

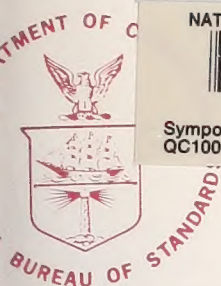
A11103 066576

NAT'L INST OF STANDARDS & TECH R.I.C.



A11103066576

Symposium on Optical/Laser Induced damage  
QC100 .U57 NO.509, 1978 C.1 NBS-PUB-C 19



NBS SPECIAL PUBLICATION

509

U.S. DEPARTMENT OF COMMERCE / National Bureau of Standards

# Laser Induced Damage in Optical Materials: 1977



STP 655



## NATIONAL BUREAU OF STANDARDS

The National Bureau of Standards<sup>1</sup> was established by an act of Congress March 3, 1901. The Bureau's overall goal is to strengthen and advance the Nation's science and technology and facilitate their effective application for public benefit. To this end, the Bureau conducts research and provides: (1) a basis for the Nation's physical measurement system, (2) scientific and technological services for industry and government, (3) a technical basis for equity in trade, and (4) technical services to promote public safety. The Bureau consists of the Institute for Basic Standards, the Institute for Materials Research, the Institute for Applied Technology, the Institute for Computer Sciences and Technology, the Office for Information Programs, and the Office of Experimental Technology Incentives Program.

**THE INSTITUTE FOR BASIC STANDARDS** provides the central basis within the United States of a complete and consistent system of physical measurement; coordinates that system with measurement systems of other nations; and furnishes essential services leading to accurate and uniform physical measurements throughout the Nation's scientific community, industry, and commerce. The Institute consists of the Office of Measurement Services, and the following center and divisions:

Applied Mathematics — Electricity — Mechanics — Heat — Optical Physics — Center for Radiation Research — Laboratory Astrophysics<sup>2</sup> — Cryogenics<sup>2</sup> — Electromagnetics<sup>2</sup> — Time and Frequency<sup>2</sup>.

**THE INSTITUTE FOR MATERIALS RESEARCH** conducts materials research leading to improved methods of measurement, standards, and data on the properties of well-characterized materials needed by industry, commerce, educational institutions, and Government; provides advisory and research services to other Government agencies; and develops, produces, and distributes standard reference materials. The Institute consists of the Office of Standard Reference Materials, the Office of Mass and Water Measurement, and the following divisions:

Analytical Chemistry — Polymers — Metallurgy — Inorganic Materials — Reactor Radiation — Physical Chemistry

**THE INSTITUTE FOR APPLIED TECHNOLOGY** provides technical services developing and promoting the use of available technology; cooperates with public and private organizations in developing technological standards, codes, and test methods; and provides technical advice services, and information to Government agencies and the public. The Institute consists of the following divisions and centers:

Standards Application and Analysis — Electronic Technology — Center for Consumer Product Technology: Product Systems Analysis; Product Engineering — Center for Building Technology: Structures, Materials, and Safety; Building Environment; Technical Evaluation and Application — Center for Fire Research: Fire Science; Fire Safety Engineering.

**THE INSTITUTE FOR COMPUTER SCIENCES AND TECHNOLOGY** conducts research and provides technical services designed to aid Government agencies in improving cost effectiveness in the conduct of their programs through the selection, acquisition, and effective utilization of automatic data processing equipment; and serves as the principal focus within the executive branch for the development of Federal standards for automatic data processing equipment, techniques, and computer languages. The Institute consists of the following divisions:

Computer Services — Systems and Software — Computer Systems Engineering — Information Technology.

**THE OFFICE OF EXPERIMENTAL TECHNOLOGY INCENTIVES PROGRAM** seeks to affect public policy and process to facilitate technological change in the private sector by examining and experimenting with Government policies and practices in order to identify and remove Government-related barriers and to correct inherent market imperfections that impede the innovation process.

**THE OFFICE FOR INFORMATION PROGRAMS** promotes optimum dissemination and accessibility of scientific information generated within NBS; promotes the development of the National Standard Reference Data System and a system of information analysis centers dealing with the broader aspects of the National Measurement System; provides appropriate services to ensure that the NBS staff has optimum accessibility to the scientific information of the world. The Office consists of the following organizational units:

Office of Standard Reference Data — Office of Information Activities — Office of Technical Publications — Library — Office of International Standards — Office of International Relations.

<sup>1</sup> Headquarters and Laboratories at Gaithersburg, Maryland, unless otherwise noted; mailing address Washington, D.C. 20234.

<sup>2</sup> Located at Boulder, Colorado 80302.



# Laser Induced Damage In Optical Materials: 1977

Special Publication No. 50

Proceeding of a Symposium Sponsored by:  
National Bureau of Standards  
American Society for Testing and Materials  
Office of Naval Research  
Energy Research and Development Administration  
Defense Advanced Research Project Agency

October 4-6, 1977  
NBS Boulder, Colorado 80303

Edited by

Alexander J. Glass  
Lawrence Livermore Laboratory  
Livermore, California 94550

and

Arthur H. Guenther  
Air Force Weapons Laboratory  
Kirtland AFB, New Mexico 87117



---

U.S. DEPARTMENT OF COMMERCE, Juanita M. Kreps, Secretary

Dr. Sidney Harman, Under Secretary

Jordan J. Baruch, Assistant Secretary for Science and Technology

U.S. NATIONAL BUREAU OF STANDARDS, Ernest Ambler, Director

Issued December 1977



**Library of Congress Catalog Card Number: 78-600021**

**National Bureau of Standards Special Publication 509**

Nat. Bur. Stand. (U.S.), Spec. Publ. 509, 561 pages (Dec. 1977)

CODEN: XNBSAV

U.S. GOVERNMENT PRINTING OFFICE

WASHINGTON: 1978

---

For sale by the Superintendent of Documents, U.S. Government Printing Office, Washington, D.C. 20434  
(Order by SD Catalog No. C13.10:509), Stock No. 003-003-01911-9 Price \$6.75  
(Add 25 percent additional for other than U.S. mailing).



## Foreword

The Proceedings contain the papers presented at the 9th Annual Symposium on Optical Materials for High Power Lasers held at the National Bureau of Standards in Boulder, Colorado, on October 4-6, 1977. The Symposium was jointly sponsored by the National Bureau of Standards, the American Society for Testing and Materials, the Office of Naval Research, the Defense Advanced Research Projects Agency, and the Energy Research and Development Administration. The Symposium was attended by about 185 scientists from the United States, the United Kingdom, France, Canada, South Africa, Australia and the Soviet Union. It was divided into sessions devoted to the following topics: Infrared window materials, mirrors and surfaces, thin films, and fundamental mechanisms. The Symposium Co-chairpersons were Dr. Alexander J. Glass of the Lawrence Livermore Laboratory and Dr. Arthur H. Guenther of the Air Force Weapons Laboratory, who also served as Editors of this report.

The Editors assume full responsibility for the summary, conclusions, and recommendations contained in the report, and for the summaries of discussion found at the end of each paper. The manuscripts of the papers presented at the Symposium have been prepared by the designated authors, and questions pertaining to their content should be addressed to those authors. The interested reader is referred to the bibliography at the end of the summary article for general references to the literature of laser damage studies.

The 10th Annual Symposium on this topic will be held in Boulder, Colorado, from September 12 to 14, 1978. It is anticipated that there will be more extensive foreign participation than in previous years. Also, a concerted effort has been made to ensure closer liaison between the practitioners of high peak power and the high average power community.

The principal topics to be considered as contributed papers in 1978 do not differ drastically from those enumerated above. We expect to hear more about improved scaling relations as a function of pulse duration, area, and wavelength, and see a continuing transfer of information from research activities to industrial practice. New sources at shorter wavelengths continue to be developed, and a corresponding shift in emphasis to short wavelength damage problems is anticipated. Fabrication and test procedures will continue to advance, particularly in the micro-machined optics and thin film areas.

At the 10th Annual Symposium we expect to pause and reflect upon the past 10 years' activities. It is our intent to have distinguished speakers who are acknowledged principal contributors in the many facets of the laser damage field. We will ask them to summarize and quantify as best as possible the state-of-the-art and the state-of-the-understanding in their specialty. These review or tutorial lectures will then be assembled and published as a separate volume on the subject of laser induced damage in optical materials. We are also contemplating having round-table discussions on those specific subjects in which there is still some question as to the correctness of our understanding. The purpose of these Symposia is to exchange information about optical materials for high power lasers. The Editors will welcome comment and criticism from all interested readers relevant to this purpose, and particularly relative to our plans for the 10th Annual Symposium.

A. H. Guenther and A. J. Glass  
Co-Chairmen

## DISCLAIMER

Certain commercial equipment, instruments, or materials are identified in this publication in order to adequately specify the experimental procedure. In no case does such identification imply recommendation or endorsement by the National Bureau of Standards, nor does it imply that the material or equipment identified is necessarily the best available for the purpose.

This publication is a contribution of the National Bureau of Standards and is not subject to copyright.







# CONTENTS

Section	Page
Foreword . . . . .	iii
A. H. Guenther and A. J. Glass	
Summary and Conclusions . . . . .	viii
A. J. Glass and A. H. Guenther	
Introduction and Welcome . . . . .	1
A. H. Guenther	
SI Conversion Units . . . . .	4
LASER WINDOWS AND MATERIALS	
Extrinsic Absorption in Infrared Laser-Window Materials. . . . .	5
M. Flannery and M. Sparks	
Possible Processes of Laser Window Degradation . . . . .	24
W. J. Fredericks	
Purification of Potassium Bromide and Alkaline . . . . .	37
W. J. Fredericks	
Frequency and Temperature Dependence of Residual Infrared Absorption in Mixed Fluoride Crystals. . . . .	56
W. G. Lipson, A. Hordvik, B. Bendow, S. S. Mitra, & J. J. Martin	
Bulk Laser Absorption Homogeneity . . . . .	62
T. J. Moravec and E. Bernal G.	
Refractive Properties of Infrared Window Materials . . . . .	74
A. Feldman, D. Horowitz, and R. M. Waxler	
Refractive Properties of CVD Zinc Sulfide . . . . .	83
M. J. Dodge	
Critical Orientation for Eliminating Stress-Induced Depolarization in Crystalline Windows and Rods . . . . .	89
R. E. Joiner, J. H. Marburger, and W. H. Steier	
Lattice Defect Equilibrium in KCl:Eu . . . . .	96
J. B. Wolfenstine and T. G. Stoebe	
Detection of Oxygen in Calcium Fluoride Laser Window Materials by XPS . . . . .	105
T. N. Wittberg, J. R. Hoenigman, W. E. Moddeman, and C. L. Strecker	
Internal-Reflection-Spectroscopy Study of Water Adsorbed on CaF <sub>2</sub> . . . . .	112
J. W. Gibson, R. T. Holm, and E. D. Palik	
Pulsed HF/DF Laser Damage in Window Materials . . . . .	118
E. W. Van Stryland, M. Bass, M. J. Soileau and C. C. Tang	
Optical Absorption in UV Laser Window Materials . . . . .	127
J. A. Harrington, B. L. Bobbs, and M. Braunstein	
UV Reflectance, Transmission, and Photoluminescence of LiYF <sub>4</sub> , and the Bulk Loss Coefficient in CaF <sub>2</sub> . . . . .	132
V. Rehn, D. L. Burdick, and V. O. Jones	
Fluence Dependence of the Absorptance of Some Alkaline Earth Fluorides at 0.36 $\mu$ m . . . . .	137
P. A. Temple and D. L. Decker	
MIRRORS AND SURFACES	
Surface Statistics of Selected Optical Materials . . . . .	142
J. M. Bennett and J. Merle Elson	
Surface Roughness Statistics of Fused Silica as a Function of Surface Preparation and Treatment. . . . .	157
R. A. House, II, A. H. Guenter, and J. M. Bennett	



The Effects of Surface Roughness on 1064-nm, 150-ps Laser Damage . . . . .	166
D. Milam, W. L. Smith, M. J. Weber, A. H. Guenther, R. A. House, and J. R. Bettis	
Low Scatter Finishing of Aspheric Optics . . . . .	174
W. P. Barnes, Jr., and R. R. McDonough	
Measurement of Mirror and Window Characteristics For Use With 10.6 $\mu\text{m}$ Lasers . . . . .	183
S. Sharma, R. M. Wood, and R. C. C. Ward	
Polishing Single Point Diamond Turned Mirrors . . . . .	196
R. E. Parks, R. E. Sumner and R. E. Strittmatter	
Pulsed-Laser Stress Phenomena on Highly Reflecting Metal and Alloy Surfaces . . . . .	204
J. O. Porteus, C. W. Fountain, J. L. Jernigan, W. N. Faith, and H. E. Bennett	
Low-Expansion Laser Mirrors . . . . .	215
P. Pirooz, G. Dube, and N. L. Boling	

#### THIN FILMS

A New Chalcogenide-Glass Antireflection Coating for KCl . . . . .	222
A. D. McLachlan and W. E. K. Gibbs	
Intrinsic and Thermal Stress Modeling for Thin-Film Multilayers . . . . .	230
A. M. Ledger and R. C. Bastien	
Hydroxyl Influence and Refractive Index Dependence in Picosecond Thin-Film Damage . . . . .	244
W. L. Smith, D. Milam, M. J. Weber, A. H. Guenther, J. R. Bettis, and R. A. House	
Further Studies of the Role of Electric Field Strength in Laser Damage of Dielectric Layers . . .	251
J. H. Apfel	
The Effects of Barrier Layers and Surface Smoothness on 150-ps, 1.064- $\mu\text{m}$ Laser Damage of AR Coatings on Glass . . . . .	255
J. H. Apfel, E. A. Enemark, D. Milam, W. L. Smith, and M. J. Weber	
Use of Non-Quarter-Wave Designs to Increase the Damage Resistance of Reflectors at 532 and 1064 Nanometers . . . . .	260
D. H. Gill, B. E. Newnam, J. McLeod	
Characteristics of R. F. Sputter-Deposited Zinc Selenide Films on Calcium Fluoride . . . . .	271
D. A. Walsh and R. V. Bertke	
A Study of Infrared Absorption in Zinc Selenide Thin Films . . . . .	276
D. F. O'Brien	
The Design and Operation of a Precise, High Sensitivity Adiabatic Laser Calorimeter for Window and Mirror Material Evaluation . . . . .	281
D. L. Decker and P. A. Temple	
Modulated Light Ellipsometer Measurements of Strain-Induced Anisotropy in the Refractive Index of $\text{As}_2\text{Se}_3$ and $\text{As}_2\text{S}_3$ Films on KCl Substrates at 10.6 $\mu\text{m}$ . . . . .	286
M. E. Pedinoff, M. Braunstein, and O. M. Stafsudd	
Damage Resistance of AR-Coated Germanium Surfaces for Nanosecond $\text{CO}_2$ Laser Pulses . . . . .	298
B. E. Newman and D. H. Gill	
10.6 $\mu\text{m}$ Laser Damage in Coatings Containing $\text{As}_2\text{S}_3$ and $\text{As}_2\text{Se}_3$ . . . . .	316
C. C. Tang, M. Bass, M. J. Soileau, and E. W. Van Stryland	
Large-Spot DF Laser Damage of Dielectric-Enhanced Mirrors . . . . .	325
D. B. Nichols, R. B. Hall, and R. A. House, II	
Defects and Impurities in $\text{As}_2\text{S}_3$ , $\text{As}_2\text{Se}_3$ , and NaF Coatings . . . . .	342
T. M. Donovan, A. D. Baer, J. H. Dancy, and J. O. Porteus	
Optical Constants of $\text{As}_2\text{S}_3$ By a Wedged-Film Technique . . . . .	352
D. L. Burdick	



Dielectric Coatings for Deformable Mirrors . . . . .	358
J. M. Rowe	
Quantitative Characterization of Coatings: Part I: Adhesion . . . . .	363
S. R. Scheele and J. W. Bergstrom	
Quantitative Characterization of Coatings: Part II: Abrasion Resistance . . . . .	378
R. A. West and C. W. Nichols	
Dielectric Enhanced Mirrors for the 2-6 $\mu$ m Region . . . . .	385
S. J. Holmes	

#### LASER GLASS AND GLASS LASERS

Temperature and Concentration Dependence of Laser Bulk Damage to Neodymium Glass . . . . .	399
J. G. Sliney, Jr., and L. G. DeShazer	
Direct Measurement of Inversion Density in Silicate and Phosphate Laser Glass . . . . .	410
J. A. Abate, D. C. Brown, C. Cromer, S. D. Jacobs, J. Kelly, J. Rinefield	
Figures of Merit and Correlations of Physical and Optical Properties in Laser Glasses . . . . .	416
D. C. Brown, S. D. Jacobs, J. A. Abate, O. Lewis, J. Rinefield	
Progress in Claddings for Laser Glasses . . . . .	434
R. B. Bennett, K. R. Shillito, and G. J. Linford	
Damage History of Argus, A 4TW Nd Laser System . . . . .	440
I. F. Stowers and H. G. Patton	

#### FUNDAMENTAL MECHANISMS

New Results on Avalanche Ionization as a Laser Damage Mechanism in Transparent Solids . . . . .	455
A. A. Manenkov	
Multiphoton Theory of Optical Breakdown in Alkali Halides . . . . .	465
A. Schmid, P. Kelly, and P. Bräunlich	
The Role of Carrier Diffusion in Laser Damage of Semiconductor Materials . . . . .	473
M. Kruer, L. Esterowitz, F. Bartoli, and R. Allen	
Multiphoton-Induced Conductivity in Ultraviolet-Transmitting Materials	
1. Free Carrier Lifetime . . . . .	481
R. T. Williams, P. H. Klein, and C. L. Marquardt	
Absolute Two-Photon Absorption Coefficients at 355 and 266 nm . . . . .	489
P. Liu, W. L. Smith, H. Lotem, J. H. Bechtel, N. Bloembergen, and R. S. Adhav	
Statistical Considerations in Laser Damage Measurements . . . . .	496
J. A. Detrio and A. P. Berens	
Multithreshold Measurement and Analysis of Pulsed Laser Damage on Optical Surfaces . . . . .	507
J. O. Porteus, J. L. Jernigan, and W. N. Faith	

#### APPENDIX I

Participants . . . . .	517
------------------------	-----



# Laser Induced Damage in Optical Materials

9th ASTM Symposium

October 4-6, 1977

The Ninth Annual Symposium on Optical Materials for High Power Lasers (Boulder Damage Symposium) was held at the National Bureau of Standards in Boulder, Colorado, from 4 to 6 October 1977. The Symposium was held under the auspices of ASTM Committee F-1, Subcommittee on Laser Standards, with the joint sponsorship of NBS, the Defense Advanced Research Project Agency, the Department of Energy (formerly ERDA), and the Office of Naval Research. About 185 scientists attended the Symposium, including representatives of the United Kingdom, France, Canada, Australia, Union of South Africa, and the Soviet Union. The Symposium was divided into sessions concerning Laser Windows and Materials, Mirrors and Surfaces, Thin Films, Laser Glass and Glass Lasers, and Fundamental Mechanisms. As in previous years, the emphasis of the papers presented at the Symposium was directed toward new frontiers and new developments. Particular emphasis was given to materials for use from 10.6  $\mu\text{m}$  to the UV region. Highlights included surface characterization, thin film-substrate boundaries, and advances in fundamental laser-matter threshold interactions and mechanisms. The scaling of damage thresholds with pulse duration, focal area, and wavelength were also discussed. Alexander J. Glass of Lawrence Livermore Laboratory and Arthur H. Guenther of the Air Force Weapons Laboratory were co-chairpersons of the Symposium. The Tenth Annual Symposium is scheduled for 12-14 September 1978 at the National Bureau of Standards, Boulder, Colorado.

Key words: Laser damage; laser interaction; optical components; optical fabrication; optical materials and properties; thin film coatings.

## 1. Introduction

The ninth annual Symposium on Optical Materials for High Power Lasers (Boulder Damage Symposium) was held, as in previous years, at the National Bureau of Standards in Boulder, Colorado, from 4 October to 6 October 1977. The Symposium was held under the auspices of the ASTM Committee F-1, Subcommittee on Laser Standards, with the joint sponsorship of NBS, the Defense Advanced Research Projects Agency, the Energy Research and Development Administration and the Office of Naval Research. This year's meeting coordinated the Damage Symposium with the DARPA Laser Window Conference. The Window Conference was held on Monday, 30 October, with the majority of the attendees remaining in Boulder for the entire week. Working sessions of the Committee F-1 Subcommittee on Lasers were held on Thursday afternoon and Friday 6-7 October. About 185 scientists attended the symposium, including representatives of the United Kingdom, France, Canada, Australia, the Union of South Africa, and the Soviet Union. The symposium was divided into sessions concerning infrared window materials, mirrors and surfaces, thin films, laser glass and glass lasers, and fundamental mechanisms. As initiated last year at the eighth symposium, two poster sessions were held. The general consensus of both those presenting poster papers and those viewing them was highly favorable. In all, over fifty technical presentations were made. Alexander J. Glass of Lawrence Livermore Laboratory and Arthur H. Guenther of the Air Force Weapons Laboratory were co-chairpersons of the symposium. The tenth symposium is scheduled for 12-14 September, 1978, at the National Bureau of Standards, Boulder. At the tenth Annual Symposium we expect to pause and reflect upon the past 10 years' activities. It is our intent to have distinguished speakers who are acknowledged principal contributors in the many facets of the laser damage field. We will ask them to summarize and quantify as well as possible the state of the art and the state of the understanding in their specialty. These review or tutorial lectures will then be assembled and published as a separate volume on the subject of laser induced damage in optical materials. We are also contemplating having round-table discussions on those specific subjects in which there is still some question as to the correctness of our understanding. The purpose of these Symposia is to exchange information about optical materials for high power lasers. The authors will welcome comment and criticism from all interested readers relevant to this purpose and particularly relative to our plans for the 10th Annual Symposium.

## 2. Principal Conclusions

The identification and development of good window materials for the infrared has been a major activity of the optical materials community over the past few years. Under Defense ARPA sponsorship, extensive research has been carried out to identify and eliminate residual impurities, which lead to deleterious absorption in the infrared. Certain conclusions can now be drawn from this activity. First, it is very difficult to reduce bulk absorption much below  $10^{-4} \text{ cm}^{-1}$ , anywhere between 10  $\mu\text{m}$  and 1  $\mu\text{m}$ . In the vicinity of 3.8  $\mu\text{m}$  and 5.5  $\mu\text{m}$ , regions occur where few impurities exhibit strong absorption, and



at 2.7  $\mu\text{m}$  the presence of OH absorption makes low absorption less probable, but overall, impurity absorption quite uniformly limits window performance. In short, bulk absorption of  $10^{-4} \text{ cm}^{-1}$  is about what systems designers will have to accept. Even this level of impurities is obtained only by an intensive effort at keeping starting materials pure, and maintaining a contamination-free environment during the entire process of material manufacture and component fabrication. Surface contamination is especially hard to prevent, since very thin layers of adsorbed  $\text{H}_2\text{O}$  or other materials, especially organics, are easily formed, and can contribute significant absorption. The picture is further complicated by synergistic effects, such as the accelerated diffusion of one impurity species into the material due to the presence of a second species. This migration can occur from the surface, or from aggregates in the bulk, or grain boundaries in polycrystalline materials.

Even if ultrapure materials are available, and ultra-clean fabrication techniques are developed for components, this may not solve the problem. First of all, the cost of fabrication must be kept at a reasonable level, and second, even if a component is clean and pure to start, it may not remain so for long in the environment of the operating system. It is clearly unproductive to design a system around a level of impurities which cannot be maintained in practice.

A variety of diagnostic tools are available for identification of surface contaminants. Both attenuated total reflection (ATR) and x-ray photoelectron spectroscopy (XPS, or ESCA) studies were reported at the conference as means of identifying impurities adsorbed on window surfaces. Combined with ion milling, and other techniques such as Auger spectroscopy, these afford powerful means for surface diagnosis.

As interest turns to shorter wavelength operation, in the visible and uv, the picture, if anything, grows bleaker. Impurity absorptions in the electronic spectrum are broader than in the IR, oscillator strengths are larger, and combined effects can become overriding. Current measurements indicate that for materials in which two-photon absorption is energetically allowed, i.e., for which the gap energy is less than twice the photon energy, absorption coefficients of  $10^{-2}$  to  $10^{-3} \text{ cm/MW}$  are expected. Thus, even at  $10\text{--}100 \text{ MW/cm}^2$ , effective bulk absorption of  $\sim 10^{-1} \text{ cm}^{-1}$  is expected, far more than can be tolerated. Note that some materials, oxides in particular, seem to exhibit two-photon absorption coefficients down by an order of magnitude from these values, even when energetically allowed. Nevertheless, it is unlikely that high-power lasers can be operated with window materials in which two-photon absorption takes place.

An example of the unpleasant surprises which await the laser builder in the uv, is the observation of a cumulative damage mechanism in  $\text{CaF}_2$  at 360 nm. Due possibly to color center formation, the absorption in fluorite materials increases linearly with prolonged exposure, reaching a value of  $2 \times 10^{-2} \text{ cm}^{-1}$  after an exposure of  $700 \text{ KJ/cm}^2$ . Further elucidation of this effect is clearly needed.

Not all the conclusions drawn from this year's Symposium are negative, however. It is possible to eliminate stress-induced birefringence, by proper choice and orientation of the window material. More and more low absorption materials are becoming available, most of them useful both in the IR and uv. The development of uv window materials has clearly been accelerated by the infrared window program. Many wide-gap materials are now available for uv windows, in ultrapure form, due to the infrared window effort. These materials should be used as the point of departure for uv window studies. The NBS measurement program, along with measurements carried out in other laboratories, has led to the accumulation of a valuable data base on optical materials, and the development of precise measurement techniques.

The very complex nature of the thin film coating of optical elements has caused this area to be the least understood as far as laser induced damage in optical materials is concerned. This is due in large measure to the numerous variables that govern the optical properties and performance of thin films. This area of investigation is characterized by the almost impossible task of attempting to isolate one factor while keeping the multitude of others constant, as well as by control of specific laser parameters used in the damage testing. However, recent work has led to several useful design tools, e.g., reduction of electric field strengths within film multilayers for pulsed laser damage resistance, reduction of coating absorption for reducing thermal distortion in high average power applications, etc. Numerous proposed figures of merit and rules of thumb have been proposed, e.g., use of low index materials in short pulse applications and the use of low thermal coefficients of expansion in mirror substrates for cw applications. However, there are undoubtedly synergistic effects taking place of which we are unaware. The only solution to this problem would be a massive undertaking that would entail the correlation of fabrication and environmental variables with resultant film structures, and a further correlation of these structural characteristics with optical properties prior to laser damage testing.



It is noteworthy that the approach being followed today contains not only well thought out parametric analyses and component testing, but the beginnings of an understanding of the correlations of optical material, fabrication variables, film structure, optical properties, and damage threshold, and from this we are encouraged. Thus the principal conclusions in the thin film area still comprise a potpourri of apparently disconnected findings. However, the great virtue of this Symposium is the beneficial synergism derived from the mutual exchange among workers in a very narrow and highly specialized field of endeavor.

One area which has received considerable attention is that of optical surfaces. Obviously it is desirable to understand the response of bare optical surfaces prior to embarking on an assessment of coated surfaces. At this year's meeting, tutorial presentations relating to the topographical characterization of surfaces were presented, particularly as relates to light scattering and absorption mechanisms. One important area discussed was the potential role of dipole scattering from isolated particles in the infrared, and its possible relation to absorption. Additional papers dealt with the topography of optical surfaces treated by difficult procedures including ion polishing, acid etching, bowl-feed and conventional polishing, flame polishing and overcoating (e.g., a film of  $\text{SiO}_2$  deposited on polished fused silica). It was seen that those techniques which tended to eliminate defects or absorbing impurities such as ion or flame polishing and acid etching resulted in higher damage thresholds. This increased damage resistance was less dependent, in these cases, on final surface roughness. An additional finding was that material properties such as surface roughness or substrate  $\text{OH}^-$  ion concentration, with certain types of deposited films, which strongly affect the damage resistance at moderate pulse lengths of 40 nsec, are not very influential at the short pulse lengths of 150 psec. This probably relates to the fact that damage thresholds at ultra-short pulse lengths are deterministic compared to the more probabilistic processes governing long pulse length damage thresholds. However, in many cases, the proposed  $\tau^{1/2}$  pulse length scaling of damage fluence (area/energy density) was reported over pulse lengths from psec to nsec in the near and mid infrared region of the spectrum.

Several papers concentrated on inter-film and film/substrate boundaries as potential regions of importance for some coated elements. The  $\text{OH}^-$  ion concentration of fused silica substrates was seen to have a relatively minor effect on the damage resistance of  $\text{ZrO}_2$ ,  $\text{ThF}_4$ ,  $\text{MgF}_2$ , and  $\text{SiO}_2$  coatings on fused silica substrates. The importance of maintaining a background environment rich in selenium to achieve proper stoichiometric films of ZnSe was identified. An additional area, somewhat related, concerns the adsorption of water layers on certain materials. The technique of attenuated total reflection spectroscopy (ATR) has been shown to be extremely valuable in these studies. Conclusions as to the nature of chemi-sorbed and physi-sorbed layers and their structure and optical properties are readily drawn. The ATR technique will undoubtedly see a continued increase in utility as one moves from the relatively pristine environment of the laboratory to the vagaries of the real world.

As equally important a concern, as damage resistance, is environmental durability. Several papers treated not only the environmental degradation of optical thin films but the development of quantitative methods for the measurement of abrasion resistance and adhesion of thin film structures. Of course, environmental durability assessment must be accomplished with the intended application firmly in mind. In some case, gross film modification can take place after exposure to the atmosphere. It was reported that some optical films containing arsenic undergo a phase modification leading to the growth of arsenic-rich absorbing crystallites after a period of atmospheric exposure. This is obviously a very important observation, yet unknown in detail as to mechanism. The behavior and response of films containing arsenic is quite perplexing. One sees crystallite growth, non-stoichiometric behavior and apparently dissimilar performance of the related materials  $\text{As}_2\text{S}_3$  and  $\text{As}_2\text{Se}_3$ . However, it was stated that  $\text{As}_2\text{S}_3$  and  $\text{As}_2\text{Se}_3$  films generally fail due to a thermal process, not directly related to the local electric field strength, with  $\text{As}_2\text{Se}_3$  being a much worse performer than  $\text{As}_2\text{S}_3$ . A somewhat similar behavior was noted for coated and uncoated germanium saturable absorbers where the pulsed damage level was directly related to a thermal mechanism. Here the culprit was identified as the substrate surface, in that the damage threshold was similar for both coated and uncoated elements. However, to further compound the picture, no relation to the structure and form of germanium was noted. Acid etching caused slight ( $\sim 10\%$ ) improvement in the damage resistance.

One rapidly developing field which will place especially stringent durability requirements on thin film coatings is the area of adaptive optics. Preliminary research efforts indicate that this may not be as serious a problem as one might expect, considering the relatively fragile nature of thin films compared to other optical elements. Cycled deformable coatings did not undergo appreciable absorption changes or mechanical failure. However, these films were not subjected to damage tests.

Several contributions treated important features of surface cleaning, film deposition conditions and resulting film structure. It was seen that sputter-etch cleaning is an excellent preparatory procedure for many materials, but bias etching is even better (the maintenance of a dc potential between the sample and sputtering source). The homogeneity and structure of ZnSe films can be greatly improved not only by employing a Se-rich-background during deposition, as has been mentioned, but through very high substrate temperatures and very slow deposition rates, less than 5 Å/sec.



Additional presentations treated the utility of novel film designs for improving pulsed laser damage resistance. These included the use of barrier layers in anti-reflection coating to shield the high index layer, in this case  $\text{TiO}_2$ , from the polished surface, suppressing possible chemical reactions. Advantageous electric field distributions were obtained by the use of nonquarterwave multilayers. Anticipated improvements and damage tests were, in general, in agreement.

New film materials were discussed including the chalcogenide glass GATS ( $\text{Ge}_{30}\text{As}_{17}\text{Te}_{30}\text{Se}_{23}$ ) proffered as an excellent high index film material at  $10.6\text{ }\mu\text{m}$ . To these materials were added new polishing procedures for producing low scatter damage resistant aspheric surfaces, a welcome revelation.

We must end our review on surfaces, mirrors and thin films by noting that several accurate and high sensitivity measurement techniques were unveiled. These instrumental procedures dealt with the development of improved calorimetric methods especially addressing the surface and film absorption problem, the use of modulated light ellipsometry to determine the strain-induced birefringence in films, and the facility of using wedged film techniques on witness plates to evaluate the optical constants of optical film as a function of thickness.

Turning our attention to Nd:glass lasers, certain conclusions can be drawn. First, bulk damage in laser glass does not limit system performance. Instead, it is the failure of multilayer dielectric coatings used in polarizers, beam splitters, and antireflection coatings, which sets the performance limits for large glass laser systems. In subnanosecond pulses, self-focusing limits the peak power density, while in long pulses, saturation limits the available fluence (areal energy density), but in both regimes, coating damage generally sets the absolute performance limit.

The effect of glass composition on optical and laser properties is becoming clearer. More compositions of laser glass are now available, silicates, phosphates, fluorophosphates, and, in limited quantity, beryllates. Thus one can choose between high and low gain, and high and low dispersion and nonlinear index values. Furthermore, these properties, within glass families, correlate with other parameters of the glass, such as thermal conductivity, density, stimulated emission cross-section, etc.

As experience is accumulated on large laser systems, certain effects are becoming manifest. This year, the experience on the Argus laser at the Lawrence Livermore Laboratory was reported, including the appearance of a film, possibly a lithium-nitrogen compound, on surfaces of ED-2 disks. The need for cleanliness in systems with hundreds of surfaces was emphasized, and the growth of beam perturbations from small particles on the optical surfaces was documented. It is now accepted that optimal placement of spatial filters throughout such a system is essential to peak performance.

Finally, there is still much to be learned regarding the ultimate failure mechanism of bulk dielectrics, breakdown and ionization. Two points of view have emerged, one emphasizing multiphoton processes, while the other views the breakdown process strictly as an electron avalanche. New experiments, such as those reported by Alexander Manenkov of the Lebedev Institute, showing damage thresholds as a function of wavelength, band gap, and temperature are very important. In both the avalanche picture and the multiphoton picture, phonon processes play an important role. The temperature dependence of the breakdown threshold is sensitive to phonon processes, and may help to discriminate among competing theories. The pulse length dependence of the damage threshold should be measured as well, for the materials currently under study, since competing theories differ in their predictions of pulse length dependence.

It is essential to carry out these investigations on ultrapure materials. Manenkov has proposed a methodology for eliminating impurity dominated damage results, one which warrants further investigation. If his view is correct, it may be nearly impossible to understand surface damage on a first principles basis, since it is surely always dominated by impurities and defects.

Detailed models of the effects of conduction electrons are emerging. These include effects like defocusing of the incident beam by the incipient plasma, diffusion of conduction electrons, and concentration dependent electron lifetimes. It appears as if the models previously proposed for optical dielectric breakdown were too naive, in ignoring these effects.

Information regarding the behavior of conduction electrons in dielectrics prior to breakdown is available from measurements like photoconductivity. In wide gap materials, two-photon induced photoconductivity is a useful technique to provide this information. Two-photon absorption, overall, is emerging as more complicated than anticipated. The relation of the measured coefficients to the structure and composition of the material remains to be elucidated, as does the density of states near the band edge, accessible to two-photon transitions.

The importance of defining what is meant by a damage threshold cannot be emphasized often enough, because people still report numbers without stating their definition. In most materials, several thresholds exist, for different competing phenomena. The characterization of the respective thresholds for these competing effects (multi threshold analysis), and how they vary with material preparation,



provides a very complete picture of the material's properties, and is especially useful in surface damage studies. However, the complexity and expense of this kind of measurement may preclude its use as a general means of surface characterization.

### 3. Summary of Papers

The 1977 Symposium was divided into five sessions at which thirty-five papers were formally presented. These sessions were augmented by two increasingly popular poster sessions, each of three hours duration, at which nineteen additional presentations were made. The general topical areas included (1) Laser Windows and Materials, (2) Mirrors and Surfaces, (3) Thin Films, (4) Laser Glass and Glass Lasers, and (5) Fundamental Mechanisms. In the following summary a concise statement of the principal results of each paper is presented. Related individual papers are grouped together within each topical area to aid in appreciation of their common thrust. Readers are directed to the topics of their particular areas of interest, and at the same time, presented with an overall view of the principal consensus of the Symposium. We have tried to provide a concise summary of the main fields of current interest and the level of understanding of the overall subject of laser induced damage in optical materials.

#### 3.1 Laser Windows and Materials

In any laser system designed to run at high average power, thermal damage to the components, due to residual absorption in the bulk materials, or at the surface, is the primary materials limitation. Window materials are chosen to operate in the region of high transparency, so it is absorption due to impurities and contaminants, rather than intrinsic causes, which is the problem. The identification of possible sources of residual absorption, and ways to avoid these impurities, is a major concern of the optical materials community. The papers presented in this section fall in three categories, bulk absorption in the IR, surface absorption due to adsorbed contaminants, and bulk absorption in the visible and uv. In addition, several papers relating to other bulk properties, such as birefringence,  $dn/dT$ , and damage resistance, are included.

It is well established that bulk absorption coefficients, in the region of transparency, are totally determined by impurity absorption. M. Flannery and M. Sparks, of Xonics, Inc., have identified and tabulated a large number of absorbing impurities, which can contribute to bulk absorption in the infrared. In particular, they have examined the properties of various anions in KCl, and their respective contributions to the residual absorption at 2.7, 3.8, 5.25 and 10.6  $\mu\text{m}$ . The resulting picture is not encouraging, from the standpoint of reducing absorption below  $10^{-4} \text{ cm}^{-1}$ .

The authors find that many impurities can contribute to absorption at 10.6  $\mu\text{m}$ , even at concentrations well below one ppm. However, at 5.5  $\mu\text{m}$  and 3.8  $\mu\text{m}$ , one would expect a lower residual absorption due to fewer coincidences with absorption lines in commonly occurring impurities. At 2.7  $\mu\text{m}$ , however, near coincidence with the absorption of the ever-present  $\text{OH}^-$  radical suggests that very few materials will be free from residual absorption. Although generally, molecular impurity cations are excluded from alkali halides due to the small size of the alkali cation, the authors do consider the case of  $\text{NH}_4^+$  in KCl, and find it especially deleterious at 3.8  $\mu\text{m}$ .

In an extension of this work, the authors tabulated 144 common molecular impurities, mostly organics, which could account for the high observed values of surface absorption. The location of the principal absorption bands of these impurities are identified. There are essentially no spectral regions between 1  $\mu\text{m}$  and 14  $\mu\text{m}$  in which impurity induced surface absorption cannot take place.

Continuing the discussion of impurity absorption in window materials, W. Fredericks of Oregon State University discussed some of the processes whereby impurities can migrate into crystalline materials, and subsequently aggregate. Of particular interest was his discussion of the diffusion of impurities. He pointed out that in general, impurity ions migrate in association with either charge compensating defects or ions of the opposite charge. Diffusion rates can be significantly enhanced by the simultaneous presence of ionic impurities of opposite sign. Thus, while mercury diffuses very little into pure KCl, the diffusion is greatly enhanced in KCl containing an hydroxide impurity. The mercuric ion bound with  $\text{OH}^-$  is much more mobile than  $\text{Hg}^{2+}$ . Other cations show similar effects. Fredericks concluded that in crystals containing divalent cation impurities, water diffusion will shorten the life of the material as a laser window.

Clustering and precipitation of impurities were also discussed. Evidence was presented from experiments on  $\text{KCl}:\text{BO}_2^-$ , showing that the spectrum exhibits features not only of the metaborate ion, but of aggregates as well. Thus, referring to the preceding paper, we see that Sparks' tabulation represents, if anything, an optimistic view of impurity absorption in the infrared. Furthermore, Fredericks points out that if grain boundaries are present, as in polycrystalline or forged materials, impurity phases can concentrate along the boundary. From the previous discussion, these regions can



be susceptible to anomalous transport of  $H_2O$ , and other pernicious impurities. We thus see the complicated and synergistic effects of impurities and defects in nominally pure and transparent materials.

Having established that impurities lead to unwanted absorption in laser window materials, and further, that synergistic effects cause the presence of one impurity to enhance the influence of another, we turn our attention to the problem of eliminating impurities from the materials to be used. W. Fredericks discussed the problem of purification of the starting materials for growth of KBr and alkaline earth fluorides for windows. He discussed the use of ion exchange resins and selective ion filters. In the latter, which is the preferred method, a series of resins is used, such that only the desired ion will be passed through them. Selective ion filters can be constructed for cations, but anion resins with differing order of selectivity for several ions do not exist. Other means for separating anions must be used.

The author discussed the prevalence of common impurities in the laboratory and presents a tabulation of impurity levels in various materials used in laboratory apparatus. As one would expect, iron is especially prevalent, but so are Cr, Co, Zn and Sb. Frederick discussed the care which must be exercised in designing a purification apparatus, to minimize further contamination of the material being prepared. The preparation of ultrapure KBr was described, and the claim made that the impurity level in the final KBr is one ppm for monovalent impurities, and much less for aliovalent impurities. The levels achievable in the system for alkaline earth fluorides have not yet been documented, but are expected to be satisfactorily low.

Among the materials of interest for high power laser windows in the infrared, the cubic perovskites have many attractive features. These are mixed fluoride crystals with the formula  $ABF_3$ , where A is an alkali metal ion, and B an alkaline earth or other divalent cation. The residual infrared absorption of these materials in the region of transparency has been studied in depth by H. Lipson, A. Hordvik, and B. Bendow, of the RADC Deputy for Electronic Technology at Hanscom Field, working in collaboration with S. Mitra of the University of Rhode Island and J. Martin of Oklahoma State University. At OSU, crystals of  $KMgF_3$  and  $KZnF_3$  have been prepared from purified starting materials. Absorption measurements were carried out from 800 to  $2000\text{ cm}^{-1}$  using a Fourier transform spectrophotometer, and compared at several CW laser frequencies to photoacoustic calorimeter measurements. Good agreement was obtained. Both the frequency and temperature dependence of the absorption coefficient were measured, from  $80^\circ\text{C}$  to  $550^\circ\text{C}$ . For  $MgF_2$  and  $KMgF_3$ , good agreement was found with a theory based on intrinsic multiphonon absorption, but the  $KZnF_3$  showed evidence of extrinsic absorption. At low levels of absorption ( $10^{-4}\text{ cm}^{-1}$ ), evidence of extrinsic absorption was also seen in the  $KMgF_3$ . The absorption properties of the perovskite  $KMgF_3$  are determined primarily by the Mg-F bond, which has a higher frequency than the K-F band. Since this crystal is strong, transparent, and chemically stable, it may prove useful for infrared coatings or as a laser window material.

In order to ascertain the homogeneity of optical absorption across a window specimen, T. J. Moravec and E. Bernal G. of the Honeywell Corporate Materials Science Center have constructed a scanning Doppler interferometer, which is used to measure thermally induced index changes in a heated sample. Heating is provided by a  $350\text{ W CO}_2$  laser. The sample is placed in the interferometer beam on a motor-driven translation stage, controlled by an HP 9825A calculator. The sample is scanned, with the heating beam and interferometer beam always remaining coincident. From the recorded phase shifts, a map of absorption homogeneity is produced. In high loss materials, deviations of the order of 50% from the average absorption are seen across the sample. For low-loss samples, deviations of 100% from the average are seen. The absolute deviation for a given material is essentially the same from sample to sample. Although not as accurate as calorimetry, this method is less sensitive to surface absorption. In fact, as these authors have previously shown, by passing the heating beam through the sample at an angle to the interferometer beam, surface contributions can be entirely eliminated. The automated scanning interferometer provides a useful technique for measuring homogeneity and sample-to-sample variation, rather than absolute absorption.

At the National Bureau of Standards in Gaithersburg, the Optical Materials Characterization Program has been established, with the purpose of providing accurate values of important optical parameters for materials of interest in laser optics. A. Feldman, D. Horowitz, and R. M. Waxler presented a review of recent results from this program, especially measurements of change in refractive index with temperature and stress. Two methods have been developed to measure refractive index, and thereby,  $dn/dT$ . One is to measure the index over a continuous range of frequencies using a precision spectrometer and minimum deviation prism. The disadvantages of this method are that it measures the index relative to that of air, and that the measurement can only be made over a limited temperature range. To circumvent these difficulties, NBS has developed a second method, based on measuring the fringe shift in a Fizeau interferometer induced by temperature change in the sample. This provides absolute values of  $dn/dT$ , but requires a coherent light source, and so is limited to a discrete set of wavelengths in the infrared, and requires a separate measurement of the thermal expansion coefficient.



Data were presented on  $dn/dT$  at 0.63, 1.15, and 10.6  $\mu m$ , obtained by the Fizeau method for  $BaF_2$ ,  $CaF_2$ ,  $KBr$ ,  $KCl$ ,  $LiF$ ,  $NaF$ ,  $SrF_2$ ,  $ZnS$ , and  $ZnSe$ . In a companion paper, M. Dodge of NBS compared  $dn/dT$  values for  $ZnS$  obtained using the precision spectrometer method to the Fizeau values obtained by Feldman et al. The agreement was satisfactory, considering the sample to sample variation in refractive index in any material. Feldman et al. compared their values to those obtained by other researchers, and found good agreement, once certain discrepancies in the assumed values of the linear expansion coefficients, used in the analysis, were taken into account.

The continuing measurements program at NBS has resulted in the evaluation of precise and accurate measurement techniques for a number of parameters of interest for laser optics, and yielded a body of data on these materials of high reliability and great utility. As the interest in laser materials extends to the visible and uv, it is essential that the measurement program continue to provide these data, in the wavelength region of interest. The maxim, "What you can't measure, you can't understand," applies with undiminished force to optical materials.

Stress-induced birefringence is a serious problem in high power laser windows and in laser rods. It was pointed out by R. E. Joiner, J. H. Marburger, and W. H. Steier, of the University of Southern California, that under certain conditions, it is possible to find an orientation of a window with respect to the crystal axes of the material such that plane-polarized light will not undergo any depolarization. This situation requires that the major and minor axes of the polarization ellipsoid in the material be uniformly oriented over the entire window. Since the stress field (or strain, in a rod) is not uniform over the aperture, one requires that the relevant coefficients vanish, so that the depolarizing terms vanish independent of the values of the stress.

The authors show that provided the material satisfies certain symmetry requirements, there is a critical angle with respect to the crystal axes at which the depolarization vanishes. This angle is determined by the relation  $\tan^2 \theta_c = -1/A$ , where  $A = q_{44}/(q_{11}-q_{12})$  is the stress-optic anisotropy ratio. Here the  $q$ 's are elements of the stress-optic tensor. Thus, in addition to symmetry requirements on the window material, the ratio  $A$  must be negative at the operating wavelength. The authors show that this condition is satisfied in  $KCl$ ,  $CaF_2$ ,  $BaF_2$  and  $SrF_2$  in the visible, and  $KCl$  at 10.6  $\mu m$ . Their analysis has been confirmed experimentally. They point out that not only is this effect useful in eliminating stress-induced depolarization in windows and rods, it also provides a sensitive measurement of the photoelastic constants.

Pure alkali halides are excellent optical materials, but exhibit poor mechanical properties. A standard method of strengthening  $KCl$  is by the addition of europium. A technique for optical monitoring of the europium concentration was advanced by J. Wolfenstine and T. Stoebe, of the University of Washington. They monitored the optical absorption of the sample at 243 nm and 343 nm, regions of strong absorption of  $Eu^{2+}$ . In order to be sure that this was the dominant charge state for the europium ion, they separately measured the absorption in the known absorption bands of the trivalent ion, in the visible. No absorption was detectable which could be attributed to  $Eu^{3+}$ . The authors find that optical monitoring is a reliable test of europium concentration, as long as the  $Eu^{2+}$  ion is the prevalent form of the impurity. They conclude that, usually, europium is present in  $KCl$  in the form of a divalent ion associated with a cation vacancy.

A comparison was made with ionic conductivity measurements, and with polarographic measurements of the europium concentration. A linear relationship was found between the ionic conductivity and the optical absorption. In three of the four samples tested, the optical absorption correlated well with the polarographic analysis. The reason for discrepancy in the fourth sample was not clear.

The role of surface contaminants in laser damage is not fully understood. The presence of contaminants at the interface between substrate and coating materials is known to affect the damage threshold, but the mechanism whereby the contaminant influences the damage level has not been identified. There is strong interest in identifying surface contaminants, measuring their concentration and distribution, and finding out the origin of the contamination.

An analysis of surface contamination in  $CaF_2$  was presented by T. N. Wittberg, J. R. Hoenigman, and W. E. Moddeman of the University of Dayton Research Institute, and C. Strecker of the Air Force Materials Laboratory. They examined  $CaF_2$  window samples, both uncoated, and coated with  $ZnSe$ , using x-ray photoelectron spectroscopy (XPS, or ESCA) as a diagnostic tool. Samples were polished with alumina, washed, rinsed with distilled water and alcohol, and cleaned with vapors. Coatings were prepared by electron beam deposition. ESCA diagnostics were measured at a vacuum of  $10^{-8}$ .



All samples showed significant oxygen and carbon contamination. Ion beam etching revealed that a high degree of carbon contamination was present at the surface on all samples, coated or uncoated. The authors ascribe this to absorption of  $\text{CO}_2$  or other carbon compounds from the air. The possibility of contamination of the surface during the cleaning process cannot be completely ruled out. Oxygen was seen at the surface, and to a lesser degree, even in the bulk, by an inspection of freshly cleaved surfaces. The authors propose that either the surface was quickly contaminated by atmospheric water or that oxygen occurs in the bulk of  $\text{CaF}_2$  at a level of a few atomic percent.

Following upon last year's exposition of the great utility of Attenuated Total Reflection (ATR) spectroscopy for the characterization of coatings, J. W. Gibson, R. T. Holm, and E. D. Palik of the Naval Research Laboratory, used ATR to study the properties and structure of water adsorbed on  $\text{CaF}_2$  crystals. From this analysis the growth of adsorbed water layers was followed, affording information about the index of refraction and the product of the extinction coefficient and film thickness. This information was derived from a detailed analysis of the unpolarized absorption and the S/P polarization ratio of the absorptance. It was concluded that the optical constants of the adsorbed water were significantly less than those for bulk water, again calling attention to the modification of films by substrate surfaces.

The principal conclusions are that adsorbed water films are less dense than bulk water ( $\rho \sim 0.7 \text{ g/cm}^3$ ) and that absorption bands shift to slightly higher frequencies with some band narrowing. Other specifics include an adsorbed water layer 4 to 6 Å in thickness, consisting of a 1.7 Å chemisorbed layer and a thicker 4.6 Å physisorbed layer, with a resulting background index of 1.21 for these water films on  $\text{CaF}_2$ . Discussions as to the possible effects of impurities in the films were included. This paper continued to show the many attributes of careful ATR analysis.

There has been a paucity of experimental data on damage thresholds in the mid-IR. The availability of HF and DF lasers make it possible to probe that region of the spectrum. E. Van Stryland, M. Bass, M. Soileau and C. Tang of USC contributed a study of pulsed HF/DF laser damage in a number of transparent dielectrics. Their laser source operated with either gas, radiating at 2.7  $\mu\text{m}$  or 3.8  $\mu\text{m}$  in a Gaussian beam with a 22 mm diameter (full width at  $1/e^2$ ). The temporal pulse shape was complex, but was carefully monitored. The equivalent pulse duration was about 170 ns.

The materials examined included NaCl, KCl, KBr,  $\text{MgF}_2$ ,  $\text{BaF}_2$ ,  $\text{SrF}_2$ ,  $\text{CaF}_2$ , sapphire, spinel, quartz, ZnSe, and  $\text{As}_2\text{S}_3$ . Damage tests were carried out with various spot sizes, 27  $\mu\text{m}$ , 38  $\mu\text{m}$ , and 59  $\mu\text{m}$ . Damage was identified as intrinsic or extrinsic, on the basis of morphological investigation.

Both bulk and surface damage were investigated. Sapphire and the divalent fluorides exhibited high damage thresholds in the bulk, on the order of 10-15  $\text{kJ/cm}^2$  at the 27  $\mu\text{m}$  spot size, approximately half that value at 59  $\mu\text{m}$  spot size, in keeping with the scaling law previously proposed by Bettis et al. For the lower threshold materials, this scaling is not as apparent, but this may be due to the presence of impurities.

The authors attempt to correlate their results with damage data on the same materials taken at other wavelengths by other investigators. Unfortunately, they fail to apply the scaling in spot size and pulse duration which their own measurements tend to bear out. Thus it is difficult to draw meaningful conclusions from these comparisons.

As interest shifts from IR lasers to shorter wavelength operation, in the visible and uv, the problem of window absorption grows more severe. Impurity absorptions are not as well localized in frequency as they are in the IR, so that the tables of contaminants generated by Sparks and co-workers are not as instructive as at longer wavelengths. As was borne out in this year's discussion, cumulative and synergistic effects of impurity absorption are more severe in the uv.

Using both an argon ion laser calorimeter and wavelength modulation spectroscopy, J. A. Harrington, B. L. Bobbs, and M. Braunstein of the Hughes Research Laboratories, and R. Braunstein, R. Y. Kim, and R. Stearns of UCLA, measured the residual absorption in 11 large-gap, uv window materials, including KCl, NaCl, NaF, LiF,  $\text{LaF}_3$ ,  $\text{CaF}_2$ ,  $\text{SrF}_2$ ,  $\text{MgF}_2$ ,  $\text{SiO}_2$ ,  $\text{Al}_2\text{O}_3$  and MgO. The absorption decreased monotonically with increasing wavelength, from 250 to 515 nm, in almost every case. Some evidence of structure in the absorption spectrum is seen by wavelength modulation spectroscopy. The values obtained for the best materials, essentially those developed for the infrared window program, to have low IR absorption, show absorption coefficients near  $10^{-4} \text{ cm}^{-1}$  in the visible. Higher absorption values are seen for forged materials than for single crystal samples. For the best materials, the values observed are significantly lower than extrapolations from previous measurements, attesting to the higher purity of the samples.



Two photon absorption effectively excludes the use of any high-power window material for which the band gap is less than twice the photon energy. At wavelengths shorter than 300 nm, the availability of optical materials is limited. Thus there is great interest in new, wide-gap materials for potential uv applications. V. Rehn, D. L. Burdick, V. O. Jones of the Michelson Laboratories reported the first studies of the vacuum ultraviolet transmission, reflectance, and photo luminescence of  $\text{LiYF}_4$ , a tetragonal crystal with a 10.4 eV absorption edge. This material is birefringent, with refractive indices close to that of  $\text{CaF}_2$ , about 1.45 in the visible.

The measurements were made over the range 4 eV to 25 eV, using synchrotron radiation from the Stanford Synchrotron Radiation Project. The material was not especially pure, and significant impurity effects were observed near the uv edge. As purer material is available, the intrinsic properties of  $\text{LiYF}_4$  will become more accessible from measurements of this kind.

In a parallel study, the uv absorption of  $\text{CaF}_2$  was measured over the range from 390 nm to 230 nm. A strong absorption band at 305 nm was observed in two samples of diverse origins. This absorption was attributed to the presence of  $\text{Ce}^{3+}$  ionic impurities in both samples.

Infrared window materials suffer from absorption in the bulk and birefringence. The bulk absorption is typically less than  $10^{-4} \text{ cm}^{-1}$  in good window materials, almost entirely due to residual impurities. With increased interest in short wavelength lasers, however, new phenomena must be considered in bulk absorption. One such new phenomenon, not previously reported, was the subject of a paper by P. A. Temple and D. L. Decker of the Michelson Laboratories. They reported that when fluoride windows ( $\text{CaF}_2$ ,  $\text{SrF}_2$ ,  $\text{MgF}_2$ ) were irradiated at 360 nm, using an argon ion laser, with a power density of  $350 \text{ W/cm}^2$ , the loss coefficient was seen to increase linearly with the cumulative fluence,  $\int I dt$ , until it had reached a value of  $2 \times 10^{-2} \text{ cm}^{-1}$  after  $7 \times 10^5 \text{ J/cm}^2$  exposure. Before exposure, the materials absorbed less than  $10^{-3} \text{ cm}^{-1}$ . The loss was identified as absorption, since it was measured calorimetrically, but could have arisen from one of two causes, the formation of organic polymers on the surface, due to pump oil contamination, or the formation of absorbing defects such as color centers in the bulk material. Further work is required to elucidate the exact mechanism. The implication for high average power lasers is severe. At  $10^3 \text{ W/cm}^2$ , a reasonable operating level, the windows would have to be replaced after an exposure of about  $10^5 \text{ J/cm}^2$ , an operating time of 100 sec. This is clearly unacceptable. It is noteworthy that a similar darkening of  $\text{CaF}_2$  windows was reported in uv lasers by Tachisto, Inc., a laser manufacturer, after 100 hours of operation at a peak power density of  $5 \text{ nW/cm}^2$ , which corresponded to a cumulative exposure of  $10^5 \text{ J/cm}^2$ .

### 3.2 Mirrors and Surfaces

Surfaces still appear to be sensitive areas in which damage will first appear. Therefore, a complete understanding of the response of surfaces is necessary before one can feel comfortable in appreciating all the many details of threshold interactions. In some cases, experimental and theoretical research has indicated some properties which play a dominant role in minimizing the deleterious aspects of intense laser illumination, such as the desirability of low expansion mirror substrates to reduce thermal distortion in high average power lasers. It is, as well, generally conceded that surface characteristics dominate many facets of the laser damage scenario for exposed surfaces of reflective and transparent optical elements. However, a comprehensive understanding of the exact relationship is not at hand. Part of this problem stems from the difficulty of experimentally characterizing the surface and isolating one particular feature to determine its exact role. Thus, several papers at this year's meeting dealt with surface characterization (primarily topographical statistics) and attempts to correlate certain features with the damage sensitivity. To this were added contributions on surface finishing procedures and the efficacy of various techniques for the improvement of damage resistivity. Diamond turned elements were highlighted again this year.

In a rather elegant exposition J. M. Bennett and J. M. Elson of the Naval Weapons Center discussed the salient features of surface statistics and how they relate to scattering behavior. Besides being a very complex subject, it is most important for characterizing optical surfaces prior to either damage testing or overall system performance. Subjects covered included the traditional properties such as total integrated scattering, rms roughness, rms slope and rms height as well as the height, slope and auto-covariance functions. Specific materials evaluated included fused silica, molybdenum, potassium chloride, copper and silicon carbide.



Characterization included correlation of scattering behavior with large defects, isolated defects and micro-irregularities corresponding to the cases where the wavelength of light is smaller than, comparable to, and less than the dimensions of the defect. To this analysis was added the importance of surface-plasmon excitation which can lead to second order light scattering. By far the greatest contribution to scattering for high quality optical surfaces arises from microirregularities.

After a discussion of the above points, tests of scattering for typical materials were reported. It was concluded that, for many materials, the total scattering in the infrared is dominated by dipole scattering from isolated particulates as opposed to surface microirregularities. Concerning the correlation between theory and experimental observation, it is frequently possible to predict the shape of angular scattering curves using measured surface statistics. The auto-covariance function is by far the most important property in describing an optical surface.

Two years ago at the 1975 Damage Symposium, a systematic study of the effects of surface roughness and finishing techniques on laser induced damage thresholds were described. At this year's meeting R. A. House, II, and A. H. Guenther of the Air Force Weapons Laboratory and J. M. Bennett of the Naval Weapons Center reported on the surface roughness statistics of fused silica substrates as a function of surface preparation and treatment. The samples studied were a representative selection of those previously employed in the earlier damage studies. They reported on a detailed statistical and topographical analysis to more fully characterize the surfaces and search for any correlation which might elucidate the underlying factors affecting the previous results.

The analysis included a determination of the mean slope, slope distribution function, mean height, height distribution function, autocovariance function and rms surface roughness as determined by total integrated scattering, Talystep profilometry, and Nomarski microscopy. Conclusions as to surface character were as follows. For flame polished and conventionally polished samples, the height and slope distribution functions were not Gaussian, since surface statistics were dominated by strongly bound particles with a very smooth background. On the contrary, bowl-feed polished samples were relatively free of particles, surface scratches, etc., characterized by a Gaussian slope distribution function and a slightly skewed height distribution function.

For Xe-ion polished surfaces, the surfaces were characterized by nearly Gaussian statistics, while  $\text{HNO}_3$  acid etched surfaces were, relatively speaking, very rough and contained many holes, up to 1.5  $\mu\text{m}$  in diameter and 1-2  $\mu\text{m}$  deep. These artifacts skew otherwise normal distribution functions.

The last set of samples evaluated were  $\text{SiO}_2$  overcoated surfaces. Here the surfaces were extremely smooth (much smoother than the polished substrate) and they exhibited the most Gaussian distributions of all of the surfaces studied.

The only obvious conclusion to be made at the present time, in this continuing study, is that techniques which have a tendency to eliminate impurities, i.e., flame polishing and acid or ion etching, lead to improved damage resistance, while those other techniques (compared to conventional polishing) such as bowl feed or overcoating lead to reduced damage thresholds. Much additional work is necessary to more fully describe this most complex state of affairs and allow us to theoretically predict appropriate surface character/damage threshold relationships.

In a paper assessing the effects of surface roughness on laser induced damage threshold of bare silica surfaces and coated optical elements for 150 ps pulses at 1064 nm, D. Milam, W. L. Smith, and M. J. Weber of the Lawrence Livermore Laboratory together with A. H. Guenther, R. A. House and J. R. Bettis concluded that although there was a general trend in the correlation, the effect was much less pronounced than previously observed when 40 ns pulses were utilized. Bare substrate roughnesses ranged from 15 Å to 350 Å rms. At roughnesses comparable to normal optically polished surfaces (< 50 Å rms) no positive effect was suggested by the experimental data. This effect "surface roughness vs. damage threshold" as a function of pulse length should be pursued over a greater range of sample types and roughnesses in which the sample topography is more fully characterized and accurately determined. It is in this latter situation that the greatest error is introduced in scaling and correlation experiments such as these, i.e., inaccuracy in adequately describing the surfaces. For the case of coated elements no correlation was evident at all. However, pulse length scaling between the 150 ps and 40 ns did follow the previously proposed square root of pulse length dependence put forth by Bettis, House, and Guenther at the 1976 Damage Symposium.

Aspheric surfaces have always been difficult optical elements to polish effectively since they do not readily permit the close fitting of lap and work surfaces normally required. To overcome this deficiency W. P. Barnes, Jr., and R. R. McDonough of the Itek Corporation discussed the utility of short term polishing with colloidal silica and non-woven poromeric (flexible) laps for producing high quality (low scatter) aspheric surfaces. Test results on three f/2 paraboloids polished in this manner indicated the achievement of low scatter surfaces whose quality is nearly equal to the best bowl-feed finished elements as determined by scattered light and damage threshold measurements.



Last year at this symposium the group from the General Electric Co., Ltd., outlined their program on laser induced damage thresholds at 10.6  $\mu\text{m}$ . This year S. Sharma, R. M. Wood, and R. C. C. Ward of that organization reported on the mirror and window characterization portion of that program. Their report specifically dealt with the development of accurate reflectance and transmittance apparatuses, and the correlation of these measurements with absorption, surface finish and laser induced damage thresholds employing a  $\text{CO}_2$  TEA laser emitting a 60 ns FWHM pulse focused to approximately 100  $\mu\text{m}$  at the 1/e intensity points.

For diamond turned OFHC copper mirrors, a SEM examination of uncoated elements indicated a generally high quality surface which contained numerous small shallow spherical holes (approximately 500 Å in diameter and 250 Å deep). There was a strong indication of reduced damage threshold at these pin holes compared to clean surfaces. Similarly, correlation of damage resistance with absorptivity, reflectance, and scatter were evident. Other samples analyzed included gold coated OFHC and  $\text{ThF}_4$  overcoated, diamond-turned copper mirrors as well as ZnSe window specimens.

In an attempt to remove the high frequency ripple from diamond turned surfaces, R. E. Parks, R. E. Sumner, and R. E. Strittmatter of the University of Arizona investigated the utility of hand polishing techniques employing laps of sufficient rigidity to bridge the micro ripple yet soft enough not to scratch the metal mirror surface. This technique can require that substantial material be removed, in which case careful testing must be done throughout the polishing. Phase contrast micrographs show that the polished surface is "almost" as free of mechanical defects as the original machined surface. This polishing technique can lead to large reductions in surface scatter and roughness. Unfortunately, previous reports by other individuals indicate that this polishing, while improving surface cosmetics will generally lead to a considerable decrease in the damage resistance of such diamond turned metal mirrors. No laser damage tests were performed during the course of this program to date.

In addition to the papers dealing with surface statistics and finishing, presentations on the mechanical response of metallic reflectors and the utility of low expansion glass ceramic substrates for reflectors were heard.

In their continuing investigation of the threshold response of metal and alloys surfaces to intense short duration (100 ns) 10.6  $\mu\text{m}$  laser pulses, J. O. Porteus, C. W. Fountain, J. L. Jernigen, W. N. Faith and H. E. Bennett of the Naval Weapons Center reported on the stress induced aspects of laser interactions. This interaction can produce many material modifications. These many responses include production of slip bands, intergranular slip melting, pit or crater production, ion emission, light emission, and finally work function changes. Which one of these responses is the first to appear as incident laser power is raised, is governed by many influences such as intrinsic material properties, impurities, processing variables in fabrication, environmental factors, handling, laser parameters, etc. They reported that many of the metallurgical modifications such as slip were seen to arise at laser powers less than those required for melting, and furthermore these types of responses may be significant in evaluating total system performance. Structural alloys were seen to have comparatively low damage thresholds.

Results of testing specially prepared surfaces indicate that diamond turning and ion-implantation are generally ineffective against slip, but sputtering, ion milling and forging may be effective. However, these later treatments may lead to increased sensitivity to other types of damage. Most noteworthy was a study of the damage threshold for copper tested in a 1 atm  $\text{N}_2$  environment and under vacuum. A substantial increase in the threshold for melting and other catastrophic effects due to increased shielding was evidenced when tested in the  $\text{N}_2$  atmosphere. However at lower energy densities where slip first occurs, no plasma was detected and damage thresholds were comparable in the two cases.

It has long been recognized that a most important characteristic of high power laser mirrors should be low expansion. P. Pirooz, G. Dubé, and N. L. Boling of Owens-Illinois evaluated a unique concept for producing low expansion IR laser mirrors. The technique studied involved the self-generation of thin copper films by diffusion from the bulk on "very" low expansion glass-ceramic (Cervit) substrates previously doped with copper. Under these conditions, excellent adhesion was achieved for the  $\text{Li}_2\text{O}-\text{Al}_2\text{O}_3-\text{SiO}_2$  system but poor for the  $\text{ZnO}-\text{Al}_2\text{O}_3-\text{SiO}_2$  system. If one assumes that all candidate mirror materials can achieve approximately the same reflectivity, then a figure of merit for minimizing thermal distortion is  $\text{FM} = \rho C / \alpha$  where  $\rho$  = material density,  $C$  is the heat capacity, and  $\alpha$  the thermal expansion coefficient. On this basis, with copper normalized to 1;  $\text{SiC} = 2.5$ ;  $\text{Mo} = 2.2$  while  $\text{Cervit} > 6.5$ . This advantage stems almost totally from the glass-ceramics low coefficient of thermal expansion. There is unfortunately the question of figure stability during the various fabrication steps remaining to be addressed.



### 3.3 Thin Films

As might be expected, the largest number of papers presented at this years damage symposium were concerned with thin films, as they represent the weakest optical feature in any optimally designed high power laser system. In point of fact, they can be considered the prime constraint to improved system performance. While optical surfaces are weaker than within the bulk of a material, the addition of coatings for anti-reflection, high reflection or environmental protection has in general caused a reduction in the laser induced damage resistance of the element. The papers dealing with thin films at this years symposium can be loosely grouped into the following categories; new film materials and designs, including analysis and experiments dealing with various parameters which might affect the damage sensitivity; methods of film characterization and property determination; recent damage investigations; and finally, the mechanical response and behavior of coatings as affects their environmental durability.

The first group of papers are concerned with the development of new coating materials for use in the infrared, thermal stress modeling of film structures, film/substrate chemistry, and the influence of the electric field distribution on the pulsed laser induced damage threshold for specific and unique multilayer designs.

A new chalcogenide-glass coating material, suitable as the high index material in two-layer anti-reflection (AR) coatings on KCl for use at 10.6  $\mu\text{m}$ , was described by A. D. McLachlan and W. E. K. Gibbs of the Materials Research Laboratories, Melbourne, Australia. The new material GATS ( $\text{Ge}_{30}\text{As}_{17}\text{Te}_{30}\text{Se}_{23}$ ) has a refractive index of about 3.11 at 10.6  $\mu\text{m}$ . In the course of their study, the compositional homogeneity, structure, refractive index, optical dispersion, absorption and pulsed/cw damage threshold of GATS films were determined. AR coatings employing GATS and  $\text{As}_2\text{S}_3$  (low index material) exhibited absorptions ranging from 0.02% to 0.07% at 10.6  $\mu\text{m}$  and reflectivities as low as 0.025%. These films were electron beam deposited at a base pressure of 0.1 mPa ( $1 \times 10^{-6}$  torr).

Employing a TEA  $\text{CO}_2$  laser, operating in the  $\text{TEM}_{00}$  mode, and characterized by a 0.2  $\mu\text{sec}$  gain switched spike followed by a 3  $\mu\text{sec}$  decaying nitrogen tail, focused to a  $1/e^2$  diameter of 280  $\mu\text{m}$ , the pulsed damage threshold was  $\sim 7 \text{ J/cm}^2$ . For the cw case, the laser was focused to an area 3 mm square ( $9 \text{ mm}^2$ ) for three seconds. Failure started to occur at  $7 \text{ KW/cm}^2$ . The obvious advantage of these coatings are their very low absorptance, offering a distinct benefit when one is concerned with minimizing thermal distortion.

It is well established that one of the many parameters that affect not only laser induced pulsed damage resistance but the durability of thin films, as well, is the film's residual stress structure. On this subject, A. M. Ledger and R. C. Bastien of the Perkin-Elmer Corporation examined several models of both intrinsic and thermal stress in thin-film multilayer stacks. Such theoretical models are widely employed for stress compensation in the design of multilayers. To perform these analyses several important film properties must be evaluated. To this end, a system of *in situ* cat's eye stress interferometers have been developed to measure the intrinsic stress, thermal expansion coefficient and Youngs modulus, the thin film properties of prime importance. Material in thin film form exhibits properties considerably different than those reported for the bulk material. In point of fact, thin film stress levels often exceed the self-breaking strength of the material in bulk form. The resultant stress is comprised of the intrinsic stress of the material, together with the stress contributed by the difference in thermal expansion coefficients of the film and substrate. This latter factor is of obvious importance considering the thermal cycling which occurs during deposition and cool-down. In many cases to obtain films of high quality they must be deposited at elevated substrate temperatures. To more fully describe the stress scenario, one should include the effects of adhesive forces between the individual layers and substrate and other factors.

After a discussion of the analytical models and experimental techniques, detailed measurements of the stress levels in  $\text{ThF}_4$ ,  $\text{ZnSe}$ , and  $\text{TlI}$  materials as a function of deposition conditions (rate, temperature, etc.) were given. The unit stress  $\sigma(t)$  was found to fit to the following equation:

$$\sigma(t) = Ae^{-Bt} (1 - e^{-Ct})$$

where  $t$  is the film thickness.

Another paper addressing the differences between the short ( $\sim 150 \text{ ps}$ ) and long ( $\sim 40 \text{ ns}$ ) pulse duration response of coated elements was performed by W. L. Smith, D. Milam, and M. J. Weber of the Lawrence Livermore Laboratory and A. H. Guenther, J. R. Bettis, and R. A. House, of the Air Force Weapons Laboratory. This work attempted to quantify the role of the  $\text{OH}^-$  ion content of commercially available fused silica substrates on the damage resistance of fluoride and oxide coatings to 1064 nm, 150 ps irradiations. Four substrate materials were employed, being Suprasil-W1, Optosil-2, Homosil, and Suprasil-1 with  $\text{OH}^-$  concentrations of approximately 5, 130, 130, and 1200 ppm respectively.



Coatings included  $\lambda/2$  (at 1.06  $\mu\text{m}$ ) layers of  $\text{ZrO}_2$ ,  $\text{SiO}_2$ ,  $\text{ThF}_4$ , and  $\text{MgF}_2$ . Bare uncoated substrates were tested as well. Unlike the previous 40 ns data by House, et al., there was no evident correlation between  $\text{OH}^-$  concentration and damage threshold, as might be expected from anomalous production of  $\text{SiO}$ , in the case of  $\text{SiO}_2$  films or  $\text{MgO}$  in the case of  $\text{MgF}_2$  films, etc., again pointing out the relative insensitivity of short pulse experiments to parametric variations which are quite obvious at long pulse durations. As discussed in the paper, this may indicate that at 40 ns the presence of  $\text{OH}^-$  (as well as surface roughness) may cause a weakening of the  $\text{SiO}_2$  structure leading to an assistance in the liberation of charge carriers during the breakdown process. This could cause a bottlenecking effect during the early phases of long duration breakdown studies. Conversely, in the picosecond regime, the higher field strengths required to provide faster ionization and sufficient incident flux for heating more effectively drive initial nonlinearities to provide numerous free carriers early in the pulse. This indicates a highly deterministic behavior, due to the high fields required.

A second aspect of the study did corroborate the previously observed  $\sqrt{t}$  pulse length and refractive index dependences observed at 40 ns. A principal conclusion is that low index coatings (fluorides) are quite damage resistant at short pulse lengths, i.e.,  $\text{ThF}_4$  and  $\text{MgF}_2$  were found to be twice as damage resistant as  $\text{ZrO}_2$  with  $\text{SiO}_2$  70% more damage resistant than  $\text{ZrO}_2$ . For the substrates, Suprasil W1 damaged at  $12.7 \pm 2.7 \text{ J/cm}^2$  while the other fused silicas damaged between 7.2 and 9.8  $\text{J/cm}^2$ . This study also indicates that coating a surface reduces the damage threshold below the value observed for the bare substrate.

In a companion paper J. H. Apfel of Optical Coating Laboratories investigated the role of electric field strength in laser damage of dielectric layers. Films tested included a  $\text{SiO}_2/\text{TiO}_2$  quarter-wave stack reflector, a four layer anti-reflection (AR) coating and a combination of the two. Tests were performed using a 180 ps, 1064 nm pulsed laser. At damage threshold the field is highest for the reflector stack and lowest for the AR coating with the combination film in appropriate order compared to the reflector. Damage thresholds for the eleven layer quarter-wave reflector, four layer anti-reflection coating and combination AR and HR coating were  $7.0 \pm 0.5 \text{ J/cm}^2$ ,  $3.2 \pm 0.3 \text{ J/cm}^2$ , and  $5.1 \pm 0.5 \text{ J/cm}^2$ , respectively. The anomalously low threshold for the AR coating is attributed to a vulnerability at the substrate-film interface.

In a continued effort to employ our increasing but still scant knowledge of those factors affecting the damage sensitivity of thin film coatings, J. H. Apfel and E. A. Enemark of Optical Coating Laboratory and D. Milam, W. L. Smith, and M. J. Weber of the Lawrence Livermore Laboratory evaluated the utility of barrier layers at the film substrate interface for both AR and HR coatings. The damage threshold difference between these two cases is attributed in part to the coating substrate interface region being illuminated for the AR case and protected by interference reflection when HR coated.

Experiments were performed using 150 ps, 1064 nm laser on coatings of  $\text{SiO}_2$  and  $\text{TiO}_2$ . Conclusive evidence was found that the introduction of a barrier layer of  $\text{SiO}_2$  on BK-7 substrates improved the damage resistivity, from zero to 90% depending on the materials used, film design, and thickness of the barrier layer. As covered in another paper at this meeting, no conclusive evidence was found for a surface roughness dependence on the damage threshold using 150 ps laser pulse lengths.

Through the use of non-quarter wave thin film designs D. H. Gill, B. E. Newnam, and J. McLeod of the Los Alamos Scientific Laboratory studied the possible improvement in laser damage resistance of reflectors at 532 and 1064 nm. The non-quarter wave designs were employed to reduce the electric field in the normally damage sensitive high index materials as well as move the field maxima from film layer interfaces where possible. The results were quite positive for films supplied from several vendors. Damage thresholds for  $\text{TiO}_2/\text{SiO}_2$  and  $\text{ZrO}_2/\text{SiO}_2$  stacks tested with 21 ps, 532 nm, and 30 ps, 1.06  $\mu\text{m}$  exhibited improvements as high as 2.6 over their all quarter wave counterparts. It was noted that these modified designs are quite sensitive to errors in coating thickness but they were quick to point out that several vendors supplied non-quarter wave stacks with thickness errors of less than 1%. Appropriate equations governing the design and behavior of these novel films were presented.

As we have said before, if you can't measure it, you can't understand it. This applies doubly to thin films, where methods to quantify the properties and behavior of thin films are needed, before any real advancement can be made. In this regard, the next group of papers were concerned with the characterization of ZnSe films from a structural and absorption standpoint, together with the development of new measurement techniques such as modulated light ellipsometry and adiabatic calorimetry.



A study of the optical, physical and chemical properties of R.F. bias-sputtered CVD ZnSe films on polycrystalline  $\text{CaF}_2$  as a function of sample preparation procedures and deposition parameters was reported by D. A. Walsh and R. V. Bertke of the University of Dayton Research Institute. Optical measurements at  $5.3 \mu\text{m}$  on coated polytran  $\text{CaF}_2$  substrates indicate that the absorption of bias-sputtered films were consistently lower than when non-biasing techniques were employed. Rutherford backscatter analysis of the ZnSe film indicates it was  $\sim 11\%$  rich in Zn. For the bias-sputtered samples, oxygen was found at the film/substrate interface, but its origin is not known. *In situ* sputter etching of the substrate surface immediately before coating produces optimum film adhesion and lowest absorption. More detailed studies of this type would be very beneficial.

It is well recognized that ZnSe is a most useful material in the infrared. Along this line D. F. O'Brien of the Air Force Materials Laboratory reported on the infrared absorption of ZnSe thin films as a function of deposition conditions. It had been previously reported that high absorption in ZnSe film probably arose from a variation in stoichiometry. In this study ZnSe was deposited on  $\text{CaF}_2$  under a variety of conditions. It was shown that the IR absorption decreased as the deposition rate was lowered, from as high as  $40 \text{ cm}^{-1}$  at  $40 \text{ \AA/sec}$  to  $< 5 \text{ cm}^{-1}$  at  $\sim 1 \text{ \AA/sec}$ . Furthermore, deposition in a Se rich vapor environment increases the probability of producing a stoichiometric film since high absorption films tend to exhibit a high Zn/Se ratio indicating an excess of Zn in the film. Although not specifically demonstrated in this paper, it was pointed out that higher substrate temperatures should also be beneficial in improving stoichiometry of ZnSe films. A final comment, through the use of AES and ESCA profile measurements of the Zn and Se concentration, it was determined that stoichiometry variations were found to exist as point to point differences in the Zn/Se ratio and not as a uniform deviation throughout the film. Thus, ZnSe films tend to exhibit highly localized absorption regions.

One area of continuing interest and utility is calorimetry as employed to evaluate new candidate window and mirror materials or finished components. To this purpose, D. L. Decker and P. A. Temple of the Naval Weapons Center reported on the design and operation of a precise, high resistivity adiabatic laser calorimeter. Features of this vacuum calorimeter, normally employed for low-absorption materials under low illumination levels, are given together with a detailed description of the theoretical equilibrium temperature response. The calorimeter exhibits a sensitivity of  $10^{-5}$  in absorbance at laser illumination levels of 1 watt. The calorimeter is capable of absolute electrical calibration. Major sources of systematic error arise from calibration of the external laser power meter and uncontrolled sample scatter. Accuracy is thus limited to  $\sim \pm 5\%$  for high quality low scatter samples. By careful attention to the stray light problem this instrument should be suitable from the near UV to the mid IR.

Another property of thin films, of which knowledge is important, concerns their anisotropy in refractive index. Addressing the measurement of this feature, M. E. Pedenoff and M. Braunstein of Hughes Research Laboratories and O. H. Stafsudd of the University of California at Los Angeles presented a most comprehensive discourse on the use of elasto-optical modulated light ellipsometer measurements of strain induced refractive index anisotropy in films of  $\text{As}_2\text{Se}_3$  and  $\text{As}_2\text{S}_3$  deposited on KCl substrates at  $10.6 \mu\text{m}$ . The instrument and computational produces developed by them allow one to estimate the anisotropic change in refractive index due to a uniaxial stress applied to the substrate. Preliminary measurements indicate anisotropies of  $\sim 0.6\%$  are generated in films of  $\text{As}_2\text{Se}_3$  and  $\text{As}_2\text{S}_3$  deposited on KCl by strains of  $4 \times 10^{-5}$  induced in the substrate.

As they say, "the proof of the pudding is in the testing." One might add, it is a way to understanding and validate our theories, as well as assessing our ability to fabricate damage resistant elements. Thus, several papers were concerned with the damage response of thin film coatings at several wavelengths in the infrared, with heavy emphasis on  $\text{As}_2\text{S}_3$  and  $\text{As}_2\text{Se}_3$ , and a characterization of the optical constants of these materials.

An evaluation of the damage resistance of gallium-doped germanium saturable absorbers at  $10.6 \mu\text{m}$  was reported by B. E. Newnam and D. H. Gill of the Los Alamos Scientific Laboratory. Employing laser pulses of 1.2 ns FWHM they found several interesting results. Damage was observed for bare Ge substrates (reflectivity  $\sim 1\%$  at  $10.6 \mu\text{m}$ ) at a threshold ranging from  $0.65$  to  $0.70 \text{ J/cm}^2$  and for anti-reflection (AR) coated surfaces at  $0.49 \pm 0.3 \text{ J/cm}^2$  employing fourteen coating designs using eight film materials from nine coating manufacturers. In all cases, only front surface damage for these 6 mm thick samples were observed, with the damage limited by the germanium surface properties. An  $\text{HNO}_3$  acid treatment raised the damage threshold of bare Ge about 10%. Multi-shot conditioning (n on 1) produced the same threshold as single shot (1 on 1) tests. There was no appreciable difference in damage sensitivity for samples of varied doping or crystallinity (single crystal, p-doped and undoped, and undoped polycrystalline) for three different conventionally polished substrates. In an additional experiment performed at a pulse width of 70 nsec a pulse width dependence  $E_D(\text{J/cm}^2) \sim \tau^{1/2}$  was observed, in agreement with previously proposed scaling relationships.



Pulsed laser damage testing of  $\text{As}_2\text{S}_3$  and  $\text{As}_2\text{Se}_3$  coatings at  $1.6 \mu\text{m}$  was the subject of a paper by C. C. Tang, M. Bass, M. J. Soileau and E. W. VanStryland of the University of Southern California. In particular the role of mode locked pulses on the damage threshold and process was assessed. For  $\text{As}_2\text{S}_3$  coatings, damage was noted only concurrently with a visible spark. However, for  $\text{As}_2\text{Se}_3$  coatings, two distinct thresholds were found. In this case the sparking threshold occurred for large diameter damage sites while at an intensity level  $\sim 30\%$  lower, small discreet damage sites were noted in the absence of any spark or incandescence. For  $\text{As}_2\text{S}_3/\text{KCl}/\text{As}_2\text{S}_3$  anti-reflection (AR) coatings on KCl, substrate damage was  $\sim 430 \text{ MW/cm}^2$  and was independent of the presence of a mode locked train of pulses. By comparison three layer AR coatings containing  $\text{As}_2\text{Se}_3$  damaged at  $\sim 20 \text{ MW/cm}^2$ . The independence of damage thresholds of these two materials on coating designs strongly indicates that damage is not related to field strength nearly as much as the energy absorbed/unit mass i.e., a predominantly thermal failure mechanism. An examination of the morphology of the damage sites indicates that damage is initiated at either microscopic defects or absorbing inclusions.

The growing interest in high power chemical lasers pointed the way for a study of dielectric coated mirrors in the  $2\text{--}5 \mu\text{m}$  region by D. B. Nichols and R. B. Hall of the Boeing Aerospace Company and R. A. House II of the Air Force Weapons Laboratory. Using a photo-initiated HF/DF laser emitting a FWHM pulse of  $4.0 \mu\text{sec}$ , they tested two substrate materials (molybdenum and Cer-Vit) and five coating designs deposited by Coherent Radiation and Northrop Corporation [ $\text{Cr} + (\text{Al}_2\text{O}_3/\text{Si})^3$ ;  $\text{Cr} + \text{Ag} + (\text{SiO}/\text{Si})^1$ ;  $\text{Cr} + \text{Au} + (\text{SiO}/\text{Si})^1$ ;  $\text{Ag} + (\text{ThF}_4/\text{ZnS})^3$ ; and  $\text{Ag} + (\text{ThF}_4/\text{ZnSe})^3$ ] which exhibited reflectivities between 0.9792 and 0.9978.

Irradiations began at exposures less than  $4 \text{ J/cm}^2$  ( $1 \text{ MW/cm}^2$ ) and proceeded at the same site with a nominal increase of 50 to 100% until small scale and then catastrophic damage was observed. Based on these tests the following conclusions were drawn: firstly, the two coatings having the lowest absorption, namely,  $\text{Ag} + (\text{ThF}_4/\text{ZnS})^3$  and  $\text{Ag} + (\text{ThF}_4/\text{ZnSe})^3$  were the most damage resistant, secondly, the absolute value of damage thresholds for the best mirror coating are comparable to thresholds for formation of surface plasmas on bare metals, thirdly, there was no discernible threshold difference between Cer-Vit or molybdenum substrates inferring that the thermal conductivity of the metal substrate gave no significant advantage for these single exposure experiments, which is not surprising considering these are not cw experiments and finally, damage thresholds for these class of materials under these experimental conditions are not appreciably different for 1.0 and 0.1 cm beam spot diameters.

In a very revealing and important paper, T. M. Donovan, A. D. Baer, J. H. Dancy, and J. O. Porteus of the Naval Weapons Center presented results from a very detailed analysis of formation and characteristics of defects and impurities in  $\text{As}_2\text{S}_3$ ,  $\text{As}_2\text{Se}_3$  and NaF coatings. It was noted that the damage thresholds of chalcogenide glass thin films are less than for corresponding thin films of NaF even though the absorption of NaF films is relatively high. Conclusions drawn from these two observations were explained by noticing that: first, chalcogenide glass films form  $\mu\text{m}$  size, arsenic rich crystallites over a period of a few days after deposition (these are sulfides and selenides, and not oxides as previously reported), and secondly the high absorption of NaF films is probably due to a thin layer of adsorbed water which rapidly forms upon exposure to the atmosphere. Attempts to eliminate these problems by stabilizing the chalcogenide coating by depositing thin layers of Ag or NaF *in situ* or employing water-free  $\text{As}_2\text{Se}_3$  evaporant both failed. In the case of NaF, it was suggested that by eliminating surface oxygen, film absorption approaching that of bulk NaF might be attained.

The disparity in absorption coefficients for materials in bulk and thin film form probably indicates better than any other measure the vast difference between materials in these two forms. Both measurements can be difficult, e.g., very low absorption in bulk materials, versus very thin samples for films. D. L. Burdick of the Naval Weapons Center has attacked the thin film side of this divergence in properties through the development of a novel wedged-film technique in which the film is deposited in a wedge form (i.e., wedged in thickness). Through careful measurement of film properties as a function of thickness on this one sample, he has been able to accurately measure optical constants of  $\text{As}_2\text{S}_3$  films in the visible spectral region, including absorption coefficients ranging from  $3 \text{ cm}^{-1}$  to  $10^4 \text{ cm}^{-1}$ , and refractive indices from 2.47 to 2.72 with precisions ranging from 0.3 to 1%. He pointed out a number of advantages of this method over other methods of measuring optical constants of thin films.

The final group of papers dealing with thin films is best described as being related to the environmental durability of coated elements. Included are papers on the performance of coatings on deformable mirrors, the degradation of coated elements subjected to real world environments of humidity, dust and sand, temperature cycling and flexure.



Recognizing the impending advent of adaptive optic systems, J. M. Rowe of the Northrop Research and Technology Center reported on dielectric coatings for deformable mirrors. In this study the results of an experimental program to determine the optical and physical properties of high-reflectance dielectric coatings subjected to as many as  $10^4$  deformation cycles was discussed. Films studied included  $(\text{SiO}/\text{Si})^2$  and  $(\text{Al}_2\text{O}_3/\text{Si})^2$  designs for operation at  $3.8 \mu\text{m}$  on top of silver coated mo substrates. Measurements included residual coating stress (taken immediately after deposition), spectral reflectance, absorptance at  $3.8 \mu\text{m}$  and Normarski interrogation. Investigations included so called "DC" cycling in which deformation was of one sign only by use of a bias e.g., flat to convex and back to flat. Zero to peak displacements of  $10.9 \mu\text{m}$  at 10 Hz were employed leading to a peak stress of  $9.9 \times 10^7 \text{Pa}$  comparable to the residual stress produced as a result of the deposition on these types of substrates. No physical degradation (cracking, etc.) nor appreciable reflectance variation was observed. However, in some cases, a slight variation in absorptance was noted. Additional work is underway on the study of other candidate film systems, to evaluate adhesion and humidity properties as well.

It is only appropriate at an ASTM sponsored meeting that one discuss measurements and standards along with the more fundamental interaction mechanisms. In this light S. R. Scheele and J. W. Bergstrom of the Hughes Aircraft Company reported on the initial phase of a program dealing with the broad category of quantitative characterization of the mechanical properties of coatings. The specific topic of their presentation dealt with film adhesion testing. After a thorough literature search, survey and review of existing test procedures, three specific mechanical pull-off tests were compared on a large number of coated glass optical substrates as potential replacements for the current MIL-Spec tests. The tests included direct pull-off, a topple test and finally a peel test. Present tests are generally qualitative and subjective, as well as not being well controlled, a generally undesirable situation.

A variety of coatings and substrates were utilized in comparing the various adhesion tests. An interesting generality was that it was difficult to remove coatings with good adherence to glass substrates, but relatively easy to remove coatings from infrared substrates. Comparitively speaking, the plug pull test was least desirable because of relatively poor repeatability and high forces involved. The topple test gave better results and was less expensive; however, unexplained substrate damage was frequently observed. While the peel test was relatively expensive to implement it required the lowest force and had the advantage of affording highly localized sampling.

In a companion paper, R. A. West and C. W. Nichols also of the Hughes Aircraft Company treated another aspect of coating characterization, abrasion resistance. In this instance the ASTM falling sand test was modified to perform abrasion resistance tests in a controlled manner. Quantification was achieved by correlation with transmittance degradation. The final carefully evaluated test procedure was correlated with other existing tests such as the military eraser and cheesecloth abrasion tests.

Abrasion resistance, like adhesion, is an important indicator of a film's durability when exposed to a range of real world environments and a need for a quantitative test is readily identified. After evaluation of many types of test specimens, the modified falling sand test was seen to be an easily implemented, sensitive, repeatable and adequately quantitative test procedure. There was little obvious correlation of the results of this test with those presently used, which are more subjective and more poorly controlled.

Continuing their interest in the near-infrared, S. J. Homes reported on Northrop's latest activities in dielectric enhanced mirrors for use in the  $2\text{--}6 \mu\text{m}$  region. Of major concern in this paper was a cataloging of performance characteristics such as reflectivity and absorption of a large variety of dielectric multilayers for high reflectivity metallic mirrors ( $> 99.9\%$  reflectivity at  $2.8 \mu\text{m}$ ,  $3.8 \mu\text{m}$  and  $5.3 \mu\text{m}$ ) together with a testing of their environmental durability. This study was performed to evaluate the reduced cooling requirements afforded by higher reflectivity mirrors, for high average power applications, over uncoated thermally conducting substrates. At least ten different dielectric enhanced mirror designs were evaluated at each of the three laser wavelengths. There were deposited on conventionally and bowl feed polished  $(\text{Al}_2\text{O}_3)/\text{Ag}$  overcoated molybdenum substrates. Cleaning and deposition parameters were covered in detail. The environmental evaluation included tests according to Mil-m-13508C for durability, adhesion, and humidity resistance. No laser damage testing was reported.

### 3.4 Laser Glass and Glass Lasers

With the continued emphasis on large, high power Nd:Glass lasers in the laser fusion laboratories around the world, interest persists in the properties of Nd:Glass as a laser material. Obviously, the damage threshold of laser glass is of importance, although in all large glass laser systems operating today, the damage limit for the system is determined by failure of optical coatings, rather than bulk failure in the glass itself. Other properties of laser glasses are also of importance, especially now that several compositions with significantly different properties are available. The laser designer must ask, which is the best glass for the system I want to design, given the system architecture and desired operating parameters. These, in turn, must be related to composition.



Adding another parameter to the growing list of relevant variables, J. G. Sliney, Jr., and L. G. DeShazer of the University of Southern California have studied the bulk damage threshold of various Nd-doped laser materials, both crystalline and glass. Samples were irradiated with a 10 ns pulse from a Nd:YAG laser oscillator, amplified by a Nd:glass rod amplifier. The beam was focused with a 25.4 mm focal length lens which unfortunately was plano-convex. Accordingly, significant spherical aberration was generated.

Nd-doped, ED-2 laser glass was tested at room temperature and at 110°K, at four concentrations of Nd, 0, 1, 2, and 3%. At room temperature, some decrease in the damage threshold was noted with increasing concentrations, while at reduced temperature, the threshold was 33% higher, and seemed less sensitive to Nd concentration. It should be pointed out that due to uncertainties in this experiment, the reported concentration dependence of damage is not well established. The increase in damage threshold with lowered temperature is similar to that observed in NaCl by Manenkov.

Of the various host materials tested,  $\text{LiYF}_4$  and ED-2 glass showed the highest thresholds, 1.9 and 1.7 times that reported for YAG, while  $\text{YVO}_4$  and GGG showed the lowest, at about 0.6 times the value for YAG. The computed power densities at which damage occurred seem small,  $7.6 \text{ GW/cm}^2$  for NaCl, for example, but the actual focal spot size and peak intensity are somewhat uncertain in these experiments.

Although not directly concerned with the damage properties of optical materials, two papers which were presented by the University of Rochester Laboratory for Laser Energetics concerning the other properties of laser glass were of great interest. J. A. Abate, D. C. Brown, C. Cromer, S. D. Jacobs, J. Kelly, O. Lewis, and J. Rinefierd contributed to the two papers.

The first concerned correlations of physical and optical properties of laser glasses and the statement and evaluation of figures of merit for laser materials. The authors pointed out that simply considering the nonlinear index,  $n_2$ , or even including the gain or cross-section for the glass did not suffice to define the utility of a given glass in a laser system. They defined eight merit factors, including the effects of nonlinear phase distortion, specific gain, heat dissipation, quantum efficiency, thermal diffusivity, heat capacity, thermo-optic distortion, and stress birefringence. In any system evaluation, these eight factors would have to be combined in some weighted sum, and cost factors taken into account to obtain a true economic figure of merit. In the present work, these eight merit factors were evaluated for five commercial laser glasses, ED-2 and four phosphates. The phosphates have higher cross-section and lower  $n_2$  values, as well as lower values of thermo-optic distortion and stress birefringence, but poorer thermal diffusivity and heat capacity factors. Furthermore, phosphate glasses show a lower resistance to thermal shock. Other factors considered included the ease of manufacture and chemical stability, which can be improved by slight compositional changes.

The authors examined correlations among the properties of these glasses and fluorophosphates to see if they can discover why some compositions show better thermal properties, and others better optical properties. They observe that low index (and low index nonlinearity) glasses show higher thermal expansion and less hardness. For phosphates and silicates, decreasing  $n_2$  correlates with a decreasing Young's modulus and decreasing thermal conductivity, however, this trend does not extend to fluorophosphates.

The difficulty in establishing these correlations seems to be the fact that differences in band polarizabilities have been ignored. The optical properties of oxide glasses, whether silicate or phosphate, reside in the oxygen bonds. Non-bridging oxygens are more polarizable than bridging oxygens, while certain network modifiers strengthen and densify the glass. Thus stronger, more compact glasses tend to be more polarizable, with higher values of  $n$  and  $n_2$ . For fluorides, however, the fluoride bond takes the place of the oxide, and a new set of correlations apply.

This paper does point up the necessity for examining all relevant factors in choosing a laser glass for a system. Cost cannot be ignored, nor can surface damage in the system elements. The isolation of the individual merit factors allows the glass user to emphasize those properties of greatest importance for his application. Correlation of these desired properties with glass composition is then a task for the manufacturer.

The second paper by the same authors reported the measurement of inversion density in both silicate and phosphate laser glass. The purpose of this measurement was to check the validity of assumptions made in the computer code GENEFF, used at the Lawrence Livermore Laboratory to model the efficiency of conversion of absorbed flashlamp light into population inversion.

The laser glass samples used were cut in the shape of a rectangular parallelepiped, with a 1 cm x 1 cm square base, and 16 cm length. Collimated flashlamp light was incident from one end. The inversion density was monitored by recording the fluorescence as a function of distance along the side of the sample. Nd concentration of the sample was determined by wet chemical and x-ray fluorescence analyses.



The Argus laser at the Lawrence Livermore Laboratory has been in operation since late in 1975. The system has been fired about 600 times, at power levels in excess of 4 TW in 0.1 ns pulses, and energy levels up to 2 kJ in one ns. I. Stowers and H. Patton of the Lawrence Livermore Laboratory reported on the experience accumulated on the Argus system in the identification and analysis of damage phenomena.

Three kinds of damage phenomena were noted. These can be described as surface damage due to foreign particles, film growth on laser glass surfaces, and coating damage.

The surface damage arises from particles deposited on optical surfaces either by dislocation from the surrounding surfaces or from the cooling nitrogen stream. Damage was seen to be more prevalent on upward facing surfaces, due to gravitational settling of particles, and on the first surface encountered by the gas stream. No significant aging effect was seen. After ten to twenty firings, no subsequent accumulation of particulate damage was seen, as long as the system was kept clean.

The phenomena of film growth on laser glass had not been extensively investigated previously. It was found that a cloudy film develops on ED-2 laser glass, even when it is not exposed to flashlamp or laser light. The film is found to consist of fibers of 2 to 5  $\mu\text{m}$  diameter and up to 0.5 mm length, containing Li and N in high concentration. Since ED-2 is rich in Li, this suggests that the film evolves due to decomposition of the glass, perhaps under attack by a moisture-laden atmosphere. The film can be removed by washing in ethanol.

Coating damage remains the major impediment to high power laser performance. Due to heavy use of spatial filtering, the Argus system has not experienced severe coating damage, however. The spatial filter lenses, especially on the input side, are most vulnerable to damage. Some evidence has been seen of a greater tendency to damage on coatings in vacuum, possibly due to removal of absorbed materials from the pores of the coating.

The most important measure for the prevention of damage in a large laser system is seen to be the maintenance of cleanliness throughout the system. Coating damage can be held to an acceptable level by maintenance of beam quality through spatial filtering.

### 3.5 Fundamental Mechanisms

The ultimate limit to the optical flux which can be transmitted through a transparent dielectric is determined by the onset of optical breakdown. A plasma forms at the dielectric and quickly grows to a density sufficient to absorb the laser light strongly. The consequent heating of the lattice by the plasma causes irreversible physical damage. This problem has been studied intensively for at least a decade. It is well known that at very short pulse durations, multiphoton ionization plays a major role in promoting electrons to the conduction band, where they can be subsequently accelerated by the optical field. It is also well known that at long pulse durations, where carrier lifetimes in the conduction band are important, avalanche ionization can occur, with the electrons gaining energy by successive collisions with the lattice, until they are sufficiently energetic to cause secondary ionization. Two points of view have emerged, however, regarding the relative importance of multiphoton ionization and avalanche ionization in causing material breakdown. These two points of view are represented by the first two papers in this section.

Alexander Manenkov of the Lebedev Physical Institute in Moscow reported on recent results obtained in his laboratory on avalanche ionization in crystalline dielectrics. Based on a detailed investigation of the quantum kinetic equation for the electric energy distribution, Manenkov derived the dependence of the breakdown threshold on the various parameters of the experiment, including laser frequency, sample temperature, ionization potential, and pulse duration. The predicted pulse duration dependence is very weak, rather than scaling like  $\tau^{1/2}$ , but this is due to the absence of transport terms in the original theoretical analysis.

Experiments were carried out for a large number of dielectric crystals with pulses of a few ns in duration at 10.6  $\mu\text{m}$ , 1.06  $\mu\text{m}$ , 0.69  $\mu\text{m}$  and 0.53  $\mu\text{m}$ . The sample temperatures were varied from 100°K to 800°K. The damage threshold was expected to decrease with increasing temperature at optical frequencies well above the effective electron-phonon collision frequency, and to increase, but weakly, with increasing temperature for optical frequencies below the collision frequency. For selected samples of alkali halides, this dependence was observed from 1.06  $\mu\text{m}$  to 0.69  $\mu\text{m}$ , but no temperature dependence was seen at 0.53  $\mu\text{m}$ . This anomaly was attributed to multiphoton processes.

Manenkov tested hundreds of samples. He found that only those with high damage thresholds exhibited consistent dependence on temperature and frequency. The low-threshold damage was attributed to impurities. The threshold in these materials could be raised by heating the materials, which Manenkov felt was due to dispersal of absorbing aggregates. The thresholds observed in the high-threshold materials were significantly higher than those reported elsewhere.

Although any theoretical analysis of damage is limited, due to the difficulty of treating all possible effects simultaneously, this paper put forward a concrete model of avalanche ionization. The experimental data are of particular interest, representing the first simultaneous and consistent study of the temperature and frequency dependence of bulk damage by pulsed lasers.

The point of view that optical breakdown in alkali halides is solely due to multiphoton excitation of polarons, followed by phonon heating of the lattice, was put forward by A. Schmid and P. Kelly of the National Research Council of Canada, and P. Braunlich of Washington State University. They calculated the rate at which conduction electrons are generated by multiphoton absorption, and the consequent heating by polaron-phonon scattering. From this calculation, they obtain a predicted dependence of the breakdown field at threshold on pulse duration and laser wavelength. The results are significantly different from those of Manenkov. A strong dependence on pulse duration is predicted, with the energy density at threshold increasing roughly as  $t_p^{2/3}$  at the ruby wavelength. Whereas the avalanche theory predicts a monotonic increase of threshold with increasing optical frequency, the multiphoton theory predicts a decrease for short wavelengths. It is of interest to note that Manenkov's measurements deviate from the pure avalanche model at high frequency, raising the possibility that multiphoton processes are contributing to the damage, as the model of Schmid et al would indicate.

With increased interest in short wavelength lasers, the consequence of promoting significant numbers of electrons into the conduction band in dielectric solids is of increasing importance. This phenomenon arises due to multiphoton absorption in window materials, but much can be learned about it by looking at semiconductors, where interband absorption occurs via one-photon absorption. M. Kruer, L. Esterowitz, F. Bartoli, and R. Allen of the Naval Research Laboratory have studied laser-induced damage in semiconductors (Ge, Si, In, Sb) irradiated at 0.69  $\mu\text{m}$ , 1.06  $\mu\text{m}$ , 5  $\mu\text{m}$  and 10.6  $\mu\text{m}$ . Pulse durations ranged from a few ns to several seconds (CW). Damage occurred due to surface melting. It was found that for very high absorption ( $10^5 \text{ cm}^{-1}$  or more), the effective depth of heating is greater than the absorption depth due to carrier diffusion. Diffusive distances of the order of 0.5  $\mu\text{m}$  were observed. These are much shorter than values obtained using room temperature material parameters. The high concentration of conduction electrons generated in these experiments shorten the carrier lifetime, due to Auger recombination, and so greatly reduce the diffusion length.

The question of the concentration dependence of free carrier lifetimes in insulators was explored in depth by K. Williams, P. Klein, and C. Marquardt, of the Naval Research Laboratory. They considered the effects of shallow traps, deep traps, and electron-hole recombination on the kinetics of conduction electrons in insulators. Shallow traps reduce the electron mobility, but do not affect the lifetime. They show that in both insulators and semiconductors, deep traps reduce the lifetime to an extrinsic value which is essentially independent of carrier density, depending only on trap density, at high trap concentrations. The intrinsic lifetime of conduction electrons is different in semiconductors and insulators. In semiconductors, it is determined by the equilibrium concentration of carriers, and so, although temperature dependent, it is not sensitive to the initial concentration of photo-electrons produced in a pulse of illumination, except through the Auger process indicated above. In insulators, however, the equilibrium concentration of carriers is zero, so an inverse dependence of carrier lifetime on concentration is expected. The authors present arguments indicating that the Auger process is not important in alkali halides, even at carrier concentrations of  $5 \times 10^{17} \text{ cm}^{-3}$ .

They present experimental data on measurements of multiphoton-induced photo-conductivity in alkali halides, using a doubled ruby laser with a pulse duration of 20 ps. They observe a decrease of the carrier lifetime from 20 ns, at low carrier concentration, to less than 10 ps at carrier concentrations which are high ( $> 10^{12} \text{ cm}^{-3}$ ), but well below those expected at the level of optical damage. At high concentrations, the authors expect their measurements to be uncertain, due to space charge effects. They emphasize the importance of using concentration-dependent carrier lifetimes in theories of optical damage.

They further report a dependence of carrier lifetime on the method of material preparation in the regime of extrinsic lifetime. In NaF, purification of the material shortened the carrier lifetime, ostensibly due to an increase in carrier mobility, while in  $\text{Al}_2\text{O}_3$ , the lifetime was sensitive to small deviations from stoichiometry in the crystal. The measurement technique is advanced as a sensitive, non-destructive test for the evaluation of wide-gap materials.



Two-photon absorption coefficients have been measured at Harvard University for a variety of wide-gap materials, again mostly fluorides and oxides, using third and fourth harmonic generation from a 30 ps, Nd: YAG laser. The authors included P. Liu, H. Lotem, and N. Bloembergen of Harvard University, W. L. Smith, now at the Lawrence Livermore Laboratory, J. H. Bechtel, of the General Motors Research Laboratory, and R. S. Adhav, of Quantum Technology. At 355 nm, the results were consistent with the expectation, in that for materials with band gap greater than twice the photon energy, negligible absorption was seen, while for materials with band gap less than  $2h\nu$ , coefficients from  $10^{-2}$  to  $10^{-3}$  cm/MW were observed. At 266 nm the same results were obtained for alkali halides and  $\text{CaF}_2$ , but for oxides and phosphate materials, the two-photon absorption coefficients were observed to be from  $5 \times 10^{-5}$  to  $3 \times 10^{-4}$ , even when the gap was significantly less than  $2h\nu$ . The authors caution against ignoring two-photon-absorption attenuation in measuring bulk damage at short wavelengths.

The final two papers in this section deal with a general methodology for identification of damage mechanisms and definition of damage thresholds. It is essential that when a damage threshold is quoted, everyone agree on the significance of the terminology. It is also important to know which of several possible effects was responsible for the damage. The threshold is thus defined as the illumination level at which a certain phenomenon will take place with a certain probability.

The problem of determining the damage threshold from a finite sample of observations was considered by J. A. Detrio and A. P. Berens of the University of Dayton Research Institute. The objective of the study is to evolve a strategy requiring the smallest number of observations to determine the damage threshold with the greatest confidence level. The damage threshold is defined, in this work, as the power or energy level at which the probability of damage (observed by some predetermined criterion) is one-half. The objective of a damage test can also be to determine which of two specimens has the higher threshold.

The authors conclude that, to determine the threshold, the "up-and-down" method is the most efficient. In this method, if the sample does not damage on a given shot, the power is raised for the next shot. If it does damage, the power is lowered. A requirement of this method is that the experimenter is able to choose the incident power level within some range of values. The choice of increment and sample size is discussed.

In determining the damage threshold of either a reflecting or transmitting surface at  $10.6 \mu\text{m}$ , a number of competing effects can give rise to damage. J. Porteus, J. Jernigan, and W. Faith of the Michelson Laboratories have developed a method of measurement and analysis, called the "multi-threshold" method, for determining the effective threshold value for each of these competing effects. They have constructed an ultra-high vacuum irradiation chamber, with the following diagnostics: a 20 power optical microscope, Faraday cup for charge collection, and Auger analyzer with an electron imager, which is sensitive to variations of the work function over the surface. Targets are exposed to a train of pulses from a mode-locked  $\text{CO}_2$  laser. Up to 50 sites are irradiated with one pulse each, and the observer notes the appearance of either visible plasma formation or pitting. The incident power density varies from shot to shot over a substantial range of values. After irradiation, the type of damage, if any, at each site is characterized.

A computer algorithm has been devised to then determine the effective threshold value and standard deviation for each of the identified damage phenomena. For each process, it is assumed that the single-shot probability of damage is zero, for fluences less than  $\phi_0 - \sqrt{3} \sigma$ , (where  $\phi_0$  is the threshold fluence, and  $\sigma$  the standard deviation) increases to unity for  $\phi_0 + \sqrt{3} \sigma$  and is unity above that value. The effective sample values of  $\phi_0$  and  $\sigma$  are then determined from the principle of maximum likelihood.

The procedure has been calibrated using a gold surface electroplated on diamond-turned copper. The results are highly reproducible. A number of materials have been examined by this process, and the results are presented in a companion paper by the same authors.

The multi-threshold method is particularly valuable, because rather than identifying the damage threshold of a surface as a single number, it provides a profile of the various damage thresholds, which can be correlated with surface treatment, material purity, aging, or other parameters of the surface preparation.

#### 4. Recommendations

The ultimate objective of laser materials studies is better lasers, better in the sense of higher power and energy, greater reliability, and reduced cost. Much of the research reported in the nine volumes of these Symposia Proceedings has been motivated by the high power laser programs in the DoD and DOE (formerly ERDA). These programs center around the construction of very large, very expensive lasers, so that considerations of performance, reliability and economy are of great importance.

Large systems with single-pulse energies of tens of kilojoules are in operation or under construction at several national laboratories around the country. Both CO<sub>2</sub> lasers and Nd:Glass lasers are involved. Even larger systems, with single-pulse energies of hundreds of kilojoules, are being planned. This raises problems for the optics industry and laser community, as well as affording new opportunities. The manufacturers and users of special optics can anticipate heavy pressure on the fabrication capability of the U.S. in the area of high power laser components. This pressure will undoubtedly divert work to manufacturers not hitherto involved in high power laser optics. It is essential that the expansion of the special optics industry be carried out with due attention to the lessons of the past, as recorded in these proceedings and elsewhere in the literature.

The flow of information back to these symposia is essential, also. As more experience is gained on large laser systems, we would like to hear more reports like that of Patton and Stowers of LLL at this symposium, recounting the damage history of an operating system. We strongly encourage the high power laser laboratories to keep their resident experts in laser damage in touch with the day-to-day experience of the operating system. There is a tendency, once the laser is operating, to turn it over to the applications group, and only to call in the damage experts when the system has failed. This Symposium needs feedback from the laser laboratories regarding the operating experience of large laser systems.

We still lack a reliable rule of thumb, predicting the lifetime of a laser component as a function of the fraction of the nominal damage level at which it is operated. What is a "safe" level of operation for thousand-shot lifetime? This question must be answered if laser systems are going to operate reliably for reasonable periods of time in fusion power plants, for example. (At 1 pps, a laser fires almost 10<sup>5</sup> shots per day.) This safe operating level must reflect the actual operating environment of the laser, obviously.

As higher yield fusion experiments are carried out, it becomes possible to conduct experiments on the effect of target debris on optical elements. Metal mirrors, dielectric multilayers, and "blast shields" are the elements most likely to be exposed to target debris. These experiments should be carried out with due attention to characterization of the samples, both before and after exposure. Here again, close cooperation between the laser damage specialist and the applications group is of great benefit to all concerned.

At present, large laser system performance is severely limited by component damage, thin film failure in glass systems, surface damage in single shot CO<sub>2</sub> systems, and thermal damage in high average power systems. We will consider each of these areas in detail as we proceed through our recommendations.

Let us turn our attention to surfaces and mirrors. While it is generally conceded that thin films are presently the most damage sensitive element in optical systems, it should be obvious that one must understand surfaces and their characteristics before one can assess the role they play as substrates for coated elements. In addition, much of the present interest in surfaces is concerned with surface absorption, environmental contamination, and adsorbed impurities (both a physics and chemistry problem), and the characterization and maintenance of the surface structure. These are all problems common to thin films. One obvious area of corollary interest is in fiber optics, where all of these topics can greatly influence the performance of fiber elements. Fiber optics will undoubtedly play a major role as control and instrumentation components in laser fusion systems. To this one might add adaptive optics. One must assess the long term modification of surfaces by mechanical fatigue of these deformable optic elements.

From a systems standpoint, there is a need to transfer laboratory experience to the real world scene. Much of the material presented at these symposia deal with very basic research efforts, and the development of improved processing procedures designed to approach the intrinsic qualities of optical materials. However, one must back off from these "idealized" levels to safe operating levels which can be utilized, taking into account potential environmental degradation. This concern is certainly application dependent. Consider if you will the space scenario, the laser fusion target chamber, or the high average power laser used in materials working such as welding in a machine shop. Each of these arenas imposes uniquely different environmental constraints on safe operating levels. We see a need for studies on fully characterized optical elements, in realistic environmental conditions, along with subsequent careful laser damage testing.



To return to our initial point, i.e., the careful characterization of surfaces in order to assess surface quality and monitor gradual modifications, scattering techniques still appear to be the best tool for quantifying surface topography. Unfortunately the theory is incomplete and measurements made at different laboratories are usually far apart in the values obtained for such simple indicators as RMS surface roughness. About the best that can be said is that they usually agree in relative smoothness. This disagreement arises in part from the fact that different techniques give different answers. To date there has been no standardization of measurement technique or even agreement on theory. This is a very fruitful and important area for research and development. Scatter measurements will become of even greater utility as we move to the uv, where, due to the shorter wavelength of light, there is an increase in scattering which constitutes a loss in the optical system. The uv will also place a greater burden on fabrication due to the more stringent tolerances required. Some accepted diagnostic method is needed. We might add that long term or environmental degradation of optical tolerances must be assessed as well to realize the full benefit to be obtained from ultraviolet lasers. We must demand tighter tolerance specifications and improve our evaluation of system performance.

From the interaction standpoint, scaling laws have been enunciated relating surface damage thresholds to laser parameters (frequency, pulse duration, spot size) and material parameters (surface roughness, refractive index). Additional work is required to define the range of applicability of these scaling laws and to refine their predictive value, both to improve their utility in arriving at realistic system specifications as well as an aid in defining theoretical bases. A word of caution is appropriate. We should not greatly extend scaling laws beyond the range of experimental determination, i.e., to grossly different conditions, for they may no longer be valid.

Thin films have been described as the Achilles Heel of high power laser systems. In large measure this is because they themselves contain many Achilles Heels. We start by considering a substrate surface. Prior to coating it is cleaned, ground, polished, and cleaned again. New and better methods of cleaning are needed in order to remove surface impurities and improve film adhesion. This requires the attention of both the surface physicist and surface chemist. The properties of the film/surface interface greatly influence both the structure of the films and film adhesion. The latter continues to be a problem in the durability of coated elements and requires continuing attention, especially for machined optics where cutting oils, etc., must be scrupulously removed. Environmental degradation occurring after the film is put into use has already been discussed.

Over the past several years we have seen many new coating materials introduced and novel design concepts suggested. At the time they seemed most noteworthy. However, in many cases these improvements have not been put into use. We don't know if this is a result of overselling, a reluctance on the part of manufacturers to deal with new materials or design, or the consequence of trying new ideas and materials and finding them wanting. Unsuccessful attempts to implement new ideas are not usually reported. One must transfer knowledge of failure as well as success. Without question more materials and design concepts are needed, together with a careful and complete evaluation of their performance and characteristics. It is hard to imagine that all possibilities have been explored.

An area which received some attention this year was the modeling of film stress. In the proposed models, the stress arising from dissimilar coefficients of expansion of the substrate and film was treated together with the intrinsic stress of the film materials. Work should be continued in this area, including stress generated by entrapped gas or impurity atoms, stress introduced by the freezing-in of lattice defects (which probably arise in good measure from the substrate surface properties) and purely surface effects. The last arises from a variety of causes including surface tension effects due to small thickness, the hindrance of dislocation motion, and the influence of oxide or other chemically bound surface layers, similar to that arising from inter-layer forces. This analysis must as well be corroborated by careful measurement and appropriate damage testing.

Of even greater concern to the burgeoning field of adaptive optics is film performance under continued deformation cycling. Initial studies were reported this year, but only extended over a few thousand cycles and did not include damage testing. If adaptive optics is to become practical, we will probably need "rubber" films.

There is still need for further parametric studies of films to develop appropriate scaling laws. The subject of thin films in itself is so complex we cannot hope to understand the full picture prior to a film's employment. What has been done to date has provided helpful guidelines for the selection of candidate film materials, multilayer designs, and deposition procedures. The choice of film materials and design is determined by the application. These studies have also uncovered new unexpected results which need to be addressed further, such as the separation of thermal and electric field induced damage in the arsenic sulfides and selenides and on the coatings of germanium saturable absorbers where the exact crystalline form of the substrate was found to be unimportant. This is one case in which a coating did not have an overwhelming deleterious effect on the damage threshold. We might add it did not have a beneficial effect either.

A question we can ask is "Can you make the material in thin film form behave as it does in the bulk?" Probably not. But how close we can come, can only be determined by a most comprehensive and detailed research program. One must begin with starting materials of known purity and proceed from known substrate character through a carefully controlled preparation procedure to a detailed evaluation of film performance. From this we must correlate the physical structure with the optical properties exhibited by the film. The studies must include damage testing and potential environmental or aging effects. This a major undertaking and probably can only be realized by the intelligent infusion of money, organization, and technology transfer by the government. This will require the development of diagnostic instrumentation, consensus definitions, and standard evaluation techniques suitable for reduction to widespread practice.

Although surface damage and thin film failure limit laser performance, especially in high peak power systems, investigation of bulk properties remain a central concern. The efforts to relate the optical and mechanical properties of laser glasses, and optical materials in general, to composition, purity, and structure should continue, primarily because great progress is being made in this area. The technological payoff of these investigations extends beyond the high power laser field. Research in fiber optics materials is proceeding along very similar lines. Low-loss optical fibers have been developed with alternation as low as 0.7 dB/km, corresponding to an attenuation coefficient of  $0.16 \times 10^{-4} \text{ cm}^{-1}$ . From arguments presented at this symposium, the impurity content of these fibers, which are made of a germanate glass, must be extremely low. Surface losses must be extremely low, as well. Laser materials researchers may be able to learn much about low-loss materials from the fiber community.

Conversely, as fiber optics users try to propagate increasing amounts of energy through monomode fibers, questions of laser damage will surely arise. A few milliwatts in a monomode fiber corresponds to megawatts/cm<sup>2</sup>. Similarly, manufacturers of junction diodes are already concerned with damage processes. We want to emphasize that laser damage considerations are not restricted to the world of high power lasers.

As far as infrared window materials are concerned, the problem has been identified as essentially one of impurities. The solution, in so far as the problem can be solved, lies in the processes of manufacture of the material and fabrication of the component. To do this economically is a challenge to the industry. In future, emphasis should be placed on questions of process control, to ensure low impurity levels, and on detection techniques, to monitor those levels. Reduction of surface contamination remains a serious problem.

The extensive research carried out on infrared window materials provides an excellent point of departure for the development of ultraviolet materials. Wide gap materials of high purity have been developed and should be used in uv studies. The methodology of the studies should also follow the procedures developed in previous work. This is especially true for damage studies. Presently, there is very sparse data on damage levels at short wavelengths. These data will not be useful unless obtained with well-characterized lasers, on well-characterized materials, with a clear definition of what constitutes damage. "Those who fail to study history are doomed to relive it" and perhaps even more painfully.

New phenomena occur in the uv which require investigation. The fact that electronic transactions are involved and that electrons can easily be promoted to the conduction band, either by multiphoton or multi-step processes, leads to new and complicated effects. It is not clear that many of the scaling laws previously observed apply at short wavelengths. Scaling with wavelength, bandgap, pulse duration, and spot area must be re-examined. The cumulative loss mechanism reported at this conference clearly warrants further investigation. There may be other cumulative or aging processes which degrade uv optics over prolonged exposure. Here again, feedback from the system builder is of great value. Further development of new uv window materials should continue.

The fundamental mechanism of two-photon absorption is generally understood. Due to the importance of this phenomenon in limiting uv laser performance, further study is clearly desired. The results reported this year or the difference in behavior of halides and oxides is a challenging subject for further investigation. The effects of impurities on two-photon absorption, especially near the band edge, is poorly understood. The general question of the density of states accessible to two-photon processes, at non-zero temperature, near the band edge is both interesting and important. Scaling studies, showing the dependence of two-photon absorption on frequency, composition and structure, and temperature, are required. Above all, as in any study, the principal requirement is for good data, on well-characterized materials.

Unresolved issues still remain in the subject of the optical breakdown of solids. This subject may be essentially academic, since other damage mechanism occur before bulk breakdown. Furthermore, the relevance of bulk breakdown to surface breakdown has been called into question, especially by Manenkov, since it is unlikely that the surface can be made free of defects, inclusions, and absorbed impurities. Nevertheless, it is important to obtain a complete understanding of the physics of this process, as part of our fundamental understanding of materials.



The scaling of breakdown thresholds with temperature and wavelength is of great importance in discriminating between competing theories. Scaling in pulse duration is needed to complete the picture. As Kelly and co-authors point out, careful attention must be paid to focusing conditions, and to defocusing by the incipient plasma. Pre-breakdown studies, like those reported by the NRC group using photoconductivity, provide valuable data on the behavior of electrons in the conduction band, data which must be fed back into the models used to describe the breakdown process.

Finally, it is not clear why different investigators get such widely disparate values for damage thresholds in alkali halides. The attribution of this disparity to the presence of impurities should be investigated, and an exchange of samples, if feasible, would clearly be of great benefit.

As stated in previous years, the need exists for a documentation project, consolidating the data which has been obtained over the past decade on laser materials, new coating materials, impurity effects, and damage thresholds. Without such a project, valuable information on optical materials may be overlooked, with an unnecessary repetition of measurements as a consequence.

## 5. Acknowledgment

The editors would like to acknowledge the invaluable assistance of Dr. Harold S. Boyne, Ms. Marilee Hood, Ms. Margaret Wooley, Ms. Sheila Aaker, and Ms. Florence Indorf and the other involved staff members of the National Bureau of Standards in Boulder, Colorado, for their interest, support, and untiring efforts in the professional operation of this Symposium and in the preparation and publication of the Proceedings. To these we must add Dr. James Harris, Ms. Patsy Collins, and others from the University of Dayton Research Institute. The continued success of the Damage Symposia would not have been possible without the enthusiastic support of those named above.

## 6. Bibliography

- [1] "Damage in Laser Glass," A. J. Glass and A. H. Guenther, Editors, ASTM Special Technical Publication 469, ASTM, Philadelphia, PA (1969).
- [2] "Damage in Laser Materials," A. J. Glass and A. H. Guenther, Editors, NBS Special Publication 341, U.S. Government Printing Office, Washington, D.C. (1970).
- [3] "Fundamentals of Damage in Laser Glass," N. Bloembergen, National Materials Advisory Board Publication NMAB-271, National Academy of Sciences, Washington, D.C. (1970).
- [4] "High Power Infrared Laser Windows," N. Bloembergen, National Materials Advisory Board Publication NMAB-292, National Academy of Sciences, Washington, D.C. (1972).
- [5] "Damage in Laser Materials: 1971," A. J. Glass and A. H. Guenther, Editors, NBS Special Publication 356, U.S. Government Printing Office, Washington, D.C. (1971).
- [6] "Laser Induced Damage in Optical Materials: 1972," A. J. Glass and A. H. Guenther, Editors, NBS Special Publication 372, U.S. Government Printing Office, Washington, D.C. (1972).
- [7] "Laser Induced Damage of Optical Elements, A Status Report," A. J. Glass and A. H. Guenther, Applied Optics 12, pp. 637-649 (1973).
- [8] "Laser Induced Damage in Optical Materials: 1973," A. J. Glass and A. H. Guenther, Editors, NBS Special Publication 387, U.S. Government Printing Office, Washington, D.C. (1973).
- [9] "Laser Induced Damage in Optical Materials, 1973: A Conference Report," A. J. Glass and A. H. Guenther, Applied Optics 14, pp. 74-88 (1974).
- [10] "Laser Induced Damage in Optical Materials: 1974," A. J. Glass and A. H. Guenther, Editors, NBS Special Publication 414, U.S. Government Printing Office, Washington, D.C. (1974).
- [11] "Laser Induced Damage in Optical Materials: 6th ASTM Symposium," A. J. Glass and A. H. Guenther, Applied Optics 14, pp. 698-715 (1975).
- [12] "Laser Induced Damage in Optical Materials: 1975," A. J. Glass and A. H. Guenther, Editors, NBS Special Publication 435, U.S. Government Printing Office, Washington, D.C. (1975).
- [13] "Laser Induced Damage in Optical Materials: 7th ASTM Symposium," A. J. Glass and A. H. Guenther, Applied Optics 15, No. 6, pp. 1510-1529 (1976).
- [14] "Laser Induced Damage in Optical Materials: 1976," A. J. Glass and A. H. Guenther, Editors, NBS Special Publication 462, U.S. Government Printing Office, Washington, D.C. (1976).
- [15] "Laser Induced Damage in Optical Materials: 8th ASTM Symposium," A. J. Glass and A. H. Guenther, Applied Optics 16, No. 5, pp. 1214-1231 (1977).

A. J. Glass  
A. H. Guenther





## INTRODUCTION AND WELCOME

Arthur H. Guenther  
Air Force Weapons Laboratory/CA  
Kirtland AFB, New Mexico 87117

Haynes Lee, Chairman of Subcommittee 2 on Lasers of the ASTM, has asked me to welcome you on behalf of the ASTM. Unfortunately he will not be able to join us this week.

The ASTM is pleased to again collaborate in cultivating the interchange of information vital to its primary aims. The ASTM looks to this conference as one of the most important inputs to the development of standards relating to lasers and related fields. Obviously one must develop standards from a basis of knowledge soundly developed, freely discussed and finally tested. This is a prime goal of the ASTM.

The Subcommittee on Lasers will be holding their working session this Thursday afternoon and Friday at the conclusion of this meeting, including the working groups on optically pumped lasers, light emitting diodes, energy and power measurement and finally infrared lasers and laser materials. These groups have collectively produced several standards this past year with many more in various stages of preparation. Don Liebenberg of the Los Alamos Scientific Laboratory, Chairman of the Optically Pumped Group, has asked me to mention their plans for a mini-symposium early next year at the next ASTM meeting in Florida on the manual and automatic reduction of interferograms. You can contact him for further details.

Haynes Lee has also asked me to invite anyone interested in the development of standards in the laser or allied fields to participate in these working sessions, particularly the infrared laser and laser materials group under the chairmanship of Herb Lipson. This group will be working on standard specifications for light scattering as well as methods of testing optical absorption by calorimetry for both bulk materials and coated surfaces. Initial discussions on loss or refractive index variations in fiber optics may also take place.

Finally I'd like to mention that the ASTM is a voluntary standards group consisting of members from government, industrial and academic institutions. It is the only organization with a concentrated effort underway in developing standards in the laser field. At the present time discussions are underway concerning possible joint ventures in the standards area between the Optical Society of America and the ASTM, probably using the existing ASTM mechanism for the development of consensus standards. We hope many of you will stay for the working sessions, become familiar with our operation, and participate in our activities.

Now to the subject at hand, speaking for Alex Glass and myself, I would like to welcome you to the Ninth Annual Boulder Damage Symposium. After eight years of operating this meeting one wonders how he gets his adrenalin up to go through the pains of yet another symposium, now formally entitled "Materials for High Power Lasers." But upon reflection, it is quite easy to understand. It is because of the support that we have received not only from the National Bureau of Standards and the ASTM but perhaps more important the energetic and cooperative attitude of those individuals who aid us in the operation of this meeting, and this, of course, includes you the participants.

I have already talked of the ASTM under whose aegis this series of meetings was initiated. The prime mover here at the National Bureau of Standards is Dr. Hal Boyne, Chief of the Electromagnetics Division. To him and his staff we are grateful for the hospitality and the use of these excellent facilities. Those NBS individuals to whom we are especially indebted include Florence Indorf, Margaret Woolley, and Marilee Hood who are concerned with the details of the operation of the meeting, the assembling of the proceedings, and financial management, respectively. Of course, there are others to whom Alex and I are also thankful for making the operation of this meeting a most rewarding experience. They are those sponsors who have tangibly supported this meeting through underwriting the expense of its operation. They include Joel Weiss at ERDA, Harry Winsor at ARPA, and Herschel Piloff of the Office of Naval Research. We would be remiss in not acknowledging the active participation of Jim Harris, Patsy Collins and others from the University of Dayton Research Institute who have aided not only in the operation of this meeting, but certainly and most important in coordinating activities during this week between ARPA, the ASTM, and the National Bureau of Standards.

We fully expect this to be our biggest and best symposium, i.e., until next year when we hold our tenth annual meeting. At that time we expect to pause and reflect upon the past ten years' activities. It is our intent to have distinguished speakers who are acknowledged principal contributors in the many facets of the laser damage field. We will ask them to summarize and quantify as best as possible the state-of-the-art and the state-of-the-understanding in their specialty. These review or tutorial

lectures will then be assembled and published as a separate volume on the subject of laser induced damage in optical materials. We are also thinking of the possibility of having round-table discussions on those specific subjects in which there is still some question as to the correctness of our understanding. Of course, we will have contributed papers as well. We solicit your thoughts on this proposed approach and comments or criticisms on the operation of this meeting and our intentions for our tenth annual meeting next year are welcomed.

Returning to this year's meeting, I would like to mention some pertinent features. Because of the economies and improved communications realized last year by holding several meetings on related subjects consecutively at the same location, we again closely coordinated the activities of this meeting with ARPA and its contractors. After initial paper selections by a joint committee, those papers most appropriate because of content were identified to be presented at the recently concluded ARPA meeting. Greater than 60 papers remained as submitted to this, the ASTM meeting. Of these, roughly 32 were selected for oral presentation to the participants at this meeting, while 20 were selected for presentation in a poster format. Other papers were selected by title only, with some rejected outright. The sum total of this effort was to hold the meeting to two days, allowing the ASTM to conduct their business meetings Thursday afternoon and Friday.

As a result of the highly successful initiation and popularity of poster sessions last year and the very favorable comments received from both presenters and participants at the meetings, we selected those papers which contained detailed data, descriptions of complex instruments, and particularly those papers dealing with comparative data which is best viewed side by side in close proximity for presentation in two poster sessions. These types of papers would be difficult to present effectively using slides or vugraphs. There were, as well, many papers submitted specifically requesting presentation at a poster session. In general, they were from people who had presented poster papers last year and appreciated the personal interest, the close interaction and idea exchange that was evidenced at those sessions.

It has always been our intention to avoid concurrent sessions or unduly short presentations. Furthermore, this meeting has had a trademark of remaining on schedule while leaving ample time for discussion. The increase in poster sessions follows naturally from these objectives. Each poster paper will be manned approximately 3 hours as indicated on your program. These sessions are interspersed to break up long periods which would be necessary for your attendance in the auditorium. My one note of caution is to ask you to please return, however, to the presented papers session on time at the conclusion of each poster session.

Alex and I would like to issue an especially warm welcome to our foreign participants from Canada, England, South Africa, France, Australia, and the Soviet Union. We would particularly like to thank Prof. Manenkov for taking the time to travel this great distance to present a paper on his recent work dealing with avalanche breakdown. His paper will be presented on Thursday morning.

We have seen a dynamic yet gradual change from one year to another in this meeting. We have always left room to develop a detailed appreciation of factors and interactions of new features, revealed by greater understanding, from the establishment of a solid foundation arrived at through an open and frank discussion of previous contributions. As can be anticipated, papers presented at this meeting continue to concentrate on those areas of most importance to the high power, high energy laser community, those being infrared laser window, surfaces and mirrors, thin films, and finally the theoretical aspects of fundamental mechanisms describing the threshold laser interaction with optical media. This year, as expected, we note a continued trend from the infrared to shorter wavelengths, and this trend has been programmed into this meeting so that it will flow smoothly from yesterday's meeting toward the shorter wavelengths at the end of the week. You will note additional scaling laws presented this year and verification where possible of those surfaced last year. Several papers deal with pulse length, surface roughness, area, and wavelength dependence of laser induced damage. These contributions are principally covered in the poster sessions.

Last year in his opening remarks, Alex Glass speculated on why the same topics keep appearing. It is obviously because we are dealing with real materials in the real world. In some cases, mechanisms are sufficiently understood that the salient material property has been identified; thus detailed information concerning materials properties is now of prime importance, that is, the achievable material properties, not the ideal, perfect material properties. While in other areas we are searching for clues through theoretical analysis and through careful parametric studies and derivation of scaling laws which will form the basic data to which future theories can be compared, still others have become so complex that no theory is universally accepted. Here I speak of avalanche breakdown mechanisms and particularly in the related case of breakdown statistics. There just appears to be too many variables and the identification of a new unexpected influence only uncovers a much more complex situation. An appreciation of this complexity is particularly evident when dealing with real world materials. You will find in this meeting that we have attempted to strike a balance between performance, properties and understanding of the laser damage process in materials. I don't wish to leave



you with the impression that we haven't made progress, for today little is said of the influence of absorbing inclusions in the bulk as a pulsed breakdown mechanism or of self-focusing. Improved processing has solved the first and an adequate theory has allowed design around the second, pointing the appropriate direction in which to go for developing improved materials.

I would like to dwell, however, a moment or two on one of Alex's and my favorite subjects, that is, thin films and its place in the arena of laser induced damage. Laser interaction studies with thin films have revealed a lack of basic understanding regarding thin films. These films represent effectively a new state of matter since in layers, from 100 to 1,000 nanometers thick, electronic and structural properties are significantly different than in the bulk material. This is in general the reason why no material has been found to damage at the same level in the bulk and thin film form. One way of assessing the reason why the state of knowledge of optical thin films is as it is would be by contrasting them with electronic materials in thin film forms. I would like to quote from a paper entitled "The Importance of Being Defective" by Shulman and Schlifkin of the University of North Carolina. They state "Because solids are rather susceptible to the occurrence of atomic scale defects in their structures, impurity atoms, vacant lattice sites, interstitial atoms and aggregations of these imperfections, they are actually much more interesting and versatile materials than they would otherwise be. Thus the useful electronic behavior of insulating and semi-conducting crystals comes about in the vast majority of cases from imperfections built into them in a controlled fashion. These defects exert and influence physical properties quite out of proportion to the low concentrations in which they are incorporated." Thus, you see that it is viewed that the important electronic properties of thin films depend in large measure on defects, that is, their departure from a perfect structure and pure material. Furthermore, the properties of interest are generally those which describe some average behavior, such as conductivity. This is usually measured in the long dimension parallel to the surface. (In addition, these materials are almost always employed in very small sizes, such as chips.) While electronic materials may be made in large sizes, it is a simple matter to reject any micro-sized element which does not exhibit the desired properties. There is no question that great advances have been made in our understanding of electronic materials in thin film form because of their tremendous commercial value. Thus there is an economic incentive for research and development in this field, that is, the electronic characterization of materials in thin film form.

In contrast, optical materials when employed in thin film form at high levels of optical radiation will fail at some Achilles heel, that is, at a defect or structure modification such as crystal disorder, vacancy, impurity, dislocation, etc. This factor compounds the difficulty in producing these coatings for large optical elements or components in which the cost of the substrate may exceed by many times that of the deposited thin film. Generally one is concerned with the properties of the film in the short dimension perpendicular to the surface, but spatially resolved. In addition, there is no commercially intensive market for large quantities of optics to be used under intense levels of radiation at the present time. For this reason there is insufficient payoff for large industrial research and development activities, particularly when one realizes that the majority of optical coatings are produced by a handful of generally small commercial organizations. The whole picture is compounded when one realizes that optical thin films may be multi-layers of many elements each having different physical as well as optical properties and can be deposited on surfaces of other than plane geometry where varying angles of incidence may produce undesirable or non-uniform characteristics. We could list a multitude of other factors too long and probably incomplete that influence the ultimate behavior of deposited thin films, that is, their optical behavior.

There appears to be only one sufficiently fundamental thread of knowledge which would help unravel the above described state of affairs. That would be to understand the correlation between the detailed structure and purity of the thin film and its resultant optical properties. This appears to be a very appropriate area in which funding agencies could establish some measurable research effort since it will probably not be sufficiently attacked by industry. Its solution could lead to real advances in the utility of coated elements. The principal questions regarding thin films are the following: How do the optical properties of the film, such as refractive index, absorption, scattering, breakdown threshold relate to the physical and chemical parameters such as morphology, composition, phase, porosity, impurity and defect composition? And secondly, how do these physical parameters depend on the preparation methods and on the basic materials and substrate utilized? To these two principal questions I would add the following comment, that the cost of characterization and instrumentation required may exceed that of the optical element itself or the research project as well. But this is the only way that we can identify those parameters which are important in correlating structure and real world optical behavior. With that thought I would like now to turn the meeting over to what was bound to happen as can be noted in your program - your chairman for the first session on Infrared Laser Window Materials - Arthur Glass.

## SI CONVERSION UNITS

In view of present accepted practice in this technological area, U. S. customary units of measurement have been used throughout this report. It should be noted that the U. S. is a signatory to the General Conference on Weights and Measures which gave official status to the metric SI system of SI units in 1960. Readers interested in making use of the coherent system of SI units will find conversion factors in ASTM Standard Metric Practice Guide, ASTM Designation E 380-76 (available from American Society for Testing and Materials, 1916 Race Street, Philadelphia, Pennsylvania 19103). Conversion factors for units used in this paper are:

### Length

$$1 \text{ in} = 0.0254^* \text{ meter}$$

$$1 \text{ ft} = 0.3048^* \text{ meter}$$

$$1 \text{ microinch} = 2.5400^* \times 10^{-8} \text{ meter}$$

### Area

$$1 \text{ in}^2 = 6.4516^* \times 10^{-4} \text{ meter}^2$$

$$1 \text{ ft}^2 = 9.2903 \times 10^{-2} \text{ meter}^2$$

### Force

$$1 \text{ lb (lbf)} = 4.448 \text{ newton}$$

$$1 \text{ kip} = 4448 \text{ newton}$$

### Pressure Stress

$$1 \text{ psi} = 6895 \text{ pascal}$$

$$1 \text{ psf} = 47.88 \text{ pascal}$$

$$1 \text{ torr (mmHg. } 0^{\circ}\text{C)} = 133.32 \text{ pascal}$$

### Energy

$$1 \text{ ft-lbf} = 1.3558 \text{ joule}$$

### Moment

$$1 \text{ lbf-ft} = 1.3558 \text{ newtonmeter}$$

### Temperature

$$T_{\circ}\text{C} = 5/9 (T_{\circ}\text{F} - 32)$$

### Heat

Thermal conductivity,  $\kappa$

$$1 \text{ cal (thermochemical) cm.s. } ^{\circ}\text{C} = 418.40^* \text{ watt/meter kelvin}$$

specific heat, C

$$1 \text{ cal (thermochemical)}/\text{gm. } ^{\circ}\text{C} = 4184.00^* \text{ joule/kilogram-kelvin}$$

---

\*Exact Value



## EXTRINSIC ABSORPTION IN INFRARED LASER-WINDOW MATERIALS

M. Flannery and M. Sparks  
Xonics, Incorporated  
Santa Monica, California 90401

Duthler's analysis and tabulation of molecular-ion-impurity lines is updated and extended to include infrared wavelengths other than  $10.6\ \mu\text{m}$ , to include other molecular ions, and to include other types of impurities. The results support our previous suggestion that the most likely explanation of typical lower absorptance at  $5.25\ \mu\text{m}$  than at  $10.6$ ,  $3.8$ , or  $2.8\ \mu\text{m}$  is simply the difference between the extrinsic absorptance at the different frequencies. The results are displayed in correlation-type charts to allow either the identification of impurities to avoid at a given wavelength or the selection of a wavelength at which impurity absorption is likely to be small. Absorption at the low level of  $\beta = 10^{-4}\ \text{cm}^{-1}$  can occur at frequencies many line widths from an absorption peak.

Key words: Infrared absorption; laser windows; molecular impurities; molecular ions; molecular spectra; optical materials; surface absorption.

### Introduction

Deutsch [1]<sup>1</sup> has studied the infrared absorptance of various impurities on the surfaces of window samples, and Duthler [2] proposed that an important class of impurities limiting infrared transmission in alkali-halide laser window materials is molecular-ion impurities which substitute for the halide ion in these crystals. In the present investigation, we extend Duthler's analysis and tabulation to include other materials and other infrared laser frequencies, in addition to  $10.6\ \mu\text{m}$ .

Recently there has been considerable interest in reducing the absorption coefficient  $\beta$  of transparent materials used in high-power infrared laser systems. Laser windows can fail catastrophically by fracturing due to inhomogeneous internal stresses, or less dramatically due to thermal defocusing of the beam which result from heating by absorbed radiation.

Among the promising materials for use with high-power  $10.6\ \mu\text{m}$  wavelength  $\text{CO}_2$  lasers are the alkali halides, in particular  $\text{KCl}$  and  $\text{KBr}$ . The mechanism for intrinsic infrared absorption in these materials is multiphonon absorption, with the fundamental Reststrahl frequency  $\nu_L$  being 6 to 8 times smaller than the  $\text{CO}_2$  laser frequency of  $943\ \text{cm}^{-1}$ . It has been established experimentally [1] and theoretically [3] that for  $\nu > \nu_L$ , the intrinsic multiphonon absorption coefficient  $\beta_{\text{int}}$  decreases nearly exponentially with increasing frequency. Extrapolation of the measured low-frequency intrinsic absorption coefficients yields  $\beta_{\text{int}} = 8 \times 10^{-5}\ \text{cm}^{-1}$  for  $\text{KCl}$  and  $\beta_{\text{int}} = 5 \times 10^{-7}\ \text{cm}^{-1}$  for  $\text{KBr}$  at  $10.6\ \mu\text{m}$ . However, absorption in the best presently available  $\text{KBr}$  is impurity dominated with  $\beta > 10^{-5}\ \text{cm}^{-1}$  at the  $\text{CO}_2$  laser frequency, while  $\text{KCl}$  has been produced with intrinsic absorption at this frequency. At higher frequencies the absorption in both materials is extrinsic.

The purposes of the present paper are to study the important class of infrared-absorbing polyatomic molecular-anion impurities which substitute for the halide ions in the crystal lattices and to identify those ionic impurities that absorb most strongly at the infrared laser frequencies:  $\text{HF}$ ,  $2.7\ \mu\text{m}$  ( $3704\ \text{cm}^{-1}$ );  $\text{DF}$ ,  $3.8\ \mu\text{m}$  ( $2630\ \text{cm}^{-1}$ );  $\text{CO}$ ,  $5.25\ \mu\text{m}$  ( $1905\ \text{cm}^{-1}$ ); and  $\text{CO}_2$ ,  $10.6\ \mu\text{m}$  ( $943\ \text{cm}^{-1}$ ). Particular emphasis will be given to the  $\text{HF}$  and  $\text{CO}_2$  laser frequencies. The influence of absorbing inclusions on the bulk absorption coefficient and the failure of materials containing inclusions have been considered in previous publications [4,5].

Nominally pure commercial crystals are commonly observed to contain molecular-anion impurities, such as the metaborate ion ( $\text{BO}_2^-$ ) [6,7] and the carbonate ion ( $\text{CO}_3^{2-}$ ) [6], using conventional absorption spectroscopy. The hydroxyl ion ( $\text{OH}^-$ ) is especially difficult to remove from alkali halides during purification [8], and may be the ion limiting absorption at  $2.7\ \mu\text{m}$ . These anion impurities along with divalent metal cation impurities [8,9] are most likely still present in small concentrations in

1. Figures in brackets indicate the literature references at the end of this paper.

specially purified laser window materials since less than one part per million of certain anions can result in the presently observed extrinsic absorption.

Molecular-cation impurities are less likely to be found in alkali-halide crystals because of the small size of the alkali ions which they replace, although  $\text{NH}_4^+$  in  $\text{KCl}$  has been studied [10]. Monatomic impurities can also absorb infrared radiation either through local modes of vibration or by activating phonons other than the fundamental Reststrahl phonon [11]. However, absorption due to monatomic impurities from  $943\text{ cm}^{-1}$  to  $3704\text{ cm}^{-1}$  is expected to be negligible because phonon and local mode frequencies are generally much smaller than the laser frequency: The local mode of  $\text{H}^-$  in  $\text{KCl}$  (U center) at  $500\text{ cm}^{-1}$  has the highest frequency of this group. Absorption due to electronic transitions of impurities is not considered in this paper [12].

### Impurity Spectra

The infrared absorption spectrum of a crystal containing substitutional molecular-anion impurities typically consists of a number of sharp lines corresponding to the infrared active internal vibration modes of the polyatomic molecular ion. Generally the internal vibrations of the impurity ions are only slightly affected by the host crystal: There are small shifts in frequency and increases in the line width which depend upon the particular host. As a result of a lowering of the symmetry when the ion interacts with the host, infrared inactive modes may become weakly absorbing and degenerate modes may be split into several components. In fact, the technique of alkali-halide matrix isolation has been used extensively to isolate and concentrate these ions for study by infrared absorption spectroscopy.

The probability of the laser frequency being exactly coincident with the peak of a given impurity absorption line is extremely small, the laser line usually falling in the wings of the absorption line. In order to estimate the absorption coefficient  $\beta$  at the laser frequency  $\nu$  due to an absorption line centered at frequency  $\nu_0$ , a Lorentzian line shape

$$\beta(\nu) = \frac{\beta(\nu_0)(\Delta\nu/2)^2}{(\nu - \nu_0)^2 + (\Delta\nu/2)^2} \quad (1)$$

is assumed, where  $\Delta\nu$  is the full width at half maximum. With 0.1 percent impurity concentration, the absorption coefficient  $\beta(\nu_0)$  at the center of an allowed transition typically ranges from  $10^2\text{ cm}^{-1}$  to  $10^3\text{ cm}^{-1}$  and  $\Delta\nu$  ranges from  $4\text{ cm}^{-1}$  to  $50\text{ cm}^{-1}$ , depending on the particular molecular species and host.

Although experimentally observed line-shapes near resonance are described quite accurately by eq. (1) using a constant relaxation frequency  $\Delta\nu$  [13-16], for extrapolation to the wings it is used with certain reservations. Widths of the fundamental absorption lines of matrix-isolated molecular impurities are in general a result of weak coupling between the internal molecular vibrations and the lattice vibrations of the host crystal [17]. With  $|\nu - \nu_0| < \nu_m$ , where  $\nu_m$  is the maximum phonon frequency ( $210\text{ cm}^{-1}$  for  $\text{KCl}$ ), there will be structure in  $\Delta\nu$ , hence in  $\beta(\nu)$ , reflecting the one-phonon density of states and phonon selection rules. This will be important for extrapolation of narrow lines ( $\Delta\nu \lesssim 10\text{ cm}^{-1}$ ), since the measured line width in this case samples only a small part of the phonon spectrum.

For extrapolation far from the line center  $|\nu - \nu_0| > \nu_m$ ,  $\Delta\nu$  is expected to decrease with increasing  $|\nu - \nu_0|$  resulting in a more rapid decrease in  $\beta$  than is predicted by eq. (1). In this region it is likely that  $\beta$  will decrease exponentially with increasing  $|\nu - \nu_0|$  in analogy with intrinsic multiphonon absorption [3]. Nevertheless, judicious use of eq. (1) together with measured impurity line strengths and line widths from the experimental literature is felt to be reliable for order-of-magnitude upper-bound estimates of  $\beta$  at any particular laser frequency.

The fundamental absorption lines of molecular-ion impurities are often accompanied by other nearby lines, which may not be resolved at room temperature and may be confused with the fundamental line width. In the case of small ions such as  $\text{OH}^-$  and  $\text{NO}_2^-$  the additional lines arise from rotational and local translational motions of the ions [17-23]. (Recall that for a freely rotating diatomic molecule, the angular momentum selection rule requires that the vibrational transition be a doublet.) The fundamental absorption lines of large polyatomic ions are often accompanied by nearby "hot" bands from transitions originating from low-energy excited states, and by isotope lines [7,24].



A number of the molecular-ion impurities that have been isolated in KCl crystals are listed together with their measured absorption frequencies in the first two columns of table 1 [25-51]. The third through sixth columns present the estimated impurity concentrations in parts per million for each ion that are required to produce  $\beta = 10^{-4} \text{ cm}^{-1}$  at 300 K and 2.7, 3.8, 5.25, and 10.6  $\mu\text{m}$ , respectively. These estimates were obtained by extrapolating the measured absorption lines using an assumed Lorentzian line shape with measured line widths where they were available. The estimates that appear in brackets are especially low because the laser line is more than 10  $\Delta\nu$  from any impurity line. Details of the spectra can be found in the original literature references which are listed in the last column.

Isolated diatomic ions typically have fundamental absorption frequencies that are far removed from the  $\text{CO}_2$  laser frequency  $943 \text{ cm}^{-1}$ . As a result, impurities such as  $\text{OH}^-$  that are commonly observed in alkali halides should have little effect on absorption at  $943 \text{ cm}^{-1}$  in spite of the large line width of typically  $50 \text{ cm}^{-1}$  at room temperature. Using  $\beta(\nu_0) \approx 30 \text{ cm}^{-1}$  and  $\Delta\nu = 50 \text{ cm}^{-1}$  in eq. (1) for 1000 ppm,  $\text{OH}^-$  in KCl yields  $\beta(943 \text{ cm}^{-1}) \approx 10^{-4} \text{ cm}^{-1}$  at 40 ppm [22].

The polyatomic impurities  $\text{BO}_3^{3-}$ ,  $\text{HCO}_3^-$ ,  $\text{SO}_4^{2-}$ ,  $\text{CrO}_4^{2-}$ ,  $\text{MnO}_4^{2-}$ , and  $\text{ClO}_3^-$  yield  $\beta(943 \text{ cm}^{-1}) > 10^{-4} \text{ cm}^{-1}$  at concentrations less than 0.1 ppm. These impurities, if present in alkali-halide laser windows, will result in a severe limitation in the laser transmission.

The case of  $\text{BO}_3^{3-}$  illustrates the effect of near coincidence of the laser frequency with an absorption line of the molecular ion. Here approximately 45 percent of the absorption at  $943 \text{ cm}^{-1}$  is contributed by the strong absorption line at  $\nu_3 = 1222 \text{ cm}^{-1}$  (with  $\Delta\nu = 30 \text{ cm}^{-1}$ ) while most of the remaining absorption is from the weak absorption at  $\nu_1 = 949 \text{ cm}^{-1}$  (with  $\Delta\nu = 5 \text{ cm}^{-1}$ ), which is only  $6 \text{ cm}^{-1}$  from the laser frequency.

With  $\text{HCO}_3^-$  the principal absorption at  $943 \text{ cm}^{-1}$  is from the  $\nu_5 = 971 \text{ cm}^{-1}$  fundamental. Estimating from published absorption curves that  $\beta(971 \text{ cm}^{-1}) = 10^3 \text{ cm}^{-1}$  and  $\Delta\nu = 12 \text{ cm}^{-1}$  with 400 ppm, eq. (1) yields  $\beta(943 \text{ cm}^{-1}) = 29 \text{ cm}^{-1}$ . Including additional contributions from  $\nu_3 = 1218 \text{ cm}^{-1}$  and  $\nu_4 = 1346 \text{ cm}^{-1}$  which have  $\Delta\nu \approx 15 \text{ cm}^{-1}$  and  $\Delta\nu = 50 \text{ cm}^{-1}$ , respectively, results in  $\beta(943 \text{ cm}^{-1}) = 10^{-4}$  with a concentration of 0.1 ppm.

The  $\text{ClO}_3^-$  ion produced a  $\beta(943 \text{ cm}^{-1}) = 10^{-4} \text{ cm}^{-1}$  at a concentration of only 0.001 ppm, the lowest concentration for any ion studied. This was produced by the two strong, broad absorptions just below the laser frequency:  $\nu_3 = 970 \text{ cm}^{-1}$  with  $\Delta\nu = 45 \text{ cm}^{-1}$  and  $\nu_1 = 940 \text{ cm}^{-1}$  with  $\Delta\nu = 15 \text{ cm}^{-1}$ .

The polyvalent ions listed in table 1 each have several absorption lines near  $943 \text{ cm}^{-1}$ . In order to preserve the charge neutrality of the crystal, divalent impurity anions must be accompanied by compensating anion vacancies, or as is frequently observed, by a divalent cation impurity (such as  $\text{Mg}^{2+}$ ,  $\text{Ca}^{2+}$ ,  $\text{Ba}^{2+}$ ,  $\text{Pb}^{2+}$ , or  $\text{Sr}^{2+}$ ) which are usually located at neighboring lattice sites. In heavily doped crystals, the solubility of the divalent anions is enhanced by simultaneous doping with divalent cations. The exact absorption frequencies and relative line strengths of the anions are dependent on the particular accompanying cation, especially in the case of  $\text{CO}_3^{2-}$  which is strongly perturbed with different metal ions.

The group of divalent ions  $\text{SO}_4^{2-}$ ,  $\text{CrO}_4^{2-}$ ,  $\text{MnO}_4^{2-}$ ,  $\text{SeO}_4^{2-}$ ,  $\text{MoO}_4^{2-}$ , and  $\text{WO}_4^{2-}$  have similar spectra with the strong  $\nu_3$  fundamental of these ions falling very near to  $943 \text{ cm}^{-1}$ . Due to their large size,  $\text{MoO}_4^{2-}$  and  $\text{WO}_4^{2-}$  are reported to be insoluble in KCl and KBr [52]. Depending on the particular perturbing cation impurity, the normally threefold degenerate  $\nu_3$  fundamental of  $\text{SO}_4^{2-}$  is split into three strongly absorbing components from  $1050 \text{ cm}^{-1}$  to  $1200 \text{ cm}^{-1}$  each with  $\Delta\nu \approx 15 \text{ cm}^{-1}$ . The otherwise forbidden  $\nu_1$  fundamental becomes weakly absorbing in the crystal with frequencies from  $975 \text{ cm}^{-1}$  to  $980 \text{ cm}^{-1}$  and with  $\Delta\nu \approx 15 \text{ cm}^{-1}$ . Additional absorption lines due to the  $\nu_4$  and  $\nu_2$  fundamentals are observed near  $600 \text{ cm}^{-1}$  and  $500 \text{ cm}^{-1}$ , respectively. The components of the  $\nu_3$  fundamental of  $\text{CrO}_4^{2-}$  are even closer to the laser line than  $\text{SO}_4^{2-}$  with frequencies in this case varying from  $880 \text{ cm}^{-1}$  to  $950 \text{ cm}^{-1}$ .

As table 1 shows, the CO laser operating at  $1905 \text{ cm}^{-1}$  has the lowest absorption from molecular ions. The  $\text{BO}_3^{3-}$  ion is the only one predicted to give an absorption of  $\beta = 10^{-4} \text{ cm}^{-1}$  at a

concentration of 0.1 ppm. For this ion, 80 percent of the absorption at  $1905\text{ cm}^{-1}$  comes from the fundamental at  $\nu_3 = 1222\text{ cm}^{-1}$  with  $\Delta\nu = 30\text{ cm}^{-1}$ , with an additional 15 percent from the  $\nu_2 + \nu_3$  summation band at  $\nu = 1944\text{ cm}^{-1}$  with  $\Delta\nu = 5\text{ cm}^{-1}$ . Since such a large portion of the absorption at  $1905\text{ cm}^{-1}$  comes from the  $\nu_3$  fundamental which is over twenty line widths away, the estimate of 0.1 ppm  $\text{BO}_3^{3-}$  might reasonably be revised upward to 0.3 ppm.

At the CO laser frequency, only four other ions produce an absorption of  $\beta = 10^{-4}\text{ cm}^{-1}$  at concentrations less than 1 ppm:  $\text{BH}_4^-$  and  $\text{NH}_4^+$  at 0.3 ppm, and  $\text{BO}_2^-$  and  $\text{HCO}_3^-$  at 0.5 ppm.

At the DF laser frequency,  $\nu = 2632\text{ cm}^{-1}$ , only  $\text{SH}^-$ ,  $\text{NH}_4^+$ , and  $\text{NCO}^-$  yield  $\beta(2632\text{ cm}^{-1}) = 10^{-4}\text{ cm}^{-1}$  at concentrations less than 0.1 ppm. For  $\text{SH}^-$  and  $\text{NH}_4^+$  the absorption is from the fundamental S-H and N-H stretching modes at  $2590\text{ cm}^{-1}$  and  $3100\text{ cm}^{-1}$ , respectively. The absorption of  $\text{NCO}^-$  at  $2632\text{ cm}^{-1}$  is expected to be particularly sensitive to the host and its preparation because the absorption at  $2632\text{ cm}^{-1}$  is dominated by a weak fourth harmonic at  $2613\text{ cm}^{-1}$  ( $\Delta\nu = 9\text{ cm}^{-1}$ ) of the  $\nu_2$  fundamental.

The absorption coefficient of KCl at the HF laser frequency,  $\nu = 3704\text{ cm}^{-1}$ , will certainly be dominated by absorption from the hydroxyl radical. Using  $\beta(\nu_0 = 3640\text{ cm}^{-1}) = 30\text{ cm}^{-1}$  and  $\Delta\nu = 50\text{ cm}^{-1}$  in eq. (1) for 1000 ppm,  $\text{OH}^-$  in KCl yields  $\beta(3704\text{ cm}^{-1}) = 10^{-4}\text{ cm}^{-1}$  at 0.03 ppm. This ion will be particularly difficult to exclude from the alkali halides because of the ubiquitous nature of water and the similarity in size and electronegativity of the halide and hydroxyl ions.

At concentrations of 0.1 ppm the ammonium ion yields an absorption of  $\beta(3704\text{ cm}^{-1}) = 10^{-4}\text{ cm}^{-1}$  from a broad N-H stretching fundamental at  $3100\text{ cm}^{-1}$ , but this ion is less likely to be present than the hydroxide ion.

#### Temperature Dependence

Absorption frequencies and line widths of matrix-isolated ions are observed to be temperature dependent, which can result in temperature-dependent absorption at the laser frequency. In the case of ions which have broad absorption lines resulting from coupling to the lattice phonons, and ionic fundamentals within the approximate range of  $50\text{ cm}^{-1}$  to  $300\text{ cm}^{-1}$  from the laser frequency, the temperature dependence can be simply predicted. With  $|\nu - \nu_0| \gg (\Delta\nu/2)$ , eq. (1) can be written

$$\beta(\nu) = \beta(\nu_0)(\Delta\nu/2)^2/(\nu - \nu_0)^2 \quad (2)$$

Above 100 K, the line widths  $\Delta\nu$  of the nitrite [13] ( $\text{NO}_2^-$ ), nitrate [13] ( $\text{NO}_3^-$ ), cyanate [14] ( $\text{NCO}^-$ ), and hydroxyl [22] ( $\text{OH}^-$ ) ions are observed to vary as  $T^n$  with  $n \approx 1.6$ , and will dominate the small temperature-dependent changes in  $\nu_0$  in eq. (2). As an example of this result,  $\beta(943\text{ cm}^{-1})$  will vary as  $T^{1.6}$ , especially in the important case of  $\text{NO}_2^-$ , where the approximations are fairly well satisfied. For  $\text{OH}^-$ , the use of the Lorentzian line shape is well justified only at  $3704\text{ cm}^{-1}$ . The absorption at the longer laser wavelengths due to this ion should have a stronger temperature dependence with  $n > 1.6$ , in analogy with intrinsic multiphonon absorption [53].

With the ions  $\text{SO}_4^{2-}$ ,  $\text{CrO}_4^{2-}$ , and  $\text{HCO}_3^-$  at the  $\text{CO}_2$  laser frequency and  $\text{NCO}^-$  and  $\text{BH}_4^-$  at the CO laser frequency the laser is operating near many relatively narrow lines and the temperature dependence of the absorption is more difficult to predict. Published spectra of these ions taken at different temperatures show small increases in line width and small shifts in frequency. In these cases changes in  $\nu_0$  can be nearly as important as changes in  $\Delta\nu$ , and it is not clear that the observed line widths are entirely due to phonon coupling. That is, part of the absorption in the wings which contributes at  $943\text{ cm}^{-1}$  could be due to hot bands, and, in the case of divalent ions, to different perturbing impurities accompanying the molecular ion. As a result, the  $943\text{ cm}^{-1}$  absorption of crystals containing these ions is expected to be less temperature dependent than crystals containing smaller, monovalent ions. It is interesting to note that figures 2 and 3 of Dem'yanenko, et al. [48], indicate that with  $\text{CrO}_4^{2-}$  in KCl, the  $943\text{ cm}^{-1}$  absorption could even decrease with increasing temperature.



## Additional Ions and Crystal Structures

The list in table 1 of some of the absorbing impurities that have been isolated and studied in KCl crystals illustrates the importance of substitutional molecular-anion impurities on infrared laser transmission. Other ions that are likely to limit transmission at  $943\text{ cm}^{-1}$  are  $\text{BeF}_4^{2-}$ , which has absorptions at approximately 909, 870 and  $770\text{ cm}^{-1}$  in KCl, the exact frequencies depending on the compensating ion, and  $\text{BF}_4^-$ , which absorbs at  $1131\text{ cm}^{-1}$  in KCl [54]. The molecular ion  $\text{PO}_4^{3-}$  has a strong absorption near  $1050\text{ cm}^{-1}$ , while  $\text{AsO}_4^{3-}$  probably absorbs at somewhat lower frequencies [55]. Also  $\text{SiO}_4^{4-}$  has a strong absorption near  $1000\text{ cm}^{-1}$  in several glasses [56].

There may be significant absorption at the CO laser frequency,  $1905\text{ cm}^{-1}$ , from  $\text{SCN}^-$ , which has a strong absorption at  $2038\text{ cm}^{-1}$  in KI and is known to be at least sparingly soluble in all the alkali halides despite its large size [57]. The  $\text{SeH}^-$  ion has an absorption at  $2294\text{ cm}^{-1}$  in KCl, which could produce significant absorption at both CO and DF laser frequencies [58]. Finally, there may be absorption at the HF laser frequency,  $3704\text{ cm}^{-1}$ , from  $\text{NH}_2^-$  or  $\text{NH}^{2-}$  ions which have bond-stretching frequencies near  $3400\text{ cm}^{-1}$  [55].

These results for molecular ions isolated in KCl can be expected to hold for other alkali halides if the laser frequency is not close to an impurity absorption frequency. As a general rule the absorption frequency of a molecular-ion impurity shifts by less than 5 percent as the host is changed from NaCl to CsI [53], while the solubility of the ion greatly increases. Since the solubility is controlled by the relative sizes of the impurity ion and the host ion it replaces, the solubility decreases precipitously when the host anion is smaller than the impurity ion. With the exception of  $\text{OH}^-$  and possibly  $\text{CN}^-$ , the molecular-ion impurities listed in table 1 have ionic radii larger than those of  $\text{F}^-$ , 0.136 nm, or  $\text{O}^{2-}$ , 0.140 nm, but smaller than  $\text{Cl}^-$ , 0.181 nm. Even in very thick samples only the strongest impurity absorption lines are detected when the ions are isolated in alkali fluorides, while very weak absorption lines are detected in KCl at concentrations of 1000 ppm. Since the ratio of strong to very weak absorptions often exceeds  $10^3$ , we estimate that the solubility limit of the molecular ions in fluorides and oxides is in the range 0.1-1 ppm. Therefore, most molecular-ion impurities are not expected to be a major source of absorption in alkaline-earth fluorides or oxides such as  $\text{Al}_2\text{O}_3$  used in HF, DF, or CO laser components. However, considerable concentrations of  $\text{OH}^-$  could be present in the alkaline-earth fluorides or  $\text{Al}_2\text{O}_3$ , which would account for the higher absorption observed at  $2.7\text{ }\mu\text{m}$  compared to that at  $3.8$  or  $5.25\text{ }\mu\text{m}$  [59].

There has been little systematic experimental work done on the effects of molecular-ion impurities on absorption in materials used for high-power laser components. Further studies of impurity-induced absorption at all the laser frequencies are needed to more firmly establish the relationship between the absorption in the wings and the fundamental absorption at the line centers. The temperature dependence of the absorption at laser frequencies found in intentionally doped crystals can possibly be used as a guide in identifying unknown impurities in other crystals.

A study of Pb-doped KCl found little correlation between absorption at  $943\text{ cm}^{-1}$  and the Pb concentration [60]. Isolated Pb ions are not expected to absorb at this frequency, but complexes of  $\text{Pb}^{2+}$  with the divalent anions listed in table 1 do absorb. The reason for the negative result of this experiment could be that there were no uncompensated divalent anions in the samples studied. In crystals containing divalent anions without accompanying divalent cations, the introduction of  $\text{Pb}^{2+}$  could have a significant effect, particularly in the case of  $\text{CO}_3^{2-}$ .

Doping KCl crystals with  $\text{OH}^-$  and  $\text{CO}_3^{2-}$  was found to have little effect on  $943\text{ cm}^{-1}$  absorption when the ions were introduced separately, but a significant increase in  $\beta(943\text{ cm}^{-1})$  was observed when both ions were present [51]. It is possible that in this case the enhanced absorption was due to the formation of  $\text{HCO}_3^-$  which is much more strongly absorbing at  $943\text{ cm}^{-1}$  than either  $\text{OH}^-$  or  $\text{CO}_3^{2-}$ .

In internally stressed KCl crystals it was observed that  $\beta(943\text{ cm}^{-1})$  was larger by a factor of two than after the same crystals were annealed [8]. This is difficult to explain on the basis of intrinsic absorption. Although there is little information available regarding the effects of inhomogeneous stresses on molecular-impurity absorption, we may speculate that the increased absorption observed in stressed crystals could be due to increased molecular-ion line widths and shifts in frequencies.

In addition to the substitutional ionic impurities, there are other possible molecular impurities that will limit infrared laser transmission. Neutral molecules such as  $H_2O$  or  $CO_2$  can exist at interstitial sites or at anion vacancies accompanied by cation vacancies in the bulk of the crystal [61-63]. Absorption from organic or inorganic molecules condensed on crystal surfaces is considered in the next section [64].

### Surface Contamination

Recent measurements of bulk and surface absorption, particularly at 2.8 or 3.8  $\mu m$ , are dominated by large surface absorptions as the total absorption approaches  $\beta = 10^{-4} \text{ cm}^{-1}$  [65-67]. Efforts have been made to correlate this surface absorption with crystal-growth techniques, mechanical or chemical polishes, and chemical surface cleaners [68-70]. Although specific culprits have been found and eliminated in some cases, there remains a high surface absorption which generally increases on prolonged exposure to the atmosphere. We propose that a large portion of this residual absorption is due to a conglomeration of impurities from the local environment deposited on the surface. This conglomeration may vary widely in its specific chemical composition, but must be heterogeneous enough to produce a fairly uniform absorption throughout the infrared spectral region.

The expected absorption from impurity compounds deposited on infrared optical surfaces is a complicated function of the number of chemical structures that absorb at a given frequency, the strength and width of their absorptions, the occurrence frequency of these chemical structures among all chemical compounds, the relative abundances of these compounds, and the dispersion characteristics of chemicals in the environment, such as vapor pressure, reactivity with other chemicals, etc. Figure 2 shows the absorption peaks of many of the ions in table 1, a few simple compounds, and some common chemical structures arranged in the order of their highest frequency absorption between 2 and 10  $\mu m$ . The leading edge of the absorptions in this type of correlation chart tends to have steps, which occur at frequencies where few types of chemical structures absorb, and plateaus, which occur at frequencies where large numbers of chemical structures absorb. Figure 1 has plateaus at  $\sim 2.9 \mu m$ ,  $\sim 4.6 \mu m$ , and  $\sim 6.8 \mu m$  which correspond quite nicely to distinct peaks in the total number of absorption bands at 2.8 - 3.0  $\mu m$ , 4.4 - 5  $\mu m$ , and 6.6 - 7.8  $\mu m$ .

Unfortunately this simple picture becomes clouded as one assembles simple chemical structures into complex chemicals. As the number of atoms increases, the number of strong fundamental vibration modes increases, bringing an increase in the number of weak difference modes. Beyond a certain point, adding atoms to large molecules tends not to increase the number of strong fundamental modes because remote parts of the molecule become weakly coupled. However, this weak coupling between adjacent structures increases the anharmonicity of the local fundamental modes which increases the strengths of overtone and combination modes [71]. These interactions in concert with external hydrogen or ionic bonding also tend to broaden the absorption bands. Therefore, to evaluate the absorption from a conglomeration of molecules, a correlation chart including some indications of the strength and width of the absorptions is needed. Such a chart is shown in figure 2 for a large number of chemical bonds, molecular ions, radicals and compounds between 0.5 and 15  $\mu m$ . The approximate spectrum of a complicated molecule can be assembled by a superposition of the spectra of its component parts. Additional correlation charts arranged by chemical structure can be found in references [55], [72], and [73]. Figure 2 tends to show that there is a rather even distribution of absorptions throughout the infrared region except for gaps at 4 - 5  $\mu m$  and 10 - 11  $\mu m$ . However, there do appear to be large numbers of strong absorptions at 2.9 - 3.5  $\mu m$ , around 6  $\mu m$ , and again around 8  $\mu m$  which could lead to increased absorption in these regions.

In addition to the location and strength of infrared absorption bands, it is necessary to have estimates of how frequently different chemical structures occur in compounds. Figure 3 shows the occurrence frequency of elements in 13520 organic chemicals listed in The CRC Handbook of Chemistry and Physics [72]. Of these compounds, 99 percent contained hydrogen, 74 percent oxygen, 42 percent nitrogen, and 16 percent chlorine, while no other element was present in more than 8 percent of the compounds. Therefore chemical bonds among this short list of elements should dominate the infrared surface absorption from organic compounds. Unfortunately, single bonds often suffer shifts in frequency and changes in absorption strength when they are combined in complex structures, necessitating the classification of the infrared absorptions of a much larger number of more complex structures which have consistent group absorption frequencies. Figure 4 lists 8462 organic chemicals according to their principal chemical group [73]. Generally compounds in a group may contain the chemical structures listed above it, but not those listed below. Most of the groups of compounds listed in this figure have well defined infrared frequencies commonly listed in infrared correlation charts. It is interesting to note that most of the structures listed contain only the four most common elements in figure 3: carbon, hydrogen, oxygen, and nitrogen.

Similar figures could be made for inorganic chemicals, but the results are less definitive. Oxygen is certainly the most pervasive element, probably followed by nitrogen or sulfur and then the halides [74]. But there is also a long list of metals which can cause rather large shifts in group frequencies and thus relatively poor correlations with simple structures.



## Acknowledgments

We are especially grateful to Dr. C. J. Duthler for discussion of previous work on this topic and for supplying a large amount of literature. This work was supported by the Defense Advanced Research Projects Agency.

## References

- [1] T. F. Deutsch, *J. Phys. Chem. Solids* **34**, 2091 (1973).
- [2] C. J. Duthler, *J. Appl. Phys.* **45**, 2668 (1974).
- [3] For theories of intrinsic multiphonon absorption see M. Sparks and L. J. Sham, *Phys. Rev. B* **8**, 3037 (1973) and references therein.
- [4] M. Sparks and C. J. Duthler, *J. Appl. Phys.* **44**, 3038 (1973).
- [5] C. J. Duthler, *Appl. Phys. Lett.* **24**, 5 (1974).
- [6] H. W. Morgan and P. A. Staats, *J. Appl. Phys.* **33**, 364 (1962).
- [7] J. C. Decius, J. L. Jacobson, W. F. Sherman, and G. R. Wilkinson, *J. Chem. Phys.* **43**, 2180 (1965).
- [8] R. C. Pastor and M. Braunstein, Hughes Research Laboratories Technical Report No. AFWL-TR-72-152, Vol. II, July (1973) (unpublished).
- [9] T. I. Maksimova, *Phys. Stat. Sol.* **33**, 547 (1969).
- [10] W. Vedder and D. F. Hornig, *J. Chem. Phys.* **35**, 1560 (1961).
- [11] A. A. Maradudin in *Solid State Physics*, Vol. 18, p. 274 and Vol. 19, p. 1, ed. by F. Seitz and D. Turnbull; M. A. Ivanov, M. A. Krivoglas, D. N. Mirline, and I. I. Reshina, *Sov. Phys.-Solid State* **8**, 150 (1966).
- [12] See for example J. T. Vallin, G. A. Slack, S. Roberts, and A. E. Hughes, *Phys. Rev. B* **2**, 4313 (1970).
- [13] V. P. Dem'yanenko and Yu. P. Tsyashchenko, *Sov. Phys.-Solid State* **11**, 3043 (1970).
- [14] I. I. Kondilenko, Yu. P. Tsyashchenko, and V. A. Pasechnyi, *Sov. Phys.-Solid State* **12**, 2990 (1971).
- [15] V. Schettino and I. C. Hisatsune, *J. Chem. Phys.* **52**, 9 (1970).
- [16] M. Tsuboi and I. C. Hisatsune, *J. Chem. Phys.* **57**, 2087 (1972).
- [17] R. Metselaar and J. van der Elsken, *Phys. Rev.* **165**, 359 (1968).
- [18] R. Bonn, R. Metselaar, and J. van der Elsken, *J. Chem. Phys.* **46**, 1988 (1967).
- [19] V. Narayanamurti, W. D. Seward, and R. O. Pohl, *Phys. Rev.* **148**, 481 (1966).
- [20] W. D. Seward and V. Narayanamurti, *Phys. Rev.* **148**, 463 (1966).
- [21] G. R. Field and W. F. Sherman, *J. Chem. Phys.* **47**, 2378 (1967).
- [22] B. Wedding and M. V. Klein, *Phys. Rev.* **177**, 1274 (1969).
- [23] M. V. Klein, B. Wedding, and M. A. Levine, *Phys. Rev.* **180**, 902 (1969).
- [24] D. F. Smith, J. Overend, J. C. Decius, and D. J. Gordon, *J. Chem. Phys.* **58**, 1636 (1973).
- [25] G. K. Pandey and D. K. Shukla, *Phys. Rev. B* **4**, 4598 (1971).
- [26] A. I. Stekhanov and T. I. Maksimova, *Sov. Phys.-Solid State* **9**, 2900 (1968).
- [27] C. K. Chau, M. V. Klein, and B. Wedding, *Phys. Rev. Lett.* **17**, 521 (1966).
- [28] C. K. Chi and E. R. Nixon, *J. Phys. Chem. Solids* **33**, 2101 (1972).
- [29] I. C. Hisatsune and N. H. Suarez, *Inorg. Chem.* **3**, 168 (1964).
- [30] J. C. Decius, C. R. Becker, and W. J. Fredericks, *J. Chem. Phys.* **56**, 5189 (1972).
- [31] K. O. Hartman and I. C. Hisatsune, *J. Chem. Phys.* **44**, 1913 (1966).
- [32] J. I. Bryant and G. C. Turrell, *J. Chem. Phys.* **37**, 1069 (1962).
- [33] A. Maki and J. C. Decius, *J. Chem. Phys.* **31**, 772 (1959).
- [34] R. Kato and J. Rolfe, *J. Chem. Phys.* **47**, 1901 (1967).
- [35] A. R. Evans and D. B. Fitchen, *Phys. Rev. B* **2**, 1074 (1970).
- [36] A. Strasheim and K. Buijs, *J. Chem. Phys.* **34**, 691 (1961).
- [37] J. van der Elsken and S. G. Kroon, *J. Chem. Phys.* **41**, 3451 (1964).
- [38] V. P. Dem'yanenko, Yu. P. Tsyashchenko, and E. M. Verlan, *Sov. Phys.-Solid State* **13**, 767 (1971).

- [39] N. G. Politov and B. M. Trakhbrot, *Sov. Phys.-Solid State* 14, 483 (1972).
- [40] S. C. Jain, A.V.R. Warriar, and H. K. Sehgal, *J. Phys. C* 6, 189 (1973).
- [41] V. P. Dem'yanenko, Yu. P. Tsyashchenko, and E. M. Verlan, *Phys. Stat. Sol.* 48, 737 (1971).
- [42] D. L. Bernitt, K. O. Hartman, and I. C. Hisatsune, *J. Chem. Phys.* 42, 3553 (1965).
- [43] E. H. Coker and D. E. Hofer, *J. Chem. Phys.* 48, 2713 (1968).
- [44] J. C. Decius, E. H. Coker, and G. L. Brenna, *Spectrochimica Acta* 19, 1281 (1963).
- [45] E. H. Coker, J. C. Decius, and A. B. Scott, *J. Chem. Phys.* 35, 745 (1961).
- [46] D. N. Mirlin and I. I. Reshina, *Sov. Phys.-Solid State* 10, 895 (1968).
- [47] V. P. Dem'yanenko, Yu. P. Tsyashchenko, and E. M. Verlan, *Sov. Phys.-Solid State* 12, 2527 (1971).
- [48] V. P. Dem'yanenko, Yu. P. Tsyashchenko, and E. M. Verlan, *Sov. Phys.-Solid State* 12, 417 (1970).
- [49] S. C. Jain, A.V.R. Warriar, and S. K. Agarwal, *J. Phys. Chem. Solids* 34, 209 (1973).
- [50] P. Manzelli and G. Taddei, *J. Chem. Phys.* 51, 1484 (1969).
- [51] H. G. Lipson, J. J. Larkin, and B. Bendow, *J. Electronic Mat.* 4, 1 (1975).
- [52] I. I. Kondilenko, V. A. Pasechny, and Yu. P. Tsyashchenko, *Phys. Stat. Sol.* 54, 783 (1972).
- [53] M. Sparks and L. J. Sham, *Phys. Rev. Lett.* 31, 714 (1973).
- [54] S. C. Jain, A.V.R. Warriar, and S. K. Agarwal, National Bureau of Standards, NSRDS-NBS 52, U.S. Government Printing Office, Wash. D.C., 1974.
- [55] N. B. Colthup, L. H. Daly, and S. E. Wiberley, *Introduction to Infrared and Raman Spectroscopy*, Academic Press, N.Y., 1975.
- [56] F. Matossi and O. Bronder, *Z. Physik* 111, 1 (1938).
- [57] M. A. Cundill and W. F. Sherman, *Phys. Rev.* 168, 1008 (1968).
- [58] F. Z. Fischer, *Z. Phys.* 187, 262 (1965).
- [59] C. Willingham, D. Bua, H. Statz, and F. Horrigan, Raytheon Research Division Final Technical Report, Contract DAAH01-74-C-0719, August 1975.
- [60] F. W. Patten, R. M. Garvey, and M. Hass, *Mat. Res. Bull.* 6, 1321 (1971).
- [61] T. J. Neubert and D. L. Roskelley, *J. Phys. Chem. Solids* 34, 493 (1973).
- [62] H. Gründig and C. Rühenbeck, *Z. Physik* 183, 274 (1965).
- [63] C. Rühenbeck, *Z. Physik* 207, 446 (1967).
- [64] T. F. Deutsch and R. I. Rudko, Raytheon Research Division Final Technical Report, Contract No. DAAH01-72-C-0194 (1973) (unpublished).
- [65] A. Hordvik, B. Bendow, H. G. Lipson, L. H. Skolnik, and R. N. Brown in *Laser Induced Damage in Optical Materials: 1976, 13-15 July 1976, Boulder, Colo.*, ed. by A. J. Glass and A. H. Guenther, NBS Special Publication 462, U.S. Government Printing Office, Wash. D.C., 1976, p. 50.
- [66] J. A. Harrington in *Laser Induced Damage in Optical Materials: 1976, 13-15 July 1976, Boulder, Colo.*, ed. by A. J. Glass and A. H. Guenther, NBS Special Publication 462, U.S. Government Printing Office, Wash. D.C., 1976, p. 45.
- [67] J. Harrington, D. Gregory, and W. Otto in *Fifth Annual Conference on Infrared Laser Window Materials, 1-4 Dec. 1975, Las Vegas, Nev.*, DARPA, Arlington, VA, Feb. 1976, p. 872.
- [68] M. Soileau, P. Temple, J. Bethke, and J. Shaffer in *Fifth Annual Conference on Infrared Laser Window Materials, 1-4 Dec. 1975, Las Vegas, Nev.*, DARPA, Arlington, VA, Feb. 1976, p. 91.
- [69] R. Turk, R. Pastor, A. Timper, M. Braunstein, and G. Heussner in *Fifth Annual Conference on Infrared Laser Window Materials, 1-4 Dec. 1975, Las Vegas, Nev.*, DARPA, Arlington, VA, Feb. 1976, p. 103.
- [70] J. Davisson in *Fifth Annual Conference on Infrared Laser Window Materials, 1-4 Dec. 1975, Las Vegas, Nev.*, DARPA, Arlington, VA, Feb. 1976, p. 113.
- [71] N. B. Colthup, L. H. Daly, and S. E. Wiberley, *Introduction to Infrared and Raman Spectroscopy*, Academic Press, N.Y., 1975, Chapter 1.
- [72] Robert C. Weast, ed. for *Handbook of Chemistry and Physics*, 55th ed., The Chemical Rubber Co., Cleveland, Ohio, 1973, pp. C-609 - C-638.



[73] Handbook of Tables for Organic Compound Identification, 3rd ed; compiled by Zvi Rappoport, The Chemical Rubber Co., Cleveland, Ohio, 1967.

[74] Robert C. Weast, ed. for Handbook of Chemistry and Physics, 55th ed., The Chemical Rubber Co., Cleveland, Ohio, 1973, pp. C-609 - C-638.

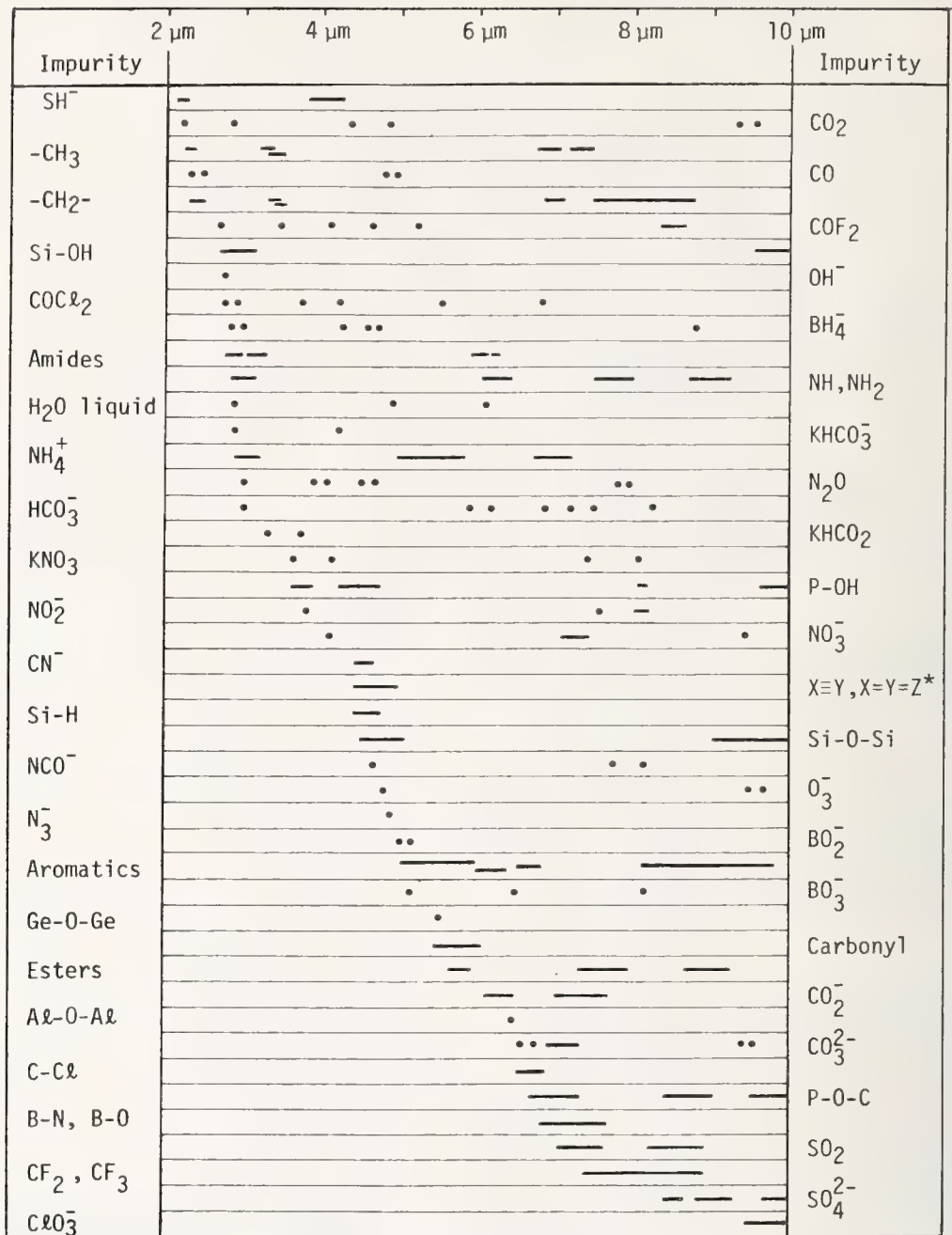
Table and Figures

Table 1. Experimentally observed absorption frequencies of some impurity ions isolated in KCl crystals with the estimated impurity concentration to produce  $\beta = 10^{-4} \text{ cm}^{-1}$  at the HF, DF, CO, and CO<sub>2</sub> laser frequencies at 300 K. Estimated concentrations in square brackets are more than ten full line widths from any impurity absorption line.

ION	FREQUENCIES ( $\text{cm}^{-1}$ )	$\nu = 3704 \text{ cm}^{-1}$ $\lambda = 2.7 \text{ }\mu\text{m}$	$\nu = 2632 \text{ cm}^{-1}$ $\lambda = 3.8 \text{ }\mu\text{m}$	$\nu = 1905 \text{ cm}^{-1}$ $\lambda = 5.25 \text{ }\mu\text{m}$	$\nu = 943 \text{ cm}^{-1}$ $\lambda = 10.6 \text{ }\mu\text{m}$	REFERENCES
H <sup>-</sup>	500	[40]	[20]	[10]	[1]	11
OH <sup>-</sup>	3610, 3640	0.03	[5]	[20]	[40]	22, 23, 25, 26, 27, 51
SH <sup>-</sup>	2578, 2590	[5]	0.01	[3]	[10]	28
CN <sup>-</sup>	2089, 4151	> 100	[20]	2	[80]	20, 21
BO <sub>2</sub> <sup>-</sup>	590, 1964, 1972	> 100	[70]	0.5	[70]	6, 29, 30
CO <sub>2</sub> <sup>-</sup>	1676	> 100	[30]	[2]	[20]	31
N <sub>3</sub> <sup>-</sup>	642, 2049	> 100	[40]	3	> 100	32
NC <sub>3</sub> <sup>-</sup>	631, 1211, 1297, 2182, 2403, 2499, 2613, 3373, 3459	1	0.03	[5]	[10]	15, 14, 24, 7, 33
NO <sub>2</sub> <sup>-</sup>	806, 1287, 1327, 2580	[20]	0.5	[1]	0.3	19, 13, 34, 18, 35
NO <sub>3</sub> <sup>-</sup>	843, 1062, 1396, 2446, 2789	[10]	0.5	[3]	0.3	16, 17, 13, 34, 18, 36, 37, 9
CO <sub>2</sub> <sup>2-</sup>	680-720, 883, 886, 1058, 1064, 1378, 1416, 1488, 1518	> 100	[80]	[10]	5	6, 38, 9, 39, 51
BO <sub>3</sub> <sup>-</sup>	736, 949, 1222, 1247, 1944	[3]	[1]	0.1	0.01	40
SeO <sub>3</sub> <sup>2-</sup>	~ 780, ~ 850	> 100	[100]	[30]	0.3	41
HCO <sub>3</sub> <sup>-</sup>	589, 672, 713, 840, 971, 1218, 1346, 1701, 3339	[5]	[5]	0.5	0.1	42
BH <sub>4</sub> <sup>-</sup>	1142, 2256, 2321, 2425	[5]	0.3	[0.3]	0.3	43, 29
SO <sub>4</sub> <sup>2-</sup>	978, 1083, 1149, 1188	> 100	[90]	[20]	0.01	44, 45, 46, 9
CrO <sub>4</sub> <sup>2-</sup>	862, 890, 930, 941	> 100	> 100	> 100	0.05	47, 48, 49, 46
SeO <sub>4</sub> <sup>2-</sup>	834, 861, 904, 924	> 100	> 100	> 100	0.3	41
MnO <sub>4</sub> <sup>2-</sup>	899, 909, 914, 925	> 100	[80]	[30]	0.02	50
CrO <sub>3</sub> <sup>-</sup>	640, 940, 970	[10]	[5]	[1]	0.001	51
NH <sub>4</sub> <sup>+</sup>	1405, 3100	[0.1]	0.05	0.3	[1]	10

a. Intensity for the most intense band assumed to be  $\beta = 10 \text{ cm}^{-1}$  for 100 ppm of impurity.

b. Exact frequencies and intensities very dependent on compensating  $\text{Me}^{2+}$  ion.



\*X, Y = C, N; Z = C, N, O, S; X $\equiv$ Y means C $\equiv$ C, C $\equiv$ N, etc.

Figure 1. Correlation chart showing the absorption lines between 2 and 10  $\mu\text{m}$  of some chemical bonds, molecular ions, radicals, and compounds.  
Key: • peak positions; — range of peak positions in various materials.



Figure 2. Correlation chart showing the absorption lines between 0.5 and 15  $\mu\text{m}$  of some chemical bonds, molecular ions, radicals, and compounds.

• peak positions

— range of peak positions in various materials

Absorption strength:

S strong

M medium

W weak

V variable

Absorption line width:

B broad

Sh sharp

Numbers associated with an absorption band indicate the number of peaks occurring within that band.

If several designations apply to one peak, they are separated by commas.

If a designation applies to two adjacent peaks, it may be written between them.

aliph. = aliphatic

arom. = aromatic

Me = metal atom.

Impurity	Wavelength ( $\mu\text{m}$ )													
	1	2	3	4	5	6	7	8	9	10	11	12	13	14
Phenols	••	-	-	S, 1-2	← Bonded (B)			M	S					
Alcohols	••	-	-	Monomer (Sh) M S				- W		S		← Unbonded		
													Dimer (B)	
Tertiary alcohols	••	-	-	M S, B				M	S					
Secondary alcohols	••	-	-	M S, B				M	M					
-CH <sub>3</sub>	•••••	-	-	S			S	M						
-CH <sub>2</sub>	•••••	-	-	S			S	W		← CH <sub>2</sub> chains →			M	
Aromatic C-H	••	••	••	W-M										
Allene: >C=C=CH <sub>2</sub>	•••••	-	-	-	S, 1-2									
>C=CH <sub>2</sub>	•••••	-	-	M, 1-2		M	V	S		S	S			
Amines: NH, NH <sub>2</sub>	•	1-2	•	1-2		M		S	M			M, B		
-C≡C-H	••		Sh		M			M, B						S, B
Epoxides, oxiranes	•••••	-	-					S				M		

Impurity	Wavelength ( $\mu\text{m}$ )													
	1	2	3	4	5	6	7	8	9	10	11	12	13	14
$\geq\text{CH}$	..	.	<u>M</u>				<u>W</u>							
$-\text{Cl}-\text{H}$	-	-												
$\text{H}_2\text{O}$ (liquid)	.	.	S,B		M,B	S,B							S,B	
Imides: $-\text{CO}-\text{NH}-\text{CO}-$	.	.	-			<u>S</u>	.		<u>---</u>				-	
$-\text{HC}=\text{CH}-$	.	.	<u>M</u>			<u>V</u>	<u>M</u>		<u>S</u>				<u>M</u>	
$\geq\text{P}-\text{H}$		-		<u>M</u>										
$\geq\text{C}=\text{O}$		.				<u>S</u>								
Aromatic aldehydes		..	..			<u>S</u>		<u>---</u> <u>M</u> <u>---</u>			<u>---</u> <u>M</u> <u>---</u>			
Aliphatic aldehydes		..	..			<u>S</u>		<u>---</u> <u>M</u> <u>---</u>		<u>---</u> <u>M</u> <u>---</u>		<u>---</u> <u>M</u> <u>---</u>		
$\text{SH}^-$		-		<u>W</u>								<u>---</u> <u>W</u> <u>---</u>		
$\text{CO}_2$		<u>W</u>	<u>S</u>		<u>S</u>	<u>W</u>				<u>W</u>	<u>W</u>		<u>M</u>	
$\text{CO}$		<u>W</u>			<u>S</u>									

Impurity	Wavelength ( $\mu\text{m}$ )													
	1	2	3	4	5	6	7	8	9	10	11	12	13	14
$-\text{C}\equiv\text{N}$		.		<u>S</u>										
$-\text{F}-\text{H}$			-											
$\text{COF}_2$			.	.	.	<u>S</u>			<u>S</u>					
Benzene			<u>W</u>	<u>S</u> <u>M</u> <u>W</u>			<u>S</u>	<u>W</u> <u>M</u>	<u>W</u> <u>M</u>		<u>S</u>			
$\text{C}_3\text{O}_2$			.	.	.		.							
$\text{Si}-\text{OH}$			<u>---</u>							<u>W</u>		<u>S</u>		
$\text{SD}^-$		<u>W</u>			<u>M</u>									
$\text{OH}^-$			.											
$\text{CO Cl}_2$			..	.	.	<u>S</u>	<u>W</u>							<u>S</u>
Acetone			<u>W</u> <u>M</u> <u>W</u>			<u>S</u>	<u>S</u>	<u>S</u>	<u>M</u>		<u>W</u>		<u>W</u>	
$\text{BH}_4^-$			<u>W</u>		<u>S</u> , <u>B</u>				<u>S</u> , <u>B</u>					
Amides: $-\text{CO}-\text{NH}_2$			<u>M</u>			<u>S</u> <u>M</u>								



Impurity	Wavelength (μm)													
	1	2	3	4	5	6	7	8	9	10	11	12	13	14
$\text{KHCO}_3^-$			.	.										
$\text{SO}_2 \text{NH}_2$			<u>M</u>			<u>M</u>					-			
Amides: $-\text{CO}-\text{NH}-$			<u>M</u> <u>W</u>			<u>S</u> <u>M</u>								
$\text{NCO}^-$			<u>W</u>		<u>S</u>			<u>S</u>						
n-butyl alcohol			<u>S, B</u> <u>S</u>				<u>M</u>	<u>W</u>	<u>M</u> <u>S</u> <u>M</u>			<u>W</u>		<u>M, B</u>
$\text{NH}_4^+$			<u>S</u>		<u>W</u>		<u>S</u>							
Formamide			<u>S, B</u> <u>M</u> <u>W</u>			<u>S, B</u>	<u>S, B</u>		<u>M</u>				<u>M, B</u>	<u>S, B</u>
$\text{N}_2\text{O}$			<u>W</u>	<u>M</u> <u>S</u>			<u>S</u>							
$\text{HCO}_3^-$			<u>B</u>			<u>B</u>	<u>B</u>							
$\text{NH}_3^+$ salt			<u>S</u>	<u>W</u>		<u>M</u>								
$\text{K}_2\text{CO}_3$			.	.										
P-NH <sub>2</sub>			<u>M</u>			<u>M</u>			<u>M</u>					




Impurity	Wavelength (μm)													
	1	2	3	4	5	6	7	8	9	10	11	12	13	14
Lactams: $-\text{CO}-\text{NH}-$			<u>M</u> <u>W</u>			<u>S</u>								
Isopropyl: $(\text{CH}_3)_2\text{CH}-$			<u>M</u> <u>W</u>				<u>S</u> <u>M</u> <u>W</u>	<u>M</u>		<u>W</u>				
Carboxylic acid dimer			<u>S</u> <u>M</u>			<u>S</u>	<u>M</u>	<u>S</u>			<u>M, B</u>			
Ethyl: $\text{CH}_3\text{CH}_2-$			<u>S</u> <u>M</u>				<u>S</u> <u>M</u>		<u>M</u>	<u>W</u>		<u>M</u>		
Ethyl ether			<u>S</u>	<u>W</u> <u>W</u>		<u>M</u> <u>S</u> <u>M</u>	<u>S</u> <u>S</u> <u>M</u>	<u>W</u>	<u>M</u>					
Toluol			<u>S</u> <u>W</u>		<u>M</u>	<u>S</u> <u>M</u>	<u>M</u>	<u>S</u>		<u>M</u>			<u>S</u>	
$(-\text{O}-\text{Si}(\text{CH}_3)_2-\text{O}-\text{Si}(\text{CH}_3)_2-)_x$			<u>M</u> <u>W</u>				<u>W</u> <u>S</u>		<u>S, B</u>		<u>M</u>	<u>S</u>		<u>W</u>
$\text{KHCO}_2$			.	.										
Tetrahydrofuran			<u>S</u> <u>W</u>		<u>W</u>		<u>M</u> <u>W</u> <u>M</u>	<u>S</u> <u>M</u>	<u>S</u>					
$\text{HCCl}_3$			<u>M</u>	<u>W</u>			<u>W</u>	<u>S</u>	<u>W</u>	<u>W</u>		<u>S, B</u>		<u>M</u>
$\text{NH}_2^+$ salt			<u>S</u>			<u>M</u>								
$\text{NO}_3^-$			<u>W</u>				<u>S</u>				<u>M</u>			

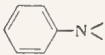
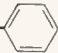

Impurity	1	2	3	4	5	6	7	8	9	10	11	12	13	14
$\text{KNO}_3$				.	.		S, B	.				M		W
P-OH				S, B				W		S				
$\text{NH}^+$ salt				S										
$\text{NO}_2^-$				.			.	S				.		
$\text{KNO}_2$				.			.	S, B				W		
C-D, $\text{CD}_2$				M					S				M	M
$\text{PH}_2$				M					M					
$-\text{C}\equiv\text{C}-$				W										
$\text{X}\equiv\text{Y}, \text{X}=\text{Y}=\text{Z}$ $\text{X}, \text{Y} = \text{C}, \text{N}; \text{Z} = \text{C}, \text{N}, \text{O}, \text{S}$				S										
Si-H				V, S										
Si-O-Si				W					S					
B..H..B bridge														

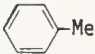
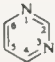
Impurity	1	2	3	4	5	6	7	8	9	10	11	12	13	14
Diborane: $\text{B} \begin{smallmatrix} \text{H} \\ \vdots \\ \text{H} \end{smallmatrix} \text{B}$				M	W	M	S							
Ge-H														
$\text{O}_3^-$				W					S					W
$\text{N}_3^-$				.										
$\text{BO}_2^-$														
$\text{Mo}(\text{CO})_6$				S, B					W	W		W		
Aromatic rings				W, 2-7	M			W, 2-6				S-W, 2-3		
$\text{BO}_3^{3-}$				.	.									.
Sn-H														
Thiol esters				S				S		S				
Cyclic anhydrides				S				S						
Anhydrides: $-\text{CO}-\text{O}-\text{CO}-$				S					S					



Impurity	Wavelength (μm)													
	1	2	3	4	5	6	7	8	9	10	11	12	13	14
Ge-O-Ge														
AlH <sub>3</sub> , AlH <sub>4</sub>														
>C=CF <sub>2</sub>						S								
Esters: -CO-O-						S			S					
Diene esters: -CO-O-						S		S						
Aromatic esters: -CO-O-						S		S						
Ketones						S	arom.	M			M	aliph.		
Nitrites: -O-NO						S						S		
C=C						S,V								
C=N, N=N						V								
FHF <sup>-</sup>						S,B								
Nitrates: -O-NO <sub>2</sub>							S					S		

Impurity	Wavelength (μm)													
	1	2	3	4	5	6	7	8	9	10	11	12	13	14
Carboxyl salt: -CO <sub>2</sub> <sup>-</sup>						S	M							
CO <sub>2</sub> <sup>-</sup>						S								
Furans: 														
Triazine ring: 						S,1-2						M-W		
Nitro-: NO <sub>2</sub>						S	M							
Nitroso-: -N=N=O														
Al-O														
Thiophenes: 														
CO <sub>3</sub> <sup>2-</sup>						S					1-2			
Azoxy: -N=NO-														
C-Cl													S	
P-O-C						M,1-4	M,1-3	S			M,V			

Impurity	1	2	3	4	5	6	7	8	9	10	11	12	13	14
B-N, B-O														
SO <sub>2</sub>														
Aromatic amines: 														
CF <sub>3</sub>														
Cyclic P=N														
Aromatic ethers														
Inorganic PO <sub>2</sub> <sup>-</sup> salts														
P=O														
CF <sub>2</sub>														
P-O- 														
S=O														
Pyridine ring: 														

Impurity	1	2	3	4	5	6	7	8	9	10	11	12	13	14
C=S														
SO <sub>4</sub> <sup>2-</sup>														
Organic PO <sub>2</sub> <sup>-</sup> salts														
Aliphatic ethers														
 -Me														
PO <sub>4</sub> <sup>3-</sup>														
Me=O														
PO <sub>3</sub> <sup>2-</sup> salts														
NF <sub>3</sub>														
C&O <sub>3</sub> <sup>-</sup>														
Pyrimidine ring: 														
P-F														



Impurity	Wavelength (μm)													
	1	2	3	4	5	6	7	8	9	10	11	12	13	14
$\text{CrO}_4^{2-}$											• • • •			
$\text{MnO}_4^{2-}$											••••			
$\text{WO}_4^{2-}$											S •	S •••••		
$\text{SeO}_4^{2-}$											• •	• •		
Ti-O-Ti														
$\text{MoO}_4^{2-}$											S •••	S • •		
Si-C														
$\text{SeO}_3^{3-}$														
$\text{BrO}_3^-$													S B	
$\text{IO}_3^-$													S W • •	
C-S														W
C-Br														S

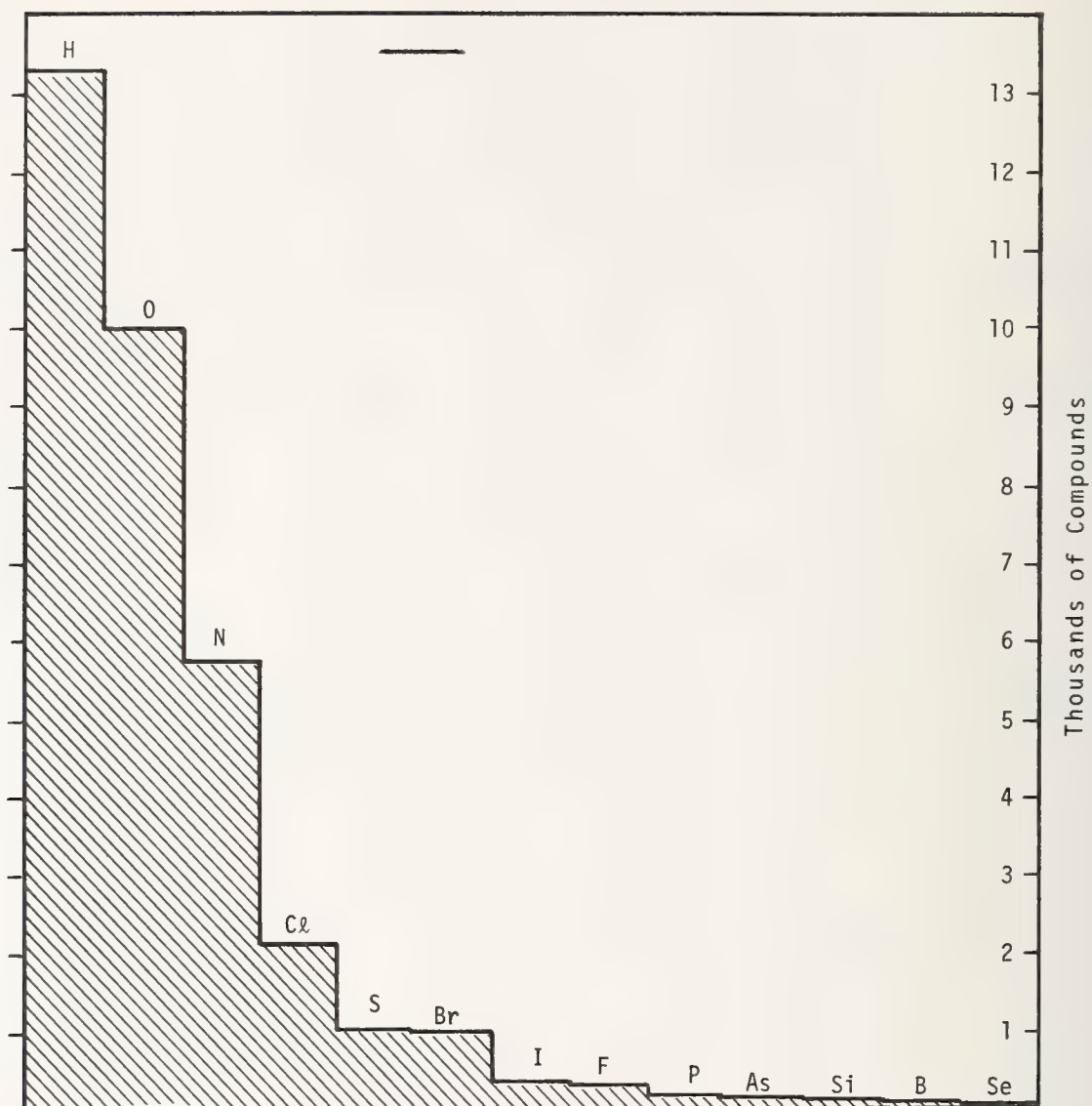


Figure 3. Occurrence frequency of elements in 13,520 organic compounds. A small number of compounds also contained Na, K, Mg, Sb, Cr, and D [72].



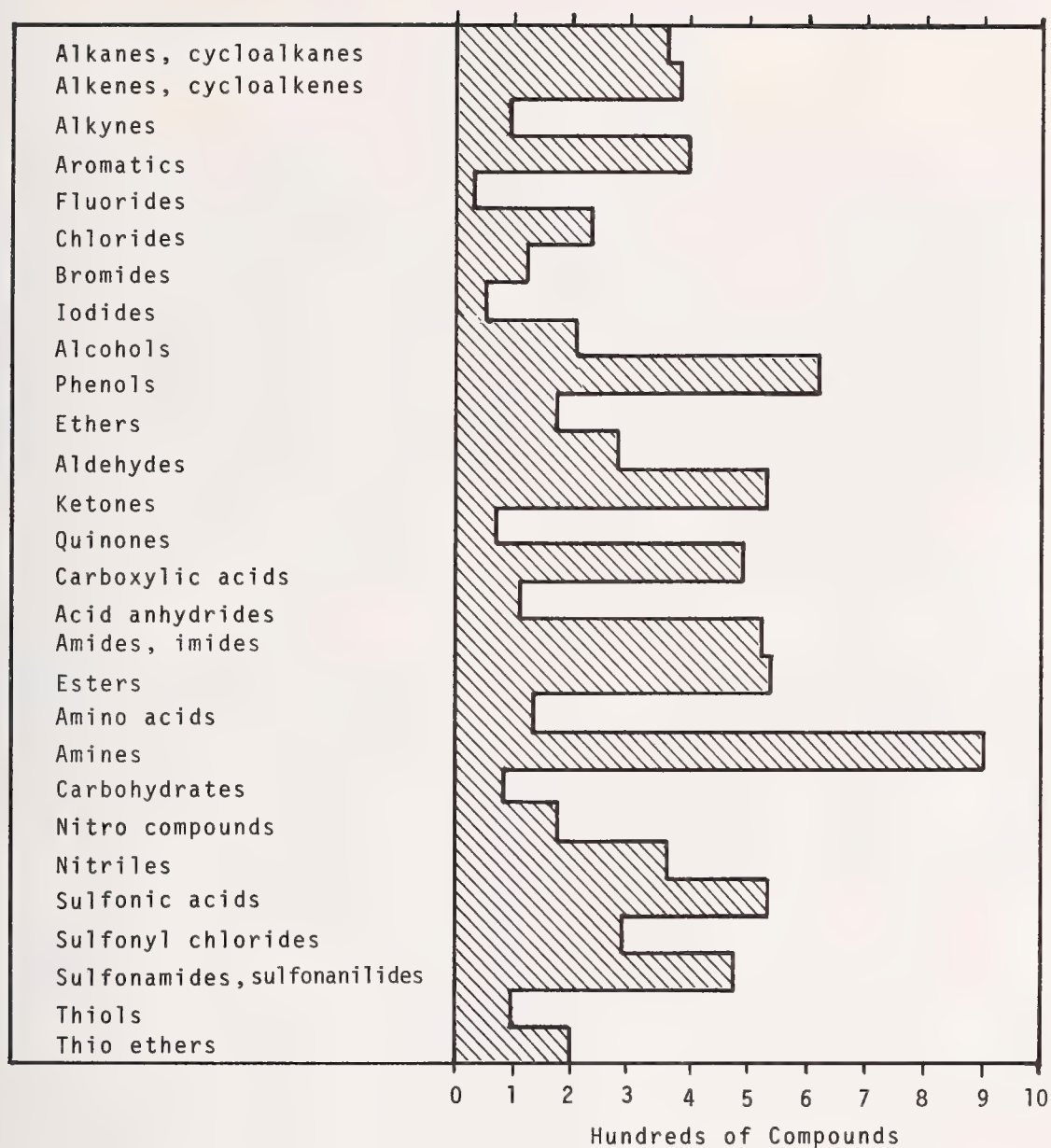


Figure 4. Occurrence frequency of the principal chemical groups in 8462 organic compounds and their derivatives. A compound may include functional groups listed above it, but not those listed below [73].

# POSSIBLE PROCESSES OF LASER WINDOW DEGRADATION

W.J. Fredericks  
Chemistry Department  
Oregon State University  
Corvallis, Oregon 97331

When judged by gross characteristics, many crystals appear to be immutable under ambient conditions. However, most crystals are continuously undergoing changes in their properties through interactions among the impurities they contain and with reactive components in their environment. These changes can cause a decrease in the transparency of the window and lead to its ultimate failure. The purpose of this paper is to consider the processes by which this may occur. A brief discussion of impurities, their interactions, and of various mass transport mechanisms (vacancy, vacancy pair, grain boundary, anomalous) in ionic crystals will be given. But most of the discussion will concern experimental evidence for such changes and their effect on optical properties. Particular attention will be given to the interactions and reactions of  $\text{OH}^-$  and  $\text{H}_2\text{O}$  and to a variety of impurity clustering effects at various stages in their development. Some of these effects occur in remarkably short times.

Key words: Clusters; deterioration; diffusion; enhanced diffusion; impurity reactions; laser window; precipitate.

## Introduction

Degradation or loss of transparency of a laser window occurs through spontaneous changes in the impurity system contained in the window. If a crystal contains very few impurities, its optical properties are stable for an extremely long time. The results given in table 1 are measurements of laser colorimetry [1] on a crystal grown in 1967. Measurements were made in 1976 or 1977.

Table 1. Additional round robin absorption in high purity KCl, Oregon State University, Sample 5-M20-3-6.

Laboratory	$\beta(10^{-4} \text{ cm}^{-1})$	Etching and drying procedure
1	$2.0 \pm .3$	10 min. conc. HCl etch, acetone rinse, heated during rinse.
5	$1.75 \pm .05$	<1 min. conc. HCl etch, filtered isopropanol spray rinse, dried with freon vapor.
3	4.4	Not etched (as received).
3	6.8	10 sec. conc. HCl etch, air dried without heating.
3	3.8	10 sec. 50/50 formic/acetic etch, 5 sec. acetic acid etch, dried 10 sec. with freon.
3	2.2	10 min. conc. HCl etch, acetone rinse, dried with hot air.

When a crystal is grown, the impurities present in it are not necessarily in equilibrium with the storage temperature of the finished crystal or necessarily in equilibrium with its external environment. As the impurity system shifts toward equilibrium, the window may change its optical properties by forming impurity compounds or the scattering centers. The fundamental process concerned with these changing properties is diffusion. Here we must consider some of the unusual mechanisms involved in diffusion in ionic crystals. The traditional diffusion mechanism associated with ionic crystals is the vacancy mechanism in which the impurity on one sublattice jumps to an adjacent vacancy in the same sublattice. While this mechanism applies to alkali halides and many other ionic crystals in some crystals such as the silver halides, the mechanism of cation migration is the interstitialcy mechanism in which a cation in an interstitial position jumps to a cation site knocking the cation in that site to an interstitial position. The jump distance in this mechanism is not limited to adjacent lattice sites. For certain small ions, an interstitial mechanism can occur in which the impurity moves through the crystal without occupying normal lattice sites. In this paper, we will discuss only the alkali halides as they are important to laser window technology. In figure 1, we show the results of a literature survey of the diffusion of divalent ions in sodium chloride [2]. The only obvious feature of this figure is that there is little agreement between the migration energies, and little agreement between various experiments. If we illustrated the migration of monovalent impurities in a similar plot, we would find the same disagreement. Even in self-diffusion, there is little agreement between the migration energies in alkali halides. Some of this scatter may be due to experimental error but most is due to differences



in the impurity content of the crystals used in the experiments. The line shown represents careful measurements of migration energies on very pure crystals for the case of diffusion by the vacancy mechanism. To understand why reasonable experiments produce such variation in migration energies we need to consider in detail the migration processes that occur in alkali halides. It is primarily impurity interactions that distort the diffusion process.

### Impurity Reactions

When an alkali halide contains an impurity, the equilibrium condition for that impurity may not be as a randomly distributed isolated ion. In the case of aliovalent impurities, there must always be a charge compensating vacancy introduced in the same sublattice. The vacancy and the impurity bear opposite charges and so undergo a mutual attraction forming impurity-vacancy complexes when in adjacent lattice sites. In the case of monovalent impurities, the impurity may be of such different size than a normal ion of the host lattice that the elastic distortion of the lattice will cause the thermally generated vacancies to preferentially associate with the monovalent ion. This effect is generally neglected in interpretation of experiments involving monovalent impurities. Most experiments have concerned aliovalent ions, in particular divalent ions, and their diffusion and association into impurity-vacancy complexes in the lattice. In table II, we show various kinds of impurity reactions that occur in the alkali halides that will distort diffusion processes. Simple association is relatively well understood, but if the crystal contains more than one divalent ion then common ion effects must be considered as shown in example 2. When a divalent ion is very much smaller than the host ion it replaces, a complex with the vacancy in the next nearest neighbor position may be more stable than the

Table 2. Impurity reactions in alkali halides.

Type	General Reaction	Examples*
1. Simple Association	$M_A^+ + V_C^- \rightleftharpoons M_A V_C$	NaCl:Pb <sup>++</sup> or NaCl:Cd <sup>++</sup> , etc.
2. Common Ion	$M_A^+ + V_C^- \rightleftharpoons M_A V_C$ $M_A^+ + V_C^- \rightleftharpoons M_B V_C$	NaCl:Pb <sup>++</sup> :Cd <sup>++</sup> or KCl:Pb <sup>++</sup> :Cd <sup>++</sup>
3. Nearest Neighbor $\rightleftharpoons$ Next Nearest Neighbor	$M_A^+ + V_C^- \rightleftharpoons M_A V_C$ $M_A^+ + V_C^- \rightleftharpoons M_A V_C (n) \text{ or}$ $M_A V_C \rightleftharpoons M_A V_C (n)$	NaCl:Mn <sup>++</sup> or KCl:Mn <sup>++</sup>
4. Cation-Anion	(1) $M_A^+ + X_B^- \rightleftharpoons M_A X_B$ or $M_A V_C + X_B V_A \rightleftharpoons M_A X_B + V_C V_A$ (2) $M_A^+ + X_B^- \rightleftharpoons M_A X_B(i) + V_a^+$ or $M_A V_C + X_B^- \rightleftharpoons M_A X_B(i) + V_C V_A$ (3) $M_A^+ + X_B^- \rightleftharpoons M_A(i) X_B(i) + V_C V_A$ etc.	KCl:HgO  KCl:Hg <sup>++</sup> :OH <sup>-</sup>
5. Polymerization	$\alpha X_A \rightleftharpoons (X_A)_\alpha$	KCl:3BO <sub>2</sub> <sup>-</sup> $\rightleftharpoons$ KCl:(BO <sub>2</sub> <sup>-</sup> ) <sub>3</sub> $V_C + KCl:Mn^{++} \rightleftharpoons KCl:(MnV_C)_3$
6. Phase Separation		
(a) Cluster	$\alpha M_A V_C + 2\alpha X \rightleftharpoons \alpha M_A X_2 + 2\alpha V_C V_D$	
(d) Ordered Phase	Phases	

nearest neighbor configuration. This is well established in the case of manganese and zinc and potassium chloride [3,4]. If the host crystal contains not only cationic but anionic impurities, they have a tendency to form compounds within the lattice. A good example is mercury and the hydroxide ion or mercury and the oxide ion [5]. If the crystal is allowed to reach equilibrium, these often cluster into large groups which we represent here as polarimization of the BO<sub>2</sub><sup>-</sup> ion [6]. The final stage occurs when a local region of the crystal becomes saturated and larger clusters or ordered phases begin to appear. All of these processes have been well established and can lead to deterioration of the optical properties of the crystal. Here we will give some examples of this type of behavior. But for purposes

of this paper the question is can these reactions occur at normal temperatures. In order to discuss this, we first need to look in detail at diffusion mechanisms in ionic crystals.

### Diffusion

The diffusion coefficient obtained from experimental observation consists of diffusion by a vacancy mechanism,  $D_v$ ; diffusion by vacancy pairs,  $D_{vp}$ ; diffusion along dislocations,  $D_d$ ; and diffusion along grain boundaries,  $D_{gb}$ ; and any other possible mechanism that may occur in the crystal. Thus the observed diffusion coefficient is given by

$$D_{obs} = D_v + D_{vp} + D_d + D_{gb} + \dots \quad (1)$$

The classic case of vacancy diffusion of monovalent cations in alkali halides is represented by equation 2.

$$D_v^c = 4a^2 f \omega_c \chi_c \exp(-g_m^c/kT) = 4a^2 f \omega_c \chi_c \exp(s_m^c/k) \exp(-h_m^c/kT) = D_o \exp(-h_m^c/kT), \quad (2)$$

where  $a$  is a cation-anion distance,  $f$  the correlation factor,  $\omega_c$  the cation attempt frequency,  $\chi_c$  the concentration of cation vacancies,  $g_m^c$  is the Gibbs free energy of migration with  $g_m^c = h_m^c - Ts_m^c$ . If the only source of cation vacancies are Schottky defects, then eq. (2) can be written as shown in eq. (3) in which the concentration of cation vacancies is expressed as a Schottky product with  $h_s$  being the enthalpy of formation of a Schottky pair and  $s_s$  the entropy of formation of a Schottky pair.

$$D_v^c = 4a^2 f \omega_c \exp\{[s_m^c + (s_s/2)/k] \exp\{[h_m^c + h_s/2]/kT\}\} \quad (3)$$

If the crystal contains both anion and cation vacancies, these experience an electrostatic attractive force and form a certain number of pairs in thermal equilibrium with the crystal at the time it was grown. The mass action expression for this is given by

$$\chi_p = z \exp[-(g_s + g_p)/kT], \quad (4)$$

where  $z$  is the configuration entropy,  $g_s$  and  $g_p$  are the free energies of formation for Schottky defects and pairs, respectively. The pairs can contribute to both anion and cation diffusion in eq. (5) the given expression for the diffusion of cations by the vacancy pair mechanism. The usual experimental

$$D_{vp}^c = 8a^2 f_{pr} \omega_c \exp\{[(s_s/2) + s_p + s_m^{cp}]/k\} \exp\{[-h_s/2 + h_p + h_m^{cp}]/kT\} \quad (5)$$

practice for separating diffusion by vacancies and diffusion by vacancy pair is to perform an electromigration experiment. As the vacancies are charged they will migrate in the electric field; the vacancy pairs will not, as they are not charged. And by analysis of diffusion profiles obtained with and without an electric field, the two contributions can be separated [7].

Diffusion along dislocations is not well developed. Often investigators use single crystals to separate the vacancy and vacancy pair contribution assuming that any difference between the observed diffusion coefficient and the sum of  $D_v$  and  $D_{vp}$  to constitute that portion of the overall diffusion process caused by diffusion along dislocations. There have been very few systematic studies of dislocation diffusion in the alkali halides.

On the other hand, there have been several excellent studies of diffusion along grain boundaries. The grain boundary diffusion coefficient as developed by Whipple [8] is given by

$$D_{gb}' \delta = \left\{ \frac{\partial \ln \chi_c}{\partial x} \right\}^{-2} \left( \frac{4D_v}{t} \right)^{1/2} \left\{ \frac{\partial \ln \chi_c}{\partial (\eta \beta^{1/2})} \right\}^2, \text{ where} \quad (6)$$

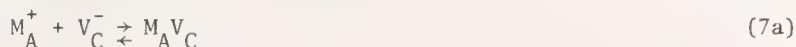
$$\eta = x/(D_v t)^{1/2} \text{ and } \beta = \frac{D_{gb}'}{D_v} \frac{\delta}{\partial (D_v t)^{1/2}}.$$

The terms  $\eta$  and  $\beta$  are defined below the equation.  $D_{gb}$  is the grain boundary diffusion coefficient,  $\delta$  is the grain boundary width,  $t$  is the time, the concentrations  $\chi_c$  are given in mole fractions, and  $x$  is the distance. L.B. Harris [9,10] has carried out extensive studies of diffusion along single grain boundaries. He finds that the ratio of the grain boundary diffusion coefficient to that for vacancy diffusion for  $^{22}\text{Na}$  in sodium chloride is 450. The magnitude of  $D_{gb}(\text{Na})$  in NaCl is  $1.2 \times 10^{-9} \text{ cm}^2$  at  $633^\circ\text{K}$ .

The diffusion of aliovalent ions in alkali halides is slightly more complex than that of monovalent ions in that the impurity and the vacancy on the corresponding sublattice associate and it is



these vacancy-impurity complexes that constitute the diffusion flux. Since the impurity has an excess positive charge and the cation vacancy has an excess negative charge, the two attract with an energy of formation for the complex  $g_k$ . The concentration of complexes is given by eq. (7a,b,c,d,e).



at concentrations  $x_A$ ,  $x_C$ ,  $x_k$  then electro neutrality requires  $x_A = C_A - k_k$  (7b)

$$k_A(T) = \frac{x_k}{x_A x_C} = z_1 \exp(-g_k/kT) ; z_1 = 12 \quad (7c)$$

$$\frac{x_k}{C_A} = p, \text{ the degree of association} \quad (7d)$$

$$k_A(T) = \frac{p}{(1-p)^2} = 12 C_A \exp(-g_k/kT) \quad (7e)$$

Since the diffusion occurs by a vacancy process the impurity flux is given by eq. (8) and note that the flux is proportional to the concentration gradient of the complexes. Since that gradient is concentration dependent the diffusion coefficients will be concentration dependent. It's convenient to consider

$$J_A = -ND_A \nabla x_k \quad (8)$$

two limiting cases of divalent ion diffusion. The low concentration limit given by eq. (9) in which the

$$D_A = \frac{1}{3} a^2 f \omega_2 p \text{ when } C_A \ll k_s(T)^{1/2} \quad (9)$$

concentration of the impurity is very much less than the concentration of thermal vacancies produced from Schottky defects and that given by eq. (10) in which the concentration of the impurity exceeds that

$$D_A = \frac{2}{3} a^2 f \omega_2 [p/(1+p)] \text{ when } C_A \gg k_s(T)^{1/2} \quad (10)$$

of the concentration of vacancies produced by Schottky defects. In the former case the diffusion coefficient is proportional to the degree of association, while eq. (10) describes the situation in which the degree of association is becoming larger and the diffusion coefficient is no longer directly proportional to the degree of association. As  $p$  approaches 1 the diffusion becomes constant, ie a saturation diffusion coefficient  $D_s$ , given by eq. (11). This describes the behavior of a simple system

$$D_A = a^2 f \omega_2 / 3 = D_s \quad (11)$$

containing a single aliovalent ion and represents the basic case of aliovalent ion diffusion. If other diffusion processes are occurring such as grain boundary diffusion, then  $D_v$  as used in eq. (5) is given by the diffusion coefficients described by eq. (8) and (9). If the crystal contains more than a single aliovalent ion on the same sublattice then the vacancy is a common ion between two reacting impurity systems and one obtains coupled diffusion coefficients, the diffusion coefficient of one ion depending on that of the second ion present.

Figure 2 shows the behavior of the diffusion coefficient of cadmium in NaCl as a function of concentration [11]. If in the interpretation of a diffusion experiment the diffusion coefficient does not reach saturation it can lead to a downward curvature in the Arrhenius plot which causes a low migration energy as illustrated in figure 3 [11]. An illustration of the dependence of the diffusion coefficient of one ion on the presence of a second ion on the same sublattice is shown in figure 4. In that particular experiment, both cadmium and lead were simultaneously diffused into purified potassium chloride. Note the initial portion of the cadmium diffusion profile and the build-up of cadmium at the termination of the lead penetration into the crystal. Under these experimental conditions the lead contributed most of the charge compensating vacancies it introduced into KCl to the cadmium and the cadmium diffused at its saturation diffusion coefficient value. Even though its concentration was well below that which would cause saturation to occur in a single ion experiment and the lead was retarded in its diffusion in KCl by the lack of vacancies with which to associate. If this experiment had been performed in a crystal containing an unsuspected quantity of lead uniformly distributed throughout the crystal, the entire profile would have been distorted and interpreted as extremely rapid diffusion with a low migration energy and a large preexponential factor.

The foregoing examples related to diffusion at high temperatures, but they indeed illustrate the peculiar behavior that can occur in diffusion studies. It's essential to understand the effect of one impurity on another in understanding diffusion processes that can occur rapidly at low temperatures. One additional high temperature example is shown in figure 5. This is the diffusion of mercury into potassium chloride [13]. Notice the extremely low concentrations of mercury that will diffuse into the purified potassium chloride, while under exactly the same conditions that 5.2 times more mercury is diffused into potassium chloride containing hydroxide. Mercury forms an anion-cation impurity compound

[5] within the lattice which is quite immobile. Notice the rapid decrease of the  $\text{Hg}^{2+}$  concentration below that in the purified crystal at a penetration distance beyond the  $\text{HgOH}_x$  maximum. The  $\text{Hg}^{2+}:\text{OH}^-:\text{O}^{2-}$  system is complex [5], but this figure illustrates that when the mercuric ion is bound with hydroxide in a potassium chloride lattice the energy of the impurity lattice compound is much lower than that of an isolated mercuric ion or a mercuric ion vacancy complex. This enhances the diffusion such that at a specific temperature and in a specific time much more mercury diffuses into the crystal than  $\text{Hg}^{2+}$  in a purified crystal. Thus we have impurity enhanced diffusion. It is this impurity enhancement of diffusion that greatly speeds low temperature diffusion into the lattice.

In keeping with its reputation for damaging the optical properties of alkali halides, the ubiquitous impurity, hydroxide, exhibits anomalous diffusion characteristics. The only values of the diffusion coefficient of hydroxide in KCl arise from effusion measurements [14] of hydroxide effusing from a KCl. The diffusion coefficient is given by equation 12. The migration energy 2.0 eV is

$$D(\text{OH}^-) = 1.2 \times 10^3 \exp(-2.0\text{eV}/kT) \text{ cm}^2/\text{sec} \quad (12)$$

characteristic of a vacancy mechanism for the diffusion process but the preexponential factor is extremely large for a simple vacancy mechanism and makes hydroxide the fastest moving ionic impurity observed in potassium chloride. These values have been confirmed by Ikeda in an independent experiment [15]. However, if the atmosphere external to the crystal is reactive, such as a chlorine atmosphere, the rate of migration of hydroxide becomes unbelievably rapid. If it is assumed that the concentration profile within the crystal is an error function complement, then the diffusion coefficient given by eq. (13) is obtained. Note that the migration energy does not change significantly but the preexponential factor increases by 100 due solely to the presence of the external reactive atmosphere. In similar

$$D(\text{OH}^-)(\text{Cl}_2\text{atm}) = 3 \times 10^5 \exp(-2.0\text{eV}/kT) \text{ cm}^2/\text{sec} \quad (13)$$

effusion measurements, Ikeda has shown that it is not the hydroxide that diffuses but that the hydroxide is destroyed more rapidly than it diffuses by forming an intermediate  $\text{O}_2^-$  impurity. The resulting diffusion profile resembles an error function complement with a displaced threshold (fig. 6). The increased magnitude of the preexponential factor in the diffusion coefficient is not real. The absorption at 204 nm is destroyed by decomposition of the hydroxide and an intermediate formation of a band ascribed to  $\text{O}_2^-$  at 240 nm. The process by which this occurs is not well understood. It may be by a hole migration in the crystal and subsequent reaction with the hydroxide. Ikeda only reported on a single experimental measurement; much more work must be done before the exact process is understood. However, this work presents a mechanism hitherto unsuspected which clearly demonstrates the effect of the external atmosphere on impurities far removed from the crystal surface. If the diffusion coefficient obtained in the vacuum experiments applies at temperatures well below those at which they were measured, the diffusion coefficient of hydroxide at room temperature is of the order  $10^{-33} \text{ cm}^2 \text{ sec}^{-1}$ . This is far too small to cause degradation of optical properties in a reasonable window lifetime. If accelerated processes occur, such as those in a chlorine atmosphere, substantially larger diffusion coefficients could occur at room temperature but still not large enough to markedly affect the properties within a year lifetime of a laser window, but in the region of the crystal through which the laser beam passes substantial changes in the impurity distribution could occur.

Gründig and Rùhenbeck [16,17,18] developed a method of studying the diffusion of water into potassium halides by observing the bleaching of the color centers in crystals to which  $\text{K}_2\text{O}$  or K had been added. Diffusion under these conditions is enhanced diffusion similar to that of mercury into  $\text{KCl}:\text{OH}^-$  discussed previously. Results of their experiments are summarized in table 3.

The temperature dependence of the solubility of water in these crystals is unusual. Initially the solubility is high then decreases as the temperature increases to a minimum at 350°C in potassium chloride, 324°C in potassium bromide, and 290°C in potassium iodide then again increases as the temperature increases. In each case the increase in solubility in the high temperature region is much greater than its decrease in the low temperature region. Note the magnitudes of W in table 3, and that water is extremely soluble in these crystals under enhanced diffusion conditions as was mercury in  $\text{KCl}:\text{OH}^-$ . They also observed that in K doped zone refined crystals the temperature solubility transition is well defined, but when  $\text{Ca}^{2+}$  is added to the crystal a temperature independent region occurs that extends well below and well above the transition temperature found in purer crystals. The solubility was enhanced in this region over that of zone refined crystals. The formation of a rather stable compound between calcium and the products of water diffused into the crystal would explain this behavior. Evidence for such a calcium hydroxide impurity compound was reported from conductivity studies by Fritz, Lùty, and Anger [19].

The diffusion coefficients reported are given in the lower part of table 3. Note the rather low migration energies for water in KCl, KBr, and KI and the very large preexponential factors. Water diffuses rapidly in these crystals when the diffusion is enhanced by the formation of a lattice compound within the crystal. Gründig and Rùhenbeck suggest that the diffusion may be by an interstitial



Table 3. Solubility and diffusion of H<sub>2</sub>O and its products in K<sub>2</sub>O- and K-doped crystals

Solubility					
Crystal	pC <sub>O</sub> (cm <sup>-1</sup> ) <sup>c</sup>	W (eV)	Temp. (°C) <sup>a</sup>	Reference	
KCl	8.9 x 10 <sup>9</sup>	-0.20	T < ~350	Rühenbeck (1967)	
	9.1 x 10 <sup>16</sup>	0.67	T > ~350		
KBr	6.2 x 10 <sup>10</sup>	-0.15	T < ~325		
	7.6 x 10 <sup>16</sup>	0.53	T > ~325		
KI	1.5 x 10 <sup>13</sup>	-0.06	T < ~290		
	1.8 x 10 <sup>16</sup>	0.33	T > ~290		
Diffusion					
Crystal	Diffusant	T(°C)	D <sub>O</sub> (cm <sup>2</sup> sec <sup>-1</sup> )	U(eV)	Reference
KCl	H <sub>2</sub> O	700-180	62	0.80	Rühenbeck (1967)
	H <sub>2</sub>	420-180	630	0.97	Gründig and Rühenbeck (1972)
KBr	O <sup>-2</sup>	---	1.5 x 10 <sup>-3</sup>	1.25	Stasiw (1935) <sup>b</sup>
	H <sub>2</sub> O	600-180	7.7	0.69	Rühenbeck (1967)
	H <sub>2</sub>	400-180	50	0.81	Gründig and Rühenbeck (1972)
KI	H <sub>2</sub> O	600-180	0.48	0.56	Rühenbeck (1967)
	H <sub>2</sub>	420-180	5.6	0.64	Gründig and Rühenbeck (1972)

<sup>a</sup>For doped zone refined crystals.<sup>b</sup>Given by Rühenbeck (1967). For OH<sup>-</sup> diffusion, see section V and table V.<sup>c</sup>p(Torr)C<sub>O</sub> (cm<sup>-3</sup>Torr<sup>-1</sup>).

process. The low migration energies for such a large molecule do indeed suggest this as do the large preexponential factors, although no other evidence is currently available to support that supposition. If these diffusion coefficients hold to lower temperatures, water can certainly damage a crystal containing an impurity that will enhance its diffusion. In figure 7 is shown the ratio C/C<sub>0</sub>, assuming an extended source of concentration C<sub>0</sub>, as a function of distance into the crystal at 25°C for 180 days, and 360 days for KCl, and 180 for KBr. For comparison the diffusion profile for OH<sup>-</sup> under a chlorine atmosphere is also shown. In order for the concentration of OH<sup>-</sup> to be comparable with that of water it must diffuse at 327°C for 180 days. There is significant penetration of water into the crystals to a depth of 0.6 mm at room temperature. This would produce a significant amount of absorption in a crystal used for a laser window.

There have been no direct experiments on the measurement of the diffusion of water into a divalent cation doped alkali halide. However, evidence does exist that it occurs at room temperature to a significant degree in a period of a year. In figure 8 the relaxation time  $\tau$  versus the reciprocal temperature is shown for a cadmium doped KCl crystal that had been exposed to atmospheric water for a period of 12 months [20]. This measurement occurred inadvertently in that a crystal that had been stored in a closed container for the period of a year was measured in a double crystal dipole relaxation measurement and exhibited a new relaxation process shown near A of figure 8 with a relaxation energy of 0.57 eV. The line near B is the normal cadmium-vacancy complex relaxation. To confirm that this relaxation was due to water, an additional experiment was conducted using a freshly grown KCl:Cd<sup>2+</sup> crystal and exposing to water vapor for 1.5 hr at 400°C. The same relaxation at A appeared in this crystal which previously had only the relaxation B. Further experiments showed that exactly the same type of behavior occurred when a KCl:Pb<sup>2+</sup> crystal was exposed to water vapor for a similar period of time. Since most divalent ions form stable impurity-hydroxide compounds when they are incorporated in alkali halides as impurities this experiment suggests that a crystal containing a divalent ion will have a much shorter lifetime as a laser window than a purer crystal. From these measurements, it appears that a period of a year in a reasonably humid atmosphere would be sufficient to destroy the optical quality of a single crystal laser window.

## Clusters and Precipitates

In addition to the degradation of the optical properties crystal by the absorption of water, another process, clustering, can reduce the optical quality of a laser window. It is convenient to divide this process into two stages, microclusters and macroclusters or precipitates. It is often assumed that when an impurity is incorporated in an ionic crystal it is rather homogeneously distributed throughout the crystal. This is not the case [21] and the discussion of the microclustering behavior of impurities in crystals will clearly demonstrate this.

The classic case of the formation of microclusters concerns manganese. For years work showed that manganese clusters by a third order process [22,23] and only recently has experimental evidence been presented to show that there is an initial stage in which dimers are formed and then a second stage in which trimers are formed [24,25,26]. However, manganese is not a common impurity in alkali halides and we will discuss in detail a more common impurity, strontium. The same processes occur for many other aliovalent impurities. The evidence for clustering of strontium comes from ionic thermal current measurements. These measurements determine the temperature at which a field oriented a dipole relaxes within a crystal and the magnitude of the charge stored in that particular relaxation process. In figure 9 are shown the results of studies of strontium in KCl by Jacobs, et al [27]. In diagram (a) is shown the current versus the temperature for depolarization of the crystal. Initially at (a) we have one rather large relaxation peak. As time passes the peak shifts to higher temperature and decreases in amplitude through (a), (b), (c), (d). This change in relaxation properties occurs in 17 hours at 250°K, well below room temperature. The quantitative analysis of this change in relaxation properties is given in the table included in this figure. There not only is a shift in the energy at which this relaxation occurs, but a decrease in the total amount of charge that can be stored in the crystal. At this temperature the change in relaxation properties cannot be due to the diffusion of an additional impurity into the crystal from an external source. It could be due to the formation of an anion-cation lattice compound such  $\text{Sr}(\text{OH})_x$  only if the hydroxide were in close proximity to the strontium initially. Crystals used in this experiment were not produced under a reactive atmosphere and could indeed contain hydroxide. However, Jacobs et al. assigned this change in dipole relaxation to the formation of impurity-vacancy complex dimers as shown at the bottom of figure 9. Recent measurements [28] on the diffusion of strontium in KCl gave a diffusion coefficient represented by eq.(14). From the magnitude of the

$$D_S(\text{Sr}^{2+}) = 1.20 \times 10^{-3} \exp(-0.871\text{eV}/kT) \text{ cm}^2/\text{sec} \quad (14)$$

diffusion coefficients its clear that this change cannot be due to a normal diffusion process occurring at 250°K. Optical studies were not reported which could have eliminated the possibility of the hydroxide formation. Whatever the mechanism of this change in the dipole relaxation properties of  $\text{KCl}:\text{Sr}^{2+}$  the significant point is that it occurs in such a short time at such low temperatures that it cannot occur by any normal diffusion process. One must conclude that either an unknown mechanism of diffusion exists in the alkali halide or that the impurities are distributed within the crystal in such a way that they are nearly adjacent to each other. While this type of clustering will only increase the general background scattering of the crystals slightly, another type of clustering can significantly alter the optical properties of the crystal.

It has been amply demonstrated that the vibrational spectrum of an anionic molecular impurity in an alkali halide depends on the cation associated with it as a charge compensating cation [29,30,31]. Another type of clustering occurs with molecular anionic impurities that has been less well discussed in the literature. The only documented case of polymerization of an anion molecular impurity is a case of metaborate in sodium chloride, potassium chloride, and potassium bromide [6]. The metaborate ion introduces a spectrum with well known fermi doublet due to an isolated  $\text{BO}_2^-$  impurity [3]. However, that spectrum is often accompanied by a very complex spectrum that extends over a wide region of the infrared. This is shown in figure 10. The complexities of this spectrum can be explained by the formation of a complex of  $\text{BO}_2^-$  ions. While the exact structure of the complex leading to this spectrum is being debated by the investigators, the consequences of such polymerization are obvious in examining the curves for the annealed crystal. As the crystal is annealed the spectral lines broaden until they produce absorption over a large portion of the infrared. As the annealing continues actual clusters of metaborate can be observed by an ultramicroscope as shown in figure 11. The clustering is caused primarily by the misfit of the polymer in the lattice. Note that no clusters are shown for KCl and that the effect of annealing on  $\text{KCl}:\text{BO}_2^-$  is much less than on sodium chloride or potassium bromide. At the onset of this precipitation stage in the crystal, not only broad absorption bands but significant amounts of scattering from the forming precipitates was observed. This process is often called Ostwald Ripening [33,34,35,36] and occurs in any local region of a crystal that is supersaturated with respect to an impurity at the temperature of that region of the crystal. While such a process would not be rapid in a crystal at room temperature, if such a crystal were exposed periodically to high intensity electromagnetic radiation that heated local regions of the crystal in that region such polymerization would initially occur finally reaching a point where precipitates could form. Thus, a stepwise, but not necessarily linear, increase in absorption on repeated exposure to high intensity radiation in local regions of a laser window may be observed. It appears probable that such a crystal would fail



before the stage of actual precipitation occurred. The size distribution of the precipitate depends on mechanism (bulk, grain boundary or surface diffusion) by which the precipitate is formed [37]. None of the literature data is suitable for kinetic analysis of clustering or precipitating.

The final stages of precipitation in a crystal often results in the formation of an ordered second phase. This generally is a phase composed of a divalent cationic impurity M, their associated vacancies, and a sufficient number of host ions to produce a second phase with a composition  $MCl_2 \cdot$

6KCl. These phases are called Suzuki phases [38], and in figure 12 transmission electron micrograph [39] of such a phase is shown. Such phases are only found in relatively impure crystals that have been well annealed.

The foregoing discussion has been primarily concerned with single crystals containing trace impurities, both anionic and cationic. However, if the crystal contains a grain boundary as may occur in poorly grown crystals or may be produced in forging a crystal, other rapid low temperature degradation processes may occur. In figure 13 is shown a scanning electron micrograph of an uncoated surface of sodium chloride containing a single grain boundary [40]. The sodium chloride was nominally pure but note the impurity phases clustered along the grain boundary. This crystal was pulled from a melt from ultrapure Merk "pro analysi" sodium chloride. Analysis showed it to contain trace amounts of calcium ( $Z=20$ ) and potassium ( $Z=19$ ). Due to the similarity and electron reflection characteristics of these two ions, it is not possible to tell whether the impurity clusters contain calcium or potassium. The foregoing discussion in this paper would suggest that they are more likely calcium than potassium. If that is so, in a region of the crystal particularly penetrable by moisture, we have an ion which will enhance diffusion. It is likely that the diffusion along the grain boundary for moisture is enhanced at least as much as it is for sodium along a similar grain boundary; that is by a factor of around 450-500 times that in the bulk crystal. This would lead to more rapid deterioration of the optical properties of such a crystal than a crystal containing a similar impurity concentration in its bulk. Whether such clusters form on forged crystals is unknown, but in the forging process the effective temperature of the crystal is increased and it is reasonable to expect that the concentration of impurities would be enhanced along these grain boundaries. Measurements of the mechanical properties of such a crystal indicate that divalent impurities will increase the hardness of a crystal by precipitating at the grain boundaries.

#### Conclusion

In this paper we have attempted to draw from the body of knowledge concerning the behavior of impurities in alkali halides to discuss mechanisms which could possibly lead to deterioration of the optical properties of a laser window. These processes conveniently divide into aging which occurs at storage temperature and clustering through use. Pure single crystals should be least susceptible to these degradation processes. The inclusion of aliovalent impurities in the lattice will increase the rate of aging and eventually contribute to clustering. If the window contains grain boundaries or large numbers of dislocations as well as aliovalent impurities the useful lifetime of the window may be markedly shortened.

#### References

- [1] Lipson, H. and Ligor, P., "Round Robin on Colorimetric Measurement of  $10.6\mu m$  Absorption in KCl." Air Force Cambridge Research Laboratories.
- [2] Fredericks, W.J., in "Diffusion in Solids Recent Developments." Academic Press, New York (1975), data from p. 431.
- [3] Watkins, G.D., Phys. Rev. 113, 79 and 81 (1959).
- [4] Dreyfus, R.W., Phys. Rev. 121, 1675 (1961).
- [5] Allen, C.A. and Fredericks, W.J., Phys. Status Solidi 3a, 143 (1970).
- [6] Becker, C.R., Thesis, Oregon State University, Chemistry Department, Corvallis, Ore. (1969).
- [7] Nelson, V.C. and Friauf, R.J., J. Phys. Chem. Solids 31, 825 (1970).
- [8] Whipple, R.T.P., Phil. Mag. 45, 1225 (1954).
- [9] Harris, L.B. and Fiasson, J., Phys. Status Solidi (a) 33, 697 (1976).
- [10] Harris, L.B., J. Phys. (Paris) 37, C7-365 (1976).
- [11] Allen, C.A., Ireland, D.T., and Fredericks, W.J., J. Chem. Phys. 47, 3068 (1967).
- [12] Krause, J.L. and Fredericks, W.J., J. Phys. (Paris) 34, C9-13 (1973).
- [13] Allen, C.A. and Fredericks, W.J., Phys. Status Solidi 55b, 615 (1973).
- [14] Allen, C.A. and Fredericks, W.J., J. Solid State Chem. 1, 205 (1970).
- [15] Ikeda, T., Japan J. Appl. Phys. 12, 1810 (1973).
- [16] Gründig, H. and Rügenbeck, C., Z. Phys. 183, 274 (1965).
- [17] Rügenbeck, C., Z. Phys. 207, 446 (1967).
- [18] Gründig H. and Rügenbeck, C., Z. Phys. 249, 269 (1972).
- [19] Fritz, B., Lüty, F., and Anger, J., Z. Phys. 174, 240 (1963).
- [20] Chaney, R.E. and Fredericks, W.J., J. Solid State Chem. 6, 240 (1973).
- [21] Allnatt, A.R. and Chadwick, A.V., Trans. Faraday Soc. 63 1929 (1967).
- [22] Cook, J.S. and Dryden, J.S., Proc. Phys. Soc. London 80, 479 (1962).

- [23] Dryden, J.S. and Harvey, G.G., Proc. Phys. Soc. London (Solid State Phys.) 2, 603 (1969).
- [24] Crawford, J.H., Jr., J. Phys. Chem. Solids 31, 399 (1969).
- [25] Symmons, H.F., Proc. Phys. Soc. London (Solid State Phys.) 3, 1846 (1970).
- [26] *ibid.* 4, 1945 (1971).
- [27] Hor, A.H. Mee, Jacobs, P.W.M., and Moodie, K.S., Phys. Stat. Sol. (a) 30, 293 (1976).
- [28] Machida, H. and Fredericks, W.J., to be published.
- [29] Coker, E.H., Decius, J.C., and Scott, A.B., J. Chem. Phys. 35, 745 (1961).
- [30] Decius, J.C., Coker, E.H., and Brenna, G.L., Spectrochim. Acta 19, 1281 (1963).
- [31] Decius, J.C., Spectrochim. Acta 21, 15 (1965).
- [32] Decius, J.C., Becker, C.R., and Fredericks, W.J., J. Chem. Phys. 56, 5189 (1972).
- [33] Greenwood, G.W., in the "Mechanism of Phase Transformations in Crystalline Solids," Institute of Metals Monograph No. 33. (1969) p. 105.
- [34] Lifshitz, I.M. and Slezov, V.V., Zh. Exptl. Theor. Phys. (USSR) 35 479 (1958); translation: Sov. Phys. JETP 38 331 (1959).
- [35] Lifshitz, I.M. and Slezov, V.V., J. Phys. Chem. Solids 19, 35 (1961).
- [36] Wagner, C., Z. Electrochem. 65, 581 (1961).
- [37] Jain, S.C. and Hughes, A.E., J. Phys. (Paris) 37, C7-463 (1976).
- [38] Suzuki, K., Japan J. Phys. Soc. 16, 67 (1961).
- [39] Yacaman, M.J., Goringe, M.J., and Hobbs, L.W., UKAEA Research Report AERE-R846 (1976) Phys. Stat. Sol. (a) 39, K85 (1977).
- [40] Harris, L.B., Moncrieff, D.A. and Robinson, V.N.E., Phys. Stat. Sol. 35, 371 (1976).

Figures

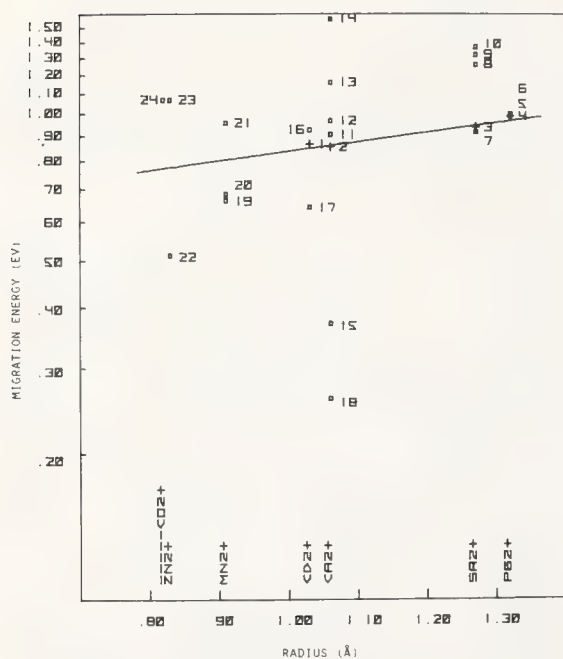


Figure 1. Migration energies of divalent impurities in sodium chloride as a function of impurity radius. Solid line shows least squares fit to  $D_s$  values.

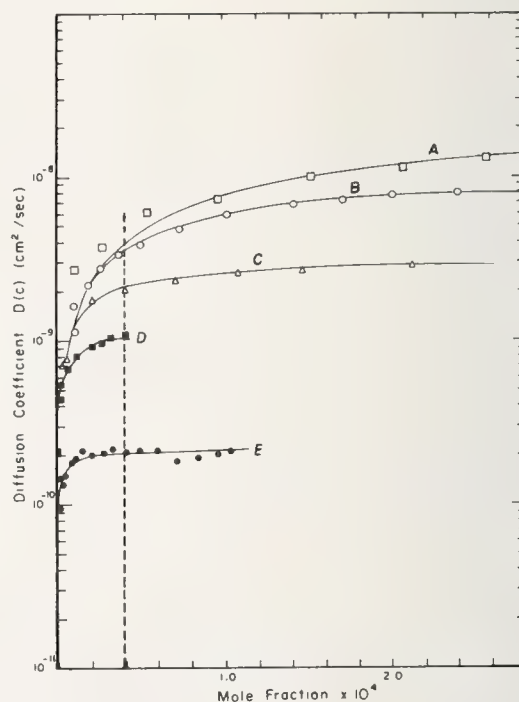


Figure 2. Diffusion coefficient of  $\text{Cd}^{2+}$  in sodium chloride as a function of cadmium concentration. The data were measured at (A) 20°C, (B) 472°C, (C) 422°C, (D) 376°C, and (E) 301°C. (ref. 11).



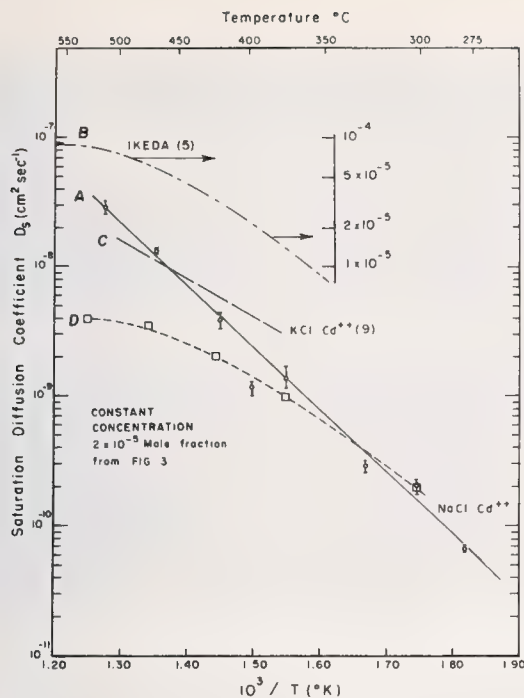


Figure 3. Log  $D_S$  vs  $1/T$  for  $\text{Cd}^{2+}$  in NaCl. (A) Saturation diffusion data. (B) Literature data with large  $D$  and bent Arrhenous plot (Ikeda, T., Japan J. Phys. Soc. 19, 858 (1964)). (C)  $\text{KCl}:\text{Cd}^{2+}$  (Keneshea, F.J. and Fredericks, W.J., J. Phys. Chem. Solids 26, 501 (1965)). (D) Arrhenous plot of constant concentration  $D$  from figure 2. (ref. 11).

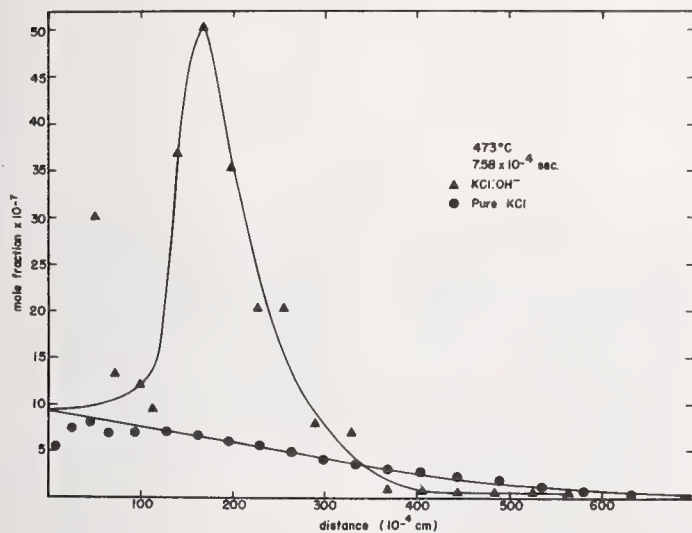


Figure 5. Comparison of mercury diffusion in pure KCl (circles) and hydroxide doped KCl ( $\text{KCl}:\text{OH}^{-}$ ) (triangles). In both experiments the crystal temperature was  $473^{\circ}\text{C}$  and the diffusion time  $7.58 \times 10^{-4}\text{s}$ . A vapor source of  $\text{HgCl}_2$  at  $180^{\circ}\text{C}$  in  $1/3$  atm  $\text{Cl}_2$  provided the diffusant. The  $\text{KCl}:\text{OH}^{-}$  profile was arbitrarily brought to the same surface concentration as found for pure KCl. (ref. 13).

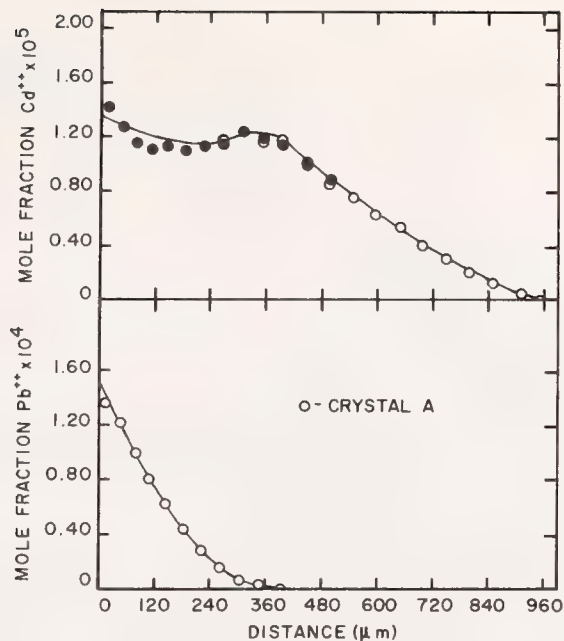


Figure 4. Penetration profile for simultaneous diffusion of cadmium and lead ions into purified KCl at  $455^{\circ}\text{C}$  for  $3.920 \times 10^5\text{s}$ . (ref. 12).

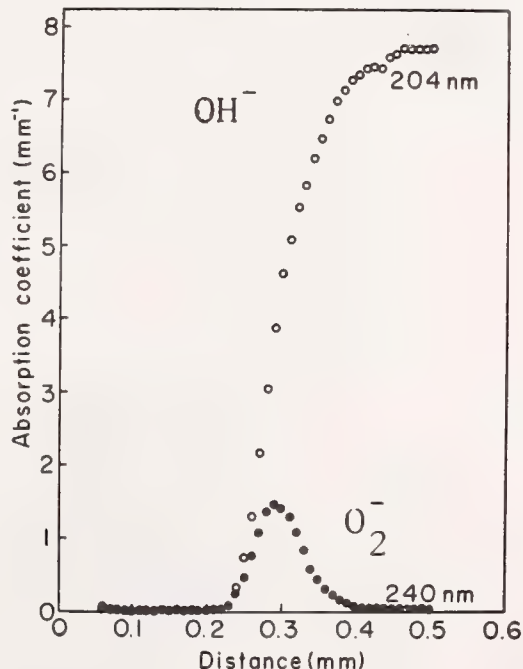


Figure 6. Distribution of the  $240\text{ nm } \text{O}_2^{-}$  band relative to the  $204\text{ nm } \text{OH}^{-}$  band after exposure of  $\text{KCl}:\text{OH}^{-}$  to  $\text{Cl}_2$  at  $1180$  torr for  $20\text{ hr}$  at  $600^{\circ}\text{C}$ . Initial  $\text{OH}^{-}$  concentration not specified. (ref. 15).

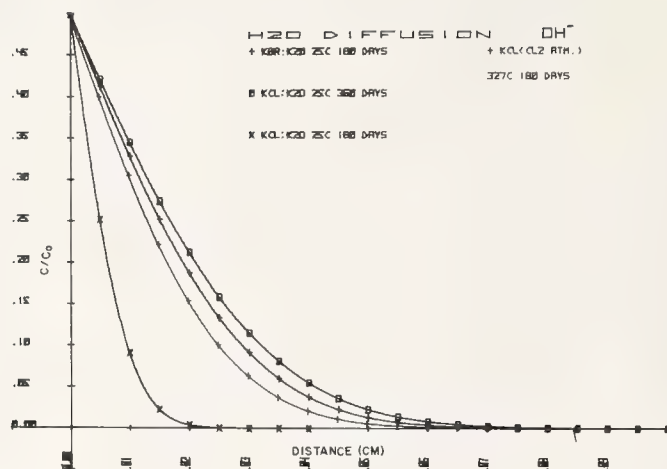


Figure 7. Fractional diffusion profiles  $C/C_0$  vs distance for  $H_2O$  and  $OH^-$  in KCl and KBr when diffusion is enhanced by impurity reactions. The lowest curve represents  $H_2O$  in  $KCl:K^+$  after 180d at  $25^\circ C$ . The next represents  $OH^-$  in KCl if enhanced by  $Cl_2$  after 180d at  $327^\circ C$ . The third curve represents  $H_2O$  in  $KCl:K^+$  after 360 d at  $25^\circ C$ . The highest curve represents  $H_2O$  in  $KBr:K^+$  after 180 days at  $25^\circ C$ . These profiles were calculated assuming the values of  $D$  and  $U$  obtained by Gründig and Rührenbeck (18) are valid at these temperatures. The figure should represent the "worst case" condition.

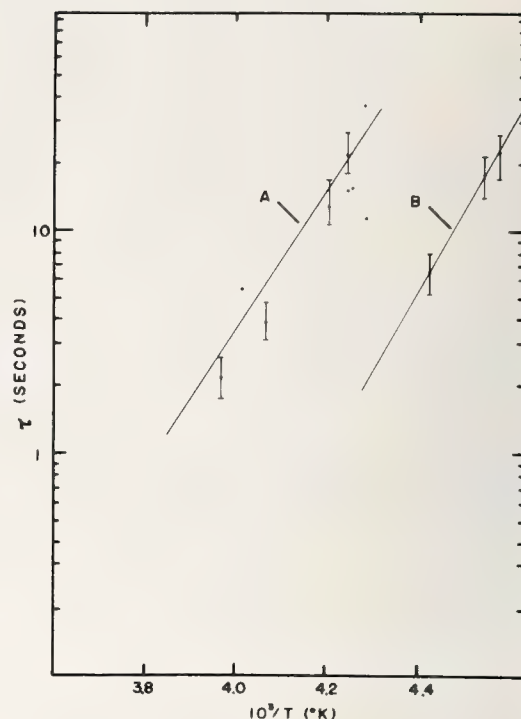
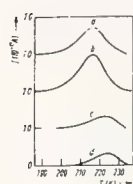


Figure 8. Dipole relaxation time  $\tau$  vs  $1/T$  for a  $KCl:Cd^{2+}$  ( $60 \times 10^{-6}$  mol fraction) showing the additional relaxation formed by exposure to atmospheric  $H_2O$  for 12 mo. (ref. 20).



Plots of the thermal depolarization current  $I$  against  $T$  for a crystal of  $KCl:Sr^{2+}$  annealed at  $623 K$  for 15 h. (a) Immediately after quenching, (b) after 1 h at  $250 K$ , (c) after a further hour at  $250 K$ , (d) after 17 h at  $250 K$ .

Thermal depolarization parameters for  $KCl:Sr^{2+}$  annealed at  $623 K$  for 15 h. Letter identifying runs are explained in the caption to Fig. 2

run	$Q_0$ ( $10^{-11} C$ )	$E$ (eV)	$\tau_0$ ( $10^{-13} s$ )
LT peak, $T_m = 216 K$			
a	1.44	0.875	30
b	2.02	0.870	30
c	0.12	0.875	30
HT peak, $T_m = 224 K$			
a	0.489	0.74	4.7
b	0.489	0.74	4.7
c	0.753	0.74	4.7
d	0.795	0.74	4.7

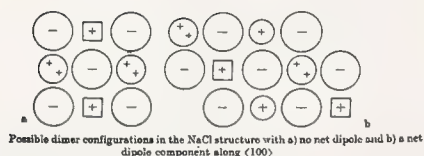


Figure 9. Thermal depolarization of  $KCl:Sr$ . (ref. 27).

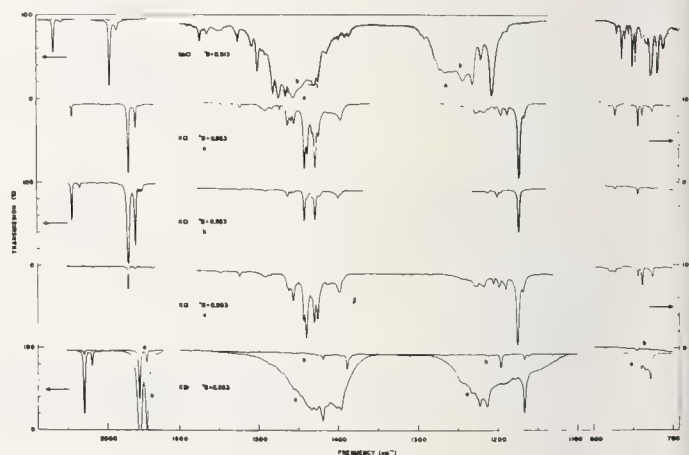


Figure 10. Spectra of boron containing species in NaCl, KCl, and KBr taken at  $T \approx 100^\circ K$  ( $700-1600 cm^{-1}$ ) and  $T \approx 300^\circ K$  ( $1930-2080 cm^{-1}$ ) which demonstrate the effect of thermal history upon the equilibria between species. a. (before quenching), b. (after quenching from  $605^\circ C$ , and c. (after annealing) denote the thermal history of a particular crystal. The small numbers near symbol refer to isotopic composition of the  $BO_2$ . (ref. 6).



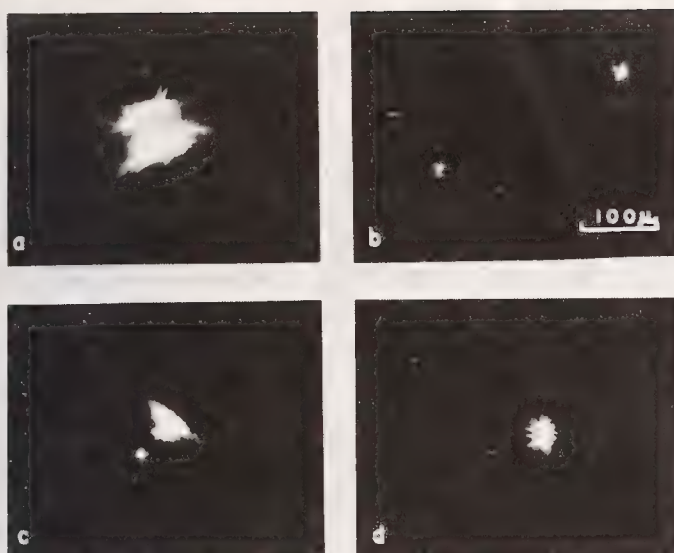


Figure 11. Light scattering observed by means of an ultramicroscope. Large clusters in (a) KBr, (b) NaCl, (c) KBr, and (d) NaCl. All crystals doped with metaborate ion. (ref. 6).

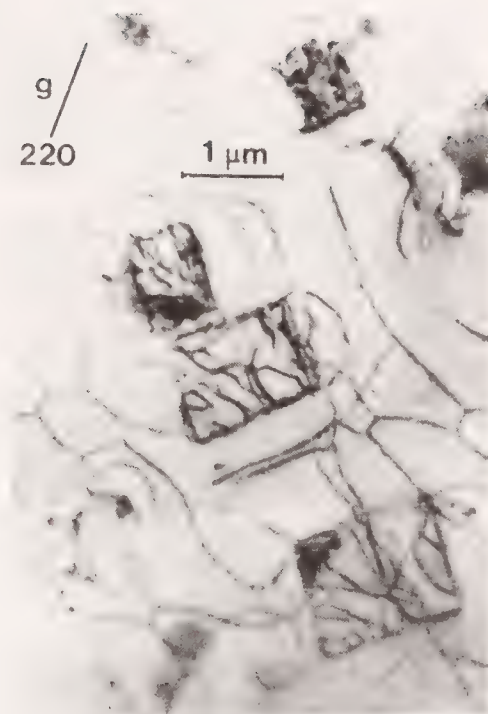
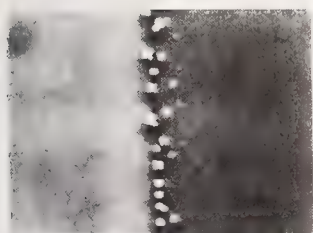
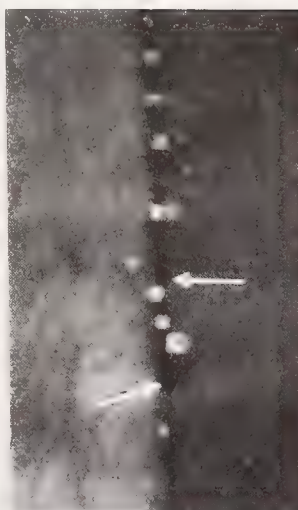


Figure 12. Suzuki phase precipitates ( $6\text{NaCl} \cdot \text{MnCl}_2$ ) showing interface dislocation structure in a TEM micrograph at  $15^\circ\text{K}$ . (ref. 39)

#### High-Resolution Examination of Uncoated Insulators by SEM



(001) bicrystal surface showing segregation of precipitates (white) to grain boundary (vertical, black). Specimen tilt  $45^\circ$  (about horizontal axis), accelerating voltage 25 kV



(001) surface showing precipitates of cubic morphology and cavities (black spots indicated by arrows) at grain boundary. Specimen tilt  $45^\circ$  (about horizontal axis), accelerating voltage 25 kV

Figure 13. Precipitation along a grain boundary in NaCl. (ref. 40).

# COMMENTS ON PAPER BY FREDERICKS

*In response to a question about possible clustering of calcium hydroxide impurities in potassium chloride windows the speaker remarked that whereas some hydroxyl compounds form clusters in a very short time, his estimations indicate that something like a year would be required for the formation of significant calcium hydroxide clusters. He further commented that the effect of ultraviolet radiation in enhancing diffusion and clustering of impurities has not been explored but since ultraviolet excitation changes the electronic structure of the lattice and of course can lead to color centering, one would expect the migration of impurities through the lattice to be affected by ultraviolet radiation.*



# PURIFICATION OF POTASSIUM BROMIDE AND ALKALINE EARTH FLUORIDES FOR LASER COMPONENTS

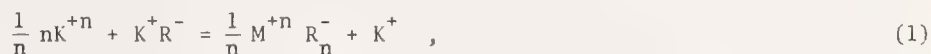
W.J. Fredericks  
Chemistry Department  
Oregon State University  
Corvallis, Oregon 97331

The use of selective ion filters and reactive gas treatment for purification of KBr  $\text{SrF}_2$  and  $\text{BaF}_2$  is considered. The principles of design of selective ion filters and the choice of materials for such systems is discussed. Examples of the construction of such systems are given. A system for removing monovalent impurities from alkaline earth fluorides is shown. A greaseless reactive gas system and a three stage reactive gas seal were developed.

Key words: Potassium bromide; strontium fluoride; barium fluoride; ion exchange purification; selective ion filters; reactive gas purification.

## Introduction

In using ion exchange resins to separate a mixture of trace ionic impurities from a desired major constituent one utilizes the property of the resin to bind these various ions to itself with varying degrees of tenacity. The common measure of the property is called selectivity. It is measured as an equilibrium quantity of the reaction of the type given by



then the selectivity E is a mass action constant given by

$$E_K^{M/n} = \frac{(a_{M+n})_R (a_{K^+})_S}{(a_{K^+})_R (a_{M+n})_S} \quad (2)$$

Where a is the activity of the various components in the resin phase R or in the solution phase S. The selectivity is not constant for a particular ion on a particular resin but is a function of any of the conditions of the resin or solution that affect the activity of the components in either phase. The major factors that affect E are given in Table 1.

Table 1. E is a function of any factor that affects the various activities.

Examples:

1. Resin type and structure (energy of sorption)
2. Extent of resin cross linking
3. Resin swelling
4. Ionic charge
5. Total ionic strength of passing solution
6. Relative ionic strength of exchanging ions
7. Extent of hydration of ions (size)
8. Strength of hydration bond
9. pH of the solution
10. Temperature

This property of differential absorption for various ions on the resin can be used in many ways to separate a mixture of such ions. In Table 2 we list the principal ways in which one employs these resins to separate mixtures of ions.

Table 2. Application of resins.

1. Ion exchange chromatography
2. Ion exclusion
3. Ion conversion
4. Frontal analysis
5. Selective ion filters (requires several stages)

Selectivity coefficients are determined by rather tedious equilibrium measurements in which a small quantity of resin is shaken for several hours with a small quantity of solution. Then the solution is removed and the resin is washed to remove the ions it has absorbed, then both solutions are analyzed. However, a more practical measurement is a quantity we call the separation coefficient which is given by equation 3.

$$S_i = \frac{C(i)}{C_0(i)} = f(\text{Resin}, C_t, T, Q, \dots, \text{etc}) \quad (3)$$

This quantity is not a thermodynamic quantity and simply the ratio of the concentration of an impurity in the elutant from a column containing a measured quantity of the resin to that in the original solution. It is not a equilibrium quantity.

Of the five methods given in table 2, the two most useful in preparation of materials for crystal growth are ion exchange chromatography and selective ion filters. For ion exchange chromatography the major component and the impurities contained in its solution are absorbed on a resin. Then the various ions are eluted from the resin in a solvent in a sequential order. This process is not particularly efficient when one of the components far exceeds the others in concentration. It is a process of last resort and purification of salt systems for crystal growth simply because of the concentration problems with overlapping elution bands and the size of the columns required. The preferred method is a selective ion filter. These operate with a combination of resins in which the orders of selectivity for various ions differ between two or more resins. In table 3 we list the selectivities of four cation exchange resins in which the order of the monovalent ions differ.

Table 3. Dilute solution selectivities.

Chelex 100	$H \gg Li > Na > K > Rb > Cs; Cu^{++}/Na^+ \gg 100$
AG50W	$Ag > Rb > Cs > K > NH_4 > Na > Li$
Bio Rex 40	$Cs > Rb > K > Na > H > Li$
Bio Rex 70	$H > Ag > K > Na > Li$

The Chelex 100 will absorb hydrogen, lithium, sodium more strongly than potassium while in the other three, in particular AG50W, silver ribidium and caesium are absorbed more strongly than potassium and potassium more strongly than ammonia, sodium, and lithium. Thus, if you pass a solution containing a mixture of these ions first through Chelex in potassium form the hydrogen, lithium, and sodium will be removed. Then passing the same solution through AG50W in the potassium form ammonia, sodium and lithium will be removed. Thus by passing a solution through the two resins we have a filter that passes only potassium ion. I list only the copper-sodium ratio of selectivities which is far greater than a hundred as it is typical of the much greater tenacity with which the divalent ions are bound to the resin than the monovalent ions.

The selectivities given in table 3 are for very dilute solutions passed under ideal conditions. In order to actually construct a selective ion filter, one must measure a property that describes a separation of the ions under actual operating conditions. For this we use the separation coefficient and measure it as a function of concentration of the solution, pH of the solution, and any other parameters that one may vary in the development of the separation process. These can be measured rather quickly on a small column. However, one must measure them over a rather wide range of conditions in order to be assured that the operating latitude of the columns will be sufficient to accommodate a large volume of solution. In figure 1 we provide an example of the type of measurements one makes to measure the separation coefficients for ion exchange filters.

Clearly for the separation of the divalent ions on an ion selective filter a chromatography column must first be used to absorb the desired divalent ions and allow the monovalent ions to elute. Note again the ratio of selectivities between divalent ions and monovalent ions are the order of a hundred or more. However, the resin has a finite capacity for the amount of ion it can absorb and thus extremely large columns are required for separation of the alkalies from the desired divalent ion. An alternative is to use a chemical process which will remove the monovalent ions to the extent that they are no longer troublesome. This sort of a system will be described later in this paper.

The anion resins are not available with differing orders of selectivity. One can build a system using several anion resins in which the initial resin absorbs most of the polyvalent ions and the anion complexes that may be present while the second resin produces an extremely strong acid solution of the salt which will have very minor amounts of other anions present. That type of system is used in both the monovalent and aliovalent ion systems. The anion resins again possess the property that they absorb the polyvalent ions much more strongly than the monovalent ions and that larger ions are much more strongly absorbed than smaller ions. Thus a solution passing through this double anion exchange resin system will be free most anionic impurities with the exception of other ions very similar to it. For example, in our systems we expect no carbonate or hydroxide or sulfate or bisulfate or bisulfite ions but we do expect other halide ions with the exception of iodine. These halogens can be removed by HBr in the reactive gas treatment occurring later in the process of purification.

#### Selection of Materials of Construction

One of the best means of preventing contamination of the solutions is to allow them to contact only materials which they do not wet and do not strongly absorb impurities. Many plastics possess these desirable qualities and are satisfactory for the construction of these systems. However, condensation polymers that contain amide or ester bonds, such as nylon or dalrin or any of the polyesters, must be avoided as these bonds are hydrolized by the solutions used in these processes. The best polymers for use in these systems are the addition polymers such as polyethylene, polypropylene, and teflon. However methylmethacrylate which contains an acid side change not involved in the polymer bond is also satisfactory. The latter has a lifetime of about 10 years in chloride systems and should be similar in bromide systems. It fails by swelling and checkering and not by decomposition of the polymer bond. Thus it does not release organics into the solution. It will not take materials such as gaseous



hydrogen bromide which cause it to crack rather quickly. Any substance used in construction contains impurities. Table 4 shows a common impurities found on and in various materials commonly used in purification and crystal growth. It contains both useful and useless materials to provide a comparison. The impurities in highest concentration are mostly iron, zinc, cobalt on the plastics listed in this table. They come from mold release compounds or extrusion greases used in forming the materials and the great portion of them are on surfaces. They will not be removed by ordinary washing but can be removed by chemical treatment. They are in the form of stearates or oleates and can be removed by first treating with a strong acid to hydrolyze the insoluble soap bond forming a soluble metal nitrate or halide then washing this portion free leaving the fatty acid behind. Next treat with a strong alkali such as potassium hydroxide that forms a soluble soap which can then be washed out of the system. Otherwise they remain on the system and slowly contribute ions to the solutions being purified. We have found the above treatments when associated with ultrasonic cleaning in the rinse cycle to be very effective in reducing the contaminants on the plastics we used. Examination of the elastimers shows them to be even more contaminated and while a good portion of this contamination is on the surface a large amount is incorporated in the compound itself. We have not successfully been able to remove this by any cleaning process to a low enough level to allow these materials to be in direct contact with the flow stream of the material being purified. Thus in the portions of the system where elastimers must be used, they should form the seal in a blind seal chamber. This is done in our systems by allowing tubing that is sealed by an o-ring to extend beyond the o-ring a half inch into a tightly pressed seat. Then the o-ring is driven against the external portion of the tubing by a compression nut. Not all elastimers are suitable for use in our systems. We have found that polyethylene-polypropylene o-rings are the only materials that hold up to our solutions without decomposition.

#### Design of the KBr Purification System

The system used for purification of the potassium bromide is shown in figure 2. It consists of seven columns, four of which are ion exchange columns and the other three are used to control the pH of the solution passing through the systems. It contains five reservoirs, one for raw KBr, one for pure KBr, one for KOH, one for water, and one for HBr. The latter four reservoirs are used in regeneration of the columns or in changing the pH of the solution as it passes through the system for purification. The first cation resin is Chelex 100 in the potassium form, the second cation resin is AG50W in potassium form, the first anion resin is AG2 and the second anion resin is AG1 both in the bromide form. All the places marked F are filters, the first is a millipore filter with five micron pores, the second is a polypropylene filter, the third is a polypropylene filter, and the fourth is a millipore filter containing five micron pores. All the millipore filters are teflon-based mitex filters. The only commercially available parts are the check valves that occur in the lines used to adjust pH or concentration. This is to prevent back flow and contamination of the reservoirs should the pressure of the KBr solution exceed that in the reservoir. If an operator inadvertently opened the wrong valve, he could cause the system to flow backwards into an unpressurized reservoir. These valves are completely made of teflon and are available from the Fluorocarbon Company. Pressurization is done by filtered regulated nitrogen. The system is usually operated at 5-10 pounds gauge pressure. All other components are constructed of polyethylene, polypropylene, methyl methacrylate, or teflon. The on and off valves are designated by a cross in a circle, the adjustable flow valves are denoted by a half-filled circle and sampling valves denoted by a cross with an external dot. The boxes marked with an M and a subscript are measuring stations. These consist of a methyl methacrylate body with a teflon plug containing a silver chloride/glass hydrogen electrode and are used to measure pH at that point. Note that all measuring stations are in a line in which a portion of the solution being purified is passed to a waste line and does not return to the main stream. This is to avoid contamination of the solution by the electrode. Not shown in the diagram is a hydrostatic head device used to assure that the electrodes are always emersed in solution. The pH adjusting columns shown in the diagram contain a series of baffles to assure that the solution which is brought in to the central portion of the bottom column cap is thoroughly mixed with the adjusting solutions that come in through side of the bottom cap. These are all constructed on the same module for efficiency in the machining of the parts. The on-off valves, the adjustable flow valves, the sampling valves and the sampling chambers are all constructed on the same module which is shown in figure 3 with the various devices that fit into it. An additional device, which converts any of the valves to a point at which resin or other materials can be inserted or removed from the system at a direction perpendicular to the plane of the drawing. In the potassium bromide system, these are used only when filling the columns with resin or removing resin from a column. Each of the columns has a polypropylene filter built into its base to prevent resins from passing through into the finer filters marked F in the system.

The hydrogen bromide is made from 15 MΩ water and electronic grade hydrogen bromide gas. It is made in a polyethylene system and analysis shows the concentration of impurities to be below the limit at which we can detect them (a fraction of a part per million). The potassium hydroxide is purified within a column system of Chelex 100 in the potassium form and AG1 in the hydroxide form. It is not ultrapure but is low in aliovalent ions and in alkalies other than potassium. The raw potassium bromide solution is 2 molar and has been passed through analytical grade filter to remove the insoluble materials always found in reagent grade chemicals. It is initially made acid by the addition of hydrogen bromide but once in the reservoir potassium hydroxide is added to it to bring its pH to 7.5 to 8. Table 5 gives an analysis the worst lot of potassium bromide obtained from Mallinkrodt Chemical Company. The raw salt contains an amazing quantity of caesium and sizable amounts

of lithium and ribidium. The aliovalent ions iron and nickel are present in larger quantities than most other impurities for which we analyzed. The analyses were done on a Perkin-Elmer 403 atomic absorption spectrograph using an HGA 2100 graphite tube furnace as the evaporation source. The detection limit is the actual measured detection limit from the statistics from the various measurements.

To place the system in operation, it is first washed with hydrobromic acid, followed by deionized water, followed by potassium hydroxide, followed by hydrobromic acid, followed by deionized water until all the pH electrodes indicate that the system is neutral. Then the resins are washed into columns one, three, five, and six. The resins are washed in as the converted form and require only further rinsing with deionized water. The potassium bromide is passed into column one and the entire amount is wasted out M1 until the pH of the effluent is greater than 9. Then it is allowed to enter the first pH column and the effluent is wasted out M2 until the pH at M2 reaches about 7.5. Then acid is added to the bottom of column two at a very small rate until the pH at M2 is less than 6 then it is allowed to enter the third column. The effluent from column three is wasted through M3 until M3 indicates a solution has reached that point then it is allowed to enter column 4 where the pH adjusted to about 6, as measured by M4 then allowed to enter the first anion column. It emerges from the first anine column rather acid and when M5 indicates it has reached that point it is allowed to pass to the second anion column. When M6 indicates an extremely acid solution of pH near 0.8 it is passed into the last column and wasted through M7 until the solution reaches M7 at the appropriate pH then M7 is closed to a slight drip as were all the previous metering stations. The solution is then collected in polypropylene container in the vacuum evaporator. The output of the glass-AgCl electrode at each metering station passes to an operational amplifier interface which converts the impedance from the 1000 M $\Omega$  of the electrode to 4000 $\Omega$  to match the John Fluke 2240A data logger. This device has separate high-low limits which operates a red (high) and a green (low) LED limit indicator at each metering station so that any variance in the operating conditions can be immediately detected by operator and corrected by adjustment of a suitable valve.

During the course of a successful run, about 3 to 4 gallons of purified potassium bromide are collected. There are two evaporators available so that the jars can be changed with only a momentary interruption in the flow process. The vacuum evaporator containing a collection jar is shown in the figure 4. After the jars of KBr solution have been collected the evaporator is placed in a nitrogen tent where the jars are covered and transferred to a vacuum oven to reduce the solution to a reasonably dry solid. The jars are closed, the vacuum oven opened, and the jar replaced in a nitrogen tent and the KBr transferred to a polypropylene bottle for storage.

The purified KBr is placed in a clean quartz crucible while in a nitrogen tent and while in the same tent the crucible is transferred to a 3-inch diameter by 18-inch long quartz test tube. This tube is sealed with a Rh-plated nickel seal which has a smaller three stage seal for a Rh-plated nickel cold finger for crystal pulling. The entire assembly is closed and placed in a crystal growing furnace and the cold finger connected to the pulling mechanism. The furnace has been described elsewhere [2]. A photograph of the three stage seal is shown in figure 5. The system is connected to the reactive gas manifold shown in figure 6. The low pressure HBr is brought in through one of the ports at the side of the cold finger seal. The first stage of cold finger seal is at the same pressure as the interior of the crystal growing chamber, the second stage is at HBr at about 5 pounds guage pressure and the final stage filled with argon at about 7 pounds guage pressure. This arrangement allows only HBr to leak past the seal into the crystal growth chamber and prevents the HBr from leaking into the laboratory. The other port in the seal connects to a separate vacuum system with a liquid nitrogen trap closed by teflon valves. The crystal growth chamber is exhausted through this second vacuum system to prevent contamination of the pure HBr. The gas manifold providing the pure HBr is arranged such that the HBr can be distilled and other gasses, such as bromine or chlorine, can be added to the crystal growth chamber if desired.

When these salts undergo reactive gas treatment there is always some sublimation from the salt in the crucible to cold walls at the top and bottom of the crystal growth chamber. It is with this salt that any volatile compounds that may remain in the system are carried away from the melt. Although the purified salt should not contain such impurities this design provides an additional safeguard against impurities such as Tl<sup>+</sup>.

#### The Alkaline Earth Fluoride Purification System

The program for purification of alkaline earth fluorides is not yet complete. However, the ion exchange systems for their preparation have been designed and constructed and will be discussed here. The materials of construction and components themselves are similar to those developed for the potassium bromide system. However, as the alkaline earth fluorides are not soluble enough for use in ion exchange purification, there are some changes. Further since the alkaline earths have a very high absorption energies on most ion exchange resins, it's necessary to remove the much less tightly bound alkalis from the solutions prior to attempting separation of the alkaline earths and other divalent ions on the exchange resins.

Figure 7 shows the first stage in the purification of the alkaline earths. This stage functions by precipitating an insoluble alkaline earth compound which can be washed free of the alkalis, then converted into an alkaline earth halide and transferred to the initial reservoir for the ion exchange system. This must be done without exposing the alkaline earth solution to an outside environment. figure 8 shows the construction of the system. The raw salt solution reservoirs are on the shelf above the filter systems at the top of this picture. The column on the left is one used to purify potassium



hydroxide and is not part of this system.

Initially a solution of a soluble barium or strontium salt such as an acetate or nitrate is prepared. It is made acidic then filtered through coarse filters to remove the major insoluble compounds, then placed in the initial reservoir and a quantity retained on top of a 1 $\mu$  hydrophobic teflon filter located in the vacuum funnels on top the two-gallon intermediate storage vessel. The solution remains on top of the 1M filter until the vacuum is applied in the container below the filter. Initially CO<sub>2</sub> is allowed to pass through the filter into the region containing the soluble alkaline earth salt. This causes the carbonates to precipitate and this process is carried out until no further precipitation occurs in the solution as observed from the upper transparent port. Then additional solution is allowed to enter the chamber, more precipitation carried out until a quantity of alkaline earth carbonate is collected on the filter. We then apply a vacuum, wash, remove the solution from the alkaline earth carbonate, and start washing with the ionized water. Washing is continued with the effluent passing into our waste system. On the way to the waste system, samples are taken of the effluent using a sampling valve. This is carried out until we no longer detect alkalies, particularly sodium, in the effluent of the system. Then purified hydrobromic acid is allowed to enter the filter chamber. This reacts with the carbonate producing the alkaline earth bromide and CO<sub>2</sub>. A vacuum is again applied to the system, and the solution passes into the intermediate storage chamber. During this time the CO<sub>2</sub> is pumped out through the vacuum and hydrobromic acid is added until the solution in the intermediate storage chamber is slightly acidic as measured on the electrode in the waste line. The alkaline earth bromide is then transferred to the lower 5 gallon container and when that has been filled, nitrogen pressure is used to force the alkali free, alkaline earth bromide into the first container of the ion exchange system.

From that first reservoir the solution is then passed through a cation exchange resin. The first column in that figure is labeled "alkali pass" but is now used to separate the barium and other ions from the strontium. The solution passes from that column into a pH adjust column thence into a second exchange resin to another pH column to a third ion exchange resin to another pH adjust column, then through two anion exchange resins and finally into the last column used to convert bromide to fluoride. At each stage in the system the pH is measured on a calomel/glass electrode. The output of these electrodes go into a separate set of channels on the Fluke data logger. There are again red and green LED lamps provided at each measuring chamber to alert the operator to deviations from permissible operating conditions for the system. The first eight columns are exactly similar to those used in the potassium bromide system and require no further discussion here. The final column is unique in that it is a countercurrent precipitation column. The bromide passes through the center of the top plate is immediately surrounded by a left swirling hydrofluoric acid solution which meets an upward right swirling hydrofluoric acid within the column and the precipitation occurs in the turbulent mixing region. The center of the lower plate is funnel shaped and collects the precipitate as it leaves the column. The precipitate then goes to a filter system similar to that used in the initial stage of this process where it is collected under a vacuum filtration. The effluent is pumped to a lime reservoir that will react with the excess hydrofluoric acid. The ion exchange system is shown schematically in figure 9 and figure 10 shows the basis of the system as constructed prior to its installation in our laboratory. Final filtrate collection chamber is shown in figure 11. In figure 11 in the upper right hand corner the bottom of the precipitation column can be seen with its externally flowing HF and internal funnel.

The anion exchange resins are exactly the same as those used in the potassium bromide system. However the cation exchange resins are different and have not been completely characterized at this time. Because of the acidity of the solution Chelex 100 may not be as useful as it is in the alkali halide purification systems and that AG50W, Bio Rex 40 and Bio Rex 70 may be the best choices for resins purification of the alkaline earths. The measurements for characterization are currently underway and will be shortly completed.

The purification systems described here when operated correctly, should reduce impurities in potassium bromide to the part per million level for alkalies and other halides and for the aliovalent ions to a much lower level. The alkaline earth fluoride systems have not been operated sufficiently to make estimates on the quality of salt they produce. We expect the operating details on the systems will be available shortly.

#### References

- |  |  |
|--|--|
| [1] Rearrangement of data from Bawyer, D.T. and J.L. Roberts Jr. "Experimental Electrochemistry for Chemists." Academic Press, New York, 1974, p. 135. | [2] Fredericks, W.J., L.W. Schuerman, and L.C. Lewis, "An Investigation of Crystal Growth Processes." Final Report, AFOSR-217-66, Chemistry Department, Oregon State University, 1967. |
|--|--|

Table 4. Trace elements in various materials.  
(concentrations in ppb)

Group A/Elements	Zn	Fe	Sb	Co	Cr	Sc	Cs	Ag	Cu	Hf
Teflon	9.3	35	0.4	1.7	<30	<0.004	<0.01	<0.3	22	--
Acrylics (Plexiglass)	<10	<140	<0.01	<0.05	<10	<0.002	<0.06	<0.03	<9.5	--
Polyethylene tubing	55	7.4	9000	140	254	11	<100	<300	--	<100
Polyethylene lab. ware	28	10400	0.18	0.07	76	0.008	<0.05	<0.1	6.6	<0.5
Polyethylene flip top vials	25	10600	0.83	0.51	19	0.56	<0.15	<0.1	15	<0.5
Polyvinyl chloride	7120	270,000	2690	45	2	4.5	<1	<5	630	--
Nylon (bulk)	I	I	I	$1.4 \times 10^5$	I	I	I	I	I	I
Group B										
Surgical rubber tubing	$3 \times 10^6$	I	<100	<50	I	<8	<100	1240	<6	--
Neoprene rubber	$1.8 \times 10^7$	I	290	2300	I	3090	I	1000	--	--
Kimwipe tissue	48,800	1000	16	24	500	14	<0.1	~0.8	--	--
Group C										
Borosilicate glass	730	$2.8 \times 10^5$	2900	81	I	106	<100	<0.001	--	597
Vycor	I	I	$1.1 \times 10^6$	I	I	I	I	I	I	I
Quartz tubing										
"Spectrosil"	1.5	595	0.05	0.44	6.5	0.05	1.1	0.05	2	<0.005
"Suprasil"	<1	I	<0.01	12	2.5	0.39	<0.01	<0.01	0.04	<0.005
Quartz Products	I	I	1940	0.89	I	I	1390	<0.1	0.09	<0.01
United States Quartz	21	--	43	0.64	230	0.18	0.30	<0.1	0.05	27
General Electric Co.	33	--	38	1.1	602	0.16	<0.1	0.1	0.05	26

-- not measured; I interfering radionuclides



Table 5. Levels of impurities in KBr mink #WD6K

(Expressed as ppm or  $\mu\text{g}$  impurity/ g KBr)

Four solutions were made, on days 3-22-77, 2-38-77, 4-1-77, and 4-4-77. The values obtained from each solution are shown in chronological order.

Element	ppm	Detection Limit <sup>3</sup>	Element	ppm	Detection Limit
Cs	1200 $\pm$ 160	242	Cu	5.2 $\pm$ .87	1.2
	1350 $\pm$ 250			5.1 $\pm$ .85	
	1280 $\pm$ 154			5.0 $\pm$ .83	
	1210 $\pm$ 121			6.5 $\pm$ .83	
Na	63.8 $\pm$ 12	10.9	Fe	91.1 $\pm$ 26	22
	68.8 $\pm$ 9.3			83.3 $\pm$ 10	
	57.9 $\pm$ 3.3			75.9 $\pm$ 10	
	64.3 $\pm$ 6.3			70.1 $\pm$ 17	
Li	224 $\pm$ 24	23	Mn	2.00 $\pm$ .22	.49
	206 $\pm$ 4.7			1.53 $\pm$ .21	
	186 $\pm$ 24			1.92 $\pm$ .21	
	181 $\pm$ 13			1.88 $\pm$ .75	
Rb	247 $\pm$ 35	55	Zn	2.30 $\pm$ .30	
	246 $\pm$ 51			2.42 $\pm$ .25	
	238 $\pm$ 25			2.21 $\pm$ .29	
	350 $\pm$ 46			1.71 $\pm$ .75	
Ca	24.3 $\pm$ 21	16.9	Co	12.1 $\pm$ 2.7	1.7
	5.5 $\pm$ 1.7			13.1 $\pm$ 1.7	
	15.0 $\pm$ 14			10.8 $\pm$ 0	
	21.7 $\pm$ 11			10.8 $\pm$ 0	
Mg	1.04 $\pm$ 1.34	2.5	Ni	151 $\pm$ 50	52.1
	.29 $\pm$ 4.7			185 $\pm$ 49	
	.58 $\pm$ .62			166 $\pm$ 25	
	3.30 $\pm$ .29			94.4 $\pm$ 23	
Cu	5.2 $\pm$ .82	1.1	Cr	0 <sup>2</sup> $\pm$ 0.0	1.3
	5.1 $\pm$ .81			0 $\pm$ 1.3	
	5.0 $\pm$ .79			0 $\pm$ 1.2	
	6.4 $\pm$ .79			0 $\pm$ 1.2	

<sup>1</sup>Four samples run on the AA gave the same peak height.

<sup>2</sup>The peak height was very small, and came where the standard curve intercepted zero.

<sup>3</sup>Detection limit calculated as  $\text{D.L.} = \sqrt{2} \sigma_{(\text{samples})} \frac{dA}{dc}$

# Figures

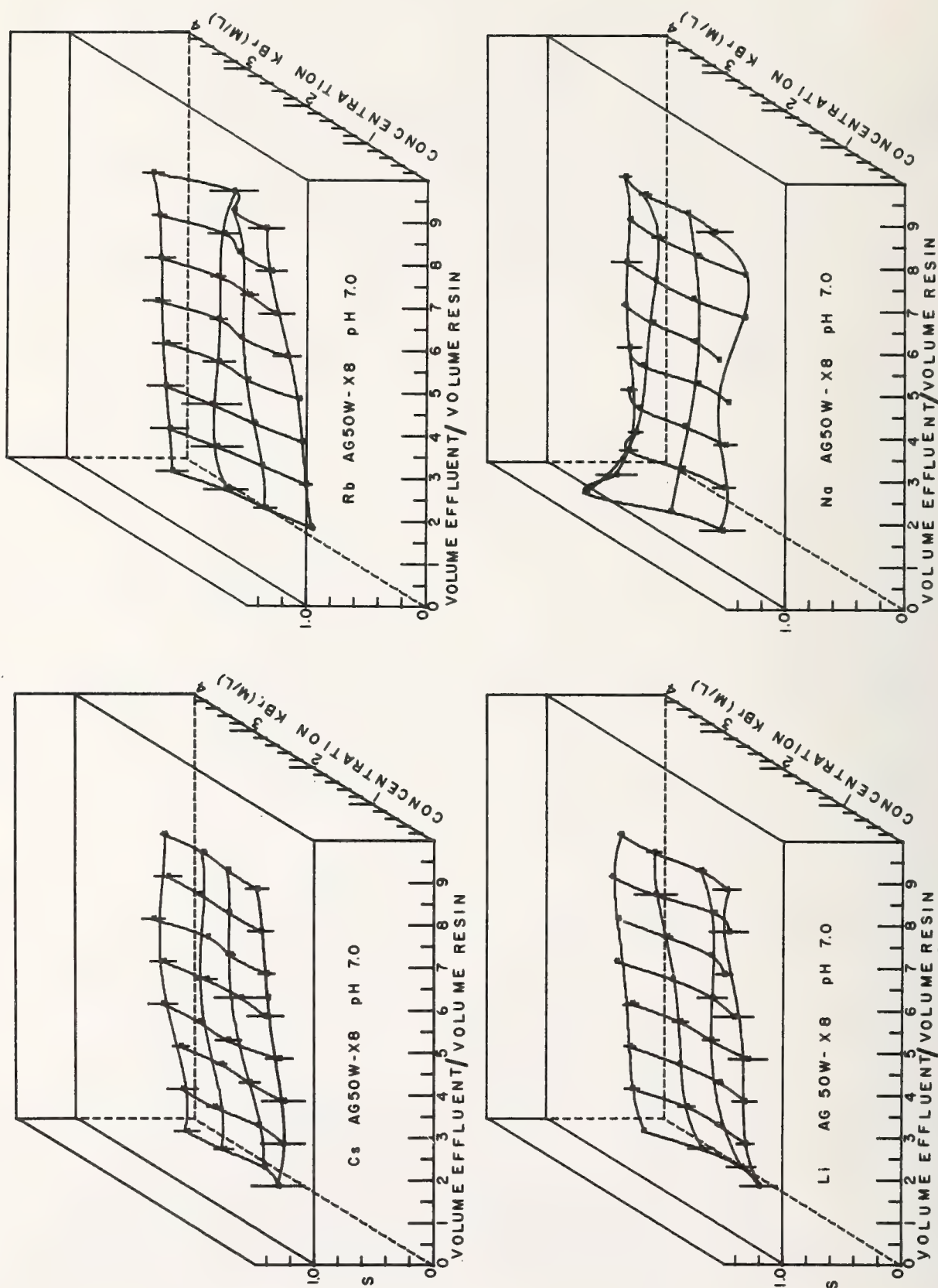
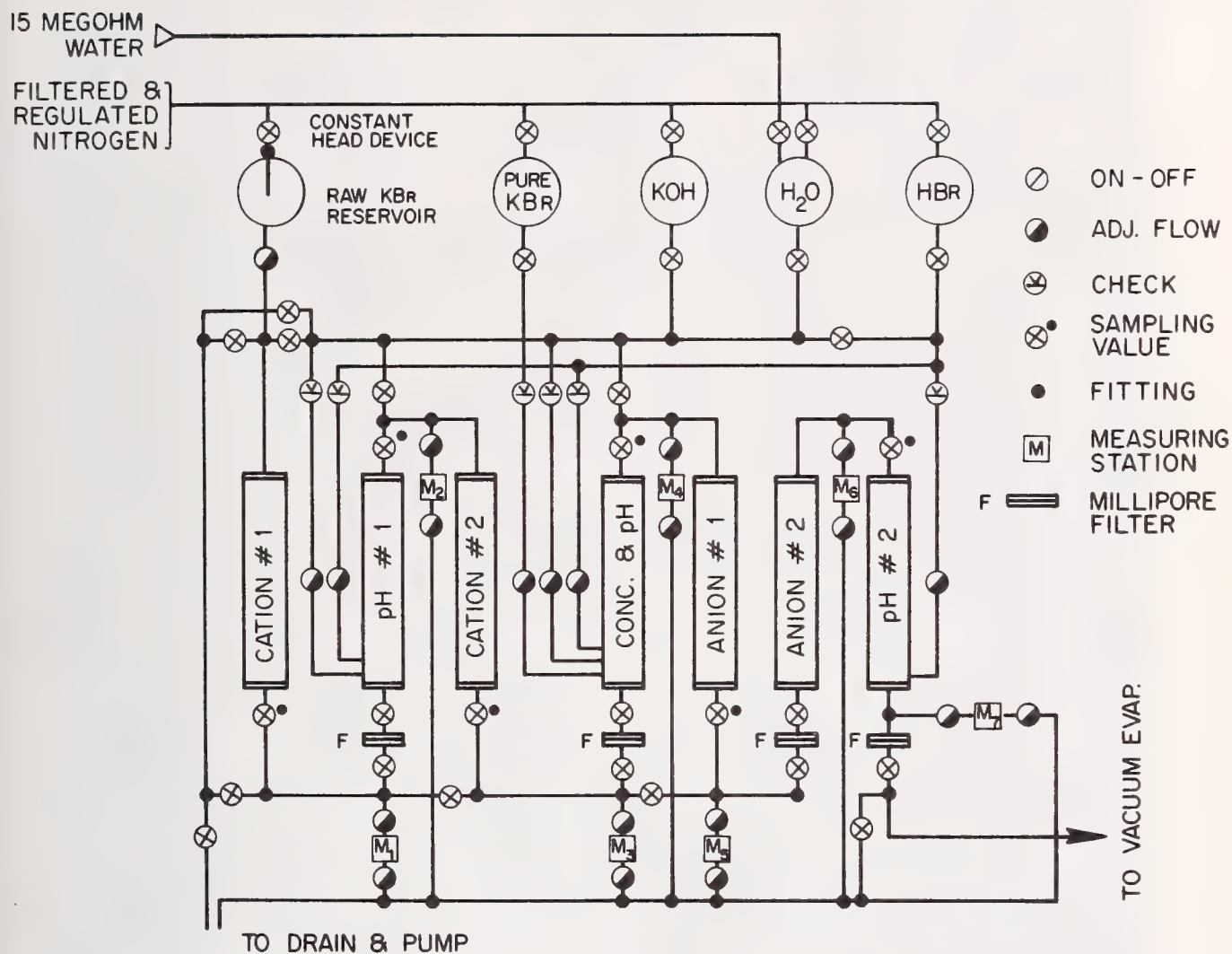


Figure 1. Separation coefficient surface for AG50W-X8 from 1M to 4M from 1 to 8 bed volumes of solution at pH of 7.





## POTASSIUM BROMIDE ION EXCHANGE SYSTEM

Figure 2(a). Flow diagram of KBr ion-exchange system.

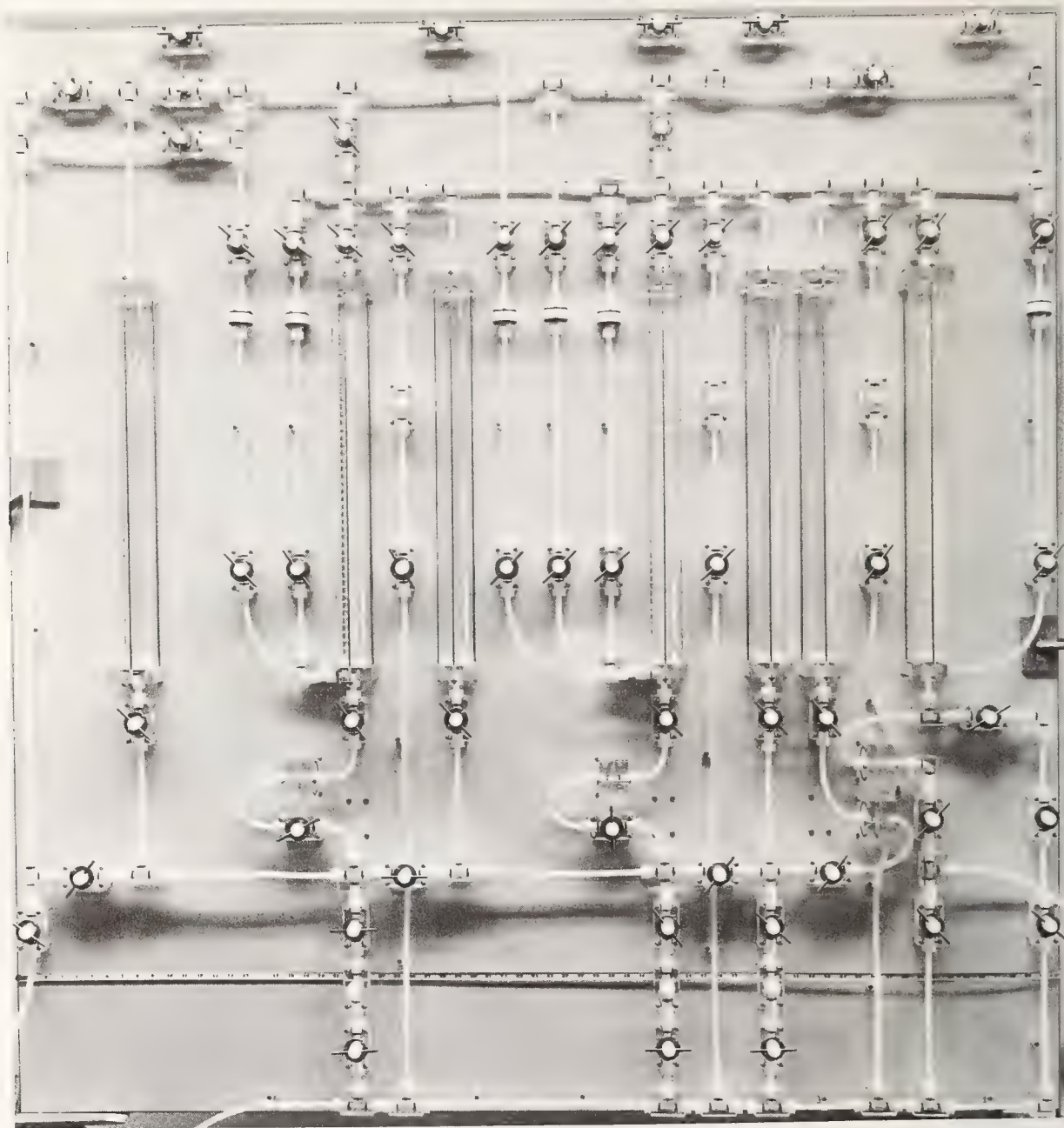


Figure 2(b). Apparatus as constructed.





Figure 3. Valve body and various attachments for sampling and measurements.



Figure 4. Vacuum collector for KBr solutions.



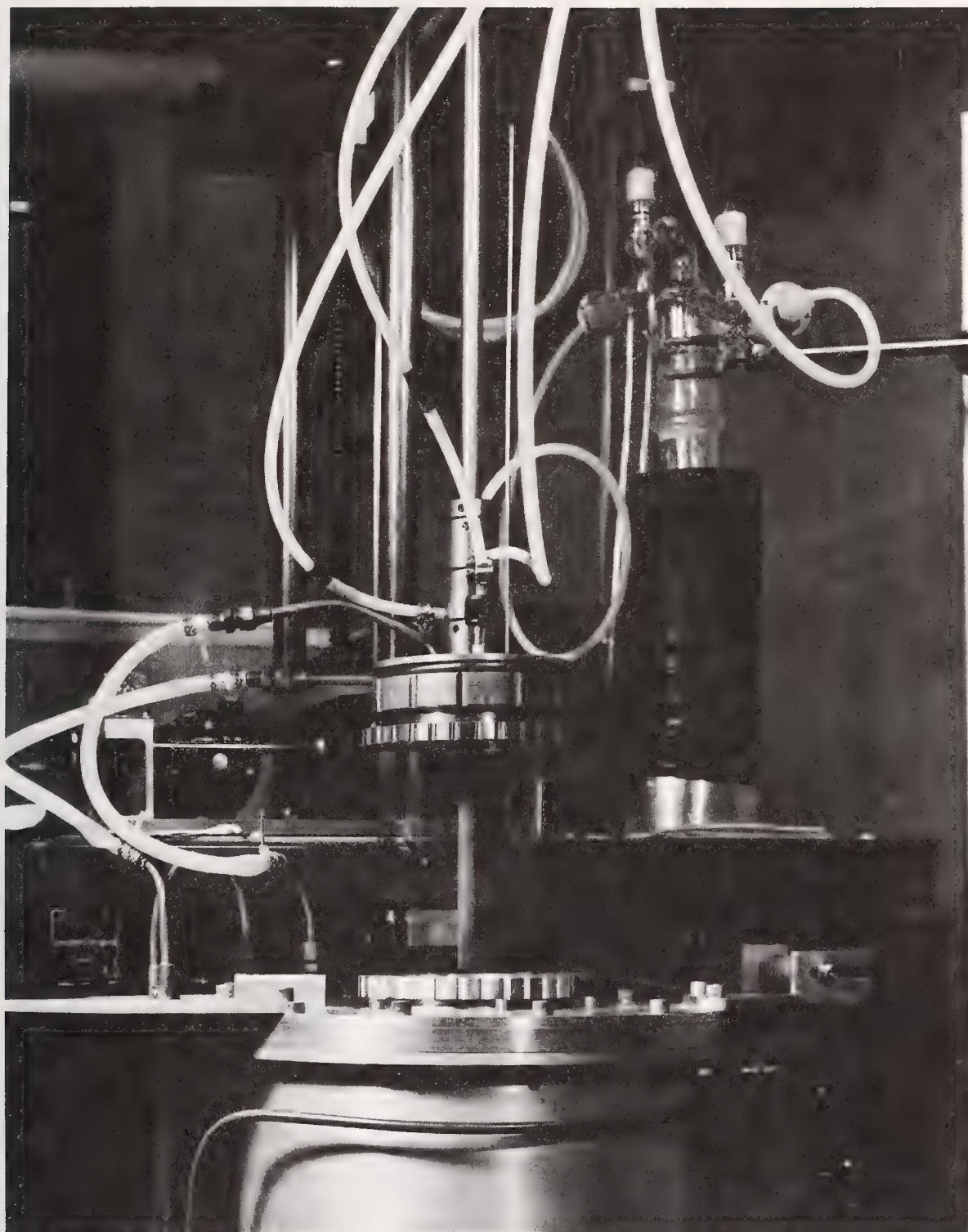


Figure 5. Crystal pulling chamber closure and cold finger seal. All metal is rhodium plated nickel. O-rings are perfluoroelastimer.

# SCHEMATIC OF GREASELESS MANIFOLD FOR CORROSIVE GAS TREATMENT

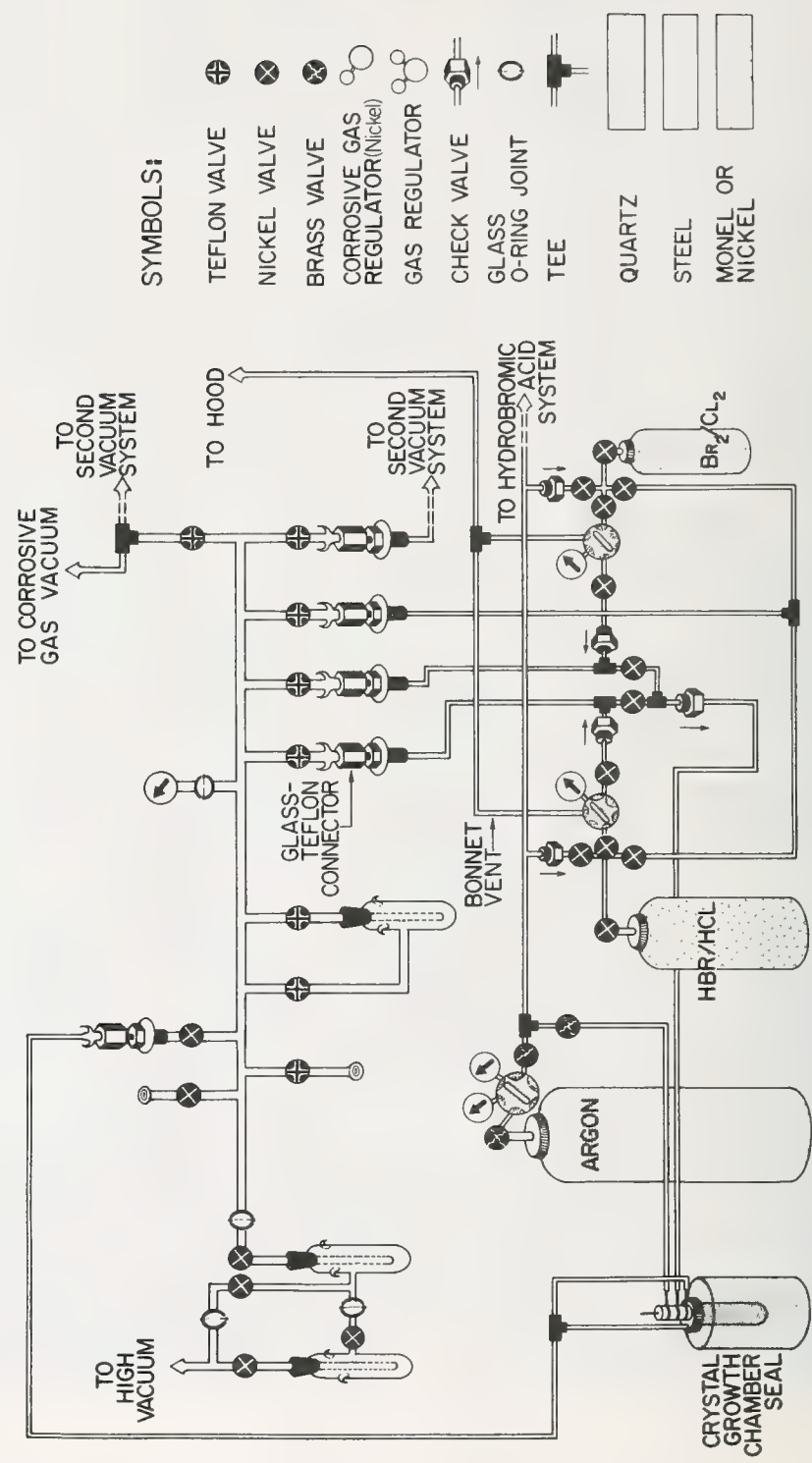
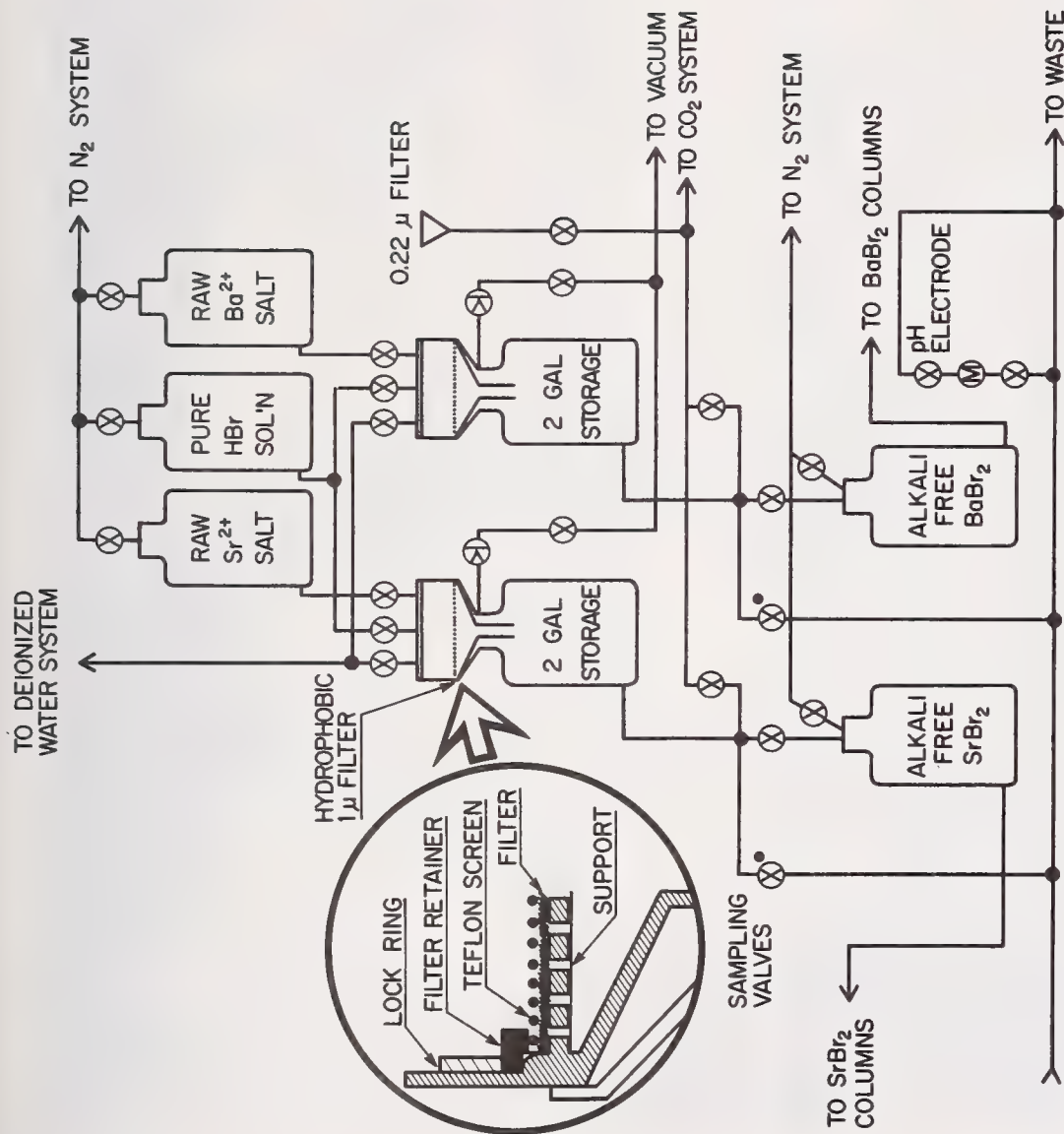


Figure 6. Reactive gas system.





# SYSTEM FOR REMOVAL OF ALKALI AND OTHER MONOVALENT IONS FROM $\text{Sr}^{2+}$ OR $\text{Ba}^{2+}$ SALTS

Figure 7. Removal of monovalent ions from  $\text{Sr}^{2+}$  or  $\text{Ba}^{2+}$ .

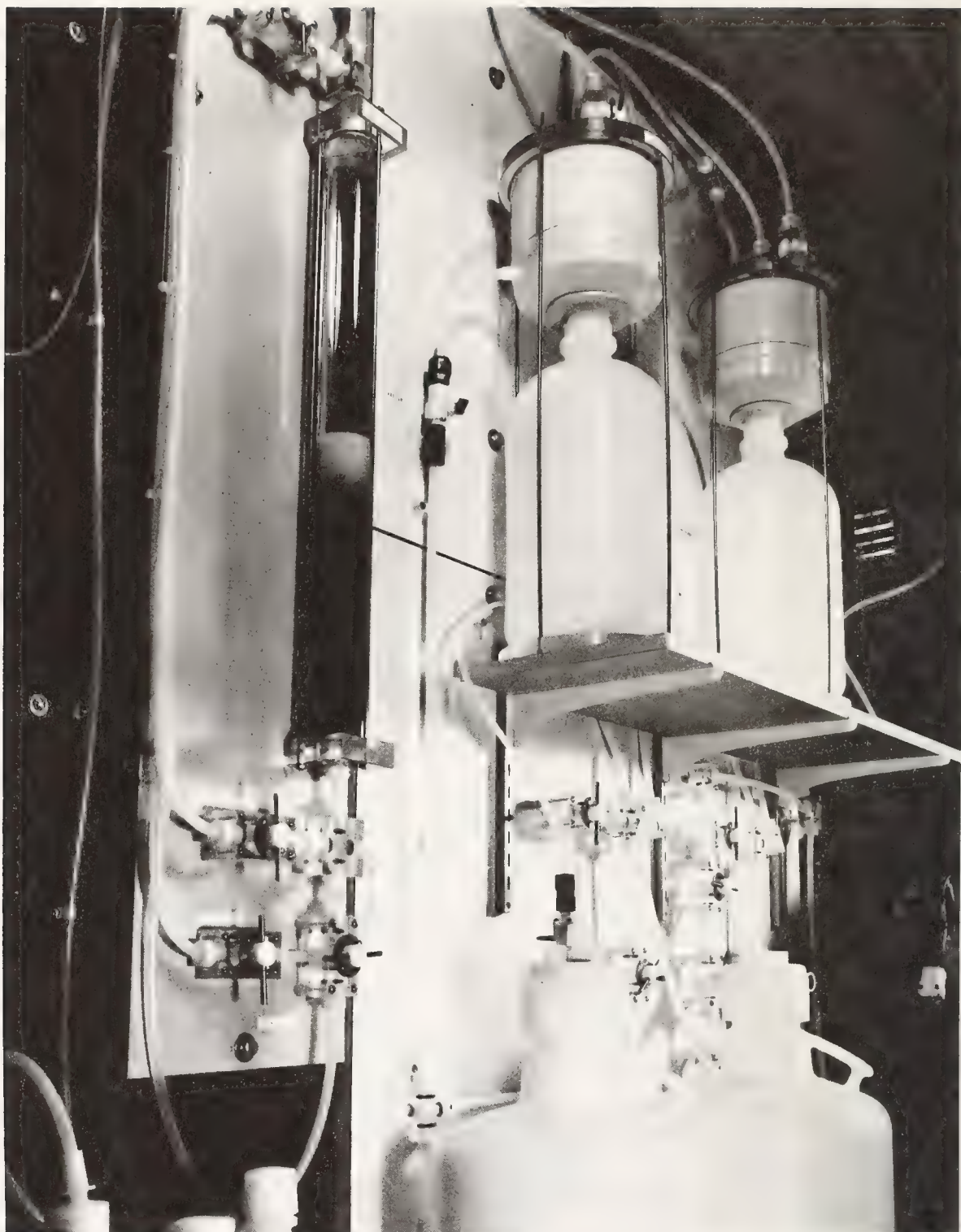
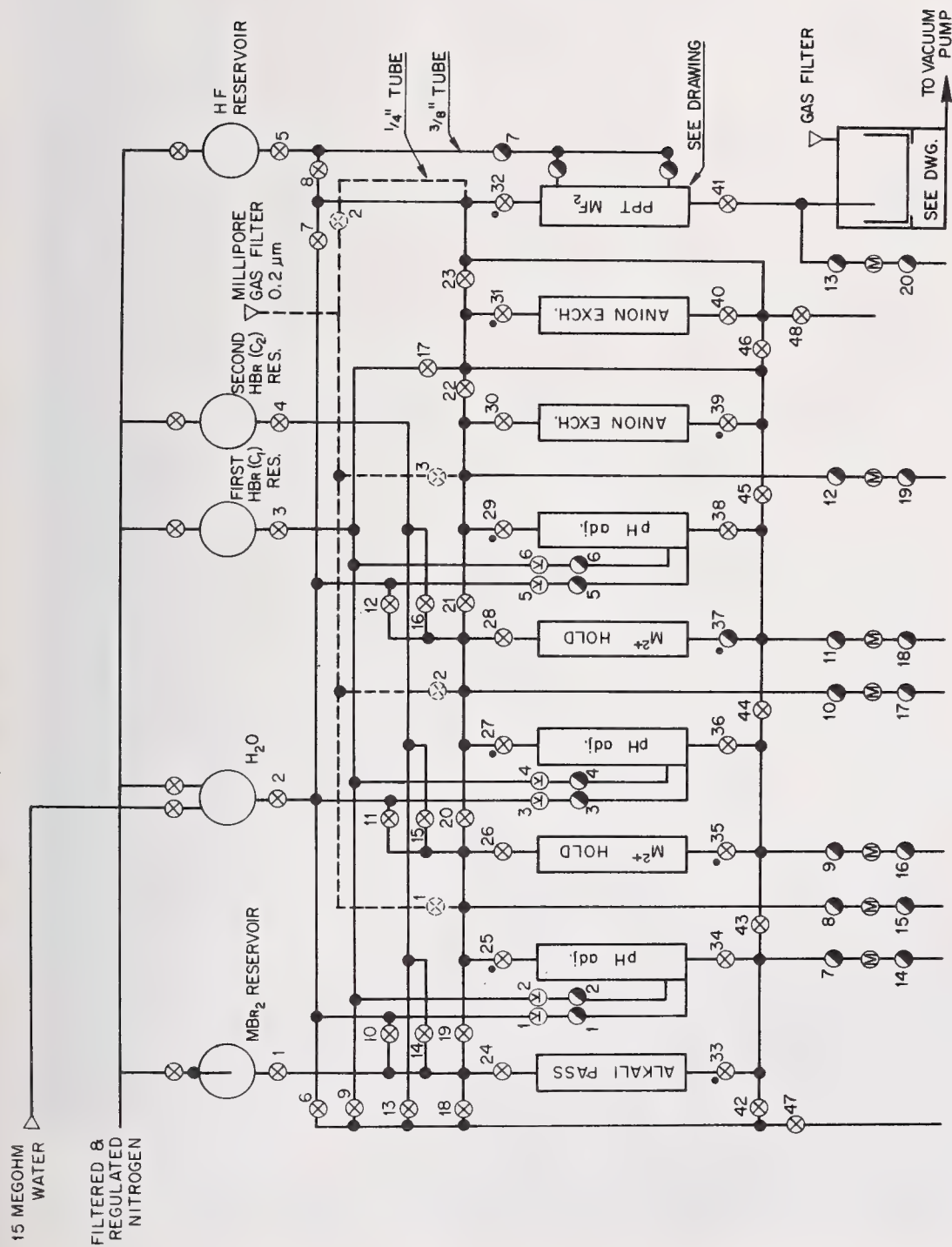


Figure 8. Apparatus for monovalent ion removal.





## STRONTIUM FLUORIDE ION EXCHANGE SYSTEM

Figure 9. Flow diagram for alkaline earth ion-exchange system.

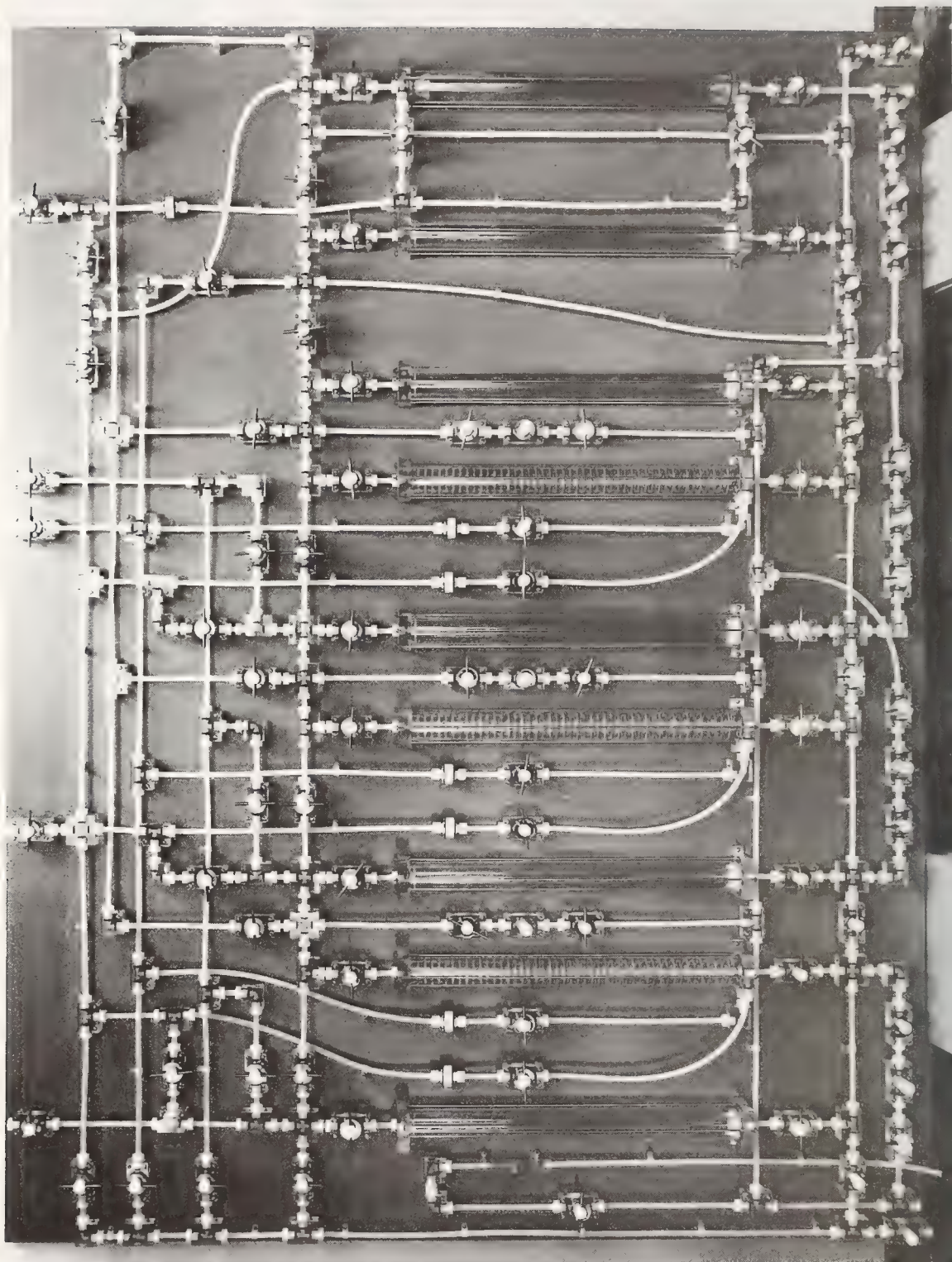


Figure 10. Apparatus for  $\text{SrF}_7$  purification.





Figure 11. Closed filter system for SrF<sub>2</sub>.

FREQUENCY AND TEMPERATURE DEPENDENCE OF  
RESIDUAL INFRARED ABSORPTION IN MIXED FLUORIDE CRYSTALS

H. G. Lipson, A. Hordvik<sup>†</sup> and B. Bendow  
Rome Air Development Center  
Deputy for Electronic Technology  
Hanscom AFB, MA 01731

and

S. S. Mitra\*  
Dept. of Electrical Engineering  
University of Rhode Island  
Kingston, RI 02881

and

J. J. Martin\*\*  
Dept. of Physics  
Oklahoma State University  
Stillwater, OK 74074

We have utilized Fourier spectroscopy and photoacoustic calorimetry to measure infrared absorption of the mixed fluoride crystal  $\text{KMgF}_3$  in the 800 to 2400  $\text{cm}^{-1}$  frequency range at temperatures from 80 to 535°K and compared the results with those obtained for binary fluorides such as  $\text{MgF}_2$  and  $\text{CaF}_2$ .  $\text{KMgF}_3$  exhibits an exponential-like decrease in absorption as a function of frequency at room and elevated temperatures characteristic of intrinsic multiphonon absorption in most ionic materials. At low temperatures, however, well-defined structural features are observed in the absorption spectrum which may be attributed to phonon density-of-states effects. The data indicate that the Mg-F interaction has the principal influence on the  $\text{KMgF}_3$  spectra. We also observe a similar exponential-like absorption vs. frequency for other mixed fluorides such as  $\text{KZnF}_3$ . However, in the 2500 to 4000  $\text{cm}^{-1}$  range our measurements suggest that residual absorption in both mixed crystals is dominated by extrinsic effects.

Key words: Infrared absorption; Magnesium fluoride; Potassium magnesium fluoride; Intrinsic multiphonon absorption; Absorption temperature dependence.

Introduction

Recent investigations have established that the residual absorption in the highly transparent regime of pure non-metallic solids is due to higher order multiphonon processes. In this regime the spectrum is often structureless and the absorption coefficient usually has a nearly exponential dependence on frequency[1]. Extensive experimental investigations of the temperature dependence of residual absorption have been carried out for a variety of ionic crystals, particularly the alkali halides [2-3]. A number of theoretical models [4-8] based on multiphonon interactions have been advanced from which the observed data can be interpreted. The temperature dependence of the absorption coefficient can be understood to a large extent in terms of phonon occupation numbers [9] and some additional considerations [6] related to crystal structure.

We have previously reported [10,11] nearly structureless exponential behavior for the frequency dependence of the absorption coefficient of alkaline earth fluorides. The temperature dependence can be understood in terms of nearly Bose-Einstein like multiphonon behavior. The purpose of the present investigation is to extend these measurements to various fluoride crystals other than those of the fluorite structure, namely,  $\text{MgF}_2$  which crystallizes in the rutile structure, and the perovskites  $\text{KMgF}_3$  and  $\text{KZnF}_3$ .

The cubic perovskites are mixed fluoride crystals of the general formula  $\text{ABF}_3$  where A is an alkali metal ion and B a divalent metal ion. Mixed crystals are known to have better mechanical properties, e.g. hardness, than the end member pure crystals [12], and can be attractive candidate window materials

<sup>†</sup>Present address: Elab, 7034 Trondheim nth, Norway

\*Supported by Deputy for Electronic Tech/RADC, under Contract F19628-75-C-0163

\*\*Supported by Deputy for Electronic Tech/RADC, under Contract F19628-77-C-0176



for high energy infrared lasers if prepared with sufficiently low absorption. Moreover, many of the perovskites are water-insoluble, similar to the alkaline earth fluorides. The perovskites studied in this investigation, viz.,  $\text{KMgF}_3$  and  $\text{KZnF}_3$  were found to be transparent in the CO and chemical laser regions, and also stronger than KCl or KCl-KBr alloys.

Infrared active lattice vibrations in the one-phonon region of  $\text{MgF}_2$ ,  $\text{KMgF}_3$  and  $\text{KZnF}_3$  as well as two-phonon infrared spectra have been reported in the literature [13-16]. First order Raman spectrum [17], and multiphonon infrared absorption [2] of  $\text{MgF}_2$  have also been reported previously. This paper presents the first measurements of temperature dependence of multiphonon absorption for  $\text{MgF}_2$  and  $\text{KMgF}_3$  as well as an analysis in terms of a simplified model [11].

### Experimental Procedure

The  $\text{KMgF}_3$  and  $\text{KZnF}_3$  crystals were prepared at Oklahoma State University from stoichiometric mixtures of KF and  $\text{MgF}_2$  and KF and  $\text{ZnF}_2$ . Crystals were grown by the Bridgman method in graphite or vitreous carbon crucibles using extreme care to minimize water pick-up in the KF during loading, and  $\text{NH}_4\text{HF}_2$  to RAP the system. The crucible was evacuated overnight while held at  $300^\circ\text{C}$ , and then it was pressured with 10 psig of gettered argon and raised to the melting point,  $1070^\circ\text{C}$  for  $\text{KMgF}_3$  and  $870^\circ\text{C}$  for  $\text{KZnF}_3$ . After a temperature cycle to freeze and remelt the material, the crystal was grown at 0.15 cm/hr. The  $\text{KMgF}_3$  crystals used for most of the optical measurements were pulled from the melt. A pull rate of  $< 3$  mm/hr was used with starting material prepared by the Bridgman technique, as described above. The  $\text{MgF}_2$  samples used for transmission measurements were commercial material obtained from Optovac, while the one used for photoacoustic measurements was obtained in polished form from A. Meller Inc.

Absorption values were determined from transmission measurements made with a Digilab Fourier transform spectrophotometer operated in the double beam mode using a nitrogen gas atmosphere. Elevated temperature measurements were made in a small furnace which was placed close to the focal point of the spectrophotometer. Temperature measurements were recorded with Cu-constantan thermocouples placed on opposite sides of the sample periphery, and temperature was controlled with a d.c. power supply. Liquid nitrogen temperature measurements were made in a Janis dewar positioned in the same way, with the sample clamped against an indium ring in contact with the coolant reservoir.

Sample thicknesses used for room and elevated temperature measurements ranged from 0.18 to 2.46 cm. Low temperature measurements on  $\text{KMgF}_3$  and  $\text{MgF}_2$  were made on samples 0.549 and 0.660 cm thick respectively. In the case of  $\text{MgF}_2$ , all transmission measurements were made with the beam directed along the c-axis.

Absorption calculations were made from transmission data stored on magnetic tape using the expression:

$$\beta = \frac{1}{d} \ln \left\{ \frac{(1-R)^2}{2T} + \left[ R^2 + \left( \frac{(1-R)^2}{2T} \right)^2 \right]^{1/2} \right\} \quad (1)$$

where  $d$  = sample thickness,  $T$  = transmission and  $R$  = reflectivity.

Corrections for small variations of the 100% line with wave number were made from comparison to measurements with no sample in the beam using the on-line computer of the spectrophotometer. Reflectivities were determined either from the maximum transmission in an adjacent spectral region where no variation was found, or from comparison with absorption values obtained by photoacoustic calorimetry. More details of the absorption measurement method are given elsewhere [18].

For absorption coefficients above  $5 \times 10^{-3} \text{ cm}^{-1}$ , little variation was found between absorption measured by photoacoustic calorimetry and that calculated from corrected transmission data. Corrections for the variation of reflectivity with wave number or the change of refractive index with temperature also included in the computer program were found to be negligible.

The photoacoustic calorimetric measurements were carried out at several CW laser wavelengths. The laser radiation incident on the sample was periodically interrupted by a chopper, and the resulting acoustic wave amplitude was measured by a piezoelectric ceramic transponder in conjunction with a lock-in amplifier. Experimental details of this method are given in previous publications [18,19].

### Results

Figure 1 shows the room temperature absorption coefficient of  $\text{MgF}_2$ ,  $\text{KMgF}_3$  and  $\text{KZnF}_3$  from 800 to  $2000 \text{ cm}^{-1}$  as obtained by Fourier spectroscopy. On the same figure are points representing absorption at selected wave numbers measured by photoacoustic calorimetry which show good agreement with the

spectroscopic data.  $\text{KMgF}_3$  and  $\text{MgF}_2$  show exponentially decreasing slopes characteristic of intrinsic multiphonon absorption with some structure evident, while  $\text{KZnF}_3$  appears to display extrinsic absorption over much of the frequency range investigated, certainly above  $1400 \text{ cm}^{-1}$ .

Photoacoustic calorimetry results obtained at DF and HF wavelengths are given in Table 1.

Table 1 Total Absorption Determined by Photoacoustic Calorimetry

	DF 3.8 $\mu\text{m}$ (2630 $\text{cm}^{-1}$ )	HF 2.7 $\mu\text{m}$ (3700 $\text{cm}^{-1}$ )
$\text{KZnF}_3$	$5 \times 10^{-2} \text{ cm}^{-1}$	
$\text{KMgF}_3$	$7 \times 10^{-4} \text{ cm}^{-1}$	$7 \times 10^{-4} \text{ cm}^{-1}$
$\text{MgF}_2^*$	$6.7 \times 10^{-4} \text{ cm}^{-1}$ (bulk) $1.2 \times 10^{-4}$ (per surface)	$2.5 \times 10^{-4} \text{ cm}^{-1}$ (bulk) $8 \times 10^{-4}$ (per surface)

\* 1.27 cm thick

The total absorption values for  $\text{KMgF}_3$  prepared at Oklahoma State University are slightly lower than those of commercial  $\text{MgF}_2$  at  $2630 \text{ cm}^{-1}$ , but at  $3700 \text{ cm}^{-1}$  the strong surface absorption of  $\text{MgF}_2$  becomes dominant and makes comparison difficult. The absorption value of  $7 \times 10^{-4} \text{ cm}^{-1}$  for  $\text{KMgF}_3$  is considerably higher than that expected from an extrapolation of the exponential slope of figure 1. This indicates extrinsic behavior resulting at least partially from the surface or bulk scattering. The relatively high value of  $5 \times 10^{-2} \text{ cm}^{-1}$  is again evidence of the extrinsic behavior demonstrated in figure 1.

The temperature and frequency dependence of the absorption coefficient of  $\text{MgF}_2$  and  $\text{KMgF}_3$  are shown in figures 2 and 3. The exponential dependence of absorption coefficient on frequency persists at higher temperatures for both materials. Above  $1800 \text{ cm}^{-1}$  additional absorption is evident which is not present in the initial room temperature data of figure 1. This absorption is attributed to changes in surface condition from temperature cycling during the measurements.  $\text{KMgF}_3$  shows more detailed structure in the absorption spectra than  $\text{MgF}_2$ , particularly at  $80^\circ\text{K}$ .

### Discussion

The perovskites  $\text{ABF}_3$  can be thought of as mixed crystals of AF and  $\text{BF}_2$ . Thus one might at first expect to obtain their optical properties by simple addition of the properties of the two end members. In figure 4 the absorption of  $\text{KMgF}_3$  is compared with that of KF and  $\text{MgF}_2$ . Actually, a close resemblance is observed for the Mg compounds and a much lower absorption and a steeper slope found for KF. This indicates that the Mg-F vibrations are dominant in the multiphonon spectrum of  $\text{KMgF}_3$ . Quantitatively, this can be understood from a comparison of the long wavelength longitudinal optical mode frequencies corresponding to frequencies in the vicinity of the cut-off of the one-phonon density of states. These are  $326 \text{ cm}^{-1}$  (KF),  $551 \text{ cm}^{-1}$  ( $\text{KMgF}_3$ ) and  $617 \text{ cm}^{-1}$  ( $\text{MgF}_2$ ). Thus at a particular frequency such as  $1300 \text{ cm}^{-1}$ , KF multiphonon absorption is a 5-phonon or higher order process whereas those of  $\text{KMgF}_3$  and  $\text{MgF}_2$  are still in the 3-phonon regime.

The temperature and frequency dependence of  $\text{MgF}_2$  and  $\text{KMgF}_3$  is next analyzed in terms of a simplified theory [11] which employs an average oscillator frequency to represent the phonon spectrum. Following Bendow [21] the absorption coefficient is expressed as

$$\beta(\omega, T) = \beta_0 \frac{[n(\omega_0) + 1] \frac{\omega}{\omega_0}}{n(\omega) + 1} \exp \left[ -\frac{\gamma\omega}{\omega_0} \right] \quad (2)$$

where  $n(\omega) = [\exp(k\omega/kT) - 1]^{-1}$  represents the phonon occupation number at temperature T,  $\beta_0$  a scaling factor,  $\omega_0$  the effective phonon frequency and  $\gamma$  the coefficient which governs the exponential decay. From the above expression it is evident that  $\beta$  increases at high T according to the usual  $T^j$  law for a  $j$  ( $= \frac{\omega}{\omega_0}$ ) - phonon process [9], provided that  $\omega_0$  is independent of T. In general,  $\omega_0(T)$  decreases with increasing T, somewhat suppressing the T dependence of  $\beta$  arising from the Bose-Einstein factors, an effect which becomes increasingly important at higher frequencies.

Before the above relation can be used to represent the T dependence of  $\beta$  it is necessary to specify  $\omega_0$ . Because the contribution of acoustic phonons are suppressed due to energy conservation,



an average optical phonon frequency such as the Brout frequency [22,11], used in our previous analysis of alkaline earth fluoride data, may be an appropriate choice. In the case of  $\text{MgF}_2$  where all of the long wavelength optic mode frequencies are known from infrared [13] and Raman [23] measurements, the Brout frequency turns out to be about  $415 \text{ cm}^{-1}$ . If this particular value is used for  $\omega_0$  in the above equation, only fair agreement is achieved with experimental data. Using the Brout frequency instead as a starting point for a least squares fit, the best agreement with experimental data is obtained for  $\omega_0 = 439 \text{ cm}^{-1}$ . The set of calculated absorption coefficients  $\beta$  versus temperature at various values of frequency,  $\omega$ , are shown in figure 5. The experimental data designated with points are seen to agree quite well over the frequency range  $1300$  to  $1800 \text{ cm}^{-1}$  and from  $300$  to  $500^\circ\text{K}$ . Deviations occurred at  $80^\circ\text{K}$  where structure was clearly evident in the spectra of figure 2 and the simple expression (2) for  $\beta$  is no longer applicable, and also above  $1800 \text{ cm}^{-1}$  where extrinsic absorption begins to dominate. Furthermore, the agreement might well be improved if the T dependence of  $\omega_0$  is included, but this has not been attempted in the calculations displayed here. The long wavelength optic mode frequencies for  $\text{KMgF}_3$  are not as well known as those for  $\text{MgF}_2$ . However, if the value  $\omega_0 = 439 \text{ cm}^{-1}$  for  $\text{MgF}_2$  is scaled by the ratio of the corresponding maximum longitudinal optic mode frequencies, (viz.,  $551 \text{ cm}^{-1}$  for  $\text{KMgF}_3$  and  $617 \text{ cm}^{-1}$  for  $\text{MgF}_2$ ), a value of  $392 \text{ cm}^{-1}$  is obtained for the  $\omega_0$  for  $\text{KMgF}_3$ . This roughly determined value yields only fair agreement between the calculated and observed absorption coefficients. However, the best fit is obtained for  $\omega_0 = 402 \text{ cm}^{-1}$  as indicated in figure 6, where good agreement is found between calculated and experimental  $\beta$  values, except at  $80^\circ\text{K}$ . Again the discrepancy at low temperature may be attributed to the pronounced structure in the absorption spectrum of  $\text{KMgF}_3$  (figure 3).

A comparison of structure in the absorption spectrum of  $\text{KF}$ ,  $\text{MgF}_2$  and  $\text{KMgF}_3$  at  $80^\circ\text{K}$  is shown in figure 7. The  $\text{KMgF}_3$  and  $\text{MgF}_2$  data are our experimental data, and the  $\text{KF}$  curve is that obtained theoretically by Boyer, et al [8]. It is evident that at  $80^\circ\text{K}$   $\text{KMgF}_3$  has the most structure and  $\text{KF}$  the least. The lack of structure in  $\text{KF}$  is characteristic of a rather smooth phonon density of states. In the case of  $\text{KMgF}_3$  presumably the contribution of  $\text{KF}$  combined with that of  $\text{MgF}_2$  introduces a gap in its phonon density of states and, as a result, persistent structure in the multiphonon spectrum as well.

With good transmission throughout the CO and chemical laser wavelength ranges and a lower absorption than  $\text{MgF}_2$ ,  $\text{KMgF}_3$  may be also a good possibility for a coating material, especially with the additional strength inherent in the mixed crystal.

#### Acknowledgement

The authors would like to thank Mr. D. Bandes of Parke Mathematical Laboratories for his assistance with the computer programming.

#### References

- [1] See for example, "Optical Properties of Highly Transparent Solids" edited by S.S. Mitra and B. Bendow, pp. 3-127 (Plenum Press, New York, NY, 1975).
- [2] T.F. Deutsch, J. Phys. Chem. Solids 34, 2091 (1973).
- [3] J.A. Harrington and M. Hass, Phys. Rev. Lett. 11, 710 (1973).
- [4] B. Bendow, S.C. Ying and S.P. Yukon, Phys. Rev. B8, 1679 (1973).
- [5] T.C. McGill, R.W. Hellwarth, M. Mangir and H.V. Winston, J. Phys. Chem. Solids, 34 2105 (1973).
- [6] K.V. Namjoshi and S.S. Mitra, Phys. Rev. B9, 815 (1974).
- [7] L.J. Sham and M. Sparks, Phys. Rev. B9, 827 (1974).
- [8] L. Boyer, J.A. Harrington, M. Hass and H.B. Rosenstock, Phys. Rev. B11, 1665 (1975).
- [9] J.R. Hardy and B.S. Agrawal, Appl. Phys. Lett. 22, 236 (1973).
- [10] K.V. Namjoshi, S.S. Mitra, B. Bendow, J.A. Harrington and D.C. Stierwalt, Appl. Phys. Lett. 26, 41 (1975).
- [11] H.G. Lipson, B. Bendow, N.E. Massa and S.S. Mitra, Phys. Rev. B13, 2614 (1976).
- [12] J.N. Plendl, Appl. Opt. 10, 1134 (1971).
- [13] A.S. Barker, Jr., Phys. Rev. 136, A1290 (1964).
- [14] G.R. Hunt, C.H. Perry and J. Ferguson, Phys. Rev. 134, A688 (1964).
- [15] C.H. Perry and E.F. Young, J. Appl. Phys. 38, 4616 (1967).
- [16] E.F. Young and C.H. Perry, J. Appl. Phys. 38, 4624 (1967).
- [17] S.P.S. Porto and J.F. Scott, Phys. Rev. 157, 716 (1967).
- [18] H.G. Lipson, Applied Optics, to be published.
- [19] A. Hordvik, B. Bendow, H.G. Lipson, L.K. Skolnik and R.N. Brown, "Laser Induced Damage in Optical Materials: 1976, A.J. Glass and A.H. Guenther, editors (NBS Special Publication 462, 1976 p. 50).
- [20] A. Hordvik & H. Schlossberg, Appl. Opt. 16, 101 (1977).
- [21] B. Bendow, Phys. Rev. B8, 5821 (1973).
- [22] See, for example, S.S. Mitra, in Optical Properties of Solids, edited by S. Nudelman and S.S. Mitra (Plenum, New York, 1969).
- [23] S.P.S. Porto, P.A. Fleury and T.C. Damen, Phys. Rev. 154, 522 (1967).

# Figures

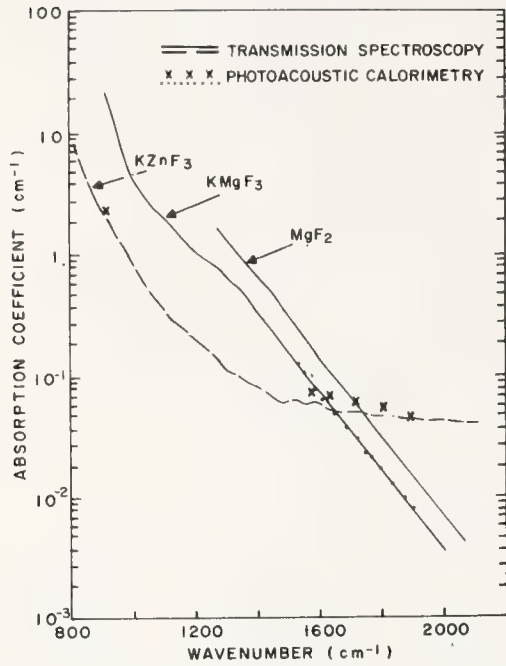


Fig. 1. Absorption coefficient vs. wavenumber for  $\text{KZnF}_3$ ,  $\text{KMgF}_3$  and  $\text{MgF}_2$  measured by Fourier spectroscopy (solid and dashed lines) and photoacoustic calorimetry for  $\text{KMgF}_3$  (dots) and  $\text{KZnF}_3$  (crosses).

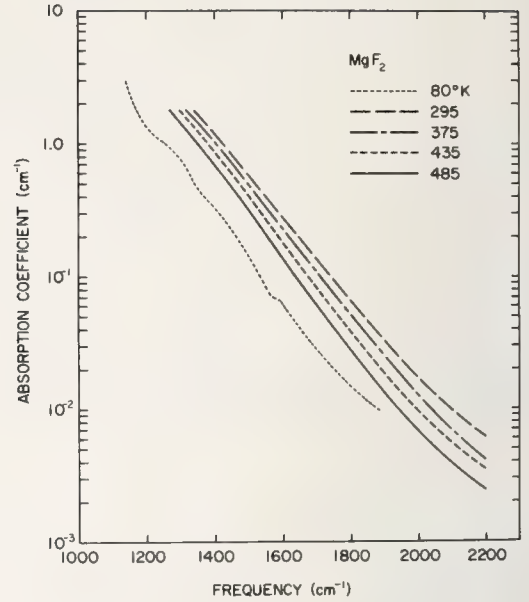


Fig. 2. Measured absorption coefficient versus frequency for  $\text{MgF}_2$  at various temperatures.

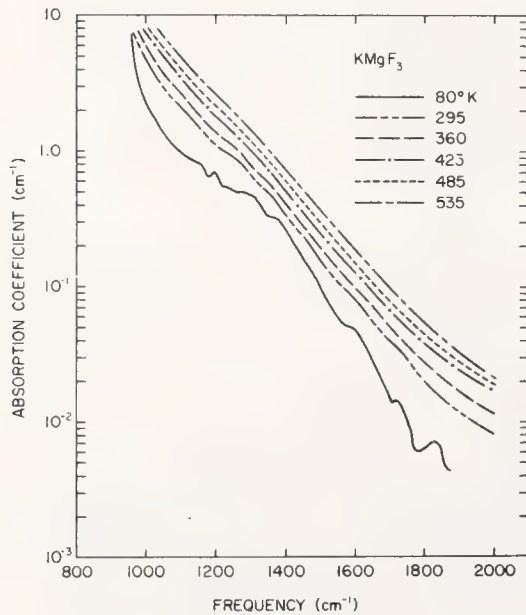


Fig. 3. Measured absorption coefficient versus frequency for  $\text{KMgF}_3$  at various temperatures.

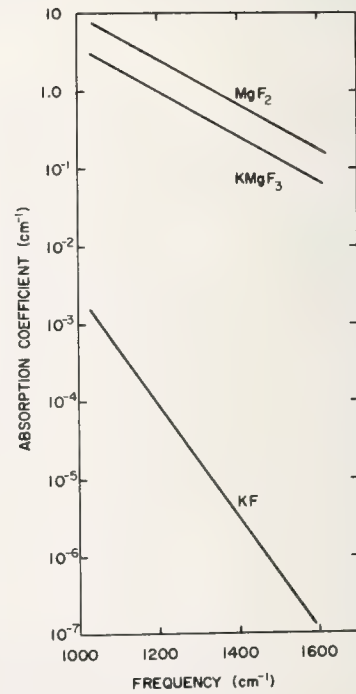


Fig. 4. Comparison of absorption coefficient versus frequency behavior of  $\text{MgF}_2$ ,  $\text{KMgF}_3$  and  $\text{KF}$ .



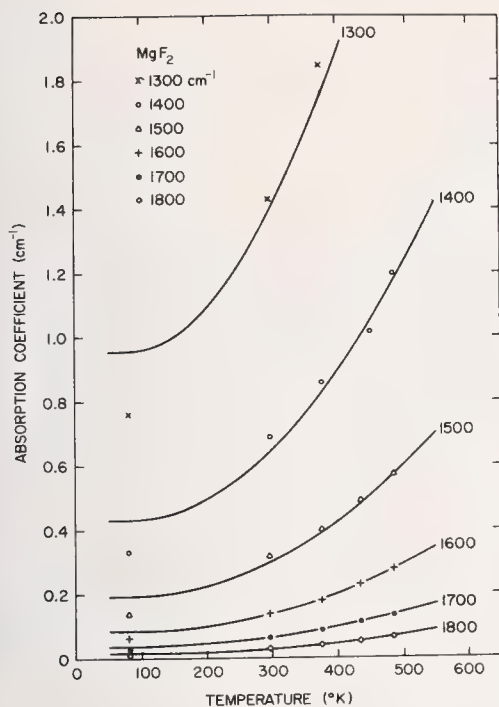


Figure 5 - Absorption coefficient versus temperature for MgF<sub>2</sub> at various representative frequencies. The solid lines are calculations obtained from equation (2) utilizing  $\omega_0 = 439 \text{ cm}^{-1}$ ,  $\beta_0 = 29,922$ ,  $\gamma = 3.496$ , while the individual points are experimental data.

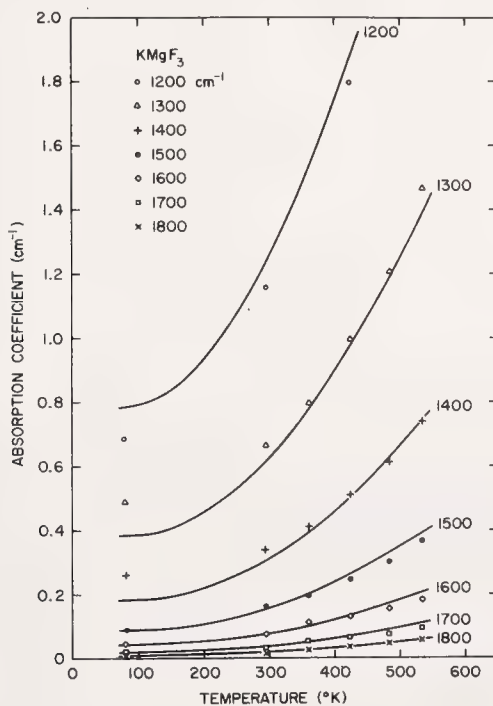


Figure 6 - Absorption coefficient versus temperature for KMgF<sub>3</sub> at various representative frequencies. The solid lines are calculations obtained from equation (2) utilizing  $\omega_0 = 402$ ,  $\beta_0 = 5328$ ,  $\gamma = 2.953$ , while the individual points are experimental data.



Figure 7 - Comparison of structure in low temperature spectra of  $\text{KMgF}_3$  and  $\text{MgF}_2$  (experimental data) and  $\text{KF}$  (theoretical calculation from reference 8).  $\text{KF}$  data plotted on a reduced scale relative to  $\text{KMgF}_3$  and  $\text{MgF}_2$ .

#### COMMENTS ON PAPER BY LIPSON, HORDVIK, BENDOW, MITRA, AND MARTIN

*It was pointed out in the discussion that potassium magnesium fluoride is a mixed fluoride crystal which appears attractive for use as a coating material. It was indicated that investigation of this material for coatings is underway.*



## BULK LASER ABSORPTION HOMOGENEITY\*

T. J. Moravec and E. Bernal G.  
Honeywell Corporate Materials Science Center  
Bloomington, Minnesota 55420

Doppler Interferometry has been used to measure the optical change in path upon CO<sub>2</sub> laser irradiation and thus the absorption. This absorption has been measured at many points over the full aperture of several laser windows and materials. The entire experiment is under control of an HP9825A calculator. Details are given of the experiment and its operation.

Key words: Automated calorimetry, calorimetry, Doppler interferometry, laser absorption uniformity.

### 1. Introduction

The objective of this experiment is to examine the spatial variation of absorption in infrared laser window materials and coatings. Our approach is to measure by interferometric techniques the localized change in optical path induced by irradiation of a window by a focused laser beam.

### 2. Experimental Description

Figure 1 shows the experimental arrangement. The idea is to bring the interferometric beam in coincidence with the CO<sub>2</sub> beam so the point of irradiation can be changed. The measurements are normalized to the time of irradiation and power transmitted, i.e. the energy. The experiment & X-Y table used for mounting and positioning the sample are under computer control.

A sample can be scanned and the change in optical path length due to CO<sub>2</sub> laser irradiation can be measured at many points over the clear aperture of the sample. The number of points is limited by the size of the CO<sub>2</sub> beam. The change in path length is proportional to the absorption coefficient of the sample. Thus, a plot of the homogeneity of the absorption can be obtained by plotting the change in optical path length. Because the interferometer measures optical path by heterodyning two light beams of different frequency, we will refer to this experimental technique as scanning Doppler interferometry (SDI). The experimental approach is similar to that of Skolnik et. al. [1]<sup>1</sup>

### 3. Noise Limitations

An extensive program was undertaken during the first part of this year to determine the accuracy and noise limitations of the instrument. The interferometer has an instrument resolution of 0.016  $\mu$ m determined by the wavelengths and electronics used.

To test the instrument, a program was written that does not move the X-Y table, but rather samples the readings of the interferometer consecutively. Without any induced changes or motions, the readings are essentially the background fluctuations or noise of the interferometer. Figure 2 shows a typical plot of 100 consecutive readings spaced 0.3 second apart that are the difference (or change) from the zero reading. Large fluctuations are evident. These fluctuations are independent of the floating of the optical table and thus are not due to mechanical vibrations. However, they appear to be due to air currents. Figure 3 shows a typical run with the room air circulating system turned off. It was also determined that the same effect could be obtained with the interferometer beam enclosed in beam pipes and thus protected from air currents. The experiment then can be run with the room air circulating.

Some drift can be noted in Figure 3 which we believe is due to thermal changes in the optical table. We have eliminated this by sending the interferometer reference beam over the same path as the sample beam. With this configuration, data as shown in figure 4 is obtained. This shows sufficient stability to perform the homogeneity experiment. The absolute resolution and stability now is about 0.03  $\mu$ m with the present configuration.

---

\* This work was supported by the Defense Advanced Research Projects Agency under Contract No. DAHC15-73-C-0464, ARPA Order No. A02416.

1. Figures in brackets indicate the literature references at the end of this paper.

#### 4. Experimental Results

In order to examine the homogeneity of a sample, a program was written that moves the sample and irradiates each point for a fixed length of time determined by the operator. Thus the change in optical path length per transmitted laser power at each point is measured by the scanning interferometer. As derived in reference [2] this is given by

$$\frac{\Delta L_i}{P_i} = \frac{2}{P_i} \frac{dn}{dT} + d(n-1) t(x_i, y_i) \Delta T(x_i, y_i) \quad (1)$$

where  $n$  is the refractive index,  $t(x_i, y_i)$  is the thickness and  $\Delta T(x_i, y_i)$  is the change in temperature at  $(x_i, y_i)$ . This is directly proportional to the temperature rise at  $(x_i, y_i)$ , and hence the local absorption coefficient.

The present program will sample points in a 3 by 3 matrix up to a 9 by 9 matrix. The distance between points is set by the operator and the size of the sample. The order of the data points for a 5 by 5 and a 7 x 7 matrix is shown in table 1. The others are done in a similar fashion. The procedure is very fast with a 7 x 7 array taking about 12 minutes for a 10 second irradiation at each point. The data is plotted as an isographic projection of the  $x$  and  $y$  coordinates on the sample and the value of  $\Delta L_i/P_i$  (time).

Figures 5 thru 9 are data taken on forged KCl samples and Figure 10 is that for a ZnSe sample. In each case, a photograph of the sample through crossed polarizers is shown in the upper right hand corner. The area scanned is delineated by a white border whose dimensions are ~1" x 1". No correlation with birefringence can be detected. The min. and max. are given in micrometers per joule units.

Table 2 presents a summary of the results along with CO<sub>2</sub> calorimetry measurements taken near the center of each sample.

#### 5. Conclusions

We conclude that there are no order of magnitude effects but variations of the order of three are common in state-of-the-art materials. Change in path in alkali halides can be extremely small, but fluctuations are then large. Materials that have larger changes have smaller variations. We note that values for average path change scale with the absorption calorimetry measurements. So complete evaluation of potential laser windows should include these tests for checking the expected laser absorption. It should be pointed out that while this technique is faster than adiabatic techniques, it requires a large laser with an output of ~200 watts.

#### 6. References

- [1] L. H. Skolnik, A. Hordvik, and A. Kahan,  
Appl. Phys. Lett. 23, 477 (1973)
- [2] E. Bernal G., R.H. Anderson, B.G. Koepke,  
T.J. Moravec, R.A. Skogman, D. Wertman,  
R.J. Stokes, J.S. Loomis, Honeywell Semi-  
annual Technical Report No. 6 on ARPA  
Contract DAHCl5-73-C-0464, 31 December 1976.



TABLE 1: LASER ABSORPTION SCANNING PATTERN

5 X 5							
Y-Axis	24	14	4	9	19		
	22	12	2	7	17		
	21	11	1	6	16		
	23	13	3	8	18		
	25	15	5	10	20		
X-Axis							
7 X 7							
Y-Axis	48	34	20	6	13	27	41
	46	32	18	4	11	25	39
	44	30	16	2	9	23	37
	43	29	15	1	8	22	36
	45	31	17	3	10	24	38
	47	33	19	5	12	26	40
	49	35	21	7	14	28	42
X-Axis							

TABLE 2 SUMMARY OF SAMPLE HOMOGENEITY AT 10.6 $\mu$ m

Sample		Path Change ( $\times 10^{-4}$ $\mu$ m)				Calorimetry $\beta$ ( $\times 10^{-4}$ cm $^{-1}$ )	
		<u>Min</u>	<u>Max</u>	<u>Ave</u>	<u>Std.Dev.</u>	<u>Ave</u>	<u>Std.Dev.</u>
ZnSe	#353	11.28	43.96	21.58	9.12	66.8	1.3
KCl	#520	0.37	1.65	0.77	0.71	21.7	2.1
KCl	#482	0.76	3.70	2.09	0.52	44.7	3.2
KCl	#K-8	0.34	2.89	1.32	0.50	16.4	2.7
W/RbCl							
KCl	#476	2.75	5.18	3.50	0.52	55.7	2.3



# DIAGRAM OF SCANNING DOPPLER INTERFEROMETER

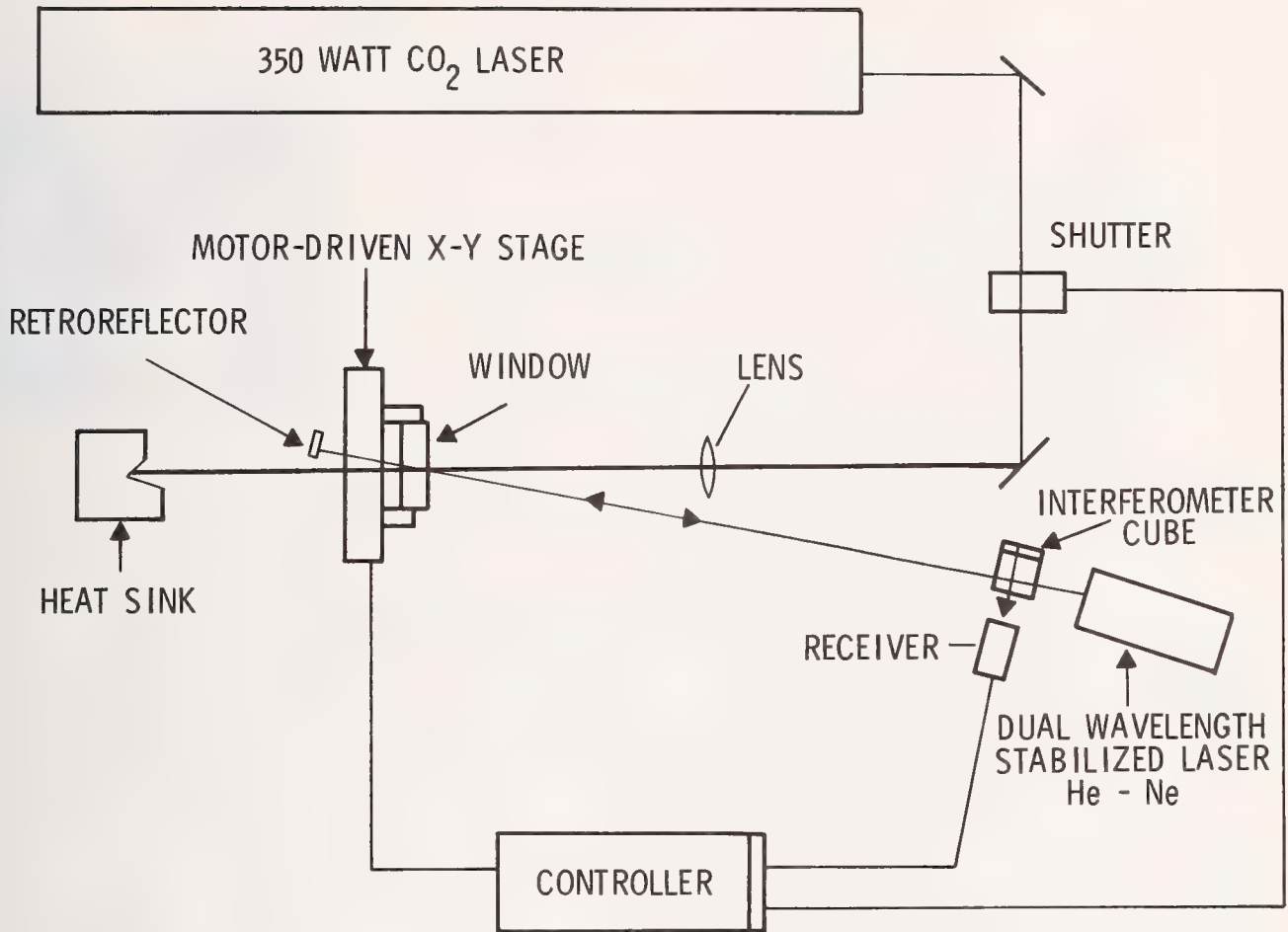


Figure 1 Experimental arrangement of scanning Doppler Interferometer

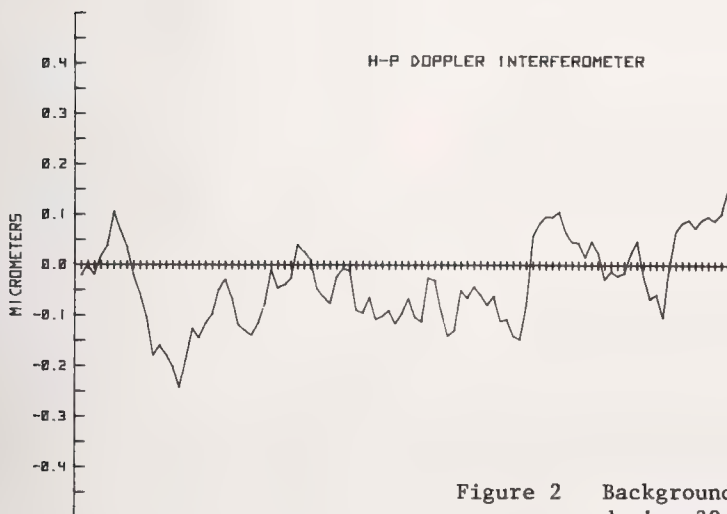


Figure 2 Background Noise Fluctuations of Optical Path Difference during 30-Second Time Interval Represented by 100 Data Points on x-axis

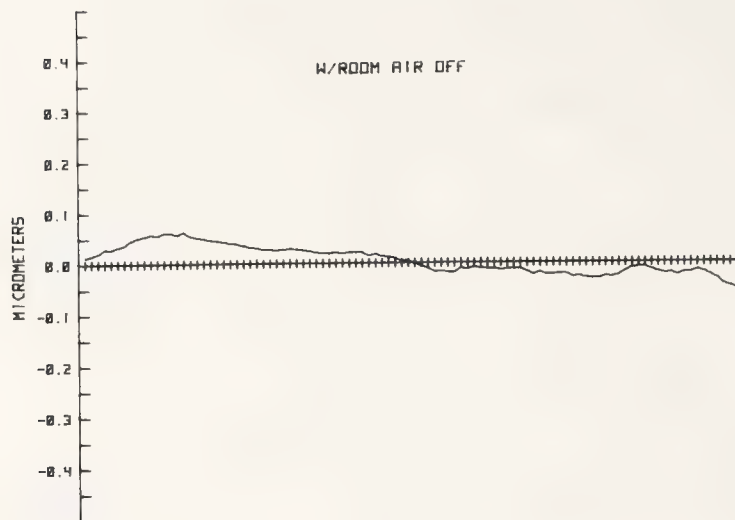


Figure 3 Same as Figure 2 but with Room Air Circulating System Turned Off

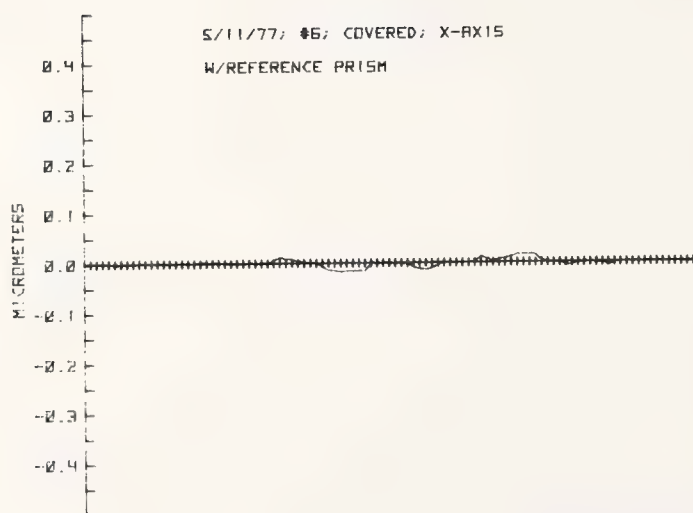


Figure 4 Same as Figure 3 but with Reference Beam Sent over Same Path as Sample Beam (but not through sample) and Interferometer Enclosed in Box



INSERT77 #482; 200WATT5  
 MAX= 3.695582E-04 MUM/J  
 MIN= 7.563217E-05 MUM/J

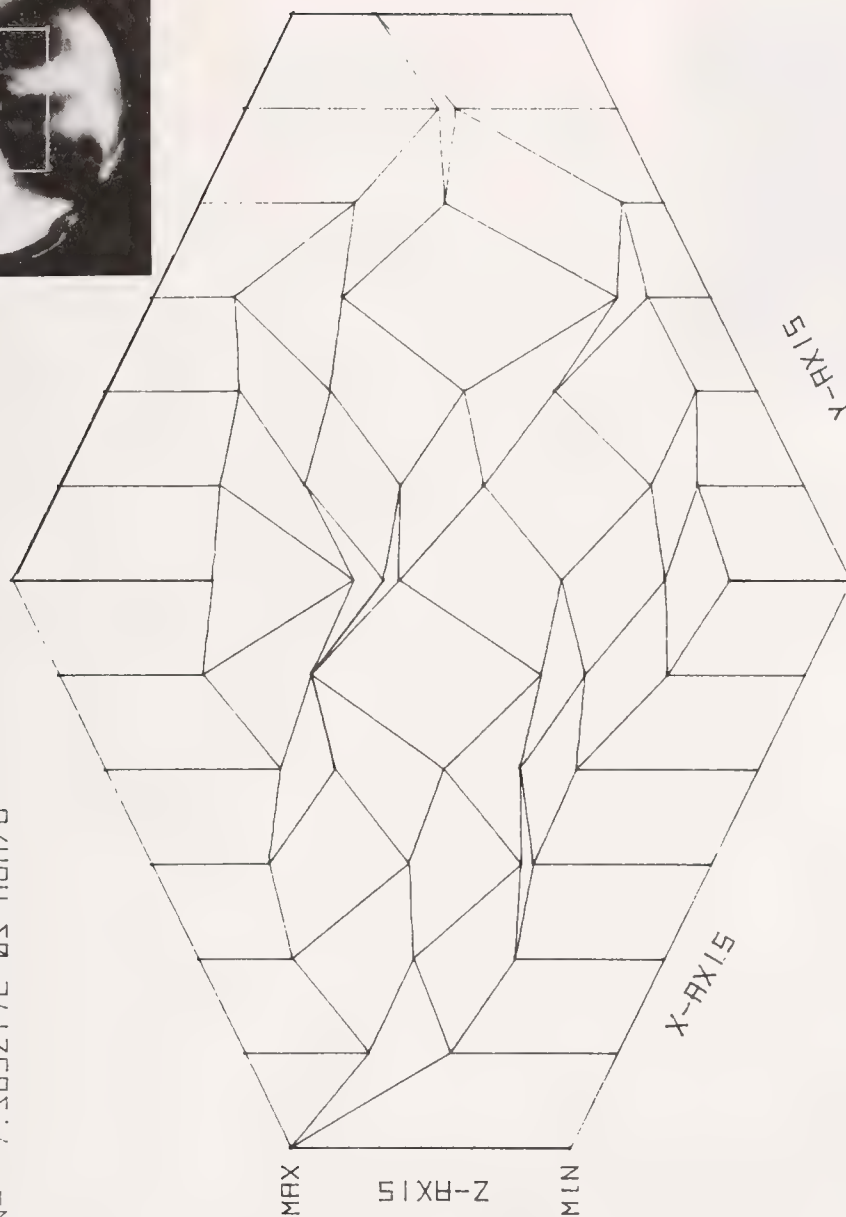


Figure 5 SDI data for forged KCl sample #482

145EPT77 #520; 200WATTS  
 MAX= 1.652289E-04 MUM/J  
 MIN= 3.731634E-05 MUM/J

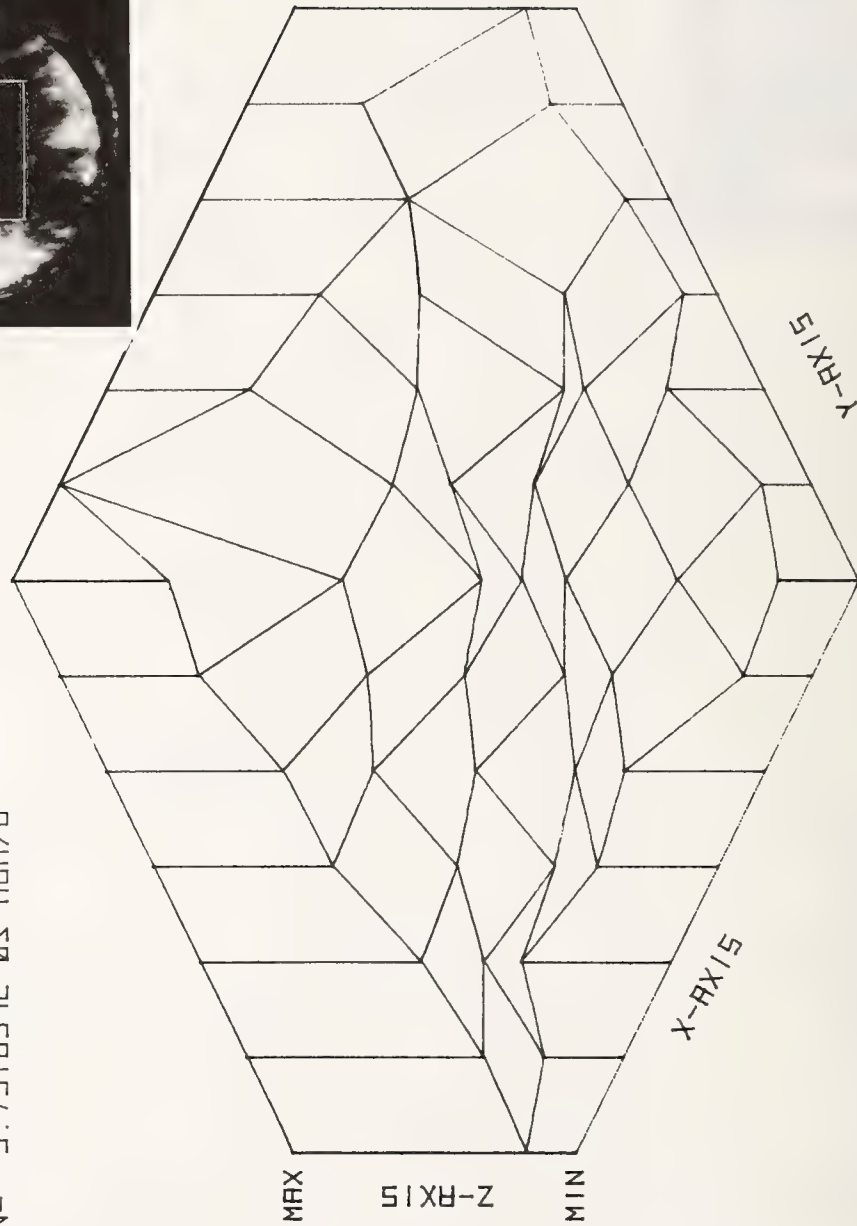


Figure 6 SDI data for forged KCl sample #520



14SEPT77 #K-8; 200 WATTS  
 MAX= 2.888323E-04 MUM/J  
 MIN= 3.448010E-05 MUM/J

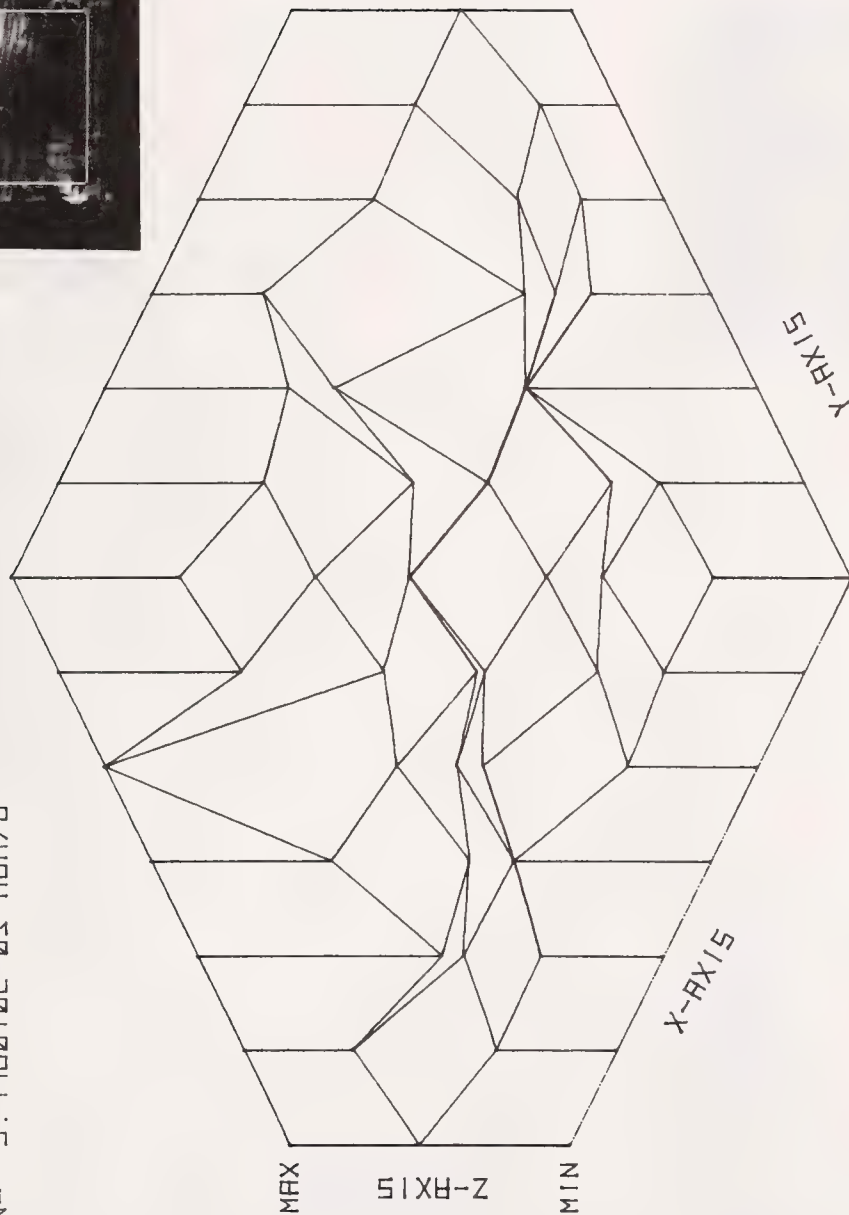
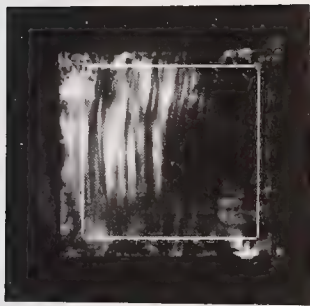
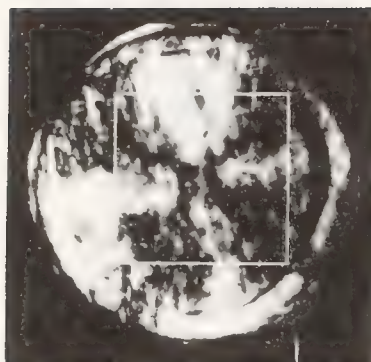


Figure 7 SDI data for forged KCl sample #K-8



30AUG77 #473 100WATTS  
 MAX= 3.899270E-03 MUM/J  
 MIN= 1.609760E-03 MUM/J

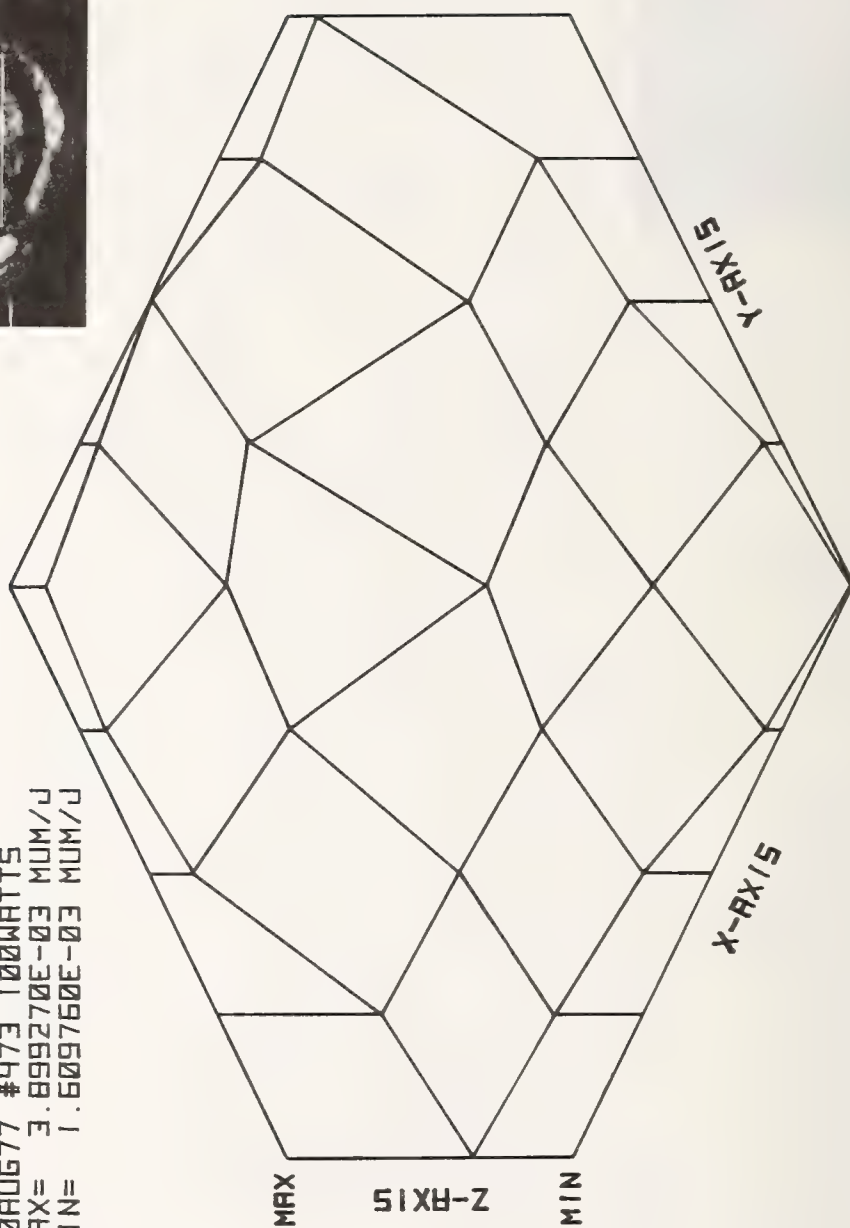


Figure 8 SDI data for forged KCl sample #473



14SEPT77 #476, 200 WATTS  
 MAX= 5.179413E-04 MUM/J  
 MIN= 2.753107E-04 MUM/J

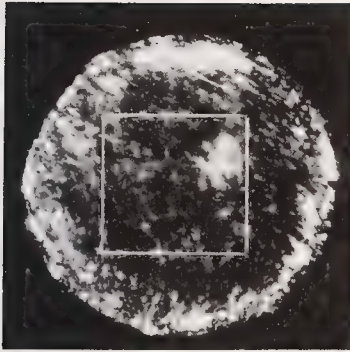
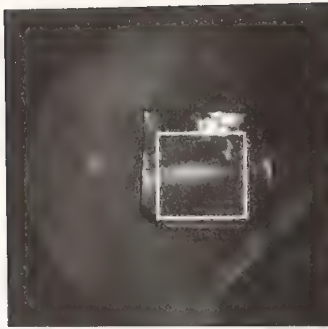


Figure 9 SDI data for forged KCL sample #476



14SEPT77 ZNSE; 200 WATTS-#353  
 MAX= 4.395538E-03 MUM/J  
 MIN= 1.128170E-03 MUM/J

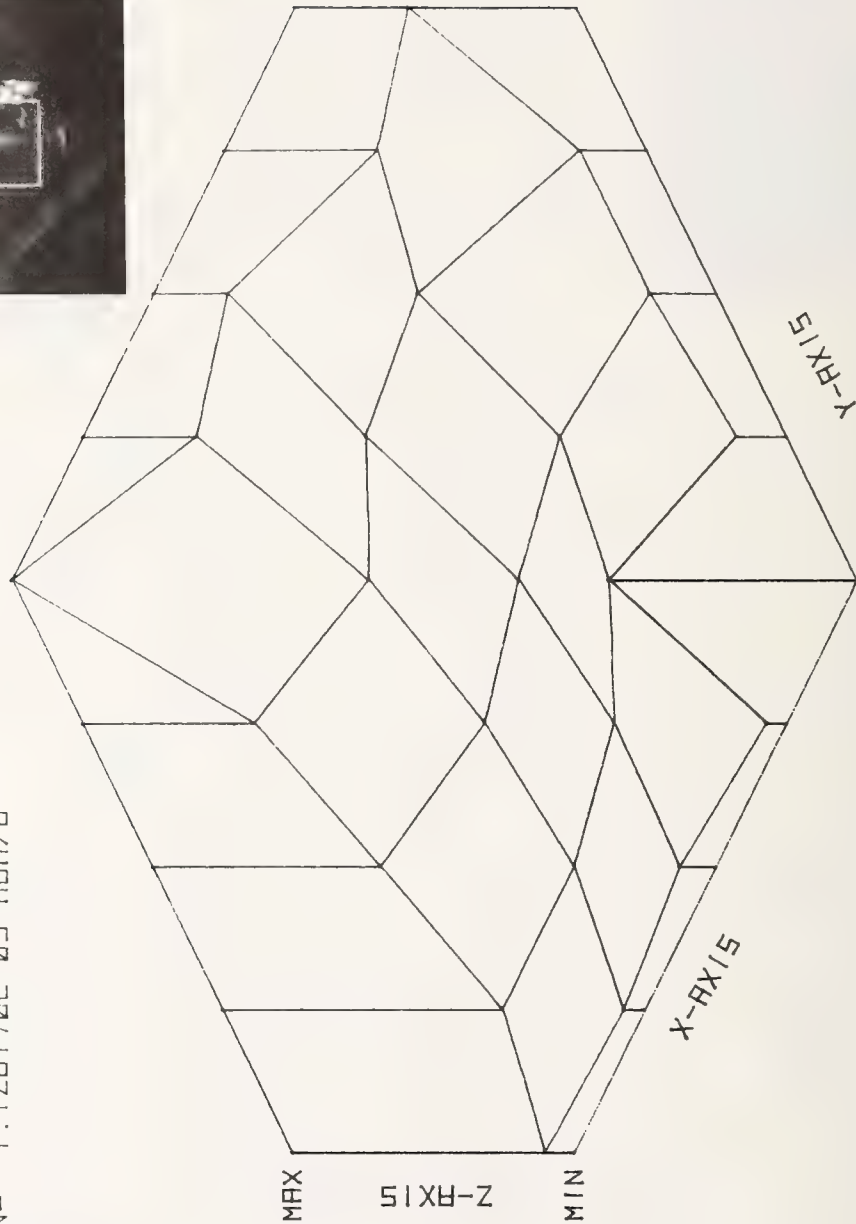


Figure 10 SDI data for ZnSe sample #353

#### COMMENTS ON PAPER BY MORAVEC AND BERNAL G.

In response to a question about scattering, the speaker emphasized that the measurement detected the thermally induced path change and was therefore not sensitive to scattering but only to absorptive mechanisms.

# REFRACTIVE PROPERTIES OF INFRARED WINDOW MATERIALS\*

A. Feldman, D. Horowitz, and R. M. Waxler  
Institute for Materials Research  
National Bureau of Standards  
Washington, D. C. 20234

The results of the Optical Materials Characterization Program at the National Bureau of Standards are reviewed. The techniques for measuring refractive index and the change of refractive index with stress and temperature are enumerated and the materials on which these measurements have been made are listed. Data are presented for the change of refractive index with temperature of single crystal specimens of  $\text{BaF}_2$ ,  $\text{CaF}_2$ , reactive atmosphere processed (RAP)  $\text{KCl}$  and  $\text{KBr}$ ,  $\text{LiF}$ ,  $\text{NaF}$  and  $\text{SrF}_2$ , and polycrystalline chemical vapor deposited (CVD)  $\text{ZnSe}$  and  $\text{ZnS}$ . The measurements were done by the method of Fizeau interferometry over the temperature range  $-180$  to  $200^\circ\text{C}$  at the wavelengths  $0.6328\ \mu\text{m}$ ,  $1.15\ \mu\text{m}$ ,  $3.39\ \mu\text{m}$  and  $10.6\ \mu\text{m}$ . The results were compared to the results of other workers and found to be in general agreement. We attempt to explain disagreements with other workers.

Key words:  $\text{BaF}_2$ ;  $\text{CaF}_2$ ;  $\text{KBr}$ ;  $\text{KCl}$ ;  $\text{LiF}$ ;  $\text{NaF}$ ; refractive index;  $\text{SrF}_2$ ; thermal coefficient of refractive index;  $\text{ZnS}$ ;  $\text{ZnSe}$ .

## 1. Introduction

When high-power laser radiation propagates through a laser window, the residual absorption in the window leads to a temperature rise. The temperature distribution is, in general, nonuniform; hence, it will cause a nonuniform optic path variation across the window aperture resulting in a distortion of the beam wavefront. The distortion arises from the change of refractive index with temperature, the change of thickness with temperature, and the change of refractive index and thickness produced by stress caused by thermal gradients. In order to predict the optical distortion due to thermal gradients it is important to determine the refractive index,  $n$ , the change of refractive index with temperature,  $dn/dT$ , the linear thermal expansion coefficient,  $\alpha$ , the piezo-optic constants,  $q_{ij}$ , and the elastic constants,  $s_{ij}$  or  $c_{ij}$ , of laser window materials. The Optical Materials Characterization Program has been established at the National Bureau of Standards to measure these quantities.

In this paper are listed the methods we have used for measuring these parameters and materials on which measurements have been made. We do not discuss the details of the experimental procedures [1]<sup>1</sup> or the experimental data that have appeared in the literature, but we do present our most recent data of  $dn/dT$  on  $\text{BaF}_2$ ,  $\text{CaF}_2$ ,  $\text{KBr}$ ,  $\text{KCl}$ ,  $\text{LiF}$ ,  $\text{NaF}$ ,  $\text{SrF}_2$ ,  $\text{ZnS}$ , and  $\text{ZnSe}$ . A comparison is made with the data of other workers. The results of refractive index measurement on  $\text{ZnS}$  are presented in an accompanying paper by M. J. Dodge.

## 2. Experimental Methods

### 2.1. Refractive index

The refractive indices of prismatic specimens are measured by the method of minimum deviation on the following instruments: Precision spectrometer with glass optics - The ultimate accuracy is several parts in  $10^6$ ; the wavelength range is  $0.4\ \mu\text{m}$  to  $1.08\ \mu\text{m}$ . Precision spectrometer with mirror optics - the ultimate accuracy is several parts in  $10^5$ ; the wavelength range is  $0.21\ \mu\text{m}$  to  $50\ \mu\text{m}$ .

As part of the infrared laser window program, we have measured the refractive indices of the following materials: commercial  $\text{KCl}$  [2], reactive atmosphere processed (RAP)  $\text{KCl}$  [3],  $\text{KCl}$  nominally doped with 1.5%  $\text{KI}$  ( $\text{KCl:KI}$ ) [3], chemical vapor deposited (CVD)  $\text{ZnSe}$  [4], CVD  $\text{ZnS}$  (see paper by M. J. Dodge in these proceedings), hot forged  $\text{CaF}_2$  [5], fusion cast  $\text{CaF}_2$  [6], and eight specimens of  $\text{CaF}_2$  doped with from 0.001% to 3%  $\text{Er}$  [7]. The spectrometer with mirror optics was used. All of the refractive index values obtained were relative to the refractive index of air,  $n_{\text{air}}$ , that is, we measured  $n/n_{\text{air}}$ .

\* Research supported in part by the Defense Advanced Research Projects Agency.

1. Figures in brackets indicate the literature references at the end of this paper.



## 2.2. Temperature coefficient of refractive index

The temperature coefficient of refractive index,  $dn/dT$ , is measured by either of two methods. In the first method we measure the refractive index at 20 °C and at 30 °C on a precision spectrometer. This method has the advantage of giving values for  $dn/dT$  over the entire wavelength range. It has several disadvantages: (1) Values can be obtained only near room temperature; (2) Because the values of refractive index are obtained relative to the refractive index of air, in order to obtain  $dn/dT$  for a material, a correction must be applied to the measured value as shown by the equation

$$\frac{dn}{dT} \approx \frac{d}{dT} \left( \frac{n}{n_{\text{air}}} \right) + n \frac{dn_{\text{air}}}{dT} \quad (1)$$

where the measured quantity is the first term on the right. Theoretical expressions for  $dn_{\text{air}}/dT$  can be obtained from the literature and these have been verified in the visible and the near infrared, however, it is uncertain whether these expressions are correct further into the infrared. (3) The technique depends on the subtraction of two numbers of comparable magnitude. If the accuracy of these numbers for some reason is less than optimum, large errors in the values for  $dn/dT$  could ensue. For example, an error of  $10^{-4}$  in refractive index would lead to an error greater than  $10^{-5}K^{-1}$  in  $dn/dT$ .

The second method we use for measuring  $dn/dT$  overcomes many of the problems listed above. In this method, we measure the shift with temperature of the Fizeau fringes generated by the reflections of laser radiation from the surfaces of a flat plate of specimen material. This method has several advantages: (1)  $dn/dT$  data can be obtained over a wide range of temperature. We presently have two systems that cover the temperature ranges -180 °C to 200 °C and 20 °C to 800 °C, respectively. (2) The value obtained for  $dn/dT$  is for the material itself and is independent of  $n_{\text{air}}$  and its temperature derivative. The method has the following disadvantages: (1) Measurements can be made only at the discrete wavelengths of spectral lamps or lasers because coherent radiation must be used. In the infrared, we are presently limited to measurements at 1.15  $\mu\text{m}$ , 3.39  $\mu\text{m}$  and 10.6  $\mu\text{m}$ . (2) The method relies on accurate values for the linear thermal expansion coefficient. Thermal expansion data are obtainable from the literature or are measured by a Fizeau interferometer technique in this laboratory. The technique for measuring the thermal expansion is similar to the technique for measuring  $dn/dT$ .

The results of our latest measurements of  $dn/dT$  by the interferometric method are given in section 3.

## 2.3. Photoelastic constants

The photoelastic constants describe the effect of stress or strain on the refractive indices of a solid. In glasses and most cubic solids the coefficients  $q_{11}$  and  $q_{12}$  describe the absolute change of refractive index with stress, whereas the coefficients  $q_{11}-q_{12}$  and  $q_{44}$  (in glasses  $q_{44} = q_{11}-q_{12}$ ) describe the stress-induced birefringence. We measure these coefficients by a variety of techniques depending on the wavelength of measurement and the sensitivity of measurement required. These techniques, which have been described in the literature, are listed below.

Twyman-Green interferometer - we measure the shift of interference fringes for different polarizations of the radiation as a function of uniaxially applied stress.

Fizeau interferometer - we measure the shift of Fizeau fringes as a function of uniaxially applied stress or as a function of hydrostatic pressure. These measurements together with the Twyman-Green interferometer measurements permit us to calculate the elastic constants as well as the photoelastic constants.

Modified Twyman-Green interferometer - this interferometer permits us to measure fractional fringe shifts in the infrared.

Modified Dyson interferometer - this interferometer permits us to measure fractional fringe shifts in the visible.

Babinet-Soleil compensator or DeSenarmont compensator - these instruments are used for measuring stress-induced birefringence in the visible and near infrared.

Stress-Birefringent compensator - this device is used for measuring stress-induced birefringence in the infrared. In this technique a specimen subjected to a varying uniaxial load functions in a manner similar to a Babinet-Soleil compensator.

The above techniques have been used to measure the photoelastic constants of the following materials in the infrared:  $\text{As}_2\text{S}_3$  glass [2], a chalcogenide glass (Ge 33%, As 12%, Se 55%) [2], fused  $\text{SiO}_2$  [8], Ge [9], KCl (RAP) [9,10], and ZnSe (CVD) [11]. Measurements are presently underway on  $\text{CaF}_2$ ,  $\text{BaF}_2$ , and  $\text{SrF}_2$ .

### 3. Temperature Derivative of Refractive Index of Infrared Window Materials

We have obtained  $dn/dT$  of the following materials over the temperature range  $-180\text{ }^{\circ}\text{C}$  to  $200\text{ }^{\circ}\text{C}$ :  $\text{BaF}_2$ ,  $\text{CaF}_2$ ,  $\text{KBr}$  (RAP),  $\text{KCl}$  (RAP),  $\text{LiF}$ ,  $\text{NaF}$ ,  $\text{SrF}_2$ ,  $\text{ZnS}$  (CVD), and  $\text{ZnSe}$  (CVD). Measurements were made at the wavelengths  $0.6328\text{ }\mu\text{m}$ ,  $1.15\text{ }\mu\text{m}$ ,  $3.39\text{ }\mu\text{m}$ , and  $10.6\text{ }\mu\text{m}$  with the exception that measurements on  $\text{ZnS}$  were not made at  $0.6328\text{ }\mu\text{m}$  and measurements on  $\text{CaF}_2$ ,  $\text{LiF}$ , and  $\text{NaF}$  were not made  $10.6\text{ }\mu\text{m}$ . The results of these measurements are presented in figures 1-9.

We have also measured  $dn/dT$  of hot-forged  $\text{CaF}_2$  and  $\text{KCl}$  nominally doped with 1.5% KI, but these measurements were indistinguishable from the measurements on the unmodified materials.

In table 1 we list values of  $dn/dT$  that we have obtained at  $40\text{ }^{\circ}\text{C}$  for comparison with earlier work. We compare our results only with the results obtained interferometrically by other workers. We find that our measurements on  $\text{BaF}_2$ ,  $\text{CaF}_2$ , and  $\text{SrF}_2$  agree within experimental error with the values of Lipson, Tsay, Bendow, and Ligor [12].

Table 1.  $dn/dT$  ( $10^{-5}\text{K}^{-1}$ ) of infrared transmitting materials at  $40\text{ }^{\circ}\text{C}$

Material	$0.6328\text{ }\mu\text{m}$	$1.15\text{ }\mu\text{m}$	$3.39\text{ }\mu\text{m}$	$10.6\text{ }\mu\text{m}$	Reference
$\text{BaF}_2$	$-1.63 \pm 0.02$	$-1.66 \pm 0.03$	$-1.62 \pm 0.03$	$-1.48 \pm 0.03$	Present work
	$-1.67 \pm 0.04$	$-1.71 \pm 0.05$	$-1.68 \pm 0.04$	—	[12]
	$-1.64 \pm 0.01$	$-1.68 \pm 0.01$	$-1.63 \pm 0.1$	—	[13]
$\text{CaF}_2$	$-1.15 \pm 0.02$	$-1.18 \pm 0.02$	$-1.14 \pm 0.03$	—	Present work
	$-1.18 \pm 0.07$	$-1.20 \pm 0.05$	$-1.15 \pm 0.07$	—	[12]
	$-1.31 \pm 0.04$	$-1.34 \pm 0.04$	$-1.28 \pm 0.04$	—	[13]
	$-1.16$	$-1.19$	$-1.15$	—	[13] corrected
$\text{KBr}$ (RAP)	$-4.16 \pm 0.03$	$-4.23 \pm 0.03$	$-4.25 \pm 0.03$	$-4.16 \pm 0.06$	Present work
$\text{KCl}$ (RAP)	$-3.65 \pm 0.02$	$-3.68 \pm 0.02$	$-3.69 \pm 0.02$	$-3.54 \pm 0.04$	Present work
	$-3.33 \pm 0.02$	$-3.41 \pm 0.02$	$-3.38 \pm 0.01$	$-3.13 \pm 0.01$	[13]
	$-3.64$	$-3.72$	$-3.69$	$-3.43$	[13] corrected
$\text{LiF}$	$-1.70 \pm 0.02$	$-1.73 \pm 0.04$	$-1.48 \pm 0.04$	—	Present work
$\text{NaF}$	$-1.30 \pm 0.05$	$-1.34 \pm 0.06$	$-1.27 \pm 0.05$	—	Present work
$\text{SrF}_2$	$-1.25 \pm 0.02$	$-1.28 \pm 0.01$	$-1.26 \pm 0.03$	$-1.03 \pm 0.05$	Present work
	$-1.20 \pm 0.07$	$-1.27 \pm 0.05$	$-1.30 \pm 0.05$	—	[12]
$\text{ZnS}$ (CVD)	—	$4.6 \pm 0.2$	$4.3 \pm 0.2$	$4.1 \pm 0.2$	Present work
	$6.35 \pm 0.10$	$4.98 \pm 0.11$	$4.59 \pm 0.10$	$4.63 \pm 0.12$	[13]
$\text{ZnSe}$ (CVD)	$10.7 \pm 0.1$	$7.0 \pm 0.1$	$6.2 \pm 0.1$	$6.1 \pm 0.1$	Present work
	$9.11 \pm 0.11$	$5.97 \pm 0.12$	$5.34 \pm 0.11$	$5.20 \pm 0.12$	[13]

Harris, Johnston, Kepple, Krok, and Mukai (HJKKM) [13] have recently reported values of  $dn/dT$  for a series of materials including  $\text{BaF}_2$ ,  $\text{CaF}_2$ ,  $\text{KCl}$ ,  $\text{ZnS}$  (CVD) and  $\text{ZnSe}$  (CVD). A comparison of our results with theirs shows agreement within experimental error for  $\text{BaF}_2$  and reasonably good agreement for  $\text{ZnS}$ , but larger deviations for the other materials. We will discuss the results for each of these materials separately in an attempt to account for the discrepancies.

The values that HJKKM report for  $\text{CaF}_2$  appear to be larger than our values by about 12%. But, an examination of table II in their paper, which lists the parameters used in their calculations, shows that the values of  $n$  for  $\text{BaF}_2$  and  $\text{CaF}_2$  are interchanged. If we recalculate their value of  $dn/dT$  by assuming that the index for  $\text{BaF}_2$  had been mistakenly used in the original calculation, and furthermore, if we change the value of  $\alpha = 19.5 \times 10^{-6}\text{K}^{-1}$ , the value they had used, to  $\alpha = 19.05 \times 10^{-6}\text{K}^{-1}$ , the value we have used, the resulting value, as shown in table 1, is in excellent agreement with our value. A similar correction to their data on  $\text{BaF}_2$  makes a negligible change in the values.



The values that HJKKM report for KCl appear to be larger than our values by about 10%. This discrepancy can be almost completely eliminated by changing the value of  $\alpha = 35.5 \times 10^{-6} \text{K}^{-1}$ , the value they had used, to  $\alpha = 37.6 \times 10^{-6} \text{K}^{-1}$ , the value we have used. In table 1, a comparison of their corrected values with ours shows deviations of no more than 3%. We believe our value of  $\alpha$  is more nearly correct because measurements of  $\alpha$  made in our laboratory agree with values in the AIP Handbook [14].

A comparison of HJKKM's values for ZnSe with our values indicates a discrepancy of about 15%. However, HJKKM have reported that they obtained different results on some materials when measuring  $dn/dT$  in air and when measuring  $dn/dT$  in an immersion bath. We, therefore, decided to remeasure  $dn/dT$  of ZnSe at  $0.6328 \mu\text{m}$  using an immersion technique. We found no significant difference between the data we had obtained previously and the data obtained by the immersion technique.

Tsay, Lipson, and Ligor [15] have recently reported measurements of  $dn/dT$  on  $\text{CaF}_2$  as a function of temperature. These data appear to be in good agreement with ours.

#### 4. Summary

We have enumerated the techniques we have used for measuring refractive index and the change of refractive index with stress and temperature. We have listed the materials on which measurements have been made. Data of  $dn/dT$  as a function of temperature have been presented for nine infrared transmitting materials. The results were compared with the results of other workers and found to be in general agreement. We attempted to explain disagreements with other workers.

#### 5. Acknowledgments

We thank the following for the specimen materials: E. Bernal G. of Honeywell, C. Pitha of the Rome Air Development Center, P. Klein of the Naval Research Laboratory, J. Fenter and R. Harris of the Air Force Materials Laboratory, P. Miles and B. DiBenedetto of Raytheon, and J. Fontanella of the U.S. Naval Academy. The support from the Defense Advanced Research Projects Agency is greatly appreciated.

#### 6. References

- [1] For a description of apparatus and the experimental procedures see the proceedings of these conferences starting in 1974. See also, A. Feldman, Electro-Optical Systems Design **8**, 36 (1976). In this reference the caption in figure 7 is incorrect. The wavelength  $10.6 \mu\text{m}$  should be changed to  $0.6328 \mu\text{m}$ .
- [2] A. Feldman, I. Malitson, D. Horowitz, R. M. Waxler, and M. J. Dodge, in Laser Induced Damage in Optical Materials: 1974, NBS Special Publication 414, edited by A. J. Glass and A. H. Guenther (U.S. G.P.O., SD Catalogue No. C13.10:414, 1974) pp. 141.
- [3] M. J. Dodge, in Proceedings of the Fifth Annual Conference on Infrared Laser Materials, Las Vegas, Nevada, December 1975 (1976) pp. 215.
- [4] M. J. Dodge and I. H. Malitson, in Laser Induced Damage in Optical Materials: 1975, NBS Special Publication 435, edited by A. J. Glass and A. H. Guenther (U.S. G.P.O. SD Catalogue No. C13.10:435, 1975) pp. 170.
- [5] M. J. Dodge, in Laser Induced Damage in Optical Materials: 1976, NBS Special Publication 462, edited by A. J. Glass and A. H. Guenther (U.S. G.P.O., SD Catalogue No. C13.10:462).
- [6] A. Feldman, D. Horowitz, R. M. Waxler, M. J. Dodge, and W. K. Gladden, Optical Materials Characterization, NBSIR 77-1030 (ARPA) (Aug. 1977).
- [7] A. Feldman, D. Horowitz, R. M. Waxler, M. J. Dodge, and W. K. Gladden, Optical Materials Characterization, NBSIR 77-1219 (ARPA) (March 1977).
- [8] to be published.
- [9] A. Feldman, D. Horowitz, and R. M. Waxler, in Laser Induced Damage in Optical Materials: 1975, NBS Special Publication 435, edited by A. J. Glass and A. H. Guenther (U.S. G.P.O., SD Catalogue No. C13.10:435, 1975) pp. 164. In table 1, the values for  $p_{11}$  and  $p_{12}$  have been interchanged.
- [10] A. Feldman, D. Horowitz, and R. M. Waxler, Appl. Optics, to be published.
- [11] A. Feldman, R. M. Waxler, and D. Horowitz, in Optical Properties of Highly Transparent Solids, edited by S. S. Mitra and B. Bendow (Plenum Publishing Corp., New York, 1975) pp. 517. The following corrections should be made: last line, page 519, change [111] to [110]; page 520, eq. (3), change [110] to [100].
- [12] H. G. Lipson, Y. F. Tsay, B. Bendow, and P. A. Ligor, Appl. Optics **15**, 2352 (1976).
- [13] R. J. Harris, G. T. Johnston, G. A. Kepple, P. C. Krok, and H. Mukai, Appl. Optics **16**, 436 (1977).
- [14] American Institute of Physics Handbook, 3rd edition (McGraw-Hill Book Company, 1972) p. 4-137.
- [15] Y. F. Tsay, H. G. Lipson, and P. A. Ligor, J. Appl. Phys. **48**, 1953 (1977).



# 7. Figures

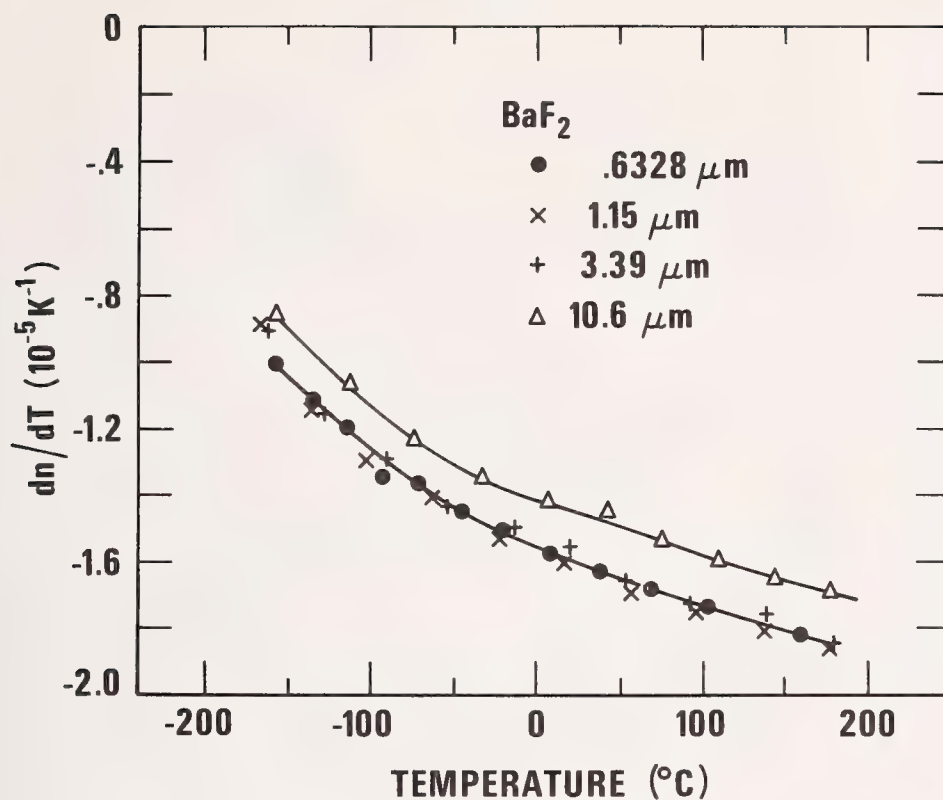


Figure 1.  $\frac{dn}{dT}$  of BaF<sub>2</sub> as a function of temperature.

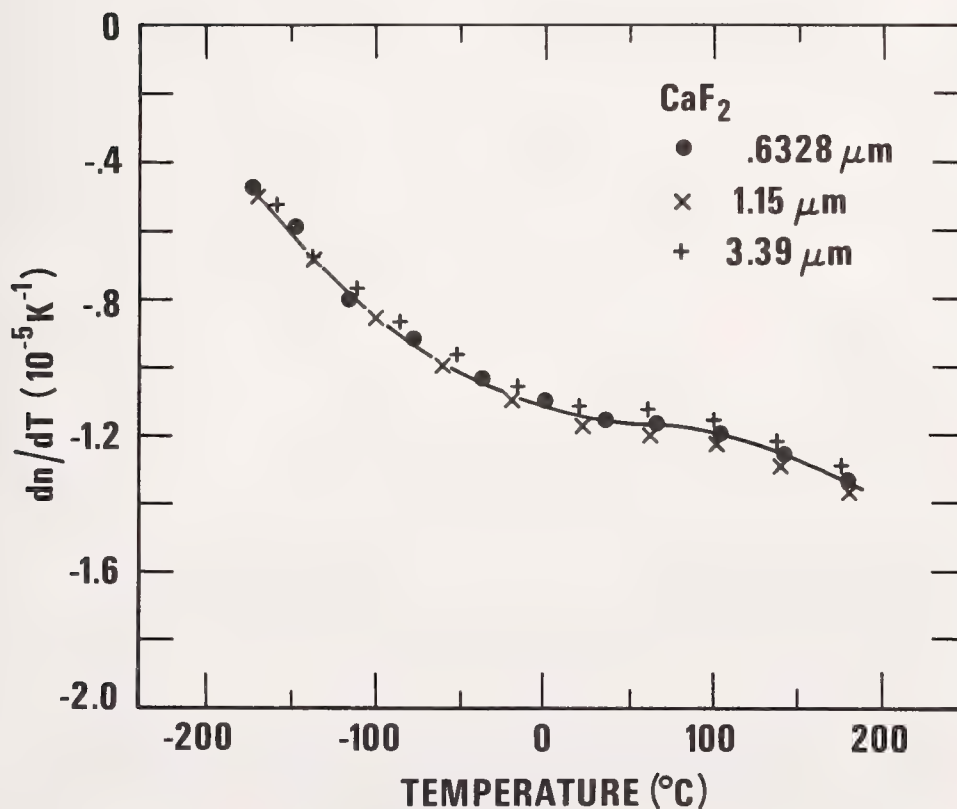


Figure 2.  $\frac{dn}{dT}$  of CaF<sub>2</sub> as a function of temperature.

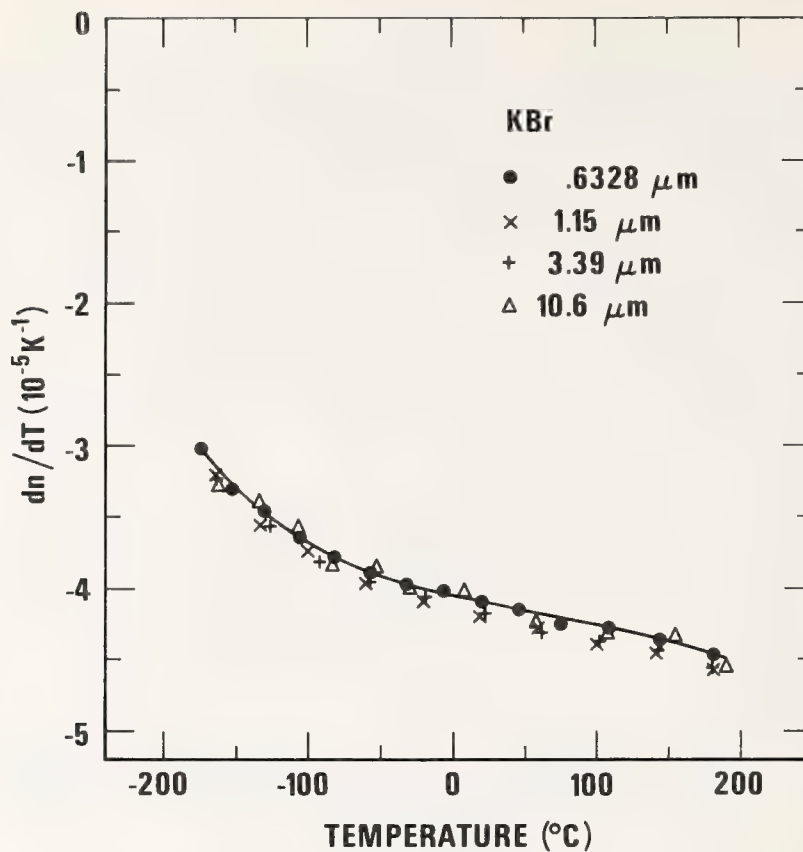


Figure 3.  $dn/dT$  of KBr (RAP) as a function of temperature.

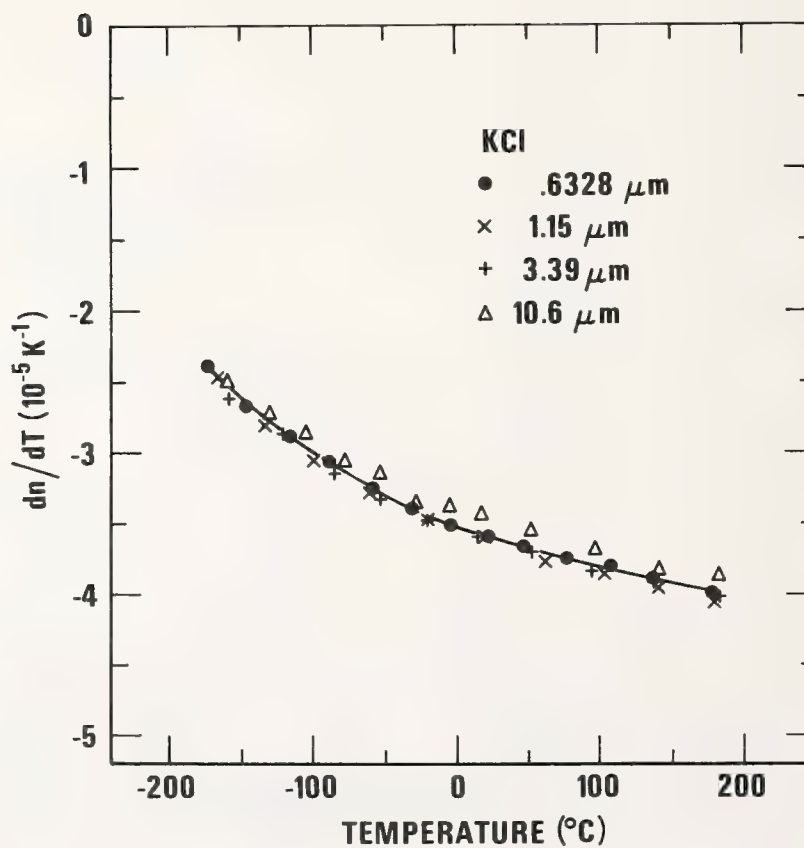


Figure 4.  $dn/dT$  of KCl (RAP) as a function of temperature.

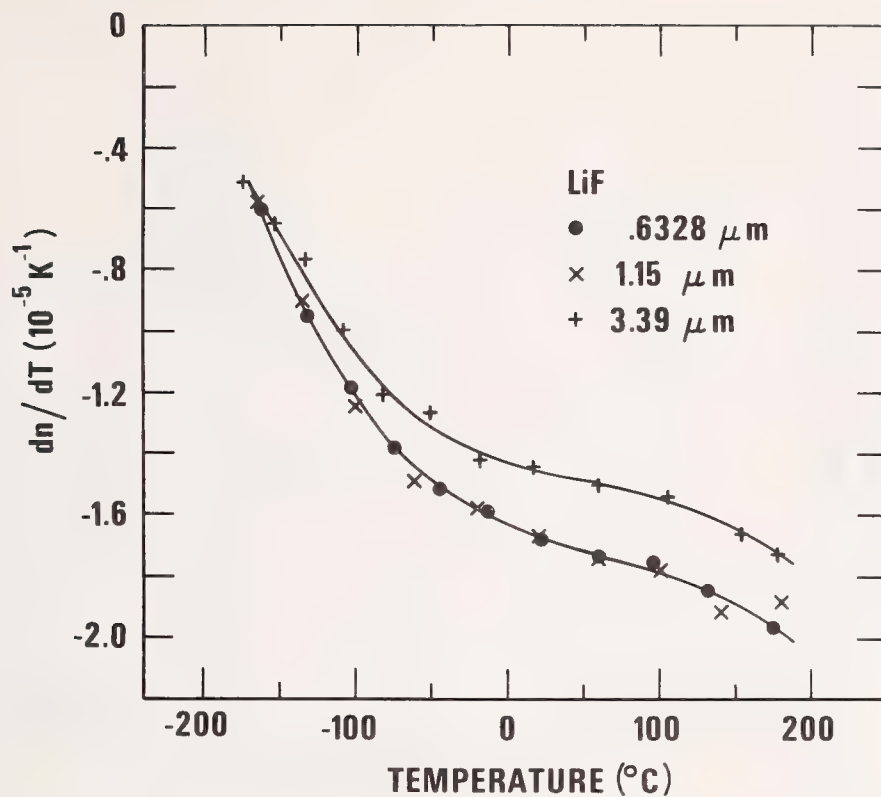


Figure 5.  $dn/dT$  of LiF as a function of temperature.

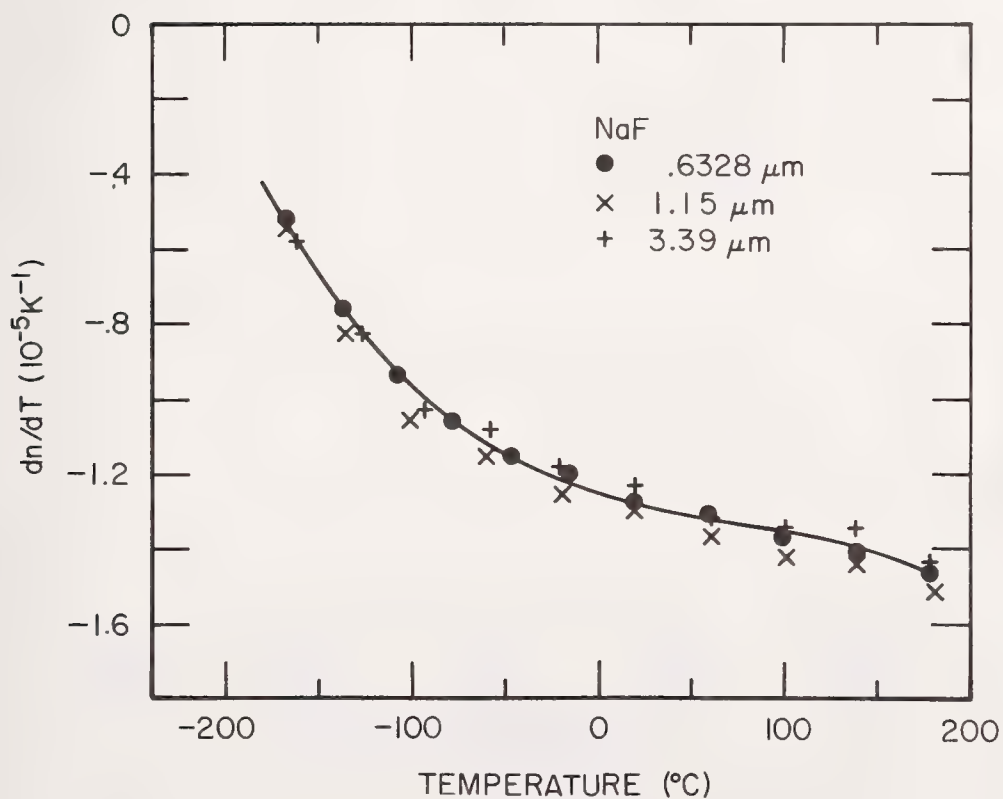


Figure 6.  $dn/dT$  of NaF as a function of temperature.



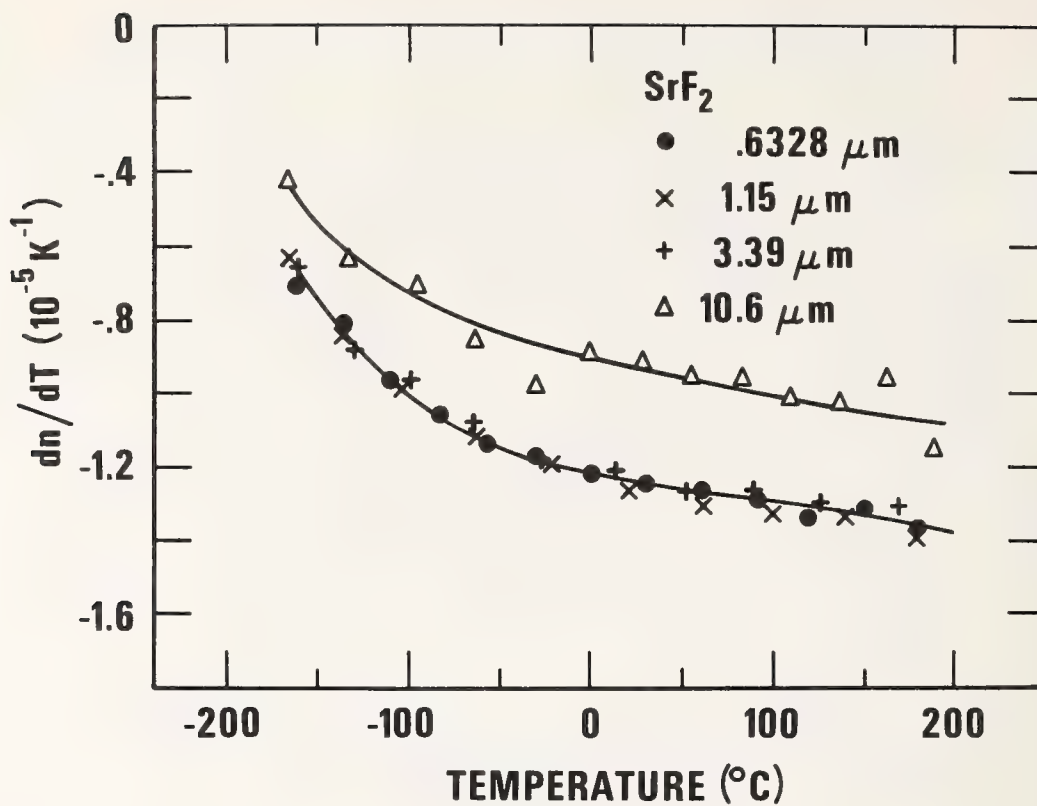


Figure 7.  $\text{dn}/\text{dT}$  of  $\text{SrF}_2$  as a function of temperature.

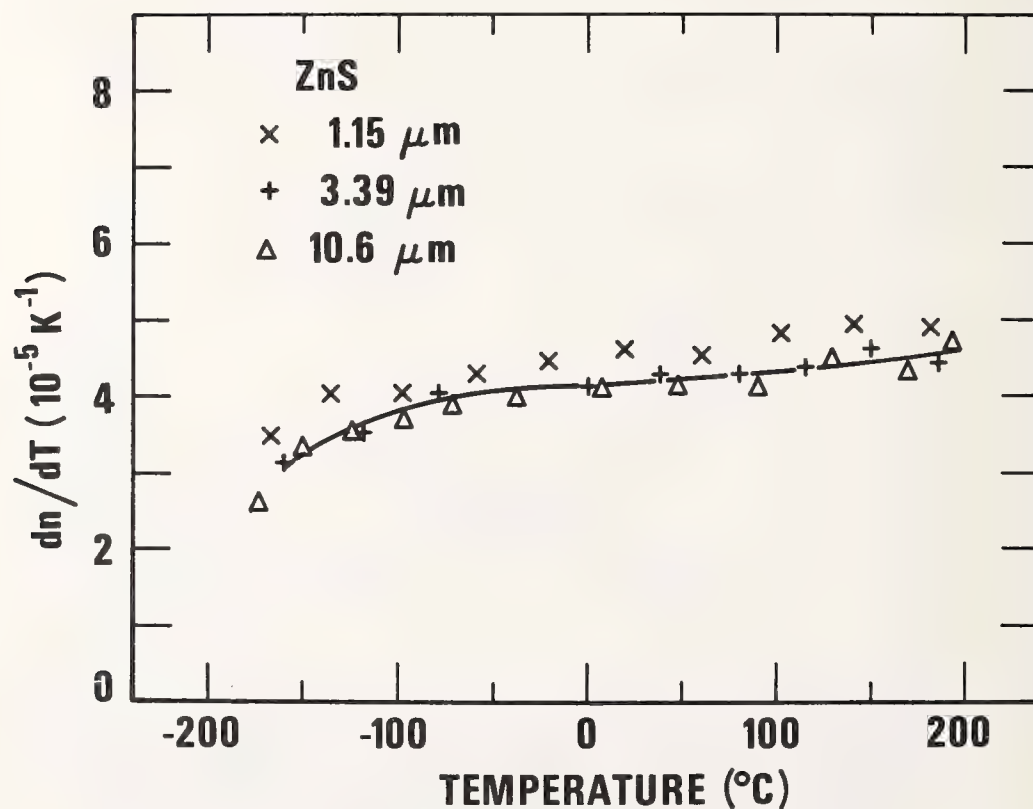


Figure 8.  $\text{dn}/\text{dT}$  of ZnS (CVD) as a function of temperature.

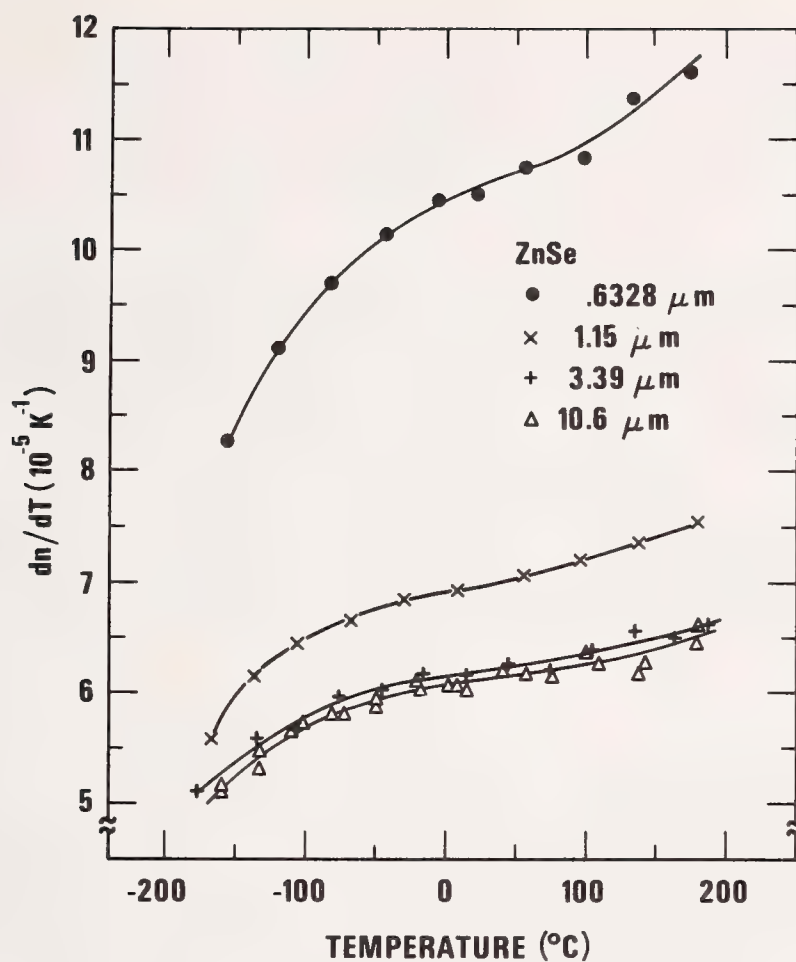


Figure 9.  $dn/dT$  of ZnSe (CVD) as a function of temperature.

COMMENTS ON PAPER BY FELDMAN, HOROWITZ, AND WAXLER

No discussion on this paper.

# REFRACTIVE PROPERTIES OF CVD ZINC SULFIDE\*

Marilyn J. Dodge  
National Bureau of Standards  
Washington, D. C. 20234

The refractive index of two samples of zinc sulfide made by the technique of chemical vapor deposition (CVD) was determined from 0.5461 to 11.475  $\mu\text{m}$ . Measurements were made relative to air by means of the minimum-deviation method on a precision spectrometer at temperatures near 22°C and 34°C. Each set of experimental data was fitted to a Sellmeier-type dispersion equation which permits refractive index interpolation within several parts in  $10^{-5}$ . The calculated data at the two temperatures was used to determine the temperature dependence of the refractive index of ZnS. The index and  $dn/dT$  of the ZnS will be compared with those properties of CVD ZnSe.

Key words: Dispersion; refractive index; temperature coefficient of refractive index; zinc sulfide.

## 1. Introduction

The performance of a high-power laser system is dependent on the optical and mechanical stability of the optical components within the system. Optical distortion of a component can occur as a result of absorptive heating, and if the distortion is severe enough the component can become unusable. New and better optical materials are being developed to help alleviate this problem.

Theoretical calculations of optical distortion in laser windows depends on the knowledge of the absorption coefficient, refractive index (RI), change of index with temperature ( $dn/dT$ ), thermal expansion coefficient, stress-optical constants, elastic compliances, specific heat, thermal conductivity and density of the material under consideration. An optical materials characterization program [1]<sup>1</sup> is currently in progress at NBS to determine their pertinent optical properties. The refractometry laboratory is determining the RI and  $dn/dT$  of selected window materials over a limited temperature range.

Chemical vapor deposited (CVD) ZnS is a possible candidate window material. A comprehensive study of the refractive index of bulk ZnS is not readily available in the open literature. This paper will present RI and  $dn/dT$  data on two samples of this material. The prismatic samples, designated "A" and "B" were made available by B. A. di Benedetto of Raytheon Company.<sup>2</sup> Sample B appeared to be of much better optical quality than sample A.

## 2. Transmission

This material has a practical transmission range from 0.6 to 12  $\mu\text{m}$ , with the exception of the 6  $\mu\text{m}$  region where there is a strong absorption band. Figure 1 shows a transmission curve of a sample of A-type material, 1.5 cm thick [2]. The 6  $\mu\text{m}$  region absorption band is considered to be due to a hydride [3], a common impurity in the CVD ZnS currently available.

\* This work was supported in part by the Defense Advanced Research Projects Agency.

1. The numbers in brackets represents references at the end of this paper.
2. The use of company and brand name in this paper are for identification purposes only and in no case does it imply recommendation or endorsement by the National Bureau of Standards and it does not imply that the materials used in this study are necessarily the best available.



### 3. Experimental Technique

Each prismatic sample had a refracting angle near  $32^\circ$ , and two polished faces approximately 2.5 cm square. The refractive indexes were determined by means of the minimum-deviation method on a precision spectrometer shown schematically in fig. 2 [4]. In the visible and near infrared regions of the spectrum, the index was determined at known emission wavelengths of mercury, cadmium and helium. Beyond 2  $\mu\text{m}$ , a glo-bar was used for the radiant-energy source, and measurements were made at known absorption bands of water, carbon dioxide, polystyrene, methocyclohexane, and 1, 2-4 trichlorobenzene. A series of narrow-band interference filters was also used between 3.5 and 10.6  $\mu\text{m}$ . A thermocouple with a cesium iodide window was used for the detector. The scale of this spectrometer can be read to 1 second of arc and the instrument is considered to have an equivalent precision and negligible systematic errors. This will permit refractive indexes accurate within a few parts in  $10^{-5}$  over a wide wavelength range, to be determined for good optical material. All measurements were made relative to air under normal laboratory conditions.

### 4. Refractive Index

The RI of sample A was determined from 0.5461 to 11.475  $\mu\text{m}$  and from 0.5461 to 11.862  $\mu\text{m}$  for sample B. Measurements were initially made on each sample at a controlled-room temperature near  $22^\circ\text{C}$  and repeated near  $34^\circ\text{C}$ .

Each set of experimental data from 0.5461 to 10.6  $\mu\text{m}$  was fitted to a three-term Sellmeier-type dispersion equation [5] of the form:

$$n^2 - 1 = \sum_{j=1}^3 \frac{A_j \lambda^2}{\lambda^2 - \lambda_j^2}.$$

The index of refraction is represented by  $n$ ,  $\lambda$  is the wavelength of interest in  $\mu\text{m}$ , the  $\lambda_j$ 's are the calculated wavelengths of maximum absorption and the  $A_j$ 's are the calculated oscillator strengths corresponding to the absorption bands. The  $\lambda_j$ 's and  $A_j$ 's are not intended to have any physical significance. Primary emphasis is given to procuring a mathematical fit of the measured data useful for interpolation.

The constants calculated for the dispersion equation for each specimen at two temperatures, the number of wavelengths fitted and the average absolute residual (the average difference between the experimental values and the calculated values) are given in table 1.

Table 1. Dispersion equation constants for calculating refractive index of CVD ZnS relative to air.

	Sample A		Sample B	
	21.6°C	33.6°C	21.9°C	33.4°C
$A_1$	0.33904026	0.19924242	0.24199447	0.79907896
$A_2$	3.7606868	3.9029481	3.8575584	3.3033398
$A_3$	2.7312353	2.7620669	2.5433609	2.8028661
$\lambda_1$	0.31423026	0.34058701	0.33005445	0.28020665
$\lambda_2$	0.17594174	0.18057756	0.17899635	0.16205174
$\lambda_3$	33.886560	34.059326	32.849275	34.288073
No. of wavelengths fitted	25	25	30	27
Average absolute residual $\times 10^5$	5.5	5.0	4.6	4.2

The average absolute residual is an indication of the overall accuracy of the experimental data. The largest residuals were in the region between 5.5 and 6.5  $\mu\text{m}$  which could be expected because of the strong absorption in this region. The Sellmeier equation will fail when a fit is attempted too close to an absorption edge, but will attempt to fit through a band when some data exists on either side of the band. It was possible to obtain experimental index data within the 6  $\mu\text{m}$  region of absorption, but the equation could not adequately fit the data in this region because of the anomalous index effect which occurs in regions of absorption. Experimental data were obtained for both specimens beyond the 11  $\mu\text{m}$  absorption band, but because of the natural cutoff of the material not enough data could be obtained in this region to facilitate a fit through the band. Instead, the anomalous index effect within this weak band put undo influence on the IR parameters of the equation and an adequate fit was impossible at all wavelengths. Therefore, a satisfactory fit could not be accomplished beyond 10.6  $\mu\text{m}$ .

After a fit was obtained, the refractive index was calculated at regular wavelength intervals. Figure 3 shows the dispersion curve for specimen B.

Figure 4 compares sample B with sample A which is represented by the zero line. The index of specimen B is lower than that for sample A below 2  $\mu\text{m}$  and higher at all wavelengths beyond 2  $\mu\text{m}$ . This behavior could be indicative of extended useful transmission, or less absorption, in sample B beyond the absorption edges of sample A.

### 5. Temperature Coefficient of Index

The calculated data for the two average temperatures at which each sample was measured were used to calculate  $dn/dT(^{\circ}\text{C})^{-1}$  for each specimen. The resultant  $dn/dT$  values are shown graphically in fig. 5. The data points in this figure represent the  $dn/dT$  values which were calculated from the experimental data. With the exception of between 6.5 and 10  $\mu\text{m}$  the values for both samples agree within  $5 \times 10^{-6}$ . This discrepancy is still well within the stated experimental errors for the index determinations from which the  $dn/dT$  was calculated. Corrections for the  $dn/dT$  of air have not been applied in the determination of the  $dn/dT$  values for the ZnS samples in this study. In table 2, the  $dn/dT$  of these two specimens are compared with those of Feldman, et al. [6], and Harris, et al. [7] at specific laser wavelengths.

Table 2. Comparison of  $dn/dT \times 10^{-5}(^{\circ}\text{C})^{-1}$  for CVD ZnS

WAVELENGTH ( $\mu\text{m}$ )	DODGE*		FELDMAN (30 $^{\circ}\text{C}$ )	HARRIS (45 $^{\circ}\text{C}$ )
	A (28 $^{\circ}\text{C}$ )	B		
1.15	5.0	5.2	4.6	5.0
3.39	4.6	4.8	4.2	4.6
10.6	4.7	5.0	4.1	4.6

\* These values have not been corrected for the  $dn/dT$  of air.

### 6. Comparison of CVD ZnS and CVD ZnSe

The refractive index and temperature coefficient of refractive index of CVD ZnSe has been previously reported [8]. Because ZnSe and ZnS are similar materials, a comparison of the RI and  $dn/dT$  of the two materials measured in this laboratory is made in table 3.

Table 3. Comparison of the refractive properties (relative to air) of CVD ZnS and CVD ZnSe.

WAVELENGTH ( $\mu\text{m}$ )	ZnS	ZnSe
	REFRACTIVE INDEX	
1.0	2.2923	2.4891
3.0	2.2572	2.4375
5.0	2.2462	2.4294
10.6	2.1921	2.4027
$dn/dT \times 10^5 (^{\circ}\text{C})^{-1}$		
1.0	5.2	8.9
3.0	4.9	7.2
5.0	4.3	7.3
10.6	5.0	7.4

## 7. Conclusion

The refractive properties of CVD ZnS presented in this paper refer to the specific samples in this study. Although these findings are probably representative of the material, caution should be used when applying any of these values to other samples of ZnS. As growth techniques are improved, better material will result with possible changes in the refractive properties, especially near the regions of absorption.

## 8. References

- [1] Feldman, A., Malitson I., Horowitz, D., Waxler, R. M. and Dodge, M., Laser Induced Damage in Optical Materials: 1974, NBS Special Pub. 414, 141, (1974).
- [2] Raytheon Company, In-Line Transmission, Run ZS-157P, PBN-74-607; provided through the courtesy of B. A. di Benedetto, Advanced Materials Department.
- [3] Personal communication with D. A. di Benedetto, Raytheon Company.
- [4] Stephens, Robert E., Phylar, Earle K., Rodney, William S., and Spindler, Robert J., J.O.S.A. 43, 110, (1953).
- [5] Sutton, Loyd E. and Stavroudis, Orestes N., J. Opt. Soc. Am. 51, 901 (1961).
- [6] Feldman, A., Horowitz, D., Waxler, R. M., "Refractive Properties of Infrared Window Materials," Proceedings of the Ninth Symposium on Materials for High Power Lasers, 1977, NBS Publication.
- [7] Harris, R. J., Johnston, G. T., Kepple, G. A., Krok, P. C., and Mukai, H., Applied Optics 16, 436 (1977).
- [8] Dodge, Marilyn J. and Malitson, Irving H., Laser Induced Damage in Optical Materials: 1975, NBS Special Pub. 435, 170, (1976).

## 9. Figures

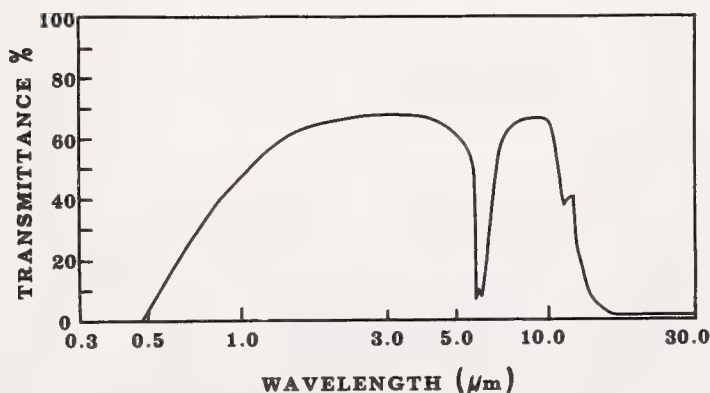


Fig. 1 - Transmission curve of CVD ZnS taken from "In Line Transmission Run" provided through the courtesy of B. A. di Benedetto, Ratheon Company.



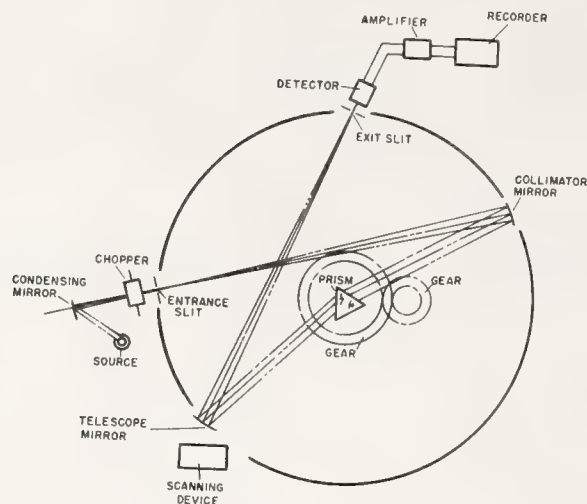


Fig. 2 - Schematic diagram of the modified Gaertner precision spectrometer showing optical path. The prism is rotated at one-half the rotation rate of the telescope assembly by gear system, thus maintaining the condition of minimum deviation for any wavelength. The scanning device drives the assembly which scans the spectrum to identify lines or bands and determine their approximate scale positions.

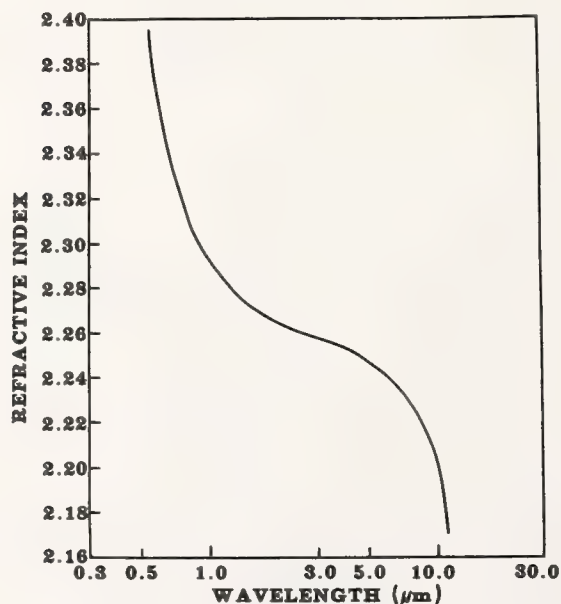


Fig. 3 - Refractive index of CVD ZnS as a function of wavelength (logarithmic scale). Data near 22°C were calculated from the dispersion equation.

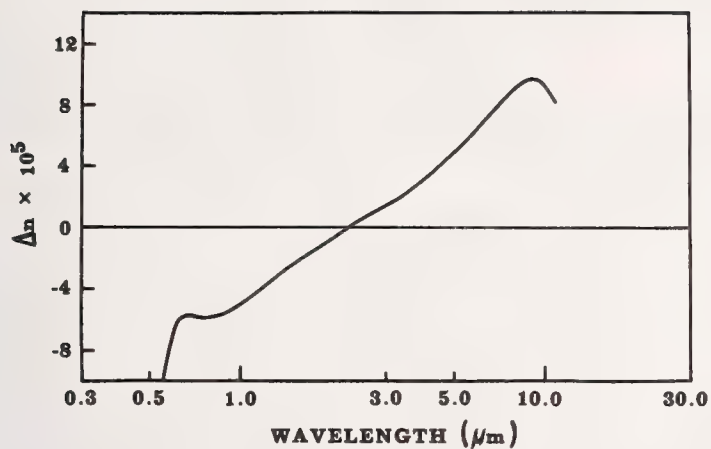


Fig. 4 - Comparison of the refractive index of sample B ZnS with sample A. The index of sample A is represented by the zero-line.

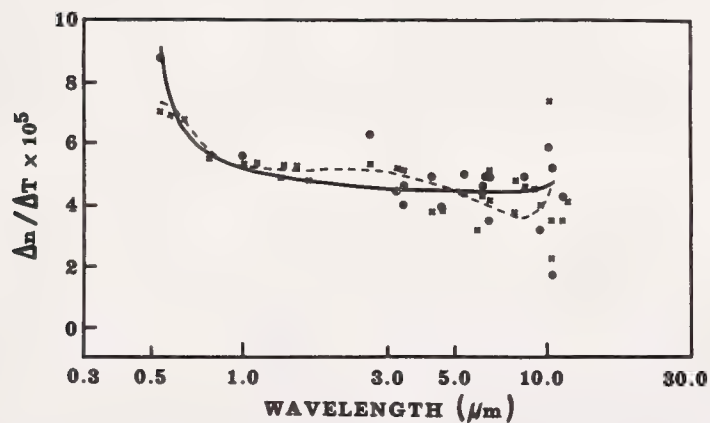


Fig. 5 - Temperature coefficient of refractive index of CVD ZnS near 28°C. Sample A: ———  $dn/dT$  from index data calculated by the dispersion equation; ●  $dn/dT$  from experimental index data. Sample B: -----  $dn/dT$  from calculated index data; ✱  $dn/dT$  from the experimental data.

# CRITICAL ORIENTATIONS FOR ELIMINATING STRESS-INDUCED DEPOLARIZATION IN CRYSTALLINE WINDOWS AND RODS\*

R. E. Joiner, J. H. Marburger, and W. H. Steier  
Departments of Electrical Engineering and Physics  
University of Southern California  
Los Angeles, California 90007

The amount of depolarization resulting from stress-induced birefringence in crystalline materials can be extremely dependent upon orientation. In windows and rods made of certain materials, critical orientations exist for which the depolarization effect is eliminated.

Key words:  $\text{BaF}_2$ ;  $\text{CaF}_2$ ; crystalline windows and rods; depolarization; optical distortion; photo-elastic constants; stress-induced birefringence.

## 1. Introduction

Depolarization of beams transmitted through optical elements rendered birefringent by applied, induced, or frozen in stresses is a frequent nuisance in laser system design. In high power laser windows, this form of optical degradation effectively creates two distorted beams, one for each polarization. Each beam has a different focal point, and any attempt to focus one defocuses the other. In laser rods, the effect appears as a loss in the cavity for polarized output. We have found that the depolarization effect can be eliminated in crystalline windows made of certain materials by properly orienting the window. A similar critical orientation can also be found for a rod made of the same material, where the strains are confined to the plane perpendicular to the axis of the rod.

## 2. Experiment

The experimental set-up shown in figure 1 was used to investigate the effect of crystal orientation upon the depolarization resulting from thermally induced stresses in a window made of  $\text{BaF}_2$ . A 25 W Gaussian mode  $\text{CO}_2$  beam ( $10.6\text{ }\mu\text{m}$ ) was used to thermally induce the stresses, while a polarized and collimated HeNe beam ( $632.8\text{ nm}$ ) with uniform intensity was used to probe the birefringence. Within experimental limits, no intensity was observed in the orthogonal polarization of the HeNe beam when the heating beam was blocked. With heating, a cloverleaf pattern in the orthogonal polarization was observed as shown in figure 2. For normal incidence, the propagation vectors for both beams were along the  $\langle 111 \rangle$  crystallographic direction, and the electric displacement  $\vec{D}$  of the HeNe beam was along some undetermined direction in the  $\langle 111 \rangle$  plane. For this orientation, the resultant intensity pattern is independent of crystallographic direction along  $\vec{D}$  [1]. The intensity pattern for the  $\langle 111 \rangle$  orientation is shown in figure 2(a). Other orientations were observed by rotating the window by the angle  $\varphi$  about its normal ( $\langle 111 \rangle$ ) and by tilting the window about the horizontal axis of the mirror mount holding the window, such that the propagation vector inside the window made an angle  $\theta$  with the window normal, as shown in figure 3. As the window was rotated by  $\varphi$  and  $\theta$ , the intensity pattern in the orthogonal polarization would rotate and change dramatically in intensity, as shown in figure 2(b). For a particular orientation  $(\theta_0, \varphi_0)$ , the pattern vanished, showing a null in the depolarization effect. This null was also observed for  $(\theta_0, \varphi = \varphi_0 + n(120^\circ))$  for  $n = 1, 2$ , consistent with the 3-fold symmetry at the  $\langle 111 \rangle$  direction.

## 3. Analysis (General Case)

For a given propagation vector  $\vec{k}$  in a naturally birefringent material, there are two directions for the electric displacement  $\vec{D}$  which result in a linearly polarized beam. In the index ellipsoid formalism [2], these directions correspond to the major and minor axes of an elliptical cross-section of the index ellipsoid, perpendicular to  $\vec{k}$ , as shown in figure 4. In phase plate terminology, these axes correspond to the fast and slow axes of the phase plate. If  $\vec{D}$  is along one of these axes, then the beam remains linearly polarized as it propagates through the material. If  $\vec{D}$  is along any other direction, the beam becomes elliptically polarized.

If the birefringence is induced by stresses, the shape of the ellipsoid will depend upon crystal orientation and the amount of stress. For non-uniform stress, both the magnitude and direction of the fast and slow axes will vary from point to point, and the window appears as a collection of differently oriented phase plates, as shown in figure 5(a). In general, it is not possible for a beam to be polarized along a single direction over the entire cross-section of the beam. The resultant polarization state is usually a complicated function of position, depending upon the distribution of stresses in the window.

\*Work supported by DARPA under Contract No. F19628-77-C-0094.



For the special case of a circularly symmetric heating beam, normally incident upon a  $\langle 111 \rangle$  oriented window, the axes are along radial and azimuthal directions, as shown in figure 6, and the magnitudes are a function of the radial coordinate only. Hence, a cloverleaf intensity pattern in the orthogonal polarization is observed.

We have discovered that in certain materials, for certain critical orientations, the axes of the effective phase plates become uniform in direction, independently of stresses in the plane of the window, as shown in figure 5(b). A beam passing through such a window will become distorted (because there are still index variations along the fast and slow axes) but not depolarized. To understand how such an orientation could exist, we investigate the equation for the index ellipsoid.

In cartesian coordinates, the index ellipsoid for a cubic crystal is given by

$$(1/n^2 + \Delta B_{xx})xx + (1/n^2 + \Delta B_{yy})yy + (1/n^2 + \Delta B_{zz})zz + 2\Delta B_{xy}xy + 2\Delta B_{xz}xz + 2\Delta B_{yz}yz = 1, \quad (1)$$

where  $n$  is the index of refraction, and

$$\Delta B_{ij} = -2\Delta n_{ij}/n^3 \quad (2)$$

is the stress-induced change in the ellipsoid. If the wave vector  $\vec{k}$  is along the  $z$  direction, then the elliptical cross-section of the ellipsoid perpendicular to  $\vec{k}$  is given by

$$(1/n^2 + \Delta B_{xx})xx + (1/n^2 + \Delta B_{yy})yy + 2\Delta B_{xy}xy = 1. \quad (3)$$

If  $\Delta B_{xy} = 0$ , then equation (3) describes an ellipse with major and minor axes along  $x$  and  $y$ . For the existence of critical orientations as described,  $\Delta B_{xy}$  must be zero, independent of stress.

The relationship between  $\Delta B$  in the  $xy$  plane and stresses  $\sigma$  in the  $xy$  plane is given by

$$\begin{bmatrix} \Delta B'_{xx} \\ \Delta B'_{yy} \\ \Delta B'_{xy} \end{bmatrix} = \begin{bmatrix} q'_{11} & q'_{12} & q'_{16} \\ q'_{21} & q'_{22} & q'_{26} \\ q'_{61} & q'_{62} & q'_{66} \end{bmatrix} \begin{bmatrix} \sigma'_{xx} \\ \sigma'_{yy} \\ \sigma'_{xy} \end{bmatrix}, \quad (4)$$

where the prime denotes a quantity which varies with crystal orientation. The  $q$ 's are elements of the stress-optic tensor [3]. The condition for  $\Delta B'_{xy} = 0$  independent of stress is

$$q'_{61} = q'_{62} = q'_{66} = 0. \quad (5)$$

Starting from some arbitrary orientation and rotating the coordinate system about the  $y$  axis by the angle  $\theta$ , one finds [4] that

$$q'_{61} = -\sin\theta(q_{41}\cos^2\theta + q_{43}\sin^2\theta - q_{45}\sin 2\theta/2) + \cos\theta(q_{61}\cos^2\theta + q_{63}\sin^2\theta - q_{65}\sin 2\theta/2) \quad (6)$$

$$q'_{62} = -\sin\theta(q_{42}) + \cos\theta(q_{62}) \quad (7)$$

$$q'_{66} = q_{44}\sin^2\theta + q_{66}\cos^2\theta - ((q_{46} + q_{64})/2)\sin 2\theta, \quad (8)$$

where the unprimed  $q$ 's denote elements of the stress-optic tensor before the rotation. If the rotation axis is a 2-fold axis or an axis perpendicular to a mirror plane, the unprimed  $q$ 's in eqs. (6, 7) are identically zero, and both  $q'_{61}$  and  $q'_{62}$  are zero independent of  $\theta$ . The angle  $\theta$  is determined by setting  $q'_{66} = 0$  in eq. (8).

#### 4. $\bar{4}3m$ Cubic Symmetry Windows and Rods

##### 4.1 Windows

The window materials currently of interest have  $\bar{4}3m$  cubic symmetry. The  $\langle 100 \rangle$  and  $\langle 110 \rangle$  directions satisfy the symmetry requirements in section 3. For  $z$  and  $y$  along  $\langle 100 \rangle$  directions,  $q_{46} = q_{64} = 0$ , and  $q_{66} = q_{44}$ ; hence from eq. (8),  $q'_{66} = q_{44}$  independent of a rotation by  $\theta$  about the  $y$  axis, and no critical orientation exists. For  $z$  along a  $\langle 100 \rangle$  direction and  $y$  along a  $\langle 110 \rangle$  direction, shown in figure 7,  $q_{64} = q_{46} = 0$ ,  $q_{66} = q_{11} - q_{12}$ , and  $q'_{66}$  is given by

$$q'_{66} = (q_{11} - q_{12})\cos^2\theta + q_{44}\sin^2\theta. \quad (9)$$

The value of  $q'_{66}$  varies from  $(q_{11} - q_{12})$  when  $z'$  is in the  $\langle 100 \rangle$  direction to  $q_{44}$  when  $z'$  is in the  $\langle 110 \rangle$  direction. If  $(q_{11} - q_{12})$  and  $q_{44}$  are opposite in sign, then there exists a critical angle  $\theta_c$  for which  $q'_{66}$  vanishes, namely

$$\tan^2\theta_c = -1/A_q, \quad (10)$$

where

$$A_q = q_{44}/(q_{11} - q_{12}) \quad (11)$$

is the stress-optic anisotropy ratio. Thus critical orientations exist in materials for which  $A_q$  is negative. For  $\vec{k}$  along  $z'$  and  $\vec{D}$  along either  $x'$  or  $y'$ , no depolarization will occur, independent of stress in the  $x'y'$  plane. To insure the plane stress approximation, the window should be thin, and the window normal should be in the  $z'$  direction.

Stress-optic anisotropy ratios and critical angles were computed using experimental values for stress-optic coefficients [5, 6, 7, 8] for several window materials at wavelengths where data was available. The results are shown in table 1. Experimental results in  $\text{BaF}_2$  [9], shown in figure 8, are in good agreement with the theoretical estimate of  $\theta_c$ . The angle measured from the  $\langle 111 \rangle$ ,  $\theta_0$ , was  $11^\circ$ , corresponding to a value of  $65.7^\circ$  for  $\theta_c$  measured from the  $\langle 100 \rangle$ . Also note that the estimated value of  $\theta_0$  for  $\text{CaF}_2$  at 632.8 nm is within  $1\frac{1}{2}^\circ$  of the  $\langle 111 \rangle$  direction. Measurements by Bernal [10] and Detrio [11] show negligible depolarization for  $\langle 111 \rangle$  oriented  $\text{CaF}_2$  windows, and significant depolarization for other orientations.

Table 1. Critical angles for stress-insensitive birefringence axes

	NaCl	KCl	KCl	$\text{CaF}_2$	$\text{BaF}_2$	$\text{SrF}_2$	CdTe	GaAs
$\lambda$	633 nm	633 nm	10.6 $\mu\text{m}$	633 nm	633 nm	633 nm	10.6 $\mu\text{m}$	10.6 $\mu\text{m}$
A	+0.68	-2.16	-2.12	-0.44	-0.19	-0.25	+0.84	+1.10
$\theta_c$	—	34.2°	34.5°	56.3°	66.4°	63.4°	—	—

#### 4.2. Rods

Analogous to thin windows, critical orientations should also exist for beams propagating down the axis of a long rod. For long rods, it is the strain rather than the stress that is confined to the plane perpendicular to the rod axis. For this case

$$\begin{bmatrix} \Delta B'_{xx} \\ \Delta B'_{yy} \\ \Delta B'_{xy} \end{bmatrix} = \begin{bmatrix} p'_{11} & p'_{12} & p'_{16} \\ p'_{21} & p'_{22} & p'_{26} \\ p'_{61} & p'_{62} & p'_{66} \end{bmatrix} \begin{bmatrix} e'_{xx} \\ e'_{yy} \\ e'_{xy} \end{bmatrix}, \quad (12)$$

where the  $p_{ij}$ 's are strain-optic coefficients, and the  $e$ 's are strains. For  $z'$  in the  $\langle 110 \rangle$  plane,  $p'_{61}$  and  $p'_{62}$  are zero independent of  $\theta$ , and

$$p'_{66} = \frac{1}{2}(p_{11} - p_{12})\cos^2\theta + p_{44}\sin^2\theta. \quad (13)$$

The factor of one half comes from the definition of  $p_{44} = p_{1212}$  as opposed to  $q_{44} = 2q_{1212}$ . The critical orientation  $\theta_c$  is given by

$$\tan^2\theta_c = -1/A_p \quad (14)$$

where

$$A_p = 2p_{44}/(p_{11} - p_{12}) \quad (15)$$

is the strain-optic anisotropy ratio.

The  $p$ 's and  $q$ 's are related by

$$p_{IJ} = q_{IK}c_{KJ}, \quad (16)$$

and the anisotropy ratios are related by

$$2p_{44}/(p_{11} - p_{12}) = (q_{44}/(q_{11} - q_{12})) * (2c_{44}/(c_{11} - c_{12})). \quad (17)$$

The  $c$ 's are the elastic stiffness coefficients. Since the elastic anisotropy ratio is always positive, the stress-optic and strain-optic anisotropy ratios have the same sign. So if a critical orientation exists for a thin window made out of a certain material, a critical orientation also exists for a long rod made of the same material.

Koechner, Rice, and DeShazer [12] first appreciated the orientation dependence of strain-induced birefringence in YAG rods and investigated the depolarization of a HeNe beam (632.8 nm) for rods oriented along symmetry axes. At this wavelength,  $A_p$  in YAG is positive, and therefore, only a minimum depolarization was observed.

## 5. Conclusions

The amount of beam depolarization resulting from stress-induced birefringence in thin windows and long rods can vary significantly with crystallographic orientation. For certain critical orientations the depolarization can be eliminated. In  $\bar{4}3m$  cubic symmetry materials, the necessary condition is a negative photo-elastic anisotropy ratio. If such an orientation exists for a window made of a certain material, a critical orientation will exist for a rod made of the same material.

Apart from its application in the design of optical elements free from stress-induced depolarization, the effect should also prove useful in connection with the measurement of photo-elastic constants. These constants are relatively difficult to measure. A simple measurement of  $\theta_c$  yields a ratio of constants, and if one constant is known, the other is easily and accurately determined. A measurement of  $\theta_c$  while varying the wavelength would also give the dispersion in the stress-optic anisotropy ratio.

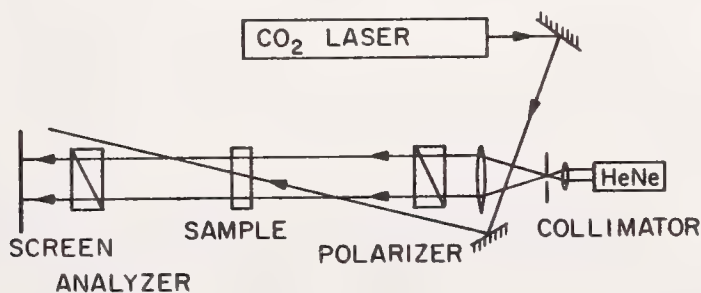
## 6. Acknowledgement

The authors are grateful to Professor Jan Smit for stimulating discussions of this effect.

## 7. References

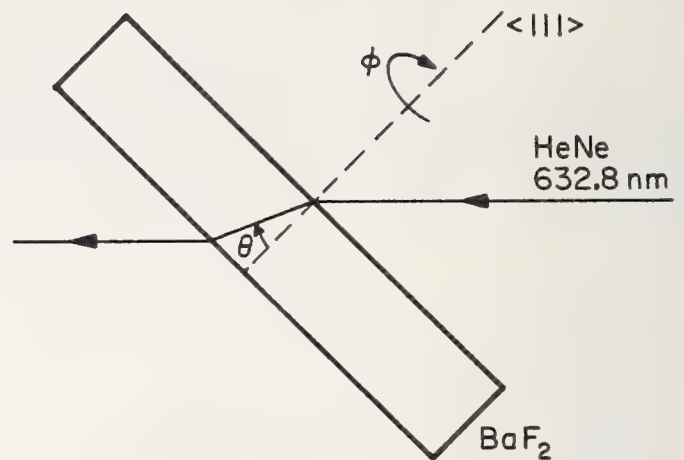
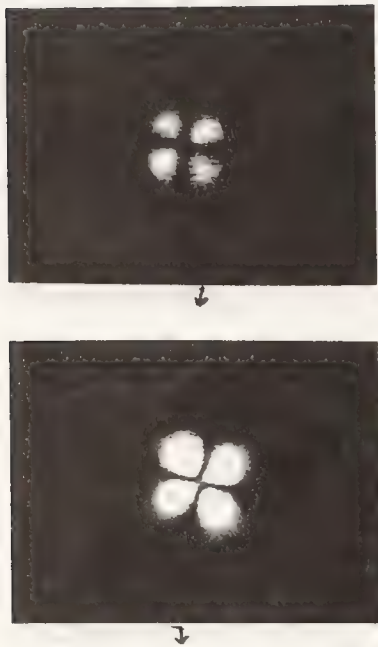
- [1] Bendow, B., Gianino, P.D., Flannery, M., and Marburger, J., Proceedings of the 4th Annual Conference on Infrared Window Materials, compiled by C.R. Andrews and C.L. Strecker (Air Force Materials Lab., Wright-Patterson Air Force Base, Ohio 1975), p. 299.
- [2] Yariv, A., Quantum Electronics, 2nd ed. (Wiley, New York, 1975), pp. 354-355.
- [3] Nye, J. F., Physical Properties of Crystals, (Oxford University Press, Ely House, London W.1, 1969), pp. 235-254.
- [4] Joiner, R. E., "The Elimination of Stress-Induced Birefringence Effects in High-Power Laser Windows," dissertation, University of Southern California, Los Angeles, 1977.
- [5] Pitha, C., Friedman, J., Szcsensniak, J., Cutteback, D., and Corielli, J., Proceedings of the 5th Annual Conference on Infrared Window Materials, compiled by C.R. Andrews and C.L. Strecker (Air Force Materials Lab., Wright-Patterson Air Force Base, Ohio, 1976), p. 927.
- [6] Joiner, R. E., Steier, W. H., and Christensen, C. P., in ref. [5], p. 937.
- [7] Feldman, A., Horowitz, D., and Waxler, R. in ref. [5], p. 943.
- [8] Dickinson, S. K., Infrared Laser Window Materials Property Data for ZnSe, KCl, NaCl, CaF<sub>2</sub>, BaF<sub>2</sub>, SrF<sub>2</sub>, (Air Force Cambridge Research Labs, Bedford, Mass., 1975).
- [9] Joiner, R. E., Marburger, J., Steier, W. H., Appl. Phys. Lett. **30**, 485 (1977).
- [10] Bernal G., E. and Leung, K., private communication, Honeywell Corporate Research Center, Bloomington, Minnesota, August 1977.
- [11] Dietrio, J. A., private communication, University of Dayton, Research Institute, Dayton, Ohio, October 1977.
- [12] Koechner, W., Rice, D. K., and DeShazer, L. G., U. S. patent.

## 8. Figures



1. Experimental set-up used to investigate orientation effects upon depolarization in BaF<sub>2</sub>.

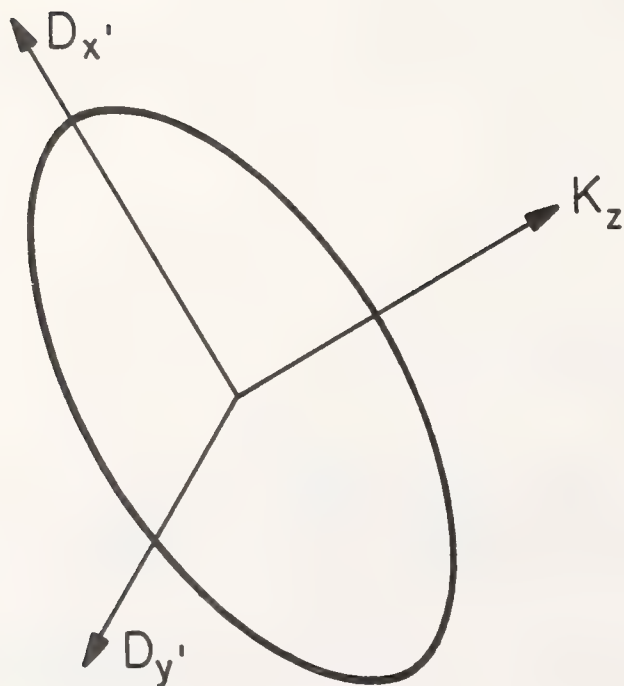




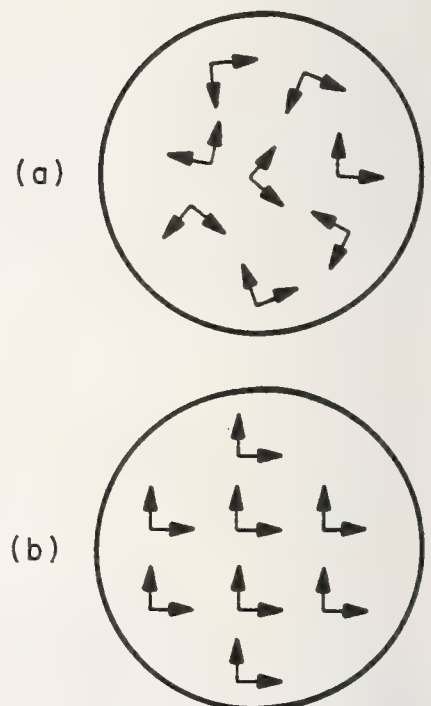
3. Rotations used to investigate other orientations.

2. Intensity pattern in the orthogonal polarization.

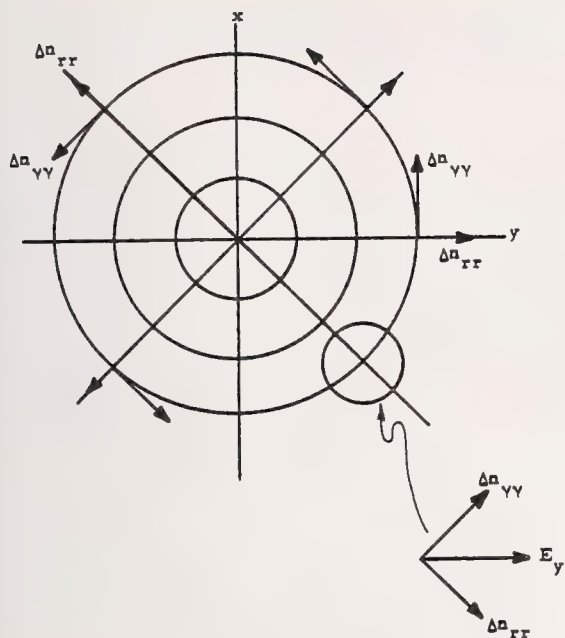
- (a)  $\vec{k}$  along  $\langle 111 \rangle$
- (b) arbitrary orientation



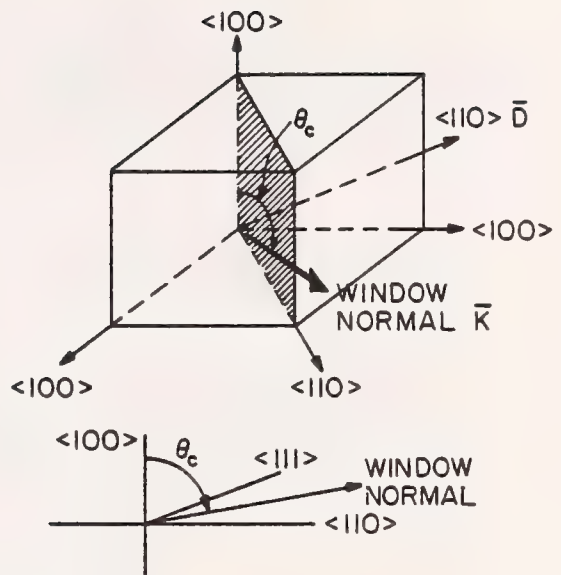
4. Major and minor axis of elliptical cross-section in index ellipsoid formalism.



5. "Fast" and "slow" axes in a stressed window.  
 (a) arbitrary orientation and stress  
 (b) critical orientation



6. "Fast" and "slow" axes for a circularly symmetric heating beam propagating in the  $\langle 111 \rangle$  direction.

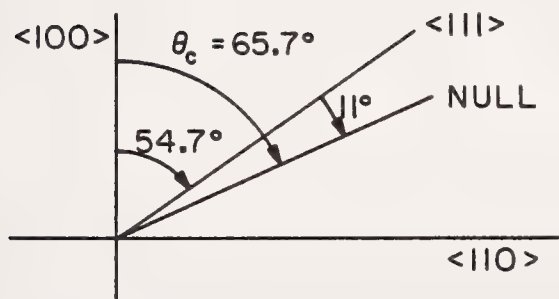


$$q'_{61} = q'_{62} = 0$$

$$q'_{66} = (q_{11} - q_{12}) \cos^2 \theta + q_{44} \sin^2 \theta = 0$$

$$\text{For } \tan^2 \theta_c = \frac{-(q_{11} - q_{12})}{q_{44}} = -\frac{1}{A}$$

7. Critical orientations in windows made of material with  $\bar{4}3m$  symmetry.



CRITICAL ANGLE IN  $\text{BaF}_2$  AT 632.8 nm  
 THEORETICAL  $66.4^\circ$   
 EXPERIMENTAL  $65.7^\circ$

8. Experimental value of  $\theta_c$  in  $\text{BaF}_2$ .

COMMENTS ON PAPER BY JOINER, MARBURGER, AND STEIER

The speaker was asked if a critical angle determination had been carried out for YAG. He responded that they had looked for a critical angle effect in YAG at  $6328 \text{ \AA}$ , but none had been observed. John Detrio of the University of Dayton Research Institute pointed out that in experiments carried out at UDRI, results similar to those presented in this paper had been obtained.



# LATTICE DEFECT EQUILIBRIUM IN KCl:Eu\*

J. B. Wolfenstine and T. G. Stoebe  
Department of Mining, Metallurgical, and Ceramic Engineering  
University of Washington  
Seattle, WA 98195

A study of lattice equilibria in Harshaw-grown KCl:Eu laser window material has been undertaken using optical absorption and ionic conductivity. Ionic conductivity was determined using an A.C. method with a Wayne-Kerr bridge on 5 samples each taken from four different regions containing Eu impurity contents between 30 and 60 ppm.  $\text{Eu}^{++}$ -ion concentrations were determined from the position of the "knee" in the conductivity plots. Optical absorption measurements were undertaken using a Cary 14 spectrometer at room temperature using samples from the same four regions of the original crystal. The optical absorption coefficients,  $\alpha$ , were determined at 343 and 243 nm and compared with the  $\text{Eu}^{++}$  contents determined using ionic conductivity. The results for the 243 nm band indicate a linear relationship between these two measurements such that

$$\text{Mole \% Eu}^{++} = 4.3 \times 10^{-4} \alpha.$$

For the 343 nm band, the proportionality constant is  $4.5 \times 10^{-4}$ .

This result disagrees with other work using different Eu-ion analysis techniques. This may indicate the presence of additional Eu in some of the crystals, present in a state of agglomeration, which would not be measured using ionic conduction.

Key words: Eu impurity, ionic conductivity, KCl, laser window materials, optical absorption.

## 1. INTRODUCTION

Recent advances in infrared laser technology have demanded the development of a suitable window material for the high powered  $\text{CO}_2$  gas laser system. The window materials under consideration are primarily alkali halides, with the most promising of these being NaCl, KBr, NaBr and KCl [1].<sup>1</sup> These alkali halides are preferred in that they have very low optical absorption coefficients over a wide portion of the infrared spectrum. However they do have the drawback that in their single crystal state they are quite weak. Therefore in order to use these alkali halides for window materials it is important to increase their strength without decreasing their transparency. Some of the strengthening methods being investigated are recrystallization, alloying and radiation hardening [1]. In KCl, one of the main strengthening methods used involves alloying with europium (Eu).

In order for the europium-doped KCl (KCl:Eu) material to be used in a laser window system, either in single crystalline or polycrystalline form, it is important to characterize its lattice defect state and to relate the lattice defect structure to the optical properties of the material. This characterization should include the determination of the Eu impurity distribution throughout the crystal, the nature of the charge and state of the Eu impurity content. These crystal characterization goals are the basis of this present work in KCl:Eu single crystals.

## 2. BACKGROUND

Various studies in KCl:Eu have indicated the presence of  $\text{Eu}^+$ ,  $\text{Eu}^{++}$ , and  $\text{Eu}^{+3}$  ions in this material. The predominant ion present at room temperature appears to be  $\text{Eu}^{++}$  present in the form of  $\text{Eu}^{++}$ -vacancy dipoles [2-5].

The  $\text{Eu}^{++}$  ion has two characteristic ultraviolet absorption bands that are due to electronic transitions from the  $4f^7$  ground state to the  $e_g$  and  $t_{2g}$  components of the  $4f^6 5d^1$  configuration, with the former being at higher energy [6]. These bands occur at 243 nm and at 330 nm. A typical room temperature absorption spectrum of the KCl:Eu<sup>++</sup> is shown in Fig. 1, where the more intense curve (H) is from the heel section and the lower curve (C) is from the cone section Harshaw KCl:Eu crystal KC.01ECH97. The 3300 Å band consists of a staircase structure that can be partially resolved at room temperature; at low temperatures it is composed of peaks at 3290, 3430 and 3640 Å [7]. The 2400 Å band

---

\*Work sponsored in part by Air Force Office of Scientific Research under grant AFOSR-76-2977.

1. Figures in brackets indicate literature references at the end of this paper.

can only be resolved at low temperatures; at 77°K it consists of five individual peaks at 2340, 2400, 2440, 2510 and 2580 Å [7]. All of the samples from our KCl:Eu crystal showed the blue luminescent color characteristic of  $\text{Eu}^{++}$  [6].

The absorption spectrum of trivalent Eu ions has been observed only in europium salts [8] and in  $\text{LaCl}_3:\text{Eu}^{+++}$  [9]. The principal absorption lines that are of interest are at 5790, 5260, 4650 and 3960 Å. Of these, the absorption at 4650 Å has been reported as being about twice as intense as the others, while the presence of the absorption of 5790 Å seems questionable. Stoebe and Spry [10] made attempts to observe the  $\text{Eu}^{+++}$  absorption bands 5790, 5260, 4650 and 3960 Å in as-received KCl:Eu crystals by annealing the crystals at 650°C for 4 hours and then rapidly cooling them to room temperature (cooling accomplished in about 30 sec.). Honeywell Corporation development work [1] had indicated that KCl:Eu becomes brittle after annealing at 650°C in air; Honeywell speculated that this was caused by the oxidation of  $\text{Eu}^{++}$  to  $\text{Eu}^{+++}$ . However, no  $\text{Eu}^{+++}$  absorption bands were observed by Stoebe and Spry [10] and any change in the  $\text{Eu}^{++}$  content (243 nm peak) was small and virtually undetectable. These observations suggest that the concentration of  $\text{Eu}^{+++}$  as compared to the total Eu concentration is negligible.

The optical absorption bands of the  $\text{Eu}^{++}$  (243 nm and 330 nm), if calibrated, can allow for a non-destructive determination of the  $\text{Eu}^{++}$  content. Stoebe and Spry [10] calibrated the peak absorption coefficient of the 243 nm band against the Eu concentration as determined by the Honeywell polarographic analysis [11]. The 243 nm band was chosen rather than the 330 nm band, since from fig. 1, the 243 nm band has less structure at room temperature. A linear relationship was obtained as follows:

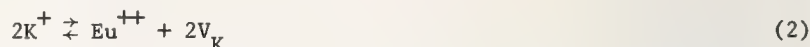
$$\text{mole \% Eu} = 4.2 \times 10^{-4} \alpha \quad (1)$$

where  $\alpha$  is the peak absorption coefficient of the 243 nm band in  $\text{cm}^{-1}$  at room temperature. The relative comparison of optical absorption results and polarographic analysis using eq. (1) is shown in fig. 2 [10].

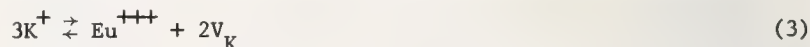
Using peak absorption coefficients and polarographic data, Stoebe and Spry [10] were able to determine the Eu impurity distribution in the edge, heel and cone regions of the KCl:Eu crystal KC.01ECH97. They found that the  $\text{Eu}^{++}$  content through the crystal generally followed the expected variations for an impurity with a distribution coefficient of less than one, except for the rise in concentration near the surface. The initial Eu content in the melt was 100 mole ppm; this decreased to indicated concentrations in the crystal on the order of 30 mole ppm near the cone and 60 mole ppm near the heel, as shown in fig. 2. The relative intensities of the absorptions in fig. 1 also indicate the variation of  $\text{Eu}^{++}$  content from heel (H) to cone (C).

Ionic conductivity is another technique that may be used to investigate lattice defect configurations and divalent (or trivalent) ion concentrations. Ionic conductivity data can thus provide another calibration check on the  $\text{Eu}^{++}$  content.

A simple theory of ionic conductivity, which is adequate for most of our work, has been well summarized by Lidiard [12] and Süptitz and Tetlow [13]. The main point is that the variation of the concentration of free cation vacancies as a function of temperature for doped crystals enables the calculation of the impurity content. Of the three possible species of the Eu-ion present in KCl:Eu, only the  $\text{Eu}^{++}$  and the  $\text{Eu}^{+++}$  can be detected by ionic conductivity, since only these two ion valences increase the concentration of free cation vacancies. If  $\text{Eu}^+$  is introduced into the KCl lattice to replace  $\text{K}^+$ , no extra cation vacancy is needed to maintain charge neutrality and hence  $\text{Eu}^+$  cannot be detected by ionic conductivity. However, if  $\text{Eu}^{++}$  is introduced into the KCl lattice to replace  $\text{K}^+$  an extra cation vacancy is also created to maintain charge neutrality, according to the charge balance equation,



where  $\text{V}_\text{K}$  indicates a cation vacancy. This extra cation vacancy can contribute to ionic conductivity and allows detection of  $\text{Eu}^{++}$  ions. If  $\text{Eu}^{+++}$  is introduced into the KCl to replace  $\text{K}^+$ , 2 extra cation vacancies are also created to maintain charge neutrality, according to the charge balance equation,



Hence these extra cation vacancies can also contribute to ionic conductivity and allow detection of the  $\text{Eu}^{+++}$  ion.

Ionic conductivity is usually plotted as  $\ln \sigma T$  ( $\text{ohm}^{-1}\text{cm}^{-1}\text{K}$ ) versus  $1/T$  ( $\text{K}^{-1}$ ). For our purpose, only regions I and II of the conductivity plot need be considered. In region I the concentration of cation vacancies is governed only by the thermal statistics of the lattice and is independent of the impurity doping level. The slope of the  $\ln \sigma T$  vs.  $1/T$  plot in region I is  $(H_s/2 + H_m)$ , where  $H_s$  is the Schottky energy of formation, and  $H_m$  is the energy of motion of the cation vacancy. Region II is known as the extrinsic region and is where the concentration of cation vacancies is equal to the concentration of divalent impurities; the slope in this region is  $H_m$ . The temperature at which regions I and II



intersect is known as the knee temperature and at this point the concentration of intrinsic cation vacancies equals the concentration of extrinsic vacancies (concentration of divalent impurities). Thus the determination of the knee temperature and the slopes of regions I and II allows the calculation of the concentration of divalent impurities present.

### 3. EXPERIMENTAL

The KCl:Eu crystals used in this study were from KCl:Eu ingot KC.01ECH97 [10], a 17-inch diameter by 7-inch high single crystal grown by the Harshaw Chemical Company for the AFML-monitored laser window development program. The sectioning plan for this ingot is shown in fig. 3. The KCl:Eu samples were taken from locations shown in more detail in fig. 2; samples from the heel (last part to solidify) are shown in fig. 2 [10], as H2 and H4, while samples from the cone section (first part to solidify) are shown in fig. 2 as C2 and C4. Also available were several Harshaw-grown undoped KCl single crystals.

The techniques used to investigate the crystals consisted of optical absorption, electron paramagnetic resonance and ionic conductivity. Polarographic analysis of the Eu-ion content was obtained by Honeywell, Inc. [11] on samples immediately adjacent to those used for the current work. The polarographic analysis results for heel and cone scans along with the earlier optical absorption determinations of Eu-ion content have been shown in fig. 2.

The samples used for optical absorption measurements were cleaved to thicknesses 5 mm and 1 mm. Samples were used in the unpolished condition; however, care was taken so that the part of the crystal in the beam contained no cleavage steps. Some of the crystals that were used in the unpolished condition were also mechanically polished to an optical finish using 0.6  $\mu$ m alumina polishing powder and compared to measurements made in the unpolished condition; no differences were observed. All optical absorption measurements were made on a Cary-14 spectrophotometer at room temperature and the optical absorption coefficient was calculated from the optical density and the thickness of the crystal. The effect of reflectance in KCl is approximately 3.5% and therefore can be neglected; thus,  $\alpha$  can be calculated from the peak absorption coefficient [14] using the relation:

$$\alpha = \frac{2.303(O.D.)}{t} \quad (4)$$

Here  $t$  is the sample thickness and O.D. represents the optical density of the sample. Optical absorption measurements were also made on a few of the Harshaw-grown undoped KCl single crystals for comparative purposes.

Ionic conductivity measurements were made using an A.C. method at 1592 Hz using a Wayne-Kerr Universal Bridge which measured both conductance and capacitance of the sample. Conductivity values were determined by multiplying the measured conductance by  $L/A$ , where  $L$  is the length of the sample and  $A$  is the cross sectional area of the sample. The crystal was coated with a colloidal graphite and then mounted between two nickel electrodes in the conductivity jig [15]. The conductivity jig was placed inside a horizontal Vycor tube which was heated by a Marshall furnace. The furnace temperature of the crystal was measured by means of a chromel-alumel thermocouple placed next to the crystal and connected to a digital volt meter. Before making the conductivity measurements, the crystals were annealed for 1 hr. at 420°C to allow for sample equilibrium. During the annealing treatment and the conductivity measurements the furnace was continually flushed with dry helium gas. The conductivity measurements were made in equilibrium on heating from 420°C to 750°C at 25°C intervals.

### 4. RESULTS AND DISCUSSION

Ionic conductivity plots of the KCl:Eu crystals from samples H2, H4, C2 and C4 are shown in fig. 4 where the intrinsic slope is determined from that of the Harshaw crystals. The slope in region II,  $H_m$ , is 0.81eV from crystal C2 [16]. This value seems high compared to some recent work [17-19] but agrees fairly well with earlier studies [20-22]. From the slope of region I and this value of  $H_m$ ,  $H_s$  was determined as 2.56 eV. This agrees well with recent work. Using this value and the knee temperatures, the  $\text{Eu}^{++}$  content of these KCl:Eu crystals was then determined.

Assignment of a  $\text{Eu}^{++}$  content from the above is valid only if no  $\text{Eu}^{+3}$  contributes to the ionic conductivity data. Again the optical absorption bands at 5790, 5260, 4650 and 5960 Å were checked for  $\text{Eu}^{+3}$  absorptions. As with the work of Stoebe and Spry [10], none were observed.

The optical absorption coefficients at room temperature of both the 243 and 330 nm band were calculated for the KCl:Eu crystals H2, H4, C2 and C4. The optical absorption coefficient of the 243 nm band is calibrated against the  $\text{Eu}^{++}$  content determined by ionic conductivity using a least squares analysis, as shown in fig. 5. The result indicates a linear relationship between these two measurements such that:

$$\text{mole \% Eu}^{++} = 4.3 \times 10^{-4} \alpha \quad (5)$$



This result agrees well with the work of Stoebe and Spry [10] and is probably more accurate than their value. This result may also be compared to the polarographic analysis of the adjacent samples as in fig. 6. The comparison agrees to within 10% in three of the locations but varies 25% at the fourth (Sample H4). The reasons for this discrepancy are not clear.

When the optical absorption coefficient of the 330 nm band is calibrated against  $\text{Eu}^{++}$  content determined by ionic conductivity, a linear relationship exists as follows:

$$\text{mole \% Eu}^{++} = 4.5 \times 10^{-4} \alpha \quad (6)$$

This compares well with the calibration of the 243 nm band given in eq. (5).

The result in eq. (5) may also compare to the results of Sill et al. [23], who used atomic absorption spectroscopy to measure the  $\text{Eu}^{++}$  impurity content. Compared to the optical absorption coefficient of the 243 nm band, Sill et al. obtained a proportionality factor that was 8 times higher than that in eq. (5). This may indicate the presence of additional Eu in their crystals, present either as  $\text{Eu}^+$  or in a state of agglomeration, neither of which would be measured using ionic conductivity. However, this discrepancy is not seen in the polarographic analysis of our samples, noted above.

## 5. CONCLUSIONS

The 243 and 330 nm absorption bands in  $\text{KCl:Eu}$ , when calibrated by polarographic analysis and ionic conductivity data, can yield a non-destructive determination of  $\text{Eu}^{++}$  content in  $\text{KCl:Eu}$  laser window materials. The concentration of  $\text{Eu}^{+3}$  is negligible when compared to the total Eu concentration in the  $\text{KCl:Eu}$  samples studied. The results also indicate that at room temperature the  $\text{Eu}^{++}$  is in the form of  $\text{Eu}^{++}$ -vacancy dipoles.

The discrepancy between the Eu content determined by polarographic analysis, by atomic absorption, and by ionic conductivity may be due to cation vacancies that are trapped by some type of complex that would not allow detection by ionic conductivity, or by the presence of some of the Eu in the form of  $\text{Eu}^+$  ions. These possibilities are being investigated further.

## 6. ACKNOWLEDGEMENTS

The authors wish to thank Dr. Robert Spry of the Air Force Materials Laboratory for his input in formulating this program.

## 7. REFERENCES

- |  |  |
|--|--|
| [1] Harrison, W. B. Halide Material Processing for High Power Infrared Laser Windows, Final Technical Report AFML-TR-75-104, Honeywell, Inc., July 1975. | [10] Stoebe, T. G., Spry, R. J., and Lewis, J. F., Optical Properties of Europium-doped Potassium Chloride Laser Window Materials, Technical Report AFML-TR-76-20, April 1976. |
| [2] Rohrig, R., Phys. Lett. <u>16</u> , 20 (1965).   | [11] Harrison, W. B., Alkali Halide Materials for High Power Infrared Laser Windows, Final Technical Report AFML-TR-76-106, Honeywell Inc., June 1976.                         |
| [3] Nair, P. G., Lingam, K. V., and Venkataraman, R., J. Phys. Chem. Solids <u>29</u> , 2183 (1968).   | [12] Lidiard, A. B., Handbuch der Physik, edited by S. Flosse (Springer-Verlag, Berlin 1957) Vol. 20, p. 246.  |
| [4] Aguliar, G., Munoz, E., Murrieta, H., Boatner, L. A., and Reynolds, R. W., J. Chem. Phys. <u>60</u> , 4665 (1975).                                   | [13] Süptitz, P., and Tetlow, S., Phys. Stat. Sol., <u>23</u> , 9 (1967).  |
| [5] Maevskii, V. M., Kalabokhova, E. N., Zhukov, A. N., and Krulilovskii, B. N., Sov. Phys.-Solid State <u>17</u> , 150 (1975).                          | [14] Townsend, P. D., and Kelly, J. C., <u>Colour Centers and Imperfections in Insulators and Semiconductors</u> , Sussex University Press, London (1973).                     |
| [6] Reisfield, R., and Glasner, A., J. Opt. Soc. Amer. <u>54</u> , 331 (1964).   | [15] Vora, H., Ph.D. Thesis, University of Washington (1974).  |
| [7] Chowdri, B. V. R., and Itoh, N., Phys. Stat. Sol. (b) <u>46</u> , 549 (1971).  | [16] Stoebe, T. G., and Pratt, P. L., Proc. British Ceramic Soc. <u>9</u> , 181 (1967).  |
| [8] Kim, B. F., and Moos, H. W., Phys. Rev. <u>161</u> , 869 (1967).   |  |
| [9] DeShazer, L. G., and Dieke, G. H., J. Chem. Phys. <u>38</u> , 2190 (1963).   |  |

- [17] Beaumont, J., and Jacobs, P., J. Chem. Phys. 45, 149 (1966).
- [18] Chandra, S., and Rolfe, J., Can. J. Phys. 48, 412 (1970).
- [19] Fuller, R., and Marquardt, C., Phys. Rev. 176, 1036 (1968).
- [20] Beniere, M., Beniere, F., and Chemla, M., J. Chem. Phys. 67, 1312 (1970).
- [21] Dreyfus, R., and Nowick, A., J. Appl. Phys. 33, 473 (1962).
- [22] Allnatt, A., and Jacobs, P., Trans. Faraday Soc. 58, 116 (1962).
- [23] Sill, E. L., Martin, J. J., and Al. Shaieb, Z., Phys. Stat. Sol. (A) 39, K 131 (1977).
- [24] Pawdey, S. D., J. Chem. Phys. 47, 3094 (1967).

## 8. FIGURES

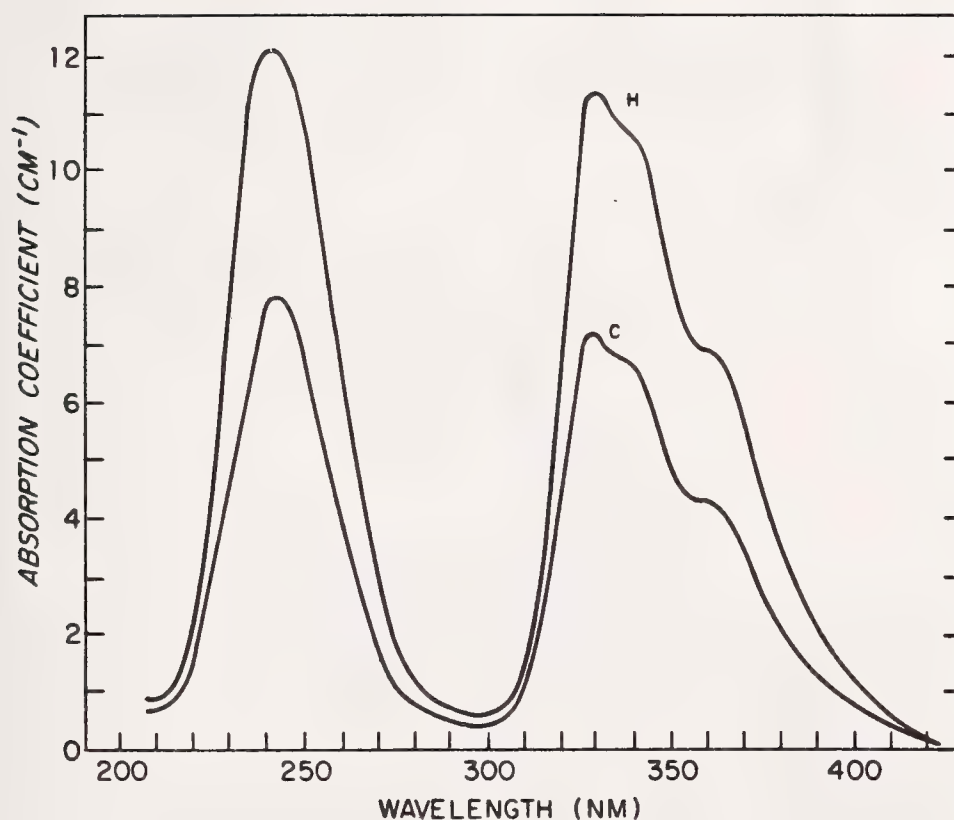


Figure 1. Optical absorption spectrum of  $\text{KCl:Eu}^{++}$  at room temperature. Spectrum H is from the heel section and spectrum C is from the cone section of sample KC.01ECH97.

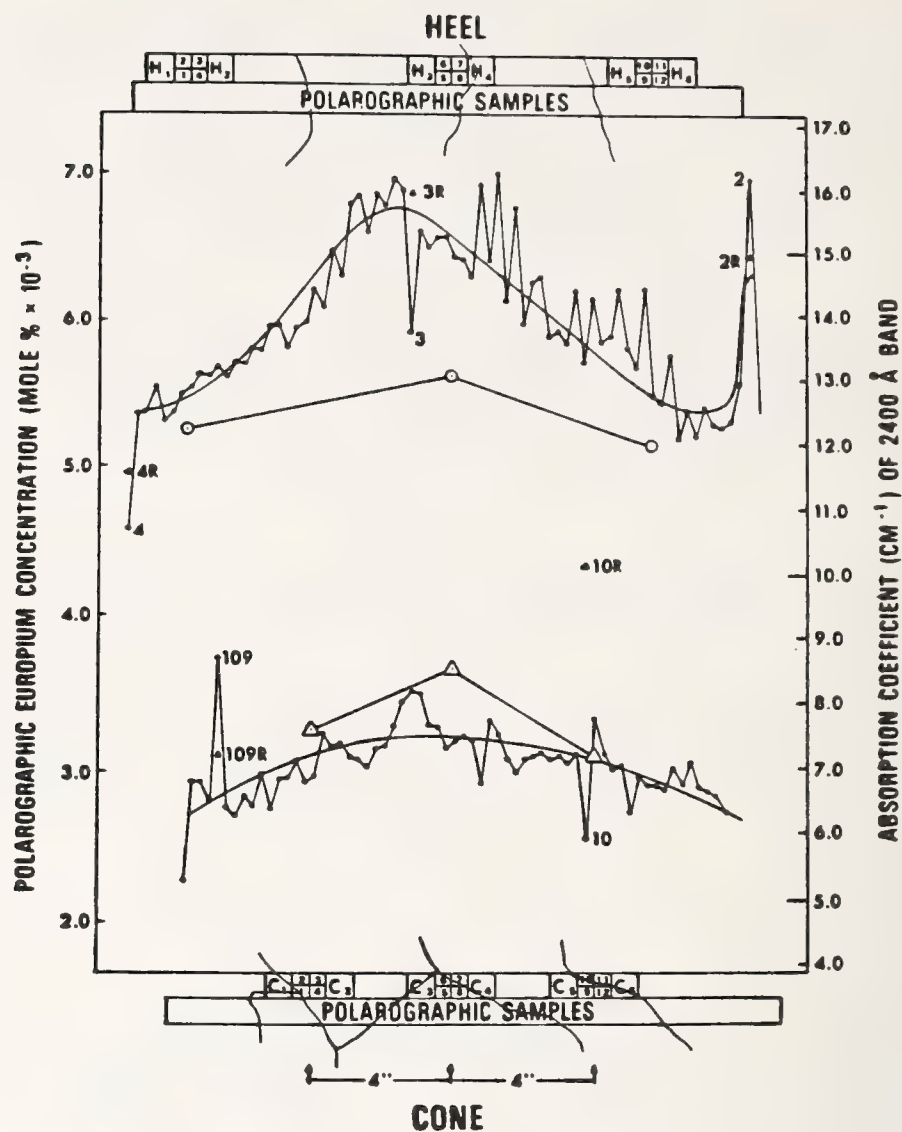


Figure 2. Concentration vs. crystal location determined using absorption and polarographic results, from ref. 10. Schematic sections at heel and cone show sample locations and grain boundaries (see also fig. 3).



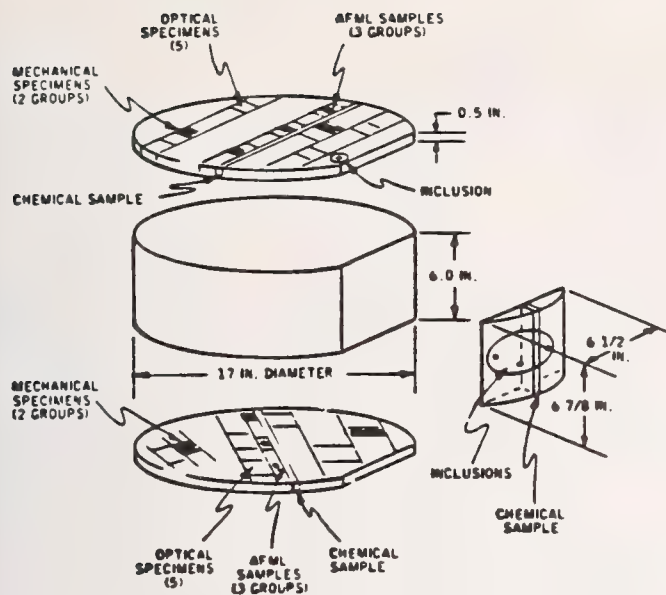


Figure 3. Sectioning plan for Harshaw-grown ingot KC.01ECH97. See fig. 2 for specific sample locations in cone and heel sections.

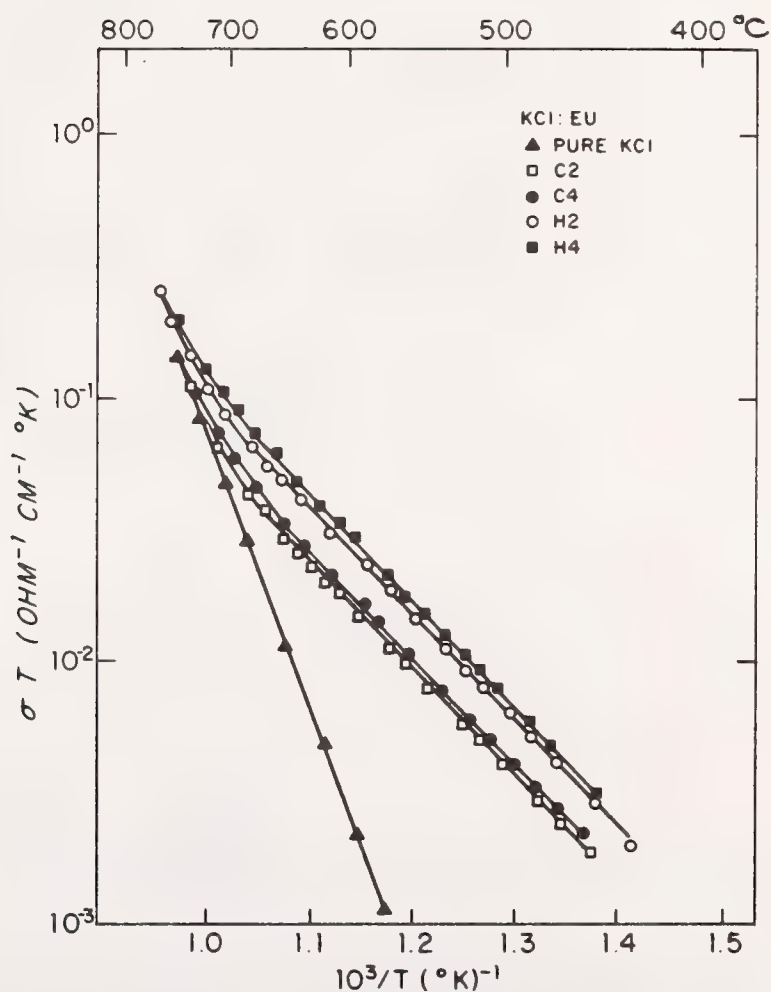


Figure 4. Ionic conductivity plots of pure KCl and KCl:Eu crystals from the heel and cone sections of Harshaw-grown ingot KC.01ECH97. Sample numbers from fig. 2.

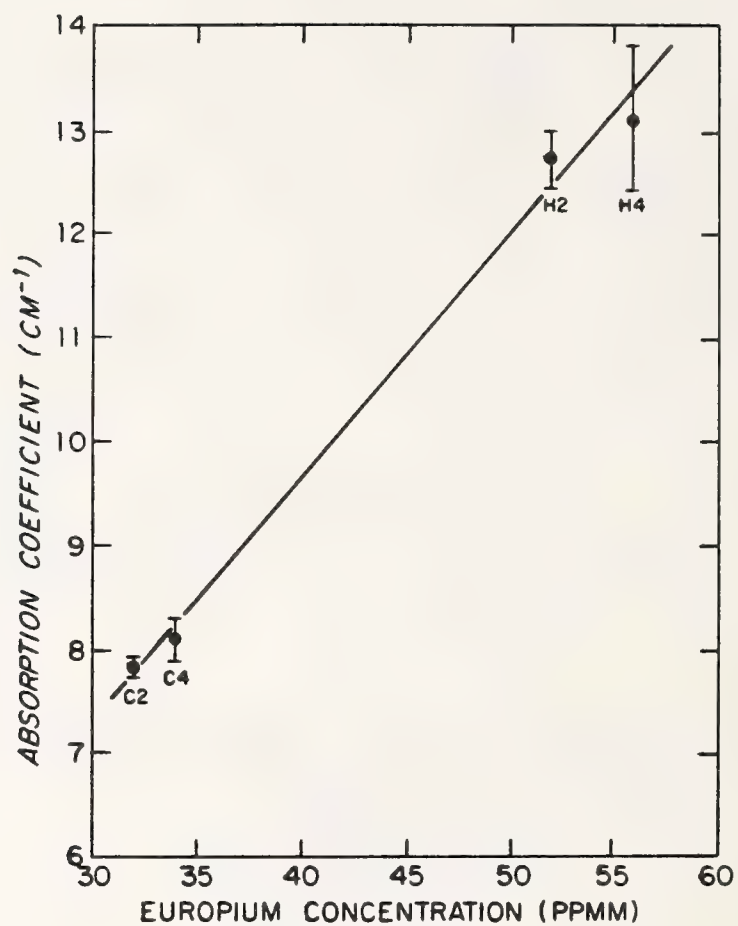


Figure 5. Absorption coefficient of the 243 nm band versus  $\text{Eu}^{++}$  concentration, as determined by ionic conductivity. The slope, determined by least squares curve fitting, is 0.234; the slope inverse gives proportionality constant in eq. (5).

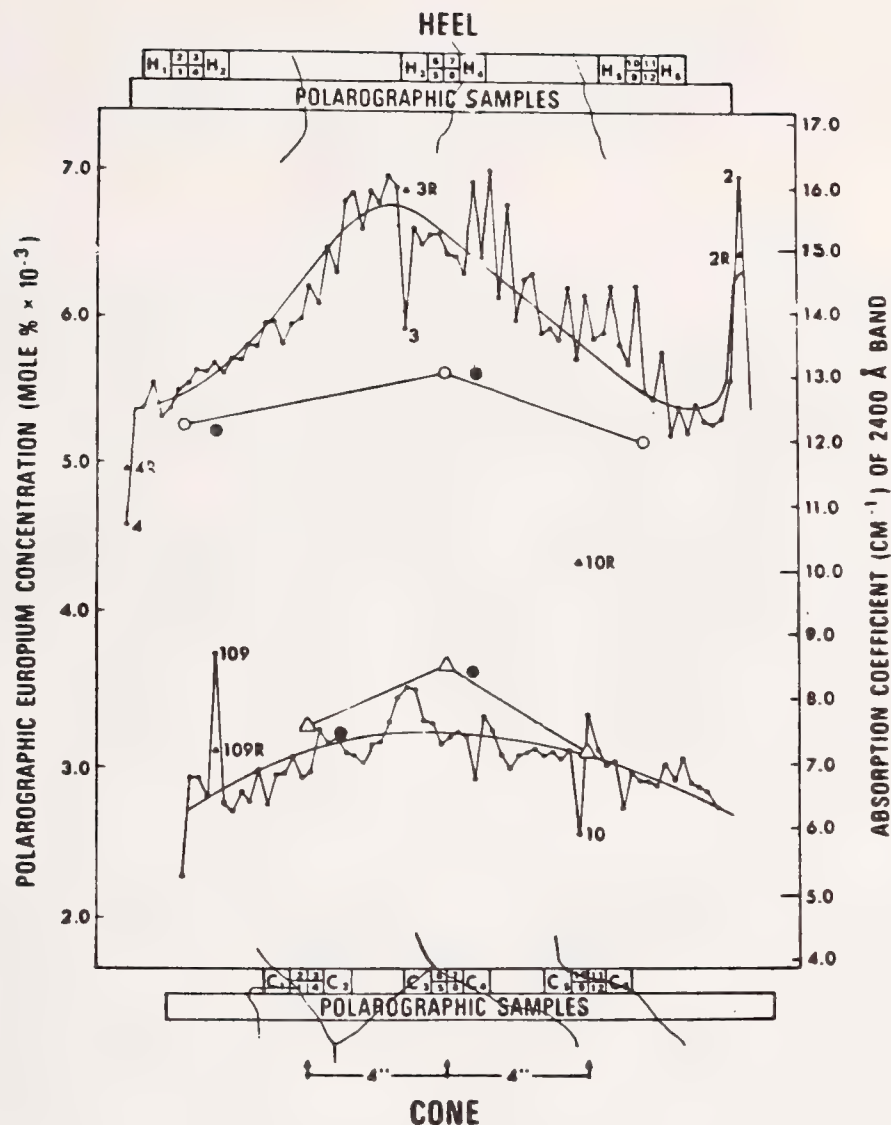


Figure 6. Same as fig. 1 with addition of points •, which represent  $\text{Eu}^{++}$  concentration determined by ionic conductivity (fig. 5) compared to polarographic  $\text{Eu}$ -ion content.

#### COMMENTS ON PAPER BY WOLFENSTINE AND STOEBE

The principal point brought out in the discussion was that the determination of the charge state of the europium ion by absorption measurements is very difficult. The oscillator strength of the doubly ionized europium is much greater than that for the trivalent ion. A much more sensitive method of detecting  $\text{Eu}^{3+}$  would be to look for fluorescence of the ion, because the fluorescence spectra of the divalent and trivalent states of the ion are well separated. The speaker responded that this experiment had not been carried out.



# DETECTION OF OXYGEN IN CALCIUM FLUORIDE LASER WINDOW MATERIALS BY XPS

T.N. Wittberg, J.R. Hoenigman, and W.E. Moddeman  
University of Dayton Research Institute, Dayton, Ohio 45469

and

C.L. Strecker  
Air Force Materials Laboratory, Wright-Patterson AFB, Ohio 45433

The three most important criteria used in evaluating materials for laser window applications are high mechanical strength, high optical transmission, and the existence of applicable antireflective coating systems. In the case of calcium and strontium fluoride, oxygen impurities can play a strong role in determining these characteristics.

XPS data are presented on  $\text{CaF}_2$  substrates, ZnSe coatings, and ZnSe/ $\text{CaF}_2$  interfaces. XPS data on  $\text{CaF}_2$  show the presence of oxygen on surfaces that have been argon ion sputtered and on surfaces that have been cleaved in an inert atmosphere. Oxygen has also been noted at the ZnSe/ $\text{CaF}_2$  interface. These data can be related to previous results on the optical transmission of the coated laser windows.

Key words: Adsorption, atmospheric contaminants, calcium fluoride coatings, laser window, oxygen contaminants, x-ray photoelectron spectroscopy (XPS), zinc selenide.

## 1. Introduction

A typical laser window consists of a substrate, such as  $\text{CaF}_2$ , which is given an antireflective coating. The boundary region between the coating and the substrate is referred to as the coating/substrate interface. Theoretical investigations have shown that two molecular layers of adsorbed water at the coating/substrate interface would give rise to an optical adsorption of  $10^{-4}$  which is unacceptable for transmission applications at  $10.6 \mu\text{m}$  [1]. Also, the chemical composition of the substrate's surface influences the adhesion of laser window coatings. To date, little experimental information is available as to the role that surface-adsorbed impurities at the interface play in adhesion. In this paper, data on changes in elemental surface composition are presented on  $\text{CaF}_2$  samples with different surface preparations. The preparations include: (1) polishing, (2) exposing to high humidity, (3) sputtering to a depth of approximately 30 nanometers, and (4) cleaving in different environments.

In addition, two ZnSe coated  $\text{CaF}_2$  specimens were analyzed for elemental variations in the coating and at the interface. The technique used to analyze these materials was X-ray Photoelectron Spectroscopy (XPS)\*. The technique is well documented for its analytical capabilities [2,3].

## 2. Experimental Procedures

High purity polycrystalline  $\text{CaF}_2$  materials were obtained from the Harshaw Chemical Corporation. These samples were used in the analysis unless otherwise indicated. Emission spectroscopy was used to analyze for bulk impurities. Samples for XPS analysis were cut with a diamond bladed saw without the use of a lubricant. The samples were cut into rectangular specimens, approximately  $10 \times 5 \times 1 \text{ mm}$ . The surface of each sample was sequentially polished with 20, 9, and  $1 \mu\text{m}$  alumina polishing compounds. Each polished specimen was then washed with detergent (Alconox), which was followed by three distilled water rinses and three isopropyl alcohol rinses. Following the washing and rinsings, the samples were cleaned with vapors. Each sample was then analyzed with XPS.

Two of the polished specimens were removed from the XPS analyzer and exposed to a high humidity environment. This was accomplished by holding each specimen above boiling water for approximately one minute. These samples were then re-analyzed with XPS. Approximately thirty nanometers of the surface of one sample were removed by argon ion sputtering and the sample was re-analyzed by XPS. The ion sputtering and depth profiling were accomplished with a Varian 3 keV variable potential ion gun.

The two ZnSe coated  $\text{CaF}_2$  specimens were prepared by electron beam deposition [4]. The thickness of each film was determined by a Sloan automatic deposition controller, model OMNI, which uses a quartz crystal frequency oscillator for thickness monitoring. The thickness of each film was 50 nanometers [4]. One coating was deposited at 0.1 nanometers/second and the other at 2 nanometers/second. Both of these coatings survived a water immersion test [5].

\* This acronym is often used interchangeably with Electron Spectroscopy for Chemical Analysis (ESCA).

The XPS spectrometer is a modified AEI ES-100 instrument. This spectrometer with the accompanying argon ion sputtering capability has been discussed in more detail elsewhere [6]. The system is pumped by two 250ℓ/sec diffusion pumps and a 260ℓ/sec turbomolecular pump. Vacuum achievable in the sample chamber is  $10^{-8}$  torr. The chamber is bakeable to  $>150^{\circ}\text{C}$ . Reactive vapors can be minimized in the system by baking, by a Ti sublimation pump, and by two liquid  $\text{N}_2$  cryostations. The anode used for all XPS measurements was magnesium.

### 3. Results and Discussion

#### 3.1. Calcium Fluoride Substrate

The first part of this study involved the examination of the calcium fluoride substrate itself. The second part of the study concerned the zinc selenide coated calcium fluoride materials. Figure 1 illustrates the overall XPS spectra of a polycrystalline  $\text{CaF}_2$  sample polished and cleaned (1a), following exposure to high humidity (1b), and following argon ion sputtering, (1c). These data are summarized in Table I. The data represented in Table I are given in atomic percent [7]. The scan in Figure 1a shows that the surface of the  $\text{CaF}_2$  is contaminated mainly with carbon and oxygen, and with smaller amounts of other elements (Na, Cl, Si, S, and P). Upon exposure to high humidity, (Figure 1b), the carbon and oxygen signals were found to increase by approximately a factor of two, relative to the calcium or fluorine. These data, for both the polished and exposed samples, suggest that  $\text{CaF}_2$  has a high affinity for components of the atmosphere. Possible atmospheric sources for oxygen contamination are  $\text{O}_2$  and water. For carbon, possible sources include atmospheric dust and  $\text{CO}_2$ . The origin of the adsorbate species has not been identified. From the results of Edelhock and Taylor [8] the increased oxygen contamination is most probably chemisorbed water and not atmospheric molecular oxygen.

The data following sputtering to a depth of  $<30$  nm are also included in Table I. The decrease in the carbon and oxygen signals relative to the calcium and fluorine signals indicate oxygen and carbon are surface contaminants adsorbed from the atmosphere.

In order to examine these surface contaminants more closely, two experimental approaches were taken. One involved a detailed, in-depth profile analysis of  $\text{CaF}_2$ , and the second involved the comparison of cleaved surfaces\*. Some of the samples used in these analyses had been annealed previously to approximately  $1000^{\circ}\text{C}$ .

The XPS data from the in-depth profiling for annealed and non-annealed samples are given in Table II. Only four elements were monitored during sputtering. These in-depth profiles illustrate that oxygen is not only present on the surface of  $\text{CaF}_2$ , but is a contaminant below the surface. Carbon is obviously a surface contaminant that is removed to less than one atomic percent, by sputtering.

A similar conclusion concerning the presence of oxygen in  $\text{CaF}_2$  can be derived from the comparison of XPS data taken on cleaved surfaces with those of outside surfaces<sup>2</sup>. These data are given in Table III. The cleaving was performed in air and in dry nitrogen. All cleaved surfaces of  $\text{CaF}_2$  were found to contain approximately six atomic percent oxygen. The level of oxygen was found to be approximately a factor of two higher on the outside surface.

J. Estel et al [9] examined water adsorption on cleaved samples of alkali halides with Secondary Ion Mass Spectroscopy (SIMS). He examined the (100) planes of  $\text{LiF}$ ,  $\text{NaF}$ , and  $\text{NaCl}$  under a variety of conditions: air and vacuum cleaved; with and without annealing; and with and without exposure to water at various crystal temperatures. The main results were that cleaved crystal surfaces were found to be free of water and hydroxide layers even in the submonolayer region under ultra-high vacuum conditions. They found that water vapor would only adsorb on cooled cleaved samples, thus concluding that water physically adsorbs to  $\text{LiF}$ ,  $\text{NaF}$  and  $\text{NaCl}$  and the water is easily removed by evacuation.

Upon examining Estel's spectra more closely, one notes the presence of  $\text{O}^-$  and  $\text{OH}^-$  in the negative SIMS spectra of a cleaved surface of  $\text{LiF}$ . These  $\text{O}^-$  and  $\text{OH}^-$  signal intensities were found to be  $\sim 1/100$  of the  $\text{F}^-$  intensity and the signals roughly decreased by only a factor of two upon in-depth profiling. Estel rationalized from the low oxygen signals and the profiling information that the surface of  $\text{LiF}$  did not contain large concentrations of  $\text{O}^-$  and  $\text{OH}^-$ . He attributed these  $\text{O}^-$  and  $\text{OH}^-$  signals as resulting partly from oxygen bulk impurities.

Estel's SIMS results, showing the presence of oxygen in alkali halide materials, agree qualitatively with the XPS results on  $\text{CaF}_2$ . Since the quantitative capabilities of SIMS are questionable [10], signal intensity comparisons made by Estel may have little correlation to actual sample composition.

---

\* Preferential cleaving in  $\text{CaF}_2$  occurs along the (III) face.



Table 1  
Qualitative and Semi-Quantitative ESCA Results On  
Nonexposed, Exposed and Ion Sputtered Nonannealed Calcium Fluoride\*

Element	Level	Binding Energy (eV)	Atom Percent					
			Surface Scan Before Exposure	Element Ca	After Exposure to High Humidity	Element Ca	After Sputtering	Element
Fluorine	1s	688	4.7	0.7	1.8	0.6	25.3	0.8
Oxygen	1s	533	7.1	1.1	7.1	2.4	12.7	0.4
Calcium	2p	348	6.4	1.0	3.0	1.0	32.9	1.0
Carbon	1s	285	75.6	11.8	85.5	28.5	2.5	<0.1

\*Chlorine, sulfur, phosphorus, sodium, and silicon were found present in amounts on the surface of these materials.

Table 2  
In-Depth Profile Analysis of O, C, F, and Ca In Annealed And  
Non-Annealed CaF<sub>2</sub> Polycrystalline Laser Window Substrate Materials  
(Data Given in Atomic %)\*

Sputtering Time (Min)**	Annealed								Non-Annealed							
	F	O	Ca	C	F/Ca	O/Ca	C/Ca		F	O	Ca	C	F/Ca	O/Ca	C/Ca	
Surface	15	15	10	60	1.5	1.5	6.0		3	30	2	65	1.2	1.2	32.	
0.5	56	9	23	11	2.4	0.40	0.50		48	19	18	15	2.7	1.0	0.8	
1	57	10	26	7	2.2	0.38	0.27		54	15	22	7	2.4	1.70	0.32	
2	59	12	24	5	2.5	0.50	0.21		57	15	23	3	2.5	0.65	0.13	
4	56	13	26	4	2.2	0.50	0.15		58	12	27	3	2.1	0.44	0.11	
8	56	12	28	4	2.0	0.43	0.14		57	13	29	1	2.0	0.45	0.03	
16	58	10	30	2	1.9	0.33	0.07		58	12	30	<1	1.9	0.40	0.03	
32	58	11	29	1	2.0	0.38	0.03		59	12	28	<1	2.1	0.43	0.04	

Table 3  
Qualitative and Semiquantitative ESCA Results on Cleaved Specimens Of  
Single Crystal\*\*And Polycrystalline Calcium Fluoride\*\*\*

Element	Level	Single Crystal				Polycrystalline					
		Cleaved in Air	†	Cleaved in Air Plus Baking at ~100°C	†	Cleaved in Nitrogen Gas	†	"Outside" Surface	†	Cleaved in Air	†
Fluorine	1s	49.4	2.5	39.2	2.3	57.4	2.6	14.4	1.7	44.2	2.2
Oxygen	1s	7.5	0.39	6.0	0.34	6.2	0.28	13.7	1.7	7.9	0.40
Calcium	2p	19.5	1.0	17.3	1.0	22.2	1.0	8.2	1.0	20.0	1.0
Carbon	1s	23.6	1.2	37.5	2.2	14.3	0.64	63.6	7.7	27.9	1.4

\*\* Single crystal from Harshaw Chemical Company

\*\*\* Fusion cast material from Raytheon Company, See, C. L. Strecker, "Analysis for Oxygen in Calcium and Strontium Difluoride Utilizing X-ray Photoelectron Spectroscopy," Air Force Materials Laboratory Report, AFML-TM-LP-77-1, January 1977, Wright-Patterson Air Force Base, Ohio.

† Ratio of elements relative to Ca.

### 3.2 Coatings

The data given in Table IV are the results of in-depth profiling two ZnSe/CaF<sub>2</sub> systems. The data are also plotted in Figure 2. The results show a zinc enrichment at the interface as well as a significant amount of oxygen (on the order of 12 atomic percent) and carbon (on the order of 8 atomic percent) in the first few hundred angstroms of the CaF<sub>2</sub> substrate. The oxygen and carbon at the interface are probably due to atmospheric adsorption by CaF<sub>2</sub> substrate prior to ZnSe PVD deposition.



Johnston, et al [11], measured the absorption of sputtered films of ZnSe on KCl. They found little increase in film absorptance as the thickness of the film was varied from 0.4 to 2 $\mu$ m. They concluded that the origin of the majority of the measured absorption was the interface region. These absorption measurements are consistent with the XPS results on the ZnSe/CaF<sub>2</sub> system which showed significant contamination and apparent stoichiometric deviations at the coating/substrate interface. Ritter [1] has shown that preparation of substrate surfaces can have a marked effect on coating adhesion.

Table 4  
ESCA Intensity Results of In-Depth Elemental Profile  
Analysis On ZnSe Coatings Evaporated On CaF<sub>2</sub>  
(Intensity Given in Atomic Percent)

Sputtering Time	Element					
	Oxygen	Carbon	Zinc	Selenium	Calcium	Fluorine
Data for 0.1 nm/sec.						
Surface	17.2	42.8	19.4	20.6	---	---
30 sec	2.7	19.2	39.9	38.2	---	---
2 min	2.2	10.9	38.6	48.3	---	---
10 min	4.5	4.9	26.7	17.2	12.5	34.2
11 min	13.2	7.1	12.5	7.9	17.6	41.8
12 min	8.2	7.6	9.8	5.0	21.7	47.5
14 min	8.9	7.6	4.4	4.6	23.2	51.3
20 min	13.3	4.5	0.5	<0.4	27.1	54.2
Data for 2 nm/sec						
Surface	7.0	76.0	7.2	9.8	---	---
30 sec	1.6	34.6	45.7	17.9	---	---
1 min	1.2	18.8	50.0	30.0	---	---
2 min	0.9	8.7	58.9	31.5	---	---
4 min	0.6	15.6	53.9	29.9	---	---
6 min	1.8	10.7	46.7	40.8	---	---

#### 4. Conclusions

The XPS data presented here show that there is a significant amount of oxygen present on fresh surfaces which have been formed either by argon ion sputtering or by cleaving in an inert atmosphere. For a sample that has been sputtered to a depth of >6 nanometers, oxygen has been found present at a concentration of ~12 atomic percent. For cleaved polycrystalline CaF<sub>2</sub> specimens the level of oxygen was measured to be ~6 atomic percent. On coated samples in which the coating was removed by sputtering the level of oxygen in the CaF<sub>2</sub> was measured to be >10 atomic percent. In the coating itself the oxygen was measured to be 2  $\pm$  1 atomic percent.

The conclusion that can be drawn from the XPS data on the profiled and cleaved surfaces is that either (1) a fresh surface of CaF<sub>2</sub>, created either by sputtering in a very high vacuum or by cleaving in dry nitrogen, is extremely reactive to very low concentrations of environmental components (such as water), or (2) oxygen is present in the bulk of CaF<sub>2</sub> as an impurity.

#### 5. References

- [1] E. Ritter, *Physics of Thin Films*, 8, 1 (1975).
- [2] K. Siegbahn, C. Nordling, A. Fahlman, R. Nordberg, K. Hamrin, J. Hedman, G. Johansson, T. Bergmark, S. Karlson, I. Lindgren, and B. Lindberg, "ESCA: Atomic, Molecular, and Solid State Structure Studied by Means of Electron Spectroscopy," Almquist and Wiksells Boktrycker: A.B. Uppsala, Sweden, 1967.
- [3] C. D. Wagner, *Anal. Chem.*, 49, 1282, (1977).
- [4] Samples supplied by Major David F. O'Brien, Air Force Materials Laboratory, Wright-Patterson Air Force Base, Ohio to be published as an Air Force Materials Laboratory Technical Report (AFML-TM- ).
- [5] D. A. Walsh, J. A. Detrio, P. J. Larger, and C. E. Hill, "Water Immersion Adhesion Evalua-
- [6] T. N. Wittberg, J. R. Hoenigman, W. E. Moddeman, C. R. Cothorn and M. R. Gullett, "AES and XPS of Silicon Nitride Films of Varying Refractive Indices," accepted in *J. Vac. Sci. and Tech.*
- [7] H. Berthou and C. K. Jorgensen, *Anal. Chem.*, 47 (3), 482 (1975).
- [8] H. Edelhock and H. S. Taylor, *J. Phys. Chem.*, 58, 344 (1954).
- [9] J. Estel, N. Hoinkes, H. Kaarmann, H. Nahr, and W. Wilsch, *Surf. Sci.*, 54, 393 (1976).

- [10] C. A. Anderson, Int. J. Mass Spect. and Ion Physics, 3, 413 (1970).
- [11] G. T. Johnston, D. A. Walsh, R. J. Harris, and J. A. Detrio, University of Dayton Research Institute Semi-annual Progress Report No. 4, Contract No. F33615-74-C-5001, June 1975, Dayton, Ohio.

## 6. Figures

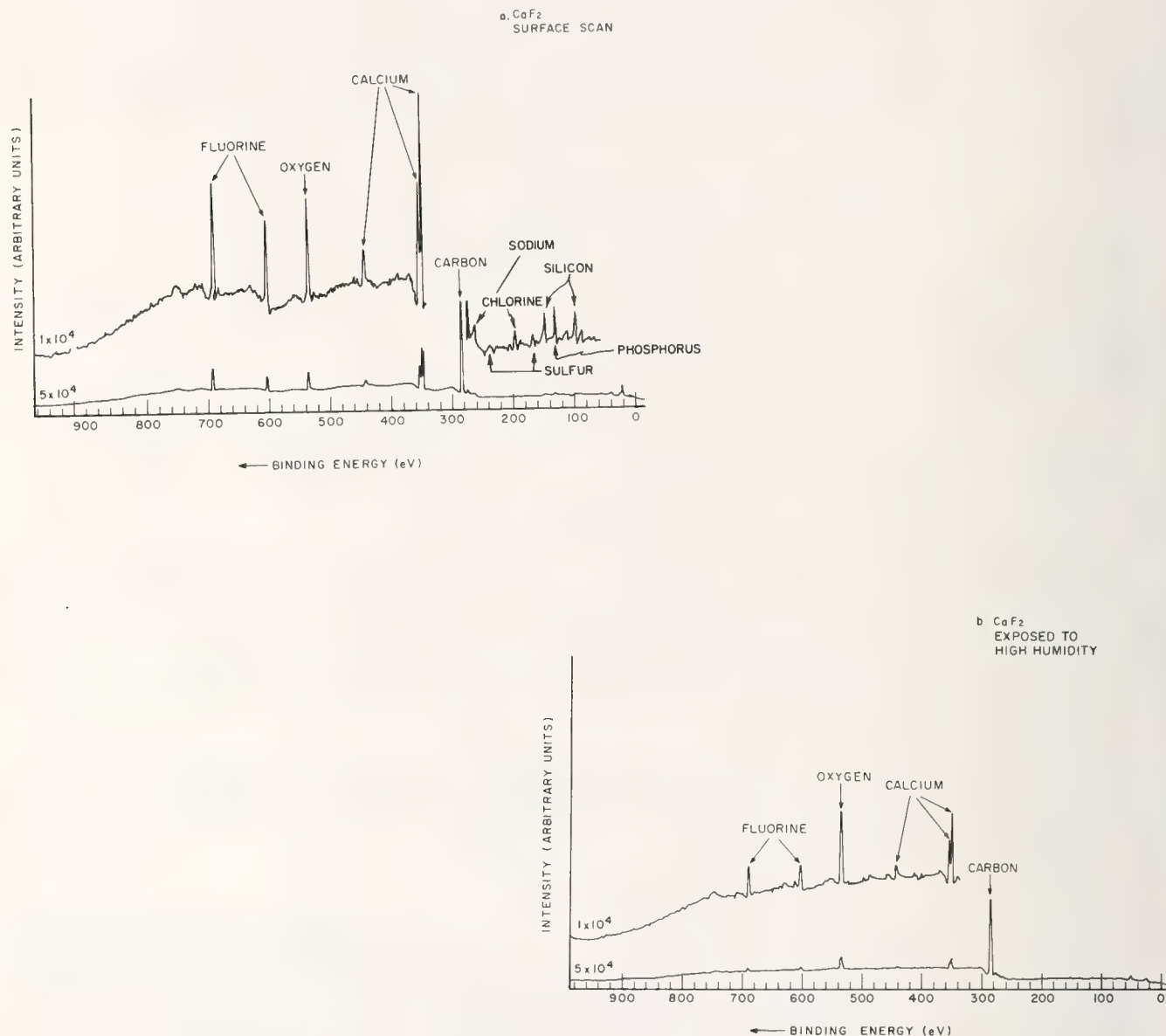


Figure 1. XPS Scans on (a) freshly polished  $\text{CaF}_2$ , (b) exposed to high humidity, and (c) argon ion-sputtered to a depth  $>6$  nanometers. The two observed fluoride peaks can be associated with the F 1s photopeak at  $\sim 690$  eV and with the F Auger peak at  $\sim 600$  eV. The three calcium peaks are due to Ca 2p doublet at  $\sim 345$  eV and Ca 2s at  $\sim 440$  eV. The oxygen and carbon are 1s photoelectrons. The anode used was magnesium.

c.  $\text{CaF}_2$   
AFTER SPUTTERING  $\sim 6\text{ nm}$

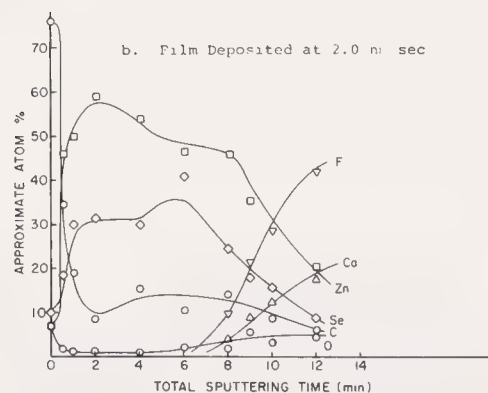
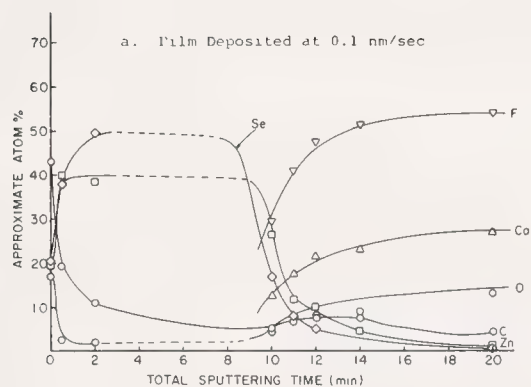
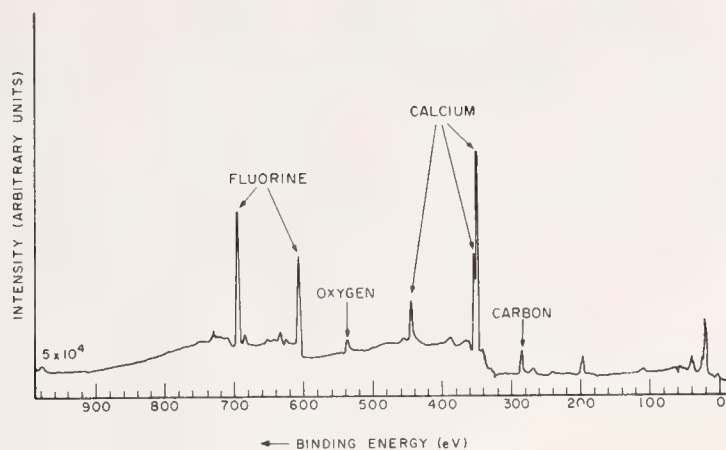


Figure 2. In-Depth Profile Analysis of Electron Beam Deposited ZnSe Films on  $\text{CaF}_2$ . (2a) Film Deposited at 0.1 nm/sec. (2b) Film Deposited at 2.0 nm/sec.



COMMENTS ON PAPER BY WITTBERG, HOENIGMAN, MODDEMAN, AND STRECKER

*The discussion of this paper centered around the relative merits of Auger spectroscopy versus ESCA. The speaker pointed out that great care has to be exercised in using Auger spectroscopy on fluoride materials because of the possibility of desorbing fluorides during the Auger measurement. This difficulty is not encountered with ESCA. Furthermore, if the chemical shifts can be resolved, ESCA provides more information on the chemical binding of the individual elements than is available using Auger spectroscopy, which only identifies a species.*

# INTERNAL-REFLECTION-SPECTROSCOPY STUDY OF WATER ADSORBED ON $\text{CaF}_2$

J. W. Gibson, R. T. Holm and E. D. Palik  
Naval Research Laboratory  
Washington, D.C. 20375

The infrared internal-reflection spectrum of  $\text{CaF}_2$  trapezoids in air indicate the presence of an adsorbed water film. The absorption near  $3\ \mu\text{m}$  has been studied in a vacuum system in which the trapezoids were cleaned by baking and then water vapor was allowed to the surface. Measurements of the unpolarized absorptance and the s/p polarization ratio of the absorptance indicate that the index of refraction of the film and the product of the extinction coefficient and film thickness can be obtained. Analysis implies that the optical constants are significantly less than those of bulk water. The simplest conclusion is that the film is porous.

Key words: adsorbed water;  $\text{CaF}_2$  surfaces; infrared spectrum; internal reflection; optical constants; water absorption.

## 1. Introduction

The infrared (IR) absorption due to adsorbed water on surfaces of various materials has been extensively studied [1,2,3]<sup>1</sup>. The sample was typically a polycrystalline material such as  $\text{CaF}_2$  precipitated from an aqueous solution [4], a porous film of NaCl formed by deposition on a cold substrate [5], or a porous glass with large surface area [1,2]. One-angle ellipsometry has been used to determine the monolayer thickness of an adsorbed water film on alkali-halide surfaces under the assumption that the index of refraction of the film is the same as for bulk water [6]. We have used the phenomenon of attenuated total reflection (ATR) to determine the optical constants of the adsorbed water film on  $\text{CaF}_2$ . They are found to be significantly less than those of bulk water. Inferences are drawn as to the structure of the adsorbed film.

## 2. Experimental Techniques

Trapezoids illustrated in the inset of figure 1 were used in a double-pass mode in a double-beam spectrometer for experiments in air. The base angles were  $\theta_1 = 48^\circ$ ,  $\theta_2 = 56.5^\circ$ , the mean length  $l$  was 5.0 cm, the width  $w$  was 0.18 cm, the index of refraction was 1.42 and the number of reflections  $m$  was 25 for one pass and 38 for double pass. Trapezoids in air invariably have water and hydrocarbons on the surfaces which give rise to characteristic absorption lines as illustrated in figure 1. Prominent OH,  $\text{H}_2\text{O}$  and CH absorption frequencies are indicated by the arrows even though this particular trapezoid may not clearly display all the bands. Such trapezoids were also used single-passed in an ultra-high vacuum (UHV) system and cleaned by baking to remove water. Then pure water vapor was admitted into the chamber to saturated vapor pressure and unpolarized and polarized absorption measurements were made.

The trapezoids were [111] oriented on the large surface but mechanically polished, so the damaged surface probably consisted of unoriented crystallites.

The spectra were analysed with a multilayer model [7], for which we assumed a layer of liquid water on the surface of  $\text{CaF}_2$  and bulk optical constants.

## 3. Results

### 3.1. Measurements in air

We measured a number of double-pass trapezoids in air [8] and always found the peak unpolarized absorptance near  $3400\ \text{cm}^{-1}$  to be  $(6.5 \pm 0.4)\%$ . This is measured from the dotted background level shown in figure 1. The laboratory temperature was  $21^\circ\text{C}$  and the relative humidity was about 50%. Assuming the optical constants of bulk water [9], we computed the equivalent water film thickness to be  $4.0\ \text{\AA}$ . In the analysis of HF-laser calorimetry experiments, Horrigan and Deutsch [10] estimated from an absorptance per surface of 0.029% for  $\text{CaF}_2$  a film thickness of about  $6\ \text{\AA}$ .

We placed a trapezoid into the UHV chamber at  $\sim 5 \times 10^{10}$  Torr initial pressure and measured single-pass spectra after baking at  $200^\circ\text{C}$  for 24 hr. The absorption due to water was removed to the degree

1. Figures in brackets indicate the literature references at the end of this paper.

of experimental sensitivity. When the surfaces were exposed to laboratory air, an s absorptance  $A_s + a_s = 5.6\%$  was obtained which upon evacuation decreased to  $a_s = 2.3\%$ . This residual absorptance could not be decreased further by pumping but was removable by baking. This indicates [4] a thinner chemisorbed layer about  $1.8 \text{ \AA}$  thick with absorptance  $a_s$  and a thicker physisorbed plus chemisorbed layer about  $4.6 \text{ \AA}$  thick with absorptance  $A_s + a_s$ .

As it was time consuming to bake the sample to clean the surface, we chose to measure the polarized absorptance of the physisorbed film, since water could be removed from and returned to the surface easily. This was done by s- or p-polarizing the radiation with the chemisorbed layer present and then allowing water vapor into the chamber to saturation. Since we measured absorptance from the level of the chemisorbed layer, we were actually measuring  $A'_{s,p} \approx A_{s,p}/(1 - a_{s,p})$ . If the chemisorbed absorptance is small, then  $A'_{s,p} \approx A_{s,p}$ . We can make a better assumption that  $a_s = a_p$ , which we did not actually determine for this type of film. Lastly, we could assume  $a_s/a_p = A'_s/A'_p$ . An analysis indicates that the  $A'_s/A'_p$  ratio as well as the values of  $A'_{s,p}$  are not sensitive functions of the various above approximations. We measured  $A'_s/A'_p = 0.75$ . The calculated value of this ratio is  $A_s/A_p = 1.6$ . This discrepancy is well beyond the experimental error and implies that the film is not bulk water. It also throws suspicion on the film thickness calculated from the observed unpolarized absorptance.

### 3.2. Measurements in pure water vapor

The bulk of our experiments were done by exposing a clean surface to pure water vapor. The unpolarized absorptance at  $3335 \text{ cm}^{-1}$  is shown in figure 2 as a function of vapor pressure. Near saturation the absorptance also saturates at  $A + a = 16.6\%$ . Upon pumping, the absorption reduces to  $a = 4.3\%$ , but cannot be reduced by further pumping at room temperature. Baking does remove the absorption. The calculated chemisorbed film thickness is  $3.4 \text{ \AA}$  and the total film thickness (chemisorbed plus physisorbed) is  $14.7 \text{ \AA}$ . The  $A'_s/A'_p$  polarization ratio for the physisorbed film was measured to be 1.37, which corrects to 1.35 if we assume  $a_s/a_p = A'_s/A'_p$ . We have ignored this correction in view of the overall experimental uncertainties in the measurements of  $A'_s/A'_p$ . The values of unpolarized absorptance  $a$  and  $A$  are determined by measuring from the clean-surface level first as shown in figure 3. Then, values of  $A'_s$  and  $A'_p$  are measured from the absorption level of the chemisorbed film with the radiation s polarized and allowing saturated water vapor into the chamber. Then the vapor is pumped out so that the absorptance returns to its previous (chemisorbed) level; the radiation is p polarized and the water vapor is re-admitted. The calculated  $A_s/A_p = 1.6$  is in much better agreement with  $A'_s/A'_p$  for the water film formed from pure water vapor than for the water film formed from air.

We measured the unpolarized and p-polarized absorption of the chemisorbed film at  $3335 \text{ cm}^{-1}$  and found  $a_s/a_p = 1.1 \pm 0.1$ . However, there is a large uncertainty due to poor signal-to-noise ratio and the small magnitude of the absorptance.

We next measured the wavelength dependence of the  $A'_s/A'_p$  ratio with the results given in figure 4b by the experimental data points. The solid curve is calculated assuming the bulk optical constants shown in figure 4a. Note that the calculation is for a water film on a  $\text{CaF}_2$  surface while the experiment is for a thick physisorbed water film on a thin chemisorbed water film on a  $\text{CaF}_2$  surface. If the chemisorbed film has the same polarization properties as the physisorbed film, the presence of the chemisorbed film does not affect the calculated results for  $A_s/A_p$  significantly.

The data of figure 4b are in qualitative agreement with the calculation with the s/p ratio being both larger and smaller than unity over the region of anomalous dispersion. This gives a clue as to why the water film formed from air gave  $A'_s/A'_p = 0.75$  at  $3335 \text{ cm}^{-1}$  and the water film formed from pure water gave  $A'_s/A'_p = 1.37$ . If the air film were "dirty" with dissolved hydrocarbons, oxygen, nitrogen, etc., it is possible that this solute effect [1] could shift the band enough to lower frequency, so that at  $3335 \text{ cm}^{-1}$  the  $A_s/A_p$  ratio is now less than unity. In effect we slide along the frequency scale of figure 4b.

In the thin-film approximation it is easy to see that the  $A_s/A_p$  ratio is a direct measure of the index of refraction  $n_f$  of the film and is independent of the extinction coefficient  $k_f$  and film thickness  $d$ . It depends only on the indices of refraction of the film and substrate and the internal angle of incidence [3]. The calculated  $A_s/A_p$  ratio approaches 1.35 far away from the absorption band where absorption is small. We measured this ratio only in the spectral range  $3000\text{--}3800 \text{ cm}^{-1}$  because absorption was too small elsewhere or absorption due to water vapor interfered. We feel that the



discrepancy in figure 4b is well beyond experimental or analytical error.

We analyzed the data of figure 4b to obtain the index of refraction of the film as shown in figure 4d. Comparison with figure 4a shows that the index of refraction is generally smaller for the film than for bulk water. In figure 4c is shown the unpolarized absorptance. By smoothing the  $n_f$  data of figure 4d, we could use the values of  $n_f$  to determine the product  $k_f d$  from figure 4c which is shown in figure 4e. Thus, the analysis yields  $n_f$  and  $k_f d$ .

We now applied a Lorentz-oscillator model to analyze  $n_f$  and  $k_f d$ . This model is not strictly appropriate for water, since at least two vibration modes contribute to the absorption, and when these bands are separated in liquid H<sub>2</sub>O, a Gaussian shape fits better [12]. The form of the dielectric function is

$$\epsilon = (n - ik)^2 = \epsilon_\infty \left[ 1 + \frac{\Omega^2}{\omega_0^2 - \omega^2 - i\gamma\omega} \right], \quad (1)$$

where  $\epsilon_\infty = n_\infty^2$  is the high frequency dielectric constant in the visible,  $\omega_0$  is the resonant frequency,  $\gamma$  is the damping constant (the full width at half maximum of  $nk$  is  $2\gamma$ ), and  $\Omega^2$  is an oscillator-strength term. Analysis of the data of figure 4a yields  $n_\infty = 1.32$ ,  $\omega_0 = 3390 \text{ cm}^{-1}$ ,  $\gamma = 200 \text{ cm}^{-1}$ , and  $\Omega^2 = 1.56 \times 10^{-3} \text{ cm}^{-2}$ . For the adsorbed film, the analysis of the data of figure 3b-3e gives  $n_\infty = 1.21$ ,  $\omega_0 = 3405 \text{ cm}^{-1}$ ,  $\gamma = 185 \text{ cm}^{-1}$  and  $\Omega^2 = 7.57 \times 10^{-4} \text{ cm}^{-2}$ . These analyses suggest that there is a significant decrease in background index of refraction, a slight increase in resonant frequency, a slight narrowing of the line width, and a substantial decrease in the oscillator strength. With these optical constants the total water-film thickness nearly doubles compared to the value obtained assuming bulk optical constants.

#### 4. Discussion

There are numerous references in the literature [13] indicating that evaporated solid films can have anomalous optical constants compared to the starting bulk material. This can be porosity, size effect, anisotropy, surface roughness, for example. However, it is not obvious that an adsorbed water film is analogous.

If the film is porous, we can determine from the Clausius-Mossotti equation

$$\frac{n_\infty^2 - 1}{n_\infty^2 + 2} = \frac{4\pi}{3} \sum_i N_i \alpha_i \quad (2)$$

that the number  $N$  of electronic oscillators/cm<sup>3</sup> must be reduced to about 0.7 of the number in bulk water to allow the background index of refraction to decrease from 1.32 to 1.21. Here, we assume that the atomic polarizability  $\alpha_i$  remains the same for both kinds of material. This is not at all obvious for a film of water only a few monolayers thick because of the changes in bonding at the nearby interfaces. In fact, the concept of bulk dielectric constant probably is suspect. This magnitude of packing density is not unusual for solid evaporated films deposited on heated substrates [14], but again, we do not know if an adsorbed water film behaves in a similar manner. In a porous water film the hydrogen bonding is reduced, thus allowing the resonant frequency to increase and the line width to narrow. Also, the oscillator strength term  $\Omega^2$  varies as  $N$ , where  $N$  is the number of vibrational oscillators [15], so a porous film would lead to a weaker vibration band. To reduce  $\Omega^2$  by a factor of two in equation 1 requires a reduction of  $N$  by a factor of two, which is comparable to, but smaller than the value of  $N$  suggested by the decrease in  $n_\infty$ .

From the large body of work on the IR properties of bulk water [11] we can make some comparisons with the adsorbed water film. In general, a solute perturbs the water band at  $3390 \text{ cm}^{-1}$ . Various molar solutions of alkali halides and other materials [11] cause the band to shift to higher frequency and narrow or to shift to lower frequency and widen. However, the band always weakens in intensity, and the background index of refraction always increases slightly. Solute effects could then be invoked to explain our results except for the observed decrease in background index of refraction. Solutes are a possibility since the film is no doubt a complicated mixture of Ca and F ions, hydrocarbons, and perhaps chemical compounds such as  $\text{Ca}(\text{OH})_2$ .

There is a one-angle ellipsometry measurement of water adsorbed to alkali-halides which yields the film thickness assuming bulk optical constants for water [6]. A monolayer thickness is  $3.7 \text{ \AA}$ . There are non-optical studies (SIMS) of water on low-temperature alkali halides which suggest irregular films with clusters of water on the surface [16]. But it is not obvious if this type of structure persists at room temperature at high vapor pressures.

## 5. Conclusions

Analysis of ATR data indicate that for an adsorbed film, the absorption band of water shifts to slightly higher frequency and narrows a little. The peak extinction coefficient is reduced about a factor of two and the background index of refraction decreases significantly to 1.21. While the film is probably a complicated mixture of ions, impurities and chemical compounds, the simplest way to explain these features is to assume a porous film with about 0.7 the water molecules of bulk water.

## 6. Acknowledgment

We thank P. H. Klein for useful discussions regarding adsorbed water on  $\text{CaF}_2$ . J. N. Harrick provided information about internal-reflection-spectroscopy techniques.

## 7. References

- [1] Little, L. H., Infrared Spectra of Adsorbed Species, (Academic Press, New York, 1966).
- [2] Hair, M. L., Infrared Spectroscopy in Surface Chemistry, (Marcel Dekker, New York, 1967).
- [3] Harrick, N. J., Internal Reflection Spectroscopy, (Wiley, New York, 1967).
- [4] Barracough, P. B. and Hall, P. G., J. Chem. Soc. Faraday Trans. I 71,2266(1975).
- [5] Smart, R. St. C. and Sheppard, N., J. Chem. Soc. Faraday Trans. II 72,707(1976).
- [6] Bayh, W. and Pflug, H., Z. Angew. Physik 25,358(1968).
- [7] Holm, R. T. and Palik, E. D., Appl. Opt. (in press).
- [8] Palik, E. D., Gibson, J. W., R. T., Hass, M., Braunstein, M. and Garica, B., Appl. Opt. (in press).
- [9] Downing, H. D. and Williams, D., J. Geophys. Res. 80,1656(1975).
- [10] Horrigan, F. A. and Deutsch, T. F., "Research in Optical Materials and Structures for High-Power Lasers", Final Technical Report. Contract No. DAAH01-70-C-1251 ARPA, Sept. 1971, p. 82.
- [11] Rhine, P., Williams, D., Hale, G. M. and Querry, M. R., J. Phys. Chem. 78,238,1405 (1974), and references therein.
- [12] Eisenberg, D. and Kauzmann, W., The Structure and Properties of Water, (Oxford, New York, 1969), Chap. 5.
- [13] Roberts, E. F. I. and Ross, D., Surf. Sci. 56,425(1976).
- [14] Ritter, E., "Dielectric Film Materials for Optical Applications" in Physics of Thin Films. Edited by G. Haas, M. H. Francombe and K. W. Hoffman (Academic Press, New York, 1975) p.1.
- [15] Burstein, E., "Optical Properties of a Dielectric Medium", in Dynamical Processes in Solid State Optics, edited by R. Kubo and H. Kamimura (W. A. Benjamin, New York, 1967) p.1.
- [16] Estel, J., Hoinkes, H., Kaarmann, H., Nahr, H. and Wilsch, H., Surf. Sci. 54,393(1976).

## 8. Figures

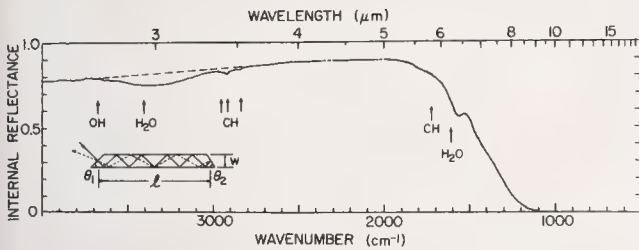


Figure 1. Internal-reflection spectrum of a double-passed  $\text{CaF}_2$  trapezoid in air. The inset defines the trapezoid parameters.

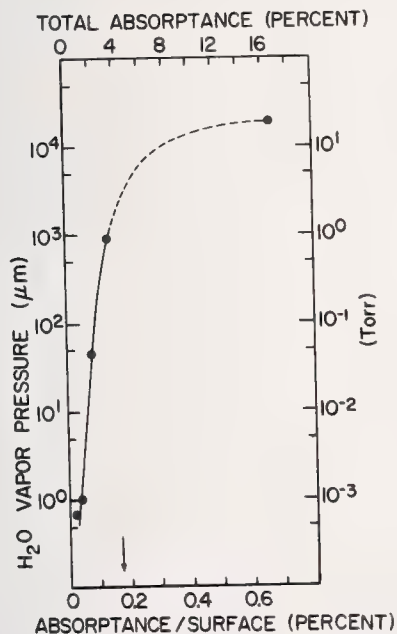


Figure 2. The unpolarized total absorbance of a clean surface of  $\text{CaF}_2$  exposed to water vapor. When the water vapor is pumped out, the absorbance decreases to 4.3% indicated by the arrow, rather than 0% implying a chemisorbed layer tightly bound to the surface.

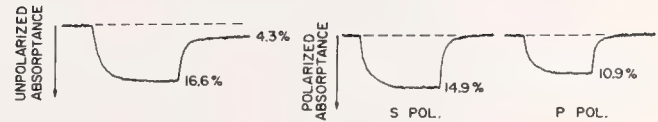


Figure 3. The sequence used to measure the absorbance at  $3335 \text{ cm}^{-1}$  of a water film formed on  $\text{CaF}_2$  from saturated water vapor.

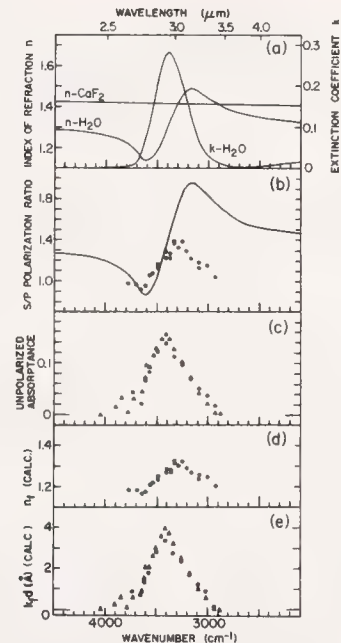


Figure 4. a) The index of refraction  $n$  and extinction coefficient  $k$  of pure water and the index of refraction of  $\text{CaF}_2$ . b) The calculated and observed absorbance polarization ratio for a water film on  $\text{CaF}_2$  surrounded by saturated water vapor. c) The experimental unpolarized absorbance obtained in two separate runs. d) The index of refraction  $n_f$  extracted from the  $A'_S/A'_P$  ratio given in Figure 4b. e) The  $k_f d$  product determined from the unpolarized absorbance in Figure 4c.



#### COMMENTS ON PAPER BY GIBSON, HOLM, AND PALIK

*It was pointed out that the results presented in this paper on adsorbed water layers have been confirmed on other substrates by ellipsometry. The speaker pointed out that the seeming invariance of these results on different substrate materials was due to the fact that the principal absorption detected was attributed to a hydrogen vibration, so that the bonding of the oxygen end of the water molecule to the surface, which would be expected to be different for different substrates, could not be detected by this technique.*

## PULSED HF/DF LASER DAMAGE IN WINDOW MATERIALS\*

E.W. Van Stryland, M. Bass, M.J. Soileau and C.C. Tang<sup>†</sup>  
Center for Laser Studies, University of Southern California  
University Park, Los Angeles, California 90007

Laser damage thresholds are reported for several alkali-halides, alkaline earth fluorides, ZnSe, As<sub>2</sub>S<sub>3</sub>, sapphire, spinel and quartz at HF (2.7  $\mu$ m) and DF (3.8  $\mu$ m) wavelengths. A low pressure, transversely excited, double discharge laser and two different focal length lenses were used. A Gaussian spatial beam distribution was obtained by spatially filtering out high order modes in the far field of an unstable resonator cavity. Sapphire was found to have the highest bulk damage threshold of the materials tested, 100 GW/cm<sup>2</sup> at 2.7  $\mu$ m (peak intensity on axis). The damage threshold was found to vary as the inverse of the spot diameter which supports the model of Bettis, et. al. (NBS Spec. Publ. 462). The measurements also show that all of the materials evaluated in this effort are surface damage limited when exposed to pulsed HF or DF laser radiation. Evidence concerning the roles of material manufacture, surface finishing and laser irradiation conditioning in the damage process are presented.

Key words: Alkali-halides, alkaline earth fluorides, As<sub>2</sub>S<sub>3</sub>, DF, electric breakdown, HF, laser damage, quartz, sapphire, spinel, ZnSe.

### 1. Introduction

Measurements were made of the pulsed laser damage resistance of several candidate window materials at HF and DF laser wavelengths. Of the materials tested sapphire and the alkaline earth fluorides have the highest resistance to laser damage. A major part of the experimentation was devoted to modification and characterization of the HF/DF chemical laser. The damage irradiations were performed with total powers less than 1/10 of the critical powers for self-focusing by tightly focusing the Gaussian laser beam. At 2.7  $\mu$ m, the HF laser wavelength, a single triangular pulse waveform was used, however, at 3.8  $\mu$ m, the DF wavelength, a double pulse was obtained because the laser oscillated on several lines simultaneously. The occurrence of surface damage set the practical use limit for the materials that were studied and in general there was a considerable effect of laser preconditioning (N on 1 effect) for the surface damage threshold.<sup>(1)</sup>

### 2. Experiment

In the damage threshold measurements a transversely excited HF (or DF) pulsed chemical laser was used as the irradiation source. The output wavelength of the HF laser was multiline and centered about 2.7  $\mu$ m; the output is considerably more dispersed for DF and is centered about 3.8  $\mu$ m. The only change made in the system to go from HF to DF lasing was to switch from H<sub>2</sub> to D<sub>2</sub> gas. The power supply, laser cavity and all other optics remained the same. The relevant laser parameters and cavity design employed are shown in figure 1.

The laser was manufactured by Lumonics (2) and has been described previously, however, the cavity has been modified as shown in figure 1. The unstable resonator employed a 100% reflector with focal radius of 14m and an NaCl output coupler of focal radius .8m. The NaCl lens was uncoated and the 4% reflection from the surface was the only feedback into the cavity. A series of Fresnel rings were observed in the near field of the laser output. These were sensitive to adjustment of either reflector as well as to the size and position of the intracavity aperture. The output traversed the path shown in figure 2. It propagated to a focus 5.76 m "downstream" where a 1.7 mm diameter spatial filter was positioned to block any off axis output modes. This spatially filtered output was then attenuated by two pair of Brewster angle ZnSe slabs; the first pair of which was rotatable to vary the attenuation, and the second was used to assure that the polarization in the beam reaching the target remained constant. After these, bulk attenuators such as quartz, Ge or As<sub>2</sub>Se<sub>3</sub> were inserted as necessary. The energy in each pulse was monitored after the attenuators by a calibrated pyroelectric energy meter. At a total distance of 9.0m from the laser output coupler lens the far field spatial distribution was the Gaussian desired for meaningful damage experiments. At this point the output was focused by a ZnSe meniscus lens (2 different focal length lenses were used) on or inside the samples.

A beam scan of the output of the HF laser at the position of the damage lens with a 0.4 mm aperture gave the data points in figure 3. Each point represents the average of 10 laser shots. The drawn in curve shows a fit of the data to a Gaussian. The 1/e<sup>2</sup> full width of the Gaussian fit curve is 22.0 mm.

\*This work was supported by D-ARPA under contract No. F 19628-77-C-0094.

<sup>†</sup>Current address: Aerospace Corporation, El Segundo, California.

<sup>1</sup>Figures in brackets indicate literature references at the end of this paper.

A pinhole scan of the laser output was also performed in the focal planes of ZnSe lenses of focal lengths 38.0 and 127 mm. A scan of the focal plane of the 38.0 mm focal length ZnSe lens is shown in figure 4 using a 9.1  $\mu\text{m}$  diameter pinhole. This pinhole was made in thin Al foil by the focused laser output, and its diameter measured in an optical microscope. Each data point represents a single laser shot measured with the pyroelectric energy monitor. The pinhole was moved by a differential micrometer in 12.7  $\mu\text{m}$  intervals. The data has been folded with respect to the maximum. Since the pinhole size was not small compared to the beam size, corrections were made to account for the finite size aperture. (3) It was found by numerical integration (of a circular aperture with a Gaussian weighting function) that the beam width appeared 5% larger using a 9.1  $\mu\text{m}$  diameter pinhole than if the scan had been performed with a much smaller aperture (e.g.: 1  $\mu\text{m}$ ). The Gaussian, uncorrected for a finite size aperture is shown as points in figure 4. Even using an aperture as large as one third the  $1/e^2$  width causes very little distortion of the observed beam profile.

The temporal pulse waveform was monitored at two points, one before the spatial filter and one after transmission through the sample as shown in figure 2. The HF laser produced a triangular pulse with some irregular spiking which has a full width at half maximum (FWHM) of 175 nsec as shown in figure 5. The HF waveforms were monitored using fast pyroelectric detectors with risetimes of  $\sim 1$  nsec (Ge photon drag detectors cannot be used at 2.7  $\mu\text{m}$ ). The second pulse in the HF waveform is due to ringing in the pyroelectric detector. The DF waveforms were monitored using Ge photon drag detectors and consisted of the double pulse also shown in figure 5. Damage occurred on the second part of the pulse as observed by monitoring the waveform distortion upon transmission through the sample. An equivalent pulse width for the DF pulses of 176 nsec was obtained by finding the total normalized pulse area (nsec) and multiplying by the percentage of the area under the second part of the pulse. This is mathematically equivalent to the FWHM obtained for a triangular pulse of the same area. An example of the transmitted pulse waveforms when damage occurred is shown in figure 5 for both HF and DF pulses.

The pulse waveforms for both HF and DF operation were critically dependent on gas mix, pressure, discharge voltage and laser repetition rate. The operating parameters listed in figure 1 were chosen because they resulted in the best HF waveform and this could be reproducibly obtained from day to day. A single DF pulse could not be obtained by simply varying these parameters and, as demonstrated previously, the double pulse DF output is attributed to the multiline nature of the laser oscillation.

### 3. Calculation

The definition of a damage threshold level of irradiation used in this paper is that flux which produces damage at 50% of the irradiated sites. An example of data is shown in figure 6. The plus or minus values are a measure of the overlap that occurred in all of the samples tested. The 1 on 1 threshold corresponds to one irradiation per site. The n on 1 threshold is where a given site is irradiated by a pulse or pulses with insufficient energy (or intensity) to damage prior to the pulse that produces damage. From the measured energy which caused damage the intensity thresholds were determined in the following way. The energy E in terms of the energy density  $\epsilon(r)$  at the focal plane is given by

$$E = \int_0^{\infty} \epsilon(r) 2\pi r dr. \quad (1)$$

For the Gaussian beam used in these experiments

$$\epsilon(r) = \epsilon_0 e^{-2(r/\omega_0)^2} \quad (2)$$

where  $\epsilon_0$  is the peak on axis energy density and  $\omega_0$  is the  $1/e^2$  half width point in intensity. Thus,

$$E = \omega_0^2 \epsilon_0 \pi/2 \quad (3)$$

giving the peak on axis energy density  $\epsilon_0$  as

$$\epsilon_0 = 2E/\pi\omega_0^2 \quad (4)$$

This equation gives the damage threshold in  $\text{J}/\text{cm}^2$ . To obtain the intensity damage threshold I in  $\text{watts}/\text{cm}^2$ ,  $\epsilon_0$  is simply divided by the normalized area, T, of the temporal waveforms; 175 nsec for the HF pulse, and 176 nsec for the DF as discussed previously. Thus

$$I = 2E/(\pi\omega_0^2 T) \quad (5)$$

(Again, this is equivalent to performing the temporal integral for a triangular pulse waveform). The transmission of the ZnSe lenses at both 2.7 and 3.8  $\mu\text{m}$  was measured to be 0.80. The energy E in the previous equation was corrected for this lens transmission in the calculation. In addition for bulk or exit surface damage thresholds the energy was corrected for the front surface reflection. (i.e.:

$4n/(1+n)^2$  of the incident energy is transmitted through an interface where n is the index of refraction of the sample at the appropriate wavelength). In all the samples tested, with the possible exception of quartz at 2.7  $\mu\text{m}$ , absorption was entirely negligible.

### 4. Data

Table 1 gives the damage thresholds at 2.7  $\mu\text{m}$  (HF) as measured with a 38 mm focal length ZnSe lens (measured  $1/e^2$  full width spot size of 27  $\mu\text{m}$ ). Also presented is the increase in threshold when a single site was preconditioned by pulses of insufficient energy (energy or intensity) to produce damage (labeled N on 1 increase). The number quoted multiplied by the 1 on 1 damage threshold in  $\text{J}/\text{cm}^2$  or



$\text{GW}/\text{cm}^2$  gives the n on l damage threshold. The final two columns give our assessment of whether the bulk damage was due to macroscopic inclusions or was intrinsic. This information was deduced from microscope examination of the damage morphology. For example; if damage occurred at different positions along the focal beam path the damage was deemed inclusion induced. If on the other hand as the sample was traversed perpendicular to the beam all the damage sites appeared similar and lay in a single plane, we deemed the damage to be intrinsic.

Table 1. Bulk thresholds with 27  $\mu\text{m}$  spot size ( $\lambda = 2.7 \mu\text{m}$ )\*

Specimen	$\text{J}/\text{cm}^2$	$\text{GW}/\text{cm}^2$	N on l	Increase	Inclusions	Intrinsic
NaCl (Harshaw)	$3.6 \times 10^3$	21	no			X
KCl (Harshaw)	$2.9 \times 10^3$	16	no			X
KBr (Naval Research Lab)	$1.2 \times 10^3$	6.6	x 1.12		X	
MgF <sub>2</sub> (Optovac)	$13 \times 10^3$	75	no			X
BaF <sub>2</sub> (Optovac)	$13 \times 10^3$	78	no			X
SrF <sub>2</sub> (Optovac)	$13 \times 10^3$	76	no			X
CaF <sub>2</sub> (1 Raytheon)	$15 \times 10^3$	88	no			X
CaF <sub>2</sub> (2 Harshaw)	$14 \times 10^3$	85	no			X
CaF <sub>2</sub> (3 Harshaw)	$0.47 \times 10^3$	2.8	x 1.7		X	
Sapphire (Optovac)	$17 \times 10^3$	103	no			X
Spinel (Union Carbide)	$12 \times 10^3$	68	no			X
Quartz (1 NWC)	$8.7 \times 10^3$	52	no			X
Quartz (2 General Electric)	$1.4 \times 10^3$	8.5	x 3.0		X	
ZnSe (Raytheon)	$0.46 \times 10^3$	2.7	x 1.3		X	
As <sub>2</sub> S <sub>3</sub> (Servo)	$0.29 \times 10^3$	1.7	no		X	
MgF <sub>2</sub> (pressed, NWC)	$0.05 \times 10^3$	0.29	x 1.7		X	

\* $1/e^2$  full width intensity

Table 2 gives bulk damage thresholds in the same format at 2.7  $\mu\text{m}$  for a  $1/e^2$  full width spot size of 59  $\mu\text{m}$  (the focal spot size of a 127mm lens). The greater than signs (>) in front of some of the damage thresholds indicates that there was insufficient laser energy (or intensity) to damage the sample and thus the numbers represent lower limits. No N on l data could be obtained for these samples.

Table 2. Bulk thresholds with 59  $\mu\text{m}$  spot size\* ( $\lambda = 2.7 \mu\text{m}$ )

Specimen	$\text{J}/\text{cm}^2$	$\text{GW}/\text{cm}^2$	N on l	Increase	Inclusions	Intrinsic
NaCl	$1.7 \times 10^3$	10	no			X
KCl	$0.84 \times 10^3$	5.0	x 1.1			X
KBr	$0.21 \times 10^3$	1.2	x 2.9		X	
MgF <sub>2</sub>	$>5.8 \times 10^3$	$>34$	-----			X
BaF <sub>2</sub>	$6.1 \times 10^3$	36	no			X
SrF <sub>2</sub>	$6.4 \times 10^3$	38	no			X
CaF <sub>2</sub> (1)	$>5.8 \times 10^3$	$>34$	-----			X
CaF <sub>2</sub> (2)	$2.9 \times 10^3$	17	no			X
Sapphire	$>6.0 \times 10^3$	$>35$	-----			X
Quartz (1)	$3.3 \times 10^3$	19	x 1.1			X

\* $1/e^2$  full width intensity

Table 3 shows surface damage thresholds again using a 59  $\mu\text{m}$   $1/e^2$  full width focal spot size at the 2.7  $\mu\text{m}$  wavelength. Surface damage was labeled inclusion induced since near threshold more than one damage site was observed within the focal area. The anomalously high threshold quoted for KBr (as compared to the bulk) may have been due to improper focusing.

Table 3. Surface threshold 59  $\mu\text{m}$  spot size\* ( $\lambda = 2.7 \mu\text{m}$ )

Specimen	$\text{J}/\text{cm}^2$	$\text{GW}/\text{cm}^2$	N on 1 Increase	Inclusions	Intrinsic
NaCl	$1.3 \times 10^3$	7.4	x 1.6	X	
KCl	$0.27 \times 10^3$	1.6	x 2.7	X	
KBr	$0.44 \times 10^3$	2.6	x 1.5	X	
<hr/>					
$\text{MgF}_2$	$1.3 \times 10^3$	7.4	x 1.6	X	
$\text{BaF}_2$	$0.36 \times 10^3$	2.1	x 1.0	X	
$\text{SrF}_2$	$0.43 \times 10^3$	2.5	x 1.2	X	
$\text{CaF}_2$ (1)	$2.6 \times 10^3$	15.2	x 1.2	X	
$\text{CaF}_2$ (2)	$1.2 \times 10^3$	7.0	x 1.3	X	
<hr/>					
Sapphire	$0.65 \times 10^3$	3.8	x 1.2	X	
Quartz (1)	$^\dagger 1.0 \times 10^3$	$^\dagger 6.1$		X	
<hr/>					
				* $1/e^2$ full width	
				$^\dagger$ exit surface data	

Table 4 shows damage thresholds obtained at 3.8  $\mu\text{m}$  (the DF laser wavelength) at the focus of the 38 mm focal length ZnSe meniscus lens. The  $1/e^2$  full width focal spot size of 38  $\mu\text{m}$  was calculated from the measured spot size at the 2.7  $\mu\text{m}$  wavelength and scaled according to wavelength. At the right of the chart the damage threshold in  $\text{GW}/\text{cm}^2$  at the HF laser wavelength is compared to the damage threshold at the DF wavelength after multiplying by the ratio of the spot sizes, 38  $\mu\text{m}/27 \mu\text{m}$ . The theory of Bettis, et. al. (4) predicts that the damage thresholds should be inversely proportional to the spot diameter. The HF and DF damage thresholds are nearly the same when scaled according to this rule.

Table 4. Bulk thresholds at 3.8  $\mu\text{m}$ 

Specimen	38 $\mu\text{m}$ Spot*		N on 1 Increase	Intensity ( $\text{GW}/\text{cm}^2$ ) Scaled to a 27 $\mu\text{m}$ Spot Size	HF Damage Threshold ( $\text{GW}/\text{cm}^2$ ) For a 27 $\mu\text{m}$ Spot Size
	$\text{J}/\text{cm}^2$	$\text{GW}/\text{cm}^2$			
$\text{MgF}_2$ (single crystal)	$7.4 \times 10^3$	43	no	60	75
$\text{MgF}_2$ (pressed)	$0.12 \times 10^3$	0.7	x 1.7	1.0	0.3
Sapphire	$13 \times 10^3$	72	no	102	103
Spinel	$6.9 \times 10^3$	39	no	55	68

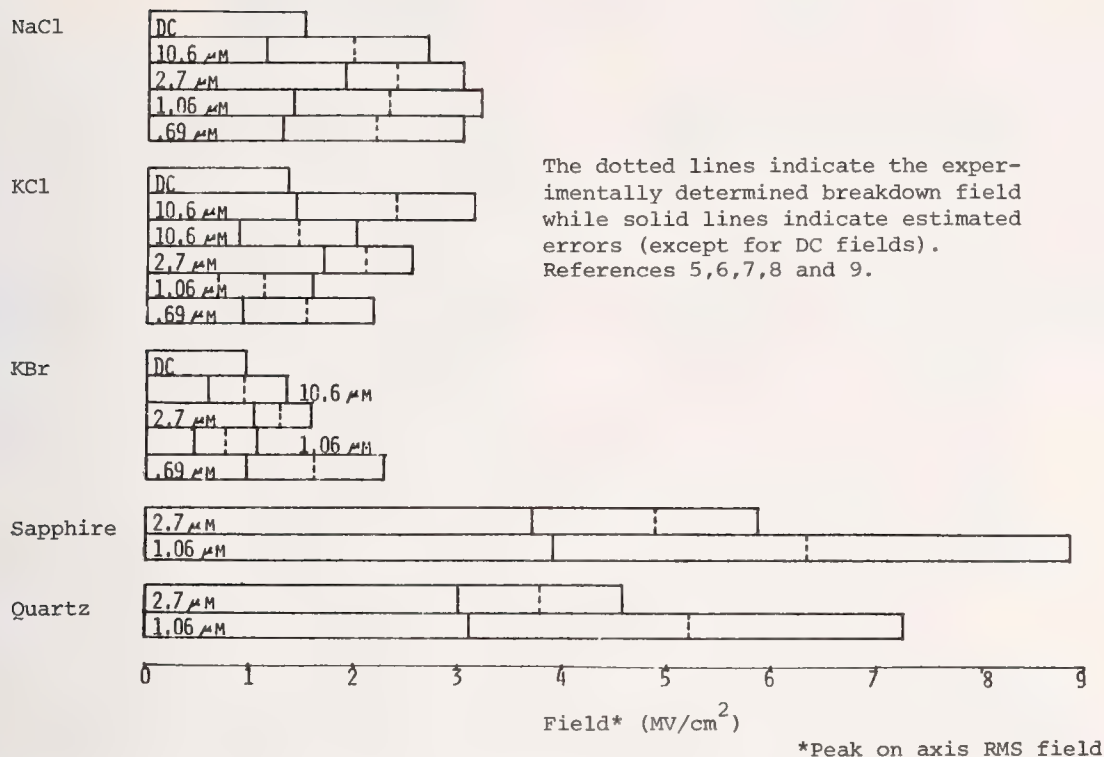
\* $1/e^2$  full width intensity

In table 5 we present a bar diagram showing the electric field at which breakdown occurred in the bulk material at various wavelengths including DC. This RMS field was calculated from the intensity damage thresholds, I, and the indices of refraction n, substituted in the equation

$$\text{Field}_{(\text{breakdown})} (\text{Volt}/\text{cm}) = 19.41 \sqrt{I(\text{Watts}/\text{cm}^2)/n} \quad (6)$$

The 2.7  $\mu\text{m}$  data is from this work. Data at other wavelengths is from the referenced literature. No attempt has been made to reduce the data to account for spot size or pulse width.

Table 5. Breakdown fields vs wavelengths



The .69 μm Ruby laser data (7,9) used a focal spot diameter ( $1/e^2$  full width in intensity) of approximately 12 μm. The pulse durations were 14 nsec FWHM. At 1.06 μm, the damage threshold appeared spot diameter independent using a spot diameter of from 16 μm to approximately 50 μm. The pulses were about 10 nsec in duration (FWHM). The 2.7 μm and 3.8 μm laser parameters are listed in this paper. The 10.6 μm damage data was taken using a CO<sub>2</sub> laser focal spot diameter of ~100 μm and a pulse length of ~100 nsec. (7,8)

The estimated errors on damage threshold intensities quoted in this paper are ~30%, which implies an uncertainty of ~14% in the fields.

### 5. Conclusions

The damage data survey presented here shows that sapphire and the alkaline earth fluorides have the highest damage thresholds at both HF and DF laser wavelengths. This is a fortunate result since both are rugged materials. In particular sapphire is extremely strong and hard.

Bettis, et. al. (4) determined that the damage intensity threshold is proportional to the inverse of the spot diameter. Although their model was developed for surface damage, they attempted to show that their model also applied to bulk damage. From this we expect that the ratio of the damage intensities for the 27 μm and 59 μm spot diameters should be 2.2. The average value of this ratio determined by this experiment is 2.5 which is in good agreement.

Using this spot diameter scaling and extending it to the 3.8 μm wavelength our DF damage thresholds are nearly the same as the HF thresholds (see table 4). Damage thresholds for some of the materials tested were obtained previously (2) at 3.8 μm using a 130 μm spot diameter ( $1/e^2$  full width). Scaling these values with spot diameter according to reference 4 also gives excellent agreement with the 2.8 μm data presented here. Thus it appears that the damage thresholds are insensitive to wavelength between 2.7 μm and 3.8 μm. We should note, however, that due to the time structure of the DF laser pulse (see figure 5) this data is less reliable.

As has been noted at other wavelengths optical materials are limited by surface damage thresholds. Our data of table 3 confirms this at 2.7 μm. The large laser conditioning effect (n on 1), the low thresholds relative to the bulk values, and microscopic examination show that surface damage is defect limited. Here again the fact that sapphire and the alkaline earth fluorides have high thresholds is helpful since we expect that with careful surface preparation the damage thresholds of these hard materials can be substantially increased. (10)

It is interesting to note that to within experimental error the raw data of table 5 shows a damage field independent of wavelength.



## 6. References

- (1) M. Bass and K.M. Leung, J. Quantum Electr. QE-12, 82 (1976).
- (2) M. Bass, K.M. Leung and C. Tang, "Pulsed Laser Induced Damage at the DF Laser Wavelength", NBS Special Publication 462 (1976).
- (3) E.W. Van Stryland, J.A. Gunderson, G. Benedict, to be published.
- (4) J.R. Bettis, R.A. House II, A.H. Guenther, "Spot Size and Pulse Duration Dependence of Laser Induced Damage", NBS Special Publication 462 (1976).
- (5) A.Von Hippel, J. Appl. Phys. 8, 815 (1973).
- (6) D.W. Fradin, E. Yablonobitch and M. Bass, Appl. Optics, 12, 700, April, 1973.
- (7) D.W. Fradin, Laser Focus, February, 1974.
- (8) S.D. Allen, M. Braunstein, C. Guiliano and V. Wang, p. 66, NBS Special Publication 414.
- (9) D.W. Fradin and M. Bass, p. 225, NBS Special Publication 387.
- (10) M.J. Soileau, A. Bennett, J. Porteus, P. Temple, "Laser Damage to HEL Window Materials as Related to Surface Damage", Fifth Annual Conference on Infrared Laser Window Materials, Las Vegas, 1975, page 351.

## 7. Figures

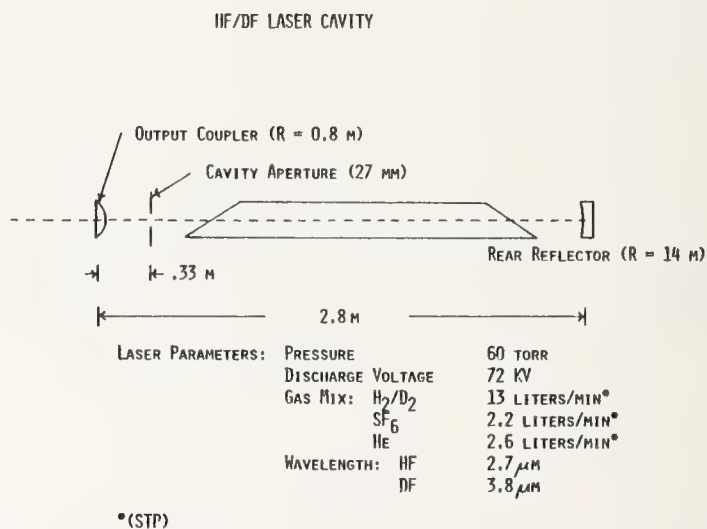


Figure 1. HF/DF Laser Cavity.

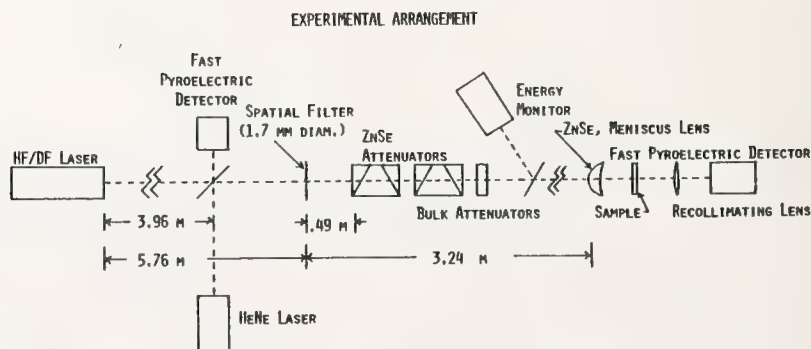


Figure 2. Experimental Arrangement.

HF LASER SPATIAL PROFILE  
(PRIOR TO ZnSe LENS)

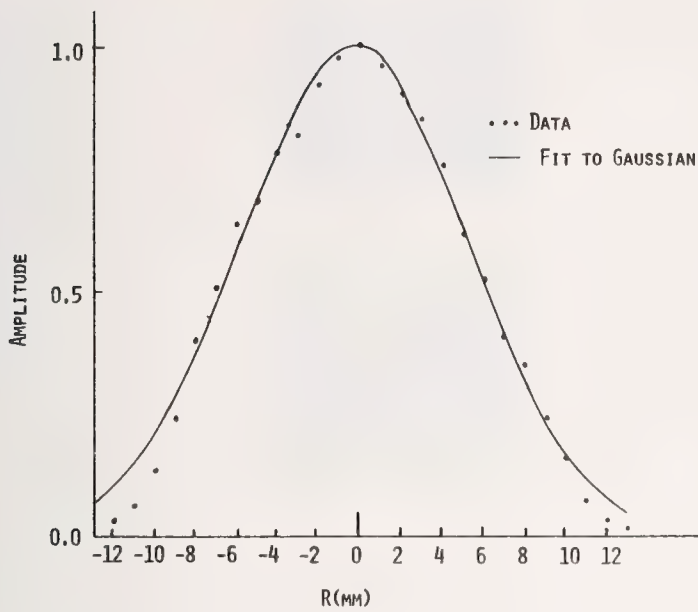


Figure 3. HF Laser Spatial Profile (Prior to ZnSe Lens).

PINHOLE SCAN OF FOCAL PLANE

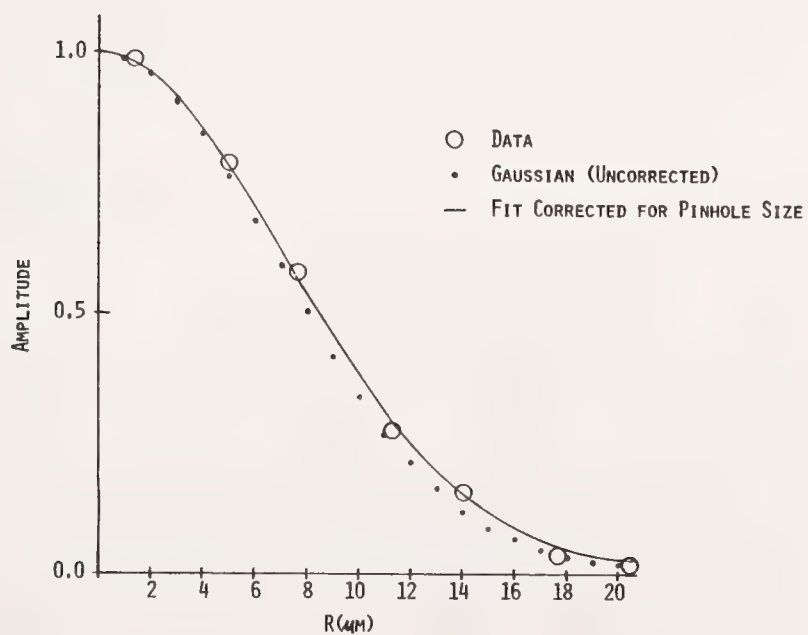


Figure 4. Pinhole Scan of Focal Plane.

# PULSE WAVEFORMS

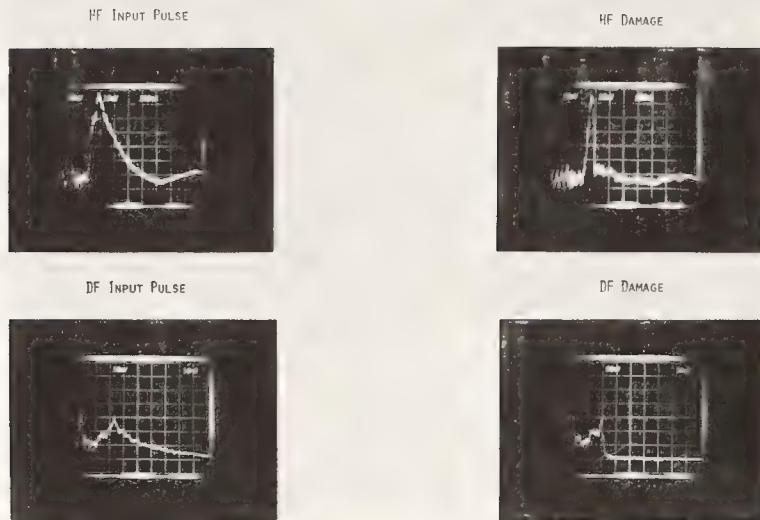
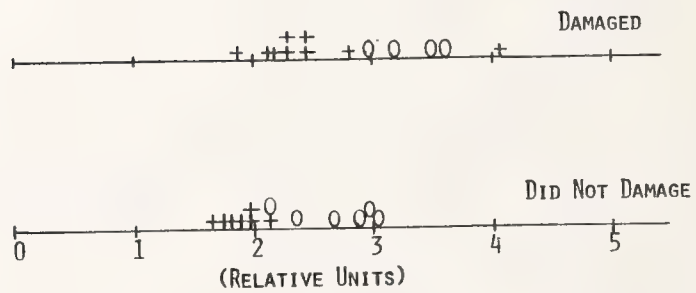


Figure 5. Pulse Waveforms.

# THRESHOLD DEFINITION



+ 1-ON-1 THRESHOLD  $2.0 \pm 0.2$   
 O N-ON-1 THRESHOLD  $3.0 \pm 0.1$

Figure 6. Threshold Definition.



COMMENTS ON PAPER BY VAN STRYLAND, BASS, SOILEAU, AND TANG

*It was pointed out that the frequency dependence of the damage threshold, even when all other factors are held constant, is not expected to obey any simple scaling relation. The role of absorbing impurities and competitive processes at different wavelengths tends to obscure the simple scaling relation predicted by the very naive theory of avalanche ionization. The speaker indicated that when he mentioned pure material he meant the best RAP-grown material available, which was as free from visible scattering as it was possible to obtain.*

# OPTICAL ABSORPTION IN UV LASER WINDOW MATERIALS

James A. Harrington, Bradley L. Bobbs, and Morris Braunstein\*  
Hughes Research Laboratories  
Malibu, California 90265

and

Rubin Braunstein, R.Y. Kim, and R. Stearns  
Department of Physics  
University of California  
Los Angeles, California 90024

The requirements for low-loss optical components for high-power excimer lasers has stimulated the investigation of optical absorption in a variety of highly transparent materials at visible and uv wavelengths. The absorption coefficient  $\beta$  has been measured, using laser calorimetric techniques, for  $\text{CaF}_2$ ,  $\text{SrF}_2$ ,  $\text{BaF}_2$ ,  $\text{LaF}_3$ ,  $\text{CeF}_3$ ,  $\text{MgF}_2$ ,  $\text{SiO}_2$ ,  $\text{MgO}$ ,  $\text{Al}_2\text{O}_3$ ,  $\text{NaF}$ ,  $\text{LiF}$ ,  $\text{NaCl}$ , and  $\text{KCl}$  at 3511, 3638, 4579, 4880, and 5145 Å. The absorption was found to decrease with increasing wavelength to a low value of  $4 \times 10^{-5} \text{ cm}^{-1}$  for  $\text{SrF}_2$  at 5145 Å. In addition, wavelength modulation spectroscopy was used to obtain absorption coefficients for some of the samples. In this technique, the energy derivatives of  $\beta$  are integrated, using the calorimetrically determined values of  $\beta$  as constants of integration to fix  $\beta$  at the laser wavelengths, to obtain absorption coefficients continuously from 2500 to 5000 Å.

Key words: Extrinsic uv absorption; laser calorimetry; laser windows; Urbach tail; uv laser components; wavelength modulation spectroscopy.

## 1. Introduction

There has recently been considerable interest in low-loss optical components for uv excimer lasers. To provide reliable coating and window materials that have high damage thresholds at uv laser wavelengths requires making a systematic study of the optical absorption in a wide variety of transparent materials. The materials with large band gaps that have been investigated include alkali halides, alkaline earth fluorides, oxides, and some rare earth fluorides. The small, residual absorption coefficients ( $\beta$ 's) were measured at five visible and uv wavelengths using Ar ion laser calorimetry; they were also measured continuously from approximately 400 to 250 nm using wavelength modulation spectroscopy. A comparison of our data with published data (Urbach tail region) indicates that, although the spectral regions of the Urbach tail data and our data do not overlap, our absorption data is significantly lower than a simple extrapolation of the "extrinsic" Urbach tail. These results suggest that the materials studied are considerably more transparent around 350 nm than originally expected from published data.

## 2. Experimental Procedure and Techniques

The small optical absorption coefficients were measured in a variety of single- and polycrystalline samples using laser calorimetric techniques [1]. A Coherent Radiation Laboratories model CR-12 Ar ion laser equipped with visible or uv optics was used in conjunction with a simple air calorimeter to obtain absorption results at 514.5, 488.0, 457.9, 363.8, and 351.1 nm. The schematic of the uv calorimeter shown in figure 1 also contains the quartz half-wave plate utilized to maximize the power in each uv line. The procedure yielded about 1 W at each uv wavelength and between 5 and 6 W for the strong blue-green lines. Wavelength modulation spectroscopy was performed on some of the samples that had been measured calorimetrically. The basic principles of this technique are discussed elsewhere [2]. Certain refinements in the original apparatus have been made to provide the greater sensitivity required to measure these extremely small absorption coefficients [3].

## 3. Experimental Results

### 3.1 Calorimetric Measurements

Eleven different materials were measured at visible and uv wavelengths. In some cases, more than one source or different forms of the same material were studied. Figures 2 and 3 display all the calorimetric data for the various samples studied. In each case, absorption increases with increasing energy. The lowest absorbing crystals are the alkaline earth fluorides,  $\text{KCl}$ ,  $\text{NaCl}$ , and  $\text{SiO}_2$  (one sample), where  $\beta$ 's in the low  $10^{-4} \text{ cm}^{-1}$  region were measured at visible wavelengths. The single crystal

\*Research supported in part by Hughes Independent Research and Development Projects.

1. Figures in brackets indicate the literature references at the end of this paper.

KCl grown in the Hughes Laboratories, for example, had absorption coefficients that were unmeasurable in the blue-green region (cf. fig. 3) but were estimated, based on the sensitivity of the calorimeter, to be no greater than  $2 \times 10^{-5} \text{ cm}^{-1}$ . The highest absorbing materials tended to be certain oxides, NaF, and LiF. The NaF and LiF samples (obtained from Optovac, Inc., and Adolf Meller Co.) had surprisingly high absorptions, especially considering the large band gap in these materials. The most probable explanation is that these materials are not as pure as the alkaline earth fluorides and other alkali halides, which have been more highly purified because of the emphasis on these hosts for applications as infrared laser windows. In no case, however, was it found that the absorption increased with increasing exposure to the uv laser radiation, as might occur if color centers were being continuously produced.

### 3.2 Wavelength Modulation Spectroscopy

Absorption coefficients for some of the sample samples measured calorimetrically were obtained by wavelength modulation spectroscopy from approximately 450 to 280 nm. The results of this work for several materials are shown in figures 4 and 5. The raw data is returned as a derivative of the absorbance with respect to wavelength. These spectra are then integrated to yield the relative absorption coefficients, shown as the upper curves in figures 4 and 5. An absolute calibration of these curves is then obtained by comparing these to the calorimetric data of figures 2 and 3 (reproduced as the dashed-bottom curves in figs. 4 and 5). In general, there is excellent agreement between the calorimetric and  $\lambda$ -modulation data for each host material studied.

The increasing absorption at uv wavelengths is clearly evident in figure 4 for  $\text{LaF}_3$ ,  $\text{Al}_2\text{O}_3$ , and  $\text{SiO}_2$ . The high sensitivity of  $\lambda$ -modulation methods in comparison to other forms of spectroscopy may also be seen by noting the spectra of some older  $\text{LaF}_3$  material measured on a conventional (Cary 14) spectrometer. Contrasting the conventional spectroscopic data and the calorimetric/ $\lambda$ -modulation data, one can see that some structure is visible in the integrated  $\lambda$ -modulation spectrum that is impossible to observe in the Cary 14 data because the Cary 14 is less sensitive than derivative spectroscopy. For  $\text{Al}_2\text{O}_3$ , one observes another complementary feature of  $\lambda$ -modulation spectroscopy. The peak in the absorption near 380 nm is missed by calorimetry because of the lack of laser lines at this energy. By comparison,  $\text{SiO}_2$  data in figure 4 merely indicates a monotonic increase in absorption with increasing energy. This is in agreement with the calorimetric results (i.e., no sharp absorption bands appear in the spectra).

$\text{CaF}_2$  data (cf. fig. 5) exhibits a peak in the absorption near 370 nm. This is not entirely evident from calorimetry alone, but derivative spectroscopy clearly delineates this band. A likely explanation for this absorption is that it is due to F-centers. The absorption in  $\text{SrF}_2$ , even though it is at an extremely low level, indicates some structure on an otherwise monotonically increasing absorption with increasing energy.

### 3.3 Comparison with Band Edge Data

The alkaline earth fluorides were singled out for comparison with data in the Urbach tail region taken from existing literature. Figure 6 includes the band edge data of Tomiki and Miyata [4] and our  $\lambda$ -modulation/calorimetric data. Unfortunately, the two spectral regions do not overlap; however, the data from this study is significantly lower than any extrapolation of the "extrinsic" Urbach tail data would imply. Presumably, the purity of the samples has increased and, with more sensitive techniques being used, this has led to the "extrinsic" absorption observed by us being less than that previously observed. Experiments are underway to extend our measurements to 11 eV so that an accurate comparison can be made. The attenuation due to scattering, calculated theoretically [5], is negligible when compared to the other absorption losses.

## 4. Conclusions

Our absorption studies of highly transparent solids for use as low-loss components on uv excimer lasers has led us to conclude that the lowest absorbing materials near 350 nm are the alkaline earth fluorides, NaCl, KCl, and  $\text{SiO}_2$ . More highly absorbing materials are  $\text{Al}_2\text{O}_3$ , MgO, alkali fluorides, and rare earth fluorides. One reason for this is that the low absorbing uv materials are also those that have been extensively studied and purified for low-loss at infrared laser wavelengths. A comparison of our experimental data with "extrinsic" Urbach tail region data indicates less extrinsic absorption than previously expected.

## References

- |   |  |
|---|--|
| [1] Hass, M., Davisson, J.W., Klein, P.H., and Boyer, L.L., J. Appl. Phys. <u>45</u> , 3959 (1974). | [4] Tomiki, T. and Miyata, T., J. Phys. Soc. Japan <u>27</u> , 658 (1969). |
| [2] Welkowsky, M. and Braunstein, R., Rev. Sci. Inst. <u>43</u> , 399 (1972).                       | [5] Rich, T.C. and Pinnow, D.A., Appl. Phys. Lett. <u>20</u> , 264 (1972). |
| [3] To be published.  |  |



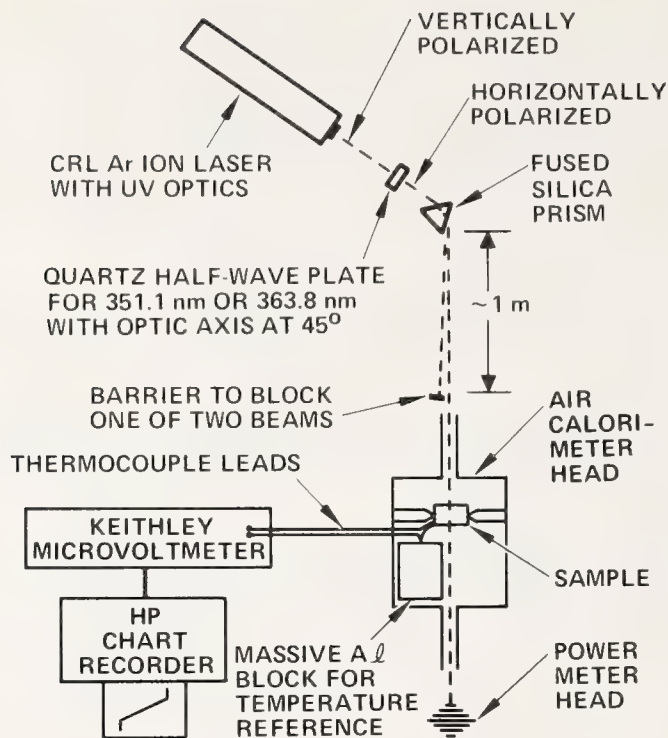


Figure 1. UV Calorimeter.

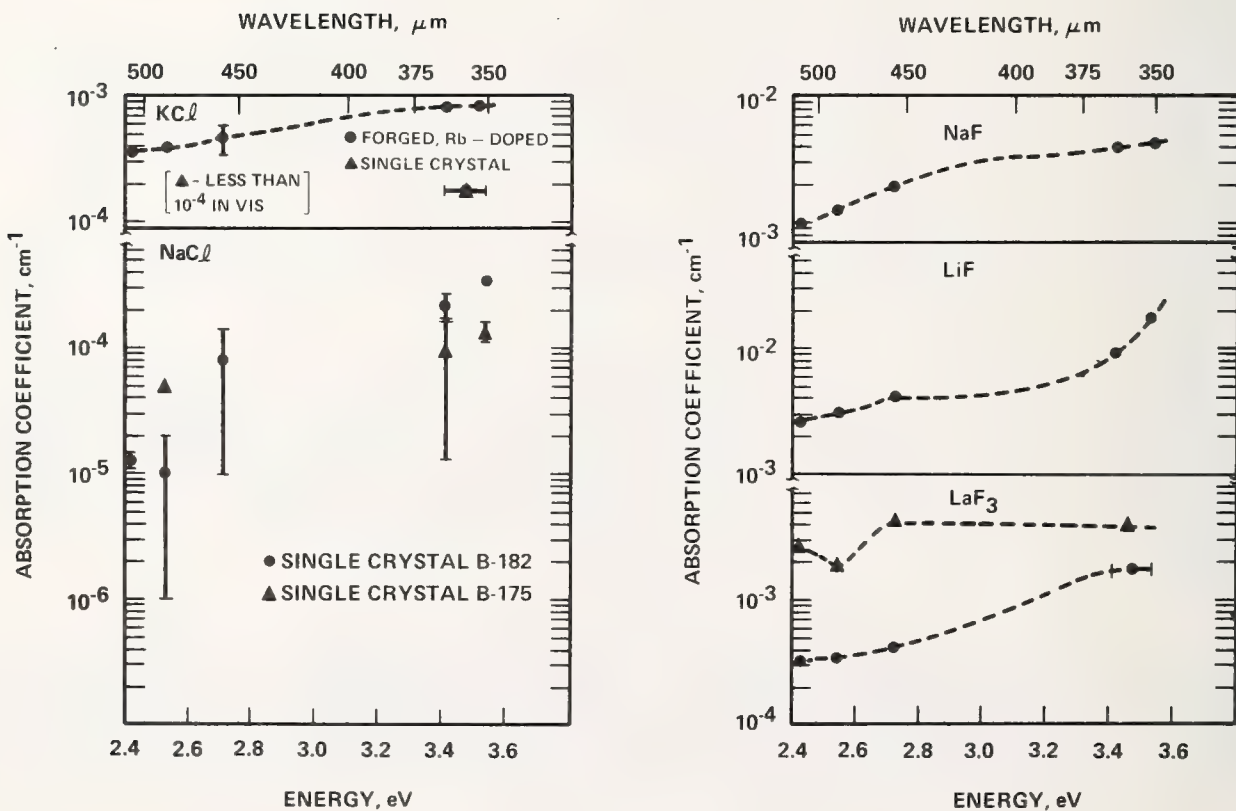


Figure 2. Calorimetric measurements of uv-visible absorption in alkali halides and LaF<sub>3</sub>.

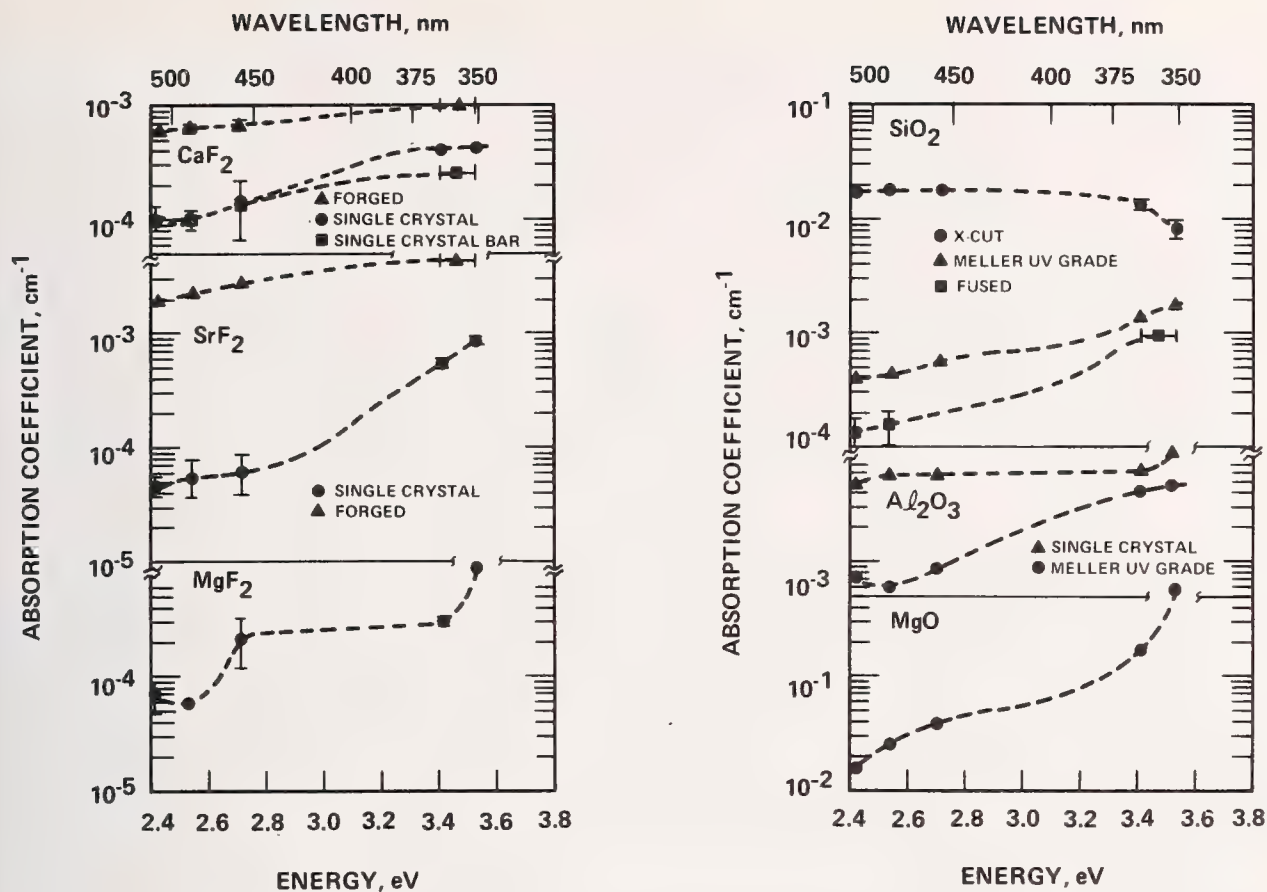


Figure 3. Calorimetric measurements of uv-visible absorption in alkaline earth fluorides and various oxides.

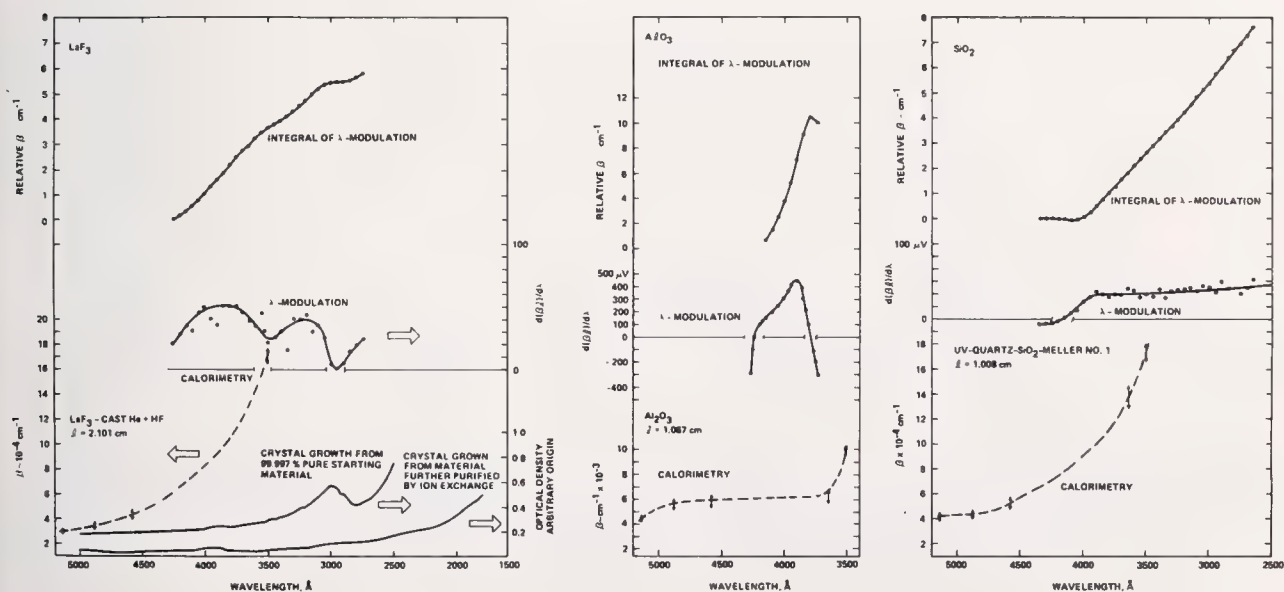


Figure 4. Absorption in LaF<sub>3</sub>, Al<sub>2</sub>O<sub>3</sub>, and SiO<sub>2</sub>.

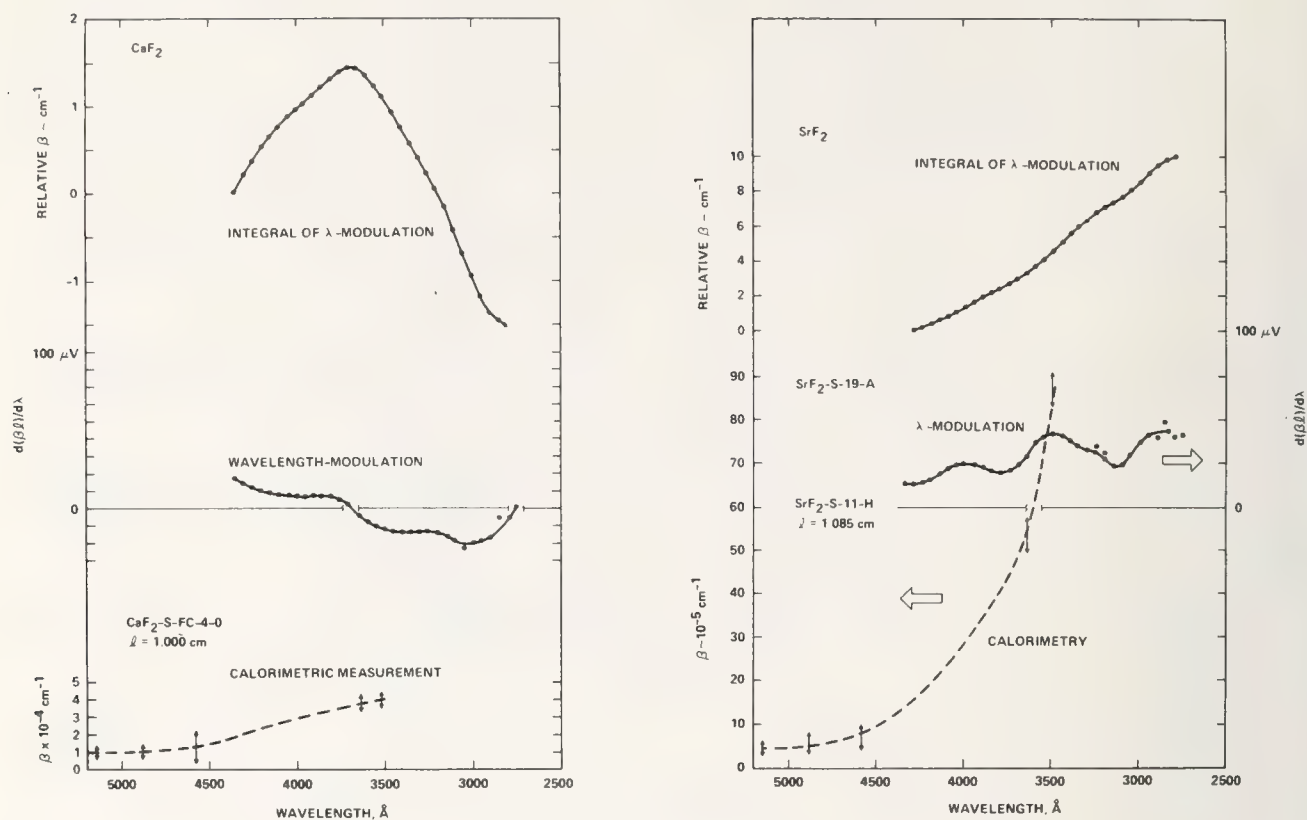


Figure 5. Absorption in  $\text{CaF}_2$  and  $\text{SrF}_2$ .

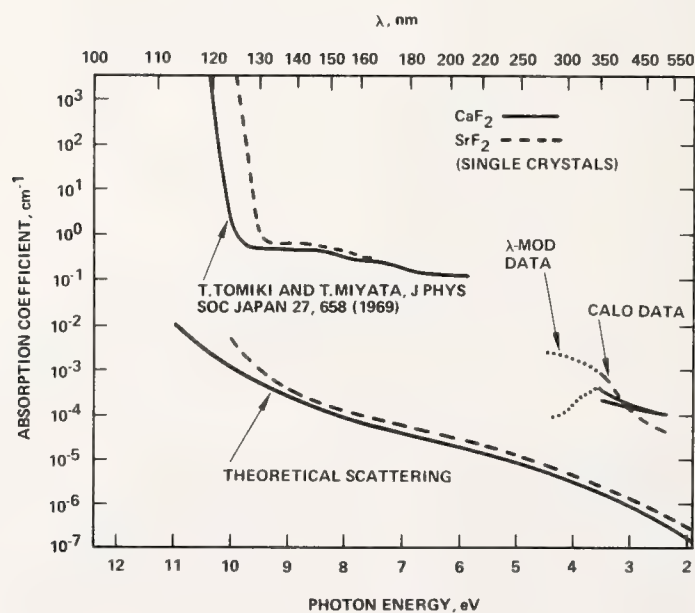


Figure 6. UV and visible absorption in  $\text{SrF}_2$  and  $\text{CaF}_2$ .



UV REFLECTANCE, TRANSMISSION, AND PHOTOLUMINESCENCE OF  $\text{LiYF}_4$ ,  
AND THE BULK LOSS COEFFICIENT IN  $\text{CaF}_2^*$

Victor Rehn, David L. Burdick, and Vernon O. Jones  
Physics Division, Michelson Laboratories  
Naval Weapons Center, China Lake, California 93555

Measurements have been made of the bulk loss coefficient in two  $\text{CaF}_2$  samples. The measurements were made between 200 and 400 nm using the prism technique. The results show a strong peak at 305 nm against a background loss of  $10^{-3}$  to  $10^{-2} \text{ cm}^{-1}$ . The peak is tentatively assigned to  $\text{Ce}^{3+}$ . In addition, VUV measurements of the transmission, reflectance, and photoluminescence of  $\text{LiYF}_4$  have been performed for the first time. The fundamental absorption edge is at 10.42 eV. The transmission and photoluminescence spectra show structure at 7.1, 8.0 and 8.6 eV.

Key words: Bulk loss coefficient;  $\text{CaF}_2$ ;  $\text{Ce}^{3+}$ ;  $\text{LiYF}_4$ ; photoluminescence; prism technique; reflectance; transmission.

Materials which transmit vacuum ultraviolet (VUV) radiation without coloration or degradation are in short supply. This is especially true for intense beams such as laser beams or beams of synchrotron radiation from large electron storage rings. Hence, it was a pleasant surprise to find that a new material, developed by Sanders Associates as a laser host, also has the third highest fundamental optical absorption edge energy among available optical materials. Here we report the first studies of the VUV transmission, reflectance and photoluminescence of  $\text{LiYF}_4$ . The transmission measurements show that the fundamental absorption edge is very sharp at about 10.42 eV (1190 Å). Both transmission and photoluminescence measurements show that the particular sample we have contains an appreciable impurity concentration. These impurities contribute to the absorption coefficient below the absorption edge, which diminishes from  $3 \text{ cm}^{-1}$  at 10 eV to  $0.1 \text{ cm}^{-1}$  at 5 eV. The reflectivity and transmittivity in the range 4 to 10.4 eV are used to deduce the optical constants for the polarization direction  $\hat{e} \perp \hat{c}$ . The reflectance spectrum is shown for the range 4 to 25 eV.

$\text{LiYF}_4$  forms in a tetragonal (scheelite or a-13) crystal structure with  $\text{Li}^+$  ions arranged among  $\text{YF}_4^-$  tetrahedra [1]<sup>1</sup>. Known physical properties include the density ( $3.99 \text{ g/cm}^3$ ), hardness (4 to 5 on Moh's scale), strength ( $3.3 \times 10^7 \text{ N/m}^2$ ) and Poisson's ratio (0.33) [2]. Optically, the crystal is clear and transparent from 0.21 to 10.4 eV (0.119 to  $5.88 \mu\text{m}$ ). It is uniaxial and birefringent, with  $(n_e - n_o)/n_o = 0.0153$  at  $2 \mu\text{m}$ , 0.0157 at  $0.5 \mu\text{m}$ , 0.0167 at  $0.3 \mu\text{m}$  and 0.0175 at  $0.25 \mu\text{m}$  [3]. The refractive index for the ordinary ray rises from 1.4424 at  $2 \mu\text{m}$  to 1.4567 at  $0.5 \mu\text{m}$  and 1.4754 at  $0.3 \mu\text{m}$ , slightly higher than the refractive index of  $\text{CaF}_2$ .

The sample [4] was cut from an undoped a-axis rod about 2-cm diameter by 15-cm long. The  $\hat{c}$  direction was marked by an unusual ridge along the side of the boule. The sample was oriented via x-ray Laue photographs with the  $\hat{a}$  and  $\hat{c}$  directions in the plane of the coin-shaped disc 1.56-mm thick x 2-cm diameter. It was mechanically polished on both sides using Syton [3] on a short-nap cloth as the final polish. The surface appeared smooth and shiny, but slightly rounded. Before mounting in the UHV reflectometer [5] the sample was rinsed in electronic grade acetone and electronic grade methanol, and blown dry with dry  $\text{N}_2$ . The sample was mounted with  $\hat{c}$  vertical. The measurements were carried out at the Stanford Synchrotron Radiation Project [6] using the  $8^\circ$  VUV beam line. The synchrotron radiation (SR) is 96 to 97% polarized in the horizontal direction as it emerges from the monochromator, so that the optical properties measured are characteristic of the "ordinary ray," for which  $\hat{e} \perp \hat{c}$ .

In figure 1 we compare the transmittivity of the sample with the photoluminescence excitation spectrum. The transmittivity remains high to 7 eV, above which there is a gradual reduction to about 50% at 10 eV, and then a sharp decrease to 10% at 10.42 eV. The gradual decline is marked by dips, most notably at 7.1, 8.0 and 8.6 eV. The photoluminescence excitation shows peaks at these same photon energies.

The photoluminescence emission was collected from  $1.8\pi \text{ sr}$  in the backward direction and focussed on a glass-fiber light pipe with a coating of sodium salicylate on the input end. The detector on the output end was an EMI 9514S photomultiplier. Hence, the spectral sensitivity for emitted photoluminescence extended from less than 2 eV to the soft x-ray region. No effort was made to narrow this spectral range. Photons scattered by the sample were eliminated from the photoluminescence response by electronically gating the photon counting system to accept photons only in the time period from 30 to 180 nsec after

\* Work supported by NWC Independent Research Funds, the Office of Naval Research, and Defense Advanced Research Projects Agency.

1. Figures in brackets indicate the literature references at the end of this paper.

the exciting light pulse. (The exciting light pulse is typically 0.3 nsec in duration.) In this way, the total effect of stray light and dark count contributed only 50 to 60 Hz (1 to 10%) of the counting rate in the photoluminescence spectrum. The spectrum shown in figure 1 has been approximately normalized to incident intensity, but because of uncertainties in phosphor efficiency, reflectance and scattering losses, pulse pile-up and the relatively slow response of the photomultiplier, the absolute luminescence yield shown is only an order-of-magnitude estimate. The relative yield across the spectrum is probably accurate to  $\pm 10\%$ .

Figure 2 shows the sample reflectivity in the 4 to 11 eV range, as well as the reflectance deduced from the transmittivity and reflectivity data. Figure 3 shows the absorption coefficient in this range as also deduced from the data of figures 1 and 2. In order to obtain the reflectance R and absorption coefficient  $\beta$ , the equations for transmittivity T and reflectivity R' of a plane-parallel plate of thickness d is incoherent radiation,

$$T = \frac{(1 - R)^2 \exp(-\beta d)}{1 - R^2 \exp(-2\beta d)} \quad (1)$$

$$R' + R = \frac{1 + (1 - 2R) \exp(-2\beta d)}{1 - R^2 \exp(-2\beta d)} \quad , \quad (2)$$

were combined into a quartic equation:

$$0 = a_4 y^4 + a_3 y^3 + a_2 y^2 + a_1 y + a_0 \quad , \quad (3)$$

where  $y \equiv \exp(-\beta d)$ ,  $a_0 = a_4 = -1/2$ ,  $a_1 = 1/T$ ,  $a_3 = 1 - (1 - R')/T^2$ . This equation was solved by successive approximations in which the  $y^4$  and  $y^3$  terms were ignored first, then evaluated with the first y value obtained from solution of the residual quadratic equation and added to  $a_0$  before solving the residual quadratic again. This procedure was very fast. With a programmable calculator about 10 successive approximations were made per second, and even with  $\beta d$  as small as .02, convergence to six significant figures was obtained within 200 successive approximations. As  $\beta d$  becomes larger, less and less approximations are necessary.

The reflectance, R, was obtained subsequently using the equation

$$R = \frac{Ay - 1}{Ay - y^2} \quad , \quad (4)$$

where  $A \equiv (1 - R')/T$ , obtained from eqs. (1) and (2) in a straightforward manner. Table 1 summarizes the optical constants implied by the R and  $\beta$  values of figures 2 and 3, compared with the previous results of ref. 3. Note that the  $k_0$  and  $\epsilon_2$  values are characteristic of this sample and probably not characteristic of pure  $\text{LiYF}_4$ .

The reflectance from 10 to 25 eV is shown in figure 4. Beyond 10.5 eV the sample is so opaque that no back-surface correction is necessary, and  $R = R'$ . The dashed portions of figure 4 near 12 eV and above 24 eV are regions where stray light or second-order problems reduce the accuracy of the data. In the 12 eV region the problem is mainly second-order, which could not be filtered out by any available filter. Above 24 eV the component of stray long-wavelength radiation becomes a significant fraction of the monochromatic radiation.

#### Bulk Loss Coefficient Measurements in $\text{CaF}_2$

We have made preliminary measurements of the total bulk loss coefficient of two  $\text{CaF}_2$  samples over the spectral range from 400 to 210 nm. The measurements were performed at the Stanford Synchrotron Radiation Laboratory in order to utilize the highly collimated monochromatic radiation available there on the 8° beam line.

The measurement technique is based upon the use of prism-shaped samples. This technique has been developed with both a double-beam configuration [7] (for differential measurements) and a single-beam version. A schematic diagram of the single-beam system is shown in figure 5; this is the method used at Stanford Synchrotron Radiation Laboratory for the preliminary  $\text{CaF}_2$  measurements.

Referring to figure 5, the beam passes through a  $\text{BaF}_2$  splitter, a tuning fork chopper, and the sample. After reflecting from the mirror it retraces its path and proceeds to the photomultiplier tube. The prism-shaped sample is placed on a translation stage such that it can be translated parallel to the bisector of the prism angle, and so that the radiation is incident at the angle of minimum deviation. This latter requirement prevents the beam from moving about on the mirror as the sample is translated.

The data analysis for the single-beam experiment is relatively simple. Let  $I(t)$  be the intensity at the detector as a function of the beam path length in the sample. Then



$$I(t) = I_0 G(1 - R_1 - A_1 - S_1)^2 (1 - R_2 - A_2 - S_2)^2 e^{-2\beta t} \quad (5)$$

where R, A, and S are the surface reflectivity, absorption, and scatter coefficients. We assume that the two polished surfaces are uniform but not necessarily identical; hence, the subscripts "1" and "2". G is a factor which accounts for all the properties of the other optical elements, such as back-mirror reflectivity, beam splitter reflectivity, and so on.  $\beta$  is the bulk loss coefficient, composed of absorption and scatter. In highly transparent materials  $\beta t \ll 1$ ; therefore, to first order we find that

$$\beta = -\frac{1}{2} \frac{1}{I_0 G(1-R_1-A_1-S_1)^2 (1-R_2-A_2-S_2)^2} \frac{dI}{dt} \quad (6)$$

Both  $dI/dt$  and the denominator in eq. (2) are directly measurable. Note that the surface parameters need not be measured as they are eliminated by ratioing. Variations in  $I_0$  are eliminated by real-time ratioing of the photomultiplier output to the storage ring current, a quantity directly proportional to  $I_0$ .

The bulk loss coefficients calculated from eq. (1) are shown in figures 6 and 7. The curves drawn through the experimental points are least-squares fits to all but the points on the large peak at 305 nm. These curves have an approximate wavelength dependence of  $\lambda^{-2.5}$ .

In spite of the diverse origins of the two samples, the similarity of the spectra is striking. The Raytheon material shows slightly lower losses overall. Based on the 305-nm peak, the tentative identification of the impurity responsible is  $Ce^{3+}$ . The spectra of rare-earth ions in  $CaF_2$  have been extensively studied by Loh [8,9]. Loh has observed the lowest  $4f \rightarrow 5d$  absorption band of  $Ce^{3+}$  in  $CaF_2$  to be located at 307 nm; the analogous bands in the remaining rare-earths are at shorter wavelengths (the next closest is  $Pr^{3+}$  at 219 nm). The increase in absorption observed in figures 6 and 7 as one goes to wavelengths shorter than 305 nm may be due to the  $4f - 5d$  transition associated with clusters of  $Ce^{3+}$  ions. In an interesting experiment on the concentration dependence of  $4f - 5d$  absorption due to  $Ce^{3+}$  in  $CaF_2$ , Loh finds peaks between 250 to 210 nm which he assigns to the  $4f - 5d$  transition of clustered  $Ce^{3+}$  ions. He found that as the concentration of  $Ce^{3+}$  increased, the 307-nm band decreased in intensity while the higher energy clustered ion band increased. This suggests that  $Ce^{3+}$  prefers to cluster rather than to exist as isolated ions.

#### References

- [1] Shand, W. A., J. Crystal Growth (Netherlands) 5, 143 (1969).
- [2] Folweiler, R. C. *et al.*, Report #1-1413-76-L-1025A, Sanders Associates, Inc., July 1976.
- [3] Castleberry, D. E. and Linz, A., Appl. Opt. 14, 2056 (1975).
- [4] We are grateful to R. C. Folweiler of Sanders Associates for supplying us with samples. Mr. Folweiler has informed us that no special precautions were taken to make an especially pure crystal.
- [5] The UHV absorption/reflectance/scattering reflectometer was designed and built by J. L. Stanford, Naval Weapons Center.
- [6] Supported by NSF Grant No. DMR73-07692 in cooperation with SLAC and ERDA.
- [7] Burdick, D. L., Rehn, V., Kyser, D. S. and Jones, V. O., in *High Energy Laser Mirrors and Windows*, Semi-Annual Report No. 6, Sept. 1974-March 1975, DARPA, Order #2175, pp. 32-101.
- [8] Loh, Eugene, Phys. Rev. 147, 332 (1966).
- [9] Loh, Eugene, Phys. Rev. 154, 270 (1967).



TABLE 1. Optical Constants for the Ordinary Ray  
( $\hat{e} \perp \hat{c}$ ) in the Range 4 - 10.4 eV.

$h\nu$	$\lambda$	$n_o$		$k_o \times 10^7$ $\pm 1.0$	$\epsilon_1$ $\pm 0.009$	$\epsilon_2 \times 10^7$ $\pm 2.1$
		$\pm 0.004^a$	$\pm 0.0002^b$			
4.00	3100	1.472		2.6	2.165	7.7
4.133	3000	1.473	1.4754		2.170	
4.50	2755	1.479		2.3	2.187	6.8
4.959	2500	1.487	1.4895		2.210	
5.00	2480	1.487		2.1	2.212	6.3
5.50	2254	1.497		2.8	2.241	8.4
5.510	2250	1.498	1.5014		2.242	
6.00	2066	1.506		3.4	2.269	10.2
6.50	1907	1.521		4.4	2.316	13.4
7.00	1771	1.540		6.9	2.372	21.3
7.50	1653	1.565		8.5	2.449	26.6
8.00	1550	1.604		13.7	2.573	44.0
8.50	1459	1.660		18.0	2.756	60.0
9.00	1378	1.724		22.4	2.972	77.0
9.50	1305	1.796		25.4	3.226	91.0
10.00	1240	1.883		27.7	3.546	104.0
10.20	1216	1.937		33.2	3.752	128.0
10.40	1192	2.080		124.0	4.326	516.0

<sup>a</sup> This work.

<sup>b</sup> Ref. 3.

Figures

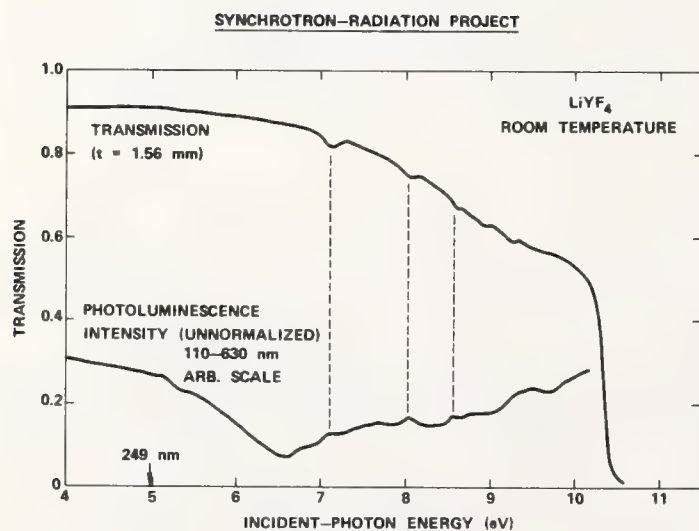


Figure 1. Transmission and photoluminescence spectra of  $\text{LiYF}_4$  showing correspondence between the structure in each spectra.

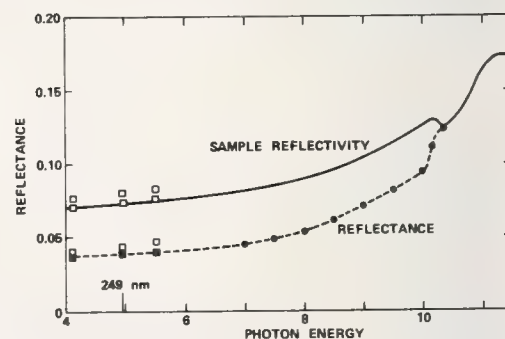


Figure 2. Reflectivity and reflectance of  $\text{LiYF}_4$ .

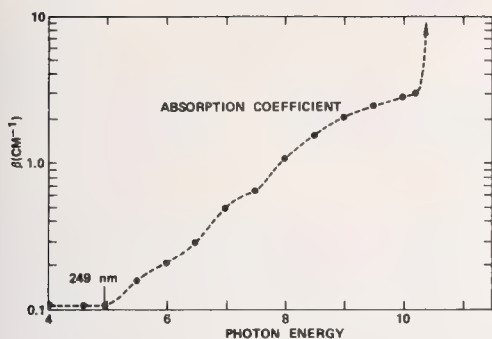


Figure 3. Absorption coefficient of  $\text{LiF}_4$  as deduced from the data in figures 1 and 2.

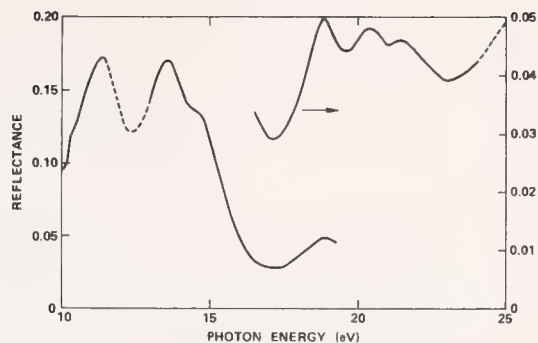


Figure 4. Reflectance of  $\text{LiF}_4$  from 10 to 25 eV. The dashed portions are regions where stray light or second-order effects reduce the accuracy of the data.

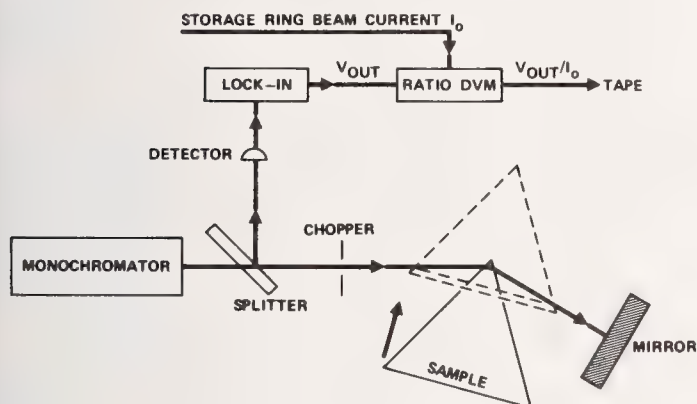


Figure 5. Single-beam version of the prism technique. Highly collimated light passes through the prism-shaped sample at the angle of minimum deviation.

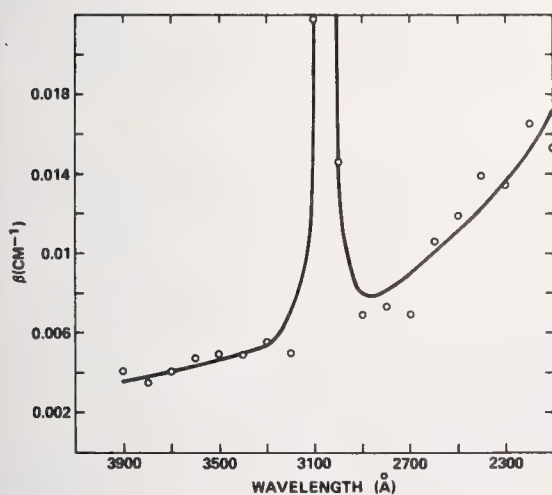


Figure 6. Absorption coefficient of Harshaw  $\text{CaF}_2$ .

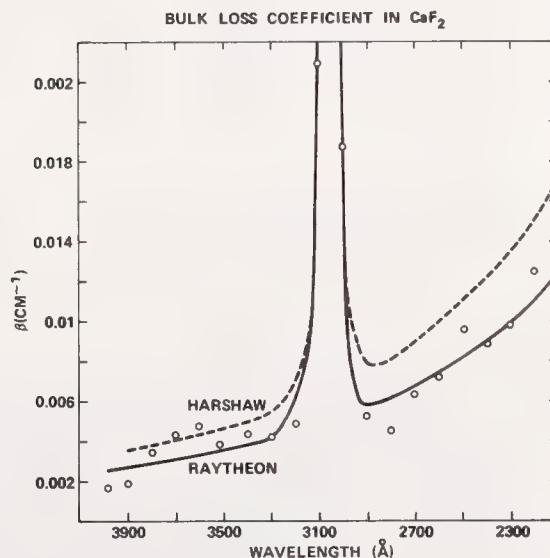


Figure 7. Absorption coefficient of Raytheon  $\text{CaF}_2$  (circles) with that of Harshaw  $\text{CaF}_2$  superimposed as a dashed line. The large peak at 305 nm may be due to  $\text{Ce}^{3+}$  ions.

P. A. Temple and D. L. Decker  
Physics Division, Michelson Laboratories  
Naval Weapons Center, China Lake, California 93555

The absorptances of  $\text{MgF}_2$ ,  $\text{SrF}_2$  and  $\text{CaF}_2$  have been measured at 0.351 to 0.364  $\mu\text{m}$ . The absorptance is found to increase with each successive absorptance measurement due to sample coloring by the 351 to 364 nm beam. This is found to be linear with  $\int P dt$  for a given beam diameter over the power range tested. Increases in absorption of nearly two orders of magnitude to  $1 \times 10^{-1}$  were seen after a total central beam fluence of  $3.5 \times 10^6 \text{ J/cm}^2$ . Under the beam and sample configuration used all three materials were found to have an absorptance of approximately  $1 \times 10^{-2}$  after approximately  $3.5 \times 10^5 \text{ J/cm}^2$  had been incident upon the sample. Possible absorption mechanisms will be discussed, including photochemically generated polymer films, impurities, and color centers.

Key words: Alkaline earth fluorides; color centers; laser calorimetry; photochromic; polymer films.

## 1. Introduction

This work was done on the Naval Weapons Center high sensitivity adiabatic calorimeter to be described in another paper [1]<sup>1</sup>. In this instrument the sample is in thermal equilibrium with its surroundings (a temperature-controlled can) and calibration is accomplished by observing the temperature rise of the sample after laser irradiation and comparing it to the temperature rise caused by the deposition of a precise amount of electrical energy. By using this technique it is not necessary to know the mass or specific heat of the sample [1]. The light source was the undispersed UV output of a Spectra Physics 171-19 argon ion laser. The two predominant lines are at 351 and 364 nm. For all these measurements the power was limited to 50 mW and all exposures were for a period of 100 seconds. This gave a total incident energy per exposure of 5 J. The Gaussian beam was condensed by two long focal length lenses to a  $1/e^2$  full width of 0.190 mm at the sample position [2]. The power density in the center of this beam was then  $350 \text{ W/cm}^2$  and the energy fluence per exposure was  $3.5 \times 10^4 \text{ J/cm}^2$ . All samples were 1-cm thick.

## 2. Experimental

The materials investigated were  $\text{CaF}_2$ ,  $\text{MgF}_2$  and  $\text{SrF}_2$ . The  $\text{CaF}_2$  and  $\text{SrF}_2$  were prepared by Raytheon using a reactive atmosphere process and had very low absorptance at 3.8  $\mu\text{m}$ . The  $\text{MgF}_2$  was purchased from Optovac. The raw data for  $\text{SrF}_2$  are shown in figure 1. Each data point represents a 5-J exposure. The figure shows the temperature rises for 13 successive exposures at a fixed point on the sample. The step changes in temperature are the result of individual 100-sec laser exposures. The horizontal portions are equilibration times between laser exposures during which the sample came into equilibrium with the surroundings. This figure shows the successively larger temperature rises for equal laser exposure, indicating that the absorptance is increasing with each measurement.

As seen in the lower left of figure 1, the uncolored absorptance of the sample is small, and is bracketed between zero and  $1 \times 10^{-3}$ . This uncolored absorptance is consistent with the data reported by Rehn *et al.* at this conference [3].

Figure 2 shows the data in figure 1 on a log-log plot. The solid line has a slope of 1. The data follow this line closely, indicating that the absorptance is directly proportional to the fluence in the range investigated.

Figure 3 shows the absorptance of  $\text{CaF}_2$ , and figure 4 shows the absorptance of  $\text{MgF}_2$ . The higher dose points in figures 2 and 3 were obtained by a factor of 10 higher power exposure ( $1/2 \text{ W}$ ) for the appropriate period of time to obtain the indicated dose. The absorptance was then measured in the usual way with 0.050 W power for 100 sec. The linear increase in absorptance, within experimental accuracy, indicates that the sample darkening is proportional to fluence or total incident energy, that is  $\int P dt$ , rather than power. The coloring rate is assumed to be proportional to the local intensity  $I$ . If this is true, it can be shown rigorously that the measured absorptance is inversely proportional to the beam area when the beam is Gaussian. Therefore, these data were all measured with the same beam diameter in order to retain the same relationship between total power and central beam intensity.

\* Work supported by Defense Advanced Research Projects Agency.

1. Figures in brackets indicate the literature references at the end of this paper.



Figure 3 contains points gathered the next day. These data indicate there had been no loss in absorbance of the sample over that time period.

For the three materials shown in figures 2, 3 and 4, the absorbance after 20 exposures, or  $7 \times 10^5$  J/cm<sup>2</sup> fluence, are shown in table 1.

Table 1. Window absorbances after 20 exposures.

CaF <sub>2</sub>	$2.7 \times 10^{-2}$
MgF <sub>2</sub>	$2.2 \times 10^{-2}$
SrF <sub>2</sub>	$2.0 \times 10^{-2}$

### 3. Discussion

Two possible fluence-dependent absorption mechanisms will be discussed. They are photochemical production of an absorbing polymer film and the generation of bulk absorbing sites due to impurity atoms or vacancy-related sites (color centers).

#### 3.1 Polymer Films

The growth of polymer films on plasma tube windows by UV-activated crosslinking of monomers is well known in the laser industry [4]. These films are the result of an in situ photochemical reaction on the window surface and are not directly related to prior cleaning procedure. If organic impurities are present in the plasma tube the action of ion and UV bombardment results in a slow degradation of the output due to this film production [4].

The pressure in the calorimeter during these measurements was  $4 \times 10^{-6}$  torr. The system is ion pumped. There is a limited amount of organic material present in the system, including methane from the ion pump. While data do not exist on the growth rate of such films, it is possible that there is sufficient organic material present to cause the generation of absorbing polymer films. The fluence dependence of the absorbance is consistent with film growth, if one assumes a linear growth rate with incident energy.

#### 3.2 Impurity and Color Center Absorption

As noted in a recent compilation by Sparks [5], there are a large number of atomic impurity species which give rise to absorption in the UV. In addition, various color center bands exist in the UV. Color centers are generally associated with charge trapped at lattice vacancy sites.

Concerning the growth of absorption with dose, while lattice displacements would probably result in the generation of color center sites, it is unlikely that atomic displacements can be caused by the  $\sim 3.5$  eV photon beam. However, color centers may also be "activated" by the transfer of charge from impurity atoms to already existing lattice vacancies. Photons of 3.5 eV are quite capable of such charge transfer as color center bleaching experiments have shown [6]. In addition, charge transfer can take place between various impurity species, resulting in the growth of absorption bands with dose. As notes by Sparks, if the oscillator strength is high, even ppb impurity concentrations can result in absorption coefficients as high as  $10^{-1}$ .

#### 3.3 Implications

The data shown above have serious implications to large laser behavior. For example, a laser of 10 MW/cm<sup>2</sup> power density, 1  $\mu$ sec pulse length, and 1 kHz repetition rate has a fluence of 10 J/cm<sup>2</sup> per pulse, or a fluence of  $10^4$  J/cm<sup>2</sup> per minute. With windows of CaF<sub>2</sub> behaving as shown in figure 4, the window absorbance will have risen to  $2 \times 10^{-2}$  in 70 sec of operation.

Similar results have been observed empirically by Tachisto, Inc., who market a commercial UV laser with an output power density of approximately 5 MW/cm<sup>2</sup> with a total flux of 1000 J/hr [7]. CaF<sub>2</sub> has been used as a Brewster window material. The beam dimension is 0.4 cm x 1.5 cm which results in a Brewster window dose per unit area of approximately  $8 \times 10^5$  J/cm<sup>2</sup> in 100 hr of operation (assuming the output coupler has  $R = 0.7$ ). Typically, 100 hr of use results in a drop in output of 20%. This is equal to a Brewster window absorbance of  $7 \times 10^{-2}$ . This is quite similar to the darkening with fluence observed in the work reported here. It must be kept in mind, however, that there are tremendous power density differences between the Tachisto device and that repeated here, and that the lack of dependence on power which we report here was shown to be true over a limited power range. In addition, other coloring mechanisms may be acting in the Tachisto laser where the window is exposed to hard UV, electrons, and x-rays.

### 4. Conclusion

By proper calorimeter beam conditioning we have simulated the photon fluence anticipated in larger laser systems. We report here the observation of a fluence-dependent absorption coefficient in CaF<sub>2</sub>,

$\text{SrF}_2$  and  $\text{MgF}_2$  at 351 to 364 nm. Material exhibiting the fluence-dependent behavior discussed above would be unsatisfactory for laser window material. We have discussed two possible darkening mechanisms, polymer films and impurity or color centers. If the absorption is due to polymer film production it should be possible to reduce the effect by appropriate care. If the absorption is due to impurity or color center sites, on the other hand, it will be necessary to determine the precise nature of the absorption and then to reduce the concentration of the offending species.

## 5. References

- [1] Decker, D. L. and Temple, P. A., "The Design and Operation of a Precise, High Sensitivity Adiabatic Laser Calorimeter for Window and Mirror Material Evaluation," this conference.
- [2] Yashida, A. and Asakura, T., in *Optics and Laser Technology* (December 1976), p. 273.
- [3] Rehn, V., Burdick, D. L. and Jones, V. O., "UV Reflectance, Transmission and Photoluminescence of  $\text{LiYF}_4$  and Bulk Loss Coefficient in  $\text{CaF}_2$ ," this conference.
- [4] Wright, Dave, Spectra Physics, Inc., Mountain View, California. Private communication.
- [5] Sparks, M., Vora, H. and Flannery, M., *Tabulation of Impurity Absorption Spectra--Ultraviolet and Visible*, Vol. 1, 9th Technical Report, June 1977, Defense Supply Service, Washington, DC.
- [6] Schulman, J. H. and Compton, W. D., *Color Centers in Solids* (Pergamon, New York, 1963).
- [7] Chase, Charles, Techisto, Inc., Needham Heights, Massachusetts. Private communication.

## 6. Figures

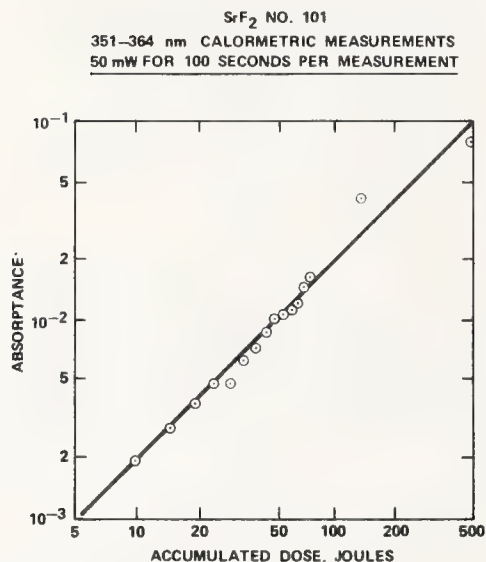


Figure 1. Calorimetric data for  $\text{SrF}_2$  No. 101 at 351 to 364 nm showing the increase in absorptance with each successive exposure. Thirteen individual absorptance measurements are shown. The vertical scale is an arbitrary temperature scale.

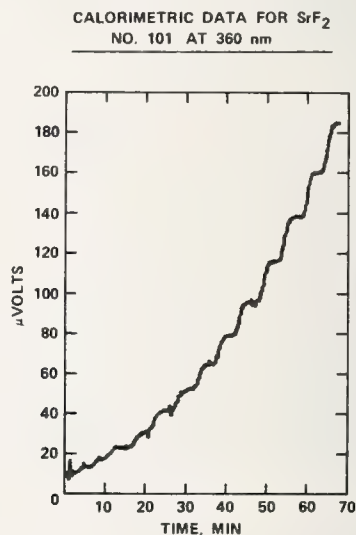


Figure 2. The 351 to 364 nm absorptance of  $\text{SrF}_2$  No. 101 as a function of total incident energy.

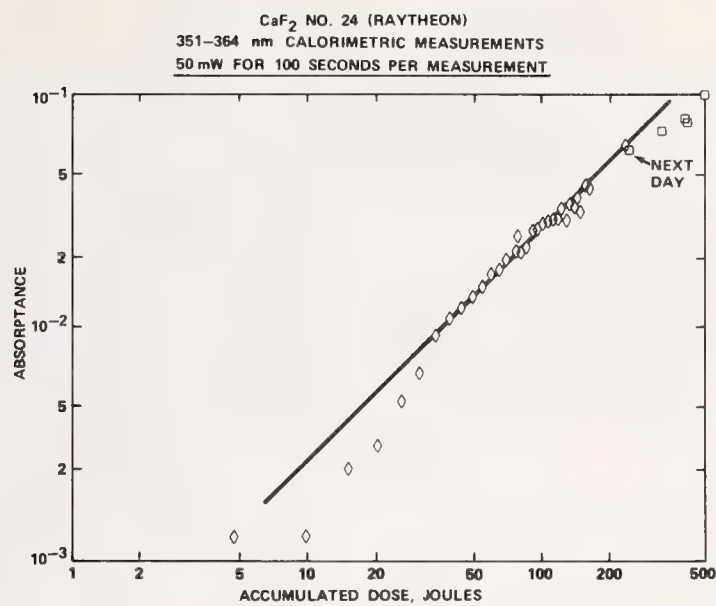


Figure 3. The 351 to 364 nm absorbance of CaF<sub>2</sub> No. 24 (Raytheon) as a function of total incident energy.

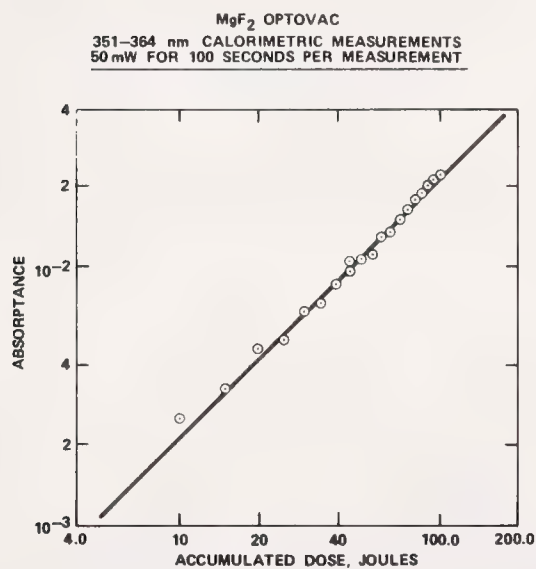


Figure 4. The 351 to 364 nm absorbance of MgF<sub>2</sub> (Optovac) as a function of total incident energy.



#### COMMENTS ON PAPER BY TEMPLE AND DECKER

The discussion in this paper centered around the question of whether a polymer film on the surface of the sample or color centers in the bulk of the sample was responsible for the observed absorption. It was noted that polymer films which could lead to such an absorption are well known in synchrotron radiation studies and are due to the polymerization of hydrocarbon compounds into heavy hydrocarbons. A similar formation of a film is seen in laser tubes where a large amount of ultraviolet radiation from the laser discharge is present. Bulk coloring is seen in the Brewster angle windows used in many gas lasers, especially in quartz windows. In the experiments described in this paper the spot size was very small, approximately a tenth of a millimeter in diameter. It was very difficult therefore to take the sample out of the apparatus, make a parallel investigation, and then replace it in exactly the same location. This prevented any investigation of the effect of annealing, which would indicate that the discoloration was due to color center formation. The speaker described the effect as permanent, that is, that no reduction in the attenuation was seen over a period of several days. He indicated that experiments to determine whether or not the attenuation was reduced by annealing would be carried out in the near future.

## SURFACE STATISTICS OF SELECTED OPTICAL MATERIALS\*

Jean M. Bennett and J. Merle Elson  
Physics Division, Michelson Laboratories  
Naval Weapons Center, China Lake, California 93555

In order to understand and predict the scattering properties of laser mirrors and windows, it is necessary to know the statistical properties of the surface microroughness. The rms roughness of the surface determines the total integrated scattering, while the slopes of the surface irregularities determine the autocovariance function and hence the angular dependence of the scattered light. The rms roughness, rms slope, height and slope distribution functions and autocovariance function have been measured for materials of interest in infrared, visible, and ultraviolet laser applications. These include fused quartz, molybdenum, potassium chloride, copper, and silicon carbide. Variations between the statistics of different samples of the same material as well as between samples of different materials have been found. The calculated scattering to be expected from different samples will be discussed and related to that measured for some samples.

Key words: Mirrors; scattering; surface roughness; surface statistics.

### 1. Introduction

Scattered light from the surfaces of laser optical components can arise from various sources: (1) Defects whose dimensions are large compared to the wavelength of light give rise to so-called macro-scattering, which is governed by the laws of geometrical optics. (2) Isolated defects whose dimensions are comparable to the wavelength of light can be considered as dipole scatterers whose scattering characteristics are predicted by Mie (dipole) scattering theory. (3) Microirregularities whose heights are small compared to the wavelength of light produce scattering which is predicted by diffraction theory. (4) From certain types of rough metal surfaces, for example, silver and aluminum, there can be radiative excitation and subsequent decay of surface plasmons yielding second-order light scattering. Although all of these sources of scattered light are important, the most prevalent source is (3) because all surfaces have some sort of microirregularities remaining from the finishing process, whether it be mechanical polishing, diamond turning, electropolishing, chemical polishing, ion polishing, or some other process. These microirregularities are distributed over the entire surface and hence contribute a larger fraction of the scattering, particularly in the visible and ultraviolet, than do isolated surface defects such as scratches, digs, dust particles, etc. We are attempting to find ways to predict the scattering from an optical component based on knowledge of its surface statistics. The theory relating total integrated scattering (TIS) to surface statistics has proven to be valid in many cases, and the advantages and limitations of this theory will be discussed. In order to predict the angular distribution of scattered light, more information about the surface statistics is necessary, and the theory is much more difficult. Progress is being made in this area, some of which will be discussed in this paper. Finally, examples will be given of some of the wide variety of surface statistics which can occur on optical surfaces.

### 2. Total Integrated Scattering

Figure 1 gives a schematic representation of scattering from a rough surface. The incident beam is assumed to be normal (or nearly normal) to the surface and the specular beam is in the appropriate direction so that the angle of reflection equals the angle of incidence. The rest of the light is scattered in all directions by the surface. For smooth but wavy surfaces the scattered light peaks about the specular direction; rougher or matte surfaces scatter the light more equally in all directions. For surfaces whose roughness is small compared to the wavelength and whose height distribution is Gaussian, the TIS into a hemisphere is related to the rms roughness of the surface by the simple relation [1]<sup>1</sup> shown in figure 1. Most polished surfaces satisfy this relation and have height distribution functions similar to that shown in the upper left of figure 2. (In this type of presentation the histogram is obtained from the measured height data. The length of each bar represents the fraction of the total number of surface features which have heights equal to the value given on the abscissa, which is measured relative to the mean surface level (dashed vertical line). The smooth Gaussian curve encloses the same total area and has a half width derived from the measured rms roughness of the surface.) Some very soft materials such as polished KCl have proportionately too many large bumps or deep scratches. This distorts the measured histogram (upper right of fig. 2), putting too much contribution in the tails. The influence of the extrema on the surface makes the rms roughness proportionately too large,

\* Work supported by NWC Independent Research Funds and Defense Advanced Research Projects Agency.

1. Figures in brackets indicate the literature references at the end of this paper.



so the half width of the Gaussian is also too large and the Gaussian does not fit the measured histogram. For surfaces of this sort, the agreement between measured values of the rms roughness and those calculated from TIS measurements is not very good. TIS-derived values tend to be higher. Relatively few surfaces have the problems illustrated by the histograms shown in the lower part of figure 2. If a surface is extremely smooth but has rather large dust particles on it, one can obtain a distorted height distribution histogram with the maximum shifted to negative values (because the particles have influenced the placement of the mean surface level). Similarly, an etched or pitted surface which is nominally smooth but has deep holes in it can have a distorted histogram with the peak shifted in the other direction. Neither of these two types of surfaces would satisfy the assumptions in figure 1 and hence the simple relation between TIS and rms roughness would not be expected to hold.

Fortunately, most surfaces have gaussian height distribution functions and in this case it makes sense to talk about an rms roughness for the surface. In figure 3 are shown the range of rms roughnesses, mostly derived from TIS measurements, which have been measured for polished optical surfaces. In all cases it is easy to obtain larger roughnesses, but reducing the lower limit is much more difficult. (In the case of KCl, there is such a wide range of roughnesses that the difference between the value measured directly and that derived from TIS measurements is relatively insignificant.)

Two unusual height distribution functions have been obtained from polished molybdenum and TZM samples [2], and are shown in figure 4. The molybdenum sample on the left had a smooth but wavy surface with a predominance of small bumps and absence of small holes. The TZM sample on the right had the only bimodal height distribution we have seen with a relative absence of surface features whose heights were very close to the mean surface level.

### 3. Angular Scattering

Figure 5 shows the relation [3] between the scattering per unit solid angle  $dP/d\Omega$  as a function of wavelength  $\lambda$ , the optical constants of the mirror surface (given in terms of the dielectric constants  $\epsilon_1$  and  $\epsilon_2$ ), the scattering angle  $\theta$ , the rms roughness  $\delta$ , and the spectral density function  $g(k)$ , which is the Fourier transform of the autocovariance function measured for the surface. The autocovariance or autocorrelation function of the surface roughness is a measure of the average relationship between two values of surface height separated by a finite distance. If the two surface height values are sufficiently separated so as to be completely independent, then the autocovariance function is zero for that separation distance. As the separation distance decreases, eventually one value of the surface height will be influenced by the value of the other; then they are correlated. The autocovariance function has argument  $\rho$ , the separation distance, and as  $\rho$  approaches 0 the surface heights become completely correlated. The autocovariance function is defined in a mathematical manner elsewhere [3]. In the relation for  $dP/d\Omega$  given in figure 5, we are assuming that the light is normally incident and polarized, and that the scattered light is measured in the plane perpendicular to the direction of polarization of the incident beam. Note that the expression for  $dP/d\Omega$  is composed of two parts: an optical factor which is a function only of wavelength, optical constants of the material and scattering angle, and a surface factor which contains the statistical properties of the surface. In figure 5 the optical factor is plotted for a silver-coated mirror for three selected laser wavelengths. The separation between the curves is caused by the  $\lambda^{-4}$  wavelength dependence, while the curling over of each curve at large scattering angles is caused by the  $\cos^2\theta$  term in the numerator. The entire shape of each optical factor curve is primarily determined by the above-mentioned  $\cos^2\theta$  term. Since the contribution from the optical factor is nearly constant for scattering angles from  $0^\circ$  to about  $60^\circ$ , all the variation in the angular scattering is caused by the contribution from the surface structure by way of the spectral density function,  $\delta^2g(k)$ . A typical curve of a spectral density function for polished fused quartz is shown in the lower right of figure 5. Here  $\delta^2g(k)$  is plotted versus  $k$ , the net change in the wave vector component along the surface between the incident and scattered photon. For normal incidence an incoming photon has no wave vector component parallel to the surface and therefore  $k$  in this case represents the wave vector component, parallel to the surface, of the scattered light. Since  $k = (2\pi/\lambda)\sin\theta$ , the value of  $\delta^2g(k)$  can be obtained for any wavelength and scattering angle from the curve. The dashed line marked FECO limit is the upper limit of  $k$  values for which  $\delta^2g(k)$  can be obtained from interferometric measurements.

The calculated values of angular scattering are shown for three laser wavelengths in figure 6. These curves are products of the curves shown in figure 5. The vertical separation between the curves comes from the  $\lambda^{-4}$  term, while the variation in the shapes of the curves for angles from  $0^\circ$  to about  $60^\circ$  is caused by the spectral density function. For larger scattering angles the downward curl is caused by the downward curl in the optical factor curves.

From the curves in figures 5 and 6, it is clear that the measured surface statistics form the most important part of the calculations of the angular scattering. Hence it is appropriate to look more closely at the different types of spectral density functions produced by surfaces having different types of statistics. In figure 7 are shown the three basic constituents of surface structure: short range random roughness, long term waviness, and periodicity. The short range random roughness is the predominant type on most polished surfaces and produces a large initial spike on the autocovariance function. This is because the features on the surface are uncorrelated and the only correlation is between points on a given feature (bump or hole). The Fourier transform of this type of autocovariance



function is slowly varying with no initial spike, and produces the type of scattering curve shown in the lower center of figure 7. Waviness on a surface produces an autocovariance function with a much larger correlation distance (zero intercept). The spectral density function and angular scattering curves both show a very large spike for small  $k$  values and scattering angles. Periodicity in a surface produces an oscillatory autocovariance function and a spike in the angular scattering curve at the scattering angle corresponding to the relation  $\sin\theta = \lambda/\tau$ , where  $\tau$  is the spacing between features on the surface. This relation is a special case of the grating equation for normally incident light and first-order diffracted light. For a periodic surface whose contour is close to a sine wave and whose amplitude is small compared to  $\lambda$ , such as the one shown, the second- and third-diffracted orders are essentially completely suppressed, even though the first-order is very strong [4].

If a surface having short range random roughness is considered to be composed of many periodic components of different amplitude, spacing, and phase [4], one can calculate the separation of surface features that will produce scattering at a particular angle and wavelength. This information, obtained from the grating equation for normal incidence illumination, is contained in the nomogram in figure 8. The dashed lines show an example of how to use this nomogram: features which produce scattering at  $5^\circ$  from the specular direction at a wavelength of  $0.5\text{ }\mu\text{m}$  have separations of about  $5.7\text{ }\mu\text{m}$ . This nomogram emphasizes that for a particular wavelength, scattering between  $1^\circ$  and  $90^\circ$  can only be produced by features on the surface having a finite range of separations whose ratio is less than 60. For example, scattering between the angles of  $1^\circ$  and  $90^\circ$  at a wavelength of  $0.5\text{ }\mu\text{m}$  is produced by surface features having separations ranging from  $0.5\text{ }\mu\text{m}$  ( $d = \lambda$ ) to  $29\text{ }\mu\text{m}$ . Thus, evaporated films which consist of particles having diameters in the  $400$  to  $1000\text{ }\text{\AA}$  range should not affect the angular scattering in the visible. Generally, the evaporated film contours the underlying substrate, so that the scattering is produced by features on the substrate having larger separations.

#### 4. Measured Surface Statistics

Based on the results of the preceding section, surface statistics should be measured with an instrument having a lateral resolution adequate to detect surface features which produce scattering at the desired wavelength and scattering angle. At Michelson Laboratory the instrumentation available for the measurement of surface statistics includes a scanning interferometer employing multiple beam fringes of equal chromatic order (FECO) [5], a profilometer with a diamond stylus [6], and stereo electron microscopy [7]. The height sensitivity and lateral resolution of these various instruments is given in figure 9 along with the maximum length on the surface for which statistical information can be obtained at one time. Stereo electron microscopy is useful when one is considering angular scattering in the vacuum ultraviolet and x-ray regions. Conversely, FECO interferometry is useful chiefly for predicting microirregularity scattering in the infrared and near-angle scattering in the visible. In the infrared, microirregularity scattering from many surfaces is so small that other scattering mechanisms, for example, dipole scattering from isolated particulates, dominate. Thus, the Talystep profilometer currently seems to be the best tool for measuring statistics of surfaces whose irregularities produce scattering in the visible and ultraviolet. The remainder of this paper will be devoted to a discussion of statistics for various types of surfaces.

##### 4.1 Fused Quartz

One might think that the surface statistics for a given material might be quite similar for different types of surface preparation. That this is not so is well illustrated by polished fused quartz. The surface profiles range from the smooth but wavy type for a bowl feed polished [8] surface to the type with short range random roughness for a normal fresh feed polished surface. The former type of surface profile produces an autocovariance function such as that shown in figure 10 (also, fig. 7, left-hand column), while the latter type has an autocovariance function such as that shown in figure 11 (and fig. 7, center column). All variations in between are possible and have been observed, including an extremely smooth fresh feed polished surface that was wavy and had very fine polishing scratches. All of these polished fused quartz surfaces had normal Gaussian height (and slope) distribution functions, such as that shown in figure 2, upper left.

The measured and calculated angular scattering curves for the two silvered polished fused quartz surfaces whose autocovariance functions were shown in figures 10 and 11 are shown in figure 12. The measured and calculated curves for the rougher, fresh feed polished surface were matched in the  $20$  to  $40^\circ$  range of scattering angles, but no other adjustments were made. The agreement between theory and experiment is encouraging, but not yet quantitative. In particular, it appears that there may be another unaccounted for scattering mechanism operating in the case of the smoother bowl feed polished sample. One possibility is dipole scattering from isolated particulates such as dust on the surface which may increase the entire scattering level without drastically affecting the shape of the scattering curve.

##### 4.2 Molybdenum and TZM

Molybdenum [2] and one of its alloys, TZM (containing titanium and zirconium) [2], have quite interesting surface statistics and predicted angular scattering properties. Two unusual height distribution functions were shown in figure 4. A third sample of polished molybdenum obtained from stock

made by a different process also had a skewed height distribution function similar to that of the molybdenum sample shown in figure 4. The initial portions of the autocovariance functions for these three polished molybdenum samples are shown in figure 13. With the exception of the very near angle scattering (less than  $1^\circ$  from the specular direction), the entire angular scattering curve in the visible seems to be determined by the initial positive portion of the autocovariance function. Thus, the predicted angular scattering from these three polished molybdenum samples should be quite different, as shown by the three calculated curves in figure 14. However, the measured angular scattering for these three samples is remarkably similar, as shown by the three additional curves in figure 15. The reason for the discrepancy between theory and experiment is not clear and is currently being studied.

#### 4.3 Potassium Chloride

Potassium chloride is a very soft material, and polishing it has been likened to polishing peanut butter. However, using a polishing process developed at Michelson Laboratory [9], it has been possible to obtain surprisingly smooth surfaces. KCl is one of the few polished materials that does not have Gaussian height and slope distribution functions (see fig. 2, upper right). A more unusual type of KCl surface has been produced by Honeywell [10]. The sample has been made by pressing between optical flats in a two-step process with no additional polishing or surface treatment following the second pressing operation. The height and slope distribution functions for the plano surface of a plano-concave lens produced by this process [11] are shown in figure 16. These have a non-Gaussian character similar to that of polished KCl. The corresponding autocovariance function for this material, figure 17, looks similar to that of a fresh feed polished fused quartz sample (fig. 11), although the surface seems to be more wavy.

Since KCl is so soft, it is important that the diamond stylus used to obtain the surface statistics does not gouge the surface. Extensive experiments have been performed to determine the magnitude of the stylus loading which will not damage KCl surfaces when styluses having various radii are used [12]. All the measurements reported here were made using loadings that did not permanently mark the KCl surface.

Surface scans on a diamond turned KCl sample produced the autocovariance functions shown in figure 18. For this sample tool chatter apparently was the dominant feature since the scan made parallel to the grooves did not look appreciably different from the scan made perpendicular to the grooves. In both autocovariance functions the dominant feature is the very short range correlation,  $\sim 2 \mu\text{m}$ , showing that the machining grooves are much less important than are uncorrelated surface features.

#### 4.4 Diamond Turned Copper

Single point diamond machining is much easier on soft metals such as gold, silver, and copper, and the surface statistics of several diamond turned copper samples have been measured at Michelson Laboratory. Two examples will be given here. In figure 19 is shown the initial portion of the autocovariance function for a diamond turned copper sample made at the Lawrence Livermore Laboratory. A periodicity of about  $14 \mu\text{m}$  is evident in parts of the surface scan and in the oscillations of the autocovariance function. This periodicity would produce a spike in the angular scattering curve at about  $2.7^\circ$  for a wavelength of  $0.6471 \mu\text{m}$ . In figure 20 a longer portion of an autocovariance function is shown for a diamond turned copper sample produced by the Moore Tool Company. As in figure 19, the scan was made perpendicular to the grooves. Two other periodicities are present in addition to the  $\sim 14\text{-}\mu\text{m}$  one. The submultiple,  $6.9 \mu\text{m}$ , is not as distinct as the  $14\text{-}\mu\text{m}$  periodicity. The very long periodicity,  $290 \mu\text{m}$ , manifests itself as a beat frequency. As shown in the table in figure 20, this long periodicity would only be important if the mirror were being used for very near angle scattering. We have not yet measured angular scattering curves on diamond turned samples, but measurements of this type have been reported elsewhere [4]. Most of the diamond turned copper samples whose statistics we have measured have nearly Gaussian height and slope distribution functions [5].

#### 4.5 Silicon Carbide

Silicon carbide is a promising low scatter material, particularly in the ultraviolet and at shorter wavelengths where its reflectance is higher than that of platinum [13] and its scattering much lower than that of molybdenum [13,14]. The surface profiles on the smoothest polished silicon carbide samples are similar to those for bowl feed polished fused quartz, very smooth but wavy. Thus, the autocovariance function is also similar, as shown in figure 21. Angular scattering measurements have not yet been made on this material, but they would be expected to have a shape similar to that shown in figure 12. Work in this area is continuing.

#### 5. Summary

In summary, the relation between TIS and rms roughness has been given, and the roughnesses of a variety of optical materials have been presented. We have shown that it is possible to predict the shape of angular scattering curves for several optical materials using measured surface statistics in the calculations. The most important surface statistic is the autocovariance function, and these have been presented for several optical materials.



## 6. References

- [1] Bennett, H. E. and Porteus, J. O., J. Opt. Soc. Am. 51, 123 (1961).
- [2] Klugman, A., "Surface Finishing of Molybdenum Substrates," presented at High Power Laser Optical Components and Component Materials Meeting, 3-4 October 1977, National Bureau of Standards, Boulder, Colorado.
- [3] Elson, J. M. and Bennett, J. M., Appl. Opt., to be published.
- [4] Church, E. L. and Zavada, J. M., Appl. Opt. 14, 1788 (1975); Stover, J. C., Appl. Opt. 14, 1796 (1975).
- [5] Bennett, J. M., Appl. Opt. 15, 2705 (1976).
- [6] Talystep Step Height Measuring Instrument (Metric), Model No. 75-1001, obtained from Rank Precision Industries, Inc., 411 East Jarvis Avenue, Des Plaines, Illinois 60018.
- [7] Dancy, J. H. and Bennett, J. M., "Investigation of Electron Stereomicroscopy as a Method for Determining Heights of Features on Evaporated and Sputtered Films and on Polished Surfaces," in *High Energy Laser Mirrors and Windows* (Semi-Annual Report No. 7-8, Defense Advanced Research Projects Agency Order 2175, Naval Weapons Center, 1976), p. 166.
- [8] Dietz, R. W. and Bennett, J. M., Appl. Opt. 5, 881 (1966).
- [9] Soileau, M. J., Bethke, J. W., Shaffer, J. and Bennett, H. E., "Polishing of Alkali-Halide Windows," in *High Energy Laser Mirrors and Windows* (Semi-Annual Report No. 6, Defense Advanced Research Projects Agency Order 2175, Naval Weapons Center, 1975), p. 75.
- [10] Anderson, R. and Bennett, J. M., "Properties of KCl Optical Elements Forged Between Optically Polished Dies," presented at High Power Laser Optical Components and Component Materials Meeting, 3-4 October 1977, National Bureau of Standards, Boulder, Colorado.
- [11] Honeywell isostatically forged, flat-pressed samples provided by Enrique Bernal G. and Rogers Anderson, Honeywell Corporate Research Center, Bloomington, Minnesota.
- [12] Dancy, J. H. and Bennett, J. M., "Study of Diamond Styluses for a Talystep Profilometer," in *High Energy Laser Mirrors and Windows*, Annual Report No. 9, April 1976-May 1977, NWC TP 5988, October 1977, in press.
- [13] Choyke, W. J., Partlow, W. D., Supertzi, E. P., Venskytis, F. J. and Brandt, G. B., Appl. Opt. 16, 2013 (1977).
- [14] Rehn, V., Stanford, J. L., Baer, A. D., Jones, V. O. and Choyke, W. J., Appl. Opt. 16, 1111 (1977).

## 7. Figures

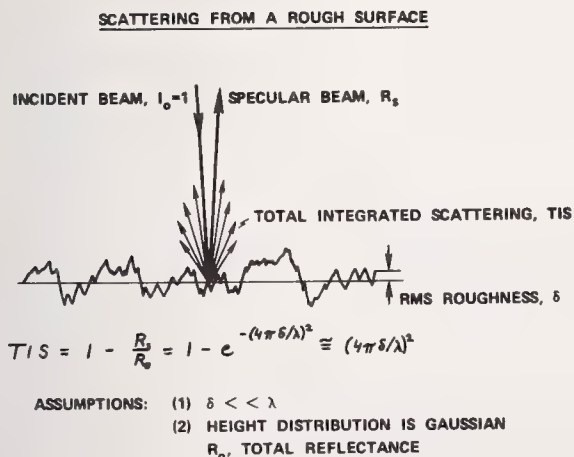


Figure 1. Schematic representation of scattering from a rough surface, and the relation between total integrated scattering and rms roughness. The assumptions implicit in the expression for TIS are given.

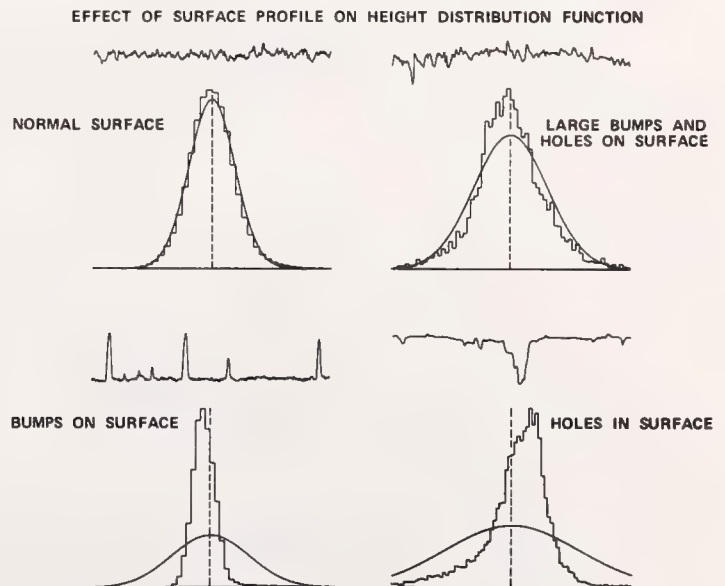


Figure 2. Effect of the surface profile on the height distribution function for four types of surfaces. The surface profiles are shown above the corresponding histograms.



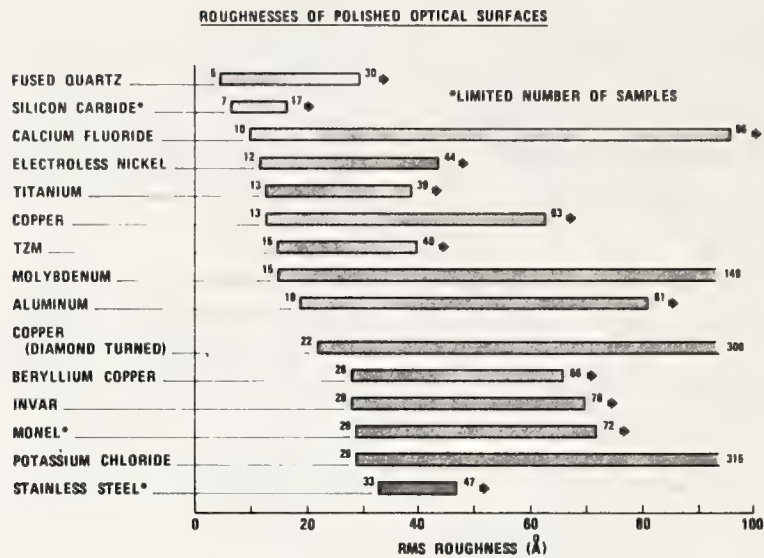


Figure 3. Range of rms roughnesses measured for polished optical surfaces.

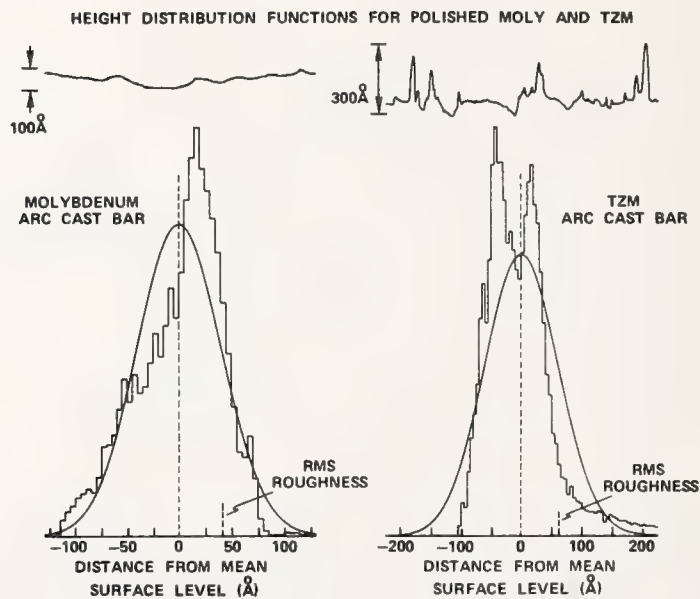


Figure 4. Surface profiles and height distribution functions for two unusual molybdenum and TZM surfaces (see reference 2).

# RELATE SURFACE STATISTICS TO OPTICAL SCATTERING

$$\frac{dP}{d\Omega} = \underbrace{\frac{16\pi^2}{\lambda^4} \frac{|1 - \sqrt{\epsilon}|^2 \cos^2 \theta}{A + \cos^2 \theta - 2\sqrt{A} \sin(\alpha/2) \cos \theta}}_{\text{OPTICAL FACTOR}} \cdot \underbrace{\delta^2 g(k)}_{\substack{\text{SPECTRAL} \\ \text{DENSITY} \\ \text{FUNCTION} \\ \text{(SURFACE FACTOR)}}} \quad \begin{aligned} A &= [(\sin^2 \theta - \epsilon_1)^2 + \epsilon_2^2]^{1/2} \\ \tan \alpha &= -\epsilon_2 / (\sin^2 \theta - \epsilon_1) \end{aligned}$$

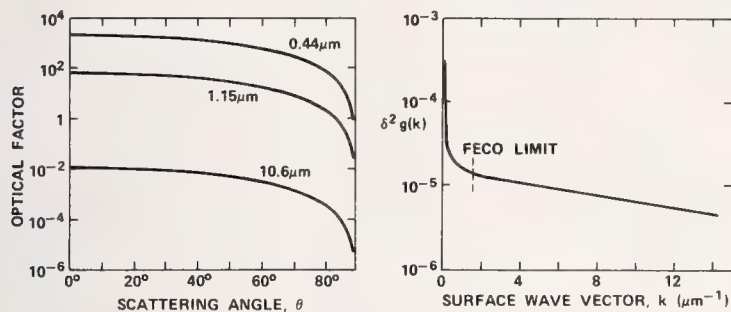


Figure 5. Expression for the angular scattering per unit solid angle for normally incident polarized light. The symbols are explained in the text. Typical graphs for the optical factor and surface factor are shown below.

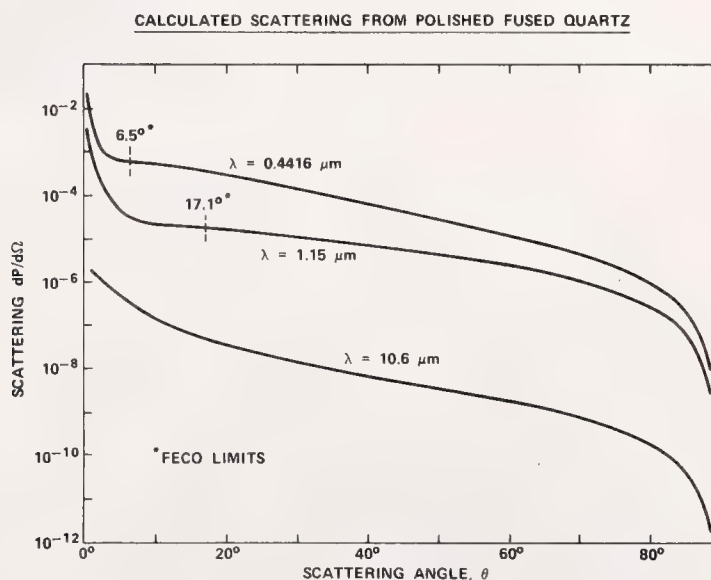


Figure 6. Angular scattering curves for polished fused quartz calculated from the optical and surface factors in figure 5.

# EFFECT OF SURFACE PROFILE ON AUTOCOVARIANCE FUNCTION AND ANGULAR SCATTERING

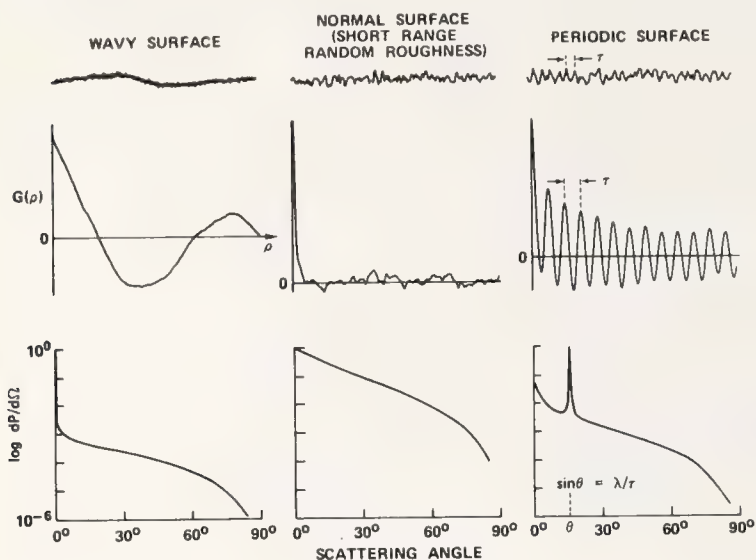


Figure 7. Three basic types of surface profiles and their corresponding autocovariance functions and angular scattering curves.

## SEPARATIONS OF SURFACE FEATURES WHICH PRODUCE SCATTERING

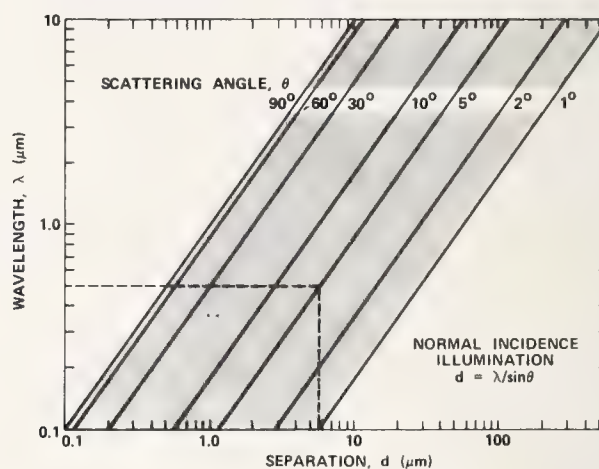


Figure 8. Nomogram giving separation of surface features that produce scattering at a particular angle and wavelength. The dashed lines are an illustrative example.

## COMPARISON OF STATISTICAL METHODS

	HEIGHT SENSITIVITY	LATERAL RESOLUTION	MAXIMUM LENGTH
FECO INTERFEROMETER	$\sim 3\text{\AA}$ RMS	$\sim 2\ \mu\text{m}$	1 mm
TALYSTP PROFILOMETER	$\sim 1\text{\AA}$ RMS	$\sim 0.1\ \mu\text{m}$	2 mm
STEREO MICROSCOPY	$\pm 20\text{\AA}$	$\sim 5\text{\AA}$	$\sim 1\ \mu\text{m}$

Figure 9. Comparison of three techniques used to obtain surface statistics.



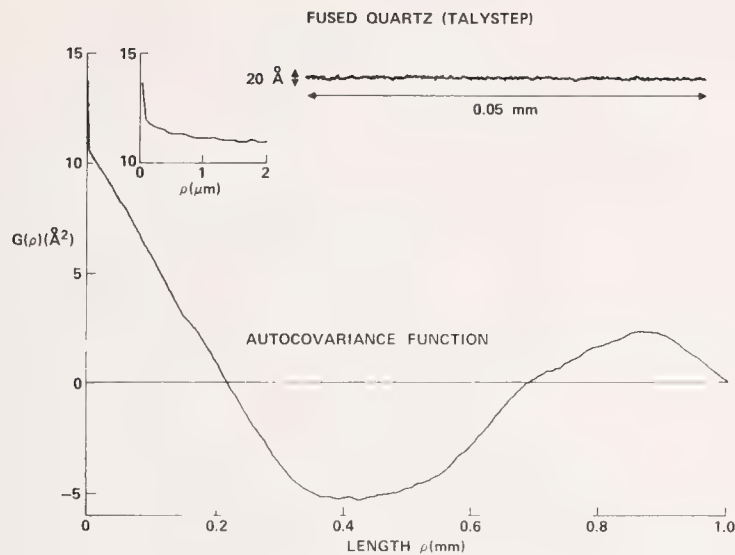


Figure 10. Surface profile and autocovariance function for a smooth but wavy bowl feed polished fused quartz surface.

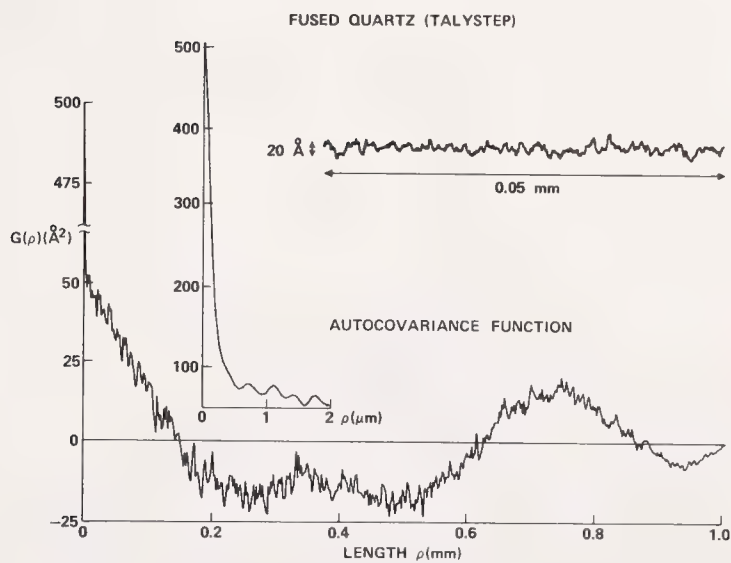


Figure 11. Surface profile and autocovariance function for a fresh feed polished fused quartz surface having short range random roughness.

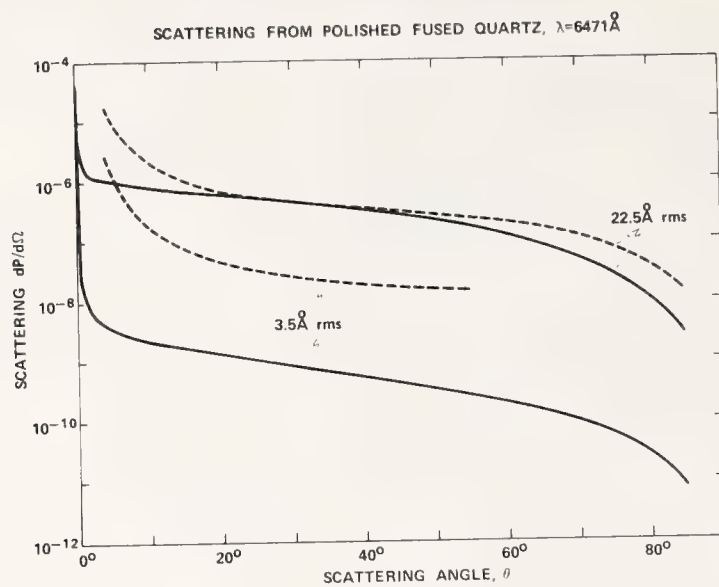


Figure 12. Calculated (solid) and measured (dashed) curves showing angular scattering for the polished fused quartz surfaces whose auto-covariance functions were shown in figures 10 and 11.

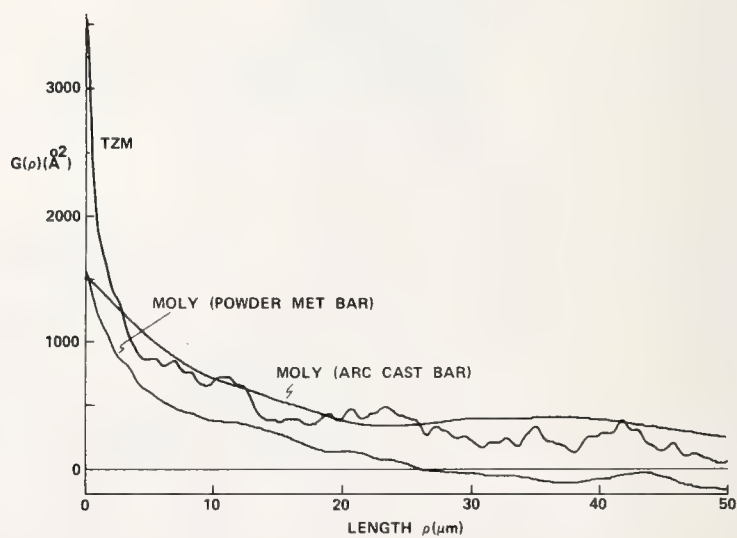


Figure 13. Initial portions of the autocovariance functions for two molybdenum samples and a TQM sample.

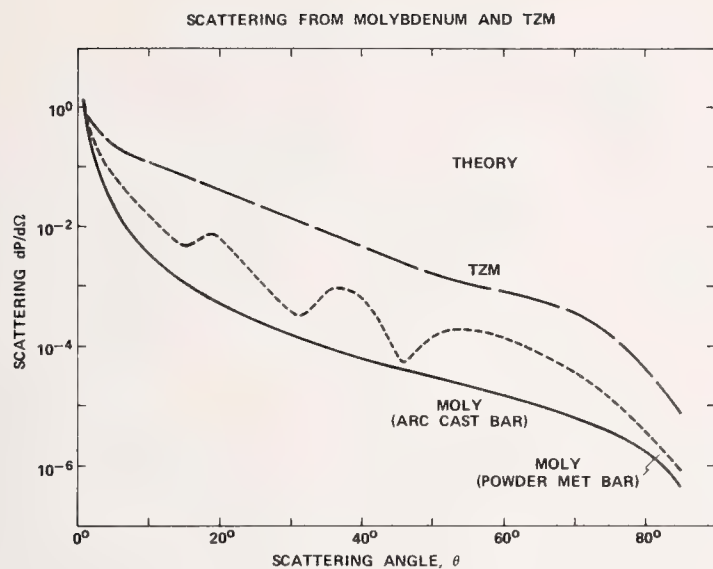


Figure 14. Calculated angular scattering curves for the molybdenum and TZM samples whose autocovariance functions were shown in figure 13.

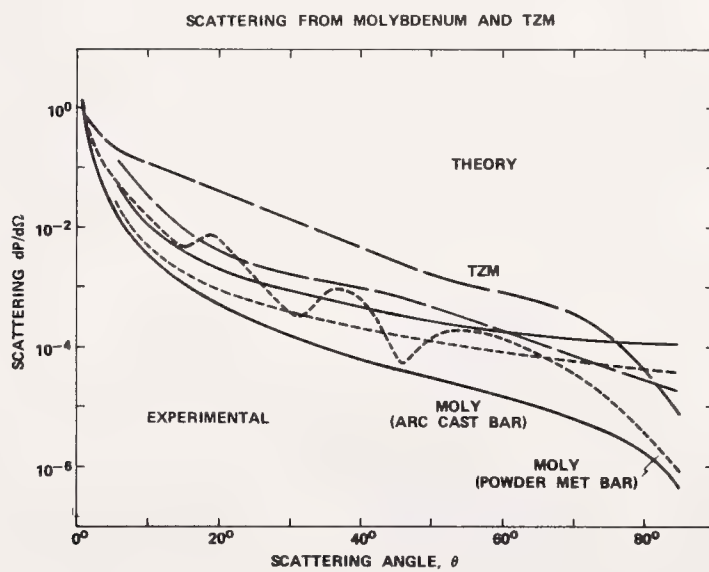


Figure 15. Same as figure 14 except that three measured scattering curves have been added.



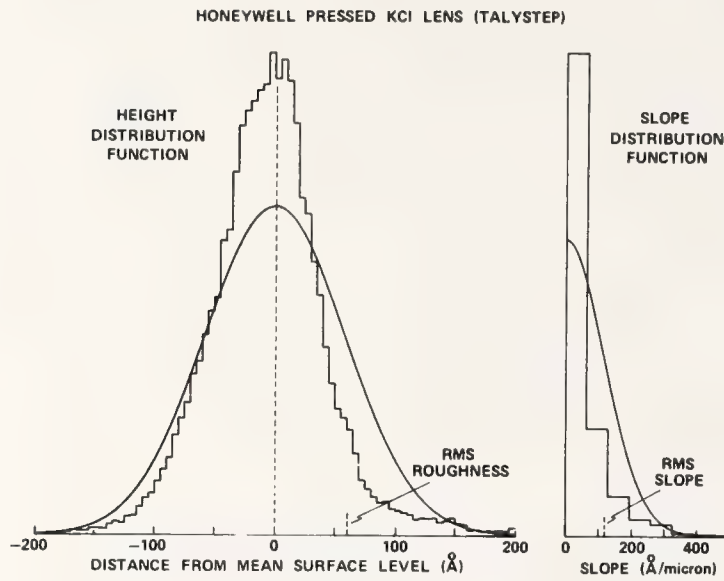


Figure 16. Height and slope distribution functions for the plano surface of a pressed KCl lens (see reference 10).

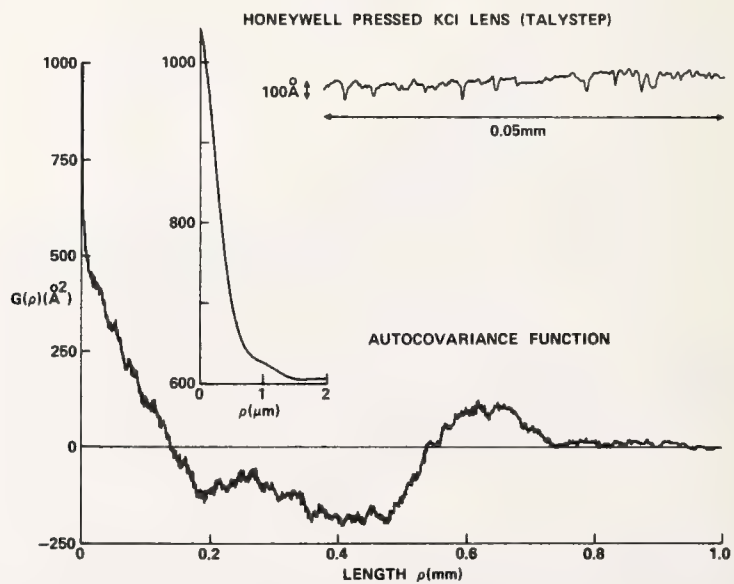


Figure 17. Surface profile and autocovariance function for the same KCl lens as in figure 16.

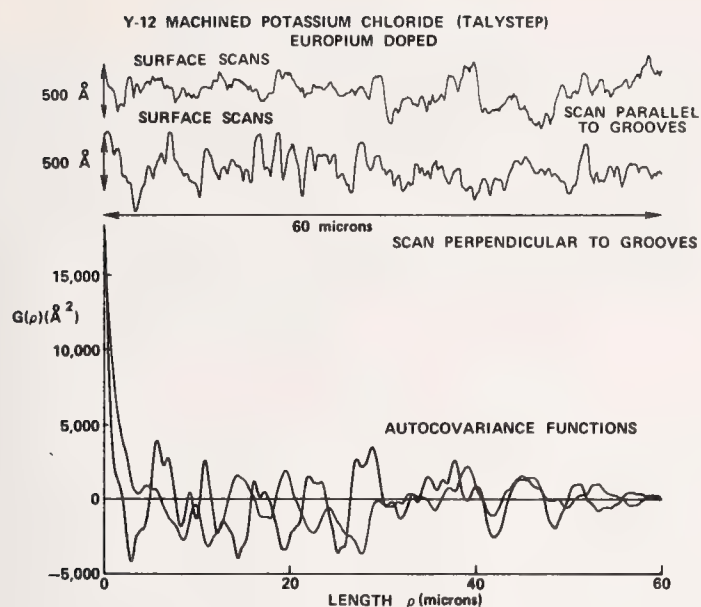


Figure 18. Surface profiles and autocovariance functions for a diamond turned, europium doped KCl sample.

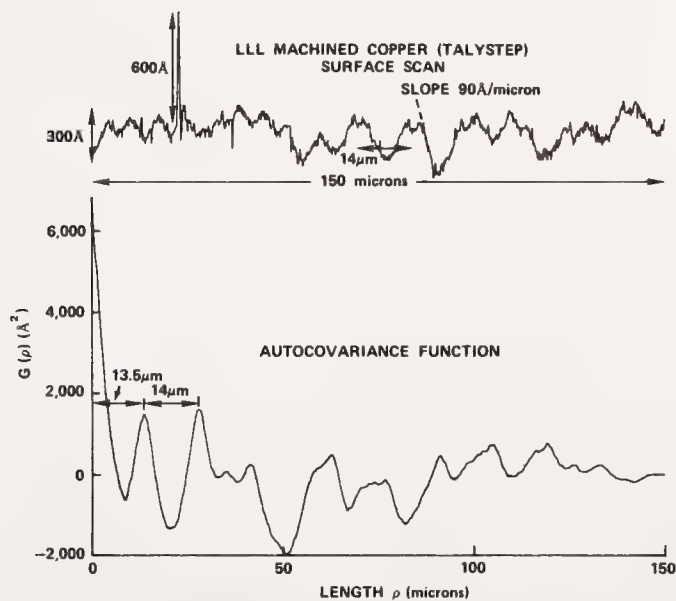


Figure 19. Surface profile and initial portion of the autocovariance function for a diamond turned copper sample made at the Lawrence Livermore Laboratory.

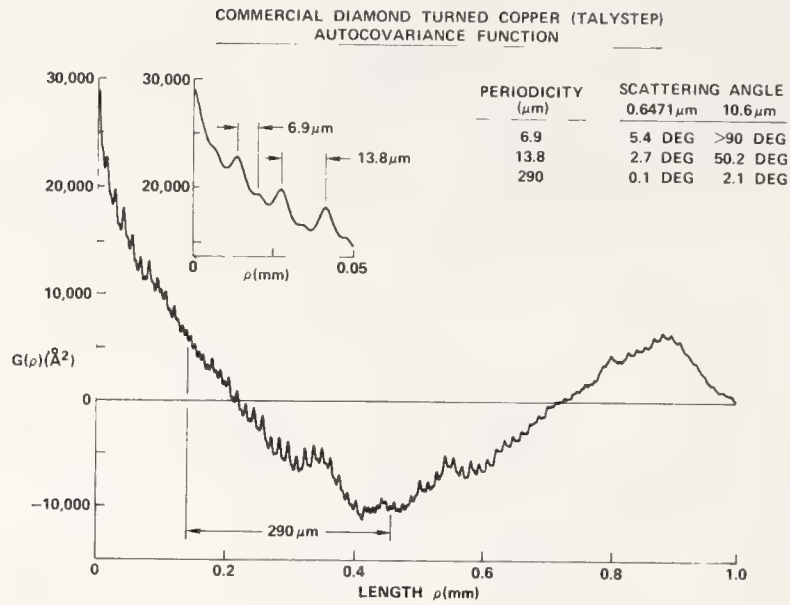


Figure 20. Autocovariance function for a diamond turned copper sample made by the Moore Tool Company.

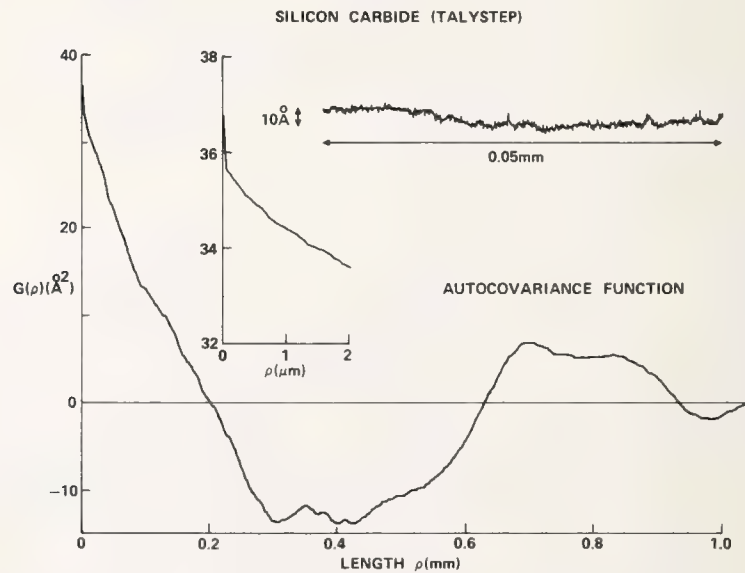


Figure 21. Surface profile and autocovariance function for polished silicon carbide.



#### COMMENTS ON PAPER BY BENNETT AND ELSON

The comparative virtues of FECO, talystep profilometry, and scattering measurements were discussed. Both FECO and profilometry measurements gave good agreement with each other and yielded the same results for the autocorrelation function. In response to a question as to which technique would be the measurement of choice, the speaker responded that, in a real system, one is really interested in scattering, therefore total integrated scattering or the angular scattering spectrum would be the measurements of interest. However, for the determination of surface character and surface statistics, profilometry is by far the best method to use. The question was asked if the autocorrelation function was uniquely related to the surface profile. The speaker replied that of course the scattering spectrum and autocorrelation function are uniquely related, but that different surface profiles can give very similar, although possibly not identical, autocorrelation functions, or equivalently very similar scattering spectra. A given profile of course, must yield a unique scattering spectrum, but the reconstruction of the surface profile from the scattering spectrum or autocorrelation function may not be uniquely defined.

SURFACE ROUGHNESS STATISTICS OF FUSED SILICA AS  
A FUNCTION OF SURFACE PREPARATION AND TREATMENT

R. A. House, II, and A. H. Guenther  
Air Force Weapons Laboratory  
Kirtland AFB, NM 87117

and

J. M. Bennett  
Naval Weapons Center  
China Lake, CA 93555

Samples of fused silica which had previously been laser damage tested on portions of their surfaces were subjected to a detailed statistical topographic analysis. These samples had been fabricated using a variety of surface preparation techniques, and the primary final characteristic of interest was the rms surface roughness of each sample. The present study focused on the height and slope distribution functions and an autocovariance length evaluation resulting from the differing surface treatments. The basic conclusion of the study is that the type of surface finishing used strongly influences the surface structure, causing a wide variation in light scattering properties and topography.

Key words: Correlation length; fused silica; polishing; roughness; slope; surfaces.

#### Introduction

Previously reported work [1] indicated a strong correlation between laser damage threshold and rms surface roughness. The experiments were performed on fused silica using a wavelength of 1.06  $\mu\text{m}$  and a pulse length of 40.5 ns. A graphical summary of the experimental data is presented in Figure 1, where the functional dependence is  $E\sigma^m = \text{constant}$ .  $E$  is the threshold (in MV/cm) and  $\sigma$  is the rms roughness (in Å). For most of the surface treatments used on the substrates, the exponent  $m$  had a value of about 0.5, while the value of the constant varied considerably with surface finishing procedure. In the cases of ion polishing and bowl feed polishing, the samples were polished as smooth as possible. Therefore, these samples all exhibited low rms roughness values having insufficient spread to clearly delineate a threshold-roughness relationship. The specific samples examined in detail during the present effort are indicated in Figure 1.

Four significant observations from Figure 1 indicated that further surface characterization of the samples would be desirable: 1) The value of  $m$  for the flame polished samples was considerably different than 0.5; 2) The behavior of the etched samples was erratic; 3) The constants varied considerably with surface preparation; 4) There was undoubtedly a wide range in the surface contamination levels introduced during the final surface finishing. It was hoped that, as a result of detailed topographic evaluation, the functional dependence of  $E$  on  $\sigma$  would be clarified. It was also hoped that variations in the structures of surfaces prepared in different manners could be assessed and correlated with previously reported laser-induced damage results.

#### Procedures and Data

Selected samples that had previously been laser damage tested were subjected to detailed topography measurements at the Michelson Laboratory, Naval Weapons Center. Measurements were made using Total Integrated Scattering (TIS) and Talystep profilometry. The samples were also examined visually using Nomarski microscopy [2].

Data resulting from the investigation of the six samples indicated in Figure 1 are presented in Table 1 and in Figures 2-7. The symbols used in Table 1 are as follows:  $\sigma_b$  is the background roughness (i.e., the roughness excluding particles);  $\sigma_t$  is the overall roughness including the particles;  $\sigma_t$  is the TIS-determined roughness (at the wavelength 5682 Å);  $s$  is the rms slope of the surface topography, in Å/ $\mu\text{m}$ , with the equivalent angle given in parentheses;  $l$  is the correlation length in  $\mu\text{m}$ ;  $h_p$  is the rms height of the gross surface features (i.e., particles or holes);  $f$  is the fraction of the surface area covered by these gross features;  $E$  is the measured damage threshold of the surface (previously determined); and  $\sigma_i$  is the initial roughness value for the surface (also previously determined). Roughness values  $\sigma_b$  and  $\sigma_t$  were determined from analysis of the Talystep data obtained in the present study.

Table 1. Summary of surface statistics.

SAMPLE TREATMENT	$\sigma_b$ (Å)	$\sigma_t$ (Å)	$\sigma_t$ (Å)	s (Å/μm)	ℓ (μm)	$h_p$ (Å)	f	E (MV/cm)	$\sigma_i$ (Å)
Flame	5.62	75.4	20.9	208.4 (1.19°)		231.8	0.0718	2.24	13.32
Conventional	2.27	16.27	12.4	63.93 (0.37°)	0.90	75.6	0.0422	1.60	13.75
Bowl Feed	30.2	30.2	24.8	118 (0.68°)	0.89			0.86	13
Overcoated	2.68	2.68	9.3	28.85 (0.17°)	0.82			0.89	13.75
Ion-Etched	60.8	60.8	16.5	260 (1.49°)	0.48			1.34	36
Acid-Etched	15	111	216	1870 (10.59°)	1.5			0.41	243

Figures 2-7 show typical raw and composite data for the samples. Part "a" of each figure presents the surface height and slope distributions measured for the sample. Also shown are the fitted Gaussian curves, the fit being made by requiring each Gaussian to have the same area and rms value as the corresponding histogram. Note that the histograms represent the as-measured surface (i.e., they include the measured particles or holes). Parts "b" for Figures 3-7 are the autocovariance functions for the samples. The autocovariance function for the flame polished sample was not actually measured; however, this sample's visual and surface scan characteristics were essentially the same as those of the conventionally polished sample (Fig. 3), so that its autocovariance function is estimated to be the same as Figure 3b.

A feature typical of the samples investigated was the presence of large amounts of very small particulates (of the order of 1000 Å or less in size). Some of these particles were very tenaciously bound to the surfaces and could not be removed using dry nitrogen and a low-energy electron gun. This cleaning process was the only one used on the conventionally polished and flame polished samples. Since the particles were not removed by this treatment their statistics were examined. Figures 2b and 3c show the measured (histogram) and fitted (Gaussian) distributions of the particles on these samples. The other four samples were cleaned in soap and water, and most of the particles were removed. Parts "c" of Figures 4-7 for these samples show typical Talystep surface scans. Note that several such scans were made on each sample and that the data were averaged to obtain the height, slope, and autocovariance functions. Note also that the scan for the etched sample shows not only the background surface but also one of the deep holes present in the surface.

Surface scan raw data consisted of 17,000 Talystep data points per scan length of 1.037 mm. The resulting data-point spacing of 0.061 μm is much smaller than the typical spacing for FECO (2 μm) and TIS (1 mm) measurements. That is, the Talystep stylus probes the surfaces in much finer detail than do the other standard measurements. Each surface was scanned several times at various surface locations, and stylus pressures were kept light enough to avoid leaving tracks. The data were analyzed by computer program and then plotted.

### Conclusions

For the flame polished and conventionally polished samples, the height and slope distribution functions were not Gaussian. Surface statistics were dominated by many strongly-bound particles, although the background surfaces were extremely smooth. The overall distribution functions were considerably skewed by the particles, which themselves exhibited non-Gaussian height distributions. The majority of particles on the conventional sample were 20-30 Å high, with the largest measured particle being 205 Å. For the flame polished sample the corresponding numbers were 30-55 Å and 906 Å.

Although the particles could not be blown off, they apparently were easily removable using soap and water. This technique was successfully applied to the other four samples.

The bowl feed polished sample was apparently free of particles, scratches, and surface blemishes under Nomarski; but it exhibited surface scan characteristics of fresh feed surfaces (i.e., it contained considerable structure). The height distribution was skewed because of small (100-500 Å) particles, although the slope distribution was Gaussian. The Talystep and TIS roughness values were comparable (probably because of the particles), and there was little long-term waviness in the surface.



The  $\text{SiO}_2$  overcoated sample was extremely smooth and Gaussian in its statistics. The surface appeared to have no defects under Nomarski, and it exhibited the same character as the best bowl feed polished samples. Although the surface was very smooth and showed very little long-term waviness, the fact that its damage threshold was about half that of the conventional sample or the flame polished sample clearly indicates that thin films introduce significant laser damage susceptibility at an optical surface.

The Xenon ion polished sample had nearly Gaussian statistics and was flat but very rough. Talystep roughness was significantly greater than TIS roughness and is probably explainable by the height variations being too closely spaced to be resolved by the wavelength used (5682 Å). Holes and bumps were of the order of 200-400 Å in height or depth. There was also little long-term waviness.

The etched sample was very rough, primarily due to large numbers of holes in the surface. These holes were as much as 1.5  $\mu\text{m}$  in diameter and as much as 1-2  $\mu\text{m}$  deep. However, the background surface was fairly smooth. The holes clearly skewed the height and slope histograms.

Except for the overcoated and ion polished samples, the statistical distributions were definitely not Gaussian. It is clear that the type of surface finishing technique used strongly influences the structure and light scattering properties of the surface of a given type of optical glass. No definite correlations have yet been found between laser damage threshold and rms slope or correlation length; however, the sample space so far examined is quite small. Future measurements presently underway on other samples of a given type of surface treatment may yield such correlations.

One additional observation is warranted. If one normalizes damage thresholds to those characteristic of conventionally polished surfaces, then later treatments such as flame-polishing and acid or ion etching afford more damage resistant surfaces while those other techniques, e.g., bowl-feed and overcoating generally lead to increased damage sensitivity. This certainly appears to be the rule of thumb for coatings.

In any event, considerable additional work is needed to fully describe this most complex situation before we can predict and quantify the appropriate surface character/damage threshold relationship.

#### References

- [1] House, R. A., II, Bettis, J. R. and Guenther, A. H., IEEE J. Quant. Elec. QE-13, #5, 361-363 (May 1977).
- [2] Bennett, J. R., and Elson, J. M., this proceedings.

#### Figures

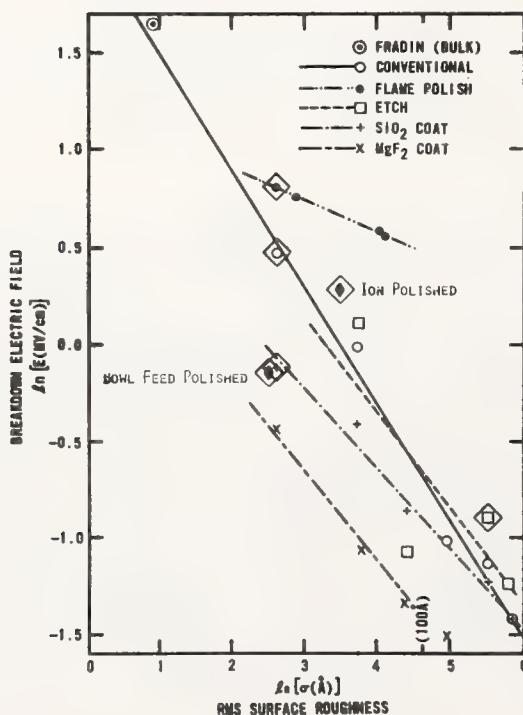


Fig. 1. Laser damage threshold vs. rms roughness for 40.5 ns, 1.06  $\mu\text{m}$  irradiations on fused silica. Details of the sample preparation technique is discussed in reference 1. Briefly, etch refers to a dilute  $\text{HNO}_3$  and etch and  $\text{SiO}_2$  and  $\text{MgF}_2$  coat refer to  $\lambda/2$  at 1.06 single film layers on substrates whose roughness is indicated on the abscissa. The points indicated in the endorsed diamond correspond to the samples examined in this study.

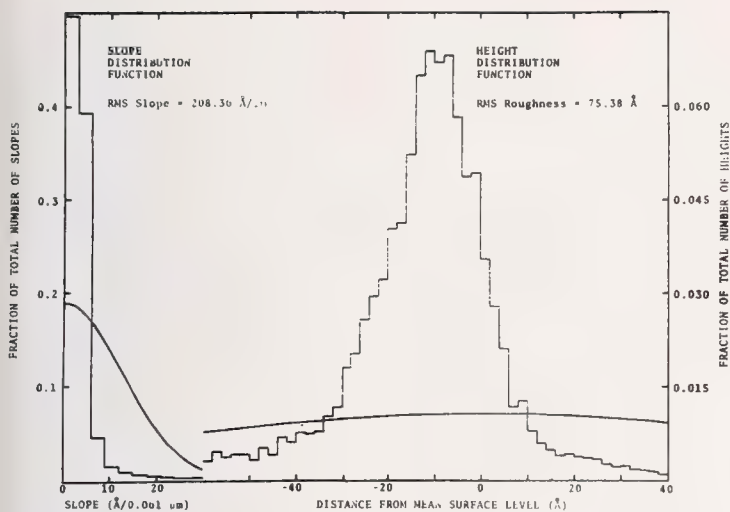


Fig. 2a. Height and slope distribution: flame polished sample.

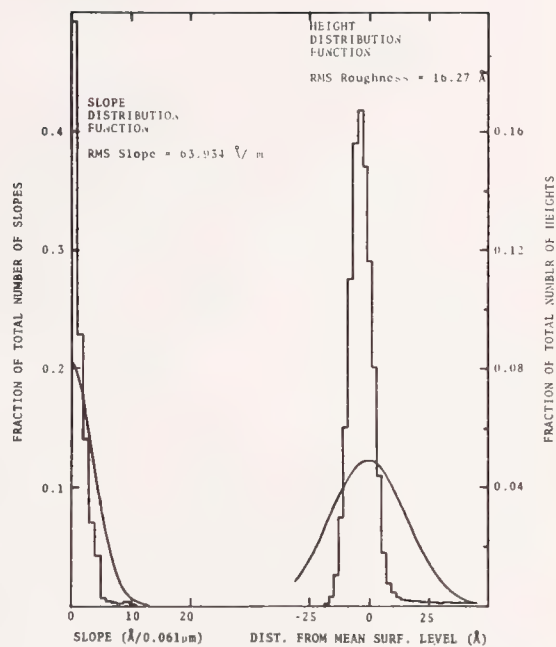


Fig. 3a. Height and slope distributions: conventional sample.

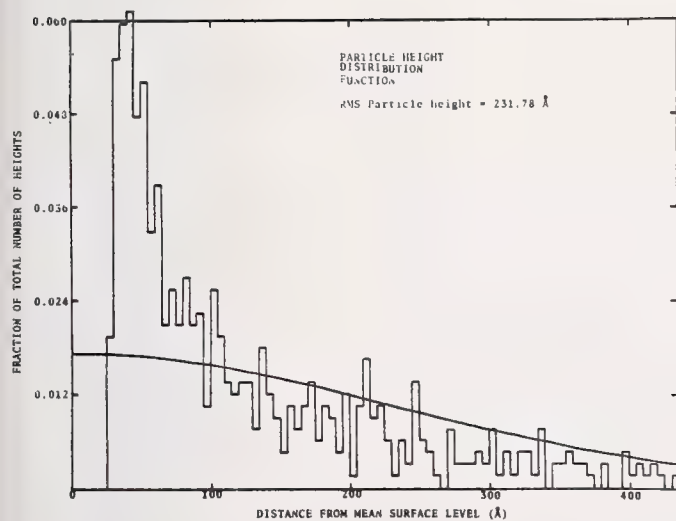


Fig. 2b. Particle height distribution: flame polished sample.

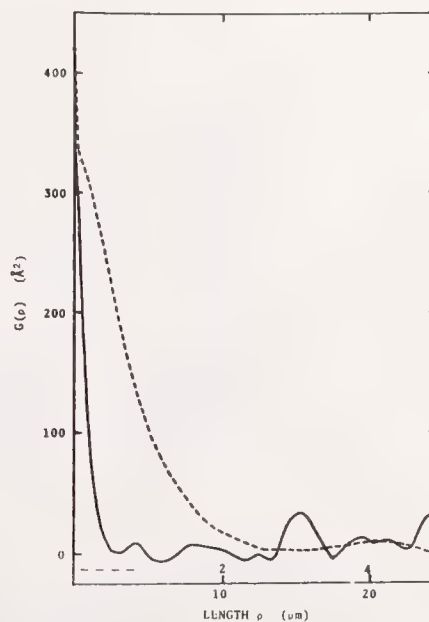


Fig. 3b. Autocovariance function: conventional sample.

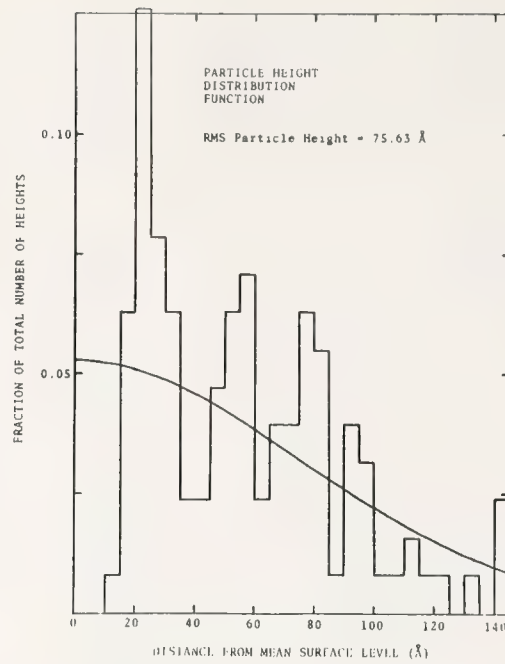


Fig. 3c. Particle height distribution: conventional sample.

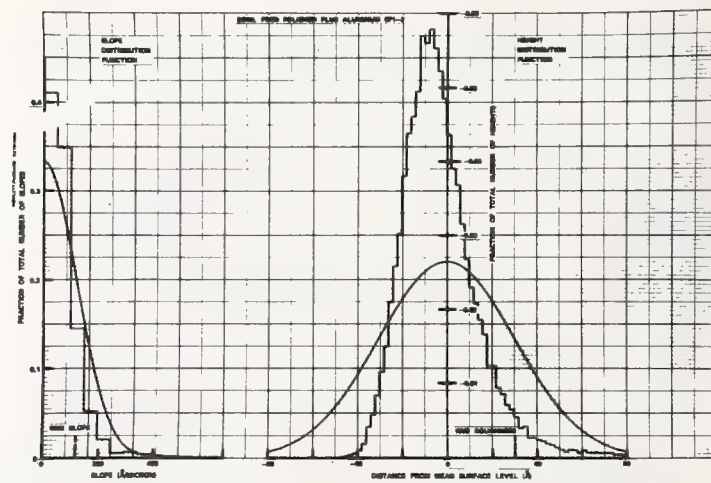


Fig. 4a. Height and slope distributions: bowl feed polished sample.



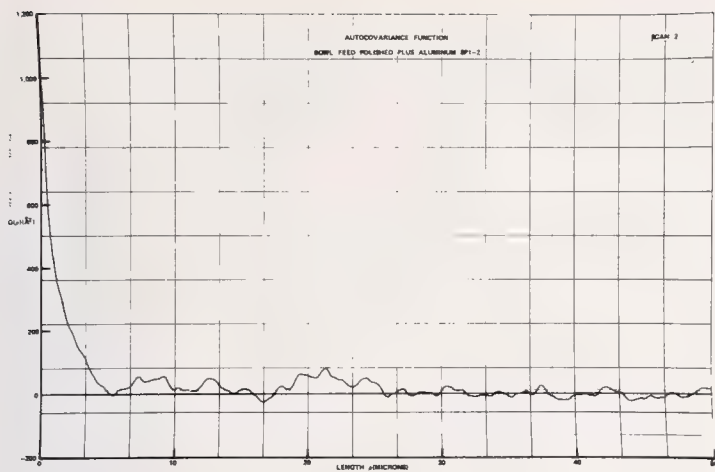


Fig. 4b. Autocovariance function: bowl feed polished sample.

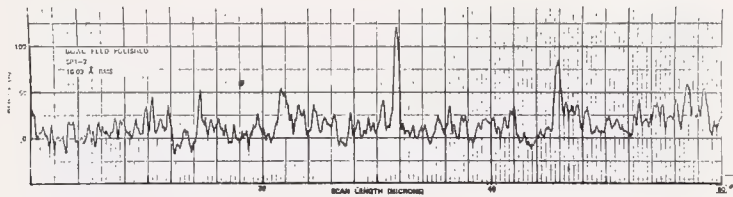


Fig. 4c. Typical surface scan: bowl feed polished sample.

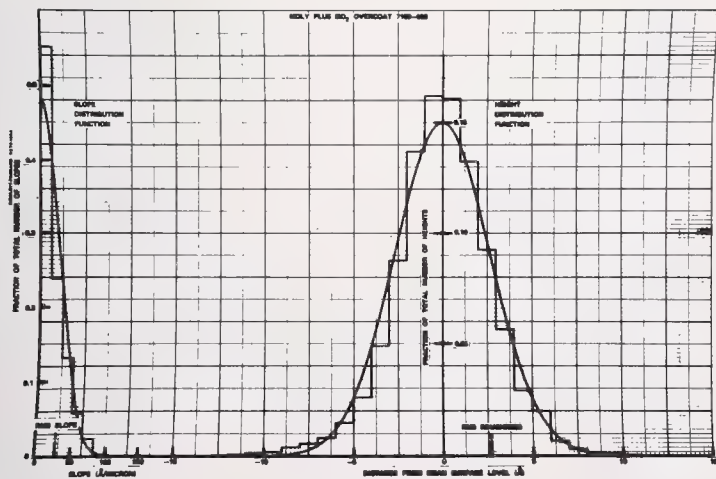


Fig. 5a. Height and slope distributions: SiO<sub>2</sub>-overcoated sample.

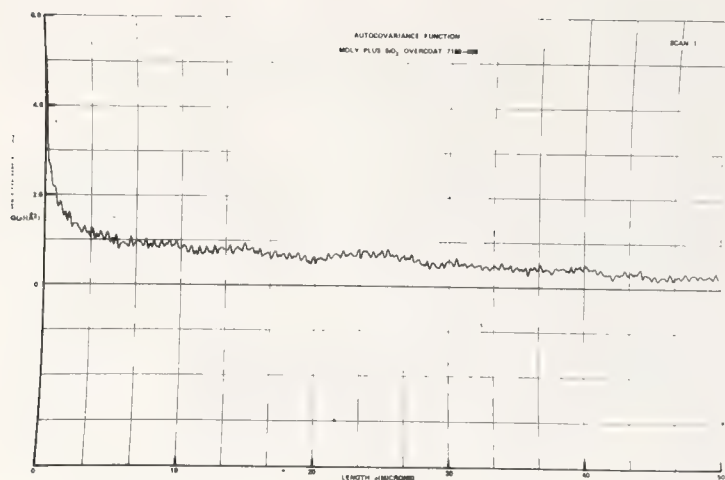


Fig. 5b. Autocovariance function: SiO<sub>2</sub>-overcoated sample.

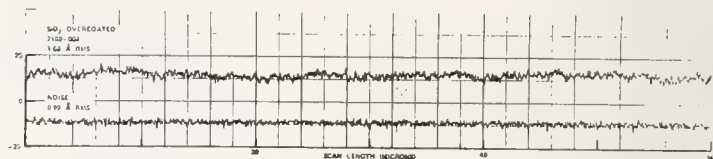


Fig. 5c. Typical surface scan: SiO<sub>2</sub>-overcoated sample.

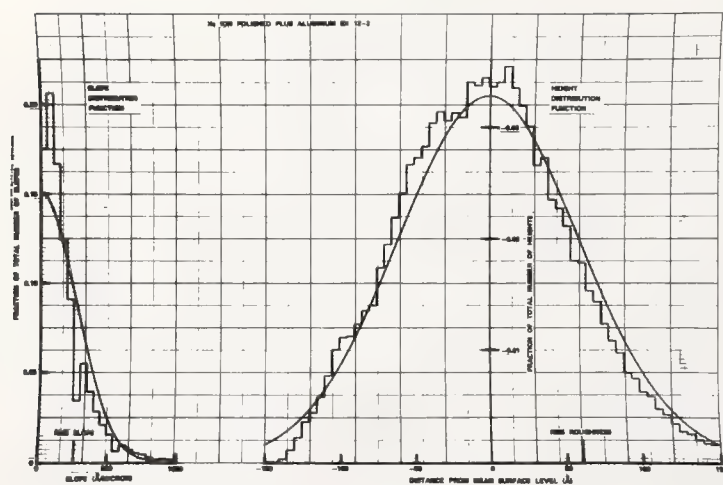


Fig. 6a. Height and slope distributions: Xenon polished sample.

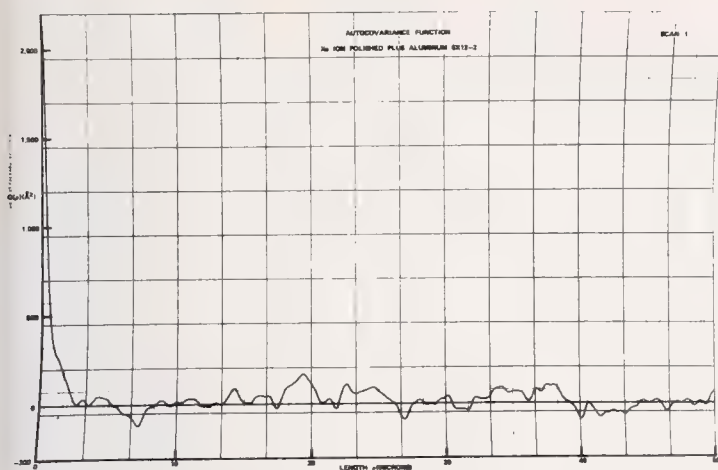


Fig. 6b. Autocovariance function: Xenon polished sample.

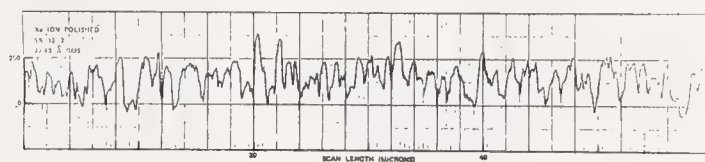


Fig. 6c. Typical surface scan: Xenon polished sample.

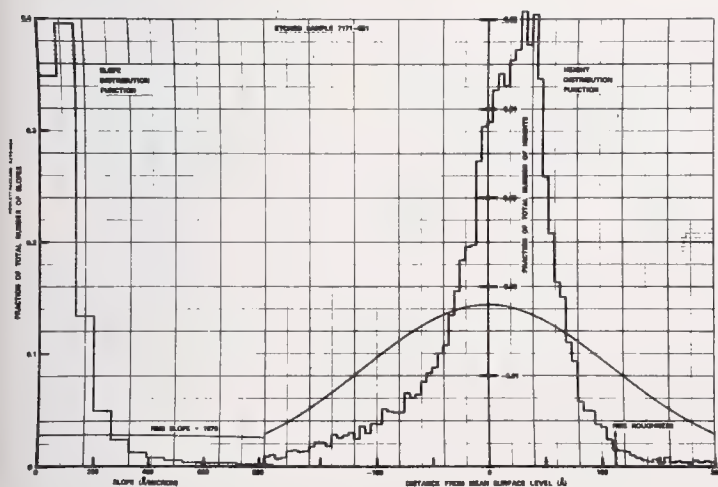


Fig. 7a. Height and slope distributions: etched sample.



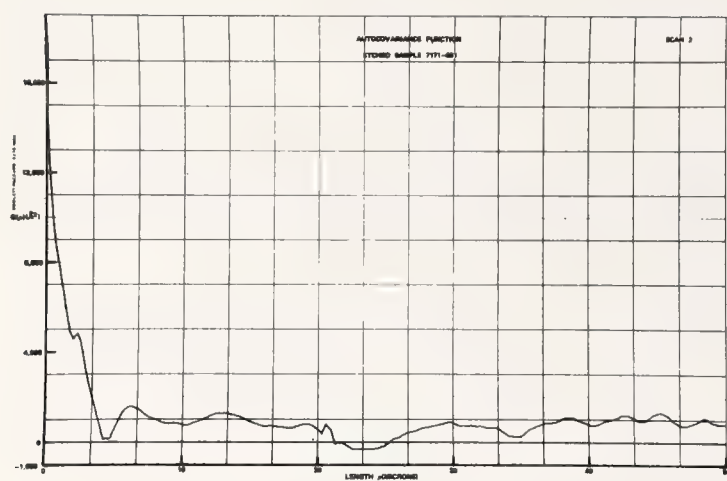


Fig. 7b. Autocovariance function: etched sample.

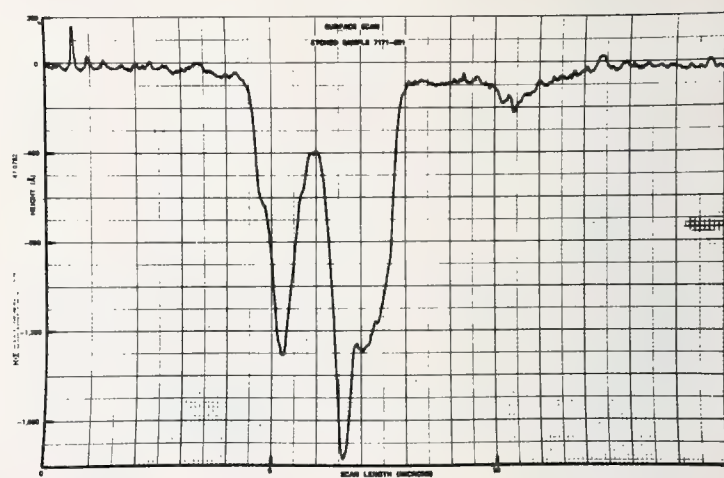


Fig. 7c. Typical surface scan: etched sample.

D. Milam, W. L. Smith, and M. J. Weber  
Lawrence Livermore Laboratory  
University of California  
Livermore, California 94550

and

A. H. Guenther, R. A. House, and J. R. Bettis  
Air Force Weapons Laboratory  
Kirtland Air Force Base  
New Mexico 87115

We report the first measurements of the influence of surface roughness on surface damage thresholds for damage induced by subnanosecond 1064-nm laser pulses. Samples included carefully characterized bare polished silica surfaces and glass surfaces which were used as substrates for antireflection coatings. Where possible, data is correlated with earlier work performed with 40-ns, 1064-nm laser pulses.

Key words: Breakdown field; coating substrate; damage morphology; fused silica; Normarski micrographs; pulse duration; surface damage threshold; surface roughness.

### Introduction

Polished bare surfaces on optical components damage at flux levels below that which causes bulk damage. Furthermore, exit surfaces usually damage more easily than entrance surfaces, provided the damaging beam is collimated and normally incident on the sample. Serious efforts to understand the vulnerability of polished surfaces began after Crisp, Boling, and Dubé successfully explained the lower threshold for exit surfaces. They showed [1] that the optical electric field strengths at the exit surface were greater than those at the entrance surface because the wave reflected from the exit surface is in phase with the incident wave as opposed to the entrance surface where the reflected wave is out of phase with the incident wave.

Bloembergen [2] extended the notion of enhanced electric fields by calculating the local field strengths near dielectric discontinuities whose shapes were similar to the surface disruptions which result from polishing. The electric fields near grooves in a material with index of refraction  $n$  can be  $n^2$  times greater than the field in the undisturbed material itself. Local intensities, which are proportional to the square of the electric fields, could be enhanced by  $n^4$ . Accordingly, surface damage thresholds, irrespective of the mechanism, should be reduced by surface irregularities. The exact magnitude of threshold reduction would depend on whether the mechanism was linear or nonlinear, and on whether heat or electrons could diffuse away from the high-field regions during the pulse interval. Bloembergen estimated that defects less than 100 Å in size would be unimportant because of electron diffusion.

Two subsequent experimental studies produced disagreement as to the universality of Bloembergen's model as an explanation of laser damage. First, Fradin and Bass [3] reported that the damage thresholds of very smooth surfaces on fused silica and BSC-2 glass were equal to that of the bulk material. Second, Boling, Ringlien, and Dubé [4] demonstrated that chemical contamination could reduce the threshold even on very smooth surfaces, and that leaching processes could yield rough surfaces with good damage resistance.

The most comprehensive study to date on the effect of surface finish on surface damage threshold was that conducted at the Air Force Weapons Laboratory (AFWL) by House, Guenther, and Bettis [5]. This work included surfaces prepared by conventional polishing, bowl-feed polishing, ion polishing, flame polishing, and acid etching. Damage tests were made on bare and coated surfaces using 40-ns, 1064-nm pulses focused to a spot size of  $\approx 150 \mu\text{m}$  at the  $e^{-2}$  intensity level. It was invariably found that the damage threshold increased as the quality of the finish improved. One obvious result was that cleaning of the surfaces by flame, polishing, and ion or acid etching markedly improved the damage threshold at a given surface roughness. This was probably due to the removal of easily ionized surface impurities. The excursions of damage thresholds observed in that study are the largest ever reported in a single material. For example, reducing the roughness on conventionally polished fused silica from 335 Å rms to 15 Å rms increased the damage threshold by a factor of 6.3 in breakdown field strength, or  $(6.3)^2 = 40$  in intensity.

\*The work at the Lawrence Livermore Laboratory was performed under the auspices of the Materials Sciences Programs of the U.S. Energy Research and Development Administration and Contract W-7405-eng-48.

A recent study [6] of surface damage induced by 150-ps, 1064-nm pulses suggested that surface roughness might be less important in determining short-pulse thresholds. Near-threshold damage with 1064-nm, 125-ps pulses created a randomly distributed array of micropits. The initial surface morphology was preserved intact, and the damage pits were only weakly associated with residual polishing artifacts such as streaks. Even when fresh scratches having widths of approximately 1-10  $\mu\text{m}$  were scribed on polished surfaces, damage thresholds in the immediate vicinity of the induced scratches were at least one-half as large as the threshold for undisturbed areas on the surface.

To quantify this apparent difference between the effect of surface roughness on damage induced by 40-ns and 150-ps pulses, replica samples from the AFWL 40-ns study were tested at LLL using 150-ps pulses. Results of this comparison are reported below. In addition, measurements were made to determine whether substrate roughness was a dominant effect in damage to antireflection films.

#### Samples

Four bare fused silica surfaces which had been prepared using a controlled grinding process to insure that each sample had approximately the same subsurface structure were tested. Different roughnesses were obtained by removing the samples at various times during the final lapping. Barnsite abrasives were used. Surface roughnesses reported here were determined by the FECO technique (Fringes of Equal Chromatic Order) at the Naval Weapons Center.

Six  $\text{TiO}_2/\text{SiO}_2$  antireflective (AR) films were also tested. Films of two designs were simultaneously deposited on three substrates of varied roughness. Film deposition and measurement of substrate roughness were done by the Research Division of Optical Coating Laboratory, Inc. (OCLI). Substrate roughness was determined at OCLI by relative scatter measurements. Calibration of the scattering apparatus was done by testing a 10-Å surface supplied by Dr. Jean Bennett of the Naval Weapons Center. The smoothest sample in the coating deposition test compared favorably with the 10-Å rms sample. The roughest substrates had an estimated roughness of  $\sim 100$  Å. These samples were part of a joint LLL/OCLI test of the use of barrier layers with AR films. A description of this study by Apfel et al. is reported elsewhere in these Proceedings.

The silica samples were dusted with a freon spray prior to testing. The smoothest silica sample was washed with high-purity ethanol since it had been previously tested at 40 ns. Previously damaged sites were carefully avoided during this experiment. The thin films were all cleaned using ethanol-wetted strips of tissue.

#### Damage Experiments

Damage experiments at 150 ps were performed using an apparatus and techniques described in detail elsewhere [6]. The laser beam was gently focused to spot sizes of 2-3 mm diameter at the  $e^{-1}$  intensity level. The beam was incident on the surface with measured roughness at  $\sim 5^\circ$  from the normal. Complete spatial and temporal beam profiles were recorded on photographic film for each firing. The energy density on axis was determined absolutely to within 7%. From the streak camera image, the pulse shape and peak intensity was determined. The total absolute uncertainty in the intensity measurement is  $\pm 15\%$ .

In the 150-ps tests, three methods to detect damage were employed. (1) The sample was observed during each irradiation. Near-threshold irradiation produced a faint, but visible, glow. (2) Immediately after each firing, the site was inspected visually using a focused white light source. Since large areas were irradiated, the scattering from the few pits created by the laser was easily visible, except for sites on the roughest sample in the set. (3) The final determination of damage was made by Nomarski microscopy. The three tests agreed for all but the roughest sample. The surface of that sample was so rough that scatter and microscopic examinations were of little value. The 40-ns experiments, performed previously at AFWL, are described in detail in Ref. 5.

#### Results

Nomarski micrographs of damage sites on each of the silica samples are shown in figure 1. The 15-Å surface was free of the usual polishing streaks when viewed at a magnification of 360 X. Streaks could be seen on the 40-Å surface. Damage on both of these surfaces consisted of randomly distributed micropits. There was a weak correlation between streaks and damage on the 40-Å surface. The 140-Å sample was covered with raised polishing structure; damage was initiated at these structural features. We could not determine what specific features on the 350-Å surface were related to the damage at threshold. There was no obvious difference in the microscopic appearance of the immediate surroundings of damaged and undamaged regions of the sample.



Damage thresholds for the silica samples are reported in Table 1 in terms of energy flux, intensity, and rms breakdown electric field strength. All beam parameters are those computed in air at the sample surface; that is, the values have not been adjusted to account for the refractive index of the silica.

Damage thresholds of the four fused silica samples at both 150 ps and 40 ns are shown in figure 2. The primary feature of the earlier 40-ns data is the close agreement between the data and the functional form

$$E_{th} \sigma^{0.61} = \text{constant},$$

where  $\sigma$  is the rms roughness and  $E_{th}$  is the rms breakdown electric field strength. Based on the limited data available, it is not clear that the 150-ps data obeys a simple power law dependence on surface roughness since the 150-ps threshold of the smoothest surface ( $\sigma = 15 \text{ \AA}$ ) is less than that of the sample with 40- $\text{\AA}$  roughness. It is obvious that a roughness  $> 100 \text{ \AA}$  rms causes a reduction in damage threshold at either pulse duration. But the total excursion in damage field strengths is much less for the 150-ps data than for the 40-ns data. As regards Bloembergen's hypothesis, it should be noted that surfaces with an rms roughness of  $< 100 \text{ \AA}$  can have topographical features  $>> 100 \text{ \AA}$ .

Damage thresholds for the six antireflection films are shown in figure 3 as a function of relative scattering intensity. In this case, there is no correlation between the roughness of the substrate and the damage threshold of the film.

Table 1. 150-ps, 1064-nm damage threshold of fused silica as a function of surface roughness.

Sample	Roughness, rms, $\text{\AA}$	$\text{J/cm}^2$	Damage Threshold	
			$\text{GW/cm}^2$	$\text{mV/cm}$
016	15	$8.5 \pm 0.5$	$56 \pm 4$	$4.6 \pm 0.2$
078	40	$11 \pm 1.0$	$73 \pm 7$	$5.2 \pm 0.3$
090	140	$3.5 \pm 0.5$	$23 \pm 3$	$3.0 \pm 0.2$
098	350	$2.5 \pm 0.5$	$17 \pm 3$	$2.5 \pm 0.2$

#### Conclusions

1. Surface roughness greater than  $100 \text{ \AA}$  rms reduces the 1064-nm, 150-ps surface damage threshold of conventionally polished fused silica.
2. Additional 150-ps tests will be required to determine whether a strong and convincing threshold vs. roughness correlation exists for the "smooth" surfaces (rms roughness  $< 50 \text{ \AA}$ ) on normally available optics at  $1.064 \text{ \mu m}$ .
3. The 150-ps damage thresholds of  $\text{TiO}_2/\text{SiO}_2$  antireflection films are not correlated with roughness of the BK-7 glass substrates on which they were deposited.
4. Damage thresholds (MV/cm) at 150 ps are related by the fourth root of the pulse duration to the thresholds found at 40 ns. Extrapolated breakdown fields at 40 ns agree with measured fields to within 30% for the smoother surfaces.
5. The extrapolation of Smith's [7] threshold for bulk breakdown at 30 ps in fused silica yields a predicted 150-ps breakdown threshold in air at the silica surface of  $9.4 \text{ MV/cm}$ . This, when compared with the largest value observed here,  $5.2 \text{ MV/cm}$ , suggests that breakdown fields for surfaces are about half the bulk values. The average interatomic spacing (smoothest possible surface) for fused silica is  $3.57 \text{ \AA}$ .

#### Acknowledgments

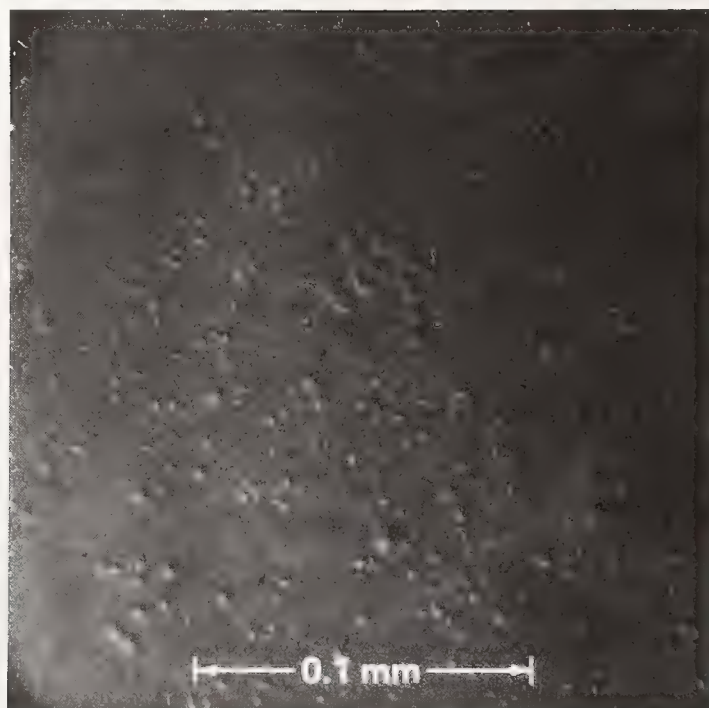
We thank G. E. Murphy for his excellent technical assistance with the laser-damage measurements and J. H. Apfel and E. A. Enemark of Optical Coating Laboratory, Inc., for their collaboration on the substrate surface roughness--thin-film damage studies.

## References

- [1] Crisp, M. D., Boling, N. L., and Dubé, G., Appl. Phys. Lett. 21, 364 (1972).
- [2] Bloembergen, N., Appl. Opt. 12, 661 (1973).
- [3] Fradin, D. W., and Bass, M., Appl. Phys. Lett. 22, 159 (1973).
- [4] Boling, N. L., Ringlien, J. A., and Dubé, G., "Laser-Induced Damage in Optical Materials," in *Laser-Induced Damage in Optical Materials*: 1974, A. J. Glass and A. H. Guenther, eds., Nat. Bur. Stand. (U.S.) Spec. Publ. 414, p. 119 (1974).
- [5] House, R. A., Bettis, J. R., Guenther, A. H., and Austin, R., "Correlation of laser-induced damage with surface structure and preparation techniques of several optical glasses at 1.06  $\mu\text{m}$ ," in *Laser-Induced Damage in Optical Materials*: 1975, A. J. Glass and A. H. Guenther eds., Nat. Bur. Stand. (U.S.) Spec. Publ. 435, pp. 305-320 (1975); also R. A. House, "The effect of surface structural properties on laser-induced damage at 1.06  $\mu\text{m}$ ," Ph.D. dissertation, Air Force Institute of Technology, Wright-Patterson AFB, Ohio, 1975 (now available as report AFWL-TR-76-62, Kirtland AFB, NM 87117); also R. A. House, J. R. Bettis and A. H. Guenther, "Surface roughness and laser damage threshold," IEEE J. Qu. Elect. QE-5, pp. 361-363 (1977).
- [6] Milam, D., Appl. Opt. 16, 1204 (1977).
- [7] Smith, W. L., Bechtel, J. H., and Bloembergen, N., Phys. Rev. B12, 706 (1975).

## Figures

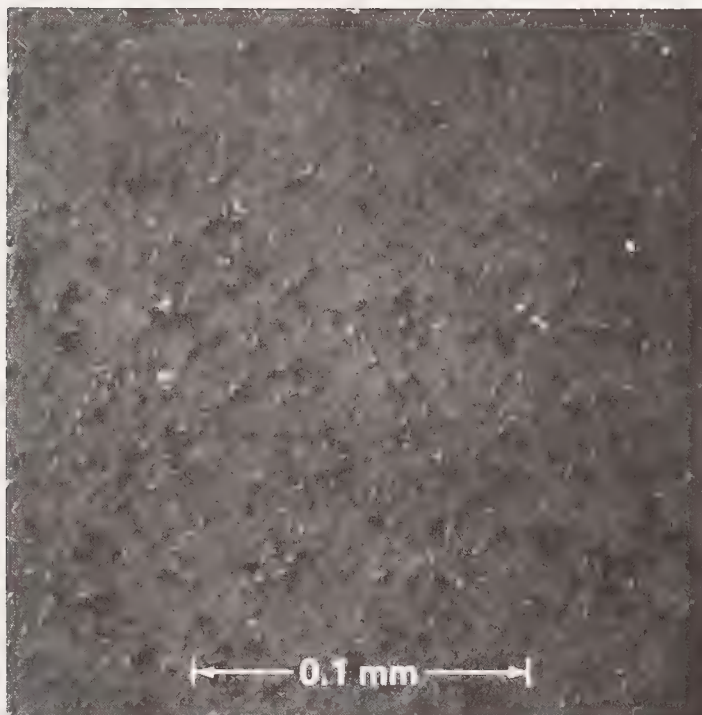
Fig. 1. Nomarski photographs of damage induced on polished fused silica surfaces by 1064 nm, 150 ps laser pulses. a) Damage on a surface with roughness of 15 Å consisted of randomly distributed micropits. b) Damage on a 40 Å surface. Finishing streaks are visible, but there is no strong obvious correlation between the streaks and the damage induced pits. Damage on the 140 Å surface occurred at rough features visible on sites which were not irradiated. Frames c) and d) show respectively damaged and undamaged sites on the 140 Å sample.



1(a)

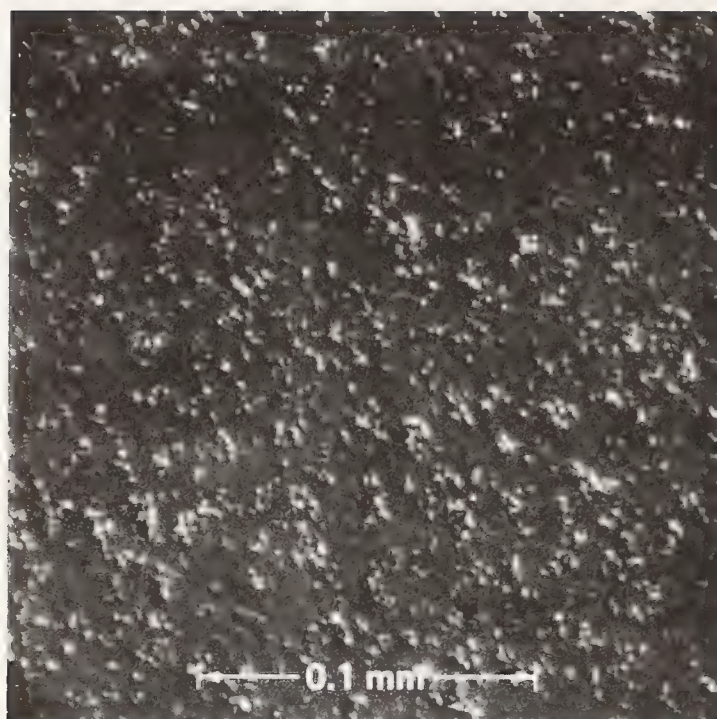


1(b)



1(c)





1(d)

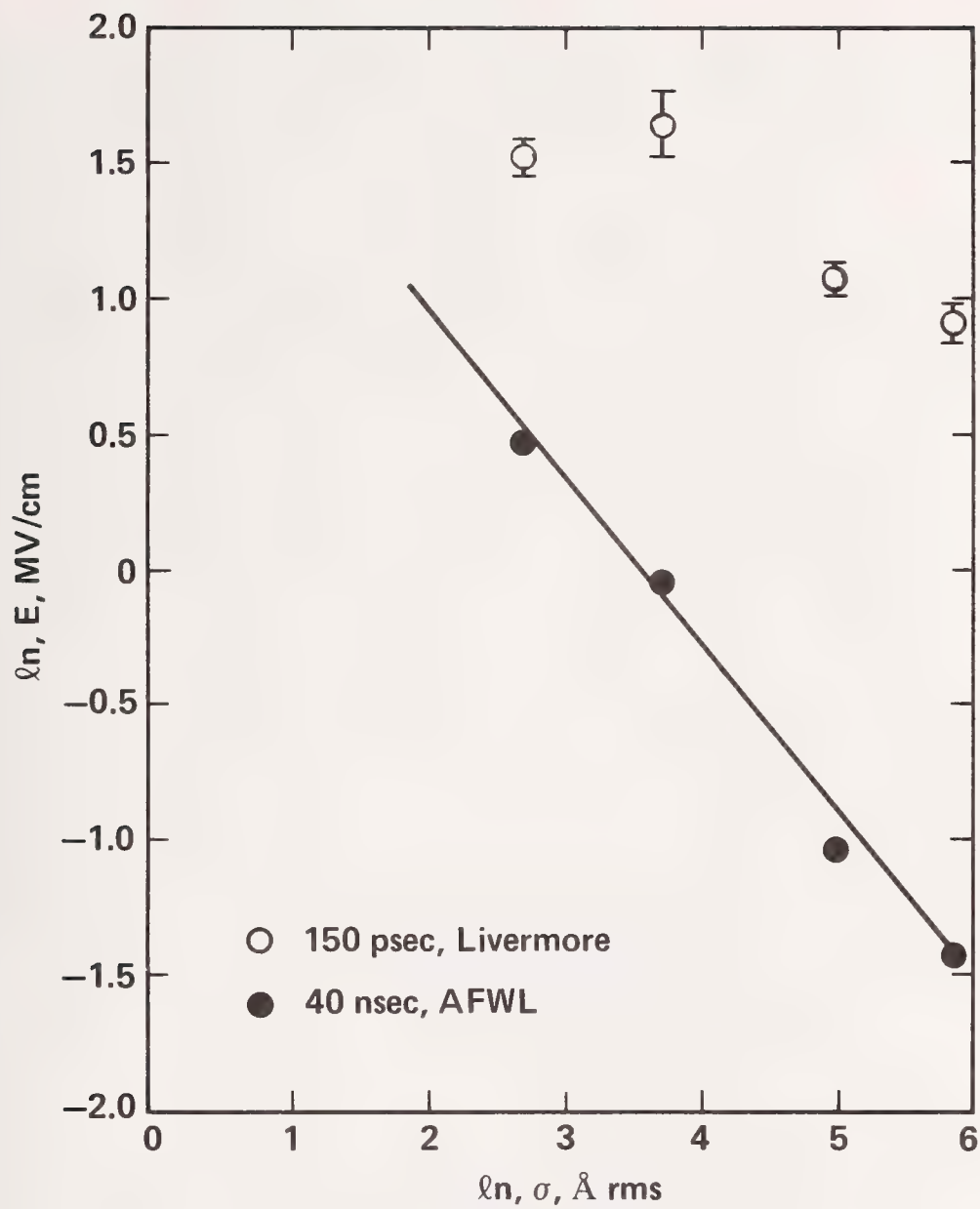


Fig. 2. Surface damage thresholds of four fused silica surfaces as a function of surface roughness for two different pulse durations.

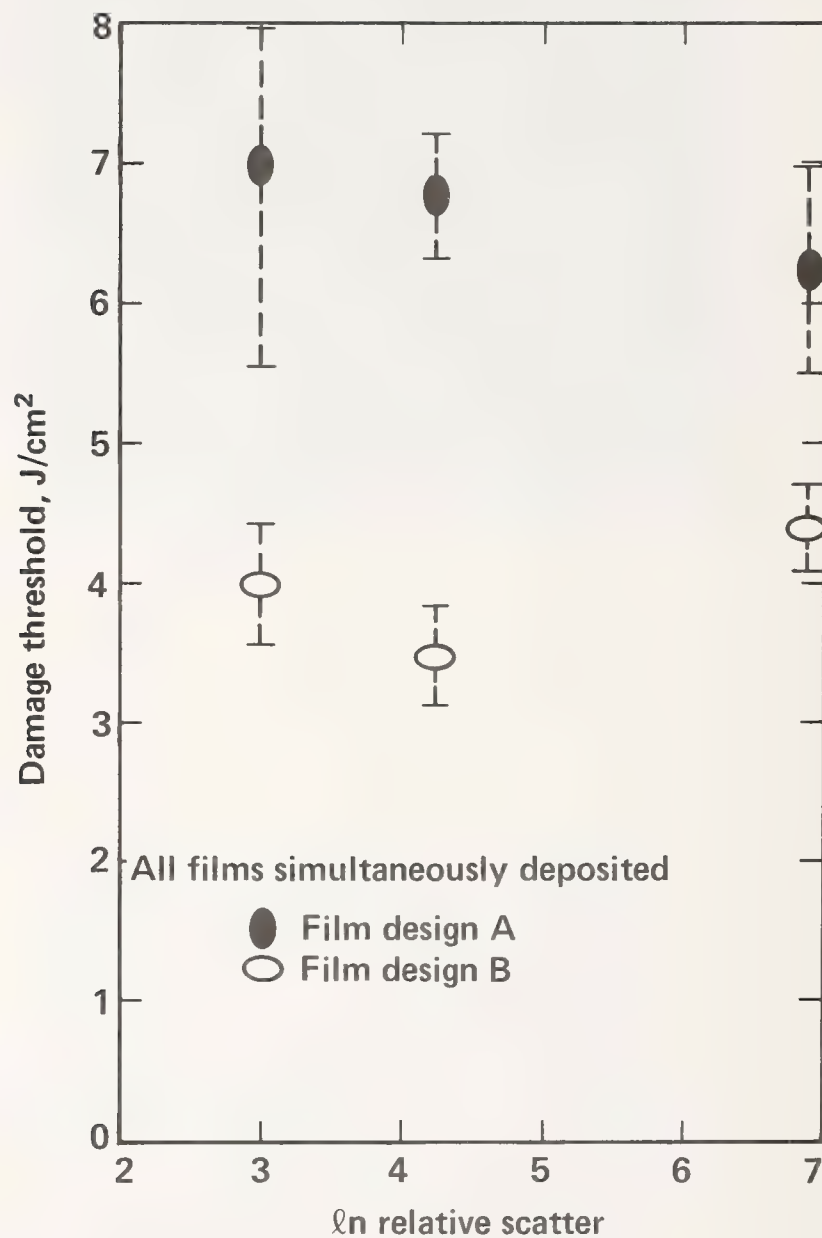


Fig. 3. 150-ps, 1064-nm damage thresholds of  $\text{TiO}_2/\text{SiO}_2$  anti-reflection coatings of two designs as a function substrate roughness. Relative values of roughness were determined by relative scatter measurements. By comparison tests using a sample of known roughness, the roughness of the smoothest substrate was inferred to be  $\approx 10$  Å rms.



## LOW SCATTER FINISHING OF ASPHERIC OPTICS

W. P. Barnes, Jr., and R. R. McDonough  
Itek Corporation  
Lexington, MA 02173

Bowl-feed or settling slurry polishing operations are commonly used for low scatter finishing of flat and shallow spherical optical surfaces. Aspheric surfaces are a powerful optical design option, but they do not permit the development of the closely fitting lap and work surfaces required for effective bowl-feed polishing. Previous IR&D work at Itek had indicated that short term polishing with colloidal silica and a non-woven poromeric lap produced surfaces comparable to bowl-feed surfaces, as determined by scattered light and 1.06  $\mu\text{m}$  damage threshold measurements.

To test the applicability of this approach for low scatter finishing of aspherics, three f/2 paraboloids were given a short final polishing using colloidal silica and full sized flexible laps. No degradation of surface figure was detected, and surface scatter was reduced to values nearly equal to best practice in bowl-feed finishing.

Key words: Aspheric optics; laser damage; low scatter; optical fabrication.

# LOW SCATTER ASPHERIC FINISHING

- 12-INCH-DIAMETER,  $f/2$  PARABOLOIDS
- FUSED SILICA, ULE, CER-VIT
- CONVENTIONAL HAND POLISH TO  $1/2$  TO 1 WAVE FIGURE
  - ASPHERICITY IS 14.6 WAVES
- COLLOIDAL SILICA (SYTON, LUDOX) POLISH
  - TWO 15-MINUTE RUNS
  - ALUMINUM,  $1/4$ -INCH CLOSED CELL FOAM RUBBER, POLITEX LAP



# CER-VIT

## Interferogram Before Syton Polishing



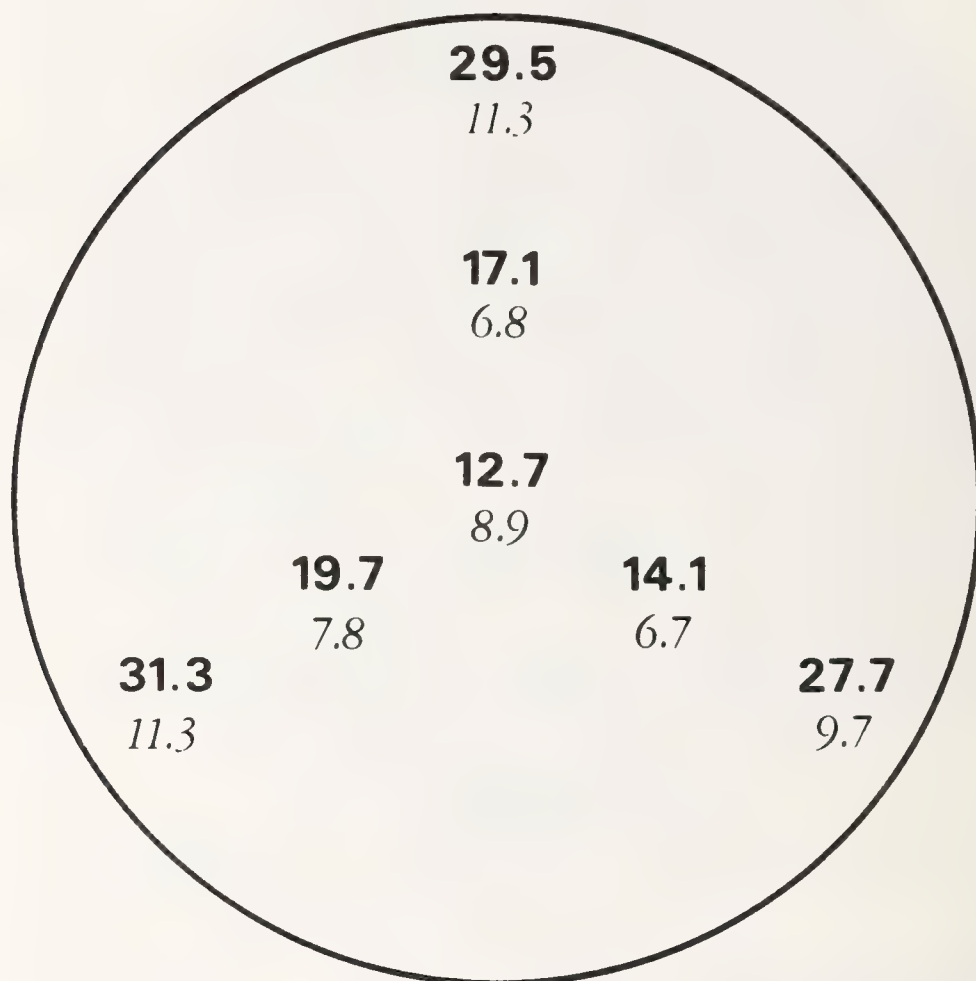
Surface Deviations From True Paraboloid  
(wavelengths at 633 nm):

	<u>Before</u>	<u>After</u>
$r^4$ component	0.45	0.38
Cylinder	0.14	0.03
Other	0.05	0.05



# CER-VIT

Indicated Surface Roughness ( $\text{\AA}$ )  
Before / *After* Syton Polishing



	<u>Before</u>	<u>After</u>
Average	21.7	8.9
Standard Deviation	7.7	1.9

# FUSED SILICA

Interferogram Before Syton Polishing

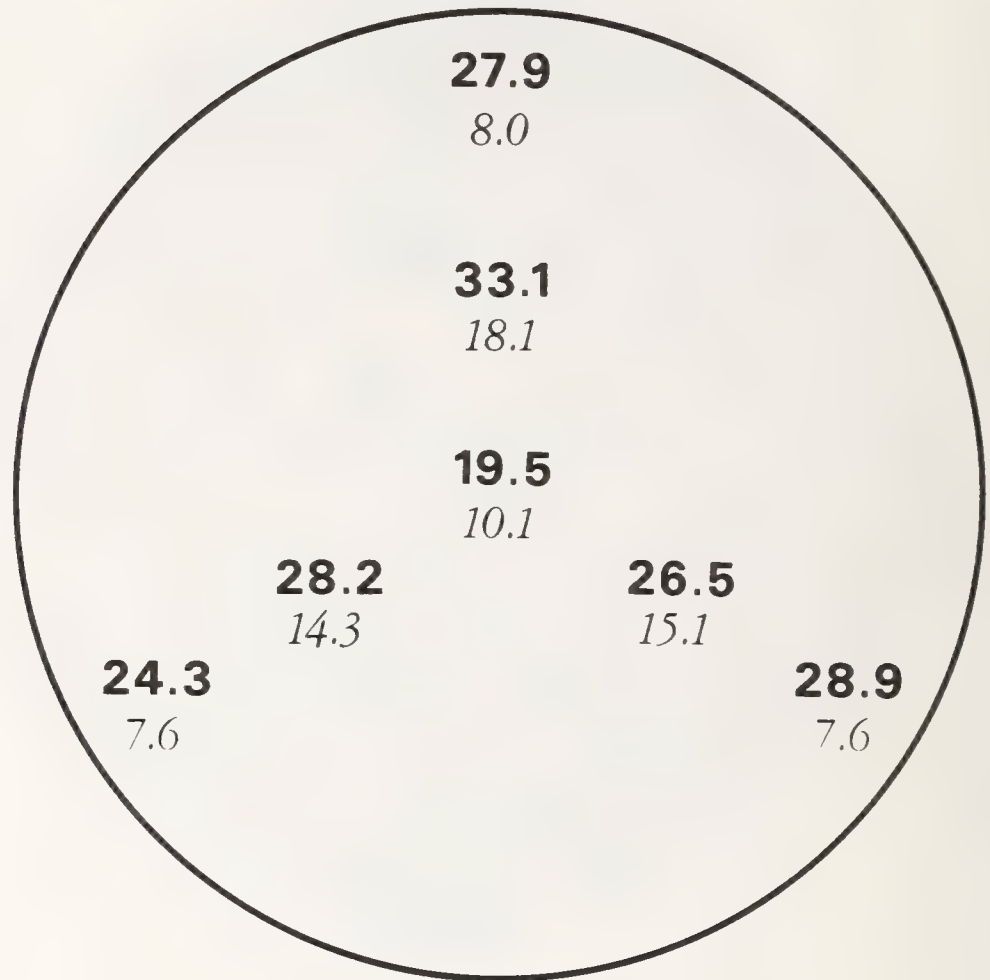


Surface Deviations From True Paraboloid  
(wavelengths at 633 nm):

	<u>Before</u>	<u>After</u>
$r^4$ component	0.83	0.78
Cylinder	0.29	0.03
Other	0.07	0.07

# FUSED SILICA

Indicated Surface Roughness ( $\text{\AA}$ )  
Before / *After* Syton Polishing



	<u>Before</u>	<u>After</u>
Average	26.9	11.5
Standard Deviation	4.2	4.3



# ULE

## Interferogram Before Syton Polishing

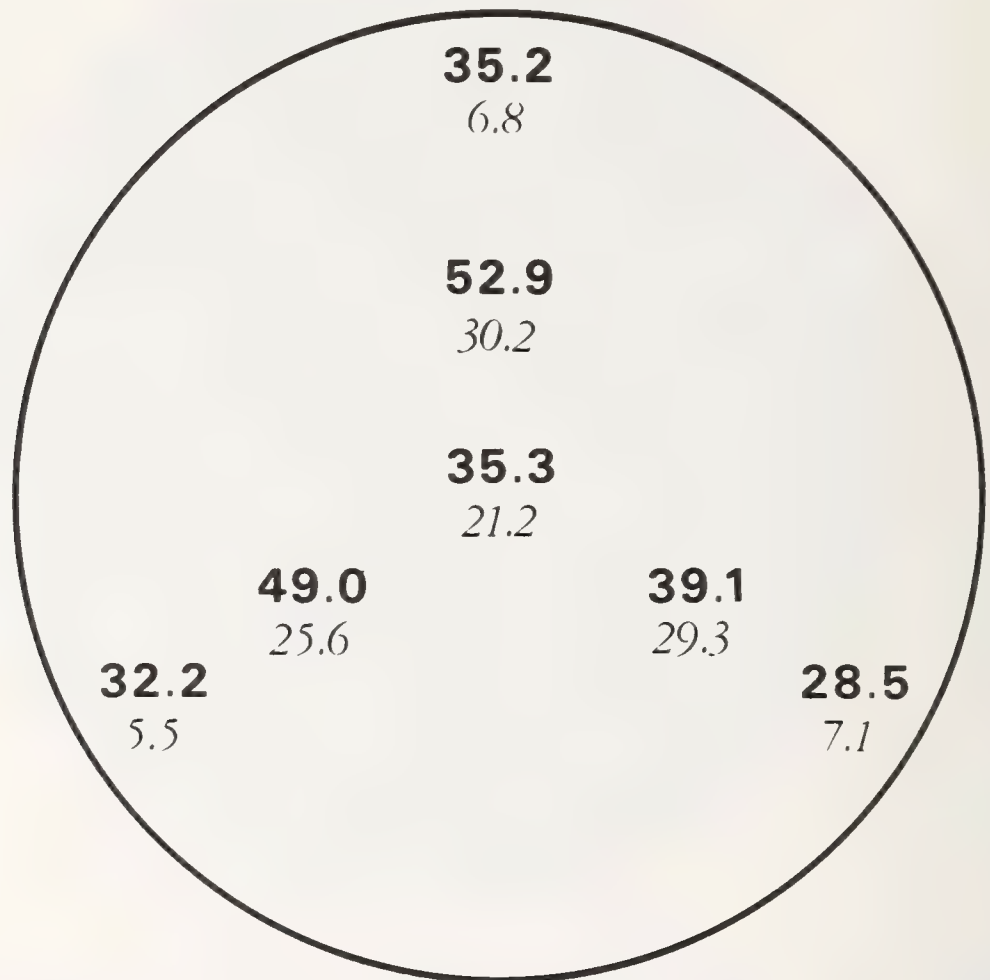


Surface Deviations From True Paraboloid  
(wavelengths at 633 nm):

	<u>Before</u>	<u>After</u>
$r^4$ component	0.15	0.19
Cylinder	0.17	0.17
Other	0.03	0.03

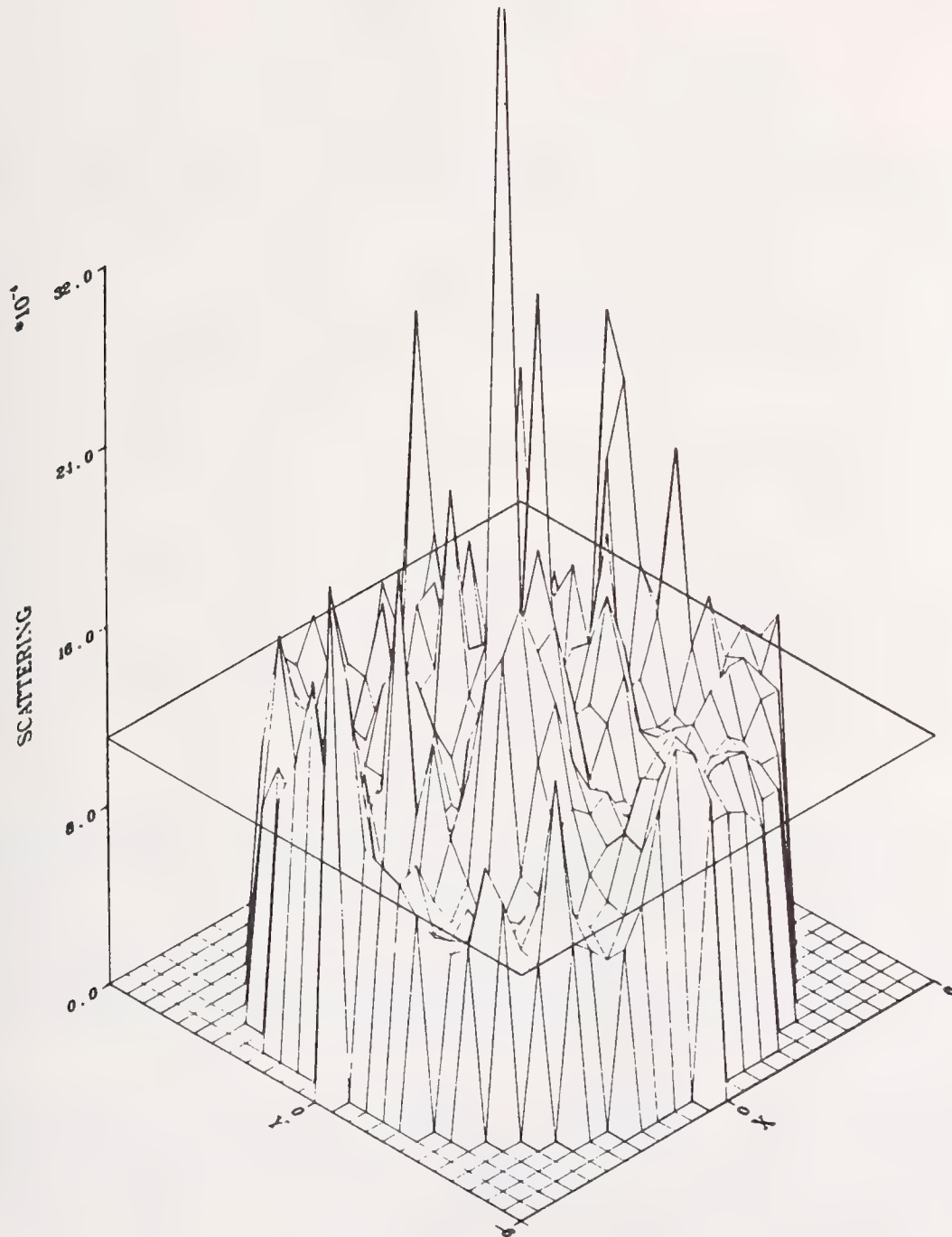
# ULE

## Indicated Surface Roughness ( $\text{\AA}$ ) Before / *After* Syton Polishing



	<u>Before</u>	<u>After</u>
Average	38.9	18.0
Standard Deviation	8.9	11.1

# NWC RESULTS FOR CER-VIT



Indicated Average Surface Roughness =  $14.8 \text{ \AA rms}$   
(469 Points Measured)



S. Sharma, R.M. Wood and R.C.C. Ward

The General Electric Co. Ltd.,  
Hirst Research Centre,  
Wembley, England.

The absorption, reflectance and transmission characteristics of a range of infra-red mirrors and windows have been measured accurately using apparatus developed at the Hirst Research Centre based on a 10W CO<sub>2</sub> c.w. laser. The above characteristics have been related to the methods of fabrication (diamond turning, polishing, etching, dielectric coatings) and to pulsed laser-induced damage thresholds measured using a CO<sub>2</sub> TEA laser, (60 ns FWHH).

The reflectance/transmittance measurement technique will be discussed and the results, together with the absorption data, correlated with the damage threshold measurements. These latter measurements will in turn be shown to correlate with surface quality (measurements made using optical and electron beam microscopy, visible scatter and X-ray topographs) and with surface films or dielectric coatings.

Key words: absorptance; dielectric coated mirror; infrared laser windows; laser mirrors; pulsed CO<sub>2</sub> laser damage; reflectance; 10.6  $\mu\text{m}$  optical components.

## 1. Introduction

This paper is a continuation of the work presented last year [1]<sup>1</sup> when the programme of research on 10.6  $\mu\text{m}$  laser induced damage thresholds at the Hirst Research Centre of The General Electric Company Ltd. under DCVD sponsorship was outlined.

This paper reports work on the development of an accurate reflectance/transmittance measurement apparatus and the correlation of these measurements with absorption, surface finish and laser induced damage thresholds.

## 2. Reflectance/Transmittance Measurements

A laser window or mirror can only be characterised fully when all the elements of the equation  $R + T + A + S = 1$  have been measured accurately at the wavelengths of interest. As a logical sequence of the development, use and experience gained with apparatus set up at HRC to measure reflectance and transmittance accurately at 1  $\mu\text{m}$  it was decided to extend this facility into the 10  $\mu\text{m}$  region in order to back up the absorption measurements reported previously [1].

An apparatus has been developed capable of directly measuring both transmittance and reflectance to a high degree of accuracy (i.e.  $\pm 0.02\%$ ). This apparatus is shown schematically in figure 1 and basically consists of a 10W CO<sub>2</sub> c.w. laser, a chopper, beam splitter, two pyroelectric measurement heads and associated electronics and ratiometric logic and display.

The c.w. laser, chopper and pyroelectric detector heads in conjunction with simultaneous digital logic are used in order to facilitate the making of accurate measurements without the need for a highly stable laser, optical bench etc.

The pyroelectric measurement heads are shown in figure 2. They consist of shot-blasted, gold plated integrating spheres with pyroelectric detectors. This arrangement gives a spatial and angle insensitive measurement. The outputs of these have been shown to be linear with respect to input power.

The processing electronics are shown in figure 3. The beams are either directly compared, D/R, or subtracted (R-D)R, using a high quality analogue divider, depending on the relative values and accuracy required.

The apparatus is first calibrated with the detector heads in positions R and D<sub>0</sub> (see fig. 1) with no sample. The variable gain on the reference beam is changed until a signal ratio of 1.0000 has been

---

1. Figures in brackets indicate the literature references at the end of this paper.

set. The sample is now put in the beam and the new signal (transmittance) read off (in the case of a window). The detector head D is now moved to  $D_1$  and the reflectance read off. Finally the same is removed back to  $D_0$  for a zero check. In the case of high reflectance mirrors the ratio  $(R-D)/R$  gives even greater accuracy.

### 3. Absorption Measurement

The absorption apparatus previously described [1] has been further refined in order to give higher accuracy and repeatability [2]. A schematic of the apparatus is shown in figure 4.

### 4. Damage Threshold Measurement

A schematic of the laser induced damage threshold apparatus is shown in figure 5. The laser is sealed off  $CO_2$  TEA laser [3] with a 60 ns FWHH main pulse and is focussed to 100  $\mu m$  1/e intensity diameter using a 50 mm focal length germanium meniscus lens. The beam power may be varied either continuously using a gas cell (propylene) or by means of thin polythene attenuators.

### 5. Surface Examination

Various techniques have been employed to characterise the substrate surfaces viz:

Optical microscopy - (up to 1000) using a Reichert MEF microscope with dark field illumination - a standard inspection technique on all samples.

Scanning electron microscopy - (up to  $\times 60,000$ ) - this technique has mainly been used on metal mirror surfaces. The microscope has an energy dispersive attachment for detection of elements present on the surface.

Visible scatter measurement - using a He/Ne gas laser probe and integrating sphere/photomultiplier, capable of making scatter measurements down to 0.005%. This has mainly been used to characterise and evaluate dielectric coatings but has also been used with metal mirrors.

X-ray topography - used for evaluating the crystallographic perfection of the surface (controlled penetration down to 20  $\mu m$  for germanium) of single crystals.

Infra-red spectrophotometer measurements - (Perkin-Elmer Type 325 grating I-R spectrophotometer) on windows and dielectric coatings.

X-ray fluorescence measurements - analysing thin films and deposits on mirrors.

### 6. Metal Mirrors

The characteristics of a series of high quality metal mirrors have been measured. In order to eliminate variations in substrate quality etc. a number of mirrors were produced by single-point diamond turning OFHC copper blanks by Heliotrope Ltd. Some of these were tested bare, some were gold-plated, by Mirror Techniques Ltd. and others were overcoated with  $ThF_4$ .

The characteristics have been tabulated, see table 1, and correlation has been found between the various surface measurement techniques and the laser damage thresholds. Table 1 shows the summary of results made on two mirrors of each type, one as near perfect as has been obtained and one of slightly worse quality. These results illustrate the ways in which the surface quality affects the reflectance and the damage thresholds of good quality mirrors.

The optical and scanning electron microscopy examination showed that the uncoated diamond turned OFHC copper mirrors were of very good quality (no scratches visible by either technique). The SEM micrographs (figure 6a and b) showed that the surfaces contain numerous very small shallow spherical holes (approximately 500  $\text{\AA}$  dia., 250  $\text{\AA}$  deep). These holes are typical of the diamond turning procedure. Under optical examination mirror number 2 exhibited a slightly patchy surface, attributed to a thin oxide layer. This slight difference between the samples is repeated in absorptivity, reflectance, scatter and damage thresholds.

The gold-plated mirrors exhibited visible turning marks (not visible on unplated surfaces), although the SEM micrographs (figures 6c and d) show that the plating procedure fills in the turning 'holes' and replaces them with a gently undulating surface. The height of these undulations is estimated to be about 100  $\text{\AA}$ . The visible scatter measurements were higher for these surfaces than for the uncoated surfaces. Both gold-plated mirrors have higher absorptivity than the uncoated copper mirrors in line with previous results [1]. Mirror 4 had a 'milky' looking surface and a higher absorptivity than mirror 3. The laser induced damage thresholds were shown to be uniform ( $\sim 8 \text{ MW mm}^{-2}$ ). The lower damage levels for these mirrors (relative to the uncoated copper values of  $\sim 10 \text{ MW mm}^{-2}$ ) are due to their greater absorptivities and are in agreement with previously measured results[1].

A  $ThF_4$  dielectric coating on a diamond turned surface should, apart from microscopic coating



defects, allow the high reflectance and damage thresholds of uncoated copper to be realized whilst giving protection from oxidation. In practice care must be taken both to coat the copper surface, as soon as possible after machining to stop a thin film of oxide forming, and also to coat with a thick enough layer to stop 'pinholes' penetrating through the protective layer. Table 1 includes results on mirrors 5 and 6, one of which developed a 'bloom' on the surface after exposure to air. The absorption, reflectance and damage threshold values reflect the differences between the surfaces.

The composition of the surface film on degraded mirrors has been investigated and film thicknesses of the order of 0.5  $\mu\text{m}$  have been examined using a scanning electron microscope fitted with an energy dispersive system for the detection of elements present.

Oxide, nitrate and chloride layers have been identified. Figure 7 shows a SEM micrograph of a badly tarnished surface of a Be/Cu mirror. This layer was analysed using the energy dispersion elemental analyser to be chloride and copper nitrate.

## 7. Window Materials

During the last year our attention has been mainly concentrated on measurements on CVD grown zinc selenide and on surface improvement of germanium.

CVD grown zinc selenide from two sources (Raytheon and AWRE) has been tested. Table 2 illustrates that both sources have reduced the absorption.

One of the principle areas of concern is the relative magnitudes of the possible surface layer absorption and the bulk absorption.

Most of the surface absorption (of the order of  $4 \times 10^{-4}$  per surface for a diamond polished sample [2]) may be attributed to a thin broken-up layer. This layer can be improved by polishing. Inspection of figure 8 shows, for example, that measurements made on 1974 ex Raytheon ZnSe, after etch polishing to a high standard indicated that the maximum surface absorption was less than  $1.8 \times 10^{-4}$  per surface. Other measurements [4] however, have indicated that it is possible to detect the effect of a water layer on the surface and it has been suggested that one cause of discrepancy between measurements made at different laboratories may lie in differences in relative humidity.

Inspection of the absorption and damage thresholds, table 2, indicates that the absorption is not the dominating damage mechanism, the threshold being peak power density rather than energy density dependent. The disappointing factor in this improvement is that the damage threshold has not improved markedly over the years. This is presumed to be because of the microscopic structure of the ZnSe (X-ray measurements show that the crystallite sizes are typically 20  $\mu\text{m}$  (max. 50  $\mu\text{m}$ ) on samples from both sources).

The relationship between surface finish and laser damage threshold has also been sought for germanium. Previous results [1] indicated that the laser-induced surface damage threshold for 'Syton' polished germanium was low and variable (0.7 to 4  $\text{MW mm}^{-2}$ ). When ion-beam etched the damage threshold was raised to between 3 and 5  $\text{MW mm}^{-2}$ . SEM micrographs indicated that the etched surface looked marginally better. X-ray topographs have been taken of the etched and unetched surface layers. Several reflection topographs were obtained, using different Bragg reflections to vary the angle of incidence of the X-ray beam with the crystal surface. These give differing pictures depending on the penetration depths of the X-rays. The X-ray topographs reproduced in figure 9 show the difference between etched and unetched crystal using two different Bragg reflections. Figure 9a is a 311 topograph (i.e. Bragg reflection from {311} planes, penetration depth  $\sim 0.5 \mu\text{m}$ ) and figure 9b is a 511 topograph (Bragg reflection from {511} planes, penetration depth  $\sim 10 \mu\text{m}$ ). The surface etching was of the order of 1 to 2  $\mu\text{m}$ .

The unetched area (9b) shows a large number of polishing scratch images (not visible using an optical microscope) superimposed on images of grown-in dislocations. The etched area shows the continuation of the strain associated with the most severe scratches superimposed on the dislocation pattern.

In contrast to this the unetched area in Figure 9a, looking at the top 1  $\mu\text{m}$  on the surface of the crystal, shows a greater scattering of the X-ray intensity than the etched area. The mottled appearance of the etched area indicates that the surface is now no longer flat. The dislocation images are still visible in this area but have a much reduced contrast compared with the 511 topograph (9b). The dislocation images are not visible in the unetched layer. Careful interpretation of the X-ray topographs indicates that the unetched, Syton polished, surface is disturbed and a broken-up, physically deformed layer (rather than amorphous) of about 0.5  $\mu\text{m}$  depth exists. Further investigation is being made into the optimum technique of polishing/etching in order to arrive at a single crystal, flat surface.

## 8. Conclusions



The absorption, reflectance and transmission characteristics of a range of infra-red mirrors and window materials have been measured and related to the methods of fabrication and to measured pulsed laser-reduced damage thresholds. The mirror characteristics have been shown to correlate with surface quality and surface films.

#### 9. Acknowledgement

This work has been carried out with the support of Procurement Executive, Ministry of Defence, sponsored by DCVD.

#### 10. References

- [1] Gibbs, R and Wood, R.M., Laser-induced damage of mirror and window materials at 10.6  $\mu\text{m}$ . Proc. 8th Symp. on Laser Induced Damage in Optical Materials. NBS Special Pub. 462, 181, (1976).  
 [2] Gibbs, R and Lewis, K.L., Laser calorimeter for the determination of the absorption coefficients of thin 10.6  $\mu\text{m}$  windows (to be published J. Phys. E.).  
 [3] Stark, D.S., Cross, P.H. and Foster, H., IEEE J.Q. Elec., QE.11(9), 774, (1975).  
 [4] Lewis, K.L., (private communication).

Table 1. Characteristics of metal mirrors

Mirror	Percentage Absorption % A @ 10.6 $\mu\text{m}$	Percentage Reflectivity % R @ 10.6 $\mu\text{m}$	Percentage Absorption % A @ 0.63 $\mu\text{m}$	Damage Threshold MW $\text{mm}^{-2}$		Comments
				Defect Site	Clear Area	
Diamond-turned OFHC copper (1)	0.7	99.2	0.27 $\rightarrow$ 0.47	-	11	Very good visual quality. 500 $\text{\AA}$ dia., 250 $\text{\AA}$ deep 'turning holes'.
Diamond-turned OFHC copper (2)	0.9	99.0	0.50 $\rightarrow$ 0.69	7.6	8.7 $\rightarrow$ 9.8	Patchy surface. 500 $\text{\AA}$ dia., 250 $\text{\AA}$ deep 'turning holes'.
Diamond-turned gold-plated (3) OFHC copper	1.0	98.9	0.75 $\rightarrow$ 0.81	-	7.8	Turning marks. Gently undulating surface, 100 $\text{\AA}$ height.
Diamond-turned gold-plated (4) OFHC copper	1.2	98.7	0.59 $\rightarrow$ 0.82	4.2	8.1	'Milky' looking surface, turning marks, gently undulating surface, 100 $\text{\AA}$ height.
ThF <sub>4</sub> overcoat diamond turned (5) OFHC copper	1.37	98.5	1.0 $\rightarrow$ 1.6	2.0 $\rightarrow$ 3.4	3.5 $\rightarrow$ 5.0	20 $\mu\text{m}$ diameter coating defects, 'bloom' on surface.
ThF <sub>4</sub> overcoat diamond turned (6) OFHC copper	1.241	98.8	0.1 $\rightarrow$ 0.5	3	>11	Very good mirror with no visual defects.

Table 2. Absorption and damage thresholds for ZnSe

Source	Date	Absorption Coefficient $\text{cm}^{-2}$	Damage Threshold MW $\text{mm}^{-2}$
Raytheon	1974	$4.9 \times 10^{-3}$	3.2 $\rightarrow$ 7.5
	1974	$4.9 \times 10^{-3}$	1.5 $\rightarrow$ 3.8
	1974	$4.9 \times 10^{-3}$	3.2 $\rightarrow$ 5.5
	1976	$2.1 \times 10^{-3}$	3.5 $\rightarrow$ 7.0
AWRE	1975	$20 \times 10^{-3}$	0.8 $\rightarrow$ 4.5
	1976	$5.0 \times 10^{-3}$	2.2 $\rightarrow$ 4.7
	1977	$1.6 \times 10^{-3}$	3.6 $\rightarrow$ 11.2

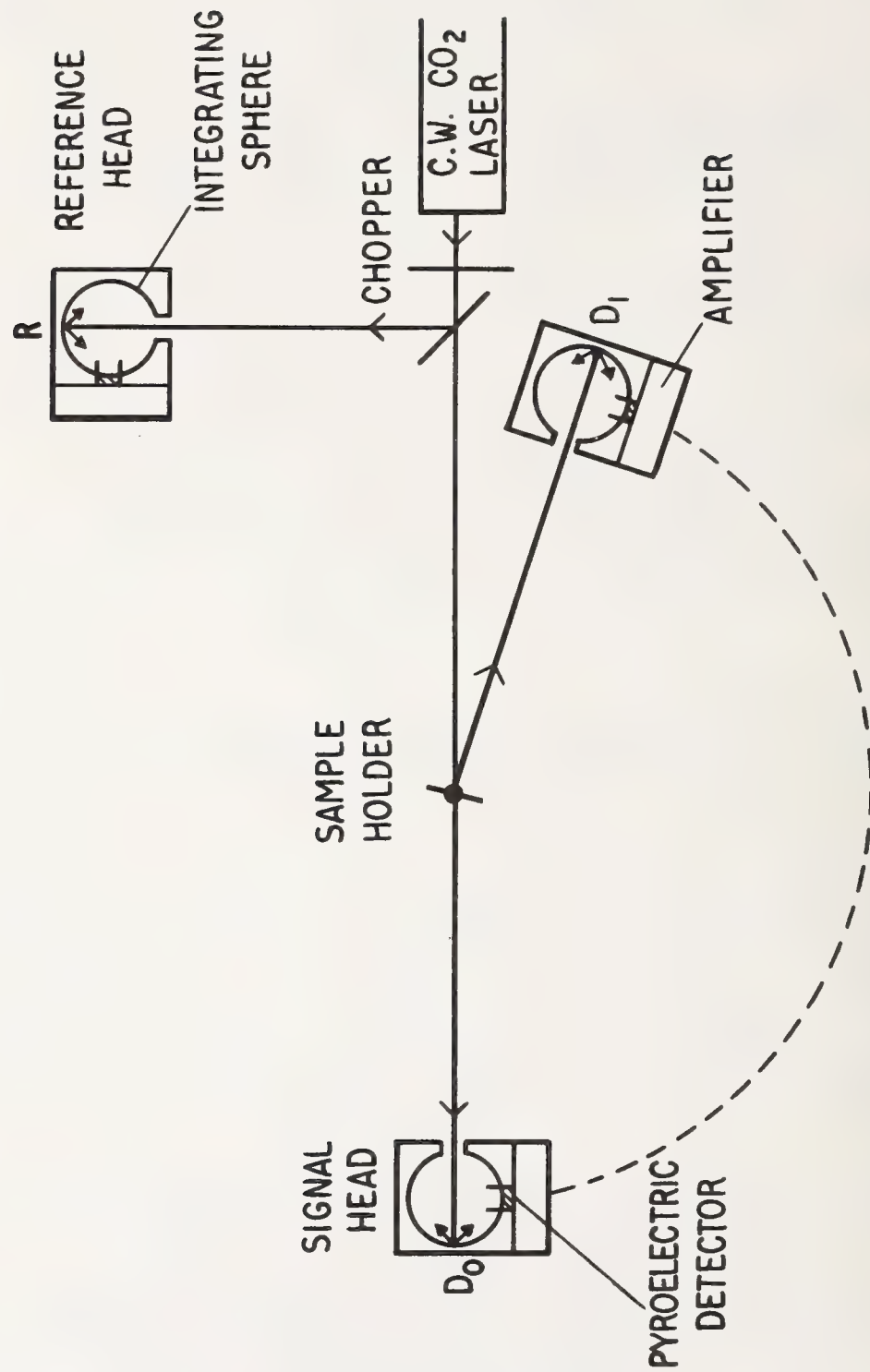
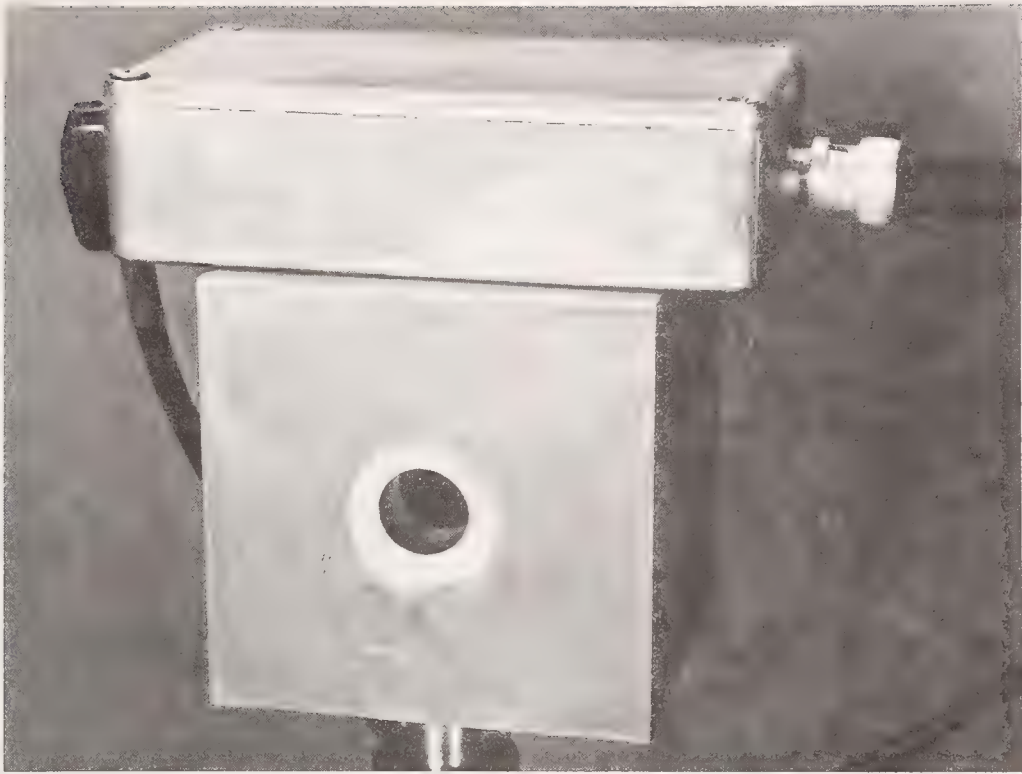
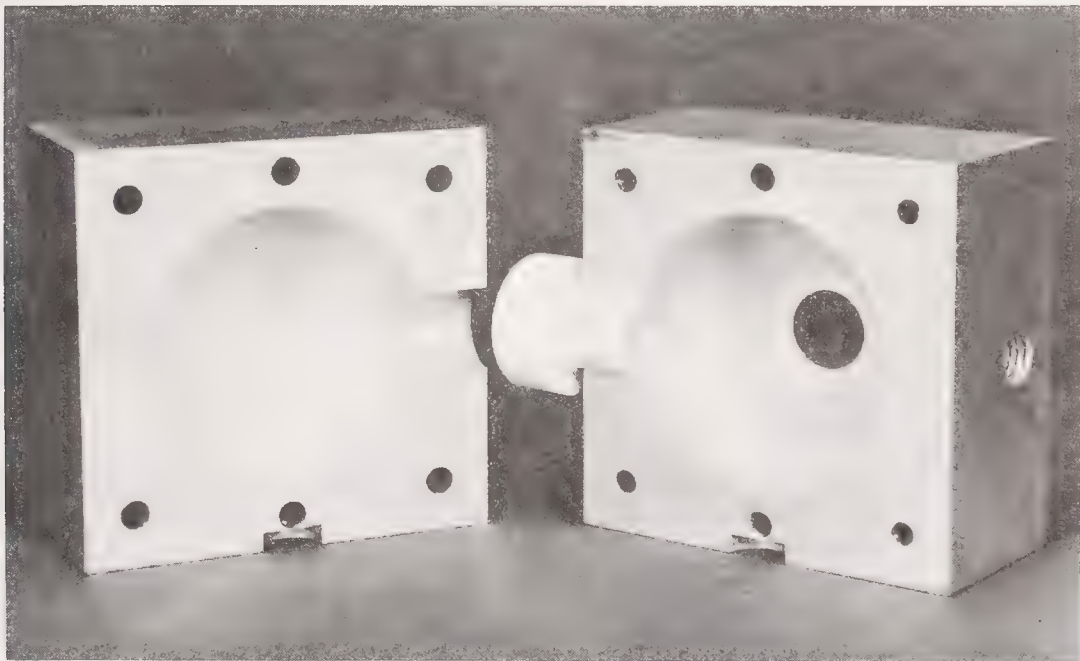


Figure 1. Schematic of reflectance/transmittance measurement apparatus.



(a)



(b)

Figure 2. Pyroelectric measurement head.



PYROELECTRIC  
DETECTOR  
HEADS

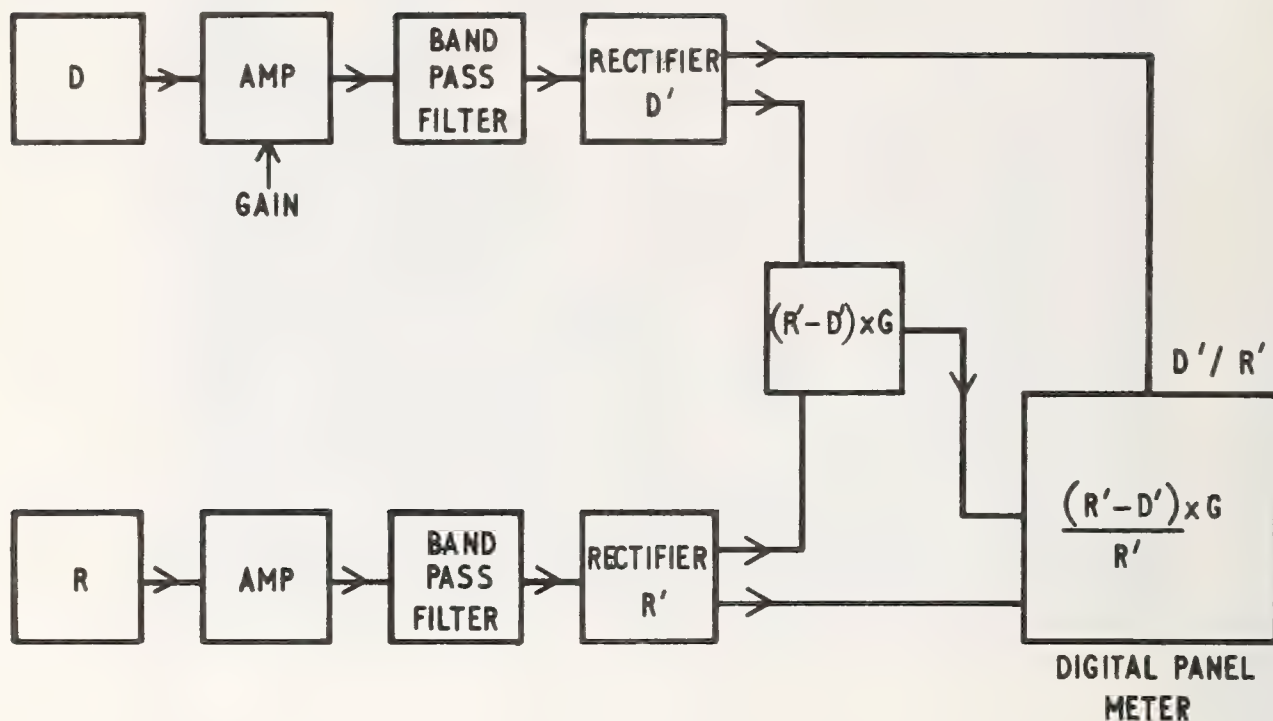


Figure 3. Reflectance measurement processing electronics.

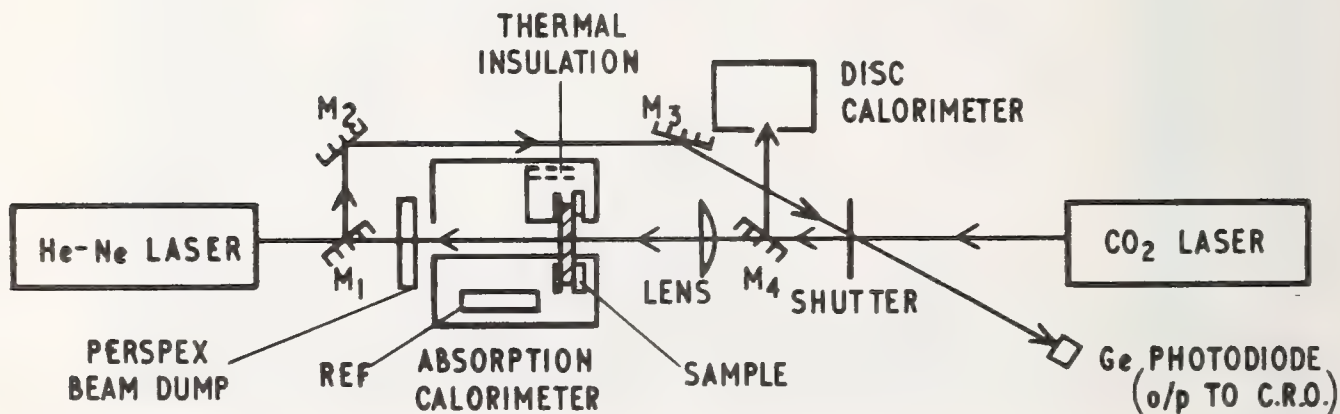


Figure 4. Absorption measurement apparatus.

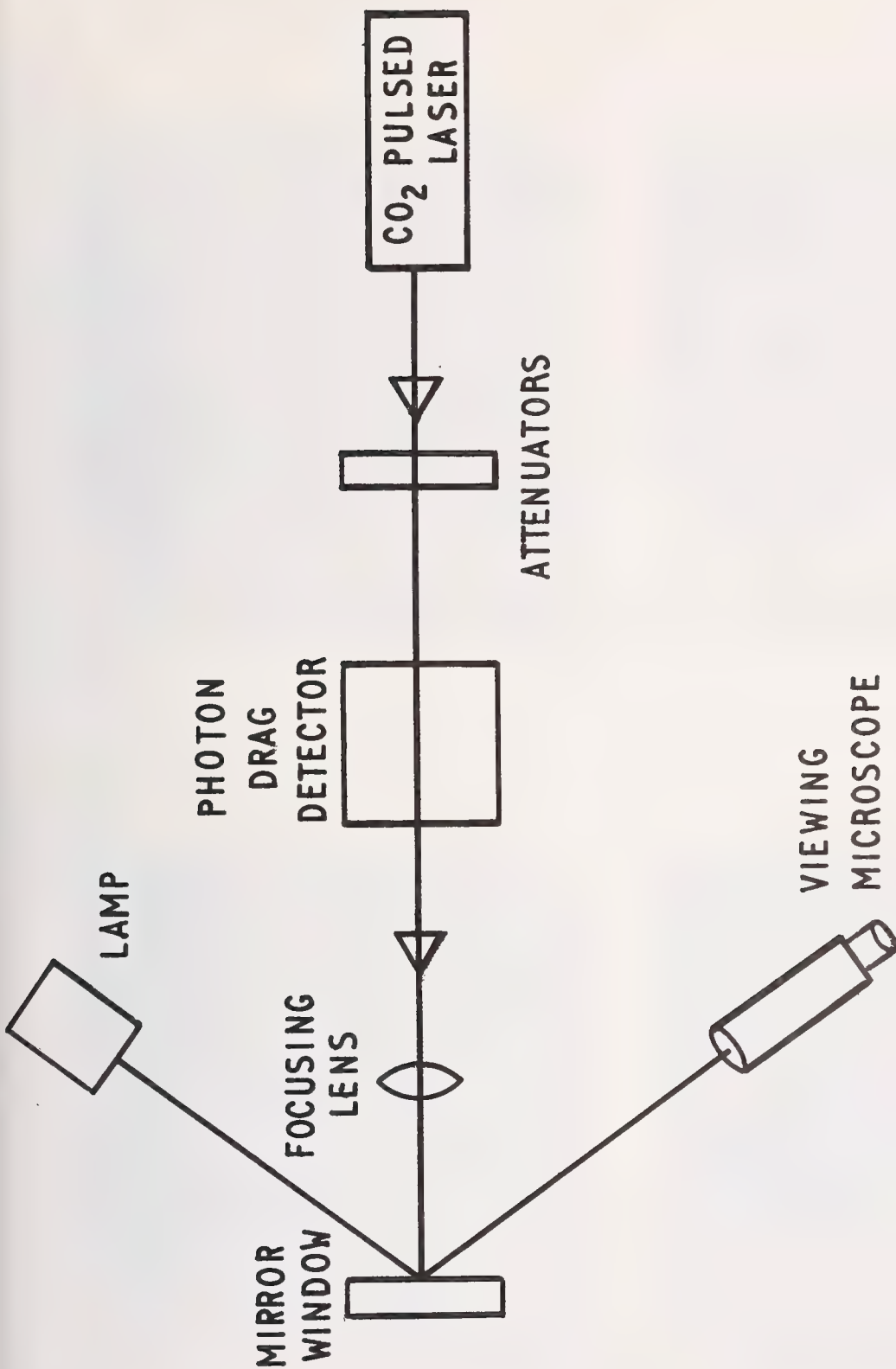
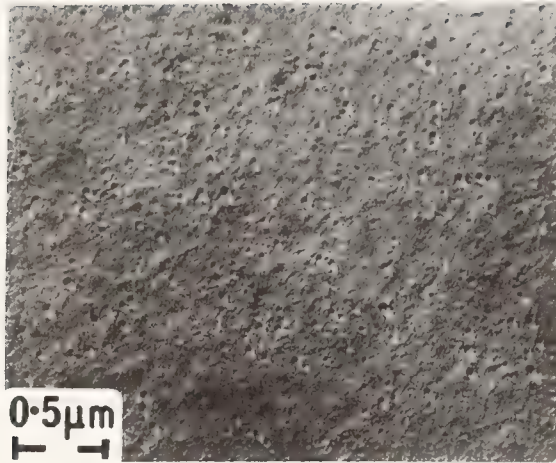
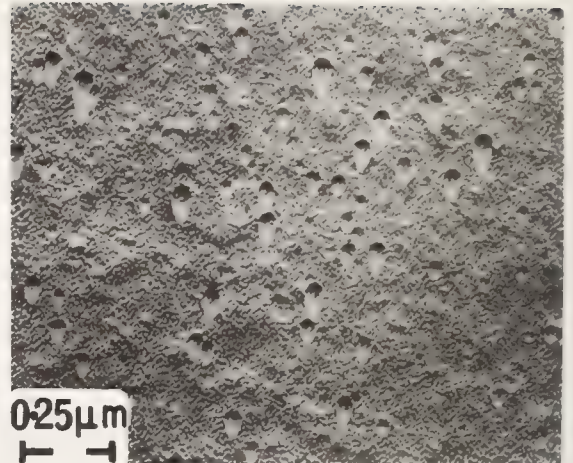


Figure 5. Schematic of pulse damage measurement apparatus.

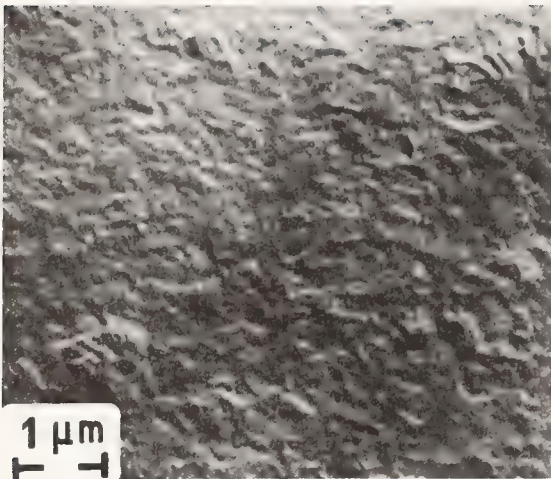


(a)

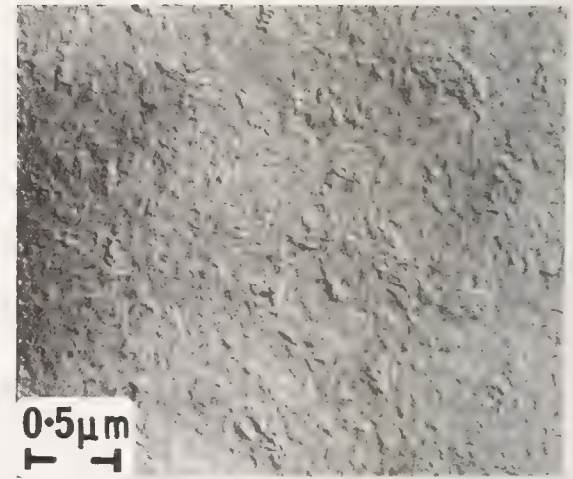


(b)

(a) & (b) Diamond-turned OFHC copper mirrors.



(c)

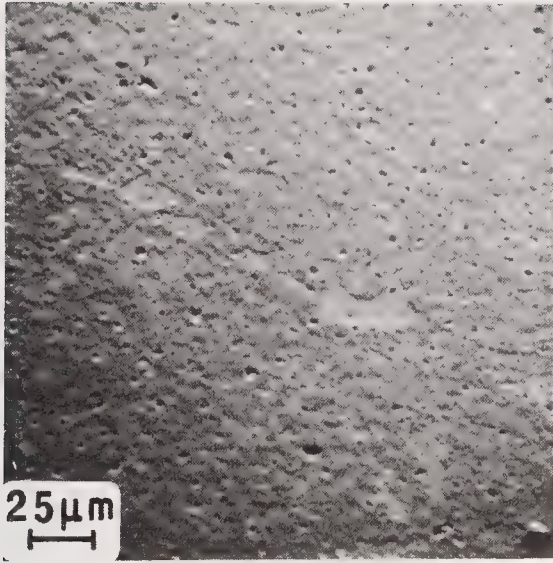


(d)

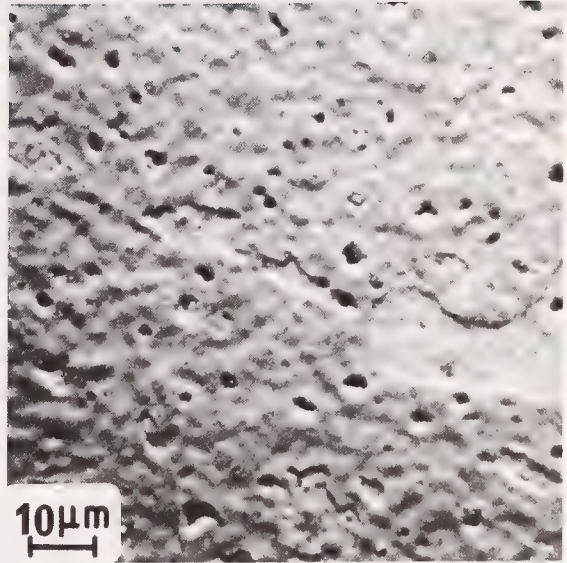
(c) & (d) Gold-coated, diamond-turned OFHC copper mirrors.

Figure 6. Scanning electron micrographs.

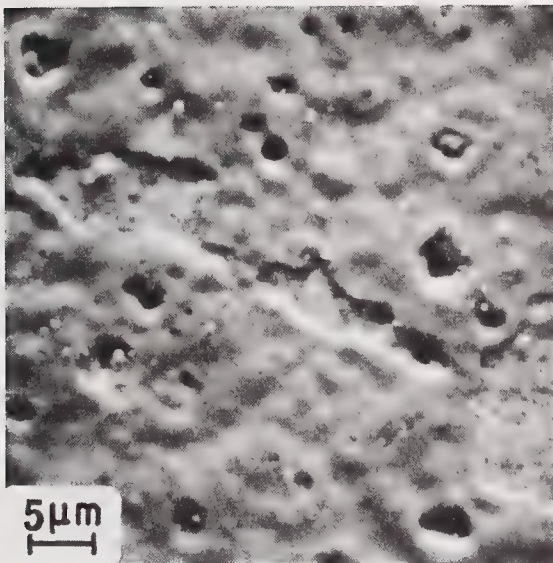




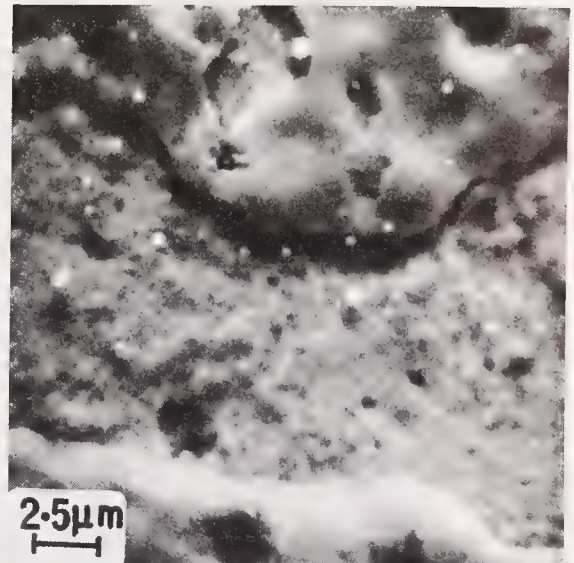
(a)



(b)



(c)



(d)

Figure 7. Scanning electron micrographs of surface layer of BeCu mirror.

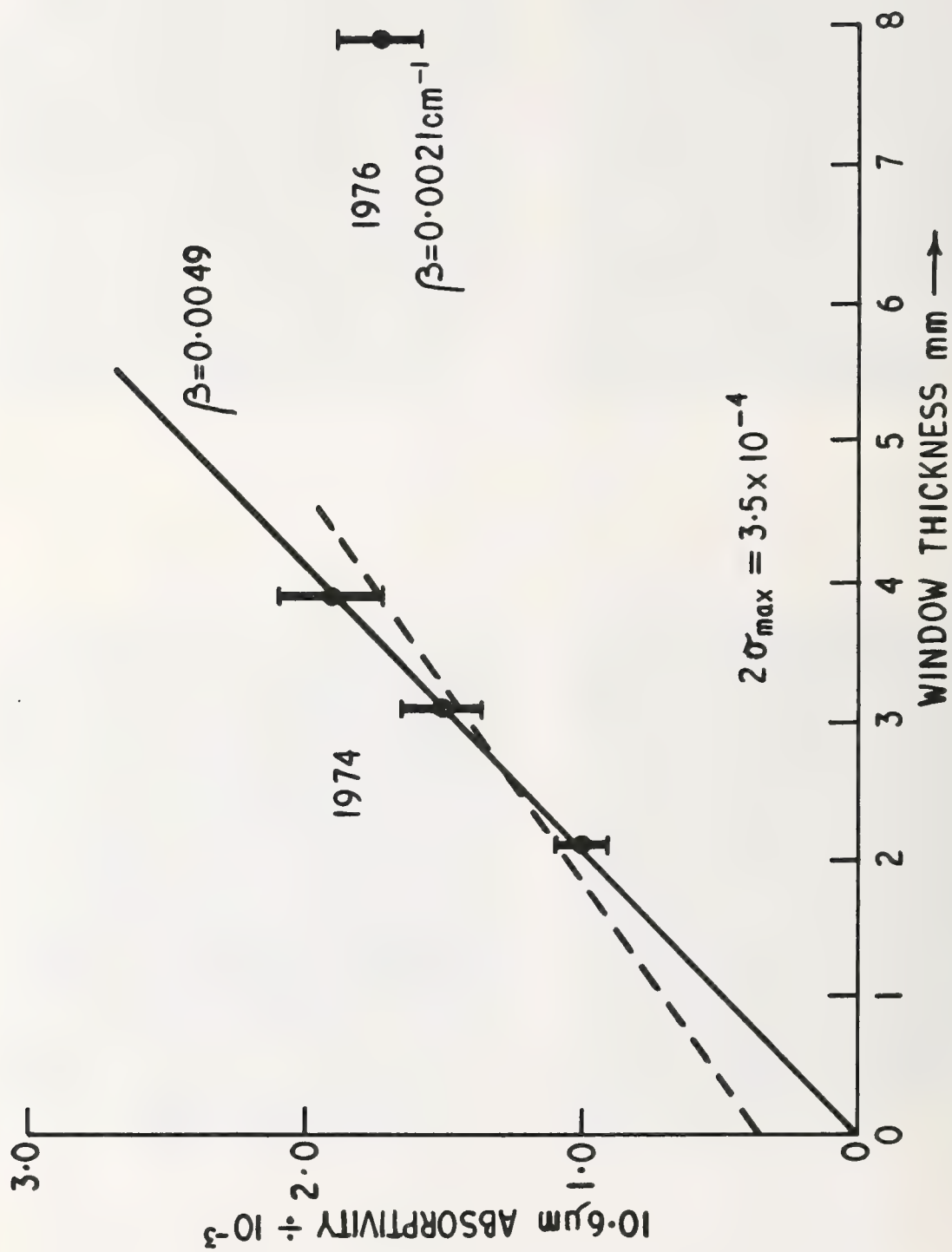
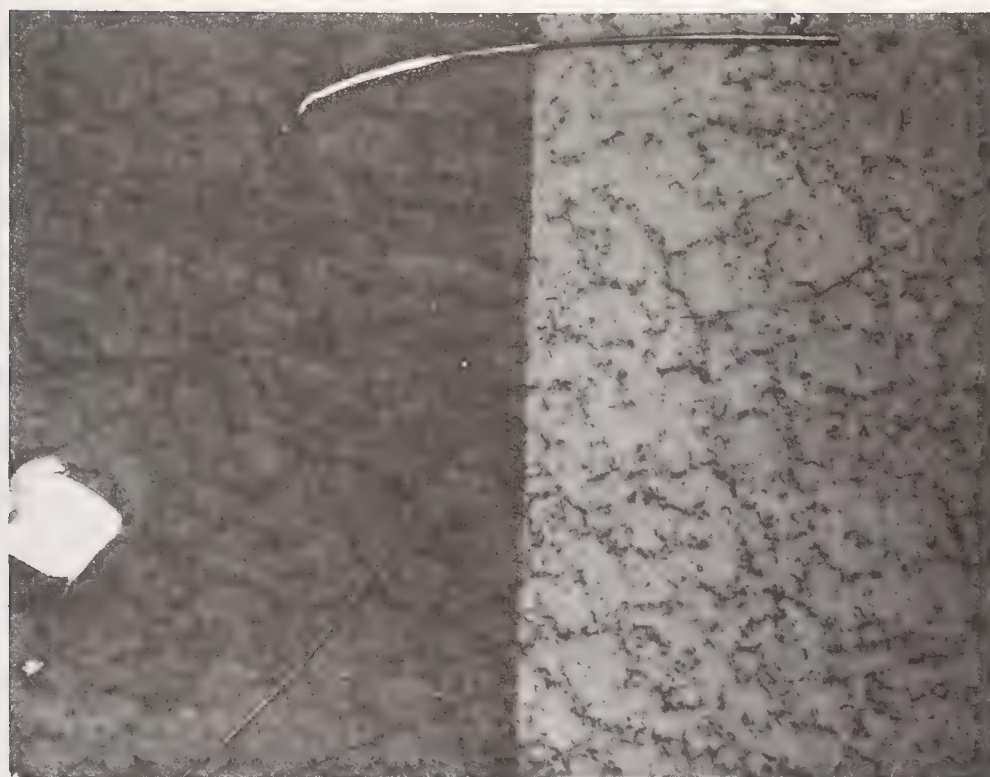


Figure 8. Zinc selenide absorption.



(a) Surface topograph [0.5  $\mu\text{m}$  penetration] unetched and etched (X30).



(b) Topograph [10  $\mu\text{m}$  penetration] unetched and etched (X30).

Figure 9. X-ray topographs of germanium mirror.



COMMENTS ON PAPER BY SHARMA, WOOD, AND WARD

The speaker indicated that the depth of the pits seen on the scanning electron microscope pictures was estimated by measuring the angle of the shadow cast into the hole, and that this measurement technique was good to about 10%. He was asked about the observed damage level of the germanium surface. He indicated that as received, the germanium surfaces damaged at about 4 joules per square centimeter, while after etching, the damage level was raised to about 25 joules per square centimeter.

## POLISHING SINGLE POINT DIAMOND TURNED MIRRORS

R. E. Parks, R. E. Sumner and R. E. Strittmatter  
Optical Sciences Center  
University of Arizona  
Tucson, Arizona 85721

A method of removing the high frequency micro-ripple from single point diamond machined mirrors has been developed. The process uses conventional hand polishing techniques and laps of sufficient rigidity to bridge the microripple yet soft enough not to scratch the metal mirror surface. Substantial material must be removed from the mirror surfaces in some cases and the surface figure may be degraded unless careful testing is done during the process. We present photographs showing the reduction in scattering and improvement in mirror surface roughness as the result of the polishing. Phase-contrast microphotographs also show that the polished surface is almost as free of mechanical defects (scratches and pits) as the original virgin turned metal surface.

Key words: Metal mirrors; microripple; polishing; scattering; single point diamond turned mirrors.

### 1. Introduction

We present a series of pictures of 400mm diameter single point diamond turned copper off axis parabolas before, during and after polishing to remove the microripple. Before polishing, the scattered light in the visible is sufficiently intense to make proper alignment difficult to impossible. Double pass interferograms contain little useful information.

After polishing, the image forms a tight core, a double pass interferogram is easy to interpret and a microphotograph of the surface shows the absence of turning marks.

### 2. Test Methods

In order to assess the results of the polishing procedures, several methods of testing the off axis parabolas were used. A point source microscope was used to examine the image formed by the mirrors while a modified Fizeau type interferometer was used to measure the surface contour. In order to study the surface on a smaller scale, a Leitz metallographic microscope with a 10X differential interference contrast objective was used.

Figure 1 shows the parameters of the mirror and its optical test. The focus of the test instrument is placed in coincidence with the focus of the parabola. The light, after being collimated by the parabola, is autoreflected by an optical flat placed perpendicular to the optical axis of the parabola. After a second reflection in the parabola the light returns to the original focus after suffering twice from the defects in the surface of the parabola.

In order to examine the return image from the parabola, a point source microscope was placed with its objective focus at the focus of the parabola. Figure 2 shows the design of the microscope and the position of the camera used to photograph the image. A 20X objective was used to insure filling the f/1.9 cone angle of the mirror. Illumination was provided by an optical fiber drawn down to a diameter of 0.3mm and bent parallel to the axis of the microscope. The image size projected by the 20X objective was 15 $\mu$ m.

In figures 4(a,b,c) the upper spot of light is light back scattered by the fiber and is not representative of the source size itself. The lower spot of light (elongated horizontally in figures a and b) is the return image from the mirror at several stages of polish.

In order to assess the surface figure of the mirror, a modified Fizeau type interferometer<sup>[1]</sup> was used as illustrated schematically in figure 3. In this application the advantage of this interferometer is that the f/1.9 acceptance cone of the parabola can easily be filled without resorting to a rather expensive fast diverging lens required by some interferometers. The pinhole spatial filter in the interferometer as reflected in the beamsplitter cube is placed at the focus of the parabola. Interference is then obtained between the return wavefront from the parabola and the reflection off of the spherical reference surface on the beamsplitter cube. The fringes may then be photographed directly using a 35mm camera equipped with an f/1.5 or faster lens or by projection through a large Erfle eyepiece onto Polaroid film. The results of this test procedure with the

interferometer are shown in figures 5(a,b,c). The improvement in fringe representation is a result of polishing the mirror.

In order to examine the surface of the mirror itself, a Leitz metallographic microscope was used. The microscope was equipped with a 10X differential interference contrast (Nomarski type) objective. Results of this examination are shown in figures 6(a,b,c) all to the same scale.

### 3. Polishing Procedure

Before discussing the process worked out for polishing the microripple from these mirrors a possible misunderstanding should be clarified. The impression has perhaps been given that these mirrors do not represent the state-of-the-art or are in some way much worse in terms of microripple than can be generally expected of diamond turning. In fact these mirrors do represent something very close to the state-of-the-art for what these mirrors are; namely they represent a parent parabola of  $f/0.37$  some 2 meters in diameter with a mass in the neighborhood of 300kg. This piece was turned on a modified Excella N/C lathe accurate to  $\pm 0.4\mu\text{m}$  of the desired average contour over an annular band 40cm wide. Components smaller in size and whose contours are not aspheric have vastly superior surface finishes. Small spheres and flats generally look as good and often much better than can be obtained using conventional polishing techniques.

These remarks regarding the polishing of these mirrors are intended to illustrate that methods exist to improve the quality of large aspheric mirrors which suffer from scattering in the visible rather than degrading in any way the extremely powerful technique that diamond turning has shown itself to be. In fact we consider the turning and polishing processes to be complimentary techniques rather than competing ones.

The polishing process we have developed is a two step procedure; the first removes the microripple with a firm or stiff lap but somewhat degrades the cosmetic appearance of the surface, the second step restores the cosmetic appearance to that obtained from the turning lathe but less the microripple.

The stiff lap was made by melting a quantity of beeswax and straining the same through cheese-cloth. To the molten wax, an equal volume of  $0.3\mu\text{m}$  alumina (Linde A) was added and thoroughly mixed. If a lesser quantity of alumina is used, the mixture may be too thin to stay mixed and the compound will settle out. The mixture is then poured onto a lap base; we used a 10cm diameter base.

After the mixture has cooled, the lap is beveled and channeled to give 2.3cm facets. The lap is then softened by moistening with kerosene. After 5 minutes or so the lap is ready for use. We found that if the wax had been softened with a small quantity of turpentine when it was molten, the lap would be almost soft enough that it could be used on copper with soapy water as a lubricant without scratching. Extreme care was needed with this lap to avoid damage. This is why we simply turned to kerosene as a lubricant. The lap slowly dissolves in use but it takes real effort to make the lap scratch copper deeply.

Before applying the lap to the work, the mirror should be carefully beveled with a clean, fine file and the bevel polished out using Pellon or felt and Linde C. The risk of picking up a burr from the edge is too great to forget this step. After beveling, the filled wax lap is rubbed perpendicularly to the turning marks using a generous amount of kerosene for lubrication. The slurry should turn black immediately indicating a good cutting action. To judge progress, simply flush the surface with clean kerosene. The surface will appear scuffed or lightly brushed and the evenness of polishing is indicated by the uniformity of the brushed appearance. This surface degradation has no particular depth and will polish out quickly during the second step of the process.

The idea of a lap that slowly dissolves may not sound like a good idea at first but it has several definite advantages. For one, it is very soft, something necessary for a metal as soft as copper. In addition, being an oil, the kerosene keeps the metal from oxidizing allowing one to leave his work for a time without the worry of corrosion or etching. Further, one of the easiest ways of picking up a scratch is for some of the metal that has been polished off the mirror to cake up on the lap. This is avoided because there are no hard surfaces on the lap for the metal to affix to. Finally, the lap continues to supply fresh compound at a uniform rate as the lap is used. We have found the alumina filled wax lap and kerosene to be a very successful method for removing the microripple in diamond turned mirrors.

Once the ripple is reduced to the desired level and the figure is satisfactory, we proceed to the second step of the process to restore the original brightness to the copper surface. First clean up the surface by a thorough flushing with kerosene followed by acetone. It is difficult to completely remove the wax film. Don't worry and don't be tempted to wipe it off with any sort of physical means. This usually spells disaster. Any remaining wax film will come off during the second step.

For a lap we use 2 to 4mm thick open cell polyurethane sheeting which we obtain from upholstery or fabric shops for something like \$2 a square meter. Cut the sheeting into a piece 30cm square and wash thoroughly with filtered water. The least contaminant at this point can ruin everything. Make a paste of Linde A, dishwashing detergent (Liquid Ivory, etc.) and water. Make a ball of the foam sheeting, dip into the paste and uniformly scrub the mirror surface. Use mild to moderate pressure and a buffing motion. Too great a pressure will eventually scratch, too light a pressure will take too long.

Very quickly the slurry will turn black indicating material removal. Continue a uniform polishing action while keeping the surface wet with additional filtered water. To inspect progress, flush



the surface with well filtered water. A clean piece of the polyurethane sheeting thoroughly wet may be used to help with the clean-up. The remarkable thing about the polyurethane sheeting is its ability to be used as a cleaning cloth on soft copper without scratching.

Discretion must be used when polishing with the urethane sheeting. Ideally, polishing should be continued until the brushed appearance from step one is gone but no farther. The second step should not be used for removing heavier scratches but rather the first step carried on longer until a uniform brushed surface is obtained with no heavy scratches. The problem with using the foam sheeting too long is the same problem that arises whenever a "soft" lap is used, the softer areas of the surface polish faster than the harder areas. This leads eventually to an orange-peel surface. Before reaching this stage the copper begins to show evidence of low level wide angle scatter. A high intensity light focused on the surface will show a haze developing on the surface if the foam is used too long. The only solution then is to go back to the soft filled wax lap to get a smooth but brushed surface and then repeat the foam lap treatment for a shorter time.

If the wax lap finish on the surface is well done to start with, the finish obtained with the foam lap can be spotless, not a sign of scratches or pits. The finish or specularly is at least as good as the virgin turned surface except now of course all the ripple and consequent scattering are removed.

After finishing with the foam lap, wash the mirror thoroughly (including all the edges) with filtered water followed by distilled water. The water should bead off the clean surface. Then flush with CP acetone or CP methanol and blow dry in a sheet with dry nitrogen. This final cleaning step is important so that no water or other residue is left on the copper to potentially stain or etch the surface.

#### 4. Results and Conclusions

Now that the polishing process has been explained we would like to return to the photographs obtained during the testing of various stages in polishing. The photographs in Fig. 4 show the reduction in scattering as the microripple is removed. Fig. 4a shows a mirror just as it came from the SPDT lathe. The light, in fact, scattered far off the illustration, this being the central third. The herringbone pattern is caused by the deeper of the turning marks. Because these mirrors are off-axis sections, the turning marks are roughly unidirectional and thus the scattering is principally perpendicular to the grooves as in the case of a diffraction grating. This preferential scattering is particularly bothersome in the visible because astigmatism is the principle aberration caused by misalignment of an off-axis parabola. The astigmatism also causes a lengthened image and it is very difficult to separate the effects of the scattering from the astigmatism due to misalignment. This makes it all but impossible to line up a SPDT off-axis section if the microripple is too severe.

Fortunately, the polishing procedure very quickly corrects this problem, the finest microripple structure being the first to polish out. Fig. 4b shows the return image after polishing one of the 400mm copper mirrors for about an hour with the filled wax lap. Although the image is still considerably longer than it is high, the herringbone pattern is gone and there is a definite although elongated core. After another 3 hours polishing with the wax lap and then cleaning up the surface with polyurethane foam sheet, we get the image shown in Fig. 4c. Here the image is 3-4 times the source size of 15 $\mu$ m and is in fact geometrically small enough that this mirror will give diffraction limited performance at 10.6 $\mu$ m.

The interferograms in Fig. 5a through c show the same mirror at the same stages described above. Again in Fig. 5a notice the difficulty in trying to sort out astigmatism from other effects. Even the interferometer is not useful for alignment purposes when used double pass off of the parabola. After the high frequency ripple has been polished off, the fringes become readable with some difficulty in Fig. 5b. Residual turning marks are still easily apparent in the surface of the mirror as seen in the fringes. At the completion of the polishing in Fig. 5c the surface appears smooth with only the slightest indication of residual ripple at the edges of the mirror.

The microphotographs in Fig. 6a through c show equally dramatic changes in the surface of SPDT mirrors. Fig. 6a shows the untouched mirror while Fig. 6b is after 1 hour of polishing. On a small scale all the ripple is gone, there being just a hint of occasional residual ripple. Following further polishing including work with the foam lap, the surface looks almost as homogeneous as the turned except that the ripple is gone.

In conclusion, we have developed a method of removing the microripple from single point diamond turned surfaces in an easily performed, conventional manner. The method leaves the surfaces cosmetically as clean and bright as the originally turned surfaces yet free from the scattering caused by the microripple. Although the figure of the surfaces can be changed by the polishing, careful monitoring and correction can be used to avoid figure degradation and in fact if need be the figure can be improved.

#### Acknowledgments

We would like to acknowledge the help of useful discussions with Drs. J. C. Wyant and Roland Shack and with R. C. Shagam.

This work was partially funded by LASL Contract #NP6-46285-1.

# Reference

- [1] Shack, R. V. and G. W. Hopkins, "The Shack Interferometer", SPIE Proc., Vol. 126, "Clever Optics", 1977.

# Figures

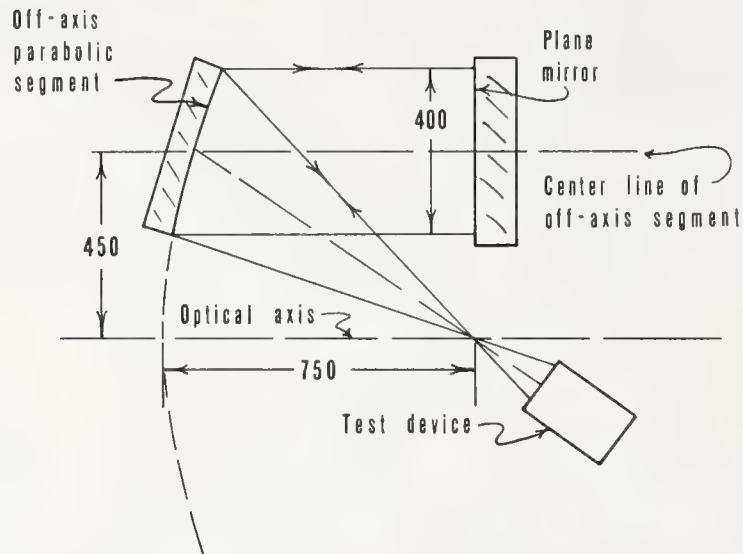


Figure 1. Parameters of the double pass autocollimation test of a 400mm diameter parabolic segment.

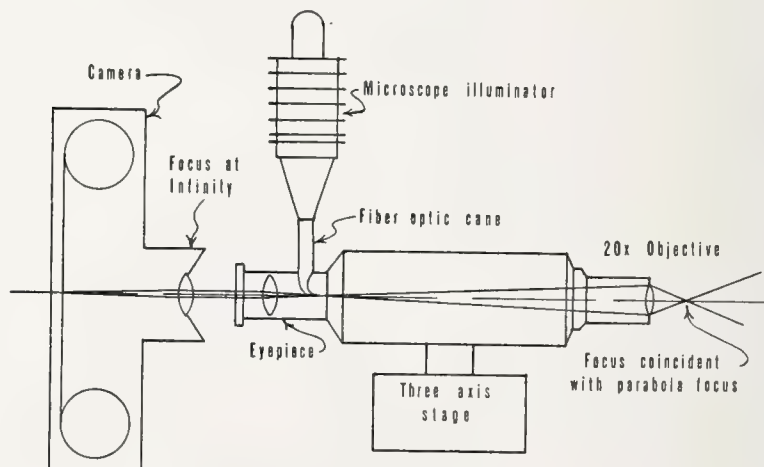


Figure 2. Schematic diagram of the point source microscope used to examine the return image from the off-axis parabolic segment. The source is a fiber optic cane drawn down to a 0.3 mm point.

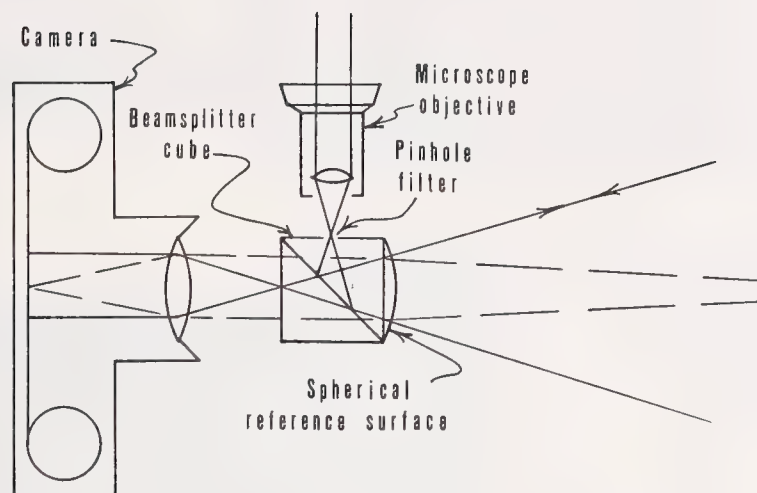


Figure 3. Schematic diagram of the Shack interferometer used to measure the wave-front errors produced by the off-axis parabolic segments.



Figure 4. Return images off of parabolic segments as photographed using the point source microscope. The upper light spot is scattered light from the source itself. a) Very elongated return image from an unpolished SPDT off-axis parabola. b) Return image from the same mirror after removing the majority of the microripple using a Linde A filled wax lap. The polishing time was about one hour.



4(a)

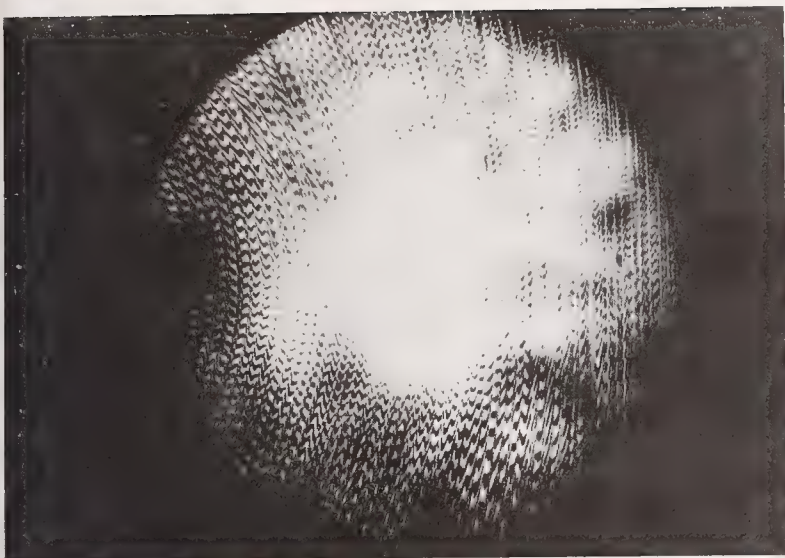


4(b)

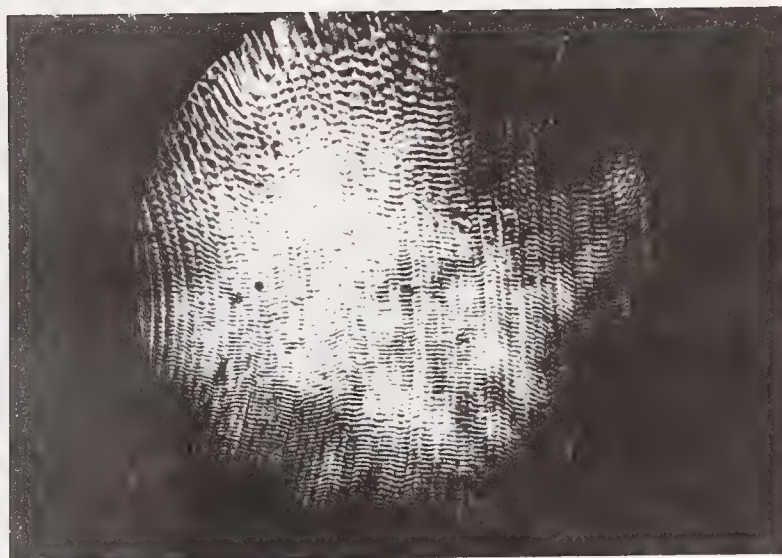


4(c)

Figure 5. Double pass interferograms obtained with the Shack interferometer showing the mirror surface ripple as a function of polishing time. a) Typical surface irregularity of an unpolished SPDT off-axis parabola. b) Same mirror surface after one hour of polishing. c) Same mirror after the completion of the second step of polishing.



5(a)



5(b)



5(c)



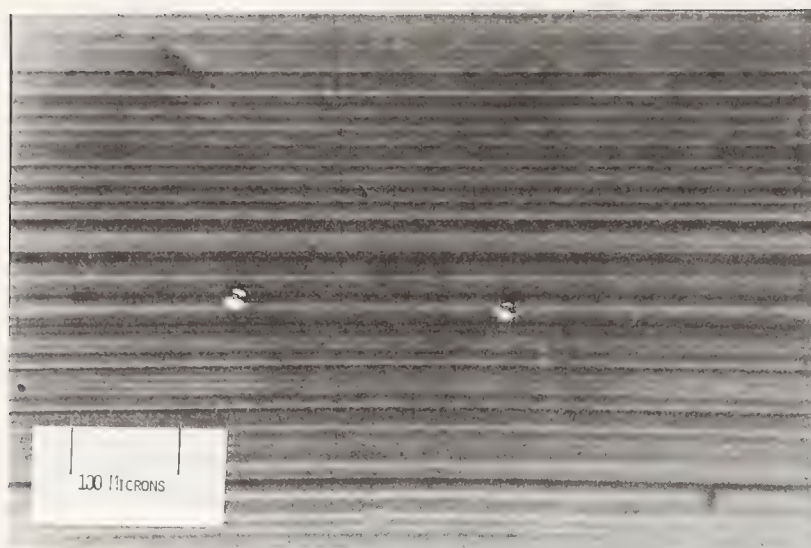
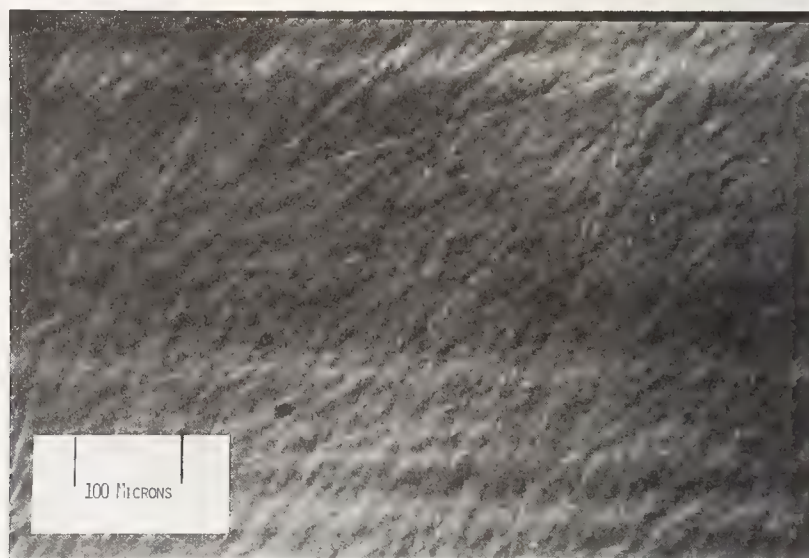
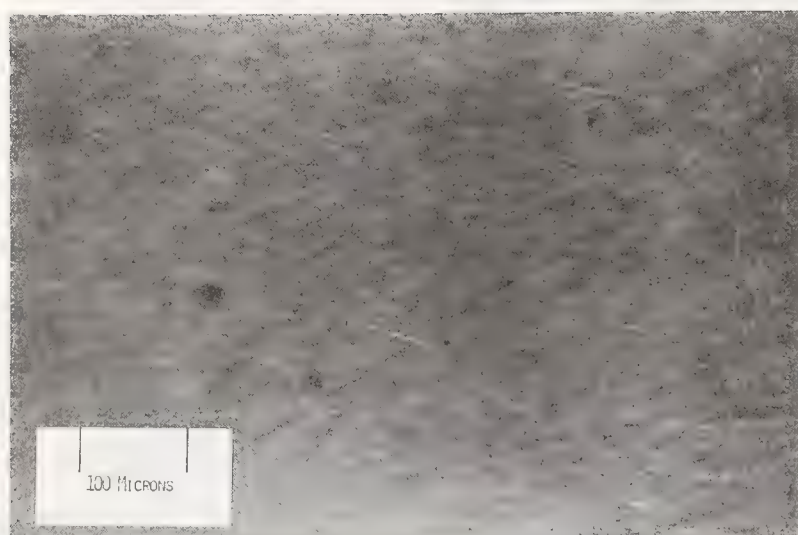


Figure 6. Microphotographs of the surface of a SPDT copper off-axis parabola at different polishing times. A 10X differential interference contrast objective was used. a) A virgin SPDT mirror. b) Surface after polishing one hour with filled wax lap. c) Surface at the completion of polishing.

6(a)



6(b)



6(c)



J. O. Porteus, C. W. Fountain, J. L. Jernigan, W. N. Faith, and H. E. Bennett  
Physics Division, Michelson Laboratories  
Naval Weapons Center, China Lake, California 93555

Modification of bare metal surfaces by laser-induced stress has been observed well below the threshold for melting with 100 nsec, 10.6  $\mu\text{m}$  laser pulses. Resulting optical and mechanical properties may be very significant for the performance of laser-optical systems and for structural components under stress. A multi-threshold approach to damage testing is used to interrelate phenomena associated with different damage mechanisms, and to help establish a relationship to material characteristics. In general, the threshold for plastic deformation as indicated by intragranular (banded) slip was found to increase with crystalline disorder, while thresholds for melting and other types of catastrophic damage decrease. The melt threshold calculated from heat-flow considerations is in reasonably good agreement with experiment on a clean, annealed, single-crystal Cu target. Possible effects of elastic and inelastic strain on the melt threshold are considered. Under certain conditions the target plasma may influence the observed slip via shielding, "scrubbing" or compression. Transient reflectance data, single-crystal slip-band patterns and air breakdown thresholds support a discussion of these effects. Finally, multithreshold results are presented for a variety of metal and alloy surfaces prepared by different methods. Target preparation techniques are evaluated in terms of their apparent effectiveness in providing resistance to slip, melting and other forms of damage.

Key words: Al 7050; crystalline disorder; Cu mirrors; dislocations; laser-induced stress; melt threshold; Mo mirrors; plasma scrubbing; plasma shielding; slip; surface preparation; Ti-6Al-4V.

## Introduction

When a metal target is exposed to a pulsed laser a variety of damage-related effects begin to appear as the fluence is gradually increased. In general, the thresholds for the various effects can be quite different, and depend on the material, the condition of the surface and the conditions of irradiation. Much basic information concerning damage mechanisms can be obtained from the relative and absolute magnitudes of these thresholds as conditions are varied. The means of obtaining this multithreshold information are discussed in another paper at this conference [1]<sup>1</sup>. The present paper deals mainly with results we have obtained by applying the multithreshold approach to the thermal stress problem.

The first type of damage usually to appear when a high quality bare Cu mirror is exposed to 100 nsec, 10.6  $\mu\text{m}$  laser pulses is plastic deformation resulting from thermal stress. Normally this appears as one of the two types of slip shown in figure 1: (a) slip bands which occur as a result of displacement along crystallographic planes and (b) intergranular slip resulting from displacement along grain boundaries. Such effects often appear well below the thresholds for melting and other forms of catastrophic damage. The importance of slip for mirror technology is that it roughens the surface, which leads to increased scattering and increased absorption via the anomalous skin effect [2]. Laser-induced slip is also found in structural alloys where it may influence the failure of thin metal components subject to mechanical stress.

## Slip Versus Melting

Figure 2(a) shows the damage profile [1] of a high quality Cu mirror. Shaded bars represent damage thresholds for the various observable damage-related effects, while the diagonally hatched boxes indicate standard deviations. Generally, the major contribution to the standard deviation is a threshold variation over the sample surface rather than experimental uncertainty. Notice that the thresholds fall into two groups, one consisting of the two types of slip, and another which includes melting and other forms of catastrophic damage.

Figure 2(b) shows similar results from a clean single-crystal Cu target, sputter-cleaned and annealed in ultrahigh vacuum. The disparity between the thresholds for slip and melting is even more

\* Work supported by the Army Missile Command, the Naval Air Systems Command and NWC Independent Research Funding.

1. Figures in brackets indicate the literature references at the end of this paper.

dramatic in the single crystal, amounting to almost a factor of 5 in fluence. This makes it quite clear that the slip observed near threshold is not related to melting or other catastrophic damage, and must be attributed to thermal stress. Furthermore, it is quite evident that slip and melt thresholds are related to the surface condition in different ways. The higher thresholds for catastrophic damage, including melting, on the single crystal are evidently the result of lower absorption associated with the higher degree of crystalline order and cleanliness. It is well known that a low yield stress is also associated with order. This evidently offsets the effect of low absorption in producing a lowered threshold for slip bands. There is, of course, no intergranular slip in a single crystal.

#### Intrinsic Melt Threshold

An intriguing question is whether or not the melt threshold indicated in figure 2(b) is representative of intrinsic single-crystal Cu. Using conventional heat flow theory, and temperature-dependent thermal and optical parameters, we calculate a melt threshold of 74 J/cm<sup>2</sup> for pure Cu. Although this is considerably higher than the measured 45.3 J/cm<sup>2</sup>, the agreement must be considered reasonably good in view of the uncertainty in the material parameters.

One possibly important effect which was neglected in the calculation is the influence of strain on the absorption coefficient. In the case of elastic strain the effect can be easily estimated, and turns out to be quite small. Using the Hagen-Rubens relationship [3] between absorptivity  $\alpha$  and electrical resistivity  $\rho$ , one finds the relationship to the strain  $\epsilon$  is given by

$$\frac{\Delta\alpha}{\alpha} \cong \frac{1}{2} \frac{\Delta\rho}{\rho} \cong \frac{1}{2} \frac{d\rho}{\rho d\epsilon} \times \Delta\epsilon \quad , \quad (1)$$

where  $d\rho/\rho d\epsilon$  is the strain coefficient of resistivity ( $\sim 1$  for Cu). With a fixed constraint the strain is related to the temperature  $T$  through the linear absorption coefficient  $\beta$  ( $\sim 10^{-5}$  for Cu).

$$\Delta\epsilon \sim \beta \Delta T \quad . \quad (2)$$

Assuming a temperature change  $\Delta T \sim 10^3$  required to produce melting, we find  $\Delta\alpha/\alpha \sim 0.5\%$ .

The effect of inelastic strain is much harder to evaluate since the dynamics of the problem are important and difficult to determine. We have attempted transient reflectance measurements on polished Cu samples, but have not been able to detect a reduction in reflectance attributable to slip. However, the sensitivity of our photographic data recording technique is limited to effects  $\sim 10\%$  or larger. A transient analyzer, which we will acquire soon, will provide much improved sensitivity to time-dependent absorbance effects. It should be emphasized that the failure to observe a transient absorbance does not necessarily preclude a residual change in absorbance resulting from slip damage. Unfortunately, the latter is difficult to measure accurately because of the small damaged area (diameter = 629  $\mu\text{m}$ ).

#### Plasma Effects

One transient effect which can be easily observed is the reduction in specular reflectance produced by the target plasma. Figure 3 compares incident and reflected laser pulses from a polished Cu target where the fluence exceeds the thresholds for ion and light emission. The dropout in the upper trace results from plasma interference. This part of the pulse, which is available for generating thermal stress at lower fluences, is blocked by the plasma.

The above interpretation is supported by the single-crystal slip-band pattern, which undergoes a drastic change when the plasma forms. Figure 4 compares dark-field micrographs of three different sites on a Cu (111) surface, each shot once at a fluence which increases proceeding from left to right. On the left, only slip has occurred. In the middle, slight melting has also occurred. On the right, a crater has formed and emission was observed, indicating plasma formation. Notice that the six-fold-symmetric slip pattern, which appears in the first two micrographs, is replaced by a three-fold-symmetric pattern on the right. The six-fold pattern is produced by compressive thermal stress acting along the target surface [4]. The three-fold pattern, however, is inconsistent with ordinary thermal stress and requires a different mechanism [5,6]. Possible mechanisms for the three-fold pattern are pressure from the plasma or, as was recently suggested to us, by a surface tensile stress produced by resolidification of the melt pool [7].

The most curious aspect of figure 4, which has also been observed with Nomarski [5,6], is the absence of six-fold-symmetric slip when the plasma forms. Presumably, thermal stress should produce this characteristic pattern early in the pulse, regardless of whether or not the plasma threshold is reached at the higher temperatures which occur later on. The explanation apparently requires a non-equilibrium or dynamical mechanism. The one we propose is illustrated schematically in figure 5. Here curves 1, 2 and 3 represent the magnitudes of the thermal stress versus time for the three fluences represented in figure 4. Although these plots are qualitative, the essential features were verified by calculation. The dashed curve  $\sigma_c$  represents the possible time dependence of the critical shear stress, which is believed to be a decreasing function of time since dislocations have a nonzero response time [8].



Six-fold slip occurs at points labeled S, where the rising stress curves intersect  $\sigma_c$ . Points labeled M and P indicate melting and plasma formation, respectively. We hypothesize that in the case of curve 3 vaporization occurs before slip. Plasma shielding then causes the stress to drop rapidly, as indicated, so that no intersection with  $\sigma_c$  is possible in this case. Vaporization is promoted by higher strain rates, so that the plasma may actually precede melting. This has been observed with the target at atmospheric pressure, as discussed below. If the vaporization is sufficiently prompt the assumption of a  $\sigma_c$  which decreases with time is, of course, not required.

An alternative explanation of the change in slip patterns is that slip due to thermal stress is obscured by "scrubbing," a term used to describe laser-induced reduction of background scatter. An example of this effect can be seen in the dark-field micrograph of figure 6, where an area of reduced scatter appears outside the clearly defined zone of melting. Here the plasma has caused removal or redistribution of material, resulting in elimination of some of the scattering centers originally present. However, the Nomarski micrograph shows no evidence of extensive surface smoothing in the scrubbed area. In fact, careful examination reveals a subtle increase in texture due to slip outside the melt zone on this fine-grained surface. This evidence suggests that obscuring of slip due to plasma scrubbing is minimal, especially when viewed with Nomarski.

An important result for practical applications is that the slip threshold is not appreciably influenced by the presence of atmosphere. This was demonstrated on a mechanically polished Cu sample, which was tested first in vacuum, and subsequently in one atmosphere of  $N_2$ . The results are shown in figures 7(a) and (b), respectively. Comparison of these figures shows a substantial increase in the thresholds for melting and other catastrophic effects due to the additional shielding provided by the  $N_2$  plasma. However, at the lower energy density where slip first occurs, no plasma could be detected in either case. Judging from the near equality of the light-emission threshold in  $N_2$  and in vacuum, the  $N_2$  plasma is triggered by the target plasma. Since the target-plasma threshold lies above the slip threshold associated with thermal stress, the latter is not influenced by shielding in either case.

#### Specially Prepared Mirrors

In an effort to identify surface treatments which provide resistance to plastic deformation, as well as other forms of laser damage, we have tested mirrors prepared by less conventional methods. In figure 8 we show the damage profile of a diamond-turned (D-T) Cu mirror. Comparison with figure 2 shows that D-T Cu is qualitatively similar to single-crystal Cu in that thresholds for melting and other catastrophic effects are high relative to that for slip bands when compared to the polished sample. This strongly suggests that D-T Cu also has a high degree of surface order leading to a lower inherent absorption, and also to a lower yield strength. The net effect is a threshold for slip bands which is virtually identical to that of polished Cu. These arguments do not necessarily apply to the thresholds for pits and intergranular slip, which may be influenced by random inclusions or segregated impurities [1].

A more extensive multithreshold study of D-T metal mirrors has already been reported [9], including samples where the metal to be turned was electrolytically deposited on bulk Cu substrates. Au and Ag mirrors prepared in this way show very uniform damage thresholds (small standard deviations), but are not without problems. The chief difficulty with the D-T Au mirror, for example, is a high background scatter, which can be seen in figure 6. The Ag mirror produced a slip threshold of only 12 J/cm<sup>2</sup>, although the catastrophic thresholds compare favorably with D-T bulk Cu.

Unfortunately, we do not have multithreshold results on sputter-deposited Cu surfaces, and must therefore base our discussion of this preparation method on Mo, which generally exhibits much lower thresholds than Cu. Figures 9(a) and (b) show damage profiles of bulk and sputter-deposited Mo mirrors, respectively, where the same polishing method was used in both cases. On the sputtered sample we find no visible evidence of slip, but the melt threshold is much lower than on the bulk sample. Light emission and, to some extent, ion emission are associated with pitting on the bulk sample and are not representative of the surface in general. In view of our previous results the implications are that the sputtered sample is highly disordered, resulting in a slip threshold which is indistinguishable from the melt threshold. However, it is quite possible that slip simply cannot be observed on the sputtered sample because of the very small grain size.

We have also tested Cu mirrors that have been ion-implanted and one that was ion-milled. No significant improvement in slip threshold was ever achieved by ion-implantation with any of various combinations of energy, dosage and ion type. Ion-milling, on the other hand, did produce a marked increase in the slip threshold, but melting and other thresholds were low. However, since the purity of the Cu was suspect on this sample, the possible benefits of ion-milling cannot be disregarded.

#### Structural Alloys

In order to evaluate laser-induced stress damage in structural alloys we polished and tested samples of two materials. The damage profile of Ti-6Al-4V, shown in figure 10, indicates a slip threshold of only 0.6 J/cm<sup>2</sup>. This is the lowest we have seen on any well polished metallic sample. The threshold for work function change, which is also very low, is attributed to surface oxide removal,



based on Auger results. The intergranular slip in this alloy can be seen quite clearly in Nomarski (fig. 11) as an enhancement of the grain boundaries near the center of the field. Slip bands are difficult to observe on this sample because of the small grain size, but are faintly visible in the dark-field micrograph.

Figure 12 gives the damage profile of hand-forged Al 7050-T73652 from Alcoa. The lowest threshold which could be observed was for work function change associated with a change in the state of surface oxidation. No slip was visible, evidently as a result of the high dislocation density. Although hardening has minimized slip, this has been at the expense of the thresholds for melting and pit formation. Pure, clean Al, for example, has a melt threshold of  $14 \text{ J/cm}^2$  [5,6]. The lack of homogeneity and resulting pits are apparent in figure 13. Auger analysis shows isolated Si, possibly from SiC which collected in voids during polishing.

#### Summary

In summary, it has been demonstrated that thermal stress can damage mirror surfaces in the absence of melting. Stress damage may be indicated by slip bands, roughening or displacement along grain boundaries, as seen by Nomarski or other types of microscopy. Surface condition, as influenced by the surface preparation method used, can affect the thresholds for slip and for melting differently. Typically, slip thresholds are low and melt thresholds high on clean, well ordered surfaces. The target plasma provides shielding and scrubbing, but only above the threshold for slip due to thermal stress. Consequently, slip thresholds are about equal in atmosphere and in vacuum. The plasma introduces another mechanism for slip, which produces a different slip band pattern on a (111) single-crystal Cu surface. Results of testing on specially prepared surfaces indicate that diamond-turning and ion-implantation are generally ineffective against slip. Sputtering, ion-milling and forging may be effective, but may also reduce thresholds for other types of damage. The structural alloys tested have low damage thresholds. Ti-6Al-4V is extremely susceptible to slip damage.

#### Acknowledgments

The authors are indebted to W. R. Compton and J. B. Patton for heat-flow and stress calculations.

#### References

- [1] Porteus, J. O., Jernigan, J. L. and Faith, W. N., this conference.
- [2] Bennett, H. E., Bennett, J. M., Ashley, E. J. and Motyka, R. J., Phys. Rev. 165, 755 (1968).
- [3] Bennett, H. E. and Bennett, J. M., in *Optical Properties and Electronic Structure of Metals and Alloys* (North-Holland Publishing Co., Amsterdam, 1966), p. 179.
- [4] Haessner, F. and Seitz, W., J. Mater. Sci. 6, 16 (1971).
- [5] Porteus, J. O., Soileau, M. J. and Fountain, C. W., Appl. Phys. Lett. 29, 156 (1976).
- [6] Porteus, J. O., Soileau, M. J. and Fountain, C. W., in *Laser Induced Damage in Optical Materials: 1976*, A. J. Glass and A. H. Guenther, eds. (NBS Spec. Publ. 462), p. 165.
- [7] Glicksman, M. E. and Breinan, E. M. Private communication.
- [8] Steverding, B. and Dudel, H. P., J. Appl. Phys. 47, 1940 (1976).
- [9] Porteus, J. O., Decker, D. L., Jernigan, J. L., Faith, W. N. and Bass, M., IEEE/OSA Conference on Laser Engineering and Applications, held in Washington, D.C., 1-3 June 1977.

## Figures

### SLIP BANDS AND INTERGRANULAR SLIP

#### BULK Cu, DIAMOND-TURNED

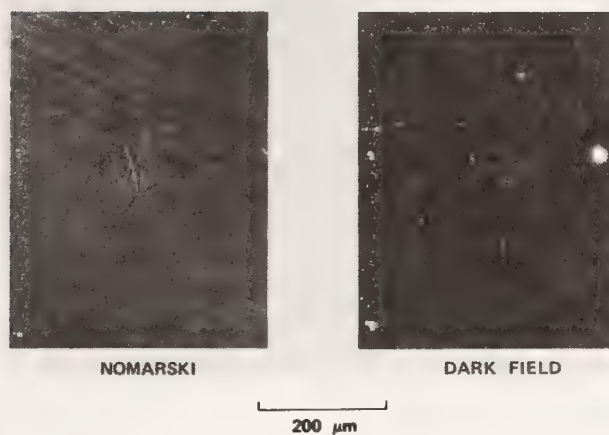
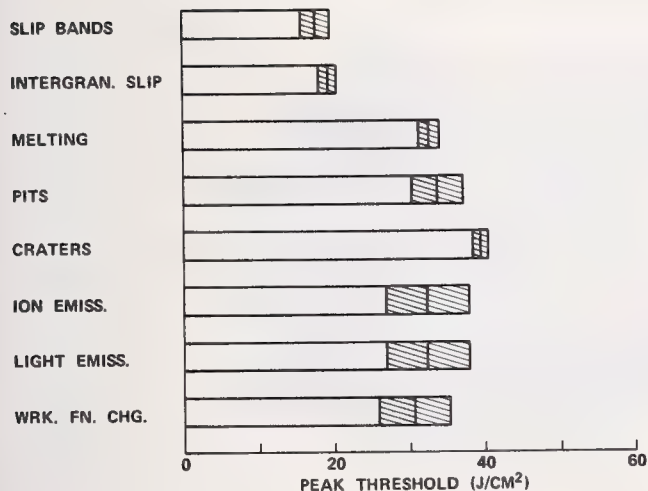


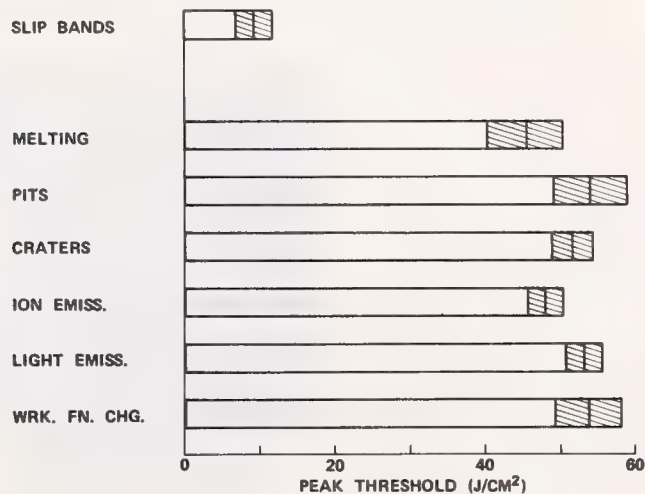
Figure 1. Nomarski and dark-field micrographs of a damage site on diamond-turned bulk Cu below the threshold for melting. Crack-like features are grain boundaries which have undergone intergranular slip. The roughened appearance just left of center is due to slip bands.

#### BULK Cu, OPTICAL POLISH



(a)

#### (111) SINGLE-CRYSTAL Cu, UHV-PREPARED



(b)

Figure 2(a). Damage profile of polished Cu, showing damage thresholds and their associated standard deviations for eight damage-related effects. All results in this paper were obtained with the target in vacuum, unless otherwise indicated.

Figure 2(b). Damage profile of a (111) single-crystal target prepared and tested in ultrahigh vacuum.

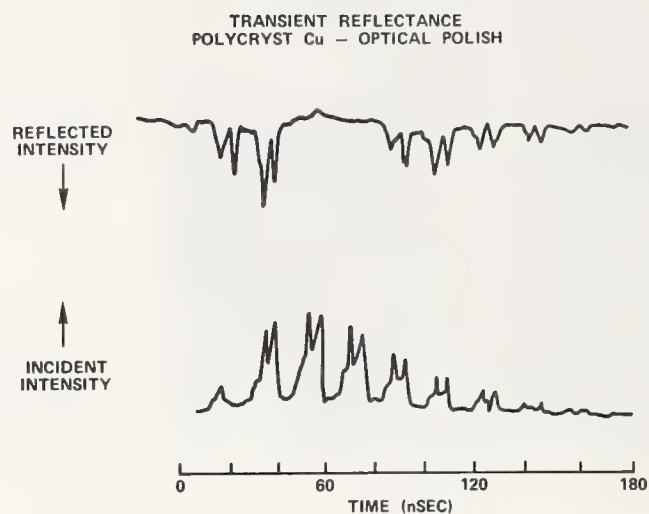


Figure 3. Comparison of the laser pulse at normal incidence (bottom) with the back-reflected pulse (top) from a polished bulk Cu target above the threshold for plasma formation.

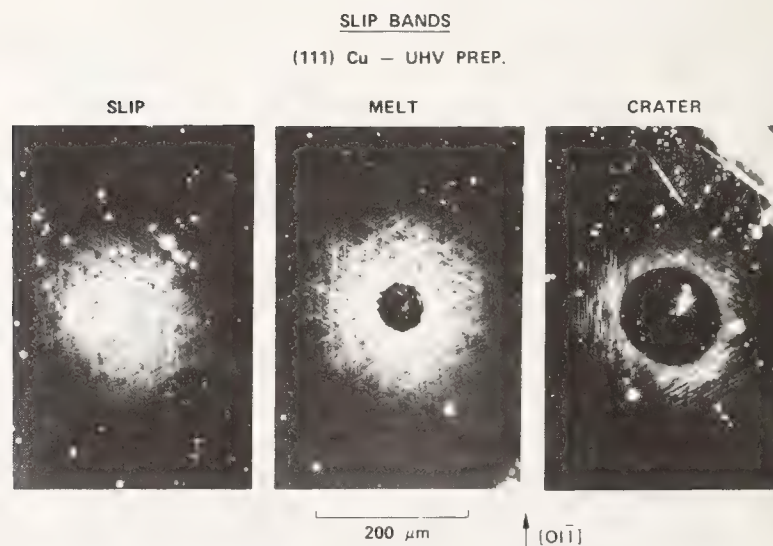


Figure 4. Dark-field micrographs of three sites on (111) Cu damaged at 47, 50 and 56 J/cm<sup>2</sup>, respectively, proceeding from left to right. Bright lines are caused by scattering from slip bands.



#### PLASMA SHIELDING

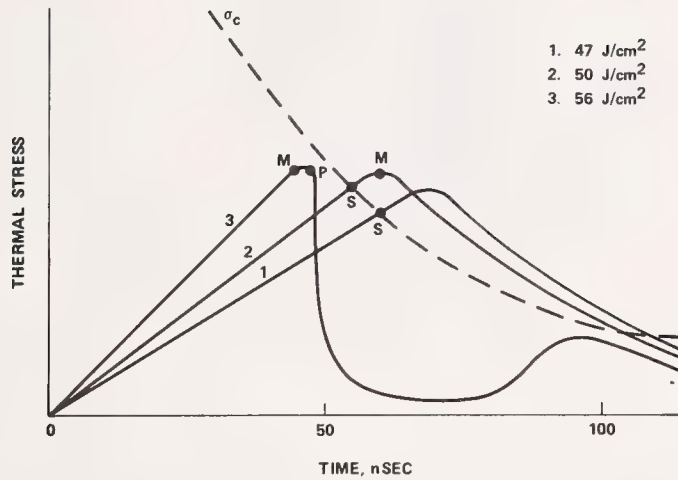


Figure 5. Time dependences of thermal stress, illustrating the plasma shielding effect. The dashed curve  $\sigma_c$  represents the limiting stress for elastic deformation.

#### MELTING, SLIP, SCRUBBING

ELECTRODEP. Au ON BULK Cu, DIAMOND-TURNED

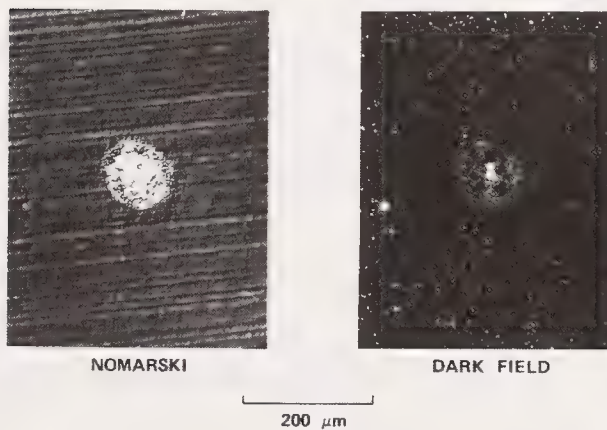


Figure 6. Nomarski and dark-field micrographs of a heavily damaged site on diamond-turned Au, electrolytically deposited on bulk Cu. Slip, which is obscured by the small grain size and inherent surface texture is indicated by a subtle increase in texture in Nomarski. The term "scrubbing" refers to the area of low-scatter in the dark-field micrograph as explained in the text.

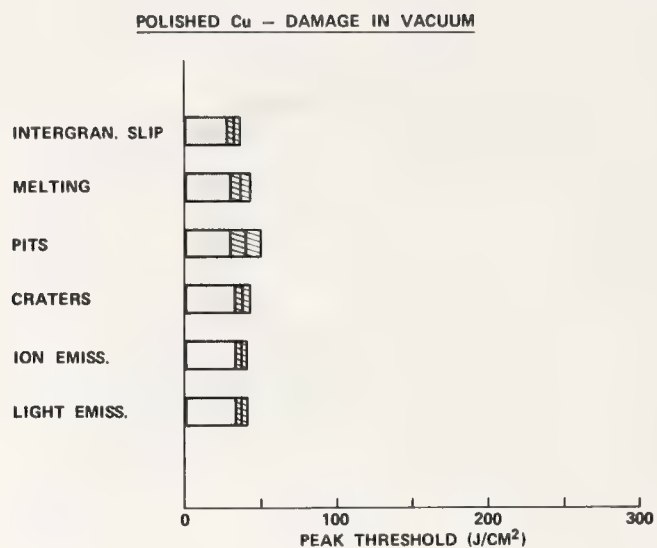


Figure 7(a). Damage profile of mechanically polished Cu damaged in vacuum. Note that the scale differs from previous figures.

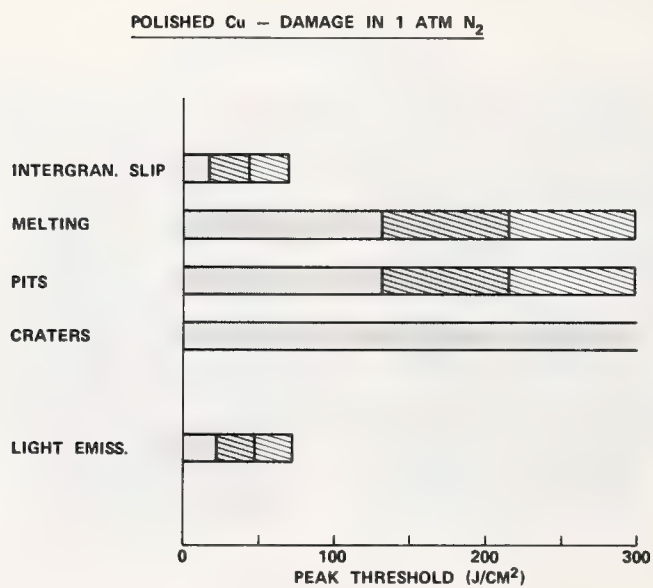


Figure 7(b). Damage profile of the target of 7(a) damaged in one atmosphere of N<sub>2</sub> for comparison.

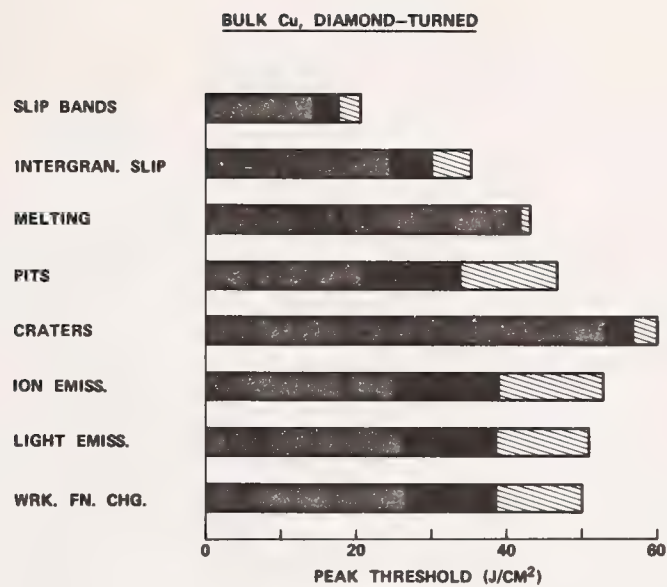
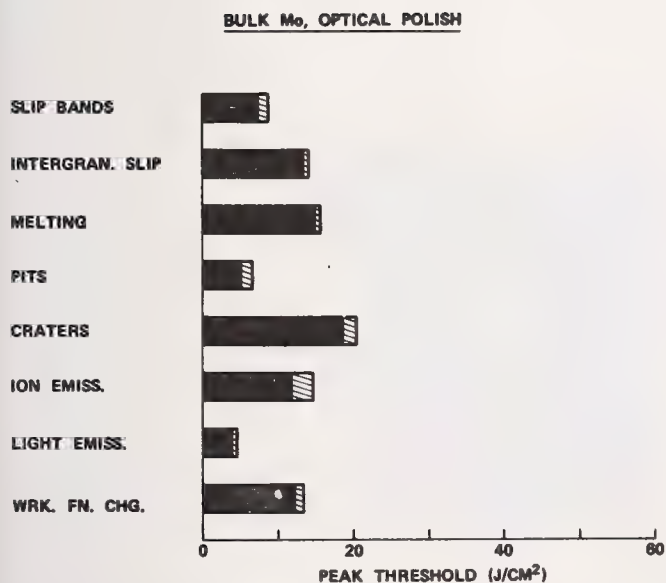
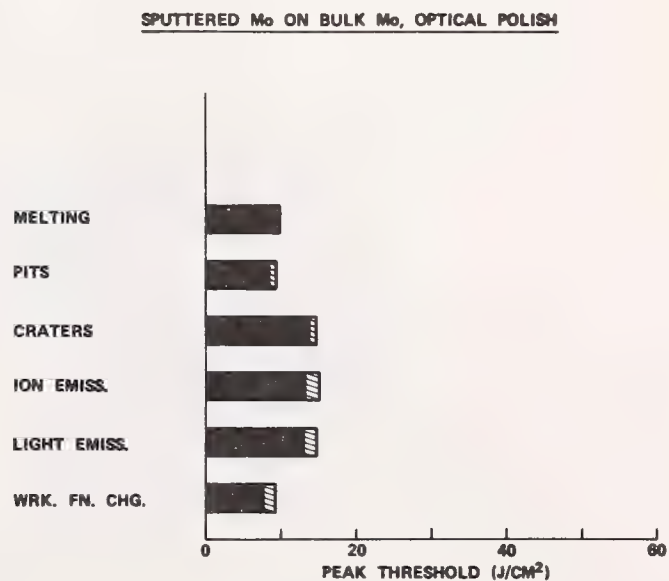


Figure 8. Damage profile of diamond-turned bulk Cu, for comparison with figure 2.



(a)



(b)

Figure 9(a). Damage profile of polished bulk Mo.

Figure 9(b). Damage profile of polished Mo which has been sputter-deposited on bulk Mo.



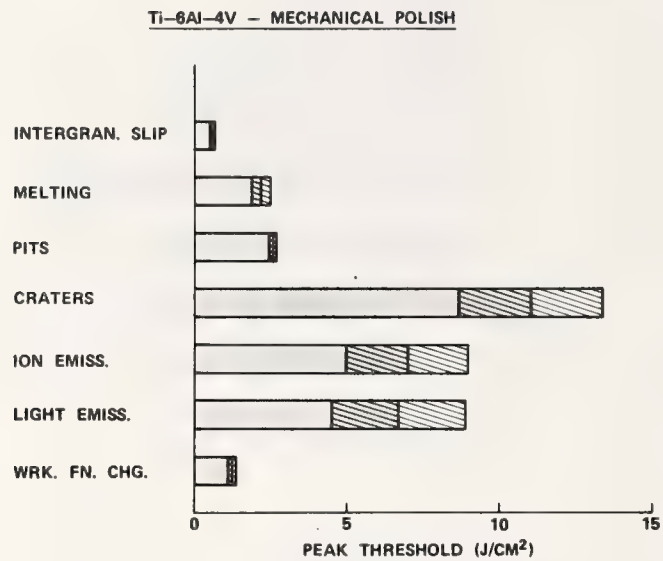


Figure 10. Damage profile for mechanically polished Ti-6Al-4V. Note the small scale compared to previous figures.

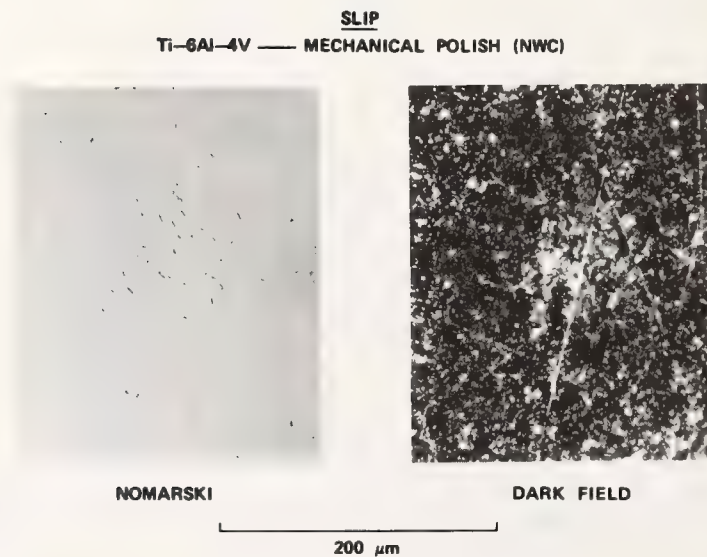


Figure 11. Nomarski and dark-field micrographs of a damage site on Ti-6Al-4V at  $1.6 \text{ J/cm}^2$  peak fluence, showing intergranular slip and faint slip banding.

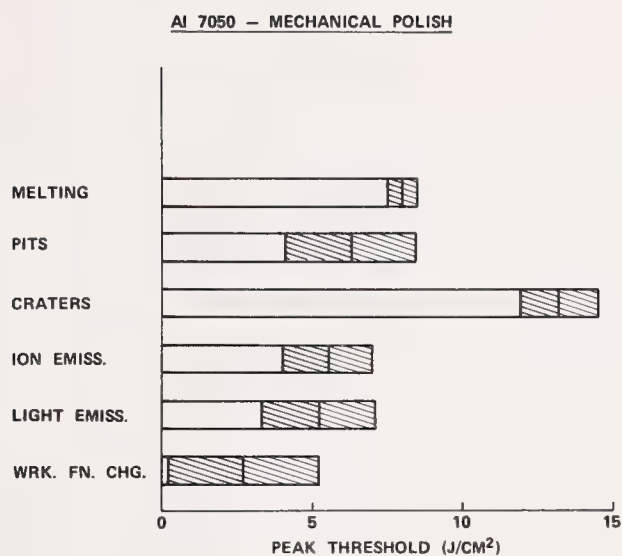


Figure 12. Damage profile if mechanically polished Al 7050.

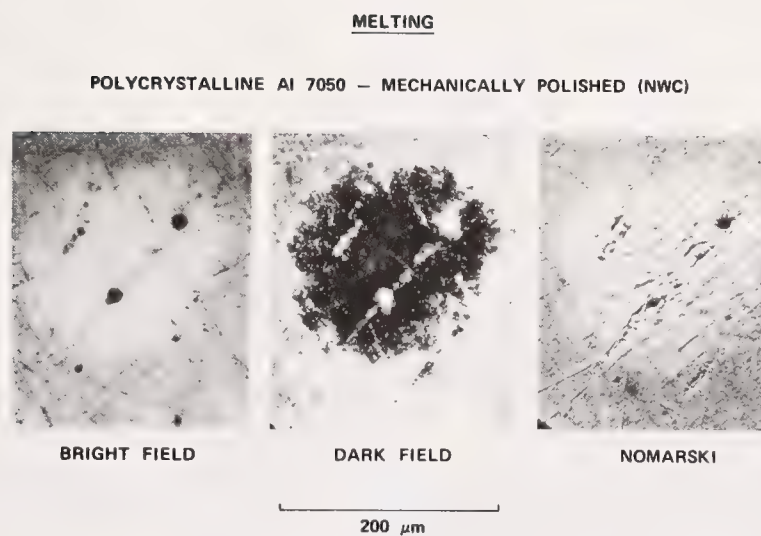


Figure 13. Bright-field, dark-field, and Nomarski micrographs of a melted site on Al 7050 at a peak fluence of  $10.9 \text{ J/cm}^2$ .

COMMENTS ON PAPER BY PORTEUS, FOUNTAIN, JERNIGEN, FAITH, AND BENNETT

*No discussion on this papers.*

# LOW-EXPANSION LASER MIRRORS\*

P. Pirooz, G. Dubé and N. L. Boling  
Owens-Illinois, Inc.  
Toledo, Ohio 43666

A unique concept for producing low-expansion IR laser mirrors was evaluated. This concept involved the self-generation of thin copper films on very low-expansion glass-ceramic substrates previously doped with copper. Exploratory studies of two major glass-ceramic systems:  $\text{Li}_2\text{O-Al}_2\text{O}_3\text{-SiO}_2$  and  $\text{ZnO-Al}_2\text{O}_3\text{-SiO}_2$ , doped with copper have resulted in the development of mirrors with good film-to-substrate adhesion and high specular reflectance at  $10.6 \mu\text{m}$ . The effects of surface finish and process parameters on the film properties were also investigated.

Key words: Copper film; film adhesion; glass-ceramics; IR reflectance; laser mirrors; low-expansion materials.

## 1. Introduction

The recent increase in demand for high-power IR lasers has prompted a number of studies directed towards the advancement of the state of the art of polished metal mirrors. Yet other workers have attempted to replace the metal mirrors with alternate materials in an effort to minimize the serious thermal distortion problem encountered by the metal mirrors subjected to high-power laser irradiation.

H. E. Bennett [1]<sup>1</sup> has concluded that, for a mirror, the thermal distortion is given by the expression,

$$\frac{I t (1-R)}{\sqrt{2}} \cdot \frac{\alpha}{\rho C} \cdot \left[ 1 + \frac{3}{\sqrt{\pi}} \left( \frac{b}{\ell} \right)^2 + \frac{3}{\pi} \left( \frac{b}{\ell} \right)^4 \right]^{1/2} \quad (1)$$

where  $I$  is the irradiance,  $t$  the pulse length,  $R$  the reflectance,  $b$  the mirror radius,  $\ell$  the mirror thickness,  $\rho$  the material density,  $C$  the heat capacity, and  $\alpha$  the thermal expansion.

If we assume that all mirror materials can achieve the same reflectance, a figure of merit for minimizing thermal distortion becomes the following expression

$$\text{F.M.} = \frac{\rho C}{\alpha} \quad (2)$$

Table 1 lists these parameters and the figure of merit for several common laser mirror materials and for CER-VIT<sup>®</sup> material which is a low-expansion glass-ceramic.

Table 1. Properties of laser mirror materials

	<u>Cu</u>	<u>SiC</u>	<u>Mo</u>	<u>C-V</u>
$\rho$	8.9	3.2	9.01	2.5
$C$	0.385	0.75	0.248	0.21
$\alpha (\times 10^{-7})$	170	43	50	< 4
$\rho C / \alpha$	1	2.5	2.2	> 6.5

The significantly higher F.M. for the CER-VIT material explains the interest in a mirror system which consists of a reflecting film such as copper supported by a very low-expansion substrate such as CER-VIT material. Such a system offers the potential of a significant reduction in the thermal distortion.

This study was undertaken specifically to determine feasibility of producing low-expansion glass-ceramic mirrors in which the reflective copper film is self-generated on the surface by a unique diffusion controlled process. It was anticipated that the copper film generated by the subject process would exhibit superior film-to-substrate adhesion and laser damage threshold. This was borne out by the results obtained in a limited study which is the subject of this report.

\* This study was funded by the Defense Advanced Research Projects Agency, Department of Defense, under the contract No. F33615-76-C-5343.

1. Figures in brackets indicate the literature references at the end of this paper.

® A registered trademark of Owens-Illinois, Inc.



## 2. Background

The process of copper-film generation presented here is based on a phenomenon which results in the selective migration of copper ions to the glass surface by diffusion.

In a previous study [2], attempts were made to delineate the basic mechanism for this migration. The following discussion is based on the findings obtained from light microscopy and electron microprobe analysis of samples fired in oxidizing, reducing and neutral atmospheres.

Basically, these results have led to the conclusion that said migration is a diffusion-controlled process as indicated by the linear dependence of the depth of copper depleted layer on the square root of the heat-treatment time.

The colors produced as the result of this migration support the opinion that the migrating species are only the  $\text{Cu}^+$  ions. A series of additional heat treatments have also strongly suggested that the driving force for the migration is the atmosphere in contact with the glass surface which can readily change the oxidation state of the  $\text{Cu}^+$  ions. As depicted in figure 1, if the surface is exposed to an oxidizing atmosphere, the  $\text{Cu}^+$  ions are converted to  $\text{CuO}$  which forms a continuous black layer on the surface. If the immediate atmosphere is reducing, such as hydrogen, the  $\text{Cu}^+$  ions will then convert to metallic copper which will form a continuous copper film on the glass surface. In either case, the reaction depletes the surface glass of  $\text{Cu}^+$  ions which are in turn replenished from the adjacent layers driven by the resultant concentration gradient. This hypothesis was verified by the heat treatment of samples in nitrogen and argon atmospheres which produced no detectable migration of the copper ions.

What is not readily explained by this hypothesis is the profile of the depleted layer as shown in figure 2. This layer appears to increase in depth as a function of the heat-treatment time and/or temperature, but, as indicated by the color change and the electron microprobe data, it does not cause a progressive change in the copper ion concentration. This suggests that each ion would be required to travel the entire depth of the depleted region after it has come under the influence of the driving force which is located at the surface. This type of mechanism is further supported by the diminishing rate of the growth of the surface layer as a function of the heat-treatment time, or the depth of the depleted layer.

It should be noted that the actual film generation behavior will also strongly depend on the host material and process parameters.

## 3. Experimental

### 3.1. Preparation of the original glasses

The compositions of the host glasses were selected on the basis of their ability to crystallize into a glass-ceramic body possessing a very low coefficient of thermal expansion, near zero if possible. For this purpose, two compositions were selected from totally different families of glass-ceramics; one from the  $\text{Li-Al-Si}$  system and the other from the  $\text{Zn-Al-Si}$  system. Both of these were expected to produce a high-quartz solid-solution crystalline phase resulting in very low thermal expansions. To these compositions were added  $\text{CuO}$  at 2 and 4% levels (by weight). The experimental glasses were prepared from these compositions by melting a 5000 g batch in a platinum crucible heated in an electric furnace for approximately 25 hours. At the completion of the melting process, each glass was cast in a steel mold to obtain a relatively large billet which was then annealed.

### 3.2. Crystallization studies

In crystallizing the  $\text{Li}_2\text{O-Al}_2\text{O}_3\text{-SiO}_2$  glass, best results for the billet samples were obtained by either an isothermal heat treatment at  $625^\circ\text{C}$  - 16 hours, or a two-stage heat treatment at  $580^\circ\text{C}$  - 16 hours plus  $650^\circ\text{C}$  - 4 hours, resulting in thermal expansion coefficients ranging from -1 to  $-3 \times 10^{-7}$ .

### 3.3. Film generation studies

The task of generating a copper film on the surface of these materials involves two major processes: 1) migration of the copper ions to the glass surface and their accumulation thereon, and 2) conversion of the copper oxide layers to the metallic copper.

To study these phenomena and the related process variables, flat samples approximately  $4 \times 4 \times 0.3$  cm were sawed from the glass billet. The initial studies were made with the saw-cut surface, after which surface ground and polished samples were used for the detailed property studies.

#### 3.3.1. Cupric oxide generation

There are two basic process modes for generating the  $\text{CuO}$  layer: 1) the glass is subjected to the necessary crystallization heat treatments in the form of raw stock, after which the crystallized bulk material is shaped into the desired figure and subjected to a second heat treatment to generate the  $\text{CuO}$  layer, and 2) the final figure is produced from the raw glass (noncrystalline) which will then see a combined heat treatment for bulk crystallization as well as the  $\text{CuO}$  generation.

Since the majority of glasses has a tendency to undergo a significant volume change (1-5%) due to crystallization which can cause disfiguring and warpage of plate samples, the first alternative discussed above is preferred and thus was used for most of the present studies.

All CuO generation heat treatments were conducted in air atmosphere. Samples were placed on a flat ceramic plate inside an electrically heated muffle furnace. The top surface of the sample was labeled so that it only would be utilized for all the subsequent tests and evaluations. This procedure was used to eliminate the effect of the setter material on the metal film as an additional parameter.

The CuO film generated on these materials was extremely hard and durable which, combined with its very strong bond to the substrate, made it difficult to remove. Hydrofluoric acid solution was found to be the only medium capable of attacking this CuO layer. However, since this acid also readily attacks the substrate material, it was not practical to make a determination of the thickness of this layer.

### 3.3.2. Copper metal film generation

The generation of the metallic copper was done by the direct reduction of the CuO layer in a hydrogen bearing atmosphere at elevated temperatures. Once the critical parameters for the CuO generation were determined and optimized, the metallizing process was controlled essentially by the following parameters: 1) firing temperature schedule, 2) firing time schedule, and 3) ambient atmosphere.

In this study the optimum conditions were determined by the study of a matrix which included a total of 21 samples. These samples, 12 mm wide, 2 mm thick and varying in length, were all cut from a block of  $\text{Li}_2\text{O}-\text{Al}_2\text{O}_3-\text{SiO}_2$  glass previously heat treated at  $600^\circ\text{C}$  (4 hrs) +  $650^\circ\text{C}$  (32 hrs) +  $700^\circ\text{C}$  (32 hrs). At this point, all samples bore a surface layer of CuO.

The metal generation heat treatments were all conducted in a Lindberg muffle furnace equipped with a conveyor belt and atmosphere control provisions. The temperature profile observed by the sample as it traveled through the furnace was programmed by tuning the three independent heating zones. Figure 3 shows a typical temperature profile that was used for the majority of the samples. The residence time at the maximum temperature was determined by the speed of the conveyor belt.

The overall ranges of conditions used for said matrix studies consisted of: a) temperature:  $275-540^\circ\text{C}$ , b) time: 5-30 minutes, and c) atmosphere: 8-25% hydrogen mixed with nitrogen.

The primary criterion for the evaluation of these samples was film adhesion since no material was thought to be worthy of consideration for the subject application without good film-to-substrate adhesion. The detail procedure for the adhesion test is described in a separate section.

Based on the film adhesion tests, the most favorable conditions for the metal copper generation on this type of material are: a) temperature:  $275-300^\circ\text{C}$ , b) time: 5-10 minutes, and c) atmosphere: 8-10%  $\text{H}_2/\text{N}_2$ . This information was later utilized to prepare the final samples for the film property evaluations.

### 3.4. Film property evaluations

A relatively large number of samples were prepared and studied with respect to the manufacturing process variables and physical properties such as: film adhesion, thickness, roughness and light reflectance.

#### 3.4.1. Sample preparation

The final samples were plates  $35 \times 35 \times 3$  mm sawed from the precrystallized billet. Once the precrystallized plates were either ground or polished, the CuO generation and the final conversion to Cu was carried out by the procedures previously described.

The various surface finishes examined here are: as saw-cut, ground with No. 600 grit silicon carbide, ground with No. 1000 grit silicon carbide, polished with cerium oxide, and polished with diamond paste.

#### 3.4.2. Film adhesion test

The relative film-to-substrate adhesion was checked using the unsophisticated, but common, "Scotch Tape Test." This test consisted of pressing a section of the tape (Scotch Magic Transparent Tape No. 810) on the copper film, making sure that no air remained trapped at the interface. The tape was then peeled from the sample by pulling up slowly with a force normal to the film surface. The results were subjectively categorized as follows: excellent (no removal of the film), good (minor peeling), moderate (partial peeling with moderate force), and poor (major peeling requiring no significant force).

#### 3.4.3. Film thickness and surface roughness

A Clevite Brush Surf-Analyzer 150 was used to measure the roughness of the sample surfaces and the thickness of the copper coating. This instrument drives a stylus across a horizontal surface and records the vertical motion of the stylus in microinches. It can record both profile and roughness. Roughness refers to the short-range profile, but does not record longer-range slants or undulations of the surface.

To measure the thickness of the copper coating, a small section of the copper coating was chemically removed by dipping in a solution of  $\text{FeCl}_3$  for 1 minute. The Surf-Analyzer was then driven across this step to measure the thickness of the coating. Because the coating was fairly thin, only polished samples could be used for the thickness measurement. Three measurements were made on each sample.



### 3.4.4. Reflectance at 10.6 $\mu\text{m}$

A Perkin-Elmer Model 621 Grating Infrared Spectrophotometer was used to measure the reflectance of the samples using light with wavelengths from 2.5  $\mu\text{m}$  to 20  $\mu\text{m}$ . The reflectance reported is relative to a silver-coated reference mirror. The absolute reflectance of this mirror is not known, but is believed to be  $98\% \pm 0.5\%$ . Because this instrument measures specular reflectance, only the polished samples gave meaningful results. The relative reflectances at 10.6  $\mu\text{m}$  of the polished samples ranged from 101 to 90%.

Most samples were measured approximately three days after their manufacture and a few days before the laser damage tests. Many samples had their reflectivity measured again about three weeks later to see if the oxidation, which was quite apparent on some samples, had lowered the reflectivity at 10.6  $\mu\text{m}$ .

### 4. Discussion of results

Table 2 summarizes the preparation conditions and the results of tests and measurements for some of the flat plate samples made in this investigation. The three significant heat-treatment parameters tabulated are: the initial crystallization heat treatment, the CuO generation heat treatment conducted in air, and the Cu generation heat treatment performed in  $\text{H}_2/\text{N}_2$  atmosphere. The surface finish shown is that of the crystallized sample prior to the CuO and Cu generation processes.

Table 2. Process and physical properties data for copper-coated glass-ceramic samples

Sample No. †	Surface Finish	CuO Generation °C (hrs)	Cu Generation °C (min)	Electrical Resistivity ( $\Omega/\square$ )	Adhesion	% Reflectance at 10.6 $\mu\text{m}$		Roughness ( $\text{\AA}$ )		Average Thickness of Copper Film ( $\mu\text{m}$ )
						Fresh	Aged	Substrate	Copper	
1	G (600)	625 (16)	275 (5)	0.2	Exc.	65	64	$\approx 15000$	same	ND
2	"	625 (32)	275 (5)	0.2	Exc.	63	--	$\approx 15000$	same	ND
3	P (Ce)	625 (16)	275 (5)	0.2	Pr.	100	102	$< 200$	same	0.48
4	"	625 (32)	275 (5)	0.2	Pr.	101	90	$\approx 500$	same	0.36
5	G (600)	625 (16)	300 (10)	0.2	Exc.	63	62	$\approx 15000$	same	ND
6	"	625 (32)	300 (10)	0.2	Exc.	60	58	$\approx 17000$	same	ND
7	P (Ce)	625 (16)	300 (10)	0.2	Pr.	98	96	$< 200$	same	0.31
8	"	625 (32)	300 (10)	0.2	Exc.	100	100	$< 200$	same	0.46
9	G (600)	625 (16)	275 (6)	0.2	Exc.	67	72	$\approx 15000$	same	ND
10	"	625 (32)	275 (6)	0.3	Exc.	54	64	$\approx 15000$	same	ND
11	"	625 (16)	275 (7)	ND	Exc.	ND	ND	ND	ND	ND
12	"	625 (32)	275 (7)	0.2	Exc.	ND	ND	ND	ND	ND
13	P (Ce)	625 (16)	275 (6)	0.3	Exc.	90	86	$\approx 2500$	same	ND
14	"	625 (16)	275 (7)	0.4	Exc.	ND	ND	ND	ND	ND
15	G (600)	625 (16)	300 (10)	0.1	Exc.	76	76	$\approx 15000$	same	ND
16	"	625 (32)	300 (10)	ND	Exc.	72	62	$\approx 15000$	same	ND
17	P (Ce)	625 (16)	300 (10)	0.2	Exc.	95	94	$\approx 1200$	$< 200$	0.24
18‡	saw-cut	650 (32)	300 (16)	0.05	Md.	ND	--	$\approx 3000$	$\approx 1000$	17.1

Legends: G (600) = ground with No. 600 silicon carbide grinding powder

P (Ce) = polished with cerium oxide powder

Pr. = poor

Md. = moderate

Exc. = excellent

ND = not determined

† Crystallization heat treatment:  $60^\circ\text{C/hr} \rightarrow 580^\circ\text{C}(16) + 30^\circ\text{C/hr} \rightarrow 650^\circ\text{C}(4) + 30^\circ\text{C/hr} \rightarrow 500^\circ\text{C}(0)$   
+ furnace rate  $\rightarrow$  room temperature.

‡ New copper was electrochemically deposited on the original film.

#### 4.1. Film adhesion

In general, film adhesion was excellent for the unpolished (ground) samples and poor for the polished samples with the exception of samples 8, 13 and 17 which exhibited excellent adhesion. It is noteworthy that all samples prepared from the  $\text{ZnO-Al}_2\text{O}_3\text{-SiO}_2$  glass, whether ground or polished, showed very poor film adhesion.

Preliminary studies conducted on a matrix of samples showed that the time, temperature and atmosphere parameters of the Cu generation heat treatments are critical factors affecting the film adhesion.



In general, excessive time, temperature or  $H_2$  content of the atmosphere contributed to poor adhesion. The optimum conditions were found to be: 8-10 minutes, 275-300°C and 8-10%  $H_2$ .

#### 4.2. Electrical sheet resistivity

Electrical sheet resistivity which is a measure of copper film thickness and surface purity was measured on the majority of the samples. The resistivity values ranged from 0.05 to 0.36  $\Omega/\square$ .

#### 4.3. Surface roughness

Surface roughness of the polished glass-ceramic substrate ranged from  $< 200 \text{ \AA}$  to  $500 \text{ \AA}$ . Samples 13 and 17 were exceptions with 2500 and 1200  $\text{\AA}$  roughness. The ground samples showed a range of 1500-1700  $\text{\AA}$ . With the exception of sample 17, the surface roughness did not change significantly with the generation of the copper film. In sample 17, the average roughness was  $< 200 \text{ \AA}$  with the copper film, as compared with 1200  $\text{\AA}$  for the bare substrate. Sample 18 is a special case, in which a relatively large amount of copper was electrolytically deposited on the original copper film. The substrate surface finish was obtained from a saw cut. The plated surface was lightly polished with alumina powder and diamond paste.

#### 4.4. Film thickness

The average film thickness was determined only for the polished samples. These ranged from 0.24 to 0.51  $\mu\text{m}$ . That of the copper-plated sample was 17.1  $\mu\text{m}$ , most of which was due to the electroplating. Although the actual film thickness was not determined for the unpolished samples, it is also expected to be  $< 1 \mu\text{m}$ .

#### 4.5. Reflectance at 10.6 $\mu\text{m}$

Light reflectance was measured on ground as well as polished samples shortly after their preparation and again after about three weeks of aging. The first measurements on the polished samples resulted in 95-101% reflectance versus a silver-coated reference. That of the ground samples ranged from 54-76% apparently due to considerable scattering. It is interesting to note that the values obtained from two samples (not shown in the table) were extremely low, despite their bright appearance. This is believed to be due to a thin dielectric coating present on the copper film which is absorbing the 10.6  $\mu\text{m}$  radiation.

Although the visual appearance of the samples indicated a major discoloration due to aging, the reflectance data shown in the table do not present a clear direction. A mixed effect is shown by the data including a significant drop in three samples, a significant rise in two samples and no significant change in the remaining eight samples.

#### 5. Conclusions

1. In a brief study, compositions from  $\text{Li}_2\text{O}-\text{Al}_2\text{O}_3-\text{SiO}_2$  and  $\text{ZnO}-\text{Al}_2\text{O}_3-\text{SiO}_2$  systems doped with copper at 2 to 4% levels were investigated.

2. Copper metal films were successfully generated on glass-ceramic plates exhibiting characteristics highly favorable to the laser mirror application. These included good film adhesion and high reflectance at 10.6  $\mu\text{m}$ .

3. It was demonstrated that, if desired, the copper film may be built up by electroplating of additional metal to several micrometers without deterioration of the critical properties.

4. It is conceivable that such mirrors can be repaired by refinishing and subsequent regeneration of the copper film.

5. Extremely small thermal expansion/contraction coefficient of the substrate material will allow the utilization of very steep temperature gradients across the wall for high heat transfer rates.

#### 6. References

- [1] Bennett, H. E., NBS Special Publication No. 462 (1976). [2] Pirooz, P. P., Owens-Illinois, Inc., Internal Report (1973).

#### 7. Figures

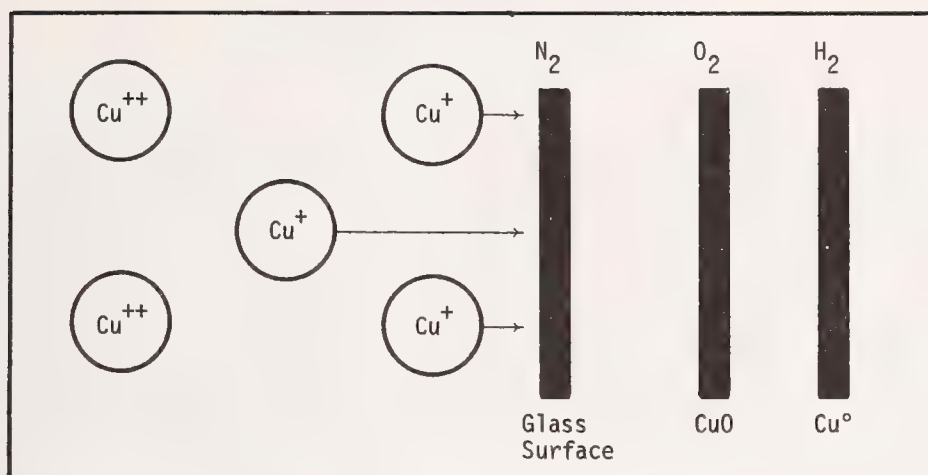


Figure 1. Schematic presentation of copper ion migration in glass.

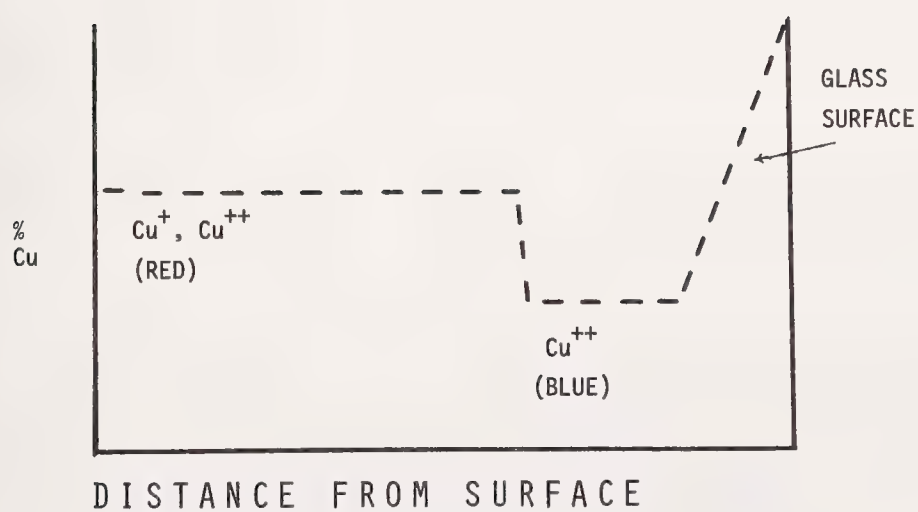


Figure 2. Copper ion concentration profile in a heat-treated glass-ceramic.

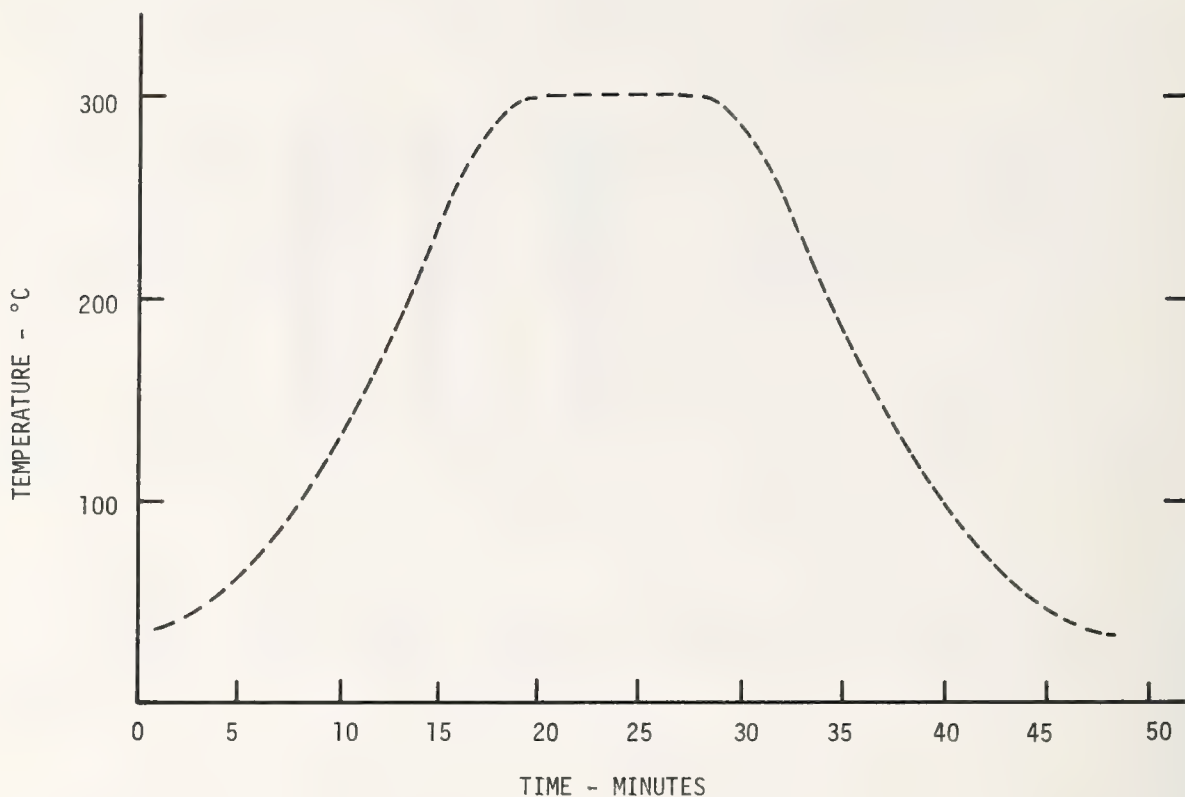


Figure 3. Heat-treatment schedule for copper film generation.

#### COMMENTS ON PAPER BY PIROOZ, DUBE, AND BOLING

The speaker indicated that although the surfaces of the samples were observed to tarnish visibly over a period of days after the preparation, no deleterious effect on the reflectivity at 10.6 microns was observed. He was also asked if the conductivity of the cervit matrix was affected by the inclusion of copper ions. He indicated that time had not permitted the investigation of this point although it would certainly be an interesting affect to examine.



## A NEW CHALCOGENIDE-GLASS ANTIREFLECTION COATING FOR KCl

A.D. McLachlan and W.E.K. Gibbs  
Materials Research Laboratories  
Defence Science and Technology Organisation  
Melbourne 3032, Australia

The design, preparation and performance of new low-absorption antireflection (AR) coatings for KCl at 10.6- $\mu$ m wavelength are described. These coatings are of the two-layer type and utilize the chalcogenide glasses  $\text{As}_2\text{S}_3$  and a newly-developed thin-film material  $\text{Ge}_{30}\text{As}_{17}\text{Te}_{30}\text{Se}_{23}$  (GATS) for the low-index and high-index layers respectively. The compositional homogeneity, structure, refractive index and optical dispersion of thin-films of the GATS material are reported.

The absorption of the AR coatings at 10.6- $\mu$ m wavelength was determined by laser calorimetry and found to be in the range 0.02% to 0.07%. Fine tuning of the deposition procedures enabled coatings with reflectances of 0.025% to be produced. The damage thresholds for pulsed and cw  $\text{CO}_2$ -laser radiation were also determined.

Key words: Absorptance; antireflection coatings; chalcogenide glasses; laser damage; potassium chloride; 10.6- $\mu$ m lasers.

### 1. Introduction

Potassium chloride is widely used as a window material in  $\text{CO}_2$ -laser systems due to its low optical absorption at the operating wavelength of 10.6  $\mu$ m. However, in many applications antireflection (AR) coatings are required, and it is desirable that the absorption in such coatings be kept to a minimum. Antireflection coatings of the two-layer type have a reasonable design flexibility that is illustrated in the Schuster diagram [1]<sup>1</sup> shown in figure 1. The shaded areas represent the range of refractive indices of the layer materials for which zero reflectance may be obtained. Most coating designs utilize a material (e.g.  $\text{ZnSe}$ ,  $\text{As}_2\text{S}_3$ ) for the inner layer with a refractive index,  $n_2$ , of about 2.5 and this is coupled with a material (e.g.  $\text{ThF}_4$ ,  $\text{BaF}_2$ ) with a low refractive index ( $n_1$ ) to produce the desired AR coating. However, there are difficulties in obtaining low refractive-index materials with absorptions as low as the other materials used. Materials such as  $\text{ThF}_4$ , TlI and NaF have been used [2,3,4] with varying degrees of success.

The approach followed in this paper has been to develop a thin-film material for the inner layer with a refractive index,  $n_2$ , greater than 2.9 which can then be used in conjunction with an outer layer of  $\text{As}_2\text{S}_3$ , a material that has been studied extensively in these laboratories [5]. An earlier example [6] of this approach by the present authors was to use quarter-wave thicknesses of the chalcogenide glass  $\text{Ge}_{45}\text{Se}_{55}$  and  $\text{As}_2\text{S}_3$  for the inner and outer layers respectively. The composition of the Ge-Se glass was chosen so that its refractive index,  $n_2$ , satisfied the zero-reflectance condition for quarter-wave layers. Some test results on this AR coating were presented [7] at last year's Symposium by J.F. Lewis and M.C. Ohmer of the Air Force Materials Laboratory. In the present paper, the development is reported of another chalcogenide glass with a suitable refractive index,  $n_2$ , greater than 2.9, that results in an AR coating with an absorptance significantly lower than that reported previously [6,7].

Earlier measurements [8], which are summarized in table 1, at these laboratories have shown differences in the optical absorption between thin films and corresponding materials. In general, the reason for the higher thin-film absorption is not known, although it has been suggested [9] that the presence of water vapour in the pores of polycrystalline films may be a significant factor. Some support for this explanation may be obtained by noting that the difference between thin-film and bulk absorption is least for glassy materials, e.g.  $\text{As}_2\text{S}_3$ . It is well known [5] that films of this material are impervious to water vapour and thus protect KCl surfaces from attack by atmospheric water vapour. For these reasons, effort has been concentrated on low-absorption chalcogenide glasses as candidate thin-film materials.

---

1. Figures in brackets indicate the literature references at the end of this paper.

Table 1. Thin-film absorption coefficient at 10.6  $\mu\text{m}$  and corresponding bulk values.

MATERIAL	ABSORPTION COEFFICIENT ( $\text{cm}^{-1}$ )	
	THIN FILM	BULK
$\text{As}_2\text{S}_3$	3.6	1.1
GeSe	11.9	-
$\text{BaF}_2$	33	0.14
ZnSe	33	0.13
CdTe	59	0.08

The particular material investigated here is a 4-component Ge-As-Te-Se glass of composition  $\text{Ge}_{30}\text{As}_{17}\text{Te}_{30}\text{Se}_{23}$  designated as GATS. This material has a refractive index  $\approx 3.1$  (thus satisfying the requirements for zero reflectance), and a low bulk absorption coefficient [10]  $\approx 0.0075 \text{ cm}^{-1}$ . It is somewhat similar to the Texas Instruments' glass "TI-20" in which some of the Se component is replaced by Te. The addition of Te lowers the absorption in the wavelength region of 11.5 and 13.0  $\mu\text{m}$  and increases both the refractive index and the reciprocal dispersive power [10].

The KCl substrates used in this work were prepared from forged polycrystalline blanks supplied by the U.S. Air Force Materials Laboratory. The surfaces were mechanically polished on soft pitch laps with sub-micron alumina abrasive in a glycerol medium.

## 2. Coating Preparation

### 2.1 GATS Thin Films

Samples of the GATS material were prepared by melting the four components in an evacuated, sealed, silica ampoule that was rocked in a furnace at a temperature of  $650^\circ$  for 6 hours. Procedures were followed that minimized oxygen contamination of the components during preparation [11]. The composition of the resulting glassy ingot was found from electron microprobe measurements to be reasonably uniform. Evaporated thin films of the GATS material adhered to the KCl substrates and appeared to be of good optical quality. No evidence of crystalline structure was revealed by X-ray diffraction, and SEM micrographs of transverse sections of fractured films showed conchoidal fractures characteristic of glassy materials. A representative SEM micrograph is shown in figure 2. The composition of the thin films was found by electron microprobe measurements to be  $\text{Ge}_{28}\text{As}_{21}\text{Te}_{29}\text{Se}_{22}$  and this composition could easily be reproduced. The slight difference in composition between the thin film and the bulk material could be due to the high volatility of the As component.

The optical dispersion of the GATS thin-films was determined from measurements of special transmittance and film thickness. The results are shown in figure 3 where it can be seen that the refractive index at 10.6  $\mu\text{m}$  is 3.11, which is very close to that of the bulk material. The absorption of a number of GATS thin films was determined by calorimetry at 10.6- $\mu\text{m}$  wavelength. The average value for the absorption coefficient was found to be  $2.5 \text{ cm}^{-1}$  which, although considerably higher than the bulk value of  $0.008 \text{ cm}^{-1}$ , is suitable for low-absorption coatings. It may be noted that the absorption coefficient of  $\text{As}_2\text{S}_3$  thin films prepared under similar conditions was found to be  $2.5 \text{ cm}^{-1}$ . This may suggest that a limiting value has been obtained which is determined by contamination from the vacuum system rather than by the intrinsic absorption of the bulk material.

### 2.2 Coating Design and Deposition

The thickness required for zero reflectance for a two-layer coating on KCl are obtained by solving the relevant equations [12]. In general, there will be two solutions which result in the thicknesses shown in table 2 and designated Designs I and II respectively. It was decided to investigate AR coatings specified by Design I since this design is less susceptible to errors in the thickness of the GATS layer. With values of the thin-film absorption coefficients obtained above, the absorptance of the AR coating is calculated to be  $6 \times 10^{-4}$  i.e. 0.06%.

Table 2. Design alternatives for GATS/As<sub>2</sub>S<sub>3</sub> Antireflection Coatings on KCl

MATERIAL	REFRACTIVE INDEX	THICKNESS	
		DESIGN I	DESIGN II
As <sub>2</sub> S <sub>3</sub>	2.374	1.468	0.764
GATS	3.11	0.483	1.222
KCl	1.454	-	-

Deposition of the coating was performed in a turbo-pumped, liquid N<sub>2</sub>-trapped vacuum system by an electron-beam gun source under conditions specified in table 3.

Table 3. Coating deposition parameters

Vacuum system	Turbo-pumped Liq. N <sub>2</sub> trapped 0.1 mPa (1 x 10 <sup>-6</sup> Torr) base pressure
Evaporation source	Electron Beam Gun
Evaporation rate	GATS 1 nm/s As <sub>2</sub> S <sub>3</sub> 2 nm/s

Knowledge of the shape of the dispersion curves of the two materials enabled the required layer thicknesses to be deposited by monitoring the optical thickness at a wavelength of 1.62 μm. The monitoring wavelength was chosen to avoid termination of the deposition on a transmission maximum or minimum. Greater precision can be achieved in this way, since sensitivity to thickness change is greatest at thicknesses midway between transmission maxima and minima.

The spectral transmittance of the completed coating is shown in figure 4, together with values computed from the measured optical constants and design thicknesses of the coating materials. The close agreement indicates that the required layer thicknesses have been correctly deposited.

### 3. Coating performance

#### 3.1. Absorptance

The coating absorptance was determined by calorimetry at a wavelength of 10.6 μm by means of a conventional experimental arrangement which has been reported previously [8]. The results obtained for four AR coatings are shown in table 4. The values obtained are among the lowest ever reported for AR coatings on KCl [4,13,4], and are lower than the expected value of 0.06%. The reason for the discrepancy between the absorptance of the AR coating and the measured absorptances of the coating components is currently under investigation. Not all of the GATS/As<sub>2</sub>S<sub>3</sub> AR coatings that we have produced have shown the low absorptance of the samples tabulated. However, for seven AR coatings deposited at different times and on different KCl substrates, the highest absorptance measured was 0.07% and the mean was 0.035%.

Table 4. GATS/As<sub>2</sub>S<sub>3</sub> AR Coating Absorption at 10.6 μm

COATING NO.	SUBSTRATE	ABSORPTION (%)
MRL 77-8	KCl	0.02
MRL 77	KCl	0.02
MRL 77-10	KCl	0.03
MRL 77-11	KCl	0.02



### 3.2. Reflectance

The reflectance of the AR coatings can be estimated from spectrophotometer transmittance charts; however, for the commercial instruments available, this method is only accurate to about 1%. For more accurate measurements of the AR coatings, an experimental arrangement as shown in figure 5 was utilized. A wedged ( $1^\circ$ ) KCl substrate was used to eliminate interference in the reflected rays between the front and rear surfaces, and was AR coated on one-half of the front surface as shown. This arrangement spatially resolved the front and rear surface reflections so that a power meter could be positioned to record the front surface reflection. A sensitive measurement of the reflectance of the AR coating could be obtained from the ratio of the power levels when the coated and uncoated portions of the samples are present in the beam.

The reflectances of a number of GATS/ $\text{As}_2\text{S}_3$  coatings were measured and found to be less than 0.1%; the lowest measured reflectance was 0.025%. Further improvement should be possible with fine tuning of the coating-deposition procedures.

### 3.3 Damage threshold

The laser-induced damage threshold was determined for both pulsed and continuous-wave  $\text{CO}_2$  laser radiation. The experimental arrangement for the measurement of damage threshold for pulsed radiation is illustrated in figure 6. A TEA  $\text{CO}_2$  laser was operated in the  $\text{TEM}_{00}$  mode and produced a typical pulse, i.e. a sharp gain-switched spike of width 0.2  $\mu\text{s}$  followed by a decaying nitrogen-pumped tail ( $\approx 3\mu\text{s}$ ). The energy in this pulse can be approximated by a square pulse of width 0.6  $\mu\text{s}$  and height equal to the height of the gain-switched spike. The intensity distribution at the sample plane was Gaussian with a  $(1/e^2)$  diameter of 280  $\mu\text{m}$ . The damage threshold was defined as the peak-on-axis energy density that just failed to damage the coating as revealed by subsequent Nomarski microscopy. The damage threshold thus determined was found to be  $\approx 7 \text{ J/cm}^2$ . For energy densities near the damage threshold, the coating was damaged only at a few isolated points within the beam area, as shown in figure 7. This behaviour suggests that the presence of inclusions may be the determining factor in this assessment of damage. For conditions well above threshold the mode of failure was the complete removal of the coating from the substrate.

Values of damage threshold for continuous-wave irradiation must be carefully interpreted since spot size, time of irradiation, cooling, etc. all influence the value obtained. The damage threshold determined in any particular experiment has the merit of ranking the performance of various coatings, but cannot necessarily be taken as a firm design parameter. In our measurements, an area on the coating, 3 mm square, was irradiated uniformly for a fixed time of 3 seconds. This configuration is more representative of many practical situations than is the case with a smaller irradiated area. The GATS/ $\text{As}_2\text{S}_3$  coatings were observed to fail at power densities  $\approx 7 \text{ kW/cm}^2$ . The mode of failure was the removal of portions of the coating within the irradiated area and catastrophic cleavage of the KCl substrate did not occur, although some melting of the film was evident. This behaviour suggests that induced stresses in the films may be responsible for their removal. The figure of  $7 \text{ kW/cm}^2$  is not particularly high. However, it must be borne in mind that our previously reported  $\text{GeSe/As}_2\text{S}_3$  AR films exhibited [9] a damage threshold  $\approx 60 \text{ kW/cm}^2$  when irradiated with a spot size of 0.8 mm, yet their threshold in the large beam-size experiment described above was somewhat less than  $7 \text{ kW/cm}^2$ .

### 4. Conclusion

Two-layer AR coatings on KCl for 10.6- $\mu\text{m}$  wavelength have been produced that utilize the chalcogenide glasses  $\text{Ge}_{30}\text{As}_{17}\text{Te}_{30}\text{Se}_{23}$  and  $\text{As}_2\text{S}_3$  as coating materials. The absorptance and reflectance of these coatings have been measured to be as low as 0.02% and 0.025% respectively. The laser-induced damage threshold has been measured to be  $\approx 7 \text{ J/cm}^2$  for pulsed and  $\approx 7 \text{ kW/cm}^2$  for cw irradiation (9 mm<sup>2</sup> spot). Whilst these damage thresholds are not particularly high, it should be noted that, in applications where thermally-induced optical distortion rather than coating damage is the main limitation, the extremely low absorptance exhibited by the coatings could be of advantage.

### 5. Acknowledgements

The authors would like to thank Mr. W.C. Schoonover of Air Force Avionics Laboratory and Dr. M.C. Ohmer of Air Force Materials Laboratory for arranging for the supply of the substrate materials used in this work.

## 6. References

- [1] Schuster, K., Ann. Phys. 6th series, 4, 352 (1949).
- [2] Braunstein, M., Allen, S.D., Braunstein, A.I., Giuliano, C.R., Turk, R.R., Wang, V., and Zaccaro, D., Air Force Cambridge Research Laboratories Report No. AFCRL-TR-75-0429 (1975).
- [3] Baer, A.D., Donovan, T.M., Green, A.K. and Turner, G. in *Laser Induced Damage in Optical Materials*: 1976, NBS Special Publication 462, p. 214.
- [4] Detrio, J.A., Petty, R.D., Ohmer, M.C. and Swensen, O.F. in *Laser Induced Damage in Optical Materials*: 1976, NBS Special Publication 462, p. 283.
- [5] Young, P.A., Thin Solid Films, 6., 423 (1970).
- [6] McLachlan, A.D., Appl. Opt. to be published.
- [7] Lewis, J.F. and Ohmer, M.C. in *Laser Induced Damage in Optical Materials*: 1976, NBS Special Publication 462, p. 279.
- [8] Gibbs, W.E.K. and Butterfield, A.W., Appl. Opt., 14., 3043 (1975).
- [9] Sparks, M. in *Laser Induced Damage in Optical Materials*: 1976, NBS Special Publication 462, p. 203.
- [10] Savage, J., Royal Signals and Radar Establishment (Malvern), United Kingdom. Private communication.
- [11] Webber, P.J. and Savage, J.A., J. of Non-Crystalline Solids, 20, 271 (1976).
- [12] Cox, J.T. and Hass, G., in *Physics of Thin Films*, 2 (Academic Press, N.Y., 1964), p. 257.
- [13] Loomis, J.S. and Huguley, C.A., in *Laser Induced Damage in Optical Materials*: 1974, NBS Special Publication 414, p. 94.
- [14] Wang, V., Rudisill, J.E., Giuliano, C.R., Braunstein, M. and Braunstein, A. in *Laser Induced Damage in Optical Materials*: 1974, NBS Special Publication 414, p. 59.

## 7. Figures

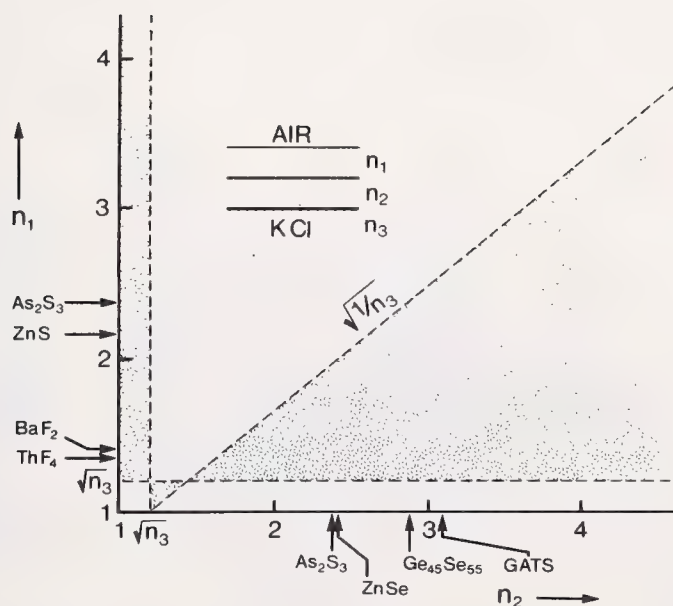


Figure 1. Schuster Diagram for 2-layer AR coatings on KCl. The shaded areas indicate areas for which zero reflectance may be obtained. The refractive indices of several candidate coating materials are shown.

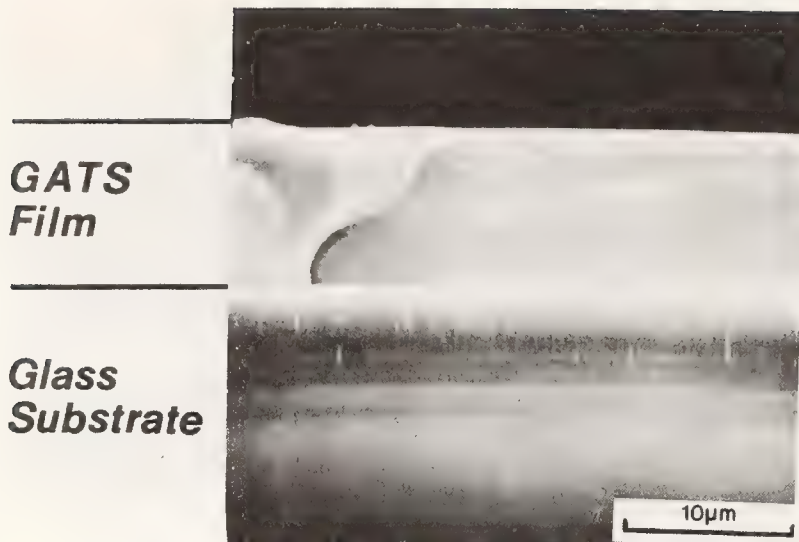


Figure 2. Scanning Electron Micrograph of the transverse section of a fractured GATS film on a glass substrate. The fracture surface of the film is characteristic of glassy materials.

Figure 3. The optical dispersion relationship for the chalcogenide glass film  $\text{Ge}_{23}\text{As}_{21}\text{Te}_{29}\text{Se}_{22}$  (GATS).

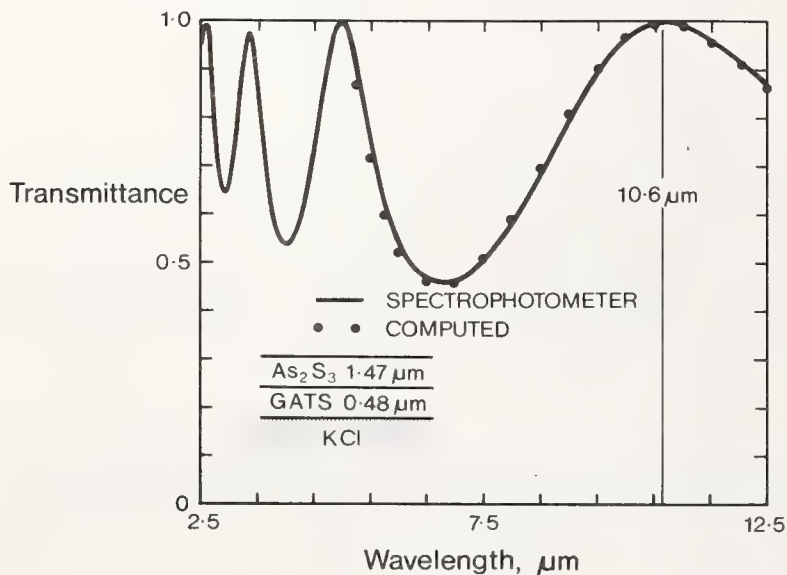
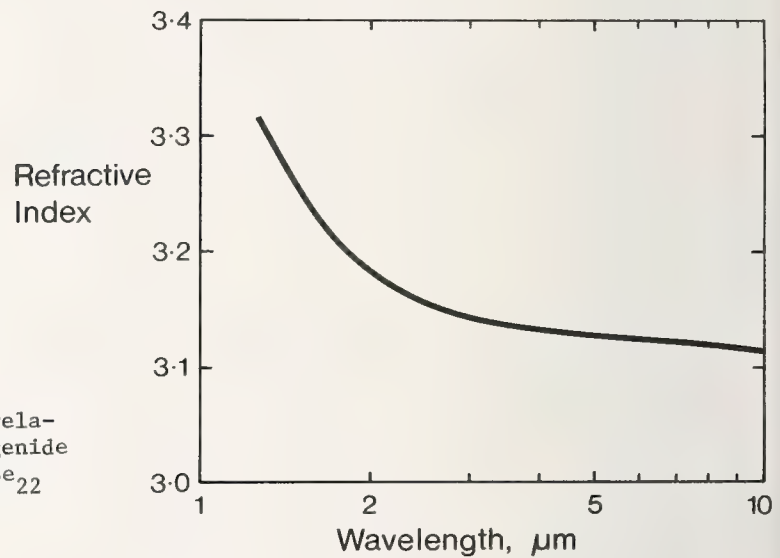


Figure 4. The spectral transmittance of a GATS/ $\text{As}_2\text{S}_3$  AR coating on KCl as measured by a spectrophotometer (—) compared with values (...) computed from the measured optical constants and design thicknesses.



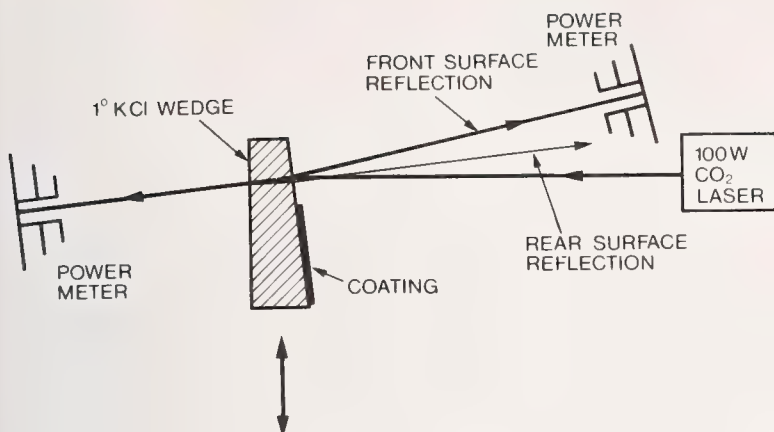


Figure 5. Experimental arrangement for the measurement of AR coating reflectance.

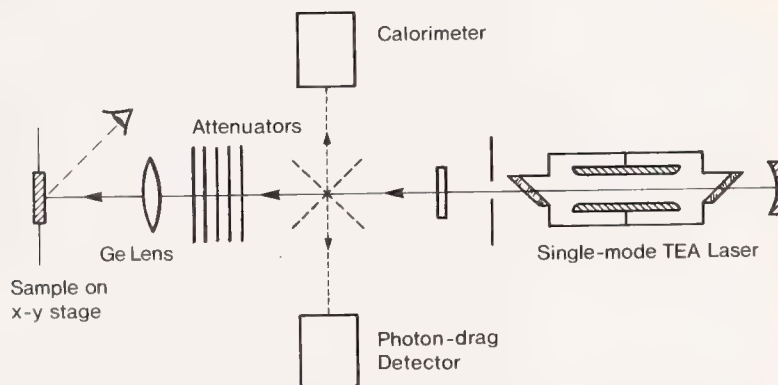
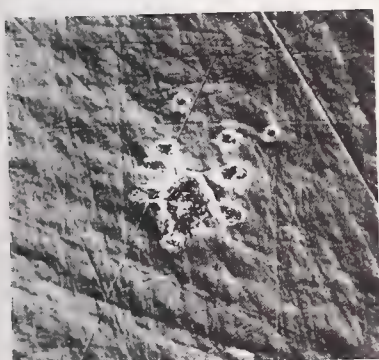


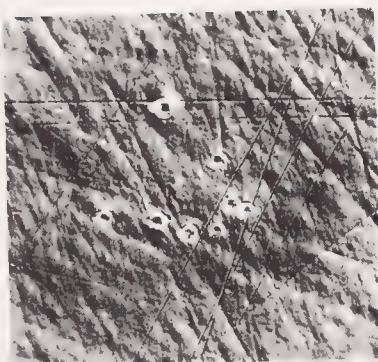
Figure 6. Schematic diagram of damage-threshold measurements.

ABOVE THRESHOLD



280  $\mu\text{m}$   
( $1/e^2$ ) diameter

NEAR THRESHOLD



280  $\mu\text{m}$   
( $1/e^2$ ) diameter

Figure 7. Nomarski micrograph of damage sites within the irradiated beam area. The site on the right shows the damage near, but just above, the threshold level. The site on the left shows damage for power levels somewhat higher than threshold.

COMMENTS ON PAPER BY McLACHLAN AND GIBBS

*No discussion on this paper.*

# INTRINSIC AND THERMAL STRESS MODELING FOR THIN-FILM MULTILAYERS

Anthony M. Ledger and Roy C. Bastien  
The Perkin-Elmer Corporation  
Norwalk, Connecticut 06856

## Abstract

Theoretical models of stress effects in thin films have been developed that can be used as a framework of a computer model for stress addition in multilayer films. A system of stress interferometers has been developed which enables intrinsic stress, thermal expansion coefficient, and Young's Modulus to be obtained for thin films. Data on these mechanical properties have been obtained for films of Thorium Tetrafluoride, Zinc Selenide, and Thallium Iodide materials.

Key words: Film stress; infrared interferometer; stress interferometer; thin film thermal expansion coefficient; Young's modulus; zinc selenide.

## 1. Introduction

Multilayer dielectric coatings fabricated by thermal evaporation or sputtering exist in a stressed condition. The stress levels often exceed the breaking strength of the bulk form of the material. The total stress in such a deposited film is the sum of two basic contributions: an intrinsic stress characteristic of the thin film material; together with a thermal stress contribution caused by a difference in thermal expansion coefficient between the thin film and its substrate. These stress levels can greatly influence the durability of thin film structure, although a complete model of film durability must include a description of the adhesive forces at each film interface and in particular at the boundary between the film stack and its substrate.

The initial impetus for the development of durability models for thin film structure was provided by the difficulty in producing antireflection coatings for high expansion window material ( $KCl$ ,  $CaF_2$ , etc.) using traditional infrared coating materials. Although this particular difficulty has since been overcome by the use of high expansion films of Thallium Iodide and Potassium Chloride<sup>1</sup>, the fundamental problem remains of predicting the durability of a thin film structure when exposed to intense laser beams.

During the past year, a program was initiated to investigate durability models for thin films and primary emphasis was directed towards the following areas.

- Stress addition models for multilayer coatings
- Development of a stress measuring interferometer system
- Mechanical property measurements of  $ThF_4$ ,  $ZnSe$ ,  $TlI$  infrared coating materials

A system of stable stress interferometers suitable for use at high temperatures was developed during the program and utilized to provide stress measurements during film deposition, together with measurements of the thin film thermal expansion coefficient of several infrared coating materials. Before discussing these specific measurement techniques, a brief review is presented in the following text of the theoretical framework pertaining to stress effects in thin films.

## 2. Stress Measurements and Stress Effects in Thin Film Multilayers

Many different measurement techniques have been used for the measurement of intrinsic stress, most of which depend upon detecting the minute deflections of a thin glass beam or disc upon which the film is being deposited. Optical interference methods provide a very sensitive method of measuring such small deflections although capacitive and electro-mechanical methods can also provide comparable sensitivities. Comprehensive review of various stress measurement techniques have been given by Hoffman<sup>2</sup> and more recently by Kinoshita<sup>3</sup> and Hoffman<sup>4</sup>.

1. Figures in brackets indicate the literature references at the end of this paper.



A stressed film depositing onto a flexible disc can be described in terms of a unit stress  $\sigma(t)$  at some film thickness  $t$  as shown in figure 1. If the growing film produces a deflection  $\omega(t)$  of the flexible disc due to the integrated effect of the unit stress function  $\sigma(t)$ , up to a thickness  $t$ , the average stress  $\langle S(t) \rangle$  is given by the following expression.

$$S(t) = \frac{4E_s}{3(1-\nu_s)} \left( \frac{h}{D} \right)^2 \left( \frac{\omega(t)}{t} \right) \left[ 1 + \frac{E_f}{E_s} 3(1-\nu_s) \frac{t}{h} \right] \quad (1)$$

The deflection of the disc is governed principally by the aspect ratio  $(h/D)$  and to a lesser extent by the values of Poissons ratio  $\nu_s$  and Young's modulus  $E_s$  of the substrate material. A second order term,  $3 E_f (1-\nu) t / h E_s$  is included in the expression for the effective film stress and arises from stress relief effects. When a stressed film is deposited onto an uncoated disc, the deflection of the disc during the measurement produces a small amount of stress relief in the thin film material. Alternatively, if an external force is applied to the center of the disc so that the deflection produced by a tensile film is removed, the film will elongate. In this case, the true value of film stress is larger than if the plate were allowed to bend freely. The small magnitude of such stress relief effects in practice ( $t/h \ll 1$ ) implies that the addition of a film to an existing multilayer stack will have little influence upon the stress levels of previously deposited films. In a similar manner, the deflection of a deformable mirror substrate will not produce measurable stress change in a mirror coating.

Although stress determinations using flexible substrates provide a measure of the total effective film stress  $S(t)$ , nonuniformities in intrinsic stress as a function of film thickness are more conveniently described in terms of the unit stress function  $\sigma(t)$ . This function cannot be measured directly for a film material but can be computed from the measured data as follows:

$$\sigma(t) = \langle S(t) \rangle + t \frac{d}{dt} \langle S(t) \rangle \quad (2)$$

The total film stress in a deposited film contains an additional contribution arising from thermal stress caused by a difference in expansion coefficient between the thin film and substrate material.

If the film/substrate combination undergoes a uniform temperature change  $\Delta T$ , the difference in unit elongation of film and substrate is given by  $(\alpha_f - \alpha_s)$  which leads to the existence of a thermally induced stress  $\sigma_{TH}$  given by

$$\sigma_{TH} = E_f (\alpha_f - \alpha_s) \Delta T \quad (3)$$

where  $\alpha_f$  and  $\alpha_s$  are the expansion coefficients of the film and substrate material and  $E_f$  is the value of Young's modulus for the film material.

The total stress in a thin film material which is deposited at a temperature  $T$  and subsequently reduced to an ambient temperature  $T_0$  can be expressed as

$$\sigma(t) = \langle S(t) \rangle + t \frac{d}{dr} \langle S(t) \rangle + E_f (\alpha_f - \alpha_s) (T - T_0) \quad (4)$$

and this expression forms the basis for the addition of stress effects in multilayer coatings.

When film materials are combined to form optical multilayer stacks, the stress levels in each film combine to produce a total bending moment at the film/substrate boundary which tends to tear the film from the substrate. This moment can be expressed in terms of the individual stress levels in each film for a stack of  $m$  films as

$$M_{STACK} = \sum_{i=1}^m \int_{t_{i-1}}^{t_i} \sigma_i(z) dz \quad (5)$$

where, the stresses  $\sigma_i(z)$  are defined according to eq. (4). The effect of this total moment on a flexible disc is such as to produce a deflection given by

$$\omega_{TOTAL} = \frac{3}{2} \left( \frac{1-\nu_s}{E_s} \right) \frac{D^2}{h^3} M_{STACK} \quad (6)$$

In some cases this deflection can be minimized or reduced to zero resulting in so-called zero stress multilayer designs but more properly denoted as zero moment multilayer structures.

From the preceding discussion it is evident that a durability model for thin film multilayers requires, at the very least, experimentally measured data for intrinsic stress levels, the thin film expansion coefficients, and the Young's modulus of each layer, together with adhesion and film breaking stress levels. The present program addressed the measurement of the first three quantities using a new stress interferometer system described in the following sections.

### 3. Interferometric Stress Measurements

The intrinsic stresses developed in metallic films have been measured by many authors to aid in developing theories of film nucleation and growth. Stresses developed in dielectric films, however, have not been investigated as thoroughly, particularly for thick films used in infrared coating designs. The two most comprehensive investigations of stress effects in dielectric films were carried out by Campbell<sup>5</sup> and Ennos<sup>6</sup>. The stress behavior of various fluorides, bromides, and iodides, have been measured by Campbell using a capacitance bridge whereas Ennos<sup>6</sup> utilized a laser interferometer to measure intrinsic stress in a large variety of coating materials as a function of the deposition conditions.

This type of laser interferometer configuration was found to be sensitive to vibration. Distortion of the interferometer occurred at high temperatures. Recently, a high temperature Michelson interferometer designed for UHV applications has been described by Roll and Hoffman<sup>7</sup>. Thermal distortions are minimized in this design by obtaining an interferogram of the full aperture of the bending disk and by deducing the deflection from successive photographs of the fringe pattern. Tilts and axial displacements of the substrate can be removed by computation, but the method requires substantial data reduction time for each successive fringe pattern taken during deposition.

The problems of vibration and temperature disturbances have been minimized by designing a new interferometer capable of continuous stress measurements during deposition at temperatures up to 250°C.

#### 3.1 Cats-Eye Interferometer

The cats-eye interferometer consists simply of a glass element whose front surface is polished to focus an incident laser beam onto two reflecting surfaces formed by the base of the cat's eye lens and the substrate upon which the film is being deposited (figure 2). The base of the lens is coated with a hard dielectric reflector to reflect ~50% of the incident beam at 6328Å and the deformable substrate is coated on its top surface with a partially reflecting metal coating. In most experiments a gold coating was used for this purpose since, when cold-deposited, gold has a low stress and has such poor adhesion to the substrate that it can be easily wiped from the surface. In addition, gold films can withstand high temperature baking without the occurrence of excessive recrystallization.

This interferometer configuration acts in a manner similar to a retroreflecting mirror, and alignment is a simple task. The reflected light consists of a set of circular interference fringes that either expand or contract from the center as the substrate is deformed, depending upon the tensile or compressive nature of the film stress. A single silicon detector mounted in the center of the return fringe pattern enables not only the amount of deflection to be measured but also allows the direction of motion to be determined automatically from the fringe change recording.

The interferometer is illuminated with a 4-mm diameter collimated laser beam (6328Å) produced by the interferometer laser source illustrated in figure 3. The polarized beam from a 2-mW He-Ne laser is chopped by a synchronous chopper wheel and expanded to 4-mm diameter by a beam expander and spatial filter. A polarizing beamsplitter reflects approximately 1 percent of the "p" polarized laser beam to a silicon synchronous reference detector and transmits the remaining energy to the cat's-eye interferometer. A quarter-wave plate located between the polarizing beamsplitter and interferometer rotates the polarization from "p" to "s" after two passes, and the return fringe pattern is reflected by the polarizing beamsplitter to a fringe-count detector and display screen. The polarizing beamsplitter/quarter-wave plate system is used only to maximize the amount of light on the viewing screen and is not fundamental to the operation of the interferometer system.

A system of four cat's-eye interferometers has been constructed to monitor film stress at four radial positions in a 36" vacuum box coating system. An optical-thickness monitor is located on the



centerline of the chamber, and optical film thicknesses are monitored at any desired wavelength up to  $1.0\mu\text{m}$  by suitable choice of line filters. Optical thicknesses of the composite films of multilayers are individually monitored using fresh glass microscope slides for component films during an evaporation cycle. The entire assembly of interferometers, rigid substrate holders, and optical monitor slides are enclosed in stainless-steel shields and can be treated to  $250^\circ\text{C}$  by a Calrod heater located at the top of the vacuum chamber. Temperature control is obtained using an SCR proportional controller and a thermistor mounted close to the interferometer housings.

Stress changes in the films during deposition cause the bull's-eye fringe patterns at the fringe-count detector to expand or contract depending upon the nature of the stress (tensile or compressive). Changes in intensity of the central fringe are detected by PIN diodes and are fed to lock-in amplifiers that synchronously demodulate the chopped signals using a reference signal from a second silicon diode in the laser source housing. The outputs of the optical monitor and stress interferometers are recorded on a six-channel chart recorder and are also applied to the input of a data-logger/punched tape recorder system. This stress interferometer system provides stable bull's-eye fringes at the fringe count detector with all vibration effects eliminated. Stress measurements at equilibrium temperatures up to  $250^\circ\text{C}$  are reproducible although changes in temperature can cause erroneous fringe counts during heat up or cooling cycles.

A unique feature of this type of interferometer is that of the magnitude and sign of the fringe changes that can be detected using a single detector. The wavefront generated by the detector as the fringes either contract or expand possesses waveform asymmetry which occurs each cycle. The sign of the asymmetry depends upon the direction of motion of the flexible disc. Figure 4 shows this effect for a Magnesium Fluoride film deposited onto a Cervit disc at ambient temperature and illustrates the fringe count waveform at the time the film undergoes cracking. Before the film deposition point, the stress is tensile, and the positive going slope is greater than the negative going slope. After the film cracks, the disc deflects in the reverse direction and the waveform asymmetry changes sign. This effect can be explained theoretically by the radial shearing which occurs in the focussed beam at the two interferometer reflecting surfaces.<sup>8</sup>

### 3.2 Stress Measurements

Stress measurements have been made for films of Thorium Tetrafluoride ( $\text{ThF}_4$ ), Zinc Selenide ( $\text{ZnSe}$ ) and Thallium Iodide ( $\text{TlI}$ ) under a wide range of deposition conditions. The influence of vapor incidence angle, evaporation rate, and substrate temperature have been investigated for  $\text{ThF}_4$ . A number of stress measurements have also been made for Thallium Iodide material evaporated from an electron beam gun.

Data from the stress interferometer system is reduced using an IBM 70 and plots are obtained of the sampled data, the average stress  $\langle S(t) \rangle$  and the unit stress curve  $\sigma(t)$  by best fit procedures. The unit stress data can be well described in terms of three film stress coefficients A, B, and C according to

$$\sigma(t) = Ae^{-Bt} (1 - e^{-Ct}) \quad (7)$$

Examples of the stress data obtained are shown in figures 5 and 6 for  $\text{ThF}_4$  and  $\text{ZnSe}$  materials as a function of the film mechanical thicknesses (microns). The experimental data for these materials show a nonuniformity of stress with thickness for small film thicknesses. Examination of cracked films of  $\text{ThF}_4$  and  $\text{ZnSe}$  deposited onto  $\text{KCl}$  substrates by microinterferometry show that flakes of  $\text{ThF}_4$  material are usually highly curved whereas  $\text{ZnSe}$  film flakes are predominantly flat. This behavior conforms to the experimental stress curves since the nonuniform stress region is much wider in  $\text{ThF}_4$  than  $\text{ZnSe}$ . Such stress nonuniformities may be caused by the flexible substrate being heated by the source as the film is being deposited onto the surface and theoretical investigation of this effect are continuing.

Stress data obtained for  $\text{ThF}_4$  shows little dependence upon deposition rate, angle of incidence, or deposition temperature, whereas the results obtained for Zinc Selenide films show a marked dependence upon evaporation rate. The possibility that this rate dependence is influenced by source heating cannot be ignored at the present time. Thallium Iodide material exhibits extremely low stress levels when deposited at  $100^\circ\text{C}$  from an electron beam gun source. Table I summarizes the stress data obtained for these three materials in terms of the film stress coefficients A, B, and C defined in eq. (7).



#### 4. Experimental Measurement of The Thin Film Expansion Coefficients and Young's Modulus

Experimental values of the thermal expansion coefficient ( $\alpha_f$ ) and Young's modulus ( $E_f$ ) for a thin film can be obtained using the four-channel interferometer system by observing the total deflection caused by thermally induced stress. Figure 7 shows the output from two interferometer channels during deposition of a film of  $\text{ThF}_4$  ( $\lambda/4$  at  $10.6 \mu\text{m}$ ) and during subsequent cooldown. This film is deposited onto Cervit and  $\text{KCl}$  discs and the thermally induced stress contribution is sufficient to produce a large tensile stress ( $+3400 \text{ kg/cm}^2$ ) for the  $\text{ThF}_4$  on Cervit and a large compressive stress ( $-1400 \text{ kg/cm}^2$ ) for  $\text{ThF}_4$  deposited onto  $\text{KCl}$ . When zinc selenide films are deposited onto  $\text{KCl}$  in this manner the large initial intrinsic stress - ( $1500 - 3000$ )  $\text{kg/cm}^2$  together with a thermally induced stress of  $\sim 2400 \text{ kg/cm}^2$  is usually sufficient to crack the films by compressive film failure at the  $-4000$  to  $-5000 \text{ kg/cm}^2$  stress level.

Initial experiments using uncoated discs of various materials showed that substantial fringe changes occurred upon heating and cooling presumable due to temperature gradients (radial and front to back) existing in the flexible discs. Experimental measurements were therefore made using all four interferometers and coated and uncoated discs of each substrate material. Fringe changes were utilized on cooldown since this results in a much lower cooling rate than during the heatup cycle.

The values of expansion coefficient and Young's modulus can be obtained from the expressions for the thermally induced deflection of a thin disc, i.e.,

$$\omega = \frac{3(1-\nu_s)t}{4E_s} \left( \frac{D^2}{h} \right) E_f (\alpha_f - \alpha_s) (T_i - T_o) \quad (8)$$

where  $(T_i - T_o)$  is the total temperature change,  $\alpha_s$ ,  $\nu_s$ , and  $E_s$  being the expansion coefficient, Poisson's ratio, and Young's modulus, respectively, of the substrate.

For two different substrate materials each coated with a film of thickness  $t$ , the thermally induced deflections are

$$\omega_1 = \frac{3(1-\nu_s)t}{4E_1} \left( \frac{D_1^2}{h_1} \right) E_f (\alpha_f - \alpha_1) (T - T_o) \quad (9)$$

$$\omega_2 = \frac{3(1-\nu_s)t}{4E_2} \left( \frac{D_2^2}{h_2} \right) E_f (\alpha_f - \alpha_2) (T - T_o) \quad (10)$$

Consequently, the values of the film constants  $\alpha_f$  and  $E_f$  are given by

$$\alpha_f = \frac{\alpha_2 \omega_1 \Lambda_2 - \alpha_1 \omega_2 \Lambda_1}{\omega_1 \Lambda_2 - \omega_2 \Lambda_1} \quad (11)$$

$$E_f = \frac{\omega_2}{\Lambda_2 (\alpha_f - \alpha_2) t (T - T_o)} \quad (12)$$

where

$$\Lambda_1 = \frac{3(1-\nu_1)}{4E_1} \left( \frac{D_1^2}{h_1} \right) \quad \text{and} \quad \Lambda_2 = \frac{3(1-\nu_2)}{4E_2} \left( \frac{D_2^2}{h_2} \right) \quad (13)$$

characterize the substrate properties.

In all experimental determinations the deflections  $\omega_1$  and  $\omega_2$  correspond to the differences in deflection between the coated and uncoated substrates, i.e.,

$$\omega_1 = (\omega_1)_c - (\omega_1)_{uc} \quad (14)$$

$$\omega_2 = (\omega_2)_c - (\omega_2)_{uc} \quad (15)$$

The typical changes that occur during heating, cooling, and reheating of coated and uncoated discs of different materials are shown in figure 8. Here, discs of Cervit and  $\text{KCl}$  are coated with  $\text{ThF}_4$  material, and the fringe changes as a function of temperature are used to compute the expansion coefficient and Young's modulus of the thin-film material as shown above.

Measurements were made of thin films of  $\text{ThF}_4$ ,  $\text{ZnSe}$ ,  $\text{TlI}$  in this manner and the results are summarized in Table II.

Emphasis was placed on obtaining values of  $\alpha_f$  for thorium tetrafluoride since measurements of this material in single crystal form by Van Uitert<sup>9</sup> show that the expansion coefficient is small and negative in the region from 0 to 200°C. The experimental values for thin films consistently showed a large positive value both for measurements made during cooldown and immediately after the film was deposited and during subsequent reheating cycles. Different pairs of substrates ( $\text{KCl} + \text{Cervit}$  and  $\text{KCl} + \text{ZnSe}$ ) were also used for these experiments and gave similar results.

The expansion coefficient of thallium iodide material was so closely matched to that of the  $\text{KCl}$  substrate that no discernible difference in the fringe changes could be seen for the coated and uncoated substrates as the temperature was varied.

## 5. Summary and Conclusions

The framework of a computer model for stress addition in thin film multilayers has been completed which uses measured data on film stress, thin film thermal expansion coefficients and Young's modulus for each coating material.

A new cat's-eye stress interferometer has been developed which enables measurements to be made at high temperatures (250°C) during film deposition. This interferometer offers simple alignment, immunity from vibrations, and fringe counting sensitivity.

A system of four interferometers has been used to measure the stress levels in the  $\text{ThF}_4$ ,  $\text{ZnSe}$ , and  $\text{TlI}$  materials as a function of film deposition conditions (rate, temperature). Data has been presented for these materials in terms of three stress coefficients.

The interferometric system has also been used to measure the thermal expansion and Young's modulus of thin films of the above materials. Thermal expansion values for  $\text{ThF}_4$  films in particular have been shown to be much larger than the bulk single crystal values previously measured.

## 6. Acknowledgements

The authors are grateful for the dedicated assistance of M. R. Porier who conducted the experimental measurements and reduced copious amounts of data to significant essentials. This work was sponsored by Captain Henry Winsor, under ARPA Contract DAA25-76-C-0410.

## 7. References

1. M. C. Ohmer, Laser Induced Damage in Optical Materials Symposium, 1977, Boulder, Colorado, *ibid*.
2. R. W. Hoffman, Physics of Thin Films, 3, 211 (1966).
3. K. Kinoshita, Thin Solid Films, 12, 17 (1972)
4. R. W. Hoffman, Thin Solid Films, 34, 185 (1976)
5. R. S. Carpenter and D. S. Campbell, J. Mat. Sci., Vol. 2, p. 173, (1967)
6. A. E. Ennos, Applied Optics, Vol. 5, No. 1, p. 51, (1966).
7. K. Roll and H. Hoffman, Rev. Sci. Inst., Vol. 47, No. 9, (1976).
8. A. M. Ledger, Applied Optics, to be published
9. L. Van Uitert, et al., Mat. Res. Bull. 11, 699 (1976)

## 8. Figures

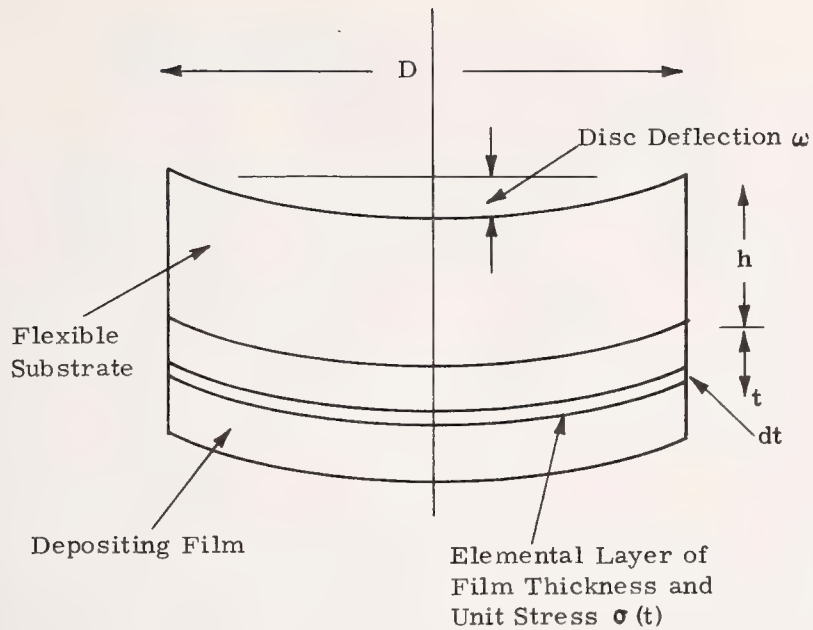


Figure 1. Deflection of a thin flexible disc by a growing film of material deposited in a stressed condition. The film stress is described in terms of a unit stress  $\sigma(t)$  acting in an element of thickness  $dt$  at any thickness  $t$ .

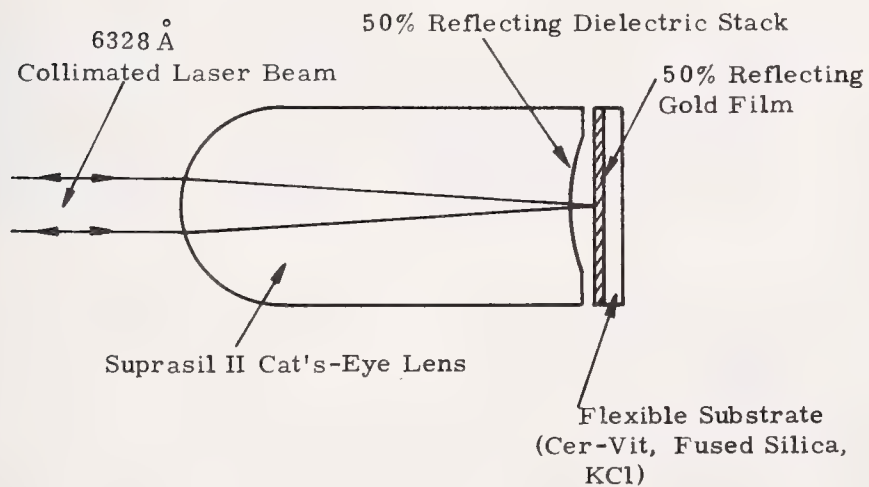


Figure 2. Cat's-Eye stress interferometer configuration utilizing interference effects in a focussed beam to generate bull's-eye fringes.



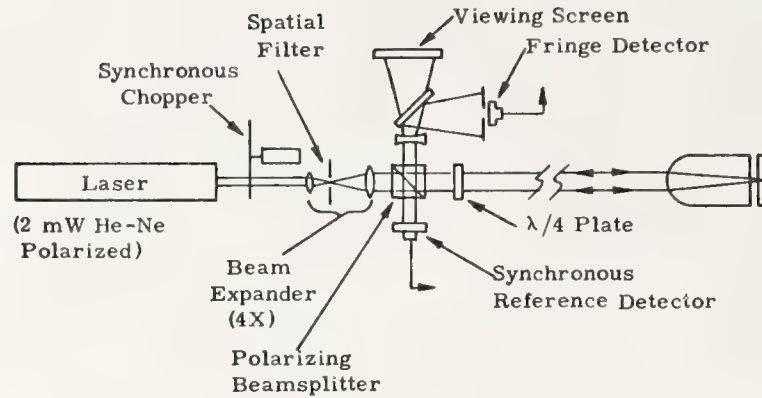


Figure 3. Cat's-Eye stress interferometer system. A chopped circularly polarized laser beam is used to illuminate the interferometer element which produces a set of circular fringes in reflection. Fringe changes produced by deflections of the disc during coating deposition are sensed by a synchronous detection system to provide coating stress information.

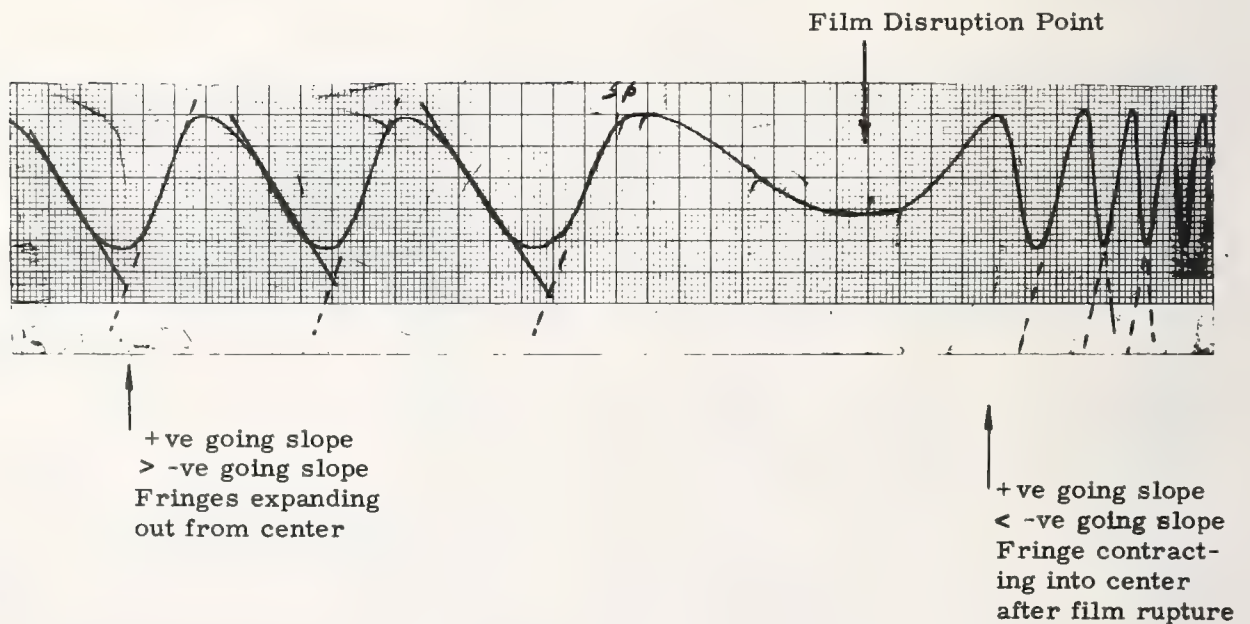


Figure 4. Fringe count for a 0.5-mm thick Cervit disc during deposition of  $\text{MgF}_2$  (Note waveform asymmetry indicating direction of fringe motion before and after film cracking).

EXPONENTIAL MODEL:  
 $A = 1057.10$   
 $B = 0.000000050$   
 $C = 12.49699$   
 $STD. DEV. = 44.202$

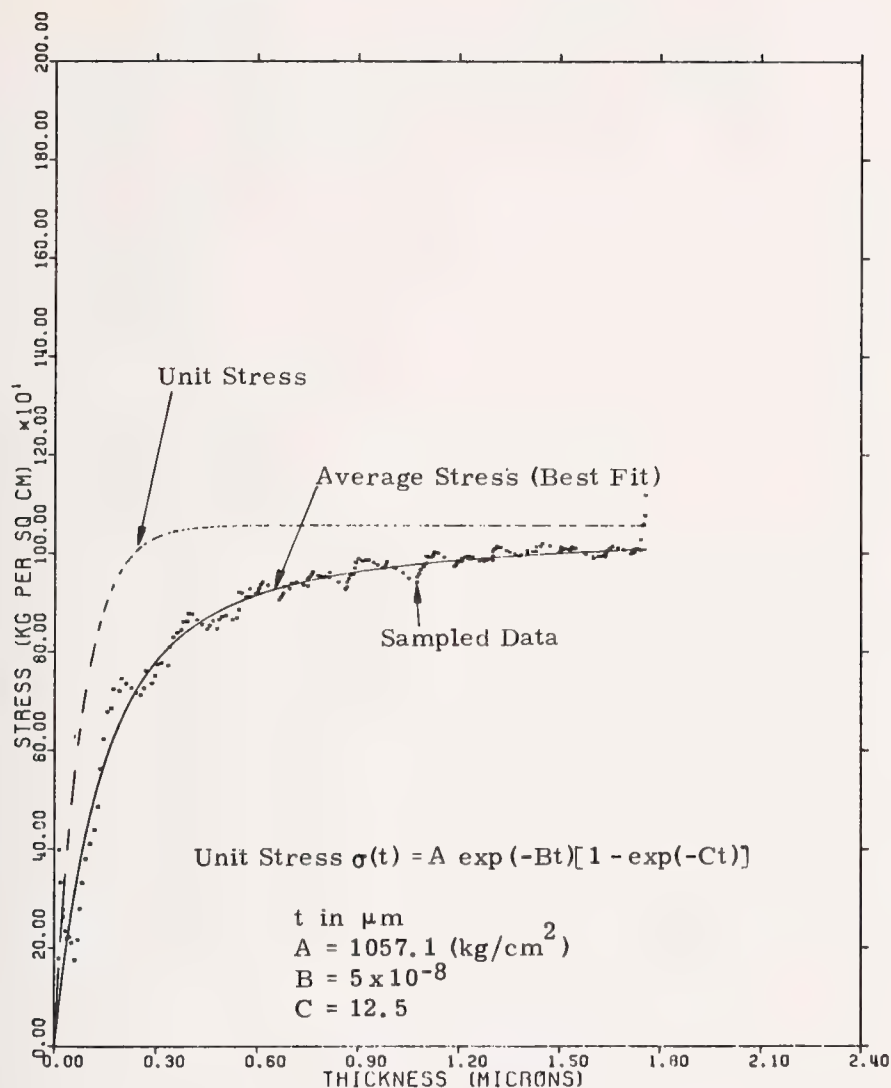


Figure 5. Tensile stress produced in Thorium Fluoride film material deposited at 37 Å/s at 200°C. Stress measured from the deflection of 0.5-mm thick Cervit substrate.

EXPONENTIAL MODEL:  
 $A = -3300.00$   
 $B = 0.199999680$   
 $C = 80.00000$   
 STD. DEV. = 83.205

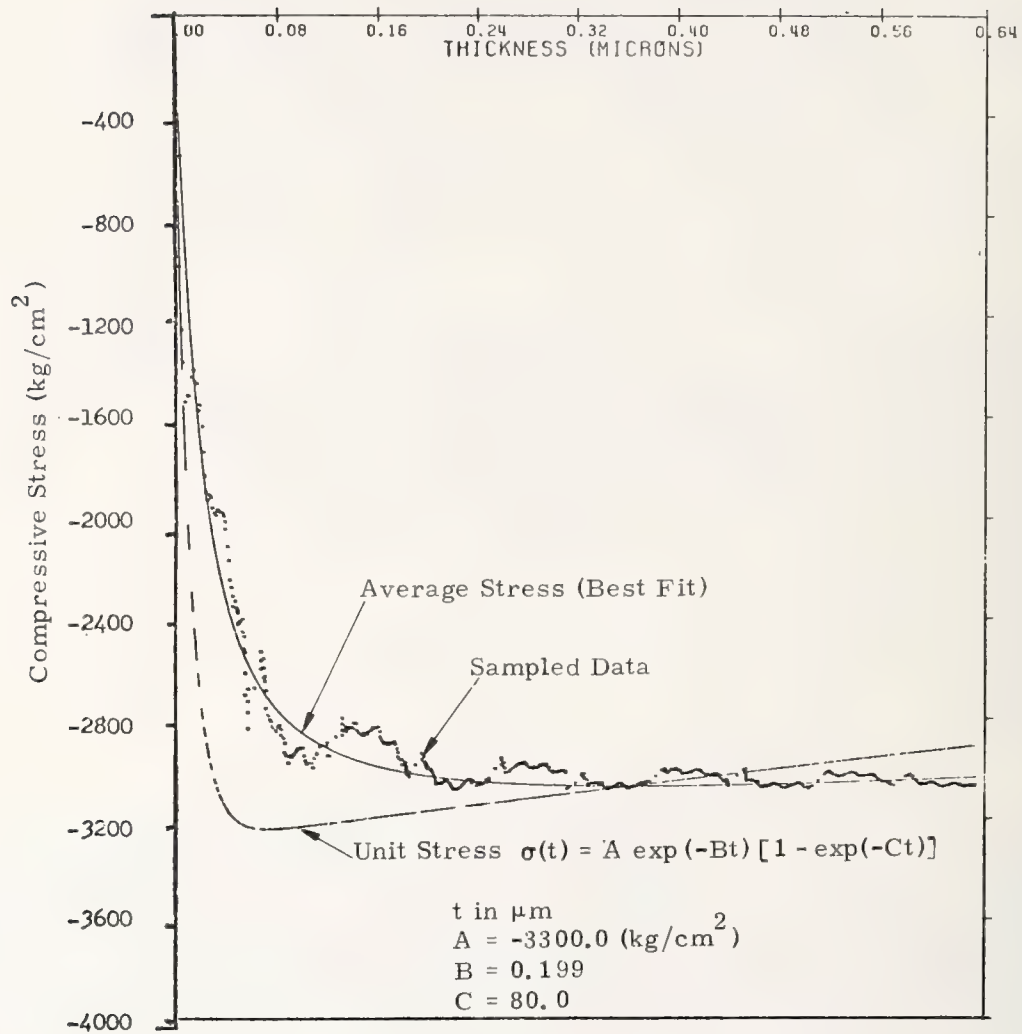


Figure 6. Compressive stress produced in Zinc Selenide thin film material deposited at 4.4 Å/s at 150°C. Stress measured from deflection of 0.25-mm-thick Cervit substrate.



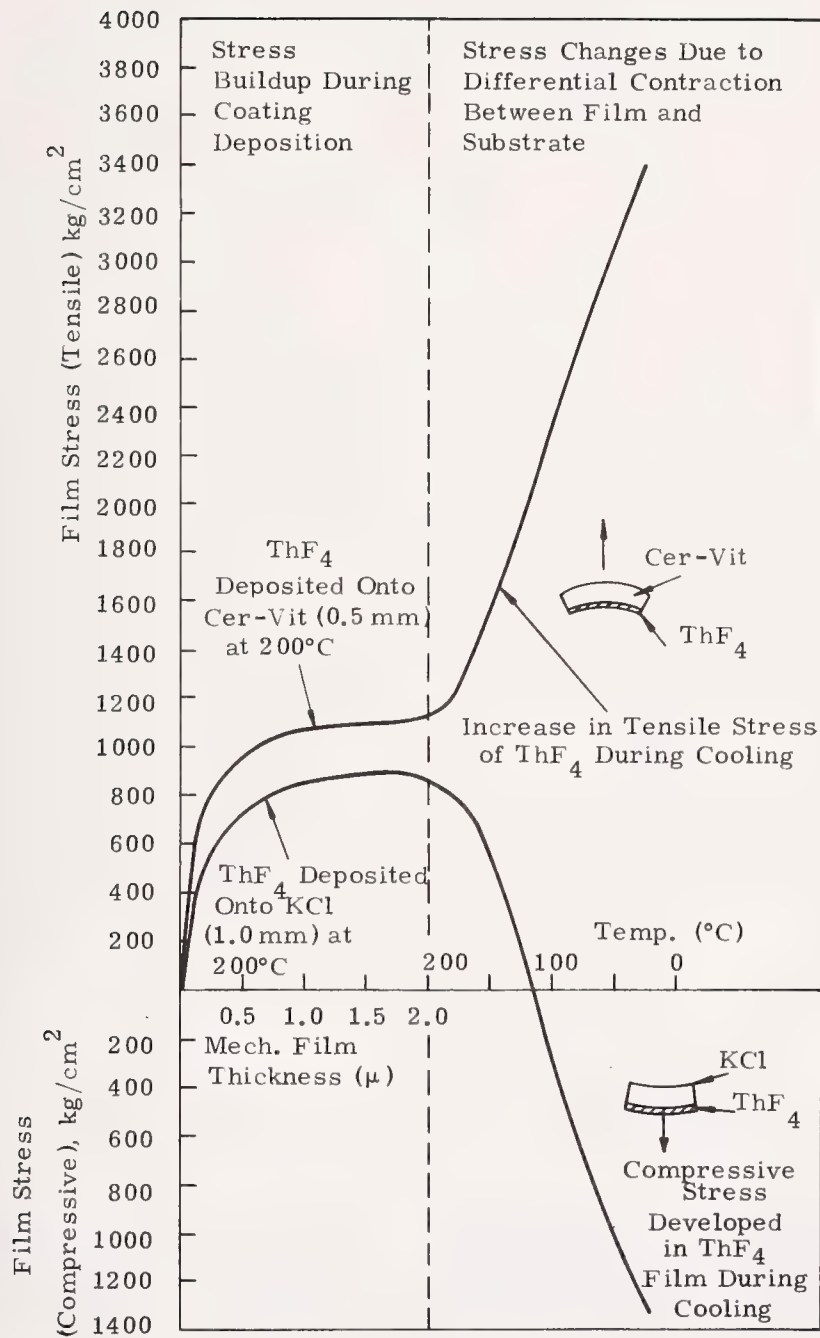


Figure 7. Intrinsic and Thermally Induced Stresses in ThF<sub>4</sub> films deposited onto Cervit and KCl substrates at 200°C followed by cooling to ambient temperature.

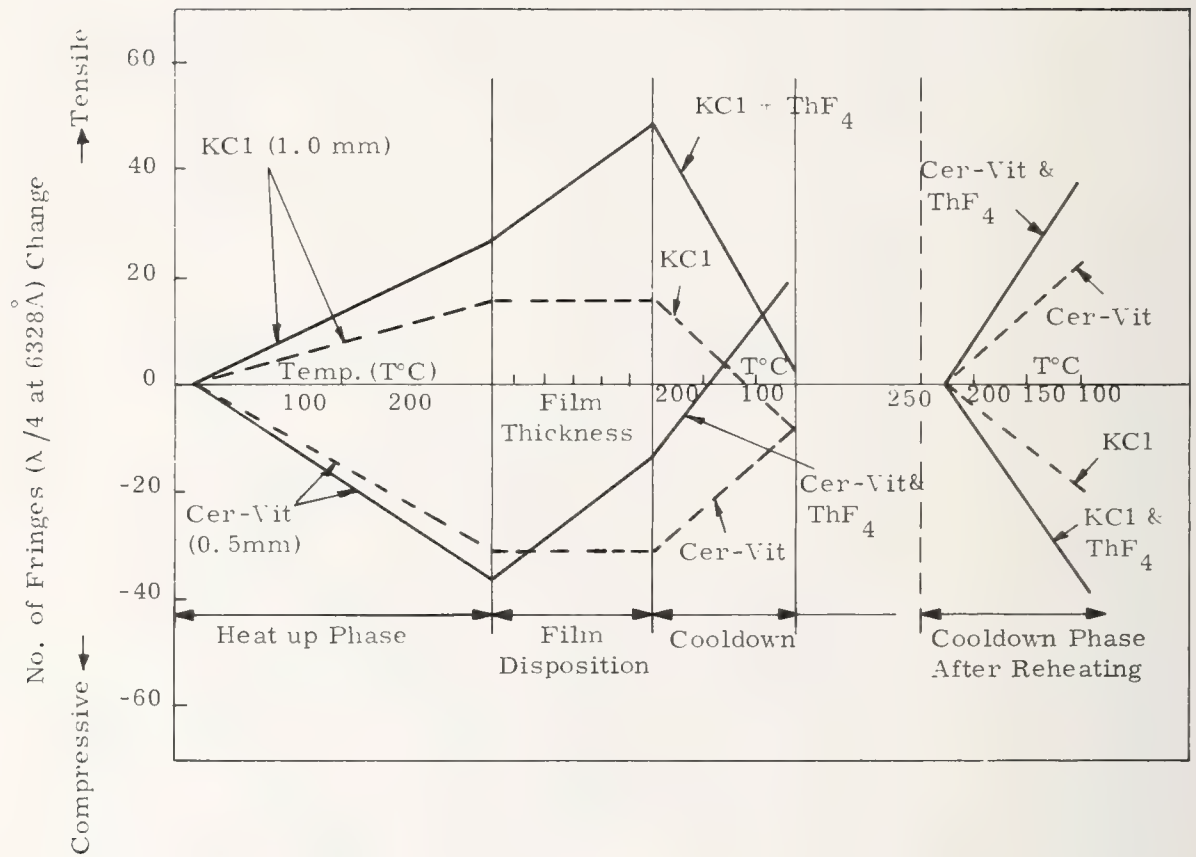


Figure 8. Fringe changes for  $\lambda/4$  film of  $\text{ThF}_4$  deposited onto  $\text{KCl}$  and Cervit during heating, deposition, and heat cycling. Full curves indicate the fringe changes for cocked discs of  $\text{KCl}$  and Cervit

Table I. Film Stress Data for ThF<sub>4</sub>, ZnSe and TlI Thin Films

Material	Rate Å/Sec	Temp °C	Stress Coefficients		
			A (kg/cm <sup>2</sup> )	B (microns) <sup>-1</sup>	C (microns) <sup>-1</sup>
ZnSe	2.6	100	-2900	2.0	25.0
ZnSe	18.0	100	-2100	0.95	56.0
ZnSe	4.4	150	-3300	0.2	80.0
ZnSe	9.0	150	-2610	0.4	75.0
ZnSe	20.0	150	-2200	0.9	68.2
ZnSe	24.4	150	-2384	0.9	74.3
ZnSe	3.0	200	-4640	~0.0	9.0
ZnSe	19.0	200	-3800	~0.0	21.5
ZnSe	24.0	200	-3020	0.4	82.5
ThF <sub>4</sub>	30A/Sec	150°C	+1057	~0.0	12.5
TlI	-	100°C	~150	-	-

Table II. Expansion Coefficient and Young's Modulus Values for ThF<sub>4</sub>, ZnSe, and Thallium Iodide Materials

Substrates Utilized	Film Material	Film Expansion Coefficient ( $\alpha_f$ )	Young's Modulus ( $E_f$ )
KCl, Cervit	ThF <sub>4</sub>	$13.3 \times 10^{-6}/^{\circ}\text{C}$	$4.3 \times 10^5 \text{ kg/cm}^2$
KCl, Cervit	ThF <sub>4</sub>	$11.1 \times 10^{-6}/^{\circ}\text{C}$	$3.9 \times 10^5 \text{ kg/cm}^2$
KCl, ZnSe	ThF <sub>4</sub>	$18.1 \times 10^{-6}/^{\circ}\text{C}$	$6.8 \times 10^5 \text{ kg/cm}^2$
KCl, ZnSe	ThF <sub>4</sub>	$15.1 \times 10^{-6}/^{\circ}\text{C}$	$4.3 \times 10^5 \text{ kg/cm}^2$
KCl, ZnSe	TlI	$36.0 \times 10^{-6}/^{\circ}\text{C}$	$2.3 \times 10^5 \text{ kg/cm}^2$
KCl, Cervit	ZnSe	$8.1 \times 10^{-6}/^{\circ}\text{C}$	$4.2 \times 10^5 \text{ kg/cm}^2$



#### COMMENTS ON PAPER BY LEDGER AND BASTIEN

The question was raised concerning the fact that thorium fluoride shows a negative expansion coefficient in the bulk, while the measured value in the thin film was positive. The speaker indicated first, that the accuracy of the expansion coefficient measurement was estimated to be approximately 30%, and that the difference in sign between the expansion coefficient in the thin film form and the bulk form was attributed to the fact that the film was not purely  $\text{ThF}_4$ . He indicated that it would be very interesting to perform the experiment using a film of thorium fluoride deposited on a substrate of  $\text{ThF}_4$ .

HYDROXYL INFLUENCE AND REFRACTIVE INDEX DEPENDENCE  
IN PICOSECOND THIN-FILM DAMAGE\*

W. Lee Smith, D. Milam, and M. J. Weber  
Lawrence Livermore Laboratory  
University of California  
Livermore, California 94550

and

A. H. Guenther, J. R. Bettis, and R. A. House  
Air Force Weapons Laboratory  
Kirtland Air Force Base  
New Mexico 87115

Results of a study of the influence of  $\text{OH}^-$  content of silica substrates on the damage resistance of thin films under  $1.06\text{-}\mu\text{m}$ ,  $150\text{-ps}$  pulse illumination are presented. The  $\text{OH}^-$  content variation was provided by the use of four types of commercial silica (Suprasil-W1, Optosil-2, Homosil, and Suprasil-1) as substrates. The  $\text{OH}^-$  concentrations, as indicated by IR absorption spectroscopy, are approximately 5, 130, 130, 1200 ppm, respectively. For each of the substrate materials, a set of four samples was made by depositing  $\lambda/2$  (at  $1.06\text{ }\mu\text{m}$ ) films of  $\text{ZrO}_2$ ,  $\text{SiO}_2$ ,  $\text{ThF}_4$ , and  $\text{MgF}_2$ . Furthermore, an uncoated but otherwise identical sample of four uncoated silica materials was tested to provide baseline surface damage data. The results of this study are discussed in regard to earlier work of House et al. concerning hydroxyl chemistry at film-substrate interfaces. A new interpretation of the role of  $\text{OH}^-$  in the breakdown process for nanosecond and picosecond pulses is introduced.

A second important aspect of this study is the correlation of thin-film damage threshold with film material refractive index. On each substrate type, films covered the index range of 1.37 to 2.0. The threshold range observed in this picosecond study is discussed with regard to possible improvements in coating damage thresholds by use of low-index materials.

Key words: Thin-films; damage thresholds; hydroxyl content; half-wave films;  $\text{SiO}_2$ ;  $\text{ZrO}_2$ ,  $\text{MgF}_2$ ;  $\text{ThF}_4$ ; refractive index.

#### Introduction

In this study two basic questions were addressed:

I. To what extent does hydroxyl chemistry at a film-substrate interface affect damage resistance? By using a commercially available family of silica materials as substrates for the coated test samples, one has the ability to alter the hydroxyl ( $\text{OH}^-$ ) concentration of the substrate by a factor  $\sim 250$  and, hence, to possibly alter the oxidation state of deposited thin-film materials at the interface. In a previous investigation, the possibility was entertained that the production of a different refractive-index component at the thin-film/substrate interface could significantly influence the damage threshold. For example, when  $\text{SiO}_2$  is deposited onto a substrate,  $\text{SiO}$  is formed to a small extent [1]. Because  $\text{SiO}$  has a higher refractive index than  $\text{SiO}_2$ , its damage threshold should be lower than  $\text{SiO}_2$  [2]. Increasing the oxygen availability (in the form of  $\text{OH}^-$ ) therefore allows the possibility of increasing the damage resistance of the thin-film system by more complete oxidation of the silicon. Another oxide depositant,  $\text{ZrO}_2$ , would be expected to behave in the same fashion. Conversely,  $\text{MgF}_2$  and perhaps  $\text{ThF}_4$  thin-film damage resistance could be expected to fall with increasing oxygen availability, due to production of  $\text{MgO}$  or  $\text{ThOF}_2$  due to the production of higher index, less damage resistant coating.

Later in this report data gained from a  $1064\text{-nm}$ ,  $150\text{-ps}$  pulse length damage study will be employed to advance a new interpretation of the role of substrate  $\text{OH}^-$  content in the damage process.

II. To what extent can the high damage thresholds of low-index materials, e.g., fluorides, in the bulk form be retained in thin-film systems? For several years data have been published which show that materials with low refractive index offer generally high damage resistance. The bulk damage thresholds of fluorides have been measured using both picosecond and nanosecond pulses, and fluoride thin film thresholds have been measured using nanosecond pulses. Much of this data is summarized in recent publications which document the dependence of damage threshold on refractive index [2].

\*The work at the Lawrence Livermore Laboratory was performed under the auspices of the Materials Sciences Programs of the U.S. Energy Research and Development Administration and Contract W-7405-eng-48.

Yet to what degree the relative strength of the fluoride materials would be retained, or diminished in thin-film form under picosecond pulse illumination was not yet investigated. Thus this picosecond investigation of  $\text{OH}^-$  influence is an extension of work with 40-ns, 1.06- $\mu\text{m}$  pulses by Bettis, House, and Guenther [4], and the results of the two studies will be compared later in this report. As recent progress in thin-film antireflection (AR) coating design [3] has provided new possibilities for use of lower index materials in practical AR coatings, the importance of the fluorides as coating constituents can be expected to increase. One area of obvious concern is the production of homogeneous fluoride coatings. In this sense homogeneous means uniform in refractive index throughout the film. The bigger question is the development of understanding and preparation techniques that will allow materials in thin film form to exhibit bulk-like behavior and characteristics.

## Sample Characteristics

### A. Substrate Materials

Five samples (3.8 cm diameter, 9 mm thick) of each of four types of fused silica (Suprasil-W1, Optosil-2, Homosil, Suprasil-1) were obtained from a commercial supplier [5]. The vendor's literature lists the  $\text{OH}^-$  content of these materials to be approximately 5, 130, 130, and 1200 ppm, respectively. Spectrophotometer investigation between 1 and 3  $\mu\text{m}$  verified that the relative concentrations of  $\text{OH}^-$  in our samples agreed approximately with the vendor's literature. Table 1 summarizes that data. The absorption coefficients listed pertain only to  $\text{OH}^-$  absorption [6] and are therefore proportional to the  $\text{OH}^-$  concentration in each sample. The ratios of coefficients of the various types agree with the relative concentrations indicated by the vendor.

Table 1. Hydroxyl absorption coefficient ( $\text{cm}^{-1}$ ) of silica substrates.

Silica Type	Absorption Peak Wavelength		
	1.38 $\mu\text{m}$	2.22 $\mu\text{m}$	2.72 $\mu\text{m}$
Suprasil-W1	--	--	0.11
Optosil-2	0.02	0.08	4.18
Homosil	0.02	0.08	3.94
Suprasil-1	0.16	0.58	--

The twenty substrates were polished by identical bowl-feed procedures with  $\text{ZrO}_2$  abrasives to specifications of  $\lambda/20$  smoothness in the visible and 0/0 scratch/dig. The possible implications of using  $\text{ZrO}_2$  abrasive in a test involving  $\text{ZrO}_2$  as one of four coating materials is discussed in a later section. Prior to coating, the substrates were rinsed with alcohol, washed in nitric acid and/or acetone. Immediately before insertion into the coating chamber, an alcohol-wetted tissue was pulled across each surface.

### B. Coating Procedure

The coatings prepared by CVI, Inc., Albuquerque, New Mexico, employed in this study were single layer films  $\lambda/2$  in optical thickness at 1.06  $\mu\text{m}$  of  $\text{ZrO}_2$ ,  $\text{SiO}_2$ ,  $\text{ThF}_4$ , and  $\text{MgF}_2$ . In all cases, high-purity starting materials were employed. Prior to coating, the chamber was pumped down to  $10^{-7}$  torr. During coating, a pressure of  $5 \times 10^{-5}$  torr of oxygen was maintained as is standard practice. The coating was electron-beam deposited at a rate of 16-20 minutes/half-wave. Substrate temperatures were 400°C; cooling to room temperature was slow (overnight). Just prior to damage testing, the samples were air-jet dusted and dragged with an alcohol laden tissue.

### C. Optical Characteristics of Coatings

Figure 1 exhibits the calculated optical standing electric fields for these  $\lambda/2$  coatings [7]. Along each vertical axis is plotted the time-averaged square of the electric field,  $\overline{E^2}$ , of a wave (incident from the air) as a function of distance into the film-substrate composite.  $\overline{E^2}$  is normalized to unity at the air-coating interface. The arrows point to the internal positions where various extrema of  $\overline{E^2}$  are reached. Note that  $\overline{E^2} = 0.666$  occurs at each air/coating and coating/substrate interface. Thus, all four of the coatings experience identical  $\overline{E^2}$  values at the coating/substrate interface--the location of primary interest in this experiment. Furthermore, to within 11%, the maximum values of  $\overline{E^2}$  are the same in all the specimens. The  $\overline{E^2}$  values in the middle of the  $\text{ZrO}_2$  and  $\text{ThF}_4$  layers are reduced because their refractive index exceeds that of the  $\text{SiO}_2$  substrate.  $\overline{E^2}$  in  $\text{MgF}_2$  is conversely enhanced by 11% over its interface value. This series of  $\lambda/2$  coatings is ideal for providing uniform irradiation of the different samples at the interface of interest and minimizing variations in the maximum of  $\overline{E^2}$  reached throughout the thin films.



## Experimental Apparatus and Procedures

Linearly polarized, 1.06- $\mu\text{m}$ , 150-ps damage tests were performed with a laser system and techniques described in detail elsewhere [8]. The beam was gently focused to a spot size of 2-3 mm diameter at the  $e^{-1}$  intensity level. A photographic recording of the sample-plane flux distribution is made for each shot. Microdensitometric and computer analyses then yield the flux value at the spatial maximum of each pulse. The single-shot flux uncertainty is  $\pm 7\%$ . Streak camera data of the temporal profile of each shot were not available for this experiment. An average pulse duration (intensity FWHM) of 150 ps should be used to convert flux to intensity [9]. However, for the laser used in the present experiment, as is true of generally all lasers that are mode-locked by a saturable absorber, a distribution of durations (with width  $\sim \pm 30\%$  of the average) is actually produced [10].

Typically 30 sites were irradiated per sample. Identification of damage was made by breath fogging the surface while illuminating it with a high-intensity microscope light. This method was more reliable than observing a breakdown plasma, as some samples never yielded visible sparks unless irradiated appreciably above the threshold indicated by fogging light-scattering. Nomarski microscopy was employed occasionally on borderline sites, but consistent indications were always obtained with the fogging/light scattering method.

The damage threshold for each sample was defined to be the flux value midway between the highest flux which did not damage the sample and the lowest flux which damaged the sample. The uncertainty in the threshold position (due to insufficient resolution from a limited number of shots) was summed with the uncertainty for the individual shot flux to yield the final threshold uncertainty. For the occasional situation in which overlap occurred between the damaging and non-damaging ranges of flux, the midpoint of the overlap region was defined as the threshold position. The largest overlap width encountered was  $\pm 5\%$  of the assigned threshold position, an amount less than our single-shot flux uncertainty.

The complete experiment was performed twice in two consecutive weeks. Thresholds agreed for the two separate runs for every material, thus indicating that potential changes in damage threshold due to  $\text{OH}^-$  content alteration by exposure to air or breath-fogging were negligible.

## Damage Results

Results for the 150-ps, 1064-nm damage thresholds are tabulated in Table 2 and displayed in Figure 2. All flux values discussed herein are values achieved in air at the sample surface; no refractive index corrections have been applied. The notation for the coatings and substrate materials is as follows: Z, S, T, M, SW, O, H, and S1 denote  $\text{ZrO}_2$ ,  $\text{SiO}_2$ ,  $\text{ThF}_4$ ,  $\text{MgF}_2$ , Suprasil-W1, Optosil-2, Homosil, and Suprasil-1, respectively. Note that the common logarithm of the substrate  $\text{OH}^-$  concentration is plotted along the segmented horizontal axis in Fig. 2. The Optosil-2 and Homosil data are displaced from each other for the sake of presentation only, as they have nominally the same  $\text{OH}^-$  concentration. The large uncertainty bars on the SO and SSI data in Fig. 2 are due to unfortunate coarse bracketing of the threshold resulting from less than optimum beam splitting ratios.

Table 2. Damage threshold flux data.

Coating-Substrate	Flux ( $\text{J}/\text{cm}^2$ )	Coating-Substrate	Flux ( $\text{J}/\text{cm}^2$ )
ZSW	$2.9 \pm 0.3$	TSW	$6.4 \pm 0.7$
ZO	$3.6 \pm 0.3$	TO	$5.6 \pm 0.4$
ZH	$2.8 \pm 0.4$	TH	$6.1 \pm 0.7$
ZS1	$2.9 \pm 0.3$	TS1	$5.9 \pm 0.5$
SSW	$4.6 \pm 0.5$	MSW	$6.0 \pm 0.6$
SO	$5.6 \pm 1.3$	MO	$5.3 \pm 0.5$
SH	$5.4 \pm 0.5$	MH	$5.8 \pm 0.7$
SSI	$3.8 \pm 0.9$	MS1	$6.0 \pm 0.7$

Bare Substrate	Flux ( $\text{J}/\text{cm}^2$ )
SW	$12.7 \pm 2.7$
O	$8.7 \pm 0.6$
H	$8.2 \pm 1.5$
S1	$9.8 \pm 1.4$

It was discovered after the completion of the experiment that the coating vendor used  $\text{ZrO}_2$  as the polishing compound on all the substrates. Concern was expressed initially by us that the  $\text{ZrO}_2$  usage might conceivably have affected the damage behavior of the samples in a significant way. However, the different patterns of the data shown in Fig. 2 for the two oxide films (including  $\text{ZrO}_2$ ), the two fluoride films, and the bare substrates, probably rule out any major compromise in the behavior of the various samples resulting from the use of  $\text{ZrO}_2$  polishing abrasive.

In answer to our initial questions, specifically the first query, the data in Fig. 2 illustrates that no obvious correlation is evident between the thin-film damage thresholds and substrate  $\text{OH}^-$  concentration for 150-ps, 1064-nm pulses. This result is to be contrasted with the 40-ns, 1064-nm work of Bettis, House, and Guenther [4]. In that earlier work the breakdown flux changed monotonically in the  $\text{SiO}_2$ -coated samples by a factor of 4.8 as the substrate  $\text{OH}^-$  concentration was varied through approximately the same range as in this study. In their  $\text{MgF}_2$ -coated samples, a flux change of 40% was observed. The apparent independence of the breakdown threshold on  $\text{OH}^-$  concentration in this subnanosecond experiment is consistent with results in a different 150-ps experiment reported in these proceedings [11]. There, a diminution in the dependence of the damage threshold on surface roughness was found for 150-ps pulses vis-a-vis that found for 40-ns pulses.

The results from these two 150-ps studies lead us to a new interpretation of the probable role of the  $\text{OH}^-$  species at the coating-substrate interface. It is no longer clear that the manner in which the  $\text{OH}^-$  affects damage resistance is via chemical production of a species with a different refractive index (e.g.,  $\text{SiO}$  in an  $\text{SiO}_2$  film). In fact, from avalanche ionization considerations, it is difficult to argue that a part per million  $\text{SiO}$  in a  $\text{SiO}_2$  medium would affect the overall lattice impact ionization development. Only once in every  $10^6$  collisions would an  $\text{SiO}$  molecule be involved in the breakdown process. That is true, unless the breakdown initiation is facilitated by  $\text{OH}^-$  presence as could be affected through a modification of the  $\text{SiO}_2$  structure, i.e., a weakening. Consistent interpretation of the damage dependence on  $\text{OH}^-$  concentration in the 40-ns and 150-ps experiments is obtained only if one assigns the  $\text{OH}^-$  role to be assistance in the liberation of charge carriers in the earliest stage of the breakdown process. The results of the 40-ns and 150-ps experiments indicate strongly that at 40 ns the bottleneck to the breakdown process is its initial phase--the plasma inception which depends on the promptness and difficulty with which initiating electrons are liberated [12]. Hence, phenomena such as (1)  $\text{OH}^-$  concentration--which may function primarily in few ppm concentration to influence the number of unsaturated bonds (states within the band "gap")--or (2) surface roughness--which concentrates field distributions at all times during the pulse and thus enhances initial carrier production--are probably of greater importance for nanosecond pulse durations than for picosecond durations, if the proposed hypothesis is correct.

For the picosecond regime, the higher field strengths required to provide fast ionization and sufficient incident flux for the heating stage (melting the lattice via the plasma) more effectively drive initial nonlinearities [12] to provide numerous initiating carriers early in the pulse [13]. Hence, the importance of  $\text{OH}^-$  presence or surface roughness would be expected to decrease for subnanosecond pulses.

As regards our second question, the data displayed in Fig. 2 show a general correlation with refractive index. One should remember the  $\overline{E}^2$  graphs of Fig. 1 when comparing the  $\text{MgF}_2$  thresholds with those of the other materials. According to the standing-wave analysis, the  $\text{MgF}_2$  films experienced 11% greater electric fields than the other materials, per unit flux. Thus an  $\overline{E}^2$  correction would raise the  $\text{MgF}_2$  thresholds by 11% to positions exceeding the  $\text{ThF}_4$  values, as one would expect from previously reported refractive-index dependences of the damage threshold [2]. However, the thresholds of the  $\text{SiO}_2$  and  $\text{ThF}_4$  groups do not lie in the relative positions predicted by the refractive-index dependence. The  $\text{SiO}_2$  and  $\text{ThF}_4$  indices differ only by 0.04, however, apparently allowing other effects (e.g., porosity, surface chemistry, inhomogeneity) to assume comparable importance.

The data displayed in Fig. 2 are encouraging for operational prospects of improved thin-film damage resistance. In many current high-power laser systems,  $\text{TiO}_2/\text{SiO}_2$  are the coating materials used for thin-film applications. It is generally observed that  $\text{TiO}_2$  and  $\text{ZrO}_2$  have roughly the same damage resistance, so we may view  $\text{ZrO}_2$  and  $\text{SiO}_2$  in Fig. 2 as representing the present wide-usage high-index and low-index coating materials. The  $\text{ZrO}_2$  and  $\text{SiO}_2$  films damaged at average levels of about 3.0 and 5.0  $\text{J}/\text{cm}^2$ , respectively. As damage often occurs at the threshold of the high-index material, roughly 3.0  $\text{J}/\text{cm}^2$  characterizes the damage resistance of such films. Hence AR film designs which could employ exclusively the low-index ( $n < 1.5$ ) materials such as the fluorides present a distinct opportunity for improved 1.06- $\mu\text{m}$  damage resistance. For example, a three-layer [3] or alternate AR design employing  $\text{ThF}_4$  and  $\text{MgF}_2$



layers on a silica substrate may raise the 1.06- $\mu\text{m}$ , AR damage resistance to the level of about 6 J/cm<sup>2</sup>. In a field where even 30% improvements come only with struggle, such a 100% advancement would be significant for many applications. Hence, the data shown in Fig. 2 are valuable in pointing out potential routes for improvement.

On the other hand, a look at the absolute damage thresholds in Fig. 2 relative to perhaps the ultimate achievable thresholds--those of the bulk materials--reminds us of our primitive state of understanding of (particularly) the thin-film damage mechanism details. Consider the SiO<sub>2</sub>-on-silica series. The 30-ps bulk damage threshold inside silica (Suprasil-1) [14] is 13 J/cm<sup>2</sup> which converts to 35 J/cm<sup>2</sup> in air for 150 ps by the square-root of the pulse duration [15]. Therefore, the bare surface threshold average of our silica series from Table 2 is a factor of 3 to 4 lower than bulk, but the thin-film average of about 5 J/cm<sup>2</sup> is a factor seven lower than bulk. Much work remains to delineate convincingly the origins of these large differences between bulk and film behavior.

#### Conclusions

1. Within experimental uncertainty, no evident correlation of damage threshold with OH<sup>-</sup> concentration in silica substrates was observed for ZrO<sub>2</sub>, SiO<sub>2</sub>, MgF<sub>2</sub> and ThF<sub>4</sub> films in 150-ps, 1064-nm experiments.
2. Two fluoride materials, ThF<sub>4</sub> and MgF<sub>2</sub>, in thin-film form were found to be roughly twice as damage-resistant as ZrO<sub>2</sub>. SiO<sub>2</sub> was found to be ~ 70% more damage-resistant than ZrO<sub>2</sub>, in general agreement with an earlier oxide-film, picosecond study [16].
3. The absence of a strong correlation of damage thresholds with OH<sup>-</sup> concentration at 150 ps and the presence of correlation at 40 ns is a further indication that the initial stage of charge-carrier buildup is the breakdown process bottleneck at 40 ns but not at 150 ps. This observation implies that efforts to increase damage resistance by eliminating sources of initial electrons (by annealing to reduce color center populations, ultrapurification, etc.) would be more effective for supernanosecond pulses than for subnanosecond pulses.

#### Acknowledgments

We thank G. E. Murphy of LLL for his able technical assistance during the several hundred laser firings for this experiment. Dr. J. H. Apfel of OCLI is acknowledged appreciatively for providing our Fig. 1. For the manuscript preparation, we thank Ms. K. Wenzinger.

#### References

- |  |  |
|--|--|
| <p>[1] Ritter, E., in Physics of Thin Films, (Hass, Froncombe, and Hoffman, Eds., Academic Press, New York, 8) p. 6 (1975).</p> <p>[2] Bettis, J. R., Guenther, A. H., and Glass, A. J., Nat. Bur. Stand. Spec. Publ. (U.S.) 414, p. 214; also Bettis, J. R., House, R. A., Guenther, A. H., and Austin, R., NBS Spec. Publ. 435, p. 289; also Bettis, J. R., Laser Induced Damage as a Function of Dielectric Properties at 1.06 <math>\mu\text{m}</math>, Ph.D. dissertation Air Force Institute of Technology, Wright Patterson AFB, OH (1975).</p> <p>[3] Baer, A. D., NBS Spec. Publ. 462 (1976) p. 221.</p> <p>[4] House, R. A., Bettis, J. R., and Guenther, A. H., NBS Spec. Publ. 462 (1976) p. 310; Bettis, J. R., Final Report AFWL-TR-76-61, NTIS, Washington, D.C. (1976).</p> <p>[5] Amersil, Inc., 685 Ramsey Ave., Hillside, N.J. 07205, product literature.</p> | <p>[6] The absorption coefficients (<math>\alpha</math>) listed in Table 1 were obtained by inverting a Beer's law relation, <math>T_1/T_2 = e^{-\alpha x}</math>, where <math>T_1</math> is the transmission (%) at the wavelength of a given absorption peak. <math>T_2</math> is a transmission (%) obtained by constructing on the transmission graph a straight line tangent to the flat base at the sides of the absorption peak. The transmission denoted by the straight line, at the wavelength of the absorption peak, is <math>T_2</math>. <math>T_1/T_2</math> is independent of Fresnel losses or intrinsic (non-OH<sup>-</sup>) silica absorption.</p> <p>[7] Apfel, J., OCLI, Inc., Santa Rosa, CA, private communication.</p> <p>[8] Milam, D., Appl. Opt. 16, 1204 (1977).</p> <p>[9] Apfel, J. H., Enemark, E. A., and Milam, D., Smith, W. Lee, and Weber, M. J., this proceedings.</p> |
|--|--|



- [10] Smith, W. Lee, and Bechtel, J. H., Phys. Lett. 55A, 203 (1975).
- [11] Milam, D., Smith, W. Lee, Weber, M. J., Guenther, A. H., Bettis, J. R., and House, R. A.
- [12] Milam, D., NBS Spec. Publ. 462, p. 350 (1976).
- [13] Smith, W. Lee, Bechtel, J. H., and Bloembergen, N., Opt. Comm. 18, 592 (1976).
- [14] Smith, W. Lee, Bechtel, J. H., and Bloembergen, N., Phys. Rev. B15, 706 (1975).
- [15] Expressions of  $\sqrt{\tau}$  dependence of breakdown threshold are found in a) Bettis, J. R., House, R. A., and Guenther, A. H., NBS Spec. Publ. 462, p. 338 (1976), b) Laser Program Annual Report, Lawrence Livermore Laboratory Report UCRL-50021-76 (1977), c) reference 13 above.
- [16] Newnam, B. E., and Gill, D. H., NBS Spec. Publ. 462, p. 292 (1976).

Figures

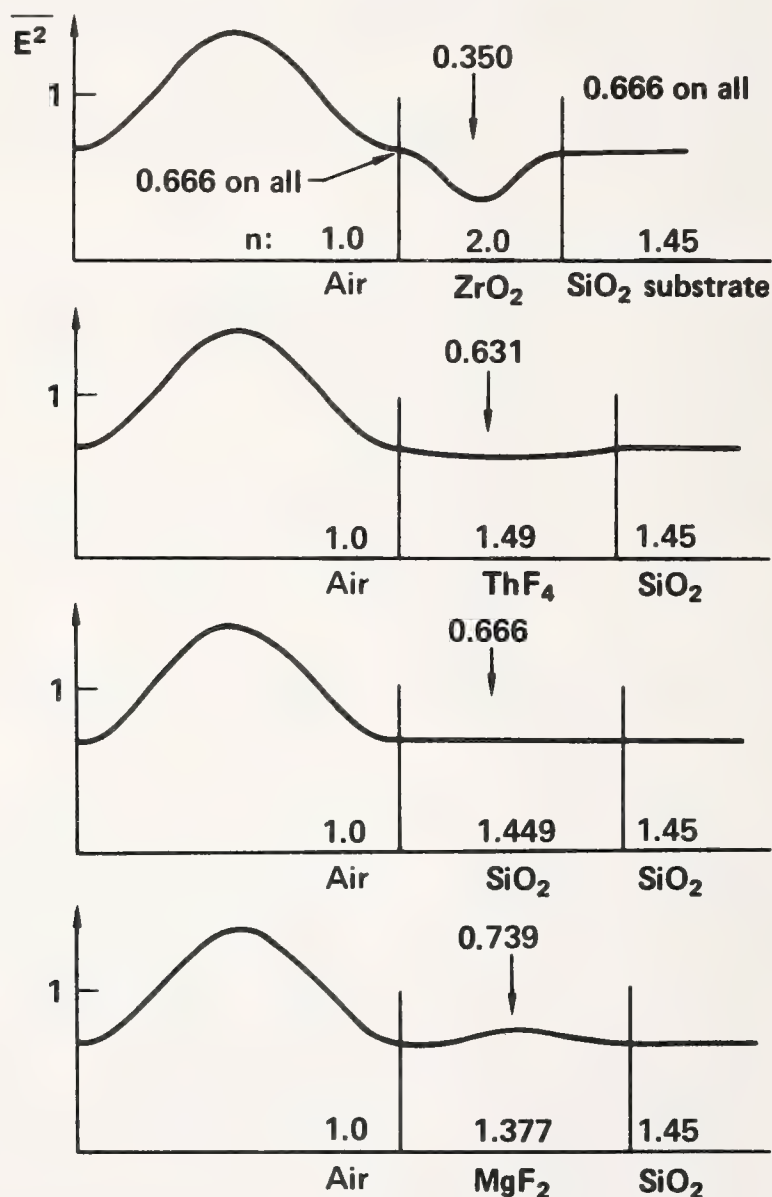


Fig. 1. Illustrations of the time-averaged electric field squared as a function of distance into  $\lambda/2$  coated samples [7].  $\overline{E^2}$  is normalized to unity at the air-coating interface. The arrows indicate positions where various values of  $\overline{E^2}$  are obtained. The refractive indices of each material are included in each illustration.

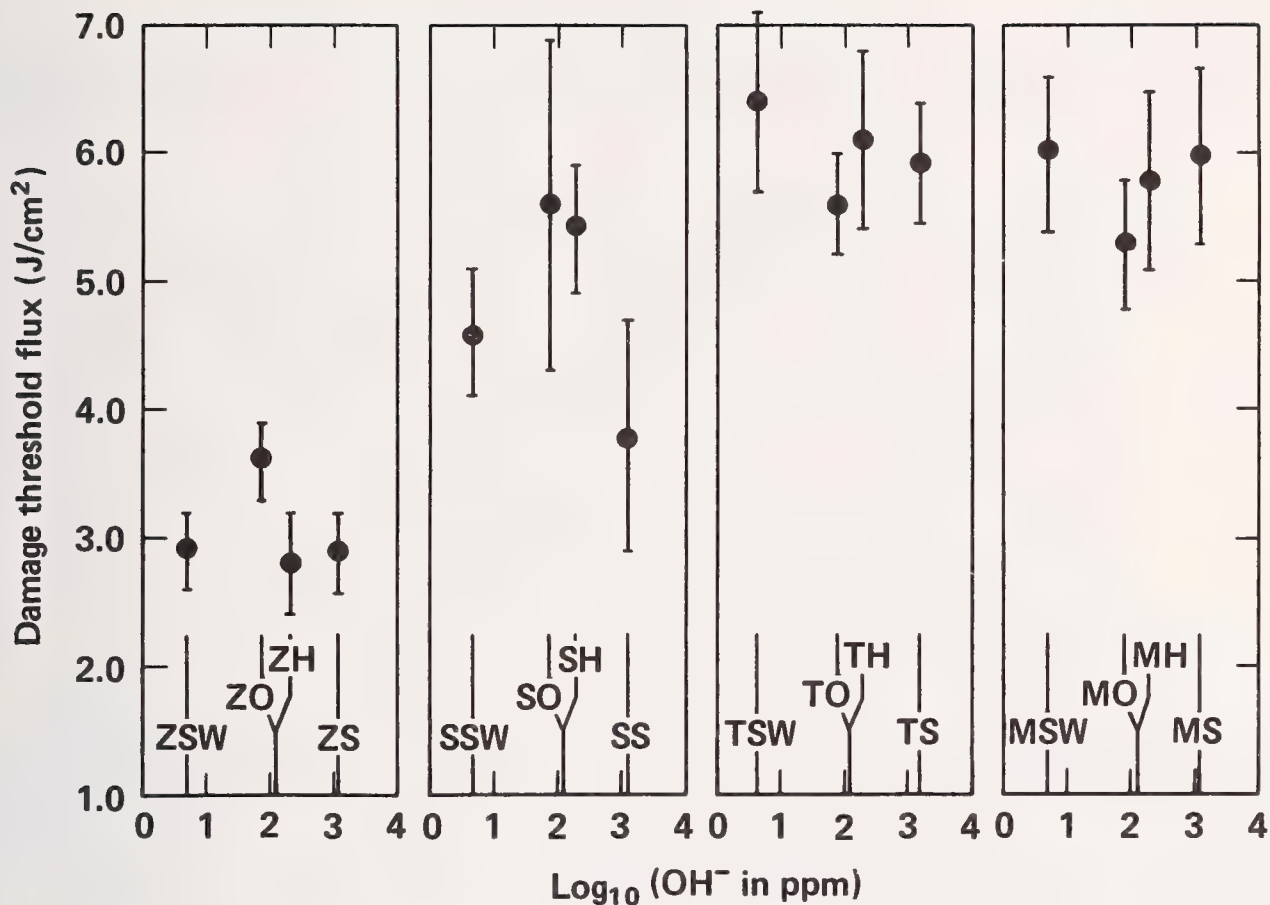


Fig. 2. Damage threshold flux results for the  $\lambda/2$ -coated samples. Note that the common logarithm of  $\text{OH}^-$  concentration is plotted along the segmented horizontal axis. The Optosil and Homosil samples are displaced horizontally from each other only for clarity. Their  $\text{OH}^-$  contents are essentially equal  $\text{Z} = \text{ZrO}_2$ ;  $\text{S} = \text{SiO}_2$ ;  $\text{T} = \text{ThF}_4$ , and  $\text{M} = \text{MgF}_2$  for the films. SW = Suprasil-W1; 0 = Optosil-2; H = Homosil, and S1 = Suprasil-1 for the fused silica substrates.

#### COMMENTS ON PAPER BY SMITH, MILAM, WEBER, GUENTHER, BETTIS, AND HOUSE

There was extensive discussion concerning the question as to whether the damage threshold was clearly defined in the short pulse measurements, or whether the damage measurements exhibited cross-over. Cross-over is the term describing the situation in which some pulses at a higher energy do not produce damage, while others at a lower energy do. It was reported that at 40 nanoseconds the cross-over was always observed in damage testing. The speaker indicated that in tests at 30 and 150 picoseconds, cross-over was never observed. Brian Newnam, from LASL, indicated that in his measurements carried out in the picosecond regime, cross-over was always observed. Therefore the point remains unresolved. The question of short pulse damage versus long pulse damage was reviewed, and the speaker once again indicated that sub-nanosecond damage measurements seemed far less sensitive to extraneous sources of electrons than long pulse damage measurements, and also that at short pulses, damage thresholds seemed to be totally insensitive to the linear absorption of the medium. However, he did acknowledge that it is very difficult to measure the linear absorption of materials in thin film form.

FURTHER STUDIES OF THE ROLE OF  
ELECTRIC FIELD STRENGTH IN LASER DAMAGE  
OF DIELECTRIC LAYERS

JOSEPH H. APFEL  
Optical Coating Laboratory, Inc.  
Santa Rosa, California 95402

In this study a silica/titania quarterwave stack reflector, a four-layer antireflection coating, and a combination of the two were prepared in a single evaporation coating run and damaged with 180-ps, 1.064 $\mu$ m laser pulses. The peak pulse intensity at the threshold of damage was highest for the reflector stack and lowest for the AR coating. Although relative thresholds of the reflector stack and the combination are in the order predicted by the model of damage occurring at the location of peak field intensity in the titania layers, the AR coating damaged at an anomalously low value.

The results indicate that the substrate/coating interface is vulnerable when illuminated by the laser pulse as in the case of the AR coating.

Key words: Antireflection coatings; dielectric films; electric fields; laser damage; nonlinear absorption; optical coatings.

## 1. Introduction

In studies of damage to optical coatings by 125-ps 1.064 $\mu$ m laser pulses, Milam [1], found that antireflection (AR) coatings generally fail at lower pulse intensities than dielectric reflectors. This is contrary to expectations based upon an analysis of the internal electric fields [2]. In this study we evaluated the damage threshold of these two types of coatings and a combination of them which were composed of silica and titania films prepared under controlled circumstances. These results provide for a quantitative comparison of the threshold versus the computed electric field intensity in each of the coatings.

To explain the discrepancy between these results and the previously reported correlation between peak field intensity and damage [2], we consider two models; nonlinear absorption in the high index titania layers and substrate/coating interface vulnerability. The nonlinear absorption model is shown to be incompatible with experimental results.

Another study reported at this conference [3], which describes the effect of barrier layers at the substrate/coating interface, supports our conclusion that the interface is especially vulnerable to damage.

## 2. Experimental

Using equipment and procedures described previously [2], we prepared three different multilayer coatings in a single evaporation run on super polished substrates of BK-7 glass.

The three coatings were an eleven layer quarterwave stack high reflector (AR), and a combination of the two in which the AR coating was deposited on top of the HR coatings (see figure 1).

By means of externally actuated masks, the vapor from the electron beam heated silica and titania sources was allowed to deposit onto substrates A and B for the eleven layer HR coating and then onto A and C for the AR coating. Although, the combination AR+HR coating has no practical application it was included to demonstrate that the low threshold of the AR is not inherent in its design.

After coating, the three samples were delivered to the Lawrence Livermore Laboratory where they were tested for damage threshold by the techniques described pre-



viously [1,3]. For these samples only one laser beam was incident during each shot and every shot was subjected to streak camera recording.

### 3. Experimental Results

Table 1 contains the results of damage testing. Thresholds are quoted as laser pulse energy density (Joules/cm<sup>2</sup>) and laser pulse peak power density (GW/cm<sup>2</sup>). From the streak camera recordings which were used to convert the energy density data to power density data, the average pulse width (FWHM) was found to be 180 picoseconds.

Table 1. Measured Damage Threshold  
for 180-ps, 1.064 $\mu$ m

<u>Sample</u>	<u>Description</u>	<u>Energy Density (J/cm<sup>2</sup>)</u>	<u>Peak Intensity (GW/cm<sup>2</sup>)</u>
B	11 Layer Quarterwave Stack Reflector (HR)	7.0 $\pm$ 0.5	45 $\pm$ 5
C	4 Layer Antireflection Coating (AR)	3.2 $\pm$ 0.3	17 $\pm$ 3
A	Combination AR+HR	5.1 $\pm$ 0.5	28 $\pm$ 4

### 4. Discussion

Figures 2,3, and 4 are the electric field profiles of the three coatings at threshold. The incident intensities for these three profiles are proportional to the pulse energy densities at threshold. Due to variations in the pulse length and shape, the peak intensities are not exactly proportional to the pulse energies; if the profiles were plotted using peak intensities the combination coating (Sample A) would have slightly greater amplitude than shown.

Clearly, the three samples do not have the same peak electric field intensity in the high index titania layers as observed by Apfel, et. al. [2]. In that study, four assemblies of quarter and half-wavelength thick layers were prepared simultaneously and found to have approximately equal peak electric field intensities at threshold.

Since the AR design contains non-quarterwave layers we sought an interference compatible mechanism that would somehow make the three coatings similar under intense radiation. It was hypothesized that nonlinear absorption in the high index titania layers might cause sufficient absorption to modify the electric field profiles, and thus the absorption, to a greater extent in the reflector (B) and the combination coating (A) than in the AR coating (C).

Figures 5 and 6 show the results of the analysis. The high index layers of all designs were subdivided and given absorption values proportional to the local field intensity and the internal field was recomputed and then the process was repeated until no significant change in field occurred. Figures 5 and 6 resulted after five cycles. The proportionality constant was chosen to just cause melting of titania(1830 $^{\circ}$ C) in the sample with the highest peak field. The computed peak temperatures are shown in the figures. Even with these rather high absorption coefficients the interference generated electric field profiles for the three coatings are not significantly changed from the original curves which assume essentially zero absorption.

The AR coating, which failed at the lowest pulse energy density, is different from the other two coatings in that there is intense radiation at the substrate surface. We postulate that the substrate/coating interface is vulnerable to damage because of contamination from the substrate polishing process or from an undefined chemical reaction between the substrate and the adjacent titania layer. Our experiments with barrier layers of silica and alumina are reported at this symposium [3].

## 5. Conclusions

An antireflection coating for  $1.064\mu\text{m}$  composed of evaporated silica and titania has anomalously low damage threshold relative to a quarterwave stack reflector and a combination coating consisting of the AR on top of the HR coating. It is proposed that the low threshold is due to an unexplained vulnerability of the substrate/coating interface.

## 6. Acknowledgments

The damage threshold measurements were made by D. Milam and W.L. Smith of the Lawrence Livermore Laboratories.

## 7. References

- [1] Milam, D. Appl. Opt. 16, 1204 (1977)
- [2] Apfel, J.H., Matteucci, J.S., Newnam, B., and Gill, D., NBS Special Pub. No. 462, 301 (1976)
- [3] Apfel, J.H., Enemark, E.A., Milam, D., Smith, W.L., and Weber, M.J., "The Effects of Barrier Layers and Surface Smoothness on 150-ps,  $1.064\mu\text{m}$  Laser Damage of AR Coatings on Glass." Presented to 1977 Boulder Damage Symposium.

## 8. Figures

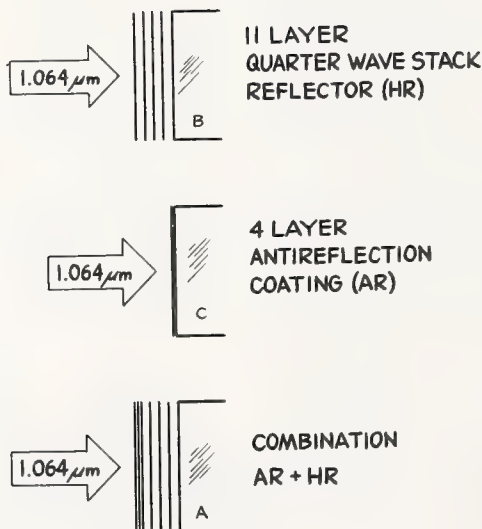


Fig. 1. Schematic representation of the three coatings.

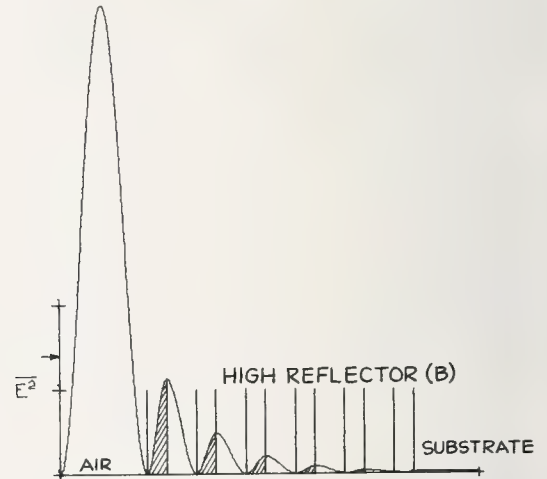


Fig. 2. The time averaged square of the electric field in an eleven layer quarterwave stack high reflector (HR) coating at the threshold of damage as a function of distance measured normal to the surface of the layers for radiation incident from the left. The high index titania layers are indicated by shading and the incident laser beam intensity is indicated by the arrow.

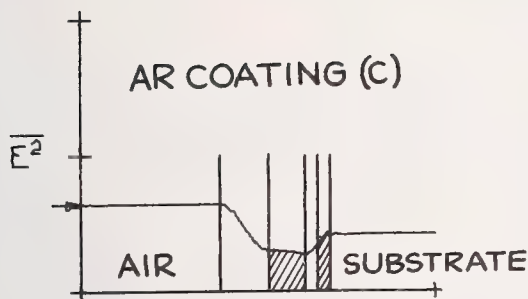


Fig. 3. The time averaged square of the electric field in a four layer antireflection (AR) coating at the threshold of damage as a function of distance measured normal to the surface of the layers for radiation incident from the left. The high index titania layers are indicated by shading and the incident laser beam intensity is indicated by the arrow.

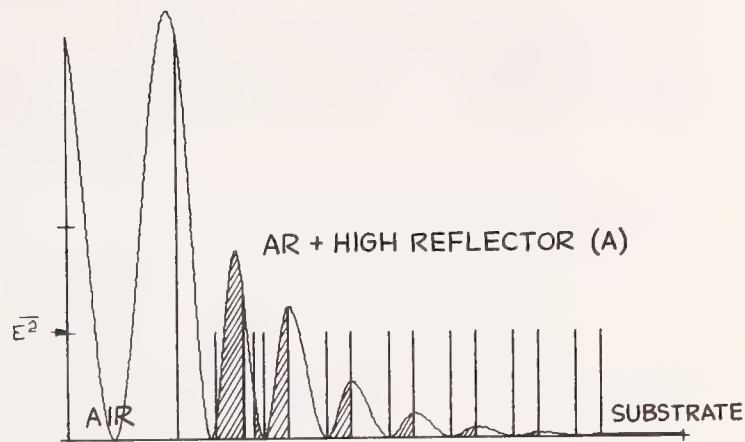


Fig. 4. The time averaged square of the electric field in a combination (AR+HR) coating as a function of distance measured normal to the surface layers for radiation incident from the left. The high index titania layers are indicated by shading and the incident laser beam intensity is indicated by the arrow.

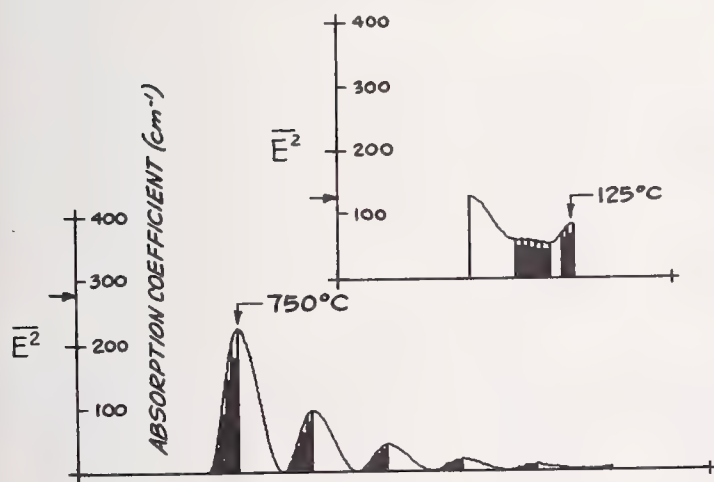


Fig. 5. The electric field intensity profile for radiation incident on a high reflector (HR) and an antireflection (AR) coating with nonlinear absorption in the high index layers as a bar graph overlay. The incident laser beam intensity is indicated by the arrow at the left and the peak temperature is shown for a nonlinear absorption coefficient adjusted to cause melting of  $\text{TiO}_2$  on the combination (AR+HR) coating.

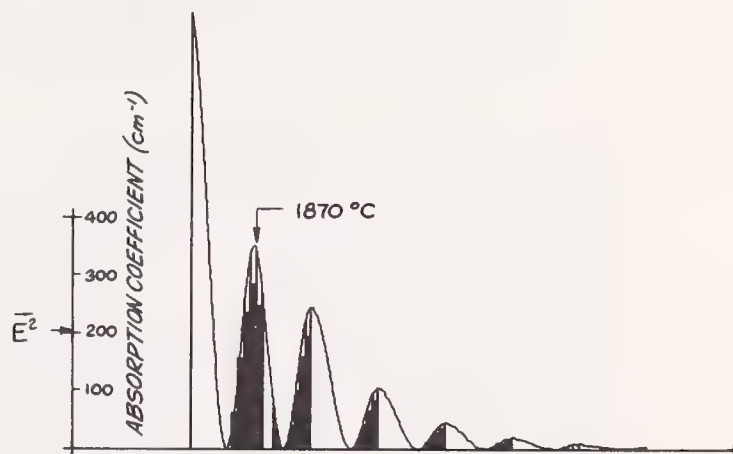


Fig. 6. The electric field intensity profile for radiation incident on a combination (AR+HR) coating with nonlinear absorption in the high index layers as a bar graph overlay. The incident laser beam intensity is indicated by the arrow at the left and the peak temperature is shown for a nonlinear absorption coefficient adjusted to slightly exceed the melting point of  $\text{TiO}_2$ .



THE EFFECTS OF BARRIER LAYERS AND SURFACE SMOOTHNESS  
ON 150-ps, 1.064- $\mu$ m LASER DAMAGE OF AR COATINGS ON GLASS\*

J. H. Apfel and E. A. Enemark  
Optical Coating Laboratory, Inc.  
Santa Rosa, California 95402

and

D. Milam, W. L. Smith, and M. J. Weber  
Lawrence Livermore Laboratory  
University of California  
Livermore, California 94550

We observed that the maximum internal electric field at the threshold of damage in antireflection (AR) coatings, as calculated from our measured threshold flux, is lower than for high reflector (HR) coatings. The difference in damage vulnerability is attributed to the coating-substrate interface which is illuminated when AR coated but is protected by interference reflection when HR coated. To test this postulate, experiments were designed using evaporated interference coatings of silicon oxide (silica) and titanium oxide (titania) of different compositions on glass substrates of different surface smoothnesses. These were damage-tested with 150-ps, 1.064- $\mu$ m laser pulses. We find that for silica/titania AR coatings on BK-7 glass, a barrier or protecting layer of silica adjacent to the substrate improves the damage threshold whereas the substrate surface smoothness is not critical for short pulses. In one experiment, aluminum oxide (alumina) was used for the barrier layer between the AR coating and the substrate.

Key words: Antireflection coatings; barrier layer; damage thresholds; glass substrate; optical coating design; optical coating materials; substrate smoothness.

## INTRODUCTION

In studies of damage to optical coatings by 125-ps, 1.064- $\mu$ m laser pulses, Milam [1] found that antireflection (AR) coatings generally fail at lower pulse intensities than dielectric reflectors. This is contrary to expectations based upon an analysis of the internal electric fields. Previous work [2] with several silica/titania multilayers demonstrated a correlation between 1.064- $\mu$ m pulsed laser damage threshold and the maximum electric field strength produced in the titania layers. Because the maximum internal electric field for AR coatings is a lower multiple of the incident electric field than for quarter-wave-stack reflectors (HR), the damage threshold should be higher.

We suspected that the above differences are due to the damage vulnerability at the interface between the substrate and the coating. This interface is subject to full pulse intensity for an AR coating but is protected by interference for a dielectric reflector. Coleman [3] found that the slight optical absorption of sputtered titania films on soft glass microscope slides was reduced when a silica layer was deposited prior to the titania. Although glass substrates, such as BK-7, are compositionally different from the soft alkali-bearing glass used by Coleman, the presence of a titania first layer prompted our investigation of the effect of introducing silica and alumina barrier layers on the substrate prior to depositing AR coatings. A series of coatings was designed in which the barrier layer thickness, barrier material, and deposition process were varied. Damage thresholds were measured using 150-ps, 1.064- $\mu$ m laser pulses.

For the initial experiments on barrier layers, coatings were placed on conventional polished surfaces. However, we observed variations in thresholds for different experiments involving supposedly similar coating. House *et al.* [4] have reported variations in damage thresholds with surface smoothness. To investigate this, a second series of experiments were performed in which controlled, and widely different, substrate surface smoothnesses were used.

## EXPERIMENTAL

### Coatings

For glass, the simplest monochromatic AR coating which is composed of silica and titania films is a two-layer V-coat consisting of a first-deposited thin titania layer and a thicker silica second layer. This design is capable of zero reflectance at one wavelength for the design incidence angle. The reflectance of a V-coat increases rapidly for wavelengths and incidence angles departing from the design values. Accordingly, imprecise layer thicknesses or variations in layer thickness over a single surface can result in unacceptably high reflectance values. A four-layer coating, similar to that described by Rock [5], is more practical for large laser components because it maintains uniformly low

\* Work at the Lawrence Livermore Laboratory was performed under the auspices of the Materials Sciences Programs of the U. S. Energy Research and Development Administration and Contract W-7405-eng-48.

reflectance for angle and thickness variations encountered in normal production of flat and gently curved lens surfaces. The designs used in this study were composed of (1) four layers beginning with high-index titania on the glass substrate or (2) five layers when a low-index silica or alumina barrier layer was interposed between the glass and the first high-index layer.

Most of the AR coatings were prepared in a special vacuum facility equipped with externally actuated masks which can be interposed in the coating vapor stream. In this way, both a control coating and a barrier layer coating were prepared in the same run with the four-layer AR coating simultaneously deposited on both substrates. In the coating run made to compare the effects of silica and alumina barrier layers, the vacuum was broken when the source material was changed.

To demonstrate the applicability of this work, three "production" runs were also made with regular coating equipment and sample spatial filter lenses similar to those required for the LLL Shiva laser. In one run the barrier layer plus a regular four-layer AR was coated on one surface of the lens and, in another run, the opposite surface was coated with only the four-layer AR.

### Substrates

The substrates for the research coatings were BK-7 glass disks of 38 mm diameter and 7 mm thick. The disk faces were ground and polished by standard optical shop procedures to yield three degrees of surface smoothness which will be referred to as commercial, conventional, and super-polish. All disks had one surface prepared with a commercial polish and the other polished to a higher degree. The smoothness was characterized by applying a silvered surface and measuring the diffusely scattered intensity of a He-Ne laser beam. With the polarized laser beam incident at 30°, the collimated detector accepted a narrow cone of diffusely scattered light in the plane of incidence at an angle near the specularly reflected beam. Relative roughness values are quoted in parts-per-million intensity compared to a ground surface of boron nitride.

The silver coating was dissolved with hot nitric acid prior to applying the experimental coating. Extended hot nitric acid immersion was previously shown to be beneficial to the damage threshold for 40-ns pulses [6] and is effective in removing all optical traces of the silver layer.

### Damage Threshold Determination

The damage tests at 1.064  $\mu\text{m}$  were carried out with the laser facility previously described [1]. Streak camera recordings of 37 laser shots made during one of the damage experiments show that the laser pulse length (FWHM) varied from 110-210 ps with an average value of 149 ps. Experimental results are quoted as maximum energy flux ( $\text{J}/\text{cm}^2$ ) measured at the surface in a plane perpendicular to the beam. When streak camera pulse-length data were available, intensities ( $\text{GW}/\text{cm}^2$ ) are also given.

An experimental configuration was used in which three beams having relative intensities 1:2:3 were incident on the sample for each firing of the laser. Several techniques were employed to detect damage. The sample was visually observed during each irradiation to detect laser-induced light or sparks. Immediately after each firing the focal sites were examined using a focused white light source. The damage experiment was continued until damage was detected by one of these two tests. Typically, this procedure required four to seven laser firings and the irradiation of twelve to twenty-one sites per sample.

Final determination of damage was made by using Nomarski microscopy to examine each focal site. Since a fixed array of sites was used during sample irradiation, the spatial coordinates of each site were known. Damage was assessed by noting systematic differences in the morphology of irradiated sites and non-irradiated portions of the film. Threshold damage consisted of a few micropits  $\approx 1 \mu\text{m}$  in diameter or, in some cases, of a few areas 5-10  $\mu\text{m}$  in diameter which appeared as raised "mounds." The tops of these mounds were ruptured in some instances. There is an uncertainty in the microscopic assessment because all dielectric films examined to date have a few small pinholes which resemble laser damage. Mounds were never found except on irradiated sites. Depending on sample quality, obvious damage was observed for sites irradiated at flux levels 10-20% above the assigned threshold. The usual precision of threshold values was 10-12%.

Thresholds were defined as the midpoint between highest flux not producing damage and the lowest flux causing damage. The assigned error accounts for uncertainties in the relative flux levels ( $\sim 5\%$ ) and the microscopic examination. The boundary between flux levels which cause damage and those which cause no damage was always sharp to within experimental uncertainty. In no case did we observe large scale variations of threshold over the sample surface.

## RESULTS

Table 1 summarizes the results of three coating runs in which different thicknesses and materials were used for the barrier layers. In every case the threshold was either unchanged or improved by the addition of the barrier layer. Comparable benefit is seen for alumina and silica barrier layers.



Table 2 shows the results for three samples coated on both surfaces in production vacuum equipment. Again, the coatings with a barrier layer demonstrated higher thresholds. Note that similar coatings did not yield identical thresholds.

The control samples in Table 1 (566A, 565A, and 568A) were identical coatings made in separate runs on conventionally polished substrates. Similarly, samples 566D and 568B had identical half-wave optically thick silica barrier layers. Differences in the measured damage thresholds of these similar coatings suggested that substrate surface roughness might be important.

Table 3 shows the effect of surface smoothness on the threshold for AR coatings with and without barrier layers. In these experiments the laser pulse length was determined from streak camera data; thus, it was possible to calculate pulse intensities ( $\text{GW}/\text{cm}^2$ ) at the threshold of damage. The data in Table 3 are arranged into groups with similar coatings and in order of increasing roughness within each group. Although the thresholds vary by a factor of two, there is no consistent correlation with surface smoothness.

## DISCUSSION

The present results in conjunction with previous results [1] show that for silica/titania films the damage thresholds for 150-ps, 1.064- $\mu\text{m}$  laser pulses are lower for AR coating than for silica/titania multilayer reflectors. This is opposite to predictions based upon internal electric field strengths in the film. As mentioned earlier, one obvious difference between the two types of coatings is the intensity at the coating/substrate interface which is high for AR coatings and zero for HR coatings. Since uncoated BK-7 disks damage at  $\approx 10 \text{ J}/\text{cm}^2$ , any interface vulnerability must be due to the presence of the coating.

Table 1. Experimental damage thresholds ( $\text{J}/\text{cm}^2$ ) for coatings from research equipment.

Sample	Barrier*	Threshold	Improvement
566A	none	$4.2 \pm 0.3$	--
566B	$\lambda/50 \text{ SiO}_2$	$4.0 \pm 0.3$	none
566C	$\lambda/4 \text{ SiO}_2$	$4.0 \pm 0.3$	none
566D	$\lambda/2 \text{ SiO}_2$	$4.8 \pm 0.5$	15%
565A	none	$3.2 \pm 0.4$	--
565B	$2 \times \lambda/4 \text{ SiO}_2$	$6.3 \pm 0.7$	90%
565C	$4 \times \lambda/4 \text{ SiO}_2$	$6.3 \pm 0.7$	90%
568A	none	$3.2 \pm 0.3$	--
568B	$\lambda/2 \text{ SiO}_2$	$5.6 \pm 0.6$	75%
568C	$\lambda/4 \text{ Al}_2\text{O}_3$	$4.0 \pm 0.4$	25%
568D	$\lambda/2 \text{ Al}_2\text{O}_3$	$5.1 \pm 0.4$	60%

\* Barrier layers stated in optical thicknesses. Barrier layers in 565B and 565C were deposited as an accumulation of several discrete thin films.



Table 2. Experimental damage thresholds ( $\text{J}/\text{cm}^2$ ) for coatings from production equipment.

Sample	Barrier	Threshold	Improvement
Asphere A	none	$2.7 \pm 0.3$	--
Asphere B	$\lambda/4 \text{ SiO}_2$	$4.7 \pm 0.8$	70%
6974A	none	$3.5 \pm 0.5$	--
6974B	$\lambda/4 \text{ SiO}_2$	$4.3 \pm 0.5$	20%
6977A	none	$3.3 \pm 0.4$	--
6977B	$\lambda/4 \text{ SiO}_2$	$4.0 \pm 0.4$	20%

Table 3. Dependence of damage threshold on surface roughness of substrate.

Sample	Surface Preparation	Barrier Layer	Diffuse Intensity (ppm)	Threshold	
				$\text{GW}/\text{cm}^2$	$\text{J}/\text{cm}^2$
600A	Superpolish	none	160	$27 \pm 7$	$4.0 \pm 0.6$
599A	Commercial	none	> 1000	$37 \pm 9$	$5.5 \pm 0.7$
599 B14	Superpolish	$2 (\lambda/4) \text{ SiO}_2$	20	$28 \pm 7$	$4.1 \pm 0.6$
600 AA1	Superpolish	$2 (\lambda/4) \text{ SiO}_2$	40	$36 \pm 9$	$5.4 \pm 0.7$
599 A16	Superpolish	$2 (\lambda/4) \text{ SiO}_2$	70	$23 \pm 6$	$3.4 \pm 0.5$
599 AA1	Commercial	$2 (\lambda/4) \text{ SiO}_2$	> 1000	$29 \pm 7$	$4.4 \pm 0.6$
599 B8	Superpolish	$\lambda/2 \text{ SiO}_2$	20	$47 \pm 18$	$7.0 \pm 2.0$
599 A13	Superpolish	$\lambda/2 \text{ SiO}_2$	70	$45 \pm 9$	$6.7 \pm 1.3$
600 B6	Superpolish	$\lambda/2 \text{ SiO}_2$	230	$26 \pm 8$	$3.9 \pm 0.8$
599 B6	Commercial	$\lambda/2 \text{ SiO}_2$	> 1000	$42 \pm 10$	$6.3 \pm 0.8$

In the above experiments, several different barrier layer designs were tried. These layers did not significantly affect the reflectivity of the AR coating or the electric field intensity at the boundary. They do, however, provide physical and chemical isolation from the substrate and a different surface for the deposition of the first titania layer. In Tables 1 and 2, the addition of the barrier layers always yielded positive results in terms of increased damage thresholds.

From the limited data available, the thickness of the barrier layers seems to be important. That is, up to the  $\lambda/2$  thicknesses investigated, the thicker layers had the higher damage thresholds. We have chosen the  $\lambda/2$  barrier layer thickness for subsequent production applications.

The effects of depositing the barrier as (1) one continuous layer and (2) a series of discrete  $\lambda/4$  layers separated by a time interval of several minutes are included in Table 1. The small improvement by the latter technique evident in Table 1 was not repeated in Table 3. At present, the interruption of layers appears to offer no benefit.

To investigate the effects of substrate surface irregularities, AR coatings were prepared with and without  $\lambda/2$  barrier layers on substrates with various degrees of roughness. The roughness was determined by light scattering. The quoted scatter intensity of each disk is the average of five measurements made at different locations within a 2.5-mm-diameter central region. Two disks were evaluated at several locations within the central one-inch-diameter region to verify that the surface scatter intensity was uniform. To correlate the scatter intensity measurements with surface roughness, we examined three samples (generously provided by J. Bennett, Michelson Laboratory, Naval Weapons Center) whose RMS roughnesses were all about  $10\text{\AA}$  as determined by TIS and FECO techniques. Our best superpolish surfaces scattered slightly less than the Bennett samples and were, therefore, assumed to be at least as smooth.

From the results shown in Table 3, the quality of substrate surface polish did not affect the damage threshold for 150-ps pulses. House *et al.* [4], on the other hand, found a correlation between damage threshold and surface smoothness for 40-ns pulses.

## CONCLUSIONS

The addition of a silica barrier layer between a BK-7 glass substrate and the first titania layer of a four-layer AR coating improved the average threshold for 150-ps,  $1.064\text{-}\mu\text{m}$  laser damage. The improvement varies from insignificant to nearly double when simultaneously coated samples were compared. There is a trend toward higher threshold with increased silica barrier layer thickness. On the basis of results for the two samples, alumina barrier layers are as effective as silica in raising the damage threshold. Contrary to the results of House *et al.* [4] for damage by 40-ns pulses, for 150-ps pulses we found no correlation between damage thresholds and surface smoothness either with or without a barrier layer.

## REFERENCES

- [1] D. Milam, Appl. Opt. 16, 1204 (1977).
- [2] J. H. Apfel, J. S. Matteucci, B. Newnam, and D. Gill, "The Role of Electric Field Strength in Laser Damage of Dielectric Multilayers," NBS Spec. Pub. #462, 301 (1976).
- [3] W. J. Coleman, Appl. Opt. 13, 946 (1974).
- [4] R. A. House, J. R. Bettis, and A. H. Guenther, IEEE J. Quant. Electron. QE-13, 361 (1977).
- [5] U. S. Patent 3,432,225.
- [6] R. A. House, "The Effects of Surface Structural Properties on Laser-Induced Damage at  $1.06\text{ }\mu\text{m}$ ," AFWL-TR-76-62, Air Force Weapons Laboratory final report, Kirtland AFB, NM (October 1976).

## COMMENTS ON PAPER BY APFEL, ENEMARK, MILAM, SMITH, AND WEBER

The speaker indicated that the damage threshold of the barrier layer alone had not been investigated. He felt that the effect which had been observed might be due to the interposition of the barrier layer between the titanium dioxide film and the ground and polished Bk-7 surface, and implied that in the absence of the barrier layer some chemical interaction might be taking place between these two constituents. This would seem to be supported by slight improvements seen when the surface was cleaned by sputter etching, prior to the deposition of the  $\text{TiO}_2$  film. Newnam from LASL indicated that in experiments he had carried out in which a barrier layer of  $\text{SiO}_2$  was applied prior to putting down a sputtered coating of  $\text{TiO}_2$ , no improvement due to the barrier layer was seen. It may be that the sputtering process in itself cleans the surface, and so the barrier layer becomes redundant.

## NOTICE

"This report was prepared as an account of work sponsored by the United States Government. Neither the United States nor the United States Energy Research & Development Administration, nor any of their employees, nor any of their contractors, subcontractors, or their employees, makes any warranty, express or implied, or assumes any legal liability or responsibility for the accuracy, completeness or usefulness of any information, apparatus, product or process disclosed, or represents that its use would not infringe privately-owned rights."

USE OF NON-QUARTER-WAVE DESIGNS TO INCREASE THE DAMAGE RESISTANCE OF REFLECTORS  
AT 532 AND 1064 NANOMETERS\*

Dennis H. Gill, Brian E. Newnam and John McLeod  
Los Alamos Scientific Laboratory  
Los Alamos, New Mexico 87545

The damage resistance of multilayer dielectric laser reflectors has been increased by using non-quarter-wave thicknesses for the top few layers. These designs minimize the standing-wave electric field in the high-index layers, which are generally the weaker layers. Algebraic equations have been derived for optimum film thicknesses and for the resulting peak electric fields.

Five sets of reflectors for 532 and 1064 nm were fabricated according to these designs by two vendors using two different material combinations. Each set contained one reflector of standard all-quarter-wave design and three reflectors each with a different number of modified layers. The damage thresholds of the modified designs were found to be higher than the all-quarter-wave designs, in some cases by a factor greater than 2. The damage thresholds have been analyzed and explained in terms of standing-wave electric field patterns.

Key words: Damage thresholds; electric fields; laser damage; non-quarter-wave designs; picosecond pulses; standing waves; thin films.

### 1. Introduction

A substantial increase in the damage resistance of multilayer dielectric laser reflectors has been attained by using non-quarter-wave thickness designs for the top few layers. The principle of these designs is to minimize the standing-wave (SW) electric field in the high-index layers, which are generally less damage resistant than low-index layers. Algebraic equations were derived for the optimum film thicknesses and for the resulting peak electric fields. Reflectors for 532 nm and 1064 nm were fabricated according to these designs, and their measured damage thresholds were compared with those of similar reflectors with all quarter-wave (QW) thicknesses.

To the knowledge of the authors, the first suggestion for using non-QW top layers was made by Gary DeBell for the purpose of minimizing the total linear absorption in reflector stacks [1]. Newnam suggested non-QW thicknesses to obtain minimum peak fields in high index layers in order to raise the damage threshold [2]. Costich and Bloom designed and supplied test samples of  $\text{TiO}_2/\text{SiO}_2$  reflectors to LASL with one pair of non-QW layers, but these were not the optimum design [3]. Newnam and Gill presented the threshold data for these samples along with suggestions for improvement at Asilomar [4] and reported on the first set of reflectors with optimum designs at CLEA [5]. Apfel did a very elegant job of mathematically deriving the optimum designs [6].

### 2. Theory

The standard dielectric reflector is composed of alternate layers of relatively high- and low-refractive indices which have QW optical thicknesses. In this design, the SW-electric field maxima occur at the layer interfaces and are largest in the top layers nearest the incident radiation (see fig. 1a). Previous experiments [2,7,8] have shown that the damage threshold of QW stacks of  $\text{TiO}_2$  and  $\text{SiO}_2$  is determined by the peak internal SW electric field in the high-index material ( $\text{TiO}_2$ ). In the visible and near infrared the high-index material is usually weaker than the low-index material, thus, it is highly desirable to shift the position of the SW field maxima away from the film interfaces of the top layers of a reflector and into the low-index (stronger) layers. This is accomplished by the use of non-QW thicknesses for the top layers.

If the thicknesses of the top pair of layers are modified so that the high-index layer is thinner and the low-index layer is thicker than a QW, the SW field maximum is shifted into the low-index material, as shown in figure 1b. Note that the amplitude of the peak has increased, so that the low-index material is being stressed harder than for the all-QW case. The maximum value of E occurring in high-index material has been reduced to  $0.652/0.833 = 0.78$  of its previous value. (These numbers depend on the indices of refraction of the materials. This example uses 2.40 and 1.46.) The peak E occurring in low-index material has increased to  $1.073/0.833 = 1.29$  times its previous value. Further shifting can be accomplished by modifying the thicknesses of the top two pairs of layers, as shown in figure 1c. Here the peak E value in high-index material has been further reduced and the peak E in low-index material has increased again. This procedure can be extended to the modification of as many

\*Work supported by the U. S. Department of Energy.

1. Figures in brackets indicate the literature references at the end of this paper.



layers as desired. However, at some point the stronger material will break and no further improvement can be obtained. This will be discussed in more detail below.

One can analyze the SW electric-field pattern in a reflector and derive equations for the peak fields and the reflectance. To minimize the peak field in the high-index layers while maintaining maximum reflectance, the thicknesses of the top two layers are given by

$$\sin \theta_L = \frac{1}{N} \quad \theta_L > \frac{\pi}{2} \quad (1)$$

and

$$\tan \theta_H = \frac{N}{\sqrt{N^2 - 1}} \quad \theta_H < \frac{\pi}{2}, \quad (2)$$

where

$$N = \frac{n_H}{n_L} \quad (3)$$

and

$$\theta_i = \frac{2\pi n_i d_i}{\lambda} \quad (4)$$

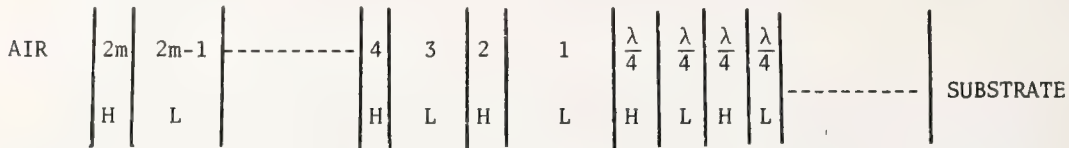
Here, the subscripts L, H refer to the low- and high-index layers and d is the film thickness. Similar expressions have also been derived by Apfel [6]. For the thicknesses specified by eqs. (1,2), the peak E-field in the first high-index layer is reduced by a factor of

$$\frac{N}{\sqrt{2N^2 - 1}} \quad (5)$$

compared to the standard all-QW case. At the same time the peak E-field in the first low-index layer is increased by a factor of

$$\frac{N^2}{\sqrt{2N^2 - 1}} \quad (6)$$

The equations above apply to the modification of the top pair of layers. For further improvement one can modify additional pairs of layers. The thicknesses, however, are different for each layer. In order to generalize the equations, a convention is chosen for numbering the layers. Assume that some number of QW layers are deposited on the substrate (i.e., a standard reflector), then m pairs of modified layers are deposited on top of the QW stack. Number the modified layers outward, starting with layer 1 adjacent to the QW stack and ending with layer 2m next to the air, as shown below.



For this general case, the optimal thicknesses for the modified layers are given by

$$\text{Low Index Layers: } \sin \theta_{2i-1} = \frac{1}{\sqrt{iN^2 - (i-1)}} \quad \begin{cases} 0 < i \leq m \\ \theta_{2i-1} > \pi/2 \end{cases} \quad (7)$$

$$\text{High Index Layers: } \tan \theta_{2i} = \frac{N}{\sqrt{i(N^2 - 1)}} \quad \begin{cases} 0 < i \leq m \\ \theta_{2i} < \pi/2 \end{cases} \quad (8)$$

where eqs. (3,4) still hold. The maximum E-field occurring in any high-index layer, relative to the incident E-field in air, is

$$\left| \frac{E_H}{E_o^+} \right| = \frac{2}{n_L \sqrt{(m+1)N^2 - m}} \quad (9)$$

Similarly, for a low-index layer,

$$\left| \frac{E_L}{E_o^+} \right| = \frac{2}{n_L} \sqrt{\frac{mN^2 - (m-1)}{(m+1)N^2 - m}} \quad (10)$$

Equations (9) and (10) can be used to determine the decrease or increase in the peak E-field occurring in either material, relative to the field in a standard all-QW ( $m = 0$ ) reflector. These ratios are plotted in figure 2 as a function of  $N$ . Because of the relationship between damage threshold and peak E-field, we define the reciprocal of the reduction in the peak E-field in the high-index material as the improvement,  $I$ . This is the expected increase in the damage threshold, as compared to the all QW case, for a reflector with an  $m$ -pair modified design. This expected increase is given by

$$I \equiv \frac{E_Q}{E_H} = \frac{\sqrt{(m+1)N^2 - m}}{N} \quad (11)$$

This assumes that damage occurs due to failure of the high-index material. Figure 3 shows the improvement  $I$  as a function of  $N$ , as well as the ratio of the peak E-field in the low-index material to that of the high-index material. Note that  $I$  relates to the E-field damage threshold. If one thinks of damage threshold in units of joules per square centimeter, the improvement is  $I^2$ .

Whether or not these modified designs will yield higher damage thresholds than the all-QW design depends on the ratio of the damage thresholds of the two materials. As has been shown, increasing the value of  $m$  increases the E-field in the low-index material. As  $m$  is increased, at some point the (stronger) low-index material will break. Define the parameter  $\rho$  to be the ratio of the damage threshold (expressed in MV/cm) of the low-index film to the damage threshold of the high-index film. Using eqs. (9,10) we can show that if

$$\rho \geq \sqrt{mN^2 - (m-1)} \quad , \quad (12)$$

then full advantage can be taken of an  $m$ -pair modification. For most practical cases in the visible and near ir, the value of  $\rho$  limits the useful designs to  $m = 1, 2$  or  $3$ . If a value of  $m$  is used such that eq. (12) does not hold, then the damage threshold will decrease from its optimum value. If  $m$  is high enough, the damage threshold can actually be lower than for the all QW case.

### 3. Experiment

#### 3.1. Test Procedure

In order to test the theory, five sets of reflectors were obtained from two vendors. Each set (except one) contained four reflectors, one each of  $m = 0$  (all QW),  $m = 1$ ,  $m = 2$  and  $m = 3$ . All four reflectors were coated in the same coating run by using shutters, thus, all four reflectors have the same stack of quarter wave layers. Then the modified layers are added, and as each reflector is completed, it is shuttered off to protect it from the remaining modified layers. This rather complicated procedure was used to assure that each reflector was as nearly identical to the others in its set as possible. In this way, differences in damage threshold should be due to design differences only, assuming that the material in the outer layers is identical to that in the QW layers. The reflectors obtained were  $\text{TiO}_2/\text{SiO}_2$  and  $\text{ZrO}_2/\text{SiO}_2$  at 1064 nm and 532 nm.

The reflectors were tested using a laser damage test facility that has been described elsewhere [8,9]. The laser was a mode-locked Nd:YAG system. The fundamental or second harmonic was used as appropriate. Pulse lengths were 30 ps for 1064 nm and 21 ps for 532 nm. Considerable effort was taken to assure a good gaussian beam profile, and the profile of the focal spot was measured on every shot using a linear array.

#### 3.2. Data at 1064 nm

Table 1 lists the data obtained on one set of  $\text{TiO}_2/\text{SiO}_2$  reflectors at 1064 nm. One can see that the  $m=1$  design doubled the damage threshold compared to the  $m = 0$  case. The  $m = 2$  case was not quite as good as  $m = 1$ , but still better than  $m = 0$ . The  $m = 3$  case provided a damage threshold 2.6 times as large as the QW reflector. The lower threshold for  $m = 2$  followed by an increased threshold for  $m = 3$  does not follow the pattern predicted by the last column, using the exact design thicknesses. At least part of the explanation lies in the lack of ability of the vendor to maintain accurate film thicknesses on non-quarter-wave coatings. These modified-layer designs are much more sensitive to errors in coating thicknesses than are standard QW designs. By consulting with the vendor and carefully reading his coating run sheets, we were able to estimate the magnitude and location of several thickness errors. Also, some of these could be verified by comparing spectral transmission curves with theoretically predicted curves. The modified-layer designs have very distinct spectral signatures. Both of these methods can be used to estimate thickness errors. It was determined that there were thickness errors in both the  $m = 2$  and the  $m = 3$  reflectors. Without ideal thicknesses, eqs. (9-11) no longer apply. The actual (as best we could determine) thicknesses were used in a LASL computer code that calculates the complete E-field distribution in an arbitrary stack of dielectric films. The results were used to predict the improvement shown in the "Theoretical as Coated" column. It should be noted that the theoretical improvements in all of the tables assume high-index layer

failure, unless otherwise noted. At higher m-values it is expected that the low-index layer will fail, and these predicted improvements will be larger than those actually obtained. In table 1, the measured improvement does not agree exactly with the "Theoretical as Coated" improvement, but the trends agree well. Specifically, the lower improvement for m = 2 is apparently explained by the thickness errors. While these errors cause trouble in exact agreement between experiment and theory, all of the modified-design reflectors had substantially higher damage thresholds than the standard QW reflector.

Table 1.  $\text{TiO}_2/\text{SiO}_2$  reflectors at 1064 nm.

Layers	Design	Measured Damage Threshold ( $\text{J}/\text{cm}^2$ )	E-field at threshold		Improvement Measured	Relative to all QW	
			H-Layer (MV/cm)	L-Layer (MV/cm)		Theoretical as coated	Theoretical ideal thick.
11	All QW	$1.0 \pm .1$	3.0	3.0	---	---	----
13	m=1	$2.0 \pm .2$	3.4	5.4	2.0	1.59	1.59
15	m=2	$1.7 \pm .2$	3.5	6.2	1.7	1.31	2.18
17	m=3	$2.6 \pm .5$	3.1	6.7	2.6	2.47	2.77

Table 2 lists the data obtained on a set of  $\text{ZrO}_2/\text{SiO}_2$  reflectors at 1064 nm. Here, again, coating thickness errors play a major role. Note the rather dramatic drop in the threshold for the m = 2 case, which is explained by a thickness error. The m = 3 design provided a 74% increase in the damage threshold. It is likely that the m = 3 design failed in the low-index layer.

Table 2.  $\text{ZrO}_2/\text{SiO}_2$  reflectors at 1064 nm.

Layers	Design	Measured Damage Threshold ( $\text{J}/\text{cm}^2$ )	E-field at threshold		Improvement Measured	Relative to all QW	
			H-Layer (MV/cm)	L-Layer (MV/cm)		Theoretical as coated	Theoretical ideal thick.
17	All QW	$1.3_5 \pm .3$	4.2	4.2	---	---	----
19	m=1	$1.4_2 \pm .3$	3.8	5.0	1.05	1.27	1.42
21	m=2	$1.0 \pm .1$	3.8	5.3	.74	.88	1.84
23	m=3	$2.3_5 \pm .6$	3.8	6.7	1.74	2.10	2.26

Table 3 lists the data for another set of  $\text{TiO}_2/\text{SiO}_2$  reflectors at 1064 nm. This set was chronologically the first set obtained. The results were somewhat dubious because of the larger range of the damage threshold. Note that the lower end was constant for the three samples. This was attributed to defects. The samples had a high scatter level, which is often due to the presence of large numbers of defects. The upper end of the range did show an improvement for the modified samples. The improvement obtained for m=1 is consistent with that predicted for either L- or H-layer failure, and the improvement obtained for m=2 is consistent with that predicted for low-index layer failure. The column predicting improvement if the L-layer fails appears in table 3 because we have a measured value of  $\rho$  for this vendor and these materials. Recall that  $\rho$  is the ratio of damage thresholds for the two materials. Previous to this experiment, single QW layers of  $\text{TiO}_2$  and  $\text{SiO}_2$  had been obtained from this vendor and damage tested. The value of  $\rho$  was found to be 1.5 - 1.6. The next-to-last column in table 3 was calculated using 1.58 and seems to be consistent with the data. For other vendors the value of  $\rho$  for  $\text{TiO}_2/\text{SiO}_2$  has been measured to be in the range 1.5 - 1.6, also. Because of the constant threshold on the low end, it was decided to obtain samples from another vendor. All of the other samples reported in this paper were from the second vendor.

Table 3.  $\text{TiO}_2/\text{SiO}_2$  reflectors at 1064 nm.

Layers	Design	Measured Damage Threshold ( $\text{J}/\text{cm}^2$ )	E-field at Threshold		Improvement Measured (Top of Range)	Relative to all QW	
			H-Layer (MV/cm)	L-Layer (MV/cm)		Theoretical H-Layer Fails As Coated	Theoretical L-Layer Fails $\rho = 1.58$ H-Layer Fails Ideal Thick.
15	All QW	4.5-5.4	7.0	7.0	---	----	----
15	m=1	4.5-8.0	7.1	11.1	1.5	1.44	1.4
15	m=2	4.5-6.4	5.6	10.7	1.2	1.82	1.2



### 3.3. Data at 532 nm

Table 4 lists the data obtained from a set of  $\text{TiO}_2/\text{SiO}_2$  reflectors at 532 nm. Once again coating thickness errors reduced the expected improvement. As designed, the set would have shown a range of improvements from 1.63 to 2.88, although the L-layer should have broken for  $m = 3$ . However, as coated, the expected improvements were all roughly the same, and indeed this was observed experimentally. Even so, a factor of 1.6 increase in damage threshold is well worthwhile.

Table 5 lists the data for a set of  $\text{ZrO}_2/\text{SiO}_2$  reflectors at 532 nm. The maximum improvement of 30% was obtained with the  $m = 1$  design followed by a slow decrease in the threshold for  $m = 2$  and 3.

Table 4.  $\text{TiO}_2/\text{SiO}_2$  reflectors at 532 nm.

Layers	Design	Measured Damage Threshold ( $\text{J}/\text{cm}^2$ )	E-Field at Threshold		Improvement Measured	relative to all QW	
			H-Layer	L-Layer		Theoretical as coated	Theoretical Ideal Thick.
11	All QW	$1.3 \pm .1$	3.9	3.9	---	----	---
13	$m=1$	$1.8 \pm .1$	4.0	5.6	1.4	1.31	1.63
15	$m=2$	$2.2 \pm .2$	5.1	7.0	1.6	1.18	2.26
17	$m=3$	$2.1 \pm .2$	4.7	7.2	1.6	1.38	2.88

Table 5.  $\text{ZrO}_2/\text{SiO}_2$  reflectors at 532 nm.

Layers	Design	Measured Damage Threshold ( $\text{J}/\text{cm}^2$ )	E-Field at Threshold		Improvement Measured	relative to all QW	
			H-Layer	L-Layer		Theoretical as coated	Theoretical Ideal Thick.
17	All QW	$1.9 \pm .1$	5.7	5.6	---	----	---
19	$m=1$	$2.5 \pm .5$	6.2	7.1	1.3	1.13	1.46
21	$m=2$	$2.3 \pm .4$	5.5	6.7	1.2	1.21	1.91
23	$m=3$	$2.1 \pm .3$	5.5	6.7	1.1	1.12	2.37

### 3.4. Discussion of results

Since most of the samples showed the effects of coating thickness errors, the tolerance for error in these designs was studied. Table 6 presents the results of an error analysis for one specific case,  $\text{TiO}_2/\text{SiO}_2$  with indices of 2.26 and 1.44, respectively. The analysis is done for an 11-layer, all-QW reflector, and for a 15-layer,  $m=2$  design. The all QW reflector is quite insensitive to thickness errors, with negligible field changes for 3% errors. The  $m = 2$  design has field changes of the order of 2% to 8% for the various 1% errors and field changes of 5% to 23% for various 3% errors. These are obviously not insignificant. Since the designs are optimized with regard to the high-index layers, thickness errors always produce higher E-fields in the H-layer, but may produce either higher or lower E-fields in the L-layer.

The effect of errors in index of refraction was also studied. The modified designs are not at all sensitive to an error in  $n$  if  $nd$  is correct, as might be expected. Thus, an accurate measurement of the optical thickness  $nd$  is important, but an accurate knowledge of  $n$  is not so critical.

Tolerances of 1% in coating thickness are not unreasonable. Most coaters are capable of maintaining this tolerance. In some previous experiments using non-QW layers we have obtained samples from vendors with thicknesses accurate to better than 1%. The primary difficulty is in the monitoring techniques, which may require some changes. These changes should be worthwhile, however, considering the possible gains (factors of 2 and more increase in damage threshold).

The amount of improvement that one can expect depends upon the relative damage thresholds of the two materials, as has been shown earlier. It is expected that greater improvements can be obtained in the uv and ir where one material tends to be much weaker than the other. Throughout this paper it has been assumed that the high-index material was weaker. The theory presented here works equally well for combinations where the low-index material is weaker. One simply modifies the thicknesses so as to push the peak of the E-field distribution into the high-index layer. Equations for the optimal thicknesses can be derived in a similar manner.

The reflectances for these modified designs will always be greater than the reflectance of the corresponding all QW reflector, although not by very much. This is true because one is adding the modified layers to the QW stack.

Table 6. Coating thickness error analysis. Theoretical errors in E-field due to thickness errors in coating, for  $\text{TiO}_2/\text{SiO}_2$ ,  $n_H = 2.26$ ,  $n_L = 1.44$ ,  $N = 1.57$ . Primes refer to fields in coating with errors.

Design	Thickness	$\frac{E_H'}{E_H}$	$\frac{E_L'}{E_L}$
m=0 (All QW)	All layers 3% thick	1.003	1.011
	All layers 3% thin	1.006	1.003
m=2	Mod. layers 1% thick	1.036	1.023
	All layers 1% thick	1.060	1.033
	Mod. layers 1% thin	1.058	0.979
	All layers 1% thin	1.078	0.973
m=2	Mod. layers 3% thick	1.124	1.083
	All layers 3% thick	1.225	1.125
	Mod. layers 3% thin	1.167	0.948
	All layers 3% thin	1.218	0.935

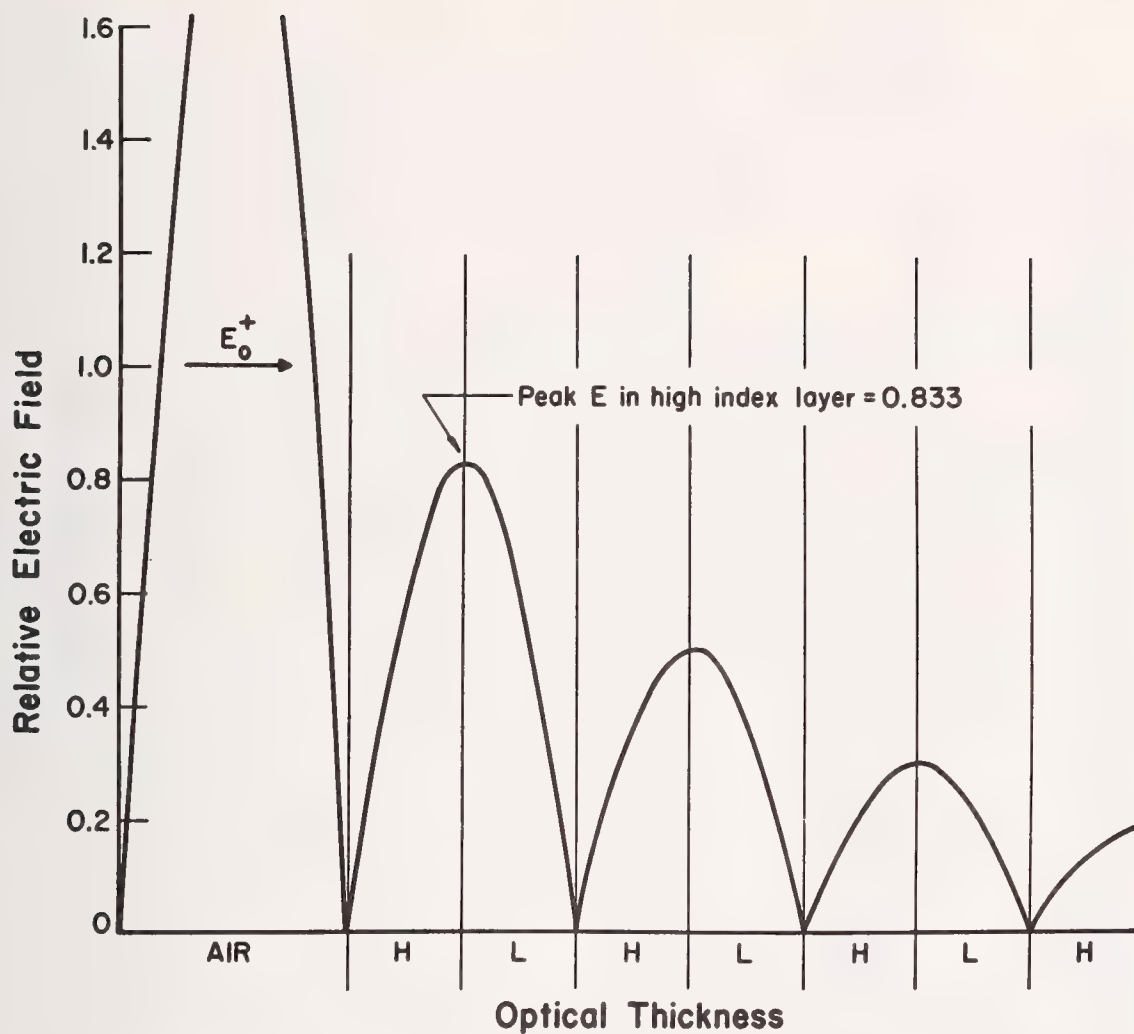
#### 4. Conclusions

It has been shown both experimentally and theoretically that a substantial increase in the damage threshold of a reflector can be obtained by using non-QW layers in the design. Factors of improvement as large as 2.6 (in the energy density threshold) were obtained. The modified designs are sensitive to errors in coating thickness, and many of the samples showed less improvement than they might have due to this. Even so, out of 5 sets of reflectors from 2 vendors, made of 2 different material combinations for 2 different wavelengths, only one reflector had a lower threshold than its all-QW counterpart. Non-QW thickness samples have been obtained with thickness errors less than 1%.

These experiments were done in the visible and near ir. It is expected that even greater improvements could be seen in the uv and ir where the weak layers are relatively weaker.

#### 5. References

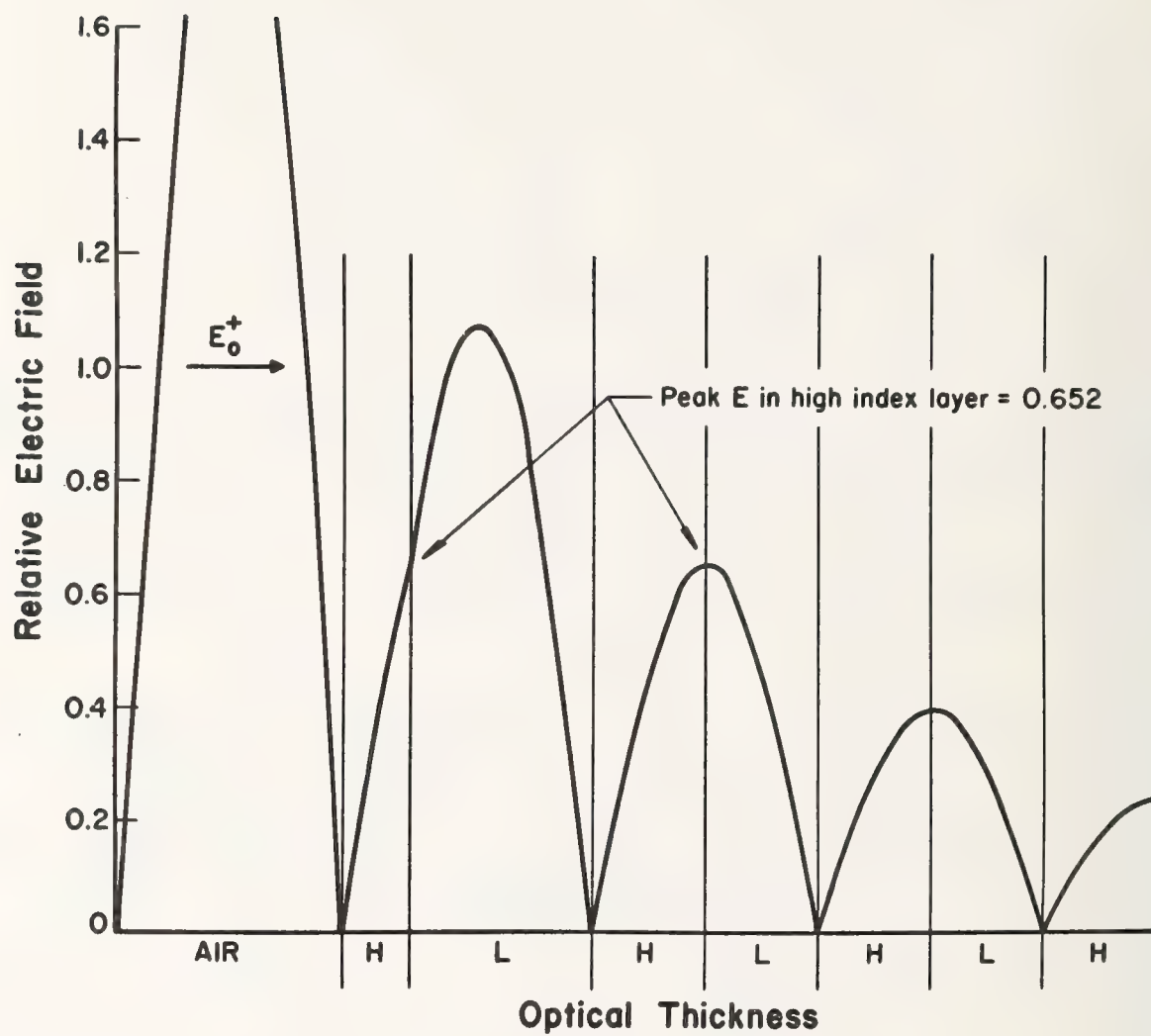
- [1] DeBell, G., Ph.D. Dissertation, Univ. of Rochester, University Microfilms, Ann Arbor, Mich. (1971).
- [2] Newnam, B. E., Ph.D. Dissertation, Univ. Microfilms, Ann Arbor, Mich. (1973).
- [3] Costich, V. R. and Bloom, A., personal communication (1974).
- [4] Newnam, B. E. and Gill, D. H., J. Opt. Soc. Am. 66, 166 (1976).
- [5] Gill, D. H., Newnam, B. E., and McLeod, J., 1977 IEEE/OSA Conf. on Laser Eng. and Applications Digest of Tech. Papers, 54 (1977).
- [6] Apfel, J. H., Appl. Opt. 16, 1880 (1977).
- [7] Apfel, J. H., Matteucci, J. S., Newnam, B. E. and Gill, D. H., NBS Special Publication 462, 301 (1976).
- [8] Newnam, B. E., Gill, D. H. and Faulkner, G., NBS Special Publication 435, 254 (1975).
- [9] Newnam, B. E. and Gill, D. H., NBS Special Publication 462, 292 (1976).



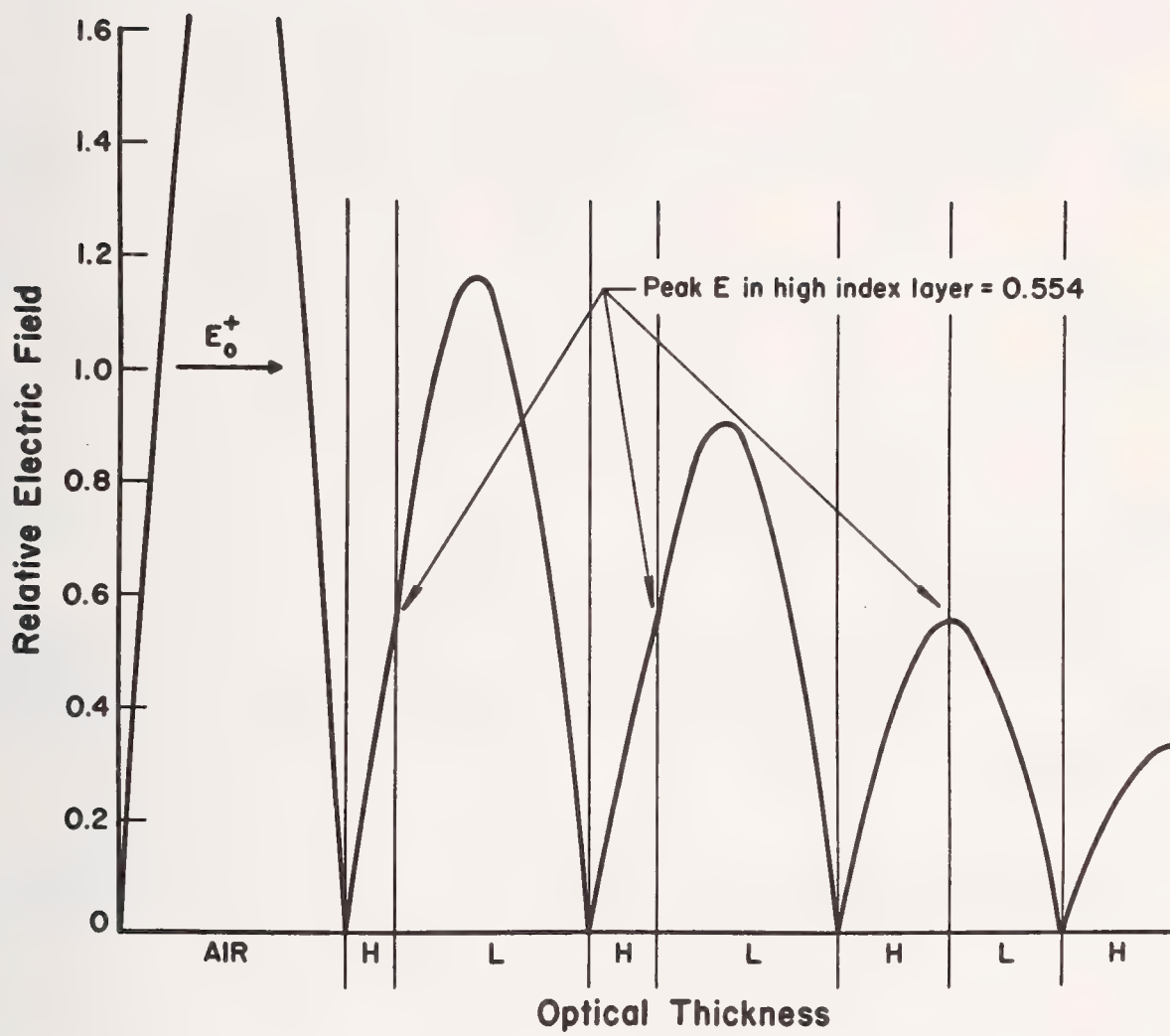
(a)

Fig. 1. Standing-wave electric field distribution in a multi-layer dielectric reflector.  $E_0^+$  is the incident electric field in air. Indices are 2.40 and 1.46. (a) Standard all-quarter-wave reflector,  $m=0$ . (b) One pair of layers modified in thickness,  $m=1$ . (c) Two pairs of layers modified in thickness,  $m=2$ .





(b)



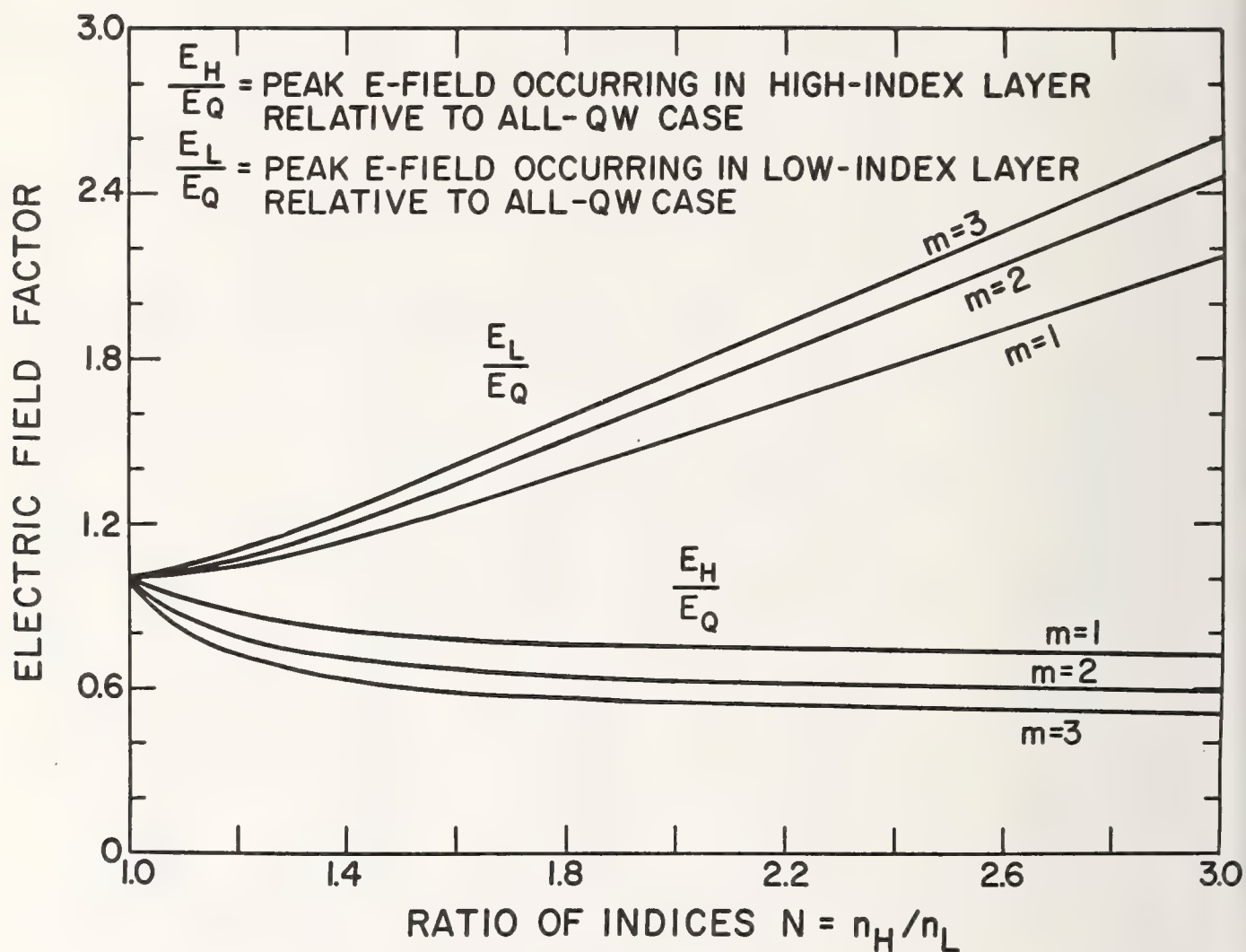


Fig. 2. Peak E-fields occurring in high- and low-index materials, relative to an all-QW reflector, as a function of the index ratio  $N$  and the degree of modification  $m$ .



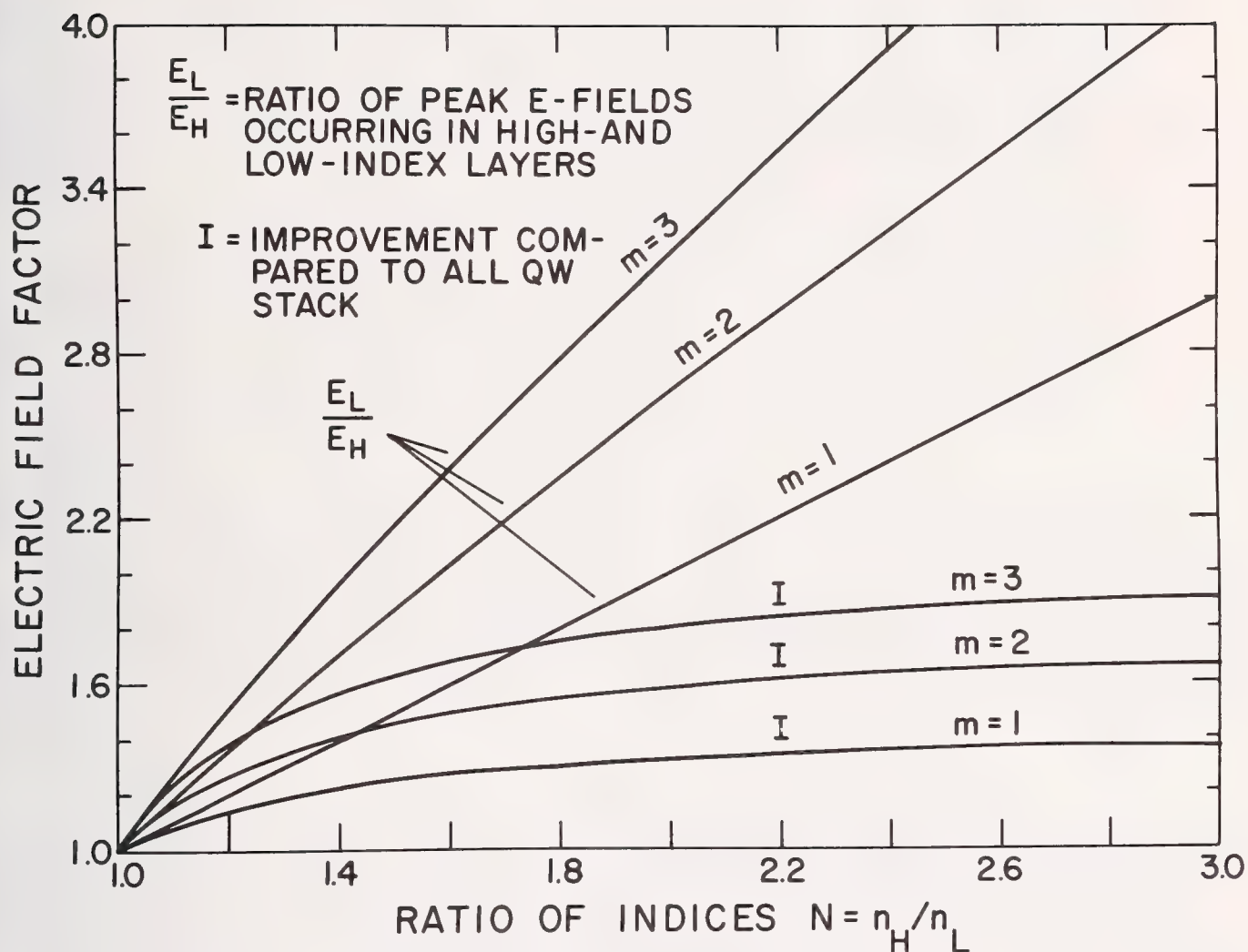


Fig. 3. Ratio of peak E-fields occurring in high- and low-index materials and the improvement (E-field), in the damage threshold, as a function of index ratio  $N$  and degree of modification  $m$ .

# CHARACTERISTICS OF R. F. SPUTTER-DEPOSITED ZINC SELENIDE FILMS ON CALCIUM FLUORIDE\*

D. A. Walsh and R. V. Bertke  
University of Dayton Research Institute  
Dayton, Ohio 45469

A study has been made of the optical, physical and chemical properties of R. F. bias-sputtered CVD Zinc Selenide thin films on polycrystalline  $\text{CaF}_2$  laser window material as a function of sample preparation and deposition parameters. Optical performance of the coatings has been evaluated by measurement of coating absorption, physical integrity by topple-test and Scotch Tape adhesion, and chemical properties by Rutherford Backscattering and Auger Spectroscopy.

A comparison is made between bias-sputtered and non bias-sputtered coatings. It is shown that a lower coating absorption is produced when the sample surface is sputter-etched in-situ immediately prior to coating. A zinc to selenium ratio of 1.13 to 1 has been found for the initially deposited coating material and the presence of oxygen at the coating/substrate interface has been detected for bias-sputtered films.

Key words: Auger analysis; bias-sputtering; calcium fluoride; Rutherford backscattering; sputter-etching; zinc selenide.

## 1. Introduction

The deposition of coatings by the sputtering technique offers a number of potential advantages over resistive or electron beam methods. Inherent in sputtering is the higher kinetic energy of the coating material as it arrives at the substrate. This promotes tighter bonding to the substrate surface and should result in a coating of higher density, improved adhesion and better durability. Along with these benefits should also follow better homogeneity and lower absorption in the deposited film. Lower deposition temperatures could also be possible and by utilizing production-type equipment with vacuum interlocks, a decrease in coating cycle time might also be realized. Of particular value is the ability to subject the substrates to a final cleaning by means of in-situ sputter-etching.

## 2. Experimental

In this investigation three techniques were studied in a modified sputtering apparatus equipped with an optical monitor for film thickness control. [1]<sup>1</sup> Representative coatings of zinc selenide were fabricated on standard samples of  $\text{CaF}_2$  window material by straight RF sputtering and RF-Bias sputtering both with and without sputter-etching of the substrate surface. The absorption of each coating was measured at  $5.3\mu$  and representative films were evaluated by Auger Analysis to determine coating composition and by Rutherford Backscattering to determine the stoichiometry of the initially deposited  $\text{ZnSe}$ . All of the samples were subjected to the Scotch Tape Test but in most cases were not given further adhesion tests to allow additional optical measurements to be performed.

### 2.1 Sample Preparation

Substrates were 38 mm O.D. by 6 mm thick Harshaw Polytran  $\text{CaF}_2$  with a 3-5 fringe flat standard IR finish. Prior to coating each sample was washed in a Liquinox detergent solution using a lens paper swab and given three rinses in both distilled water and isopropyl alcohol. Samples were then stored in a Freon degreaser until ready to coat. One set of samples was further cleaned by in-situ sputter-etching immediately before coating. Coating conditions used in sample fabrication are shown in table 1. The apparatus used in this work is equipped with a vacuum interlock which allows the target to remain under vacuum at all times following its initial sputter-cleaning. After the pre-heating of the specimen in the vacuum interlock, it is automatically loaded into the sputtering chamber where it is outgassed immediately prior to coating deposition or sputter-etching if this step is included.

\* Work supported by the Air Force Materials Laboratory.

1. Figures in brackets indicate the literature references at the end of this paper.

## 2.2 Bias-sputtered Coating Absorption

The absorption values measured for three sets of ZnSe coatings as a function of the optical thickness at  $5.3\mu$  are shown in figure 1. These were determined by subtracting the uncoated substrate absorption,  $A_o$ , from the coated sample absorption,  $A_c$ . These observations were not compensated for coherence effects as only comparative values were being sought in these studies.

Absorption in the non-bias sputtered coatings increases rapidly as thickness becomes greater. The trend in the bias-sputtered coatings is also an increase in absorption but at an overall lower rate. This could be attributed to the inherent cleaning action of the bias-sputtering method.

While a good bit of scatter is evident in the readings, the bias-sputtered films clearly display lower values. It may also be seen that neither of the absorption curves plotted for the two modes will extrapolate to zero. This could imply a higher absorption in the initially deposited material or an appreciable contribution due to interfacial effects between the coating and the substrate - or possibly a combination of both.

## 2.3 RBS and Auger Analyses

Two experiments were undertaken to allow a closer look at the film/substrate interface and the initially deposited film material.

A series of thin ZnSe coatings was deposited on  $\text{CaF}_2$  in the nominal range of 25 - 175 Å in 25 Å steps. These were evaluated by the Rutherford Backscattering technique in an attempt to determine the stoichiometry of initially deposited ZnSe material.

The results of this evaluation are shown in figure 2, which is a plot of the measured ratio of Zn to Se for each coating thickness. This ratio was found to be in the range 1.05 to 1.18 with an average of 1.13.

This ratio may improve as the film becomes thicker; but since the RBS technique can only be used for very thin films, an alternate method of measurement will have to be found.

Another method of determining the composition of the interface is shown in figure 3. This is a plot of a series of Auger scans through a 4300 Å ZnSe film on  $\text{CaF}_2$ . As the interface is approached and penetrated, the presence of oxygen is clearly evident. The Auger method can thus be used to detect the presence of this element but cannot differentiate between an oxide, a hydroxide, (such as water), or some other oxygen compound.

Regardless, the presence of any contaminant is undesirable and it must be removed from the substrate to afford the coating material the cleanest possible surface on which to deposit.

## 2.4 Sputter-etching Results

One method of cleaning the surface which appears to produce a lower ZnSe film absorption is in-situ sputter-etching. This portion of the study employed exactly the same coating and measurement procedures as used for the bias-sputtered coatings but with a sputter-etching step added. Shown in figure 4 is a semi-log plot of the absorption coefficients of films deposited after the substrates had been sputter-etched for the times shown. All of the coating thicknesses are the same and are approximately half-wave at  $5.3\mu$ . The initial data point represents a non-etched sample used as a control.

Following a 15 second sputter-etch the  $\beta_f$  decreased rather sharply to  $1.1 \text{ cm}^{-1}$ . There was an increase with further etching up to about 2 minutes. A second decrease was found at 4 minutes followed by a rapid rise. Visual inspection of similar  $\text{CaF}_2$  samples etched for the same times and aluminized for Total Integrated Scattering measurements showed that after 16 minutes the surface became roughened and this would contribute to the higher  $\beta_f$  for the last sample.

All of the coatings produced in this study pass the Scotch Tape Test. Two special test samples were fabricated using sputter etch times of 30 seconds and one minute. These were to be tested [2] but no qualitative results were forthcoming since either the adhesive bonding material separated without removing the film from the substrate or, as happened on two trials, a large chunk of the substrate material was torn from the specimen. In no case was the film pulled away from the substrate.



### 3. Conclusions

The absorption of bias-sputtered films has been found to be consistently lower than those deposited by non-bias techniques. RBS evaluation of the initially deposited zinc selenide material has shown that it is rich in zinc by approximately 11%. Oxygen was found at the film/substrate interface of bias-sputtered specimens but its form has not been determined.

In-situ sputter-etching of the specimen surface immediately before coating produced optimum film adhesion and the lowest absorption values measured to date.

### 4. Acknowledgements

The authors wish to gratefully acknowledge the assistance of Dr. Patrick Hemenger of the Air Force Materials Laboratory and Dr. C. E. Christodoulides of the University of Salford, England, for the Rutherford Backscattering Analyses and Dr. W. E. Moddeman of the University of Dayton for the Auger Electron Spectroscopy evaluations.

### 5. References

- [1] Walsh, D.A., Pukite, E.U. and Fenter, J.R., Rev. of Sci. Instru., 47, 8, 932 (1976). [2] Butler, D.W., J. Phys. E., 3, 979 (1970).

### 6. Figures

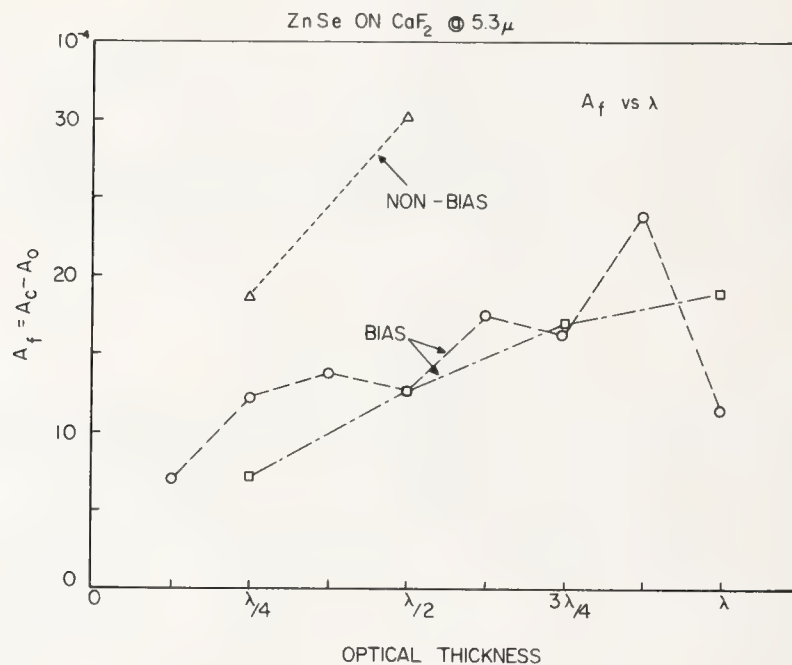


Figure 1. Absorption of sputter-deposited zinc selenide films on non-etched substrate surfaces.

BIAS SPUTTERED ZnSe ON CaF<sub>2</sub>

RBS  $\frac{N_{Zn}}{N_{Se}}$  RATIO vs.  $t$

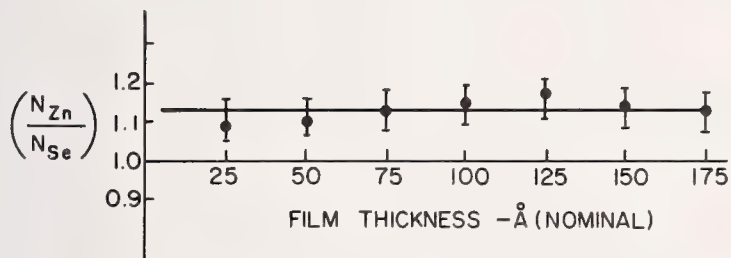


Figure 2. Ratio of zinc to selenium for thin layers of zinc selenide on calcium fluoride by Rutherford Backscattering analysis.

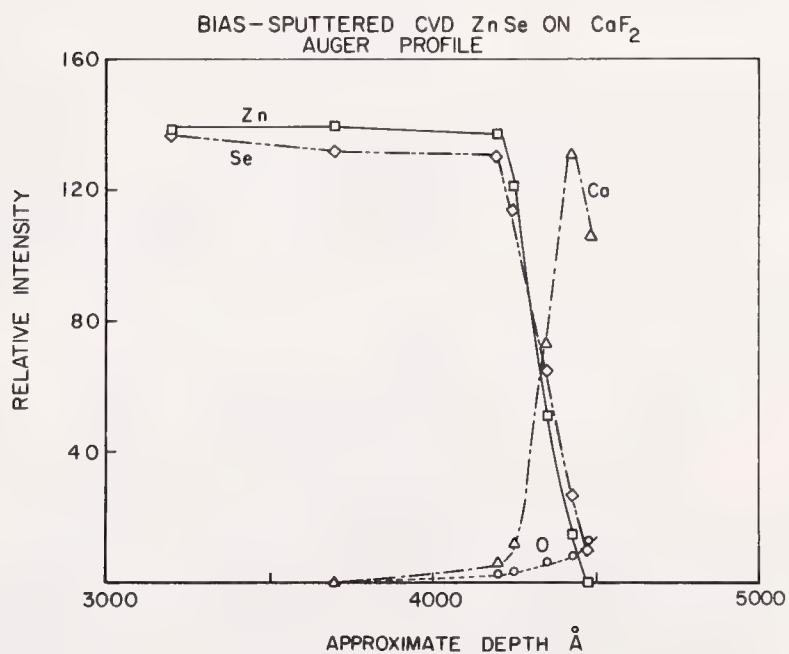


Figure 3. Auger profile of zinc selenide film on calcium fluoride showing presence of oxygen at interface.

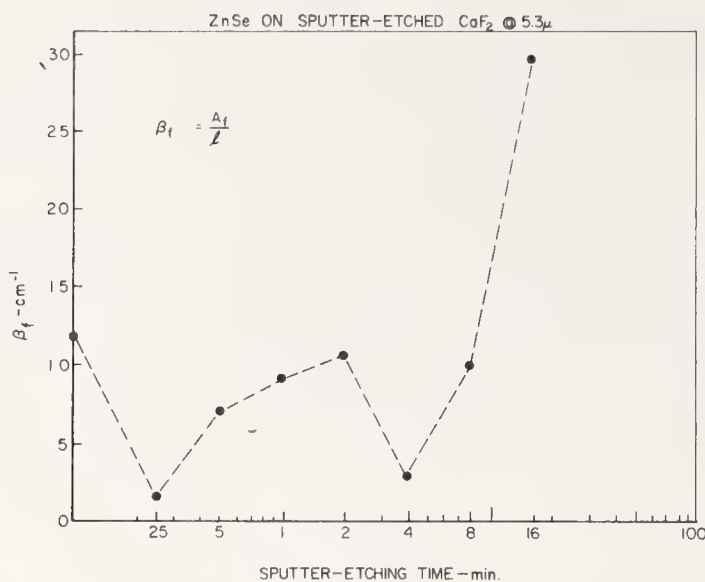


Figure 4. Comparative absorption coefficients for equivalent coated samples based on sputter-etching times.

Table 1. Processing conditions used in the fabrication of coating test specimens

Precoating:

Preheat to 150°C, 5 min. @ 10 $\mu$

Outgas to 1 x 10<sup>-6</sup> Torr

Coating:

Target Voltage = 1000V

Bias Voltage = 50V

R.F. Power = 520W (1.6 W/cm<sup>2</sup>)

Pressure = 10 $\mu$  Argon

Spacing = 7 cm

Etching:

Platform Voltage = 350V

RF Power = 300W (1.0 W/cm<sup>2</sup>)

Pressure/Spacing = as above

COMMENTS ON PAPER BY WALSH AND BERTKE

There was considerable discussion on the conclusion that an 11% excess of zinc existed in the zinc selenide film as determined from Rutherford back-scattering. In answer to a question from the floor, the speaker indicated that the Rutherford back-scattering measurements were carried out with 4 MeV helium ions, and that the accuracy of this technique was estimated to be a few percent. The zinc excess was also noted on the Auger spectrometry for this material, the Auger method however is not quantitative.



# A STUDY OF INFRARED ABSORPTION IN ZINC SELENIDE THIN FILMS\*

David F. O'Brien  
Air Force Materials Laboratory  
Wright-Patterson AFB, Ohio 45433

Zinc Selenide coatings for infrared laser windows have effective absorption coefficients which are three to four orders of magnitude higher than was predicted from bulk material optical constants. Prior growth studies and theoretical descriptions of binary compound deposition indicated that variations of the stoichiometry of the zinc selenide films were a possible cause for the high absorption measured in these coatings. An experimental program was conducted in which the absorption in zinc selenide deposited onto calcium fluoride under a variety of deposition conditions was measured. It was shown that the infrared absorption decreased as the deposition rate was lowered. This directly correlated with theoretical predictions based upon changes in stoichiometry caused by different film deposition conditions. Surface and chemical analyses using state-of-the-art techniques indicated that the most probable cause for the anomalous absorption in the films was an increase in the zinc to selenium ratio which could be controlled to some degree by the proper selection of the vacuum deposition conditions.

Key words: Absorption; dielectric coatings; thin films; zinc selenide.

## Introduction

It has become acknowledged that most commonly used infrared, low absorption coating materials display orders of magnitude differences between the effective absorption coefficients measured in the bulk material and those measured in the thin film form of this same material. Several explanations for the higher absorption in the thin films have been proposed [1]<sup>1</sup>, and all of these appear to have a certain degree of validity. The greatest emphasis seems to have been placed on thin film contamination as being a primary source of the increased absorption. It is somewhat surprising that although a large number of these coating materials are binary compounds eg.  $As_2S_3$ ,  $As_2Se_3$ ,  $KCl$ ,  $ThF_4$ ,  $TlI$ ,  $ZnSe$ , very little emphasis has been placed on investigating whether or not stoichiometric deviations of these materials could be affecting the thin film absorption. This work was undertaken to determine if stoichiometric variations possibly occurring during the thin film deposition of  $ZnSe$  could be identified and related to increased infrared absorption in these coatings.

Karl-Georg Gunther has reported that for depositions involving evaporation of binary compounds where the individual constituents have different vapor pressure, it can be expected that the deposited coating will have a tendency to exhibit an excess of the less volatile material[2]. Zinc is known to have a substantially lower vapor pressure than selenium; therefore, for the particular case of depositions involving  $ZnSe$ , Zn rich coatings might be expected. In describing the deposition process for binary compounds, Gunther indicates that the degree of nonstoichiometry can be affected by three deposition parameters, substrate temperature, deposition rate, and component flux ratio. Specifically, the following behavior can be inferred from his description:

High substrate temperatures tend to produce a more nearly stoichiometric film.

Low deposition rates tend to produce a more nearly stoichiometric film.

An excess of the more volatile component (Se) introduced into the vapor stream increases the probability of producing a stoichiometric film.

## Deposition Studies

The experimental program was designed to investigate if the calorimetrically measured infrared absorption in  $ZnSe$  thin film coatings could be varied by changing the above mentioned deposition parameters, and if so could these variations be correlated to the predicted stoichiometric variations.

---

\* The material reported herein is based on portions of the author's dissertation submitted in partial fulfillment of the requirements for the Doctor of Philosophy degree at the Air Force Institute of Technology, Wright-Patterson Air Force Base, Ohio

1. Figures in brackets indicate the literature references at the end of this paper.

The substrates used in this investigation were 5cm diameter by 1cm thick polycrystalline  $\text{CaF}_2$  manufactured by Harshaw.  $\text{CaF}_2$  was selected for its relative stability (as compared with alkali halides) and for its low absorption coefficient. Each substrate was polished using successively a 1.0, 0.3, and  $0.05\mu\text{m}$   $\text{Al}_2\text{O}_3/\text{H}_2\text{O}$  slurry and subsequently cleaned using a standard procedure described elsewhere[3]. Depositions were carried out in a diffusion pumped vacuum system which with liquid nitrogen trapping maintained a vacuum of  $1.33 \times 10^{-4}$  Pa ( $1 \times 10^{-6}$  Torr). Electron beam evaporation was used since it provided the easiest means for controlling the evaporation rate of the Raytheon CVD ZnSe source material. ZnSe was deposited onto substrates heated to a predetermined temperature between  $20^\circ\text{C}$  and  $255^\circ\text{C}$  and at rates which were varied from 55 to 2000 Å/min. Additionally, some depositions were carried out with excess Se in the vapor stream, accomplished by performing a separate thermal evaporation of high purity elemental selenium simultaneously with the electron beam evaporation of the ZnSe. Coating thicknesses of nominally 0.15, 0.30, 0.60, and  $1.0\mu\text{m}$  were deposited for each of the separate sets of deposition parameters. Deposition rate was monitored by means of a quartz crystal rate monitor, and final film thickness was determined using a Sloan Dektak Surface Profile Measuring Systems.

The use of  $\text{CaF}_2$  as a substrate precluded calorimetric measurements at a wavelength of  $10.6\mu\text{m}$  and alternatives available were limited to a  $5.3\mu\text{m}$  CO system or a  $1.06\mu\text{m}$  Nd:YAG system. The latter was selected when it was found that the  $\text{CaF}_2$  displayed a significantly lower absorption at  $1.06\mu\text{m}$  thus offering a potential increase in the sensitivity of the thin film absorption measurement. The effective absorption coefficient of the ZnSe coating  $\beta_c (\text{cm}^{-1})$  was determined by measuring the absorption  $A$  of the uncoated and the coated substrates using standard calorimetry techniques [4] and dividing the difference of these two values by the film thickness  $t$ . This is expressed as

$$\beta_c = \frac{A_c}{t} = \frac{A_{\text{coated}} - A_{\text{uncoated}}}{t}$$

All calorimetry measurements on the coated substrates were made with the coated surface facing the incident laser beam, and no corrections for coherence effects were used since only comparisons of data from measurements on coatings of similar thickness were made.

The first phase of experimentation was to determine if coating absorption would decrease when ZnSe depositions were made onto heated substrates as would be expected from stoichiometric considerations. Table 1 shows the results of this portion of the study. Comparisons of coating absorption for depositions performed at two different temperatures and at low, intermediate, and high rates were made.

Table 1. Effect of substrate temperature on coating absorption

Rate (Å/sec)	Substrate Temp( $^\circ\text{C}$ )	$A_c/t$ ( $\text{cm}^{-1}$ )	Coating Condition
0.9	76	5.5	Intact
0.9	181	6.3	Crazed
3.6	67	9.3	Intact
2.1	255	No data	Crazed
17.0	22	29.4	Intact
14.0	75	30.7	Intact

The data in table 1 show that the results of this phase were inconclusive. This was due to two factors. In the two cases where high substrate temperatures were used,  $181^\circ\text{C}$  and  $255^\circ\text{C}$ , thermal expansion coefficient mismatch between the ZnSe coating and the  $\text{CaF}_2$  substrate caused crazing to occur which either completely prevented a calorimetry measurement or rendered the data invalid. The third entry in table 1 shows the results of an attempt to make a comparison between a room temperature deposition and a deposition onto a slightly heated substrate which presumably would have reduced the problems caused by the thermal mismatch. The absorption data from these depositions were essentially identical. It is possible that this negative result was caused by the two substrate temperatures being too close to reveal the sought after trend.

The second phase of the experiment was designed to determine if a correlation existed between the measured coating absorption and the predicted variations of film stoichiometry based upon differences in deposition rate. A positive correlation would be indicated by a tendency for low deposition rates to produce lower absorbing films. In this case, the  $\text{CaF}_2$  substrates were all heated to approximately



75°C, a value selected as being the highest temperature at which integrity of the film could be assured and which provided a heated surface which would decrease the probability of having condensable impurities deposited in the films. Deposition rates between 55 and 2000 Å/min were used and the measured 1.06µm absorption coefficient for each coating was determined and plotted against the deposition rate. Figure 1 displays the results of this comparison and includes a third degree polynomial fit to the data. Clearly evident from the figure is the definite decrease in absorption at the lower deposition rates. This agrees directly with predictions which attribute changes in stoichiometry to changes in deposition rate.

As a final attempt at establishing the correlation between coating absorption and stoichiometry, evaporations were made using excess Se in the vapor stream. Since predictions based upon the Gunther model indicated that an increase in the Se/Zn flux ratio would aid in producing a more nearly stoichiometric film, it was felt that the addition of excess Se would result in a relative decrease in coating absorption. Thermal evaporation of high purity Se from a tantalum boat was used to provide the excess Se in the evaporant stream. Electron beam evaporation of the ZnSe was conducted simultaneously with the Se evaporation, but because of geometry and control factors only a qualitative estimate of the amount of excess Se could be made. It was estimated that from 10 to 30 percent excess Se was being introduced. Figure 2 shows the results of absorption measurements made on the coatings where, as in the previous study, depositions were made at several different rates. Included in the figure is the curve previously shown in figure 1 for the case of no excess Se. The results show that except for the lowest deposition rates an improvement in coating absorption was achieved by providing the excess Se. Again this agrees with predictions based upon stoichiometry behavior.

#### Surface Chemical Analyses

The results of this study produced evidence supporting predictions that related theoretical stoichiometric deviations to absorption within the coatings. It was still desirable, however, to directly confirm that these stoichiometric deviations were actually occurring within the films. Several surface chemical analysis techniques were employed in an attempt to accomplish this. Prior to making these measurements, estimates were made to determine, on an order of magnitude scale, what amount of stoichiometric deviation would be required to increase the ZnSe absorption to the levels observed in the thin film coatings. The estimates were made using an approach described by Sparks [5] where, in this case, the absorption was attributed to microscopic Zn inclusions existing in a stoichiometric ZnSe medium. Based on this model, it was estimated that from 0.01 to 0.1 percent excess Zn would be sufficient to increase the ZnSe absorption coefficient from a value at 1.06µm of approximately  $0.02 \text{ cm}^{-1}$  to a value greater than  $1 \text{ cm}^{-1}$  which was typical of the increase measured in the coatings.

Five different surface analysis techniques were used in an attempt to measure stoichiometric deviations in the films. These were x-ray fluorescence, electron microprobe, Rutherford backscattering(RBS), electron spectroscopy for chemical analyses (ESCA), and Auger electron spectroscopy (AES); the latter two methods included an ion sputtering attachment which provided a capability for performing profile analyses of the films. One drawback existed, however, for all of the techniques. For each one the estimated lower limit of detection was at best 0.001 atomic fractions, and it could be presumed that it was even higher than this for measurements of stoichiometric variations. Since this lower limit was the same order of magnitude as the highest estimated amount of excess Zn required to cause the observed level of ZnSe thin film absorption, measurement of the stoichiometric deviations were expected to be rather difficult. Table 2, which lists the conclusions based on results of these measurements, bears this expectation out.

Table 2. Summary of stoichiometry analyses

<u>Technique</u>	<u>Dependence of Zn to Se Ratio on Deposition Rate</u>
X-Ray Fluorescence	Possibly Higher for High Rate
Electron Microprobe	Possibly Higher for High Rate
RBS	No Dependence Detected
ESCA	Higher for High Rates; Variation Within a Single Film Noted
AES	No Dependence Detected; Variation Within a Single Film Noted

In each case measurements were made on two or more coatings deposited at different rates. Because of ambiguities in the background corrections, interpretations of the x-ray fluorescence and the electron microprobe results are very qualitative. Although still qualitative, the ESCA and AES measurements provided the most interesting results. Figure 3 gives an example of data from one AES measurement and reveals perhaps one of the most significant findings resulting from the profile analyses of both the AES and the ESCA measurements. The figure shows only the final portion of an AES analysis of a ZnSe coating



where the rapid decrease in the Zn and Se concentration is indicative of the fact that the coating/substrate interface had been penetrated by the ion beam. The fact that the overall Zn level in this figure appears higher than that of the Se is only a result of the measurement technique and does not indicate a difference in concentration. Evident in this data, however, is the indication of a significant point to point variation in the Zn concentration which is far greater than any variation in the Se concentration. From these results it was felt that the nonstoichiometry of the ZnSe coatings existed not in a uniform manner throughout the film but rather as local variations in the Zn concentration and that changes in the deposition parameters affect the magnitude of these variations.

### Conclusions

The observed behavior of ZnSe coating absorption at a wavelength of  $1.06\mu\text{m}$  as a function of deposition parameters was found to be consistent with a model which explains the behavior on stoichiometric variations. This conclusion is based on a comparison of changes observed in the measured thin film absorption with predicted stoichiometry deviations and on qualitative measurements of coating stoichiometry using several surface analysis techniques. The results of this study indicate that there are three controllable deposition parameters available which affect and, hence, can aid in minimizing the absorption in ZnSe coatings. These parameters and their relationship to absorption are

Deposition Rate:	Lowest rates produced lowest absorbing films.
Se/Zn Flux Ratio:	Inclusion of excess Se in vapor stream produced lower absorbing films
Substrate Temperature:	High substrate temperatures should aid in lowering absorption. Not confirmed because of thermal expansion problems.

Finally, it should be noted that the AES and ESCA profile measurements of the Zn and Se concentrations within the coatings indicated that the stoichiometry variations were found to exist as point to point variations in the Se/Zn ratio and not as a uniform deviation throughout the film. This would imply that the absorption of infrared radiation, which is likewise affected by the distribution of Zn and Se, occurs nonuniformly throughout the coating and is concentrated at localized high absorption points.

### References

- [1] Sparks, M., Theoretical Studies of High Power Infrared Window Materials. Seventh Technical Report 30 June 1976, DARPA Order No. 1969 Amendment No. 7, Program Code No. 6D10, (1976), pp 206-217.
- [2] Gunther, Karl Georg, "Interfacial and Condensation Processes Occurring with Multicomponent Vapors," in The Use of Thin Films in Physical Investigations. J. C. Andrews ed., Academic Press, New York (1966).
- [3] O'Brien, David F., "Infrared Absorption in Zinc Selenide Thin Films," to be published as Air Force Materials Laboratory Technical Report.
- [4] See for example Kraatz, P. and Mendoza, P. J. "CO Laser Calorimetry for Surface and Coating Evaluation," in Proc. Fourth Conf. on Infrared Laser Window Materials, 1974, C. R. Andrews and C. L. Strecker, eds. Defense Advanced Research Projects Agency, Arlington, Va., (1975), pp 214-230.
- [5] Sparks, M., Theoretical Studies of High Power Infrared Window Materials. Final Technical Report December 1972, ARPA Order No. 1969-Program Code No. 2D10 (1972), pp 90-110.

# FIGURES

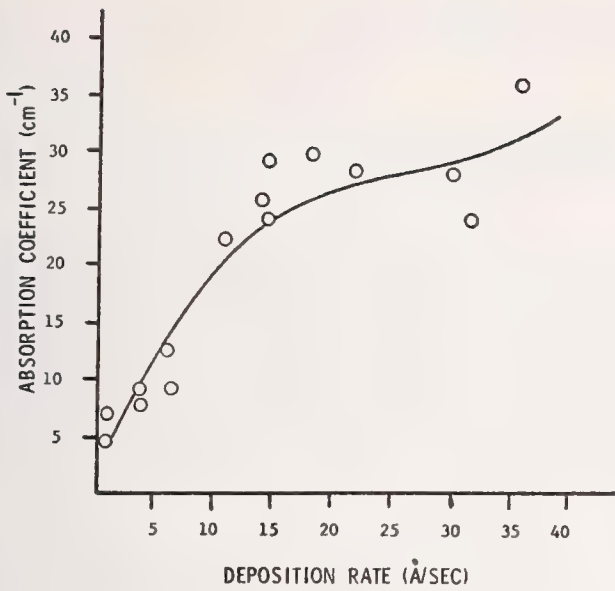


Figure 1. Coating absorption coefficient versus deposition rate of ZnSe.

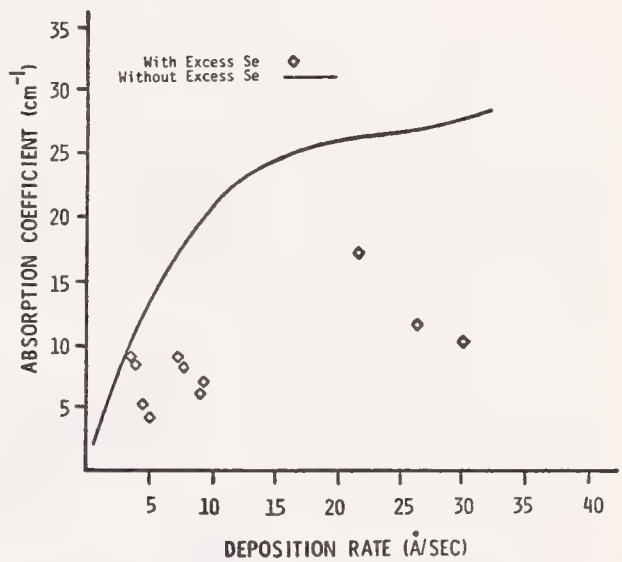


Figure 2. Coating absorption coefficient versus deposition rate of ZnSe with excess selenium in the vapor stream.

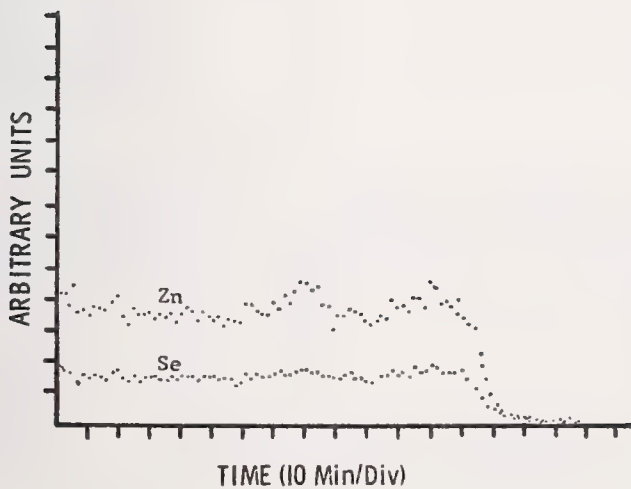


Figure 3. Auger electron profile analysis of ZnSe thin film showing Zn variations.

THE DESIGN AND OPERATION OF A PRECISE, HIGH SENSITIVITY ADIABATIC LASER  
CALORIMETER FOR WINDOW AND MIRROR MATERIAL EVALUATION\*

D. L. Decker and P. A. Temple  
Physics Division, Michelson Laboratories  
Naval Weapons Center, China Lake, California 93555

Important design details of a vacuum calorimeter intended for use with low absorption materials and using only low power laser illumination are given. Much attention has been given to the requirements for high sensitivity and to sources of systematic error including bulk and surface scatter, resulting in a number of improvements over existing instruments. Calorimetric measurements are now possible in the visible and ultraviolet, and as a function of temperature. The calorimeter output is capable of absolute electrical calibration, which is ordinarily an integral part of an absorption measurement sequence. The system thermometry is sensitive to a change in temperature of  $2 \times 10^{-5}^{\circ}\text{C}$ . For a typical 1.5-inch-diameter sample, this corresponds to an absorptance sensitivity in the very low  $10^{-5}$  range using one watt of laser power. The design of the instrument permits the variation in absorptance across the sample to be determined. This paper presents examples of the operational capability of the instrument.

Key words: Absorption; calorimeter; laser; scattering.

This paper discusses the design philosophy, some construction details and actual performance of a very sensitive laser calorimeter. The goals in the design of this instrument were to provide accurate, absolute absorptance data as a function of temperature in the  $10^{-3}$  to  $10^{-5}$  range for window or mirror materials, using only low power ( $< 1$  watt) laser sources over a wide range in wavelengths, and to provide the capability to spatially scan the sample. Since the rate at which energy is dissipated in the sample during laser irradiation can be as low as a few tens of microwatts, it is clear that very careful attention to heat flow and to thermometry is mandatory. The design of necessity must approach an adiabatic ideal, requiring control over both radiation and conduction heat exchange from the sample to its surroundings. Since the heat flows are so small, stray laser radiation reflected from calorimeter windows, or scattered from the sample or baffles must be carefully accounted for and minimized to the extent possible. In addition to minimizing systematic error sources, it was felt that some form of absolute calibration was necessary to reach the accuracy levels required. This design approach thus differs from the usual rate type calorimeter, and although much more difficult to construct, has capabilities and advantages which have not been heretofore available.

The design which has been implemented is based upon techniques similar to those employed in low temperature specific heat calorimetry. The sample is in vacuum at a pressure of  $10^{-6}$  Torr, and is surrounded by a low emissivity isothermal enclosure which is temperature controlled to  $\pm 10^{-3}^{\circ}\text{C}$ . The sample, which can be as large as 2 inches in diameter and 3/8-inch thick, is suspended in this can by a clamp ring supported by very fine steel wires. The sample temperature sensing thermistor and a calibration resistor are thermally connected to the clamp ring and hence the sample (see fig. 1). The thermal link from the sample to the isothermal can has a conductance of  $< 10^{-3}$  watts/ $^{\circ}\text{C}$ , with radiation being a factor of five or so more important than conduction for temperatures near room temperature. The input window to the calorimeter is in fact a lens which focusses the laser beam onto the sample, the radiation passing into and out of the isothermal can through small holes. The calorimeter output is taken as the incremental change in sample temperature accompanying a laser irradiation of known beam power and duration. This incremental response is heating rate independent to very high order. Absolute electrical calibration is obtained by dissipating a known quantity of joule heat in the resistor attached to the ring (see fig. 2). The transient response of the system to such a heat input is obviously different than if the heat were deposited in the actual sample by laser irradiation. But since to high accuracy both processes are adiabatic, the final equilibrium temperature increment is independent of the means, rate or location of heat input. This is shown clearly in figure 3 where the same quantity of joule heat is supplied to the calibration resistor on the clamp ring and to an identical resistor epoxied into a hole in the center of a fused quartz disc. The fused quartz sample was chosen as a "worst case" since this material has a very small thermal conductivity. The incremental temperatures measured in these two cases differ by only 2%, and in fact agree very well with a calculation of the theoretical temperature increment using the calculated heat capacity of the sample and addenda and the sensitivity of the thermistor (see Appendix). Absolute electrical calibration of the calorimeter response is thus possible, making it unnecessary to know the sample mass, specific heat or thermal diffusivity.

\* Work supported by Defense Advanced Research Projects Agency and NWC Independent Research Funds.



Since the equilibrium temperature response is rate independent, it is unnecessary to irradiate the sample only with a simple fixed geometry, and in fact the sample can be scanned point by point from one side to the other by the beam, providing information on the spatial uniformity of the sample absorptance with a resolution limited only by the laser beam diameter.

Figure 4 shows the spatial response of a very uniform coated  $\text{CaF}_2$  window with an average absorptance of  $4.8 \times 10^{-4}$  and a maximum spatial variation of  $0.6 \times 10^{-4}/\text{mm}$ . Also shown on figure 4 is the excellent repeatability of the measurement, the average absorptance difference between runs 1 and 2 being less than  $1 \times 10^{-5}$ . The  $3.8 \mu\text{m}$  laser power used in these measurements was less than 1 watt.

The spatial scan is actually accomplished by moving the isothermal can with respect to the beam. This same motion permits the sample and can to be withdrawn completely from the beam, so that after calibration of the losses in the windows, a direct measure of the laser beam power at the sample is possible using a power meter at the output window of the instrument.

Figure 5 shows a typical run which includes a preliminary calibration. To compute the absorptance one needs merely to ratio the incremental temperature response to laser irradiation  $\Delta T_{\text{laser}}$  to that of calibration  $\Delta T_{\text{cal}}$ . One then computes the energy deposited during irradiation  $\Delta Q_{\text{laser}}$ :

$$\Delta Q_{\text{laser}} = \frac{\Delta T_{\text{laser}}}{\Delta T_{\text{cal}}} \times \Delta Q_{\text{cal}},$$

where  $\Delta Q_{\text{cal}}$  is just the calibration heat increment. If the laser power is  $P_{\text{laser}}$ , averaged over the irradiation time  $\Delta t_{\text{laser}}$ , the absorptance  $A$  is just:

$$A = \frac{\Delta Q_{\text{laser}}}{P_{\text{laser}} \times \Delta t_{\text{laser}}}.$$

For the data in figure 5,

$$A = \frac{4.3}{5.4} \times \frac{.051}{1.13 \times 120} = 3.00 \times 10^{-4}.$$

There are two sources of systematic error in this calorimeter design which are important: (1) stray light which is absorbed on the clamp ring giving a false signal and (2) improper calibration of the external power meter. The use of an electrically calibratable power meter such as the Scientech 361 is a step in the right direction, but the absorptance of the disc in this power meter is usually taken more or less on faith as being 0.96. This assumption is not easily verified and constitutes significant uncertainty in the present approach.

The stray light problem is present in calorimeters of all types, but especially in vacuum calorimeters because of the additional sources of scattered and reflected light coming from the entrance and exit windows which are necessarily present. Carefully designed and aligned baffles can solve these problems and the performance of the system can be directly verified by illuminating a sample which has a hole through which the beam passes. Figure 6 is a run showing that under such conditions there is no detectable heating of the sample or ring. This test seems a trivial one, but is highly recommended as one of the important "proof tests" of any calorimeter.

The other major source of stray light is light scattered from the surface or bulk of the sample itself. For many samples most of the scattered light comes from the surfaces, and it is possible to absorb much of this light directly in conical receivers attached to the isothermal can. However, bulk scatter is potentially more of a problem, with light scattered possibly directly to the clamp ring. Solutions to this problem include making the ring from material of lower absorption and limiting the area of the ring which looks into the sample. Sample scatter becomes much more serious as the wavelength is reduced, but as is demonstrated in a companion paper given at this conference by the same authors, the present instrument with no additional modification is capable of the same high performance reported here at wavelengths into the near UV.

All measurements reported here were made at a temperature near  $24.5^\circ\text{C}$ . However, since the sample "sees" primarily only its isothermal enclosure, similar measurements to those reported here can be made at any temperature at which the enclosure temperature can be regulated. For the present apparatus this temperature range extends from laboratory ambient ( $\sim 24^\circ\text{C}$ ) to  $100^\circ\text{C}$ . This a capability not found in the usual rate type calorimeter in which the sample is not thermally shielded. In such a device, measurements only very near to the ambient temperature are possible.

The calorimeter described in this paper meets all original design goals, and has a sensitivity using laser power levels of one watt of  $\sim 10^{-5}$  in absorptance. The calorimeter itself is capable of absolute electrical calibration. The major sources of systematic error are associated with the calibration of the external laser power meter and uncontrolled sample scatter and limit the absolute accuracy of the measurements to perhaps  $\pm 5\%$  for high quality, low scatter samples. Careful attention

to the stray light problem permits the use of this instrument into the near UV with the same accuracy and sensitivity reported here for IR measurements.

#### Appendix

The following is a calculation of the theoretical equilibrium temperature response of the adiabatic calorimeter with the quartz sample as reported in figure 3 of the text.

1) Calculation of the heat capacity of the sample and addenda

Addenda (mostly aluminum alloy) mass, 6.18 gm  
Heat capacity of addenda, 6.18 gm x .90 J/gm°C = 5.56 J/°C  
Sample mass, 23.52 gm  
Heat capacity of sample, 23.52 gm x .787 J/gm°C = 18.50 J/°C

Total Heat Capacity, 24.1 J/°C

2) Calculation of thermistor bridge sensitivity

For an equal arm bridge with arm resistance R, the output voltage  $\Delta V$  near balance is

$$\Delta V = \frac{1}{4} V_o \frac{\Delta R}{R}, \text{ where } \Delta R \text{ is the out-of-balance resistance of one arm, and } V_o \text{ is the bridge supply voltage.}$$

or

$$\frac{\Delta V}{\Delta T} = \frac{1}{4} V_o \frac{1}{R} \frac{\Delta R}{\Delta T}$$

for the particular thermistor used (at 35°C)

$$\frac{1}{R} \frac{\Delta R}{\Delta T} = 0.0400/^\circ\text{C}$$

so

$$\frac{\Delta V}{\Delta T} = \frac{1}{4} (1.35) (0.0400) = 0.0135 \text{ V}/^\circ\text{C}$$

3) Calculation of the system response

For the runs in figure 3 an average incremental voltage of 60  $\mu\text{V}$  was seen

$$60 \times 10^{-6} \times \frac{1}{0.0135} = 4.44 \times 10^{-3} ^\circ\text{C}$$

$$4.44 \times 10^{-3} \times 24.1 = 0.107 \text{ J}$$

Computed Heat Input, 0.107 J

4) Calculation of the calibration heat input

5.856 V was applied across the calibration resistor (31.14 k $\Omega$ ) for 100 seconds.  
The heat input was therefore

$$\frac{(5.856)^2}{31.14 \times 10^3} \times 10^2 = 0.110 \text{ J}$$

Calibration Heat Input, 0.110 J

5) Intercomparison of results

Computed heat input, 0.107 J  
Actual heat input, 0.110 J

Difference is then 0.003 J or 2.77%.

## Figures



Figure 1. Two views of the adiabatic calorimeter with the vacuum container open. The view on the right shows the isothermal can with the top in place, showing the sliding top with beam exit aperture and the chain and sprocket translation mechanism. The view on the left is with this cover removed, showing details of the interior including sample clamp ring.

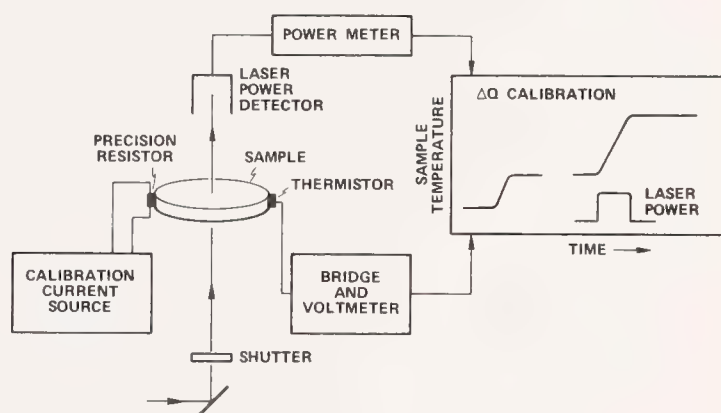


Figure 2. Operational schematic of the adiabatic calorimeter. The calibration resistor and temperature sensing thermistor are in intimate thermal contact with the sample rim. The system response to either a calibration pulse or to sample absorption of laser energy is an incremental temperature change which is as shown.

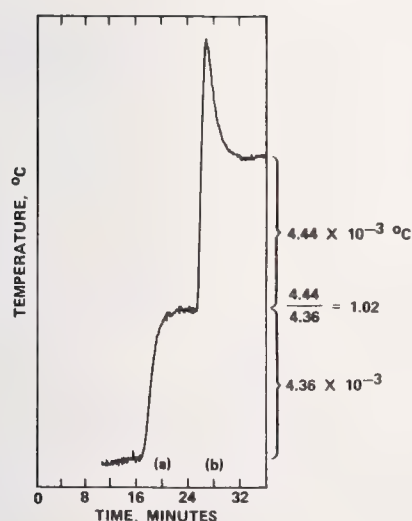


Figure 3. This data indicates the effect of depositing joule heat at the center of a fused quartz sample (a) or at the rim on the clamp ring (b). The equilibrium response differs by only 2% in these two cases, indicating that the system response to high accuracy is indeed adiabatic.



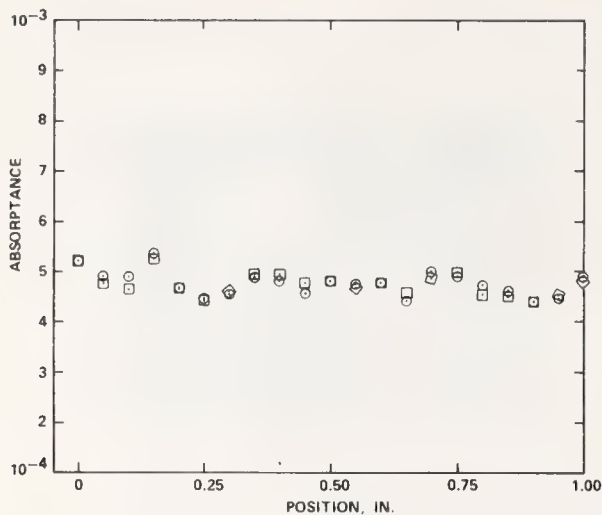


Figure 4. Spatial variation of the absorbance of a Northrop-coated  $\text{CaF}_2$  window sample 1-cm thick at  $3.8 \mu\text{m}$ . The average absorbance is  $4.8 \times 10^{-4}$  and the maximum spatial variation is  $.6 \times 10^{-4}/\text{mm}$ . Two different runs are plotted which were made one day apart:  $\odot$  first pass;  $\square$  second pass. Beam diameter ( $1/e^2$  points) was 1.35 mm.

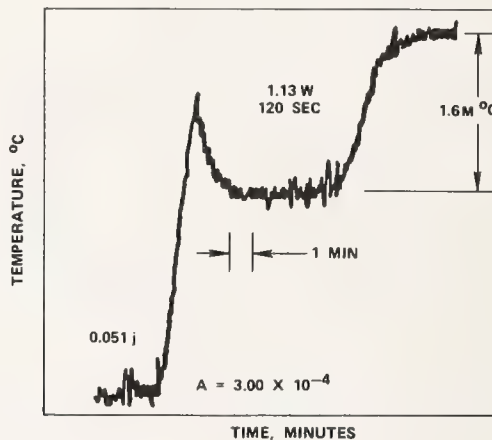


Figure 5. Shown in this figure is a typical measurement run on a  $\text{CaF}_2$  sample at  $3.8 \mu\text{m}$  which includes a preliminary calibration. The absorbance computed directly from this data is  $3.00 \times 10^{-4}$  (see text).

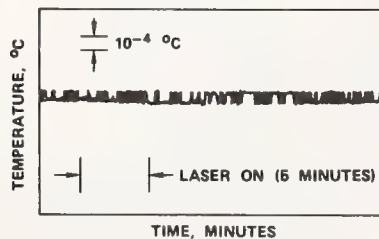


Figure 6. No detectable heating of the sample or ring is evident in this data, taken by allowing the beam to pass through a hole in the sample. This is a very sensitive test for the presence of unwanted stray laser light in the instrument originating at windows or baffles.

MODULATED LIGHT ELLIPSOMETER MEASUREMENTS OF STRAIN-INDUCED  
ANISOTROPY IN THE REFRACTIVE INDEX OF  $\text{As}_2\text{Se}_3$  AND  $\text{As}_2\text{S}_3$   
FILMS ON KCl SUBSTRATES AT  $10.6 \mu\text{m}^*$

M.E. Pedinoff and M. Braunstein  
Hughes Research Laboratories  
Malibu, California 90265

and

O.M. Stafsudd  
Engineering Department  
University of California at Los Angeles

The measurement of strain-induced anisotropy in the refractive index of thin films by means of an Elasto-optic modulated light ellipsometer is discussed.

Ellipsometers of this type yield refractive index information indirectly in terms of ratios of signals  $V_\omega/V_{dc}$  ( $R_1$ ) and  $V_{2\omega}/V_{dc}$  ( $R_2$ ) where  $\omega$  is the modulation frequency.

Computational routines have been developed that (differentially) relate changes in film and substrate refractive index to changes in the signal ratios  $R_1$  and  $R_2$ . These calculations enable us to estimate the anisotropic change in the refractive index,  $\Delta n$ , of an optical film due to a unidirectional stress applied to the substrate. Assumed anisotropies of 1%, give signal ratio changes of 1% to 120%, depending on the experimental conditions. Preliminary ellipsometric measurements show anisotropies of 0.6% generated in films of  $\text{As}_2\text{S}_3$  and  $\text{As}_2\text{Se}_3$  on KCl by strains of  $4 \times 10^{-5}$  induced in the substrate.

An exact calculation of the change in signal ratios  $R_1$  and  $R_2$  was obtained using D. Den Englestone's model of reflection from a uniaxial anisotropic film with the strain axis in the film orthogonal to the plane of incidence.

The presence of large refractive index anisotropy cannot be discerned from measurements made on a single film thickness sample by ellipsometric techniques. Experimental data is presented for various thickness samples.

Key words: Anisotropy; ellipsometer; infrared; refractive index.

#### Introduction

The measurement of strain induced anisotropy in the refractive index of thin films by means of an Elasto-optic modulated light ellipsometer will be discussed.

Ellipsometers of this type [1,2,3,4] yield refractive index information indirectly in terms of ratios of signals  $V_\omega/V_{dc}$  ( $R_1$ ) and  $V_{2\omega}/V_{dc}$  ( $R_2$ ) where  $\omega$  is the modulation frequency. These ratios are used in a suitable set of equations [1,2] to calculate the equivalent sets of  $\Delta$  and  $\psi$  which in turn are used in conventional computer programs [5] to calculate the refractive index of substrates and the refractive index and thickness of films.

Computational routines [6] have been developed that (differentially) relate changes in film and substrate refractive index to changes in the signal ratios  $R_1$  and  $R_2$ . These calculations enable us to estimate the anisotropic change in the refractive index,  $\Delta n$ , of an optical film due to a unidirectional stress applied to the substrate, from a measurement of the signal ratio changes  $\Delta R_1$  and  $\Delta R_2$ .

An exact calculation of the change in signal ratios  $R_1$  and  $R_2$  has also been obtained using a variation of D. Den Englestone's [7] model of electromagnetic reflection from a uniaxial anisotropic film. In this case, the optic axis lies in the plane of the film and is orthogonal to the plane of incidence. Assumed anisotropies of 1%, give rise to signal ratio changes of 10% to 300%, depending on the film thickness, film index, and the angle of incidence. Preliminary ellipsometric measurements on this effect show that anisotropies of the order of 1/2% have been generated in films of  $\text{As}_2\text{S}_3$  on KCl by strains of the order of  $2.5 \times 10^{-5}$  piezoelectrically induced in the substrate.

\*Sponsored by the Defense Advanced Research Projects Agency and administered by RADC/ETSO, Hanscom Air Force Base, Massachusetts 07131.

1. Figures in brackets indicate the literature references at the end of this paper.

In those cases where the film is deposited on the substrate at high temperatures and then allowed to cool to room temperature, thermal expansion coefficient differences between the film and the substrate can give rise to a uniaxial anisotropy in which the optic axis is orthogonal to the plane of the film. In this "perpendicular" anisotropy, the signal ratios  $R_1$  and  $R_2$  will show a different dependence on film thickness than the signal ratios of the isotropic case. We have found that the plots of  $R_1$  versus  $R_2$  as a function of angle of incidence as a parameter, were not useful in separating isotropic and anisotropic effects. However, when the signal ratios  $R_1$  and  $R_2$  are plotted at the constant angle of incidence using the film thickness as a parameter, the cases of an isotropic film and a film with 10% anisotropy can easily be resolved. This method of measurement of perpendicular optical anisotropy requires that the measured signal ratio data be plotted on a theoretically calculated chart of the signal ratios for several values of anisotropy and film thickness. The curve which best fits the data is then the best estimate of the anisotropy. It is feasible but non-trivial to program the computer to find that set of film thickness and refractive indices which best fit the data.

#### Analysis

Analysis of an anisotropic film has been approached by several workers 7,8 and in general is very difficult due to the admixture of r and s polarized fields by the anisotropy of the film. However, a more tractable problem occurs if the film exhibits uniaxial properties and if the unique axis is either perpendicular to the surface of the film (perpendicular case) or parallel to the plane of the film and orthogonal to the plane of incidence (planar case). Using the coordinate system of figure 1 for these two cases, the index tensor can be expressed as:

$$\bar{N} = \begin{pmatrix} N_{or} & 0 & 0 \\ 0 & N_{or} & 0 \\ 0 & 0 & N_{ex} \end{pmatrix} \quad \text{for the perpendicular case}$$

$$\bar{N} = \begin{pmatrix} N_{ex} & 0 & 0 \\ 0 & N_{or} & 0 \\ 0 & 0 & N_{ex} \end{pmatrix} \quad \text{for the planar case.}$$

We will assume that the films and substrates are transparent in all cases.

#### Planar Anisotropy

Let us first examine the planar case (fig. 1). To calculate the reflection coefficients for the r and s polarizations of the film substrate system requires calculating the fresnel coefficients of the interfaces and the phase factor associated with traversal of the film for each polarization. At the first interface (air - film), the reflection coefficients are of the form:

$$r_{\perp}^{(1)} = \frac{\cos \phi_1 - N_{ex} \cos \phi_{ex}}{\cos \phi_1 + N_{ex} \cos \phi_{ex}} \quad (1)$$

$$r_{\parallel}^{(1)} = \frac{\cos \phi_{or} - N_{or} \cos \phi_1}{\cos \phi_{or} + N_{or} \cos \phi_1} \quad (2)$$

at the film-substrate interface.

$$r_{\perp}^{(2)} = \frac{N_{ex} \cos \phi_{ex} - N_s \cos \phi_3}{N_{ex} \cos \phi_{ex} + N_s \cos \phi_3} \quad (3)$$

$$r_{\parallel}^{(2)} = \frac{N_{or} \cos \phi_3 - N_s \cos \phi_{or}}{N_{or} \cos \phi_3 + N_s \cos \phi_{or}} \quad (4)$$



The phase factors associated with the two polarizations are

$$\beta_{\perp} = \frac{2\pi F t}{\lambda} \left( N_{\text{ex}}^2 - \sin^2 \phi_1 \right)^{1/2} \quad (5)$$

$$\beta_{\parallel} = \frac{2\pi F t}{\lambda} N_{\text{or}} \cos \phi_{\text{or}} \quad (6)$$

The total reflection coefficients can then be calculated from:

$$R_{\perp} = \frac{r_{\perp}^{(1)} + r_{\perp}^{(2)} e^{-2i\beta}}{1 + r_{\perp}^{(1)} r_{\perp}^{(2)} e^{-2i\beta}} \quad (7)$$

and

$$R_{\parallel} = \frac{r_{\parallel}^{(1)} + r_{\parallel}^{(2)} e^{-2i\beta_{\parallel}}}{1 + r_{\parallel}^{(1)} r_{\parallel}^{(2)} e^{-2i\beta_{\parallel}}} \quad (8)$$

All angles other than  $\phi_1$  can be eliminated from  $R_{\perp}$  and  $R_{\parallel}$  by using Snell's law:

$$\sin \phi_1 = N_{\text{or}} \sin \phi_{\text{or}} = N_{\text{ex}} \sin \phi_{\text{ex}} = N_s \sin \phi_3 \quad (9)$$

The ratio of  $R_{\parallel}$  to  $R_{\perp}$  can be used to find the usual ellipsometric variables  $\Delta$  and  $\psi$  from:

$$\frac{R_{\parallel}}{R_{\perp}} = \tan \psi e^{i\Delta} \quad (10)$$

The observable signal ratios  $R_1$ ,  $R_2$  can then be calculated directly from  $R_{\parallel}$  and  $R_{\perp}$  or from  $\Delta$  and  $\psi$  as defined above [1,2].

The results shown in figure 2 were obtained by calculating the  $R_1$ ,  $R_2$  parameters of a typical isotropic film (such as ZnSe on KCl) as a function of thickness or angle of incidence and then comparing it to a film of moderately strong anisotropy (e.g.,  $N_{\text{ex}} = 1.1 N_{\text{or}}$ ). It is somewhat more enlightening, particularly for smaller anisotropies (e.g., 1%), to plot  $R_1$  and  $R_2$  separately as functions of angle of incidence, as shown in figures 3,4,5, and 6. The parameter most easily observed experimentally is the change in  $R_1$  or  $R_2$  (i.e.,  $\Delta R_1$  or  $\Delta R_2$ ) caused by stress-induced anisotropy. Therefore, we have also plotted  $\Delta R_1/R_1$  and  $\Delta R_2/R_2$  as functions of angle of incidence in figures 3,4,5, and 6.

If a stress orthogonal to the plane of incidence is applied to the substrate film combination, anisotropy can be induced in the film index. The form of this anisotropy corresponds to our model of the planar case.

In principle, an unstressed film could be measured, a clamp (or equivalent) used to stress the film in a fixture, and then the film remeasured. The problem with this approach is that thermal effects in the fixture and additional experimental uncertainties limit the accuracy of the results. However, if the stress on the film is dynamically changed during the experiment, then the change in  $R_1$  and  $R_2$  can be easily and unambiguously measured. The change in stress and associated strain can be produced by piezoelectric transducers and measured by a strain gauge. Figures 3 and 4 represent a film of  $\text{As}_2\text{Se}_3$  ( $\lambda/4$ ) thickness on KCl and figures 5 and 6 represent  $\text{As}_2\text{S}_3$  ( $\lambda/4$ ) thickness on KCl. Figures 3 and 5 and figures 4 and 6 indicate the expected fractional change in  $R_1$  and  $R_2$ , respectively, as functions of angle of incidence. The assumed change in the index of refraction in each case is 1%. The curves show that there exists an optimum range in the angle of incidence for the measurement of this effect.

The results of our first series of measurements on planar anisotropy generated by an externally applied strain are shown in table 1. In this experiment, the strain was generated in the sample by a piezoelectric transducer and monitored by a piezoresistive strain gauge. One sample consisted of a film of  $\text{As}_2\text{S}_3$  on a KCl substrate. The mechanically induced strain in the substrate and the film was  $2.45 \times 10^{-5}$  and the attendant fractional change in refractive index was  $0.006 \pm 0.0003$ . Using these values, the experimental strain optic constant [11] defined as  $-2(\Delta N/N^3)(\Delta l/l)$  was found to be  $89 \pm 10$ . This thin-film strain optic value is more than two orders of magnitude larger than the bulk strain optic values measured at  $1.15 \mu\text{m}$  (0.31); similar results were obtained for the  $\text{As}_2\text{Se}_3$  samples.

The typical maximum values for stress in optical films [9], observed by other methods, can be of the order of  $10^9$  dyne/cm<sup>2</sup>. By assuming a stress value of  $10^7$  dyne/cm<sup>2</sup> and  $1.6 \times 10^{10}$  dyne/cm<sup>2</sup> for

Young's modulus in  $\text{As}_2\text{S}_3$  the strain in a typical film can be estimated to be as large as  $6 \times 10^{-4}$ . Using this value for the strain and the strain optic constant empirically determined above, the expected change in refractive index  $\Delta N/N$  due to the thermal expansion coefficient mismatch effect is equal to 0.14. This externally induced change in refractive index is much larger than the sample-to-sample variation observed in our conventional modulated light ellipsometer measurements of the refractive indices of  $\text{As}_2\text{S}_3$  films. However, significant sample-to-sample variations were observed in the measured refractive index of  $\text{As}_2\text{Se}_3$  films on KCl substrates. We have attributed these effects to strain-induced anisotropic, and we shall show that the existence of moderate to large perpendicular anisotropies are essentially undetectable ellipsometrically in a single-thickness film.

#### Perpendicular Anisotropy

A summary of the results of our conventional modulated light ellipsometer measurements\* on  $\text{As}_2\text{S}_3$  and  $\text{As}_2\text{Se}_3$  films is given in table 2. The variation of the measured refractive index from sample-to-sample is less than 2% for the  $\text{As}_2\text{S}_3$  film and more than 14% for the  $\text{As}_2\text{Se}_3$  film. The existence of these variations in refractive index for different film samples from the same startup materials tends to indicate that the conditions prevailing during the evaporation play a significant role in the properties of the film.

The fact that these films showed no significant variation in their refractive index when measured at various angles has led to a theoretical investigation of the effects of perpendicular anisotropy which arises when isotropic films deposited on isotropic substrates are internally strained. The tension or compression forces that produce this strain are expected to be isotropic and planar. In this case, the s-polarized wave always "sees" a constant index as a function of angle of incidence (mainly  $N_{\text{or}}$ ). The polarization component, however, sees a varying index as a function of angle of incidence due to the anisotropy of the film. Again, just as in the planar case, to calculate the reflection coefficient of the film-substrate system only requires calculating the fresnel coefficients at the interfaces and the phase factors for traversal of the film.

The fresnel coefficients of the film air interface are

$$r_{\perp}^{(1)} = \frac{\cos \phi_1 - N_{\text{or}} \cos \phi_{\text{or}}}{\cos \phi_1 N_{\text{or}} \cos \phi_{\text{or}}} \quad (11)$$

$$r_{\parallel}^{(1)} = \frac{\cos \phi_1 N_{\text{or}} N_{\text{ex}} - (N_{\text{ex}}^2 - \sin^2 \phi_1)^{1/2}}{\cos \phi_1 N_{\text{or}} N_{\text{ex}} + (N_{\text{ex}}^2 - \sin^2 \phi_1)^{1/2}} \quad (12)$$

The fresnel coefficients of the film substrate interface are

$$r_{\perp}^{(2)} = \frac{N_{\text{o}} \cos \phi_{\text{o}} - N_{\text{s}} \cos \phi_3}{N_{\text{o}} \cos \phi_{\text{o}} + N_{\text{s}} \cos \phi_3} \quad (13)$$

$$r_{\parallel}^{(2)} = \frac{N_{\text{s}} (N_{\text{ex}}^2 - \sin^2 \phi_1)^{1/2} - N_{\text{or}} N_{\text{ex}} \cos \phi_3}{N_{\text{s}} (N_{\text{ex}}^2 - \sin^2 \phi_1)^{1/2} + N_{\text{or}} N_{\text{ex}} \cos \phi_3} \quad (14)$$

and the phase factors for traversal of the film are

$$\beta_{\perp} = \frac{2\pi F_t}{\lambda} (N_{\text{or}}^2 - \sin^2 \phi_1)^{1/2} \quad (15)$$

$$\beta_{\parallel} = \frac{2\pi F_t}{\lambda} \frac{N_{\text{or}}}{N_{\text{ex}}} (N_{\text{ex}}^2 - \sin^2 \phi_1)^{1/2} \quad (16)$$

$R_{\perp}$  and  $R_{\parallel}$  can be calculated as before:

$$R_{\perp} = \frac{r_{\perp}^{(1)} + r_{\perp}^{(2)} e^{i2\beta_{\perp}}}{1 + r_{\perp}^{(1)} r_{\perp}^{(2)} e^{i2\beta_{\perp}}} \quad (17)$$

\*These are not a result of squeezing the substrate.

$$R_{\parallel} = \frac{r_{\parallel}^{(1)} + r_{\parallel}^{(2)} e^{i2\beta_{\parallel}}}{1 + r_{\parallel}^{(1)} r_{\parallel}^{(2)} e^{i2\beta_{\parallel}}} \quad (18)$$

Inserting the expressions for the phase factors and the single surface fresnel coefficients into eqs. (17,18) yields  $R$  and  $R$  as functions of  $F_t$ ,  $N_s$ ,  $N_f$ ,  $\phi$ , etc. As before, all angular variables ( $\phi_{or}$ ,  $\phi_{ex}$ , and  $\phi_3$ ) can be eliminated by using a modified Snell's law.  $R_{\perp}$  and  $R_{\parallel}$  can then be used to calculate the ratios  $R_1$  and  $R_2$ .

Figure 2 shows a plot of  $R_1$  versus  $R_2$  at a fixed angle of incidence ( $70^\circ$ ). In this plot, the parametric variable is the film thickness. The tick marks are spaced by film thickness increments of  $\lambda/20 (N^2 - \sin^2\phi_1)^{1/2}$ . The solid curve indicates the increment of calculated values of  $R_1$  and  $R_2$  for a film of ZnSe on KCl with no anisotropy. The  $\Delta$  and  $O$  marks indicate the calculated values of  $R_1$  and  $R_2$  for anisotropic films of the same thickness on a KCl substrate. In the case of  $\Delta$ , the film has planar anisotropy with  $N_{or} = 2.45$  and  $N_{ex} = 1.1 N_{or}$ . For the  $O$  marks, the film is perpendicularly anisotropic with  $N_{or} = 2.45$  and  $N_{ex} = 1.1 N_{or}$ . The figure shows that even anisotropies of 10% give relatively small shifts in the  $R_1$   $R_2$  plots. In fact, there are film thickness values for an isotropic film that give  $R_1$  and  $R_2$  values identical to those of an anisotropic film of slightly different thickness values at a fixed angle of incidence.

We have calculated the variation of  $R_1$  and  $R_2$  with angle for a series of anisotropic films with optical axes perpendicular to the surface of the film. This corresponds to the usual case of an optical film deposited at high temperature on a substrate with thermal expansion properties than the film. These calculations indicate generally that the presence of this type of anisotropy cannot be detected by measuring a single film sample. For example, figures 7 and 8 show the theoretically expected values of  $R_1$  and  $R_2$  as functions of angle of incidence for isotropic films of index values 2.4 and 2.448. Also plotted are the data points for an anisotropic film of  $N_{or}$  equal to 2.4 and  $N_{ex}$  equal to 2.448. These curves show that an anisotropic film exhibits  $R_1$  and  $R_2$  values as a function of the angle of incidence,  $\phi_1$ , that are essentially identical to the behavior of an isotropic film of slightly different index and/or thickness. This indicates that there will be very little variation in the experimentally determined refractive index as a function of the angle of incidence even though the film being measured is highly anisotropic. This conclusion only applies to the perpendicular anisotropic case.

In principle, following the work of De Smet [8] and Den Engleston [7], the anisotropy can be evaluated using a series of optically identical films of vastly different thicknesses. With reference to figure 2 for the anisotropic case, the  $R_1$ ,  $R_2$  curves will spiral rather than form a closed figure. This is analogous to the  $\Delta$ ,  $\psi$  plots for anisotropic film as shown by De Smet and Den Engleston. In practice, however, this is not feasible with a  $10.6 \mu\text{m}$  ellipsometer because the method requires films that range in thickness over many wavelengths. This film thickness variation method for determining anisotropy is viable for short wavelength ellipsometers provided the film is transparent at the measurement wavelength.

### Conclusions

We have demonstrated the feasibility of measuring the anisotropy induced in a thin optical film by piezoelectric or other external means. Measurements of these effects have been used to estimate the strain optic constants of thin optical films at  $10.6 \mu\text{m}$ . These constants, when used in conjunction with typical strains associated with optical films, predict strong anisotropies of the perpendicular type defined here. The existence of thermal expansion coefficient mismatch effects between the film and the substrate can cause the films to have perpendicular anisotropy characteristics. These effects, combined with the planar anisotropy effects that occur whenever an external stress is applied, can lead to biaxial optical anisotropy, which has not been analyzed here.

Theoretical calculations of the effects of perpendicular anisotropy on the measurement of the refractive index of films show that these measurements cannot be used to determine whether or not the film is anisotropic from a single sample. However, a series of measurements with films of various thicknesses can be used to determine the perpendicular anisotropy, provided that the strain in the films is independent of thickness. Experimental data taken on various films agrees with the theoretical result that the perpendicular anisotropy alters the index but does not yield different index values for different measurement angles.



# Table of Symbols

$F_t$	film thickness
$\lambda$	Wavelength in free air
$N_s$	index of substrate
$N_{or}$	ordinary index of refraction of the film
$N_{ex}$	extraordinary index of refraction of the film
$\phi_1$	angle of incidence
$\phi_{or}$	angle of refraction in the film of the ordinary polarization
$\phi_{ex}$	angle of refraction in the film of the extraordinary polarization
$\phi_3$	angle of refraction in the substrate
$R_1$	the reflection coefficient of film substrate for s polarization
$R_{11}$	the reflection coefficient of the film substrate for p polarization
$\beta_{or}$	phase factor for the ordinary wave
$\beta_{ex}$	phase factor for the extraordinary wave

## References

- [1] Pedinoff, M.E., Braunstein, M., and Stafsudd, O.M., "Modulated Light Ellipsometry at 10.6  $\mu$ m," Proceedings of SPIE, San Diego, CA, August 1977.
- [2] Pedinoff, M.E., Braunstein, M., and Stafsudd, O.M., "Measurements of Refractive Indices of IR Materials: 10.6  $\mu$ m Ellipsometry," Appl. Optics, to be published November 1977.
- [3] Allen, S.D., Braunstein, A.I., Braunstein, M, Cheng, J.C., and Nefie, L.A., "A 10.6 Micron Modulated Light Ellipsometer," Optical Properties of Highly Transparent Solids, S.S. Mitra and B. Bendow (Plenum Publishing Co., New York), pp. 503-513, 1975.
- [4] Jaspersen, S.N., Burge, D.K., and O'Handley, R.C., "A Modulated Ellipsometer for Studying Thin-Film Optical Properties and Surface Dynamics," 37, pp. 548, 1973.
- [5] McCrackin, F.L., "A Fortran Program for Analysis of Ellipsometer Measurements," Natl. Bur. Std. Technical Note No. 479 (1969), (U.S. Govt. Printing Office, Washington, D.C. 1969).
- [6] Pedinoff, M.E., Braunstein, M., Stafsudd, O.M., "Modulated Light Ellipsometer Measurements of the Refractive Indices of ThF<sub>4</sub> Single Crystals and As<sub>2</sub>Se<sub>3</sub> and As<sub>2</sub>S<sub>3</sub> Films on ICCL Substrates at 10.6  $\mu$ m." Topical Conf. on High Power Laser Optical Components and Component Materials, Boulder, Colorado, October 3, 1977.
- [7] Den Engleston, D., "Ellipsometry of Anisotropic Films," J. Opt. Soc. Am. 61, pp. 1460-1466, 1971.
- [8] DeSmet, D.J., "Ellipsometry of Anisotropic Thin Films," J. Opt. Soc. Am. 64, pp. 631-638, 1974.
- [9] Ennos, A.E., "Stress Developed in Optical Film Coatings," Appl. Opt. Vol. 5, pp. 51, 1966.

Table 1. Squeeze Experiment Results

Film Material	As <sub>2</sub> S <sub>3</sub>	As <sub>2</sub> Se <sub>3</sub>
Substrate	KCl	KCl
N <sub>f</sub> (film index)	2.35	2.8
N <sub>s</sub> (substrate index)	1.455	1.455
Ft (film thickness) Å	11610	9914
Δl/l (strain)	2.45 x 10 <sup>-5</sup> ± 1.2 x 10 <sup>-5</sup>	4 x 10 <sup>-5</sup> ± 2 x 6 <sup>-5</sup>
ΔN/N (index change)	0.006 ± 0.0003	0.01 ± 0.0005
Strain optic coefficient		
$P_{11} = -2 \frac{\Delta N}{N_3} / \frac{\Delta l}{l}$	89 ± 40	64 ± 32

Table 2. Results of the Conventional Modulated Light Ellipsometer Measurements

MATERIAL	OPTICAL THICKNESS	MEASURED INDEX	MEASURED THICKNESS	ACCEPTED INDEX
$\frac{AS_2S_3}{KCl}$	~ λ/8	2.34 ± 0.03	6826 ± 72 Å°	2.38
$\frac{AS_2S_3}{KCl}$	~ λ/4	2.35 ± 0.03	9916 ± 116 Å°	
$\frac{AS_2S_3}{KCl}$	~ λ	2.36 ± 0.06	39210 ± 205 Å°	
$\frac{AS_2Se_3}{KCl}$	~ λ/8	2.45 ± 0.05	6808 ± 120 Å°	2.80
$\frac{AS_2Se_3}{KCl}$	~ λ/4	2.66 ± 0.14	9683 ± 376 Å°	
$\frac{AS_2Se_3}{KCl}$	~ λ/4	2.81 ± 0.17	10170 ± 570 Å°	
$\frac{AS_2Se_3}{KCl}$	~ λ	2.85 ± 0.03	33700 ± 710 Å°	

Figures

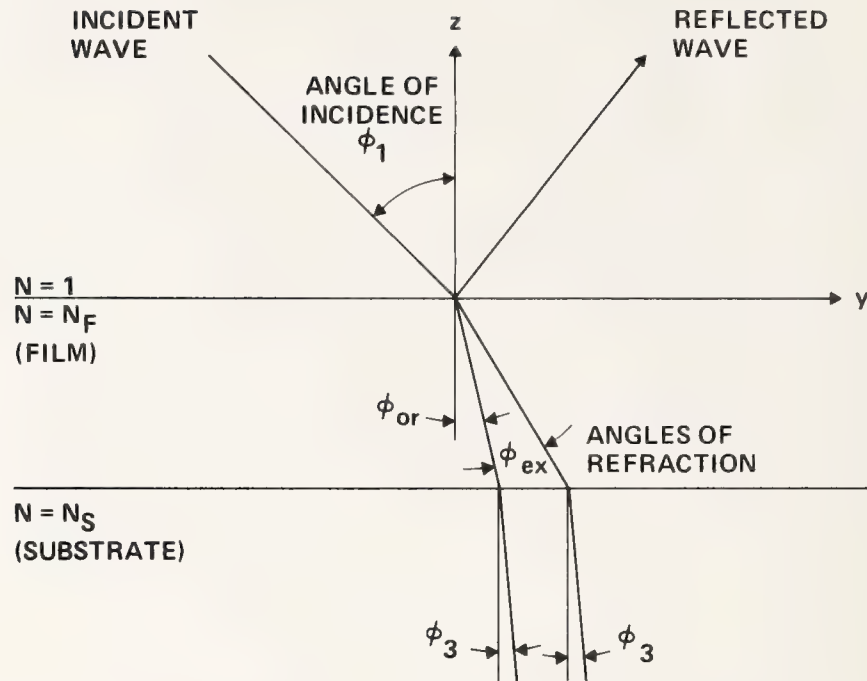


Figure 1. Theoretical model of anisotropic film.

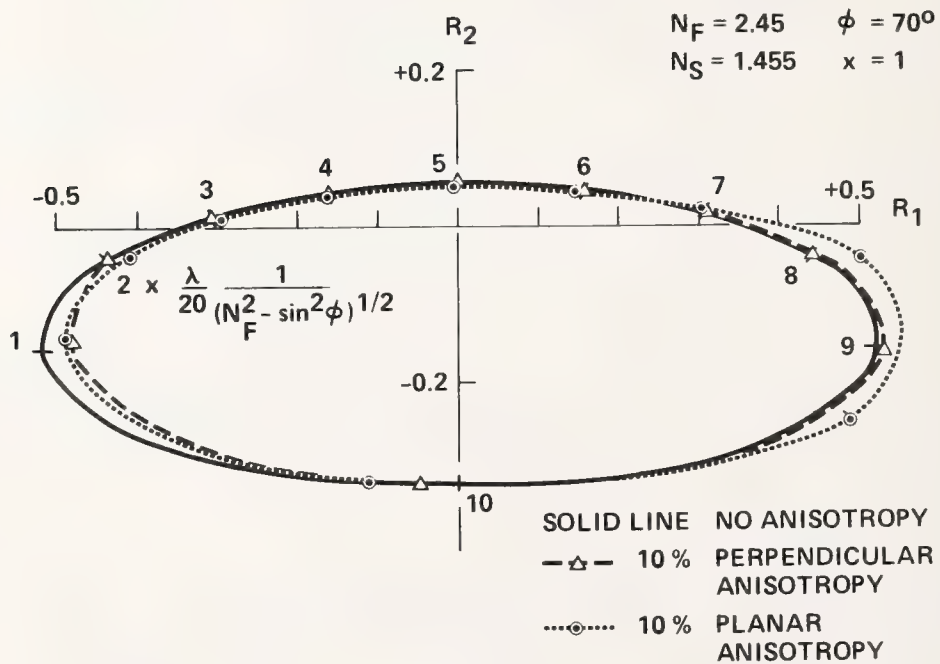


Figure 2. Plot of  $R_1$  versus  $R_2$  for  $N_F = 2.45$ ,  $N_S = 1.455$ ,  $x = 1$ .



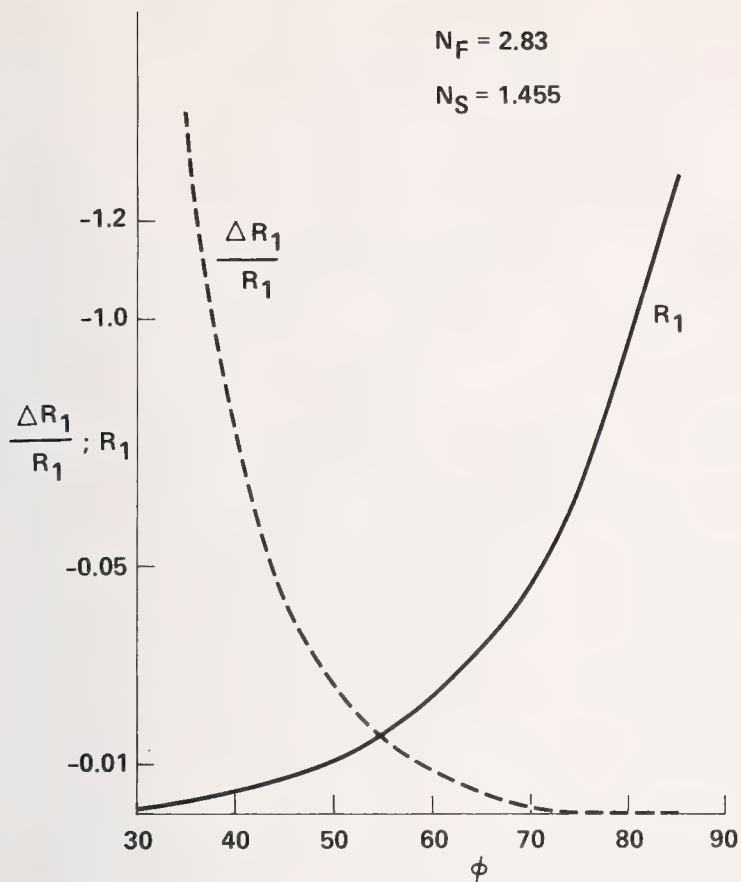


Figure 3. Signal ratio  $R_1$  and  $\Delta R_1/R_1$  versus  $\phi$  with 1% planar anisotropy.

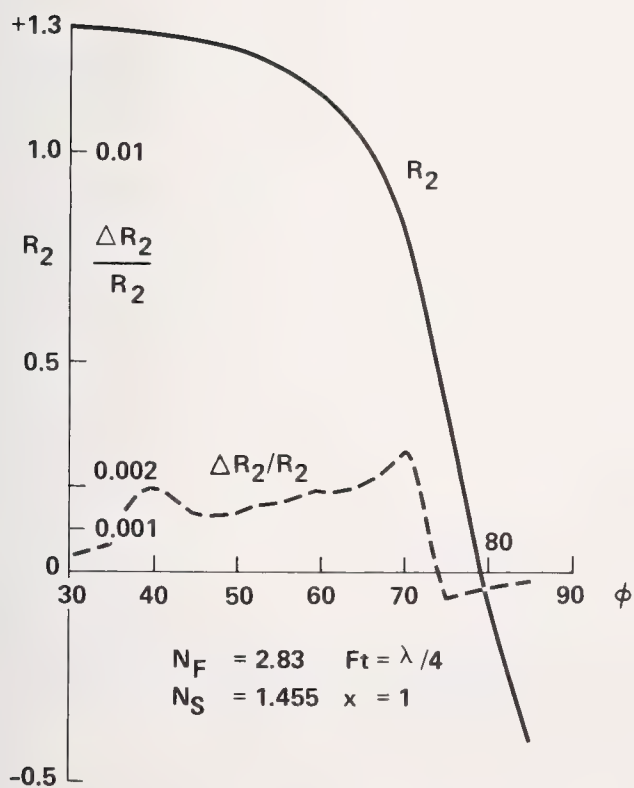


Figure 4.  $R_2$  and  $\Delta R_2/R_2$  versus  $\phi$  with 1% planar anisotropy

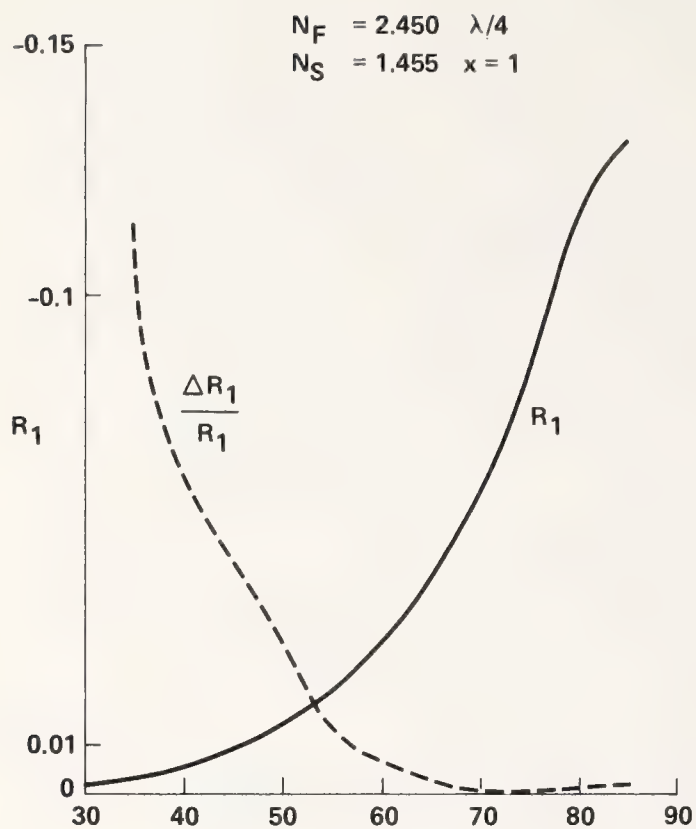


Figure 5.  $R_1$  and  $\Delta R_1/R_1$  versus  $\phi$  with 1% planar anisotropy.

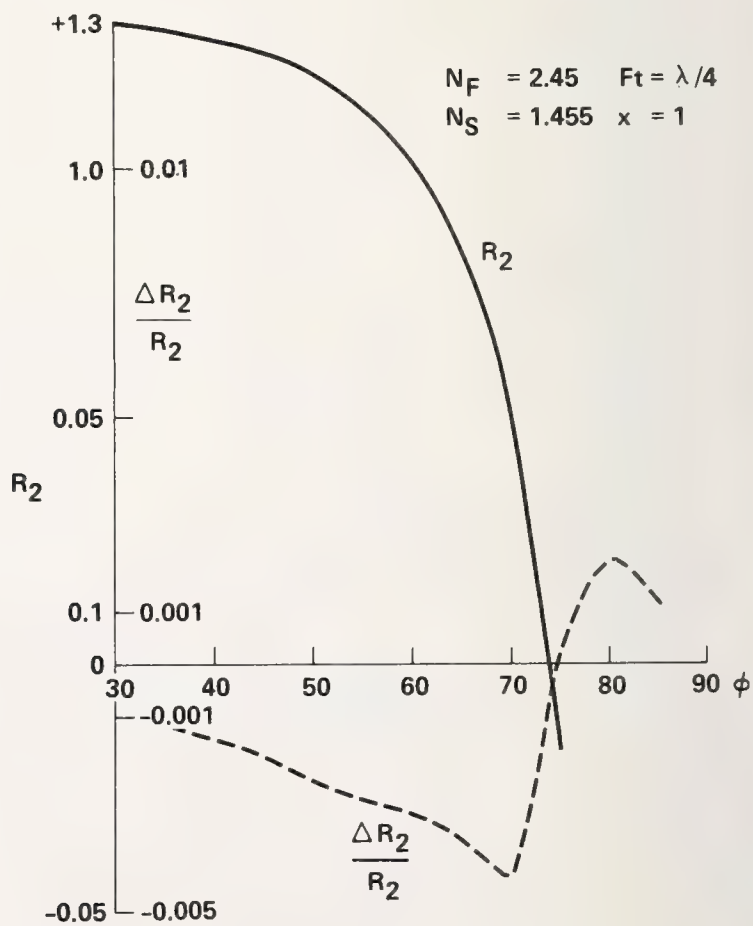


Figure 6. Signal ratio  $R_2$  and  $\Delta R_2/R_2$  versus  $\phi$  with 1% planar anisotropy.

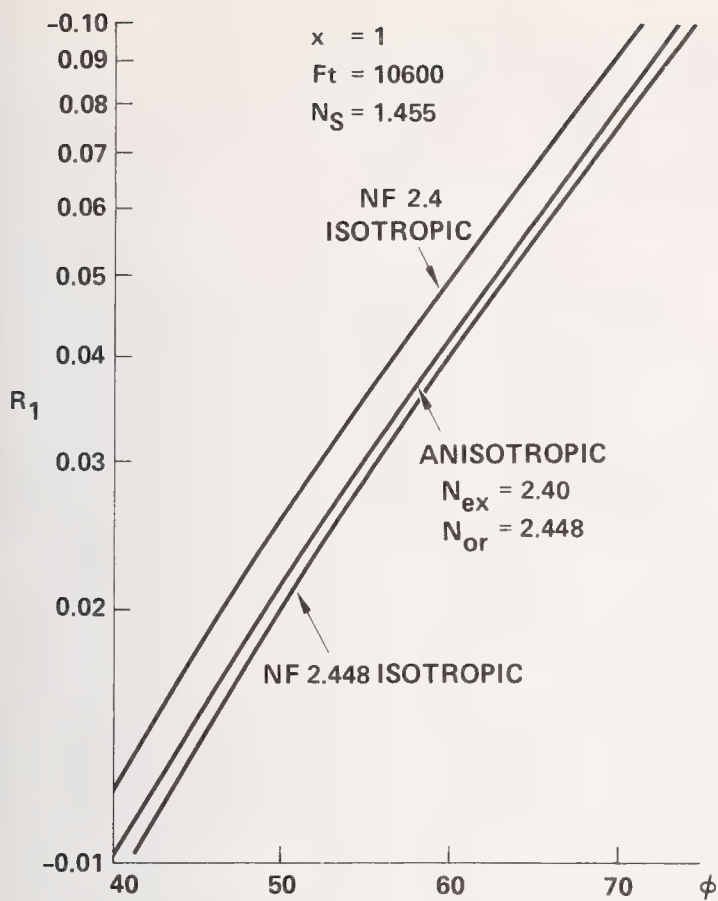


Figure 7. Perpendicular anisotropy  $R_1$  versus  $\phi$ .

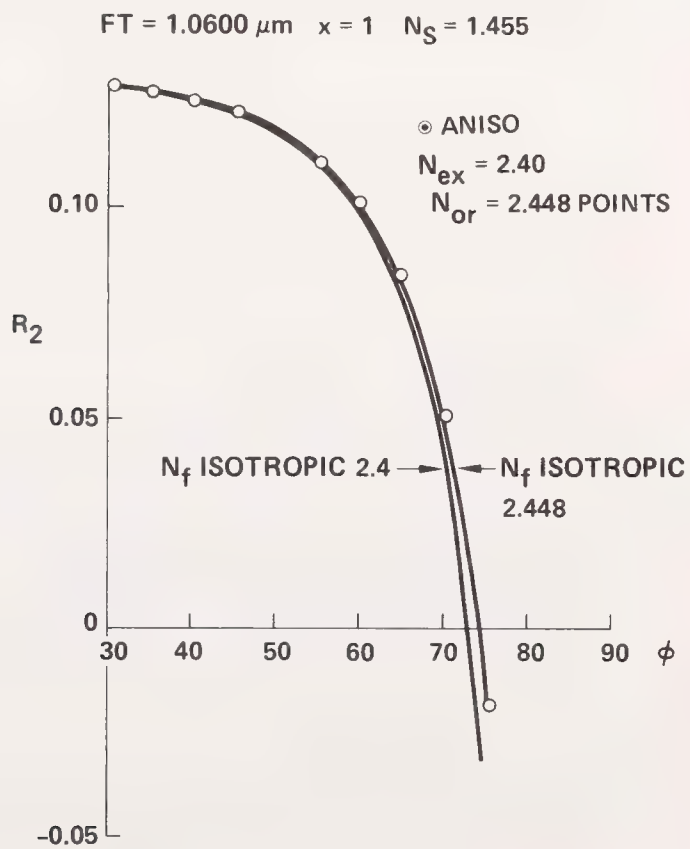


Figure 8. Perpendicular anisotropy  $R_2$  versus  $\phi$ .



COMMENTS ON PAPER BY PEDINOFF, BRAUNSTEIN, AND STAFSUDD

*The speaker pointed out that anisotropies up to 15% have been measured by this technique.*

# DAMAGE RESISTANCE OF AR-COATED GERMANIUM SURFACES FOR NANOSECOND CO<sub>2</sub> LASER PULSES\*

Brian E. Newnam and Dennis H. Gill  
Los Alamos Scientific Laboratory  
Los Alamos, New Mexico 87545

An evaluation of the state-of-the-art of AR coatings on gallium-doped germanium, used as a saturable absorber at 10.6  $\mu\text{m}$ , has been conducted. Both 1-on-1 and N-on-1 laser damage thresholds were measured with 1.2 ns pulses on bare and coated surfaces. Only front surface damage was observed. With few exceptions, the thresholds for coated surfaces were centered at  $0.49 \pm 0.3 \text{ J/cm}^2$ . Bare Ge had a threshold ranging from 0.65 to 0.70  $\text{J/cm}^2$ . No significant differences due to substrate polish, crystallinity or doping level were evident, and multiple-shot conditioning resulted in the same threshold as for single shot tests. From an analysis of standing-wave electric fields, damage of AR-coated Ge appeared to be limited by the surface properties of Ge. Measurements at both 1.2 and 70 ns indicated that the threshold ( $\text{J/cm}^2$ ) of both coated and uncoated Ge increases as the square root of the pulse-width.

Key words: Antireflection coatings, germanium, laser damage, saturable absorber, standing-wave electric field.

## 1. Introduction

Gallium-doped germanium has been developed for use as a saturable absorber to prevent pre-pulse gain depletion in the large CO<sub>2</sub> amplifiers of LASL's eight-beam fusion laser [1,2]. For use at saturating intensities for pulses 1-nanosecond in duration, the damage resistance of the AR-coated surfaces must be maximized. Accordingly, a careful evaluation of the state-of-the-art of AR coatings at 10.6  $\mu\text{m}$  was performed.

Antireflection coatings comprising fourteen coating designs using eight film materials were obtained from nine coating manufacturers. Polycrystalline, p-doped Ge substrates polished by one vendor were supplied to each. Substrates polished by a second vendor were also supplied for comparison. Additionally, single-crystal Ge, p-doped and undoped, and undoped polycrystalline Ge were coated by one vendor to evaluate the effect of crystal structure and doping. The dimensions of the test substrates were 25 mm in diameter and 6 mm thick. Coating depositions, however, were performed in chambers large enough to eventually coat amplifier-size Ge discs (41-cm diameter and 4-cm thickness) with sufficient uniformity to obtain a reflectance per surface of less than 1% at 10.6  $\mu\text{m}$  and less than 3% from 9 to 11  $\mu\text{m}$ .

## 2. Experimental Procedure

Laser damage tests were conducted with  $1.15 \pm 0.05 \text{ ns}$  pulses (FWHM) at the P(20) 10.6  $\mu\text{m}$  wavelength. These short pulses were reliably carved out of a smoothed gain-switched pulse by use of a Pockel cell arrangement. The schematic of the laser diagnostics is shown in figure 1. Pulsewidth measurements were made with a Molelectron pyroelectric detector coupled to a 5-GHz bandwidth oscilloscope of LASL design [3]. For supplementary tests with a 70-ns pulsewidth, a photon-drag detector was used. Oscillograms of the temporal pulses are shown in figure 2.

The test samples were located prior to the focus of a 1 m F.L. ZnSe lens where the beam spot-size radius was 1.1 mm. The peak value of the irradiance ( $\text{J/cm}^2$ ) at the sample plane was measured on each shot by use of a 197- $\mu\text{m}$  diameter pinhole (Optimation, Inc.). The pinhole was located in a split-off beam and placed at the same distance from an identical ZnSe lens as was the sample. The energy transmitted by the pinhole at the center of the reference laser beam was measured by a Laser Precision Energy Meter (isolated from rf noise). Prior to each test series a calibration was performed with an identical 197- $\mu\text{m}$  pinhole centered at the sample plane. During the damage tests the reproducibility of the spatial profile was monitored by comparing the energy focussed through the pinhole reference with the total energy measured by a Scientech calorimeter. The 197- $\mu\text{m}$  diameter of the pinhole was chosen to minimize the spatial averaging over the beam profile (at the pinhole perimeter the intensity of the Gaussian profile dropped to 98% of the peak value) while transmitting an adequate amount of energy for easy detection. Also, the ratio of the pinhole diameter to the wavelength was large enough to avoid significant diffraction effects. By use of the equation,

$$T = 1 - \frac{1}{\sqrt{\pi}(ka)^{3/2}} \sin(2ka - \frac{\pi}{4}) + \dots, \quad (1)$$

\*Work supported by the U. S. Department of Energy.

1 Figures in brackets indicate the literature references at the end of this paper.

where  $a$  = aperture radius [4], the transmittance of the 197  $\mu\text{m}$ -diameter aperture was calculated to be 99.98%.

Damage was detected visually by the onset of increased surface scattering of a He-Ne laser beam directed on the same site (back and front) as the pulsed laser and by examination under bright white-light illumination using the He-Ne beam as the locator. After the tests, examination of irradiated areas was also performed with a microscope (300X).

### 3. Damage Morphology

The characteristics of the laser-damaged sites viewed under 200 and 300 X magnification were very interesting. Only front surface damage was observed in these tests. In figure 3, disruption of an AR-coated (Ge/PbF<sub>2</sub>/ZnSe/Air) surface of p-doped, polycrystalline Ge, caused by a single 1-ns pulse above threshold, is examined. The AR coating has been removed rather uniformly leaving a well-defined perimeter. Linear interference ripples oriented normal to the laser polarization are grouped around circular damage pits. Temple and Soileau have identified these ripples as perturbations in the surface topography due to interference of the incident laser electric field with the time-varying (laser frequency), induced surface charges on surface scratches, voids and inclusions [5]. The diameter of the pits are mostly 8 to 12  $\mu\text{m}$  and the ripple spacing is approximately 8.5  $\mu\text{m}$  which are close to the laser wavelength. Damage sites in uncoated Ge (not shown) caused by 1-ns pulses did have faint ripples with spacing exactly equal to the laser wavelength ( $\pm 0.2$  nm).

The morphology of damage caused by 70-ns pulses was very different from the above as shown in figure 4. On the coated surface, a random distribution of irregular sites was related to damage at defect sites, and extensive cracking of the AR coating is probably thermally-caused delamination. For bare Ge (fig. 5) the damage sites were all centered on circular pits accompanied by very tightly-spaced (3.5  $\mu\text{m}$ ) interference fringes parallel to the laser polarization. The cause of these fringes has not been identified.

### 4. Results

The experimental results for coated and bare Ge substrates are presented in tables 1-3. These thresholds are for pit formation or film disruption which occurred at much lower intensities than a breakdown plasma. Only the mean value of each threshold is listed for the coated surfaces since the range, typically  $\pm 0.02$  or less, was unusually small. The absolute accuracy is considered to be  $\pm 10\%$ . All thresholds listed are for front surface damage only as we were unable to damage any rear surface, coated or uncoated. Further, we observed no difference between thresholds for 1-on-1 and N-on-1 tests, where N-1 shots (10 to 15) were fired below the single-shot threshold, before irradiating with a damaging intensity.

To compare the effects of two different conventional polishing methods, single-and polycrystalline substrate material and Ga-doping level (undoped,  $R = 30 \Omega\cdot\text{cm}$ ; doped,  $3 \Omega\cdot\text{cm}$ ), one coating vendor deposited a two-layer ThF<sub>4</sub>/ZnS Vee-coat on each different substrate during one run. As seen in table 1, no significant differences in thresholds caused by the two polishing methods were manifest. This was surprising since Polish A qualified as better than "40-20" (scratch and dig code) and Polish B was slightly worse than "40-20". Likewise, no real differences were measured between coated single-crystal and polycrystal Ge surfaces. Gallium-doping had no effect on coated single-crystal thresholds, and only a minor 10-15% threshold reduction was measured for Ga-doped polycrystalline Ge.

Table 1. Damage threshold of AR-coated Germanium substrates

Germanium Substrate	Coating: s/ThF <sub>4</sub> /ZnS/a	
	Polish A	Polish B
Single Crystal (undoped)	0.47	0.46
Single Crystal (p-doped)	0.47	0.46
Polycrystal (undoped)	0.48	0.51
Polycrystal (p-doped)	0.41	0.46

The thresholds for fourteen coating designs on p-doped, polycrystalline Ge are listed in table 2. Multiple entries represent different samples of the same coating. The values ranged from 0.41 to 0.57 J/cm<sup>2</sup> and the mean value was  $0.49 \pm 0.03$  J/cm<sup>2</sup>. Even the two-layer coating of CaF<sub>2</sub>/ZnSe had the same threshold despite the fact that CaF<sub>2</sub> has a large absorption coefficient at 10.6  $\mu\text{m}$ .

Due to the relative uniformity of thresholds for coated Ge surfaces, particular attention was paid to the thresholds of uncoated Ge presented in table 3. The values for three different bare surfaces were all greater than those of coated Ge by about 40%. In addition, it is noted that Ga-doping lowered the threshold by  $\sim 10\%$ .



Table 2. Damage thresholds of AR-coated germanium

Vendor	Design	Ge/coating/Air
		Energy Density (J/cm <sup>2</sup> )
I	ZnS	0.51, 0.46
E	ZnS	0.50, 0.47, 0.49 <sup>a</sup>
D	TlI	0.46
Two-layer coatings		
G	CaF <sub>2</sub> /ZnSe	0.50, 0.48
H	PbF <sub>2</sub> /ZnSe	0.49
E	ZnSe/ThF <sub>4</sub>	0.48, 0.46
H	ThF <sub>4</sub> /ZnSe	0.44
A	ThF <sub>4</sub> /ZnS	0.46, 0.41

a Extra Ge substrate, undoped, polycrystalline, poor polish

Three-layer coatings		
I	ZnS/Ge/ZnS	0.53, 0.50
D	TlI/KCl/TlI	0.50
F	ThF <sub>4</sub> /ZnS/ThF <sub>4</sub>	0.51, 0.48
F	ThF <sub>4</sub> /ZnSe/ThF <sub>4</sub>	0.50
	ZnS/ThF <sub>4</sub> /ZnS	0.48, 0.47
Four- and Five-Layer Coatings		
C	ZnS/Ge/ZnS/ThF <sub>4</sub>	0.57, 0.55, 0.51
B	ThF <sub>4</sub> /ZnS/ThF <sub>4</sub> /ZnS/ThF <sub>4</sub>	0.47, 0.45

Table 3. Damage thresholds of uncoated  
polycrystalline germanium  
(Front Surface Only)

	Energy Density (J/cm <sup>2</sup> )
Undoped	0.70 ± 0.05
P-doped (Gallium)	0.65 ± 0.05
P-doped -HNO <sub>3</sub> treated	0.72 ± 0.05

### 5. Analysis of Electric Fields

The experimental results indicate that the damage threshold of AR-coated Ge surfaces is 1) independent of the design and materials of the AR coatings and is 2) lower than uncoated Ge. Furthermore, damage occurred only at the front surface. These results may be explained by considering the electric fields in the Ge, coated and uncoated. Figure 6 represents the standing-wave electric fields, normalized to the incident field  $E_0^+$ , in the vicinity of the front surface of an AR-coated and uncoated Ge substrate. Although, the exact field distribution within the AR coating must be calculated for each design, the gradual decrease of  $|E/E_0^+|^2$  from 1.0 at the air-film interface to 0.25 at the film-Ge interface is the same for any design.

The normalized field in the AR-coated substrate is easily calculated using the relation

$$\left| \frac{E_s}{E_o^+} \right|^2 = \frac{1}{n_s} \quad (2)$$

where, for Ge,  $n_s = 4.0$  at  $10.6 \mu\text{m}$ . Likewise, the field-squared in the uncoated Ge substrate is 0.16 in the vicinity of the front surface as calculated from

$$\left| \frac{E_s}{E_o^+} \right|^2 = \frac{4}{(n_s + 1)^2} \quad (3)$$

Since the power absorbed per  $\text{cm}^3$  is given by

$$P_a = n\alpha |E/E_o^+|^2 \quad (4)$$

for linear absorption, damage by this mechanism (or any other involving the electric field) in Ge would predictably occur at a lower incident laser intensity for an AR-coated surface. The ratio of the fields-squared in uncoated-to-coated Ge is computed to be 0.64. The ratio of the measured damage thresholds is  $0.7 \pm 0.1$ , which is consistent. These results indicate that the damage probably occurred in the Ge at the Ge/film interface. Thus, for all but the lowest thresholds measured, it is apparent that the coatings had at least as high a damage resistance as the substrate itself.

It is informative to calculate the peak electric field present in the various coating materials at the threshold of damage of the coated Ge surfaces. These fields, listed in table 4, represent a number of samples and coating designs. In terms of electric field, it is seen that the same value, 0.2 MV/cm, existed in the coated and uncoated Ge substrates at the threshold, again implicating the substrate as the limiting factor. We also note that this breakdown field is comparable to the dc value of  $\sim 0.08$  MV/cm [6].

Table 4. Peak electric field at damage threshold of coated Ge surfaces

Coating Material	Number of Samples	10.6 $\mu\text{m}$ , 1.15 ns pulse
		$E_{\text{RMS}}$ (MV/cm)
ZnS	17	0.33 to 0.40
ZnSe	7	0.33 to 0.40
TlI	2	0.32 to 0.39
ThF <sub>4</sub>	15	0.24 to 0.40
PbF <sub>2</sub>	1	0.33
CaF <sub>2</sub>	2	0.30
KCl	1	0.23
Ge	2	0.22 to 0.26
Ge substrate coated	26	0.18 to 0.21
Ge substrate uncoated	7	0.18 to 0.19

Interestingly, the Ge films withstood 20 to 25% more electric field than the substrate. In most other cases, thin films are generally less damage-resistant than bulk material. Given a more damage-resistant substrate than Ge, it is likely that the various coating components could survive even higher electric fields than attained in these tests.

#### 6. Pulswidth Dependence

A second set of tests at a longer pulswidth,  $\sim 70$  ns, produced thresholds of  $4.2 \text{ J/cm}^2$  for PbF<sub>2</sub>/ZnSe AR-coated Ge and  $6.4 \text{ J/cm}^2$  for uncoated Ge. The ratio of these thresholds, 0.66, is still in consonance with the SW electric-field explanation. Although only two points are used in figure 7 to draw a straight line, the threshold dependence of both coated and uncoated Ge goes nearly as the square root of the Ge pulswidth:

AR-coated Ge

$$\epsilon_D = 0.455 \tau^{0.52} \quad (5)$$

Uncoated Ge

$$\epsilon_D = 0.67 \tau^{0.53} \quad (6)$$

This scaling relationship is the same as that for free electron absorption in metallic surfaces and for electron plasma absorption initiated by avalanche breakdown in dielectrics [7].

## 7. Discussion

It is a general observation that the rear surface of a transparent dielectric is damaged prior to the front surface by a collimated laser beam, assuming the surfaces have identical surface properties. For substrates like glass, this effect has been clearly demonstrated to be due to the greater standing-wave electric field at the rear surface [8]. Figure 8 illustrates the 180° phase reversal of the reflected wave at the front surface and the in-phase reflected wave at the back surface. The resultant ratio of the total electric fields at the two surfaces is

$$\frac{E(\text{rear})}{E(\text{front})} = \frac{2n}{n+1}, \quad (5)$$

a quantity greater than unity.

The magnitude of this field ratio for several dielectrics, transparent at 10.6  $\mu\text{m}$ , is listed in table 5. As reported in section 4, only front surface damage of Ge was observed for all surfaces, AR-coated or uncoated, polycrystalline or single-crystal, doped or undoped. This was very surprising considering the large ratio, 1.60, for the fields. Even for a thinner (3 mm) substrate, no rear damage could be caused. To clarify this observation, three other substrates, NaCl, CdSe and CdTe, were irradiated. The expected early rear-surface damage was observed for NaCl and CdSe, but like Ge, only front surface damage could be produced on CdTe. This was especially intriguing since the band gap of CdTe and CdSe are nearly the same, 1.50 and 1.74 eV, respectively, at 300°K [9].

Table 5. Rear versus front surface damage at 10.6 microns

Substrate	Refractive Index	Ratio of Electric Fields Rear to Front	Damage First Observed
NaCl	1.49	1.20	Rear
CdSe	2.43	1.42	Rear
CdTe	2.69	1.46	Front only
Ge	4.0	1.60	Front only

A first order examination of this phenomenon requires taking into account the gentle convergence of the laser beam at the sample and the linear absorption of the Ge using the relation for an uncoated substrate

$$\frac{E_2}{E_1} \approx \frac{2n}{n+1} \frac{w_1}{w_2} e^{-\alpha x/2}, \quad (6)$$

where 1,2 refer to front and rear surfaces,  $w$  is the spot size radius,  $\alpha$  is the absorption coefficient and  $x$  is thickness. For our experiment  $w_1/w_2 = 1.008$  and sample thicknesses were 5.6 mm. For the p-doped Ge, of resistivity 3  $\Omega\cdot\text{cm}$ , the weak signal absorption coefficient was approximately 0.6  $\text{cm}^{-1}$  at 10.6  $\mu\text{m}$ ; for undoped Ge it was 0.005  $\text{cm}^{-1}$ .

Substituting, we find that for p-doped Ge  $E_2$  was 1.15 times  $E_1$  for weak intensities and larger for higher saturating intensities. For undoped, AR-coated Ge  $E_2$  was 1.61 times  $E_1$ . Only in the case of AR-coated, p-doped Ge was  $E_2$  less (between 0.72 and 1.0) than the  $E_1$ . However, attempts to damage the rear surface of these samples by increasing the incident laser intensity were unsuccessful.

One promising explanation for the absence of rear surface damage was suggested by Phipps [10]. In a darkened room he observed a faint blue surface corona on the front surface of a Brewster Ge plate well below the threshold for damage. This corona was distinctly different from a spark associated with an electron avalanche, and no traces of damage were found. It is possible that this visible light



was emitted during carrier recombination. Further, absorption of this visible light by the Ge could increase the free carrier density (for intrinsic Ge  $n_i = 2.4 \times 10^{13}/\text{cm}^3$  at 300°K [6]) to obtain a sufficiently absorbing plasma for higher laser intensities to cause surface damage. Further experiments are obviously needed to examine this possibility.

## 8. Summary

This study has produced a number of results which are best listed under three headings.

### 8.1 General

- a. The damage threshold was limited by germanium surface properties.
- b. Front surface damage, only, occurred.
- c. A pulsewidth dependence  $E_D \text{ (J/cm}^2\text{)} \sim \tau^{1/2}$ , was observed between 1 and 70 ns.

### 8.2 Bare Ge

- a. The damage threshold at 1.2 ns ranged from 0.65 to 0.70 J/cm<sup>2</sup>.
- b. An HNO<sub>3</sub> treatment raised the threshold ~ 10%.

### 8.3 AR-Coated Ge

- a. Damage thresholds at 1.2 ns were  $0.49 \pm 0.03 \text{ J/cm}^2$  with a total range from 0.41 to 0.57 J/cm<sup>2</sup>.
- b. Multiple-shot conditioning (N-on-1) produced the same threshold as single-shot tests (1-on-1).
- c. No variation in threshold for 3 different conventionally polished substrates was observed.
- d. No large difference of the threshold between substrates with varied doping or crystallinity was observed.

## 9. Acknowledgments

The authors wish to thank the optics personnel of the optical companies listed in table 6 for producing, polishing and AR-coating the Ge test substrates. Also due credit are Ed Foley and Andrew Nowak for constructing and maintaining the CO<sub>2</sub> laser used in these tests and George Faulkner for technical assistance with the experiments. We add our appreciation to Claude Phipps for several helpful discussions.

Table 6. Participating Optical Companies

### Germanium Substrates:

Eagle-Picher

### Coatings:

Coherent Radiation

Design Optics

Exotic Materials, Inc.

Honeywell, Inc.

Optical Coating Laboratory, Inc.

Perkin-Elmer Corporation

Santa Barbara Research

II-VI, Inc.

Valtec Corporation

### Polishing:

Design Optics

Optical Systems & Technology, Inc.

## 10. References

- [1] Phipps, C.R., Thomas, S.J. and Figuera, J.F., paper WA6, 1976 Conference on Laser and Electro-optical Systems, Digest of Technical Papers, 30 (1976).
- [2] Phipps, C.R., Thomas, S.J., Ladish, J., Cuzuchlewski, S.J., and Figuera, J.F., paper 8.8, 1977 Conference on Laser Engineering and Applications, Digest of Technical Papers, 36 (1977).
- [3] McLellan, E.J. and Lunsford, J.S., paper 8.10, *ibid*, 38 (1977).
- [4] Jackson, J.D., Classical Electrodynamics, (John Wiley & Sons, New York, 1962), p. 295.
- [5] Temple, P.A., and Soileau, M.J., NBS Spec. Pub. 462, 371 (1976).
- [6] Grove, A.S., Physics and Technology of Semiconductors, (John Wiley, New York, 1967), pp. 102-103.
- [7] Bettis, J.R., House, R.A., and Guenther, A.H., NBS Spec. Pub. 462, 338 (1976).
- [8] Crisp, M.D., NBS Spec. Pub. 387, 80 (1973).
- [9] Pankove, J.I., Optical Processes in Semiconductors, (Prentice-Hall, Englewood Cliffs, NJ, 1971) pp. 412-413.
- [10] Phipps, C.R., private communications, 1977.

## 11. Figures

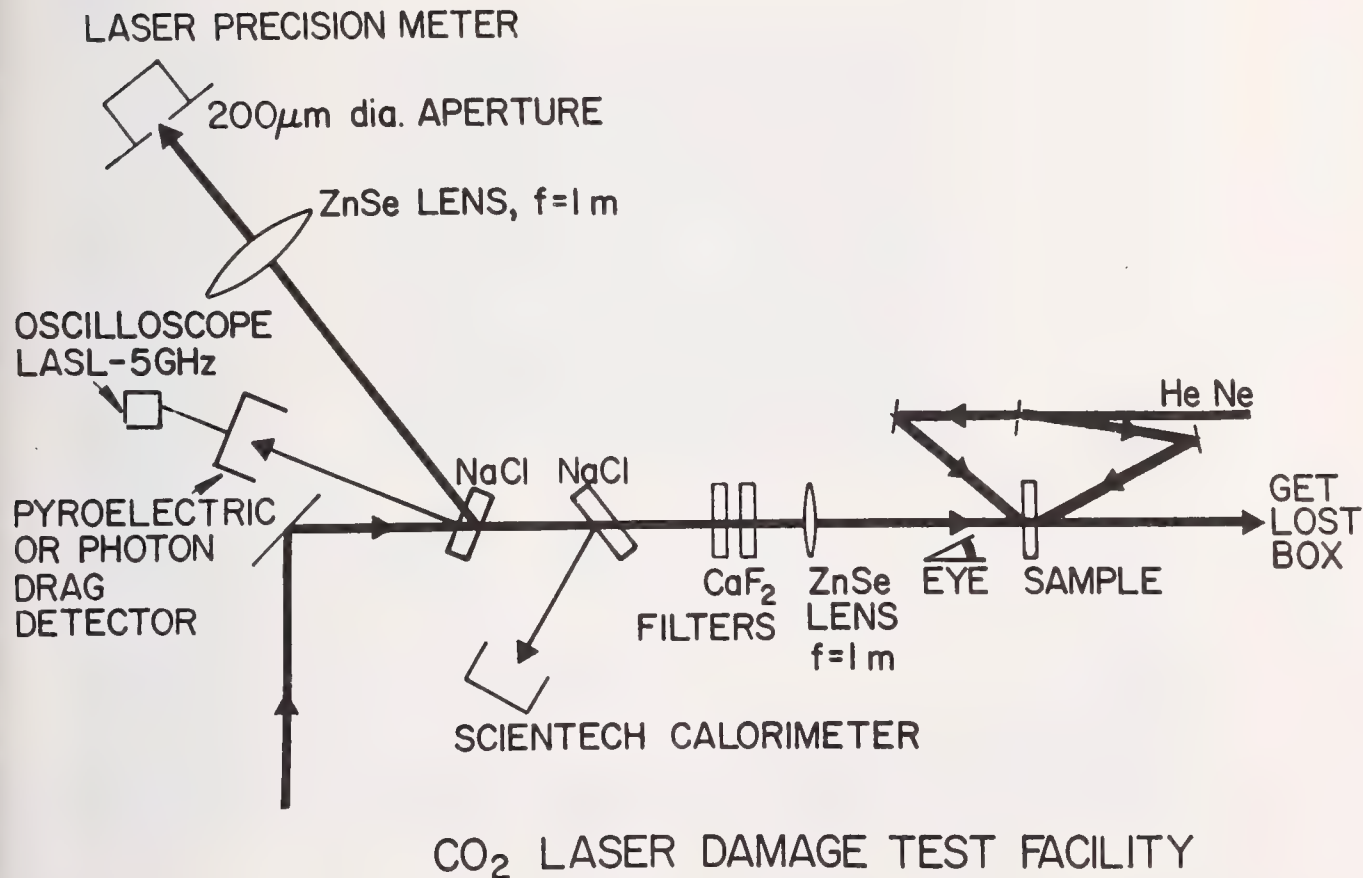
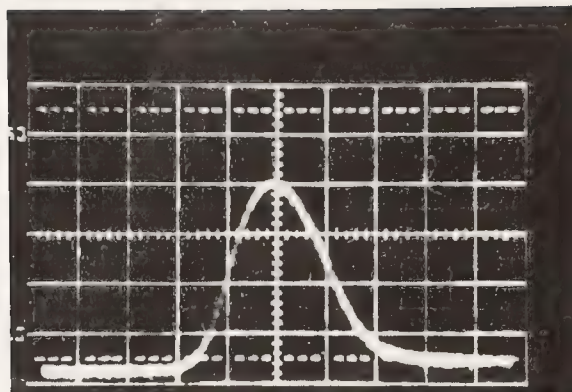
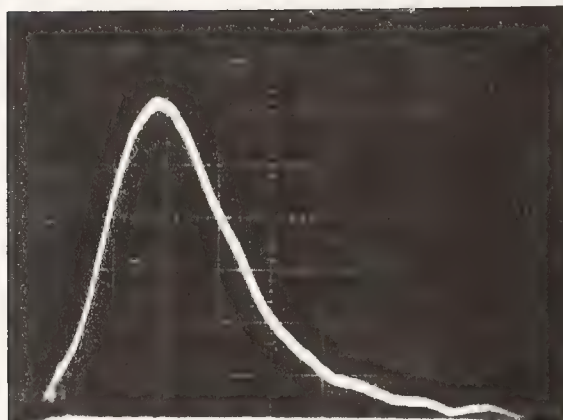


Figure 1. Schematic of the CO<sub>2</sub> laser damage test facility.



*0.5 nsec per  
division*



*20 nsec per  
division*

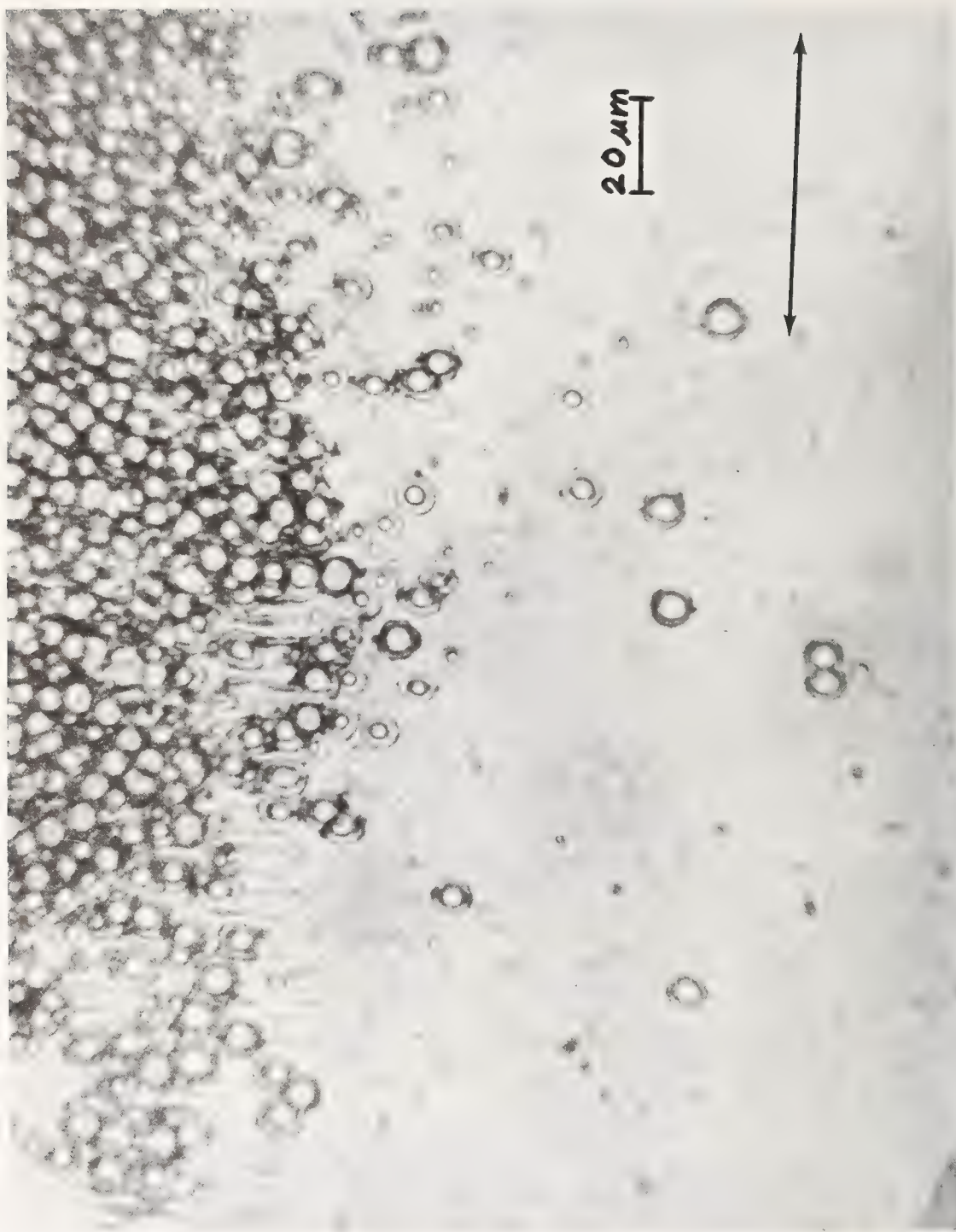
Figure 2. Oscillograms of CO<sub>2</sub> laser pulses of duration (FWHM) (a) 1.2 ns measured with a pyroelectric detector and (b) 60 ns measured with a photon-drag detector.

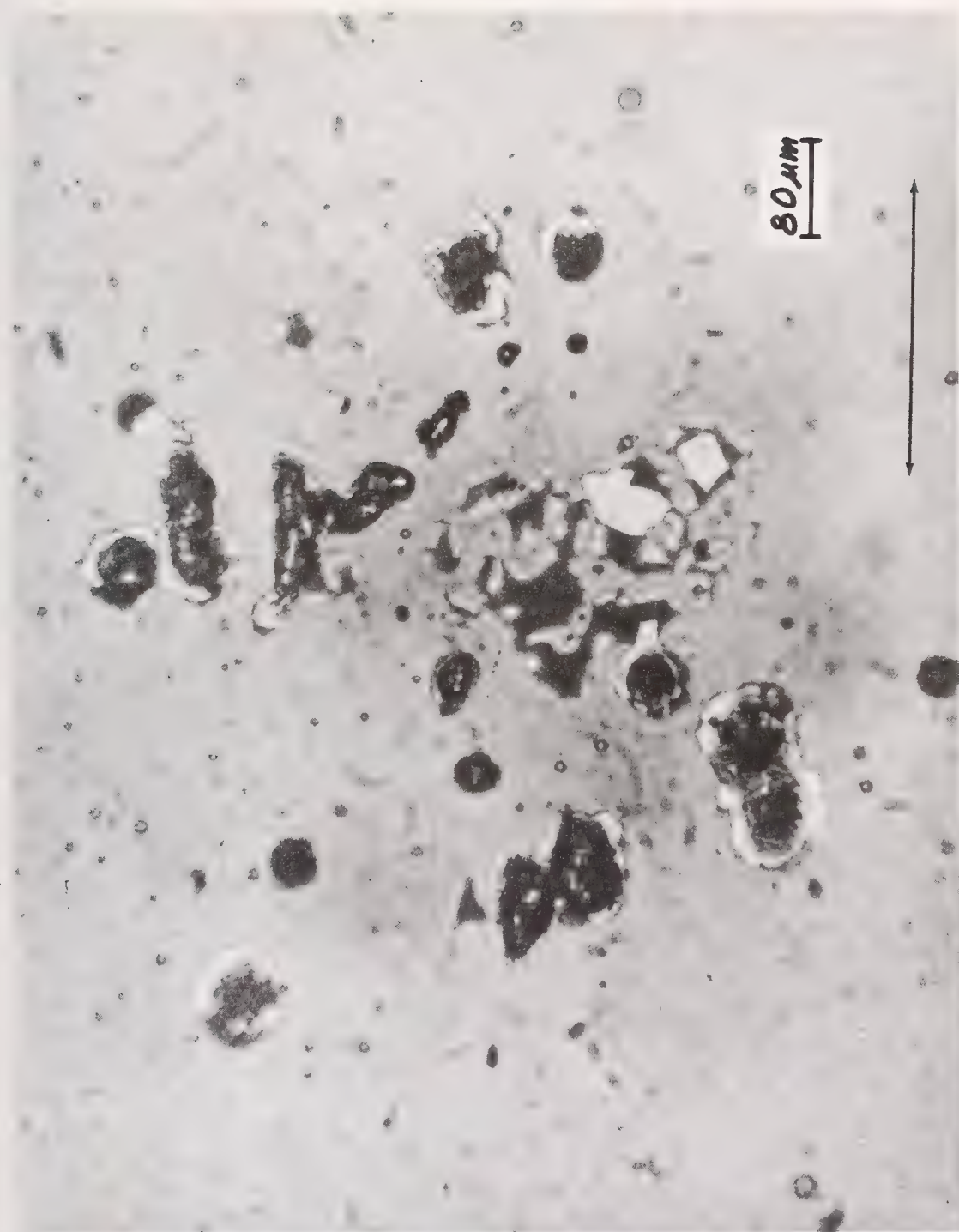




(a)

Figure 3. Damage produced by a 1-ns pulse on an AR-coated (Ge/PbF<sub>2</sub>/ZnSe)Air) surface of p-doped polycrystalline Ge. Pit diameters are mostly 8 to 12 μm and ripple spacing is ~ 8.5 μm oriented normal to the laser polarization (arrow).

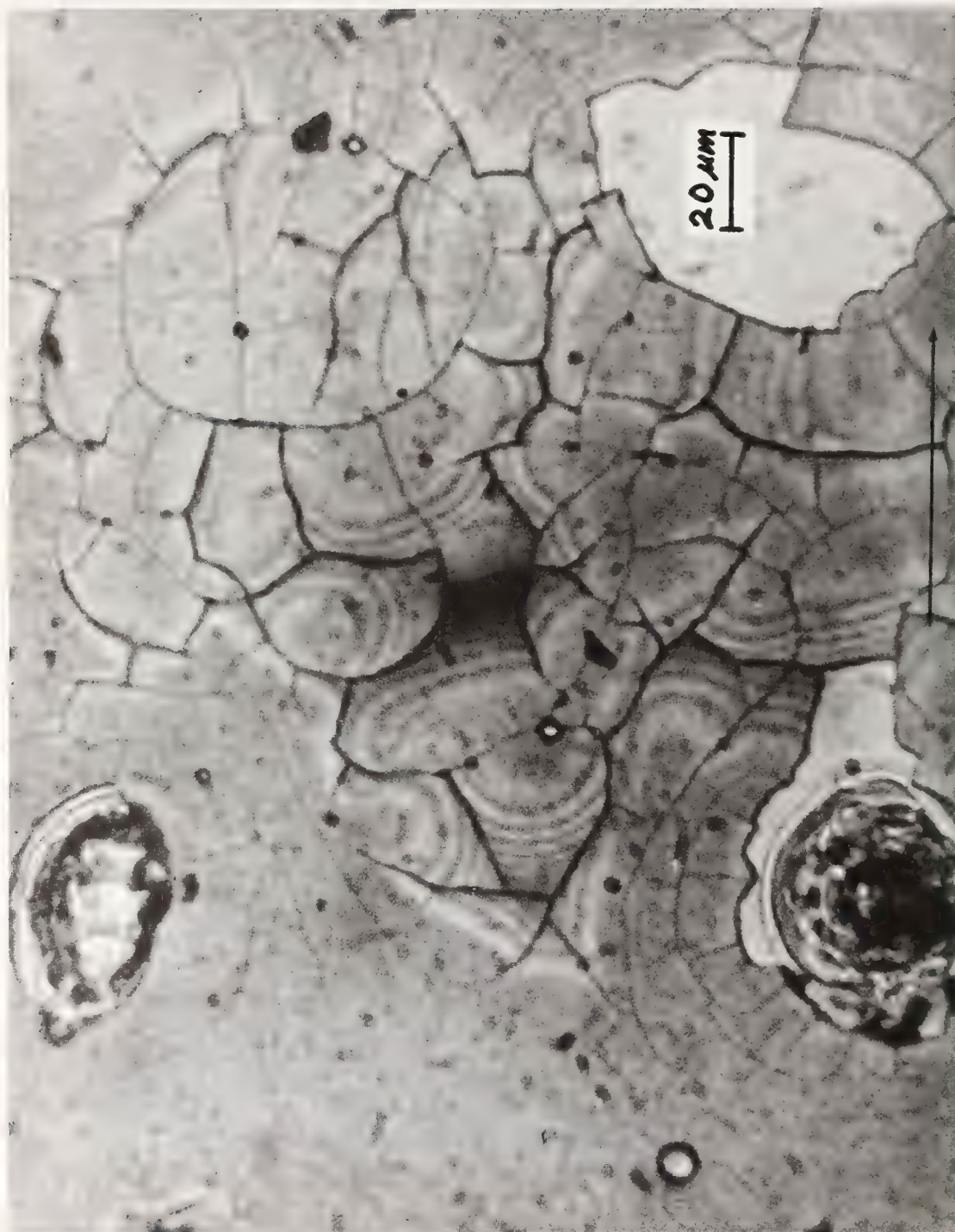




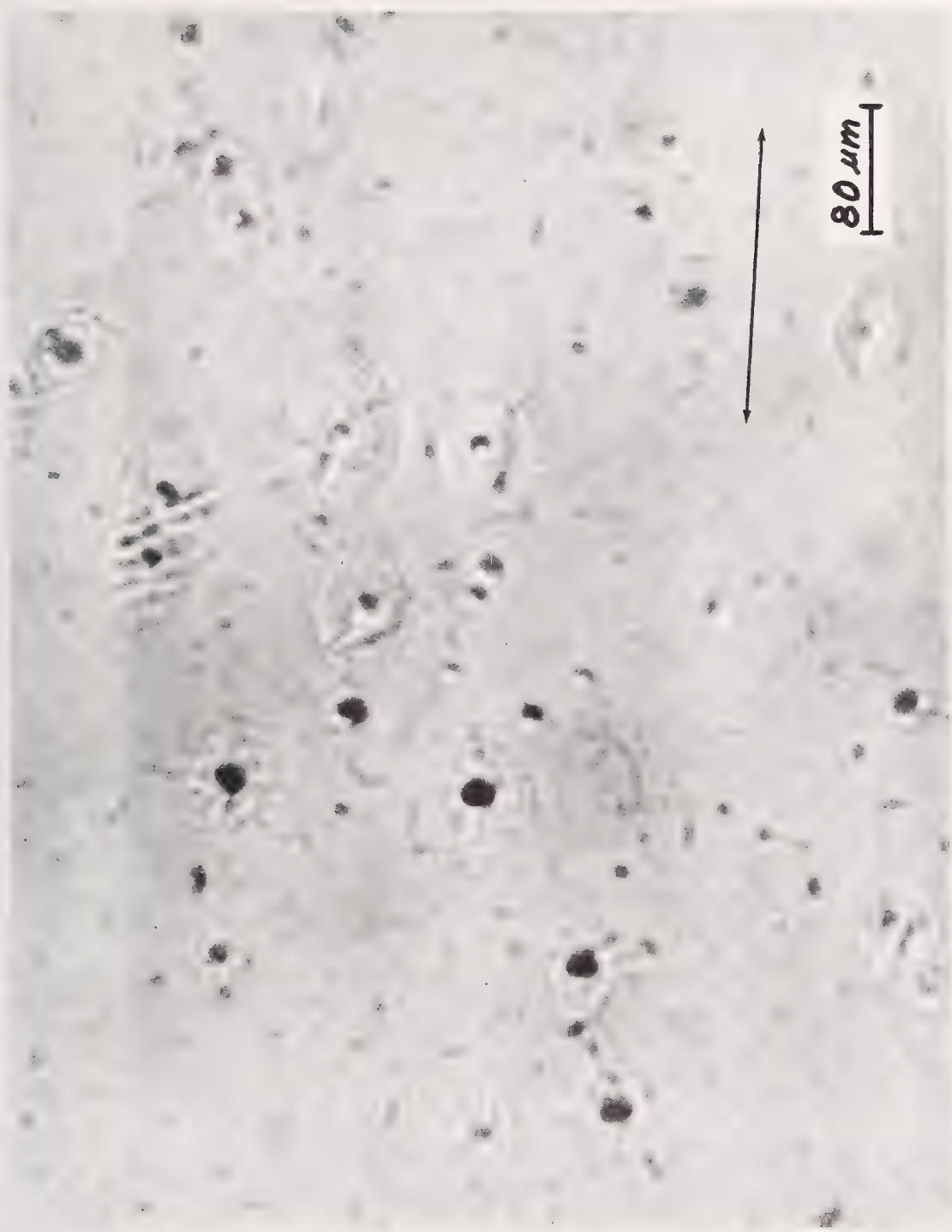
(a)

Figure 4. Damage produced by a 70-ns pulse on an AR-coated (Ge/PbF<sub>2</sub>/ZnSe/Air) surface of p-doped polycrystalline Ge. Laser polarization is along the arrow.





(b)



(a)

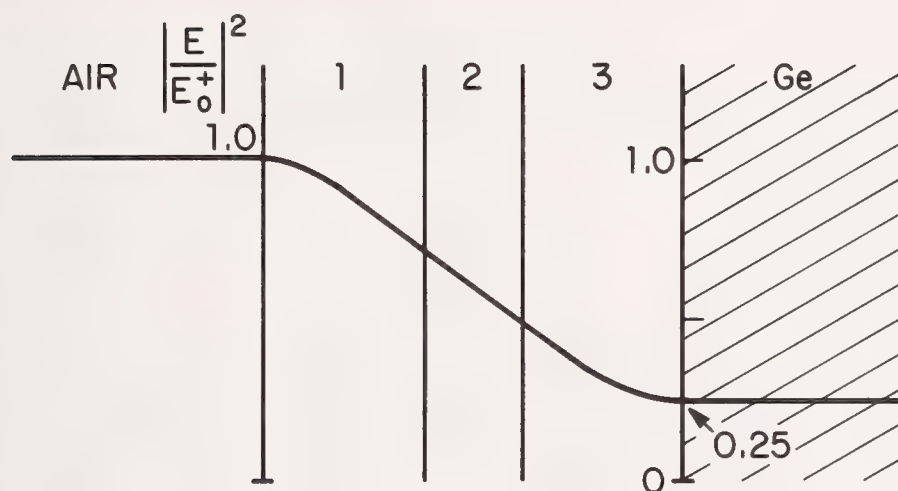
Figure 5. Damage produced by a 70-ns pulse on bare, p-doped, polycrystalline Ge. Interference ripples of spacing  $3.5\ \mu\text{m}$  are oriented parallel (arrow) to the laser polarization.



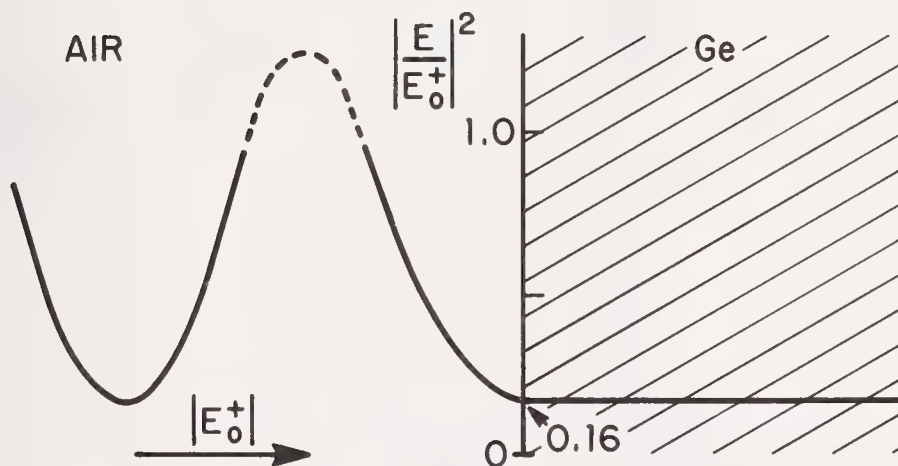
(b)



## STANDING-WAVE FIELDS



AR-COATED SUBSTRATE:  $\left| \frac{E_s}{E_0^+} \right|^2 = \frac{1}{n_s}$



UNCOATED SUBSTRATE:  $\left| \frac{E_s}{E_0^+} \right|^2 = \frac{4}{(n_s+1)^2}$

Figure 6. Standing-wave electric fields for AR-coated and uncoated Ge substrates.

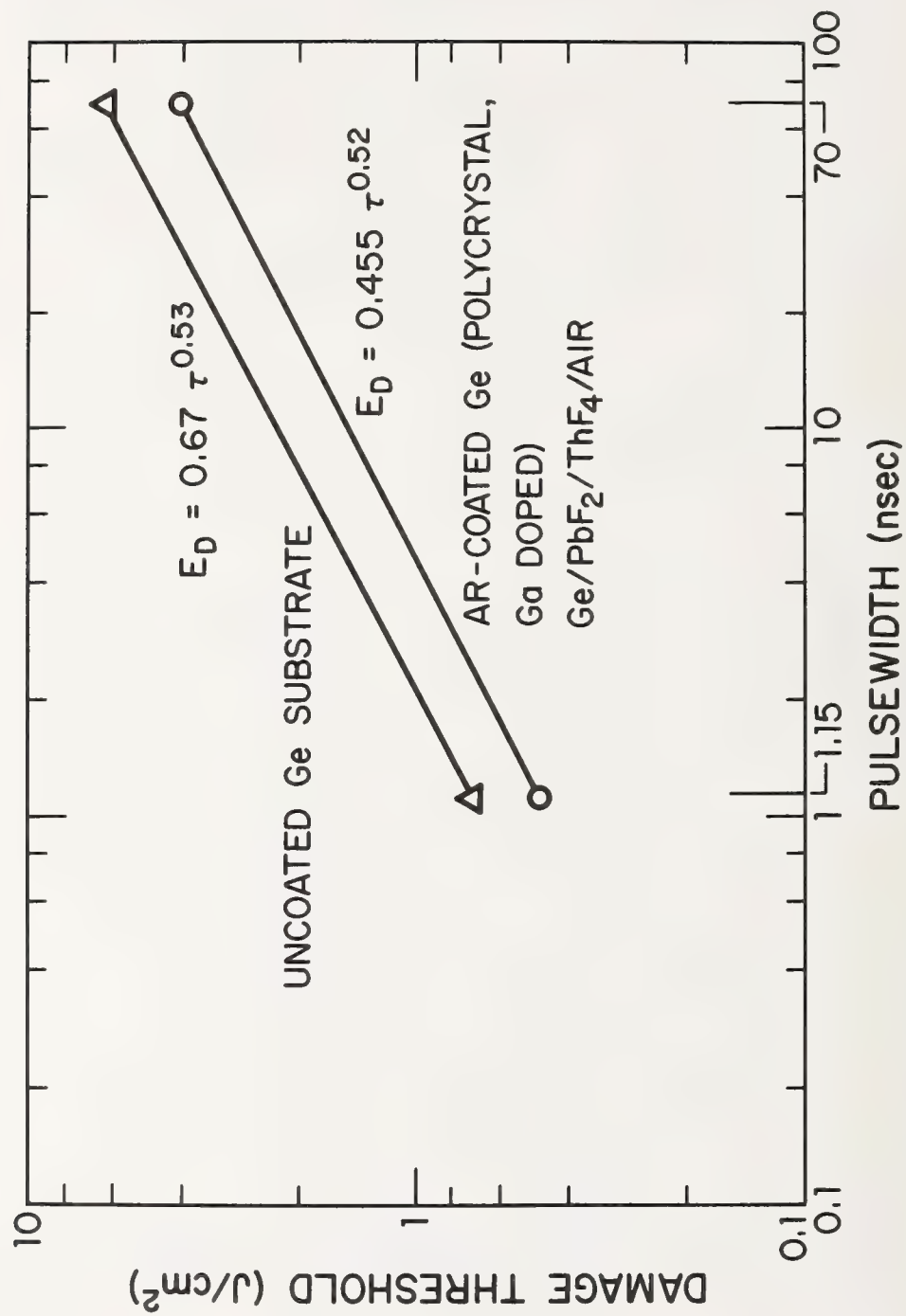


Figure 7.  $\text{CO}_2$  laser damage of AR-coated and uncoated Ge at two pulsewidths.

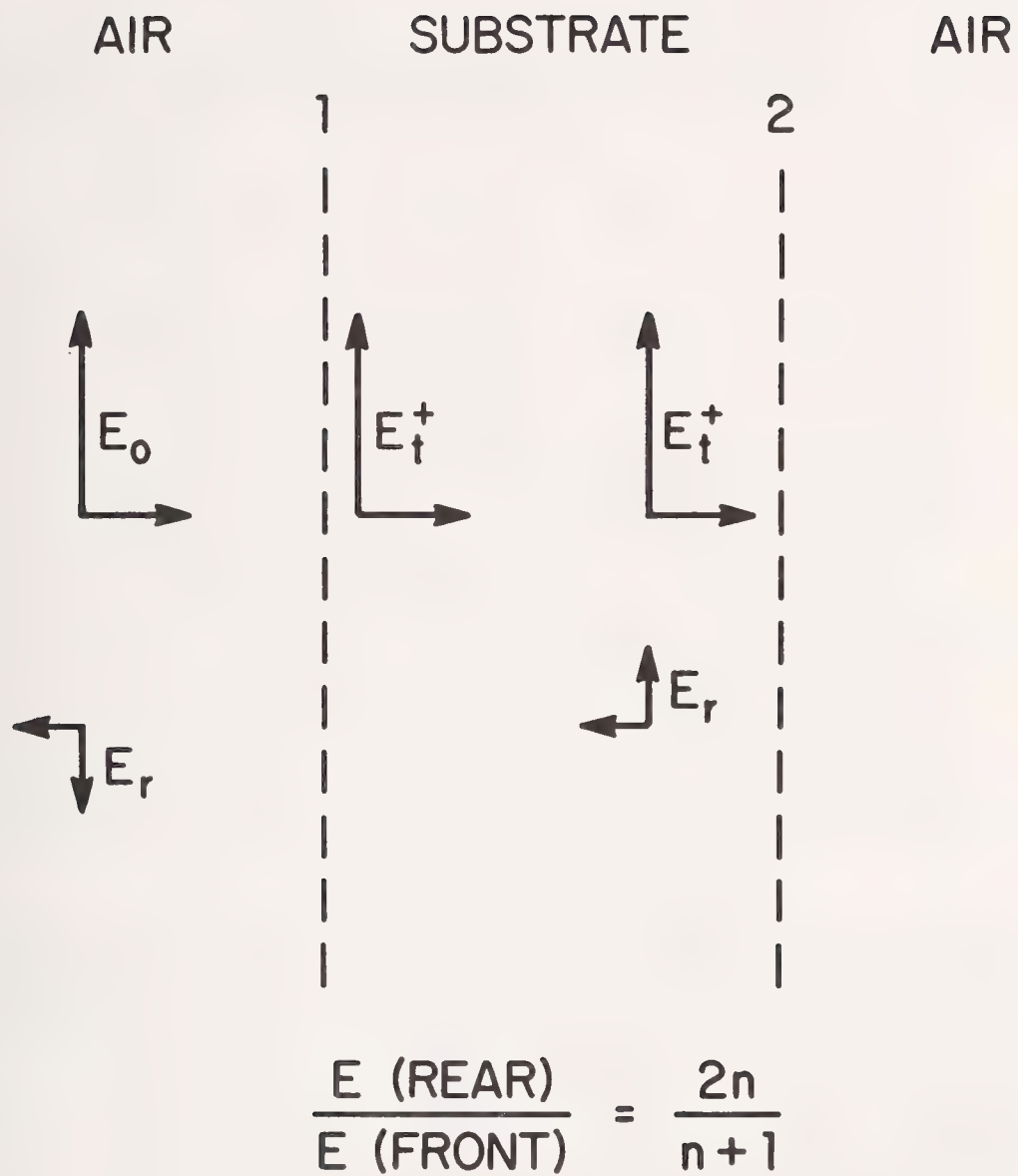


Figure 8. Electric-field vectors of a linearly-polarized laser beam at front and rear surfaces of a transparent dielectric.



#### COMMENTS ON PAPER BY NEWNAM AND GILL

Professor Manenkov pointed out that the scaling of the damage threshold with the square root of the pulse duration is not consistent with all theories of avalanche ionization, as is borne out by his subsequent presentation. Responding to questions about the morphology of the damage, the speaker indicated that for short pulses, that is of the order of 1 nanosecond, the damage at threshold took the form of well localized microscopic pits, but as the pulse duration was increased to 70 nanoseconds a more distributed form of damage was seen over the surface. This could be attributed to the excavation of the surface in the vicinity of damage sites by the longer pulse. He indicated that at power levels approximately 20% higher than that at which the small pits first occurred, damage was seen to occur over the total area of the illuminated region, which might be attributed to bulk absorption in the material.

## 10.6 $\mu\text{m}$ LASER DAMAGE IN COATINGS CONTAINING $\text{As}_2\text{S}_3$ AND $\text{As}_2\text{Se}_3$ <sup>†</sup>

C.C. Tang\*, M. Bass, M.J. Soileau and E.W. Van Stryland  
Center for Laser Studies, University of Southern California  
University Park, Los Angeles, California 90007

The laser damage properties of 10.6  $\mu\text{m}$  coatings containing  $\text{As}_2\text{S}_3$  and  $\text{As}_2\text{Se}_3$  are reported. A TEM<sub>00</sub> mode CO<sub>2</sub> TEA laser with an intracavity CW CO<sub>2</sub> discharge section was the irradiation source in these experiments. This enabled the study to include a test of the role of mode locked pulses on the damage thresholds of the sample coatings.

Coatings containing  $\text{As}_2\text{S}_3$  were damaged only after an incandescence or spark was observed during the irradiation. There was no difference in the intensity threshold,  $\sim 300 \text{ MW/cm}^2$  (peak intensity on axis) for damage in half wave or full wave thick  $\text{As}_2\text{S}_3$  coatings, with or without mode locked pulses in the laser waveform. However, evidence for laser irradiation conditioning was found in certain areas of the  $\text{As}_2\text{S}_3$  coatings.

Two different thresholds were observed for coatings containing  $\text{As}_2\text{Se}_3$ ; one where a spark was observed and a large damage site produced and a second, at  $\sim 30\%$  lower intensity which produced a very small damage site even though no incandescence was detected. The latter occurred at  $\sim 12 \text{ MW/cm}^2$  in both the full and half wave  $\text{As}_2\text{Se}_3$  coatings. Otherwise, the qualitative behavior of the threshold was similar to that of the  $\text{As}_2\text{S}_3$  coatings.

The intensity of threshold for damage to  $\text{As}_2\text{S}_3/\text{KCl}/\text{As}_2\text{S}_3$  anti-reflection coatings on KCl substrates was as high as  $430 \text{ MW/cm}^2$  and did not depend on the presence of mode locked pulses. Three layer AR coatings containing  $\text{As}_2\text{Se}_3$  damage at  $\sim 20 \text{ MW/cm}^2$ . The relationships between the coating damage thresholds and microstructure, design and measured absorption are discussed. Key words:  $\text{As}_2\text{S}_3$ ;  $\text{As}_2\text{Se}_3$ ; coating damage; coating design; defects; laser damage.

### 1. Introduction

Thin film coatings are often the most easily damaged components of an infrared laser system. The 10.6  $\mu\text{m}$ , pulsed damage thresholds of films containing  $\text{As}_2\text{S}_3$  and  $\text{As}_2\text{Se}_3$  are typically  $\sim 325 \text{ MW/cm}^2$  and  $\sim 15 \text{ MW/cm}^2$  respectively. These thresholds were found not to depend significantly on the coating design, the details of the laser pulse waveform or the sequence of the irradiation employed. Layered coating designs used to reduce coating absorption by redistributing the fields in the layers (1)<sup>1</sup> do not significantly reduce the energy absorbed per unit mass of absorptive material. Thus the heating of the coating on exposure to optical irradiation and any failure properties governed by uniform absorption should be independent of the coating design. However, an examination of the morphology of the damage sites reveals that microscopic defects or inclusions are responsible for the failure of the coatings studied to withstand intense laser irradiation. Initial "survival curve" data is consistent with this model since it rules out uniform linear absorption as the dominant pulse damage interaction.

### 2. Experimental

The experiment is shown schematically in figure 1 and the properties of the laser system are listed in table I. The low pressure CW discharge in the TEA laser cavity was used to restrict oscillation to a single longitudinal mode (2) and thus to suppress mode locked pulses in the output. Figure 2 shows the two waveforms used in these experiments.

Coatings were prepared at the Hughes Research Laboratory, (HRL), in Malibu, California, on single and poly-crystalline KCl substrates. The substrate surfaces were polished and etched. The three layer coatings were designed as anti-reflection coatings in the manner discussed later in this paper. Half

<sup>†</sup>This work was supported by D-ARPA under contract No. F 19628-77-C-0094.

\*Current address: Aerospace Corporation, El Segundo, California

<sup>1</sup>Figures in brackets indicate the literature references at the end of this paper.

Table 2. Damage Thresholds... (continued)

Material	Absorption % / Coating	Energy Density* (J/cm <sup>2</sup> )	Power Density* (MW/cm <sup>2</sup> )
As <sub>2</sub> S <sub>3</sub> - λ/2 (N on 1)	0.067	60 (88)	311 (462)
As <sub>2</sub> S <sub>3</sub> - λ (N on 1)	0.12	56 (56)	293 (293)
<sup>†</sup> As <sub>2</sub> S <sub>3</sub> /KCl/As <sub>2</sub> S <sub>3</sub> (N on 1)	0.029	83 (120)	433 (564)
<sup>†</sup> As <sub>2</sub> S <sub>3</sub> /KCl/As <sub>2</sub> S <sub>3</sub> (N on 1)	0.045	8.1 (8.1)	42 (42)

\*The thresholds quoted are the peak on axis values of the indicated quantity, and  $2W_0 = 125 \mu\text{m}$  is the diameter at the focus measured to  $1/e^2$  of the on axis intensity.

The pulse duration was 180 nsec.

<sup>†</sup>The three layer coatings are anti-reflection coatings at  $10.6 \mu\text{m}$ .

#### 4. Coating Design

Figure 3 shows the field distributions in the half wave and the three layer anti-reflection coatings containing As<sub>2</sub>S<sub>3</sub> which were studied. If the As<sub>2</sub>S<sub>3</sub> layers are responsible for absorption in the coating then the three layer design will have less absorption. This is so because there is less of the absorptive material exposed to the light field in the three layer design. However, in the three layer design less material is responsible for proportionally less absorption. Thus, the energy absorbed per unit mass of coating material is unchanged and each coating will be heated to the same temperature by the same light flux. By this argument it is possible to interpret the measured damage thresholds as being caused by uniform linear absorption. The presence of defects or inclusions in the coatings will also give rise to a damage process which is independent of coating design and as shown in the next sections is in fact the principal failure mechanism.

#### 5. Morphology of Coating Damage and Coating Uniformity

In figures 4 through 9 several representative examples of coating damage morphology are shown. Figures 4 through 9 show that in the irradiated area ( $\sim 125 \mu\text{m}$  in dia.) there were one or more randomly located sites which were easily damaged. The crazing in figures 8 and 9 is due to the polycrystalline nature of the substrate on which the coating was placed. Figure 9 shows that when a spark was produced on an As<sub>2</sub>Se<sub>3</sub> coatings, a significant portion of the coating was completely removed. In this context it is important to note the value of using more than one type of microscope illumination to examine laser damage.

In figure 5, a case of spark damage to As<sub>2</sub>Se<sub>3</sub> coating, there are interference "ripples" with spacing  $\lambda/n$  KCl similar to those described by Temple and Soileau.(4) These are due to light scattered from a defect in interfering with the incoming laser beam. The coating to substrate interface is an "exit" surface in the same sense as in reference 4 and the "ripples" are found, as expected, on the KCl substrate surface.

Figure 10 is a plot of the damage threshold as a function of position on an As<sub>2</sub>Se<sub>3</sub> coating. This data demonstrates the point-to-point non-uniformity of the coating and is additional evidence for a damage mechanism dominated by the presence of defects or inclusions.

#### 6. Survival Curve Data

A survival curve is a statistical means to examine the mechanism causing laser damage.(5) A uniform intensity pulse is used to irradiate several sites on or in a sample and the statistics of the period of time each site can survive this irradiation is used to determine the damaging interaction. If the dominant interaction is uniform linear absorption, all sites will be identical and all will survive exactly the same period of time. Figure 11 shows the distortion of a "flat-topped" laser pulse which occurs when three different sites on a ZnSe containing coatings were damaged. Clearly the three sites survive different times and so these data rule out a significant role for uniform linear absorption in the pulsed laser damage process for such a coating.

More extensive survival curve studies for bulk material and coatings are planned. The initial data presented here shows the potential for this technique to sort out damage mechanisms.

#### 7. Summary and Conclusions

The principal results of this work are summarized in table 3. Included is data from 1976 on ZnSe containing coatings (6) which show that the best currently available coatings are those containing As<sub>2</sub>S<sub>3</sub> or ZnSe. The damaging interaction in all the coatings tested is determined by the presence of microscopic defects or inclusions



and full wave layers were studied to test the role of coating design in determining the damage threshold.

The occurrence of damage was detected by an observer viewing the irradiated site through a long working distance microscope. Both white light and HeNe laser light scattering were used with comparable results. The coatings which contained  $\text{As}_2\text{Se}_3$  often damaged with no visible sparks or incandescence at fluxes 30% less than required to produce a spark. However,  $\text{As}_2\text{S}_3$  coatings only damaged after the irradiation produced a spark.

Both 1 on 1 and N on 1 irradiation sequences (3) were used but only the uncoated substrate showed a significant irradiation conditioning effect. The irradiated sites were inspected with visible microscopy to determine the damage site morphology. Normal incidence reflected, bright field transmitted, and phase contrast transmitted illumination were used to maximize the effectiveness of the morphological examinations.

Table 1.  $\text{CO}_2$  laser parameters & performance data.

TEA Section:	
Discharge Length (Double Rogowski Electrodes)	41 cm.
Energy Storage Capacitance	0.08 $\mu\text{f}$
Flow Rate Ratio ( $\text{He}:\text{N}_2:\text{CO}_2$ )	8.7:2.4:2.6 l/min.
Typical Input Energy into Pulsed Section	21 J
CW Section:	
Discharge Length	104 cm.
Gas Mixture	86%:7%:7%
Gas Pressure	3 Torr
Flowing gas, water cooled	
Mirrors	100% R - flat/Si 80% R - 10 meter/Ge
Brewster Windows	KCl
Intracavity Aperture Diameter for $\text{TEM}_{00}$ Mode	8 mm.
Total Cavity Length	307 cm.
Maximum $\text{TEM}_{00}$ Energy Available at the Target	30 mJ
Typical Width of Pulse (FWHM)	180 nsec

### 3. Measured Damage Thresholds

The damage thresholds obtained in these experiments are listed in table 2. The values for coating absorption were measured by H.R.L. as part of the coating characterization. Clearly coatings containing  $\text{As}_2\text{S}_3$  can withstand 20 times the flux that will damage one containing  $\text{As}_2\text{Se}_3$ . The data also demonstrate that the damage flux for each type of coating does not depend strongly on the coating design. The last entry for an  $\text{As}_2\text{S}_3/\text{KCl}/\text{As}_2\text{S}_3$  three layer coating represents data for a poor quality coating.

No significant laser conditioning (N on 1) effect was observed except for the uncoated KCl substrate surface. In addition, the threshold for all the listed samples did not depend on which pulse waveform was used (fig. 2).

Table 2. Damage thresholds for  $\text{As}_2\text{S}_3$  and  $\text{As}_2\text{Se}_3$  containing coatings.

Material	Absorption % / Coating	Energy Density* ( $\text{J}/\text{cm}^2$ )	Power Density* ( $\text{MW}/\text{cm}^2$ )
Surface of KCl single crystal (N on 1)		171 (329)	871 (1720)
$\text{As}_2\text{Se}_3 - \lambda/2$ (N on 1)	0.02	2.40 (2.40)	12.7 (12.7)
$\text{As}_2\text{Se}_3 - \lambda$ (N on 1)	0.018	2.60 (3.03)	13.5 (15.8)
$\text{As}_2\text{Se}_3/\text{KCl}/\text{As}_2\text{Se}_3$ (N on 1)	0.03	3.85 (3.85)	20.1 (20.1)
$\text{As}_2\text{S}_3/\text{KCl}/\text{As}_2\text{S}_3$ (N on 1)	0.02	3.3 (3.3)	17.2 (17.2)

Table 3. Summary of Coating Damage Thresholds

KCl Substrate Surface	1000 MW/cm <sup>2</sup>
Coatings on KCl Coatings:	
As <sub>2</sub> Se <sub>3</sub>	15 MW/cm <sup>2</sup>
As <sub>2</sub> S <sub>3</sub>	325 MW/cm <sup>2</sup>
ZnSe	450 MW/cm <sup>2</sup>

Cause of Coating Failure:

Mechanical Defects and/or Inclusions

#### 8. Acknowledgments

We wish to acknowledge the assistance of J. Menders, A. Stewart, K. Moravvej and M. Harvey in the damage measurements.

#### 9. References

- (1) M. Braunstein, et. al., "Laser Window Surface Finishing and Coating Science", Semi-Annual Technical Report 2, AFCRL - TR - 76 - 0048, Hughes Research Laboratory (1976).
- (2) A. Gondhalekar, N.R. Heckenberg and E. Holzhauser, J. Quantum Electr. QE-11, 3 (1975).
- (3) M. Bass and K.M. Leung, J. Quantum Electr. QE-12, 82 (1976).
- (4) P.A. Temple and M.J. Soileau, NBS Special Publication 462, p. 371.
- (5) D. Milam, R.A. Bradbury, R.H. Picard and M. Bass, NBS Special Publication 414, p. 169.
- (6) D. Zuccaro, M. Braunstein, M. Bass, K. Leung and C. Tang, "Status Report of 3 Layer 10.6  $\mu$ m A-R Coatings on KCl", Proceedings of Infrared Laser Window Materials Meeting, July 12, 1976, Boulder, Colorado.

#### 10. Figures

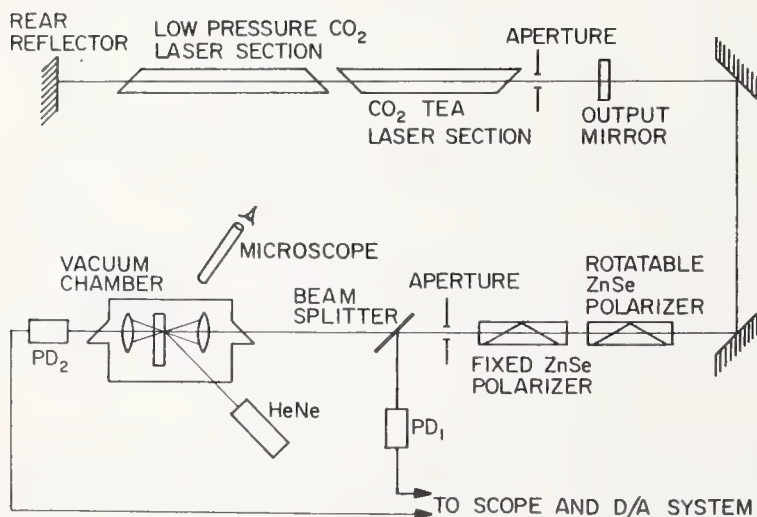
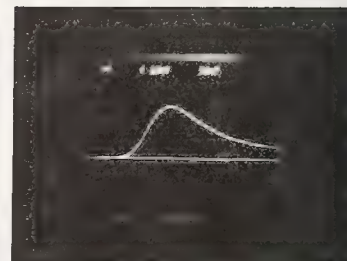


Figure 1. Schematic of the equipment.



MODE-LOCKED PULSED LASER OUTPUT



TEMPORAL PROFILE OF PULSED LASER OUTPUT  
USING CW SECTION

Figure 2. Temporal waveforms used in the damage measurements.

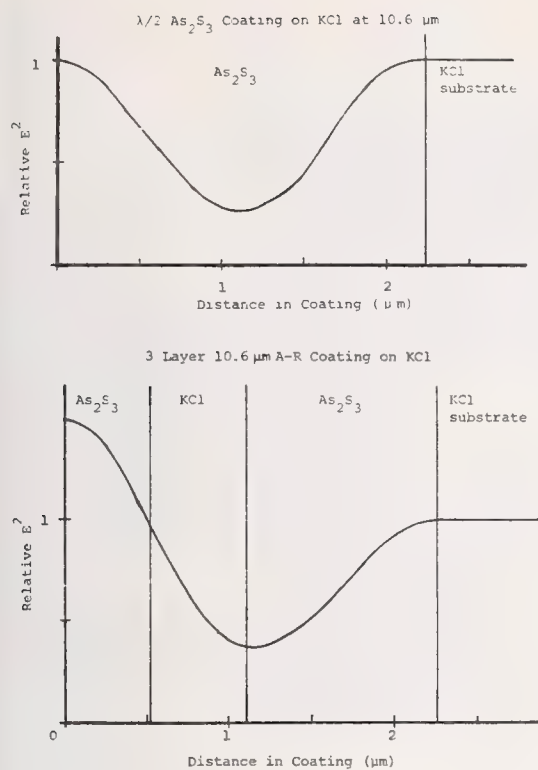


Figure 3. Electric field distributions in coatings containing  $\text{As}_2\text{S}_3$ . The electric field squared is normalized to the electric field in the substrate.

DAMAGE TO  $\lambda/2$  - THICKNESS  $\text{As}_2\text{S}_3$  ON KCL SUBSTRATE

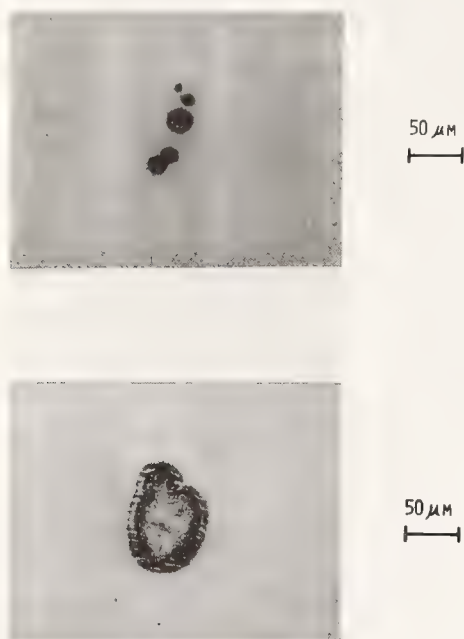


TRANSMITTED PHASE CONTRAST ILLUMINATION

Figure 4. Damage near threshold to a  $\lambda/2$   $\text{As}_2\text{S}_3$  coating on KCl at  $10.6 \mu\text{m}$ .

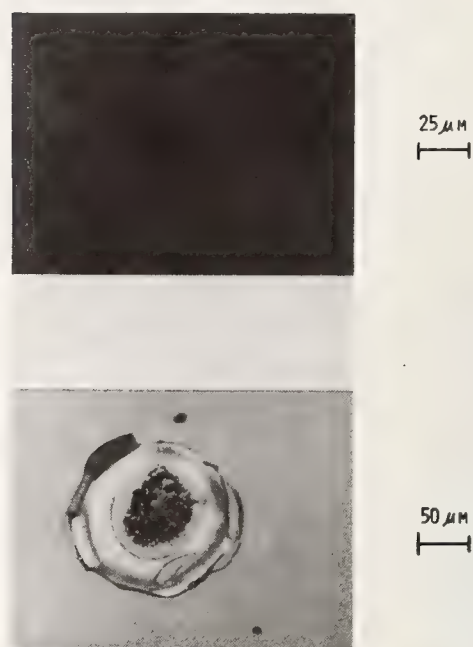


DAMAGE TO  $\lambda/2$  THICKNESS  $\text{As}_2\text{Se}_3$  ON KCL SUBSTRATE



REFLECTED NORMAL INCIDENCE ILLUMINATION

DAMAGE TO  $\lambda$  THICKNESS  $\text{As}_2\text{Se}_3$  ON KCL SUBSTRATE

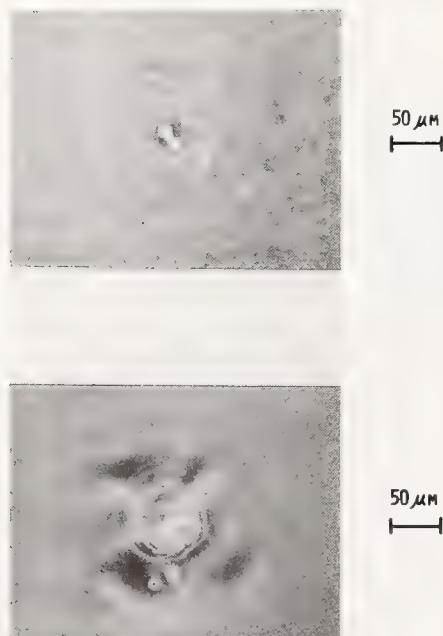


REFLECTED NORMAL INCIDENCE ILLUMINATION

Figure 5. Damage near threshold to a  $\lambda/2$   $\text{As}_2\text{Se}_3$  coating on KCl to 10.6  $\mu\text{m}$ . (Upper photo is for damage with no spark and lower is a case where a spark was observed.)

Figure 6. Damage near threshold to a  $\lambda$   $\text{As}_2\text{Se}_3$  coating on KCl and 10.6  $\mu\text{m}$ .

DAMAGE TO  $\text{As}_2\text{S}_3/\text{KCl}/\text{As}_2\text{S}_3$   
ON KCL SUBSTRATE



TRANSMITTED PHASE CONTRAST ILLUMINATION

Figure 7. Damage near threshold to an  $\text{As}_2\text{Se}/\text{KCl}/\text{As}_2\text{Se}_3$  10.6  $\mu\text{m}$  anti-reflection coating on KCl.

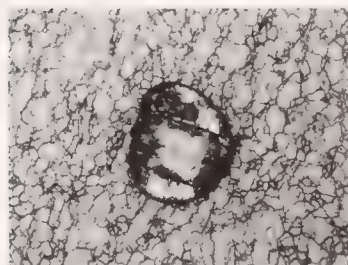
DAMAGE TO  $\text{As}_2\text{Se}_3/\text{KCl}/\text{As}_2\text{Se}_3$   
ON POLYCRYSTALLINE KCl SUBSTRATE



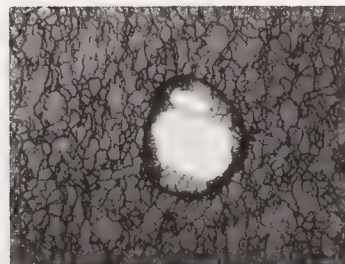
REFLECTED NORMAL INCIDENCE ILLUMINATION

Figure 8. Damage near threshold to an  $\text{As}_2\text{Se}_3/\text{KCl}/\text{As}_2\text{Se}_3$  10.6  $\mu\text{m}$  anti-reflection coating on polycrystalline KCl when no spark was produced during the irradiation.

DAMAGE TO  $\text{As}_2\text{Se}_3/\text{KCl}/\text{As}_2\text{Se}_3$   
ON POLYCRYSTALLINE KCl SUBSTRATE



REFLECTED NORMAL INCIDENCE ILLUMINATION



TRANSMITTED BRIGHT FIELD ILLUMINATION

Figure 9. Damage to an  $\text{As}_2\text{Se}_3/\text{KCl}/\text{As}_2\text{Se}_3$  10  $\mu\text{m}$  anti-reflection coating on polycrystalline KCl when a spark was produced during the irradiation.

# EFFECTS OF COATING NON-UNIFORMITY ON DAMAGE THRESHOLD

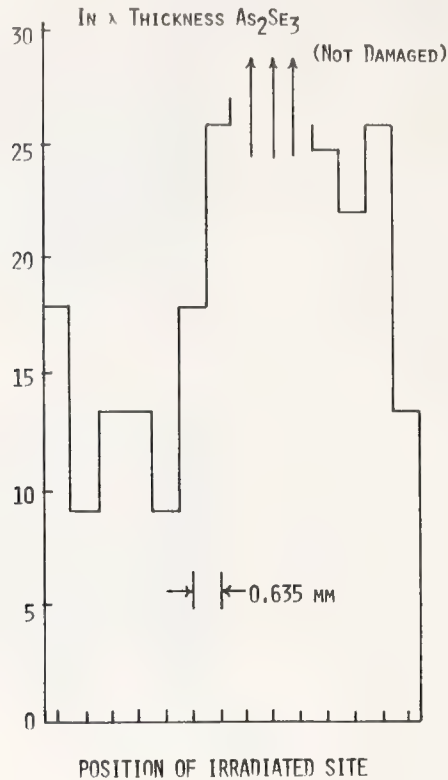


Figure 10. Laser damage threshold versus position on an  $\text{As}_2\text{Se}_3$  coating. This demonstrated the site-to-site non-uniformity of the coating.

## TRANSMITTED WAVEFORM DISTORTION DUE TO $10.6\mu\text{m}$ LASER DAMAGE ON A $\text{ZnSe/KCl/ZnSe}$ THIN FILM COATING A FLAT TOPPED PULSE WAS USED

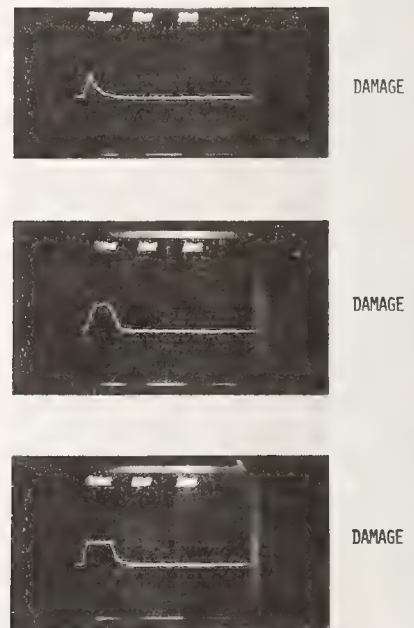


Figure 11. Transmitted waveform distortion due to  $10.6\mu\text{m}$  laser induced damage in a  $\text{Anse/KCl/AnSe}$  anti-reflection coating on  $\text{KCl}$ . The incident waveform was a flat topped pulse  $\sim 30\mu\text{sec}$  long. This demonstrates the site-to-site non-uniformity of the coating.

SURVIVAL CURVE PROOF THAT DAMAGE MECHANISM IS NOT UNIFORM ABSORPTION



COMMENTS ON PAPER BY TANG, BASS, SOILEAU, AND VanSTRYLAND

*No discussion on this paper.*

# LARGE-SPOT DF LASER DAMAGE OF DIELECTRIC-ENHANCED MIRRORS\*

D. B. Nichols and R. B. Hall  
Boeing Aerospace Company  
Seattle, WA 98124

and

R. A. House II  
Air Force Weapons Laboratory  
Kirtland AFB, NM 87117

Large-spot DF laser damage thresholds have been measured for several dielectric-coated mirrors. Five coating designs were tested, using both molybdenum and Cer-Vit substrates. Chemical laser pulses with FWHM of 4  $\mu$ sec and energies up to 70 J were focused to a target-spot diameter of 1 cm. Each test site was exposed to pulses of successively larger energies. Measured thresholds in terms of pulse peak irradiance ranged up to 21 MW/cm<sup>2</sup>, which is above the plasma formation threshold for bare aluminum. The mirrors exhibited no surface plasma during small-scale damage, but a well-defined laser-supported absorption wave during catastrophic damage. No threshold differences due to substrate material were apparent. Factor-of-ten spot-size tests were used to investigate the range of validity of the spot-size scaling laws which have successfully correlated damage data over smaller areas. Whole-target and microscopic damage morphology are examined briefly.

Key words: damage thresholds; dielectric-enhanced mirrors; large-spot laser damage; pulsed DF laser damage; substrate dependence; surface plasmas; spot size dependence.

## 1. Introduction

The emergence of high power chemical lasers has led to an increasing concern with optical components for the 2 - 5  $\mu$ m wavelength region. Experimental laser damage data, however, are still heavily concentrated at other wavelengths. Damage studies with pulsed chemical laser radiation have typically involved spots only 10 to 100  $\mu$ m in diameter due to limited total energy per pulse [1]<sup>1</sup>.

We have measured damage thresholds for dielectric enhanced mirrors with a 1 cm diameter beam spot. One objective was to investigate the large-spot limit for the size-scaling laws which have been very useful in describing dielectric damage for small spots [2]. Five coating designs were compared, with each coating on a metal and a glass substrate. Each of the ten mirrors was exposed to pulsed beams of two different diameters, giving a total of twenty damage sites. Each site received several exposures.

## 2. Laser Beam Characteristics

The laser used in this work was the Boeing PHOCL-10 photoinitiated HF/DF device [3]. Figure 1a shows the far-field burn pattern at the focus of a 200-cm mirror. The lighter curve is an analytic approximation. The overall circular shape, with four indentations, is due to the geometry of the laser itself. Figure 1b shows the configuration of a detailed beam scan. The results of this scan are shown in figure 2. The central part of the beam is quite uniform. Figures 1 and 2 are from reference [4], which includes further discussion of the spatial profile.

Figure 3 is the DF time profile, which has a generally smooth shape, and has a FWHM of 4.0  $\mu$ sec. This profile, sampled from the entire 10 cm diameter near-field beam, was measured for each laser shot and was essentially unchanged throughout these tests. Beam energy was varied by attenuation external to the laser, so that the relative time profile was independent of beam energy.

## 3. Mirror Samples

The ten mirror samples are listed in table 1. Five coating designs (designated by numbers 2 to 6) were each deposited on both molybdenum and Cer-Vit substrates (denoted by "M" and "C"). The samples were fabricated in 1975 by Coherent Radiation (coatings No. 2 - 4) and Northrop (coatings No. 5 and 6).

---

\* Work supported by the Air Force Weapons Laboratory under Contract F29650-77-90202.

1. Figures in brackets indicate the literature references at the end of this paper.

Table 1. Coating designs of ten dielectric-enhanced mirror samples. The tabulated reflectances are from absorption calorimetry measurements. Each coating design was deposited on both a molybdenum (M) and a Cer-Vit (C) substrate.

SAMPLE NUMBER	REFLECTANCE	COATING DESIGN
2M	0.9905 $\pm$ 0.0007	Cr + (Al <sub>2</sub> O <sub>3</sub> /Si) <sup>3</sup>
2C	0.9792 $\pm$ 0.0007	
3M	0.9890 $\pm$ 0.0007	Cr + Ag + (SiO/Si) <sup>1</sup>
3C	0.9880 $\pm$ 0.0007	
4M	0.9916 $\pm$ 0.0007	Cr + Au + (SiO/Si) <sup>1</sup>
4C	0.9918 $\pm$ 0.0007	
5M	0.9961 $\pm$ 0.0003	Ag + (ThF <sub>4</sub> /ZnS) <sup>3</sup>
5C	0.9909 $\pm$ 0.0003	
6M	0.9978 $\pm$ 0.0003	Ag + (ThF <sub>4</sub> /ZnSe) <sup>3</sup>
6C	0.9937 $\pm$ 0.0003	

The tabulated reflectances are from absorption calorimetry measurements made in early 1977 at the University of Alabama in Huntsville. At least two separate measurements were made for each sample. The two uncertainties indicated in table 1 reflect the maximum observed scatter between duplicate measurements within the two groups.

#### 4. Test Configuration

These tests were carried out in the focal plane of an  $f = 76$  cm mirror. The laser pulse energy and time profile were monitored by two sample beams from a CaF<sub>2</sub> wedge. Return of laser radiation from the target mirror to the laser and calorimeter was prevented by orienting the target mirror normal at a 12° angle from the incident beam axis; this angle is a function of the  $f$  number of the final focusing mirror.

Each sample was mounted with a sealed partition along a diameter, providing two isolated test areas. One side was used for 1 cm diameter beam-spot tests and the other side for 0.1 cm diameter beam-spot tests. To obtain the 1 cm diameter beam, the 45° relative profile of figure 2 was truncated at about the half-maximum point by introducing a 1-cm diameter aluminum aperture 0.1 cm in front of the test mirror. Eighty-three percent of the total energy passed through this hole. The 0.1 cm diameter beam was formed by a  $0.097 \pm 0.002$  cm aperture in a 0.025 cm-thick aluminum plate situated 0.05 cm in front of the test mirror. This 0.1 cm hole was beveled to give an effective aperture thickness of 0.01 cm.

#### 5. Procedure and Results

For each test site, exposures began below 4 J/cm<sup>2</sup>, or 1 MW/cm<sup>2</sup> peak intensity, and proceeded on the same site with nominal intensity increases of 50 to 100%. At least ten minutes elapsed between shots for the Cer-Vit samples. Small-scale and finally catastrophic damage was determined by examination of the site between each shot with strong illumination. For this inspection, the 0.1 cm aperture was removed and repositioned by a translation stage.

The tests and results are summarized in figure 4. The five groups of data correspond to the five coating designs. Molybdenum or Cer-Vit substrates are denoted by "M" or "C." A large or small circle in figure 4 indicates a 1.0 or 0.1 cm beam spot; this distinction is made by the letter "l" or "s" in site designations. Test sites are designated in the text by coating, substrate, and spot size; e.g. "site 6Cl."

For each test site the successive laser shots are indicated in figure 4 by horizontal lines. The percentage of area damaged after each shot is roughly indicated by the extent of cross hatching from that exposure down toward the previous exposure. Shading which extends completely from one shot down to the previous shot indicates that the entire central area of the mirror coating was destroyed.

The mirror surfaces were monitored for plasma formation during exposure by open-shutter photography. The large double XX in figure 4 indicates plasma formation with the nearby aperture in place, leaving in doubt whether initiation occurred on mirror or aperture or both. In several cases, plasma was anticipated due to high intensities, and the 1 cm aperture was removed before the final shot, to preclude plasma initiation on the aperture edges. In these cases, mirror surface plasma formation is indicated by a single X. The only plasma observed with the 0.1 cm aperture was a very weak event indicated by the small double xx.



## 6. Damage Site Morphology

Coatings No. 5 and 6 exhibit the highest thresholds in figure 4. Figure 5a and 5b show the sample in situ during and after an exposure with beam-axis fluence of  $54 \text{ J/cm}^2$ . Figure 5c and 5d are during and after a  $100 \text{ J/cm}^2$  shot. Figure 5a and 5c are open-shutter with room lights; figure 5b and 5d have additional illumination. The damaged area is shown in relief by oblique lighting in figure 5e.

For the same substrate and spot size figure 6 shows site 6C1 after  $50 \text{ J/cm}^2$  (fig. 6a) and  $63 \text{ J/cm}^2$  (fig. 6b). Comparison with site 5C1 shows that the replacement of ZnS with ZnSe reduces the small-scale damage threshold from  $50 \text{ J/cm}^2$  to  $30 \text{ J/cm}^2$ .

Figure 7 shows an area along the edge of the 1 cm diameter damage zone of site 5M1 after an exposure of  $88 \text{ J/cm}^2$ . At the bottom of the figure is an undamaged region. Next is a zone where the coating is fractured but still in place. The relief apparent in the next region indicates major disruption of the coating, and this zone has an overall shape which suggests blow-off effects radiating from the spot center above. Finally, the inner region at the top has the coating entirely removed.

Site 5Ms sustained the highest intensity with the least damage. The Nomarski micrograph of figure 8a shows the undamaged mirror roughness, as well as several major damage points. The peak intensity here was  $23 \text{ MW/cm}^2$ . Darkfield (fig. 8b) shows additional small damage points.

Figure 9 is the small-spot damage of the mirror shown in figure 5. The two major damage areas of figure 9a are connected by a region of fringes which is more apparent in darkfield or the Nomarski view of figure 9b. We attribute these fringes to interference between coating layers which have been delaminated by the damage event.

## 7. Conclusions

Figure 4 allows direct comparison of threshold data as a function of several variables.

### 7.1 Coating Materials

The highest damage thresholds were observed with coating designs No. 4, Ag +  $(\text{ThF}_4/\text{ZnS})$ , and No. 5, Ag +  $(\text{ThF}_4/\text{ZnSe})$ . These two coatings also exhibited low absorption in calorimetry measurements (table 1).

### 7.2 Substrate Effect

Threshold results are similar for molybdenum and Cer-Vit substrates. The thermal conductivity of the metal substrate gives no significant advantage for single pulses with FWHM of  $4 \text{ } \mu\text{sec}$ .

### 7.3 Spot Size Effect

Damage intensities  $q_{\text{thresh}}$  are similar for 1.0 cm and 0.1 cm beam spot diameters. Under the present conditions, the dielectric-damage scaling law [2],  $q_{\text{thresh}} \sim d_{\text{spot}}^{-1}$  does not extend to spot diameters larger than 0.1 cm.

### 7.4 Threshold Intensities

The absolute values of damage thresholds for the best mirror coatings,  $12\text{--}22 \text{ MW/cm}^2$ , are high, and comparable to the thresholds for formation of surface plasmas on bare metals; the threshold for unpolished aluminum under these conditions is  $15 \text{ MW/cm}^2$  [4].

Significant small-scale damage often occurred without mirror-surface plasma; the occurrence of plasma, on the other hand, was always associated with catastrophic surface damage.

## 8. References

- |   |   |
|---|---|
| [1]. Bass, M., Soileau, M. J., Tang, C. C., and Van Stryland, E. W., "Pulsed HF/DF Laser Damage in Window Materials," these Proceedings.  | [3]. Nichols, D. B., Hall, R. B., and McClure, J. D., J. Appl. Phys. <u>47</u> , 4026 (1976).   |
| [2]. Bettis, J. R., House, R. A., and Guenther, A. H., in <u>Laser Induced Damage in Optical Materials</u> : 1975, A. J. Glass and A. H. Guenther, eds. (NBS Spec. Publ. 462, 1976) p. 338. | [4]. Hall, R. B., Maher, W. E., Nelson, D. J., and Nichols, D. B., Report AFWL-TR-77-34 (Air Force Weapons Laboratory, Kirtland AFB, NM, 1977). |

## 9. Figures

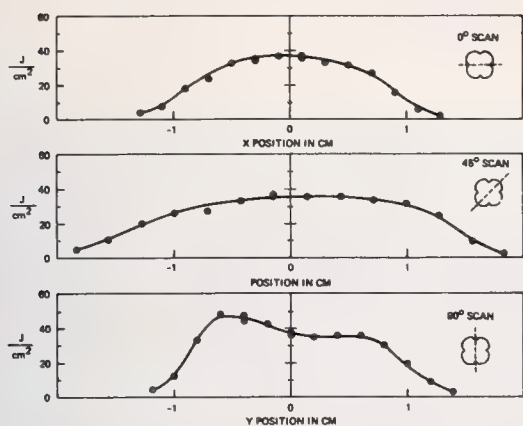


Figure 1. (a) Trace of the far-field beam profile (dark outline at the focal plane of an  $f = 200$  cm mirror. The lighter line is an analytic approximation. (b) Configuration of three beam scans.

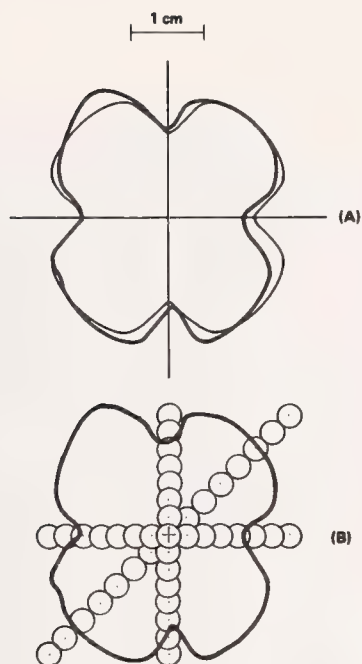


Figure 2. Results of far-field beam profile scans.

### DF Laser Pulse (70 J)

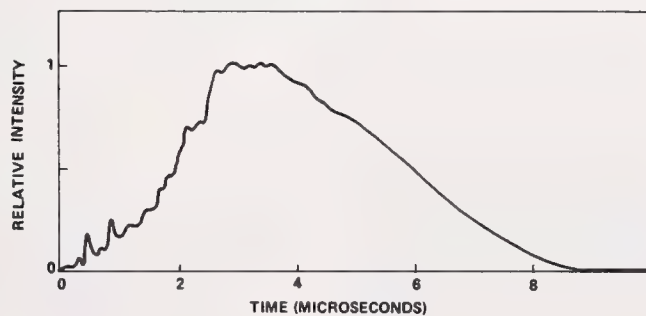


Figure 3. Time profile of the DF laser pulse.

## DF Laser Damage: Dielectric-Coated Mirrors

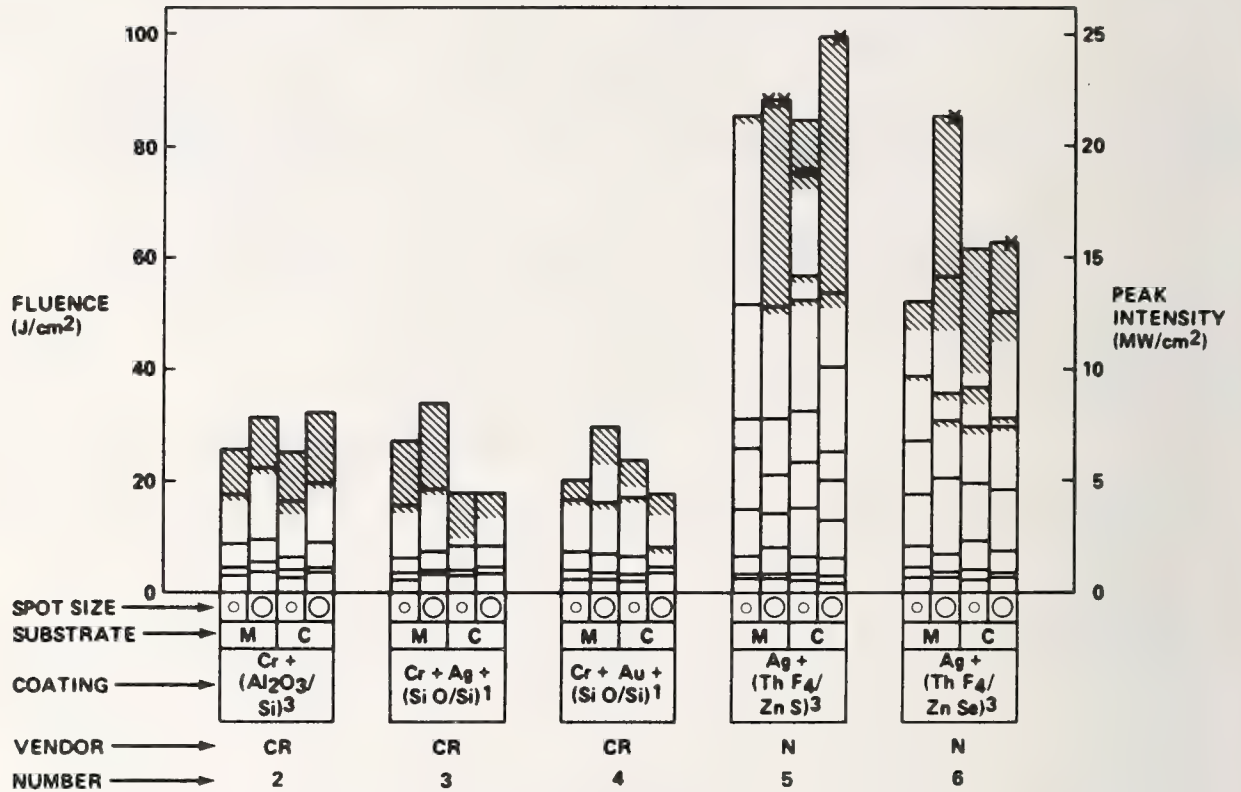


Figure 4. Summary of test sites, exposure histories, and damage results. Five coatings (No. 2 to 6), each on two substrates (molybdenum "M" or Cer-Vit "C"), were exposed to beam spots of 1 cm (large circle) or 0.1 cm (small circle) diameter. Laser shots are indicated by horizontal bars and damage is shown by shading (see text). Occurrence of surface plasma is indicated by "X."





(a)

Figure 5. Site 5C1 (coating No. 5 on Cer-Vit with 1 cm diameter spot). (a) and (b), during and after a  $54 \text{ J/cm}^2$  exposure. (c), during  $100 \text{ J/cm}^2$ . (d) and (e), after  $100 \text{ J/cm}^2$ .



(b)



(c)





(p)



(e)



(a)

Figure 6. Site 6C1, (a) after  $50 \text{ J/cm}^2$ , and (b) after  $63 \text{ J/cm}^2$ . All mirror samples were 3.8 cm in diameter.





(b)



Figure 7. Edge region of 1 cm diameter damage at Site 5M1, after an  $88 \text{ J/cm}^2$  exposure. The width of this micrograph is 0.1 cm.





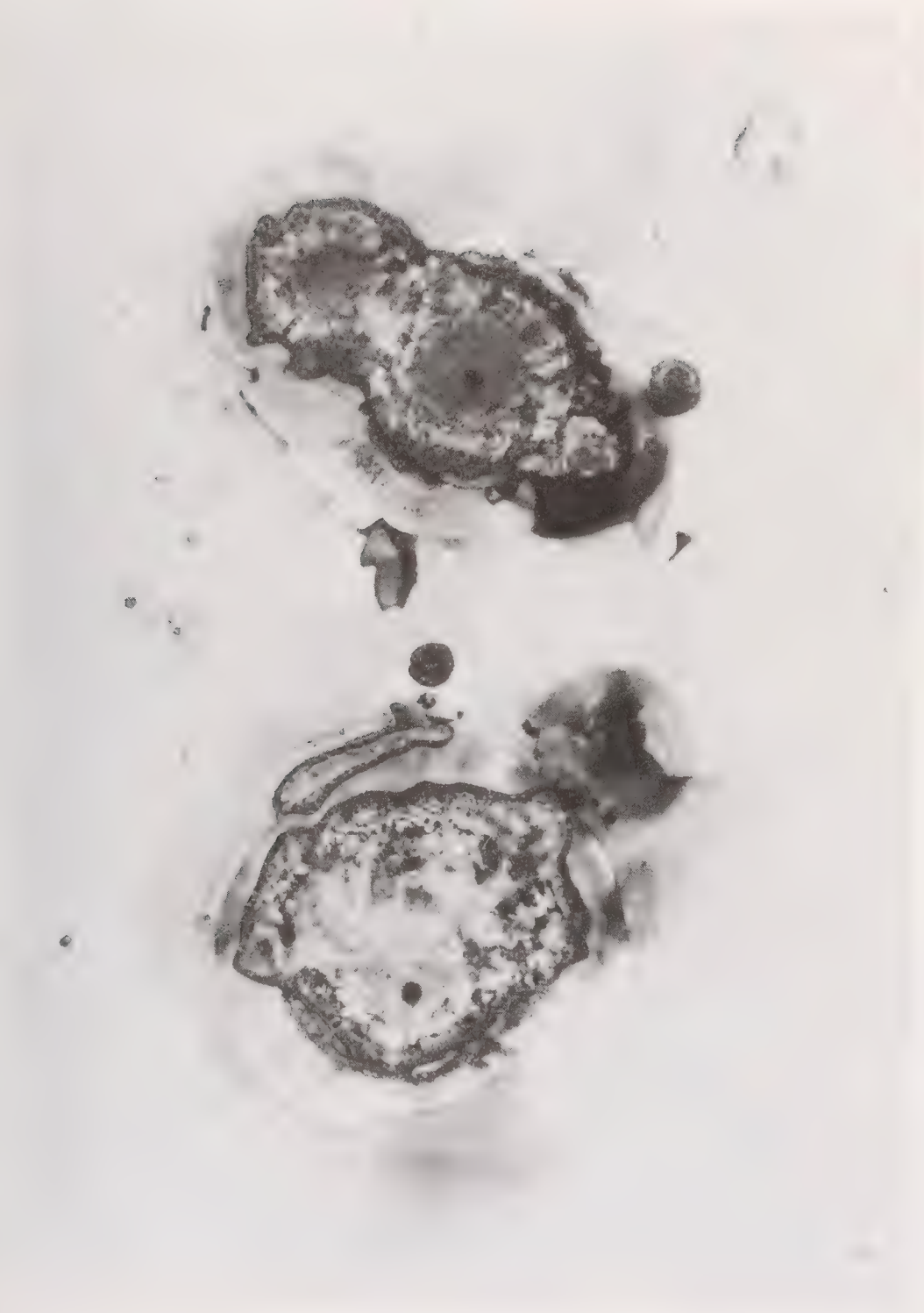
(a)

Figure 8. Nomarski (a) and darkfield (b) micrographs of Site 5Ms after  $85 \text{ J/cm}^2$ . The width of these micrographs is 0.1 cm.





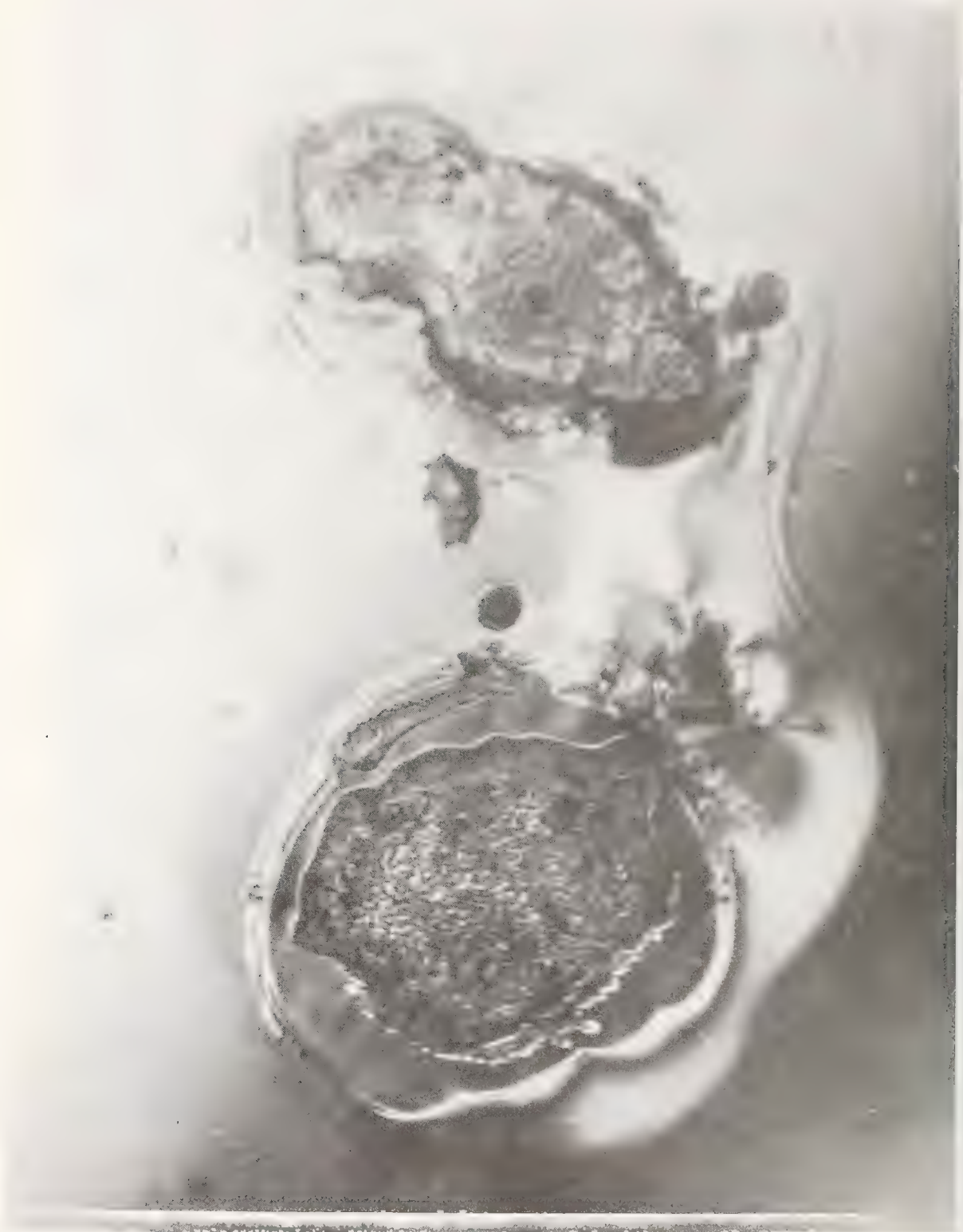
(b)



(a)

Figure 9. Brightfield (a) and Nomarski (b) views of Site 5Cs showing damage from an  $84 \text{ J/cm}^2$  pulse on a  $0.1 \text{ cm}$  diameter area. The width of this micrograph is  $0.1 \text{ cm}$ .

(b)





## DEFECTS AND IMPURITIES IN $\text{As}_2\text{S}_3$ , $\text{As}_2\text{Se}_3$ , AND NaF COATINGS\*

T. M. Donovan, A. D. Baer, J. H. Dancy, and J. O. Porteus  
Physics Division, Michelson Laboratories  
Naval Weapons Center, China Lake, California 93555

The damage thresholds of thin films of chalcogenide glasses are known to be lower than the thresholds of thin films of NaF. On the other hand, the absorptance of NaF thin films is high. The mechanisms responsible for this performance are discussed. It is suggested that the low damage threshold of chalcogenide glasses is due to the presence of micron-sized crystallites. These crystallites are not present on a fresh film, but grow on the films over a period of days, and they are an arsenic-rich sulfide, and not an oxide as has been reported. It is suggested that the high absorptance of the NaF thin films is due to a thin layer of water adsorbed on the surface, and that this water layer forms quickly when the coating is exposed to atmosphere.

Key words: Arsenic triselenide; arsenic trisulfide; Auger; damage; defects; electron microscopy; ESCA; optical coatings; thin films.

### 1. Introduction

Deposition, absorption, and  $\text{CO}_2$ -laser damage threshold for  $\text{As}_2\text{S}_3$ ,  $\text{As}_2\text{Se}_3$ , and NaF coatings and the use of these materials in three-layer antireflection designs for KCl and NaCl have been reported [1,2,3,4]<sup>1</sup>. Such coatings have been made with absorptions of  $5 \times 10^{-4}$  coated surface. The chalcogenide glasses have low absorption ( $\beta \cong 1 \text{ cm}^{-1}$  at  $10.6 \text{ }\mu\text{m}$ ) and  $\text{As}_2\text{S}_3$  is the only material reported [2] to have been deposited in thin film form with bulk-like absorption coefficients,  $\sim 1 \text{ cm}^{-1}$  at  $10.6 \text{ }\mu\text{m}$ , which is also among the lowest absorption reported in coatings. Films of  $\text{As}_2\text{S}_3$  have survived unpulsed  $\text{CO}_2$ -laser radiation with power levels in excess of  $100 \text{ kW/cm}^2$  [5]. Being insoluble in water, they form protective layers for hygroscopic KCl and NaCl [6]. A potentially serious problem with  $\text{As}_2\text{S}_3$  and  $\text{As}_2\text{Se}_3$  coatings, however, is their relatively low threshold for damage by pulsed  $\text{CO}_2$ -laser radiation [4]. NaF films have absorption levels greater than bulk NaF as well as  $\text{As}_2\text{S}_3$  and  $\text{As}_2\text{Se}_3$  coatings, and this excess absorption limits the performance of the three-layer design.

Damage-threshold limitations of a film become apparent when one examines how the damage threshold of a sample is degraded when it is coated with the film. Figures 1 and 2 show the damage thresholds of uncoated NaCl and coated NaCl, respectively. The samples, 1.5-inch diameter, single crystal, were obtained from Harshaw Chemical Company and prepared by etching for 3 min in HCl. The  $\text{As}_2\text{S}_3$  film was deposited at  $25^\circ\text{C}$  in a trapped, diffusion-pumped system. The presence of a large number of defects on the films ( $3 \times 10^4/\text{mm}^2$ ) was verified before damage testing. The damage threshold was measured by Porteus [7] using pulsed  $10.6 \text{ }\mu\text{m}$  radiation, 100 ns pulse length, and  $620 \text{ }\mu\text{m}$  spot diameter. Damage was identified according to a number of different criteria and plotted, as shown in figures 1 and 2. The cross-hatched bar on these figures indicates the average energy for damage, while the overlapping lighter bar shows the range of levels at which damage was observed. Pit formation was not observed on the uncoated sample but was observed on the coated sample. As shown, light and ion emission from the film occurred at one-third (or less) the energy density required for uncoated sample damage. The light appears to be emitted from tiny points, which could be associated with the micron-sized defects. These data demonstrate that the damage threshold of an  $\text{As}_2\text{S}_3$ -coated sample is much lower than that of uncoated samples, and that the damage mechanism for coated samples is different from that for uncoated samples.

Defects in films of chalcogenide glasses could cause the damage thresholds of the films to be reduced. Blisters and crystallites a few microns in diameter grow in fresh films of  $\text{As}_2\text{S}_3$  over a period of several days. The crystallites have diameters up to a few microns and rest on the surface of the film, and could cause a reduction in damage threshold. A few microns is large enough compared to the light wavelength of interest that interference of the incident light with light reradiated from the crystallites can increase the electric field in regions around the defect [8,9]. Consequently, dielectric breakdown can occur at lower intensities of incident radiation. We regard this model for laser damage of chalcogenide films as highly plausible but not fully verified. If the model is correct, then performance of chalcogenide films can be increased by eliminating the defects or greatly reducing their size. Much of the following discussion is a report of studies of the defects and attempts to eliminate them. The size and shape of the defects are discussed in section 2. Their chemical nature and the chemical nature of the films are discussed in section 3, and the results of some attempts to eliminate the defects are reported in section 4.

\* Work supported by Defense Advanced Research Projects Agency and NWC Independent Research Funds.

1. Figures in brackets indicate the literature references at the end of this paper.

For coatings comprised of chalcogenide glass and NaF layers, the damage threshold is limited by that of the glass but the absorptance is limited by that of the NaF [1,2,3]. The absorption coefficient of thin films of NaF is about  $6 \text{ cm}^{-1}$ , six times that of the chalcogenides and ten times that of bulk NaF [10]. The absorptance of NaF is so high that the three-layer design with the lowest absorptance is the one which minimizes the thickness of the NaF [1]. The extra absorptance could be related to the structure or porosity of the films, or impurities in the NaF. NaF films are polycrystalline and infrared-absorbing states could exist at interfaces between the NaF crystallites; however, NaF is hygroscopic and Sparks [11] has estimated that two monolayers of water in or on a material will produce an absorptance of  $1 \times 10^{-4}$  [11]. Other impurities may produce similar increases in absorptance. In section 5, the observation of impurities in NaF, attempts to eliminate them and reduce absorption from the NaF films are reported.

## 2. Crystallite Morphology and Formation

It has been known for some time that  $\text{As}_2\text{S}_3$  films deposited under standard vacuum conditions are unstable in the sense that small crystallites on the order of  $1 \mu\text{m}$  in diameter grow on the surface. The crystallites have been reported to be  $\text{As}_2\text{O}_3$  [12,13] or  $\text{As}_3\text{S}_4$  [14]. The decomposition of  $\text{As}_2\text{S}_3$  is reported to be catalyzed by the presence of water vapor and enhanced by visible (band gap) light [12]. Figure 3 shows electron micrographs of the surface of an  $\text{As}_2\text{S}_3$  film before and after it was scrubbed lightly with cotton soaked in benzene. The film was roughly  $0.5\text{-}\mu\text{m}$  thick and was deposited on a single-crystal KCl sample at  $75^\circ\text{C}$  using a rate of about  $1.3 \text{ nm/sec}$  in a trapped, diffusion-pumped system. The sample was etched for 3 min in HCl prior to deposition. Since the replication required for the micrograph is destructive, the sample was broken into several pieces. One piece was replicated 3 days after deposition without washing, while a second piece was washed (lightly scrubbed with cotton soaked in benzene) and replicated 7 days after the first samples was replicated (10 days after deposition). The micrographs show two types of defects: crystallites and blisters. On the "before" micrograph, the crystallites can be seen to agglomerate on the blisters. The "after" micrograph shows that more blisters appeared during the intervening 7 days. This illustrates how the defects grow over a period of days. Notice that after the films are washed, no evidence of the crystallites remains. There are no jagged edges of the crystallites protruding from the surface. Reflection electron diffraction patterns showed crystalline structure before, but not after, washing. Evidently the crystallites are resting on an amorphous matrix, and can be washed off.

Figure 4 gives a closer view of the shapes of defects in the  $\text{As}_2\text{S}_3$  and  $\text{As}_2\text{Se}_3$  films. The  $\text{As}_2\text{S}_3$  film shown here is the same as that shown in figure 3, but the film has been aged 86 days prior to replication. The  $\text{As}_2\text{Se}_3$  film was  $0.6\text{-}\mu\text{m}$  thick and was deposited on single-crystal, etched KCl at  $75^\circ\text{C}$  in a trapped, diffusion-pumped system; the replica was made 7 days after deposition. Notice that blisters are visible under the  $\text{As}_2\text{S}_3$  crystallites shown in both figures 3 and 4, but no blisters are visible under the  $\text{As}_2\text{Se}_3$  crystallites. The  $\text{As}_2\text{S}_3$  crystals have a distinct, pyramidal habit while the  $\text{As}_2\text{Se}_3$  crystals have a more agglomerated, triangular prism habit. The crystallites are clearly different on the two types of film, but the implications of this difference have not yet been explored.

## 3. Analytical Results

There is disagreement as to the chemical form of the crystallites appearing on  $\text{As}_2\text{S}_3$  films; they have been reported to be both  $\text{As}_2\text{O}_3$  and  $\text{As}_4\text{S}_3$  [12,13,14]. The chemical nature of the crystallites is closely related to the cause of their formation, and hence to the means for preventing their formation. If the crystallites are an oxide being formed by oxidation in contact with atmosphere, then an oxygen-impervious protective coating combined with water-free deposition should stop their formation. If the crystallites are a sulfide or selenide which form because the amorphous matrix is unstable, then some means of stabilizing the matrix must be found. Stabilization could involve altering the stoichiometry of the matrix or introducing a stabilizing impurity. Some of the passivation attempts reported in section 4 were based on the assumption that the crystallites are formed by oxidation. This assumption is not borne out by the more recent data reported in this section.

A general idea of the chemical form of the crystallites can be obtained by considering the composition and form of likely materials. Crystallites form on  $\text{As}_2\text{S}_3$  films whether the films are deposited on NaCl, KCl, quartz, Nesa glass,  $\text{Al}_2\text{O}_3$  or Al [2,4,13,14]. Evidently, constituents of the crystallites are not coming from the substrates, but must be coming from the atmosphere or the film. The list of compounds likely to form on an  $\text{As}_2\text{S}_3$  film includes  $\text{As}_2\text{O}_3$  (cubic and/or monoclinic),  $\text{As}_2\text{S}_5$ ,  $\text{As}_2\text{S}_3$  (monoclinic),  $\text{As}_4\text{S}_3$  (orthorhombic) and  $\text{As}_2\text{S}_2$  (monoclinic) [15,16]. The shape of the crystallites may give some clue as to the material involved. The crystallites shown in figures 3 and 4 are shaped roughly like octahedrons; but this by itself is not enough to discriminate between materials since the habit of  $\text{As}_4\text{S}_3$  has been described as "dipyramidal," while that of  $\text{As}_2\text{O}_3$  was described as "octahedral." Either description could apply to the crystallites; one cannot discriminate between the oxide and the sulfide with this information.

In order to identify the chemical nature of the crystallites, samples were examined at Physical Electronics, Inc. (PHI) using the Model 590 high resolution scanning Auger spectrometer. This instrument has a lateral resolution of  $0.25 \mu\text{m}$ .  $\text{As}_2\text{S}_3$  films were deposited under standard deposition conditions ( $75^\circ\text{C}$ ) on single-crystal etched KCl and sent to PHI. The crystallites were present on the films



and were easily located and identified in the scanning electron microscopy mode of the Model 590. Auger spectra of a large area in the sample were taken of the as-grown  $\text{As}_2\text{S}_3$  coating. Auger spectra then were recorded with the electron beam focused on a crystallite and with the beam focused on a region free of crystallites (matrix). The sample was then sputter-etched in purified argon to remove about 10 nm of surface film and the measurements repeated. Figure 5 compares the Auger spectra measured before and after 10 nm was removed by sputtering. The composition of the average area and the crystallite are compared in figure 6 and both show C and O contamination in the as-received conditions. After 10 nm of the crystallite surface was sputtered away, the C and O contamination is greatly reduced, and  $\text{Cl}^-$  and  $\text{K}^+$  appear. In contrast to this, in the crystallite-free region, shown in figure 5, sputter-etching does not result in the appearance of  $\text{Cl}^-$  and  $\text{K}^+$ , although C and O contamination is removed. The data indicate that these crystallites do not consist of  $\text{As}_2\text{O}_3$  as suggested in some studies. This result is consistent with data reported by Hughes Research Laboratories on films deposited by vapor transport, and with results from enhanced diffusion of the  $\text{K}^+$  and  $\text{Cl}^-$  possibly results from enhanced diffusion of the  $\text{K}^+$  and  $\text{Cl}^-$  from the substrate due to local heating of the electron beam in the defect or blistered regions. Again, this result is consistent with our electron microprobe results which also indicated enhanced diffusion of  $\text{K}^+$  and  $\text{Cl}^-$  in the crystallite region. It is of interest to note that x-ray photoemission spectroscopy (fig. 7), which does not introduce local heating or electron damage, confirms the result that O and C are present as surface contaminants. Also, there is no indication of  $\text{K}^+$  or  $\text{Cl}^-$  in what amounts to a broad area analysis. Notice also that this sputter-etch, lighter than that used for the Auger spectra, removed most of the C and O. Evidently, the C and O are in a layer roughly 2-nm thick on the surface. Previous workers also have found the O layer to be 2-nm thick [13].

Some information about the relative stoichiometry in the crystallite and crystallite-free regions can be obtained from peak height measurements of both Auger and electron microprobe spectra. The height of a particular peak is roughly proportional to the density of atoms of that material in the sample volume. By taking the ratio of peak heights on a given curve, say the S peak to the As peak, one can gain an idea of changes in the relative number of As and S atoms present. Table 1 compares peak-height ratios for an Auger spectrum measured from a crystallite with the ratios for a spectrum measured from the matrix. Ratios derived from both Auger and microprobe measurements are shown. For each type of measurement, the ratios are normalized so that the S/As ratio comes out 1.50 for the film matrix. This was done so that changes in the S/As ratio could be more easily compared with that of perfect  $\text{As}_2\text{S}_3$ , 1.50. For both Auger and electron microprobe data, the ratios on the crystallites are less than 1.50. Since the stoichiometry of the matrix is not definitely known at present, and the extent to which the electron-beam sampling is limited to the crystallites is not known, one cannot accurately estimate the stoichiometry of the crystallites. While the estimate is probably not numerically accurate, the data clearly show that the crystallites are more arsenic-rich than the matrix.

Table 1. Comparison of peak height ratios for structure associated with the film with that for structure associated with the crystallites. The sulfur 150 eV peak and the arsenic 1240 eV peak of the Auger curves were used.

Ratio	S/As peak ratio <sup>a</sup>	
	Film	Crystal
Auger (10 nm sputtered)	1.50	1.27
As-received Auger	1.50	1.20
Electron microprobe	1.50	1.36

<sup>a</sup> Arbitrarily normalized to 1.50 on the film.

These analytical results presented above resolve the disagreement concerning the composition of crystallites on  $\text{As}_2\text{S}_3$ . The crystallites are a sulfide, not an oxide. Moreover, the crystallites are more arsenic-rich than the matrix. This is consistent with the suggestion by other workers that the crystallites are  $\text{As}_4\text{S}_3$ . It now appears that crystallite formation is due to a basic instability of  $\text{As}_2\text{S}_3$ , although the details of formation are not clear at present.

#### 4. Passivation Attempts

In attempting to passivate the  $\text{As}_2\text{Se}_3$  and  $\text{As}_2\text{S}_3$  coatings against defect growth we have made the assumption, based on the literature, that crystallite formation involved the presence of water vapor and visible light; if oxygen or water could be excluded from the surface, crystallites would be prevented from forming. Two methods of excluding oxygen or water were tried. In the first, we obtained water-free starting material from the Catholic University and deposited coatings in an oil-pumped vacuum using this material. Figure 8 shows transmission traces of a commercial  $\text{As}_2\text{S}_3$  sample and a



research grade sample fashioned from a boule of high-purity  $\text{As}_2\text{Se}_3$  obtained from C. Moynihan of the Catholic University. The commercial glass clearly shows the presence of adsorbed and chemically combined O-H in the region of  $2.8\text{ }\mu\text{m}$ . There is also a small absorption band indicating the presence of H-S, which was probably introduced in the formation stage of the  $\text{As}_2\text{S}_3$ . The research grade glass, on the other hand, has an almost clean spectrum. There is a slight indication of O-H at  $2.7\text{ }\mu\text{m}$ , and this may be the surface contamination observed in the Auger/ESCA analysis. Figure 4 shows the surface of the  $\text{As}_2\text{Se}_3$  coating made using this material. Crystallites are present, but are smaller and not as well formed as those of the  $\text{As}_2\text{S}_3$ . Further efforts to reduce the presence of these defects will involve deposition in ultraclean vacuum.

The second attempt at passivation was to overcoat the  $\text{As}_2\text{S}_3$  prior to air exposure with a thin layer of either Ag or NaF in order to prevent oxygen or water vapor from contacting the chalcogenide surface. Each of these overlayers failed to prevent defect formation. A  $2\text{-}\mu\text{m}$ -thick film of  $\text{As}_2\text{S}_3$  was deposited on etched, single-crystal NaCl at  $75^\circ\text{C}$  in a trapped diffusion-pump system. Half the surface was subsequently coated with  $100\text{ nm}$  of NaF at  $140^\circ\text{C}$ . As seen in figure 9, crystallites are growing on both halves of the surface. Thus the presence of NaF did not significantly retard growth of the crystallites.

## 5. Impurities in NaF

In order to isolate the cause and reduce anomalously high absorption in NaF we have studied the effect of vacuum on the chemical contamination and absorption. Films have been deposited in standard oil-pumped vacuum, as well as baked in ultrahigh vacuum (UHV). The chemical purity has been monitored using Auger/ESCA and we have looked for the presence of surface or interface absorption using ellipsometry and total internal reflection.

We find that by using optical grade (no impurity analysis) NaF obtained from Harshaw Chemical Co., and evaporating as described previously [4], in either standard or UHV the resulting absorption was the same,  $\sim 6\text{ cm}^{-1}$  at  $10.6\text{ }\mu\text{m}$ . Measurements made at  $3.8\text{ }\mu\text{m}$  yield a slightly lower absorption, 4 to  $5\text{ cm}^{-1}$ . Auger and ESCA measurements have been made on these coatings in order to identify possible sources for this residual absorption. We found that the electron beam used in the Auger measurement alters the surface composition of the NaF, and therefore we limit our discussion to the ESCA results. Figures 10 and 11 show ESCA traces of a UHV-deposited film taken after exposure to air and the same film after approximately  $30\text{ }\text{\AA}$  of surface layer had been removed, respectively. It is clear from these figures that oxygen and carbon are present as surface contamination layers only, and can be removed by a light sputter-etch treatment. Since the calorimetry measurements were made on air-exposed samples, it is possible that O, present in the form of OH or  $\text{CO}_2$ , may be contributing to the absorption at  $10.6$  and  $3.8\text{ }\mu\text{m}$ . Even though transmission spectra do not reveal any OH or  $\text{CO}_2$  absorption bands at  $10.6$  and  $3.8\text{ }\mu\text{m}$ , both Auger and ellipsometric measurements indicate surface or interface contamination. These contaminants could be responsible for the residual absorption observed at  $3.8$  and  $10.6\text{ }\mu\text{m}$ .

## 6. Summary and Conclusions

Crystallites which form in air on  $\text{As}_2\text{S}_3$  and  $\text{As}_2\text{Se}_3$  coatings are not  $\text{As}_2\text{O}_3$ , as previously suspected, but some form of sulfide or selenide. Attempts to stabilize the coatings by depositing thin layers of Ag or NaF *in situ* failed, as did attempts using water-free  $\text{As}_2\text{Se}_3$  evaporant.

NaF as-deposited in UHV using optical grade evaporant has an absorption ten times that of bulk NaF at  $10.6\text{ }\mu\text{m}$ . This absorption may result from oxygen impurities in the form of  $\text{CO}_2$  or OH which have been found limited to the surface region. This suggests that NaF forms a dense, nonporous coating which does not take up water vapor on exposure to air. Further, it suggests that by eliminating surface oxygen, film absorption approaching that of bulk NaF might be obtained.

## 7. References

- [1] Baer, A. D., "Design of Three-Layer Antireflection Coatings," in *Laser Induced Damage in Optical Materials: 1976*, A. J. Glass and A. H. Guenther, eds. (NBS Spec. Publ. 462), p. 221.
- [2] Donovan, T. M. and Baer, A. D., " $\text{As}_2\text{S}_3$  and  $\text{ThF}_4$  Coatings on KCl and NaCl Windows," *Proceedings of the Fifth Annual Conference on Infrared Laser Window Materials: 1975*, C. R. Andrews and C. L. Strecker, eds. (Defense Advanced Research Projects Agency, Arlington, VA, 1976), p. 241.
- [3] Baer, A. D., Donovan, T. M. and Soileau, M. J., " $\text{As}_2\text{S}_3$  Coatings on KCl," in *Laser Induced Damage in Optical Materials: 1975*, A. J. Glass and A. H. Guenther, eds. (NBS Spec. Publ. 435), p. 244.
- [4] Baer, A. D., Donovan, T. M., Green, A. K. and Turner, G., "Alternate Materials for Infrared Window Coatings," in *Laser Induced Damage in Optical Materials: 1976*, A. J. Glass and A. H. Guenther, eds. (NBS Spec. Publ. 462), p. 214.

- [5] Air Force Weapons Laboratory. Private communication.
- [6] Young, P. A., Thin Solid Films 6, 423 (1970).
- [7] Porteus, J. O., Michelson Laboratory. Private communication.
- [8] Temple, P. A. and Soileau, M. J., "Resonant Defect Enhancement of the Laser Electric Field," in *Laser Induced Damage in Optical Materials: 1976*, A. J. Glass and A. H. Guenther, eds. (NBS Spec. Publ. 462), p. 371.
- [9] Bloembergen, N., Appl. Opt. 12, 661 (1973).
- [10] Klier, M., Z. Physik 150, 49 (1958).
- [11] Sparks, M., "Materials for High-Power Window and Mirror Coatings and Multilayer Dielectric Coatings," in *Laser Induced Damage in Optical Materials: 1976*, A. J. Glass and A. H. Guenther, eds. (NBS Spec. Publ. 462), p. 203.
- [12] Berkes, J. S., Ing, S. W., Jr. and Hillegas, W. J., J. Appl. Phys. 42, 4908 (1977).
- [13] Trubisky, M. P. and Nevihart, J. H., Appl. Opt. Suppl. 3, 59 (1959).
- [14] Braunstein, M., *Laser Window Surface Finishing and Coating Technology* (Semi-Annual Technical Report, Hughes Research Laboratory, Malibu, CA, 1974), AFCRL-TR-74-0425.
- [15] Palache, C., Berman, H. and Frondel, C., *Dana's System of Mineralogy*, 7th Edition (John Wiley and Sons, New York, 1944).
- [16] *Handbook of Chemistry and Physics*, 50th Edition, R. C. Weast, ed. (Chemical Rubber Co., Cleveland, OH, 1969).

## 8. Figures

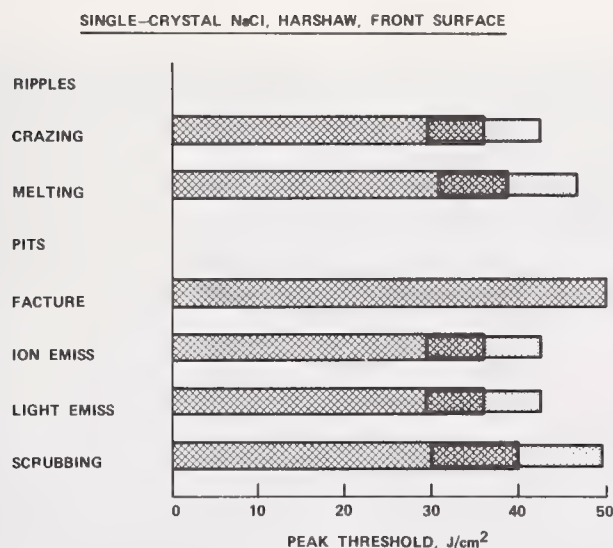


Figure 1. Laser damage at 10.6  $\mu\text{m}$  of uncoated single-crystal NaCl.

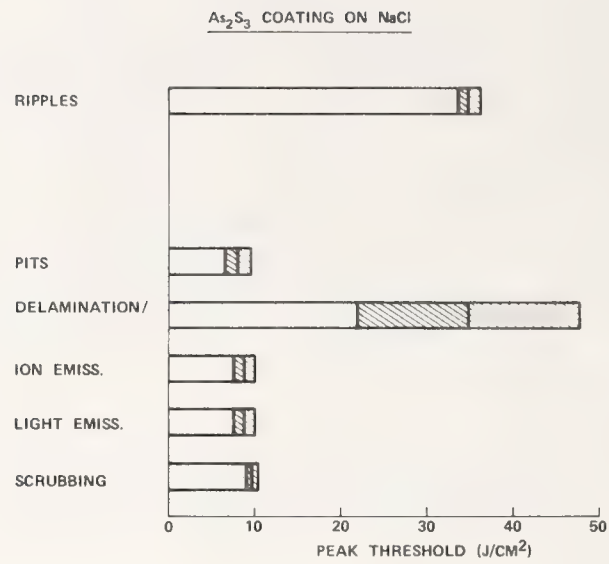


Figure 2. Laser damage at 10.6  $\mu\text{m}$  of single-crystal NaCl coated with As<sub>2</sub>S<sub>3</sub>.



Figure 3. Defects on an As<sub>2</sub>S<sub>3</sub> film before and after a light scrubbing with benzene.





Figure 4. Defects formed on  $\text{As}_2\text{S}_3$  and  $\text{As}_2\text{Se}_3$  films.

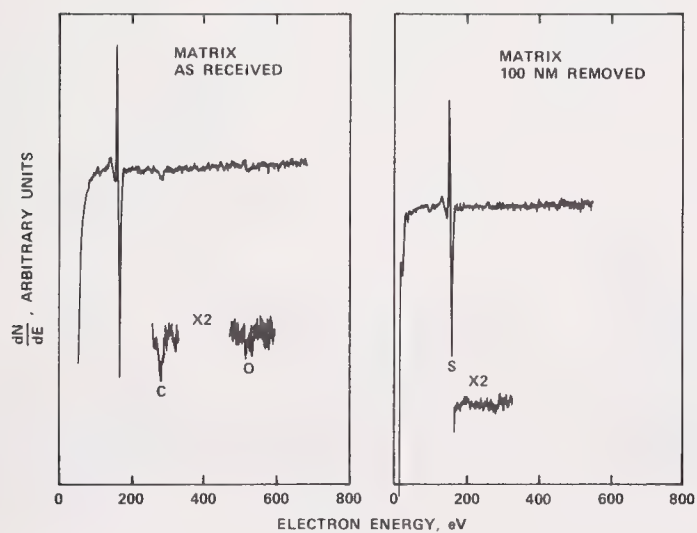


Figure 5. Auger spectra measured on an  $\text{As}_2\text{S}_3$  film before and after 10 nm of the surface was sputtered away.

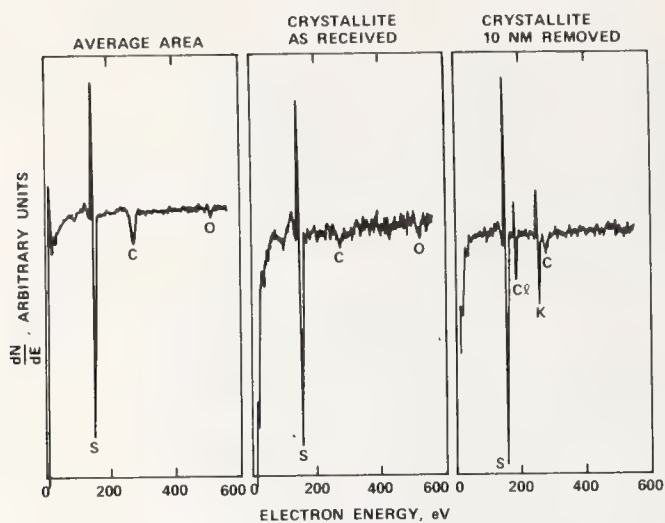


Figure 6. Comparison of Auger spectra representative of the average area of an  $\text{As}_2\text{S}_3$  film, a crystallite, and a crystallite with 10 nm removed.

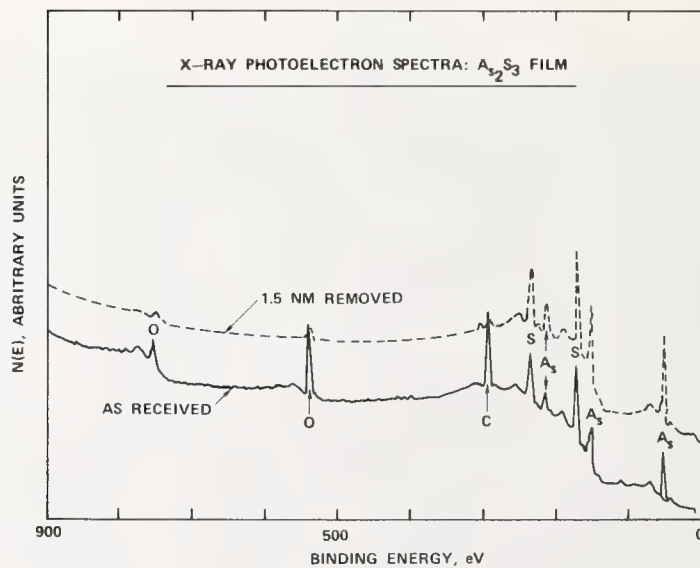


Figure 7. X-ray photoelectron spectra measured before and after 1.5 nm of  $\text{As}_2\text{S}_3$  film was sputtered off.

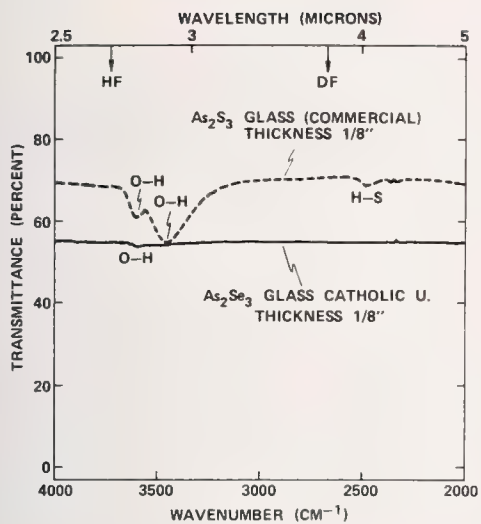


Figure 8. Transmission of commercial  $\text{As}_2\text{S}_3$  and high purity  $\text{As}_2\text{Se}_3$ .

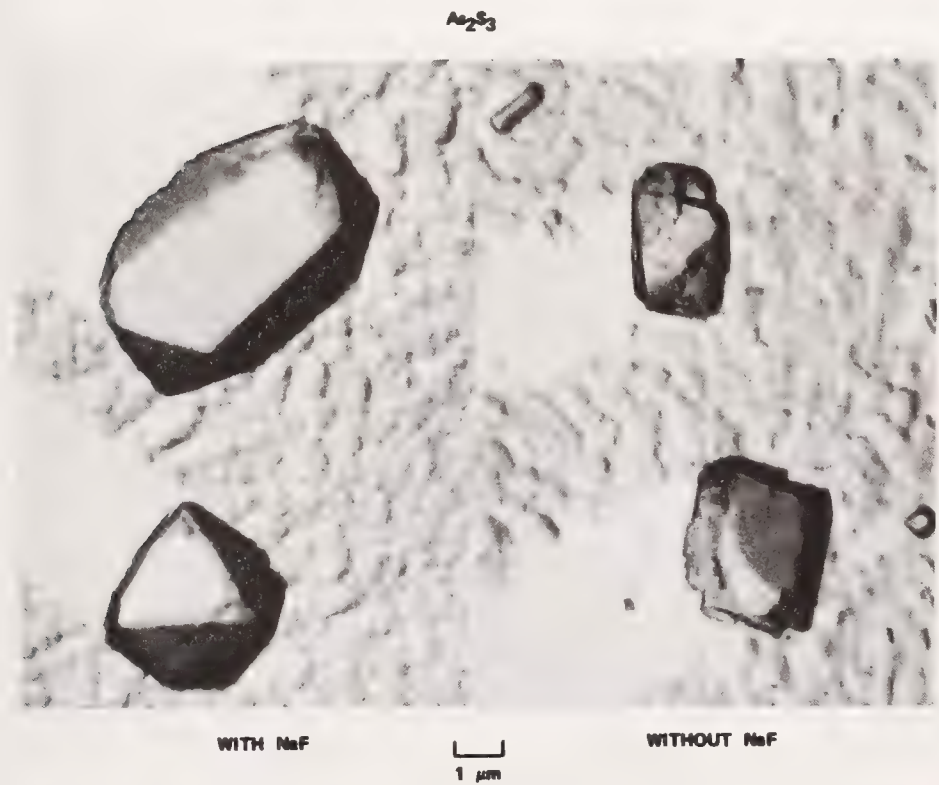


Figure 9. Micrographs of crystals on a 2- $\mu\text{m}$   $\text{As}_2\text{S}_3$  film deposited on a NaCl window. Half of the window was overcoated with NaF, 100-nm thick.



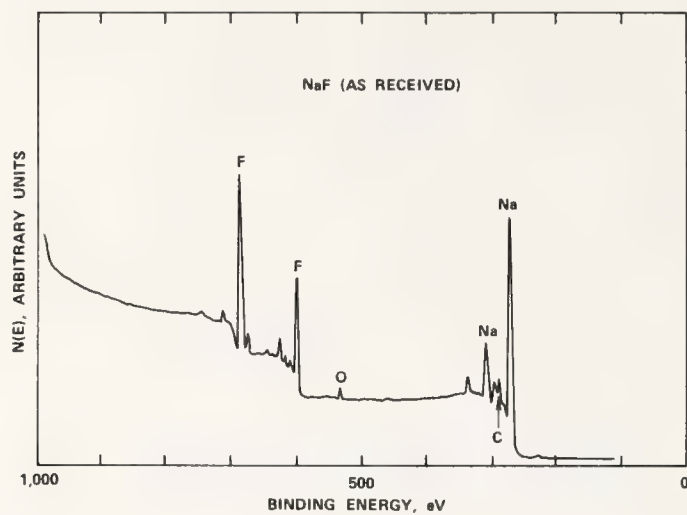


Figure 10. X-ray photoelectron spectrum recorded on a NaF film after exposure to atmosphere.

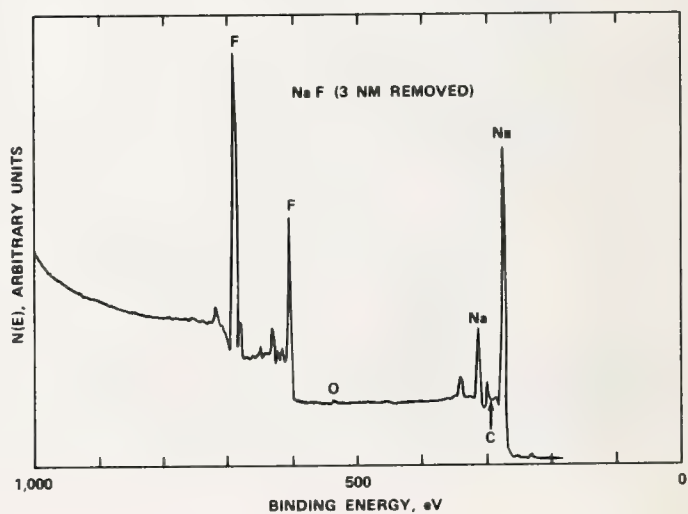


Figure 11. X-ray photoelectron spectrum recorded on a NaF film after 3 nm were removed from the surface by sputtering.

# OPTICAL CONSTANTS OF $\text{As}_2\text{S}_3$ BY A WEDGED-FILM TECHNIQUE\*

David L. Burdick

Physics Division, Michelson Laboratories  
Naval Weapons Center, China Lake, California 93555

A wedged-film technique has been developed to measure the optical constants of thin films. The technique has been applied to an  $\text{As}_2\text{S}_3$  film. Measurements in the visible spectrum have produced absorption coefficients ranging from  $3 \text{ cm}^{-1}$  to greater than  $10^4 \text{ cm}^{-1}$ , and refractive indices from 2.47 to 2.72 with precisions ranging from 0.3 to 1%.

Key words: Arsenic trisulfide; optical constants; visible spectrum; wedged film.

## Introduction

Techniques for measuring the optical constants of thin films abound. This paper describes yet another method which admits of certain advantages, and the method is applied to  $\text{As}_2\text{S}_3$  films.

The use of a wedged film on a transparent substrate is a direct descendant of the prism technique for bulk materials and, as such, shares one of the main advantages of that technique. That is, by properly ratioing the transmitted intensities one can, in principle, eliminate surface effects. It has the further advantages that film thickness need not be measured independently and that the optical constants can be measured over a wide spectral range on a single film.

## Experimental Arrangement

The experimental apparatus is shown schematically in figure 1. The wedged film on a transparent substrate is placed normal to a monochromatic beam which is focussed onto the film. The transmitted light is monitored by a detector as the substrate is translated through the beam so that the wedged film is scanned as a function of thickness. A position readout device (a linear potentiometer) measures the film position. The detector output and the position signal are ultimately fed to the x-y recorder.

## Theory of Operation

The transmission coefficient for light passing through a thin film on a transparent substrate is

$$T = \frac{16n_s(n^2 + k^2)T_s}{r^2[(e^x - \rho/r e^{-x})^2 + 4 \rho/r \sin^2(2\pi nt/\lambda + 1/2(\phi - \theta))]} \quad (1)$$

where

$$\begin{aligned} x &= 2\pi kt/\lambda \\ \rho^2 &= [(1 - n)^2 + k^2][(n_s - n)^2 + k^2] \\ r^2 &= [(1 + n)^2 + k^2][(n_s + n)^2 + k^2] \\ \tan\phi &= -k(2n + 1 + n_s)/[(1 + n)(n_s + n) - k^2] \\ \tan\theta &= -k(2n - 1 - n_s)/[(1 - n)(n_s - n) - k^2]. \end{aligned}$$

The extinction coefficient is  $k$  and  $n$  is the refractive index of the film,  $n_s$  is the substrate index,  $\lambda$  the wavelength, and  $T_s$  a transmission factor which describes how the beam leaves the substrate.

The simplest case to treat is that encountered when  $kt \ll 1$ . Assuming that  $n > n_s$  we find in this case that

$$\frac{T_{\max}}{T_{\min}} = \left( \frac{1 + \rho/r}{1 - \rho/r} \right)^2 \equiv R^2 \quad (2)$$

In this approximation both  $\rho$  and  $r$  are simple functions of  $n$  and eq. (2) can be solved for  $n$  to give

$$2n = (1 + n_s)R + \sqrt{R^2(1 + n_s)^2 - 4n_s} \quad (3)$$

\* Work supported by Defense Advanced Research Projects Agency.

This result is important for two reasons. First, it allows us to calculate  $n$  from the directly accessible ratio  $R$ , and surface effects are eliminated in the process. Second,  $n$  can be obtained without first measuring the film thickness.

Having determined  $n$  at a wavelength where the film is not absorbing, one can then calculate the film thickness profile as a function of position by using the normal interference conditions at the extrema. For instance, at the maxima,

$$t = \frac{M\lambda}{2n}, \quad (4)$$

where  $M$  is the order of the fringe.

Once  $n$  and the thickness profile have been determined, the extinction coefficient (and absorption coefficient) can be determined by using differences in  $T_{\max}$  at different film thicknesses. Thus, in the lowest approximation, and using  $T_{\max}$ , we have

$$\frac{T_1 - T_2}{T_1} \approx \frac{4\pi k}{\lambda} \left( \frac{1 + \rho/r}{1 - \rho/r} \right) \Delta t. \quad (5)$$

Solving for the absorption coefficient  $\alpha$  we have

$$\alpha = \frac{4\pi k}{\lambda} = \frac{1}{\Delta t R} (1 - T_2/T_1), \quad (6)$$

and this coefficient is determined entirely in terms of ratios, which again eliminates surface effects.

The analysis of the data takes on a much different character when  $kt$  is not small. In essence, one must use the thickness profile obtained as above and perform a least-squares fit to extract both  $n$  and  $k$ .

#### Experimental Results

The wedged-film technique has been used to obtain the optical constants of an  $\text{As}_2\text{S}_3$  film on fused quartz at six laser wavelengths. A photograph of the film is shown in figure 2 as obtained on a Zygo interferometer. The film is illuminated by 632.8 nm light to reveal the interference fringes in the film. The fringes are highly linear and uniform, a circumstance which is pleasing but not essential to the method. The film was fabricated by placing a shutter between the substrate and evaporant source. After a uniform deposition rate is established (with the shutter closed) the shutter is opened and closed at a uniform rate until the desired film thickness has been obtained.

The thickness profile of the film is shown in figure 3. The thickness was calculated from interference conditions such as given in eq. (4) at two wavelengths; the result confirms the linearity of the wedge. The greatest thickness of this film was about 1.5  $\mu\text{m}$ .

Figure 4 shows the intensity variation observed in the transmitted light at 0.6471 and 0.5682  $\mu\text{m}$  as the film is translated through the focussed beam. The film absorption at these two wavelengths is very small as evinced by the fact that the extrema do not decrease in amplitude as the film becomes thicker. The situation is markedly different, however, in figure 5. Here we show the transmission patterns obtained at 0.5208, 0.488, 0.4825, and 0.4762  $\mu\text{m}$ . The evidence for increasing absorption with increasing energy is clearly visible, ranging from a linear decrease in intensity of the extrema at 0.5208  $\mu\text{m}$  to a strong exponential character in the decrease at 0.4762  $\mu\text{m}$ .

The results obtained at 0.6471, 0.5682, and 0.5208  $\mu\text{m}$  are easily treated by eqs. (3) and (6). At 0.488, 0.4825, and 0.4762  $\mu\text{m}$  one must resort to curve-fitting. The results obtained for the optical constants are shown in figures 6 and 7. Figure 6 shows the absorption coefficient as a function of photon energy, together with the results obtained by Young [1]<sup>1</sup> for comparison. The agreement is moderately good. The refractive index is shown in figure 7, again with Young's results. Our numbers are about 3% lower. It is not uncommon to find such differences in the refractive indices of  $\text{As}_2\text{S}_3$  films grown under different conditions. Our precision is estimated to vary from 0.3% at the longer wavelengths up to 1% at the shorter. Variations in the precision are due primarily to differences in how the locations of extrema were measured.

#### Conclusions

The wedged-film technique appears to offer a number of advantages when compared with other methods of measuring optical constants of thin films. First, no independent measurement of film thickness is

1. Figures in brackets indicate the literature references at the end of this paper.



required. Second, one need not worry about dispersion in the index over some spectral range; some methods require the assumption that the index is constant over an extended spectral range. Third, measurements can be made over a large spectral range on a single film. Fourth, absorption coefficients down to 1 to 10  $\text{cm}^{-1}$  are measurable and high precision index measurements are possible. Finally, the method eliminates surface and interface effects.

#### References

- [1] Young, P. A., J. Phys. C: Solid State Phys. 4, 93 (1971).

#### Figures

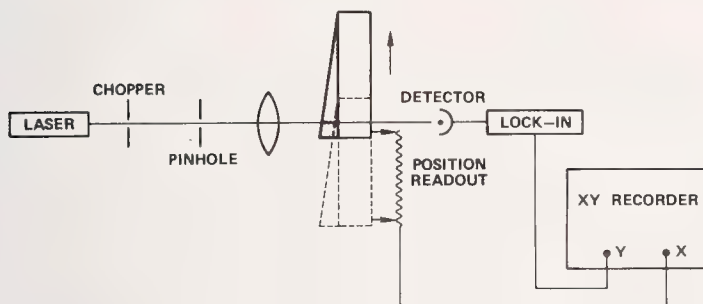


Figure 1. Schematic diagram of wedged-film apparatus. Interference fringes are observed as a wedged film is translated through a focussed monochromatic beam.

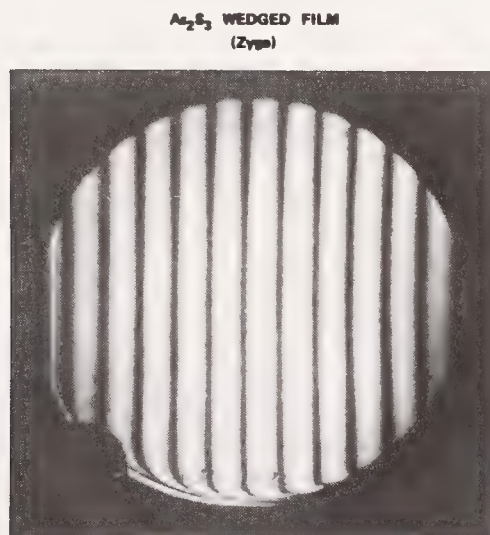


Figure 2. Photograph of As<sub>2</sub>S<sub>3</sub> film in Zygo interferometer showing fringes at 632.8 nm.

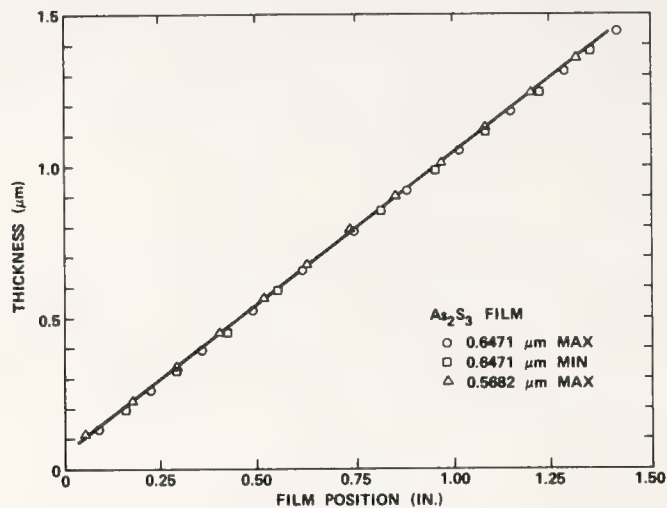


Figure 3. Thickness profile of  $\text{As}_2\text{S}_3$  film as determined from measured indices and the interference condition.

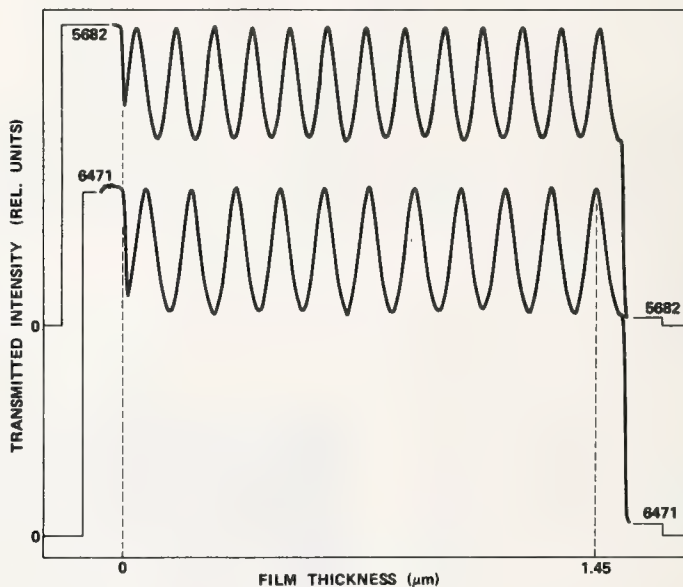


Figure 4. Intensity variations in transmission at 0.6471 and 0.5682  $\mu\text{m}$ . No absorption increase with thickness is observed at these wavelengths.

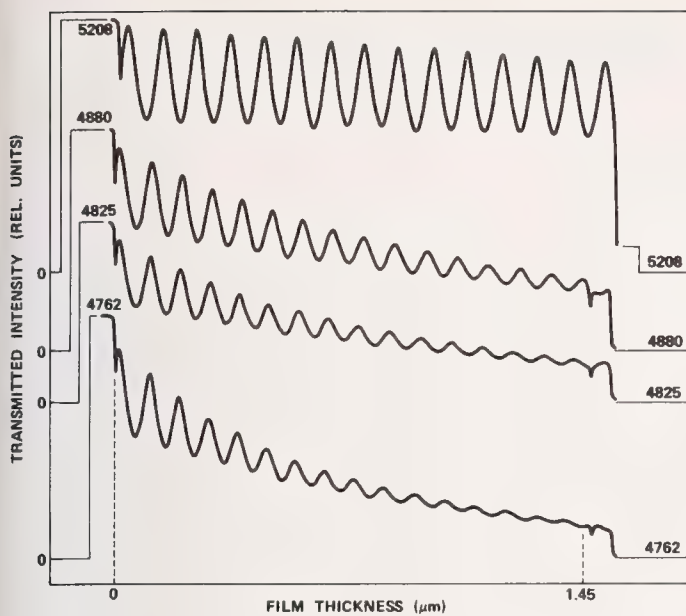


Figure 5. Intensity variations in transmission at 0.5208, 0.488, 0.4825 and 0.4762  $\mu\text{m}$ . Increases in absorption with thickness are clearly visible.

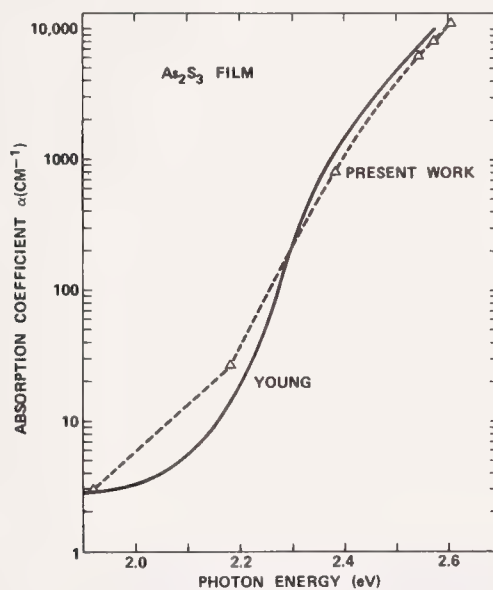


Figure 6. The absorption coefficient of  $\text{As}_2\text{S}_3$  by the wedged-film technique (six points). Also shown are Young's results [1].



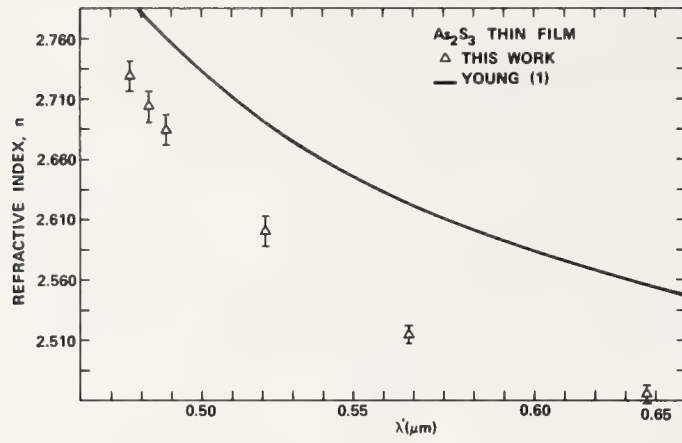


Figure 7. The refractive index of  $\text{As}_2\text{S}_3$  by the wedged-film technique, and Young's results [1].

# DIELECTRIC COATINGS FOR DEFORMABLE MIRRORS\*

J. M. Rowe  
Northrop Research and Technology Center  
Hawthorne, California 90250

Results of an experimental program to determine the optical and physical properties of high-reflectance dielectric coatings subjected to a large number of deformation cycles are reported. The effects of deforming mirrors with film stacks are difficult to predict since too many parameters are involved. Therefore, an experimental evaluation of promising designs was undertaken. Measurements included residual coating stress immediately after deposition, spectral reflectance, absorptance at the design wavelength, and examination by Nomarski microscopy. Mirror properties were evaluated at several points in a schedule of controlled deformation cycling. Coating designs consisted of dielectric enhanced silver at  $3.8\ \mu\text{m}$  deposited on molybdenum substrates. The data obtained provides a basis for choosing multilayer coating designs and deposition methods that may be applied to the fabrication of high-reflectance, deformable mirrors for mid-IR lasers.

Key words: Coating stress; deformable mirrors; dielectric enhanced reflectors; laser mirror coatings; stress cycling of coatings; thin films.

## 1. Introduction

The performance of deformable mirrors used with high power IR lasers could be improved by coating the mirrors with dielectric layers to increase reflectivity. The ability of these coatings to maintain optical and physical integrity when the mirror is deformed was investigated in a quantitative manner and results obtained to date are reported. The coatings consist of silver with reflectivity at  $3.8\ \mu\text{m}$  enhanced by dielectric quarter-wave stacks. Four candidate designs were chosen for evaluation:  $(\text{SiO}/\text{Si})^2$ ;  $(\text{Al}_2\text{O}_3/\text{Si})^2$ ;  $(\text{ThF}_4/\text{ZnS})^3$ ; and  $(\text{ThF}_4/\text{ZnSe})^3$ . Although the mirrors tested were not part of an adaptive optical system, the results will find application to that field.

## 2. Experimental

In order to provide quantitative results the coated mirror substrate must undergo only controlled, well characterized deformations. This was accomplished with the mirror and driver assembly shown in figure 1. The mirror and driver housing are molybdenum. This material was chosen because of its high elastic modulus and fatigue stress, low thermal coefficient of expansion, and because it is capable of a high quality optical polish [1]<sup>1</sup>. The polished diameter of the mirror is 3.81 cm and the web thickness is 0.762 mm. The mirror may be deformed in two ways. A stack of piezoelectric wafers is used to produce AC deflections electrically and a differential screw provides purely mechanical deflections of  $\sim 11\ \mu\text{m}$  per turn.

The differential screw is used to apply mechanical bias to the mirror during what has been called "DC" cycling. By this is meant deflections of one sign only, e.g. flat-to-convex-to-flat equals one "+" cycle. The concept is illustrated in figure 2. After application of mechanical bias, the differential screw lock nut is tightened and AC drive applied to the PZT stack with peak-to-peak deflections of twice the bias level. Zero-to-peak "DC" displacements of  $10.9\ \mu\text{m}$  at 10 Hz were used in testing the mirrors. Under these conditions a peak stress of  $9.89 \times 10^7\ \text{Pa}$  occurs at the mirror surface in the annular region directly above the edge of the central boss. All optical tests were made in this region of maximum stress. Stress induced in the coating is proportional to the ratio of coating modulus to substrate modulus since the strains are equal. For the coating materials used this ratio varies from 0.15 to 1.2. It is noted that the mechanically induced coating stresses were comparable to the residual stresses commonly produced as a result of the deposition process itself.

\*This work was supported by the Air Force Weapons Laboratory under Contract No. F29601-77-C-0015.

1. Figures in brackets indicate the literature references at the end of this paper.

A fringe counting interferometer (fig. 3) was used to measure mirror deflection. Interference between a He/Ne laser beam incident on the center of the mirror under test and a reference beam from a stationary mirror produced two maxima when the deformable mirror was deflected by one wavelength of the He/Ne light. A photodiode detected this signal which was then amplified and displayed on an oscilloscope. Drive voltage to the PZT stack was simultaneously displayed.

The following procedure was used in evaluating the mirror coatings. Coating and optical tests were done with the mirror detached from the driver. Before coating deposition, each mirror was calibrated in the driver to determine the PZT drive voltage required to produce the desired  $10.9\text{ }\mu\text{m}$  zero-to-peak displacement. The coatings were then deposited. During each coating run two stress witness samples, thin disks of fused silica, were also coated and the residual coating stress determined by well known techniques [2]. A scan of mirror reflectance vs wavelength was then made. Finally each mirror underwent a sequence of testing and controlled deformation cycling. Mirrors were examined by Nomarski microscope, double-bounce reflectometer, and DF laser calorimeter before any cycling and upon each completion of  $10^N$  cycles, where  $N = 1, 2, 3, 4$ . When not undergoing controlled cycling the mirrors were kept flat to  $\lambda/5$  at  $3.8\text{ }\mu\text{m}$ . In particular, the mirror flatness was monitored with an optical test flat during mounting and demounting to the driver.

### 3. Results

Two coating designs have completed the "DC" tests. For each design two mirrors were coated simultaneously, one for + and the other for - "DC" testing. Changes in optical performance with stress cycling were small and examination by Nomarski microscope at 167X revealed no physical degradation such as cracking or debonding of the films. The results for the  $(\text{SiO}/\text{Si})^2$  design are shown in table 1. The residual tensile stress in this coating was  $8.65 \times 10^7$  Pa. The difference in thermal expansion between the fused silica stress witness and molybdenum mirror substrate has been taken into account and the number given is for coating stress on molybdenum. It is evident from the table that the double-bounce reflectometer precision ( $\pm 0.1\%$ ) was not sufficient to measure the small changes in reflectance due to deformation cycling. The DF laser calorimetry measurements made after + "DC" cycling show a gradual increase in absorptance with number of cycles amounting after  $10^4$  cycles to 28% of the original value of  $2.14 \times 10^{-3}$ . Some of the added absorption may be due to handling of the sample although great care was taken to avoid damaging the mirror surface. It is noted that + "DC" deformation increases the tensile stress already present in the coating while - "DC" deformation reduces the coating stress. Absorptance of the - "DC" sample shows no systematic variation with cycling and equals  $2.42 \times 10^{-3}$  with a standard deviation of 3%.

Results for the  $(\text{Al}_2\text{O}_3/\text{Si})^2$  coating are shown in table 2. The residual stress in this coating was  $1.29 \times 10^8$  Pa. The measured absorptance of both the + and - cycled samples decreased through  $10^3$  cycles, an unexpected result. This apparent decrease may be within the range of experimental error, however, since the standard deviation for all absorptance measurements on either one of these samples was only  $\sim 8\%$ . No physical mechanism is proposed that would lower absorptance by stress cycling.

### 4. Work in progress

Two more coating designs,  $(\text{ThF}_4/\text{ZnS})^3$  and  $(\text{ThF}_4/\text{ZnSe})^3$ , are currently being evaluated. Once "DC" testing of all four designs is complete, two of them will be selected for "AC" testing with  $\pm 5.5\text{ }\mu\text{m}$  deflections at 1 kHz for up to  $10^7$  cycles. Adherence and humidity testing will also be done on these two designs, and the results of all measurements will be compared with a calculation of coating stresses.

### 5. Conclusion

The results obtained to date indicate that dielectric enhanced metal coatings suitable for use on high reflectance IR laser mirrors are able to withstand a large number of substrate deformation cycles without degradation. In particular, changes in absorptance were small and no physical disruption of the coating occurred. The effects of deformation cycling on the ability of the coatings to pass adhesion and humidity tests is still under investigation.



## 6. Acknowledgments

The mirror driver for this experiment was designed and fabricated by W. J. Schafer and Associates. Polishing and coating of the mirrors was done at Northrop by A. Klugman and S. Holmes. Able technical assistance was provided by M. Evangelista and F. Towns.

## 7. References

- [1] A. Klugman, "Surface Finishing of Molybdenum Substrates", 1977 Proc. High Power Laser Optical Components and Component Materials, to be published.
- [2] K. Röll, J. Appl. Phys. 47, 3224 (1976).

## 8. Tables

Table 1. Results for  $(\text{SiO}/\text{Si})^2$  coating design at  $3.8 \mu\text{m}$ .

+ "DC" TEST			- "DC" TEST		
	Reflectance	Absorptance		Reflectance	Absorptance
Cycles	(%)	$(10^{-3})$	Cycles	(%)	$(10^{-3})$
0	99.7	2.14	0	99.7	2.43
10	99.8	2.24	10	99.8	2.46
$10^2$	99.8	2.58	$10^2$	99.8	2.52
$10^3$	99.8	2.72	$10^3$	99.7	2.33
$10^4$	99.7	2.75	$10^4$	99.7	2.35

Table 2. Results for  $(\text{Al}_2\text{O}_3/\text{Si})^2$  coating design at  $3.8 \mu\text{m}$ .

+ "DC" Test			- "DC" Test		
	Reflectance	Absorptance		Reflectance	Absorptance
Cycles	(%)	$(10^{-3})$	Cycles	(%)	$(10^{-3})$
0	99.8	2.49	0	99.8	1.71
10	99.8	2.21	10	99.8	1.59
$10^2$	99.8	2.17	$10^2$	99.8	1.48
$10^3$	99.8	2.10	$10^3$	99.8	1.41
$10^4$	99.8	2.16	$10^4$	99.8	1.68

## 9. Figures

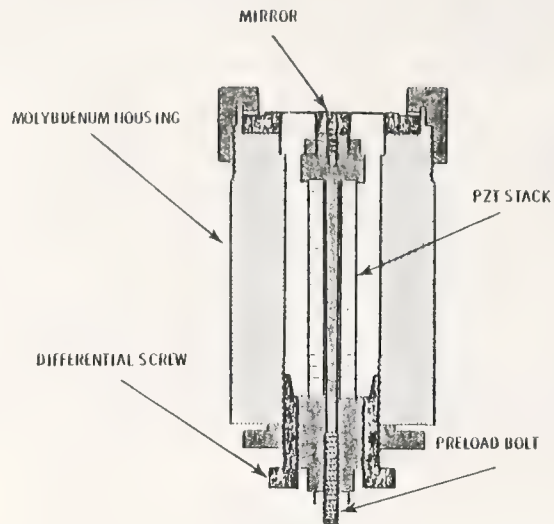


Figure 1. Driver assembly.

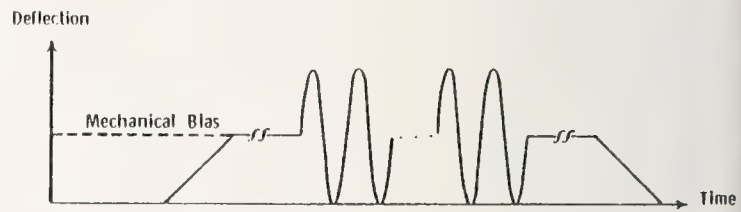


Figure 2. "DC" cycling.

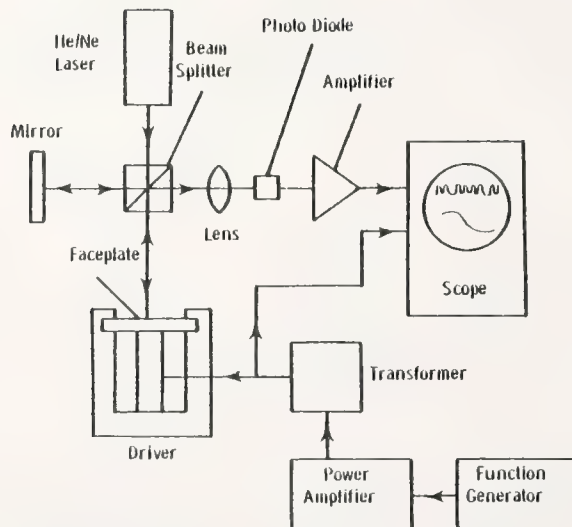


Figure 3. Fringe counting interferometer.

COMMENTS ON PAPER BY ROWE

The speaker remarked that they had not measured the stress created in the coating due to the deformation of the mirror, but felt that it would less under any circumstances than the stress in the face plate. Stress in the face plate was estimated to be no greater than 14,000 psi.



# QUANTITATIVE CHARACTERIZATION OF COATINGS:

## Part I: Adhesion\*

Stephen R. Scheele and James W. Bergstrom  
Hughes Aircraft Company  
Culver City, California 90230

Methods for quantifying the adhesion of optical coatings have been investigated with the goal of replacing the current pass-fail MIL-Spec cellophane tape tests. Three mechanical pull-off tests were compared on a large number of glass and infrared substrates with various reflection and antireflection coatings. The tests included: the direct pull-off test, in which a plug is bonded to the coating and then pulled perpendicular to the surface; the topple test, in which the top of the bonded plug is pulled parallel to the surface; and the peel test, in which an aluminum strip is bonded to, and then peeled from the surface.

Key words: Abrasion; adhesion; optical coating testing; peel test; plug-pull test; topple test.

### 1. Introduction

Efforts to predict the lifetime of optical coatings when exposed to various environments have historically been hampered by the absence of accepted quantitative testing procedures; procedures which could be used in coating development and also in quality control of production coatings. Though there have been many quantitative tests developed for nonoptical coatings such as paints and deposited electrical leads for integrated circuits, the only durability tests currently accepted throughout the optical coating industry are the qualitative MIL-Spec tests of MIL-C-675, MIL-C-48497 and MIL-M-13508. The tests include the moderate abrasion or cheese cloth test, the severe abrasion or eraser test and the adhesion or cellophane tape test. In addition to being qualitative (pass/fail) the MIL-Spec tests are also subjective; i.e., the criterion for passing the abrasion and adhesion tests is based on visual inspection for damage. Furthermore, the test procedures are not well controlled. For example, the speed at which the tape is pulled is "specified" only as slow (MIL-M-13508) or quick (MIL-C-48497). Since the pulling force is a function of the pulling speed (see sec. 5), variations in pulling speed can lead to a wide variation in results. Another example is the eraser test which is deficient in that the abrasiveness of the eraser is not well controlled and the speed and method of rubbing the surface is not specified (see part II).

The objectives of this program are to develop quantitative methods to test the adhesion and abrasion resistance of optical coatings, with particular emphasis on coatings for high powered laser windows. The tests should be relatively inexpensive, that is, inexpensive with respect to the resources of a small coating company. This includes the cost of any equipment (purchased or fabricated), the cost to develop the testing procedure (operator training, etc.) and the cost per test to run. The tests should also be accurate, i.e., repeatable (intra-laboratory), and reproducible (inter-laboratory). The tests should, if possible, simulate the action of environmental stress and the results should be relevant to optical systems.

### 2. Adhesion Testing

#### 2.1 Background

To aid in the discussion of adhesion and adhesion testing, it is useful to define three types of adhesion: basic adhesion, which is the summation of the intermolecular interactions; experimental or testing adhesion, which is measured in an adhesion test; and operational adhesion, which is a measure of the resistance of the coating to deadhesion in its operating environment. The latter two types of adhesion are similar to Mittal's [1]<sup>1</sup> definition of practical adhesion or bond strength. Though it is certainly difficult to disagree with Chapman's [2] contention that "we should try to devise tests of durability in the service conditions," it turns out to be even more difficult to devise such tests. That statement was made in an article written in 1973 and no article written before or since was uncovered which references an adhesion test that simulates the operating environment of optical coatings. If it were possible to calculate basic adhesion from measures of experimental adhesion, then perhaps the environmental adhesion could be calculated from it. While Kendal [3-6] has made some progress in relating experimental with basic adhesion by considering simple systems such as plastic in contact with gelatin, the problem of measuring basic adhesion in complicated systems remains unsolved.

The relation of practical adhesion to basic adhesion is unclear, as is the relation between various measures of practical adhesion. There is considerable analytical and experimental evidence to indicate

\* This work funded under contract to Air Force Materials Laboratory, Wright Patterson Air Force Base, Ohio. Contract No. F33615-76-C-5285.

1. Figures in brackets indicate the literature references at the end of this paper.

that all known adhesion tests are influenced by factors extraneous to basic adhesion such as coating thickness, substrate elasticity, thickness of peeling strip etc. These extraneous factors cannot be eliminated from the experimental apparatus and they cannot be analytically eliminated from the results. The best that one can do is to control these parameters so as to make the results reproducible.

## 2.2 Review of Adhesion Tests

There are good reviews of the various adhesion test by Bullett [7], Campbell [8], Chapman [9], Jacobson [10], Mittal [1,11] and Weaver [12]. The tests generally fall into two classes; mechanical and non-mechanical (nucleation). The latter tests are not applicable to this program. The mechanical tests, which are all destructive, usually involve either bonding an external element to the coating such as a plug or strip and then pulling the coating off, or the acceleration of the coating so that the momentum of the coating will tear it away. In the latter methods which include ultracentrifuge, ultrasonic, and impact tests, the results depend directly upon the thickness and density of the coating making it difficult to compare results from coatings of differing designs. There is a non-contact test called the blister method in which a hole is drilled through the sample to the film and then air pumped through until the coating fails. This technique is obviously not applicable to optical coatings. External strips or plugs can be eliminated if the coating can be gripped by its edge and peeled away. This has been done on some metal coatings [13] but cannot be done on all optical coatings and would require special coating samples which would be more expensive than the standard samples now in use. The one test which falls into none of the above categories is the stylus test. Whether or not it is a true test of adhesion has been the subject of much debate [14,15].

Thus, the available adhesion tests which meet the requirements of this program all involve bonding a member to the coating and pulling the coating off. This can be done by peeling, toppling, twisting or pulling as illustrated in figure 1. The tests that were implemented for this study were the plug pull test, topple test, and the peel test. They all have various features and drawbacks as discussed in the following paragraphs.

### Plug Pull Test

The plug pull test (variously known as the direct pull-off and flat-wise tension test) is geometrically the simplest test and would thus appear to be the easiest test to relate to basic adhesion. Detailed analysis, however, shows the test to be quite complicated. Kendall [3] studied the pull test at equilibrium, i.e., under conditions where the pulling force is just sufficient to slowly propagate cracks.\* Using two simple systems, he derived two relationships between the pulling force  $P$  and the surface free energy  $\gamma$ . For the case of a rigid disk of radius  $a$  in contact with an infinite elastic material of Young's modulus  $E$  and Poisson's ratio  $\nu$ , the relation is

$$P = \sqrt{\frac{8\pi E}{1-\nu^2}} a^{3/2} \gamma^{1/2}$$

Alternately, for a rigid disk bonded to an infinite, rigid substrate by a thin elastic film of thickness  $t$  and bulk modulus  $K$ , the relationship is

$$P = \sqrt{\frac{2\pi^2 K}{t}} a^2 \gamma^{1/2}$$

Kendall tested these equations using plastic disks (Perspex) and gelatin (for the adhesive) and found them to be accurate. However, the systems tested in this study, consisting of multi-layered coatings on flexible substrates, bonded to flexible disks, are much more complicated and no attempt was made to relate pulling force to adhesive energy.

As pointed out by Jacobssen and Kruse [16], misalignment of the plug and sample can cause additional stress  $\sigma_E$  at the bond edge due to bending moments. They give the relation as:

$$\sigma_E = \frac{4M}{\pi R^3}$$

where the moment  $M$  is:

$$M = \frac{Fa}{1 + FL^2/3EJ}$$

$$J = \frac{\pi R^4}{64}$$

where  $E$  is Young's modulus,  $a$  the misalignment,  $L$  the plug length,  $F$  the pulling force, and  $R$  the plug radius. Care was taken in implementing this test to assure good alignment.

\* If the fracture proceeds at a slow enough rate, no energy will be dissipated in viscous processes.



## Topple Test

The requirements for precise alignment are relaxed in the topple test of Butler [17]. The other advantage pointed out by Butler is that there is no net force normal to the substrate and therefore less substrate distortion than in the plug pull test. There is one other possible advantage which lacks analytical confirmation, but could be important. That is, the normal mode of failure of butt joints is crack propagation. In the plug pull test the location, size and direction of propagation of the starting crack is unpredictable, varying from sample to sample. This is undoubtedly partially responsible for the observed spread in data. In the topple test the maximum tensile stress is at one edge of the sample, greatly increasing the probability that the crack will form there and propagate in the direction of pull.

## Peel Test

The peel test, developed initially by Jacquet [18] after whom the test is sometimes called, is attractive if for no other reason than for the existing theoretical foundation. There are two quite different models for this test. The first model developed by Spies [19] and Bikerman [20] and later modified by Jouwersma [21], is based upon small bending theory applied to an elastic beam on an elastic (Winkler) foundation. The second model was derived from energy balance considerations by Kendall [3-5]. Apparent contradictions in the two models were resolved by Gent [22].

One possible source of error is energy dissipated in bending the adhering strip. This can be minimized by using thin strips or by using a roller to control the radius of bend as reported by Gent and Hamed [23]. Another source of error is energy dissipated by viscous processes. This should be a monotonically increasing function of peel speed and thus should be minimum at low speeds. Kendall [24] showed that peeling force of a rubber strip on a glass plate was independent of speed below 10  $\mu\text{m/s}$ . This is a factor of four below the slowest speed available on the Chatillon tester used for the peel tests, and therefore no measurements were made of peel force at this low speed. Also, it is impractical to set up a QC peel test at this low speed because it would take forty minutes to test a one-inch sample. This is just another example of the many extraneous factors in adhesion testing that are more amenable to control than elimination.

The results of the peel tests are given in units of peel energy per unit area (or simply referred to as peel energy). The peel energy  $E$  is related to the peel force  $F$  and length of peel  $L$  by

$$E = \int_0^L F dx$$

but the peel force, averaged over the length is

$$\bar{F} = \frac{1}{L} \int_0^L F dx = \frac{E}{L}$$

thus dividing the average peel force by the peel width

$$\frac{\bar{F}}{W} = \frac{E}{LW}$$

is equivalent to the peel energy per unit area.

## 2.3 Apparatus

The key device used in all of the adhesion tests is the universal tester, capable of measuring either tensile or compressive forces. The tests were performed with three different universal testers, all operating in the tensile mode. The Baldwin 68-TE-1300 universal tester was used only when cross-head speeds less than 0.25 cm/min or forces greater than 2000 Nt were required. Since the force sensing device and the display are mechanical, this machine has an inherently slow response. Therefore, most of the adhesion tests were performed on a Chatillon UTSM-EL electronic universal tester. Its speed range was modified from the standard model to cover the lower range of 0.25 to 3.0 cm/min. With the standard and additional load cells, several ranges were available with the following full scale force values: 5, 50, 100 and 500 pounds. An Instron TTC-M1-M4 universal tester was used for one set of tests because a crosshead speed of up to 50 cm/min was available.

With forces greater than 4000 Nt in some instances, the plug pull was the most severe test of the fixturing and universal tester. The Baldwin tester was used in all of these tests because of the high forces and slow speeds necessary.

In the plug pull and the other two adhesion tests, the bonding surfaces of the test fixtures were made of aluminum since it is easy to machine, and especially because it is a preferred surface for cleaning and bonding. The most important consideration in the design of the plug pull fixtures was maintaining perpendicular loading on the test surface. Three methods were used to help meet this criterion:

1. close tolerances in fixture fabrication
2. careful alignment during bonding
3. connections to the universal tester which only allow axial loads.



Figure 2 illustrates the design for the upper bonding plug which is bonded directly to the coating under test. Note that the bonding surface perpendicularity and roughness are specified to obtain a surface free of large stress concentrations. The lower bonding plug, which is bonded to the opposite side (bottom) of the substrate, is similar except that it has a constant 1-inch diameter over its entire length.

Alignment during bonding was made possible by a simple piece of aluminum angle as pictured in figure 3. Tests were made on a number of bonded samples to determine the concentricity of the two plugs. The maximum deviation from the axis of rotation was 0.03 cm, only slightly larger than the ellipticity of the plugs (approximately 0.018 cm). The maximum possible edge stress was calculated to be 2.4 percent higher than the average stress. This is probably less significant than the stress concentrations caused by other factors such as irregularities in the coating, and the use of glass beads in the adhesive (sec. 4). In figure 4 the entire bonded assembly can be seen held in place by two universal joints used for removal of all non-axial forces.

The advantage of the tople test is the lack of the close tolerances required in the plug pull test. The important criterion for a proper tople test is to apply only a moment at the coating surface. The tople bar/sample holder is shown in figure 5 and the entire apparatus including the turnbuckle (used to eliminate shear stress) is shown in figure 6.

Figure 7 shows the adjustable sample holder for the peel test with a one-inch diameter sample in place on a circular shim. The holder was designed to accommodate samples up to 0.5 inch thick and up to two inches in diameter. The sample holder rests on a low friction slide table so that the peeling area remains directly under the load cell and peel strip, thus maintaining the 90° angle. Figure 8 shows the entire peel test apparatus, including the Chatillon Universal Tester, and the Hewlett-Packard X-Y Recorder used for generating the peel test plots.

### 3. Coatings\*

Coatings on glass substrates were used in the initial test development phase. One hundred durable and non-durable antireflection coating samples (AR) and 100 durable and non-durable mirror coating samples were obtained for a total of 400. The durable mirror coating was  $\text{SiO}_2$ -overcoated aluminum and the non-durable mirror was gold, undercoated with 1000Å of chrome. The durable AR coating consisted of a layer of  $\text{SiO}_2$  (QWOT\*\* = 3  $\mu\text{m}$ ) followed by a layer of  $\text{TiO}_2$  (QWOT = 3  $\mu\text{m}$ ). The non-durable AR coating was a single layer of cryolite (QWOT = 3  $\mu\text{m}$ ).

Since these coatings on glass were to be used only for test development, there were no durability specifications and the only performance specification was for the two-layer AR coating, which was to have maximum reflectance of four percent at 3.0  $\mu\text{m} \pm 0.2 \mu\text{m}$ .

AR coated infrared windows were used in the final stages of test procedure development. Fifty  $\text{CaF}_2$  windows and 44 KCl windows (25.2-mm diameter by 5-mm thick) were obtained from the Harshaw Chemical Company. These samples were packed in a desiccant and arrived at Hughes with no apparent moisture damage. In addition, 16 ZnSe windows (25.4 mm diameter x 3.2 mm thick) were purchased from the II-VI Corporation. The material was Raytheon CVD-type ZnSe.

Two different AR coating designs were chosen for each substrate type for a total of 6 different coating/substrate combinations as shown in table 1. The coating materials were chosen on the basis of the ease of coating and suitability for IR laser windows.

The KCl sample coatings of  $\text{PbF}_2 + \text{ZnSe}$  were received in a severely deteriorated condition due to humidity exposure during shipment. It was also noted that the  $\text{ThF}_4 + \text{ZnSe}$  coatings on KCl were extremely sensitive to humidity. If left exposed for several minutes to the ambient laboratory humidity level of 55 to 65 percent at room temperature, blistering of the coating would occur. Because of these coating failures, several samples of each coating type were exposed for 24 hours to ambient humidity at room temperature, and other samples of each type to 100 percent humidity at approximately 50°C. Results from this test indicated that only three of the coatings procured would withstand 24-hour preconditioning at 100 percent humidity. These coatings were  $\text{MgF}_2 + \text{Ge}$  and  $\text{SiO}_2 + \text{Ge}$  on  $\text{CaF}_2$  substrates, and  $\text{ThF}_4$  coatings on ZnSe substrates. The  $\text{ZnS} + \text{Ge}$  coatings on ZnSe failed the 100 percent humidity test in only 4 hours. The  $\text{SiO}_2 + \text{Ge}$  coated  $\text{CaF}_2$  samples are listed as marginally passing the humidity test because three failed on one side only while one sample failed on both sides. Additional samples were supplied by AFML. They included ZnSe AR coatings on  $\text{CaF}_2$  and KCl (4 each) and 8 TlI-KCl-TlI AR coatings on KCl.

\* The coatings described in this section were used in both the adhesion and abrasion (following paper) phases of this program.

\*\* Quarter-wave optical thickness or the wavelength at which the phase shift upon the passage through the layer is 90 degrees. This is the accepted measure of coating thickness.

Table 1. AR coated laser windows.

Quantity	Substrate (index)	Coating Design: Material (index) QWOT, $\mu\text{m}$		Transmittance, %	Center Wave- length, $\mu\text{m}$	Humidity Test Results
		Outer Layer	Inner Layer			
19	$\text{CaF}_2$ (1.41)	$\text{SiO}_2$ (1.75) 5.63	$\text{Ge}$ (4.0) 0.45	96	3.5	Marginally Passed 100% Humidity
20	$\text{KCl}$ (1.46)	$\text{PbF}_2$ (1.72) 14.1	$\text{ZnSe}$ (2.4) 4.71	-	10.6*	Failed Shipping Environment
20	$\text{KCl}$ (1.46)	$\text{ThF}_4$ (1.5) 14.4	$\text{ZnSe}$ (2.4) 3.06	96	10.0	Failed Ambient Humidity
19	$\text{CaF}_2$ (1.41)	$\text{MgF}_2$ (1.35) -	$\text{Ge}$ (4.1) -	98	3.3	Passed 100% Humidity
7	$\text{ZnSe}$ (2.40)	$\text{ThF}_4$ (1.5) 10.6	-	96	10.0	Passed 100% Humidity
7	$\text{ZnSe}$ (2.40)	$\text{ZnSe}$ (2.15) 12.0	$\text{Ge}$ (3.8) 4.77	98	10.0	Failed 100% Humidity

\*Design goal, measurement not performed due to coating failure.

#### 4. Adhesives

Several adhesives were used in the early phases of the adhesion tests in order to pick the best one. The adhesives (all epoxies) were chosen for strength, good adhesion to glass surfaces and low curing stress (low shrinkage). Table 2 lists the adhesives used, the manufacturer, estimated yield strength, relative elasticity, curing temperature, and relative curing stress.

Table 2. Adhesives

Designation	Manufacturer	Estimated Nominal Yield Strength, $\text{Nt/cm}^2$	Relative Elasticity	Curing Temperature, $^{\circ}\text{F}$	Curing Stress
EPON 828*	Shell	4800	very stiff	70	Low
A1177-B	B.F. Goodrich	5500	stiff	70	Low
C7/W	Armstrong	5200	flexible	70	None
EC 2216	3M	3400	very flexible	70	None
EC 2214	3M	10000	stiff	225	Mod-Low

\*Catalyzed with TETA.

One of the mechanisms by which coatings fail in use is internal stress developed during coating. Additional stress due to the adhesive cure cycle would add to the internal stress and affect the test results. For this reason most of the bonding was done with room temperature curing adhesives to reduce the thermally induced curing stress. For comparison one high temperature curing adhesive was used: 3M type EC 2214 epoxy which cures between 100 and 120°C.

The aluminum plugs and strips were cleaned just prior to bonding in a hot (66°C) acid etch for 10 to 12 minutes. The acid was sulfuric with sodium dichromate added. Following the etch were two water rinses, the last in de-ionized water. The parts were then dried by placing them in a dry 66°C oven.

Most of the samples were cleaned with flowing reagent grade acetone. An ultrasonic bath was tried with no improvement in the results. In addition, a relatively mild alkaline bath was tried (Oakite 164) but was found to attack the coatings and therefore its use was discontinued.

In many of the early tests the failure occurred at the sample-adhesive interface or the plug-adhesive interface, evidence of an improper bond.\* To improve the interface, the aluminum was primed with a corrosion-resistant primer EC 3924 while the samples were primed with a silicone primer EC 3901.

The bond thickness was controlled through the use of small (0.1 mm diameter) glass beads, 0.2% by weight. Teflon shims were also tried but the results were poor. Also the shimming technique is very difficult to apply to the peel strip bonding process.

## 5. Results

### 5.1 Plug Pull Test

The results of the plug pull tests are presented in table 3. Comparing the first two entries one can see that the Al177B forms a good bond with glass. The results for the aluminized mirrors show that a good bond was formed between the plug and sample but that the yield strength of the adhesive was insufficient (for the most part) to overcome the adhesion of the coating to the glass.

Table 3. Plug pull tests\*

Sample	Quantity	Average Yield Force, Nt	Standard Deviation, %	Fraction of Coating Pulled, %	Type of Failure
None**	5	5400	10	-	Cohesive
Glass only	5	5150	19	-	Cohesive
Al + SiO <sub>x</sub> on Glass	5	4840	7	5	Mainly cohesive
Cr + Au on Glass	5	2150	30	0	Mixed adhesive and cohesive
Cryolite on Glass	5	3785	15	0	Mixed adhesive and cohesive

\* All77-B adhesive: pulling speed = 0.025 cm/min.

\*\* Direct plug to plug bond.

The tests on the gold- and cryolite-coated samples resulted in partial adhesive failure and thus low yield force. There was a strong correlation between the fraction of cohesive failure and the yield strength. This is illustrated in figure 9 which shows the results of testing two gold mirrors. The dark areas (gold) indicate adhesive failure while the light areas (adhesive) indicate cohesive failure. The measured yield force for the sample on the left was twice that of the sample on the right.

Due to the inability of the plug pull test to consistently pull coatings, the program emphasis was shifted to the topple and peel tests.

### 5.2 Topple Test

The topple test was performed on the plain glass samples, coated glass samples, and AR-coated IR substrates. Two deflection speeds (1.3 cm/min and 0.28 cm/min) were compared during the tests on plain glass. It was found that the 1.3 cm/min speed had better results. The average force was approximately ten percent higher than for the slower speed, and the standard deviation was six percent of the average as opposed to 20 percent for the 0.28 cm/min speed. Thus the 1.3 cm/min speed was used on most of the gold-, aluminum-, and cryolite-coated glass samples. From the results in table 4, it is seen that the test was successful in removing significant amounts of each coating type.

\* According to Bikerman [25], failure in a properly formed bond is always within the adhesive (cohesive failure). A failure at the boundary (adhesive failure) is indicative of an improper bond which he calls a weak boundary layer.



Table 4. Topple test results on coated glass

Quantity	Coating	Average Force, Nt.	Standard Deviation, % of Average	Average Percentage Coating Pulled	Type Failure
5	Al + SiO <sub>x</sub>	273	25	30	Cohesive
5	Cr + Au	118	30	55	Adhesive
5	Cryolite	173	24	30	Adhesive

\*All77-B adhesive, deflection speed = 1.3 cm/min for most samples.

The AR coated, laser substrates were all topple tested at the 1.3 cm/min speed. A summary of the test results is listed in table 5. The test was successful in removing either the coating or part of the substrate itself for every sample tested. Figure 10 depicts the unexplained destruction of the KCl substrates at very low topple forces. For comparison, the "slow" tape test (MIL-M-13508) was performed on the remaining coating of all of the coated samples tested by the topple method. The only samples to fail were three of the SiO<sub>2</sub> + Ge on CaF<sub>2</sub> samples, four of the AFML samples, and all of the ThF<sub>4</sub> + ZnSe on KCl samples. It has not been explained why the ThF<sub>4</sub> + ZnSe on KCl samples failed the cellophane tape test although the substrate failed in the topple test before the coating was removed.

Table 5. Topple test results on AR coated IR substrates\*

Quantity	Substrate	Coating	Average Force, Nt.	Standard Deviation, % of Average	Comments
10	CaF <sub>2</sub>	SiO <sub>2</sub> + Ge	99.6	36	coatings entirely removed, slight substrate damage
6	CaF <sub>2</sub>	MgF <sub>2</sub> + Ge	125.4	24	substrates destroyed
3	ZnSe	ZnS + Ge	43.6	28	all coatings removed
4	ZnSe	ThF <sub>4</sub>	64.1	12	substantial coating removed
9	KCl	ThF <sub>4</sub> + ZnSe	32.9	27	substrates destroyed
7	KCl	TlI + KCl + TlI	55.4	15	parts of coating layers removed
1	CaF <sub>2</sub>	ZnSe	68.1	-	substrate and coating removed
1	KCl	ZnSe	52.0	-	substrate and coating removed
1	CaF <sub>2</sub>	ZnSe	14.7	-	**coating completely removed
1	KCl	ZnSe	52.5	-	**coating completely removed

\* All77-B adhesive, deflection speed = 1.3 cm/min.

\*\* These coatings were deposited by sputtering. All the other coatings were thermally deposited.

### 5.3 Peel Test

During the development of the peel test, peel strips of varying material, thickness and temper were tried. It was found that thin (0.15 mm) aluminum strips of low temper gave the highest peel energies and were the most consistent at pulling coatings. It was also determined that a more elastic adhesive (3M EC 2216) gave better results. A summary of these results is shown in table 6 for a range of pulling speeds from 0.3 to 3.0 cm/min. There was no direct correlation between speed and the results observed, therefore a pulling speed of 1.3 cm/min was arbitrarily chosen for the subsequent tests.

Table 6. Peel test on coated glass\*

Quantity	Coating	Average Peel Energy, Nt/cm	Standard Deviation, % of Average	Coating Pulled	Comments
3	Cr + Au	4.8	11	all	-
3	Al + SiO <sub>x</sub>	19.1	12	none	Adhesive failure
3	Cryolite	10.3	10	none	Adhesive failure
3	SiO <sub>2</sub> + TiO <sub>2</sub>	19.4	17	5% on 2 samples	Adhesive failure

\*EC 2216 adhesive, 0.15 mm thick aluminum strip, various speeds.

Table 7 lists the results for these tests. For comparison the "slow" tape test was also performed on the remaining coating on these samples. All of the samples passed with the exception of the KCl windows. The peel test was therefore capable of removing coatings which had passed the tape test, and with forces low enough to avoid substrate damage.

Table 7. Peel test results on coated IR window substrates

Substrate	Coating	Average Peel Energy Nt/cm	Comments
CaF <sub>2</sub>	SiO <sub>2</sub> + Ge	0.76	all coatings removed completely
CaF <sub>2</sub>	MgF <sub>2</sub> + Ge	13.5	nothing significant removed
ZnSe	ThF <sub>4</sub>	0.70	two samples only, all coatings removed
ZnSe	ZnS + Ge	2.5	one sample, 90% coating removed
KCl	ThF <sub>4</sub> + ZnSe	0.61	two samples, >60% coating removed

### 5.4 Cellophane Tape Test

In order to compare the peel test to the established MIL-Spec cellophane tape test, measurements were made of the peel energy of the cellophane tape (Type I, Class A; Federal Specification L-T-90D) at various pulling speeds (fig. 11). Four people were asked to perform the slow pull tape test and resulting range of pulling speeds are also shown in the figure. The "quick" or snap test of MIL-C-48497 was also performed. The corresponding peel energy could not be measured because of the slow response of the tensile test machine so the value was estimated by linear extrapolation. It has been shown by Kendal [5] that the peel energy should approach a constant at high peel rates and thus the estimated value of 7.7 Nt/cm should be considered an upper limit.

Since all coating vendors do not use the approved cellophane tape, a comparison test was performed using 3M No. 6201 (Highland®) mending tape. The resulting curve in figure 11 is quite different from the cellophane curve. The tape exhibited a slip-stick peel pattern which is the reason for the relative insensitivity of the peel energy to peel rate.

All the infrared samples were tape tested and the results were compared to the results of the tople test (fig. 12) and to the results of the peel test (fig. 13).

Despite the dispersion of results there appears to be good correlation between the pull tests and the tape test. The Wilcoxon Two Sample Test [26] gives a confidence greater than 99.7% that the "passed" group of samples is really different from the "failed" group. Thus the new tests and the older tape test are testing related, if not the same, adhesion phenomena.

## 6. Summary

The basic objective of this program was to develop quantitative adhesion tests that could be used to replace the qualitative MIL-Spec tests. Though it proved difficult to remove coatings with good adherence to glass substrates, it was possible to remove coatings from infrared substrates and therefore to quantify their adhesion.

The features of the various tests are summarized in table 8. The plug pull test is perhaps the least desirable of the three because of relatively poor results and high forces involved. The topple test gave better results and is inexpensive to implement but resulted in still unexplained substrate damage. The peel test is expensive to implement but has the lowest force of the three tests; it has the advantage that it gives localized adhesion values.

Table 8. Comparison of tests

Type	Force, Nt.	Ability to Pull Coatings	Repeatability	Cost to Implement	Cost to Perform
Plug pull	4,400	Poor	Fair	High	Low
Topple	264	Fair	Good	Low	Low
Peel	22	Fair	Good	High	Moderate

## 7. References

- [1] Mittal, K.L., "A Critical Appraisal of the Methods for Measuring Adhesion of Electro-deposited Coatings," in Properties of Electro-deposits: Their Measurement and Significance, Ed. R. Sard, H. Leidheiser, Jr. and F. Ogburn, Chapt. 17, Electrochemical Society, Princeton, NJ, April 1975.
- [2] Chapman, B.N., "Thin Film Adhesion," J. Vac. Sci. Technol., 11, 106, 1974.
- [3] Kendall, K., "The Adhesion and Surface Energy of Elastic Solids," J. Phys. D., 4, 1186, 1971.
- [4] Kendall, K., "Shrinkage and Peel Strength of Adhesive Joints," J. Phys. D., 6, 1782, 1973.
- [5] Kendal, K., "The Dynamics of Slow Peeling," Int. J. Fracture, 11, 3, 1975.
- [6] Kendal, K., "Thin-Film Peeling - The Elastic Term," J. Phys. D., 8, 1449, 1975.
- [7] Bullett, T. R., and Prosser, J.L., "The Measurement of Adhesion," Progress in Organic Coatings, 1, 45, 1972.
- [8] Campbell, D.S., "Mechanical Properties of Thin Films," Handbook of Thin Film Technology, Edited by L.I. Maissel and R. Glang, Chapter 12, McGraw-Hill, New York, 1970.
- [9] Chapman, B.N., "Adhesion of Thin Metallize Films," Aspects of Adhesion, Ed. D. J. Alner, 43, CRC Press, 1969.
- [10] Jacobson, R., "Measurement of the Adhesion of Thin Films," Thin Solid Films, 34, 191, 1976.
- [11] Mittal, K.L., "Adhesion Measurements of Thin Films," Electrocomponent Sci. Technol., 3, 21, 1976.
- [12] Weaver, C., "Adhesion of Thin Films," J. Vac. Sci. Technol., 12, 18, 1975.
- [13] Poley, N.M. and Whitaker, H.L., "Adhesion of Chromium Films to Soda Lime Glass," J. Vac. Sci. Tech., 11, 114, 1974.
- [14] Butler, D.W., Stoddart, C.H. and Stuart, P.R., "The Stylus or Scratch Method for Thin Film Adhesion Measurement: Some Observations and Comments," J. Phys. D., 3, 877, 1970.
- [15] Kuwahara, K., Nakahara, S. and Nakagawa, T., "The Adhesion of Thin Evaporated Films," Int. Conf. on Strength of Metals and Alloys - Proc., 9 Supplement, 1034, 1968.
- [16] Jacobson, R. and Kruse, B., "Measurement of Adhesion of Thin Evaporated Films on Glass Substrates by Means of the Direct Pull Method," Thin Solid Films, 15, 71, 1973.
- [17] Butler, D.W., "A Simple Film Adhesion Comparator," J. Phys. E, 3, 979, 1970.
- [18] Jacquet, P.A., "Adhesion of Electrolytic Copper Deposits," J. Electrochemical Soc., 66, 393, 1934.
- [19] Spies, G.J., "The Peeling Test on Redux-Bonded Joints," Aircraft Eng., 25, 64, 1953.
- [20] Bikerman, J.J., "Theory of Peeling through a Hookean Solid," J.A.P. 28, 1484, 1957.
- [21] Jouwersma, C., "On the Theory of Peeling," J. Polymer Sci., 45, 253, 1960.
- [22] Gent, A. N. and Hamed, G.R., "Peel Mechanics," J. Adhesion, 1, 91, 1975.
- [23] Gent, A.N. and Hamed, G.R., "Peel Mechanics for an Elastic-Plastic Adherend," J. Appl. Polymer Sci.
- [24] Kendal, K., "Crack Propagation in Lup Shear Joints," J. Phy. D.: Appl. Phy., 8, 12, 1975.
- [25] Bikerman, J.J., "The Science of Adhesive Joints, 2nd Ed., Academic Press, N.Y., 1968.
- [26] Noether, G.E. Introduction Statistics, Houghton Mifflin Co., Boston, 1976.



# 8. Figures

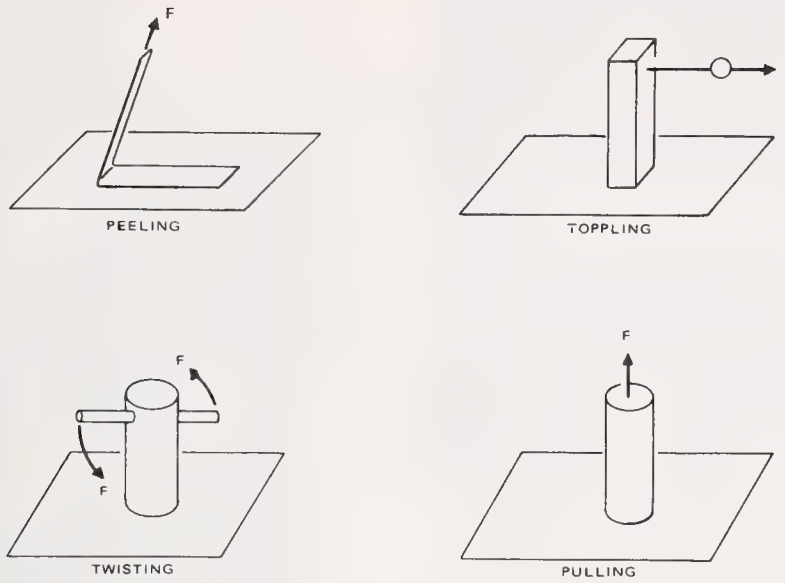


Figure 1. Various pull-off tests.

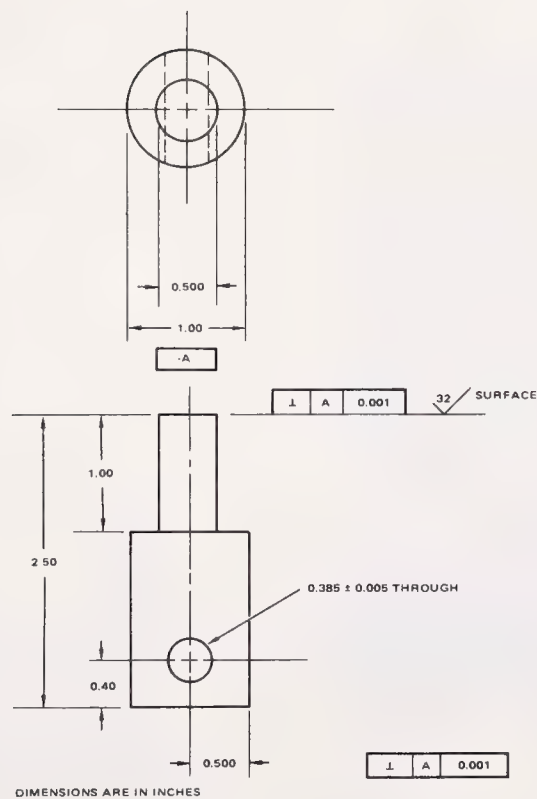


Figure 2. Upper bonding plug.

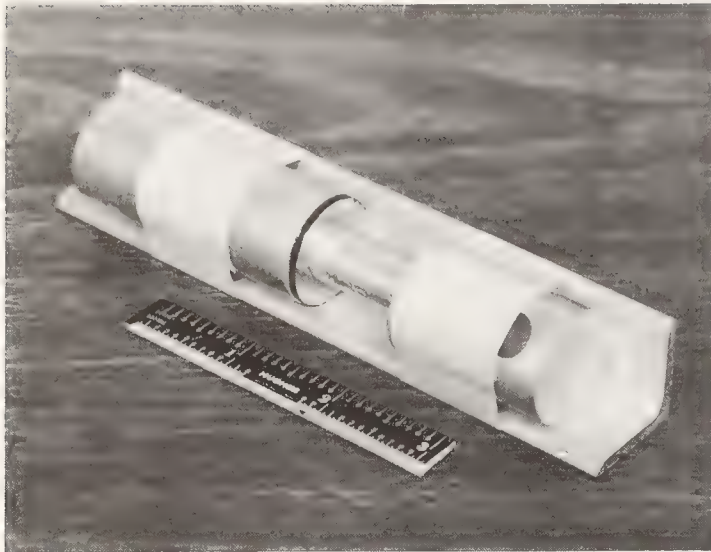


Figure 3. Bonding alignment fixture.

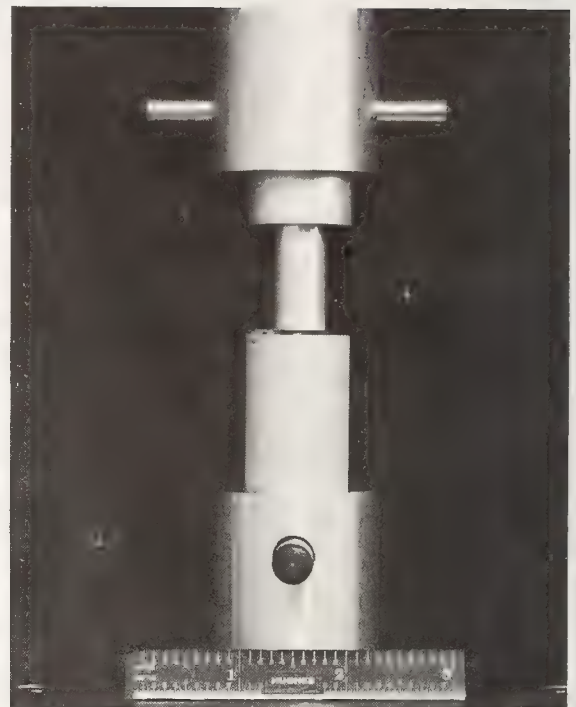


Figure 4. Bonded plug pull assembly in test fixture.

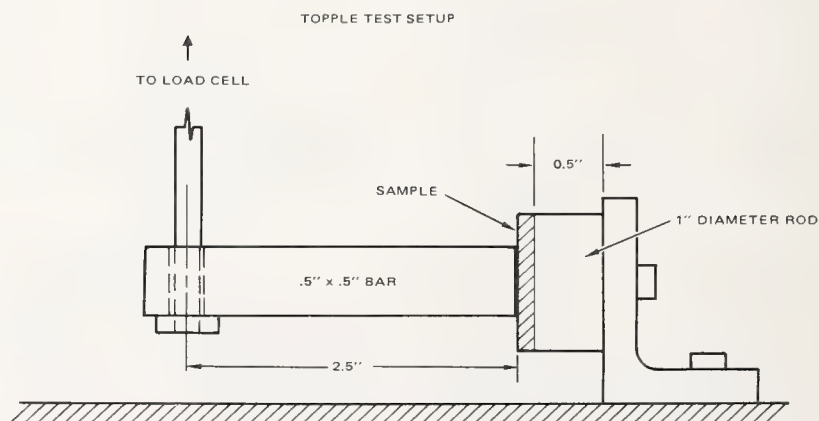


Figure 5. Topple bar/sample holder.

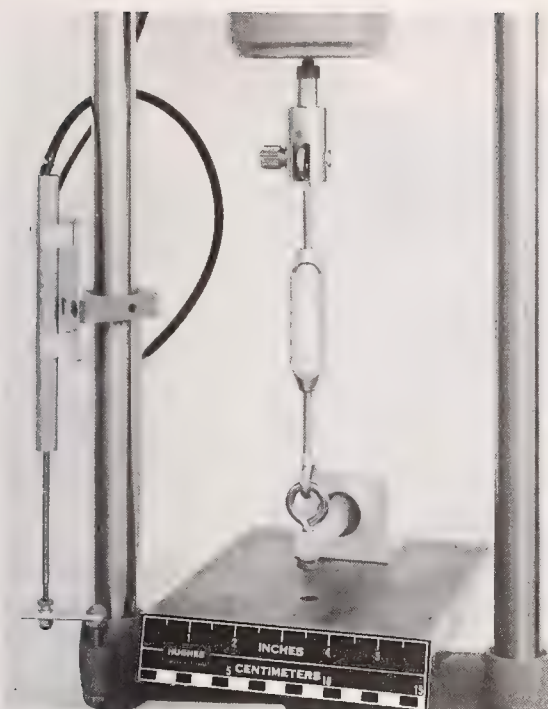


Figure 6. Topple test arrangement.

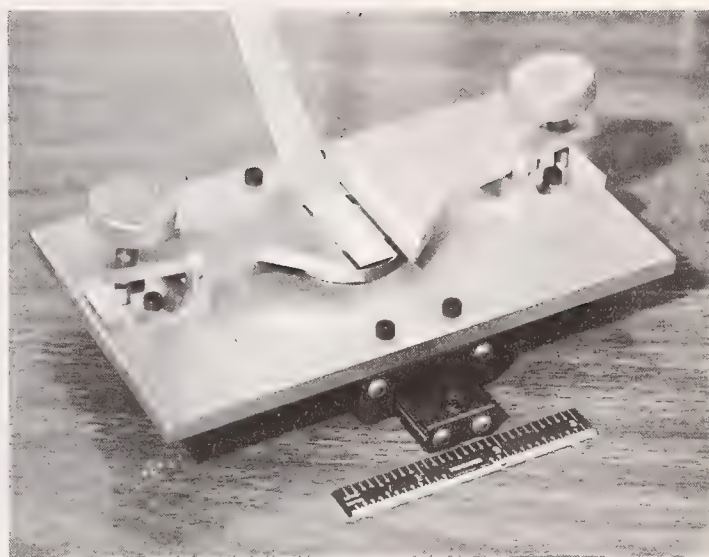


Figure 7. Sliding sample holder.

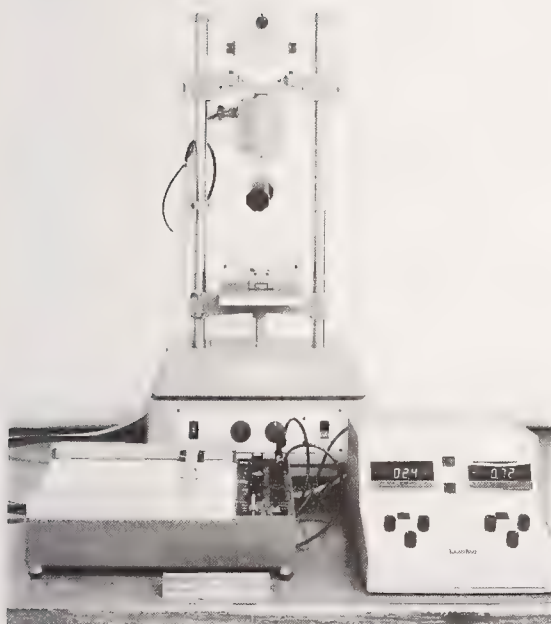


Figure 8. Peel test with Chatillon Universal Tester.



Figure 9. Variation in failure mode for two gold mirrors.



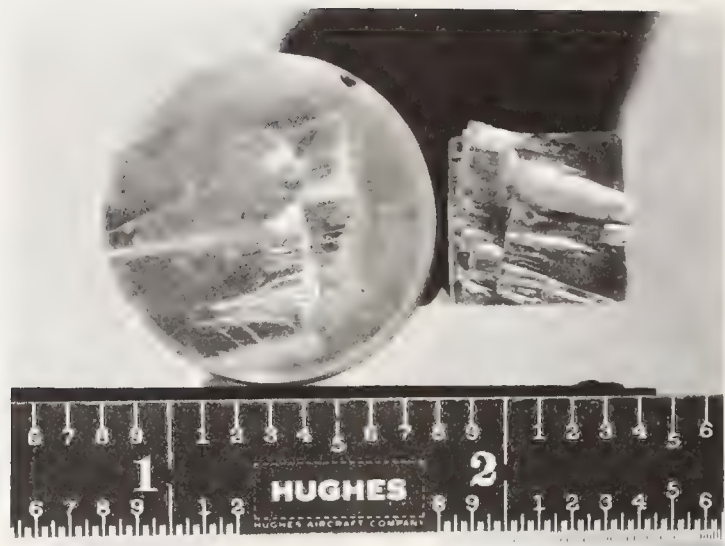


Figure 10. KCl sample damaged during topple test.

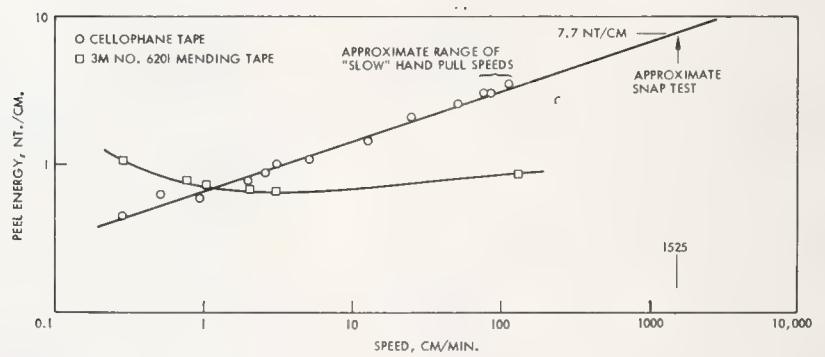


Figure 11. Tape test results.

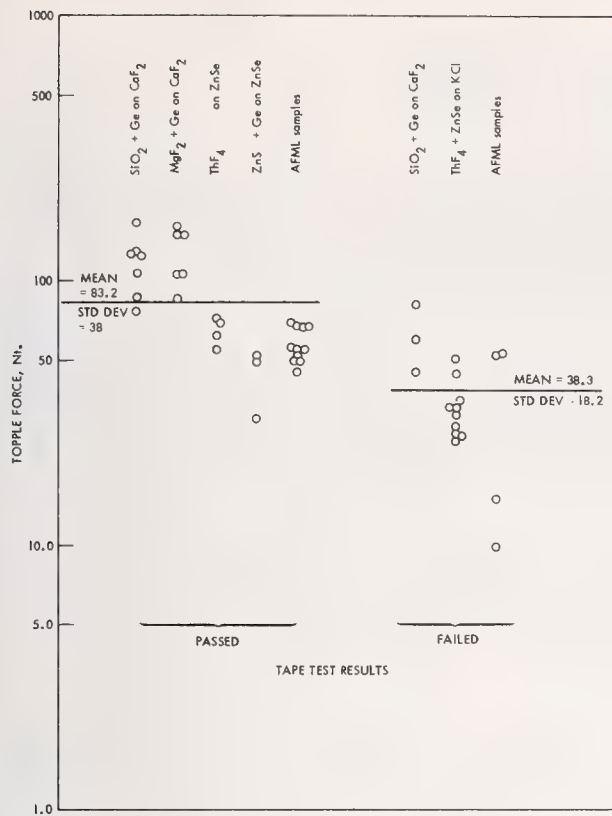


Figure 12. Comparison between topple and tape test on AR coated IR windows.

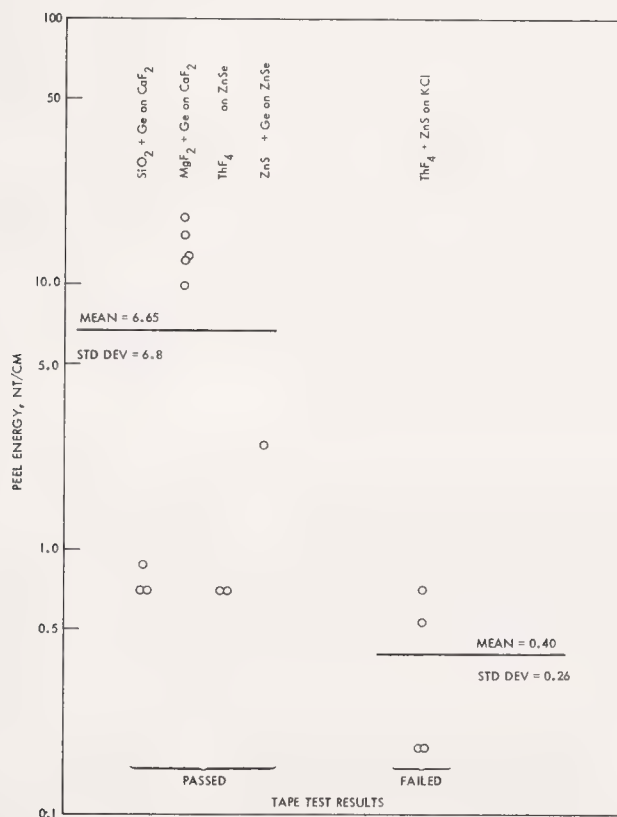


Figure 13. Comparison between peel and tape test on AR coated IR windows.

#### COMMENTS ON PAPER BY SCHEELE AND BERGSTROM

Several questions were raised concerning the nature of the adhesives used in these tests. The speaker indicated that the adhesives used were room temperature setting epoxies, chosen so as to avoid introducing thermal stress in the bond. Some tests were run using high temperature epoxies but no significantly different results were obtained. The chemical effect of the adhesive on the coating surface was not tested, although references in the literature indicated no chemical interaction for the adhesives that were employed. The epoxies used supposedly have very low shearing stress and so any shrinkage of the epoxy should not have introduced significant stress in the coating, however, no measurements were made of this effect directly. Of the three tests examined, the speaker indicated that they had a preference for the topple test, despite the fact that on some occasions it lead to substrate failure. This failure was felt to be due to bleeding of the adhesive through the coating, bonding the topple plug to the substrate. Due to this and other uncertainties, the speaker felt that it was premature to indicate a definite preference of one test over another at this time.



## QUANTITATIVE CHARACTERIZATION OF COATINGS:

### Part II: Abrasion Resistance\*

R. A. West and C. W. Nichols  
Hughes Aircraft Company  
Culver City, California 90230

A new method of quantification of abrasion resistance of antireflection coatings has been developed. The Falling Sand Test of ASTM was modified to abrade optical coatings on witness samples in a controlled manner. Quantification of the abrasion damage was accomplished by measuring transmittance degradation in the abraded area. Approximately 170 samples of antireflection coatings on various substrates including glass,  $KCl$ ,  $ZnSe$ , and  $CaF_2$ , were tested using the new method. The existing standard military eraser and cheesecloth abrasion tests were also performed on many of the samples and the degree of correlation between the existing tests and the new method was established.

Key words: Abrasion resistance; coating degradation; coatings; hardness; transmittance degradation.

#### Introduction

Whether intended for use in laboratory optical systems, military, or space applications, most coated optical elements are required to exhibit some degree of durability to insure a reasonable useful life-time for the element. One of the parameters commonly specified as a measure of this anticipated life-time is abrasion resistance of the coated surface. The resistance of a coating to abrasion allows the element to be cleaned as necessary using standard optical cleaning procedures and, in extreme cases, to operate for a reasonable period in an environment where dirt and dust impinge and accumulate on the surface.

The current tests of abrasion resistance in use throughout the optical industry include the 20-rub eraser test of MIL-C-675 and MIL-C-48497 and the 50-rub cheesecloth test of MIL-M-13508 and MIL-C-48497. Both of these tests call for a specific number of "complete strokes" of the eraser or cheesecloth pad over the surface. The force on the surface specified for the eraser test is 2.0 to 2.5 lb while that for the cheesecloth is 0.75 to 1.25 lb.

There are several problems associated with these tests. They provide only a qualitative "pass-fail" measure of a coating's abrasion resistance and the criterion for judging whether a coating is passing or failing is that "no visible deterioration" of the coating be apparent after the test. For infrared optical elements, the visible degradation criterion can be excessive since surface deterioration at infrared wavelengths is not as critical to normal performance. Furthermore, since many infrared optical elements are visually opaque and have high refractive indices, the judgement of visible degradation is highly subjective, being dependent on lighting conditions, and on the eyesight of the inspector.

Specific problems with the tests as they are currently structured include variability due to manufacturing variations in the "MIL-Spec" erasers, and lack of detail in specifying procedures to be used in preparing the tester (especially the eraser surface), rubbing speed, and limitations on useful life of erasers or cheesecloth.

#### Other Test Methods

A quantitative test of abrasion resistance of optical coatings requires two parts: first the actual abrading of the sample and then the evaluation of that abrasion. In developing a new method to provide a quantitative measure of abrasion resistance, emphasis was placed on repeatability, relevance to actual operational parameters, and ease of implementation and performance. A survey of the literature revealed many types of abrasion tests for paints, linoleum, refractory materials, etc., although few could realistically be adapted to optical coatings. Many of the tests encountered required costly equipment and/or large sample sizes, i.e., larger than 3.8 cm (1.5 in.) in diameter.

---

\* This work funded under contract to Air Force Materials Laboratory, Wright Patterson Air Force Base, Ohio. Contract No. F33615-76-C-5285.

\*\* The phrase "complete strokes" is emphasized here due to historical confusion over the definition of a complete stroke as one pass over a point on the surface as opposed to a "complete cycle" or two passes over the point.

## Falling Sand Test

The approach selected as the most readily implementable and easily variable test method to cover a wide range of coatings was the falling sand test modified from ASTM literature by Johnston and Walsh [1,2]<sup>1</sup>. Figure 1 shows the apparatus used to abrade the samples. A pyrex funnel emptied into a 10cc disposable adhesive syringe with a nominal 1.9 mm (0.075 in.) diameter opening cut in the tip. (The syringe was incorporated early in the test development to control the rate of sand entering the fall tube independent of the amount of sand in the funnel.) The syringe was inserted into a vertical 61cm (24 in.) long, glass fall tube (8.0 mm I.D.) with the bottom end located 2.54cm (1.0 in.) above the sample surface.

The sample was mounted on a rotating teflon block, belt driven by a small synchronous motor at approximately 60 rpm. (The rotation of the sample as the sand impinged on the surface was incorporated to eliminate any effects due to anisotropy of the coating, substrate material, or of the measurement technique.) The teflon block and sample were oriented at a 45° angle from the horizontal to enable each sand particle to theoretically impact the surface only once. The center of rotation of the teflon block was offset from the center of the sample by 6.4 mm (0.25 in.) to allow for abrading only one-half of the sample. A mask was designed to cover the remaining half to retain an undamaged reference area to perform spectral comparison tests.

The abrasive material selected for the abrasion process was silica sand from the Ottawa Silica Company of Ottawa, Illinois. This material was selected because it was readily obtainable, inexpensive, and was made up of relatively smooth, regular shaped particles. It is the same type of sand approved for various ASTM tests, except the range of particle sizes was smaller than the standard ASTM grades.

An extensive sieving process was used to generate a known particle size distribution and to verify that this distribution remained unchanged throughout the tests. The distribution obtained from the sieving process was as follows: 88.1 percent (by weight) of the particles were in the 180-212 µm range (#80 sieve), 2.8 percent in the 212-250 µm range (#70 sieve), and 9.1 percent in the 150-180 µm range (#100 sieve).

The method used to quantify the amount of abrasion damage achieved was the measurement of transmittance degradation. Transmittance measurements were performed on a Perkin-Elmer Model 180 spectrophotometer at the wavelength of peak transmittance for each sample. Figure 2 shows the sample holding fixture designed for mounting the samples. With this fixture, measurements could be performed on both the untested reference area and the abraded area simply by rotating the holding fixture through 180°. By using a 10x ordinate expansion and long integration times (8-16 seconds), transmittance differences as low as 0.2 percent could be accurately measured. The figure shows the abraded area of a typical sample in position in front of a 3.8 mm (0.150 in.) diameter aperture. The mount utilized indexing holes and scribe marks for proper alignment and repeatable locating of the sample for successive measurements as damage was accumulated.

### Test Results: Glass Samples

Early testing and equipment checkout was performed using glass Balzer witness plates with single layer cryolite and two layer SiO<sub>2</sub>/TiO<sub>2</sub> antireflection coatings.\* The first tests utilized measurements of specular reflectance increase instead of transmittance decrease as described above. However, erroneous results were obtained since the increase in diffuse reflectance caused a corresponding decrease in specular reflectance, counteracting the anticipated increase with coating removal. By measuring transmittance loss instead, these anomalies were eliminated since increases in diffuse and/or specular reflectance will both result in a transmittance loss.

The next variable to be quantified was the sand charge size to abrade the different coating types and measure the transmittance degradation of each type. Figures 3 and 4 show the transmittance degradation vs. sand charge for both antireflection coatings in increments of 5 grams. The points on both of these curves where peak degradation occurs represent the maximum transmittance loss due to scattering in the abraded area and correspond to the points at which coating "break through" occurred exposing the glass substrates. In order to select one fixed sand charge size to use for quantitatively ranking several coating types with wide ranging abrasion resistance characteristics it would be necessary to remain on the linear portion of the degradation curve for each coating type. It was apparent for the two coating types tested here that no one fixed charge would be appropriate for both types, since too large a charge would remove the entire cryolite coating before producing significant results on the SiO<sub>2</sub>/TiO<sub>2</sub> coating.

Hence, the method finally adopted was to select, as the independent variable, a fixed transmittance degradation level of 2 percent (considered a realistic deterioration factor from a system standpoint and also large enough to insure relative accuracy in the measurement). The dependent variable was then the amount of sand necessary to produce the 2 percent transmittance loss, which could vary widely among coating types to provide a quantitative measure of abrasion resistance. This provided a standard procedure useful for all types of coatings, visible and infrared, "soft" and hard."

1. Figures in brackets indicate the literature references at the end of this paper.

\* Details of coatings and their designs are included in Part I.



Using this method, abrasion tests were performed on a number of the glass samples with  $\text{SiO}_2/\text{TiO}_2$  and cryolite coatings. Figures 5 and 6 show histograms of the results obtained. In figure 5, the sensitivity and repeatability of the falling sand test can be demonstrated. The  $\text{SiO}_2/\text{TiO}_2$  coatings were deposited in a planetary coating chamber utilizing three separate plates on which samples were mounted. The figure shows that, in general, samples on a given plate were grouped together in the histogram indicating good repeatability in the test, although a wide spread between groups is apparent, indicating high sensitivity. It should be noted that all these samples passed the standard eraser test yet the difference in measured abrasion resistance from the "softest" to the "hardest" is more than a factor of ten.

The results for the cryolite coating in figure 6 were not as revealing since all samples were from the same plate in the coating chamber. However, since the cryolite samples also passed the standard eraser test, the ability of the falling sand test to provide useful quantitative data with which to rank samples all of which pass the eraser test was further demonstrated.

#### Test Results: IR Samples

Abrasion resistance tests were performed on laser window samples of KCl, ZnSe, and  $\text{CaF}_2$ , some purchased by Hughes from various vendors and others furnished by the Air Force Materials Lab. Table 1 summarizes the results of these tests. In order to determine if the environment in which a sample was stored prior to abrasion testing would have any effect, several samples of each coating type were stored in the ambient laboratory atmosphere (50-60%) and several in a 100% humidity environment for 24 hours prior to testing. The results show that there was indeed an effect on the test results for the  $\text{CaF}_2$  substrates and the  $\text{ThF}_4$ -coated ZnSe substrates. The other samples could not be preconditioned at 100% humidity since the coatings were not sufficiently durable to withstand that environment. Furthermore, the coatings on the KCl substrates were not able to withstand the normal lab humidity and were therefore tested by enclosing the test apparatus in a plastic bag and purging it with dry nitrogen gas (10-15% humidity). The AFML samples were evaluated in this same environment.

Many of the samples were also tested using the standard eraser or cheesecloth tests for reference. Figure 7 summarizes the sand test results compared to the eraser test results. For purposes of this comparison, samples which failed or were marginal in the cheesecloth test were included in the "failed eraser test" column.

The first thing that is apparent from the graph is the wide spread in data which results from the variations in coating type and substrate. Due to the widely varying nature of the population from which these statistics are drawn, it would require a much larger number of samples to reach any definite conclusions. This can be stated more quantitatively by testing the hypothesis that the pass and fail groups are the same. Using a test from non-parametric statistics, the Wilcoxon Two-Sample test the confidence level for rejecting this hypothesis was found to be 76 percent. It is quite apparent however that if a difference exists it is not large. There are two possible reasons for this low correlation. One is the subjective criterion for passage of the MIL-Spec tests, i.e., "no visible degradation." There is probably little correlation between this criterion and the falling sand criterion of 2 percent change in IR transmittance. The other is that the eraser or cheesecloth tests and the falling sand test might actually measure different aspects of a coating's hardness.

Table 1. Results of falling sand test

Substrate	Coating	Peak Wavelength ( $\mu\text{m}$ )	Mean Charge Size (grams)			
			Ambient Humidity	No. of Samples	100% Humidity	No. of Samples
$\text{CaF}_2$	$\text{MgF}_2+\text{Ge}$	3.3	62.8	9	44.9	8
	$\text{SiO}_2+\text{Ge}$	3.5	22.1	9	27.9	6
ZnSe	$\text{ThF}_4$	10.0	95.7	3	76.7	3
	ZnS+Ge	10.0	11.4	4	-	-
KCl	ZnSe+ $\text{ThF}_4$	10.0	15.7*	14	-	-
KCl	TlI+KCl+TlI	10.6	2.43*	7	-	-
$\text{CaF}_2$	ZnSe	4.8	1.2*	1	-	-
$\text{CaF}_2$	ZnSe	3.7	0.7*	1	-	-
KCl	ZnSe	5.0	0.3*	1	-	-
KCl	ZnSe	6.7	2.8*	1	-	-

\*Ambient Humidity 50-60%. Those marked with (\*) 10-15%.



### Summary

The falling sand test has proven to be an easily implemented, sensitive, repeatable, and quantitative test of abrasion resistance. In many cases, the test results indicated a variation among several samples within the same coating run, traceable to various locations or mounting plates within the coating chamber. Samples near each other on a given plate tended to have results close to each other indicating that test repeatability is quite good.

The lack of a definite correlation between the falling sand test and the existing tests is probably due to the fact that the two types of tests measure different damage parameters and test different damage mechanisms. The sand test is an indicator of a coating's ability to withstand a blowing grit or dust environment while the existing tests indicate scratch resistance and cleanability.

### References

- [1] ASTM D968-51, "Abrasion Resistance of Coatings of Paint, Varnish, Lacquer, and Related Products by the Falling Sand Method."
- [2] Johnston, G.T. and Walsh, D.A., "Some Effects of Environmental Factors on the Performance of Coatings for High Power IR Lasers," Interim Technical Report AFML-TR-75-15, February 1975.

### Figures



Figure 1. Falling sand apparatus.

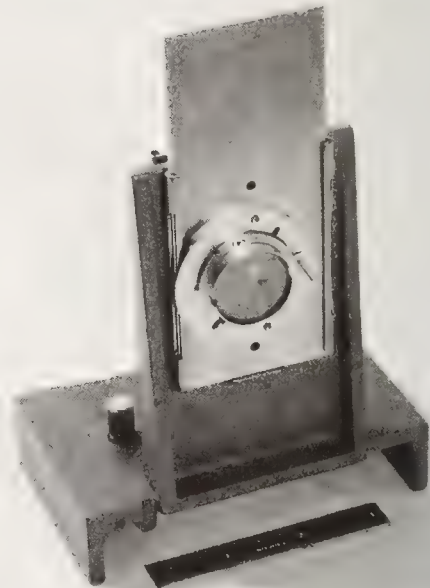


Figure 2. Sample holder for transmittance measurements.

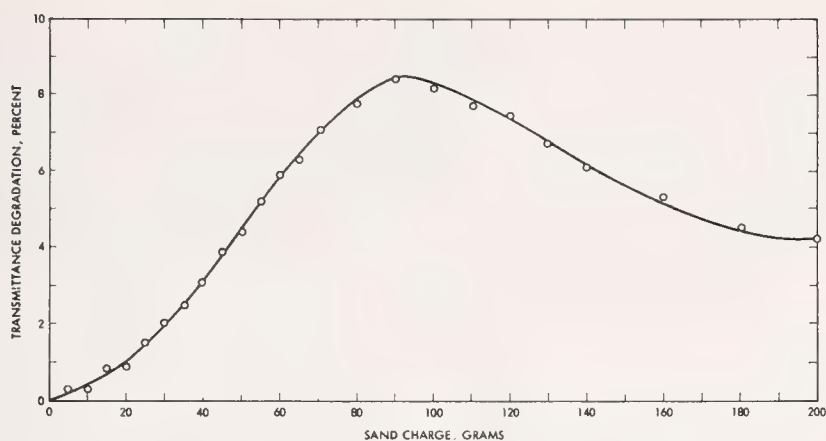


Figure 3. Transmittance degradation curve for  $\text{SiO}_2/\text{TiO}_2$  coating on glass substrate.

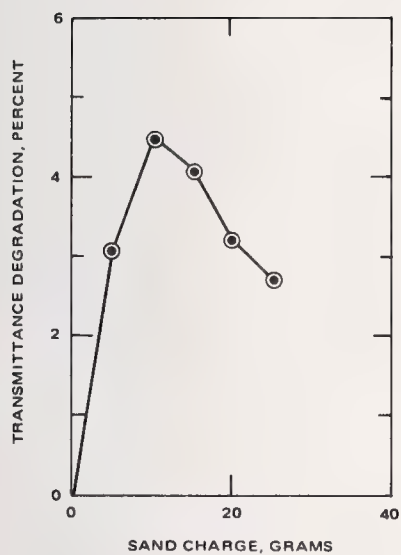


Figure 4. Transmittance degradation curve for cryolite coating on glass substrate.

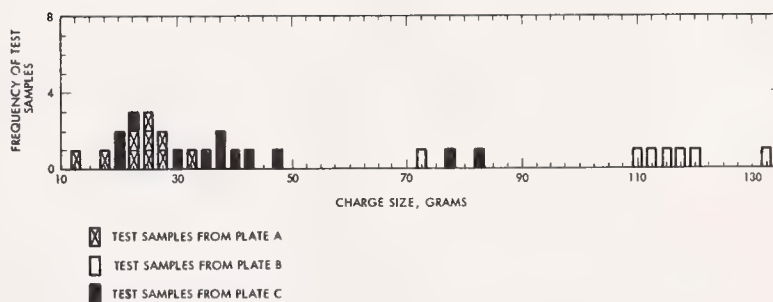


Figure 5. Histogram of 2 percent transmittance degradation results for  $\text{SiO}_2/\text{TiO}_2$  coating on glass substrates.

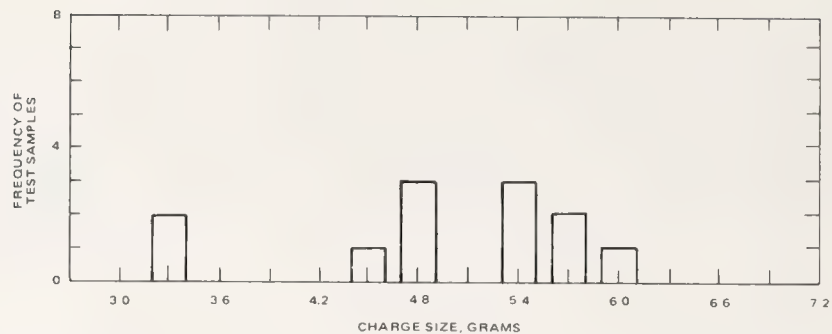


Figure 6. Histogram of 2 percent transmittance degradation results for cryolite coating on glass substrates.

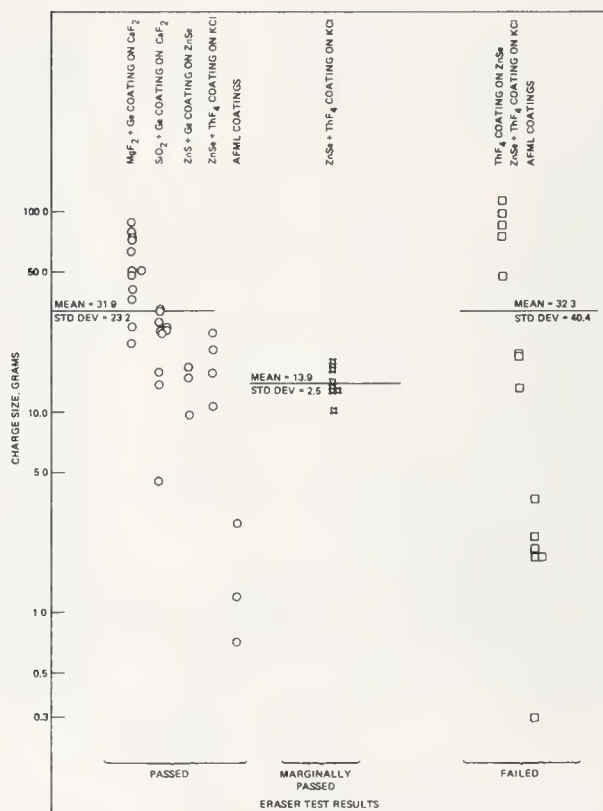


Figure 7. Comparison of sand test results to eraser test results for IR samples.



#### COMMENTS ON PAPER BY WEST AND NICHOLS

The speaker indicated that tests were carried out with Ottawa sand, which is an ASTM Abrasion Standard. The sand was passed through a No. 80 mesh and dropped from 24 inches height. The attempt was made to reduce the amount of angularity in the abrasive compound. It was suggested from the floor that it might be advisable to try glass beads as an abrasive medium. The question of the effect of the particle size on the abrasion test had not been looked at in this work, but the speaker indicated an interest in investigating that relationship.

# DIELECTRIC ENHANCED MIRRORS FOR THE 2-6 $\mu\text{m}$ REGION\*

S. J. Holmes  
Northrop Research and Technology Center  
3401 West Broadway  
Hawthorne, California 90250

This paper reports on work done to define the performance characteristics of a large variety of multilayer dielectric enhanced mirror designs. In particular, dielectric enhanced metallic mirrors have been designed and fabricated which demonstrate reflectivities of 99.9% or greater for the 2.8  $\mu\text{m}$ , 3.8  $\mu\text{m}$ , and 5.3  $\mu\text{m}$  wavelengths. Peak reflectance and description measurements are presented along with environmental testing to demonstrate the performance of these mirror coatings.

Key words: Absorptance; Cleaning procedures; Coating materials; Dielectric enhanced mirrors; Deposition parameters; Reflectance.

## 1. Introduction

Until recently the high power mirrors used on laboratory lasers have been bare metal, copper or molybdenum mirrors, which are either heat sunk or water cooled. This is adequate for short duration laboratory tests, when only a few optical elements are needed.

The difference in reflectance for uncoated versus coated mirrors represents a substantial fraction of the total laser beam output from an optical system where several mirrors are required. The increased reflectance of a coated mirror also has important implications for beam quality and component cooling. A water-cooled mirror with high reflectance will require less cooling for a given temperature induced distortion or alternatively will have less distortion for an equivalent water cooling flow. This can be important in simplifying cooling hardware or for improving the laser beam quality as well as increasing power output. The development of dielectric enhanced mirror coatings for thermally conducting substrates will provide the basis for water-cooled laser resonator mirrors required to keep pace with the high power laser technology. Similar coatings on thermally insulating substrates are needed for use as uncooled mirrors external to the laser.

Reflectivities between 98% and 99% for the 2-6  $\mu\text{m}$  region can be realized with metallic mirrors of copper, gold, or silver. When reflectivities greater than 99% are required, multilayer interference coatings are required. The most practical design for the infrared region is the enhanced metallic mirror surface coated with pairs of alternating quarter wavelengths of dielectric layers of low and high refractive indices. In principle this type of mirror can achieve reflectivity of greater than 99.9%.

## 2. Theoretical mirror designs

There are three basic multilayer dielectric enhanced mirror designs: (1) all dielectric multilayer mirrors, (2) multilayer dielectric enhancement of a highly reflecting metallic thin film deposited on a suitable substrate of metal. It is the latter design that was chosen for this work.

For the initial design of a multilayer dielectric enhanced mirror, several simplifying assumptions were made. It was assumed that all of the dielectric layers were nonabsorbing, homogeneous, plane-parallel and were illuminated by a parallel beam of linearly polarized light having an electric field strength of unity. Because of their simplicity, the equations derived by Young [1]<sup>1</sup> are used here. The reflectance  $R_m$  of a metallic film is related to its complex reflective index ( $n - ik$ ) by

$$R_m = 1 - \frac{4n}{(1+n)^2 + k^2} \quad (1)$$

\* This work was supported by AFWL, Contract No. F29601-76-C-0003.

1. Figures in brackets indicate the literature references at the end of this paper.

When a multilayer coating of  $2N$  nonabsorbing quarterwave layers having refractive index  $n_H$  (high) and  $n_L$  (low) is deposited on the thin metallic film, it can be shown that the reflectance is increased to

$$R = 1 - \frac{4xn}{(x+n)^2 + k^2} \quad (2)$$

where

$$x = (n_L/n_H)^{2N} \quad (3)$$

To obtain the maximum reflectance from a multilayer dielectric enhanced mirror, the metallic film is first coated with the low refractive index material until its reflectance decreases to a minimum at the wavelength for which the highest reflectance is desired. The optical thickness of the layer should be [2]

$$n_L d = \frac{(j+1)}{2} \frac{-\lambda}{4\pi} \arctan - \left( \frac{2n_L k}{n_L^2 - n^2 - k^2} \right) \quad (4)$$

where  $j$  is an integer or zero.

Under this condition, the low index film adjacent to the metal is effectively one quarter-wavelength. In most cases, (i.e., the infrared region), the simple quarter-wavelength coating gives adequate results. The high refractive index material is added until the reflectance reaches a maximum, in other words, until a quarter-wavelength thickness is added. For further increase of reflectance, additional quarter-wavelength film pairs must be added in the same sequence.

The reflectance of such a mirror depends on the refractive index ratio of the dielectric materials, the numbers of layers, the reflectance of the metallic thin film, and the absorption in the dielectric layers. For optimum performance, one desires coating materials with the lowest possible absorption and the highest possible refractive index ratio. The refractive index ratio which one can achieve depends on the availability of suitable coating materials. To keep the number of dielectric layers to a minimum and hence minimize the effect of absorption in the layers, the reflectance of the metallic thin film should be as high as possible.

\*

Table 1 lists the initial designs selected for the experimental coatings. Ideally one coating design should be usable for all three wavelengths with the appropriate adjustments of optical thicknesses. The effect of absorption in the dielectric layers has not been taken into account.

### 3. Experimental

The experimental investigations required the development of optimum cleaning and deposition techniques. Several experiments were conducted to develop the optimum substrate surfaces for the mirror coatings. The candidate coating designs were deposited on small scale (1.52 inch diameter) molybdenum substrates. The substrate surfaces were characterized for surface figure and finish before coating deposition. Established deposition techniques and parameters were utilized for all coating designs whenever available.

Molybdenum was chosen as a consequence of its thermal and mechanical properties. These properties are summarized in Table 2. The molybdenum used for the mirror substrates on this program was ASME 7805. This is a vacuum arc cast, low carbon content molybdenum readily available in bar stock from American Metal Climax Corporation.

\* Tables 1, 3, 4, 5, 6, 7, 8, 9, and 10 are shown following the end of the text.



Table 2. Physical properties of Molybdenum

Density	10.2 gm/cm <sup>3</sup>
Melting point	2895°C
Specific heat	0.27 J/gm °C
Thermal conductivity	1.3 J/sec cm°C
Thermal diffusivity	0.52 cm <sup>2</sup> /sec
Thermal expansion	4.9 x 10 <sup>-6</sup> /°C

The quality of the surface is the most important property of the substrate since it is here that the coating-substrate interaction occurs. It is desirable to have surfaces as smooth as possible (i.e., free of scratches and digs and with a low rms roughness). These defects are replicated by the films or propagated into the coatings. That is, each imperfection in the substrate is reproduced in each layer that is deposited on top of it which can affect both the optical and mechanical properties of the films. Surface smoothness is also important from the standpoint that it improves film adherence, decreases absorption, and minimizes light scatter.

Two polishing techniques have been developed in our optical facility which yield well figured optical surface on molybdenum mirrors. The first, based on conventional optical polishing methods (fresh feed polishing), employs a pitch lap, Al<sub>2</sub>O<sub>3</sub> abrasive and water as a polishing vehicle. We have achieved excellent results employing this technique. The second technique is continuous feed and is intermediate between the normal method of applying abrasive during the polishing process and the bowl feed technique.

The procedure that gave the best combination of smoothness and surface figure was the fresh feed technique using 0.3 µm alumina and water as the polishing vehicle on a pitch lap. The basic polishing procedure used to polish the molybdenum substrates is summarized as follows. In the grinding operation the substrates were ground flat on a cast iron tool with a slurry of #320 silicon carbide and water followed with an intermediate grind with #225 aluminum oxide and water and a final grind with #95 aluminum oxide and water. Typical grinding time required approximately 10 hours with a 10 pound overarm weight. The intermediate and final grind, typically, took one hour each using a 10 pound overarm weight. In all cases the polishing was achieved using the fresh feed technique to apply the polishing slurry to the lap. The polishing lap was of medium-hard pitch and the polishing slurry was Linde A (0.3 µm Al<sub>2</sub>O<sub>3</sub>) and water. Typical polishing time required approximately 40 hours with an overarm weight of 5 pounds with an upper spindle speed of 40 rpm and a lower spindle speed of 30 rpm. The substrates were polished until optimum surface finish was obtained as judged by Nomarski examination.

Clean substrate surfaces are a prerequisite for successful coatings. The slightest amount of contamination can cause an immense amount of harm in the coating deposition process as well as an increase in absorption and a decrease in surface adhesion. Traditionally, cleaning has been an art and there is a great diversity of opinion on what constitutes a "good" procedure for cleaning the substrates prior to coating them. A quantitative evaluation of the various cleaning methods is difficult because slight differences in procedures of apparatus can influence the results.

There are innumerable cleaning procedures which vary from one laboratory to another. Since cleaning procedures and philosophies vary widely, it is not expected that the views expressed herein will be met with universal agreement. However, it is safe to say in general, that cleaning procedures should be kept as simple as possible. With this in mind, the following procedure has been developed for cleaning metal mirror substrates.

1. Remove gross contaminants from the as-received substrates by soaking in acetone or xylene. Five to ten minutes of ultrasonic agitation will increase the rate of contaminant removal and insure a more thorough cleaning.

2. Wash with warm tap water and Liqui-nox detergent. Scrubbing the polished surface must be avoided, however, the cleaning can be assisted by ultrasonic agitation.
3. The substrate should be thoroughly rinsed in distilled water after detergent cleaning.
4. Final rinse with a reagent grade alcohol.
5. Final drying of the substrate is accomplished by inserting it in a vapor degreaser working with isopropyl alcohol. The substrate should remain in the vapor degreaser until it has reached the temperature of the vapor. The residual alcohol on the surface is immediately evaporated when the substrate is withdrawn and it is ready for loading into the coating chamber. It is a good practice to load the substrate into the chamber immediately after the cleaning process. If storage cannot be avoided, dust-free container with a lid or a desiccator should be utilized. Clean lint-free gloves should be worn during the placement of the substrate into the coating chamber.
6. Before closing the chamber, the surfaces must be checked for dust particles. If dust is evident, a small air syringe to blow off the particles can be used.

All coating depositions required for this program were carried out in a commercial vacuum system (Balzers - 710) which is equipped with an oil diffusion pump and a liquid nitrogen trap. This system is capable of routinely maintaining pressures of the order of  $10^{-6}$  Torr and is equipped with a substrate heater and a thin film monitor to control deposition rate and film thickness. Proper control of the thickness of each layer is afforded by observing the reflectance at the control wavelength of a suitably positioned monitor plate in the coating chamber and stopping deposition when the reflectance reaches a predetermined level. In all cases, care is taken to ensure the uniformity of the thickness of the layers. In order to obtain uniform layers, the window substrates are rotated above the evaporation source during the deposition process.

Deposition parameters utilized in this work are summarized for each material in Table 3. Coating materials employed in this work are listed and identified as to source and nominal purity in Table 4. No attempt was made to further purify any of these materials.

#### 4. Experimental results

Ten different dielectric enhanced mirror designs were evaluated for each of the three laser wavelengths. All of the mirror coatings were fabricated on 1.52 inch diameter molybdenum substrates. Each mirror substrate was polished as outlined in Section 3, and all of the coatings were deposited using the parameters listed in Table 3 of Section 3. Each mirror coating was evaluated for peak reflectance and absorption at the design wavelength. Environmental evaluation included tests according to Military Specifications MIL-M-13508C for durability, adhesion, and humidity resistance. The experimental results for the mirror coatings are presented in Tables 5-10.

## 5. Acknowledgments

The author acknowledges the assistance of M. Evangelista for the deposition of the mirror coatings and A. Klugman for the polishing of the mirror substrates. The absorption measurements were taken by F. Towns with the help of P. Kraatz and J. Rowe.

## 6. References

- [1] Young, L., "Multilayer Reflection Coatings on a Metal Mirror", Appl. Opt., Vol. 2, p. 445 (1964).
- [2] Parks, K. C., "The Extreme Values of Reflectivity and the Conditions for Zero Reflection from Thin Dielectric Films on Metals", Appl. Opt., Vol. 3, p. 877 (1964).



Table 1. Theoretical coating designs

		Theoretical reflectance		
		<u>2.8 <math>\mu\text{m}</math></u>	<u>3.8 <math>\mu\text{m}</math></u>	<u>5.3 <math>\mu\text{m}</math></u>
1.	$\text{Ag} + (\text{ThF}_4/\text{ZnS})^3$	0.9995	0.9995	0.9995
2.	$\text{Ag} + (\text{ThF}_4/\text{ZnSe})^3$	0.9997	0.9997	0.9997
3.	$\text{Ag} + (\text{SrF}_2/\text{ZnS})^2$	0.9993	0.9993	0.9993
4.	$\text{Ag} + (\text{SrF}_2/\text{ZnSe})^2$	0.9995	0.9995	0.9995
5.	$\text{Ag} + (\text{PbF}_2/\text{ZnS})^3$	0.9988	0.9989	0.9989
6.	$\text{Ag} + (\text{Al}_2\text{O}_3/\text{Si})^2$	0.9996	0.9997	0.9997
7.	$\text{Ag} + (\text{SiO}/\text{Si})^2$	0.9996	0.9996	0.9997
8.	$\text{Ag} + (\text{ThF}_4/\text{Si})^2$	0.9998	0.9998	0.9998
9.	$\text{Ag} + (\text{MgO}/\text{Si})^2$	0.9997	0.9997	0.9997
10.	$\text{Ag} + (\text{PbF}_2/\text{ZnSe})^3$	0.9993	0.9993	0.9993

\* Dielectric layers are quarterwave optical thickness at the design wavelength.

\* Ag layer is approximately 1000 Å thickness.

Table 3. Deposition parameters

Method of Evaporation	Material	Substrate Temperature	Deposition Pressure (Torr)	Deposition Rate
E-Beam	$\text{Al}_2\text{O}_3$	200°C	$5 \times 10^{-5}$	$\sim 600 \text{ \AA}/\text{Min}$
E-Beam	MgO	200°C	$6 \times 10^{-5}$	$\sim 1200 \text{ \AA}/\text{Min}$
E-Beam	$\text{PbF}_2$	200°C	$7 \times 10^{-6}$	$\sim 1800 \text{ \AA}/\text{Min}$
E-Beam	Si	200°C	$2 \times 10^{-6}$	$\sim 3000 \text{ \AA}/\text{Min}$
Ta Boat	SiO	200°C	$1 \times 10^{-6}$	$\sim 3000 \text{ \AA}/\text{Min}$
Mo Boat	$\text{SrF}_2$	200°C	$8 \times 10^{-6}$	$\sim 1800 \text{ \AA}/\text{Min}$
E-Beam	$\text{ThF}_4$	200°C	$4 \times 10^{-6}$	$\sim 1800 \text{ \AA}/\text{Min}$
Ta Boat	ZnS	150°C	$8 \times 10^{-6}$	$\sim 1800 \text{ \AA}/\text{Min}$
Ta Boat	ZnSe	150°C	$4 \times 10^{-6}$	$\sim 1800 \text{ \AA}/\text{Min}$
Ta Boat	Ag	25°C	$5 \times 10^{-6}$	$\sim 1000 \text{ \AA}/\text{Min}$

Table 4. Coating materials

Ag	Shot, 99.9999% Purity, American Drug and Chemical Company, Los Angeles, CA
Al <sub>2</sub> O <sub>3</sub>	Random Chunks of UV-Grade Sapphire, Union Carbide Corporation, San Diego, CA
MgO	Hot-Pressed Tablets, 99.95% Purity, Balzers High Vacuum Corp., Santa Ana, CA
PbF <sub>2</sub>	Fused Granules, 99.99% Purity, Balzers High Vacuum Corp., Santa Ana, CA
Si	Random Chunks, 99.999% Purity, Balzers High Vacuum Corp., Santa Ana, CA
SiO	Linde Select Grade, R. D. Mathis Company, Long Beach, CA
SrF <sub>2</sub>	Random Chunks, Optical Grade, EMCO Sales, Anaheim, CA
ThF <sub>4</sub>	Fused Granules, 99.9% Purity, Balzers, High Vacuum Corp., Santa Ana, CA
ZnS	Hot-Pressed Tablets, 99% Purity, Balzers High Vacuum Corp., Santa Ana, CA
ZnSe	Granules, 99.99% Purity, Balzers High Vacuum Corp., Santa Ana, CA



Table 5. Experimental results for 2.8  $\mu\text{m}$  mirrors

Sample no.	Coating design	Peak reflectance *	Absorption **	
			A	Std. dev.
170	Mo + Ag + (ThF <sub>4</sub> /ZnS) <sup>3</sup>	0.985	$1.58 \times 10^{-2}$	2.71 %
172	Mo + Ag + (ThF <sub>4</sub> /ZnSe) <sup>3</sup>	0.998	$2.27 \times 10^{-3}$	3.95 %
163	Mo + Ag + (Al <sub>2</sub> O <sub>3</sub> /Si) <sup>2</sup>	0.999	$1.05 \times 10^{-3}$	3.01 %
166	Mo + Ag + (SiO/Si) <sup>2</sup>	0.999	$1.04 \times 10^{-3}$	6.41 %
168	Mo + Ag + (PbF <sub>2</sub> /ZnS) <sup>3</sup>	0.980	$2.25 \times 10^{-2}$	6.60 %
173	Mo + Ag + (PbF <sub>2</sub> /ZnSe) <sup>3</sup>	0.996	$4.42 \times 10^{-3}$	11.15 %
179	Mo + Ag + (BaF <sub>2</sub> /ZnS) <sup>2</sup>	0.950	$5.15 \times 10^{-2}$	6.65 %
181	Mo + Ag + (ZnS/Si) <sup>3</sup>	0.973	$2.87 \times 10^{-2}$	7.97 %
183	Mo + Ag + (ZnSe/Si) <sup>3</sup>	0.997	$2.76 \times 10^{-3}$	2.84 %
176	Mo + Ag + (BaF <sub>2</sub> /ZnSe) <sup>2</sup>	0.986	$1.42 \times 10^{-2}$	2.43 %

---

\* Double-Reflection Absolute Reflectometer ( $\pm 0.001$ )

\*\* HF Laser Calorimeter

Table 6. Experimental results for 3.8  $\mu\text{m}$  mirrors

Sample no.	Coating design	Peak reflectance *	Absorption **	
			A	Std. dev.
107	Mo + Ag + $(\text{ThF}_4/\text{ZnS})^3$	0.998	$1.68 \times 10^{-3}$	3.93 %
100	Mo + Au $(\text{ThF}_4/\text{ZnS})^3$	0.996	$3.18 \times 10^{-3}$	3.67 %
105	Mo + Ag + $(\text{ThF}_4/\text{ZnSe})^3$	0.999	$6.31 \times 10^{-4}$	1.45 %
018	Mo + Au + $(\text{ThF}_4/\text{ZnSe})^3$	0.999	$6.47 \times 10^{-4}$	4.06 %
103	Mo + Ag + $(\text{AlO}_3/\text{Si})^2$	0.999	$9.99 \times 10^{-4}$	1.79 %
113	Mo + Ag + $(\text{SiO}/\text{Si})^2$	0.998	$9.64 \times 10^{-4}$	1.37 %
125	Mo + Ag + $(\text{ThF}_4/\text{Si})^2$	0.998	$1.34 \times 10^{-3}$	2.60 %
132	Mo + Ag + $(\text{SiO}/\text{ZnSe})^3$	0.993	$6.15 \times 10^{-3}$	6.14 %
133	Mo + Ag + $(\text{PbF}_2/\text{ZnS})^3$	0.998	$1.77 \times 10^{-3}$	7.04 %
111	Mo + Ag + $(\text{PbF}_2/\text{ZnSe})^3$	0.998	$1.02 \times 10^{-3}$	1.51 %
127	Mo + Ag + $(\text{BaF}_2/\text{ZnS})^2$	0.997	$2.22 \times 10^{-3}$	1.45 %
1.29	Mo + Ag + $(\text{BaF}_2/\text{ZnSe})^2$	Failed before test		

---

\* Double-Reflection absolute reflectometer ( $\pm 0.001$ )

\*\* DF laser calorimeter

Table 7. Experimental results for 5.3  $\mu\text{m}$  mirrors

Sample no.	Coating design	Peak reflectance *	Absorption	
			A	Std. dev.
001	Mo + Ag + (ThF <sub>4</sub> /ZnS) <sup>3</sup>	0.999	$9.11 \times 10^{-4}$	3.98 %
003	Mo + Ag + (ThF <sub>4</sub> /ZnSe) <sup>3</sup>	0.999	$6.40 \times 10^{-4}$	6.35 %
005	Mo + Ag + (SrF <sub>2</sub> /ZnS) <sup>3</sup>	0.995	$1.43 \times 10^{-3}$	3.04 %
007	Mo + Ag + (SrF <sub>2</sub> /ZnSe) <sup>2</sup>	0.992	$3.13 \times 10^{-3}$	3.29 %
010	Mo + Ag + (PbF <sub>2</sub> /ZnS) <sup>3</sup>	0.987	$4.11 \times 10^{-3}$	9.02 %
011	Mo + Ag + (Al <sub>2</sub> O <sub>3</sub> /Si) <sup>2</sup>	0.996	$1.72 \times 10^{-3}$	3.42 %
013	Mo + Ag + (SiO/Si) <sup>2</sup>	0.999	$1.81 \times 10^{-3}$	5.38 %
136	Mo + Ag + (ThF <sub>4</sub> /Si) <sup>2</sup>	0.997	$1.96 \times 10^{-3}$	5.15 %
019	Mo + Ag + (MgO/Si) <sup>2</sup>	Coating failed during deposition		
021	Mo + Ag + (PbF <sub>2</sub> /ZnSe) <sup>3</sup>	0.990	$1.14 \times 10^{-3}$	2.86 %

---

\* Double-Reflection absolute reflectometer ( $\pm 0.001$ )

\*\* CO laser calorimeter



Table 8. Environmental tests - 2.8  $\mu$ m mirror coatings

Coating design	Durability	Adherence	Humidity
Mo + Ag + (ThF <sub>4</sub> /ZnS) <sup>3</sup>	P	P	P
Mo + Ag + (ThF <sub>4</sub> /ZnSe) <sup>3</sup>	P	F	F
Mo + Ag + (Al <sub>2</sub> O <sub>3</sub> /Si) <sup>2</sup>	P	P	P
Mo + Ag + (SiO/Si) <sup>2</sup>	P	P	P
Mo + Ag + (PbF <sub>2</sub> /ZnS) <sup>3</sup>	P	P	P
Mo + Ag + (PbF <sub>2</sub> /ZnSe) <sup>3</sup>	P	P	P
Mo + Ag + (BaF <sub>2</sub> /ZnS) <sup>2</sup>	P	F	F
Mo + Ag + (ZnS/Si) <sup>3</sup>	P	P	F
Mo + Ag + (ZnSe/Si) <sup>3</sup>	P	P	P
Mo + Ag + (BaF <sub>2</sub> /ZnSe) <sup>3</sup>	P	P	P

---

Durability - 50 Rubs with cheesecloth 1 pound force.

Adherence - Scotch tape MLL - 13508 B.

Humidity - 95% at 120° F for 24 hours.

P - Passed

F - Failed

Table 9. Environmental tests - 3.8  $\mu$ m mirror coatings

Coating design	Adherence	Durability	Humidity
Mo + Ag + (ThF <sub>4</sub> /ZnS) <sup>3</sup>	P	P	F
Mo + Ag + (ThF <sub>4</sub> /ZnSe) <sup>3</sup>	P	P	P
Mo + Ag + (Al <sub>2</sub> O <sub>3</sub> /Si) <sup>2</sup>	P	P	F
Mo + Ag + (SiO/Si) <sup>2</sup>	P	P	F
Mo + Ag + (ThF <sub>4</sub> /Si) <sup>2</sup>	F	P	P
Mo + Ag + (SiO/ZnSe) <sup>3</sup>	F	F	F
Mo + Ag + (PbF <sub>2</sub> /ZnS) <sup>3</sup>	P	P	P
Mo + Ag + (PbF <sub>2</sub> /ZnSe) <sup>3</sup>	P	P	P
Mo + Ag + (BaF <sub>2</sub> /ZnS) <sup>2</sup>	P	P	F
Mo + Ag + (BaF <sub>2</sub> /ZnSe) <sup>2</sup>	*	*	*

---

Durability - 50 Rubs with cheesecloth 1 pound force.

Adherence - Scotch tape MIL - 13508 B.

Humidity - 95 % at 120° F for 24 hours.

P - Passed

F - Failed

\* - Failed before test

Table 10. Environmental tests - 5.3  $\mu$ m mirror coatings

Coating design	Adherence	Durability	Humidity
Mo + Ag + (ThF <sub>4</sub> /ZnS) <sup>3</sup>	P	P	P
Mo + Ag + (ThF <sub>4</sub> /ZnSe) <sup>3</sup>	P	P	F
Mo + Ag + (SrF <sub>2</sub> /ZnS) <sup>3</sup>	F	F	F
Mo + Ag + (SrF <sub>2</sub> /ZnSe) <sup>2</sup>	F	F	F
Mo + Ag + (PbF <sub>2</sub> /ZnS) <sup>3</sup>	P	P	P
Mo + Ag + (Al <sub>2</sub> O <sub>3</sub> /Si) <sup>2</sup>	P	P	P
Mo + Ag + (SiO/Si) <sup>2</sup>	P	P	P
Mo + Ag + (ThF <sub>4</sub> /Si) <sup>2</sup>	F	P	F
Mo + Ag + (MgO/Si) <sup>2</sup>	*	*	*
Mo + Ag + (PbF <sub>2</sub> /ZnSe) <sup>3</sup>	P	P	P

---

Durability - 50 Rubs with cheesecloth 1 pound force.

Adherence - Scotch tape MIL - 13508 B.

Humidity - 95% at 120° for 24 hours.

P - Passed

F - Failed

\* - Failed during coating deposition



# Temperature and Concentration Dependence of Laser Bulk Damage to Neodymium Glass\*

J. G. Sliney Jr. and L. G. DeShazer

Department of Electrical Engineering, University of Southern California  
Los Angeles, CA 90007

Bulk damage thresholds of Nd doped materials were measured using a Q-switched Nd:YAG laser with a single transverse and longitudinal mode having 7-ns pulsewidth. Damage was studied in a series of glasses of differing Nd concentrations: 0% Nd (ED4), 1% Nd (ED2.1), 2% Nd (ED2.2) and 3% Nd (ED2.3). At room temperature, the threshold decreased linearly by eleven percent as the Nd concentration increased from 0 to 3%. This variation could be explained by any one of three processes: single-photon absorption of Nd from the excited state  $4I_{11/2} \rightarrow 4F_{3/2}$ , two-photon absorption of Nd from the ground state  $4I_{9/2} \rightarrow 4G_{7/2}$  and absorption by impurities such as  $Sm^{3+}$  which typically accompany Nd doping. However, we believe the single-photon absorption to be applicable because when the glass temperature is lowered to 110°K, the damage thresholds for all concentrations are nearly equal. Bulk damage thresholds were also measured for a variety of Nd doped crystals. Nd:LiYF<sub>4</sub> had the highest damage threshold with Nd:La<sub>2</sub>Be<sub>2</sub>O<sub>5</sub> (BeL) at 55% of LiYF<sub>4</sub>'s threshold, YAG at 53% and GGG at 30%.

Key words: Damage temperature dependence; damage thresholds; GGG; La<sub>2</sub>Be<sub>2</sub>O<sub>5</sub>; LiYF<sub>4</sub>; Nd glass; YAG.

## 1. Introduction

The laser damage resistance was measured for seven Nd laser materials relevant to operation in a 10-ns Q-switch laser system. We used a Nd:YAG laser amplified by Nd:ED2 glass to damage crystal and glass cubes prepared from state-of-the-art material of Nd doped YAG, BeL, YVO<sub>4</sub>, GGG, YLF and the ED2 series of glasses.

Prior to this investigation, published reports on laser-induced bulk damage thresholds of Nd laser crystals have been surprisingly meager. The pertinent values obtained from the scientific literature are listed in Table 1. Since laser-induced damage thresholds depend on the laser pulse duration for the usual damage mechanisms, damage threshold values for different materials can be compared only at nearly equal pulsewidths of the damaging laser. The pulsewidth chosen for Table 1 is 10-ns which pertains to the usual Q-switched Nd laser.

Table 1. Comparison of Previously-published Laser Damage Thresholds under Q-switched 1.06  $\mu$ m Irradiation

Material	Damage Threshold Front Surface (GW/cm <sup>2</sup> )	Damage Threshold Bulk (GW/cm <sup>2</sup> )	Ref.
Nd:YAG	0.8 - 5.3	3.4 - 8.2	[1] <sup>1</sup>
	0.9	---	[2]
Nd:YA10 <sub>3</sub>	1.1 - 2.6	---	[1]
Nd:CaWO <sub>4</sub>	1.0 - 3.0	1.0 - 5.0	[1]
Nd:BeL	1.3	---	[2]

A majority of the reported values of damage threshold were determined in an investigation on 1.06  $\mu$ m laser damage to optical materials at the Hirst Research Centre, General Electric Co. Ltd. [1]. The GEC group used an electro-optically Q-switched Nd:YAG laser operating in the TEM<sub>00</sub> mode up to 10 mJ in 10 ns. The range of threshold values reported in reference [1] for the surface damage resulted from the surface damage thresholds being markedly affected by surface treatment and polish. The laser used in reference [2] was also a single-mode Nd:YAG laser, electro-optically Q-switched with a 10-ns pulse. Only damage thresholds for the surface were measured by R. Byer and R. Fleming [2].

\* Research supported by NASA contract number NAS 5-23698

1. Figures in brackets indicate the literature references at the end of the paper.

## 2. Experiment

### 2.1 Laser System Performance

A well-defined pulsed Nd:YAG oscillator was the source of the laser pulse which was amplified by a Nd:glass amplifier as shown in figure 1. The Nd:YAG oscillator was Q-switched passively by the Eastman Kodak dye 14015 (bis 4-dimethylaminodithiobenzil nickel). The use of a Mendenhall aperture of radius 0.5 mm and 27 cm cavity length gave a Fresnel number of 0.86 and a single transverse TEM<sub>00</sub> mode. The amplifier used a Brewster-faced Nd:glass rod (1.11 x 15.24 cm) pumped by four flashlamps in a quadruply elliptical gold-coated cavity. Two Glan-Kappa calcite polarizers were used as a variable attenuator. The pertinent operating parameters for the laser system are listed in Table 2. When the amplifier was double passed, the energy output was 6 mJ.

Table 2. Operational Characteristics of Oscillator and Single-passed Amplifier

Parameter	Oscillator (Nd:YAG)	Amplifier (Nd:glass)
Energy	2 mJ (±5%)	4 mJ (±5%)
Pulsewidth	4.6-7 ns	4.6-7 ns
Peak power (unfocussed)	0.44 MW	0.87 MW
Beam spot size	0.5 mm	1 mm
Peak energy density (unfocussed)	0.26 J/cm <sup>2</sup>	0.127 J/cm <sup>2</sup>
Peak power density (unfocussed)	106 MW/cm <sup>2</sup>	51.9 MW/cm <sup>2</sup>
Peak power density (focussed)	44 GW/cm <sup>2</sup>	347 GW/cm <sup>2</sup>

In order to measure accurately the damage thresholds, three beam quantities are needed: the total energy E, the temporal pulsewidth Δt and the focussed spot size w. When the laser pulse is well approximated by a Gaussian intensity distribution, both in space and time, as is our case, the peak power density P<sub>0</sub> is

$$P_0 = 0.598 E / (w^2 \Delta t)$$

The total energy E was measured using a ballistic thermopile (Hadron model 9) positioned after the beam-splitter and before the lens as shown by the dotted lines in figure 1. The pulsewidth Δt is defined as the full width a half maximum (FWHM) and was measured using fast photodiode with Tektronic 519 oscilloscope. Oscillograms of laser pulses from the oscillator and amplifier are given in figure 2 showing their smooth temporal profile and near Gaussian shape (within 15%).

The spatial intensity profile of the oscillator and the oscillator-amplifier system was measured using a television monitor system with a vidicon camera (Javelin NT-7310), a TV receiver (Panasonic TR910MN) and a dual-beam oscilloscope (Tektronic 555). The oscilloscope traces in figure 3 are for a single laser pulse monitored by the TV system at a distance of 135 cm from the oscillator (2.9 Rayleigh distances). As determined by the TV monitor, the spatial intensity profile was very close to the Gaussian distribution  $I_0 \exp(-2r^2/w^2)$ . The system was calibrated by a slit mask where the flat top is 1.1 mm; the slanted portion of the calibration trace is the penumbra of the shadow due to the extended size of the light source illuminating the slit.

A plano-convex lens (25.4 mm focal length) was used to concentrate the power sufficient to cause bulk damage without causing surface damage at the entrance surface. The determination of the focussed spot size is subject to the most inaccuracy arising from lens aberrations. For the diffraction limited case

$$w = \lambda f / \pi w_0$$

where f is the focal length of the lens and w<sub>0</sub> is the spot size incident to the lens. For w<sub>0</sub> = 1 mm, w = 8.6 μm. However, when NaCl was damaged at 1.06 μm using our system, the value of 40 μm was found to be the approximate value for the spot size by assuming the literature value of the damage threshold<sup>[3]</sup> of NaCl. The major cause of the difference between the diffraction-limited calculation (8.6 μm) and the spot size (40 μm) estimated by the NaCl damage is spherical aberration. Since our lens had a shape factor of +1.0, the lateral spherical aberration was calculated to increase the spot size from 8.6 μm to 9.3 μm, but the longitudinal spherical aberration was calculated to be 32 μm. The effect of the longitudinal aberration is to spread out the energy of the laser pulse along the optical path of the focussing lens, so that the peak intensity of the pulse is reduced to the intensity level one would measure if the lateral spot size had been 40 μm.

### 2.2 Low Temperature Damage Setup

For the damage measurements made at 110°K, the test samples were mounted on a copper cold finger and affixed with a highly conductive silicone heat sink compound (Dow Corning 340) as shown in figure 4. The other end of the cold finger was immersed in a bath of liquid nitrogen. The 19x19x24 cm chamber enclosing the test samples was flushed with dry nitrogen gas. The temperature was measured by a thermocouple (Omega MCJ-T copper-constantan) which was attached to the cold finger next to the sample. After the cooling down period, the samples remained at 110 ± 5°K for a period of one hour or more.



## 2.3 Damage Detection Techniques

In every case of bulk damage, the laser-induced scatter method and laser-induced change in transmittance was used to detect damage. For the case of induced scatter, evidence of damage was manifested by scattering of probe He-Ne laser light. The beam from the He-Ne laser was simultaneously used as an alignment laser for the entire laser system so it was collinear with the Nd laser pulse. The transmittance method sampled the pulse before and after the test sample so that comparison of these incident and transmitted pulses would show the occurrence of laser damage by a sharp reduction in power at the pulse peak for the transmitted pulse. Examples of the three pertinent cases above, below and at threshold for Nd:YAG are shown in figure 5. Notice that the transmittance method does not clearly mark the damage threshold since the transmitted pulse is imperceptibly distorted at threshold. Only a small portion of the transmitted beam is blocked by a small damage site near threshold. However the scattering method clearly delineated this threshold by the scatter from the damage site.

## 3. Neodymium Glass Damage

### 3.1 Concentration and Temperature Variations

Measurement of laser-induced bulk damage for ED2 laser glass showed that they were slightly concentration dependent. The samples were obtained from Lawrence Livermore Laboratories, and were of square cross section 1 cm on a side and of several different thicknesses ranging from 5 mm to 10 mm. The concentrations of Nd in the ED2 glass host include 1, 2 and 3% Nd which are designated ED2.1, ED2.2 and ED2.3, respectively. In addition, the threshold of undoped ED4 glass was measured as the 0% concentration limit. At room temperature the threshold decreased linearly by eleven percent as the neodymium concentration increased from 0 to 3%. This decrease is illustrated graphically in figure 6 in the lower set of data points which are normalized to the ED4 bulk damage threshold at room temperature. Also, the laser induced bulk damage thresholds of ED2 laser glass were measured for the several concentrations at 110°K. At this low temperature, the damage thresholds of ED2.1, ED2.2 and ED2.3 became equal at a value 20% above the room temperature threshold of ED4 glass as shown in figure 6 in the upper set of data points. The observed temperature variation of the thresholds as well as the variation of threshold with concentration could be explained by three processes: single-photon absorption by Nd from the excited state  $^4I_{11/2} \rightarrow ^4F_{3/2}$ , two-photon absorption by Nd from the ground state  $^4I_{9/2} \rightarrow ^4G_{7/2}$  and absorption by impurities such as  $Sm^{3+}$  which typically accompany  $Nd^{3+}$  doping.

### 3.2 Two Photon Process

In order for absorption to take place by a two-photon process, the  $Nd^{3+}$  would have to absorb two 1.06- $\mu m$  photons starting from the  $^4I_{9/2}$  ground state and terminate at the  $^4G_{7/2}$  excited level of  $Nd^{3+}$ . The previous work of Penzkofer and Kaiser [4] and Milam [5] does not rule out the possibility of the two photon process being operative. However, the temperature effect leads to the conclusion that the two photon process is not responsible, because if the two photon process were, then lowering the temperature from 300 to 110°K would not hinder two-photon absorption because it starts at the ground level. It should be pointed out that Penzkofer and Kaiser did light transmission experiments at 300°K and at 80°K and did not observe any change in the transmission of light at 1.06  $\mu m$ . Assuming a Boltzmann distribution, at 300°K nearly 85% of the Nd ions are in the three lowest levels of the  $^4I_{9/2}$  ground state, but at 80°K the percentage has increased to 99%. It would seem that a two-photon process in Nd glasses should proceed even better at lower temperatures, because of the greater abundance of Nd ions in the ground state compared with the number at room temperature.

### 3.3 Single Photon Process

In order for absorption to take place by a single photon process, the  $Nd^{3+}$  would have to absorb one 1.06  $\mu m$  photon starting at the  $^4I_{11/2}$  excited level and terminating on the  $^4F_{3/2}$  excited level. The population of the  $^4I_{11/2}$  level of Nd in ED2.3 laser glass was calculated at 300 and 110°K; the other spectroscopic parameters were taken from the work on Nd doped ED2 laser glass by DeShazer et al. [6]. For the low temperature it was assumed that in the case of Nd doped ED2 glass that the line centers and linewidths do not change with temperature, which is supported by the work of Mann and DeShazer [7]. The absorption lines for the  $^4I_{11/2} \rightarrow ^4F_{3/2}$  transitions of Nd in ED2.3 laser glass have been calculated theoretically and plotted for 300°K and is shown in figure 7. The smooth curve above the individual absorption lines in this figure represents the envelope of all the lines. For the Nd:YAG laser line (1.0642  $\mu m$ ) at 9397  $cm^{-1}$ , the absorption coefficient at 300°K is  $3.42 \times 10^{-4} cm^{-1}$  but at 110°K it is  $4.78 \times 10^{-11} cm^{-1}$  which is a reduction of seven orders of magnitude. This supports the belief that the single photon absorption process is responsible for initiating a portion of the laser-induced bulk damage in Nd doped ED2 laser glasses.

## 4. Bulk Damage of Neodymium Crystal Hosts

The laser-induced bulk damage thresholds of five Nd crystal hosts are listed in Table 3 along with Nd:ED2.3 glass and undoped NaCl. The 1-cm cube sample of the 1.2%  $Nd^{3+}$  in lanthanum beryllate,  $La_2Be_2O_5$  (symbolized BeL), was obtained from Allied Chemical Co. Since the polarization of laser emis-



sion from Nd:BeL is parallel to the Y-axis, the laser damage measurements were made with the incident laser pulse polarized parallel to the Y-axis. The bulk damage threshold for the Y-polarization was measured to be 4% higher than the threshold measured for Nd:YAG as shown in Table 3. Morphology of bulk damage looking down the path of the laser is shown in figure 8. The damage pattern is a six-pointed star in contrast to the damage pattern of Nd:YAG which is a four-pointed star as shown in figure 9. One interpretation of the pattern is that the fracture planes are due to the outward propagation of phonons as result of the damage process [8]. For the case of Nd:BeL with propagation in the X-direction the angles between the fracture planes measured 54°, 44° and 82°. These angles are undoubtedly a consequence of the monoclinic crystal structure of BeL (space group C2/c) but as yet we have not made a crystallographic directional analysis of these fractures.

Table 3. Bulk Laser Damage Thresholds under Q-switched 1.06  $\mu\text{m}$  Irradiation (4.65 ns pulsewidth FWHM)

Material	Power Density (GW/cm <sup>2</sup> )	Electric Field (MV/cm)	Power Density Relative to Nd:YAG
Nd:YLF	18.9	2.21	1.87
Nd:ED2.3 glass	16.9	2.2	1.67
Nd:BeL (E//y)	10.5	1.4	1.04
Nd:YAG	10.1	1.45	1.00
Nd:BeL (E//z)	9.33	1.33	0.92
NaCl (undoped)	7.64	1.39	0.76
Nd:YVO <sub>4</sub>	<6.43	<1.14	<0.64
Nd:GGG	5.56	1.08	0.55

The laser induced bulk damage threshold of Nd:YAG was measured to be third in rank after Nd:YLF and Nd:BeL as shown in Table 3. However, Nd:YAG was less than 5% lower than Nd:BeL so it is still very competitive. Examples of laser-induced bulk damage are shown in figure 9. The upper picture looks down the path of the laser and the lower figure is looking from the side. The sample of Nd:YAG was obtained from Crystal Products Department, Union Carbide Corporation.

The test sample of Nd:YLF was donated by Hughes Research Laboratories, Malibu, CA. This Nd doped host had the highest threshold, 18.9 GW/cm<sup>2</sup>, of any material tested including the Nd glasses. The Nd:YLF sample exhibited a large number of defects, mostly voids, which seemingly did not inhibit its damage resistance. In contrast to Nd:YLF, which manifested the highest bulk damage thresholds despite the obvious presence of scattering centers, Nd:YVO<sub>4</sub> placed a poor fourth among the Nd laser hosts. Apparently the iridium inclusions of the YVO<sub>4</sub> host were more favorable to the initiation of bulk damage than were the voids of the former. Allowing for the poor quality of the Nd:YVO<sub>4</sub> crystals available for these damage experiments, it is reasonable to expect that Nd:YVO<sub>4</sub> crystals of the same good optical quality as the YAG and BeL used in this research will show a higher bulk damage threshold than that which is presently being reported. Nd:GGG exhibited a low threshold, which came as a surprise because the crystal was of the highest optical quality. It showed no scattering centers before damage, when it was probe with a He-Ne laser. Neither did it show any strain patterns when viewed between crossed polarizers.

This research included laser-induced surface damage experiments on Nd doped crystals of YAG and BeL. The surface damage to Nd:BeL was conducted with the E-field of the laser parallel to the Y-axis of the crystal which is the same polarization used in the Nd:BeL laser. Both laser-quality surfaces of the BeL cube were damaged; one surface had been AR coated and the other had not been AR coated. The techniques previously used in reducing the bulk damage are not entirely applicable in the case of surface damage. The He-Ne laser scattering that was readily applicable in detecting bulk damage sites was found to be unreliable in the case of surface damage. Consequently the catastrophic break at the peak of the transmitted damage pulse has been adopted as the criterion for surface damage threshold. The values for the surface damage thresholds of the two Nd crystals were both nearly 90% of their respective bulk damage thresholds.

## 5. Acknowledgements

One of the authors (LGD) acknowledges conversations with Roger Wood, GEC, and Professor Robert Byer, Stanford, and both of the authors acknowledge the interest and support of Milton Birnbaum, Aerospace Corp. Experimental assistance on the low temperature measurements by J. A. Wunderlich was appreciated.

## 6. References

- [1] Wood, R.M., Taylor, R.T., and Rouse, R.L., Opt. and Laser Tech. 7, 105 (1975). This paper is summary of annual reports on "Laser damage investigation" by Gen. Electric Co. Ltd. to UK Ministry of Defence, CVD Research Project RP4-67 (1970-73).
- [2] Byer, R., and Fleming, R., Stanford Univ. as reported in Jenssen, H.P., et al., J. Appl. Phys. 47, 1496 (1976).  
Byer, R., private communication.

- [3] Wang, V., et al., Laser Induced Damage in Optical Materials: 1975, NBS Spec. Pub. No. 435, 118 (1975).  
 Leung, K.M., et al., Laser Induced Damage in Optical Materials: 1975, NBS Spec. Pub. No. 435, 107 (1975).
- [4] Penzkofer, A., and Kaiser, W., Appl. Phys. Lett. 21, 427 (1972).
- [5] Milam, D., in Laser Program Annual Report, Lawrence Livermore Laboratory, Livermore, CA, pp. 22-28 (1976).

- [6] DeShazer, L.G., et al., "Spectroscopy of Neodymium in Laser Glasses," USCEE Report 479, Univ. Southern Calif., Los Angeles, CA (1974).
- [7] Mann, M.M., and DeShazer, L.G., J. Appl. Phys. 41, 2951 (1970).
- [8] Draggo, V.G., et al., IEEE J. Quan. Elect. QE-8, 54 (1972).

# 7. Figures

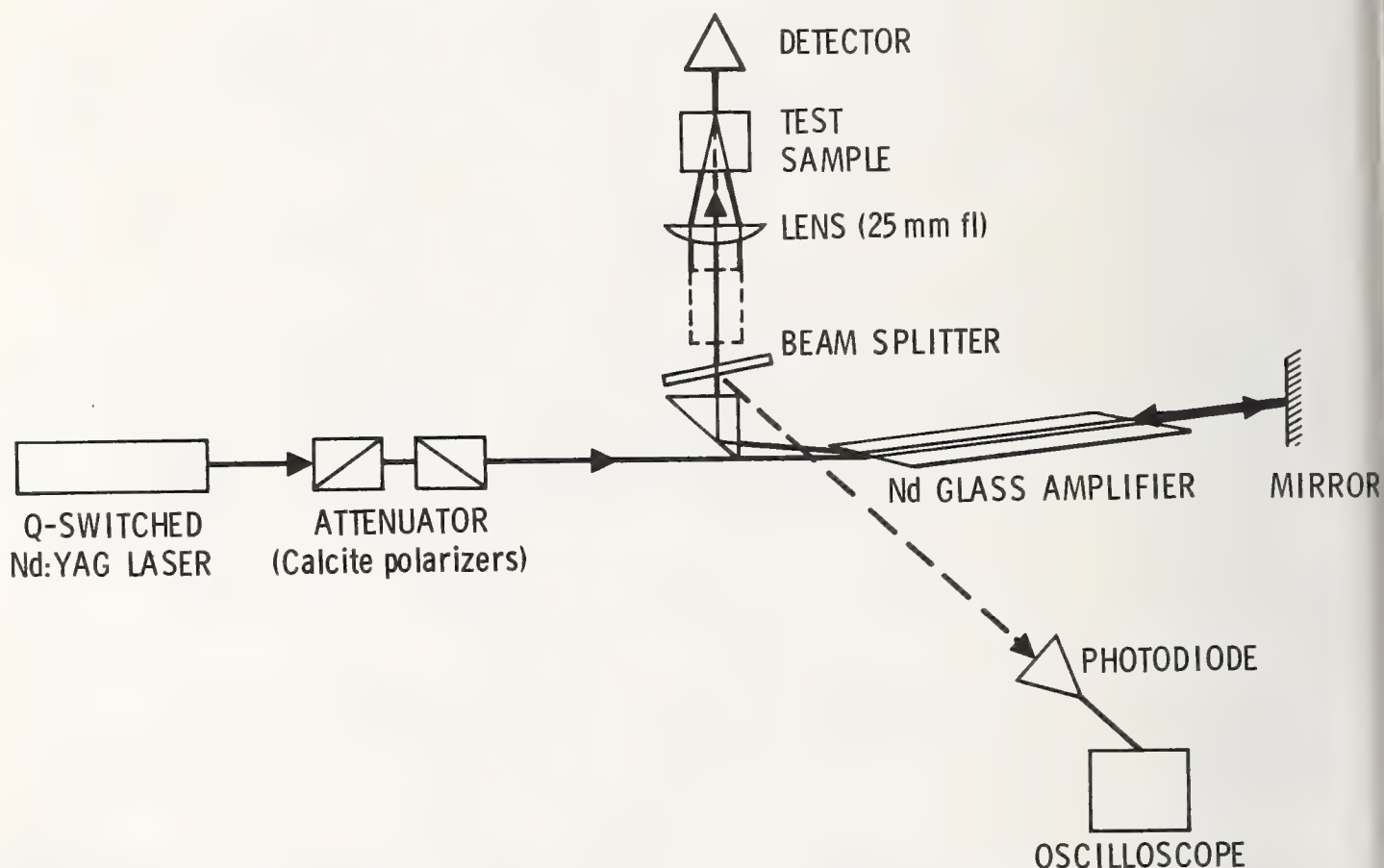
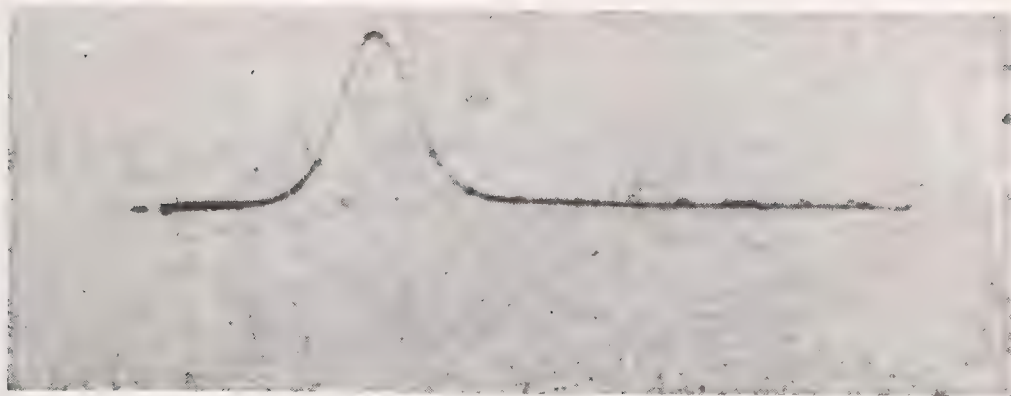
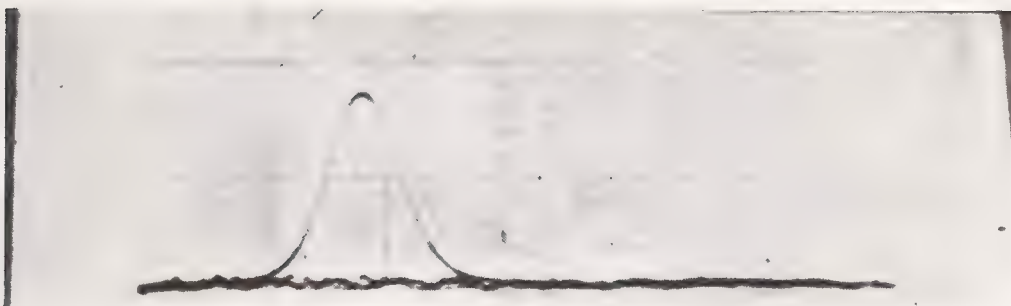


Figure 1. Schematic of Nd:YAG Oscillator, Nd:glass Amplifier, Detectors and Optics for Laser Damage Experiments



(a)

10 ns



(b)

10 ns

Figure 2. Temporal Waveforms of the Output from a) Nd:YAG Oscillator and b) Nd:glass Amplifier.



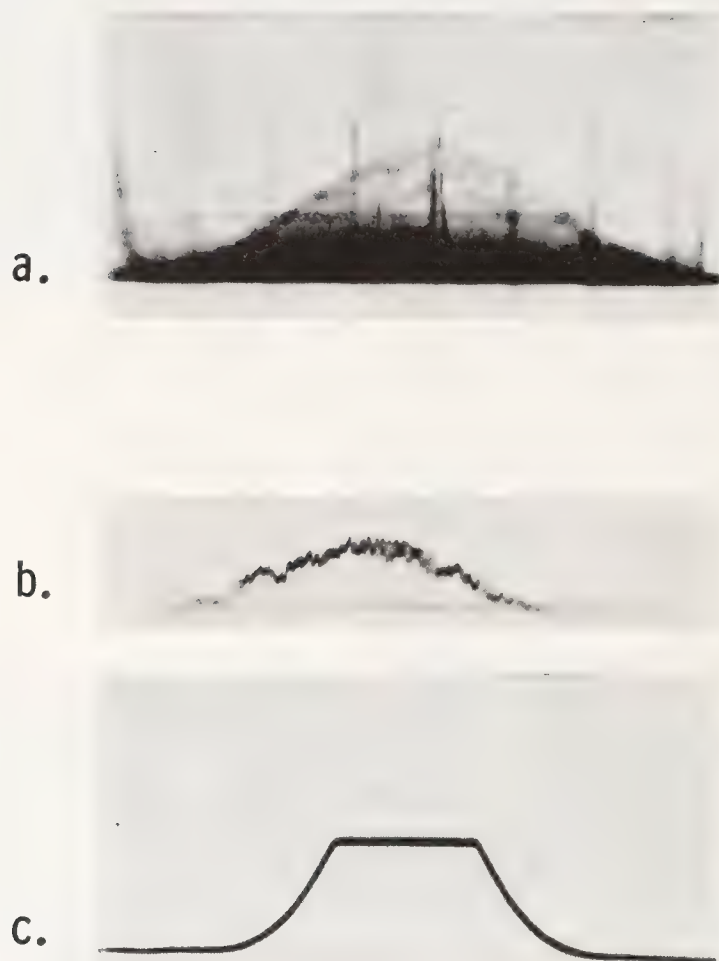


Figure 3. Transverse Intensity Profile of the Beam as Determined by TV Monitor System. a) Vertical spatial profile, b) Horizontal spatial profile at  $y = 0$ , and c) Radial distance calibration by slit.

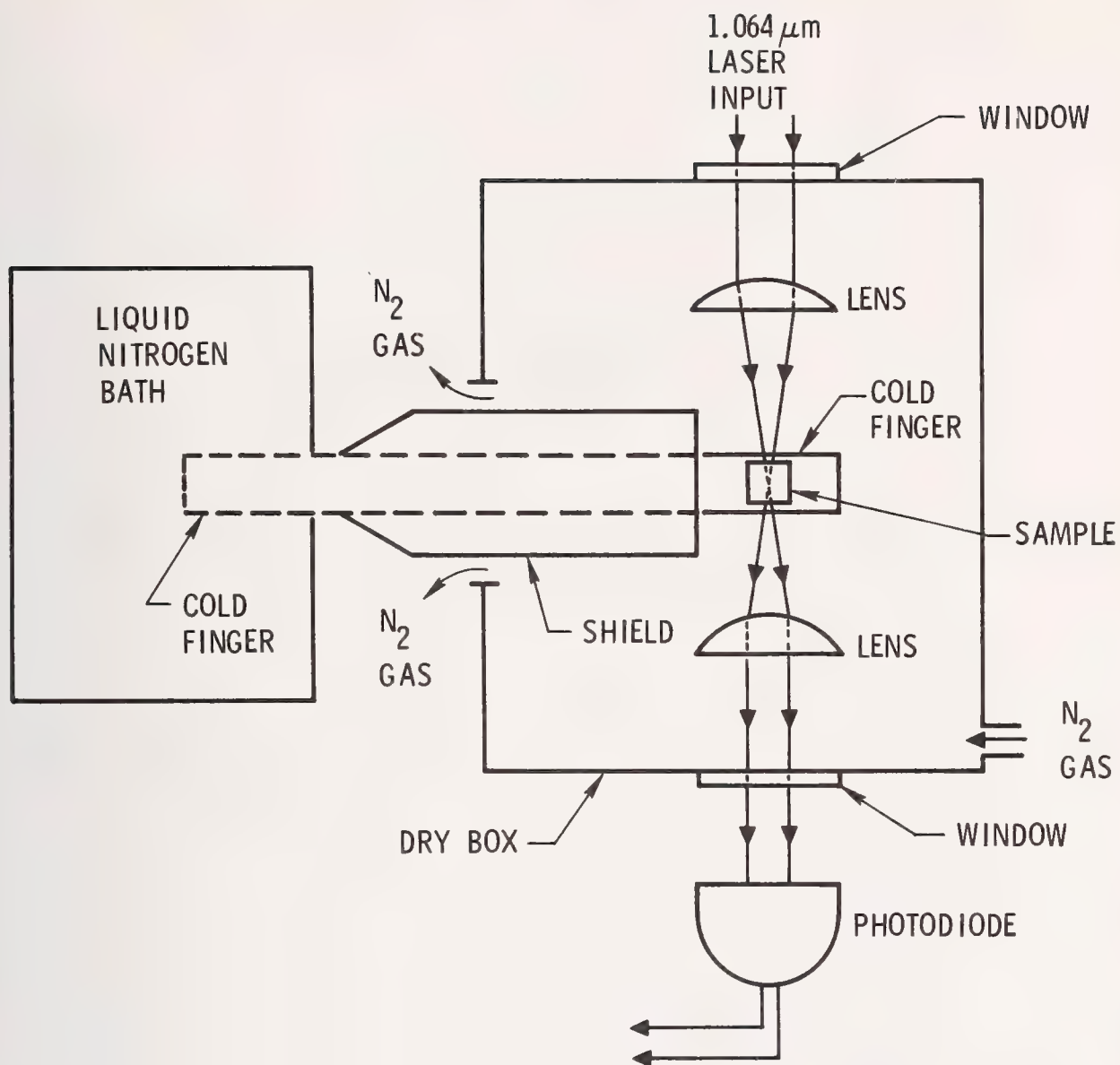


Figure 4. Schematic of Apparatus for Low Temperature Laser Damage Experiment.

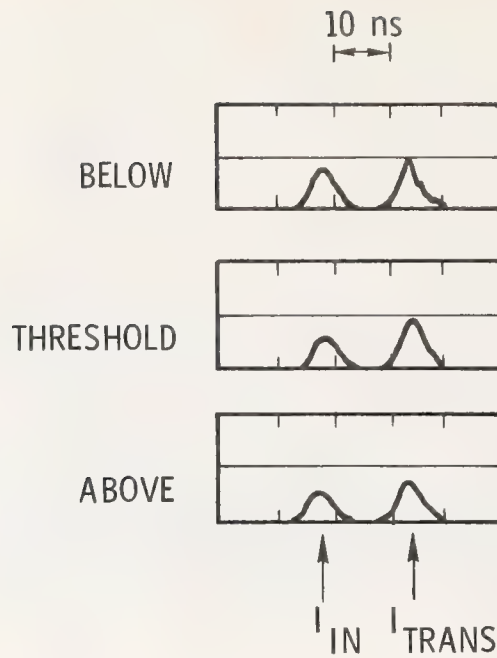


Figure 5. Distortion of Transmitted Laser Pulse by Bulk Laser Damage in Nd:YAG for the Cases Above, At and Below Damage Threshold.

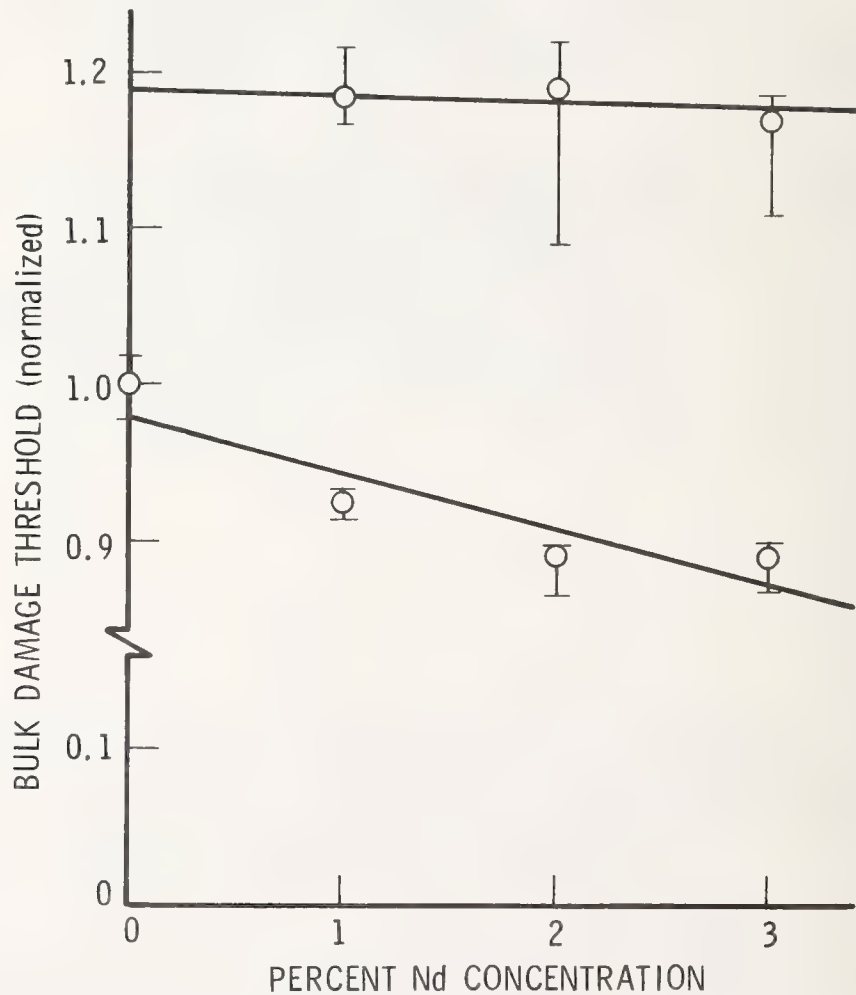


Figure 6. Laser Bulk Damage Threshold of ED2 Laser Glass as a Function of Concentration and Temperature. a) Upper data points at 110°K, and b) Lower data points at 300°K.



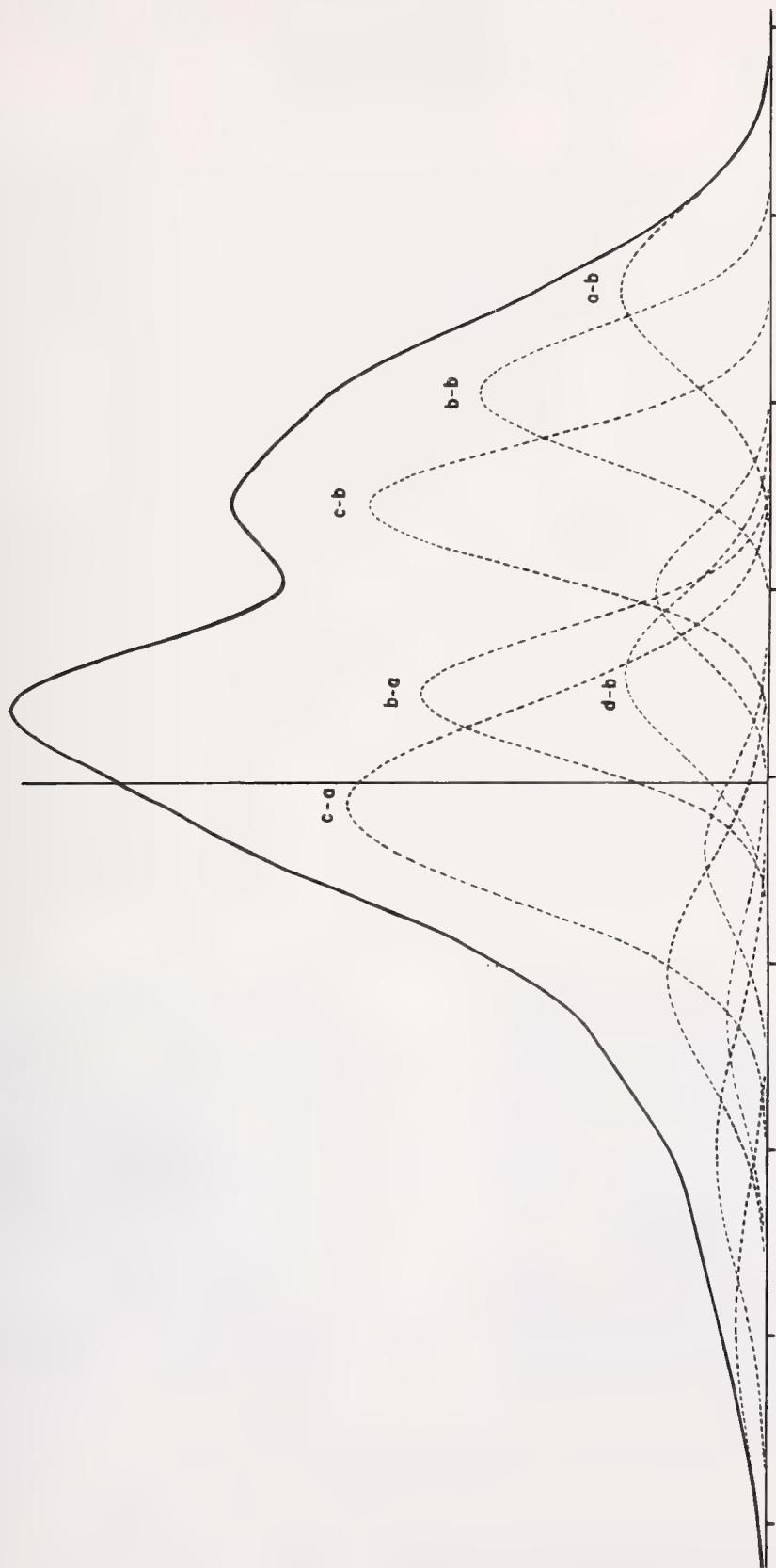


Figure 7. Plot of Theoretically Calculated Absorption Coefficient of ED2.3 Glass in the  $1.06 \mu\text{m}$  at  $300^\circ\text{K}$ .



Figure 8. Nd:BeL Bulk Damage Looking Along the Optical Path of Laser Beam.

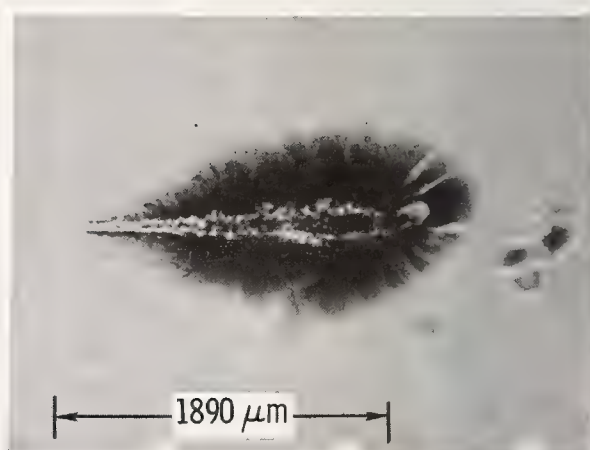
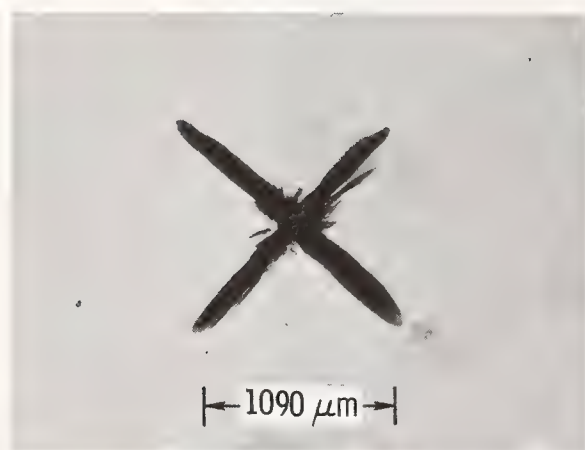


Figure 9. Nd:YAG Bulk Damage Morphology Looking a) Down the optical path and b) From the side.

## Direct Measurement of Inversion Density in Silicate and Phosphate Laser Glass

Joseph A. Abate, David C. Brown, Christopher Cromer, Stephen D. Jacobs, John Kelly, James Rinefierd  
Laboratory for Laser Energetics  
College of Engineering and Applied Science  
University of Rochester  
Rochester, New York 14623

The first direct measurements of the inversion density in ED-2, EV-2, LHG-7, and Q-88 laser glasses are reported. The data presented qualitatively confirm the validity of the Trenholme-Emmett Xe flashlamp Nd:glass pumping model and its extension to phosphate compositions. Comparison of the measured results with previously obtained analytical and computer code formulations of the variation of inversion density with optical thickness are discussed.

Key words: Inversion density; Parasitic oscillation; Phosphate laser glass; Silicate laser glass; Stored energy profiles.

### Introduction

The calculations presently used to predict the onset of parasitic oscillations in laser amplifiers depend both on the energy storage profile of the active medium as well as the geometry of the amplifier. An energy storage profile for silicate Nd laser glass has been reported by J. F. Holzrichter and T. R. Donich [1]. Their method consisted of measuring the total flashlamp light absorption, i.e., stored energy plus heat, by silicate laser glass samples of varying optical thickness. Corrections for fresnel reflections and bulk glass absorption were made to the total absorption measurements, however they could not directly measure or correct for the heat due to the quantum defect. Instead they relied on computer code corrections generated by GENEFF [2], a J. B. Trenholme and J. L. Emmett code. The GENEFF corrections were used to scale the absorption versus optical thickness data. The energy storage profile was obtained by taking the derivative of the corrected absorption versus optical thickness curve.

Certain questions arise because of this correction procedure. Some of the assumptions used in GENEFF have either not been explicitly tested or only tested in silicate laser glass. These include the assumption that the quantum efficiency is independent of the wavelength of the absorbed light. Also the model used in GENEFF did not take into account the time evolution of the flashlamp-glass system, but rather used instantaneous or averaged values of the key parameters to make its predictions. Finally the absorptivity per ion has been determined to be a constant in silicate laser glass independent of the wt-% doping up to 3% by W. Krupke [2] and no extension to other glass compositions have been made before now. It was our hope that by directly measuring the stored energy profiles, the measurement presented here will provide evidence to the validity of the GENEFF assumptions.

### Experiment

A block diagram of the apparatus used is shown in figure 1. The light from a 19mm bore water cooled Xe flashlamp was collimated by set of three pinholes and a fused quartz lens. The measured divergence of the resulting beam is smaller than .5 milliradians. The flashlamps were driven at 7Kv by a single mesh pulse forming network (PFN), and typically fired every 20 seconds. A beam splitter sent a portion of the collimated flashlamp light to a photo diode which was used by the boxcar integrator to monitor the shot to shot variation in the flashlamp output. The collimated flashlamp light struck a glass sample with an energy density typically of 40 mJ/cm<sup>2</sup>.

The glass samples used measured 1 x 1 x 16cm and were polished on all six sides. Three of the large faces were painted with black paint to minimize the effect of reflections inside the sample. A Wood's horn, filled with index matching fluid, was mounted as shown in figure 1, to minimize the back reflection of the flashlamp light. Four glass compositions were investigated; one silicate, ED-2 produced by Owens-Illinois and three phosphate EV-2, Q-88 and LHG-7 produced by Owens-Illinois, Kigre Inc. and Hoya Glass respectively. Two fiducial marks were placed on each sample to define the distance from the front edge of the sample.

A precise determination of the neodymium doping level was required in order for it to be possible to compare the stored energy profiles of the various glasses in terms of the optical thickness, i.e. weight percent doping x distance into the sample. Wet chemical and x-ray fluorescence analyses, performed by glass vendors and independent testing laboratories have been obtained to establish the doping in weight percent of Nd<sub>2</sub>O<sub>3</sub> for selected samples. Optical density measurements obtained with a Cary 14 spectrometer, permitted the calibration of additional samples from these primary standards (see figure 2). Glass density measurements (ASTM C69374) were subsequently used to generate plots of glass density versus Nd<sub>2</sub>O<sub>3</sub> weight percent doping, as shown in figure 3, so that Nd<sup>3+</sup> ion concentration may be calculated from the following:



$$\text{Nd}^{+3} \text{ (ions/cc)} = \frac{2(\text{wt. \% Nd}_2\text{O}_3) \rho N}{W}, \quad (1)$$

where  $N$  is Avagadros number ( $6.023 \times 10^{23}$ ),  $\rho$  is the glass density,  $W$  is the molecular weight of  $\text{Nd}_2\text{O}_3$  (336.48) and the factor of 2 accounts for the two  $\text{Nd}^{+3}$  ions per molecule of  $\text{Nd}_2\text{O}_3$ . Figure 3 confirms the independence of  $\text{Nd}^{+3}$  ion absorption versus doping level for ED-2, shown previously by W. Krupke [2]. Figure 3 also extends this result to the phosphates out to 4.8 wt%. This graphical data was used to determine the  $\text{Nd}_2\text{O}_3$  doping levels via optical density or physical density measurements in the four glass samples used in this experiment.

The  $1.06\mu$  fluorescence detector consisted of a microscope objective which imaged a 2mm aperture into the glass sample and as a result collected the fluorescence over an area .6mm in diameter. The fluorescence passed through a  $1.06\mu$  filter and then fell upon an InGaAsP photocathode photomultiplier tube (PMT). The InGaAsP photocathode was chosen for its high quantum efficiency, typically four to five percent at  $1.06\mu$ . The entire detector assembly was capable of being moved under stepping motor control over the entire length of the glass sample. The movement of the detector by the stepping motor was calibrated and always checked with the known position of the two fiducial marks on the glass sample.

The signal from the PMT was amplified and fed to the boxcar integrator which was gated on 300 $\mu$  seconds after the flashlamp was triggered and remained on for 500 $\mu$  seconds. The  $1.06\mu$  fluorescence from 10 to 20 flashlamp shots were averaged for a given position on the glass. A typical experimental run began with the  $1.06\mu$  detector positioned just in front of the edge of the glass sample, i.e., closest to the flashlamp. The detector was then moved along the glass sample measuring the fluorescence at greater and greater optical thickness. For a consistency check at the conclusion of a scan, the detector was moved back to one of its earlier positions and the fluorescence intensity was remeasured. In all cases the two measurements agreed well within the stated error.

### Results

In this experiment we have assumed that the stored energy density is strictly proportional to the  $1.06\mu$  fluorescence intensity as measured by the photomultiplier. This assumption is valid because the  $1.06\mu$  fluorescence is the spontaneous emission corresponding to the  ${}^4\text{F}_{3/2} \rightarrow {}^4\text{F}_1$  manifold transitions, and for all practical purposes, stimulated emission is absent in this experiment. This is expected to be the case due to the low energy flux incident on the samples, typically 40 mJ/cm<sup>2</sup>. As an experimental check on this assumption the observed fluorescence decay curves were checked and did not show any shortening or distortion as a function of the voltage applied to the PFN or of position in the glass sample. These effects would be expected if significant stimulated emission were present [3].

The measure stored energy density as a function of optical thickness is shown in figure 4 for all glasses measured. Each curve has been normalized to the fluorescence at the front edge of the glass sample. To obtain this normalization, it was necessary to extrapolate the fluorescence to zero optical thickness. We assumed an exponential fall off of the fluorescence to be a good approximation over the first few millimeters of the sample. This can be seen in figure 5 in the top portions of all curves. A least squares fit to an exponential was used to determine the value at zero optical thickness. The representative error bars shown in figures 4 and 5 are one standard deviation.

From figure 4 it can be seen that in general the phosphates (EV-2, Q-88, LHG-7) have a steeper fall off in their stored energy profiles than does the silicate ED-2, a result which has consequences for parasitic oscillations. The non-exponential character of the energy storage profiles of all four glasses is apparent from figure 5. The normalized shapes of the profiles of Q-88 and LHG-7 can be seen to be quite similar and differ most from that of ED-2.

This experiment also allowed the measurement of the relative pumping efficiency of the mentioned glasses as a function of optical thickness. Following the detailed scans of all the glasses, a measurement of the fluorescence intensity was made at a known optical thickness for each glass and used to scale the data shown in figure 4. In figure 6 the relative stored energy density profiles for the glasses measured are shown relative to that of ED-2. Q-88 was found to have a stored energy density as high as 1.45 times that of ED-2 in the surface region. Both EV-2 and LHG-7 were found to have a stored energy density 1.2 times that of ED-2 near the surface. In general these differences became less at optical thickness larger than 3 cm-wt%.

### Comparison to Theory

We will consider now previous predictions for the energy storage profile for ED-2. There have been several analytic expressions proposed to represent this profile. The purpose of these expressions is to aid the laser designer in the calculation of bulk and surface parasitic thresholds. In figure 7 we show our measured energy storage profile for ED-2 and the analytic expression used by Glaze et al. [4],

$$E_s = \frac{1}{(1 + .7708\gamma)^{1.25}} \cdot \quad (2)$$

Here  $E_s$  is the normalized stored energy and  $\gamma$  is the optical thickness (cm-wt%). There is substantial disagreement in that equation (2) predicts a less steep profile than observed.

Recently Brown et al. [5] have suggested an expression

$$E_s = \frac{1}{(1 + .7708\gamma)^{1.395}}, \quad (3)$$

for ED-2 in their study of parasitic oscillations in active mirror and disc amplifiers. Equation (2) is compared to the measured profile in figure 8. It can be seen that equation (3) is the better approximation of the energy storage profile for ED-2. In this same paper Brown et al. [5] discussed a computer code (FLASH-STORE) which models the instantaneous intensity output of a Xe flashlamp, from known operating conditions (FLASH) and then calculates the stored energy profile using measured absorption data (STORE). The FLASH-STORE code is equivalent to the Lawrnce Livermore code GENEFF. In figure 9 the measured values for the stored energy are shown along with the FLASH-STORE predictions. The agreement is seen to be quite good.

### Conclusion

The data presented here confirms the predictions of Brown et al. [5] that the phosphate laser glasses should display a more rapid fall off in stored energy density than in silicate laser glass. The higher stored energy density at the glass edge shown in figure 6 leads one to conclude that it will be important to take individual glass compositions into account in future studies of laser amplifier parasitics. The expression in equation 3 has been shown to give a very good approximation for the energy storage profile ED-2.

### Acknowledgment

The authors would like to thank Owens-Illinois, Kigre Inc., and Hoya Glass for providing us with the glass samples used. We also would like to thank Owen Lewis for his helpful discussions during the course of this work. The support of the Laboratory for Laser Energetics at the University of Rochester is gratefully acknowledged.

### References

- [1] J. F. Holzrichter and T. R. Donich, UID-16860, November (1973).
- [2] W. F. Krupke, LLL Report UCLR-714, December (1973).
- [3] J. B. Trenholme, NRL Memorandum Report, 2480, July (1974).
- [4] J. A. Glaze et al., Appl. Optics 13, 2808 (1974).
- [5] D. C. Brown et al., Appl. Optics, January (1978).

### Figures

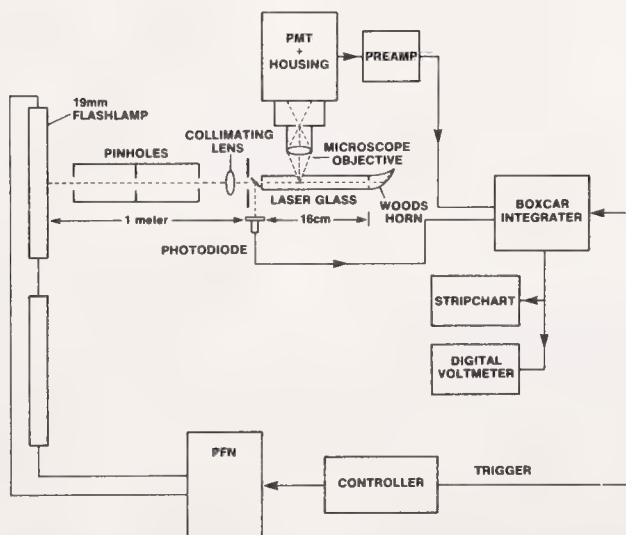


Figure 1 Block diagram of experimental apparatus.

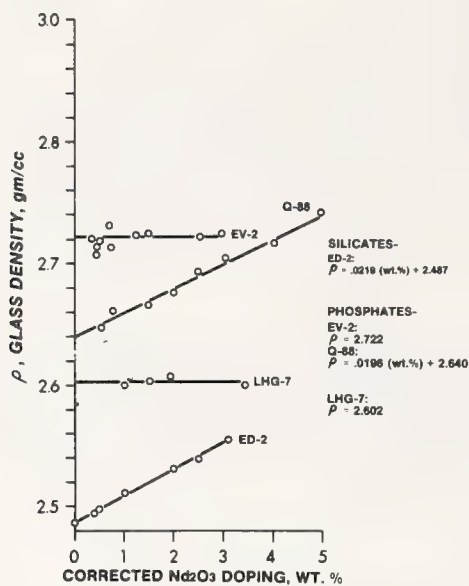


Fig. 2. Glass density for various  $\text{Nd}_2\text{O}_3$  doping levels.

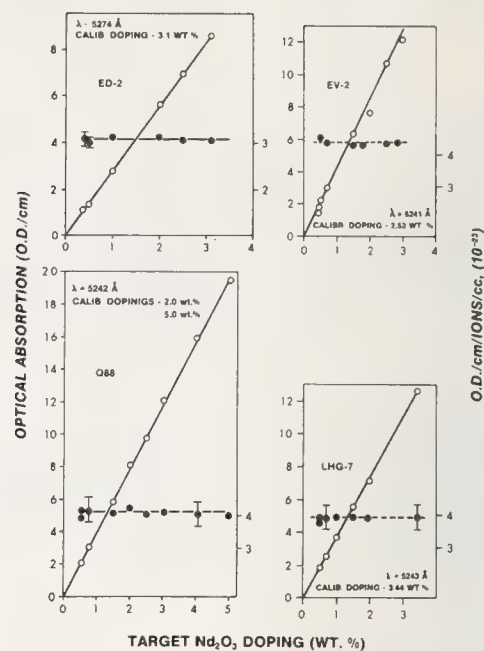


Fig. 3. Optical absorption per ion for corrected dopings.

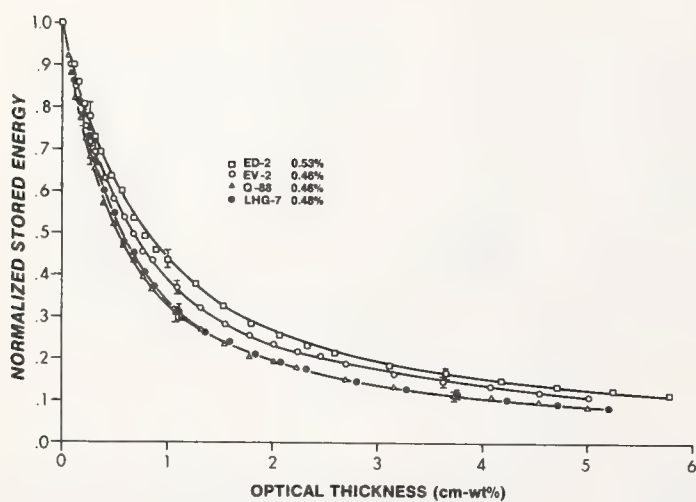


Fig. 4. Inversion profiles for silicate and phosphate laser glasses.

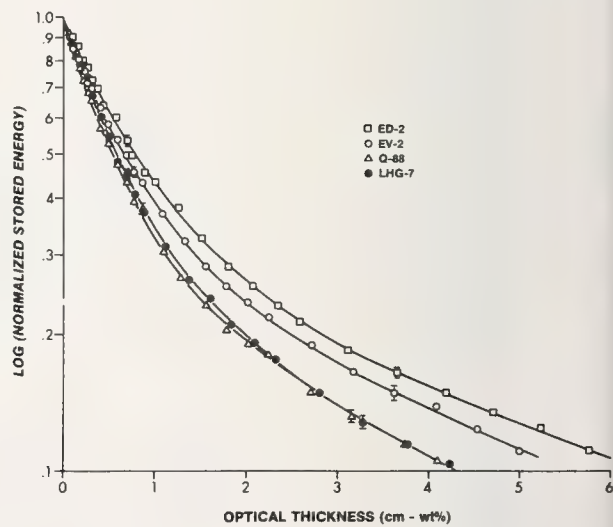


Fig. 5. Non-exponential nature of stored energy deposition.



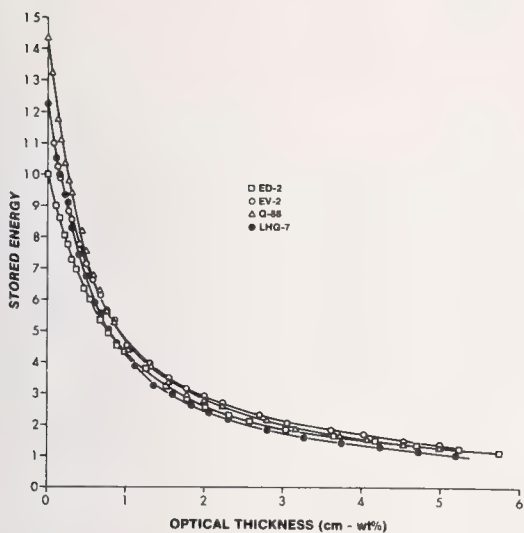


Fig. 6. Relative stored energy density profiles for silicate and phosphate laser glasses.

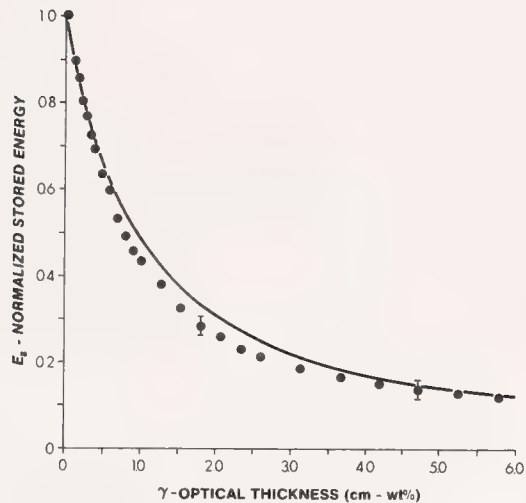


Fig. 7. Inversion data for ED-2 and the prediction of Glaze et al. [3].

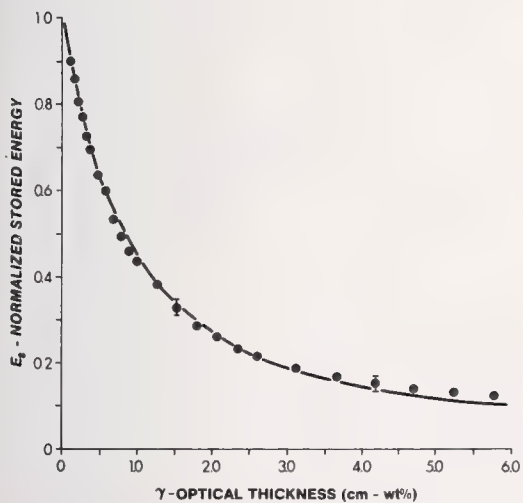


Fig. 8. Inversion data for ED-2 and the prediction of Brown et al. [4].

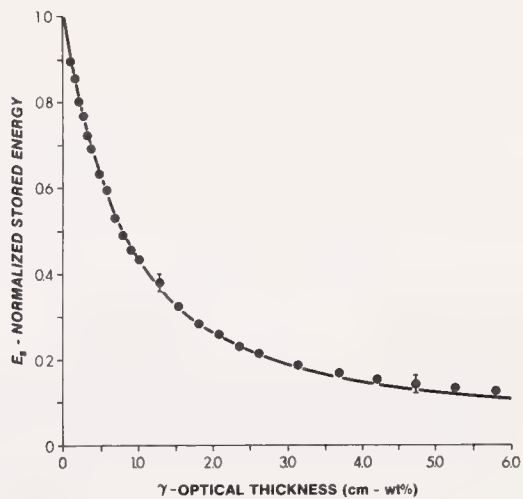


Fig. 9. Inversion data for ED-2 and the prediction of FLASH-STORE [4].

COMMENTS ON PAPER BY ABATE, BROWN, CROMER, JACOBS, KELLY, LEWIS, AND RINEFIERD

*Aside from points of clarification, there was no discussion of this paper.*

## FIGURES OF MERIT AND CORRELATIONS OF PHYSICAL AND OPTICAL PROPERTIES IN LASER GLASSES

David C. Brown, Stephen D. Jacobs, Joseph A. Abate, Owen Lewis, James Rinefied  
Laboratory for Laser Energetics  
University of Rochester  
Rochester, New York 14623

We propose a figure of merit which suggests that phosphate laser glasses have advantages over silicate compositions in that they exhibit a lower nonlinear refractive index, higher specific gain, lower thermo-optic distortion and less sensitivity to stress induced birefringence. Disadvantages of the phosphates are their tendency to heat to a greater extent under pumping, a reduced capacity to dissipate this heat, softness, high thermal expansion, low mechanical strength and reduced thermal shock resistance. From physical-optical properties correlations for a broader sampling of 120 commercially available optical glasses, we infer that one might expect lower index glasses to have poorer physical properties than higher index ones, based in part on the following:

1. there is a strong linear decrease in glass refractive index with glass density.
2. appropriate functional dependences exist which relate a low glass density to a small value of Young's modulus, and a small value of Young's modulus to a reduced hardness and rupture strength.

Preliminary data for the fluorophosphates and their high densities suggest that glasses from this composition group will be more durable than the phosphates. This trend is not well understood in light of the low refractive indices of these glasses.

Key words: Birefringence; fluorophosphate laser glass; glass density; nonlinear refractive index; phosphate laser glass; physical-optical properties; rupture strength; silicate laser glass; thermo-optic distortion; Young's modulus.

### 1. Introduction

Experiments in laser induced thermonuclear fusion are in progress at government, university, and private research facilities. Two of the largest glass laser systems in the United States are Shiva, a twenty beam silicate glass system in operation at Lawrence Livermore Laboratories, and OMEGA, a phosphate glass system under construction at the Laboratory for Laser Energetics of the University of Rochester. Fundamental to the design and performance of these and any future large, high peak power glass systems is the availability of glass compositions whose properties have been optimized for specific amplifier and staging designs.

The refractive index  $n_d$  and the nonlinear refractive index  $n_2$  of a glass set a limit on the peak power that can be propagated within the material without causing a permanent degradation in glass quality. This glass damage, caused by self-focussing of laser pulses, can be minimized for a given power level by maximizing the ratio  $n_d/n_2$  [1]<sup>1</sup>. A relationship among  $n_d$ , the Abbe value  $v_d$ , and  $n_2$  proposed by N. Boling, A. Glass, and A. Owyong [2] has provided the glass industry with a guideline for the development of compositions more suitably tailored for high power glass systems. The phosphates commercially available today are the result of an optimization program which succeeded in raising the value of  $n_d/n_2$  by roughly 50 percent when compared to established silicate compositions.

Glass development programs have suffered from a lack of attention to changes in other physical properties as compositions are optimized for low  $n_2$ . Of necessity, thermal expansion and chemical durability are adjusted so that promising compositions can be fabricated in useful sizes; but numerous other glass properties go unmonitored due to a lack of guidance as to what is important for high power glass systems. The purpose of this paper is to suggest a figure of merit for laser glasses which is sufficiently broad in scope to define desirable glass attributes for each kind of amplifier configuration required by these systems.

In what follows we present our figure of merit (FOM) formalism, justifying the importance of each component. We then turn to a comparison of silicate and phosphate laser glass compositions, using physical properties data generated at the Laboratory for Laser Energetics (LLE) and elsewhere for our FOM calculations. Advantages offered by the phosphates for medium repetition rate (2 shots/hr.) systems like OMEGA are identified, as are the potential drawbacks.

We try to understand the observed trends in the silicate to phosphate transition by plotting physical-optical properties correlations for a broad cross-section of commercially available optical glasses. We conclude with some predictions for the newly developed fluorophosphate laser glasses, based in part on the correlations presented in this paper.

1. Figures in brackets indicate the literature reference at the end of this paper.



## 2. Figure of Merit Formalism

### 2.1 Definition of Terms

The figure of merit we wish to consider may be expressed in its most general form as

$$\eta = \prod_{i=1}^n (J_i)^{W_i} \quad (1)$$

where the  $J_i$  are product factors and  $W_i$  is a weighting factor ( $0 \leq W_i \leq 1$ ). The individual  $J$  factors that we identify as being important are:

<u>J factor</u>	<u>Origin</u>
$J_1 = n/n_2$	(minimize B integral)
$J_2 = \alpha_0$	(maximize specific gain)
$J_3 = (E/H)_0$	(maximize inversion/heat)
$J_4 = \eta_0$	(maximize quantum efficiency)
$J_5 = k/\rho c$	(minimize thermal decay time constant)
$J_6 = \rho c$	(minimize induced temperature change)
$J_7 =  \Delta P_r + \Delta P_\theta ^{-1}$	(minimize average change in optical pathlength)
$J_8 =  \Delta P_r - \Delta P_\theta ^{-1}$	(minimize stress-induced birefringence)

The derivations of these  $J$  factors, discussed elsewhere [3], are based on laser rod geometries in the short pulse regime. An abbreviated description of the significance of each factor is given below:

$(n/n_2)J_1$ :	The ratio of glass refractive index, $n$ , to the nonlinear refractive index, $n_2$ , should be maximized to minimize the accumulation of B integral in a glass laser system.
$(\alpha_0)J_2$ :	It is of interest to maximize the gain per unit length in a laser glass. Small signal and saturated gain considerations lead to a desire to maximize the specific gain coefficient, $\alpha_0$ .
$(E/H)_0 J_3$ :	This is the ratio of flashlamp pump energy converted to useful inversion, $E$ , over that converted into unwanted heating of the laser glass, $H$ , evaluated for zero optical thickness.
$(\eta_0)J_4$ :	To maximize the obtained stored energy density, $E$ , one would like to maximize the quantum efficiency, $\eta_0$ (assumed wavelength independent).
$(k/\rho c)J_5$ :	For a rod geometry and an assumed parabolic temperature profile (center to edge) a characteristic thermal decay time constant can be derived which gives a measure of the time required for a glass to dissipate absorbed heat. To minimize this thermal decay time constant we want to maximize the glass thermal diffusivity, defined as thermal conductivity, $k$ , divided by the product of glass density, $\rho$ , and specific heat, $c$ .
$(\rho c)J_6$ :	One wants to minimize the induced temperature change in a volume of glass due to heat input, $H$ , by maximizing the product of glass density and specific heat.
$ \Delta P_r + \Delta P_\theta ^{-1} J_7$ :	In the absence of stress, the change in optical pathlength in a rod of length $L$ for a given uniform temperature increase $\Delta T$ of the glass is given as

$$\Delta P' = L [\beta + \alpha(n-1)] \Delta T \quad (2)$$

where  $\beta = dn/dT$ , or the temperature coefficient of refractive index; and  $\alpha$  = linear coefficient of thermal expansion. The quantity in brackets is referred to as the thermo-optic coefficient. In the presence of stress caused by an assumed radial temperature gradient, one can derive a comparable expression in terms of the change in optical pathlength per unit length per unit temperature for light polarized radially ( $\Delta P_r$ ) or tangentially ( $\Delta P_\theta$ ) within a glass rod. The average of the optical pathlength change for  $r$  and  $\theta$  polarizations with thermally induced strain present is then

$$\Delta P_r + \Delta P_\theta = 2\beta + \frac{\alpha Y}{(1-P)} (3B_\perp + B_\parallel) \quad (3)$$

where  $Y$  is Young's modulus,  $P$  is Poisson's ratio,  $B_\perp$  and  $B_\parallel$  are photoelastic constants for light polarized perpendicular or parallel to the direction of internal strain. A factor of 2 has been neglected in obtaining this equation. One wants to minimize the amount of thermo-optic distortion, and thus  $J_7$  is expressed as the inverse of equation 3.

$|\Delta P_r - \Delta P_\theta|^{-1} J_8$ :

The difference between  $\Delta P_r$  and  $\Delta P_\theta$  can be shown to give

$$\Delta P_r - \Delta P_\theta = \frac{\alpha Y}{(1-p)} (B_\perp - B_{||}) = \frac{\alpha Y B}{(1-p)} \quad (4)$$

where  $B$  is the stress-optic coefficient. Thus  $J_8$  is related to the susceptibility of the glass to stress induced birefringence, being large for glasses possessing a small stress-optic coefficient.

## 2.2 Special Cases

In most of what follows, no attempt is made to specify the weighting factors,  $W_i$ . There are, however, a number of limiting cases where certain  $W_i$  may be specified. If only optical effects are considered to be important, then by setting  $W_3=W_4=W_5=W_6=W_7=W_8=0$  and  $W_1=W_2=1$ , the FOM reduces to  $\alpha_o/n_2$ , the familiar pump limited case. Likewise, one can obtain the parasitic limited FOM,  $\eta=n/n_2$ , by setting  $W_2=0$ .

## 2.3 Physical Properties Data

The calculations presented in the following sections depend upon numerous measurements of basic physical properties. This data is readily available from vendors for their respective commercial products. It is, however, preferable to measure as many properties as possible at one facility under a given set of operating conditions, thereby improving the consistency of accumulated data and the relative comparisons which can be made. In house measurement techniques used to obtain physical properties of interest, as well as data supplied from other sources are identified as follows:

- $n$ : Refractive index measurements in the visible (dye laser), at  $.6328\mu\text{m}$  (HeNe), and at  $1.06\mu\text{m}$  (Yag) are obtained with a Hilger-Chance refractometer [4] constructed from BK-7 glass. The range of values measurable with this device is  $1.3$  to  $1.8 \pm .0005$ , as presently configured in our laboratory.
- $n_2$ : The nonlinear index of refraction is calculated from vendor supplied data for  $n_d(.588\mu\text{m})$  or  $n_D(.589\mu\text{m})$  and Abbe value  $v_d$  or  $v_D$ , using an empirical relationship [2].
- $\alpha_o$ : Specific gain is derived from stimulated emission cross section calculations and peak emission wavelength measurement data found in vendor product literature.
- $(E/H)_o$ : Calculations [5] from glass absorption band profiles predict that the ratio of stored energy to heating will be lower for phosphates versus silicates. Actual measurements of the stored energy profiles in several commercial glasses are presented elsewhere in these proceedings [6]. Until a technique for measuring heat density is developed as an alternative to calculations which convolve xenon flashlamp spectra with glass absorption spectra, this quantity will be set equal to 1 for all glasses.
- $\eta_o$ : No absolute or relative measurements of quantum efficiency have been performed for the commercial laser glasses of interest here (except ED-2[7]). Thus  $J_4$  is set equal to one in the following calculations.
- $k$ : Thermal conductivity at room temperature is measured with a commercial thermal comparator [8]. This device records the rate of cooling at the tip of a probe heated to  $20^\circ\text{C}$  above ambient, upon contact with the polished surface of interest. A thermocouple pair responds to the temperature change by generating a millivolt signal which can be converted to thermal conductivity by calibration with known reference standards. Precision achieved is  $\pm 2$  percent.
- $\rho$ : Glass density is measured according to ASTM (693 74)-Density of Glass by Buoyancy.
- $c$ : Glass specific heat near room temperature is taken from the product literature, except for EV-2 (measured in house) and Q88 (calculated from compositional and additive coefficient data [9]).
- $\alpha$ : The linear coefficient of thermal expansion is measured at the room temperature point on the expansion versus temperature curve obtained with a commercial quartz dilatometer [10]. The measurement sensitivity is  $\pm 5 \times 10^{-7}/^\circ\text{C}$ .
- $\beta$ : The change in refractive index with temperature is measured on  $60^\circ$  equilateral prisms of glass between  $10^\circ\text{C}$  and  $40^\circ\text{C}$  at  $\lambda=1.064\mu\text{m}$ . 2 cm high by 1.2 cm wide prismatic samples are oriented for minimum angle of deviation; upon heating the deflection of the laser spot is measured over a folded pathlength equivalent to 30 meters. The precision of this technique is  $\pm 6 \times 10^{-7}/^\circ\text{C}$ .
- $Y$ : Young's modulus is measured with an ultrasonic pulse technique [11]. 20mm by 4mm diameter cylindrical rods are cemented to the end of a magnetostrictive nickel alloy rod. A magnetostrictive transducer creates short duration extensional wave pulses within the rod. The velocities of these pulses within and along the rod axis together with glass density permit one to calculate  $Y$ . Measurement precision is  $\pm 130\text{kg/mm}^2$  for the present setup.



- p: The technique described above is also used to measure Shear modulus. The same precision limit applies, however, leading to a large experimental error in Poisson's ratio ( $p = \frac{Y}{2S} - 1$ ) when calculated from these measured quantities. An optical technique [12] capable of greater precision is being investigated, but for the present, vendor data for Poisson's ratio is used.
- B: Stress-Optic coefficient measurements are performed in a compression tester [13] at low values of applied stress ( $9 \text{ Kg/cm}^2$ ), using a Soleil compensation technique [3] at a wavelength of  $1.152\mu\text{m}$ . Data is good to  $\pm 0.1 \text{ nm/cm/kg/cm}^2$ .
- $B_{\perp}, B_{\parallel}$ : Fizeau interferometry is required to distinguish between the change in glass refractive index due to stress applied parallel versus perpendicular to the polarization direction of light propagating through a test sample. Experimental data taken at a wavelength of  $.6328\mu\text{m}$  is good to no better than 20 percent, due partly to a correction factor containing Young's modulus and Poisson's ratio, which is required to reduce the interferometric results.

Measured values for the above physical properties are given in table 1. The number of glasses considered is small, only because of the unavailability of photoelastic constant data at the present time for other commercial compositions (e.g. LG-700/710[17]).

Table 1. Glass physical properties data

Property	ED-2	EV-2	LHG-5	LHG-7	Q88	Data Source
Glass Source	[14]	[14]	[15]	[15]	[16]	
refractive index, $n_{1.06\mu\text{m}}$	1.5554	1.5037	1.5291	1.5050	1.5310	LLE
nonlinear index, $n_2$ ( $10^{-13}$ esu)	1.4	1.0	1.2	1.0	1.2	vendor
specific gain, $\alpha_0$ $\text{cm}^2/\text{J}$	.16	.25	.21	.20	.23	vendor
th. conductivity, $k$ $\text{cal/cm-sec-}^\circ\text{C}$ ( $10^{-3}$ )	3.00	1.08	1.75	1.46	1.76	LLE
density, $\rho$ $\text{gm/cc}$	2.51	2.72	2.64	2.60	2.67	LLE
specific heat, $c$ $\text{cal/gm-}^\circ\text{C}$	.22	.15	.17	.17	.21	vendor
th. expansion, $\alpha$ $10^{-7}/^\circ\text{C}$	77	141	77	91	90	LLE
temp. coeff. refractive index, $10^{-7}/^\circ\text{C}$	31	-100	-2	-26	-16	LLE
thermo-opt. coeff, $\beta + \alpha(n-1)$ , $10^{-7}/^\circ\text{C}$	74	-28	39	20	32	LLE
Young's modulus, $Y$ $\text{kg/mm}^2$	9620	4258	7258	6049	7123	LLE
Poisson's ratio, $p$	.24	.24	.19	.24	.24	vendor
stress-optic coeff., $B$ , $\text{nm/cm/kg/cm}^2$	1.92	1.45	2.17	2.14	2.07	LLE
photoelastic const., $B_{\perp}$ , $\text{nm/cm/kg/cm}^2$	2.6	4.9	3.5	3.5	2.9	LLE
photoelastic const., $B_{\parallel}$ , $\text{nm/cm/kg/cm}^2$	-0.2	3.1	2.2	2.0	0.0	LLE

#### 2.4 Figure of Merit Calculations

The individual J factor components for our FOM, calculated from the data in section 2.3, are given in table 2. Results are normalized relative to the silicate laser glass ED-2. The last column gives an average component FOM for the four phosphates evaluated. Based on a comparison of these averages with ED-2 we conclude the following:

- $J_1, J_2$ : Clearly the phosphates offer higher gain/lower  $n_2$  performance advantages over the silicates.
- $J_8$ : Thermally induced birefringence is less severe for phosphates versus silicates.
- $J_7$ : Thermally induced wavefront distortion is much smaller for phosphates than silicates. This may be attributed to the negative value of temperature coefficient of refractive index for these glasses. In fact,  $dn/dT$  is so negative for EV-2 that one can predict convergence for a beam propagating through an amplifier rod of this composition[18] versus predicted divergence for all other glasses in table 2.
- $J_5, J_6$ : The one disadvantage for phosphates is their tendency to heat to a higher level under flash-lamp pumping, and their diminished capacity to rapidly dissipate heat deposited in them. In practice, however, these somewhat unfavorable thermal properties do not prevent 90mm diameter by 370mm long laser rods from being fired in amplifier heads at a repetition rate of twice per hour in the Glass Development Laser system at LLE.



Table 2. Component figures of merit<sup>a</sup>

J Factor	Glass: Silicate	Phosphate <sup>b</sup>				Phosphate Average
	ED-2	EV-2	LHG-5	LHG-7	Q88	
$n/n_2, J_1$	1	1.4	1.2	1.4	1.2	1.3
$\alpha_0, J_2$	1	1.6	1.3	1.3	1.4	1.4
$(E/H)_0, J_3$	1	1	1	1	1	1
$n_0, J_4$	1	1	1	1	1	1
$k/\rho c, J_5$	1	0.5	0.7	0.6	0.6	0.6
$\rho c, J_6$	1	0.7	0.8	0.8	1.0	0.8
$(\Delta P_r + \Delta P_\theta)^{-1}, J_7^c$	1	-2.3	1.6	3.5	3.3	2.7
$ \Delta P_r - \Delta P_\theta ^{-1}, J_8$	1	1.6	1.3	1.2	1.1	1.3

<sup>a</sup>Data normalized to ED-2.

<sup>b</sup>Because of experimental uncertainties, this data is not to be construed as favoring one phosphate glass composition over another.

<sup>c</sup>Absolute value deleted to reveal special phosphate effects; see text.

### 3. Optical-Physical Properties Correlations

#### 3.1 Properties Neglected by the FOM Formalism

When phosphates were first introduced as commercial laser glass products, their biggest drawback was thought to be poor durability, characterized by softness and inadequate chemical resistance to water. In using large phosphate rods we have discovered that these are important concerns for some compositions, as are thermal shock resistance and the presence of certain types of impurities. The above are not included in the FOM formalism, but are discussed here.

Evidence of poor chemical resistance has been seen in phosphate glasses at LLE. Permanent grooves have upon occasion been etched into rod barrels by the interaction of cooling water, flashlamp radiation, and O-ring sealing materials. AR coated oscillator rod surfaces have shown evidence of moisture induced glass substrate erosion, resulting in wrinkling and cracking of the surface thin films. From chemical durability tests we have found that the chemical resistance of phosphates can be increased to a level comparable with that found in silicates by the addition of at least 50 percent by volume of ethylene glycol to any recirculating coolant cycle. The dramatic decrease in weight loss for selected phosphate glasses is shown in figure 1. Each test plotted therein was conducted on immersed glass blocks, agitated by magnetic stir bar for 18 hour time periods at 50°C.

One can calculate the thermal shock resistance of glass from its rupture strength,  $R$ , thermal diffusivity, Young's modulus, and thermal expansion [9],

$$T_{SR} = \frac{R}{Y\alpha} (k/\rho c)^{\frac{1}{2}} \quad (5)$$

A relative measure of rupture strength has been obtained at LLE using Shand's method [19], wherein flat circular specimens (1.2 mm thick by 25mm in diameter) are placed on a 19mm diameter steel ring. A load is applied from above with a concentric ring 6mm in diameter until fracture occurs. All samples in this test were fine annealed specimens whose surfaces had been uniformly damaged by application of a fine grind. The resulting rupture strength data and subsequent calculations from equation (5) show that increased care is a wise practice when subjecting phosphates to sudden temperature drops that might not harm silicate compositions (see table 3).

Table 3. Thermal shock resistance

	Glass Silicate	Phosphate			
	ED-2	EV-2	LHG-5	LHG-7	Q88
# samples tested	20	20	26	33	24
$R$ , rupture strength, $\text{kg/mm}^2$	29	14	20	17	14
$T_{SR}$ , thermal shock resistance from equation (5) (relative)	1.0	0.4	0.8	0.6	0.4

Two particularly troublesome impurities in phosphate glasses are platinum and water. There is a correlation (fig. 2) between increasing platinum level [20] and increasing glass optical absorption in the UV. The high solubility limit for platinum in phosphate glasses imparts to them an orange coloration (seen easily at low doping levels), a direct consequence of this shift of the glass UV edge toward the visible (fig. 3). A masking of the 3550 Å Nd pump band can occur, causing a reduction in energy storage and rod amplifier performance (fig. 4).

The presence of water in phosphate glass can cause a quenching of the neodymium fluorescence which is just as severe as concentration quenching. This effect is illustrated in figure 5. The sensitivity of glass to water quenching varies from one composition to another. A water content corresponding to an absorption level less than .09 optical density units per cm at  $\lambda=2.2\mu\text{m}$  will keep lifetime variations to less than about 15%.

### 3.2 Laser Glass Properties Correlations

One can ask whether there is any fundamental reason why glasses optimized for high gain and low  $n_2$  must therefore suffer from a degradation of other important physical properties. In an attempt to answer this question we look first at correlations among selected physical and optical properties for commercial laser glasses.

Plots of four physical properties versus calculated nonlinear refractive index are presented in figure 6. Two commercial silicate, six commercial phosphate, and two commercial fluorophosphate laser glass compositions are considered, as well as an experimental Nd doped beryllium fluoride glass [21]. Observed behavior can be summarized as follows:

1. There is a trend toward higher thermal expansion as nonlinear index decreases. All composition groups fit this pattern well.
2. There is a reduction in glass hardness with decreasing nonlinear refractive index. This is also seen for all glass groups.
3. For the silicates and phosphates, there is a correlation between reduced Young's modulus, thermal conductivity and decreasing  $n_2$ . These trends are reversed for the fluorophosphates.

The above observations clearly confirm the degradation in physical properties of phosphates versus silicates, as alluded to in the FOM discussions of section 2. Because nonlinear index depends upon linear index and glass dispersion in a complicated and somewhat empirical way and because of the exceptional behavior of the fluorophosphates, it would be useful to consider correlations of physical properties with more basic optical ones.

### 3.3 Optical Glass Properties Correlations

At the ERDA review of the LLE Beta Laser System held at the University of Rochester in January, 1977, Alexander Glass of LLL suggested that we evaluate the physical properties trends we observe for silicate and phosphate glasses by plotting them on a standard glass diagram. In this section we discuss the results of his suggestion.

Using the Schott Optical Glass Catalog we have selected approximately 120 optical glasses from the following composition groups: FK, PK, PSK, BK, K, ZK, BaK, BaLF, SK, KF, LLF, F, TiF, KzF, KzFS, LaSF. In addition we have included data from the experimental series E of fluorophosphates investigated at Owens Illinois [22]. The refractive index versus Abbe value for each glass has been plotted on a glass diagram. A given physical property may be examined by circumscribing the majority of glass data points possessing a common value of the property of interest. Deletion of the data points gives the type of plot shown in figures 7a, 7b, and 7c which can be analyzed as follows:

- 7a: The range of glasses examined is broad enough to illustrate the well known decrease in nonlinear index,  $n_2$ , with decreasing refractive index  $n_d$  and increasing Abbe value  $v_d$ .
- 7b: There is a strong correlation between Young's modulus and refractive index for Abbe values between 50 and 70, in agreement with the trend seen in figure 6. The lack of correlation for high index, large dispersion glasses (the region for  $Y=6000 \text{ kg/mm}^2$ ) can be linked via the high density of these glasses with the anomalous behavior of the fluorophosphates. This topic will be addressed in the next sections.
- 7c: Glass density appears to strongly follow refractive index, exhibiting little or no relationship to Abbe value.

Because of 1) its ease of measurement, 2) its fundamental nature, and 3) the strong correlation with the optical refractive index, glass density would seem to be one key to understanding the durability versus  $n_2$  problem.

### 3.4 The Importance of Glass Density

The strong dependence of glass refractive index on glass density is obvious from figure 8, wherein a least squares fit to data plotted from the glass groups used in section 3.3 gives

$$n_d = 0.1176 \rho + 1.206 \quad (6)$$

This equation is reminiscent of the Lorentz-Lorentz law under the approximation of small refractive index [23],

$$\frac{n^2-1}{(n^2+2)\rho} = \text{constant} \xrightarrow{\text{(small } n)} \frac{n-1}{\rho} = \text{constant} \quad (7)$$

A firm relationship between  $n$  and  $\rho$  enables us to qualitatively understand other trends in measured attributes.

Young's modulus is derived from a measurement of ultrasonic extensional wave velocity and glass density [11],

$$Y = (\rho V_E^2) \quad (8)$$

Thus as density drops with decreasing refractive index,  $Y$  should similarly show a decline. The correlations presented in previous sections support this relationship for glasses whose densities are less than about 3 gm/cc.

The link among refractive index (glass density), hardness, and rupture strength is accomplished by referring to the following relationship [24]

$$(\text{Hardness})H = (2/3)R \left[ 1 + \ln \frac{Y}{3(1+p)R} \right] \quad (9)$$

Glass hardness depends explicitly on rupture strength, and to a lesser degree on Young's modulus. But, because data presented here (tables 2 and 3) and elsewhere suggest that  $Y$  and  $R$  are directly proportional to each other (and frequently equated in the theoretical limit [25, 26]), we use equation (9) to support the trends observed in figure 6.

### 3.5 Exceptional Behavior of the Fluorophosphates

Preliminary results show the fluorophosphates to be more chemically durable than the phosphates [27, 28, 29]. The finding is consistent with the high density-good durability (hardness, stiffness, rupture strength) correlations presented in this paper, for the fluorophosphates have densities of around 3.6 gm/cc. But the further expectation that high density implies high index is invalid. Refractive indices for these glasses are around  $n_d = 1.45$ . One is led back to a consideration of the Lorentz-Lorentz law.

The quantity specified by equation (7) is constant only under special circumstances. If multiplied by the molecular weight ( $M$ ) of a substance, equation (7) becomes the molar refractivity  $[n]$  or [23]

$$[n] = \frac{(n^2 - 1)M}{(n^2 + 2)\rho} \quad (10)$$

In a glass  $[n]$  depends on the molecular refractivities of many constituents. This dependence can be simply additive for constituents whose electrons do not strongly interact; or it is quite possible that in for example dense fluorophosphates, electron-electron interactions are complicated by different chemical bonding, invalidating simple additivity laws and thereby breaking the  $n$ - $\rho$  correlation observed for other optical glasses.

### 4. Conclusions

We have presented the components to a figure of merit for evaluating neodymium doped glass compositions intended for use in large laser systems. Measurements of physical and optical properties and subsequent calculations point out the general attributes of phosphate versus silicate compositions. The former can offer higher gain, lower nonlinear refractive index, less sensitivity to stress induced birefringence, and lower thermo-optic distortion, while sacrificing thermal properties and durability. Correlations among physical and optical properties of other optical glasses show that some tradeoffs are a necessary consequence of low glass density. The high density fluorophosphates are an important exception to predicted trends for low  $n_2$  glasses, and illustrate the need for including a consideration of molecular polarizability in future studies.

### 5. Acknowledgements

The authors gratefully acknowledge Dr. Tetsuro Izumitani for technical discussions on this subject, and for his suggestion that we consider the link among refractive index, molar refractivity, and glass density.



# References

- [1] L<sup>3</sup> Annual Report (1974).
- [2] N. L. Boling, A. J. Glass, and A. Owyong, L<sup>3</sup> report UCRL 75628 (1974).
- [3] LLE Annual Report (1977).
- [4] J. V. Hughes, J. Sci. Inst. 18, 234 (1941).
- [5] D. C. Brown, S. D. Jacobs, N. Nee, to be published in Applied Optics, Jan. (1978).
- [6] J. A. Abate, D. C. Brown, C. Cromer, S. Jacobs, J. Kelly, J. Rinefierd, to be published in NBS Damage Symposium (1978).
- [7] L. G. DeShazer and L. G. Komai, J.O.S.A. 55, 940 (1965).
- [8] Lafayette Instrument Co., Lafayette, Indiana.
- [9] M. A. Matveev, G. M. Matveev, B. N. Frenkel, Calculation and Control of Electrical, Optical, and Thermal Properties of Glass, Ordentlich Press, Israel (1975).
- [10] Perkin Elmer Corporation, Norwalk, Conn.
- [11] L. C. Lynnworth, J. of Testing and Evaluation 1, 119 (1973).
- [12] W. T. Szymanowski, J. Appl. Phys. 15, 627 (1944).
- [13] Comten Industries, St. Petersburg, Fla.
- [14] Owens Illinois, Inc., Toledo, Oh.
- [15] Hoya Optics, USA Inc., Menlo Park, Ca.
- [16] Kigre Inc., Toledo, Oh.
- [17] Schott Optical Glass, Inc., Duryea, Pa.
- [18] text prepared for ERDA Review, Jan. 6-7 (1977).
- [19] E. B. Shand, Glass Engineering Handbook, ch. 6, 132 (1958).
- [20] platinum levels provided by P. Vergano, Owens-Illinois, and T. Izumitani, Hoya Optics.
- [21] type 816KY, provided by W. Dumbaugh and D. Morgan, Corning Glass Works, Corning, N. Y.
- [22] P. J. Vergano and C. F. Rapp, quarterly progress report to ERDA, EY-76-C-02-4080, Jan. (1977).
- [23] R. S. Longhurst, Geometrical and Physical Optics, 459 (1967).
- [24] T. Izumitani and I. Suzuki, Glass Technology 14, 35 (1973).
- [25] W. C. LaCourse, Introduction to Glass Science, 454 (1972).
- [26] R. J. Charles, Progress in Ceramic Science, 1, 4 (1961).
- [27] Owens-Illinois EVF-1, product literature June (1977).
- [28] Hoya LHG-10/11, product literature June (1977).
- [29] Schott LG-800, product literature Sept. (1977).

7. Figures

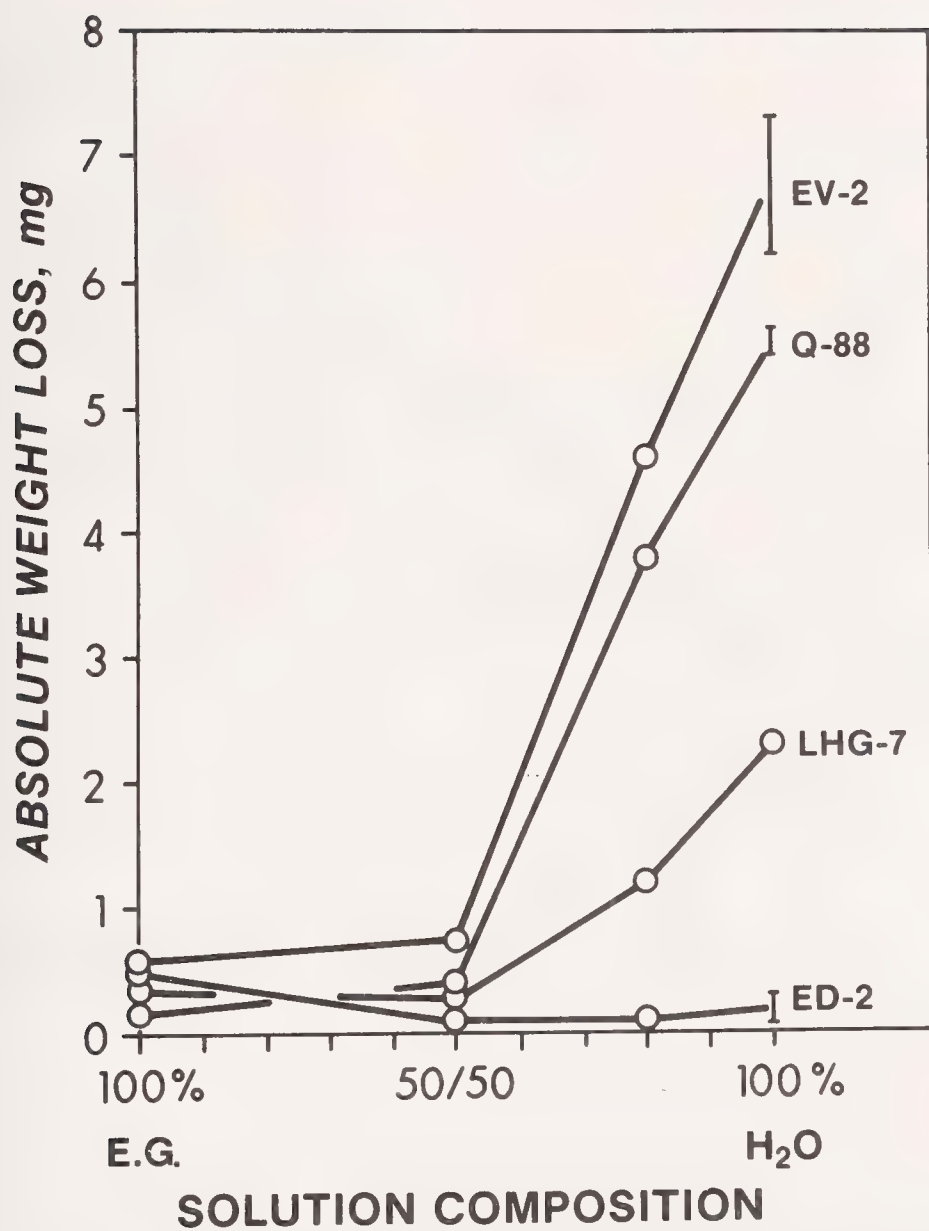


Figure 1 Laser glass durability in ethylene glycol-water solutions.

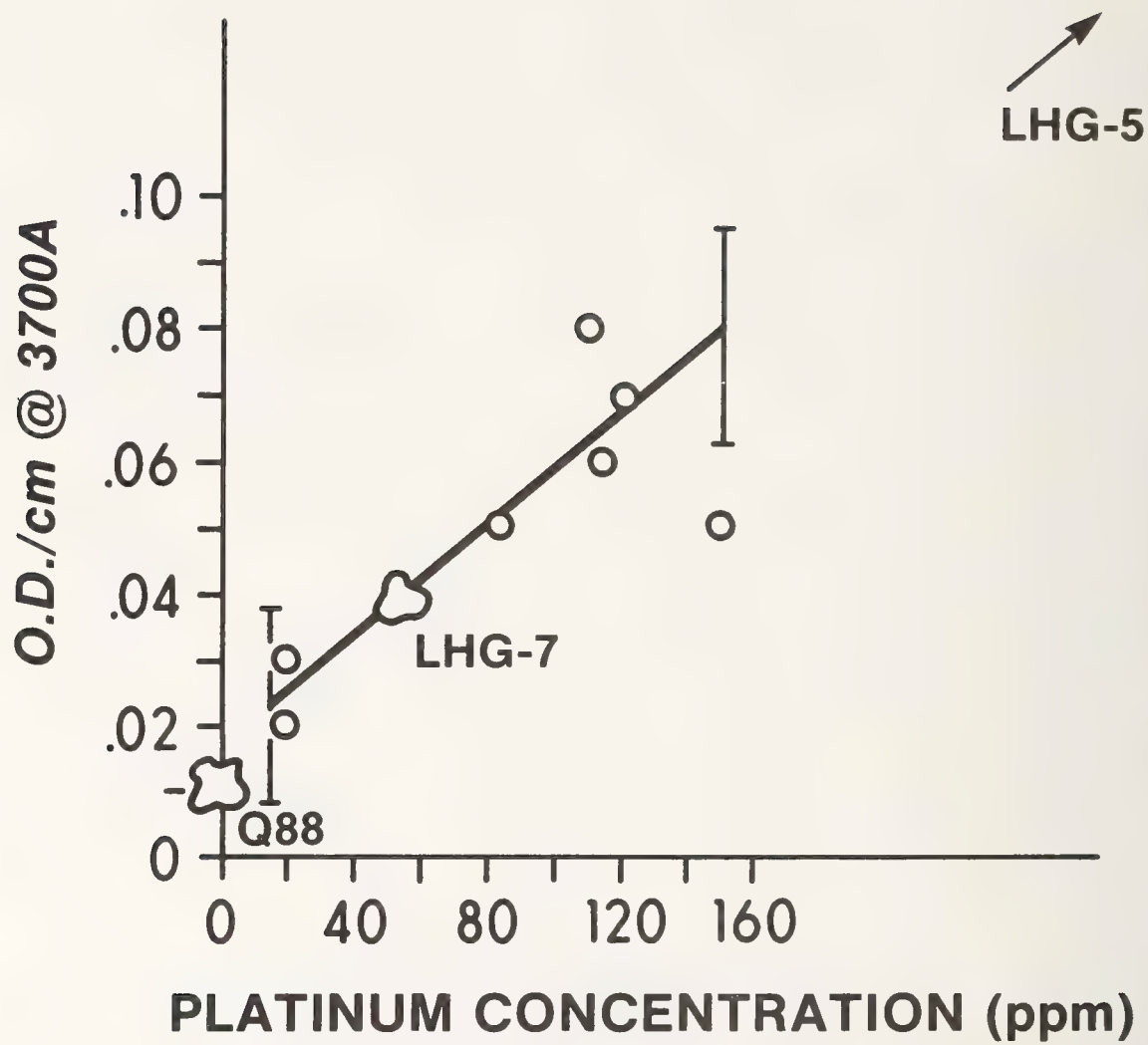


Figure 2 Platinum concentration versus absorption for EV-2 and other glasses.



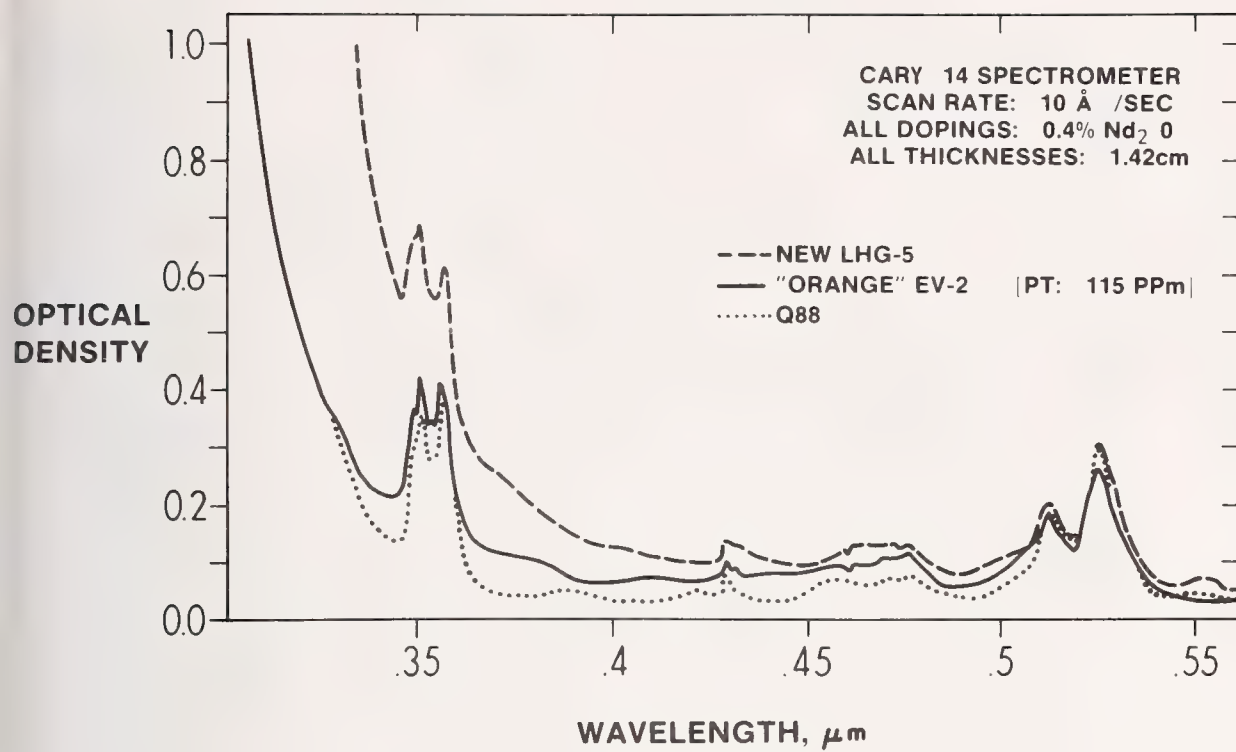


Figure 3 UV-VIS absorption in laser glasses from dissolved platinum.

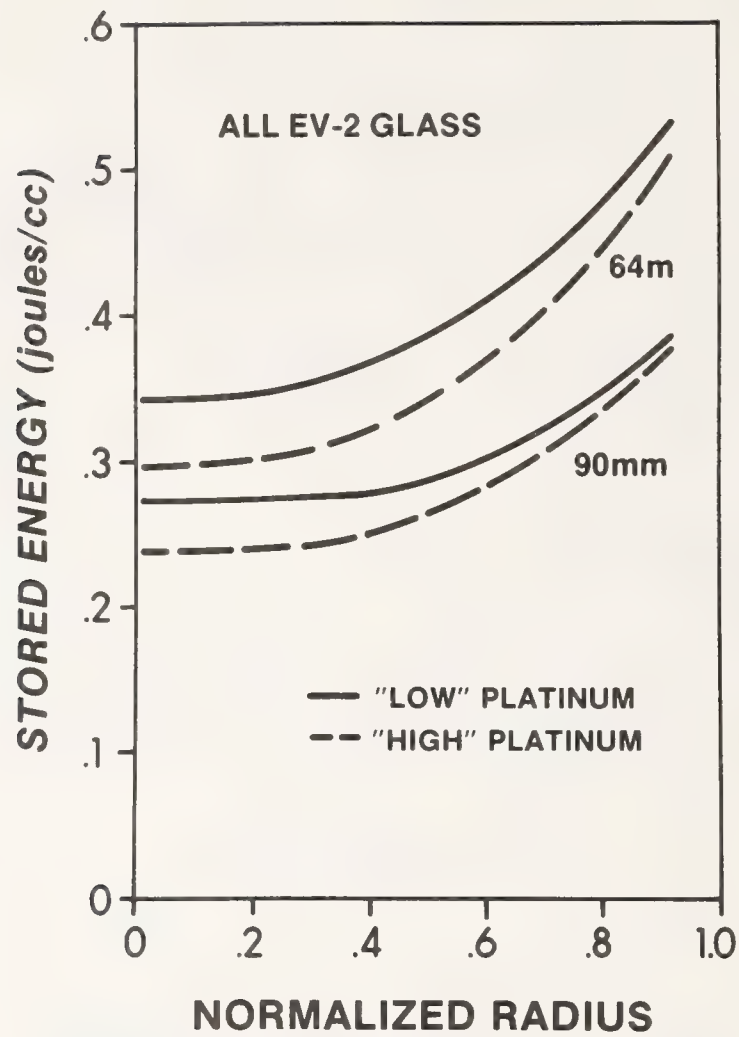


Figure 4 Gain profiles for high platinum and low platinum laser rods.

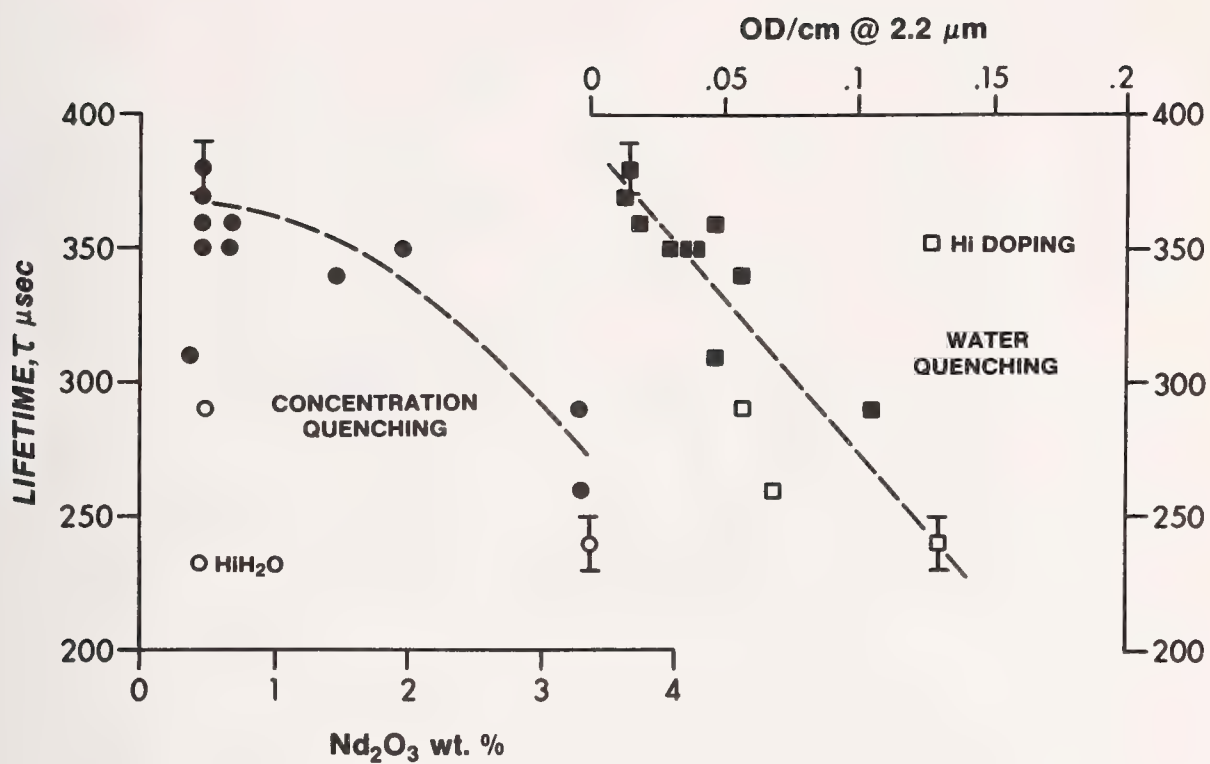


Figure 5 Fluorescent lifetime effects in LHG-5/7 glasses.



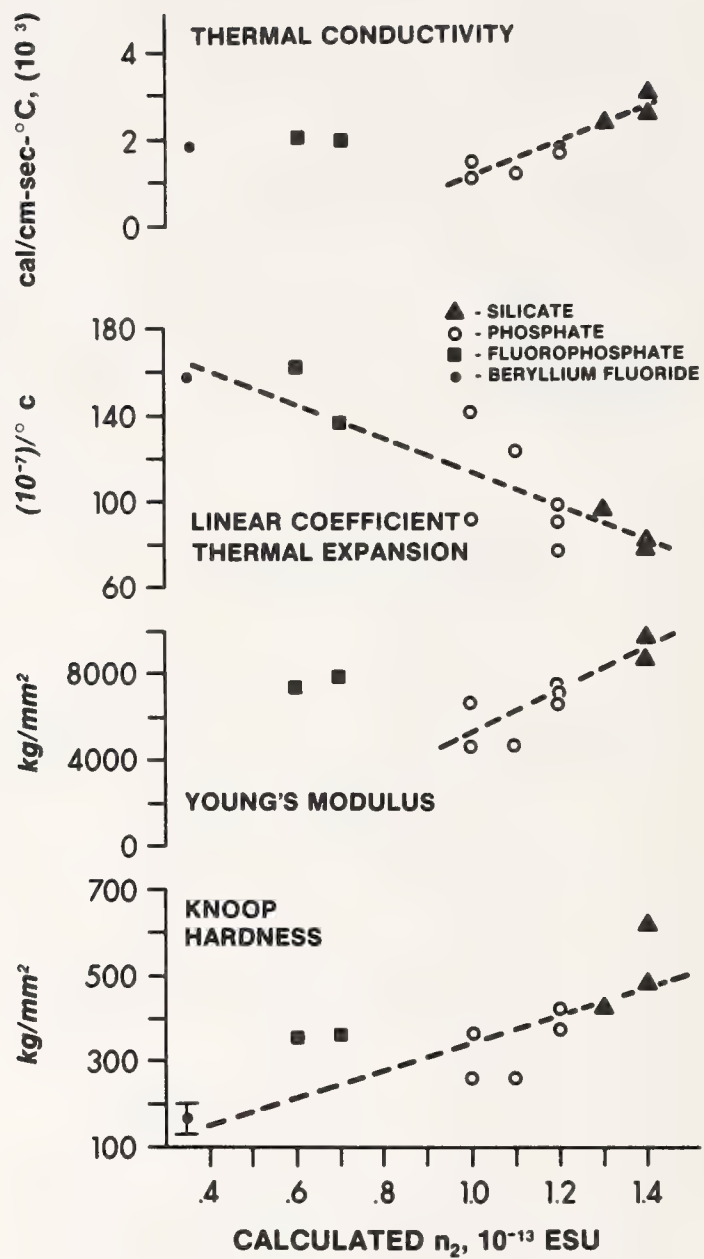


Figure 6 Laser glass physical properties correlated with  $n_2$ .

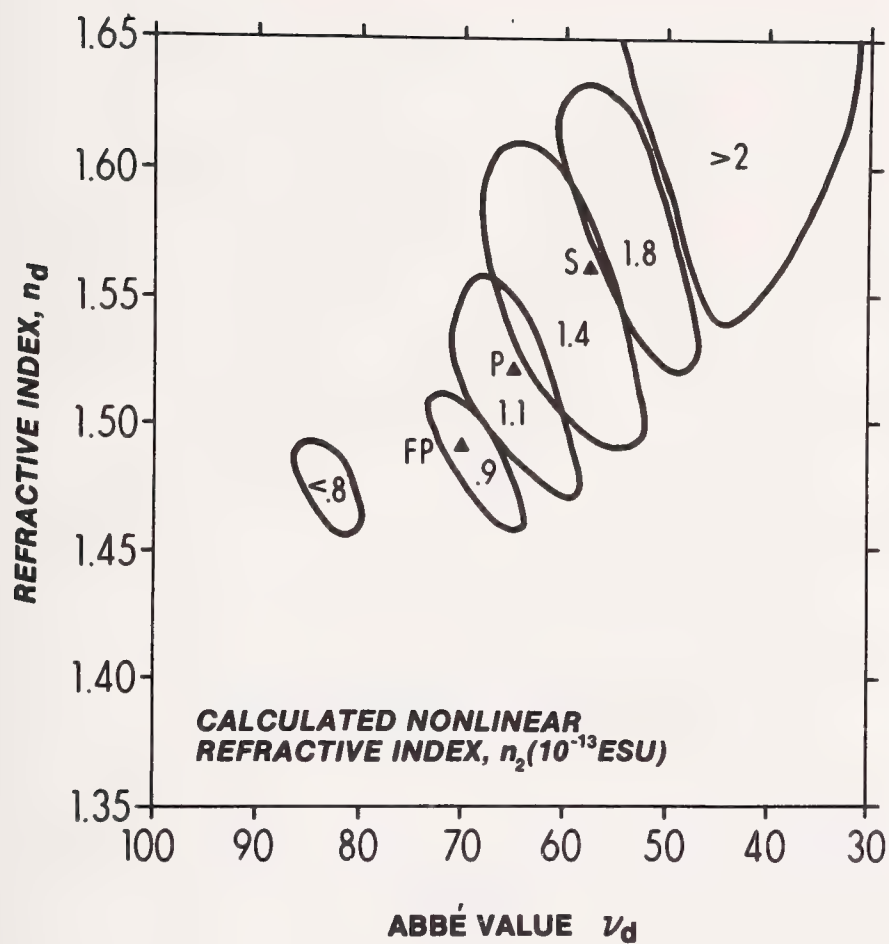


Figure 7a Regions with common  $n_2$  on the optical glass diagram.

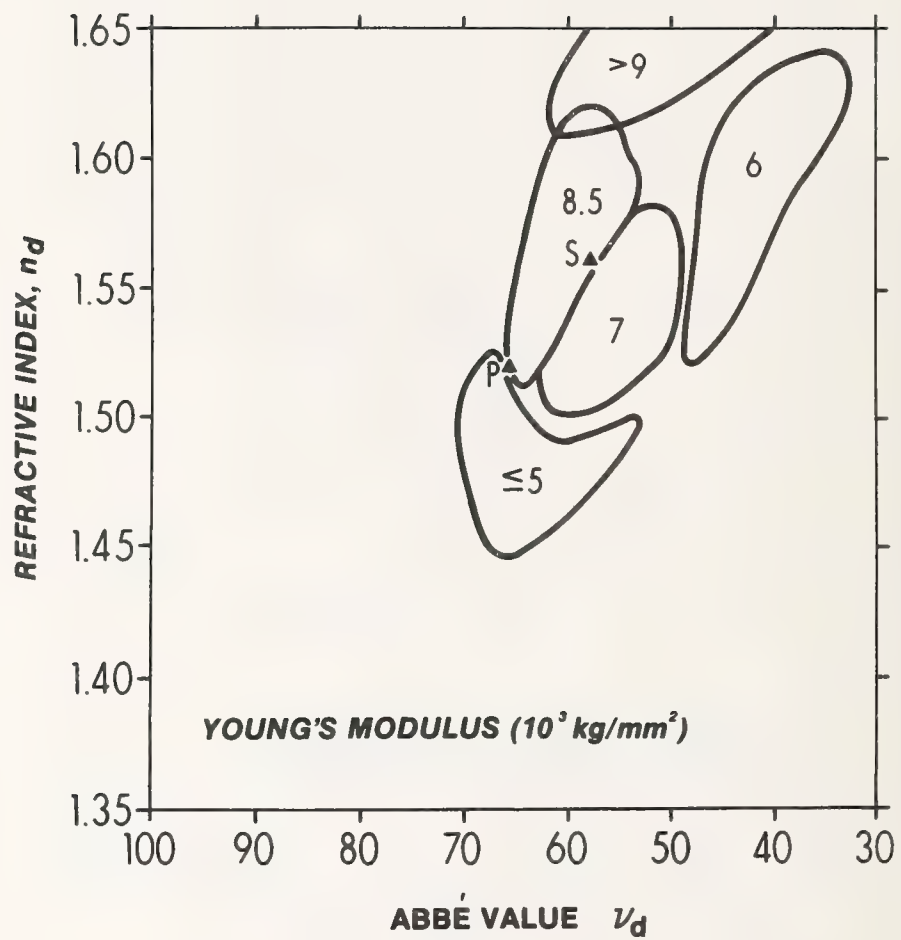


Figure 7b Regions with common Young's modulus on the optical glass diagram.



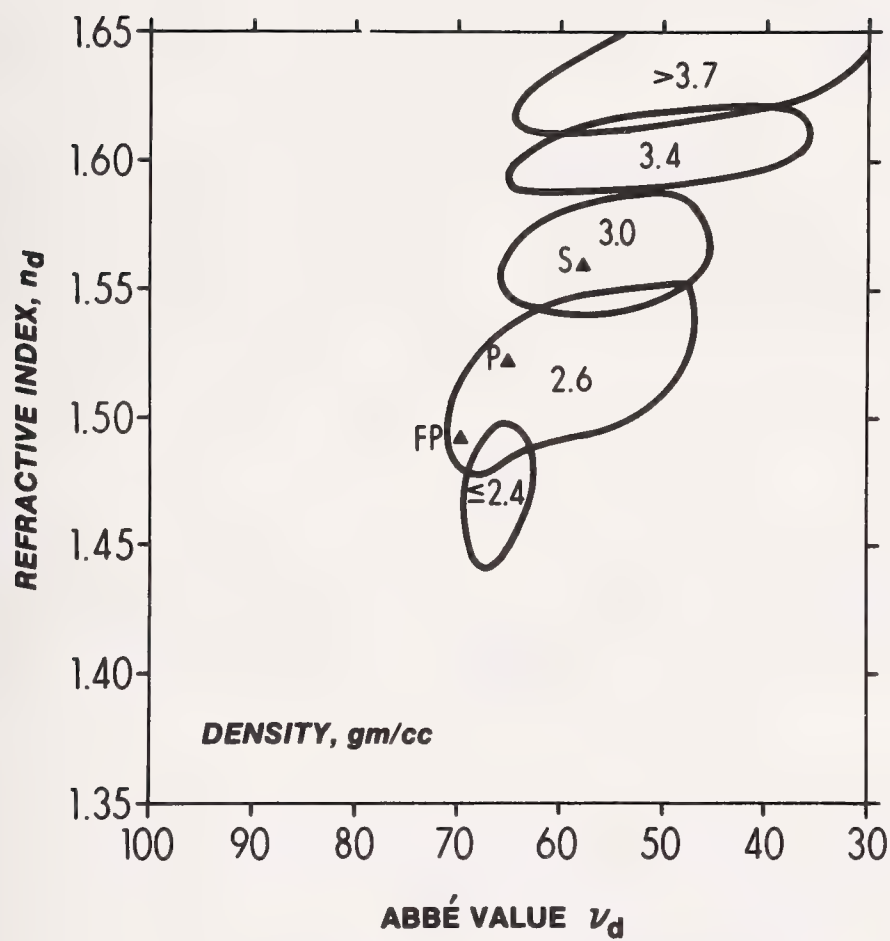


Figure 7c Regions with common density on the optical glass diagram.

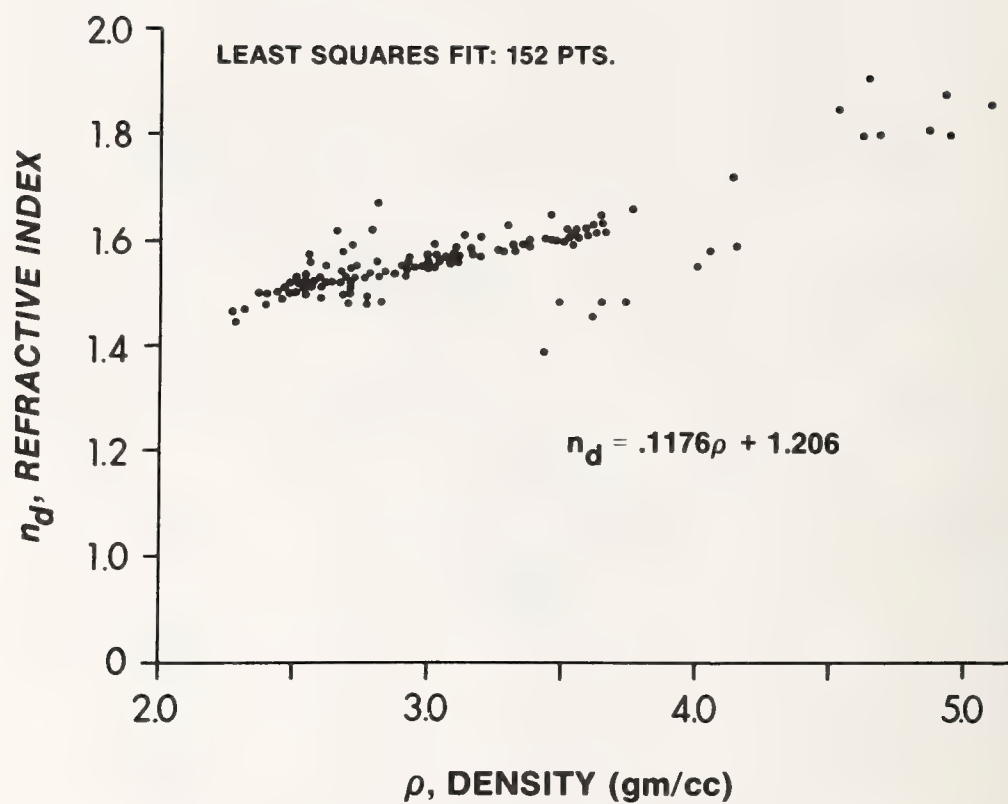


Figure 8      Refractive index versus glass density for optical glasses.

## PROGRESS IN CLADDINGS FOR LASER GLASSES\*

R. B. Bennett, K. R. Shillito  
Battelle, Columbus Laboratories  
Columbus, Ohio 43201

and

G. J. Linford  
Lawrence Livermore Laboratory  
University of California  
Livermore, California 94550

Cladding glass compositions matched in refractive index have been developed for two commercial neodymium-doped silicate laser-glass-disk amplifiers for the suppression of parasitic oscillations. Coatings based on a copper oxide-doped borate glass system satisfied specifications for single-pass optical transmission, xenon flashlamp damage threshold level, scatter, and thermal-expansion match. Commercial application for Owens-Illinois' ED-2 laser glass and Hoya Optics' LSG-91H laser glass achieved gain levels surpassing those of previously tested commercial glass claddings and equivalent to that of liquid cladding systems. Compositions and cladding design criteria are presented.

The feasibility of glass claddings for neodymium-doped fluorophosphate laser glass is also reported. Claddings based on copper oxide-doped alkali phosphate glass systems having softening temperatures below 400 C, linear thermal-expansion coefficients between  $14$  and  $18 \times 10^{-6}/\text{C}$ , refractive indices of  $1.48$ - $1.50$ , and good chemical durability have been identified. Technology is being developed to meet specific design and performance goals and to reveal the nature and extent of potential problems associated with claddings for fluorophosphate laser glass for advanced laser systems. Compositional ranges and pertinent data along with design considerations are presented.

Key words: Fluorophosphate laser glass; glass cladding; laser fusion; microstructure; parasitic oscillation; refractive index; residual stress.

### 1. Introduction

As is well known, the Lawrence Livermore Laboratory has been constructing a large neodymium glass laser system as a part of their laser fusion program. Some of the principal components of this laser glass system are disk amplifiers. The Shiva system, currently nearing completion, includes 20 laser chains of progressively larger disk amplifiers. Most of our own particular development has been targeted toward the C-size amplifier which has major and minor axes of 40 and 20 cm, respectively. The main reason for applying the claddings on these disk amplifiers is the suppression of parasitic oscillations which arise within the volume of the laser disks.

### 2. Discussion

Figure 1 illustrates the parasitic ray geometry of a laser disk with a partially transmitting cladding, illustrates several important considerations in cladding technology. In the schematic, a light ray in the laser glass disk meets the interface of the cladding glass and laser glass and is refracted by an amount varying with the refractive index mismatch. During that refraction, a portion of the light is reflected back into the laser glass, and the amount of the reflected light would be lessened, or perhaps eliminated entirely, if the refractive index match between the cladding glass and the laser glass is perfect. The cladding glass is doped with absorptive ions, usually by adding cupric oxide, which absorb the parasitic rays and dissipate the energy thermally. Any unabsorbed light will be reflected at the cladding-glass/air interface, and may reenter the laser glass after traversing the edge coating. Thus, the thickness of the cladding glass and the doping level must be coordinated so as to achieve the desired sufficient amount of light absorption, yet prevent excessive heating of the cladding glass. The cladding glass microstructure is also important. The presence of bubbles or second solid phases must be minimized, since either type of microstructural feature would be expected to reflect parasitic light back into the laser glass.

Figure 2 is another schematic which shows the alternate approach to edge cladding. This method was developed earlier because it was uncertain whether satisfactory solid claddings could be developed. Basically, this liquid cladding system involved a sealed containment ring through which a chemical solution designed to have a refractive index matching that of the laser glass was pumped. The additional complications of this approach make the liquid systems less desirable than a satisfactorily performing solid edge cladding.

---

\*Work at the Lawrence Livermore Laboratory performed under the auspices of the U.S. Department of Energy under Contract W-7405-eng-48.



The principal objective of the cladding compositional development has been to match the refractive index of the laser glass, while maintaining compatibility with commercial methods for cladding preparation and processing. The glass cladding technique is basically a glass enamel process. Preparation of the cladding glass includes several steps. The glass batch is weighed, melted, poured and cast, and annealed. After samples for optical and thermal property measurements are cut from the annealed glass, the remainder is pulverized to powder (usually -325 mesh) in preparation for its use in an alcohol-based slurry suitable for either spraying or flow coating onto the laser glass samples. Of course, the laser glass substrates require some preparation, including cutting samples of satisfactory size, polishing the surfaces to be coated, and cleaning.

Several compositional design criteria must be adhered to in developing the cladding glass. The absorption coefficient must be maximized in order to absorb parasitic light, because the commercial application process limits thickness to about 0.5 mm. The refractive index must be matched to that of the laser glass to minimize the reflection at the laser glass interface. The softening point must be minimized so that the cladding can be fused onto the laser glass at a temperature at which the laser glass itself is not distorted. Thermal contraction must be matched to that of the laser glass to prevent the formation of excessive residual stresses which would both harm lasing characteristics and also result in mechanical damage to the laser glass or the cladding. Microstructural inhomogeneities must be minimized to prevent light scatter and back reflection. Stability with respect to devitrification phase separation or possible hydrolysis by atmospheric or processing moisture must be maximized.

Table 1 shows the composition and property data for an optimized cladding applied to Hoya Optics' LSG-91H silicate laser glass. One of the significant aspects is the BaO:ZnO ratio which was balanced in order to minimize residual stress. The copper oxide was included for its absorption function. Fluorine is present to minimize the softening point of the cladding glass within an acceptable range. Al<sub>2</sub>O<sub>3</sub> was added for stability. Regarding the properties listed, the optical transmission is within the LLL specification, devitrification was avoided thus minimizing light scattering, and refractive index was within the specification of 1.56-1.60 (the refractive index of the silicate laser glasses was 1.555). The other listed properties are pertinent to the ability to apply the cladding glass by commercial practice.

Table 1. Composition and property data for cladding glass LBH-30.

Batch Composition:	5.80 NaF
	2.05 KF
	3.83 K <sub>2</sub> CO <sub>3</sub>
	1.01 Al(OH) <sub>3</sub>
	58.97 H <sub>3</sub> BO <sub>3</sub>
	12.82 PbO
	3.52 BaCO <sub>3</sub>
	12.01 ZnCO <sub>3</sub>
	4.93 CuO
Oxide Composition:	6.5 Na <sub>2</sub> O
	6.5 K <sub>2</sub> O
	1.0 Al <sub>2</sub> O <sub>3</sub>
	50.5 B <sub>2</sub> O <sub>3</sub>
	19.5 PbO
	4.15 BaO
	11.85 ZnO
	7.5 CuO
	5.0 F
Smelting Temperature	- 815 C
Softening Point	- 499 C
Thermal Exp Coeff	- 10.9 x 10 <sup>-6</sup> cm/cm/C
Refractory Index	- 1.5781 at 1.06 μm
Residual Stress	- 3 nm/cm
Devitrification	- None
Optical Transmission	- 1.1% at 1.06 μm
	5.5% at 1.35 μm

Compositional dependency of the residual stress thermally induced in the laser glass by application of the cladding glass is shown in figure 3 for both 6 percent and 8 percent copper oxide doping. Adjustment of the relative amounts of BaO and ZnO, while maintaining their total at 16 weight percent, permitted residual stress minimization. When CuO level was adjusted, a corresponding modification in the BaO/ZnO ratio maintained the low residual stress level.

The typical microstructures of the two previously available commercial coatings for silicate laser glasses are shown in figures 4 and 5. The BSDL-6 cladding section shown in figure 4 is about 0.15 mm

thick. It has a solid second phase which results in surface roughness, which is undesirable from the standpoint of mounting the claddings in the retaining rings by LLL, and also would be expected to cause some back-reflection. In addition, it contains porosity which is preferentially oriented at the interface and, therefore, would tend to maximize the amount of back-reflection off the porosity.

The competitive commercial edge cladding, as applied to ED-2 laser glass, is shown in figure 5. Typically, EI-4 is about 0.25 mm in thickness and has a significant amount of porosity, which is homogeneously dispersed in the cladding glass. A typical microstructure of LBH-30 cladding is shown in figure 6 for comparison. The cladding section shown is about 0.42 mm thick, has no second solid phase, and has less porosity than the commercial claddings. The pores in the LBH-30 cladding are homogeneously distributed through the coating. This is typical of the optimum coatings developed for both LSG-91H and ED-2.

A plot of the gain data obtained by LLL for the LB-615I cladding, which was developed for ED-2 laser glass, is given in figure 7. This is some of the early data reported by LLL and was important because it showed that when the desired properties and specifications for the cladding glass were achieved, desirable gain characteristics resulted. The data for a previously available commercial solid edge cladding, that for liquid edge cladding systems, and the data for the LB-615I which was developed and applied to ED-2 laser glass are plotted. There is a slight superiority over the liquid cladding system which, of course, allows the elimination of considerable hardware and maintenance which were needed for liquid claddings. However, there is also at least a 20 percent increase in gain over that measured for previously available solid edge claddings, resulting in quite a substantial increase in the achievable power in the laser system. As a matter of fact, using this type of solid edge cladding in the system, LLL recently achieved their first major program milestone of 500 Joules output for a single laser chain. Thus, the development of claddings for silicate laser glasses was concluded in a satisfactory fashion and both of the commercial suppliers have adapted such compositions for use on their silicate laser glasses. More recently, work has been directed toward the advanced laser glass systems being developed under the direction of ERDA. Specifically, claddings have been sought for the fluorophosphate glass compositions now being developed by at least four of the glass vendors.

Table 2 lists the cladding glass properties which would be needed for the fluorophosphate laser glasses. The refractive indices need to be lower than for silicate laser glasses, probably below 1.48. The thermal expansion coefficient will likely be in the range of  $15 \text{ to } 18 \times 10^{-6} \text{ cm/cm/C}$ . Residual stress again will need to be quite low,  $<5 \text{ nm/cm}$ . The softening point will need to be less than  $425 \text{ C}$  in order to apply the claddings at a satisfactory low temperature. Absorption coefficients again will need to be maximized and scattering minimized for efficient operation of the claddings.

Table 2. Cladding glass design criteria for advanced laser glass.

Refractive Index	- $<1.48$ at $1.06 \mu\text{m}$
Thermal Expansion Coefficient	- $15.0 - 18.0 \times 10^{-6} \text{ cm/cm/C}$
Residual Stress	- $<5 \text{ nm/cm}$
Softening Point	- $<425 \text{ C}$
Absorption Coefficient	- Maximize
Scattering	- Minimize

The compositional range for the fluorophosphate glass claddings developed to date is given in table 3. These are phosphate glasses, essentially, and they are doped with 4 to 8 percent copper oxide.

Table 3. Cladding glasses for fluorophosphate laser glass

Oxide compositions (w/o)

1.0 - 3.0	$\text{Al}_2\text{O}_3$
3.0 - 8.0	$\text{B}_2\text{O}_3$
55.0 - 65.0	$\text{P}_2\text{O}_5$
5.0 - 15.0	$\text{Na}_2\text{O}$
5.0 - 12.0	$\text{K}_2\text{O}$
0 - 7.0	$\text{ZnO}$
0 - 5.0	$\text{BaO}$
0 - 7.0	$\text{MgO}$
5.0 - 9.0	$\text{F}$
4.0 - 8.0	$\text{CuO}$

Data which have been obtained thus far for claddings developed for fluorophosphate laser glass are given in table 4. The thermal expansion coefficients are in the desired range, since the more promising laser glasses obtained from different suppliers have ranged in thermal expansion from  $14 \text{ to } 18 \times 10^{-6} \text{ cm/cm/C}$ . Residual stress of  $1.9 \text{ MN/m}^2$  (280 psi) is excessive, but the final adjustment will be made only when the desired laser glass composition(s) have been selected. Index of refraction is 1.515;

Table 4. Typical cladding data for advanced laser glass.

Thermal Expansion Coefficient	- $15.5-17.5 \times 10^{-6}$ cm/cm/C
Residual Stress	- $1.9 \text{ MN/m}^2$ (280 psi)
Index of Refraction	- 1.515 at $1.06 \mu\text{m}$
Transmission	- 0.10% at $1.06 \mu\text{m}$ 1.4% at $1.35 \mu\text{m}$
Chemical Durability ( $\text{H}_2\text{O}$ , 100 C, 1 hr)	- $0.017\% \text{ min}^{-1}$

and that is acceptably close to the target. Single-pass optical transmission is well within specifications, having 0.1 percent at 1.05 microns and 1.4 percent at 1.34 microns wavelength.

In conclusion, a solution was obtained for the problem of index matching a satisfactory glass solid edge cladding for the silicate glass laser systems, thus helping LLL to achieve a major laser program milestone. The more recent work on the fluorophosphate glass compositions has progressed sufficiently that the feasibility of obtaining a fully satisfactory cladding for the fluorophosphate glass systems has been demonstrated. Although there is work proceeding on beryllium fluoride based laser glasses, at the present time no development effort has started on claddings for these systems.

### 3. Figures

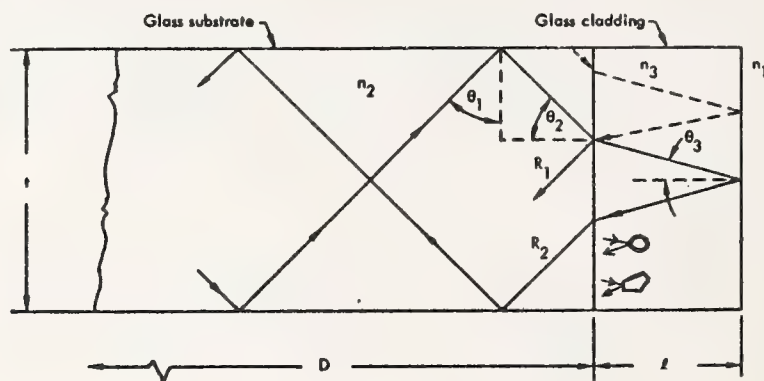


Figure 1. Schematic representation of the cladding-glass function

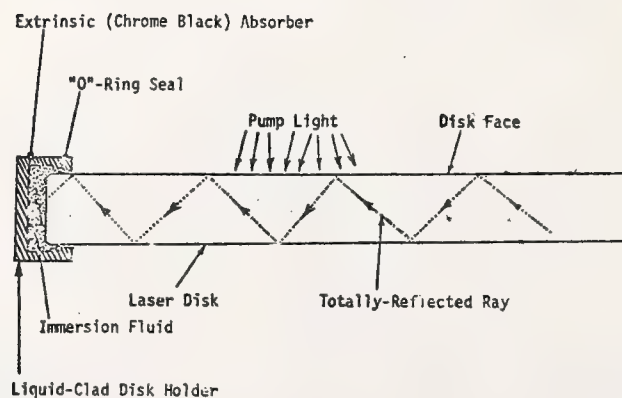


Figure 2. Cross sectional schematic of liquid-clad laser disc fixture



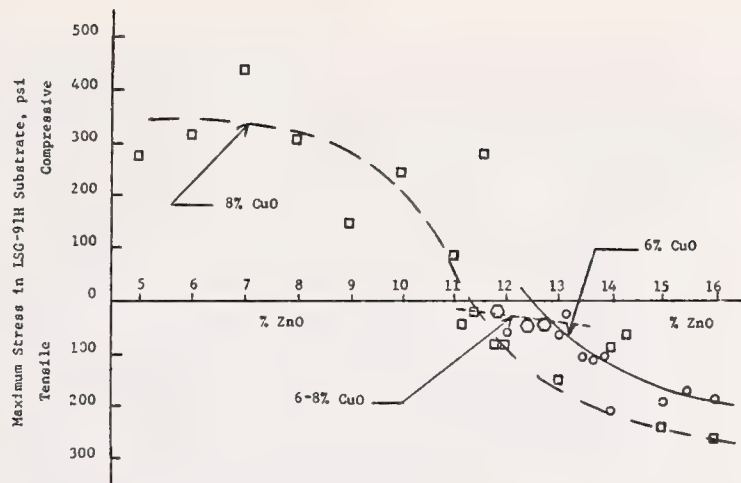


Figure 3. Effect of compositional variation on stress (annealed)



Figure 4. Typical cross-section of Owens-Illinois' EI-4 cladding, approximate 0.010-in. thickness



Figure 5. Typical cross section of Hoya BSDL-5 cladding, approximately 0.006-in. thickness

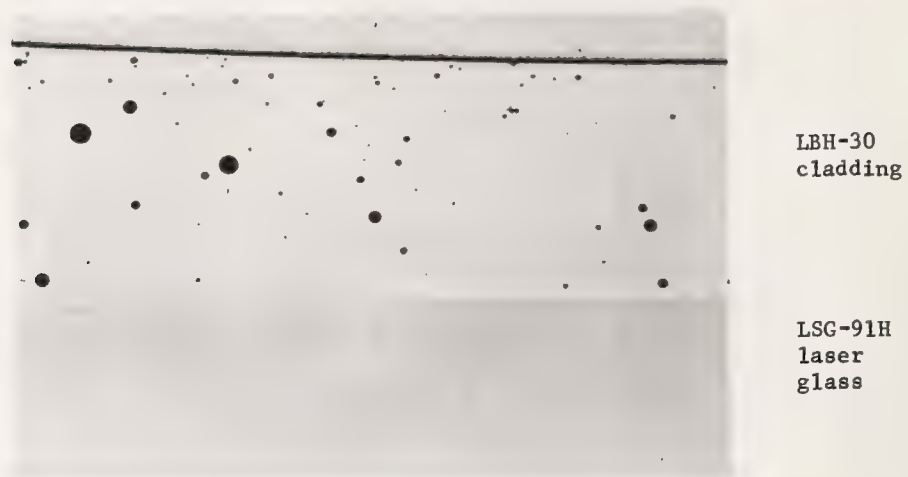


Figure 6. Typical microstructure of LBH-30 cladding

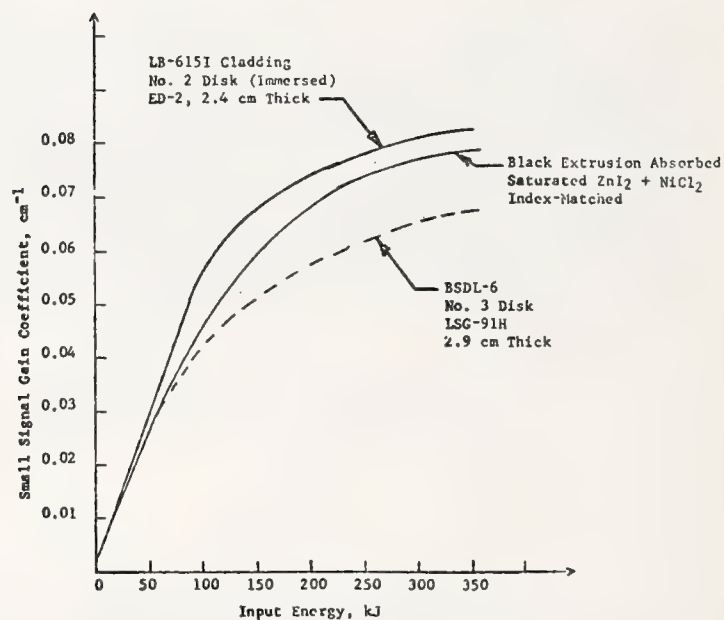


Figure 7. Comparison of gain coefficients for LB-615I experimental cladding with those for liquid cladding and commercial solid-edge claddings

#### COMMENTS ON PAPER BY BENNETT, SHILLITO, AND LINFORD

The speaker was asked why parasitic suppression was specified at 1.06 micrometers and 1.35 micrometers but not at 0.88 micrometers, which is a transition from the metastable state to the ground state. It was pointed out by Marvin Weber from LLL, that emission at 0.88 micrometers is reabsorbed by ground state neodymium ions, replenishing the inversion and therefore does not represent a net loss. Consequently there is no need to suppress radiation of fluorescence at that wavelength.

## DAMAGE HISTORY OF ARGUS, A 4TW Nd Laser System

Irving F. Stowers and Howard G. Patton  
Lawrence Livermore Laboratory  
Livermore, California 94550

Argus is a two arm Nd:glass laser built for laser fusion experiments. It operates at a power level of 4 terawatts with 100 ps pulses and has placed 2KJ on a fusion target with 1 ns pulses.

To minimize spatial modulations on the beam and damage to coated and uncoated optics, the system uses five spatial filters on each arm and the beam fluence is maintained below  $2 \text{ J/cm}^2$ . Despite these precautions, coated optics and uncoated disks occasionally still damage. Damage limits the useful life of the system and determines the frequency of maintenance.

This paper discusses the several forms of damage that have been observed, their morphology, severity and frequency of occurrence. Three distinctly different forms of damage have been observed in the system. They are: A) contamination induced damage to Nd:glass disks caused by broad-band xenon flashlamps, B) optically obscuring films on disks and C) damage to coated optics by the laser beam.

### Argus History

Each Argus arm is composed of a 4-cm rod amplifier, three 8.5-cm aperture amplifiers, (shown in figure 1) and four 20-cm aperture disk amplifiers. The disk amplifiers have 3%-Nd-doped silicate-glass disks set at Brewsters angle to minimize reflection and are enclosed in a quartz shield tube to create a clean beam cavity. The beam cavity and the flashlamp covers are flushed with dry nitrogen to exclude particulates and to cool the disks.

The first arm was placed in operation in December, 1975 and since then the system has been fired approximately 600 times. In August, 1976, after 150 shots, the disk amplifiers were disassembled, examined, and found moderately damaged and obscured by a light scattering film. The entire system was refitted in three weeks, replacing badly damaged disks with new and recleaning the remainder. In October, 1976, a planned periodic maintenance schedule was initiated<sup>1</sup> with one amplifier being rebuilt every two weeks. During this periodic maintenance, the following information was gathered on severity and frequency of damage in order to determine system reliability and to predict optimum maintenance intervals.

#### A Disk Amplifier Damage Morphology

Damage to uncoated disks occurs in a size range from  $1 \mu\text{m}$  to 1 mm and the morphology is consistent and repeatable enough to allow certain patterns to be identified.

The single most outstanding pattern is that damage sites are round, or at least circularly symmetric. The sites are always located on the surface of the glass and damage to the bulk of the glass has not been observed. Most large damage sites,  $100 \mu\text{m}$  to several millimeters in diameter, are accompanied by extensive fracturing of the glass surface. Figure 2 shows a typical large damage site which is characteristically round and fractured at the edges. In almost all cases, glass fragments from the center of the site are ejected or melted and only those attached to the edge of site remain intact.

The fractured glass produces loose chips which when ejected from the initial location fall back onto the disk and cause subsequent damage. Figure 3 shows the area immediately surrounding a large damage site, and it appears that the smaller damage sites were started by debris thrown from the initial site.

Many damage sites have melted fragments of glass attached or partially covering the damage site. These most likely represent fragments of glass from the disk itself, which have melted and resolidified, but they may also be glass fragments from the encircling quartz shield tube shown in figure 1, which have fallen onto the disk and initiated the damage. Figures 2 and 4 show typical large damage sites with melted fragments of glass of unknown origin attached to the surface.

Small damage sites,  $5\text{--}50 \mu\text{m}$  in diameter, are also very circular as shown in figure 5, and generally appear to have contaminants or foreign particles fused into their surface. Fracturing of glass is generally found to be correlated with disk position within the amplifier. That is, disk



surfaces facing upward generally sustain more damage than downward facing surfaces and several amplifiers have been found to have from 2-5 times more damage on their upward facing surfaces. This effect is attributed to gravitational settling of particles either airborne in the nitrogen or ejected from damage sites on the disks or on the quartz shield tube. It has also been noted that the first disk surface, in the direction of gas flow, generally has more damage, by as much as a factor of five, than any other disk surface in the same amplifier. This is attributed to its being the first surface upon which nitrogen-carried particles would come to rest.

Although foreign contaminant particles are rarely found attached to large damage sites, they are the cause for all of the forms of damage mentioned above. Any dielectric or metallic particle remaining on disk surfaces is rapidly heated by the flashlamp radiation and the laser pulse. The cerium-doped-quartz flashlamps, pumped with 9KJ in 600  $\mu$ s, supply in excess of 20 J/cm<sup>2</sup> at the disk surface. This is sufficient energy to heat and evaporate most particles smaller than 10  $\mu$ m. The exact mechanism by which the heated particles damage the disk is not fully understood but it is proposed that thermal diffusion of the contaminant may cause devitrification of the glass. Alternatively, a thermally induced stress caused by rapid heating and cooling of the contaminant particle in contact with the disk may be causing the cracking.

### Optical Severity of Damage

A quantitative measure of the optical severity of damage is needed to ascertain when a disk has sustained sufficient damage to warrant regrounding and repolishing. A quantitative measure of damage is also useful for correlation with proposed causes for the damage such as number of amplifier firings or incident energy.

The fraction  $\sigma$  of the optical surface obscured by damage sites is one measure of the amount of damage to the disk. It may be obtained by integrating the product of the area obscured by a damage site and the size distribution of the damage sites. The cumulative size distribution of damage sites found on both lightly and heavily damaged Nd:glass disks, shown in figure 6, follows a power function of the form,

$$C = \alpha d^n.$$

The count density  $C$  may be expressed as the number of damage sites per unit area greater than diameter  $d$ ; the parameter  $\alpha$  determines the concentration and the constant  $n$  has been experimentally found to be -1.64. The fraction of the optical surface obscured by damage is thus given by

$$\sigma = \frac{-\alpha n \pi}{4(n+2)} \left[ d_l^n + 2 - d_s^n + 2 \right]$$

where  $d_l$  and  $d_s$  are the largest and smallest damage sites on the surface, respectively. We have found that with Nd:glass,  $d_s$  may generally be taken as 1  $\mu$ m. To evaluate the function, the value of  $d_l$  is determined by finding and measuring the largest damage site on a given disk surface. The parameter  $\alpha$  is obtained by microscopically observing several representative areas and counting the number of damage sites greater than diameter  $d$ , called  $C_d$ , and calculating

$$\alpha = C_d d^{-n}$$

Since January 1977, all amplifiers overhauled have been examined to determine the extent of damage. Figure 7 shows the unaveraged data pertaining to the quantity of damage sites per disk surface as a function of the number of amplifier firings. There appears to be an upper bound of 1 damage site/cm<sup>2</sup> > 100  $\mu$ m corresponds to 0.1% obscuration per surface. The average level of damage is .20 damage sites/cm<sup>2</sup> > 100  $\mu$ m corresponding to .013% obscuration per surface or .92% per arm for the Argus system; a very acceptable level.

The low correlation of damage with number of firings, shown in figure 7, implies that only initially present contaminants or defects in the surface initiate the damage. The data also implies that there is no long term surface fatigue effect and that disks examined after the first 10-20 firings will have as much damage as after several thousand firings. This, of course, excludes the possibility of inadvertent recontamination of the optics. It also implies that, at low repetition rates, very long lifetimes can be expected if all surfaces are initially clean and remain clean.

### B. Films on Disks

In addition to damage sites found during rebuilding, many disks have been found to have a light scattering film covering their surface. Figure 8 shows this film on a 10 cm aperture disk. To

determine its composition, samples of the contaminant were collected using methyl chloroform and ethanol rinses and analyzed in a gas chromatograph mass spectrometer (GCMS). The analysis found dioctylphthalate (DOP), an unidentified terpene and a branched hydrocarbon. The concentration was quite low and corresponded to  $14 \text{ ng/cm}^2$  of area rinsed. The cooling gas, obtained from liquid nitrogen boil-off, was also sampled to determine if it was the source for any of the contaminants. Resin-filled columns were used to sample nitrogen from the operating system and any absorbed organics were eluted with ethyl ether and analyzed with the same GCMS. Very low concentrations of DOP were detected along with the same terpene detected on the disks. A homologous series of hydrocarbons was also detected which was similar to that found on the disks. The total concentration of organics measured was very low, and corresponded to only  $60 \text{ ng/g}$ . While it was at first thought that the film was a condensed gaseous contaminant brought into the amplifier with the nitrogen cooling gas, it is unlikely that these organic compounds are responsible for the film observed on the disks.

Subsequent microscopic examination of the film showed it to be composed of small spots and crystalline fibers. The largest fibers are typically  $2\text{--}5 \text{ }\mu\text{m}$  in diameter and up to  $500 \text{ }\mu\text{m}$  long. Figure 9, a photomicrograph of the crystalline film, shows the large fibers and smaller spots characteristic of the film. It is of interest that the fibrous film has been found on unfired as well as fired amplifiers and that the radiant energy from the flashlamps does not appear to diminish growth nor does the film appear to aggravate damage.

The film is readily removed using ethanol and does not appear to be chemically attached to the glass surface. Films similar to those found on disks removed from amplifiers have been artificially grown by simply leaving a Nd:glass disk in an air-conditioned clean room at 50% relative humidity for 30 days. First evidence of a film becomes visible in as short a time as 2-3 days. All growth of the film can be prevented in a vacuum dessicator. This evidence leads to the conclusion that the film is the result of an atmospheric attack, possibly water vapor, of the glass surface.

The first evidence of the composition of the fibers was obtained from an index of refraction measurement. The fibers were found to be anisotropic and one of the indexes was determined to be 1.454, using Cargille fluids. Anhydrous lithium hydroxide LiOH is a birefringent tetragonal crystal with indexes of 1.464 and 1.452. The source of the lithium is the Nd:glass which contains almost 30 mol%  $\text{Li}_2\text{O}$ .

Direct examination of fibers using an ion probe (IMMA) verified the existence of lithium and nitrogen in high concentrations in the fibers. This implies lithium nitride  $\text{Li}_3\text{N}$ , the nitrate  $\text{LiNO}_3$ , the trihydrate form  $\text{LiNO}_3 \cdot 3\text{H}_2\text{O}$ , or the nitrite  $\text{LiNO}_2 \cdot 2\text{H}_2\text{O}$ . Since lithium nitride decomposes to LiOH in the presence of water vapor, there appears to be more than sufficient evidence to support the theory of atmospheric attack of the Nd:glass. Further tests are planned to verify the composition of the film using scanning Raman spectroscopy.

To determine the optical severity of the film problem, a single small sample of Nd:glass wrapped in a lens tissue for over one year was examined with a Cary 17 Spectrophotometer. The film which had grown on the surface reduced the transmission by over 0.3% per surface as compared to an average damaged disk of 0.013%. A heavily filmed disk can, therefore, reduce transmission much more than a damaged disk. Removal of the film requires that the amplifier be removed from service, completely disassembled for cleaning, and then reinstalled and realigned. Approximately forty man-hours are required for this maintenance and this is significant for a large laser system such as the 20 arm/100 amplifier SHIVA system.

### C Damage to Coated Optics

Damage to coated optics on Argus has been minimal. On two occasions, coated spatial filter lens have been found damaged. In both cases the damage occurred on the vacuum side of the lens, suggesting damage caused by contamination due to vaporization of material around the pin hole or contamination from the ion pumps. The pattern of damage shown in Figure 10, appears as discolored areas forming several rings similar to large scale beam spatial modulations. The morphology of the damage was examined in a SEM and photomicrographs are shown in figure 11. The spatial filter coating is composed of alternating layers of  $\text{SiO}_2$  and  $\text{TiO}_2$ , and photomicrographs clearly show that the discolored areas are not surface deposits but regions in which the coating has delaminated. The delamination caused the top three layers to be removed exposing the fourth  $\text{TiO}_2$  layer. The composition of the individual layers was verified by the use of ESCA. Contaminants were not found, though, from either materials around the pin hole or materials from the ion pumps. Currently damage testing is being conducted on coated optics under vacuum conditions to determine if the coating is drying out on the vacuum side. It has been theorized that an inadequate bond, perhaps due to contamination during coating, resulted in the delamination at this particular interface. Contaminants were not found on the coated surface, and the reason for the damage occurring on the vacuum side of each lens has not yet been determined.

The circular pattern is due, apparently, to spatial modulations (noise) on the beam.

### Conclusion

It appears that the most severe (i.e. expensive) and continuing damage problem on Argus is to the surfaces of laser disks and that this damage is due to flashlamp heating of contaminants. Damage appears to create loose glass particles which can catalyze additional damage. Current cleaning and surface preparation techniques have been able to produce amplifiers with sufficiently low damage quantities that an entire laser arm will sustain less than 1% beam obscuration after 500 shots. The film crystallizing out onto the disk surfaces is currently the most significant problem from the beam obscuration point of view and an immediate solution is not available. It may be possible, though, to deplete the lithium from the glass surface and thus substantially extend the time between cleaning periods and thus increase system reliability. Damage to coated optics is rare, given that beam fluence is maintained below damage thresholds.

### REFERENCES

1. Stowers, I. F.; Patton, H. G.; Jones, W. A.; Wentworth, D.E.  
Proceedings of 9th Annual Electro-Optics/Laser 77 Conference  
Anaheim, California - October 25 - 27, 1977



# FIGURES



Figure 1. An Argus 8.5 cm aperture disk amplifier opened to show the flashlamps and the split quartz shield tubes which surround the six Nd:glass disks. During operation the flashlamp covers and beam cavity is filled with dry nitrogen.

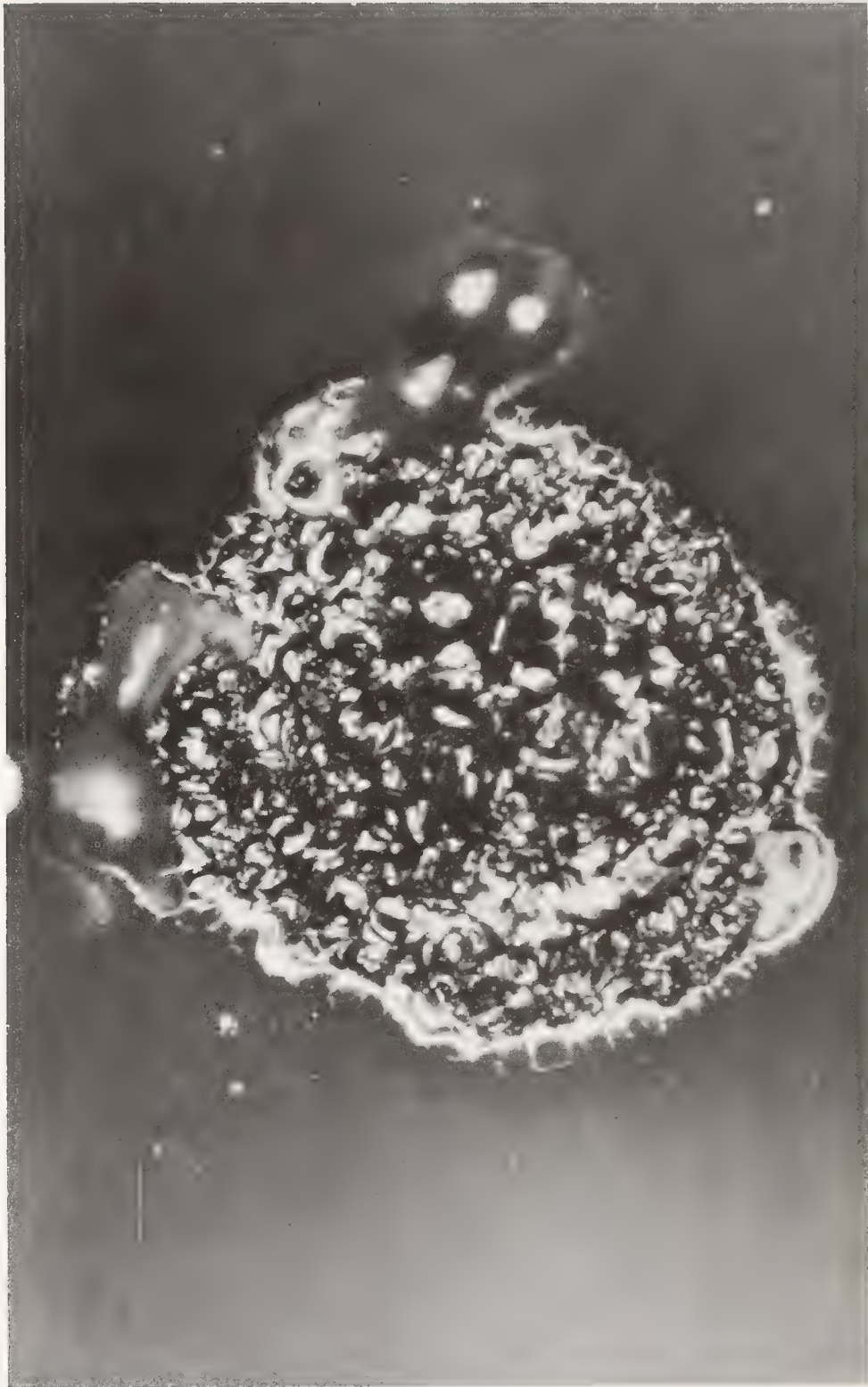


Figure 2. Circular damage site on Nd:glass disk. The edge is characteristically fractured and the ejected fragments can initiate additional damage at other locations (1 mm diameter).



Figure 3. A large (1 mm) damage site and the area surrounding it. The large number of additional smaller damage sites are due to debris ejected from the larger site.



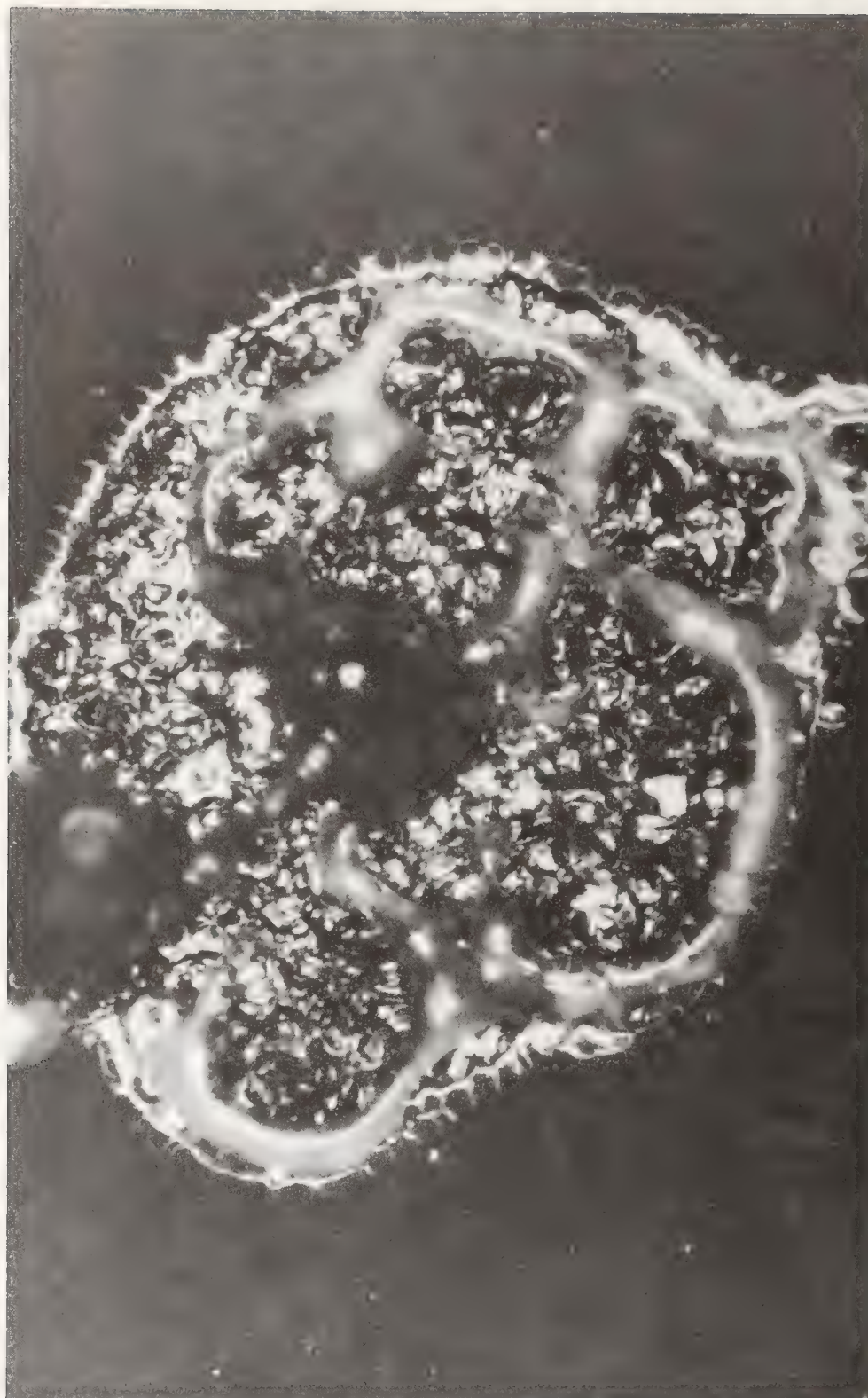


Figure 4. Large damage site on Nd:glass disk with melted fragments of glass attached to the surface. ( 1 mm diameter)



Figure 5. Small damage sites generally appear to have some form of contaminant particle fused into the surface. The small particles around the damage site are the result of partial evaporation of the contaminant particle and the glass. (50  $\mu\text{m}$  diameter spot)

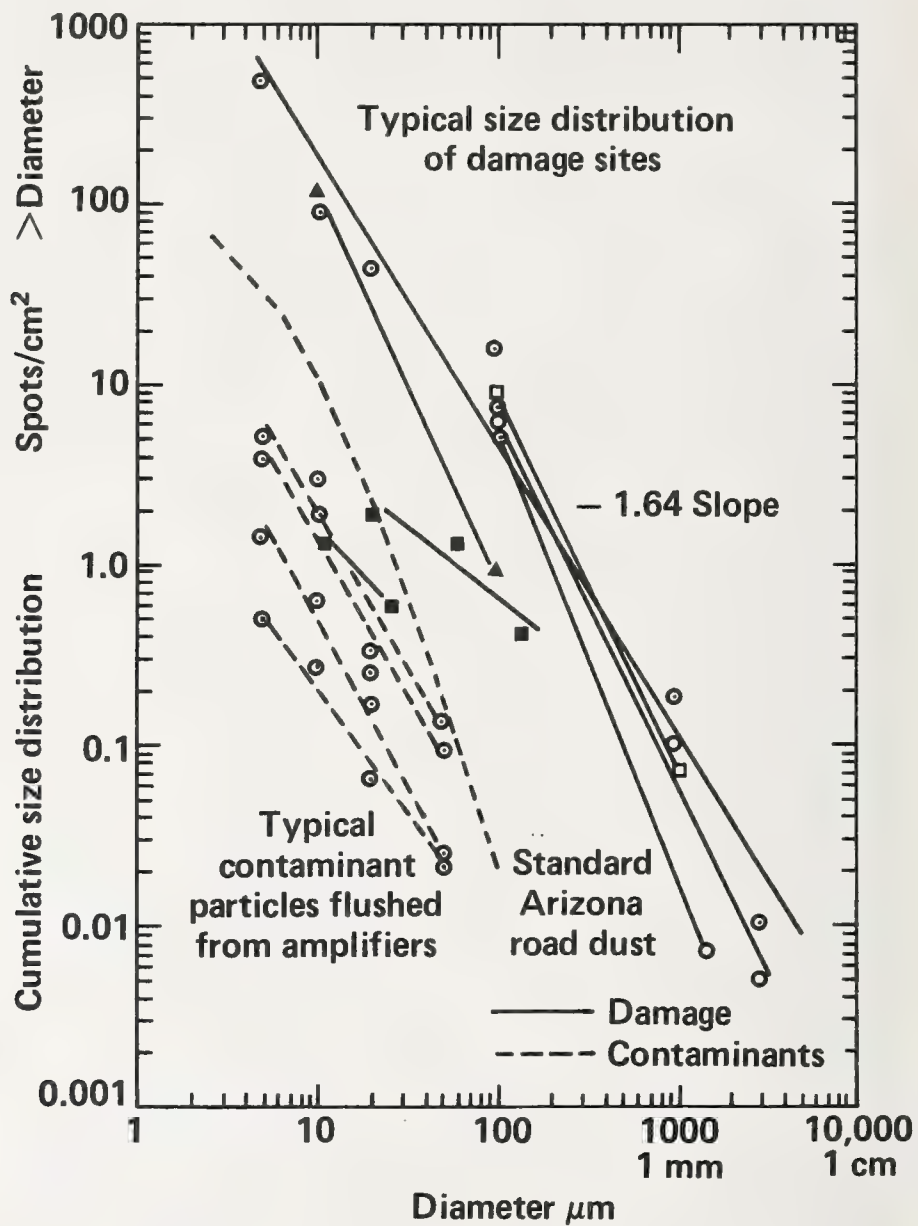


Figure 6. Cumulative size distribution of damage sites measured on several Nd:glass disks. The average slope of the curves is -1.64. The size distribution of typical contaminant particles follows the same general form as the size distribution of the damage.



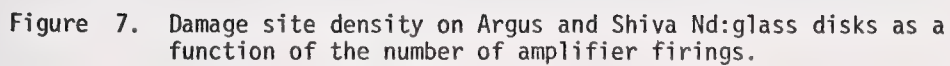




Figure 8. Nd:glass disk illuminated from above and right by a high intensity lamp. The light is scattered from the disk surface by a crystalline film that has grown after seven months exposure to a 50% RH atmosphere.





Figure 9. Crystalline fibers on Nd:glass surface after being stored in a closed and unfired disk amplifier for seven months. The atmosphere in the amplifier was air at 50% relative humidity when sealed. (2-4  $\mu\text{m}$  fibers)





Figure 10. Antireflection coated spatial filter lens. The circular pattern of the damage follows the intensity modulations on the beam.

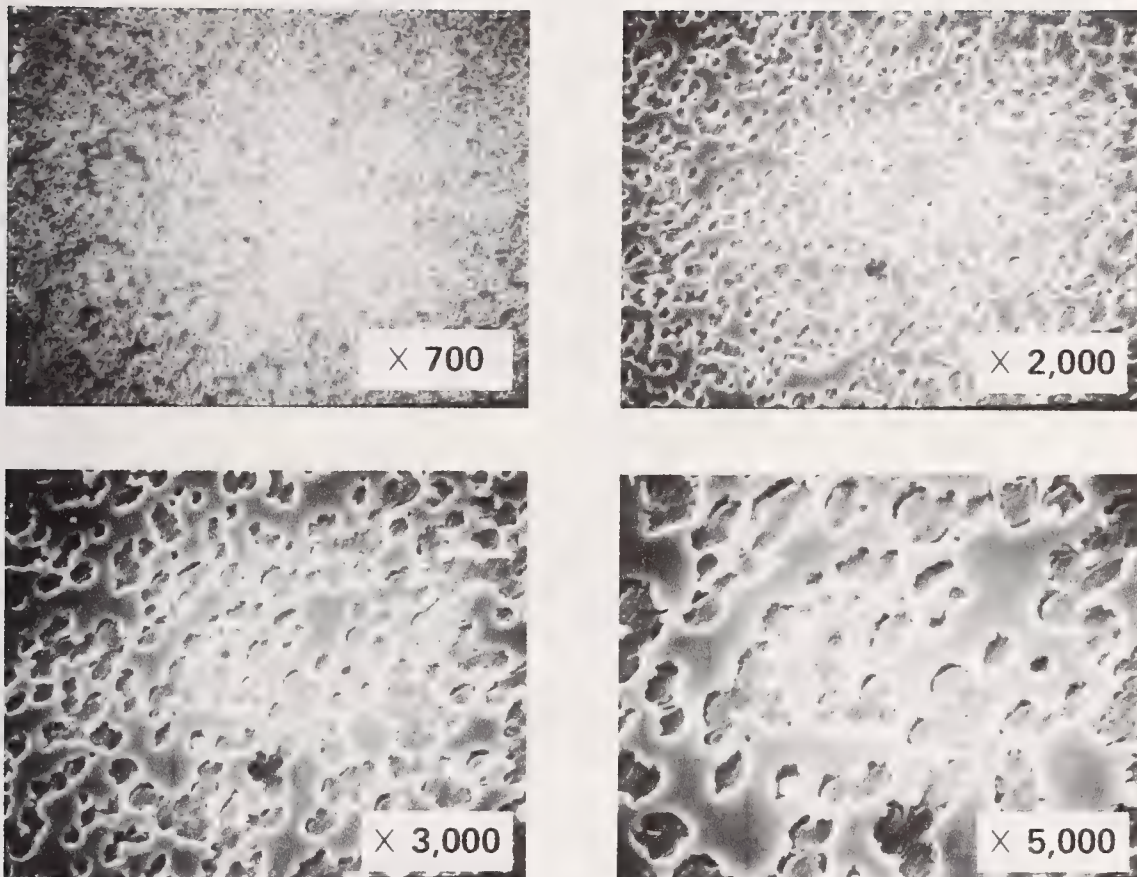


Figure 11. Scanning electron micrograph of damage on AR coated spatial filter lens. The individual layers of the coating are visible at the higher magnifications.

#### COMMENTS ON PAPER BY STOWERS AND PATTON

The speaker was asked if overcoating the surface of the ED-2 glass would suppress the growth of the lithium nitrate film. He responded that they had tried this experiment by placing samples of ED-2 glass overcoated with a protective film, in a highly humid atmosphere, the LiN seemed to form either under or on top of the protective coating, but the small fibers of LiN did not seem to appear. The speaker commented further that a conclusion one draws from this work is that given a choice for a disc amplifier, one would prefer to set it on edge, so that there were no upward facing surfaces.



# NEW RESULTS ON AVALANCHE IONIZATION AS A LASER DAMAGE MECHANISM IN TRANSPARENT SOLIDS

A. A. Manenkov

P. N. Lebedev Physical Institute  
of the Academy of Sciences of the USSR

Recent theoretical and experimental investigations carried out in the P. N. Lebedev Physical Institute of the Academy of Sciences of the USSR on electron avalanche ionization as a laser damage mechanism of solid transparent dielectrics are discussed. Formulas obtained on the basis of solution of the kinetic equation for electrons in the conduction band are given for the threshold (critical) fields  $E_c$ . The fundamental characteristics of the avalanche mechanism, namely, dependence of  $E_c$  on the sample temperature, radiation frequency and pulse duration are noted. Experimental results on the temperature dependence of damage thresholds for a number of alkali-halide crystals and other crystals used in laser optics are analyzed on the basis of avalanche ionization theory. These include NaCl, KCl, KBr, CsI, KI, RbCl, CsPr,  $Al_2O_3$ , YAG,  $SiO_2$ ,  $CaF_2$ ,  $LiIO_3$ ,  $BaF_2$ , NaF and LiF. Damage results were obtained with  $CO_2$  (10.6  $\mu m$ ), Nd:YAG (1.06  $\mu m$ , 0.53  $\mu m$ ) and ruby (0.69  $\mu m$ ) laser radiation, in pulses with duration of a few ns.

This analysis shows that for those crystals of NaCl, KCl and KBr having the highest damage thresholds, the avalanche ionization can be responsible for laser damage in the range of  $\lambda = 0.69 - 10.6 \mu m$ . This conclusion is supported by a rather good agreement between the theory and the experiment for the frequency dependence of the damage threshold over that frequency range at room temperatures and for the temperature dependence in the 100°K to 800°K range at high frequencies ( $\lambda = 1.06 \mu m$  and 0.69  $\mu m$ ). However, the theory does not explain the temperature dependence of the damage thresholds observed above 300°K at low frequency ( $\lambda = 10.6 \mu m$ ).

It is shown that at  $\lambda = 0.53 \mu m$ , the laser damage of alkali halide crystals is not explained by avalanche ionization, and it is probably attributed to multiphoton ionization.

For the other crystals investigated (in particular, for  $Al_2O_3$ , NaF, and LiF with high damage thresholds) the observed frequency and temperature dependence of the damage threshold at  $\lambda = 0.69 \mu m$  and  $\lambda = 1.06 \mu m$  do not correspond to values predicted by avalanche ionization theory. The question of the nature of the damage mechanism of these crystals is still open.

Finally, we shall discuss the previously published results on the dominant role of avalanche ionization in laser damage of the alkali halides and some other crystals. The qualitative arguments on which this conclusion was based, are shown not to be confirmed by our data, which was obtained in more detailed experiments, and analyzed using a consistent theory of avalanche ionization.

Key words: Laser damage; avalanche ionization; optical materials; damage thresholds; temperature dependence of damage thresholds.

## 1. Introduction

Electron avalanche as a laser damage mechanism of transparent solids has been discussed for over 10 years. It has been assumed that the process of avalanche ionization should be basic, and that it defines the limiting resistance of pure transparent materials to laser radiation in the nanosecond range of pulse durations. However, in spite of the rather large number of theoretical and experimental efforts which were devoted to this process, the question of whether electron avalanche is the effective damage mechanism of real optical materials was open, up to now. The reason was, that an adequate experimental study supported by a consistent theory of electron avalanche in solids was not undertaken.

Early experimental studies were restricted to measurement of the damage threshold in somewhat accidental experimental conditions (often using multimode lasers), and by quantitative analysis based on insufficiently adequate theoretical models.

Later on, more careful and informative measurements have been carried out in appropriate experimental conditions which resulted in more reliable and reproducible data (using single-mode lasers, and taking



into consideration the effects of self-focusing and absorbing inclusions). However, lack of sufficiently full and appropriate experimental data, as well as a consistent theory of the avalanche ionization process in solids did not, until recently, allow one to make well-founded conclusions on the role of this mechanism in laser damage. This, we believe, refers also to some recently published papers of American, Japanese and Soviet authors [1-6] in which it was claimed that in the alkali halide crystals investigated, intrinsic damage caused by electron avalanche ionization has been observed. Research carried out at the Lebedev Institute has shown that the qualitative arguments on which the quoted authors based their conclusions are not confirmed by more complete experimental data and an adequate theoretical analysis. In our experiments, we proceeded from the basic assumption that for a well-founded solution of the avalanche mechanism problem in laser damage, it is necessary to develop a consistent theory, which could give not only the numerical estimate of the damage thresholds, but what is more important, makes it possible to elucidate which characteristic features, specific to the mechanism, should be investigated experimentally. The developed theory [8-10] shows that the dependence of the damage threshold on frequency, pulse duration and initial temperature of the sample turned out to be characteristic for the avalanche mechanism. We studied these dependences for a great number of alkali halides, and other crystals used in laser optics (such as sapphire, YAG.Nd<sup>3+</sup>, LiIO<sub>3</sub>, SiO<sub>2</sub>) at the CO<sub>2</sub>, Nd:YAG and ruby fundamental laser frequencies, and at the second harmonic of the Nd:YAG laser in a wide temperature range (100 to 1000°K). The analysis of the experimental data on the basis of our developed theory has allowed us to make, for the first time, well-founded conclusions regarding the role of electron avalanche in laser damage.

The main results of our theoretical and experimental investigation as well as a comparison with data from the other work mentioned above are given below.

## 2. Theory

The problem of determining a critical field (or threshold intensity) of laser radiation producing a breakdown in a transparent dielectric, caused by a process of impact ionization, reduces to that of finding the electron avalanche rate  $\gamma(E)$  as a function of the electric field  $E$ , and of defining a physically adequate damage criterion. An effective procedure for finding  $\gamma(E)$  has been given by Epifanov [8]. It is based on the solution of quantum kinetic equation for the electron energy distribution function  $f(\epsilon, t)$ , which has the following form:

$$\frac{\partial f(p, t)}{\partial t} = \frac{2\pi}{h} \sum_q B^2(q) \sum_{n=-\infty}^{\infty} J_n^2 \left( \frac{eEq\tau(p)}{\hbar m \Omega (1 + \Omega^2 \tau^2(p))^{\frac{1}{2}}} \right) \{ [f(p+q)(N_q+1) - f(p)N_q] \delta(\epsilon(p+q) - \epsilon(p) + \hbar\omega_q - \hbar n \Omega) + [f(p+q)N_q - f(p)(N_q+1)] \delta(\epsilon(p+q) - \epsilon(p) + \hbar\omega_q - \hbar n \Omega) \} \quad (1)$$

$$+ [f(p+q)N_q - f(p)(N_q+1)] \delta(\epsilon(p+q) - \epsilon(p) + \hbar\omega_q - \hbar n \Omega) \} .$$

The damage criterion has been determined by consideration of the kinetics of lattice heating due to absorption of the electromagnetic field energy by free electrons, which is described as follows:

$$\frac{\partial T}{\partial t} = \beta T^{3/2} N, \quad \frac{\partial N}{\partial t} = \gamma N \quad (2)$$

The following designations were used in (1) and (2):  $e$  and  $m$  are the electron charge and mass, respectively.  $E$  and  $\Omega$  are the strength and frequency of electromagnetic field.  $P(\epsilon)$  is the momentum of an electron with energy  $\epsilon$ .  $B(q)$  is the matrix element of the electron-phonon interaction.  $N_q$  is the number of phonons with wave vector  $q$ ,  $\hbar\omega_q$  is the phonon energy,  $\tau(\epsilon)$  is the relaxation time for the longitudinal component of electron momentum in zero field, and  $T$  is the lattice temperature.

Following this research we have considered [9, 10, 7] the electron avalanche process in detail, taking into account in electron-phonon scattering, both acoustic and optical phonons. As a result, rather simple formulas have been obtained for the critical field. They describe the characteristic properties of electric breakdown in solids in a wide range of frequency from zero (the dc field) up to the frequency of visible light. Formulas in the case of electron scattering by acoustic phonons\* for various ranges of radiation frequencies and lattice temperatures are written as follows:

\*Allowance for scattering by optical phonons for typical crystal materials only slightly changes the  $E_c$  value.

$$E_c^2 = \frac{6\epsilon I m^2 V_s^2}{k T \epsilon^2} \left( \Omega^2 + \frac{I}{m l_{ac}^2} \right), \quad \hbar \Omega < \bar{\epsilon}, \quad T > T_n \quad (3)$$

$$E_c^2 = \frac{3(\hbar \Omega)^2 m^2 V_s^2}{k T \epsilon^2 \epsilon I} \left[ \operatorname{ch} \left( \frac{\hbar \Omega}{\epsilon I} \right) - 1 \right]_1^{-1} \quad \Omega \tau \gg 1, \quad T > T_n \quad (4)$$

$$E_c^2 = \frac{15 m V_s (2 m I)^{\frac{1}{2}}}{2 \epsilon^2} \left( \Omega^2 + \frac{2 I}{5 m l_{ac}^2} \right) \quad \hbar \Omega < \bar{\epsilon}, \quad T < T_n \quad (5)$$

$$E_c^2 = \frac{15 m V_s \sqrt{2 m I} (\hbar \Omega)^2 \Omega^2}{\gamma \epsilon I^2 \epsilon^2} \left[ \operatorname{ch} \left( \frac{\hbar \Omega}{\epsilon I} \right) - 1 \right]_1^{-1} \quad \Omega \tau \gg 1, \quad T < T_n \quad (6)$$

Here  $\epsilon$  is the parameter related to the damage criterion  $\gamma t_p = L$  by

$$\epsilon^{-1} = \ln \left( \frac{t_p}{L \theta} \right),$$

where  $t_p$  is the radiation pulse duration, and  $L$  and  $\theta$  are parameters whose numerical values typically are  $L \approx 15$ , and  $\theta \approx 4 \cdot 10^{-15}$  sec [10]. A transient temperature  $T_n$  separating the high and low temperatures regions is determined by the relation:

$$T_n = \frac{1}{2} V_s \sqrt{2 m I}$$

where  $V_s$  is the sound velocity in the crystal, and  $I$  is the ionization energy. Other values in (3) - (6) have the following meanings:  $\bar{\epsilon} \approx \epsilon I$  is the average electron energy,  $l_{ac}$  - is the free path of an electron with the energy of  $\epsilon = I$ . Formulas (3) - (6) are justified in the frequency range of  $\Omega \leq I / \hbar$ . For higher frequencies one must use a numerical solution of the kinetic equation.

From the given formulas it is evident, that the fundamental laws of the avalanche ionization process which can be used for experimental confirmation of its role in laser damage give rise to specific dependences of the critical field on frequency and pulse duration and on the temperature of the sample.

The frequency dependence of the critical field has a rather complex, non-monotonic form. It remains practically constant with field frequency, up to  $\Omega \approx V_{eff}$ , it grows, at first rapidly, then more slowly. (see fig. 1).

Our theory predicts very specific features for the temperature dependence of the critical fields. It is quite different in the two cases when the field frequency is higher or lower than the electron-phonon collision frequency, as it is shown in fig. 2.

The dependence of  $E_c$  on the pulse duration in the whole region where the developed theory is applicable ( $t_p = 10^{-7}$ - $10^{-11}$  sec) turns out to be very weak.

The indicated characteristics, which are predicted by avalanche ionization theory, have been used for experimental elucidation of the question of whether laser damage in optical materials is associated with electron avalanche for nanosecond light pulse duration. The frequency and temperature dependence of the damage thresholds were studied most carefully.

### 3. Experimental Results and discussion

In the experiments we have used the TEM<sub>00</sub> single-mode CO<sub>2</sub>, Nd:YAG<sup>3+</sup> and ruby lasers as well as the Nd:YAG laser with frequency doubling in a LiIO<sub>3</sub> crystal. The output characteristics of the lasers are represented in Table 1.



To produce bulk damage, the laser beam was focused into the sample by short focal length lenses. The spatial intensity distribution in the local plane of the lens was carefully measured. [7] It was close to gaussian at all laser frequencies used. Table 2 shows measured focal spot diameters (at the level of  $1/e$  of maximum intensity).

In the experiments, the effects of lens and sample aberration, optical inhomogeneity of the crystal and self-focusing were controlled. These effects proved to be negligible under our experimental conditions, which gives us assurance that the real damage threshold intensity is being measured. Such assurance is important in reaching reliable conclusions on damage mechanisms, because it is based on a quantitative comparison of the thresholds measured in experiments with widely varied parameters, such as radiation frequency and sample temperature. Measurement errors in our experiments were about 40% for the threshold frequency dependences, and 10% for the temperature dependence and relative threshold values of different samples at fixed laser parameters.

Similarly, to obtain reliable data, the experiments were conducted with a great number of crystal samples. Thus, for NaCl, we have investigated more than 100 samples grown by different techniques. These experiments showed that from sample to sample there are considerable variations of the damage threshold, indicating impurity effects.

As an example fig. 3 represents a distribution function of the damage thresholds of crystal samples of NaCl measured at the Nd:YAG laser frequency, at room temperature. The majority of samples are seen to fall into the range corresponding to a rather low optical resistance. There are some samples having a much higher threshold, which appears to be a limiting value. Note that in previously published work such high damage thresholds of NaCl were not reported, and the values represented by our first group of samples were typical. [1-6]

Investigation of the damage mechanism in low-threshold and high-threshold samples has shown that for the former, the temperature dependence of the threshold behaves typically in a non-reproducible fashion, which, in general, does not correspond to that predicted by electron avalanche theory. Figure 4 shows some typical examples of the temperature dependence, at the ruby laser frequency, for NaCl crystals. While investigating the reason for this temperature dependence non-reproducibility the effect of thermal strengthening was observed. At all frequencies under investigation except the  $\text{CO}_2$ -laser, for many samples of NaCl, KCl, and KBr, the damage thresholds increased considerably with appropriate thermal treatment, in which the sample was held for a long time at high temperature close to the melting point, followed by rapid cooling. This effect is more pronounced for the samples with low initial thresholds. The samples with maximum damage resistance are not affected by the thermal treatment. This effect of thermal strengthening is reversible. Thus, prestrengthened crystals after long annealing return to their initial threshold values.

The analysis of the described thermal effects, in the case of laser damage of low-threshold samples, showed that the latter involved the influence of impurity atoms in the crystals. Impurity clusters in a crystal can be either formed or dispersed, depending on the thermal treatment i.e., heating duration and cooling rate, and this can substantially affect the damage threshold.

The study of the frequency dependence of the damage threshold has shown that it has a considerably different character for various samples. One observes either an increase, constancy, or a decrease of the threshold with increasing frequency. Constancy or a decreasing threshold are observed, as a rule, for low-threshold samples. Figure 5 illustrates the frequency dependence observed for several NaCl samples. Obviously, the observed variation of the frequency dependence of the damage threshold, like the anomalies in temperature dependence, arises from the influence of impurities and absorbing defects.

The temperature and frequency dependence typical of intrinsic damage can be expected in samples with the highest damage thresholds at all frequencies, without thermal treatment. Accordingly, we have especially selected samples of NaCl, KCl, KBr, CsI, NaF, LiF and  $\text{Al}_2\text{O}_3$  with the desired properties, and carefully studied the temperature and frequency dependence of their damage thresholds. The damage thresholds observed for these samples at  $T \sim 300^\circ\text{K}$  are shown in table 3. For NaCl, KCl, KBr, and CsI, the observed dependence on frequency and temperature proved to be similar, and to agree qualitatively with those predicted by avalanche ionization theory, as it is seen from the data for NaCl shown in figs. 6 and 7. In fact, in the wavelength range of 10.6 to 0.69  $\mu\text{m}$ , one observes an increase of the damage threshold as well as a change of the temperature dependence character, with an increase in laser frequency. Temperature dependence is practically absent at  $\lambda = 10.6 \mu\text{m}$ , while at  $\lambda = 1.06 \mu\text{m}$  and 0.69  $\mu\text{m}$  the damage thresholds drop with increasing temperature. This allows us to assume that in the selected, high-threshold samples of alkali-halide crystals, laser breakdown is due to electron avalanche. To support this assumption, we have analyzed the experimental data on the frequency and temperature dependence by more careful and quantitative comparison with theory. The comparison has shown that there is rather good agreement between the theory and experiment for the frequency dependence of damage thresholds from 10.6  $\mu\text{m}$  to 0.69  $\mu\text{m}$ , at room temperature, if for the electron-phonon collision frequency, one assumes certain values, which seem to be rather reasonable. For NaCl crystals, as an example, the collision frequency has been found to be equal to  $6 \times 10^{14} \text{ sec}^{-1}$ . This number fits the theory and experiment rather well for both the frequency dependence of the damage threshold in the range from



10.6  $\mu\text{m}$  and 0.69  $\mu\text{m}$  at room temperature, and the temperature dependence of the thresholds observed at the wavelengths 1.06  $\mu\text{m}$  and 0.69  $\mu\text{m}$ . It gives also absolute values of the critical field, estimated from formulas (3) - (6), which are very close to the thresholds measured at 1.06  $\mu\text{m}$ . However, the collision frequency magnitude of  $6.10^{14} \text{sec}^{-1}$  does not correspond to the temperature independence of the damage threshold observed at 10.6  $\mu\text{m}$  (see fig. 7). In this case the condition  $\Omega < \nu_{\text{eff}}$  is satisfied, and hence the damage threshold should rise with increasing temperature above 200°K. We have not yet a good explanation, supported by consistent theoretical considerations, or confirmed by appropriate experiment, for this disagreement between theory and experiment. It is reasonable to note here that the temperature independence of the critical field for dc breakdown previously observed [12], is also not readily explained. One may suppose that the dc case and low optical frequency case arise from similar causes. It is obvious that further theoretical and experimental studies have to be carried out to clarify the peculiarity of low frequency breakdown.

Another result which also cannot be explained in terms of avalanche theory is the temperature independence of the threshold observed for alkali halide crystals at 0.53  $\mu\text{m}$ . (fig. 7). For that wavelength, the condition  $\Omega > \nu_{\text{eff}}$  is definitely fulfilled, and according to the avalanche theory, the damage threshold has to be a decreasing function of temperature above 200-300°K. One can reasonably suppose that at this high laser frequency, damage is associated with the multiphoton ionization mechanism, rather than with the electron avalanche process.

We have also found that experimental data obtained on the temperature dependence of damage thresholds for NaF, LiF and  $\text{Al}_2\text{O}_3$  crystals, over the range of wavelengths investigated (1.06  $\mu\text{m}$ , 0.69  $\mu\text{m}$  and 0.53  $\mu\text{m}$ ), are not fully explained by avalanche ionization theory. Thus, damage thresholds of NaF and LiF at 1.06  $\mu\text{m}$  and 0.69  $\mu\text{m}$  are practically independent of temperature, but for the avalanche mechanism such a situation can take place only in a very narrow frequency region, when  $\Omega \approx \nu_{\text{eff}}$ . For sapphire, one observes frequency independence of the damage threshold in the whole range investigated at  $T = 300^\circ\text{K}$  (see table 3), as well as a decrease in threshold with temperature at  $T = 300^\circ\text{K}$ , at all frequencies. Such dependences do not agree with the prediction of avalanche theory. Thus, the nature of the laser damage mechanism in these crystals is still an open question.

We have also analyzed data obtained previously [1-6] on laser damage of alkali halide crystals, and compare them with our results. Such an analysis has led us to a conclusion that the simple arguments on which the authors of these cited papers based their conclusions about the avalanche damage mechanism of the crystals investigated, are not confirmed by our data. For example, the lack of dependence of the threshold on frequency up to  $\Omega = 2.7 \cdot 10^{15} \text{sec}^{-1}$  ( $\lambda = 0.69 \mu\text{m}$ ) [3,4] or even up to  $\Omega = 5.4 \times 10^{15} \text{sec}^{-1}$  ( $\lambda = 0.35 \mu\text{m}$ ) [6] was taken as one of the decisive arguments in favor of the avalanche mechanism. But as we have shown, such independence indicates that the avalanche mechanism has not been realized, since it is typical of samples with relatively low optical resistance. In high threshold samples, as has been discussed above, the frequency dependence (increase) of the damage threshold is already observed on going from  $\lambda = 10.6 \mu\text{m}$  to  $\lambda = 1.06 \mu\text{m}$ , corresponding to the condition  $\Omega > \nu_{\text{eff}}$  for frequencies higher than that of the Nd laser. This condition is additionally confirmed by the character of the temperature dependence, as discussed above. Figure 8 illustrates the divergence of data on the frequency dependence of damage thresholds in NaCl, obtained by three groups: Lebedev Physical Institute, Moscow State University, and Harvard University. It seems likely that the lower thresholds measured at Moscow State University and Harvard University are associated with the effects of impurities and absorbing inclusions in their samples.

Some authors have claimed [4, 6] that they succeeded rather confidently in distinguishing between inclusion and intrinsic damage by morphological studies. Detailed investigation carried out in our laboratory by Gorshkov [11] showed, however, that a damage morphology observation could not be used as test of intrinsic damage. This is illustrated by the following experimental fact. In the samples with rather high optical resistance, the damage character is found not to change, even with considerable variation of the damage threshold. (For example, for LiF at 1.06  $\mu\text{m}$ , from  $1 \times 10^{11} \text{W/cm}^2$ ). The damage observed in these cases was similar to that referred to previously as intrinsic.

#### 4. Conclusion

The results discussed in this paper show that the problem of avalanche mechanism in laser damage is very complex, and a well-founded conclusion on its role in real crystals can only be made based on detailed investigation of the fundamental damage characteristics, and by comparison with an adequate theory. The experimental data, analyzed on the basis of a consistent theory of avalanche ionization in solids, obtained by solution of the quantum kinetic equation, shows that in those alkali halide crystals with high damage thresholds, electron avalanche is the probable mechanism of laser damage for nano-second light pulses in the wavelength range of 10.6  $\mu\text{m}$  to 0.69  $\mu\text{m}$ . The theory satisfactorily explains most of the observed characteristics concerning the frequency and temperature dependence of the damage threshold, and yield reasonable magnitudes of the principal parameter, the electron-phonon collision frequency. However, the theory does not explain all the experimental data concerning the frequency

TABLE 1.

## CHARACTERISTICS OF LASERS USED IN DAMAGE EXPERIMENTS

Laser	Wave length ( $\mu\text{m}$ )	Output Energy (mj)	Pulse duration (nsec)
CO <sub>2</sub>	10.6	60	60
Nd:YAG	1.06	15	1.5-15
Ruby	0.69	25	10
Nd:YAG with LiIO <sub>3</sub> frequency doubler	0.53	2.5	8

TABLE 2.

FOCAL SPOT DIAMETER ( $\mu\text{m}$ ) AT 1/e IN INTENSITY

Wavelength( $\mu\text{m}$ )	10.6	1.06	0.69	0.53
Focal length (mm)				
15	-	4.6	3.6	4.0
38	-	12	10	11
100	51	-	-	-

TABLE 3.

ROOM TEMPERATURE DAMAGE THRESHOLDS ( $\times 10^{10} \text{ w/cm}^2$ )

Wavelength ( $\mu\text{m}$ )	Pulse Width (nsec)	NaCl	KCl	KBr	CsI	NaF	LiF	Al <sub>2</sub> O <sub>3</sub>
0.53	8	13	2.5*	6	0.9	9	24	40
0.69	10	15	8	5.8	1.1	14	36	40
1.06	10	12	7	5	1.2	14	36	40
10.6	60	2.5	0.1	1.2	0.05*	-	-	-

\* There is some indication that the thresholds marked are not the highest at particular frequencies.

and temperature dependence over the whole range studied. A further development of the theory, which will consider, in particular, the real structure of the conduction band of dielectrics is required to explain the remaining disagreement.

Thus, the results discussed in this paper show that the problem of avalanche ionization as a laser damage mechanism proves to be more complex than previously assumed. It becomes clearer, however, since more detailed and informative experimental data and sufficiently developed theory are available, that further investigation is necessary to solve this problem, which is important both for physics, and for high power laser engineering.

## 5. References

- [1] Yablonovitch, E., App. Phys. Lett., 19, 495 (1971).
- [2] Fradin, D. W., Yablonovich, E. and Bass, M., Appl. Opt., 12, 700 (1973).
- [3] Fradin, D. W. and Bass, M., NBS Spec. Pub. 387, 225, (1973).
- [4] Bloembergen, N., IEEE J. Quant. Electr., QE-10, 375 (1974).
- [5] Yosojima, Y., Ohmari, Y., Okumura, N., and Inuishi, Y., Jap. J. Appl. Phys., 14, 815 (1975).
- [6] Aleshkevich, V. A., Akhmanov, S. A., Zhdanov, B. V., Kovrigin, A. I., Kuznetsov, V. I., and Sukhorukov, A. P., Zhurnal tekhnicheskoi fiziki, 46, 1693 (1976). [Soviet Physics, Technical Physics 21, 975 (1976)].
- [7] Gorshkov, B. A., Danileiko, Yu. K., Epifanov, A. D., Lobachev, V. A., Manenkov, A. A., and Sidorin, A. V., JETP, 72, 1171 (1977). [Translation to be published].
- [8] Epifanov, A. S., JETP, 67, 1805, (1974). [Soviet Physics JETP 40, 897 (1975)].
- [9] Epifanov, A. S., Manenkov, A. A., Prokhorov, Prokhorov, A. M., JETP Pis'ma, 21, 483 (1975). [JETP Letters, 21, 223 (1975)].
- [10] Epifanov, A. S., Manenkov, A. A., Prokhorov, A. M., JETP, 70, 728 (1976). [Soviet Physics JETP, 43, 377 (1976)].
- [11] Gorshkov, B. G., Thesis, P. N. Lebedev Physical Institute (1977).
- [12] Kuchin, V. D., FTT (Fizika tverdogo tela), 1, 450 (1959). [Soviet Physics, Solid State 1, 406 (1959)].

## 6. Figures

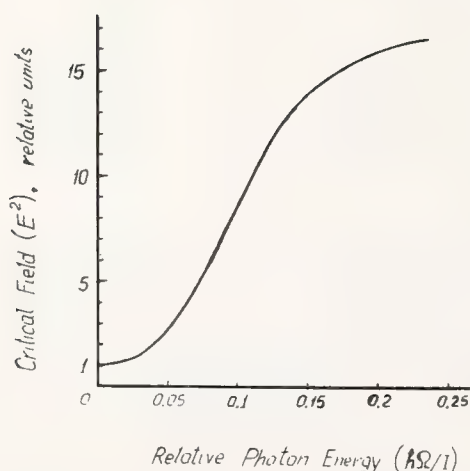


Figure 1. Dependence of critical field upon radiation frequency as predicted by avalanche ionization theory. A collision frequency of  $6 \times 10^{14} \text{ sec}^{-1}$  has been taken in the calculations.

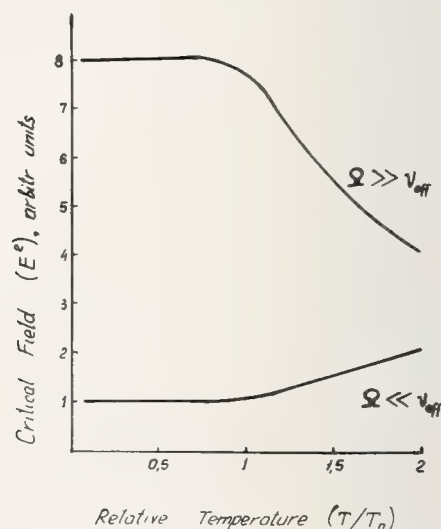


Figure 2. Dependence of critical field on lattice temperature in two limits where the radiation frequency,  $\Omega$ , is much greater or much less than the electron-phonon collision frequency,  $\nu_{\text{eff}}$ .



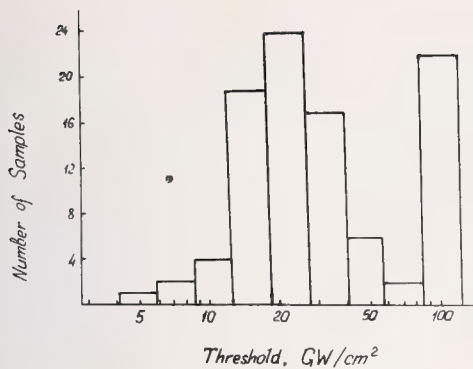


Figure 3. Distribution of laser damage thresholds at 1.06  $\mu\text{m}$  for NaCl samples.

Figure 4. Temperature dependence of damage threshold for three ordinary samples of NaCl.

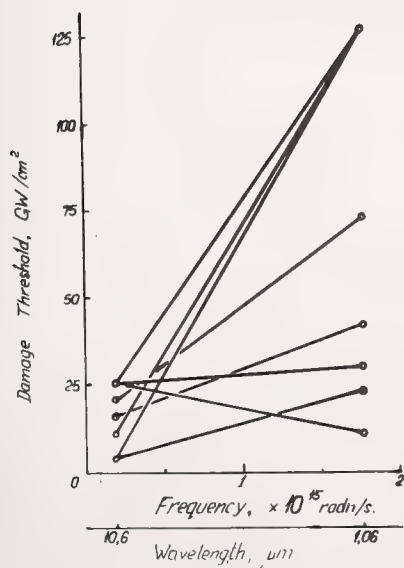
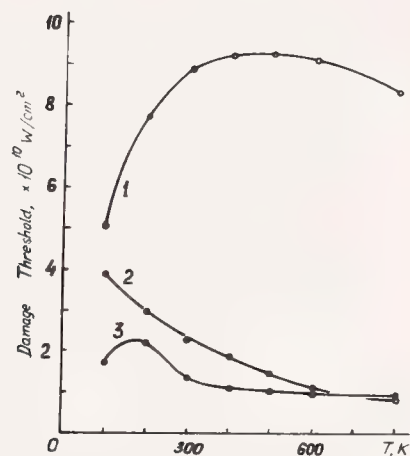


Figure 5. Damage thresholds of several ordinary samples of NaCl at the Nd:YAG<sup>3+</sup> and ruby laser wavelengths.

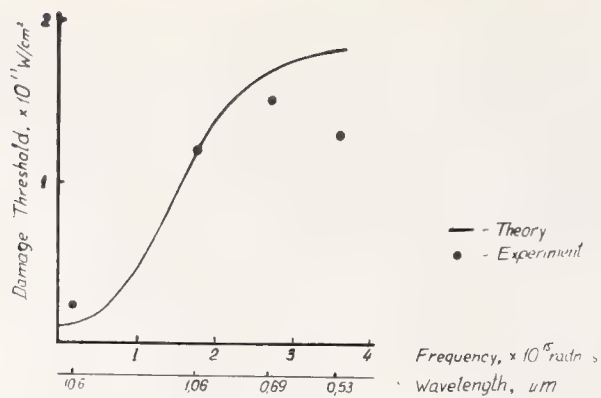


Figure 6. Frequency dependence of damage threshold for selected high optical resistance samples of NaCl at  $T = 300^\circ\text{K}$  (experiment and theory).

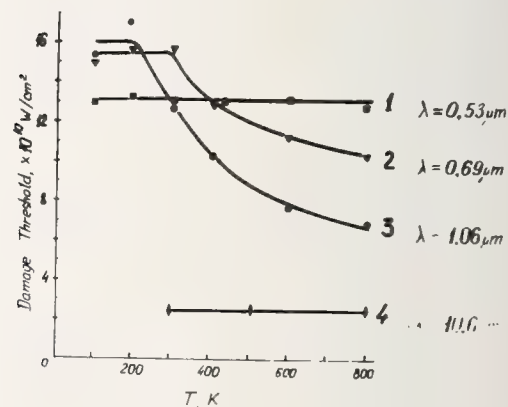


Figure 7. Temperature dependences of damage threshold for selected high optical resistance samples of NaCl at various frequencies.

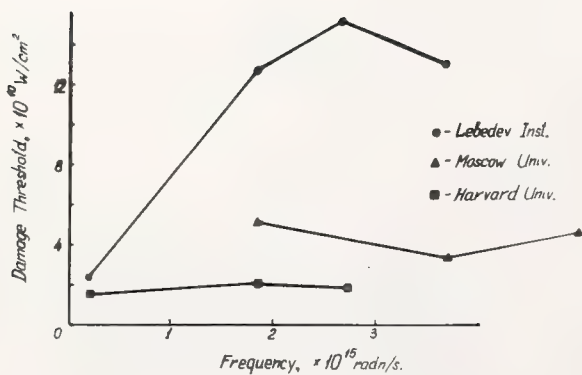


Figure 8. Dependence of damage threshold upon frequency for NaCl after measurements by three research groups: Lebedev Institute [7], Moscow University [6], and Harvard University [3,4].

#### COMMENTS ON PAPER BY MANENKOV

The speaker justified the neglect of heat transport in the theoretical model by arguing that for nanosecond pulses the distance in which heat could be expected to diffuse, using room temperature diffusion coefficients, was on the order of  $10^{-4}$  centimeters, much smaller than the focal volume. Lee Smith of LLL pointed out that experiments done with picosecond pulses show that the incipient plasma that originally forms in the breakdown process is only of a few  $\mu\text{m}$  in dimension, and therefore that heat transport over distances of the order of a  $\mu\text{m}$  could be significant in the early stages of the formation of the plasma. In addition it should be noted that the presence of conduction electrons in large numbers in the vicinity of the breakdown may also increase the thermal diffusion coefficient. In continuing discussion of the pulse length dependence question, the speaker indicated that in experiments he had carried out using YAG laser irradiation, only a very weak pulse duration dependence was seen for the breakdown threshold in very pure materials.



# MULTIPHOTON THEORY OF OPTICAL BREAKDOWN IN ALKALI HALIDES

A. Schmid and P. Kelly  
Division of Physics  
National Research Council of Canada  
Ottawa, Ontario K1A 0R1

and

P. Bräunlich  
Department of Physics  
Washington State University  
Pullman, Washington, 99163

A theory of optical breakdown in dielectrics is presented; based on multi-photon carrier generation and energy transfer from the radiation field to the lattice via polaron-photon absorption. This mechanism represents a clear alternative to avalanche breakdown models as no lattice impact ionization is involved. Breakdown field strengths calculated for various laser pulse lengths and frequencies, are fully corrected for the nonlinear refractive index  $n_2$  as well as for contributions to the refractive index resulting from a sharp increase in polaron density during a damaging pulse.

Key words: Breakdown flux and field strength; frequency dependence; intrinsic laser damage; linear and non-linear refractive indices; multiphoton absorption; polaron; pulse length dependence.

On behalf of my colleagues Drs. Peter Bräunlich and Ansgar Schmid of Washington State University, I will present the main points of our new theory of optical breakdown in the Alkali Halides. A further description will be published shortly<sup>1</sup>.

Basically we will show that intrinsic damage is caused by polaron joule heating. It is necessary, then, to define criteria for intrinsic breakdown.

As in the past<sup>2</sup> we find it useful to represent the temporal profile of a laser pulse by the relation

$$F = A^* \sin^2 (\pi t / \tau_p)$$

with  $\tau_p$  the pulse duration. We consider that breakdown occurs at the peak of the pulse i.e., when  $t = \tau_p/2$  such that  $F = A_B^*$  when a small volume of material has reached its melting point  $T_M$ .

Band-to-band excitation of electrons can take place by single or multiphoton absorption. Consider an initially empty conduction band  $n_c(0) = 0$  and a full valence band  $n_v(0) \approx 10^{22} \text{ cm}^{-3}$ . If  $\sigma_M$  is the generalized absorption cross section then the conduction band concentration is given by

$$n_c(t) = n_v(0) \cdot \left[ 1 - \exp\left(-\sigma_M \int_0^t F^M dt\right) \right]$$

An electron generated in this manner carries with it a lattice polarization field. It is necessary to consider in some detail the polaron, the composite particle of electron and phonon field, and its interaction with photons and the lattice. Multiphoton absorption by polarons has received much attention and most recently Pokatilov and Fomin<sup>3</sup> have derived expressions of the total absorption coefficient,  $K$ , for a variety of interaction mechanisms using the path integral method of Feynman et al<sup>4</sup>.

In anticipation of our results let me point out that when one considers a photon-polaron-phonon interaction whether it be with acoustical or optical modes the dominant term ( $\geq 99\%$ ) in

$$K = \sum_{N=1}^{\infty} K_N$$

is that for single photon absorption so  $K \simeq K_1$ , and aside from material parameters

$$K \simeq K_1 (T, n_c, \hbar\omega, \hbar\omega_0, V, E^2)$$

where  $\hbar\omega$  is the laser photon energy,  $\hbar\omega_0$  the respective phonon energy (dispersion is ignored),  $E$  the RMS local field intensity and  $V$  depends on the optical coupling constant  $\alpha$  or on the deformation potential constant  $\mathcal{E}_1$  dependent on the mode involved (Note well, the presence of  $E^2$ ). Generally, the local refractive index  $n_r$ , contains a non-linear contribution for high fields i.e.

$$n_r = n_o + n_2 E^2$$

where  $n_o$  is the linear refractive index (Again note the presence of  $E^2$ ).

In general the local field strength is unknown although it is related to the flux since, with  $c$  a constant, one has

$$E^2 = cF/(\lambda n_r)$$

, preceding terms in  $E^2$  can be related to the Flux.

It remains then to ascertain the effect of a large polaron concentration on  $n_o$  and then to compute the temperature rise of the sample produced by polaron joule heating since

$$dT/dt = F.K. \hbar\omega/\rho c_o$$

with  $c_o$  the specific heat and  $\rho$  the mass density.

Quite generally, the permittivity of Alkali Halides consists of a polaron contribution and a lattice contribution i.e.,

$$\mathcal{E}(\omega) \equiv \mathcal{E}_p(\omega) + \mathcal{E}_L(\omega) \equiv \mathcal{E}_1(\omega) + i\mathcal{E}_{II}(\omega)$$

The lattice contribution is given by

$$\epsilon_L(\omega) = \epsilon_\infty \frac{(\omega_1^2 - \omega^2 - i\gamma\omega)}{(\omega_t^2 - \omega^2 - i\gamma\omega)}$$

where  $\gamma$  is the damping parameter for optical vibration (and is considered negligibly small).

In the case of optical phonons the phonon contribution has been analyzed by Gurevich et al<sup>5</sup> in the limit of small coupling resulting in

$$\epsilon_p(\omega) \equiv \epsilon_{p1} + i\epsilon_{p2} = 4\pi i \sigma(\omega) / \omega$$

where the real part of the conductivity is given by<sup>5</sup>

$$R \sigma(\omega) = \left( \frac{2n_c e^2}{3m\omega_o} \right) \left( \frac{\omega_o}{\omega} \right)^{5/2} \left( 1 - \frac{\omega_o}{\omega} \right)^{1/2}$$

We have followed their procedure but we have replaced the matrix element for free-electron optical phonon scattering by that for free-electron acoustical phonon scattering and obtained

$$R \sigma(\omega) = \frac{e^2 \mathcal{E}_1^2}{3\pi^2} \frac{(kTm)^{1/2}}{\rho U_s^2} \left( 1 - \frac{\omega_o}{\omega} \right)^2 (\exp(\hbar\omega_o/kT) + 1)$$

where  $U_s$  is the speed of sound. In either case,

$$\text{Im } \sigma(\omega) = n_c e^2 / m\omega$$

The linear refractive index is then given by

$$n_o = \frac{1}{2} \sqrt{\epsilon_1 + \sqrt{\epsilon_1^2 + \epsilon_{11}^2}}$$

### Results

A comparison of optical and acoustical modes of scattering, with all the parameters the same except for the interaction term,  $V$ , shows that the dominant mechanism in NaCl is photon-polaron-acoustic phonon scattering.

Figure 1 shows the behaviour of the local refractive index as a function of time for a 30 psec Ruby pulse. The insert illustrates the self-focussing effect,  $n_2 E^2$  and the self-defocusing effect due to the rapid increase in polaron concentration,  $n_c$ . The corresponding temperature increase is also included.

Since in general the value of the refractive index has not been measured in damage experiments we show in figure 2 the breakdown Flux vs  $\tau_p^{-1}$ . The slopes are here given by  $(M+1)/2$  where  $M$  is the order of the multiphoton generation term. Please note that we used the smallest values of  $\sigma_M$  available in the literature.

Since we know the refractive index we can compute  $E_B$  and in figure 3 we show  $E_B$  vs  $\tau_p^{-1}$ . Now, at least in the nanosecond regime, the slopes are given by  $(M+1)$ . The ND line shows a large deviation from linearity.

Figure 4 illustrates the frequency dependence of the breakdown flux for different pulse lengths and in figure 5 we show the nanosecond behaviour of  $E_B$  vs  $\hbar\omega$  and compare it with existing experimental data.

In conclusion, then, we have presented a theory which fits experiment and which is a clear alternative to the avalanche mechanism.

### References

- |  |  |
|--|--|
| (1) Schmid, A., Kelly, P. and Bräunlich, P.<br>to be published (Phys. Rev. B Nov 15, 1977) | (4) Feynman, R. Hellwarth, R., Iddings, C. and<br>Platzman, P. Phys. Rev. <u>127</u> , 1004 (1962) |
| (2) Bräunlich, P., Schmid, A. and Kelly, P.<br>Appl. Phys. Lett. <u>26</u> , 150 (1975)    | (5) Gurevich, V., Lang, I. and Firsov, Y.<br>Sov. Phys. - Solid State <u>4</u> , 918 (1962)        |
| (3) Pokatilov, E. and Fomin, V.<br>Phys. Stat. Solidi, B <u>73</u> , 553 (1976)            |  |



# Figures

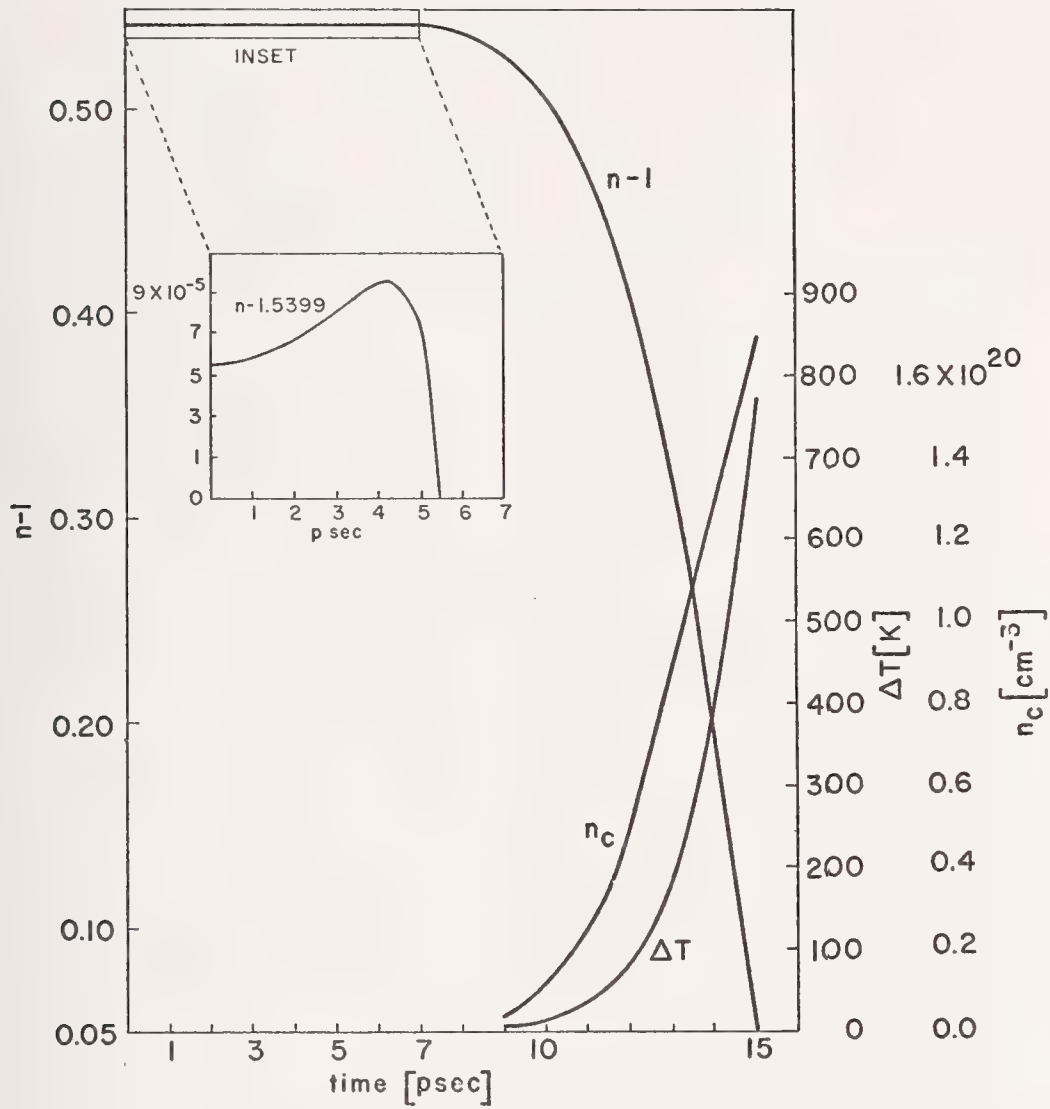


Figure 1. Time evolution of the refractive index  $n$ , the density of polarons  $n_c$  and the temperature  $\Delta T = T - 300^\circ\text{K}$  during a 30 psec ruby laser pulse of the form  $F = 8.4 \times 10^{29} \sin^2(\pi t/t_p) [\text{photons cm}^{-2}\text{sec}^{-1}]$  for which breakdown occurs at  $t = t_p/2 = 15$  psec. The insert shows details of the initial increase of the refractive index due to the non-linear refractive index  $n_2$ .

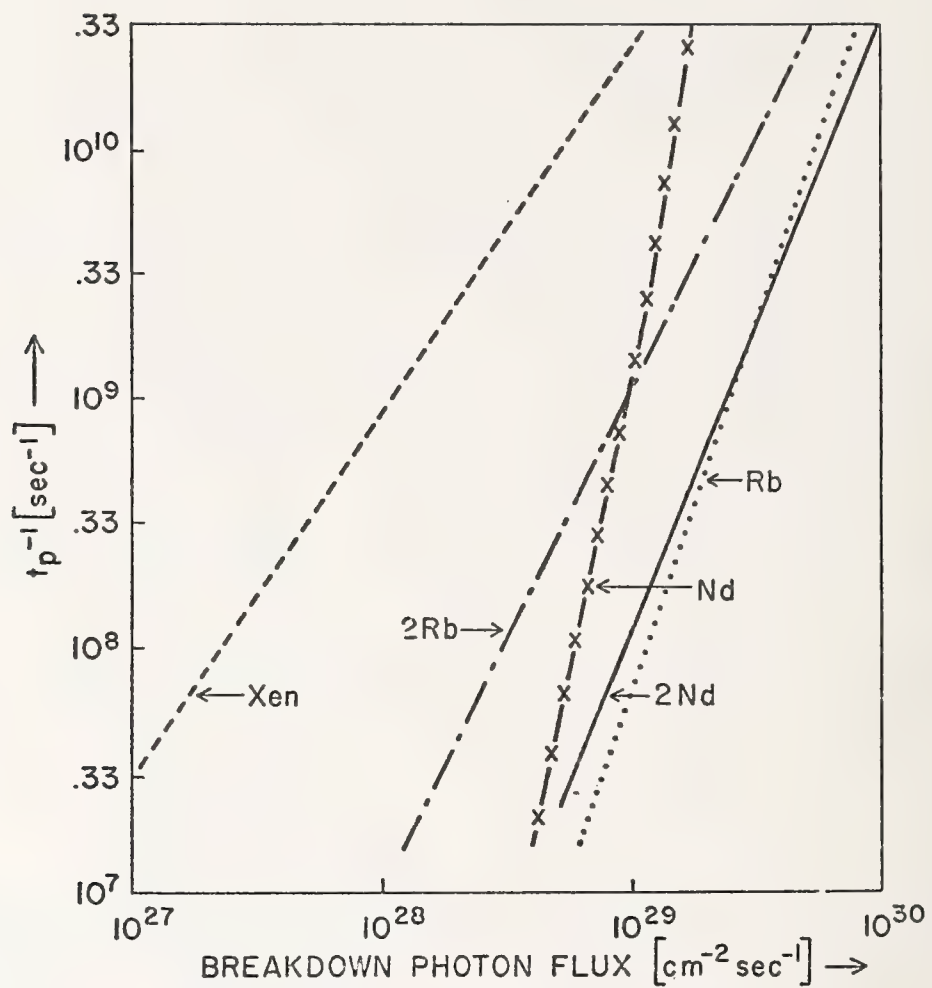


Figure 2 . Breakdown photon flux  $A_B^*$  in NaCl vs. inverse laser pulse length.

$t_p^{-1}$  calculated for different laser frequencies:

Nd: neodymium laser frequency

2Nd: doubled frequency of neodymium laser

Rb: ruby laser frequency

2Rb: doubled frequency of ruby laser

Xen: xenon laser frequency

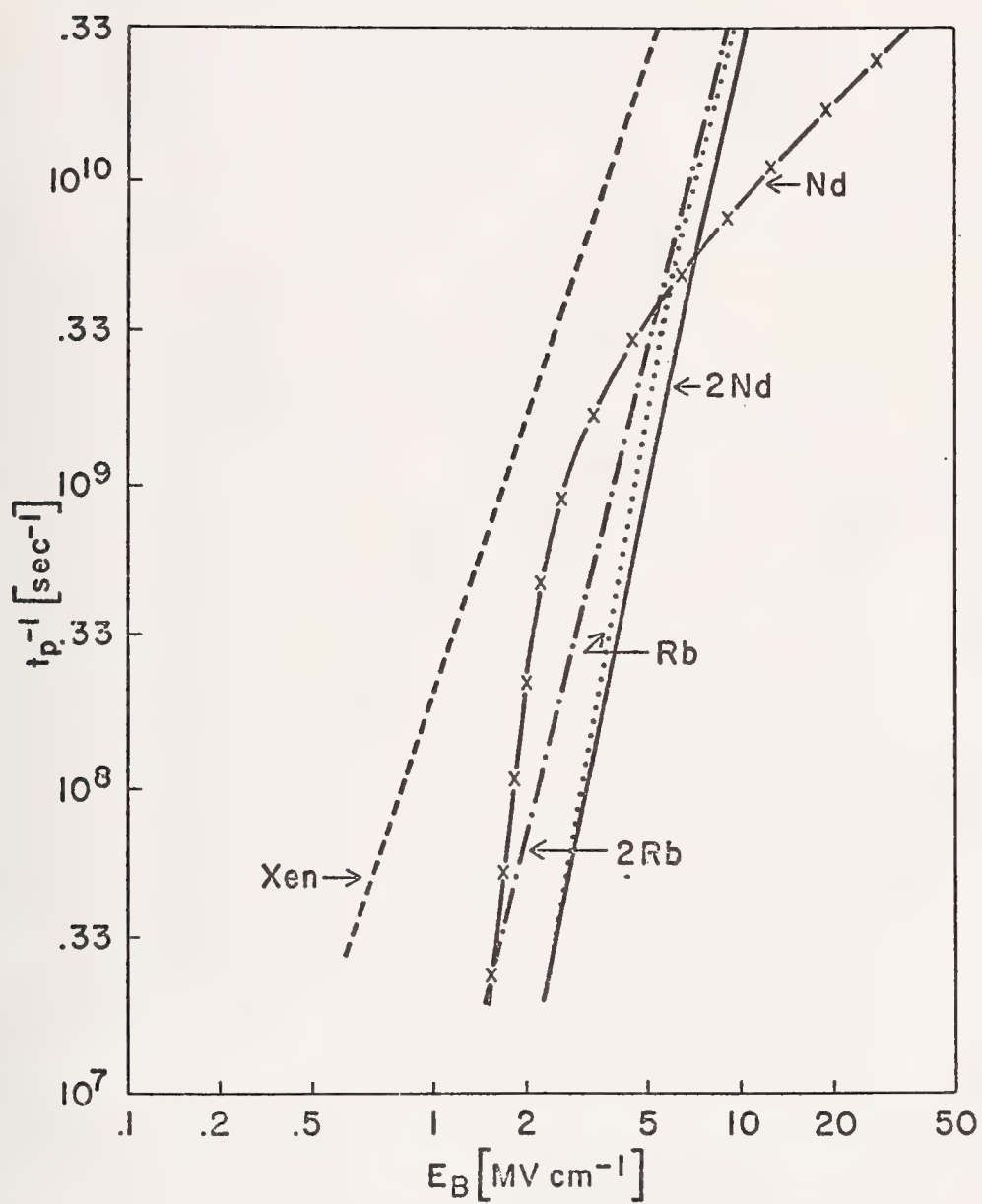


Figure 3. Breakdown field strengths  $E_B$  under the same conditions as in figure 2.



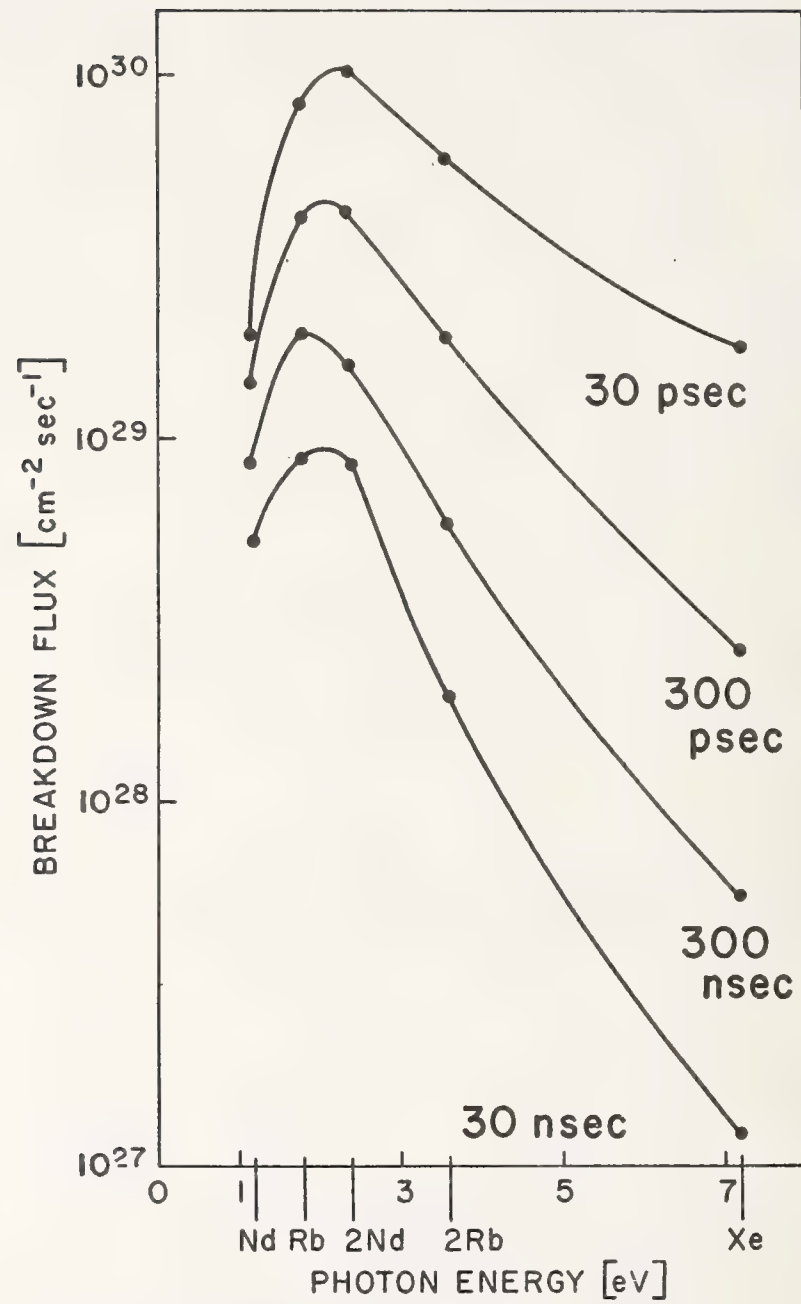


Figure 4. Breakdown flux  $A_B^*$  in NaCl vs. the energy of the laser photons for different pulse length  $t_p$ .

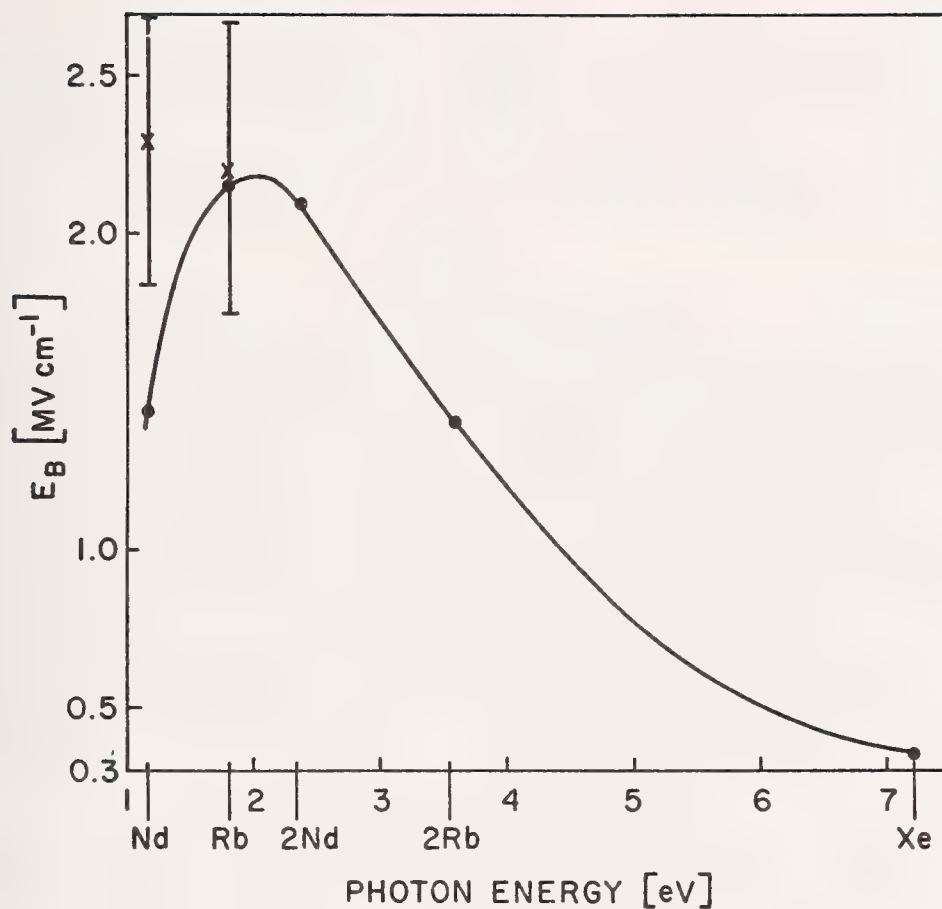


Figure 5. Breakdown field strength  $E_B$  in NaCl vs. photon energy for a  $t_p = 60$  nsec pulse. Experimental data from D.W. Fradin Harvard Univ. Tech. report No. 643, 1973 (ONR-372-0012) unpublished.

#### COMMENTS ON PAPER BY SCHMID, KELLY, AND BRAUNLICH

*It was generally agreed that in order to take full account of spatial effects a much more sophisticated calculation would be required. The authors indicated that in this calculation they were only interested in the temporal development of the ionization, and that they are presently extending their calculation to include spatial effects, including propagation through an ionized region of finite extent.*

# THE ROLE OF CARRIER DIFFUSION IN LASER DAMAGE OF SEMICONDUCTOR MATERIALS

M. Kruer, L. Esterowitz, F. Bartoli and R. Allen  
Naval Research Laboratory  
Washington, D. C. 20375

The role of carrier diffusion in laser damage of semiconductors is investigated for various laser wavelengths. The results indicate that carrier diffusion significantly affects the magnitude of the damage threshold when the optical absorption coefficient is greater than  $10^5 \text{ cm}^{-1}$ .

Key words: Laser damage; semiconductor damage; carrier diffusion; time dependence; wavelength dependence.

## 1. Introduction

The response of a semiconductor to laser pulses depends on the optical, thermal, and electronic properties of the semiconductor as well as the wavelength, duration, intensity and spatial characteristics of the laser radiation. If the photon energy is larger than the bandgap, the irradiated surface undergoes thermal damage when the laser flux is increased beyond some threshold value. In this paper such thresholds are analyzed to determine the role of carrier diffusion in laser damage of semiconductors. Thresholds for surface melting are examined since the experimental criteria for damage is well defined, the threshold temperature is accurately known and the data analysis is not complicated by phase changes. A thermal analysis is performed to calculate melting thresholds as a function of irradiation time. To investigate the role of carrier diffusion in laser damage in semiconductors it is desirable to analyze threshold data for laser pulses sufficiently short that thermal diffusion effects can be neglected. For such pulse durations, the material is heated to a depth  $\delta$  determined by the optical absorption depth and the carrier diffusion distance [1]<sup>1</sup>. The carrier diffusion distance, however, is not well known under the conditions of laser damage since both the diffusion coefficient and lifetime decrease during laser heating. Similarly the optical absorption coefficient can change for photon energies equal to or less than the bandgap, because of band shifting or free carrier effects. In this work  $\delta$  was treated as an adjustable parameter in the analysis and obtained empirically from experimental thresholds.

## 2. Thermal Analysis

We consider a homogeneous semiconductor irradiated by a Gaussian laser beam of the form:  $P(r) = P_0 \exp(-2r^2/R^2)$ . We assume that values of the material properties may be treated as constants. These are to be considered "effective values" over the wide range of temperatures and carrier densities encountered during laser heating. If heat does not diffuse to the edges of the material, the thresholds can be approximated using a thermal model in which the sample is treated as a semi-infinite solid. We have shown previously that the power density threshold  $P_0$  as a function of irradiation time  $\tau$  can be approximated by the expression [2]:

$$P_0 = E_{\Delta T} \left[ \frac{1}{\tau} + \frac{(2\pi)^{1/2} k}{R \delta \tan^{-1} (8k\tau/R^2)^{1/2}} \right] \quad (1)$$

where  $k$  is the thermal diffusivity and  $\delta$  the depth of material heated in the absence of thermal conduction. The  $\tau$ -independent value  $E_{\Delta T}$  is simply the energy density required to raise the crystal surface to the melting temperature assuming thermal conduction is negligible. Its value is given by:  $E_{\Delta T} = \Delta T \rho c \delta / (1-R')$  where  $\rho$  is the density,  $c$  the specific heat,  $R'$  the reflectance, and  $\Delta T$  is the difference between the melting temperature and ambient temperature. The energy density threshold is obtained using the expression:  $E_0 = P_0 \tau$ . The values of the parameters used to evaluate the model for all materials discussed in this paper are given in table 1.

---

1. Figures in brackets indicate the literature references at the end of this paper.



Table 1. Material properties of selected semiconductors.

Property	Germanium	Silicon	InSb
Density, $\rho$ (g/cm <sup>3</sup> )	5.33 [3]	2.33 [7]	5.78 [8]
Specific heat, $c$ (J/g - K)	0.4 [3]	0.72 [7]	0.26 [8]
Thermal Conductivity, $K$ (W/cm-K)	0.2 [4,5]	0.33 [4,7]	0.08 [4,9]
Melting Temperature, $T_m$ (°K)	1210 [3]	1683 [7]	788 [8]
Heat of Fusion, $H_m$ (J/g)	467 [3]	1650 [7]	---
Vaporization Temperature, $T_v$ (°K)	3107 [3]	3060 [7]	---
Heat of Vaporization, $H_v$ (J/g)	3921 [3]	10600 [7]	---
Reflectivity, $R'$ $\lambda = 0.69 \mu\text{m}$	0.43 [6]	0.3 [7]	0.46 [8]
$\lambda = 1.06 \mu\text{m}$	0.38 [6]	0.3 [7]	0.35 [8]
$\lambda = 10.6 \mu\text{m}$	---	---	0.35 [8]
Radius of laser beam, $R$ (cm)	0.045	0.085	0.054

### 3. Presentation of Results

#### 3.1 Germanium

Damage in germanium has been studied extensively with 0.69  $\mu\text{m}$  and 1.06  $\mu\text{m}$  lasers [10-14]. Thresholds for melting are plotted as a function of  $\tau$  in figure 1. Melting thresholds at short times were obtained by monitoring the sample reflectance which increases abruptly at the melting point [15]. The thresholds at 0.69  $\mu\text{m}$  are represented by circles in figure 1. The scatter in the data is not much larger than the experimental uncertainty which is often as large as  $\pm 30\%$ . The scatter is attributed to differences in samples and in criteria for threshold. Thresholds for 1.06  $\mu\text{m}$  radiation are presented as triangles in figure 1 and are approximately equal to the 0.69  $\mu\text{m}$  thresholds. The curve is obtained by fitting eq. (1) to the data using  $\delta$  as an adjustable parameter. The model describes the time dependence of the damage thresholds quite accurately. The value of  $\delta$  was found to be 0.5  $\mu\text{m}$  for both 0.69  $\mu\text{m}$  and 1.06  $\mu\text{m}$ .

The optical absorption depth ( $\alpha^{-1}$ ) of germanium at room temperature and low optical flux levels is presented in figure 2 as a function of wavelength. The values of  $\delta$  obtained from the damage thresholds are plotted as filled circles. The value of  $\delta$  at 0.69  $\mu\text{m}$  is about 5 times  $\alpha^{-1}$  while the value of  $\delta$  at 1.06  $\mu\text{m}$  is approximately equal to  $\alpha^{-1}$ . The difference between  $\delta$  and  $\alpha^{-1}$  at 0.69  $\mu\text{m}$  is attributed to carrier diffusion. This difference cannot be due to saturation of the optical absorption because saturation should not occur at such low flux levels. Studies of the optical absorption at 1.06  $\mu\text{m}$  using picosecond laser pulses show no deviations in linearity for flux densities below  $9 \times 10^8 \text{ W/cm}^2$  [16]. The absorption at 0.69  $\mu\text{m}$  is expected to saturate at even higher flux levels.

#### 3.2 Indium Antimonide

Laser damage thresholds of ambient temperature indium antimonide [17-20] are plotted as a function of irradiation time in figure 3. The thresholds at 0.69  $\mu\text{m}$  (circles), 5  $\mu\text{m}$  (triangles) and 10.6  $\mu\text{m}$  (squares) correspond to surface melting [21]. The thresholds at short irradiation times were determined from the abrupt increase in sample reflectance which occurs at melting. For long irradiation times, the thresholds were obtained by microscopic examination of the damaged surface. The damage thresholds for short irradiation times increase with laser wavelength as shown in figure 3. Equation (1) was fit to the 5  $\mu\text{m}$  thresholds with  $\delta$  used as an adjustable parameter. As shown in figure 3, the calculated thresholds agree with the experimental data. Using the same values of the material parameters, thresholds were calculated for 0.69  $\mu\text{m}$  and 10.6  $\mu\text{m}$  by varying  $\delta$  to obtain agreement with the data. The values of  $\delta$  obtained in this way were 0.8, 30 and 50  $\mu\text{m}$  for laser wavelengths of 0.69  $\mu\text{m}$ , 5  $\mu\text{m}$  and 10.6  $\mu\text{m}$  respectively.

The empirical values of  $\delta$  for InSb are compared to  $\alpha^{-1}$  as a function of wavelength in figure 4. The value of  $\delta$  at 0.69  $\mu\text{m}$  is almost an order of magnitude larger than  $\alpha^{-1}$ . Since the absorption depth at 0.69  $\mu\text{m}$  is expected to remain constant during irradiation, this difference is attributed to carrier diffusion. We conclude from the data that the diffusion distance is approximately 0.8  $\mu\text{m}$ . The value of  $\delta$  for 5  $\mu\text{m}$  radiation (i.e. 30  $\mu\text{m}$ ) is much larger than  $\alpha^{-1}$ . However this value is much greater than the diffusion distance (0.8  $\mu\text{m}$ ) and hence cannot be related to carrier diffusion. The 30  $\mu\text{m}$  value of  $\delta$  results from an increase in the absorption depth due to the Burstein effect. The Burstein effect is observed at 5  $\mu\text{m}$  in InSb at flux levels less than  $10^4 \text{ W/cm}^2$  [22]. The value of  $\delta$  at 10.6  $\mu\text{m}$  is much less than  $\alpha^{-1}$  indicating that the optical absorptance increases greatly during laser heating. Increases in the absorptance of InSb at 10.6  $\mu\text{m}$  due to free carriers have been observed [23] previously using lower flux levels for which sample heating was negligible. Here the optical absorptance at 10.6  $\mu\text{m}$

is further increased by shifting of the band-edge to longer wavelengths as the temperature increases. Since the value of  $\delta$  at 10.6  $\mu\text{m}$  is much larger than the diffusion distance obtained above, carrier diffusion does not significantly affect the damage thresholds.

### 3.3 Silicon

The melting thresholds of silicon [24-31] are plotted as a function of irradiation time in figure 5 for 0.69  $\mu\text{m}$  (circles) and 1.06  $\mu\text{m}$  (triangles) radiation. The theoretical curves were obtained from eq. (1) using the material properties in table 1 and varying  $\delta$  to fit the data at short irradiation times. The values of  $\delta$  were found to be 3  $\mu\text{m}$  and 200  $\mu\text{m}$  for 0.69  $\mu\text{m}$  and 1.06  $\mu\text{m}$  radiation respectively. These empirical values of  $\delta$  are compared to  $\alpha^{-1}$  as a function of wavelength in figure 6. The values of  $\delta$  and  $\alpha^{-1}$  are approximately equal at both 0.69  $\mu\text{m}$  and 1.06  $\mu\text{m}$ . These results imply that at these wavelengths the absorptance of silicon does not change appreciably during laser irradiation and that carrier diffusion does not significantly affect the damage thresholds. Grinberg, et al. have shown previously by direct measurements that the absorptance of silicon at 1.06  $\mu\text{m}$  remains essentially constant as the incident laser flux is increased to the damage level [25].

### 3.4 Other Semiconductors

The value of  $\delta$  determined here for gallium arsenide irradiated by 0.69  $\mu\text{m}$  radiation is 0.26  $\mu\text{m}$  which is about twice  $\alpha^{-1}$ . Measurements of photoconductivity and absorption by nonequilibrium carriers in GaAs excited by 0.69  $\mu\text{m}$  radiation show that the thickness of the layer containing nonequilibrium carriers is 0.3  $\mu\text{m}$  [1]. These results indicate that carrier diffusion must be considered in calculating damage thresholds of GaAs at 0.69  $\mu\text{m}$ . The values of  $\delta$  that we determined from the thresholds of HgCdTe and PbSnTe at 10.6  $\mu\text{m}$  are both  $10^{-3}$  cm. For these materials  $\delta = \alpha^{-1}$  at 10.6  $\mu\text{m}$  and the damage thresholds do not show effects of carrier diffusion.

## 4. Discussion

The comparisons of  $\delta$  and  $\alpha^{-1}$  for the semiconductors studied here show that  $\delta$  is equal to the optical absorption depth when  $\alpha$  is significantly less than  $10^5 \text{ cm}^{-1}$ . When  $\alpha \gtrsim 10^5 \text{ cm}^{-1}$ ,  $\delta$  can be greater than the absorption depth due to carrier diffusion. If  $\delta \gg \alpha^{-1}$ , then  $\delta$  is approximately the carrier diffusion distance. Values of diffusion distances were found to be on the order of 0.5  $\mu\text{m}$ . The carrier diffusion distance  $L_D$  is approximately given by the expression  $L_D = \sqrt{Dt_c}$  where  $D$  is the ambipolar diffusion coefficient and  $t_c$  is the carrier lifetime. Previous studies have assumed that carrier diffusion distances of the order of 1 mm determine the thresholds for laser damage in semiconductors [32,33]. These large distances are obtained when the expression for  $L_D$  is evaluated using initial values of the material parameters (e.g., For Si:  $D = 16 \text{ cm}^2 \text{ s}^{-1}$ ,  $t_c = 10^{-3} \text{ s}$ ). However the values of  $D$  and  $t_c$  in a semiconductor heated by laser radiation are expected to differ from those of the unexposed material. The high carrier densities generated by the in-band laser radiation shorten the carrier lifetime due to Auger recombination [34,35]. Recombination rates approaching  $10^{10} \text{ s}^{-1}$  have been measured when carrier densities of  $10^{20} \text{ cm}^{-3}$  are generated by short laser pulses which produce little heating [16]. These high recombination rates imply small carrier diffusion distances. For laser heating the diffusion distance is further reduced since both  $D$  and  $t_c$  decrease with increasing temperature.

## 5. Conclusion

The threshold laser flux for thermal damage in opaque semiconductors agrees with the predictions of the thermal model discussed for pulse durations between  $10^{-8}$  s and several seconds. The model assumes that the material is heated to a depth  $\delta$  for pulse durations sufficiently short that thermal conduction is insignificant. The magnitudes of the experimental damage thresholds indicate that  $\delta$  can be greater than the optical absorption depth if  $\alpha \gtrsim 10^5 \text{ cm}^{-1}$ . This is attributed to carrier diffusion. When  $\alpha$  is appreciably greater than  $10^5 \text{ cm}^{-1}$ ,  $\delta$  equals the carrier diffusion distance. For the materials investigated diffusion distances were found to be on the order of 0.5  $\mu\text{m}$ .

## 6. References

- [1] L.M. Blinov, V.S. Vavilov and G.N. Gaikin, Sov. Phys. - Semicond., 1(9), 1124 (1967).
- [2] F. Bartoli, L. Esterowitz, M. Kruer and R. Allen, J. Appl. Phys. 46(10), 4519 (1975).
- [3] *Handbook of Electronic Materials*, 5, M. Neuberger, (IFI/Plenum, Washington, 1971).

- [4] Determined empirically from the damage thresholds of large samples at long irradiation times. The procedure is discussed in detail in ref. 23. Second reference included in the brackets shows the temperature dependence of K.
- [5] *American Institute of Physics Handbook*, Ed. by D.E. Gray (McGraw-Hill, New York, 1972), pp 4-154.
- [6] *Handbook of Electronic Materials*, 1, A.J. Moses (IFI/Plenum, Washington, 1971).
- [7] *Silicon*, M. Neuberger and S.J. Welles (National Technical Information Service, Springfield, VA, 1969).
- [8] *Handbook of Electronic Materials*, 2, M. Neuberger (IFI/Plenum, New York, 1971), p 77.
- [9] *Thermophysical Properties of Matter*, 10, Y.S. Touloukian, R.W. Powell, C.Y. Ho and Nicolaou (IFI/Plenum, New York, 1974) p 370.
- [10] M. Birnbaum and T.L. Stocker, J. Appl. Phys. 39(13), 6032 (1968).
- [11] L.M. Blinov, V.S. Vavilov, and G.N. Galkin, Sov. Phys. Solid State, 9(3), 666 (1967).
- [12] M. Bertolotti, L. Stagni, and G. Vitali, J. Appl. Phys. 42(13), 5893 (1971).
- [13] L. Muzii, L. Stagni, and G. Vitali, Nuovo Cimento, 14(2), 173 (1973).
- [14] A.M. Bonch Bruevich, V.P. Kovalev, G.S. Romanov, Ya. A. Imas and M.N. Libenson, Sov. Phys. Tech. Phys., 13(4), 507 (1968).
- [15] J.N. Hodgson, Phil. Mag. 6, 509 (1961).
- [16] D.H. Auston, C.V. Shank and P. LeFur, Phys. Rev. Lett., 35(15), 1022 (1975).
- [17] M. Birnbaum and T.L. Stocker, J. Appl. Phys. 39(13), 6032 (1968).
- [18] M. Kruer, L. Esterowitz, R. Allen and F. Bartoli, Infr. Phys., 16, 375 (1976).
- [19] R.E. Slusher, W. Giriot and S.R. J. Brueck, Phys. Rev. 183(3), 758 (1969).
- [20] M. Kruer, L. Esterowitz, R. Allen and F. Bartoli, unpublished results on InSb at 0.69  $\mu\text{m}$  and 10.6  $\mu\text{m}$ .
- [21] We include a 10.6  $\mu\text{m}$  threshold for sparking in a vacuum. Since InSb decomposes in a vacuum only 20K above its melting temperature, this threshold is approximately equal to the threshold for melting.
- [22] The Burstein Effect in InSb at 5  $\mu\text{m}$  is discussed by A.V. Nurmikko, Opt. Comm. 16(3), 365 (1976). For laser heating the increase in absorption depth is partially counteracted by the temperature increase which shifts the bandgap to longer wavelengths.
- [23] H.J. Fossum, W.S. Chen, and B. Ancker-Johnson, Phys. Rev. B, 8(6), 2857 (1973).
- [24] M. Kruer, R. Allen, L. Esterowitz, and F. Bartoli, Opt. and Quant. Elect., 8, 453 (1976).
- [25] A.A. Grinberg, R.F. Mekhtieo, S.M. Ryvkin, V.M. Salmanov and I.D. Yaroshetskii, Sov. Phys. Sol. State 9, 1085 (1967).
- [26] Y. Matsuoka, J. Phys. D. 9, 215 (1976).
- [27] S.M. Bedair and H.P. Smith, J. Appl. Phys. 40, 4776 (1969).
- [28] Y. Matsuoka and A. Usami, J. Phys. D. 7, 1259 (1974).
- [29] M. Bertolatti, F. Depasquale, P. Marietti, D. Setti and G. Vitali, J. Appl. Phys. 38, 4088 (1967).
- [30] Y. Matsuoka and A. Usami, Appl. Phys. Lett. 25(10), 574 (1974).
- [31] M. Birnbaum and T.L. Stocker, J. Appl. Phys., 39(13), 6032 (1968).
- [32] Y. Matsuoka, A. Usami and K. Shimazaki, J. Phys. D (Appl. Phys.) 8, 1L (1975).
- [33] L. Stagni, Appl. Phys. 12, 31 (1977)
- [34] L.M. Blinov, E.A. Bobrova, V.S. Vavilov and G.N. Galkin, Sov. Phys. Sol. State 9(11), 2537 (1968).
- [35] N.G. Nilsson, Phys. Scripta 8, 165 (1973).

## 8. Figures



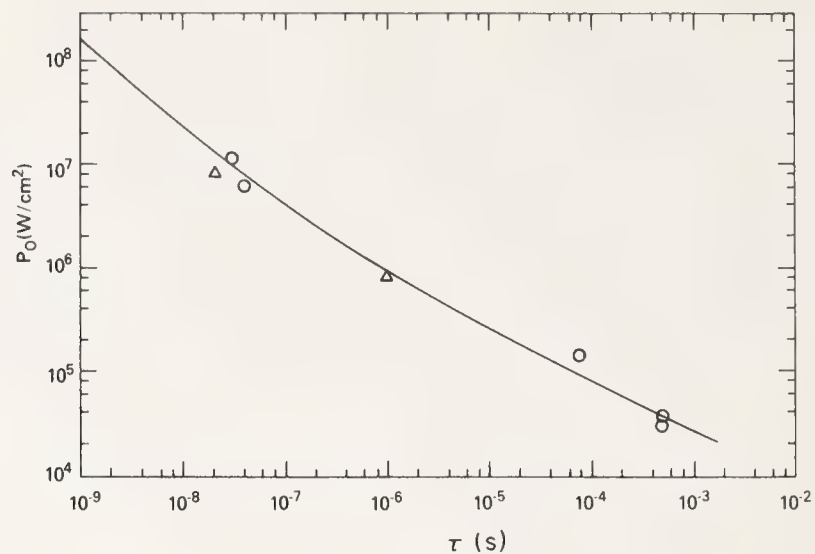


Fig. 1. Damage thresholds of germanium as a function of irradiation time. Curve A is threshold for melting and curve B is threshold for vaporization.

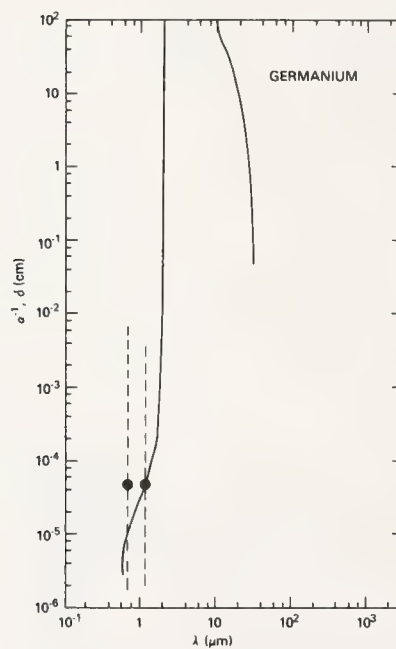


Fig. 2. A comparison of  $\alpha^{-1}$  and  $\delta$  for germanium as a function of wavelength.

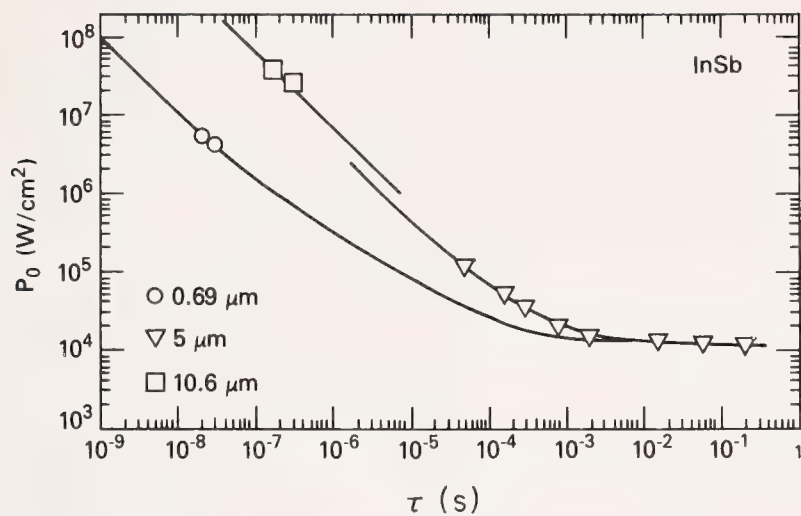


Fig. 3. Damage thresholds of indium antimonide as a function of irradiation time and laser wavelength.

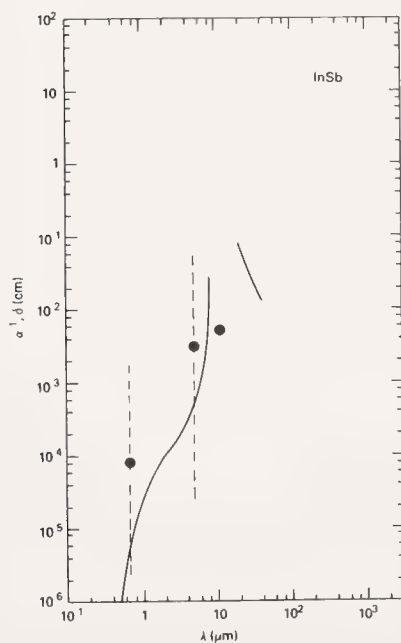


Fig. 4. A comparison of  $\alpha^{-1}$  and  $\delta$  for indium antimonide as a function of wavelength.

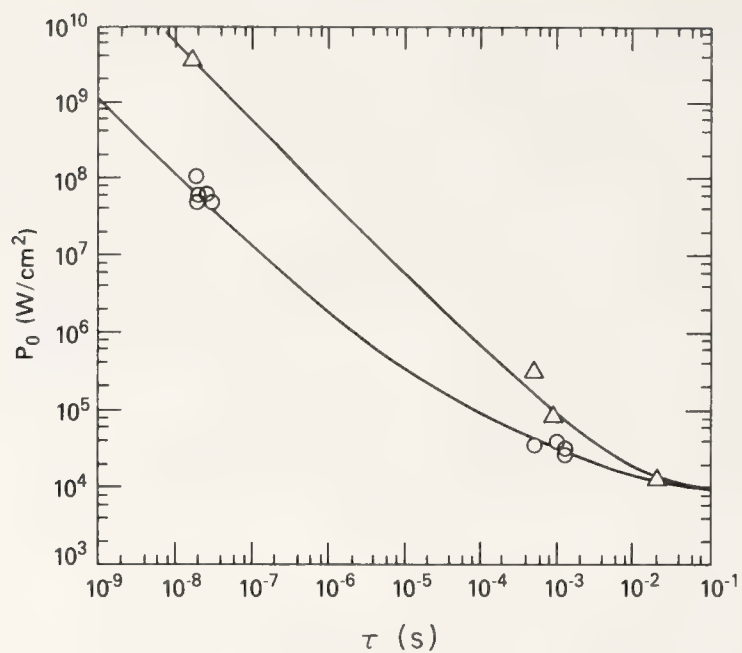


Fig. 5. Damage thresholds of silicon as a function of irradiation time. The circles and triangles represent experimental thresholds for 0.69  $\mu\text{m}$  and 1.06  $\mu\text{m}$  radiation respectively.

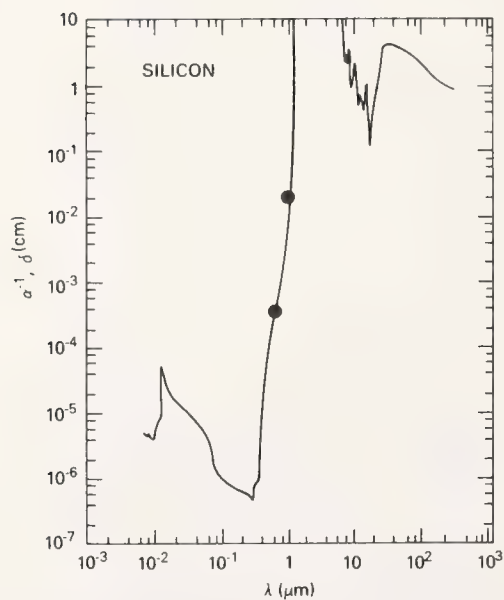


Fig. 6. A comparison of  $\alpha^{-1}$  and  $\delta$  for silicon as a function of wavelength.



COMMENTS ON PAPER BY KRUER, ESTEROWITZ, BARTOLI, AND ALLEN

*No discussion on this paper.*

MULTIPHOTON-INDUCED CONDUCTIVITY IN ULTRAVIOLET-TRANSMITTING MATERIALS 1. FREE CARRIER LIFETIME\*

R. T. Williams, P. H. Klein, and C. L. Marquardt  
Naval Research Laboratory  
Washington, D.C. 20375

Fast photoconductivity measurements are being used to characterize free-carrier recombination and trapping rates in insulators. Carriers are generated in these experiments by multiphoton absorption of a 20-ps, 347-nm laser pulse. At low carrier densities, lifetimes governed by extrinsic traps are measured to be typically 10-20 ns. Material preparation and subsequent treatment are shown to have measurable effects on carrier lifetime in the extrinsic limit. Published optical data are cited as evidence that the free carrier lifetime in alkali halides is strongly dependent on carrier concentration, changing from the extrinsic nanosecond range to less than 10 ps when the concentration is increased to about  $5 \times 10^{17}$  carriers per  $\text{cm}^3$ . Physical mechanisms giving concentration-dependent recombination times are discussed. An investigation by photoconductivity of the carrier concentration range intermediate between the two cases just cited has been attempted within limitations imposed on the present technique by space charge build-up.

Key words: Dielectrics; free carrier; laser damage; lifetime; multiphoton; ultraviolet; window materials.

### 1. Introduction

Free carriers are central to many of the failure modes of high energy laser windows and components, particularly those being considered for applications in the ultraviolet. As discussed by Sparks and Duthler [1,2]<sup>1</sup>, wavefront distortion in components subject to high optical flux can result from free-carrier contributions to the refractive index and from expansion associated with heating of the electron-hole plasma. If the heating is severe, and particularly if there is avalanche multiplication of free carriers, the material fails by fracture or melting. A key number entering calculations dealing with these failure modes is the time-dependent density of free carriers during the laser pulse. This is governed generally by a rate equation expressing a competition between source terms such as multiphoton absorption, impurity ionization, or avalanche ionization, and carrier loss terms associated with recombination and deep trapping. In recent discussions or calculations of failure thresholds by Bloembergen [3], Sparks and Duthler [4], and Braunlich, Schmid, and Kelly [5], the conduction electron lifetime due to recombination and trapping was assumed to be longer than most laser pulses and therefore the carrier loss term was neglected. Sparks and Duthler included carrier loss terms in a more recent calculation [2], but treated the conduction electron lifetime as a free parameter due to lack of experimental data for materials and temperatures of interest. Recombination times of  $10^{-2}$  to  $10^{-4}$  s in germanium were cited as an available example [2].

Catalano, Cingolani, and Minafra reported a conduction electron lifetime of about 1  $\mu\text{sec}$  in alkali halides at room temperature as measured in their experiments on multiphoton-induced photoconductivity [6]. This value was used as the constant carrier lifetime in their analysis of data on laser power dependence of integrated photocurrent. On the other hand, observations by Bradford, Williams, and Faust using picosecond optical spectroscopy of defect formation [7,8] and exciton formation and relaxation [8] in alkali halides following two-photon generation of free carriers yielded strong evidence that electron-hole recombination occurs in a few picoseconds or less when the initial carrier density is about  $5 \times 10^{17} \text{ cm}^{-3}$ . In comparison, laser damage typically involves carrier densities in the range  $10^{18}$ - $10^{19} \text{ cm}^{-3}$ . Resolution of this apparent conflict in experimental conduction electron lifetimes and progress toward an understanding of carrier annihilation under conditions of interest in laser damage were set as two of the early goals in the present study. This ordering of emphasis is also appropriate to the measurement of carrier generation cross sections by photoconductivity because the carrier lifetime must be known accurately under the relevant range of conditions if generation cross sections are to be deduced from the photoconductivity.

In addition to addressing fundamental questions of carrier lifetime and intrinsic multiphoton cross sections, photoconductivity may be developed as a diagnostic tool to be used in improving uv window materials for high-energy applications. The potential strength of this approach is that it focuses on parameters (free carrier generation and annihilation) which are known to be central to material failure. We are in the process of identifying extrinsic sources and traps with their specific effects on photoconductivity, where possible, and correlating these parameters with experimental failure thresholds to test predictive ability. The problem on which we have concentrated first is the demonstration of observable effects of material treatment and/or purity on carrier lifetime in wide-gap optical materials.

\*Work supported in part by the Advanced Research Projects Agency of the Department of Defense.

1. Figures in brackets indicate the literature references at the end of this paper.

## 2. Experiment

Although photoconductivity as a measurement technique has been developed to the point of routine technology in some classes of semiconductors, its application to extract the kind of information we want about insulators is comparatively undeveloped. The reason lies possibly in a lack of prior device motivation and in the special difficulties presented by insulators at the relatively high carrier densities encountered in failure of laser components. Problems include space charge effects, difficulty of bulk carrier generation by ordinary excitation, and short lifetimes in most of the materials studied at relevant carrier densities. Laser windows are not usually situated in a steady electric field, so ultimately we must be able to extract parameters of photo-carrier evolution in the limit of zero applied d.c. field but appropriate optical fields.

Several prior experiments on multiphoton conductivity of insulators, particularly alkali halides, have been carried out [6,9,10]. These usually involved low densities of carriers excited by a Q-switched laser pulse and did not deal extensively with the carrier lifetime. In the present work we used for excitation the second harmonic of a single 20-picosecond pulse from a mode-locked ruby laser, whose wavelength (347 nm) is reasonably close to that of the XeF\* laser (354 nm). The very short pulse permits both the resolution of shorter carrier lifetimes and the use of higher working intensities below thresholds for catastrophic failure.

The apparatus used in the present experiments is diagrammed in figure 1. The oscillator comprises a 3/8-inch Brewster-cut ruby rod in a 1.2-meter cavity with a 2.8-mm aperture selecting the lowest-order transverse mode. A contact cell with a flowing dye solution of DDI in methanol provides passive mode-locking. A single pulse is selected, amplified, and frequency-doubled (in KDP). The ultraviolet pulse then passes into the screen room where all electrical measurements are made. A pyro-electric energy meter samples the incoming uv beam and a photodiode registers the transmitted uv. Between shots, white light from a super-pressure mercury lamp is injected along the optical path, both to facilitate inspection of a magnified image of the sample for damage and to bleach trapped charges. The sample, typically 18 x 4 x 3 mm, is placed between electrodes in a shielded coaxial housing which can be flushed continuously with dry nitrogen. Light travels down the 18-mm dimension and a potential between 500 and 3000 v is applied across the shortest (~3 mm) dimension a few seconds before the laser shot. As shown in the enlarged view in figure 1, the sample was typically several millimeters longer and wider than the corresponding electrode dimensions so that the illuminated end surfaces and two side surfaces were outside the high-field region.

From known approximate mobilities, applied fields, and measured lifetimes, we find average carrier displacements of the order of  $10^{-3}$  cm or less for these experiments. Since the sample is not illuminated within about 0.5 mm of any electrode, the free charge reaching the contact areas is negligible. We are measuring charge induced on the electrodes by displacement current within the dielectric. Thus blocking contacts are appropriate. Experiments to date have utilized polished flat copper or brass electrodes pressed against the insulator sample surfaces. A thorough study of effects of specific electrodes and fused or evaporated contacts on the measurement of photoconductivity is planned. This must be investigated before we attempt to extract accurate multiphoton absorption coefficients because the nature of the contact and associated space charge is critical for deducing the true internal electric field, and because of the possibility of photo-injection from the electrodes. However, the present results on carrier lifetimes in regions of the sample well removed from the contacts should not depend significantly on the type of contact used.

We have made direct measurements of photocurrent using a Tektronix 7844 oscilloscope and 7A19 pre-amplifier for a rise time of about 0.8 ns. The data presented here are in the form of integrated photocurrent, measured by attaching a Hewlett-Packard 1120A active probe (500 MHz bandwidth) to the output electrode. From the known resistance to ground (e.g. 510 k $\Omega$ ) and the measured RC time constant for decay of the induced charge, the output capacitance to ground (integrating capacitor) was determined to be 3 pF. The ability to measure a photocharge rise time of 1 ns consistent with instrument bandwidth was verified experimentally.

## 3. Carrier Recombination

We have already cited the apparent discrepancy between microsecond lifetimes reported for free carriers created in alkali halides at relatively low density [6] and for picosecond recombination times for carriers at higher density [7,8]. The picosecond recombination times are indicated by short-pulse laser studies undertaken principally to elucidate processes of exciton relaxation and photochemical defect production in KCl, NaCl, and NaBr [7,8]. The efficiency for reaching a deep bound state of the electron-hole pair was found to be of order unity, and there was no evidence of continued reaction or recombination of free carriers beyond about ten picoseconds at room temperature. It is concluded that the observed recombination time is characteristic of essentially all free carriers at initial density  $5 \times 10^{17}$  cm $^{-3}$  in these halides [8]. Theoretical treatment of material failure requires an understanding of why the free-carrier lifetime decreases at high density, and in particular, the functional form specifying carrier lifetime at intermediate densities. Two possible mechanisms for a density-dependent free-carrier lifetime are outlined below.

### 3.1 Simple Kinetic Model

Consider an idealized semiconductor or insulator having a single type of recombination site and a single type of deep electron trap. Let  $n$  be the density of photo-generated free electrons and  $n_e$  be



the equilibrium density of electrons in the dark. Assume that all holes, generated as counterparts to free electrons, are trapped at recombination sites, and assume further that there is no re-ionization out of the recombination centers or deep electron traps. If  $n_0$  free electrons are initially created by an infinitely short optical pulse at time  $t = 0$ , then subsequent evolution of free electron concentration will be governed by a set of coupled differential equations.

$$\begin{aligned}\frac{dn}{dt} &= -v\sigma n(n_e + n_0 - n') - v\sigma_t n(n_t - n'') \\ \frac{dn'}{dt} &= +v\sigma n(n_e + n_0 - n')\end{aligned}\quad (1)$$

$$n = n_0 - n' - n''$$

Here  $v$  is the average thermal velocity of conduction electrons,  $\sigma$  and  $\sigma_t$  are the recombination and trapping cross sections, respectively,  $n'$  and  $n''$  are the numbers of conduction electrons annihilated by recombination and trapping, respectively, and  $n_t$  is the concentration of deep electron traps. The effect of shallow electron traps is also included implicitly in equation (1), since shallow trapping influences only the average velocity  $v$ .

There are several cases in which eq.(1) reduces to a very simple form. For example, in an intrinsic semiconductor  $n_t \approx 0$ , and at ordinary excitation levels  $n_e \gg n_0$ . Annihilation of the photoelectrons occurs predominantly by recombination, and is governed approximately by first-order kinetics.

$$n \approx n_0 \exp(-t/\tau), \quad \tau = (v\sigma n_e)^{-1} \quad (2)$$

Therefore, it is possible to specify a free-carrier lifetime  $\tau$  which is characteristic of the material and essentially independent of  $n_0$ .

First-order kinetics may also be obtained from eq. (1) if the density and cross section of deep electron traps are sufficiently large, such that  $\sigma_t n_t \gg \sigma(n_e + n_0)$ . In this case, eq. (1) yields

$$n \approx n_0 \exp(-t/\tau_t), \quad \tau_t = (v\sigma_t n_t)^{-1} \quad (3)$$

This behavior can be observed in insulators as well as in semiconductors, but in both cases it indicates an extrinsically determined free-carrier lifetime not characteristic of a perfect material.

If, on the other hand, we consider an intrinsic insulator, deep electron traps can be neglected ( $n_t \approx 0$ ), and at photo-excitation levels currently of interest  $n_0 \gg n_e$ . Annihilation of photoelectrons occurs by recombination as in the intrinsic semiconductor, but since  $n_0 \gg n_e$ , eq. (1) leads to second-order kinetics.

$$n \approx n_0 (1 + t/\tau)^{-1}, \quad \tau = (v\sigma n_0)^{-1} \quad (4)$$

In this case it is only possible to specify a carrier lifetime which is a function of carrier density,  $n_0$ , as well as being characteristic of the material itself. Note also that the definition of "lifetime" in eq. (4) differs mathematically from that given in eqs. (2) and (3).

Experiments to determine free carrier lifetimes in available pure insulators would be expected, in principle, to encompass two extremes. At sufficiently low carrier concentrations, trapping would be the dominant effect, and a concentration-independent lifetime would be observed, in accordance with eq. (3). At sufficiently high concentrations, however, intrinsic recombination would become dominant, and an inverse dependence of lifetime on concentration should be observed according to eq. (4). Detailed behavior of lifetime as a function of concentration depends strongly on the chemical and physical perfection of the sample. Concentration and cross section of deep electron traps are the principal factors influencing the lifetime in the trap-controlled region. They also determine the free-carrier concentration range in which the transition occurs from the trap-controlled region to the intrinsic recombination region. Shallow traps influence the lifetimes in both regions by controlling the average thermal velocity of the electrons.

### 3.2 Auger Recombination

Band-to-band Auger recombination is a well-documented channel for decay of high-density electron-hole plasmas in semiconductors [11], although very little is known of the corresponding process in insulators. Basically, an electron-electron collision in the presence of a hole (or vice-versa) results in nonradiative electron-hole recombination with the third particle gaining kinetic energy equivalent to the recombination energy. The kinetic equation for plasma recombination by this three-body interaction can be written

$$\frac{\partial n}{\partial t} = -\gamma_3 n^3 \quad (5)$$

where  $n$  is the concentration of electrons and holes. Hence the onset of Auger recombination is very

rapid with increasing carrier density, and it eventually dominates all other recombination channels. Threshold densities for onset of significant Auger recombination in semiconductors are typically quite high even in comparison to  $5 \times 10^{17} \text{ cm}^{-3}$ . Auston, Shank, and LeFur found that in germanium the Auger process is clearly observable above radiative recombination when the plasma density is  $3.4 \times 10^{20} \text{ cm}^{-3}$  but not when it is  $1.4 \times 10^{20} \text{ cm}^{-3}$  [12]. However a significantly lower threshold in HgCdTe has been reported [13].

Predicting an Auger recombination rate for plasmas in alkali halides is complicated by self-trapping of the hole. However the immediate question of whether the Auger process accounts for the rapid recombination rate in alkali halides as reported in refs. 7 and 8 can be addressed by more general arguments. In the first place, a band-to-band Auger recombination would bypass the defect production channel [14,15] with the energy going instead to the escaping electron. Thus even if the Auger process occurs appreciably at  $5 \times 10^{17}$  carriers per  $\text{cm}^3$  in KCl, it cannot account for the observation [7,8] of fast F-center production. An alternate mechanism of fast, density-dependent recombination with subsequent vibrational relaxation is still needed. In fact, the onset of Auger recombination is so sharp that in the Auger-dominated regime all F center production or population of self-trapped exciton states would be wiped out by a moderate increase in carrier density. This was specifically not observed [7,8], so we conclude that Auger recombination is probably not important in alkali halides at  $5 \times 10^{17}$  carriers per  $\text{cm}^3$ . The alternative fast recombination mechanism combines bimolecular kinetics as discussed in section 3.1 with very rapid vibrational relaxation of the self-trapped exciton to a deep level after initial electron capture.

#### 4. Photoconductivity Data

##### 4.1 Extrinsic Trap-Limited Regime

Part of our expected use of photoconductivity for characterizing wide-gap materials presupposes that some of the measured quantities will depend in a fairly sensitive way on extrinsic, hence controllable, parameters of the material. As one of the early stages of the present work, we have surveyed effects of a number of different material preparations and treatments on photoconductivity-- again looking principally at effects on carrier lifetime. Because of our shorter excitation pulse, we can look for carrier lifetimes in the range 1-20 ns which has been inaccessible in past experiments on halides. In fact most of the extrinsic trapping of carriers we have observed occurs in this range.

In figure 2 we show the integrated photocurrent in NaF from two sources. (The free-carrier density is roughly proportional to the measured photocharge.) The order-of-magnitude difference in carrier lifetime in these two samples is tentatively attributed to a reduction in the concentration of electron-trapping impurities in the highly-purified material (NRL #107E). The traps associated with these impurities are assumed to be shallow; decreasing the impurity concentration would then decrease carrier lifetime by increasing the average drift velocity.

A second dramatic effect of chemical treatment on lifetime was observed in commercial-grade sapphire, as illustrated in figure 3. A mild anneal (20 min at  $650^\circ\text{C}$ ) in a reducing atmosphere introduces a long carrier lifetime ( $\tau_c \sim 100 \text{ ns}$ ); subsequent annealing in an oxidizing atmosphere removes this long component. These observations suggest that chemical reduction of sapphire also introduces (presumably shallow) electron traps. Electron-spin-resonance experiments have demonstrated that this effect is not related to changes in the valence state of iron, which is the principal impurity. It is more likely that oxygen vacancies produced in the reducing anneal could act as electron traps.

In order to study the transition from the low-density, extrinsically-controlled regime to the higher-density regime of intrinsic recombination, we have used the unfocused uv pulse to generate carriers by two-photon excitation in high-purity KBr, varying the intensity of excitation at 347 nm from 0.05 to 50  $\text{MW}/\text{cm}^2$ . In figure 4 the maximum induced photocharge is plotted versus uv intensity, and oscilloscope traces of the build-up of integrated photocurrent are shown for three points along the curve. To stay within the dynamic range of the FET probe, the circular points in figure 2 were taken with 500 V applied as opposed to 2000 V for the square points. Independent measurements showed that the measured carrier lifetime did not depend significantly on applied voltage within this range. The ordinate values of induced charge are scaled with respect to the 2000-V data.

Consider first the lower end of the curve, where calculations indicate negligible space charge effects and where the approximate constancy of the 20-ns carrier lifetime with carrier density suggests that this is the extrinsic trap-controlled limit. The induced charge of  $10^{-13} \text{ C}$  corresponds to an initial carrier density of about  $10^{10} \text{ cm}^{-3}$  under these conditions. The 20-ns carrier lifetime we find in KBr is substantially shorter than the 1- $\mu\text{s}$  lifetime found for some alkali halides by Catalano et al. [6] in the same or higher range of carrier density. (In ref. [6], the 347-nm pulse intensity was in the range 0.1 to 12  $\text{MW}/\text{cm}^2$ , but the duration was 20 ns, or  $10^3$  times the duration of our pulse. One can deduce from the known two-photon absorption coefficient and indicated carrier lifetime that photoinduced carrier densities were in the range  $10^{13}$ - $10^{15} \text{ cm}^{-3}$ .) In view of the chemical effects mentioned above, this result suggests that the longer lifetimes measured in previous work may be due to a high concentration of shallow traps.

##### 4.2 Space-Charge/Bimolecular-Kinetics Regime

When a dielectric containing an electron-hole plasma is subjected to an electric field, the plasma will polarize to produce internal cancellation of the applied field in a time  $\tau_r = \epsilon \epsilon_0 (n_0 e \mu)^{-1}$ , some-



times called the dielectric relaxation time. Here  $n_0$  is the carrier pair density,  $\mu$  is the sum of electron and hole mobilities,  $e$  is the electron charge,  $\epsilon$  the dielectric constant, and  $\epsilon_0$  is the permittivity of free space. A criterion for whether useful transient photoconductivity measurements can be made without serious distortion by space charge effects is that either the carrier lifetime or the time for which the external field has been applied must be significantly less than  $\tau_r$ .

The dielectric relaxation time for a plasma density of  $10^{10} \text{ cm}^{-3}$  in KBr is about 3  $\mu\text{s}$ . Thus our measured carrier lifetime of 20 ns at this density should be independent of space charge effects. However the upper half of figure 4, corresponding to carrier densities above  $10^{12} \text{ cm}^{-3}$ , is getting well into the space charge region. This introduces ambiguity into interpretation of the present kind of experiment. Figure 4 indicates that the decay of the measured photocurrent becomes faster as the density of carriers increases. Extrapolation of the data in figure 4 according to eq. (4) (second-order kinetics) predicts picosecond recombination times at  $10^{16}$  carriers per  $\text{cm}^3$ , in reasonable agreement with the optical experiments cited earlier. The induced photocharge in figure 4 falls below the expected quadratic dependence on laser intensity (dashed line) in the high density range, as would be expected for shorter carrier lifetimes. These trends can be fit rather well within the kinetic model of section 3.1.

Similar behavior could also be attributed to space charge build-up. In that case, an additional mechanism would be required to account for the short lifetimes inferred from the previous defect generation experiments [7,8]. Although an Auger mechanism cannot be completely ruled out, it seems unlikely, as shown in section 3.2. In an attempt to overcome this ambiguity in interpretation of data for carrier densities in the range  $10^{14} - 10^{18} \text{ cm}^{-3}$ , we are undertaking experiments in which the electron-hole plasma evolves in zero field and is then probed by a transient electric field much shorter in duration than the dielectric relaxation time.

## 5. Summary

We have made time-resolved photoconductivity measurements on several wide-gap materials. Three major conclusions from this work are:

1. At low excitation densities, lifetimes on the order of 10 ns were found in all alkali halide samples measured at room temperature. Although extrinsically controlled, these times provide an upper limit for free carrier lifetimes which may be expected in state-of-the-art alkali halide materials.

2. Intensity dependence measurements in high purity KBr have suggested that, in the range of interest for laser damage studies, bimolecular recombination kinetics may give rise to an inverse dependence of carrier lifetime on carrier density. Extrapolation to higher intensities on the basis of this model is in agreement with results of previous defect production studies [7,8], which indicated that the free carrier lifetime in alkali halides is shorter than 10 picoseconds for carrier densities well below typical damage thresholds. Possible space charge effects in the present experiments have precluded a completely unambiguous interpretation of our initial photoconductivity data at intermediate carrier densities. More refined experiments are in progress to eliminate this ambiguity.

3. Two effects of material preparation techniques on carrier lifetimes in the extrinsic-trap-controlled regime have been observed. Chemical purification of NaF was found to shorten the carrier lifetime, presumably by lowering the concentration of shallow traps. In aluminum oxide (sapphire), the lifetime was found to be highly sensitive to oxidation-reduction conditions. In combination with electron spin resonance experiments, these data suggest that lifetimes in oxides may depend critically on small deviations from stoichiometry. These observations support the view that photoconductivity can be developed as a useful diagnostic technique for evaluation of uv laser window materials.

## 6. Acknowledgements

We wish to thank D. G. Frazier, Sr., for preparing many of the samples used in these experiments. Comments by A. Defonzo and M. N. Kabler have been very helpful.

## 7. References

- |   |   |
|---|---|
| [1] Sparks, M. and Duthler, C. J., Xonics Seventh Technical Report, Contract DAHC 15-73-C-0127, (June, 1976).   | [6] Catalano, I. M., Cingolani, A., and Minafra, A., Phys. Rev. <u>B5</u> , 1629 (1972).  |
| [2] Sparks, M. and Duthler, C. J., Xonics Eighth Technical Report, Contract DAHC 15-73-C-0127, (December 1976). | [7] Bradford, J. N., Williams, R. T., and Faust, W. L., Phys. Rev. Lett. <u>35</u> , 300 (1975).  |
| [3] Bloembergen, N., IEEE J. Quantum Electron. <u>QE-10</u> , 375 (1974).                                       | [8] Bradford, J. N., Williams, R. T., and Faust, W. L., to be published.  |
| [4] Sparks, M. and Duthler, C. J., Xonics Fifth Technical Report, Contract DAHC 15-73-C-0127, (June, 1975).     | [9] Dneprovski, V. S., Klyshko, D. N., and Penin, A. N., JETP Lett. <u>3</u> , 251 (1966).  |
| [5] Bräunlich, P., Schmid, A., and Kelly, P., Appl. Phys. Lett. <u>26</u> , 150 (1975).                         | [10] Bolte, Steven B. and Brown, Frederick C., in <u>Proceedings of the Third International Conference on Photoconductivity</u> , Pell, Erik M., ed., (Pergamon, New York, 1970), p. 139. |



- [11] Blakemore, J. S., Semiconductor Statistics (Pergamon, New York, 1962) pp. 214-248.
- [12] Auston, D. H., Shank, C. V., and LeFur, P., Phys. Rev. Lett. 35, 1022 (1975).
- [13] Bartoli, F., Allen, R., Esterowitz, L., and Kruer, M., J. Appl. Phys. 45, 2150 (1974).
- [14] Williams, R. T., Phys. Rev. Lett. 36, 529 (1976).
- [15] Kabler, M. N. and Williams, R. T., to be published.

## 8. Figures

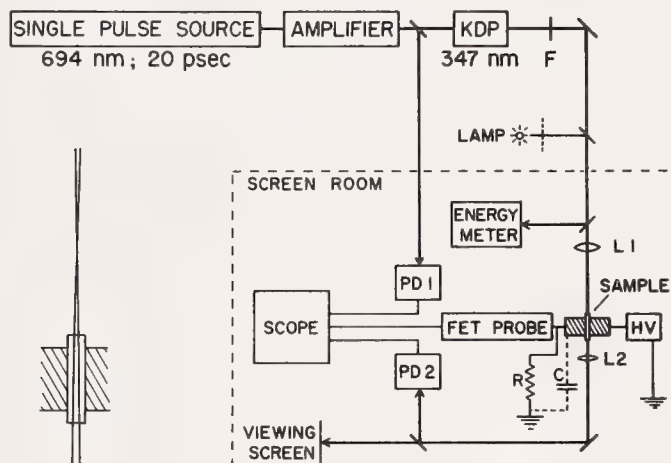


Figure 1. Apparatus for measuring photoconductivity.

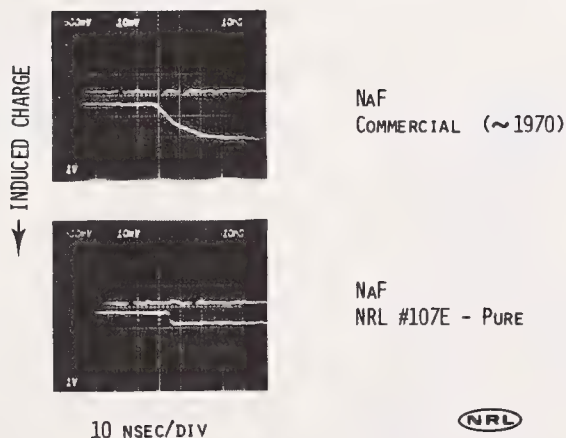


Figure 2. Photoconductivity data on samples of commercial and ultrahigh purity NaF. The lower trace in each photo shows integrated photocurrent vs. time after multi-photon excitation.

THERMAL HISTORY; OXIDATION-REDUCTION  
 $\text{Al}_2\text{O}_3$  (VERNEUIL-GROWN, COMMERCIAL GRADE)

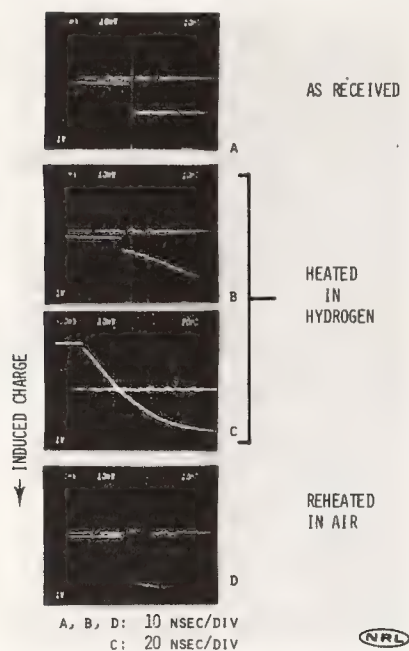
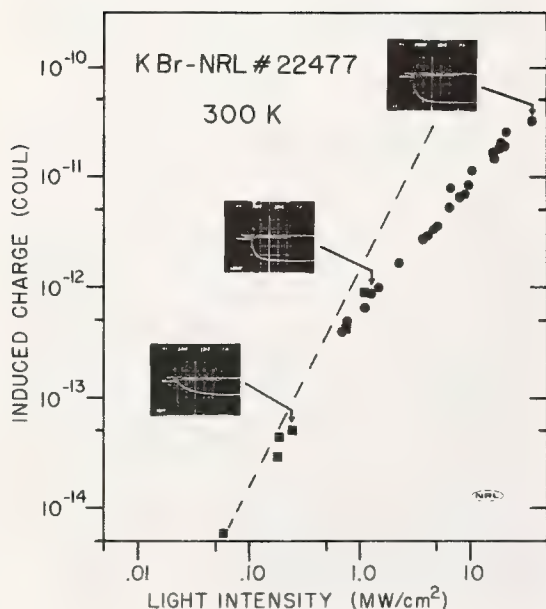


Figure 3. Integrated photocurrent vs. time after three-photon excitation of a sapphire sample as received (A), after annealing in hydrogen (B,C), and after subsequent annealing in air (D).

Figure 4. Integrated photocurrent in ultrahigh purity KBr as a function of peak intensity of the 347-nm excitation pulse. The ordinate (induced charge on the electrodes) may be scaled to free-carrier density within an order of magnitude by the multiplicative factor  $10^{23}$  carriers  $\text{cm}^{-3}$  (coulomb induced) $^{-1}$ . The inset photographs show the time dependence of integrated photocurrent (20 ns/div) for the indicated carrier densities.



COMMENTS ON PAPER BY WILLIAMS, KLEIN, AND MARQUARDT

*In response to a question concerning the role of shallow traps in liberating electrons, the speaker indicated that in the case of twophoton photoconductivity, the twophoton process clearly dominates the excitation of electrons from traps, and this can be seen by the intensity dependence of the conductivity. However in higher order processes, where the multiphoton process is weaker, the two sources of electrons compete. He indicated that among the directions in which this work would be taken would be measurements of the temperature dependence of the photoconductivity, the external photo-emission of electrons and photo-luminescence.*



P. Liu, W. Lee Smith,<sup>+</sup> H. Lotem, J. H. Bechtel,<sup>†</sup> and N. Bloembergen  
Gordon McKay Laboratory  
Harvard University  
Cambridge, Massachusetts 02138

and

R. S. Adhav  
Quantum Technology, Inc.  
Grand Island, New York 14702

The absolute two-photon absorption coefficients of ultraviolet-transmitting materials have been measured using well-calibrated single pulses at 355 nm and 266 nm from a mode-locked Nd:YAG laser system. Two-photon absorption coefficients of the order  $10^{-3}$  cm/MW were found for alkali-halides, and of order  $10^{-4}$  cm/MW for KDP and its isomorphs. Several other materials —  $\text{Al}_2\text{O}_3$ ,  $\text{CaCO}_3$ ,  $\text{SiO}_2$ , and  $\text{CaF}_2$  — were also tested. In materials with band gap greater than  $2\hbar\omega$ , no nonlinear absorption was detected up to the threshold of surface breakdown. The effects of multiphoton absorption on the breakdown of ultraviolet window materials is discussed.

Key words: Alkali-halides, avalanche ionization, breakdown, calcite, KDP, multiphoton absorption, sapphire, silica, transparency, two-photon absorption, ultraviolet windows.

## INTRODUCTION

The study of two-photon absorption (2PA) [1] will attract increasing scientific and technological interest in coming years. Because the selection rules for 2PA transitions are, in general, different from those familiar with linear spectroscopy, 2PA studies will provide much new information about the band structure and energy levels in solids, liquids, and gases. Due to widespread and growing use of high-power ultraviolet (UV) and vacuum ultraviolet (VUV) lasers, the impetus is present to understand the ramifications of multiphoton ionization for breakdown processes in large band-gap optical materials.

The interplay between multiphoton absorption and avalanche breakdown mechanisms in solids has been the subject of considerable theoretical discussion in the recent literature [2-5]. A recent experimental study [6] addressed the frequency dependence of dielectric breakdown and discussed the implications of multiphoton absorption for breakdown experiments.

This report relates a subset of aspects — dealing directly with breakdown processes — treated in a major study [7] of 2PA at 355 nm and 266 nm to be presented elsewhere. In that study, attention is given in addition to the questions of spatial anisotropy of 2PA, the relation of the 2PA coefficient to other nonlinear optical parameters, techniques for accurate relative measurements of 2PA, and comparison of the frequency dispersion of the 2PA coefficient, using Keldysh multiphoton absorption theory, with experimental results.

## THEORY

In materials with optical band gap greater than the energy of a single photon but smaller than twice the photon energy of an interacting light wave, it is possible for transitions to occur by simultaneous absorption of two (or more) photons from a single, sufficiently intense laser beam [1]. The expression for the 2PA transition rate may be written down straightforwardly from second-order perturbation theory. However, one's ability to proceed to the point of making useful predictions or precise calculations with that direct approach has been hampered in 2PA studies [1]. Linear spectroscopy theory has been similarly impeded and for the same reasons — lack of sufficient knowledge of energy band parameters, etc., of the materials.

\*This work was supported by the Advanced Research Projects Agency (F-44620-75-C-0088) and by the National Aeronautics and Space Administration (NGL-22-007-117).

<sup>+</sup>Present address: Lawrence Livermore Laboratory, Livermore, California 94550.

<sup>†</sup>Present address: General Motors Research Laboratory, Warren, Michigan 48090.

A different approach to the problem was developed by Keldysh [8], who abandoned the standard method of calculating rates using unperturbed Bloch wave functions and directly modified the wave functions to account for the strong electric field strengths required for the occurrence of 2PA. Although imperfections in the multiphoton ionization transition rate formulae derived by Keldysh have been pointed out [9] and the absolute accuracy of the theory is no doubt limited due to its simplified band structure, the Keldysh formulae are appealing in their tractability. In a solid with optical band gap  $\mathcal{E}_g$ , the Keldysh expression for the multiphoton transition rate per unit volume is

$$W = \frac{2\omega}{9\pi} \left( \frac{m^*\omega}{\hbar} \right)^{3/2} \left[ \frac{e^2 E^2}{16m^*\omega^2 \mathcal{E}_g} \right]^{\langle \frac{\Delta}{\hbar\omega} + 1 \rangle} \Phi \left[ \left( 2 \langle \frac{\Delta}{\hbar\omega} + 1 \rangle - \frac{2\Delta}{\hbar\omega} \right)^{1/2} \right] \exp \left\{ 2 \langle \frac{\Delta}{\hbar\omega} + 1 \rangle \left( 1 - \frac{e^2 E^2}{4m^*\omega^2 \mathcal{E}_g} \right) \right\}, \quad (1)$$

$$\text{where } \Delta = \mathcal{E}_g + \frac{e^2 E^2}{4m^*\omega^2}$$

and  $\langle x \rangle$  is defined as the integer part of  $x$ . The function  $\Phi$  in Eq. 1 is the Dawson integral, and  $m^*$  is the electron-hole effective reduced mass. In Eq. 1,  $E$  is the peak electric field rather than the rms electric field tabulated in many dielectric breakdown papers.

The total attenuation of a light wave as a function of distance  $z$  into a medium with linear and nonlinear absorption may be written

$$dI/dz = \sum_N \alpha^{(N)} I^N, \quad (2)$$

where  $\alpha^{(N)}$  is the  $N$ -photon absorption coefficient. The Keldysh two-photon transition rate is related to  $\alpha^{(2)}$  with the relation

$$\alpha^{(2)} = \frac{4\hbar\omega^2}{9\pi} \left( \frac{8\pi}{n} \right)^2 \left( \frac{m^*\omega}{\hbar} \right)^{3/2} \Phi \left[ \left( 4 - \frac{2\Delta}{\hbar\omega} \right)^{1/2} \right] \left( \frac{e^2}{16m^*\omega^2 \mathcal{E}_g} \right)^2 \exp \left[ 4 \left( 1 - \frac{e^2 E^2}{4m^*\omega^2 \mathcal{E}_g} \right) \right]. \quad (3)$$

Consider a material which supports only one- and two-photon absorption. If a planar slab of such a material with thickness  $\ell$  is traversed by an intensity packet

$$I(r, 0, t) = I_0 e^{-(r/\rho)^2} e^{-(t/\tau)^2}$$

at the entrance plane, then we may write [10] for the transmitted intensity at the exit surface

$$I(r, \ell, t) = \frac{I_0 (1-R)^2 e^{-(r/\rho)^2} e^{-(t/\tau)^2} e^{-\alpha^{(1)} \ell}}{1 + \alpha^{(2)} I_0 (1-R) e^{-(r/\rho)^2} e^{-(t/\tau)^2} (1 - e^{-\alpha^{(1)} \ell}) [\alpha^{(1)}]^{-1}}. \quad (4)$$

In the above equation  $R$  is the intensity reflectivity of a single surface of the medium. The energy transmission  $T$  is therefore

$$\begin{aligned} T = \frac{\mathcal{E}_{\text{out}}}{\mathcal{E}_{\text{in}}} &= \frac{2\pi \int_0^\infty r dr \int_{-\infty}^\infty I_0(r, \ell, t) dt}{I_0 \pi \rho^2 \pi^{1/2} \tau} \\ &= \frac{2\alpha^{(1)} e^{-\alpha^{(1)} \ell} (1-R)}{\alpha^{(2)} I_0 \pi^{1/2} (1 - e^{-\alpha^{(1)} \ell})} \int_0^\infty \ln \left\{ 1 + \frac{\alpha^{(2)} I_0 (1-R) (1 - e^{-\alpha^{(1)} \ell}) e^{-x^2}}{\alpha^{(1)}} \right\} dx. \end{aligned} \quad (5)$$

At low intensity we obtain

$$\lim_{I_0 \rightarrow 0} \frac{d(T^{-1})}{dI_0} = \frac{\alpha^{(2)} \ell}{2^{3/2} (1-R)}, \quad (6)$$

as long as  $I_0(1-R)(1-e^{-\alpha^{(1)}\ell})\alpha^{(2)}/\alpha^{(1)}$  is much less than unity and  $\alpha^{(1)}\ell \ll 1$  as well. Hence, the slope of experimental data of  $T^{-1}$  plotted vs. intensity  $I_0$  yields the 2PA coefficient  $\alpha^{(2)}$ . In actuality, we found the approximate value of  $\alpha^{(2)}$  from Eq. 6 for each material, and then generated a family of curves using Eq. 5 with values of  $\alpha^{(2)}$  close to the approximate value. The final 2PA coefficient was then chosen according to optimum fit of the data.

## EXPERIMENTAL EQUIPMENT AND PROCEDURE

The Nd:YAG picosecond laser oscillator — amplifier system is described in Refs. 6 and 11. Passive mode locking is employed with a laser-triggered electro-optical shutter to produce single pulses with energy up to 10 mJ. The pulses have a smooth, temporally Gaussian profile with an average full-width-at-half-intensity duration of 30 ps. During the 2PA measurements, a fast vacuum photodiode/oscilloscope was employed to eliminate data resulting from laser pulses that were not perfectly excised from the pulse train. A CDA crystal, 90° phase-matched by temperature tuning, was used to convert the 1064-nm light to 532 nm. An angle-tuned KDP crystal was used to mix the two waves to produce 355-nm pulses. A second 90° phase-matched crystal (ADP) was used to convert 532-nm light to 266 nm. Unwanted wavelengths were separated out by filter glass or by a dispersive prism set at the minimum deviation angle to avoid spatial profile distortion.

A fused silica lens (24.7 cm focal length at 355 nm) was used to increase the intensity, per unit energy, of our pulses in the sample and a second lens after the sample was used to recollimate the pulses for final energy detection. The samples were always placed behind the focal point of the first lens by at least 2 cm, i.e., many Rayleigh lengths. There are two advantages to this placement.

First, since the sample positions were well into the region describable by geometrical optics, the calculation of the area of the pulses in the sample is less susceptible to error arising from lens aberration. In these experiments the pulse area was measured at the focusing lens plane by a photodiode array with 50- $\mu$ m resolution. This measured area was used along with the carefully measured ( $\pm 0.6\%$ ) focal length of the focusing lens to calculate, using diffraction-limited theory, the pulse area in the samples. The area at the sample plane could not be measured with the photodiode array due to insufficient resolution and susceptibility to damage of the detector array.

Second, the placement of the samples far beyond the lens focal point has an advantage for the reduction of harmful self-focusing effects in the experiment. If a high-power experiment is conducted in a medium other than vacuum at (or within a Rayleigh length or so of) the focal point of a lens, then strict attention must be given to whole-beam self-focusing [6]. The input power must be kept well below the self-focusing critical power for each material in order to prevent nonlinear focal area shrinkage.

However, far away from a focal region and in thin samples such as were used in these experiments, pulses with many times the critical power may be propagated through the sample without catastrophic self-focusing. In the unfocused, thin sample geometry, small-scale self-focusing [12] is the phenomenon to be avoided.

In a medium of length  $\ell$  with a nonlinear refractive index  $n_2$ , input spatial profile modulation (noise) is augmented in intensity during propagation at most by a factor  $e^B$ . The so-called B-integral [12] is

$$B = \frac{8 \times 10^7 \pi^2 n_2 (\text{esu})}{\lambda} \int_0^\ell I(z) dz. \quad (7)$$

Values of  $n_2$  are obtainable from the literature [6] for several of the materials used in this study, and  $n_2$  of the other materials is estimable from the values in the literature. Calculations using Eq. 7 state that in these experiments it was possible, with only two exceptions, to obtain sufficient absorption and measure accurately the 2PA coefficients without incurring appreciable noise enhancement and concomitant error introduction via small-scale self-focusing (sssf). This conclusion was verified by measuring the 2PA coefficient in samples of the same material and orientation but different length  $\ell$ . The coefficients showed no variation with  $\ell$  greater than the experimental uncertainty (from all sources other than sssf) in  $\alpha^{(2)}$ . A further check was made by observing, under a microscope, the stable color pattern formed in KCl doped with U-centers by irradiation with pulses at the upper limit of intensity used in these experiments.

In SiO<sub>2</sub> at 355 nm and in LiF at 266 nm, the 2PA coefficients were so small that considerably higher intensity was passed through the samples in attempt to get measurable 2PA. In these two cases, noise fluctuations of the worst-case spatial frequency may have undergone intensity growth by as much as a factor  $e^1$  or about 3. Nevertheless, 2PA coefficients were not large enough to be measured in these two cases and upper bounds only were determined. The reader should note that the  $n_2$  values employed in the above discussion were measured at 1.06  $\mu$ m [11]. At the shorter wavelengths of 355 and 266 nm, the true



$n_2$  values may be somewhat different due to positive or negative contributions due to the nearby resonant two-photon energy bands. Resolution of that question must await  $n_2$  measurements in the UV.

In order to eliminate possible accumulative effects on the measurements, such as F-center generation, each transmission data point was performed at a fresh site in the sample. This was accomplished by translating the sample after each laser shot.

The uncertainty in the values of  $\alpha^{(2)}$  measured here is  $\pm 43\%$ , comprised of  $\pm 7\%$  uncertainty in absolute energy calibration,  $\pm 8\%$  in pulse area at the sample, and  $\pm 28\%$  in the average value at low intensity of the  $\tau A$  pulse-to-pulse fluctuation parameter [13]. Hence, the absolute uncertainty sums to  $\pm 43\%$ .

## RESULTS

At 355 nm, we measured the absolute 2PA coefficients in three alkali-halides, and in KDP and nine other harmonic generating crystals. These are all listed in Table 1. Upper limits for  $\alpha^{(2)}$  in the commonly used UV window materials, sapphire and fused silica, with band gaps greater than  $2\hbar\omega$  (7.02 eV) are also tabulated. For the materials checked with band gaps greater than  $2\hbar\omega$ , the transmission was essentially constant to intensities up to the region of about  $2 \times 10^{10}$  W/cm<sup>2</sup>. Higher beam intensities could not be used due to the onset of surface damage.

At 266 nm, we measured the 2PA in eight alkali-halides with band gap less than  $2\hbar\omega$  (9.36 eV) and in KDP, ADP, Al<sub>2</sub>O<sub>3</sub>, SiO<sub>2</sub>, and calcite. The window materials LiF and CaF<sub>2</sub> (in which no 2PA is expected) were also measured. The measured values are listed in Table 2. For alkali-halides the  $\alpha^{(2)}$  values measured are of the order of  $10^{-3}$  cm/MW while for KDP, ADP, Al<sub>2</sub>O<sub>3</sub>, and calcite they are of the order  $10^{-4}$  cm/MW. For the materials with band gaps greater than  $2\hbar\omega$ , an upper limit for  $\alpha^{(2)}$  is given. It is interesting to note that fused silica and quartz have quite small 2PA at this wavelength, even though  $2\hbar\omega$  considerably exceeds  $E_g$ .

Fluorescence is observed in all the alkali halides along the path of the beam [14]. Coloring can be seen with the bare eye after a few shots. In KCl the absorption of a monitoring beam at 532 nm by the color track is observable and can be explained by the spectral position of the absorption band of the F-center [15]. The physical process involves the generation of electron-hole pairs by two-photon excitation; the pairs recombine to form excitons with the emission of fluorescent light. The exciton energy is given up to form  $V_k$  and F-centers [16]. We have found that the F-centers generated by several hundred shots of the laser at the same site of the crystal did not influence the transmission of the crystal at the laser frequency after they had relaxed for a few seconds.

We may consider the effects of multiphoton absorption on the breakdown process via the Keldysh model. Such considerations will not be quantitative, although we may expect the Keldysh model to predict trends in the behavior of the 2PA contribution to breakdown.

The major difficulty in accurately calculating breakdown features is the diversity of the processes involved. Even if one neglects lossy facets of plasma recombination and electron and thermal diffusion, he is still faced with the coupled avalanche — 2PA dynamical problem. At 1064 nm in typical wide band gap insulators, picosecond breakdown has been interpreted in terms of an avalanche model [11]. Avalanche ionization rate data at 1064 nm has even been extracted for several materials from such breakdown experiments, yet to what extent the 1064-nm avalanche rate differs from 355-nm or 266-nm avalanche rate data is unknown.

When an experimental breakdown threshold is measured, the result may be due to combined avalanche multiplication and two (or higher-order) photon absorption. The plasma growth by the cooperative effect of 2PA and avalanche multiplication of the 2PA-generated charge carriers and avalanche-generated carriers cannot be dealt with by calculation unless the proper avalanche rate is known. Hence, even though the 2PA coefficient may be known, calculations on breakdown phenomena [3] are made difficult by our lack of data concerning the avalanche process by itself in the ultraviolet.

One approach, with perhaps the single redeeming quality of tractability, is simply to delete the avalanche considerations altogether and to model a plasma production by sole 2PA. We have used the Keldysh [8] model for such a first look at 2PA breakdown in  $\text{CaF}_2$ . Figure 1 illustrates the results. The three picosecond breakdown thresholds [6, 11] for  $\text{CaF}_2$  are plotted versus photon energy. The other bars mark the electric field necessary to generate  $10^{19}$  charge carriers per  $\text{cm}^3$  by multiphoton absorption in  $\text{CaF}_2$ . For these calculations, Eq. 1 was used with  $\mathcal{E}_g = 10$  eV and  $m^* = 0.1$  to 10 m. The range of  $m^*$  produces the range of electric field for 3PA and 5PA in Fig. 1. (Note that rms electric fields are plotted in Fig. 1, whereas peak fields actually must be used in the Keldysh expressions.)

Although the absolute positions of the multiphoton bars are not significant, the relative positions are more worthy of note. In Ref. 6 it was stated that the reduced 355-nm threshold compared to the 532-nm threshold in  $\text{CaF}_2$  was probably due to the assistance of three-photon absorption to the breakdown avalanche process. Figure 1 illustrates that the Keldysh model predicts a decrease in the electric field, necessary to make a plasma density of  $10^{19} \text{ cm}^3$ , by a factor of 2 to 3 depending on  $m^*$ . This result supports the interpretation of Ref. 6 that the three-photon absorption assistance to the avalanche process served to lower the 355-nm breakdown threshold.

One further point merits discussion here regarding 2PA and breakdown. In Ref. 6 it was surmised that in KDP at 355 nm, 2PA had caused beam depletion in front of the focal point to such an extent that an artificially high damage resistance was recorded. With the measured KDP  $\alpha^{(2)}$  of  $6 \times 10^{-6} \text{ cm/MW}$  from Table 1, we see now that, indeed, at the  $2 \times 10^{11} \text{ W/cm}^2$  intensity level, an energy loss of as much as 12% per 100  $\mu\text{m}$  will occur. Therefore, the often-used bulk breakdown geometry of tight focusing inside a sample surface will perhaps give way entirely to surface breakdown testing in the ultraviolet and vacuum ultraviolet.

#### SUMMARY

Absolute coefficients for two-photon absorption at 355 nm and 266 nm were presented for a variety of wide-band-gap optical materials. The influence of multiphoton absorption on the breakdown process was discussed. It was shown that pulse depletion due to two-photon absorption is a serious obstacle to the use in the UV and VUV of the classic bulk breakdown geometry of tight focusing inside a medium.

#### ACKNOWLEDGMENTS

We express our indebtedness to Mr. S. Maurici for his preparation of samples and to Dr. L. F. Mollenauer for a U-center doped sample. We also thank Dr. C. B. de Araujo for sharing equipment and useful discussions, and Mr. Richard Yen for assistance with the measurements. Ms. K. Wenzinger of LLL is much appreciated for preparation of this manuscript.

#### REFERENCES

- [1] Recent reviews of 2PA are found in J. M. Worlock, *Laser Handbook*, eds. T. Arecchi and F. Schulz-Dubois (North Holland, Amsterdam, 1972); and in H. Mahr, in *Quantum Electronics*, eds. H. Rabin and C. L. Tang, vol. 1 (Academic, New York, 1975).
- [2] N. Bloembergen, *IEEE J. Quant. Electron.* **QE-10**, 375 (1974).
- [3] P. Bräunlich, A. Schmid, and P. Kelly, *Appl. Phys. Lett.* **26**, 150 (1975).
- [4] P. Kelly, P. Bräunlich, and A. Schmid, *Appl. Phys. Lett.* **26**, 223 (1975).
- [5] N. L. Boling, P. Bräunlich, A. Schmid, and P. Kelly, *Appl. Phys. Lett.* **27**, 191 (1975).
- [6] W. Lee Smith, J. H. Bechtel, and N. Bloembergen, *Phys. Rev.* **B15**, 4039 (1977).
- [7] P. Liu, W. Lee Smith, H. Lotem, J. H. Bechtel, N. Bloembergen and R. S. Adhav (to be published).
- [8] L. V. Keldysh, *Zh. Eksp. Teor. Fiz.* **47**, 1945 (1964).
- [9] P. Kelly (to be published).
- [10] J. H. Bechtel and W. Lee Smith, *Phys. Rev.* **B13**, 3515 (1976).
- [11] W. Lee Smith, J. H. Bechtel, and N. Bloembergen, *Phys. Rev.* **B12**, 706 (1975).
- [12] E. S. Bliss, J. T. Hunt, P. A. Renard, G. E. Sommargren, and H. J. Weaver, *IEEE J. Quant. Electron.* **QE-12**, 402 (1976).
- [13] W. Lee Smith and J. H. Bechtel, *J. Appl. Phys.* **47**, 1065 (1976).
- [14] J. N. Bradford, R. T. Williams and W. L. Faust, *Phys. Rev. Lett.* **35**, 300 (1976).
- [15] W. B. Fowler, *Physics of Color Centers* (Academic, New York, 1968).
- [16] Y. Toyozawa, in *Proc. VI Int'l Conf. on VUV Radiation Physics*, ed. E. E. Koch (Pergamon, Vieweg, Hamburg, 1974).

Table 1. Experimental results for two-photon absorption coefficient  $\alpha^{(2)}$  at 355 nm. The orientations of sample and electric field are tabulated, along with the sample thickness  $\ell$ .

Material	$\phi_g$ , eV (approx.)	Surface Normal	$\vec{E}/ \vec{E} $	$\ell$ , cm	$\alpha^{(2)}$ , cm/MW
KI	5.0	$a \equiv [100]$	$b \equiv [001]$	0.47	$(7.3 \pm 1.5) \times 10^{-3}$
RbBr	5.4	$a$	$b$	1.0	$(2.4 \pm 0.5) \times 10^{-3}$
RbI	5.0	$a$	$b$	1.0	$(5.1 \pm 0.8) \times 10^{-3}$
ADA		$c \equiv 45^\circ$ z-cut	$d \equiv \parallel$ z axis	1.6	$(3.5 \pm 1.1) \times 10^{-5}$
ADP	6.8	$c$	$d$	2.0	$(6.8 \pm 2.4) \times 10^{-6}$
CDA		$c$	$d$	1.4	$(8.0 \pm 2.4) \times 10^{-5}$
CD*A		$c$	$d$	1.15	$(2.8 \pm 1.0) \times 10^{-5}$
KDA		$c$	$d$	1.0	$(4.8 \pm 1.4) \times 10^{-5}$
KD*A		$c$	$d$	1.0	$(2.7 \pm 0.9) \times 10^{-5}$
KDP	6.9	$c$	$d$	1.0	$(5.9 \pm 2.1) \times 10^{-6}$
KD*P		$c$	$d$	1.0	$(5.4 \pm 1.9) \times 10^{-6}$
RDA		$c$	$d$	1.25	$(5.0 \pm 1.5) \times 10^{-5}$
RDP		$c$	$d$	1.0	$< 5.9 \times 10^{-6}$
Al <sub>2</sub> O <sub>3</sub>	7.3	c-axis	--	0.5	$< 1.6 \times 10^{-6}$
SiO <sub>2</sub> (fused)	7.8	--	--	0.64	$< 1.3 \times 10^{-6}$

Table 2. Experimental results for two-photon absorption coefficients  $\alpha^{(2)}$  at 266 nm. The orientations of sample and electric field are tabulated, along with the sample thickness  $\ell$ .

Material	$\phi_g$ , eV (approx.)	Surface Normal	$\vec{E}/ \vec{E} $	$\ell$ , cm	$\alpha^{(2)}$ , cm/MW
NaCl	7-8	$a \equiv [100]$	$b \equiv [001]$	0.74	$(3.5 \pm 0.9) \times 10^{-3}$
NaBr	7.7	$a$	$b$	0.74	$(2.5 \pm 0.4) \times 10^{-3}$
KCl	6.5	$a$	$b$	0.74	$(1.7 \pm 0.3) \times 10^{-3}$
KBr	6.0	$a$	$b$	0.74	$(2.0 \pm 0.6) \times 10^{-3}$
KI	5.1	$a$	$b$	0.47	$(3.8 \pm 1.1) \times 10^{-3}$
RbCl	7.3	$a$	$b$	0.60	$(1.0 \pm 0.2) \times 10^{-3}$
RbBr	5.4	$a$	$b$	1.0	$(2.2 \pm 0.4) \times 10^{-3}$
RbI	5.0	$a$	$b$	1.0	$(2.5 \pm 0.8) \times 10^{-3}$
CaCO <sub>3</sub>	5.9	--	--	0.43	$(2.4 \pm 0.7) \times 10^{-4}$
Al <sub>2</sub> O <sub>3</sub>	7.3	c-axis	--	0.50	$(2.7 \pm 0.8) \times 10^{-4}$
SiO <sub>2</sub> (fused)	7.8	--	--	0.57	$\lesssim 4.5 \times 10^{-5}$
SiO <sub>2</sub> (crystal)	7.8	c-axis	--	0.50	$\lesssim 4.5 \times 10^{-5}$
CaF <sub>2</sub>	10.0	$a$	$b$	0.47	$< 2.0 \times 10^{-5}$
LiF	11.6	$a$	$b$	0.47	$< 2.0 \times 10^{-5}$
KDP	6.9	1.06 $\mu$ m $\rightarrow$ 0.53 $\mu$ m cut	--	0.57	$(2.7 \pm 0.8) \times 10^{-4}$
ADP	6.8	c-axis	--	0.50	$(2.4 \pm 0.7) \times 10^{-4}$



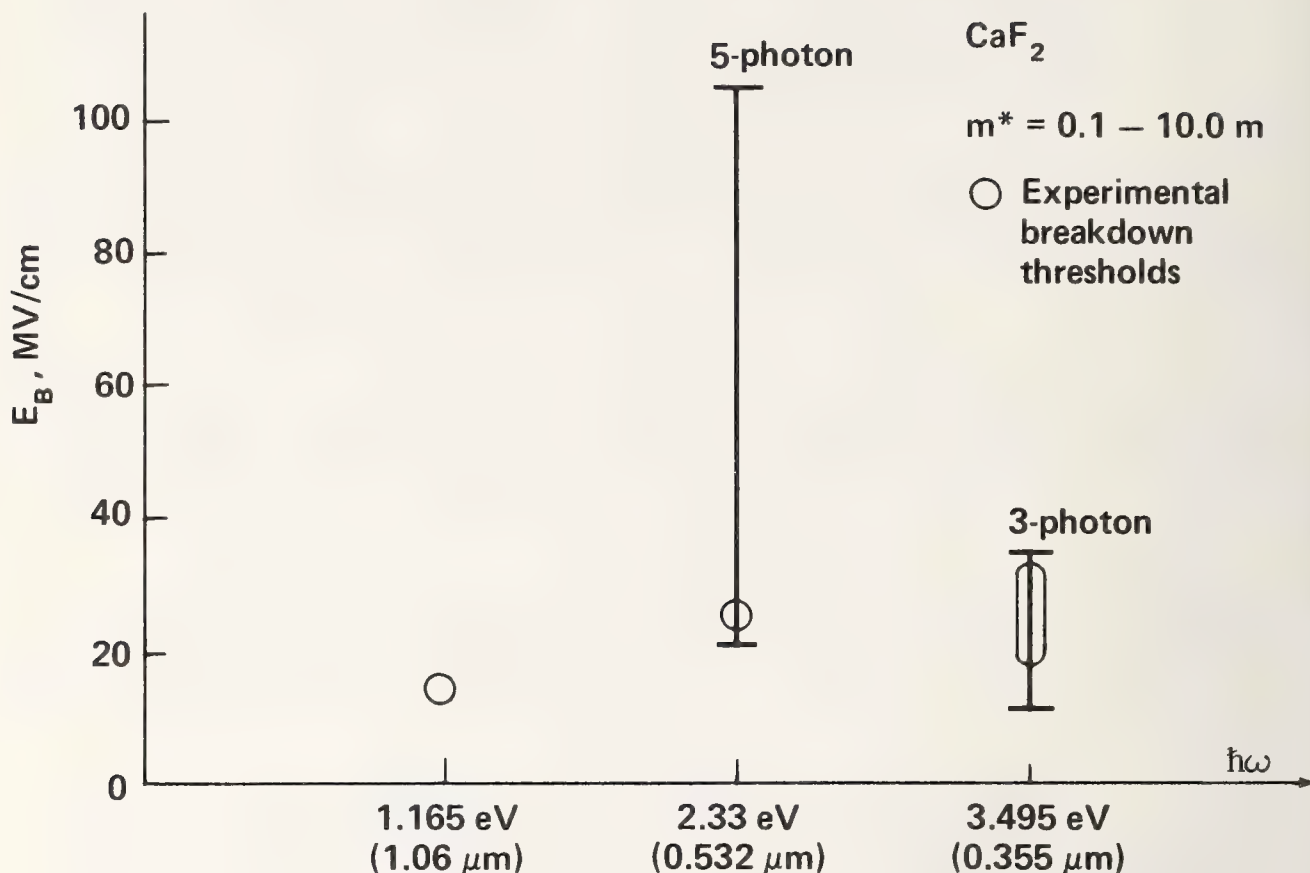


Fig. 1. Breakdown parameters versus photon energy for CaF<sub>2</sub>. The rms electric field breakdown threshold is plotted along the vertical axis. The three round data points are experimental breakdown thresholds from Refs. 6, 11. The other data bars represent the range of electric field strength needed, according to the Keldysh model, to produce  $10^{19}$  electrons/cm<sup>3</sup> in CaF<sub>2</sub>. The large uncertainty in the Keldysh bars reflects the range of  $m^*$  (0.1 to 10.0  $m$ ) considered.

#### COMMENTS ON PAPER BY LIU, LOTEM, BLOEMBERGEN, SMITH, BECHTEL, AND ADHAV

Extensive discussion was carried out concerning the definition of the band gap appropriate to multiphoton excitations. The question is really one of the density of states accessible to multiphoton transitions. It was pointed out that in alkali halides, transitions to the lowest lying exciton state are allowed for odd numbers of photons, and for even number of photons the lowest lying accessible state would be the first odd-parity state above the exciton peak. In this experiment the band gap was inferred from one-photon absorption data. The speaker indicated that there was no reason to expect any pulse duration dependence for two-photon absorption, but that no experiments have been carried out to see if this was really true. The applicability of the Keldysh theory in describing multiphoton absorption was challenged. The speaker pointed out that the Keldysh theory had been used successfully in the past to describe multiphoton absorption and was employed here as a heuristic tool.

# STATISTICAL CONSIDERATIONS IN LASER DAMAGE MEASUREMENTS\*

J. A. Detrio and A. P. Berens  
University of Dayton Research Institute  
Dayton, Ohio 45469

The measurement of the laser damage threshold for a given material or optical component is usually accomplished by testing at predetermined power levels and irradiation times and then observing whether or not damage occurs. This experimental procedure is known as sensitivity testing which attempts to determine the percentage of specimens which are damaged at the various power levels. It is not practical to determine the complete cumulative distribution curve for a given sample population because of the limited number of specimens normally available. The variability in damage level for a given optical component will influence the number of specimens required to measure the damage threshold with a given precision and with a known level of confidence or to achieve a desired degree of discrimination in comparing two different materials, preparation methods or production runs. A statistical method applicable to sensitivity testing is analyzed to permit the experimenter to determine the number of specimens required in accordance with the desired level of precision and confidence. A novel nonparametric method which is applicable to damage testing and requires few samples is also analyzed.

Key words: Laser damage testing; statistics; sensitivity testing; up and down method; probit analysis.

## 1. Introduction

Statistical considerations should be included in the planning of laser damage experiments when the purpose of the test is to select one material, component, or fabrication process over another or if the damage threshold and its standard deviation must be determined with a given precision and level of confidence. If the materials or components being tested always fail at a precise power the problem is simplified and statistics are not required. In practice, the test specimens tend to fail at random over a range of incident powers. This finite spread in the measured damage threshold makes it necessary to carefully consider the number of specimens selected. If the experimental results are used to test a hypothesis concerning the magnitude of the damage threshold for the entire population of materials from which the samples were selected, it is important to understand the consequences of an error in judgment being made on the basis of the results of the experiment.

Several constraints on the conduct of CW damage tests have encouraged a search for test strategies that are economical in the use of samples and that are compatible with the method of operation of high energy lasers (HEL). Some of the constraints are the limited numbers of samples available for testing, the expense of HEL operation, and the increase in test time which is required when frequent power level changes are used. In addition to these constraints, there are factors which influence the results and the test planning that are a consequence of the nature of the samples themselves. Some materials are sensitive to environmental conditions, others are affected by the previous history of laser irradiations and almost all samples show a spatial distribution of defects which make damage results a function of the irradiated area.

The objective of this work is to analyze a test method which is capable of yielding the required parameters and which is compatible with some of the limitations of HEL testing. A nonparametric technique for estimating the threshold with known confidence is presented. This latter method is compatible with HEL operation and is economical in the use of samples and test time.

The probabilistic nature of laser damage, which has been addressed by Bass and Fradin [1]<sup>1</sup>, is of considerable interest in the study of the fundamentals of damage processes but it is not within the scope of this paper.

\* This work supported by the Air Force Materials Laboratory, Wright-Patterson Air Force Base.  
1. Figures in brackets indicate the literature references at the end of this paper.

## 2. Problem Definition

We will define the damage threshold in accordance with conventional practice in agricultural research. It is common in the testing of pesticides to define the dosage at which 50 percent of the subjects expire as the LD50, (lethal dose 50 percent) level [2] which also corresponds to the center of the distribution of fatalities (failures) versus dosage (power). The power which corresponds to a 50 percent probability of failure is the damage threshold.

In many laser damage experiments, it is not possible to determine the power level at which damage occurs on a continuous scale of power. Rather, a power level is set, a specimen is tested at that level for a fixed time, and it is either damaged or not damaged according to the criteria selected to define "damage". This experimental procedure is called sensitivity testing. Statistical methods must be used to properly interpret such data if the required precision of the damage threshold is less than the variations in observed damage threshold. Thus, even before applying formal statistical methods to the data, the separation of the power levels at which the testing will be done must be rationally established with respect to the required precision. For example, if one wishes to resolve differences in damage threshold of  $\pm 10$  percent, then the test power levels should be spaced at no more than 10 percent increments. If the variability in the material's response is considerably greater than 10 percent, then statistical methods are necessary, and the power levels should be selected to span the region from below threshold to above the threshold.

If the required precision is stated as a percentage as in the example above, then the test levels will be spaced in a logarithmic sequence. The methods developed below are applicable to log-normal distributions and are insensitive to the assumption of a normal (Gaussian) distribution. Because the accuracy and precision of power measurements is usually expressed in percentages as are safety factors, the log sequence is in general a logical choice.

In damage experiments, the damage thresholds of the individual test specimens are the random variables and the damage threshold of the total population of the material must be defined in terms of the distribution of the random variable. The cumulative distribution displayed in figure 1 contains all the necessary information for describing the damage threshold for the particular population of specimens. Given a sufficiently large number of test samples from the population, the probability of damaging a specimen at any power level could be precisely determined. It will be assumed, that either the mean or the median of the distribution is the desired damage threshold parameter which describes a particular population of material.

The existing statistical techniques for sensitivity testing require the assumption of a normal distribution of the random variable being characterized. When the random variable is not normally distributed, transformation to an approximately normal distribution may be performed. The commonly used analytical methods require that the fixed levels of the random variable be set at equally spaced increments. Therefore, in the damage tests for which irradiation levels are set at equally spaced intervals on a logarithmic scale, it will be assumed that the power levels at which damage of the specimens is initiated will have a log-normal distribution.

The use of the mean value of the distribution as the definition of the damage threshold softens the requirement for a normal distribution and improves the efficiency of the experiment with respect to the number of specimens required.

## 3. Experimental Design

A variety of considerations affect the planning of a damage experiment. In the statistical portion of the experimental design, certain questions should be addressed. For example, are the parameters of the distribution of damage threshold as a function of power to be estimated? What is the required accuracy of the estimates? Is a hypothesis being tested? What confidence limits are required? What is the consequence of a faulty conclusion being drawn from the data? Many of these questions have a formal definition and statistical methods exist for a quantitative stating of these questions and for obtaining the answers.

There are obvious advantages to the re-use of specimens that are not damaged. The difficulty in the re-use of specimens lies in the mixing of the environmental conditions of the population being characterized. These environmental factors can be significant and could influence the estimate of a



damage threshold or may lead to a wrong conclusion in comparing two materials. This problem is normally referred to as the one-on-one versus n-on-one threshold. The effect of previous irradiations below threshold is called conditioning.

If a given material has been demonstrated to have no conditioning effect due to previous irradiation exposure, then re-use of the specimens would be possible. The verification of the presence or absence of a conditioning effect for a given material would probably be conducted during a preliminary characterization experiment to determine the appropriate damage threshold. It will be assumed the specimens are virgin and that any retest of specimens is conducted to determine a conditioning effect.

The three approaches to sensitivity testing under the restriction of testing at fixed power levels are the probit method [3], the up-and-down method [4], and a nonparametric (multilevel 3 of 4) method. The probit method is mentioned primarily because of its prominence in sensitivity experiments. In this approach, specimens are tested at several power levels and the percent damaged at each level is obtained. Assuming the data are from a normal distribution, the mean and standard deviation are derived from the best curve fit through the observed cumulative distribution. Although this method has been extensively developed [3], a minimum of 50 specimens are recommended. Since 50 specimens will probably not be available for a typical laser damage test, the probit method will not be discussed further. The up-and-down method and the nonparametric method for conducting the laser damage tests will be presented in the following.

#### 4. The Up-And-Down Method of Sensitivity Testing

##### 4.1 General Approach

The up-and-down method of testing is a sequential procedure in which the power level of the  $i+1$  test depends on the result of the  $i$ th test. If damage does not occur, the next specimen is tested at a higher level. If damage does occur, the next specimen is tested at a lower level. The effect of this sequential procedure is to provide more observations around the center of the population which allows inferences concerning the mean to be made with fewer samples. This efficiency is achieved at the cost of testing samples sequentially with a change in power between each pair of samples. A graphical display of the results of a series of up-and-down tests would appear as in figure 2.

The mean threshold is given by:

$$\bar{X} = X(\min) + \Delta X \left( \frac{A}{N} + \frac{1}{2} \right)$$

where  $A = \sum_{i=0}^k n_i$  and  $X(\min)$  is the lowest power level at which failures occur.  $n_i$  is the number of times failures occur at the  $i^{\text{th}}$  test level and  $N = \sum_{i=0}^k n_i$ . We have assumed slightly fewer failures

than survivors. The precision of the estimates of the mean and standard deviation is based on the minimum of the number of damaged or nondamaged specimens. Since the number of damaged specimens will be approximately equal to the number of nondamaged specimens, the effective sample size  $N$ , will be approximately half the number of specimens tested.

The standard error of the mean is given by the formula:

$$S_{\bar{X}} = G \sqrt{\frac{S}{N}}$$

where  $S$  is the standard deviation of the population, and  $G$  is a factor which depends on the ratio of the increment of power ( $\Delta x$ ) to  $S$  and on the difference between the true mean and the nearest  $X_i$ . For values of  $\Delta x/S \leq 2.5$ ,  $G$  is independent of the location of the true mean and is approximated by the equation

$$G = 0.85 + 0.15 \frac{\Delta x}{S}.$$

When  $\Delta x/S > 2.5$ , the location of the true mean with respect to the test intervals becomes important and the maximum and minimum  $G$  values are available as a function of  $\Delta x/S$ .

In order to determine the number of specimens required in the experiment, the objective must be stated in terms specifically related to the sampling variation of the experiment. Assume first that the objective is to estimate the median of the damage threshold distribution and that the one-sided 100 P percent confidence limit on the median will be less than 100 q percent of the estimate. Without loss of generality, assume that the upper confidence limit is being considered. The upper confidence limit on the mean of the  $\bar{X}$  distribution is given by

$$\text{U. C. L.} = \bar{X} + \frac{t_p^{\text{GS}}}{\sqrt{N}}$$

where  $t_p$  is the  $p^{\text{th}}$  percentile of the Student's t distribution. (In the calculations which follow, t values were selected for a t-distribution with 10 d. f. and a log distribution of power levels is used.) The width of the confidence interval in power units is given by  $\bar{X}$  and the upper confidence limit and, thus, the desired precision statement is

$$\frac{t_p^{\text{GS}}}{\sqrt{N}} < \log(1 + q).$$

Therefore, if

$$N \geq \left[ \frac{t_p^{\text{GS}}}{\log(1 + q)} \right]^2,$$

the desired precision will be achieved.

The sample size formula requires an estimate of the standard deviation of the power thresholds. Prior to testing and in the absence of experience for specific materials, this standard deviation is unknown. Three values which span a wide range of possibilities were assumed in the calculations. They were arrived at by assuming the range of damaging power that will be realized in the experiment span 1, 0.5, and 0.25 orders of magnitude. Assuming that the range is equal to 4 standard deviations results in log-transformed values of  $S = 0.25, 0.125, \text{ and } 0.0625$ .

Figure 3 presents N (one-half required number of specimens) as a function of q to compare sample size requirements for different levels of P at the fixed values of S. Similarly, figure 4 presents N versus q to compare values of standard deviations at a fixed level of P. Figure 3 shows that large sample sizes will be required if the width of the confidence interval is to be 10 percent or less than the estimate of the median. If the practical limit is 24 specimens and damage thresholds that have a one-half order of magnitude range ( $S = 0.125$ ), then an 80 percent confidence limit would be 13 percent of the estimate of the median and a 95 percent confidence limit would be 22 percent of the estimate of the median. The other two values of the standard deviation give less precision.

Figure 4 indicates that a smaller sample size is required for the same precision at the middle of the three standard deviation values. This result occurs due to the G factor which is a function of sample size and the spacing of the power level settings. The optimum is reached when  $S = a$ , but S is generally not known in advance so it is generally not possible to design the test to minimize sample size requirements due to this factor.

For constant values of S, figure 5 presents P as a function of q for  $N = 3, 4, 6, \text{ and } 12$ . This figure indicates that for 80 percent confidence and  $S = 0.125$ , precision for  $N = 6$  is 12 percent of the estimate while for  $N = 12$  the precision is 8.5 percent. Comparisons of this nature should be made for any prospective sample sizes to insure that the gain in precision is worth the gain in added tests.

#### 4.2 Testing Hypothesis

If the objective of the experiment is to compare the damage thresholds of two materials, sample size evaluations can be conveniently made in terms of the probability of finding a significant difference as a function of the true difference between the population means. This probability is a function of the level of significance of the test, the standard deviation of the mean, and the sample size. In particular, if  $\bar{X}_1$  and  $\bar{X}_2$  are the means of the population to be compared then the hypothesis to be tested is,

$$H_0: \mu_1 = \mu_2 \text{ vs } H_1: \mu_1 > \mu_2.$$

$H_0$  is rejected if  $Z > Z_\alpha$ , where

$$Z = \frac{\bar{X}_1 - \bar{X}_2}{S_{\bar{X}_1 - \bar{X}_2}} \quad \text{and} \quad S_{\bar{X}_1 - \bar{X}_2} = \frac{\sqrt{Z} SG}{\sqrt{n}}$$

and  $Z_\alpha$  is the  $(1-\alpha)$ th percentile from a standard normal distribution. It is assumed in the following computations that the standard deviations of the two material populations are equal and that equal sample size will be tested from both populations. The normal distribution is being used in place of Student's  $t$  to facilitate calculations, but this approximation will have little effect on the comparisons to be made.

The probability of accepting  $H_0$  as a function of  $D = \mu_1 - \mu_2$  is given by

$$P \{ Z \leq Z_\alpha \mid D \} = P \left\{ Z \leq \frac{Z_\alpha S_{\bar{X}_1 - \bar{X}_2} - D}{S_{\bar{X}_1 - \bar{X}_2}} \right\}$$

Figure 6 displays the probability of accepting  $H_0$  as a function of  $D$  for a 90 percent level of confidence test ( $\alpha = 0.10$ ), for the three assumed values of standard deviation and for  $N = 3, 4, 6$ , and  $12$ .

Let  $\beta$  denote the probability of accepting  $H_0$  when  $H_1$  is true. When  $\alpha$  and  $\beta$  are fixed, then sample size requirements to achieve a specified degree of discrimination can be determined. In particular, if

$$N \geq \frac{2(Z_\beta - Z_\alpha)^2 G^2 S^2}{D^2}$$

then the probability of accepting  $\mu_1 = \mu_2$  is  $1-\alpha$  if  $\mu_1 - \mu_2 \leq 0$ , and the probability of rejecting  $\mu_1 = \mu_2$  is  $1-\beta$  if  $\mu_1 - \mu_2 > D$ . Figure 7 presents a plot of sample size versus  $D = \mu_1 - \mu_2$  for  $\alpha = \beta = 0.1$  and the three assumed values of  $S$ .

## 5. Nonparametric 3-of-4 Approach

The problem of estimating the damage threshold of a material can also be formulated in a manner that does not require an assumption regarding the underlying distribution of damage levels of the specimens. If the population damage threshold is defined as the average of the two test irradiation levels which fall on either side of the median, then the problem is to establish these two levels with sufficient confidence. Specimens are tested at a power level and an inference would be made about the probability of damage ( $p$ ) in any single test specimen. When the analysis has indicated that the median ( $p = 1/2$ ) of the distribution has been bracketed by two of the power levels, the experiment is stopped. This approach was stimulated by a comment by Loomis [5] that 3 of 4 failures indicated a power level above threshold.

There are two methods of analyzing the results of the experiment; in the traditional approach which is the probit method, the results of experiments are used to place a lower (or upper) confidence limit on the probability of damage at that level. For example, if  $n$  specimens are tested at a level and  $k$  of the specimens are damaged, then the lower confidence limit on the probability of any one specimen being damaged is the solution for  $p$ , of the equation

$$\sum_{y=k}^n \binom{n}{y} p_1^y (1 - p_1)^{n-y} = \alpha$$

where a 100  $(1-\alpha)$  percent confidence level is sought. Values of  $p$ , are tabled in standard texts [2].



Assuming that, at most, 6 specimens could be tested at any one level, a lower 90 percent confidence limit is desired, a summary of inference for  $n \leq 6$  is as follows:

- a) For  $n \leq 3$ , regardless of result cannot be 90 percent confident that  $p > 1/2$ .
- b) For  $n = 4$ , if all four are damaged, lower 90 percent confidence limit is  $p_1 = 0.56$  and hence 90 percent confident that  $p > 1/2$ . If only 3 of the 4 are damaged,  $p_1 = 0.32$ .
- c) For  $n = 5$  and 6, all specimens must be damaged for 90 percent lower confidence limit to be greater than 0.5. In particular, if  $n = k = 5$ ,  $p_1 = 0.63$  and if  $n = k = 6$ ,  $p_1 = 0.68$ . Again, if only one specimen is not damaged, there is not 90 percent confidence that  $p$  is greater than  $1/2$ .

The above summary indicates that if this analysis method is adopted, then four specimens at each power level would be the most efficient design. Note, however, that if all specimens out of 5 or 6 are damaged, then there is 95 percent confidence (rather than 90) that  $p \geq 1/2$ . Even if this higher confidence level is desired, 5 rather than 6 specimens would be tested at each level.

The second method of analyzing the data from this experimental approach is the Bayesian approach. In this approach a distribution of possible values of the probability of damage at the particular power level is assumed and the results of the test are used to re-evaluate the distribution. In particular, the probability of obtaining the result is

$$f(k, n-k) = \int_0^1 p^k (1-p)^{n-k} g(p) dp.$$

Now assume that  $g(p)$  has a beta distribution.

$$g(p) = \frac{(a+b-1)!}{(a-1)!(b-1)!} p^{a-1} (1-p)^{b-1}$$

This family of distributions covers a wide range of shapes and, in particular, contains the uniform distribution ( $a=1$ ,  $b=1$ ) which will be assumed shortly.

Given  $f(k, n-k)$  and  $g(p)$ , the distribution of  $p$  given the result  $k$  and  $n-k$  from the experimental tests, the modified distribution of  $p$  is

$$g(p|k, n-k) = \frac{(n+a+b-1)!}{(k+a-1)!(n-k+b-1)!} p^{k+a-1} (1-p)^{n-k+b-1}$$

Now before tests are begun at a particular level, very little is known about the likelihood of the values of  $p$ . Thus, it will be assumed that prior to the experiment, any value of  $p$  between 0 and 1 is equally likely; i. e.,  $p$  has a uniform distribution. Under this assumption

$$g(p|k, n-k) = \frac{(n+1)!}{k!(n-k)!} p^k (1-p)^{n-k}.$$

Given the distribution of  $p$  as interpreted in the light of the experimental data, the question of the possibility of  $p$  being greater than 0.5 is easily answered.

$$P[p \geq 1/2] = \int_{1/2}^1 g(p|k, n-k) dp.$$

This probability is the measure of assurance that the power level setting is greater than the median of the threshold distribution.

Consider the following examples. Assume 4 specimens are tested at a level and three of them are damaged;  $n = 4$ ,  $k = 3$ . Then

$$g(p | 3, 1) = \frac{5!}{3!1!} p^3 (1-p) = 20(p^3 - p^4)$$

and

$$P(p \geq 0.5) = \int_{0.5}^1 20(p^3 - p^4) dp = 0.8125.$$

Thus, there is 81 percent confidence that  $p \geq 1/2$ .

If all four specimens are damaged, then

$$g(p | 4, 0) = \frac{5!}{4!0!} p^4 (1-p)^0 = 5 p^4$$

and

$$P(p > 0.5) = \int_0^1 5 p^4 dp = 0.96875.$$

Thus, if all four are damaged, the confidence that  $p \geq 1/2$  is definitely increased.

The results of the two methods of analysis are in close agreement. The Bayesian analysis provides a sharper insight. For example, in the classical analysis with lower 90 percent confidence limits being calculated there was no advantage in testing 5 or 6 specimens rather than 4 if the objective was to determine if  $p \geq 1/2$ . In the Bayesian analysis, however, the confidence level is not pre-set and the probability of  $p$  being greater than  $1/2$  is calculated after the experiment is conducted. Thus, the results are given different interpretations. To design the experiment for a Bayesian analysis, note that only two samples must be tested at any level below threshold for which no failures occur. Additional samples must be tested only if needed to verify that 3 of 4 fail--if 3 of 3 fail, the test is over unless one seeks the higher confidence.

In comparing two populations of materials, there is no method of evaluating sample sizes with respect to the ability to discriminate between median threshold values.

## 6. Summary

The up-and-down method of sensitivity testing can be used to obtain laser damage threshold data when the required changes in power between tests presents no great difficulty. Information on the confidence limits, sample size, test level spacing, and the ability to discriminate between different damage thresholds is presented. The curves are useful in making the appropriate trade-offs during the planning of a damage experiment. An analysis of the 3-of-4 method showed the most economical method for estimating the median of the damage threshold at an acceptable level of confidence.

## 7. References

- [1] Bass, M. and Fradin, D. W., IEEE J. Quantum Electronics, QE9 (1973) 890.
- [2] Dixon, W. J. and Massey, F. J., Introduction to Statistical Analysis, McGraw-Hill, New York, 1957.
- [3] Bliss, C. I., Ann. Appl. Bio., 22, (1935) 134 and Finney, D. J., Probit Analysis, Cambridge Univ. Press, Cambridge 1947.
- [4] Dixon, W. J. and Mood, A. M., J. Am. Statistical Assn., 43 (1948) 109.
- [5] Huguley, C. A. and Loomis, J. S., Laser Induced Damage in Optical Materials:1975, NBS Special Pub. 435, p189.

8. Figures

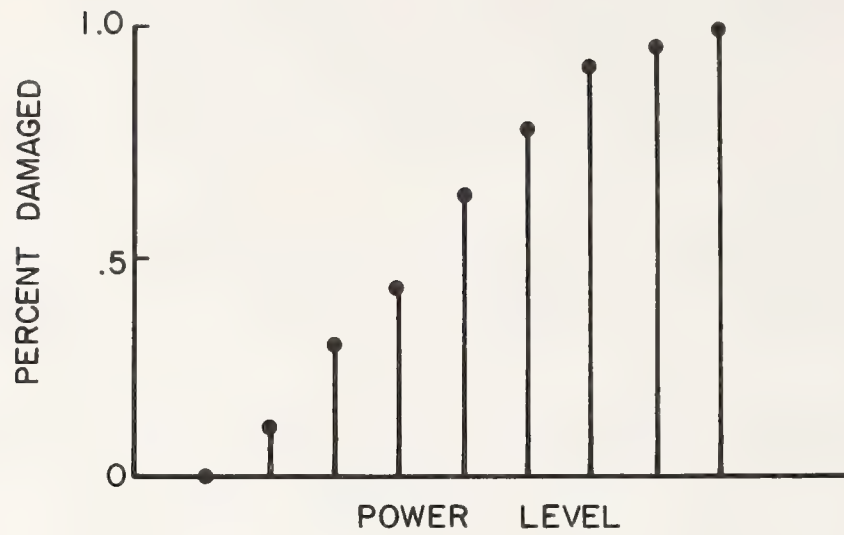


Figure 1. Example Result of Large Sample Sensitivity Experiment.

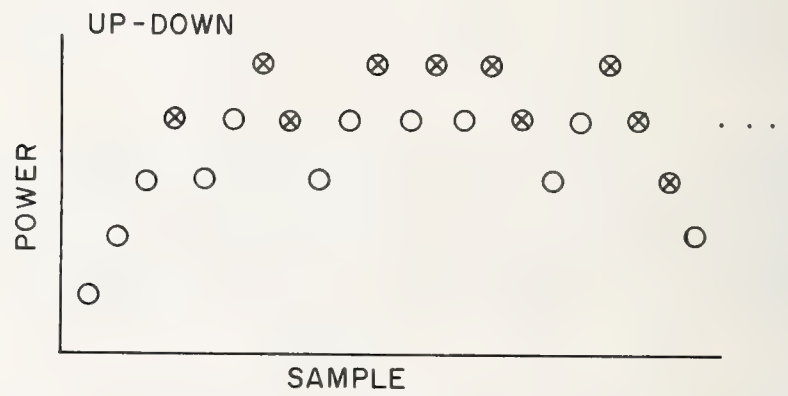


Figure 2. Example Result of Up-and-Down Testing.



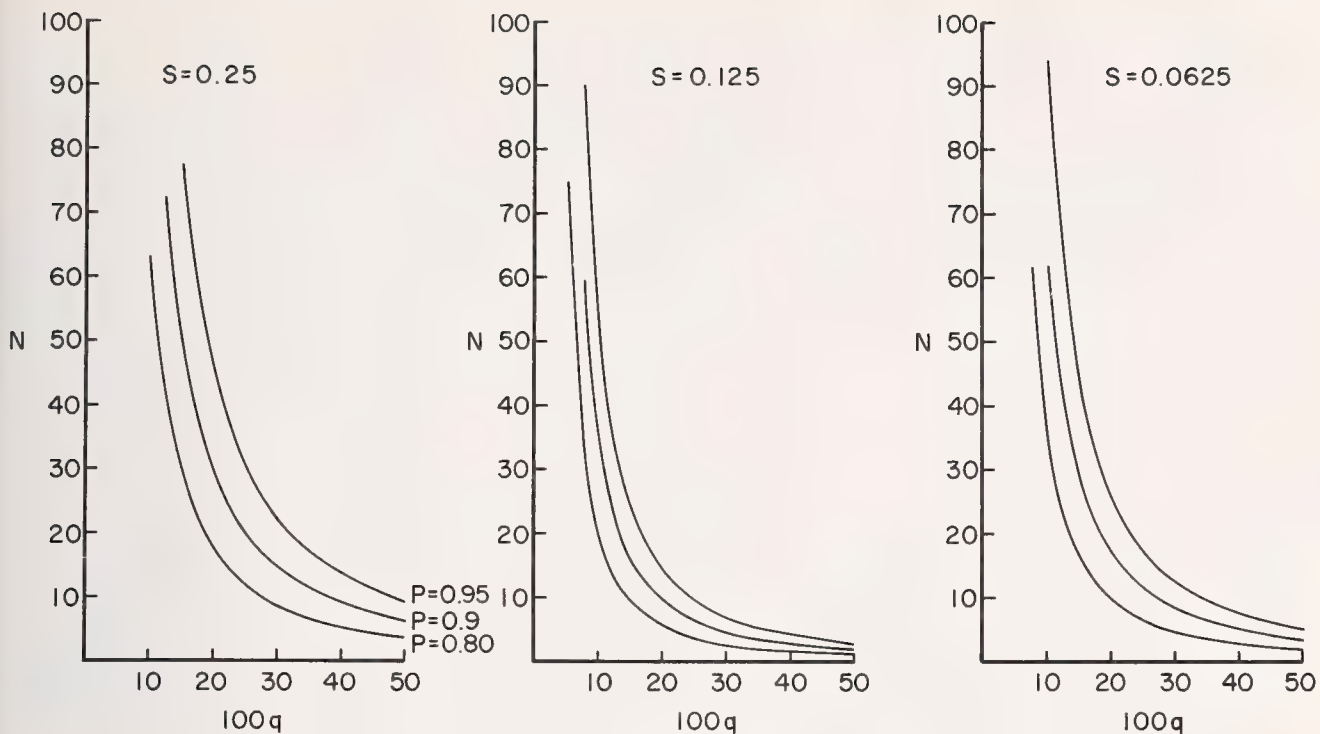


Figure 3. Comparison of Sample Size for Three Confidence Levels.

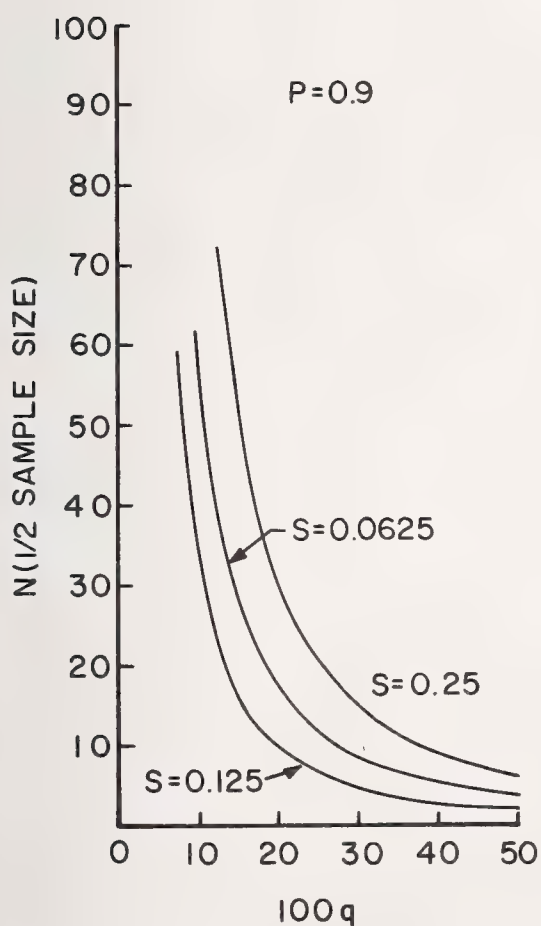


Figure 4. Comparison of Sample Sizes  
for Three Standard Deviations.

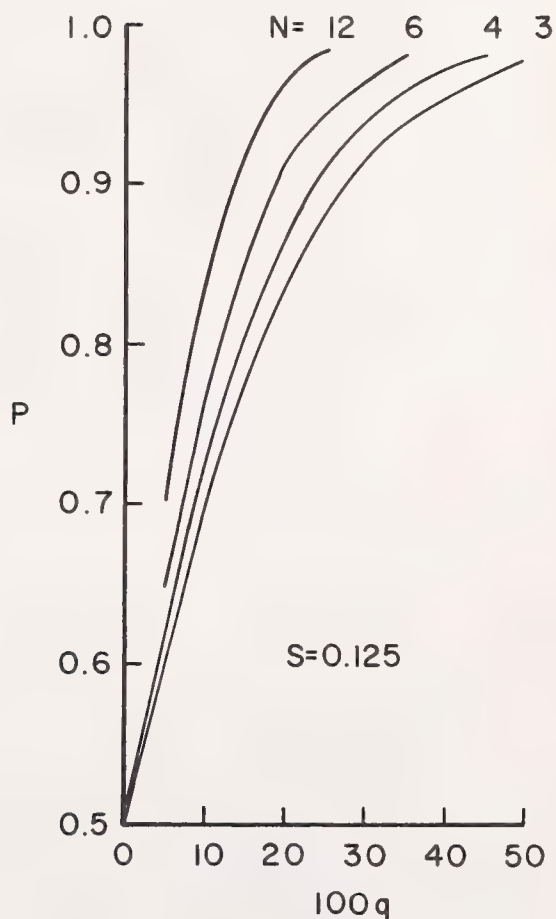


Figure 5. Comparison of Confidence Levels  
for Four Sample Sizes.

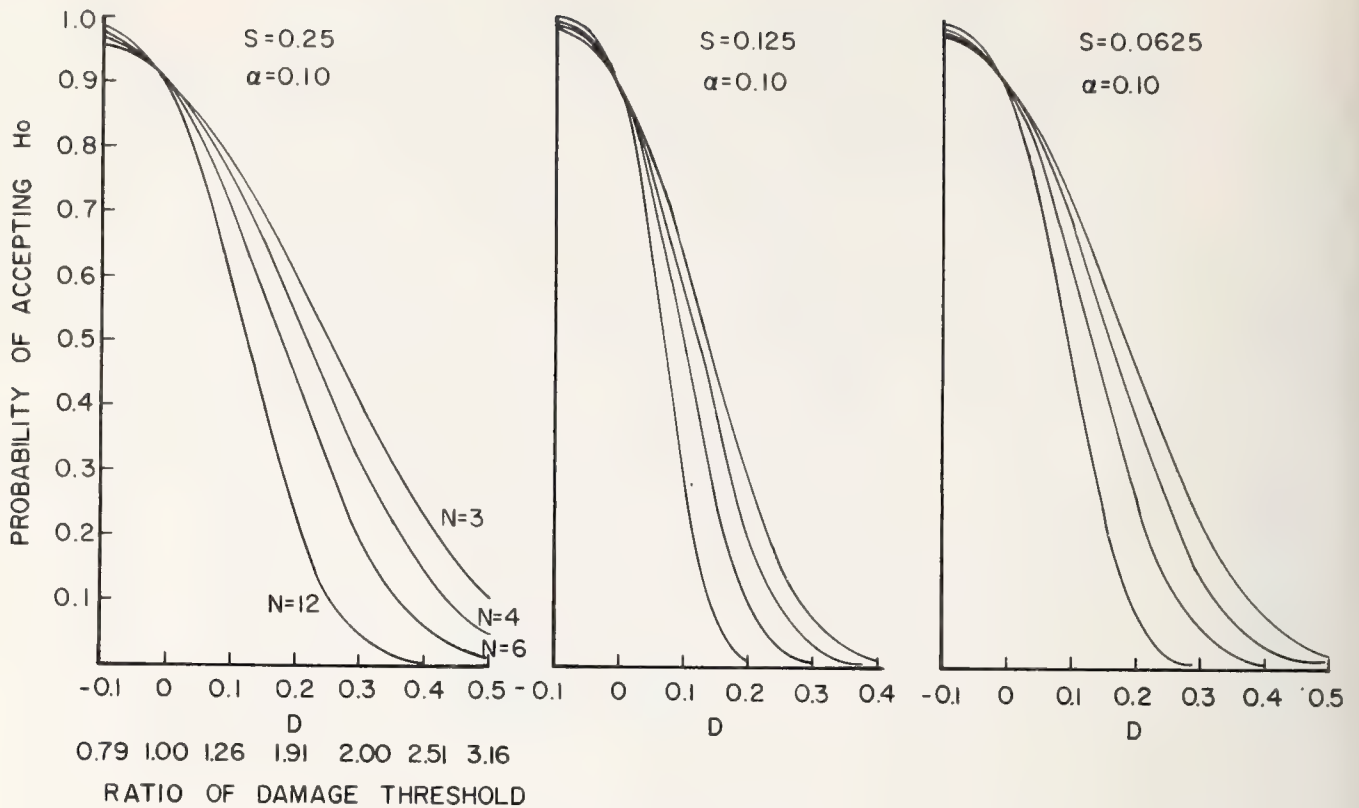


Figure 6. Probability of Accepting  $\mu_1 = \mu_2$  as Function of  $\mu_1 = \mu_2$  for  $\alpha = 0.10$  and  $N = 3, 4, 6$ , and  $12$ . Also shown on the abscissa scale is the ratio of damage thresholds that corresponds to the respective values of  $D$ . As an example, if it is assumed that  $S = 0.125$  (center graph) and 24 specimens are tested ( $N = 12$ ), if  $\bar{X}_1 - \bar{X}_2 > 0.14$ , then the probability of rejecting  $\bar{X}_1 = \bar{X}_2$  is greater than 0.90. That is, if the ratio of the damage thresholds is greater than 1.38 ( $=10^{0.14}$ ), there will be greater than a 90 percent chance of concluding that  $\mu_1$  is greater than  $\mu_2$ . On the other hand, if 6 specimens are tested ( $N = 3$ ), the ratio would have to be greater than 1.92 ( $=10^{0.282}$ ) to be 90 percent sure of rejecting equality.

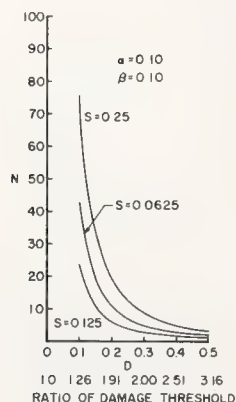


Figure 7. Sample Size Required to Yield  $\alpha$  and  $\beta$  as a Function of  $\mu_1 - \mu_2$ .

#### COMMENTS ON PAPER BY DETRIO AND BERENS

The speaker emphasized that this method is a statistical method and can be applied to any type of damage measurement. That is, it can be applied to single shot damage or to damage experiments where a particular site is irradiated many times. In the latter case, due to cumulative effects, damage may not occur on the first shot but may occur on subsequent shots. The method advanced in this paper is a means whereby the threshold for damage (however damage is defined) can be determined. He further pointed out that if a distribution of damage values over a large number of samples is obtained, then one can assign a probability of failure at any given power level of incident radiation. This is the characterization which is needed, in order to ensure safe operation over a large number of shots.



J. O. Porteus, J. L. Jernigan, and W. N. Faith  
 Physics Division, Michelson Laboratories  
 Naval Weapons Center, China Lake, California 93555

The methodology of multithreshold analysis, a new approach to laser-damage research, is described. The comparison of thresholds for various damage-related effects identifies dominant failure mechanisms and provides better guidance for laser-materials technology. After a brief description of apparatus, the procedure for routinely measuring up to eight different thresholds per sample is given. The maximum-likelihood principle is used to derive an algorithm for computing thresholds and standard deviations. The use of a standard gold sample to verify reproducibility and to maintain long-term calibration is discussed. Examples of multithreshold results on uncoated and coated infrared optical components are presented. The following are some of the effects for which thresholds are compared: slip, roughening, cracking, pits, melting, craters, delamination of coatings, ion and light emission, and work function change.

Key words: Damage thresholds; failure modes; laser-optical components; Mo mirrors; optical coatings; pitting; ripples; standard sample Au mirrors; surface characterization; surface uniformity; threshold estimation; windows.

## 1. Introduction

The damage resistance of optics for lasers may be improved with an understanding of important damage mechanisms and their relationship to material characteristics. The comparison of thresholds for the various observable damage-related effects provides a good basis for this understanding. Some of the effects typical of a bare metal mirror may be seen in figure 1. Slip bands and intergranular slip indicate susceptibility to stress damage, which can be related to yield strength, as shown in a companion paper [1]<sup>1</sup>. Melting, which produces the dark area in the dark-field micrograph, is an indicator of optical absorption. Laser-induced pitting, which occurs mainly on grain boundaries in figure 1, can be caused by segregated impurities. Cratering, identified by a raised rim around the melt zone, is usually caused by pressure associated with vaporization. Other effects measured by other techniques may also be informative. A change in surface work function, for example, can signal changes in surface composition or topography. Ion and light emission indicates plasma formation.

The present work presents the methodology of obtaining thresholds routinely and accurately for as many as eight different laser-induced surface effects. After a brief description of the apparatus, details of which are given elsewhere [2], the procedure for acquiring and reducing the data is discussed. The derivation of an algorithm based on the maximum-likelihood principle, which is used to compute thresholds and standard deviations, is also given. We then discuss the use of a standard gold sample to verify reproducibility and to maintain calibration. Finally, we present typical results and their interpretation on various infrared optical components.

## 2. Apparatus

Measurements are made in a previously described laser damage facility [2], where comprehensive target monitoring and careful beam characterization are key features. Our ultrahigh vacuum (UHV) test chamber was equipped with the following monitoring apparatus for the results presented here: (1) 20-power microscope; (2) Faraday cup with grounded entrance grid (10-mA/sr detection sensitivity at 35° off the laser beam axis) for sensing of target-emitted ions and neutrals having sufficient energy to produce secondary electrons; (3) an Auger analyzer with electron imager [2]. The electron images are generated by work function variations  $\approx 0.1$  eV over the target surface caused by variations in surface composition and topography.

Figure 2 illustrates the Gaussian spatial intensity distribution of the 10.6  $\mu\text{m}$  laser beam when focussed on the target by a ZnSe lens having a focal length of 24 cm. Temporally, each pulse consists of a train of mode-locked spikes which form an envelope of 100 nsec nominal duration. Thresholds given are peak thresholds, i.e., they refer to the time-integrated fluence of the damaging pulse at the point of maximum spatial intensity.

---

\* Work supported by the Naval Air Systems Command, the Office of Naval Research and NWC Independent Research Funds.

1. Figures in brackets indicate the literature references at the end of this paper.

The data reduction equipment consists of a Hewlett-Packard Model 9821 calculator interfaced with a Tektronix Model 4662 interactive digital plotter. Data reduction is performed entirely in the calculator, while the plotter is used only for display of final results.

### 3. Experimental Procedure

The sample is exposed to one pulse at each of approximately 50 sites spaced at 1-mm intervals along its surface. Pulse energies, which are measured for each pulse [2], are uniformly distributed over a range which includes the thresholds for each of the damage effects of interest. The occurrence of light emission (flash) and pit formation are noted by an observer as they occur, while damage features which are more difficult to identify, e.g., slip, melting and cratering, are categorized with the aid of more sophisticated optical microscopy after the sample has been removed from the test chamber (fig. 1). The damage observed at each site is summarized by a set of code numbers, each number representing a specific effect. The data is reduced by entering the damage summary and corresponding peak energy fluence for each site into the calculator and applying the algorithm derived below.

#### 3.1 Threshold Algorithm

The routine determination of up to eight thresholds per sample tested requires an algorithm permitting rapid data reduction. On the other hand, effective use of available data is important, since the fluence range of thresholds is often wide, and therefore incompatible with a high density of data points. In this section we develop an algorithm which yields reproducible results with a minimum of computational complexity.

Consider the probability  $P_i$  of obtaining a certain type of damage  $X_i$  times out of  $N_i$  shots on fresh sites (1-on-1 damage) [3,4], all at the same fluence  $\phi_i$ . This is represented by the binomial distribution

$$P_i(X_i; N_i; p_i) = \binom{N_i}{X_i} p_i^{X_i} (1 - p_i)^{N_i - X_i} \quad , \quad (1)$$

where

$$p_i = p_i(\phi_i, \phi, \sigma) \quad , \quad (2)$$

the probability of single-shot damage is a function of the damage threshold  $\phi$  and its standard deviation  $\sigma$ , in addition to the fluence  $\phi_i$ . The problem is to obtain statistical estimators for  $\phi$  and  $\sigma$  in terms of the damage data  $X_i$ ,  $N_i$  and  $\phi_i$ . Our solution is based on the method of maximum-likelihood [5]. Maximizing the logarithm of the likelihood with respect to the parameters  $\epsilon = \phi$  or  $\sigma$ , leads to two expressions of the form

$$\sum \frac{\partial p_i}{\partial \epsilon} \left[ \frac{X_i - N_i p_i}{p_i (1 - p_i)} \right] = 0 \quad . \quad (3)$$

Solving simultaneously for  $\phi$  and  $\sigma$  yields the corresponding maximum likelihood estimators  $\hat{\phi}$  and  $\hat{\sigma}$ . However, the functional form of  $p_i$  is required. For computational simplicity we assume that  $p_i$  is uniformly distributed, i.e.,

$$p_i = \begin{cases} 0 & ; \quad u_i \leq -\frac{1}{2} \\ u_i + \frac{1}{2} & ; \quad |u_i| < \frac{1}{2} \\ 1 & ; \quad u_i \geq \frac{1}{2} \end{cases} \quad , \quad (4)$$

where

$$u_i \equiv \frac{\phi_i - \phi}{2\sqrt{3} \sigma} \quad . \quad (5)$$

Substituting eq. (4) in eq. (3), one finds that only those terms  $j$  for which  $|u_j| < 1/2$  are non-zero. To further simplify the computation we neglect  $u_i^2$  terms in the denominators, which are of the form  $1/4 - u_i^2$ . As a result, our estimators differ from the true maximum-likelihood estimators in that data points near  $u_i = 1/2$  are less heavily weighted relative to those near  $u_i = 0$ . This compensates to some degree for the fact that the distribution given by eq. (4) generally represents the sample distribution less accurately near  $u_i = 1/2$ . Introducing eq. (5) and solving for  $\phi$  yields

$$\hat{\phi} \approx \frac{[\sum \phi_j^2 N_j][\sum (X_j - \frac{1}{2}N_j)] - [\sum \phi_j N_j][\sum \phi_j (X_j - \frac{1}{2}N_j)]}{[\sum \phi_j N_j][\sum (X_j - \frac{1}{2}N_j)] - [\sum N_j][\sum \phi_j (X_j - \frac{1}{2}N_j)]} \quad (6)$$

Solving for  $\sigma$  gives

$$\hat{\sigma} \approx \frac{1}{2\sqrt{3}} \frac{\sum \phi_j N_j - \hat{\phi} \sum N_j}{\sum (X_j - \frac{1}{2}N_j)} ; \quad \sum (X_j - \frac{1}{2}N_j) \neq 0 \quad (7a)$$

but gives the indeterminate form 0/0 when  $\sum (X_j - \frac{1}{2}N_j) = 0$ . Noting that eq. (6) defines the sample mean of  $\phi_j$  under the latter condition, we infer that

$$\hat{\sigma} \approx \sqrt{\frac{\sum \phi_j^2 N_j}{\sum N_j} - \left( \frac{\sum \phi_j N_j}{\sum N_j} \right)^2} ; \quad \sum (X_j - \frac{1}{2}N_j) = 0 \quad (7b)$$

It follows from the definition of  $j$  that eqs. (6) and (7) apply only to data within the interval

$$\left| \frac{\phi_j - \phi}{2\sqrt{3} \sigma} \right| < \frac{1}{2} \quad (8)$$

While the estimators  $\hat{\phi}$  and  $\hat{\sigma}$  are expressed entirely in terms of the damage data, the data interval given by eq. (8) involves the unknowns  $\phi$  and  $\sigma$ , and must be determined by trial and error. A satisfactory method for this has been developed, and is included in the routine data reduction procedure described below.

### 3.2 Data Reduction

Equations (6) through (8) are applied to each damage effect in turn via the calculator as follows. Fluences associated with the code number corresponding to a particular effect are sorted into a damaging, and the remaining fluences into a nondamaging category. Damaging fluences are then arranged and listed in order of ascending value, while the nondamaging fluences are listed in descending order. Data near the head of each list is examined for consistency by the operator and reclassified or discarded as required. Equations (6) and (7) are then applied to the revised lists. The  $j$  summations are initially taken over all data in the smallest interval which (a) includes the lowest damaging and highest nondamaging fluence, and (b) includes a damaging and nondamaging fluence as upper and lower limits, respectively. The interval is then extended as required to provide the minimum value of  $\hat{\sigma}$ , determined by applying eq. (7) to each new interval. This minimum  $\hat{\sigma}$  and the  $\hat{\phi}$  obtained by applying eq. (6) to the same interval are taken as the final results for the effect in question. In practice, it is found that  $\hat{\phi}$  is rather insensitive to the data interval. However,  $\hat{\sigma}$  depends more strongly on the number of data points used and their separation. Given adequate data the major contribution to  $\hat{\sigma}$  usually comes from the variation of the damage threshold across the sample surface, with a relatively small contribution coming from the experimental uncertainty.

Repeated application of the algorithm gives an average threshold, together with its standard deviation, for each effect. The resulting thresholds for the target are presented in the form of a bar graph or damage profile, examples of which are presented below.

### 3.3 Reproducibility and Long-Term Calibration

The reproducibility of the threshold results can be demonstrated by repeated application to a sample with uniform damage characteristics over its surface, as indicated by relatively small standard deviations of the damage thresholds. A mirror produced by electrodeposition of Au on diamond-turned bulk Cu has this desirable property. The oxidation resistance is an added advantage, which makes this sample especially attractive as a standard for calibration maintenance. The ability to directly standardize damage thresholds is an invaluable asset in the long-term development of damage-resistant optical components.

Figure 3 presents the results of two independent multithreshold measurements on the standard gold sample. Figure 3(a) was obtained before, and figure 3(b) after replacing the output coupler on the laser over one month later. After correction for a 10% change in focal spot diameter, the thresholds for all effects listed except one agree within the combined standard deviations given. Statistically, approximately half the thresholds should agree this well when the effects are independent. It is clear that changing the output coupler had negligible effect on the calibration. Furthermore, we may conclude that the threshold algorithm gives consistent and reproducible results, the accuracy of which is conservatively represented by the standard deviations.



### 3.4 Examples

Multithreshold analysis has been applied to a variety of infrared mirror and window surfaces prepared by various techniques. Both coated and uncoated samples have been studied. The present section gives a few representative examples of results obtained.

The application of multithreshold analysis to relate damage mechanisms to surface characteristics of bare metal mirrors, particularly Cu, has been amply demonstrated [1]. Certain aspects of the Au mirror represented in figure 3 were also discussed. To complete this discussion it should be pointed out that the relatively high slip threshold indicated in figure 3 may be influenced by the difficulty in observing slip on this sample [1]. In fact, the lowest threshold is for work-function change, which is attributed to evolution of water by the Au layer. This result is supported by a laser-induced diminution of oxygen as observed by Auger.

The value of multithreshold analysis in evaluating nominally equivalent mirror finishes is illustrated in figure 4, where we compare damage profiles of Mo mirrors polished by two different vendors. While mirror A exhibits higher thresholds for most types of damage, including melting, it is far more susceptible to pitting and associated plasma formation. The superior uniformity of mirror B is also evident in the smaller standard deviations.

As an example of multithreshold results from a window material we compare profiles for damage occurring on the entrance (front) and exit (back) surfaces of a polished NaCl blank (fig. 5). Only those sites where no simultaneous damage was observed on the front surface are represented in figure 5(b). All thresholds on the front are essentially the same, indicating breakdown as the only damage mechanism. Thresholds at the back surface are generally lower because of the constructive phase relationship between incident and reflected fields. Effects peculiar to the back surface are ripples, pits and fracture. Ripples result from the interference of incident and scattered radiation [6]. Present evidence shows that ripples occur only in the presence of a plasma. The pits may represent scattering sources for the ripples. The fact that pits occur only on the back surface suggest that they result from bulk, rather than from surface inhomogeneities. Scrubbing associated with the plasma, which was observed in mirrors [1], has also been observed on this sample.

A damage profile from an enhanced-reflection coating on polished bulk Cu is shown in figure 6. The thresholds are well below those for bare Cu. Pitting due to coating defects is the dominant failure mode. Almost identical damage profiles were obtained when the same coating design was applied to Mo and to ULE glass.

Figure 7 compares damage thresholds from  $\text{As}_2\text{S}_3$  in bulk form, and as a coating [7] on the NaCl. In the bulk material the coincidence of thresholds for surface pitting and bulk damage suggest that these result from the same mechanism which, surprisingly, is active below the threshold for pitting in the coating. Also, pitting in the coating tends to associate with a plasma, which is not true in the bulk material.

### 4. Summary

An efficient and reliable method has been developed for simultaneously measuring the thresholds and standard deviations for up to eight laser-damage-related effects on a single sample. An algorithm based on the maximum-likelihood principle has been derived for computing results directly from the experimental data. Reproducibility has been demonstrated by repeated measurements on a standard Au sample. The use of this sample to maintain long-term calibration was described. Examples of multithreshold results on representative optical components of each type have been given and the principal weaknesses of these components identified. The comparative analysis of such results from well characterized samples prepared from different materials and by different techniques yields the relationship between damage thresholds and material characteristics. These comparisons can also provide a better understanding of laser-damage mechanisms.

### 5. Acknowledgments

The authors are indebted to S. D. Sorenson for programming the plot routine for the damage profiles.

### 6. References

- [1] Porteus, J. O., Fountain, C. W., Jernigan, J. L., Faith, W. N. and Bennett, H. E., this conference.
- [2] Porteus, J. O., Soileau, M. J. and Bennett, H. E., in *Laser Induced Damage in Optical Materials: 1975*, A. J. Glass and A. H. Guenther, eds. (NBS Spec. Publ. 435), p. 207.
- [3] Bass, M. and Leung, K. M., IEEE J. Quantum Electron. QE-12, 32 (1976).
- [4] For n-on-1 damage the situation is obviously equivalent if nondamaging pulses leave an equivalent damage probability at each site.
- [5] Mood, A. M., *Introduction to the Theory of Statistics* (McGraw-Hill, New York, 1950), Ch. 8.

[6] Temple, P. A. and Soileau, M. J., in *Laser Induced Damage in Optical Materials: 1976*, A. J. Glass and A. H. Guenther, eds. (NBS Spec. Publ. 462), p. 371.

[7] Donovan, T. M., Baer, A. D., Dancy, J. H. and Porteus, J. O., this conference.

## 7. Figures

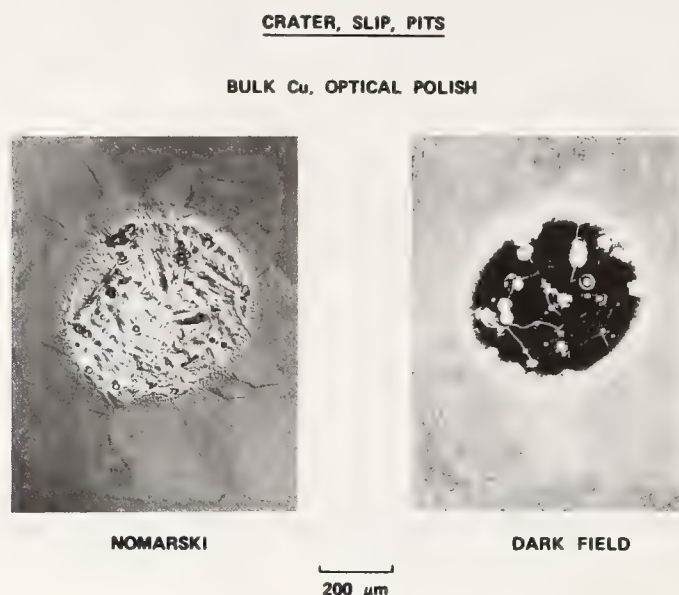


Figure 1. Micrographs of visible damage on polished bulk Cu at a peak fluence of  $68.3 \text{ J/cm}^2$ . In Nomarski slip bands appear outside the crater at the 5 o'clock position, while intergranular slip is responsible for prominent crack-like features.

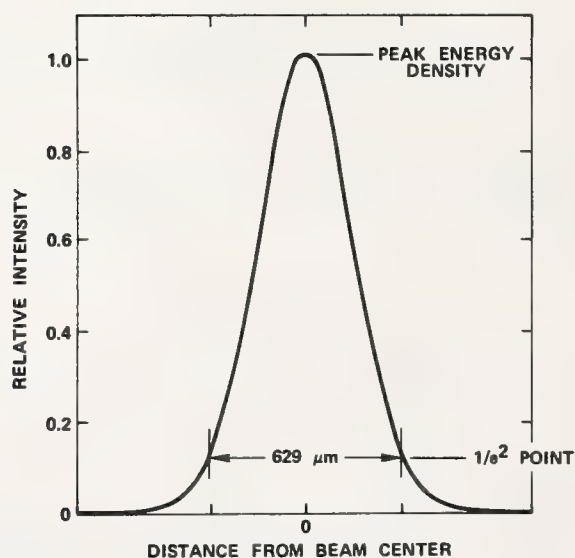


Figure 2. Gaussian spatial profile of focussed laser pulse, showing  $1/e^2$  width and peak energy density (fluence) at which thresholds are determined.

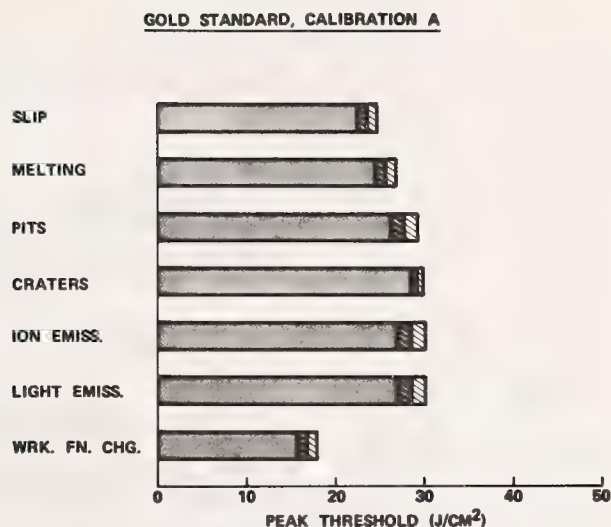


Figure 3(a). Damage profile of standard gold sample, measured for calibration with the original laser output coupler. Thresholds are indicated by the shaded bars. Standard deviations (+ or -) are indicated by the semishaded boxes at the ends of the bars.

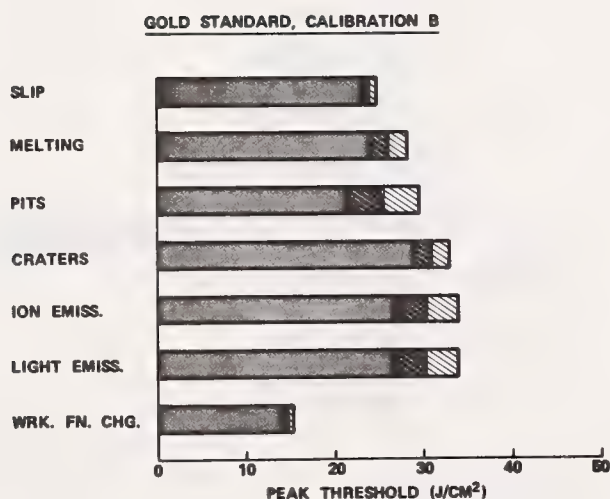


Figure 3(b). Damage profile to be compared with figure 3(a), measured for calibration with new laser output coupler.



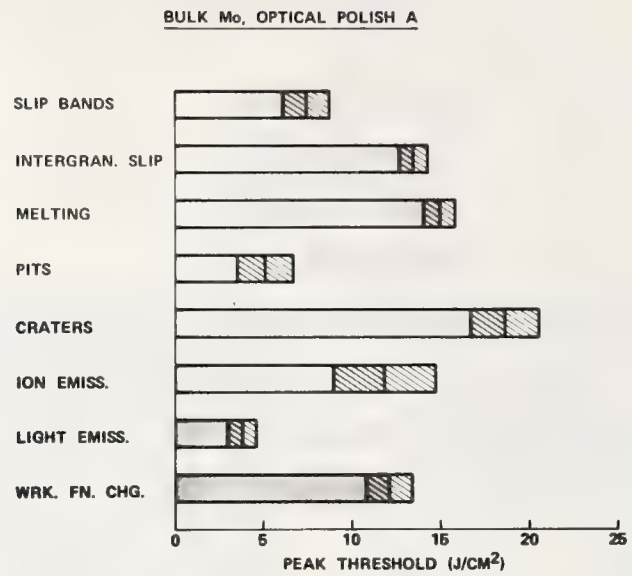


Figure 4(a). Damage profile of polished bulk Mo from vendor A.

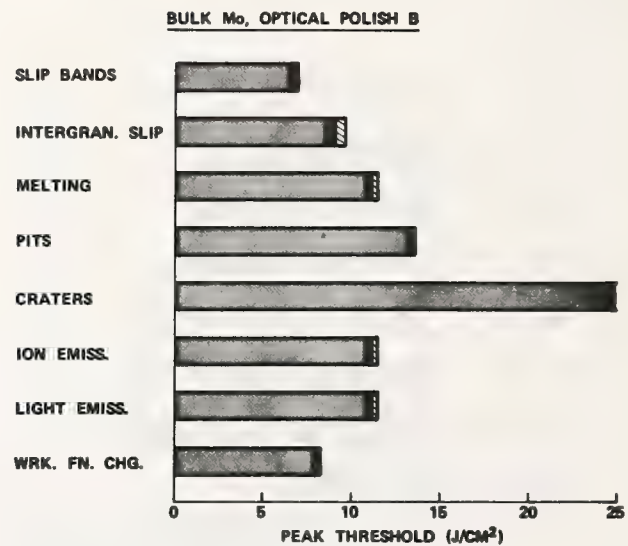


Figure 4(b). Damage profile of polished bulk Mo from vendor B.

SINGLE-CRYSTAL NaCl, HARSHAW, FRONT SURFACE

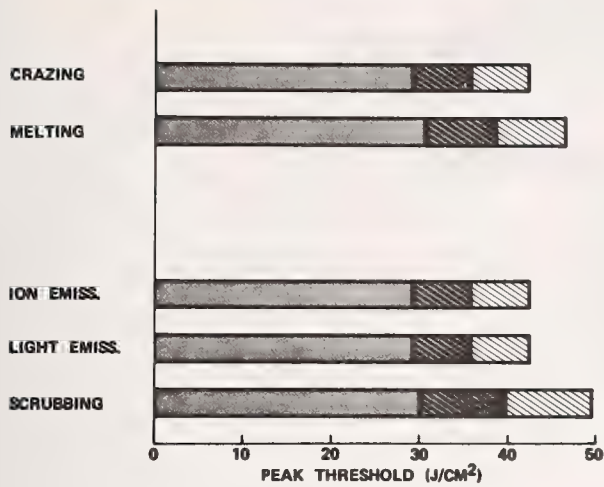


Figure 5(a). Front surface damage profile of a NaCl blank, 6.4-mm thick, polished on both surfaces.

SINGLE-CRYSTAL NaCl, HARSHAW, BACK SURFACE ONLY

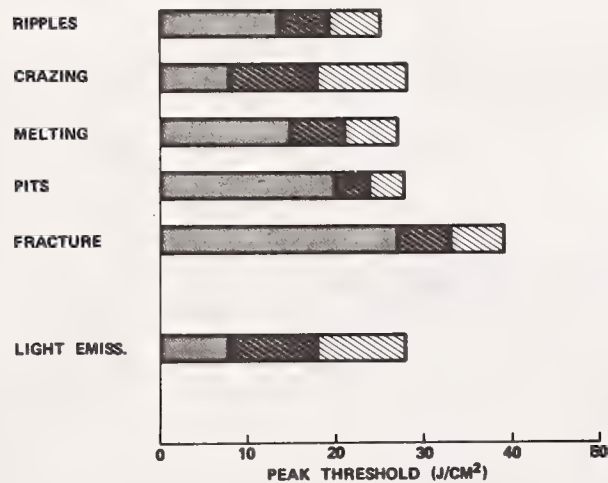


Figure 5(b). Profile of damage occurring only on the back surface of the same blank. The laser beam was focussed on the front surface.

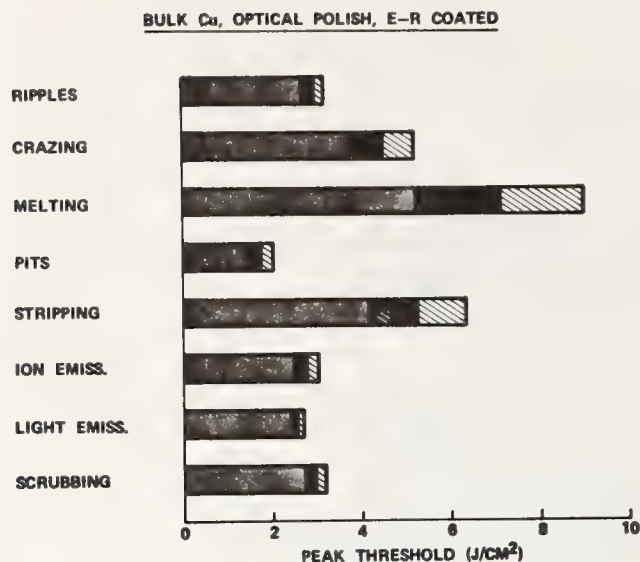


Figure 6. Damage profile of a 10.6  $\mu\text{m}$  enhanced reflection coating on bulk Cu. Coating consists of alternating layers of Ge and ZnS on a thin Ag layer.

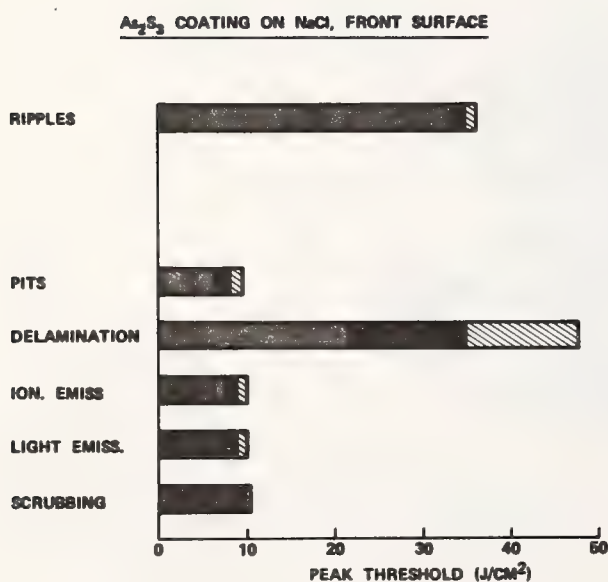


Figure 7(a). Damage profile of an As<sub>2</sub>S<sub>3</sub> coating on the front surface of NaCl.

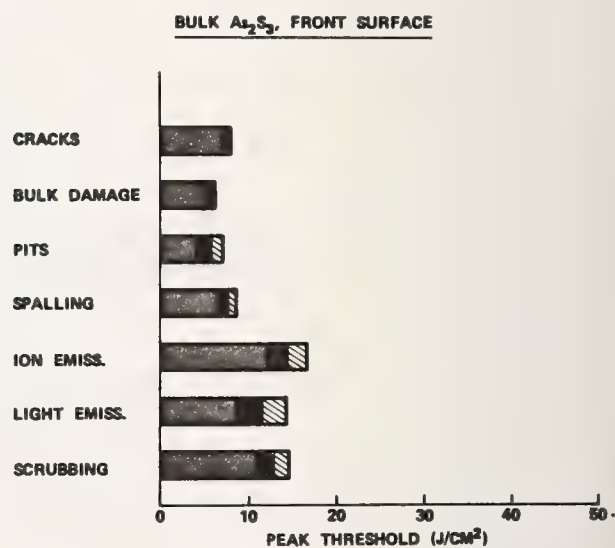


Figure 7(b). Damage profile of polished bulk As<sub>2</sub>S<sub>3</sub>.



COMMENTS ON PAPER BY PORTEUS, JERNIGAN, AND FAITH

*No discussion on this paper.*

APPENDIX I  
PARTICIPANTS

Joseph A. Abate  
Laboratory For Laser Energetics  
University of Rochester  
River Station  
Rochester, N. Y. 14627

George J. Balaschak  
Pratt & Whitney Group  
Bee Line Highway  
West Palm Beach, FL 33410

Thomas H. Allen  
Optical Coating Labs.  
P. O. Box 1599  
Santa Rosa, CA 95401

Norman Barnes  
Los Alamos Scientific Labs.  
M/S 564, P. O. Box 1663  
Los Alamos, NM 87545

C. M. Allred  
Division 276.00  
National Bureau of Standards  
Boulder, CO 80302

D. N. T. Beauchamp  
Optical Coating Laboratory Inc.  
2789 Giffen Ave.  
Santa Rosa, CA 95401

Robert J. Andrews  
University of Dayton Res. Inst.  
AFWL/LRE (UDRI)  
Kirtland AFB, NM 87117

Harold E. Bennett  
Michelson Laboratory, Code 38101  
Naval Weapons Center  
China Lake, CA 93555

Joseph H. Apfel  
Optical Coating Laboratory, Inc.  
P. O. Box 1599  
Santa Rosa, CA 95403

Jean M. Bennett  
Michelson Laboratory, Code 3818  
Naval Weapons Center  
China Lake, CA 93555

L. J. Aplet  
Hughes Aircraft Co.  
Centinela & Teale Sts.  
Culver City, CA 90230

Russell B. Bennett  
Battelle-Columbus Labs.  
Materials Technology Dept.  
505 King Ave.  
Columbus, OH 43201

Adrian Donald Baer  
Naval Weapons Center  
Code 3818, Research Dept.  
China Lake, CA 93555

Enrique Bernal G.  
Honeywell Corporation  
Material Sciences Center  
10701 Lyndale Ave. So.  
Bloomington, MN 55420

John F. Blais Jr.  
Spectrum Systems Division of Valtec  
211 Second Avenue  
Waltham, MA 02154

W. T. Boord  
Honeywell Systems & Research Center  
MN 17-2340  
2600 Ridgway Parkway  
Minneapolis, MN 55413

David Burdick  
Naval Weapons Center  
Code 3813  
China Lake, CA 93555

E. C. Borsare,  
W. J. Schafer Assoc.  
10 Lakeside Office Park  
Wakefield, MA 02090

Charles A. Burke  
Spectrum System Div. Valtec Corp.  
211 Second Ave.  
Waltham, MA 02154

Capt. Dan L. Boulet  
Air Force Materials Lab.  
USAF, AFML/LPO  
Wright-Patterson AFB, OH 45433

Pat Burke  
University of Dayton Res. Inst.  
300 College Park  
Dayton, OH 45469

Gordon Boulton  
OCLI  
P. O. Box 1599  
Santa Rosa, CA 95401

Chalot Serge, S.C.  
Laboratoires de Marcoussis C.R. C.G.E.  
Route de Nozay  
Marcoussis, FRANCE

Morris Braunstein  
Hughes Research Labs.  
Dept 30-23  
3011 S. Malibu Canyon Road  
Malibu, CA 90265

George E. Chamberlain  
Division 276.04  
National Bureau of Standards  
Boulder, Colorado 80302

R. E. Brocklehurst  
AF Materials Lab.  
AFML/LP  
Dayton, OH 45433

John W. Childress  
Northrup/N.T.C.  
MS 300-62  
3401 W. Broadway  
Hawthorne, CA 90250

David C. Brown  
Laboratory for Laser Energetics  
University of Rochester  
River Road  
Rochester, NY 14627

Terence M. Christmas  
OCLI Optical Coatings LTD.  
Hillend Fife Scotland  
Dunfermline SCOTLAND

Aaron Budgor  
Lawrence Livermore Labs.  
P. O. Box 808-L488  
Livermore, CA 94550

Patsy Collins  
University of Dayton Res. Inst.  
300 College Park  
Dayton, OH 45469

Verne R. Costich  
Design Optics  
155 Moffett Park Drive  
Sunnyvale, CA 94086



Tony Damommio  
Physics Dept.  
University of Dallas  
Braniff Rm. 42, Northgate Blvd.  
IRving, TX 75060

David Eimerl  
Lawrence Livermore Lab.  
P. O. Box 808  
Livermore, CA 94550

Donald Decker  
Naval Weapons Center  
Code 3818  
China Lake, CA 93555

Edward A. Enemark  
Optical Coating Laboratory, Inc.  
2789 Giffen Ave.  
Santa Rosa, CA 95401

Louise Decker  
Lockheed Research Labs.  
Dept. 52-54, Bldg. 202  
3251 Hanover St.  
Palo Alto, CA 94304

Richard R. Esposito  
International Laser Sys.  
Optical Coating Lab. Inc.  
Box 9316  
Albuquerque, NM 87119

John A. Detrio  
University of Dayton Res. Inst.  
KL 541  
300 College Park  
Dayton, OH 45469

Albert Feldman  
A259, Materials Bldg.  
National Bureau of Standards  
Washington, D. C. 20234

Marilyn J. Dodge  
Division 232.03  
A251, Physics Bldg.  
National Bureau of Standards  
Washington, D. C. 20234

Nics Fernelius  
University of Dayton Res. Inst.  
300 College Park  
Dayton, OH 45469

T. M. Donovan  
Naval Weapons Center  
Code 3818  
China Lake, CA 93555

John Fielman  
University of Dayton Res. Inst.  
300 College Park  
Dayton, OH 45469

C. J. Duthler  
Xonics, Inc.  
6849 Hayrenhurst Ave.  
Van Nuys, CA 91406

Dennis Fischer  
Coherent, Inc., Optics Dept.  
374 Fay  
Mountainview, CA 94043

David F. Edwards  
Los Alamos Scientific Lab.  
MS-564  
Los Alamos, NM 87545

Douglas B. Flint  
ITEK Corp. - Optical System Div.  
Dept. 535  
10 Maguire Rd.  
Lexington, MA 02173

Alan M. Frank  
University of California  
Lawrence Livermore Labs  
Optics Group  
P.O. Box 808  
Livermore, CA 94550

W. G. D. Frederick  
AF Materials Laboratory  
AFML/LPO  
Wright-Patterson AFB, OH 45433

Charles Greninger  
Rocketdyne  
521/M S BA 30  
6633 Canoga Ave.  
Canoga Park, CA 91301

W. J. Fredericks  
Oregon State University  
Chemistry Dept.  
Corvallis, OR 97331

Arthur H. Guenther  
Air Force Weapons Lab.  
CA  
Kirtland AFB, NM 87117

Francois Garaude  
CEA - CEL \_\_\_\_\_ Center France  
BP 2f 94190 Villeneuve  
St georges, FRANCE

Harold S. Gurev  
Opt. Sci. Ctr.  
University of Arizona  
Tucson, AZ 85721

R. E. Gaylord  
E-O Program Office  
U.S. Naval Material Command  
MAT 08TE  
Washington, DC 20028

Douglas Hamilton  
University of So. California  
Dept. of Physics  
University Park  
Los Angeles, CA 90007

Dennis H. Gill  
Los Alamos Scientific Lab.  
Los Alamos, NM 87545

Norman F. Harmon  
The Mitre Corporation  
P. O. Box 208  
Bedford, MA 091740

Alexander J. Glass  
Univ. of California  
Lawrence Livermore Lab.  
P. O. Box 808  
Livermore, CA 94905

Nora-Jean Harned  
AVCO Everett Research Lab.  
2385 Revere Beach Parkway  
Everett, MA 02149

Ann Glassman  
University of Dayton Res. Inst.  
Applied Physics Dept.  
300 College Park  
Dayton, OH 45468

Robert D. Harned  
AVCO Everett Research Lab.  
2385 Revere Beach Parkway  
Everett, MA 02149

Helen Gourley  
ILC Technology Corp.  
164 Commercial St.  
Sunnyvale, CA 94070

Robert J. Harrach  
Lawrence Livermore Lab.  
T-Division  
P. O. Box 808, Mail Code L-71  
Livermore, CA 94550

George A. Graves  
University of Dayton  
1930 Knoll Dr.  
Bellbrook, OH 45305

James A. Harrington  
Hughes Research Lab.  
Malibu, CA 91361

James Harris  
University of Dayton Res. Inst.  
300 College Park  
Dayton, OH 45469

Samuel J. Holmes  
Northrop Corp.  
3401 W. Broadway  
Hawthorne, CA 90250

Marvin Hass  
Naval Research Lab.  
Code 6408  
Washington, DC 20375

Capt. Richard A. House II  
AFWL/LRE  
Kirtland AFB, NM 87117

Gerard Hasserjian  
Northrop Corp.  
3401 W. Broadway  
Hawthorne, CA 90274

Richard S. Hughes  
US. Naval Weapons Center  
Code 3815  
China Lake, CA 93555

Kenneth J. Hebert  
Design Optics Inc.  
155 Moffett Park Drive  
Sunnyvale, CA 94086

Florence M. Indorf  
Division 276.00  
National Bureau of Standards  
Boulder, Colorado 80302

Don Heiman  
University of So. California  
Dept. of Physics  
University Park  
Los Angeles, CA 90007

Stephen D. Jacobs  
Laboratory for Laser Energetics  
University of Rochester  
River Station  
Rochester, NY 14627

Robert B. Hemphill  
Vought Corp., Advanced Tech. Center  
Box 6144  
Dallas, TX 75222

Robert J. Jelley  
E-A Industrial Corp.  
4500 North Shallowford Rd., NE  
Atlanta, GA 30341

Gilbert O. Hendrickson  
Honeywell Inc, Ceramic Center  
1885 N. Douglas Drive  
Golden Valley, MA 55422

Carl J. Johnson  
II-VI Incorporated  
207 Garden Lane  
Glenshaw, PA 15116

Graeme L. Hennessey  
Valtec Corp.  
1244 Highland St.  
Holliston, MA 01746

George T. Johnston  
University of Dayton Res. Inst.  
AFWL/LRE  
Kirtland AFB, NM 87117

Richard A. Hoffman  
Westinghouse Electric Corp.  
R&D Center, Beulah Road  
Pittsburgh, PA 15235

R. E. Joiner  
University of So. California  
University Park, 620 PHE  
Los Angeles, CA 90007



Paul Kelly  
National Research Center  
Physics Division  
310 Smyth Road  
Ottawa, CANADA

Neil Larsen  
Division 276.04  
National Bureau of Standards  
Boulder, Colorado 80302

John C. Kershenstein  
Naval Research Lab.  
Code 4104  
4555 Overlook Ave. SW  
Washington, DC 20375

Hubert P. Lebodo  
Laboratoire National ou Enoies  
K015 Paris, France

Claude A. Klein  
Raytheon Research Division  
28 Leym Street  
Waltham, MA 02154

Karl G. Leinberger  
University of Dayton  
KL 163C  
300 College Park Ave.  
Dayton, OH 45469

Philipp H. Klein, Code 5222  
Naval Research Lab.  
Washington, D. C. 20375

Kang M. Leung  
Honeywell Inc.  
Corporate Material Sciences Center  
10701 Lyndale Ave. S.  
Bloomington, MN 55420

Abe Klugman  
Northrop Research & Tech. Center  
3401 W. Broadway  
Hawthorne, CA 90250

Capt. Steven R. Lindle,  
USAF/AFWL/LRE  
9801 Pitt PL. NE  
Albuquerque, NM 87111

Lawrence Kopell  
Wright-Patterson AFB  
AFMC/LTE  
Dayton, OH 45433

Herbert G. Lipson  
RADC(ESD)ESE  
Hanscom AFB  
Bedford, MA 01731

Paul Kraatz  
Northrop Research & Tech. Center(375/61)  
3401 W. Broadway  
Hawthorne, CA 90250

Jim R. Logsdon  
Electronics Metal Finishing Corp.  
P. O. Box 848  
Oak Ridge, TN 37830

Melvin R. Kruer  
Naval Research Lab.  
Code 5554, Opt. Sci. Div.  
Washington, DC 20022

Ron. W. MacPherson  
Defence Research Establishment Valcartier  
Electro-Optics Division  
P. O. Box 880  
Courcellette, Quebec, CANADA GOA IRO

G. Edward Kuhl  
USAF, Air Force Materials Lab.  
AFML/LPO  
Wright-Patterson AFB, OH 45433

Robert J. McBroom  
UDRI  
AFWL/LRE (UDRI)  
Kirtland AFB, NM 87117

Richard Macklin  
EM Laboratories Inc.  
500 Executive Blvd.  
Elmsford, NY 10523 10523

Thomas J. Moravec  
Honeywell Corporate Material  
Sciences Center  
10701 Lyndale Ave. South  
Bloomington, MN 55420

William M. Madden  
Pratt & Whitney Aircraft Group  
Gov. Prod. Div.-Dept 713  
Mail Stop E-25, P. O. Box 2691  
West Palm Beach, FL 33402

Dennis Morelli  
Optical Coating Lab. Inc.  
P. O. 1599  
Santa Rosa, CA 95403

Prof. Manenkov A. A.  
Lebedev Physics Institute  
Moscow, USSR

Mouchart Jacques  
Laboratoires de Marcoussis C.R. C.G.E.  
Route de Nozay  
Marcoussis, FRANCE

Sam D. Meyerson (21t)  
USAF/AFWL/IRE  
Kirtland, AFB  
Albuquerque, NM 87117

Donald L. Mullen  
University of Dayton Res. Inst.  
AFWL/LRE (UDRI)  
Kirtland AFB, NM 87117

David Milam  
Lawrence Livermore Labs  
y Div., P. O. Box 808  
Livermore, CA 94550

C. T. Myers  
Northrop Corp.  
Electro Mechanical Div.  
Dept. 6620  
500 E. Orangethorpe Ave.  
Anaheim, CA 92801

Perry A. Miles  
Raytheon Co.  
Opt. Systems  
Hartwell Road  
Bedford, MA 01730

Brian E. Newnam  
Los Alamos Scientific Laboratory  
MS 552, P. O. Box 1663  
Los Alamos, NM 87545

S. S. Mitra  
University of Rhode Island  
Dept. of Electrical Engineering  
Kingston, RI 02881

Davis B. Nichols  
Boeing Aerospace Co.  
MS 88-46, P. O. Box 3999  
Seattle, WA 98124

W. E. Moddeman  
University of Dayton  
300 College Park Drive  
Dayton, OH 45469

Novaro narc n°  
CEA Limeil Center  
BP 2f 94190 Villeneuve St georges  
FRANCE 96790

Michael J. Monsler  
Lawrence Livermore Lab.  
L-488, P. O. Box 88  
Livermore, CA 94550

Major David F. O'brien  
USAF, Air Force Materials  
Laboratory/LP  
Wright-Patterson AFB, OH 45433

Melvin C. Ohmer  
AFML/LPE  
Wright-Patterson AFB, OH 45433

Perry P. Pirooz  
Owens Illinois  
1700 N. Westwood  
Toledo, OH 43607

Jerry R. Oldenettel  
Maxwell Labs. Inc.  
9244 Balboa Ave.  
San Diego, CA 92123

B. C. Platt  
Optical Technology Section  
AFWL/LRE (UDRI)  
Kirtland AFB, NM 87117

Russell M. Ono  
TRW  
One Space Park, 41A/CTS  
Redondo Beach, CA 90278

James O. Porteus  
Naval Weapons Center  
Code 3817  
China Lake, CA 93555

Carlo G. Pantano  
University of Dayton Res. Inst.  
KL542  
300 College Park  
Dayton, OH 45469

Lt. Col. Ronald F. Prater  
AFWL/LRE  
Kirtland AFB, NM 87117

Roger A. Paquin  
The Perkin-Elmer Corp.  
MS 420, Main Ave.  
Norwalk, CT 06856

Diamantis Preonas  
University of Dayton Res. Inst.  
AFWL/LRE (UDRI)  
Kirtland AFB, NM 87117

Robert E. Parks  
Optical Sciences Center  
University of Arizona  
Tucson, AZ 85721

Victor Rehn  
Lawrence Berkeley Labs.  
Bldg. 70A, Room 1115  
Berkeley, CA 94720

Melvin E. Pedinoff  
Hughes Research Labs.  
30-23-00  
3011 Malibu Canyon Rd.  
Malibu, CA 90265

Harold C. Reynolds Jr.  
Pratt & Whitney Aircraft  
P. O. Box 2691  
West Palm Beach, FL 33410

Roger D. Petty  
University of Dayton Res. Inst.  
300 College Park Road  
Dayton, OH 45469

Stephen G. Reynolds  
University of Dayton Res. Inst.  
AFWL/LRE, Bldg. 401  
Kirtland AFB, NM 87111

Richard Pierce  
Spawr Optical Research  
1527 Pomona Road  
Corona, CA 91720

Mort Robinson  
Hughes Research Labs.  
Chem. Phys. Dept.  
Malibu, CA 90265



Roger E. Rondeau  
WPAFB, AFML/LPJ  
Wright Patterson AFB, OH 45433

Dave R. Segawa  
Hoya Optics, USA, Inc.  
2180 Sand Hill Road  
Menlo Park, CA 94025

Terry Rosshart  
TRW Space & Defense Systems  
Hel. Optics Dept.  
One Space Park 01/1271  
Redondo Beach, CA 90278

Glenn H. Sherman  
II-VI, Inc.  
207 Garden Lane  
Glenshaw, PA 15116

James M. Rowe  
Northrop Research & Tech. Center  
375-61  
3401 W. Broadway  
Hawthorne, CA 90250

Keith R. Shillito  
Battelle-Columbus Labs.  
Materials Application Section  
505 King Ave.  
Columbus, OH 43201

J. Earl Rudisill  
Hughes Research Labs.  
3011 Malibu Canyon Road  
Malibu, CA 92650

Frederick M. Shofner  
Union Carbide/K-25  
Box #P  
Oak Ridge, TN 37830

Aaron Sanders  
Division 276.04  
National Bureau of Standards  
Boulder, Colorado 80302

Philip A. Simpson  
Division 276.04  
National Bureau of Standards  
Boulder, Colorado 80302

Stephen R. Scheele  
Hughes Aircraft  
Culver City, CA 90230

James G. Sliney, Jr.  
University of So. California  
c/o Physics Dept. SSC 302  
University Park  
Los Angeles, CA 90007

Ansgar Schmid  
Washington State University  
Dept. of Physics  
Pullman, WA 99164

Durand M. Smith  
General Electric, RESD  
P. O. Box 8555, 20A10  
Philadelphia, PA 19460

T. E. Schmid MS B08  
Pratt & Whitney Aircraft  
Box 2691  
West Palm Beach, FL 33402

W. Lee Smith  
Lawrence Livermore Lab.  
Mail Code L479  
Box 808  
Livermore, CA 94550

R. I. Seddon  
Advanced Products Dev.  
Optical Coating Lab. Inc.  
2789 Giffen Ave.  
Santa Rosa, CA 95404

John B. Sonderman  
Lawrence Livermore Lab.  
P. O. Box 808  
Livermore, CA 94550

Marshall Sparks  
Xonics, Inc.  
1333 Ocean Ave.  
Santa Monica, CA 90401

P. A. Temple  
Naval Weapons Center  
Code 3818  
China Lake, CA 93555

J. L. Stanford  
Naval Weapons Center  
Code 3818  
China Lake, CA 93555

E. Theron  
CSIR  
Optical Sciences Div. NPRL  
P. O. Box 395  
Pretoria, Republic of SOUTH AFRICA

Major James L. Stapp  
Air Force Weapons Laboratory  
AFWL/LRE  
Albuquerque, NM 87117

Normal Thomas  
Optical Coating Lab, Inc.  
P. O. Box 1599  
Santa Rosa, CA 95403

Thomas G. Stoebe  
University of Washington  
326 Roberts, FB-10  
Seattle, WA 98195

James H. Tillotson  
Maxwell Labs.  
Research & Development  
9244 Balboa Ave.  
San Diego, CA 92064

Irving F. Stowers  
Lawrence Livermore Lab.  
L-474, P. O. Box 808  
Livermore, CA 94550

Michael J. Treadaway  
IRT Corp.  
P. O. Box 80817  
San Diego, CA 92138

Charles Strecker, AFML/LPO  
Air Force Materials Laboratory  
Wright-Patterson AFB, OH 45433

H. L. Wain  
Embassy of Australia  
1601 Massachusetts Ave,  
Washington, DC 20036

Eric W. Van Stryland  
Center for Laser Studies  
University of So. California  
Los Angeles, CA 90007

Thomas W. Walker  
USAF  
Wright-Patterson AFB, OH 45433

Paul M. Sutton  
Electro-Optics Dept., L270  
Ford Aerospace & Communications Corp.  
Ford Road, Newport Beach, CA 92660

David A. Walsh  
University of Dayton Res. Inst.  
300 College Park  
Dayton, OH 45469

Wayne A. Taggart  
Rocket Dyne  
6633 Canoga Ave.  
Canoga Park, CA 91304

Marvin J. Weber  
Lawrence Livermore Laboratory  
L-479, P. O. Box 808  
Livermore, CA 94550

R. A. West  
Hughes Aircraft  
Centinela & Teale Sts.  
Culver City, CA 90230

R. M. Wolff  
Western Sales  
Valtec Corp.  
Box 2311  
Newport Beach, CA 92663

Richard T. Williams  
Naval Research Lab.  
Code 6440  
Washington, DC 20375

Shew M. Wong  
Rockwell International  
Rocky Flats Div. B/779  
P. O. Box 464  
Golden, Colorado 80401

C. B. Willingham  
Raytheon Research Div.  
28 Seyon Street  
Waltham, MA 02154

Roger M. Wood  
G.E.C. LTD., Hirst Research Centre  
Eastland, Wembley  
Midd<sup>x</sup>, England

James M. Wimmer  
University of Dayton Res. Inst.  
300 College Park  
Dayton, OH 45469

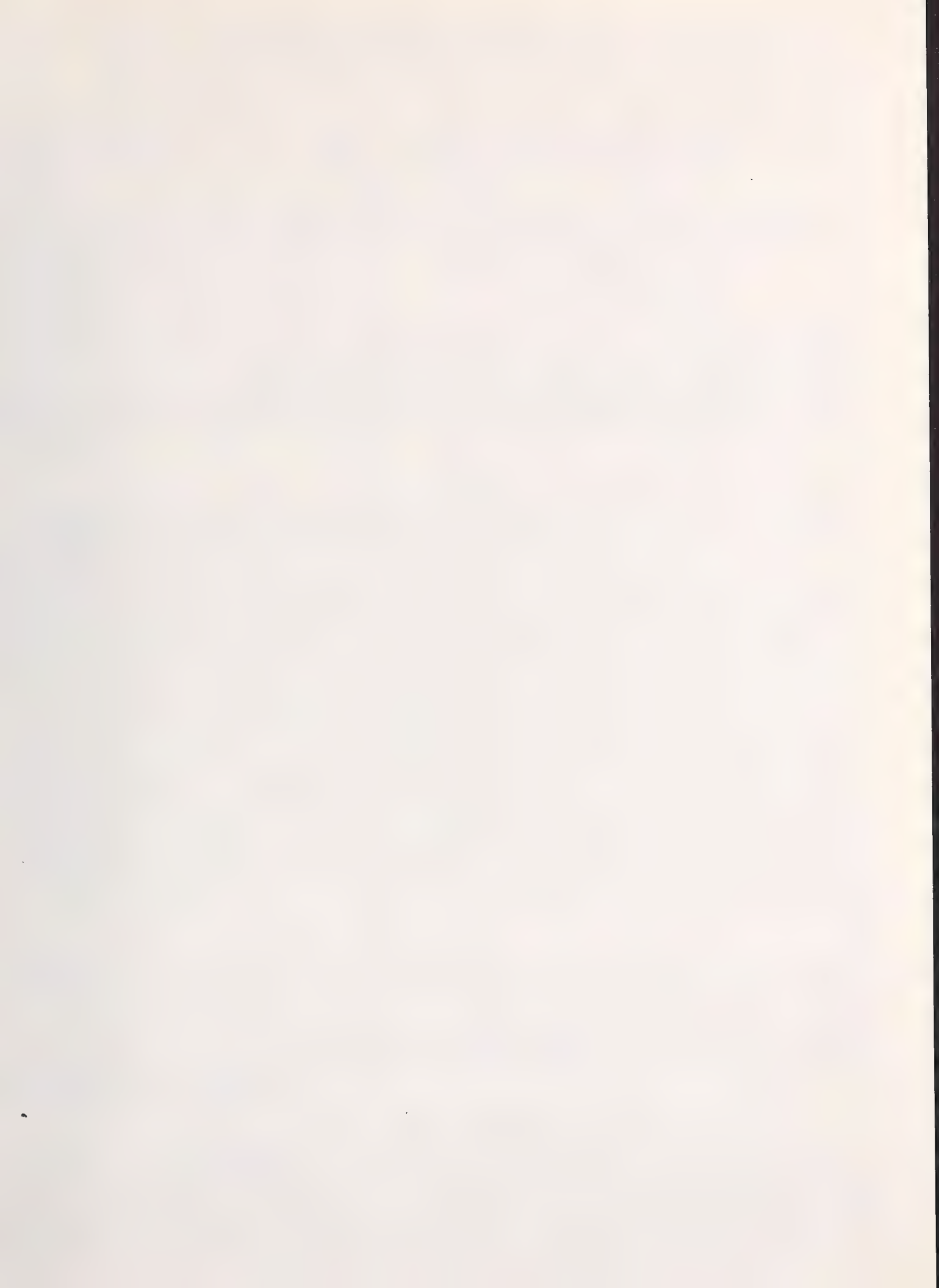
Robert W. Zimmerer  
Scientech, Inc.  
5649 Arapahoe Ave.  
Boulder, CO 80303

Capt. Harry V. Winsor  
DARPA/MSO  
1400 Wilson Blvd.  
Arlington, Washington 22209

David Zuccaro  
Hughes Research Labs.  
3011 Malibu Canyon Road  
Malibu, CA 90265

G. Richard Wirtenson  
University of California  
Lawrence Livermore Labs.  
Laser fusion?ME Dept. L-474  
P. O. Box 808  
Livermore, CA 94550





U.S. DEPT. OF COMM. <b>BIBLIOGRAPHIC DATA SHEET</b>		1. PUBLICATION OR REPORT NO. NBS SP-509	2. Gov't Accession No.	3. Recipient's Accession No.
4. TITLE AND SUBTITLE  Laser Induced Damage in Optical Materials: 1977			5. Publication Date December 1977	6. Performing Organization Code
7. AUTHOR(S) Edited by Alexander J. Glass and Arthur H. Guenther			8. Performing Organ. Report No.	
9. PERFORMING ORGANIZATION NAME AND ADDRESS  NATIONAL BUREAU OF STANDARDS DEPARTMENT OF COMMERCE WASHINGTON, D.C. 20234			10. Project/Task/Work Unit No. 2760581	11. Contract/Grant No.
12. Sponsoring Organization Name and Complete Address (Street, City, State, ZIP) Electromagnetics Div., National Bureau of Standards, Boulder, CO. American Society for Testing & Materials, Phila., PA. 19103 Dept. of the Navy, Office of Naval Research, Arlington, VA 22217 Energy Research & Development Admin., Washington, DC 20234 Defense Advanced Research Project Agency, Washington, DC 20234			13. Type of Report & Period Covered FINAL	14. Sponsoring Agency Code
15. SUPPLEMENTARY NOTES  Library of Congress Card Catalog Number: 78-600021				
16. ABSTRACT (A 200-word or less factual summary of most significant information. If document includes a significant bibliography or literature survey, mention it here.) The Ninth Annual Symposium on Optical Materials for High Power Lasers (Boulder Damage Symposium) was held at the National Bureau of Standards in Boulder, Colorado, from 4 to 6 October 1977. The Symposium was held under the auspices of ASTM Committee F-1, Subcommittee on Laser Standards, with the joint sponsorship of NBS, the Defense Advanced Research Project Agency, the Department of Energy (formerly ERDA), and the Office of Naval Research. About 185 scientists attended the Symposium, including representatives of the United Kingdom, France, Canada, Australia, Union of South Africa, and the Soviet Union. The Symposium was divided into sessions concerning Laser Windows and Materials, Mirrors and Surfaces, Thin Films, Laser Glass and Glass Lasers, and Fundamental Mechanisms. As in previous years, the emphasis of the papers presented at the Symposium was directed toward new frontiers and new developments. Particular emphasis was given to materials for use from 10.6 $\mu$ m to the UV region. Highlights included surface characterization, thin film-substrate boundaries, and advances in fundamental laser-matter threshold interactions and mechanisms. The scaling of damage thresholds with pulse duration, focal area, and wavelength were also discussed. Alexander J. Glass of Lawrence Livermore Laboratory and Arthur H. Guenther of the Air Force Weapon Laboratory were co-chairpersons of the Symposium. The Tenth Annual Symposium is scheduled for 12-14 September 1978 at the National Bureau of Standards, Boulder, Colorado.				
17. KEY WORDS (six to twelve entries; alphabetical order; capitalize only the first letter of the first key word unless a proper name; separated by semicolons)  Laser damage; laser interaction; optical components; optical fabrication; optical materials and properties; thin film coatings.				
18. AVAILABILITY  <input type="checkbox"/> Unlimited  <input type="checkbox"/> For Official Distribution. Do Not Release to NTIS  <input checked="" type="checkbox"/> Order From Sup. of Doc., U.S. Government Printing Office Washington, D.C. 20402, SD Cat. No. C13 10:509  <input type="checkbox"/> Order From National Technical Information Service (NTIS) Springfield, Virginia 22151		19. SECURITY CLASS (THIS REPORT)  UNCLASSIFIED	20. SECURITY CLASS (THIS PAGE)  UNCLASSIFIED	21. NO. OF PAGES  561
				22. Price \$6.75



# NBS TECHNICAL PUBLICATIONS

## PERIODICALS

**JOURNAL OF RESEARCH**—The Journal of Research of the National Bureau of Standards reports NBS research and development in those disciplines of the physical and engineering sciences in which the Bureau is active. These include physics, chemistry, engineering, mathematics, and computer sciences. Papers cover a broad range of subjects, with major emphasis on measurement methodology, and the basic technology underlying standardization. Also included from time to time are survey articles on topics closely related to the Bureau's technical and scientific programs. As a special service to subscribers each issue contains complete citations to all recent NBS publications in NBS and non-NBS media. Issued six times a year. Annual subscription: domestic \$17.00; foreign \$21.25. Single copy, \$3.00 domestic; \$3.75 foreign.

Note: The Journal was formerly published in two sections: Section A "Physics and Chemistry" and Section B "Mathematical Sciences."

### DIMENSIONS/NBS

This monthly magazine is published to inform scientists, engineers, businessmen, industry, teachers, students, and consumers of the latest advances in science and technology, with primary emphasis on the work at NBS. The magazine highlights and reviews such issues as energy research, fire protection, building technology, metric conversion, pollution abatement, health and safety, and consumer product performance. In addition, it reports the results of Bureau programs in measurement standards and techniques, properties of matter and materials, engineering standards and services, instrumentation, and automatic data processing.

Annual subscription: Domestic, \$12.50; Foreign \$15.65.

## NONPERIODICALS

**Monographs**—Major contributions to the technical literature on various subjects related to the Bureau's scientific and technical activities.

**Handbooks**—Recommended codes of engineering and industrial practice (including safety codes) developed in cooperation with interested industries, professional organizations, and regulatory bodies.

**Special Publications**—Include proceedings of conferences sponsored by NBS, NBS annual reports, and other special publications appropriate to this grouping such as wall charts, pocket cards, and bibliographies.

**Applied Mathematics Series**—Mathematical tables, manuals, and studies of special interest to physicists, engineers, chemists, biologists, mathematicians, computer programmers, and others engaged in scientific and technical work.

**National Standard Reference Data Series**—Provides quantitative data on the physical and chemical properties of materials, compiled from the world's literature and critically evaluated. Developed under a world-wide program coordinated by NBS. Program under authority of National Standard Data Act (Public Law 90-396).

NOTE: At present the principal publication outlet for these data is the Journal of Physical and Chemical Reference Data (JPCRD) published quarterly for NBS by the American Chemical Society (ACS) and the American Institute of Physics (AIP). Subscriptions, reprints, and supplements available from ACS, 1155 Sixteenth St. N.W., Wash., D.C. 20056.

**Building Science Series**—Disseminates technical information developed at the Bureau on building materials, components, systems, and whole structures. The series presents research results, test methods, and performance criteria related to the structural and environmental functions and the durability and safety characteristics of building elements and systems.

**Technical Notes**—Studies or reports which are complete in themselves but restrictive in their treatment of a subject. Analogous to monographs but not so comprehensive in scope or definitive in treatment of the subject area. Often serve as a vehicle for final reports of work performed at NBS under the sponsorship of other government agencies.

**Voluntary Product Standards**—Developed under procedures published by the Department of Commerce in Part 10, Title 15, of the Code of Federal Regulations. The purpose of the standards is to establish nationally recognized requirements for products, and to provide all concerned interests with a basis for common understanding of the characteristics of the products. NBS administers this program as a supplement to the activities of the private sector standardizing organizations.

**Consumer Information Series**—Practical information, based on NBS research and experience, covering areas of interest to the consumer. Easily understandable language and illustrations provide useful background knowledge for shopping in today's technological marketplace.

*Order above NBS publications from: Superintendent of Documents, Government Printing Office, Washington, D.C. 20402.*

*Order following NBS publications—NBSIR's and FIPS from the National Technical Information Services, Springfield, Va. 22161.*

**Federal Information Processing Standards Publications (FIPS PUB)**—Publications in this series collectively constitute the Federal Information Processing Standards Register. Register serves as the official source of information in the Federal Government regarding standards issued by NBS pursuant to the Federal Property and Administrative Services Act of 1949 as amended, Public Law 89-306 (79 Stat. 1127), and as implemented by Executive Order 11717 (38 FR 12315, dated May 11, 1973) and Part 6 of Title 15 CFR (Code of Federal Regulations).

**NBS Interagency Reports (NBSIR)**—A special series of interim or final reports on work performed by NBS for outside sponsors (both government and non-government). In general, initial distribution is handled by the sponsor; public distribution is by the National Technical Information Services (Springfield, Va. 22161) in paper copy or microfiche form.

## BIBLIOGRAPHIC SUBSCRIPTION SERVICES

The following current-awareness and literature-survey bibliographies are issued periodically by the Bureau:

**Cryogenic Data Center Current Awareness Service.** A literature survey issued biweekly. Annual subscription: Domestic, \$25.00; Foreign, \$30.00.

**Liquified Natural Gas.** A literature survey issued quarterly. Annual subscription: \$20.00.

**Superconducting Devices and Materials.** A literature survey issued quarterly. Annual subscription: \$30.00. Send subscription orders and remittances for the preceding bibliographic services to National Bureau of Standards, Cryogenic Data Center (275.02) Boulder, Colorado 80302.



**U.S. DEPARTMENT OF COMMERCE**  
**National Bureau of Standards**  
Washington, D.C. 20234

OFFICIAL BUSINESS

Penalty for Private Use, \$300

POSTAGE AND FEES PAID  
U.S. DEPARTMENT OF COMMERCE  
COM-215



SPECIAL FOURTH-CLASS RATE  
BOOK















